DTIC FILE COPY

AGARD-CP-437 Vol.I

AD-A211 893

AGARD CONFERENCE PROCEEDINGS No.437

Validation of Computational Fluid Dynamics

Volume 1 — Symposium Papers and Round Table Discussion

S MAR 2 3 1989 D
H



DISTRIBUTION AND AVAILABILITY ON BACK COVER

DISTRIBUTION STATEMENT A
Approved for public release;
Distribution Unlimited

89 3 22 150

AGARD-CP-437
Volume 1

NORTH ATLANTIC TREATY ORGANIZATION

ADVISORY GROUP FOR AEROSPACE RESEARCH AND DEVELOPMENT

(ORGANISATION DU TRAITE DE L'ATLANTIQUE NORD)

AGARD Conference Proceedings No.437

VALIDATION OF COMPUTATIONAL FLUID DYNAMICS

Volume 1: SYMPOSIUM PAPERS AND ROUND TABLE DISCUSSION

Volume 2 contains Poster Papers
presented at the Symposium

Papers presented and discussions held at the Symposium of the Fluid Dynamics Panel in Lisbon, Portugal, 2—5 May 1988.

THE MISSION OF AGARD

According to its Charter, the mission of AGARD is to bring together the leading personalities of the NATO nations in the fields of science and technology relating to aerospace for the following purposes:

- Recommending effective ways for the member nations to use their research and development capabilities for the common benefit of the NATO community;
- Providing scientific and technical advice and assistance to the Military Committee in the field of aerospace research and development (with particular regard to its military application);
- Continuously stimulating advances in the aerospace sciences relevant to strengthening the common defence posture;
- Improving the co-operation among member nations in aerospace research and development;
- Exchange of scientific and technical information;
- Providing assistance to member nations for the purpose of increasing their scientific and technical potential;
- Rendering scientific and technical assistance, as requested, to other NATO bodies and to member nations in connection with research and development problems in the aerospace field.

The highest authority within AGARD is the National Delegates Board consisting of officially appointed senior representatives from each member nation. The mission of AGARD is carried out through the Panels which are composed of experts appointed by the National Delegates, the Consultant and Exchange Programme and the Aerospace Applications Studies Programme. The results of AGARD work are reported to the member nations and the NATO Authorities through the AGARD series of publications of which this is one.

Participation in AGARD activities is by invitation only and is normally limited to citizens of the NATO nations.

The content of this publication has been reproduced
directly from material supplied by AGARD or the authors.

Published December 1988

Copyright © AGARD 1988
All Rights Reserved

ISBN 92-835-0489-5 Vol.1
ISBN 92-835-0490-9 Vol.2
ISBN 92-835-0491-7 Set of 2 Vols.

Printed by Specialised Printing Services Limited
40 Chigwell Lane, Loughton, Essex IG10 3TZ

PREFACE

The aerospace community has come to realize that Computational Fluid Dynamics offers great potential as an analysis and design tool for air vehicles as well as components. Great strides have been made in recent years in development of both computer hardware and solution algorithms as well as pioneering applications. Design applications are being made in today's developments. In general , CFD methods of today can simulate flows about complex geometries with simplified flow physics or flows about simple geometries with complex flow physics, however, they cannot simulate both in many cases. Significant progress still has to be made to help resolve these issues.

The ultimate goal of CFD development is a fully mature design and analysis capability that is user friendly, cost effective, numerically accurate and fully verified by detailed experimental or analytical comparisons. A critical step, as far as practical applications of CFD are concerned, is the thorough validation or calibration of the CFD tools. Through validation the design user of CFD can gain the high level of confidence that is needed to permit the capability to realize its full potential as a design tool.

AGARD's Fluid Dynamics Panel has sponsored a Symposium with the specific intent of examining activities, both computational and experimental, directed toward validating or calibrating CFD codes over a broad spectrum of fluid-dynamics study areas. The objectives of the Symposium were to identify the level of agreement of numerical solution algorithms and physical models with experimental and/or analytical data, to identify regions of validity for given flow solvers and to identify flow regions where significant gaps exist and further work is warranted.

Due to the intense interest in this subject, a large number of paper abstracts were submitted to the FDP "Call for Papers". The Programme Committee decided to accommodate this intense response by inviting authors to prepare "Poster Papers" for a special session. Poster Papers were mounted on large display stands and authors informally inter-acted with interested participants during a two hour period. This stimulating discussion period proved to be highly successful. Volume 2 contains the formal written versions of the Poster Papers. Volume 1 contains the Symposium papers and the concluding Round Table Discussion.

* * *

La communauté aérospatiale est en voie de se rendre compte des possibilités énormes offertes par le calcul en dynamique des fluides en tant qu'outil d'analyse et de conception. Des progrès considérables on été enregistrés au cours des dernières années dans le développement du matériel informatique et des algorithmes de résolution ainsi que des applications originales et des applications d'études sont en cours.

En règle générale, les nouvelles méthodes de CDF permettent soit de simuler des écoulements autour de géométries complexes selon des lois physique d'écoulement simplifiées, soit de simuler des écoulements autour de géométries simplifiées, selon des lois de physique d'écoulement complexes, mais non pas les deux, dans bien des cas. Des efforts importants sont encore demandés afin de résoudre ces problèmes.

Le but ultime recherché par ces travaux de développement du CDF serait la réalisation d'un système d'analyse et de conception à l'épreuve de toute défaillance, et qui serait en même temps convivial, d'un bon rapport qualité/prix, précis du point de vue numérique et confirmé rigoureusement par des expérimentations détaillées. En ce qui concerne les applications pratiques du CDF, la validation poussée, ou l'étalonnage des codes CDF représente une étape critique. La validation assure à l'utilisateur du CDF le niveau de fiabilité élevé dont il a besoin, et elle doit permettre à cet outil de réaliser tout son potentiel en tant qu'aide à la conception.

Le Panel AGARD de la dynamique des fluides a organisé ce s[illegible]ium pour permettre un examen des travaux de calcul ainsi que des travaux expérimentaux qui sont en cours à l'heure a[illegible]lle et dont l'objet serait de valider ou d'étalonner les codes CDF, et ceci pour la quasi-totalité des domaines de recherche en dynamique des fluides.

Le symposium a eu pour objectif principal de déterminer le niveau de concordance entre les modèles physiques et les algorithmes de résolution numériques d'une part, et les données expérimentales d'autre part, ainsi que l'identification des domaines de validation pour des résolveurs d'écoulements spécifiques et l'identification des régimes d'écoulement pour lesquels il existe des lacunes importantes, et où des recherches supplémentaires seraient justifiées.

Etant donné le vif intérêt du sujet de nombreux résumés de communications ont été soumis à l'approbation du Comité chargé du programme. Pour répondre à cette demande importante le Comité a donc décidé d'inviter des auteurs a préparer une session spéciale permettant une exposition de leurs communications. Ces communications on été présentées sur de grands et larges supports et les auteurs se sont tenus à la disposition des participants pendant environ deux heures. Cette exposition a stimulé des discussion vivantes et bénéfiques pour tous.

Le Volume 2 contient les textes complets des présentations faites lors de cette exposition et le Volume 1 contient les communications du Symposium et les conclusions de la Table Ronde.

QUALITY INSPECTED 4

A-1

AGARD FLUID DYNAMICS PANEL

Chairman: Mr D.H.Peckham
Superintendent AE2 Division
Royal Aerospace Establishment
R141 Building
Farnborough, Hants GU14 6TD
United Kingdom

Deputy Chairman: Dr W.J.McCroskey
Senior Staff Scientist
US Army Aero Flightdynamics
Directorate (AVSCOM)
Ames Research Center N258-1
Moffett Field, CA 94305
United States

PROGRAMME COMMITTEE

Dr R.G.Bradley, Jr. (Co-Chairman)
Director, Aerospace Technology Dept.
GD/FW-MZ 2888
Fort Worth Division
P.O. Box 748 Fort Worth, TX 76101, USA

Dr W.Schmidt (Co-Chairman)
Deputy Director-Dornier 328 Program
Dornier GmbH, EY
Postfach 1420
D-7990 Friedrichshafen
Federal Republic of Germany

M. l'Ing. en Chef B.Monnerie
Directeur Adjoint
Direction Aérodynamique
B.P. 72
ONERA
92322 Châtillon, France

Professor D.Papailiou
Department of Mechanical Engineering
University of Patras
Rio 26001
Patras, Greece

Dr Ing. G.Bucciantini
Aeritalia-Societa Aerospaziale Italiana
Gruppo Velivoli Combattimento
Corso Marche 41
10146 Torino, Italy

Professor Ir. J.W.Slooff
National Aerospace Laboratory, NLR
Anthony Fokkerweg 2
1059 Amsterdam, Netherlands

Professor H.Norstrud
Appt. 24
27 rue Noulet
F-31400 Toulouse, France

Professor A.F. de O.Falcao
Pavilhao de Maquinas
Instituto Superior Tecnico
1096 Lisboa Codex, Portugal

Mr P.R.Bignell
BAe PLC, Sowerby Research Centre
Naval Weapons Division
FPC 067, P.O. Box 5
Filton
Bristol BS12 7QW, UK

Dr R.A.Graves
Director, Aerodynamics Div.
NASA/HQ/Mail Code RF
Washington D.C. 20546, USA

PANEL EXECUTIVE

From Europe:
Mr M.C.Fischer
AGARD-OTAN
7 rue Ancelle
92200 Neuilly-sur-Seine, France
Tel (1) 4738 5775 – Telex 610176 (France)

From USA and Canada:
AGARD-NATO
APO New York 09777

Symposium CONTENTS

	Page
PREFACE	iii
FLUID DYNAMICS PANEL	iv
	Reference
SESSION I – CFD VALIDATION CONCEPTS Chairman: A.F. de O.Falcao	
CFD VALIDATION PHILOSOPHY by R.G.Bradley (Invited)	1
ACCURACY REQUIREMENTS AND BENCHMARK EXPERIMENTS FOR CFD VALIDATION by J.G.Marvin (Invited)	2
NUMERICAL ACCURACY ASSESSMENT by J.W.Boerstoel (Invited)	3
SESSION II – EXTERNAL FLOW I: AIRFOILS Chairman: B.Monnerie	
WIND TUNNEL EXPERIMENTS ON AEROFOIL MODELS FOR THE ASSESSMENT OF COMPUTATIONAL FLOW METHODS by P.R.Ashill, D.J.Weeks and J.L.Fulker	4
PARAMETRIC STUDY OF GRID SIZE, TIME STEP, AND TURBULENCE MODELING ON NAVIER-STOKES COMPUTATIONS OVER AIRFOILS by C.L.Rumsey and W.K.Anderson	5
ON THE VALIDATION OF A CODE AND A TURBULENCE MODEL APPROPRIATE TO CIRCULATION CONTROL AIRFOILS by J.R.Viegas, M.W.Rubesin and R.W.MacCormack	6
COMPARATIVE STUDY OF CALCULATION PROCEDURES FOR VISCOUS FLOWS AROUND AIRFOILS IN THE TRANSONIC REGIME by H.W.Stock, W.Haase and H.Echtle	7
NUMERICAL SOLUTION OF COMPRESSIBLE NAVIER-STOKES FLOWS by F.Bassi, F.Grasso and M.Savini	8
SESSION III – EXTERNAL FLOW II: VORTEX FLOWS Chairman: W.Schmidt	
THE INTERNATIONAL VORTEX FLOW EXPERIMENT by A.Elsenaar, L.Hjelmberg, K.Bütefisch and W.J.Bannink (Invited)	9
STATUS OF CFD VALIDATION ON THE VORTEX FLOW EXPERIMENT by B.Wagner et al.	10
FLOW FIELD SURVEYS OF LEADING EDGE VORTEX FLOWS by T.T.Ng, R.C.Nelson and F.M.Payne	11
A THEORETICAL AND EXPERIMENTAL EVALUATION OF A NUMERICAL METHOD FOR CALCULATING SUPERSONIC FLOWS OVER WING/BODY CONFIGURATIONS by J.L.Fulker and P.R.Ashill	12

Reference

SESSION IV – EXTERNAL FLOW III: WINGS/WING BODY
Chairman: G.Bucciantini

THE DFVLR-F5 WING EXPERIMENT – TOWARDS THE VALIDATION OF THE NUMERICAL SIMULATION OF TRANSONIC VISCOUS WING FLOWS
by W.Kordulla, D.Schwamborn and H.Sobieczky 13

ACCURATE SOLUTIONS, PARAMETER STUDIES, AND COMPARISONS FOR THE EULER AND POTENTIAL FLOW EQUATIONS
by W.K.Anderson and J.T.Batina 14

VERIFICATION OF AN IMPLICIT RELAXATION METHOD FOR STEADY AND UNSTEADY VISCOUS AND INVISCID FLOW PROBLEMS
by M.A.Schmatz, A.Brenneis and A.Eberle 15

FIABILITE ET VALIDITE DES CODES DE C.F.D. COMPARAISON AU VOL ET A LA SOUFFLERIE
par G.Heckmann 16

DECOLLEMENT SUR OBSTACLES DE TYPE ELLIPSOIDE – EXPERIENCES DE VALIDATION ET MODELISATION
par D.Barberis et B.Chanetz 17

ACCURACY STUDY OF TRANSONIC FLOW COMPUTATIONS FOR THREE DIMENSIONAL WINGS
by M.P.Carr 18

CFD APPLICATIONS IN DESIGN AND ANALYSIS OF THE FOKKER 50 AND FOKKER 100
by N.Voogt, W.J.A.Mol, J.Stout and D.F.Volkers 19

SESSION V – EXTERNAL FLOW IV: HIGH SPEED FLOWS
Chairman: P.R.Bignell

EXPERIMENTAL PROGRAM FOR REAL GAS FLOW CODE VALIDATION AT NASA AMES RESEARCH CENTER
by G.S.Deiwert, A.W.Strawa, S.P.Sharma and C.Park 20

CALCULS TRIDIMENSIONNELS DE L'INTERACTION D'UN JET LATERAL AVEC UN ECOULEMENT SUPERSONIQUE EXTERNE
par M.Dormieux et C.Mahe 21

NUMERICAL SIMULATION OF SEPARATED SUPERSONIC FLOWS AROUND TACTICAL MISSILE BODIES
(SIMULATION NUMERIQUE D'ECOULEMENTS SUPERSONIQUES DECOLLES AUTOUR DE FUSELAGES DE MISSILES TACTIQUES)
par Ph.Guillen et J.Lordon 22

DEVELOPMENT AND APPLICATION OF A WEAPONS MULTIBLOCK SUITE
by P.A.Shepherd and G.R.Tod 23

ARCJET VALIDATION OF SURFACE CATALYCITY USING A VISCOUS SHOCK-LAYER APPROACH
by A.D.Zwan, R.S.Crooks and W.J.Whatley 24

SESSION VI – INTERNAL FLOW I: TURBOMACHINERY
Chairman: H.Norstrud

CFD VALIDATION EXPERIMENTS FOR INTERNAL FLOWS
by L.A.Povinelli 25

SOLUTION ON UNSTRUCTURED GRIDS FOR THE EULER AND NAVIER-STOKES EQUATIONS
by W.Koschel, M.Lötzerich, and A.Vornberger 26

VALIDATION OF AN EULER CODE FOR HYDRAULIC TURBINES
by F.Thibaud, A.Drotz and G.Sottas 27

Reference

COMPUTATIONAL TECHNIQUES AND VALIDATION OF 3D VISCOUS/TURBULENT CODES FOR INTERNAL FLOWS
by B.Lakshminarayana, K.R.Kirtley and Mr.Warfield 28

VALIDATION A L'AIDE D'ESSAIS EN SOUFFLERIE DE CODES DE CALCUL DU CHAMP AERODYNAMIQUE DE ROTORS ET D'HELICES DANS DES CONDITIONS DE VOL VARIEES
par C.Maresca, D.Favier, M.Nsi Mba et C.Barbi 29

VALIDATION OF A 3D EULER/NAVIER STOKES FINITE VOLUME SOLVER FOR A RADIAL COMPRESSOR
by E-L.Eriksson and J.T.Billdal 30

COMPUTATION OF TRANSONIC 3D CASCADE FLOW AND COMPARISON WITH EXPERIMENTS
by H-W.Happel and B.Stubert 31

SESSION VII – INTERNAL FLOWS II: INTAKES AND DUCTS
Chairman: D.Papailiou

NUMERICAL AND EXPERIMENTAL INVESTIGATION OF ENGINE INLET FLOW WITH THE DORNIER EM2 SUPERSONIC INLET MODEL
by H.Buers, S.Leicher and P.A.Mackrodt 32

EFFORTS TOWARD THE VALIDATION OF A COMPUTATIONAL FLUID DYNAMICS CODE FOR ANALYSIS OF INTERNAL AERODYNAMICS
by R.G.Semmes, D.G.Arbiter and R.D.Dyer 33

MEASUREMENTS AND COMPUTATIONS OF SWIRLING FLOW IN A CYLINDRICAL ANNULUS
by R.J.Kind, E.M.Vowakim and P.M.Reddy 34

ON THE VALIDATION OF 3D NUMERICAL SIMULATIONS OF TURBULENT IMPINGING JETS THROUGH A CROSSFLOW
by J.M.M.Barata, D.F.G.Durão, M.V.Heitor and J.J.McGuirk 35

TIME-DEPENDENT NUMERICAL SIMULATION OF THE STARTING FLOW OF AN INCOMPRESSIBLE FLUID PAST A DOWNSTREAM-FACING STEP
by M.Ciofalo and M.W.Collins 36

A COMPARATIVE STUDY AND VALIDATION OF UPWIND AND CENTRAL-DIFFERENCE NAVIER-STOKES CODES FOR HIGH-SPEED FLOWS
by D.H.Rudy, A.Kumar, J.L.Thomas, P.A.Gnoffo and S.R.Chakravarthy 37

ROUND TABLE DISCUSSION RTD

CFD VALIDATION PHILOSOPHY

Richard G. Bradley
General Dynamics Corporation
Fort Worth, Texas 76101, USA

ABSTRACT

Computational Fluid Dynamics (CFD) is becoming an increasingly powerful tool in design and analysis of fluid dynamic and aerospace systems. Application of CFD to practical design problems requires a high level of confidence, which in turn requires focused experimentation to verify the accuracy of CFD codes. The need for CFD validation is presented from the viewpoint of the user, and a general philosophy for validation of CFD codes is introduced, highlighting the requirements for disciplined experimentation and careful evaluation of the bounds of error in CFD solutions.

INTRODUCTION

The development of aerospace vehicles, over the years, has been an evolutionary process in which engineering progress in the aerospace community was based, generally, on prior experience and databases obtained through wind tunnel and flight testing. Advances in the fundamental understanding of flow physics, wind tunnel and flight test capability, and new mathematical insights into the governing flow equations have been translated into improved air vehicle design. Two notable examples of this evolutionary process that resulted in significant improvements to air vehicles are the area rule and supercritical-wing technology. These improvements evolved from a combination of wind tunnel tests and analytical advances. The analytical advances resulted in the ability to obtain solutions to simplified forms of the appropriate supersonic and transonic flow equations. The modern day field of Computational Fluid Dynamics (CFD) is seen as a continuation of this growth in analytical capability and the digital mathematics needed to solve more rigorous forms of the flow equations.

CFD is becoming an increasingly powerful tool in the aerodynamic design of aerospace systems, owing to improvements in numerical algorithms, geometric modeling, grid generation, and physical parameter modeling, as well as dramatic improvements in supercomputer processing speed and memory. With the realization of the potential of forthcoming supercomputers, much of the current CFD work will be expanded to address more complex configurations, geometries, flight regimes, and applications. Some of the existing codes will become components of more complex systems of codes addressing problems of modeling, grid generation, flow field algorithms, and flow visualization. Thus, CFD is becoming an important aerospace design and development tool - one that requires a high level of confidence.

In order to meet the required confidence level, the existing and forthcoming CFD application codes must be verified with the best available experimental data. Because of the complexity of the aerodynamic flows that will be routinely computed, the experimental database must be expanded to include not only surface-measurable quantities, but also detailed measurements of fluid and thermal parameters throughout the flow region of interest. Focused experimental tests must be performed to obtain detailed flow quantity measurements in addition to integral checks. Also, the errors inherent in experimental testing must be identified, understood, and minimized in order to produce the high-quality, accurate benchmark data sets that are required for validation of complex CFD codes and for use in developing physical modeling data for complex flows.

The intent of this paper is to set forth some general principles for gaining the confidence in CFD that is essential for the capability to realize its full potential as a design and analysis tool in fluid mechanics. These principles constitute a foundation for defining a "general philosophy of validation" for CFD. Key definitions are suggested that set CFD validation apart from the usual concept of calibration of the analytical methods used in design applications.

Copyright © 1988 by General Dynamics Corporation.
All rights reserved.

CODE MATURATION

In order to set the stage for a general philosophy of CFD validation, it is useful to consider, along with the requirements of the user, the steps required to mature the capability.

THE DEVELOPMENT CYCLE

A recent study conducted by the National Research Council examined the current status of CFD in the United States and suggested future directions for development work (Reference 1). An extensive survey of codes, either under development or in use, formed a basis for evaluation of the state of affairs in the field. One of the key conclusions of the study is that careful "verification of flow models and algorithms" is needed.

A five-phase development cycle for CFD is set forth in Reference 1 as a guide for assessing CFD capabilities. This development cycle, shown in Figure 1, illustrates the steps generally followed to achieve a "mature" CFD capability. A mature capability is generally understood to result in codes that can be used routinely in complex design applications by engineers.

The predominant effort over the last two decades has been focused on Phases I, II, and III. Code developers have made outstanding progress in developing algorithms and physical models that allow solution of inviscid and viscous flow equations for a large number of flows of interest. In recent years industry has placed significant emphasis on learning to use the evolving capability, Phase IV. Although the success in algorithm development for the potential equations and Euler equations has been noteworthy, most codes are equipped with "knobs" that control convergence and smooth the solutions. Unfortunately, these artifices may introduce unacceptable errors. On the other hand, Navier Stokes solvers rely heavily on physical models, for turbulence as an example, that are not well understood and require additional research.

The mature CFD capability, Phase V, involves increasing the understanding and verification of the code's sensitivities to grids, convergence characteristics, spacial accuracy, reliability, robustness, ease of use, and cost effectiveness. The physical models employed for turbulence, chemical kinetics, transition, and heat transfer mechanisms are critical elements for some flows and require considerable attention. In a pragmatic sense, one key feature of maturity in CFD capability is careful comparison with experimental measurements.

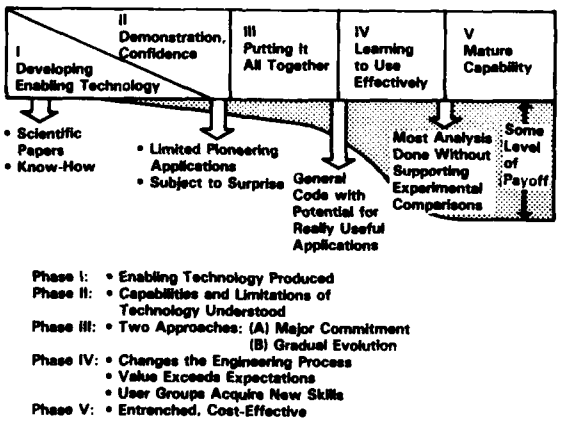


Figure 1 The CFD Development Cycle

THE USERS' VIEWPOINT

From a design manager's point of view, one obtains a perspective completely different from that of the code developer. Recall that the aerospace designer is responsible for defining the best configuration to meet performance specifications in the shortest time and at the lowest cost. He has traditionally relied upon extensive wind-tunnel and flight-test results to guide his design decisions and to supply the flight envelope database needed for comprehensive vehicle-performance calculations. Admittedly, wind tunnel test data have many limitations, but designers have years of experience to help in understanding those limitations. Today's dilemma for the designer of high-performance aircraft is illustrated in Figure 2, taken from Reference 2.

The potential of CFD is well known. For the first time in the history of aeronautics, the designer has the opportunity to generate solutions for complex flowfields and to examine the detailed "microscopic" features of the flow that influence a design. The challenge, now, is to provide usable, believable, cost- and schedule-effective codes for design application, and to integrate these codes into the designer's toolset. This is both a technical and a management challenge. A responsible designer, however, raises legitimate concerns about the benefits of CFD in helping him to meet his requirements, as shown in Figure 2.

Capability, in the context of this discussion, pertains to the usefulness of the code in modeling flowfields about complex geometries over a wide range of flow conditions, such as Mach number, Reynolds number, angle of attack, and yaw; and in producing results in a form that are meaningful to the designer.

Turnaround is the time required to set up geometries, grid meshes, and obtain converged solutions.

Availability concerns the level of expertise required to generate the flowfield solutions. (e.g., Can a design engineer run the code, or does it require a CFD specialist.)

Cost represents the cost effectiveness of a CFD approach relative to other options.

Confidence relates to the dependability of the codes to give accurate solutions over the range of design variables.

These concerns should be focal points for developers of CFD codes and for engineers who are integrating the capability into the design process. While all of the concerns are vitally important, "confidence" is perhaps the most critical at this time. "Confidence" is especially critical to the tactical aircraft designer, since he generally does not have much experience with CFD, and the flowfields of tactical aircraft are the most complicated. The required confidence level is gained by continually comparing CFD results with experimental data.

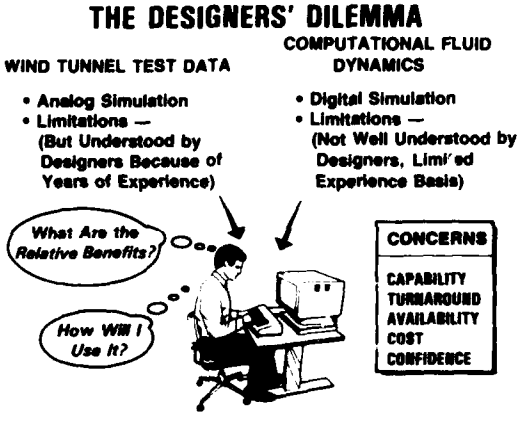


Figure 2 The Designers' Dilemma

It is, of course, important to note that CFD codes can be used in analysis and design applications long before the codes are considered to be mature in the sense of Figure 1. Engineers have always been able to use less than perfect tools to provide design guidance by using them in conjunction with experience and calibration to known physical quantities. Calibration provides an error band or correction factor that enhances the capability of a particular code or analytical method to predict specific parameters that are important to the design objectives for a particular design without verifying that all other features of the flow are modeled accurately. For example, one might calibrate a code to predict shock location, lift, and moment on a wing without any assurance that the flowfield off the surface and the wake behind the wing are properly modeled. Or, one may calibrate a code to compute gross pressure loss through a supersonic inlet-duct combination without concern for the accuracy of the distortion distribution at the compressor face. Although the use of calibrated CFD solutions is dangerous because of the subtle viscous interactions that are sensitive to geometry and flowfield, skilled engineers can obtain useful design information and guidance from relatively immature codes.

CFD VALIDATION

CFD has opened the door for precise solutions to governing equations without many of the simplifying assumptions required previously for analytical treatment. As a result, complex physical flows can be computed to a level of detail not previously possible. On one hand, this unique capability gives the designer the ability to "step inside" a flow field and understand its impact on the design. On the other hand, it poses the question of how one can be sure of the accuracy in this extraordinary capability. In other words, how can one validate a code and establish its limitations?

In response to the above concerns, a concept for gaining full confidence in CFD - termed CFD validation - is suggested. Validation must involve detailed comparisons of computed flow fields with experimental data to verify the code's capability to accurately model the critical physics of the flow. These comparisons require close coordination between the code developer and the experimentalist to ensure that the accuracy and limitations of the experiments, as well as those of the numerical algorithms and grid densities, are understood and taken into account. Through validation, one assures that the numerical physics of the code truly represents the flow physics being modeled.

NASA's Aeronautics Advisory Committee recently formed an ad hoc committee to review the CFD validation activities at three NASA research centers and assess their current and planned research programs. The committee membership was selected from the Aeronautics Advisory Committee and the ARTS (Aerospace Research & Technology Subcommittee) and SSTAC (Space Systems Technology Advisory Committee). The results are reported in an internal report to NASA (Reference 3) that is not available for public dissemination but forms the basis for the terminology and ideas presented below.

DEFINITIONS

The following definitions in Reference 3 clarify the concept for validation of CFD and help identify the unique experimental requirements:

> CFD Code Validation - Detailed surface-and-flow-field comparisons with experimental data to verify the code's ability to accurately model the critical physics of the flow. Validation can occur only when the accuracy and limitations of the experimental data are known and thoroughly understood and when the accuracy and limitations of the code's numerical algorithms, grid-density effects, and physical basis are equally known and understood over a range of specified parameters.
>
> CFD Validation Experiment - An experiment that is designed to provide detailed building block data for developing and validating CFD codes. This objective requires that the data be taken in the form and detail consistent with CFD modeling requirements and that the accuracy and limitations of the experimental data be thoroughly understood and documented.
>
> Validated CFD Code - A code whose accuracy and range of validity has been determined by detailed comparison with CFD validation experiments, so that it can be applied, without calibration, directly to a geometry and flow condition of engineering interest with a high degree of confidence.

While it is desirable to have mature, validated codes for design applications, it is recognized that code calibration remains an important part of the design process. This is especially true since most of the codes being applied today are in the development phases. A definition of calibration as it applies to CFD is suggested in order to distinguish the process from code validation:

> CFD Code Calibration - The comparison of CFD code results with experimental data for realistic geometries that are similar to the ones of design interest, made in order to provide a measure of the code's capability to predict specific parameters that are of importance to the design objectives without necessarily verifying that all the features of the flow are correctly modeled.

In the past, the terms "validation" and "calibration" have been used loosely to describe any comparison with experiment. The definitions given above are intended to clearly distinguish between the two concepts.

CFD REQUIREMENTS

The concept of CFD validation, defined in the previous section, implicitly relates a code's accuracy to its ability to predict physical features of a given flow. In this global sense, the accuracy of a solution has four limitations: (1) The appropriateness of the governing equations to represent the dominant features of the flow is, of course, a key consideration that can limit a solution. (2) The numerical algorithm, including smoothing routines and convergence acceleration schemes, may be a source of numerical error. (3) It may not be possible to generate grids that will capture the scale of the physical phenomena throughout the solution domain. (4) Many solutions require physical models to represent phenomena that are not well understood (turbulence for example), and that may lead to significant sources of error. The net effect of these four limiting factors is of primary concern for the designer who must gain confidence in a code's accuracy for specific applications.

Numerical error in CFD solutions is a strong function of the geometry, the algorithms selected, and the grid density. The truncation error decreases with an increasing number of mesh points; however, practical limitations of today's computers do not permit total elimination of this error source. Further, artificial introduction of numerical " viscosity" terms to speed convergence and provide smoothing to the solution introduces a source of error that must be understood and evaluated. Grid size distributions must be matched to the physical scales of the flow to help ensure accuracy in the solution. Often such optimum distribution is not known a priori and can be a source of error. Confidence in the solution stems from an understanding of these limitations and their effect on the solution.

Much work remains to be done in physical modeling of turbulence, transition, combustion kinetics, and heat-transfer mechanisms, including wall catalycity. Today's CFD must rely on various levels of numerical approximation to represent these basic physical phenomena, which are not completely understood. In the case of transition and turbulence, full Navier-Stokes Equation solutions are providing insight, but even this application is limited by practical computer limitations today. Much work remains to be done before one can have implicit confidence in the physical models required for a mature CFD capability.

In the light of known limitations inherent in CFD codes, validation must entail a thorough understanding of how these limitations affect the ultimate accuracy of a solution in a given application. Thus, validation is seen to include the bounds of accuracy in terms of a range of numerical and physical parameters for which an acceptable error band may be achieved. This level of confidence, then, must be related to experimental evidence that is subject to its own band of uncertainties.

EXPERIMENTAL REQUIREMENTS

Equally critical to the concept of CFD validation is the reliability of experimental data. It was noted in Reference 3 that four categories of experimentation are related to the development of CFD capability:

a. Experiments designed to understand flow physics.
b. Experiments designed to develop physical models for CFD codes.
c. Experiments designed to calibrate CFD codes.
d. Experiments designed to validate CFD codes.

All four categories of tests are important. They form the basis for building a mature CFD capability. Validation tests should be only a part of the total test focus and should be formulated to provide specific data in the form required for validating CFD codes.

Of course there is some overlap in the use of data from any given set of experiments. However, experiments that are to be used for validation require special attention to details of the facility, the measurements, the instrumentation, and the form of data reduction.

In order to provide the basis for CFD validation, the experiments must provide measurements, with adequate accuracy and resolution, under flow conditions that are representative of those for which CFD will be used. The available capabilities of various facilities to simulate realistic flow conditions of Mach number, Reynolds number, turbulence, gas composition, and other flow parameters, is an important consideration. An understanding of the effect of flow gradients in the test section, sting and wall interference effects, blockage, and noise is required to ensure the integrity of the flow measurements and to provide the proper flow and boundary conditions for the accompanying CFD calculations.

At lower Mach numbers, subsonic facilities are generally adequate, although existing measurements may lack sufficient detail or accuracy. At the higher Mach numbers, tunnels are much less capable of fully simulating Mach number, Reynolds number, real-gas effects, and combustion, for example. The phenomena of transition, turbulence, real-gas effects, unsteady flow, and combustion are all important to maturing CFD capability. Existing facilities and measurement capabilities can limit the validation of CFD codes.

The range of experiments for CFD validation must extend from simple basic ones to those covering the conditions of flight. They must be adequate to test CFD in a multi-dimensional environment, so as to provide a clear indication of what is needed to evaluate CFD's capability to predict details as well as trends, and to explore the boundaries of the range of application for specific codes.

It is essential that critical details of the flow are measured to a level of accuracy comparable to the accuracy expected from the calculations and in a form that is compatible with the CFD solutions. An understanding of the bounds of accuracy associated with the various measurements is essential. Instrumentation to provide redundant measurements for both the surface and the flow field is highly desirable for validation experiments.

In summary, CFD validation requires a disciplined form of experimentation that is closely coupled to the requirements of the codes being validated. This experimentation requires close cooperation between the code developer and the experimentalist. Each must be thoroughly familiar with the requirements and limitations of the other.

REFERENCES

1. "Current Capabilities and Future Directions in Computational Fluid Dynamics." National Research Council, National Academy Press, Washington, D.C. 1986.

2. Bradley, R.G.; Bhateley, I.C.; and Howell, G.A.: "Computational Fluid Dynamics - Transition to Design Applications." NASA Conference on Supercomputing in Aerospace, NASA Ames Research Center, Palo Alto, CA, March 1987.

3. "Computational Fluid Dynamics Validation." The Ad Hoc Committee on CFD Validation of the Aeronautics Advisory Committee, May 1987. (Not available for public dissemination.)

ACKNOWLEDGEMENTS

The concepts and definitions presented are based upon the findings of two committee studies as noted in the text. The author gratefully acknowledges the contributions of each of the U.S. researchers and scientists who served on these committees.

ACCURACY REQUIREMENTS AND BENCHMARK EXPERIMENTS FOR CFD VALIDATION

Joseph G. Marvin
Chief, Experimental Fluid Dynamics Branch
NASA Ames Research Center
Moffett Field, CA 94035

SUMMARY

The role of experiment in the development of Computational Fluid Dynamics (CFD) for aerodynamic flow prediction is discussed. CFD verification is a concept that depends on closely coordinated planning between computational and experimental disciplines. Because code applications are becoming more complex and their potential for design more feasible, it no longer suffices to use experimental data from surface or integral measurements alone to provide the required verification. Flow physics and modeling, flow field, and boundary condition measurements are emerging as critical data. Four types of experiments are introduced and examples given that meet the challenge of validation: (1) flow physics experiments; (2) flow modeling experiments; (3) calibration experiments; and (4) verification experiments. Measurement and accuracy requirements for each of these differ and are discussed. A comprehensive program of validation is described, some examples given, and it is concluded that the future prospects are encouraging.

1. INTRODUCTION

Mathematical approximations, limited computer capacity, and lack of understanding of physical modeling lead to uncertainties in the application of Computational Fluid Dynamics (CFD). Consequently, the pace of introduction and the extent of reliance on CFD in the design process depends on validation[1]; and experiments that verify CFD have become an essential element of its evolutionary development.[2]

Experimental validation is required for a number of different aerodynamic flows that occur over the full range of flight speeds. Any effective, timely program to provide the necessary data will require good planning and cooperation between various aerospace disciplines. Because of this situation the topic of validation has been intensely debated within NASA during the past year. An outgrowth of that debate resulted in the concepts of CFD validation and calibration and categories of experiments recommended by a NASA ad hoc Committee on Validation introduced by Bradley.[3] And the first NASA CFD Validation Workshop made further recommendations: (1) provide closer cooperation between CFD developers and experimentalists; (2) provide detailed measurements of the flow field and boundary conditions in addition to model surface and integral quantities; (3) provide new or improved nonintrusive measurement capabilities, especially for hypersonic or reacting flow conditions; (4) provide redundancy in both measurements and experiments whenever practical so as to clarify accuracy and credibility; (5) provide dedicated large facilities for validation research activities; and (6) provide standardized test cases with accessible data bases.

The intent of the present paper is to provide a perspective on validation using these ideas and to introduce a synergistic approach for timely accomplishment of validation. Details on experimental and accuracy requirements will be discussed using the concepts of validation, calibration, and categories of experimentation as defined in Ref. 3.

CFD code validation: Detailed surface- and flow-field comparisons with experimental data to verify the code's ability to accurately model the critical physics of the flow. Validation can occur only when the accuracy and limitations of the experimental data are known and thoroughly understood and when the accuracy and limitations of the code's numerical algorithms, grid-density effects, and physical basis are equally known and understood over a range of specified parameters.

CFD code calibration: The comparison of CFD code results with experimental data for realistic geometries that are similar to the ones of design interest, made in order to provide a measure of the code's ability to predict specific parameters that are of importance to the design objectives without necessarily verifying that all the features of the flow are correctly modeled.

Categories of experimentation: (1) Experiments designed to understand flow physics; (2) experiments designed to develop physical models; (3) experiments designed to calibrate CFD; (4) experiments designed to validate CFD.

The categories of experiments will be explained first with the aid of some examples that represent the work of the author and his colleagues at the Ames Research Center. Their cooperation in the use and preparation of this material is greatly appreciated. Following that, accuracy, instrumentation and facility requirements, and future prospects for validation experiments will be discussed.

2. EXPERIMENTAL REQUIREMENTS

2.1 Role of Experiments

A framework for describing the connection between experiment and computation was presented in Ref. 4. That framework can be depicted with the aid of Fig. 1, taken from Ref. 4, and extended to reflect new developments and the various categories of experiments defined in Ref. 3. The stages of code development are shown in ascending order of maturity and each is linked to a type(s) of experiment.

Research codes refer to those developed by integrating new enabling technology such as supercomputers, algorithms, grid methodology, and new understanding of physical modeling to solve specific problems. One or two researchers are involved in developing the code, and limited documentation is available. Experiments utilized at this stage are referred to as building blocks. These provide the data required to understand flow physics, to guide flow modeling processes, and to validate the computations for a particular problem. Two types of experiments make up the building blocks leading to the development of the research code. They are flow physics and flow modeling experiments. An additional new development at this level is the use of full and large-eddy numerical simulations[5] (FS and LES) and computational chemistry[6] to develop data bases for understanding phenomena such as a transition, turbulence, and reaction rate chemistry.

Pilot codes refer to a more mature stage of development. Documentation is more complete, the code is operated by others besides those involved in the research code development, and the envelope of application is expanded in recognition of the potential advances afforded by the research code. Benchmark experiments are the key to this stage of development. They provide the parametric information leading to the identification of the range of applicability of the code. Calibration and verification are the objectives of these experiments.

Subsequently the code would advance to its ultimate development stage when it could be used alone or in combination with codes from other disciplines such as structures or propulsion and applied confidently in the design process. Configurational, performance and system integration experimental data would be needed for verification at this stage.

The delineation of the various stages of development outlined above is idealized, and not always evident in practice, because of the dynamic nature of CFD and its wide-ranging possibilities for solving such a variety and complexity of problems; but the framework depicts how experiment and computation, working together, could accelerate the pace of development. Without question the success of such a framework depends on close coordination between experimental and computational fluid dynamicists and instrumentation developers. For this paper, the emphasis will be on the requirements for the first two stages of development.

2.2 Flow Physics Experiments

The lack of understanding of fundamental physical phenomena is limiting the pace of CFD development. Important expamples are transition from laminar to turbulent flow, turbulence, and high temperature gas physics related to hypersonic flows. Flow physics experiments are defined as those experiments that provide fundamental understanding of such phenomena so that they can be accurately modeled in the codes. As mentioned previously, computation itself is beginning to supplement data from flow physics experiments through numerical simulations that do not require any modeling of the physics. The following examples show how full simulations of the Navier-Stokes equations are being combined with experiment to provide a more fundamental understanding of turbulent boundary layers. These examples will suffice to illustrate what is meant by flow physics experiments.

The physical insight obtainable from direct Navier-Stokes simulation[7] is shown in Fig. 2. The figure highlights several important aspects of the structure of turbulence in a simulated flat-plate boundary layer. The simulation[8] was developed by P. R. Spalart of Ames, and employs no turbulence models of any kind. The complete, time-dependent Navier-Stokes equations were solved using spectral methods at each of the 9.4 million grid points in the computational domain. The Reynolds number based on momentum thickness is approximately 670. In the figure, elongated white surfaces identify the low-pressure cores of vortices. Shaded regions show where significant contributions to the Reynolds shear stress, $-\overline{uv}$, are occurring. Regions of low-speed fluid ejected outwards, and high-speed fluid swept wallward are labeled. These, and other realizations show that large hook-shaped vortical structures are clearly present in the numerical turbulent boundary layer, and the loactions of significant Reynolds stress contribution are seen to occur adjacent to these vortical structures. This level of understanding of the fundamental processes involved in the Reynolds stress generation is eventually expected to aid the development of improved statistical models that accurately reflect the underlying physical behavior of turbulence.

To gain similar physical insight, experimental techniques must generally employ multipoint measurement schemes. An example [9] of such an approach in a flow that is beyond the current capability of full simulation is shown in Fig. 3(a). Here, the large-eddy structure of a high Reynolds number, compressible turbulent boundary layer was investigated by mounting a fixed hot-wire at the wall in conjunction with another, traversing hot-wire mounted directly above the first. The objective was to map the spatial character and extent of the coherent eddies in a Mach 3 axisymmetric boundary layer, and to compare the results with low Reynolds number, incompressible flow experiments and simulations.

The long-time-averaged, space-time-cross-correlation functions between the near-wall sensor and various positions of the outer sensor are shown in Fig. 3(b). These curves show that measurable correlation between the two wires occurs up to a separation distance of at least half the boundary-layer thickness. These data suggest the presence of coherent outer-layer structures that extend well into the near-wall region, which may provide an energy transfer path between the free-stream flow and the near-wall, turbulence-producing region. The slope of these structures can be deduced from the correlation curves by using an eddy convection velocity, and is shown in Fig. 3(c) to vary from 5° near the wall to 30° in the outer layer.

The nature of these large disturbances can be studied in more detail by computing ensemble-averaged, mass-flow histories around strong, rapid accelerations and decelerations. The results for accelerations, shown in Fig. 3(d), closely resemble those of similar investigations performed in low-speed flows and in numerical simulations. This suggests confirmation of Morkovin's hypothesis that the basic structure of turbulent boundary layers is not fundamentally changed by compressibility, at least for moderate Mach numbers.

2.3 Physical Modeling Experiments

Practical CFD applications involving complex turbulent flows rely on statistical modeling of turbulence.[10] Physical modeling experiments are defined as experiments that provide guidance for and verification of the modeling process.

An example of a physical modeling experiment[11] used to improve turbulence modeling for transonic flows with strong shock-wave/boundary-layer interaction is shown in Fig. 4. The test model consisted of a cylindrical body fitted with a circular arc section similar to that of an airfoil. Shock-wave interactions of varying strengths were studied by varying free-stream Mach number. The choice of an axisymmetric geometry was made to eliminate three-dimensional effects. Mean-flow velocity and turbulence profiles, obtained with a Laser Doppler Anemometer System (LDA), and surface quantities such as pressure and oil-streak data were documented.

Computations of the flow field from a Reynolds-averaged, Navier-Stokes code revealed deficiencies in the turbulence modeling. By using a model developed primarily for attached boundary layers, the shock wave location was predicted incorrectly and consequently the pressure recovery was seriously overpredicted. The mean- and turbulence-profile data were used to explain the differences and to guide modeling improvement. The primary cause of the pressure recovery overprediction was the failure of the eddy viscosity model to adequately reflect the lag of turbulence adjustment through the shock wave. Using new modeling concepts in conjunction with the turbulence data resulted in a significant model improvement.[12] In particular, the "history effects" of the turbulence changes through the shock wave were accounted for by prescribing and solving an ordinary differential equation for the maximum shear stress development. The improved model results are shown.

2.4 Calibration Experiments

Calibration experiments are intended to reveal a code's ability to predict specific parameters. The data, in most instances, are limited with respect to their ability to determine the completeness of the flow modeling. Code calibration is prevalent and important to developing codes for real gas hypersonic applications because in this flight regime it is extremely difficult to provide ground test data for exact flight conditions and their attendant chemical and length scales. For example, facilities may duplicate flight energy levels but not match the air chemistry, or they may duplicate flight Mach number but not match the energy level.

An example of a calibration experiment intended to determine the applicability of the air chemistry model used in a parabolized Navier-Stokes code[13] is shown in Fig. 5. Drag data from 10° sharp cones fired down a Ballistic Range are shown as a function of angle of attack.[14] The angle of attack range represents the variation (uncertainty) in launch and flightpath angle of the cones from various firings done nominally at zero angle of attack. For these test conditions the flow is laminar; viscous-inviscid interaction is small; and the temperature in the viscous layer is sufficiently high to cause dissociation of the air. Drag owing to friction and pressure is about the same magnitude, so comparisons of the data with integrated pressures and skin friction from the computations provide a sensitive measure of how well the code predicts skin friction in a high-speed boundary layer. The favorable comparison with the computations performed by A. W. Strawa serves to illustrate that the code can predict drag in this chemically reacting flow field. More discussion on this experiment and its results are presented in Ref. 15.

2.5 Verification Experiments

Verification experiments provide the final validation of the codes. As such they require flow-field and surface measurements over a range of conditions and in sufficient detail to ensure that the flow physics is properly represented. The following example illustrates this category of experiment.

The improved turbulence model shown previously has recently been introduced into a transonic Navier-Stokes code and compared with data from an airfoil section. The airfoil was mounted in a specially designed test section with solid walls. Boundary-layer suction was applied upstream of the airfoil on the sidewalls to minimize interference. To further minimize wall interference, the upper and lower walls were contoured to streamline shapes that were predetermined by computation to account for the presence of the model, which further minimized interference. Tests[16] were performed at chord Reynolds number of 6×10^6 and angle of attack and Mach number were varied over a range sufficient to produce transonic flow covering weak and strong shock-wave/boundary-layer interaction and attendant displacement effects. The boundary layer was tripped on the upper and lower model surface to ensure turbulent flow beyond 7% chord. Model pressures, wall-boundary shapes and pressures, total drag, lift, and flow-field and wake velocities from an LDA system were documented. A data base of this type with minimal interference from a tunnel with solid walls provides an ideal basis for evaluating the development of codes for the transonic speed range because the codes can include wall-boundary conditions more precisely than interference corrections can be made to the data sets.

An example of some of the comparisons is shown in Fig. 6. At present the code does not include the solid wall-boundary conditions, but a preliminary assessment using these benchmark data indicates that the code provides very good simulation for the strong interaction cases when the improved turbulence model developed by Johnson and King[12] is employed. Results of the comparisons for one strong interaction case (where separation occurred at the trailing edge) are shown. The airfoil pressures, flow field velocities at constant heights above the model, and a wake profile at the trailing edge are compared with computations using two different turbulence models, a two-equation model,[17] and the Johnson-King model. The comparison shows that the computations using the improved turbulence model simulate the measurements very well. It is important to emphasize that this conclusion could not have been drawn without the complete data set composed of total drag, lift, boundary conditions and flow-field surveys. (See Ref. 16 for further discussion.)

3. MEASUREMENT REQUIREMENTS

3.1 Completeness

Each of the types of experiment discussed previously requires specific information that will enable a critical assessment of the code's capabilities at each stage of its development. Some examples of these measurements and the test conditions where they are needed are listed in Fig. 7 taken from Ref. 4. In these examples the measurements are representative and are germane to the development of Reynolds-averaged Navier-Stokes codes for fully developed turbulent flow.

Building block experiments must provide the data required for phenomenological understanding and/or modeling guidance and enable a critical test of the research code's ability to simulate important aerodynamic flows (e.g., shock-induced separation). Surface variables and flow-field variables, including turbulence data, are essential measurements. For the turbulence modeling problem, flow physics experiments and full numerical simulation of the Navier-Stokes equations carried out for simple flows at incompressible and compressible conditions can be very helpful in providing fundamental understanding and guidance of statistical modeling. But the flow modeling data must be obtained at representative flight Mach and Reynolds numbers where the codes are to be applied to ensure that the physics is modeled adequately.

Benchmark experiments must provide the parametric measurements necessary to calibrate or verify pilot code development. Surface and flow-field data at critical locations are the essential information since the objective of verification is to ensure that the code represents the correct physics or for calibration to ensure that the code adequately predicts some particular flow quantities. In order to clearly identify the applicable range of the code, parametric testing over as wide a range of flight Mach and Reynolds numbers is necessary. Experiments at extremes in such conditions are now often limited by instrumentation and facility development, as in hypersonic or high Reynolds number regimes.

Design experiments at the final stage provide the optimal configuration data necessary for performance evaluation and the experiments should be carried out as close to flight conditions as practical. CFD is expected to expedite the execution of these by eliminating the need for fine increments in parametric variations, by helping to resolve anomalous data sets, and by extrapolating the design performance data to flight conditions when facilities are unable to achieve them.

For each category of experiment careful measurements of boundary conditions are required because they may influence the flow field around test models. Moreover, they may be needed to initiate computations. Free-stream or initial conditions, wall-boundary physical location and necessary measurement variables, and precise model lines are examples of these measurement requirements.

3.2 Accuracy

Accuracy assessments for both computational procedures and experiments are essential. Otherwise there is no quantitative means for determining the limits and ranges of applicability for the codes. Uncertainty analysis is a well-established method for determining experimental data accuracy and should be a prerequisite for all levels of experiment used to develop CFD. It is useful during the planning and developmental phases of experiments, for evaluating data obtained with different instruments, and for comparing data from different experiments. (See Ref. 18 for more discussion on accuracy.)

Error estimates for test geometry dimensions, test operating and free-stream conditions, model and flow-field measured variables, and instrumentation should all be specified and the method used documented sufficiently to allow independent assessment.

Reliance on single experiments or measurement procedures for code validation purposes should be viewed with caution because of the current limitations of facilities and instrumentation needed to accomplish validation. (These limitations are especially present in hypersonic experiments.) Therefore, redundant measurement techniques and similar experiments performed in more than one facility may be required. In every case, careful substantiation and specification of experimental accuracy limits is crucial.

4. WIND TUNNEL REQUIREMENTS

The requirements for test facilities used to validate CFD were discussed in Ref. 4. The most important of these requirements are: (1) versatility, along with well-defined test and boundary conditions;

(2) appropriate scale and speed range; (3) accessibility of nonintrusive instrumentation; (4) provision for high-speed data systems; and (5) dedication of use to verification-experimentation.

5. FUTURE PROSPECTS

During the past year NASA has embarked on a comprehensive CFD validation program. Coordinated experimental and computational studies have been initiated at each of the NASA OAST Research Centers by teams comprised of computational and experimental research scientists.

At the Ames Research Center, the major thrust of the activity is supporting the development of codes employing the Reynolds-averaged Navier-Stokes equations. Data from in-house and university-funded experiments are expected to be published in the public domain and made available to other computational fluid dynamicists carrying out CFD validation. Some examples of the benchmark experiments that illustrate the scope of the program follow.

Turn-around-duct experiment: The experiment shown in Fig. 8 is under way to help guide the development of a 3-D incompressible Navier-Stokes code (INS-3D),[19] including its turbulence model. The application of the code is to study the axisymmetric flow in the Space Shuttle Main Engine turn-around-duct. The geometry consists of a constant area aspect-ratio 10 duct which turns an air flow, at high Reynolds number, through a 180° bend. The bend radius is equal to the duct height and some separation of the flow occurs on the inner corner wall near the end of the turn. A planer rather than axisymmetric geometry was chosen to permit access for nonintrusive laser instrumentation. Surface pressures, skin friction, velocity profiles, and Reynolds-averaged normal- and shear-stress profiles are being documented for a range of Reynolds numbers. Companion computations for this geometry are planned to verify the range of applicability of the code and various turbulence modeling approximations.

Transonic Wing and Wing-Body Experiments: Transonic experiments have been performed and others are now under way to guide the development of a transonic Navier-Stokes code (TNS).[20] The approach to the experiments is unique in that they are deliberately performed in solid-wall wind tunnel facilities. This test technique was chosen because the code can use the tunnel walls as boundary conditions and eliminate uncertain corrections to the data for wall interference. Once the code has been validated, it can confidently be used for free-air computations by appropriately changing the boundary conditions.

The first phase of the experimental activity was conducted several years ago.[21] A low-aspect ratio wing with a NACA 0012 profile section in the stream direction was mounted on the sidewall of a high Reynolds number facility and tested over a range of Mach numbers from 0.5 to 0.84, Reynolds numbers from 2×10^6 to 8×10^6, and angle of attack from 0° to 2°. Solid, straight, wind tunnel walls, sloped to correct for "tunnel empty" boundary-layer growth and instrumented with pressure taps were employed. Inviscid, no-slip boundary conditions along all walls were assumed for the computations, but that may not be entirely adequate as discussed later. Model pressures, wall-boundary pressures, surface oil flows, and limited velocity profiles obtained with an LDA were documented. Thus far, the data have been used by computational groups at the NASA Ames and Langley research centers.

The Ames group used comparisons with the data at the lower Mach numbers and angles of attack to establish confidence in the zonal techniques employed in the TNS code. At the higher Mach numbers and angles of attack they used comparisons with the data to sort out grid refinement and turbulence modeling issues.[22] Results of the comparisons with the high Mach number data were satisfactory only in the sense that they reproduced many of the complex flow features, but it could not be determined whether the turbulence model was solely responsible for the differences with the data. Recently the Langley group showed the importance of including the viscous, no-slip condition along the mounting wall. Their results, taken from Ref. 23, are shown in Fig. 9. A perspective view of the surface streamlines shows the influence of the viscous sidewall. The streamline patterns, especially in the side-wall region, are remarkably similar to the experimental oil flows. The comparison of computed and measured pressures on the tunnel walls and the wing shows good agreement except on the wing at the span location where a strong shock forms. These differences reflect the inadequacy of the turbulence model. Efforts are under way to improve the modeling.

A follow-on experiment conducted in a solid wall transonic test section is under way. This experiment eliminates some of the shortcomings of the one previously described: the model and the test facility are larger; the Reynolds number range can be extended; a more realistic, low-aspect, high-taper-ratio wing geometry is being used; and the sidewall boundary layer will be measured. Moreover, provision is made to test a wing-body combination. A photograph of the wing-body model mounted in the tunnel is shown in Fig. 10. The measurements to be made are also listed. The half-model body is mounted on the sidewall. The TNS computations will employ no-slip boundary conditions along the mounting wall and slip conditions on the other walls. Preliminary wing-alone and wall pressure data have been obtained recently.

3-D Supersonic Shock Interaction Experiments--Several experiments are under way to study the interaction of shock waves with turbulent boundary layers. Reference 24 presented data for a series of asymmetric separated flows on an ogive-cylinder-flare model. Shock unsteadiness was a major issue in the experiments and the reader is referred to Ref. 24 for further discussion.

Another series of experiments on a swept-wedge plate are being conducted by Settles. Figure 11 shows the geometry, test conditions and some recently published measurements.[25] The surface skin friction on the plate has been measured and compared with a computation solving the Reynolds-averaged Navier-Stokes

equations. A two-equation turbulence model with wall functions was employed and the results compare well with the data. In Ref. 25, comparisons with data for other wedge angles using both two-equation and algebraic turbulence models show that turbulence modeling is not critical to resolving the structure physics of these flows, probably because they are dominated by inviscid effects. However, the effects of viscosity are essential to reproducing the structures, and Euler codes probably cannot represent these flows adequately.

Hypersonic All-Body Experiment: The experiment depicted in Fig. 12 is being performed to guide the development of a 3-D Parabolized Navier-Stokes code[26] that uses up-wind differencing to obtain sharp shocks. The geometry is a 75° swept delta with an elliptical cross section. At the two-thirds body length station, an expansion surface forms the upper part on the model. Some recent experimental results taken from Ref. 27 are also shown in Fig. 11. Spanwise pressure distributions for 15° angle of attack and M = 10.3 over the forebody region ahead of the expansion are shown compared with the computations for a single streamwise station, assuming either laminar or turbulent flow from the leading edge. The agreement is good with either assumption because viscous-inviscid interaction has a small influence on the pressure distribution at this Reynolds number. When the remaining measurements of heating and velocity profiles are completed, other validation issues such as aerodynamic heating will be addressed.

6. CONCLUDING REMARKS

Experiments play a critical role in the development of CFD. They provide phenomenological data to help understand the physics of complex flows; they provide guidance in the modeling process where the physics is unknown or so complex that computational procedures are not practical; and ultimately they provide the verification necessary to establish the limits of applicability to various aerodynamic flows.

Four types of experiments supporting the development of CFD were described: (1) flow physics experiments, (2) flow modeling experiments, (3) calibration experiments, and (4) validation experiments. The first two types were broadly categorized as building block experiments. They provide the phenomenological and modeling data required for research code development. An additional new technological advance contributing to the building block data base is full- and large-eddy simulations and computational chemistry. The building block data base is more detailed and often requires sophisticated instrumentation and test techniques. The second two types were broadly categorized as benchmark experiments. These experiments provide the data needed to identify the accuracy and limitations on the code's ability to compute complex aerodynamic flows. The data requirements differ from the building block experiments in the sense that phenomenological and modeling issues are not investigated in detail.

The categories of experiments and corresponding measurements lead to specific requirements for facilities used for validation. Versatility, appropriate scale and speed range, accessibility for nonintrusive instrumentation, computerized data systems, and dedicated use for verification are the important requirements.

A synergistic, comprehensive approach to validation was introduced. A program is under way to provide validation experiments that can guide the development of advanced computational procedures for application to complex flows. Both computational and experimental fluid dynamicists are focusing on key aerodynamic problems whose solutions are paced by the lack of adequate understanding of the flow physics and modeling and by the lack of adequate validation data to verify code development. The major challenge for success of the program depends on timely accomplishment of the experiments, development and implementation of new instrumentation, and development of appropriate high Reynolds number and high Mach number, high-enthalpy facilities.

REFERENCES

1. Bradley, R. G., Bhateley, I. C., and Howell, G. A., "Computational Fluid Dynamics - Transition to Design Applications," Supercomputing in Aerospace, NASA Conference, Publication 2454, pp. 69-767, Mar. 1987.

2. Current Capabilities and Future Directions in Computational Fluid Dynamics, National Research Council, National Academy Press, Washington, D.C., 1986.

3. Bradley, R. G., "CFD Validation Philosophy," Paper No. 1, AGARD Symposium on Validation of Computational Fluid Dynamics, May 1988, Lisbon, Portugal.

4. Marvin, J. G., "Wind Tunnel Requirements for Computational Fluid Dynamics Code Verification," Paper 34, AGARD Symposium on Aerodynamic Data Accuracy and Quality, Requirements and Capabilities in Wind Tunnel Testing, Naples, Italy, Sep. 28-Oct. 1, 1987.

5. Moin, P. and Kim, J., "The Structure of the Vorticity Field in Turbulent Channel Flow, Part I - Analysis of Instantaneous Fields and Statistical Correlations," J. Fluid Mechanics, Vol. 155, p. 441, 1985.

6. Cooper, D. M., Jaffe, R. L., and Arnold, J. O., "Computational Chemistry and Aeroassisted Orbital Transfer Vehicles," Journal of Spacecraft and Rockets, Vol. 22, No. 1, p. 60, Jan.-Feb. 1985.

7. Kline, S. J., and Robinson, S. K., "Turbulence-Producing Coherent Structures in the Turbulent Boundary Layer: Progress of a Cooperative Evaluation," to be presented at the Zaric Memorial International Seminar on Wall Turbulence, Dubrovnik, Yugoslavia, May 1988.

8. Spalart, P. R., "Direct Simulation of a Turbulent Boundary Layer up to Rtheta = 1410," NASA TM 89407, 1986.

9. Robinson, S. K., "Space-Time Correlation Measurements in a Compressible Turbulent Boundary Layer," AIAA Paper 86-1130, Atlanta, GA, May 1986.

10. Marvin, J. G., "Turbulence Modeling for Computational Aerodynamics," AIAA Journal, Vol. 21, No. 7, pp. 941-955, Jul. 1983.

11. Bachalo, W. D., and Johnson, D. A., "An Investigation of Transonic Turbulent Boundary Layer Separation Generated on an Axisymmetric Flow Model," AIAA Paper 79-1479, Williamsburg, VA, 1979.

12. Johnson, D. A., and King, L. S., "Transonic Separated Flow Predictions Based on a Mathematically Simple, Nonequilibrium Turbulence Closure Model," IUTAM Symp. on Turbulent Shear Layer/Shock Wave Interaction, Paris, France, Sep. 1985, NASA TM 86826, Oct. 1985.

13. Prabhu, D. K., Tannehill, J. C., and Marvin, J. G., "A New PNS Code for Three-Dimensional Chemically Reacting Flows," (U), AIAA 87-1472, Honolulu, HI, Jun. 1987.

14. Intrieri, P. F., Kirk, B. K., Chapman, G. T., and Terry, J. E., "Ballistic Range Tests of Ablating and Nonablating Slender Cones," (U), AIAA Journal, Vol. 8, No. 3, pp. 558-564, Mar. 1970.

15. Deiwert, G. S., Strawa, A. W., Sharma, S. P., and Park, C., "Experimental Program for Real Gas Flow Codes at NASA Ames Research Center," Paper No. 21, AGARD Symposium on Validation of Computational Fluid Dynamics, Lisbon, Portugal, May 1988.

16. Mateer, G. G., Seegmiller, H. L., Coakley, T. J., and Hand, L. A., "An Experimental Investigation of a Supercritical Airfoil at Transonic Speeds," AIAA Paper 87-1241, Honolulu, HI, Jun. 1987.

17. Coakley, T. J., "Numerical Simulation of Viscous Transonic Airfoil Flows," AIAA Paper 87-0416, Jan. 1987.

18. Moffatt, R. J., "Contributions to the Theory of Uncertainty Analysis for Single-Sample Experiments," 1980-81 AFOSR/HTTM-Stanford Conference on Complex Turbulent Flows, Vol. 1 Objectives, Evaluation of Data, Specification of Tests Cases, Discussion, and Position Papers, edited by S. J. Kline, B. J. Cantwell, and G. M. Lilley.

19. Chang, J. L. C., and Kwak, D., "A Three-Dimensional Incompressible Flow Simulation Method and Its Application to the Space Shuttle Maine Engine, Part II--Turbulent Flow," AIAA Paper 85-1670, Reno, NV, Jan. 1984.

20. Holst, T. L., Kaynak, U., Gundy, K. L., Thomas, S. D., Flores, J., and Chaderjian, N. M., "Numerical Solution of Transonic Wing Flows Using an Euler Navier-Stokes Zonal Approach," AIAA Paper 85-1640, Cincinnati, Jul. 1985.

21. Lockman, W. K., and Seegmiller, H. L., "An Experimental Investigation of the Subcritical and Supercritical Flow About a Swept Semispan Wing," NASA TM-84367, Jun. 1983.

22. Kaynak, U., Flores, J., "Advances in the Computation of Transonic Separated Flows over Finite Wings," AIAA Paper 87-1195, Honolulu, HI, Jun. 1987.

23. Vasta, V. N., and Wedan, B. W., "Navier-Stokes Solutions for Transonic Flow Over a Wing Mounted in a Tunnel," AIAA Paper 88-0102, Reno NV, Jan. 1988.

24. Brown, J. D., Brown, J. L., Kussoy, M. I., Holt, M., and Horstman, C. C., "Two-Component LDV Investigation of 3-Dimensional Shock/Turbulent Boundary Layer Interactions," AIAA Paper 87-0553, Reno, NV, Jan. 1987.

25. Kim, K. S., and Settles, G. S., "Skin Friction Measurements by Laser Interferometry in Swept Shock Wave/Turbulent Boundary-Layer Interactions."

26. Lawrence, S. L., Chaussee, D. S., and Tannehill, J. C. "Application of an Upwind Algorithm to the PNS Equations," (U), AIAA Paper 87-1112, Honolulu, HI, Jun. 1987.

27. Lockman, W. K., Cleary, J. W., and Lawrence, S. L., "Flow Visualization and Pressure Distributions for an All-Body Hypersonic Aircraft," (U), Paper No. 53, Fourth National Aero Space Plane Technology Symposium, Monterey, CA, Feb. 1988.

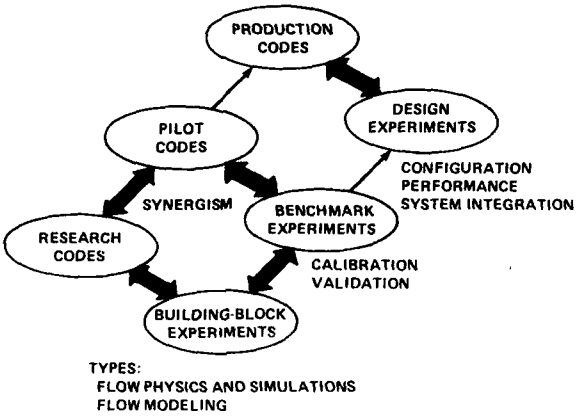


Figure 1. The role of experiment in developing CFD.

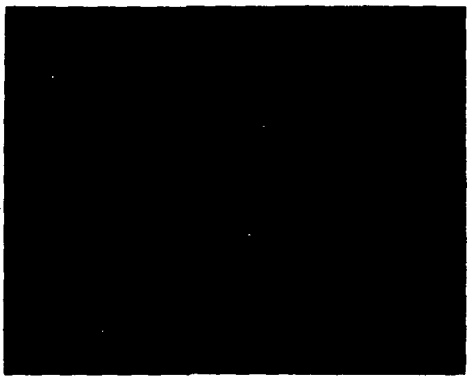


Figure 2. Turbulent flow-physics obtained from a full simulation of the Navier-Stokes equations. $M_\infty = 0$, $Re_\theta = 670$.

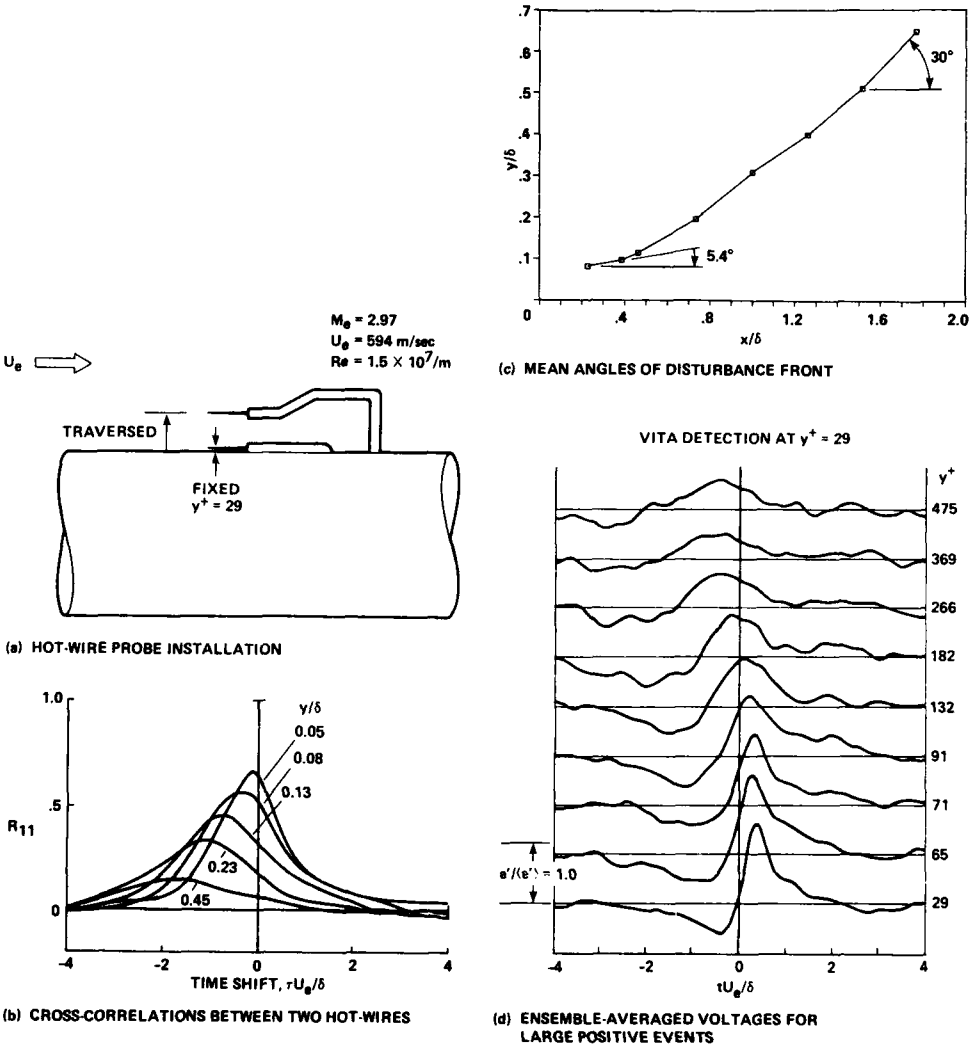


Figure 3. Turbulent flow-physics obtained from the experiment of Ref. 9 employing multiple hot-wires. M_∞ = 3; Re = 1.5 × 10^7/m.

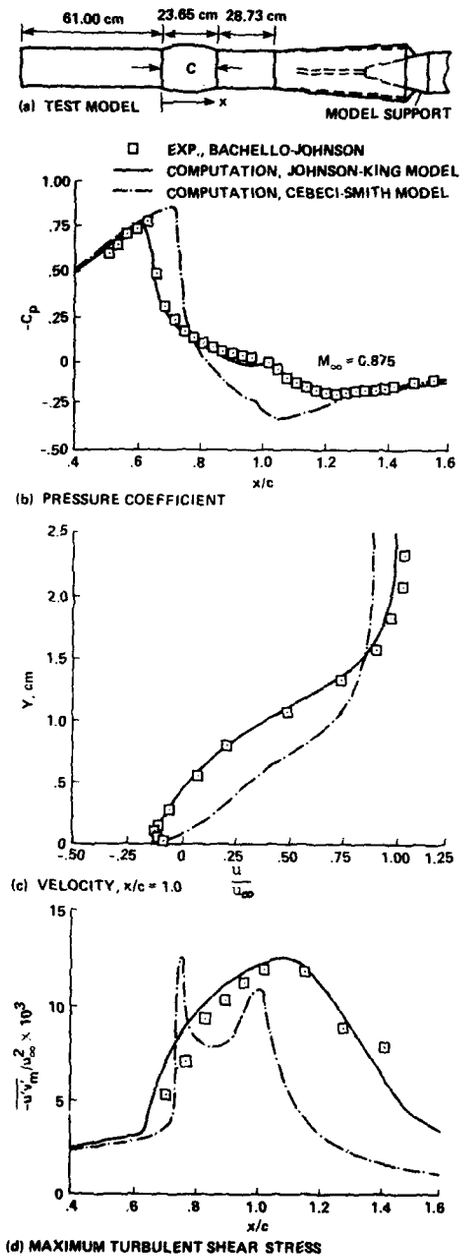
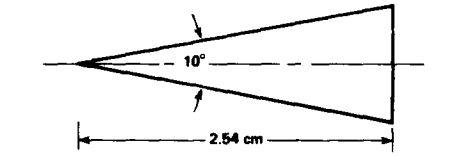
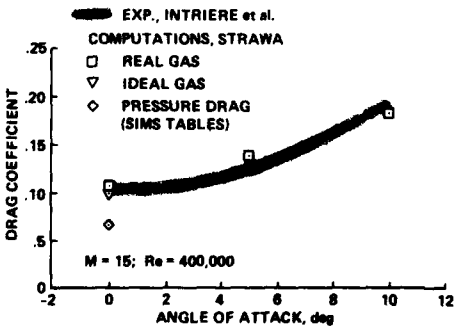


Figure 4. A flow-modeling experiment used to develop an improved turbulence model.

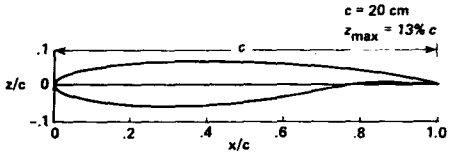


(a) GEOMETRY

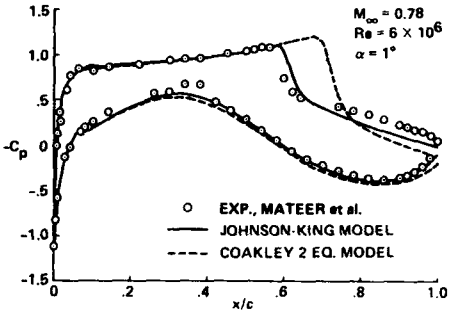


(b) DRAG DATA FOR 10° CONE

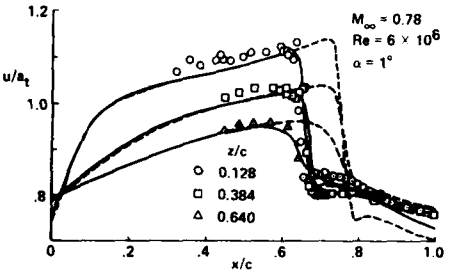
Figure 5. A calibration experiment used to evaluate a real gas chemical model in a parabolized Navier-Stokes code. 10° cone; M_∞ = 15; and Re_L = 400,000.



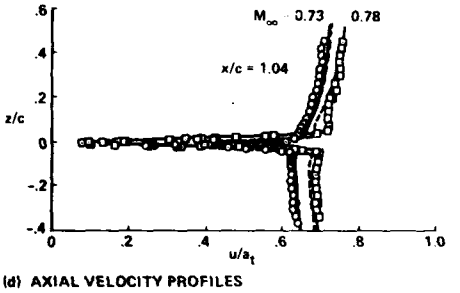
(a) TEST MODEL – MBB VA-2 AIRFOIL
TRAILING EDGE THICKNESS = 0.522% CHORD



(b) PRESSURE COEFFICIENT



(c) FLOW FIELD VELOCITIES
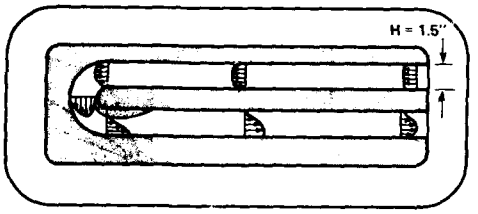


(d) AXIAL VELOCITY PROFILES

Figure 6. A benchmark airfoil experiment used to verify development of an improved turbulence model.

EXPERIMENT	MEASUREMENTS (REPRESENTATIVE FOR TURBULENCE MODELING)	TEST CONDITIONS
BUILDING BLOCK (PHENOMENOLOGICAL)	SURFACE QUANTITIES INCLUDE TRANSITION PTS. FLOW FIELD QUANTITIES TURBULENCE INDIVIDUAL STRESSES CORRELATION LENGTHS STRUCTURE BOUNDARY CONDITIONS FREE STREAM TUNNEL WALLS MODEL SHAPE	REPRESENTATIVE FLIGHT M_∞, Re_∞
BENCHMARK (PARAMETRICAL)	SURFACE QUANTITIES INCLUDE TRANSITION PTS. FLOW FIELD QUANTITIES (SELECTED LOCATIONS) BOUNDARY CONDITIONS (SEE ABOVE)	VARY M_∞, Re, α OVER FLIGHT RANGES
DESIGN (CONFIGURATIONAL)	DRAG, LIFT, MOMENTS, HEAT LOADS, SHEAR LOADS BOUNDARY CONDITIONS (SEE ABOVE)	AS CLOSE TO FLIGHT M_∞, Re, α AS PRACTICAL

Figure 7. Experimental requirements.



(a) FLOW FIELD AND GEOMETRY

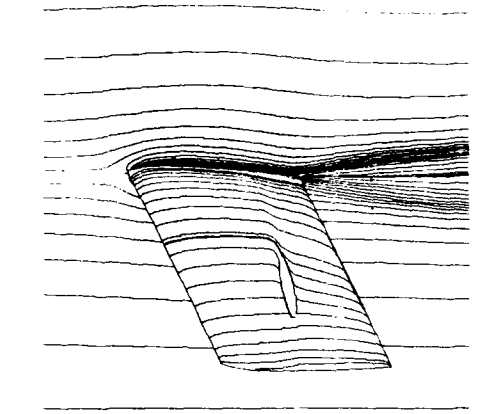
SURFACE: p_w, c_f, OIL FLOW
FLOW FIELD: U, V, $\overline{u'}$, $\overline{v'}$, $\overline{u'v'}$
$RE_H = 0.1 - 3.0 \times 10^6$, M = 0.1 - 0.3

(b) MEASUREMENTS AND TEST CONDITIONS

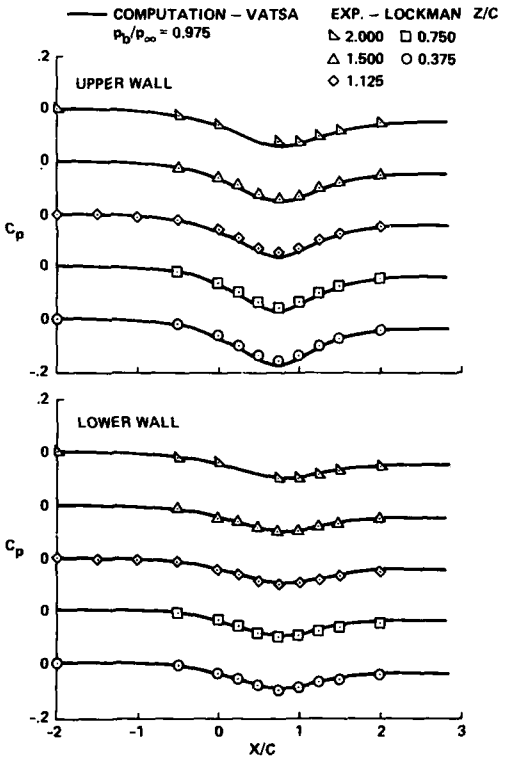


(c) VIEW SHOWING LASER SKIN-FRICTION INTERFEROMETER

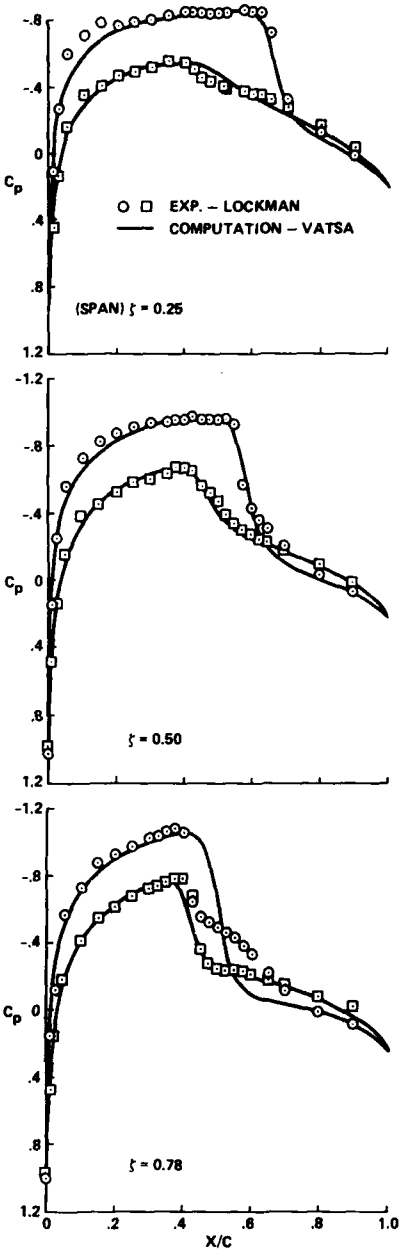
Figure 8. 2-D turn-around-duct experiment.



(a) PERSPECTIVE VIEW OF COMPUTED STREAMLINES ON WING AND WALL



(b) TUNNEL WALL PRESSURE COMPARISONS



(c) WING PRESSURE COMPARISONS

Figure 9. Comparison of Reynolds-averaged Navier-Stokes computations and data from a verification experiment. M_∞ = 0.826, Re = 8 × 10^6, α = 2°, A/R = 3.

GEOMETRY

- OGIVE-CYLINDER HALF-BODY
- WING
  - NACA 64A008 STREAMWISE SECTION
  - ASPECT RATIO = 3.2
  - TAPER RATIO = 0.25
  - L.E. SWEEP ANGLE = 36.9°

TEST CONDITIONS

- M_∞ = 0.5 TO 0.8
- $Re_{\infty,\bar{c}}$ = 1 × 10^6 TO 10 × 10^6
- α = 0° TO 15°

MEASUREMENTS

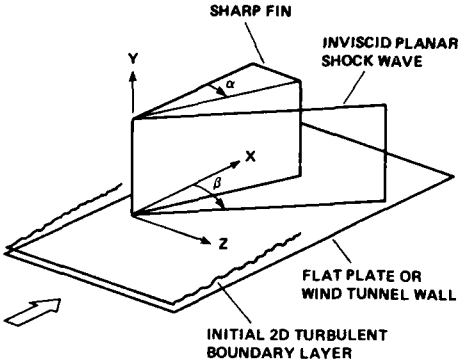
- FLOW VISUALIZATION
  - SURFACE (OIL FLOW)
  - FLOW FIELD (VAPOR SCREEN)
- SURFACE PRESSURES (WING, TUNNEL WALLS)
- MEAN VELOCITY – FLOW FIELD (LDV AND PROBES)

(a) GEOMETRY, TEST CONDITIONS AND MEASUREMENTS



(b) PHOTO OF MODEL MOUNTED IN TUNNEL

Figure 10. A low-aspect-ratio wing-body experiment.



PENN STATE EXPERIMENT:

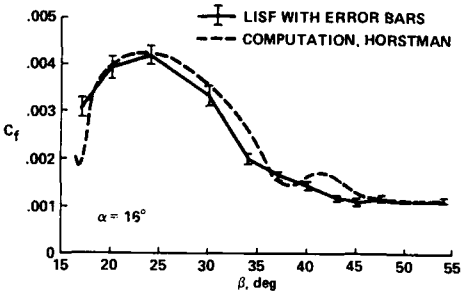
$M_\infty \approx 2.4 - 4$, $\alpha = 4 - 22°$, $Re_x \approx 10 \times 10^6$

MEASUREMENTS

SURFACE: OIL FLOW, p_w, c_f

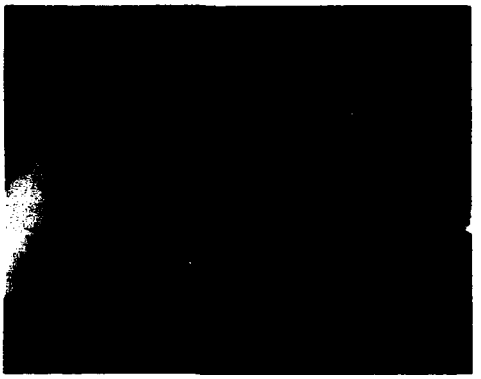
FLOW FIELD: VAPOR SCREEN, p_{t_2}, YAW ANGLE

(a) FLOW GEOMETRY

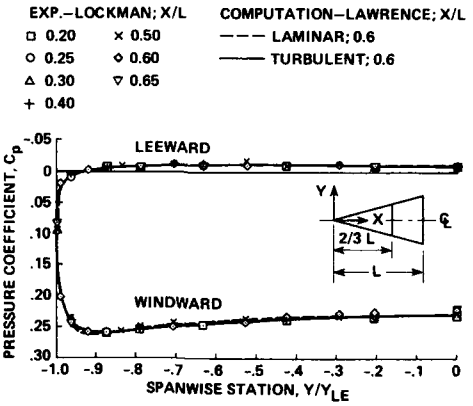


(b) SKIN FRICTION ON THE PLATE, x = 3.5 in.

Figure 11. A 3-D shock-wave boundary layer interaction experiment.



(a) ALL-BODY HYPERSONIC AIRCRAFT MODEL IN NASA/ AMES 3.5-ft HWT; LENGTH = 3 ft



(b) SPANWISE PRESSURE DISTRIBUTIONS FOR FOREBODY $\alpha = 15°$; $M_\infty = 10.3$; $Re_{\infty,L} = 5 \times 10^6$

Figure 12. A hypersonic all-body experiment.

NUMERICAL ACCURACY ASSESSMENT

J.W. Boerstoel
Senior Research Scientist
National Aerospace Laboratory NLR
Anthony Fokkerweg 2
1059 CM AMSTERDAM; The Netherlands

Summary

The first sections are devoted to putting the topic numerical accuracy assessment within a framework. Hence, the purpose of numerical flow simulations is first formulated. This formulation concerns the classes of aeronautical configurations (boundaries), the desired flow physics (flow equations and their properties), the classes of flow conditions on flow boundaries (boundary conditions), and the initial flow conditions. Next, accuracy and economical performance requirements are defined: the final numerical flow-simulation results of interest should have a guaranteed accuracy, and be produced for an acceptable FLOP-price.

Within this context, the validation of numerical processes with respect to the well-known topics of consistency, stability, and convergence when the mesh is refined must be done by numerical experimentation because theory gives only partial answers. This requires careful design of test cases for numerical experimentation.

Finally, the results of a few recent evaluation exercises of numerical experiments with a large number of codes on a few test cases are summarized.

1. Introduction

The purpose of this article is a summary of the state-of-art about the topic Numerical Accuracy Assessment.

To keep the scope of this article limited, we will restrict ourselves to external transonic (and subsonic) aerodynamics for two- and three-dimensional aeronautical applications, with an emphasis on inviscid calculations. Internal aerodynamics and hypersonic flows are thus not considered, and Navier-Stokes flows are only briefly mentioned.

In May 1985, AGARD issued the report AR-211 "Test Cases for Inviscid Flow Field Methods" [1]. This report was prepared in an effort to define test cases that may be used to validate Euler-flow calculation methods. Results of several computer codes were collected. These results were compared to each other, and best numerical solutions were identified for aerofoilflow, delta-wing flows, and the flow about an isolated transport aircraft wing.

In the open literature, other test cases are also defined. We will consider two of them,
1. the AIAA Euler Solvers Workshop survey by Margason [2], and
2. the Viscous Transonic Airfoil Workshop Compendium of Results by Holst [3].

Another interesting survey report is that of Woodward and Colella for unsteady flows with strong shocks and strong shears layers (Mach numbers larger than, say 3), [4]. This survey is of interest for hypersonic-flow test cases, and is thus not further discussed here.

2. Scope of CFD goals

Numerical methods for aeronautical CFD applications are expected to satisfy a number of primary requirements. These concern,
- the aeronautical configurations of interest,
- the physics in the flow domain, and
- the physical boundary and initial conditions to be satisfied.

The aeronautical configurations that are nowadays of interest in CFD research cover a wide range. Examples are simple configurations, like
1. aerofoils, isolated wings, like the ONERA M6 wing, delta wings, and wing-body configurations.
2. complex, full 3D transport aircraft, including tail planes and propulsion systems, various types of fighter aircraft with delta wings, missiles, etc.

The configurations define the flow-domain geometry of interest. CFD codes are usually required to handle classes of configurations, and numerical simulation methods should thus be able to accept each configuration of such classes as input.

The numerical simulation of the physics in the flow domain requires dealing with the question which physical laws and phenomena should be numerically modeled and which can be neglected. It will in general be useful to compile lists of physical laws and phenomena that should be appropriately modeled. The list below is expected to cover many laws and phenomena of interest in current CFD.
1. Steady/time-averaged/periodic/time-dependent flows.
2. Three-dimensional (two-dimensional) flows.
3. Conservation of mass, momentum, energy. Equations of state, shear-stress/rate-of-strain relations, heat conduction laws, etc.
4. In special cases, conservation of entropy, enthalpy, and/or vorticity.
5. Reversibility of flow direction and of physical processes when the flow is smooth.
6. Normal and oblique shock waves as discontinuity surfaces, or as thin layers.
7. Contact discontinuities (surfaces across which the pressure is continuous, but the density and/or the velocity vector are discontinuous) as discontinity surfaces, or as thin layers with some internal structure. Shear layers.
8. Incompressible/subsonic/transonic/supersonic flows.
9. Inviscid separation. Inviscid production of entropy, vorticity and turbulence. Stability of shear layers and inviscid vortices.
10. Viscous dissipation, heat conduction.
11. Viscous boundary layers and wakes. Viscous vortices.
12. Viscous separation, viscous production of entropy, vorticity and turbulence. Stability of viscous shear

layers.
13. Turbulence modeling. Law of the wall, law of wake, etc.

In individual studies/applications, it will usually be necessary to adapt this example list, and to remodel these requirements into forms involving measurable data.

The desired flow physics must be modeled into a discrete equation system, which discrete solutions describe the desired flow phenomena on the flow domain. Without boundary and initial conditions, this equation system has an infinity of solutions. Boundary and initial conditions should introduce auxiliary equations such that a unique discrete solution is picked out.

A few examples of physical formulations of boundary conditions are listed below.

1. Free-stream conditions (M_∞, α, β, S_∞, H_∞, etc) describing the asymptotic (time-dependent or time-independent) behaviour of a flow far from a configuration.
2. Full-slip/no-slip conditions on solid surfaces. Prescribed heat fluxes through solid surfaces. Solid surfaces steady or moving.
3. Over inlet/outlet surfaces, distributions of appropriate combinations of variables (possibly also as a function of time).
4. Flow conditions at edges of solid surfaces.

This list is by no means exhaustive. In individual studies and application, similar lists of boundary conditions must be compiled as a starting point for boundary-condition formulations.

Initial flow conditions on a given flow domain are required in time-dependent or iterative processes.

Numerical flow simulations should also satisfy certain performance requirements. These concern the accuracy of flow-simulation results and the economical performance of numerical simulations.

Final results of numerical flow simulations should have a certain minimum (engineering) accuracy. Such accuracy levels should be formulated so that they directly reflect engineering needs. It is in practice usually easy to specify precise limits that should be ideally met. A few examples of typical accuracy requirements are the next ones.

1. Calculated (for steady flows: converged) flow variables should at most have an error, on configuration surfaces, of, say,
   ½% for ρ/ρ_∞ = scaled density
   $c_p = (p - p_\infty)/p_\infty$ = pressure coefficient,
   M = Mach number,
   S/S_∞ = scaled entropy, etc.
2. Force and moment coefficients, per unit area and per unit length, and made dimensionless with free-stream dynamic pressure, should have an error of at most ½%.
3. Drag coefficient should have an error of at most 1 count (10^{-4} in C_D).

It should be observed that these requirement are formulated independent of mesh resolutions and numbers of (time) iteration steps, because it is the accuracy of a final complete flow-simulation result that is of interest in engineering practice.

The economical performance requirements concern the computational effort required to obtain a final numerical result of a *flow simulation*,

- in which, for desired classes of configurations, all required *physical laws* and phenomena are correctly simulated,
- in which all boundary (and if applicable, initial) conditions are satisfied, and
- that meets the engineering accuracy requirements.

Such results should be produced in acceptable amount of FLOPs (floating point operations). Note that this requirement is formulated in a computer-independent way, and also independent of meshes and iterations.

It is in practice useful to monitor and analyze the error level during calculations, and to measure also performance characteristics of CFD codes that are helpful in an analysis of economical performance requirements for complete flow-simulation results. Error levels may be monitored, for example, by inspecting

1. rms and max norms of $\partial\rho/\partial t$, $\partial\rho q/\partial t$, $\partial E/\partial t$, $\partial H/\partial t$, $\partial S/\partial t$, etc. as a function of (time) iteration step, and
2. dimensionless force and moment coefficients, and numbers of supersonic points as a function of (time) iteration step.

A quantity that sometimes is used to give some idea of the operational efficiency of a CFD code is the average number of FLOPs per grid point and per (time) iteration step.

CFD, limited to the areas mentioned in the introduction, is concerned with the construction of numerical models of physical processes and phenomena in flows around given aeronautical configurations, and the validation of these numerical models by analysis, numerical testing, and verification with physical test results.

3. Validation techniques

Starting from lists of requirements as formulated in the previous section, the general approach to the construction of algorithms for the numerical simulation of Euler and Navier-Stokes flows consists of five steps. First, the goals must be reformulated in numerical mathematical terms. Hence,

1. the classes of aeronautical configurations must be numerically defined,
2. computation grids in the flow domains around these configurations must be defined,
3. on these grids, discrete conservation equations must be designed such that discrete solutions of these conservation equations have desired physical properties,
4. initial conditions must be defined on these grids, and
5. on the boundaries of the flow domain, discrete time-(in)dependent boundary conditions must be defined in accordance with desired physical behaviour on the boundaries.

Moreover, the equation system formed by the discrete conservation equations, initial conditions, and boundary conditions should have a unique solution which time-dependent behaviour is stable in some useful sense.

For the numerical analyst, there are only a few strategies to verify the validity of CFD codes designed along such lines. First of all, the numerical algorithms and the data structures mapped into the computer codes should be checked to have the physical properties that can be analyzed with paper and

pencil, and a study should be made of the issues of consistency, convergence and stability. Next, a catalog of test cases should be designed, consisting of typical examples from the classes aerodynamic configurations of interest, with flow conditions exhibiting all flow phenomena of interest, and with flow-calculation results that may be used to check the accuracy and economical performance of the CFD codes by numerical experimentation. This catalog should be next used as a benchmark for code validation.

At the start of the activities of the AGARD working group that issued the test-cases report for inviscid flow-field methods [1], such a benchmark was designed. This benchmark consisted of simple aeronautical configurations for 2D and 3D flows, and specified free-stream conditions and boundary conditions. Steady inviscid Euler-flows should be computed. Initially, it was hoped that exact test cases could also be included. Here exact means that geometries and flow data should be mathematically precisely defined, without numerical approximation. The working group found that there are in fact no exact test cases, which are not too simple. Hence, in practice, one has to rely completely on validation by numerical experimentation on a well-designed catalog of test cases, and on some analysis of the algorithms used.

4. Numerical methods

General approach

Starting from lists of requirements as discussed in section 2, the general approach to the numerical simulation is to reformulate these requirements as a discrete (initial-)boundary-value problem on a computation grid around the discrete configurations of the desired classes of configurations. These problems are subsequently solved for a given discrete configuration and discrete initial-boundary data. The next sections discuss a number of related topics.

Grid generation

The first step in numerical flow simulation is the construction of computation grids in the flow domains around the configurations of interest. During the last four years, grid-generation technology has rapidly undergone major advances. Many review articles and research papers may be found in the proceedings of two grid-generation conferences, see Thompson (ed.), [5], and Häuser and Taylor (ed.s), [6].

For complex aerodynamic configurations, there are now two approaches,

1. blocked grids, with an underlying block (or domain) decomposition of the flow domain, and
2. unstructured grids, with tetrahedra cells in 3D space.

For recent review papers, see Baker [7], and the three reviews by Thompson, Weatherill and Boerstoel in the Proceedings of [8].

It is now clear that the construction of grids around complex configurations is not a major problem anymore. This situation is different from that about four years ago, when grid generation was reported to be a major pacing item for progress in CFD, see AGARD Advisory Report 209, [9].

Discretisation of conservation equations

For each cell in a computation grid, algebraic equations are defined to simulate the conservation equations. These equations may (or may not) be considered discretisations of continuum equations. The number of published discretised forms of the conservation equations is so large, that a detailed discussion of them is out of scope. Instead, only a brief review of the most important numerical topics is presented.

Semi-discretisation (method of lines) is a construction technique that most authors in aeronautical CFD literature following to derive difference equations for the conservation equations. They first discretise the conservation equations in the spatial variables (x, y, z), and obtain then a system of coupled nonlinear ordinary differential equations of the form

$$d\bar{U}/dt = f(\bar{U}),$$

where $\bar{U}$ is a time-dependent grid function. Subsequently, this system is numerically integrated, together with numerical boundary conditions, with respect to time, by some implicit or explicit integration method.

The procedure is useful for the structuring of the stability analysis of the time(like) integration, and leads to simple procedures for the construction of free-stream- (or, uniform-flow-)consistent difference equations.

Spatial differencing alternatives. There are three major approaches in the spatial discretisation of conservation equations. They are

1. 2nd-order accurate, conservative central differencing, with explicitely-added blended 2nd-order and 4th-order dissipative divergence operators, and with shock capturing.
2. 2nd-order accurate, conservative upwind differencing, with either flux-vector or flux-difference splitting to create appropriate implicit numerical dissipation, and with shock capturing.
3. 2nd-order accurate, non-conservative upwind differencing, combined with characteristic theory, and with shock- and contact-discontinuity fitting. λ-schemes and split-coefficient methods are examples of this approach.

The latter two approaches are based on the application of concepts of characteristic theory. In flux-vector and flux-difference methods, characteristic theory is used to design difference schemes with steady-state solutions that are everywhere smooth except at shocks. Over shocks, the solutions have steep-gradients. The schemes also suppress unphysical expansion shocks at sonic surfaces, if the steady flow is accelerating in downstream direction over a sonic surface. The smoothness is created by implicit numerical viscosity. At shocks, this viscosity is suitably reduced or switched off.

Numerical or artificial viscosity is a concept to be connected with the construction of difference expressions for the convective divergences in the conservation expressions. These difference expressions are designed such that, outside shocks and contact discontinuities, numerical solutions for steady flows are smooth. This smoothness is enforced by adding to the central-difference forms of the convective divergences a discrete fourth-order dissipative divergence operator. For central-difference schemes, this

operator must be added explicitly. For upwind schemes, this operator is created by the upwinding, if there are characteristic speeds of *opposite sign*; the fourth-order dissipative operator is readily found if the upwind-difference expressions for the convective divergence are written as a sum of a central-difference expression plus an additional higher-order central-difference term.

The numerical modeling of C°-discontinuities (shock waves and contact discontinuities) requires special attention. It is well-known that the physical thickness of these discontinuities can be related to the Reynolds numbers in the flow as follows.

- Thickness of shock waves $= 0\ (Re^{-1})$, including viscous effects.
- Thickness of contact discontinuities $= 0\ (Re^{-\frac{1}{2}})$,

Hence, for Reynolds numbers common in aeronautical applications ($1 - 30 * 10^6$), the thickness of shock waves can probably always be put equal to zero. However, contact discontinuities should be modeled as thin layers of finite thickness if viscous effects are accounted for, because $O(Re^{-\frac{1}{2}})$ is then not negligeable.

The numerical treatment of C°-discontinuities can be based on two different approaches.

1. Differencing over C°-discontinuities is (effectively) avoided, and the conservation equations are replaced by their limiting forms over the discontinuities. These limiting forms are the Rankine-Hugoniot relations.
2. Differencing over C°-discontinuities is accepted, and the build-up of large errors in the conservation equations is prevented by using fully conservative difference schemes. Such schemes are shock-capturing. In this case, the discontinuities are usually smeared out over one or a few meshes, and the Rankine-Hugoniot relations are approximated over these few meshes by the discrete conservation equations.

Most authors in literature apply fully-conservative shock-capturing schemes, designed such that shocks have a width of a few meshes.

To achieve that C°-discontinuities in discrete solutions are nicely modeled as steep gradients over a few meshes, more is needed than the property of fully-conservative C°-discontinuity capturing. We need more, to avoid excessive smearing out of the discontinuity over many meshes, and to avoid wiggles in discrete solutions near the shock where the discrete solutions should be smooth.

To satisfy these numerical-modeling requirements, limiters or shock-sensors are used. Limiters are procedures that limit grid-function-gradients to values corresponding to those in smooth discrete solutions. Hence, the $O(\text{mesh-size})^{-1}$ gradient values over a C°-discontinuity are not used in the discrete conservation equations, but replaced by neighbouring values near the discontinuity. Shock sensors are functions of grid functions, that measure the location and the strength of C°-discontinuities in grid functions. The use of shock sensors is popular in approaches with central differencing, limiters are much used in upwind methods.

The limiters and shock sensors are subsequently used to modify the calculation of spatial divergence operators over C°-discontinuities, compared to that in smooth flow parts. This modification should have at least two effects.

1. the numerical viscosity created by the fourth-order dissipative divergence operator, is reduced or completely eliminated over a C°-discontinuity,
2. in the direction approximately normal to a C°-discontinuity, grid-function values inside the C°-discontinuity *should continuously vary* between the grid-function values in the adjacent smooth regions, when the position of the discontinuity is varied.

A difference scheme is said to be uniform-flow consistent if, for any steady uniform flow, the difference equations for the (unsteady) conservation equations are exactly satisfied. (Boundary-conditions need not to be satisfied.) This property should be satisfied, for example, in steady-state-flow simulations on infinite domains, with a course mesh near infinity.

Free-stream consistency is uniform-flow consistency for the special case of uniform free-stream conditions.

Expansion shocks over sonic surfaces must be ruled out in numerical simulations by numerical modeling. In real physical flow, they are ruled out by an entropy inequality constraint. In numerical simulations, they are ruled out by either numerical viscosity with a fourth-order dissipative divergence operator which enforces/smooth flow, or by upwinding in such a way that fluxes per unit area are prescribed to have sonic (extreme) values on sonic surfaces.

Discretisation of boundary conditions

At grid boundaries, the discretisation of the conservation equations has to be augmented with boundary conditions. Numerical boundary-condition formulations have to satisfy a few general requirements.

1. Desired physical boundary conditions must be imposed.
2. The total number of equations in the semi-discrete equation system

$$d\bar{U}/dt = f(\bar{U})$$

(this total number is usually equal to the total number of discrete conservation equations plus the total number of boundary conditions) should be equal to the total number of unknowns in the grid-function vector $\bar{U}$.

3. Numerical extra boundary conditions should not create undesirable properties in numerical solutions, like numerical boundary layers. When the total number of physical discrete conservation equations and physical discrete boundary conditions is smaller than the total number of unknowns in the grid function $\bar{U}$ (cell-centred schemes), these extra numerical boundary conditions are required.

For inviscid calculations, the boundary conditions may be divided into three classes.

1. Conditions at solid walls (like aerofoils, wings, fuselages, windtunnel walls etc.). At solid surfaces with zero normal fluxes, various techniques are applied. In flux-vector and flux-difference methods, unsteady waves are reflected against the wall in such a way that the boundary condition becomes satisfied. Special attention is sometimes needed to evaluate the pressure in the boundary condition, because it is unknown. Higher-order accuracy in the boundary conditions may be realized by using the known derivatives of the boundary conditions with respect to time.
2. Conditions far away from the configuration, where free-stream conditions have to be approached when going to infinity, except possibly at downstream infinity behind shock waves, near convected vortex

sheets, etc. Asymptotic theory may be applied to evaluate the perturbation of the uniform flow. For supersonic and subsonic free-stream flows, this theory leads to different types of results. In current applications, three different approaches may be identified.
- The first few terms of an asymptotic expansion are explicitly used (flow around aerofoil: far-field flow uniform plus circulation perturbation).
- Differential operators are used to simulate the far-field flow. These differential operators act as radiation conditions, selecting acceptable asymptotic expansions that represent only the physically relevant outgoing disturbances.
- Characteristic theory is applied. When using flux-vector or flux-difference splitting or a λ-scheme, waves coming into the computational domain over the boundary are separated from the outgoing waves, and the incoming waves are prescribed to be those of the unperturbed far-field flow.

3. At influx and outflux boundaries, various types of boundary conditions are encountered depending on the problem (inlets, channels). Characteristic theory is usually applied to determine what boundary conditions should be applied to prevent over- or under-specification of the boundary conditions.

At boundaries where the flow behaves like a viscous flow, boundary conditions corresponding to the Navier-Stokes equations are required. No-slip conditions and a heat-flux condition are usually applied.

Initial conditions

Initial conditions are often chosen to be those of a given uniform flow, or of a given previously computed grid function.

When initial and boundary conditions for a grid function are contradictory (like in the case of an initial uniform flow, and time-independent zero-flux boundary conditions on solid walls), strong transient effects arise. These are usually not acceptable if this leads to (nonlinear) instability.

Solution, time integration

The semi-discretized equation system $d\bar{U}/dt = f(\bar{U})$ for conservation equations and boundary conditions is in literature solved by a large variety of methods. They may be grouped in three classes.

1. Time-integration by a multi-stage Runge-Kutta type integration scheme, usually combined with a post-smoothing technique, like residual averaging.
2. Time integration by an implicit ADI-like approximate factorization method. Hereby each time-integration step is decomposed into a sequence of time-integration substeps. Each substep is implicit in one spatial grid-coordinate direction, and explicit in the other directions. The implicit direction is cyclically exchanged with other spatial grid-coordinate directions during each time step.
3. For steady flows, the nonlinear discrete equations may also be solved by approximate Newton iteration. The basic iteration step is one or a few Newton iteration steps for all conservation (+ boundary-condition) equations of one grid cell, or one line of grid cells. For each overall iteration step, all grid cells are visited according to some strategy.

For the calculation of steady-flow states, convergence speed-up is an important issue. The following techniques are available in literature to improve convergence rates.

1. Local time stepping.
2. Multi-grid techniques.
3. Enthalpy damping.
4. Rational Runge-Kutta time stepping.
5. Post-smoothing, residual averaging.
6. Weakly reflecting boundary conditions.

Consistency, stability, convergence

CFD difference schemes should satisfy the three well-known criteria of consistency, stability, and convergence. These notions may be roughly defined as follows.

1. A difference-equation system is consistent, if each difference equation tends to a corresponding differential equation of the continuum model, when the mesh is decreased to zero.
2. A difference-equation system is stable if, for each initial condition, for each boundary condition from a class of admissable initial and boundary conditions, for each sufficiently fine mesh, and for all times smaller than some finite upper limit, the discrete solution exists, and is unique and bounded in some useful sense.
3. A sequence of discrete solutions on a sequence of grids is convergent if, for decreasing mesh size to zero, the differences between the discrete solutions on different grids tend to zero in a useful sense.

It is known that, under suitably defined conditions, stability and consistency may be shown to imply convergence.

The application of these issues in aeronautical CFD is not always clear. It is well-known that, in Euler and Navier-Stokes flows, all kinds of physical instabilities may appear that are related to the creation of turbulence. Flow phenomena that often give rise to such instabilities are vortices, vortex sheets, and instability regions in boundary layers and shear layers. The instabilities often arise because of bifurcation in time of solutions. Under these circumstances it is often not clear, what a consistant, stable, and/or convergent discrete solution is. Nevertheless, the questions about consistency, stability, and convergence are usually investigated by extensive numerical experimentation:
- numerical solutions on successively finer grids are compared to each other (convergence),
- all kinds of convergence histories are analyzed (stability),
- boundary shapes, boundary conditions, and initial conditions are varied over their ranges (sensitivity analysis with respect to convergence and stability).

The problem with this approach is that numerical experimental verifications are not the same as mathematical proofs about numerical algorithms.

5. Numerical experimental validation

In this section, the findings of recent validation excercizes are summarized.

Iso-Mach line plots of four typical test cases for transonic inviscid aerofoil flows of the AGARD report [1] are given in fig. 5.1. These test cases include transonic shock-free flow about a geometrically difficult aerofoil, strong shocks and strong shear layers.

Tabulated results for the shock-free flow case of AGARD report [1] and of the AIAA Euler workshop [2] are given in fig. 5.2; the drag coefficient C_D should be less than about 0.0005, the lift coefficient

should be about 0.594. Corresponding distribution functions (C_p, Mach, total pressure) of the AIAA Euler Workshop are presented in fig. 5.3. The irregularities at about 60% of the chord at the upper side of the airfoil are possibly due to error accumulation in the downstream sonic point on the aerofoil in upwind methods. These irregulaties are smeared out if a fourth-order numerical dissipation operator is used in this region [2]. Taking into account that the accuracy of the dense set of coordinates in [1] is a few units of the fifth decimal place, it may be concluded that the codes of fig. 5.3 seem to pass this test case.

AGARD-report results of the two transonic test cases with subsonic free-stream Mach numbers are presented in fig. 5.4. It may be seen, that many codes produce nearly identical results.

Inviscid transonic aerofoil-flow calculation, including strong shocks, strong shock-induced shear layers, shock-free flows, and geometrically difficult aerofoil shapes is nowadays common practice at many places.

The inclusion of viscous effects in aerofoil calculations was the topic the recent AIAA Viscous Transonic Aerfoil Workshop, [3]. There were 23 different contributing computer codes. A few results are reproduced here, and the main conclusions are summarized.

Fig. 5.5 is a comparison of the C_L-α curves of all contributors with each other and with an experiment for two aerofoils. It may be concluded that the calculation of mildly loaded aerofoils in subsonic and slightly transonic flow is no problem. Skin friction coefficients vary between rather wide limits, however. Holst reports that this scatter is acceptable with todays CFD technology because skin friction is a derivative quantity, [3], p.11.

Fig. 5.6a is a comparison of computed and experimental results for a transonic flow with a shock-induced separation. It may be seem that there is a rather wide variation in computed shock positions and, downstream of the shock, in computed distributions of the pressure, displacement thickness, and skin friction. Fig. 5.6b displays corresponding variations in sonic-line/shock positions in the flow. It may be concluded that the computed flow circulation around the aerofoil varies between wider limits than one would like. Fig. 5.6b also shows that the computed velocity profiles in the boundary layer at $x/c = 0.75$ do not show the measured reattachement of the windtunnel experiment. The figures allow the conclusion that, at least for this test case with shock-induced separation, there is a need for improving the boundary-layer/wake calculation at and downstream of the shock. Holst concludes, that apart from "physical *modeling aspects, such as turbulence modeling*", *also many* "*numerical aspects, such as artificial* dissipation, grid resolution, surface grid clustering, etc." affect skin friction, [3] page 15. It may be concluded that numerical accuracy assessment is also required to clarify the observed confusing situation with this test case.

Major conclusions of the AIAA Viscous Transonic Airfoil Workshop [3] are as follows, as far as numerical accuracy assessment is concerned.

- Computed results should be produced on sufficiently fine grids with appropriate clustering, [3], page 27.
- Computed results should be shown independent of outer-boundary position and independent of continued grid refinement, [3], page 24.

Further it is concluded that improved turbulence models for (shock-induced) separated boundary layers are required, [3], page 27.

The findings of the numerical simulations of the airfoil test cases are of interest to put validation work for transport-type wings in a proper perspective.

Fig. 5.7 presents AGARD rep. [1] results of computed transonic Euler-flow pressure distributions on the ONERA M6 wing. The results agree, except at the wing tip where mesh-topology and mesh-resolution differences give rise to significant differences in calculated results. Comparison of results of windtunnel experiments in fig. 5.8 with medium- and fine-mesh results on OO-grids shows that the medium-mesh results are already reasonable. Computed shock positions are somewhat downstream of those in the windtunnel experiments.

Fig. 5.9 gives AIAA Euler Solvers Workshop results of pressure distributions in transonic flow on the Boeing 747-200 wing-body, [2]. On so-called dense grids, away from the tip of this swept wing, the computed results mutually agree reasonably well (if shock-position differences of 7½% of the chord around an average position are considered acceptable). However, the computed rear-shock positions are 10-25% of the chord downstream of the shock positions of the windtunnel experiments, which is (too) much. In the AIAA Euler Solvers Workshop report, it is shown that, with a boundary-layer correction, computed results improve to what is called "good agreement with experimental data" ([2], page 10), although computed and windtunnel shock positions still differ by about 10% over the outer 30% of the wing span. *)

Conclusions are as follows, for transport-type wings and wing-body configurations in mildly transonic flow.

- Euler-flow calculation results with "acceptable accuracy" (see below) can be obtained, if grids have sufficiently fine meshes.
- However, for transonic flows with shocks at least, viscous effects have to be accounted for to make such results more useful for reliable design work.

It should be pointed out that accuracy requirements in terms of maximum acceptable values of errors in computation results are different for 2D and 3D flows. The qualification "acceptable accuracy" used here is not the same as within the context of 2D airfoil-flow calculations. Pressure distributions of airfoil-flow calculations are nowadays considered to have acceptable accuracy if the errors in e.g. pressure coefficients and shock positions (as a fraction of the chord) are about 1% at most. However, wing-flow calculations are considered to have acceptable accuracy if errors in pressure coefficients and shock positions are of the order of 5% to 10% at most.

For flows around delta wings, one has to deal with the calculation of shocks and/or leading-edge vortices. Results of test-case calculations are available in the AGARD report [1] and in the report of the AIAA Euler Solvers Workshop, [2].

*) During the conference, it was reported that the disagreement between windtunnel experiments and calculations would be due to geometry differences at the wing-body between windtunnel model and numerical geometry in the calculations.

Fig. 5.10 (taken from the AGARD report [1]) is an illustration of the state-of-art, as far as accuracy of Euler-flow calculations are concerned. On the wing, computed and windtunnel pressure distributions agree fairly well. However, there are numerical-accuracy questions. J.H.B. Smith analyzed in [1], that there are large total-pressure losses in vortex cores. These losses can exceed the dynamic pressure. Further, he found from fig. 8.38 in fig. 5.10, that the static-pressure behaviour on the wing in spanwise direction near the leading edge has large gradients (so that there must be large numerical viscosity, if the fourth-order dissipative operators are switched on here), and that the total pressure has (unexpected) strong gradients and variations over the leading edge.

The conclusions of the AGARD report were as follows.

a. For some three-dimensional vortex flows, convergence with respect to grid spacing needs to be established. The computed fine-grid results of Rizzi on the Dillner wing reveal flow phenomena not present in computed medium-grid results, [1].
b. In numerical Euler-flow calculations, the role of streamlines as transporting characteristics of total pressure and vorticity is not clear.
c. The role of (implicit or explicit) artificial viscosity at the leading edge, where a vortex sheet leaves the wing surface, should be clarified. It is known that, in a few circumstances, the flow pattern could be completely modified by altering the numerical viscosity at the leading edge, see Newsome, [10].

6. Concluding discussion

In order to delineate the topic of numerical accuracy assessment within the context of CFD, a methodology is sketched.

First, lists of requirements for numerical flow-simulation codes should be specified, section 2. These requirements concern the flow physics, the classes of aeronautical configurations of interest, physical initial conditions and boundary conditions, and performance requirement about required engineering accuracy levels. Further, economical performance requirements are of interest: calculation results with a guaranteed engineering accuracy should be produced for an acceptable amount of FLOPs (floating point operations).

Next, validation methods should be designed and applied, section 3. Validation includes logical verification of the numerical processes mapped in computer codes, and verification of the accuracy requirements with calculation results of a carefully designed collection of test cases. These test cases should be designed such that stability and accuracy (convergence with mesh refinement) requirements can be verified for all configurations and initial/boundary conditions of interest.

A brief survey of the popular numerical issues is presented in section 4. This includes grid generation (there are very rapid developments in the last four years), differencing alternatives (central, upwind), numerical viscosity (implicit/explicit), limiters and shock- or discontinuity sensors, numerical time integration, and the issues of consistency, stability, and convergence of solutions of the highly nonlinear discrete (flow-evolution) equation system.

Section 5 is devoted to a discussion of the results of recent validation excercises of AGARD report [1], and the AIAA workshops for Euler and Navier-Stokes codes, [2,3]. Transonic flows about aerofoils, wing and wing-body configurations for transport aircraft, and delta wings were considered. Conclusions are presented in section 5, for each configuration class.

7. References

1. – Test Cases for Inviscid Flow Field Methods, AGARD Fluid Dynamics Panel Working Group 07, AGARD-AR-211 (May 1985).

2. Margason, R.J. Review and Evaluation of Euler Methods, Test Case Results, AIAA Euler Solvers Workshop (Aug. 20-21, 1987).

3. Holst, T.L. Viscous Transonic Airfoil Workshop Compendium of Results, AIAA-87-1460 (1987).

4. Woodward, P., Colella, P. The Numerical Simulation of Two-Dimensional Fluid Flow with Strong Shocks, J. Comp. Physics 54 (1984) 115-173.

5. Thompson, J.F. (ed.) Numerical Grid Generation, Proc. Symp. Num. Grid Gen. of Curv. Coord. Syst.s and their Use in Num. Sol. of Part. Diff. Eq.s, North Holland, New York (1982).

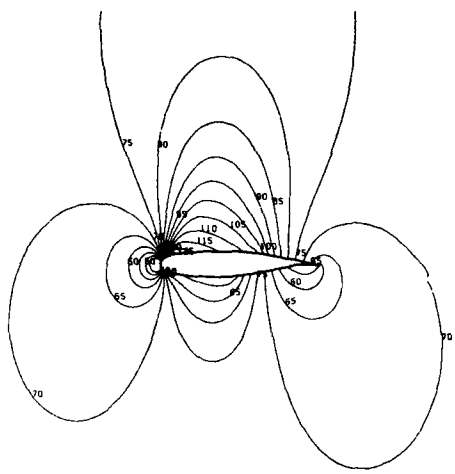
6. Häuser, J., Taylor, C. (ed.s) Numerical Grid Generation in Computational Fluid Dynamics, Peneridge Press, Swansea, U.K. (1986).

7. Baker, T.J. Developments and Trends in Three-Dimensional Mesh Generation, Review paper at Transonicum Symposium, NASA Langley Res. Center (April 1988).

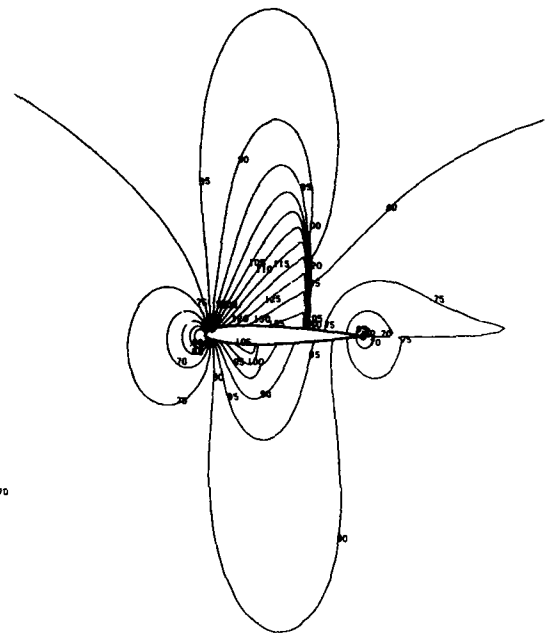
8. – Proceedings of the Conference on Numerical Fluid Dynamics, March 21-24, Inst. for Comp. Fl. Dyn. of the Univ.s of Oxford and Reading, Oxford, U.K. (to be published).

9. – Large scale computing in aeronautics, AGARD-AR-209 (June 1984), Page 1.

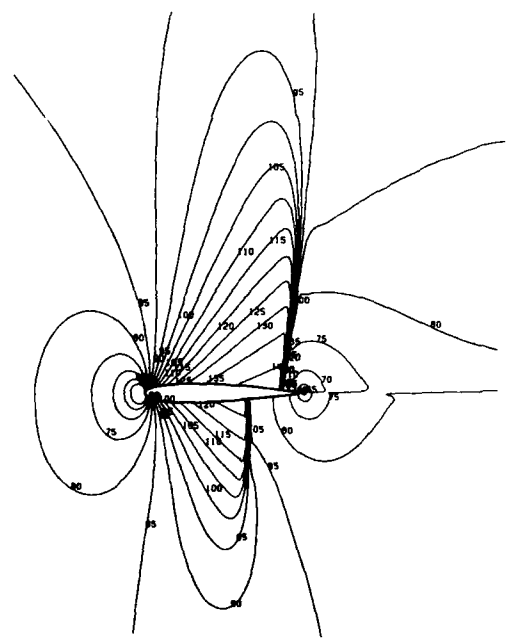
10. Newsome, R.W. A comparison of Euler and Navier-Stokes solutions for supersonic flow over a conical delta wing, AIAA 85-0111 (1985).



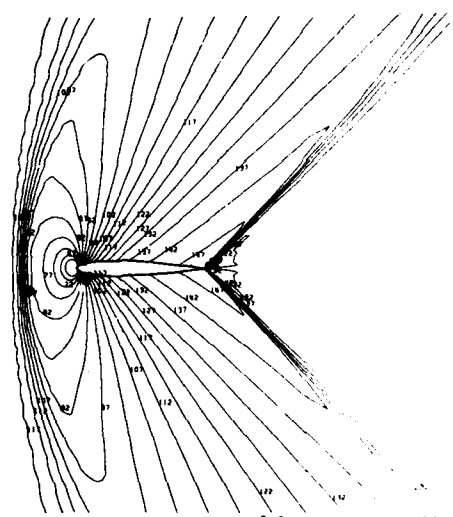
Iso-Mach lines of solution n° 9.2 for test case 07 (ΔM=0.05, curve parameter=100M) NLR 7301, M_∞=0.720957, α=-0.194°



Iso-Mach lines of solution n° 9 for test case 01 (ΔM=0.05, curve parameter=100M) NACA 0012 M_∞=0.8, α=1.25°



Iso-Mach lines of solution n° 9 for test case 02 (ΔM=0.05, curve parameter=100M) NACA 0012 M_∞=0.85, α=1°



Iso-Mach lines of solution n° 9 for test case 04 (ΔM=0.05, curve parameter=100M) NACA 0012, M_∞=1.2, α=0°

Fig. 5.1 Typical airfoil test cases of AGARD report

Table 6.1 - Numerical solutions for test case 07 (NLR 7301, M_∞=0.721, α=-0.194°)

Solution	MESH			outer boundary (chords)	C_L	Γ	C_D	C_M
	type	points or cells total	points or cells on airfoil					
1	C	251 x 35	195	4/6/7	0.5878	0.2900	0.0016	-0.1347
2.1	C	250 x 34	194	4/6/7	0.6035	0.2968	0.0014	-0.1345
2.2	C	298 x 34	230	4/6/7	0.6015	0.3012	0.0011	-0.1333
3.1	O	159 x 23	159	16	0.5591	0.2709	0.0028	-0.1290
3.2	O	159 x 23	159	16	0.5587	0.2717	0.0024	-0.1290
3.3①	O	319 x 47	319	?	0.5722	0.2834	0.0027	-0.1303
4	O	121 x 34	121	8 FS	0.4792		0.0085	-0.1298
5	C	249 x 41	181	8/12/12 FS	0.4497	0.2230	0.0017	-0.1135
6	O	192 x 39	192	50	0.6431		0.0013	-0.1350
7	C	150 x 25	120	4/5/4	0.4389		0.0104	-0.1240
8.1	O	128 x 28	128	5	0.578	0.282	0.0012	-0.128
8.2	O	128 x 32	128		0.581	0.286	0.0014	-0.130
8.3	O	160 x 32	160	5	0.587	0.287	0.0007	-0.129
8.4	O	160 x 32	160	5	0.587	0.288	0.0002	-0.130
8.5	O	160 x 32	160	5	0.588	0.300	0.0001	-0.130
9.1	O	162 x 34	160	50	0.582		0.0019	-0.132
9.2	O	322 x 66	320	50	0.594		0.0005	-0.132
10②	C	129 x 25	105	9	0.5864		0.0055	-0.1236
"exact"					0.5939	0.2987	"0.0006"	-0.1298

(1 :aerodynamic coefficients only, 2 :α=0.244°)

TEST CASE #1						
AUTHOR:	GRID:	MACH:	ALPHA:	CL:	CD:	NOTES:
CHAKRAVARTHY	64 X 24	.72	0.0	.592		WITH ADDED
" "	80 X 32	.72	-.14	.587		DISSIPATION.
" "	144 X 32	.72	-.18	.590		
" "	192 X 48	.72	-.194	.597		
THOMAS	320 X 80	.72	-.194	.6012	.00087	W/O 4TH DIFF.
" "	320 X 80	.72	-.194	.6022	.00022	WITH 4TH DIFF.
" "	160 X 40	.72	-.194	.6012	.00017	W/O 4TH DIFF.
" "	160 X 40	.72	-.194	.6028	.00035	WITH 4TH DIFF.
" "	80 X 20	.72	-.194	.6012	.00121	W/O 4TH DIFF.
" "	80 X 20	.72	-.194	.5987	.00283	WITH 4TH DIFF.
TINOCO	132 X 32	.72	-.19	.588		INVISCID MODE
" "	63 X 20	.72	.07	.595		INVISCID MODE
RAJ	241 X 65	.72	-.194			
VERHOFF	181 X 25	.72	-.194	.6018	.0039	QAZID METHOD
" "	257 X 33	.72	-.194	.5949	.0038	QAZID METHOD
" "	312 X 49	.72	-.194	.5947	.0027	QAZID METHOD
SCHMIDT	322 X 66	.72	-.194	.594	.0005	

Table 2 Numerical solutions for AIAA Euler Solvers Workshop case 1: NLR 7301 airfoil, Mach = 0.721, alpha = -0.194°

Fig. 5.2 Tables of results for NLR 7301 airfoil, design condition, AGARD report, AIAA Euler Solvers Workshop

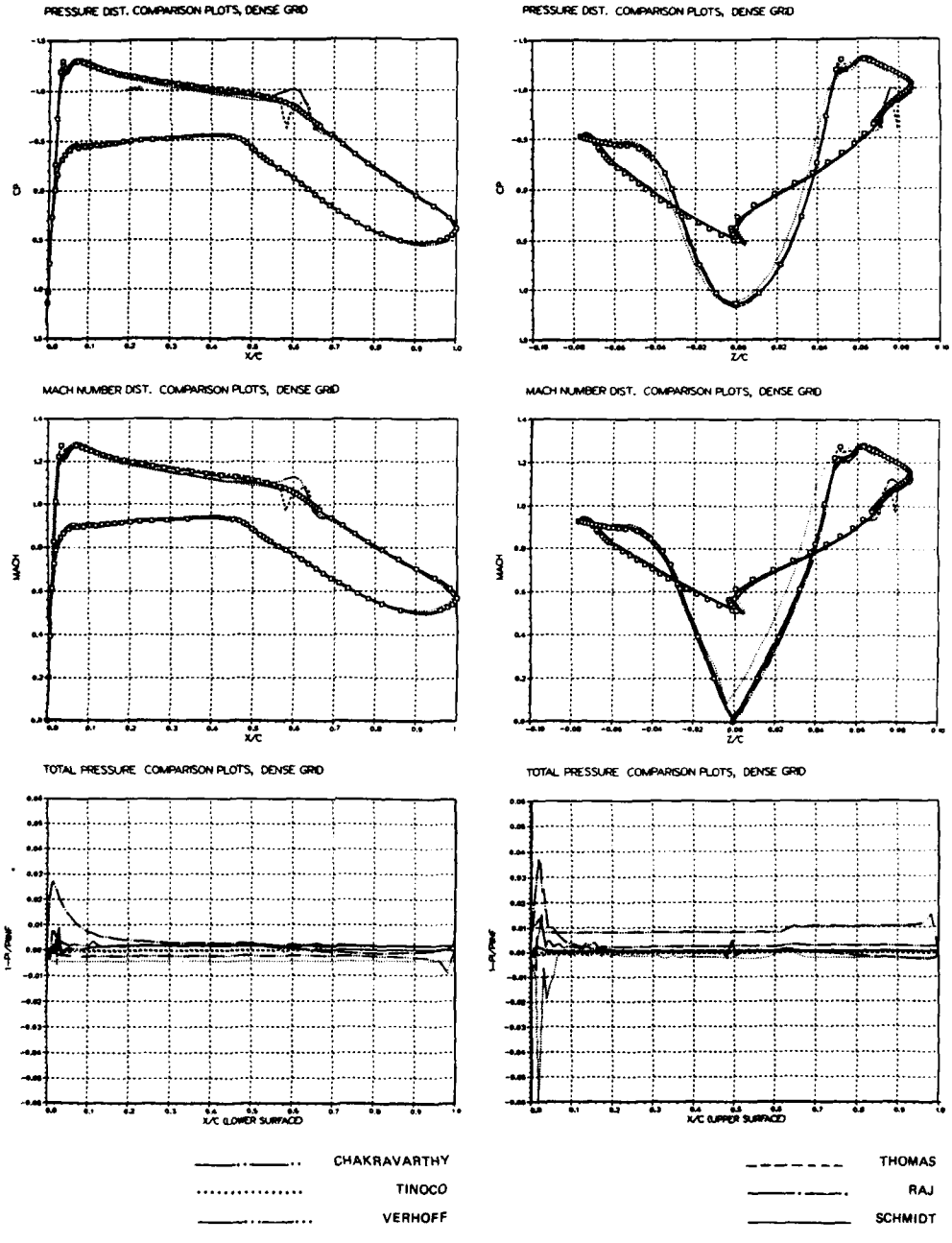
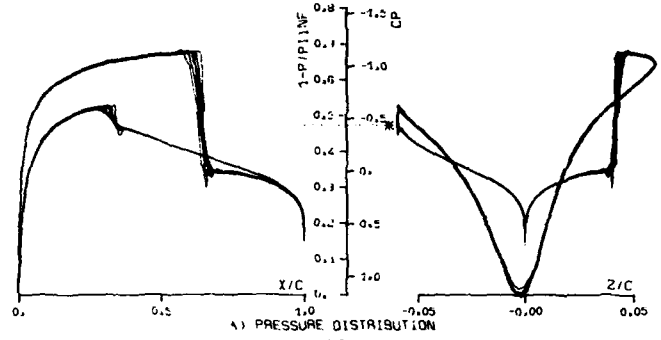
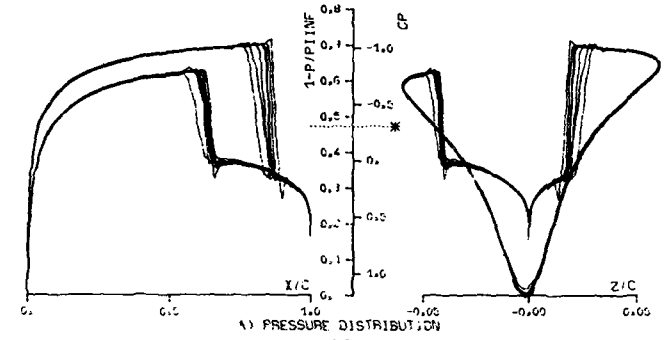


Fig. 5.3 Distributions on NLR 7301 airfoil in design condition, AIAA Euler Solvers Workshop

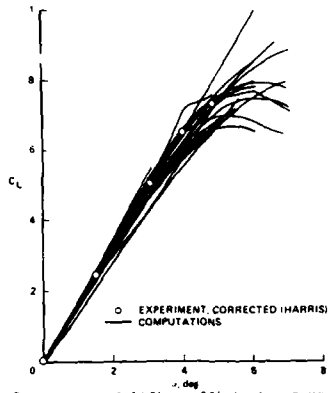


Solutions of group 2 for test case 01 (NACA 0012, Mach=0.80, α=1.25°)

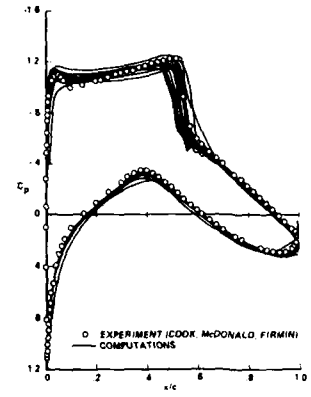


Solutions of group 2 for test case 02 (NACA 0012, Mach=0.85, α=1°)

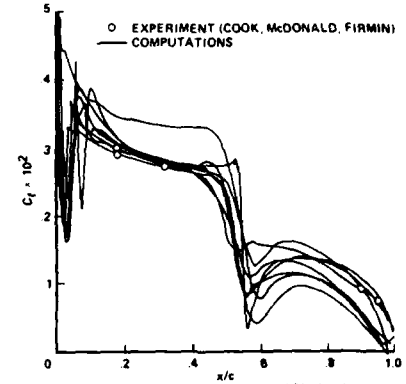
Fig. 5.4 Distributions on NACA0012 airfoil, 2 test cases, AGARD report



Comparison of lift coefficient versus angle of attack for the NACA 0012 airfoil, M_∞=0.7, Re_c=9.0x10^6, case A4

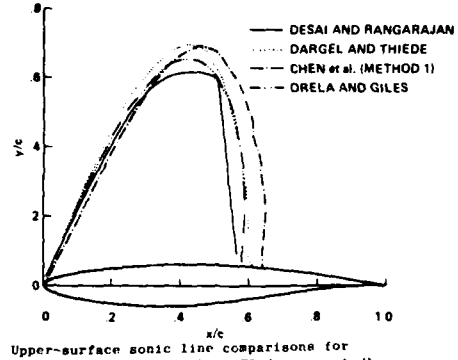


Comparison of pressure coefficient distributions for the RAE 2822 airfoil, M_∞=0.725, α=2.92° (uncorrected), Re_c=6.5x10^6, case B1

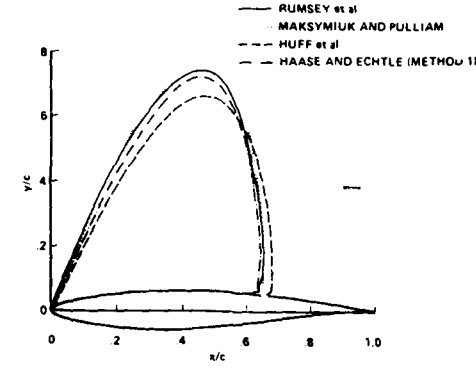


Comparison of skin-friction coefficient distributions from the RAE 2822 airfoil upper surface, M_∞=0.725, α=2.92° (uncorrected), Rc_c=6.5x10^6, case B3

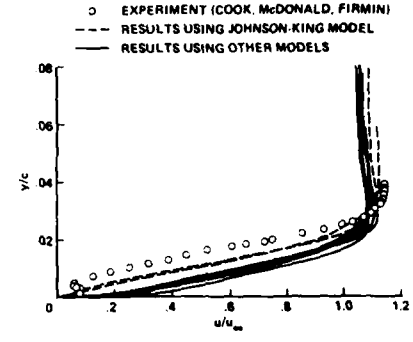
Fig. 5.5 Navier-Stokes calculations, C_L-α curves, and transonic flow without separation, AIAA Viscous Transonic Airfoil Workshop



Upper-surface sonic line comparisons for the RAE 2822 airfoil, M_∞=0.75 (uncorrected), α=3.19° (uncorrected), Re_c=6.2x10^6, case B11. a)Computations utilizing inviscid-plus-boundary-layer methods

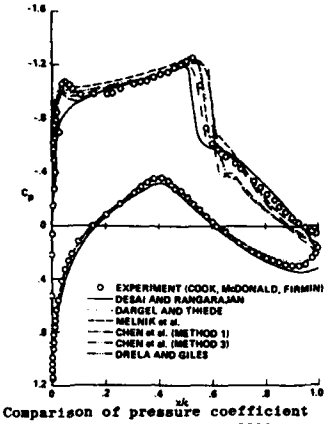


Computations utilizing Navier-Stokes methods

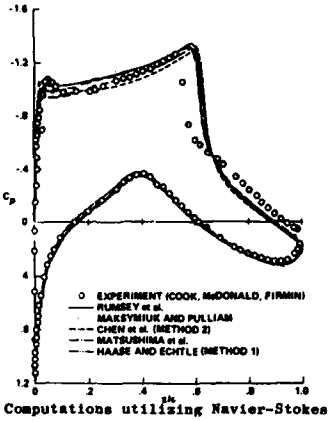


Velocity profile comparisons from the RAE 2822 airfoil upper surface at x/c=0.75, M_∞=0.75 (uncorrected), α=3.19° (uncorrected), Re_c=6.2x10^6, case B9

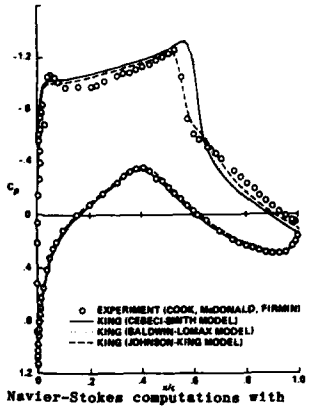
Fig. 5.6, end. Computed sonic-line positions and boundary-layer velocity profiles, AIAA Viscous Transonic Airfoil Workshop



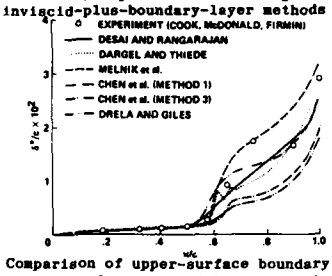
Comparison of pressure coefficient distributions for the RAE 2822 airfoil, M_∞=0.75 (uncorrected), α=3.19° (uncorrected), Re_c=6.2x10^6, case 86 a)Computations utilizing inviscid-plus-boundary-layer methods



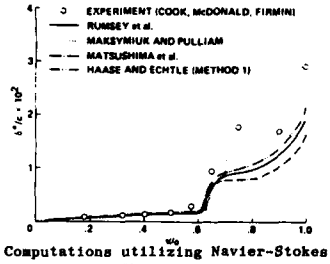
Computations utilizing Navier-Stokes methods on fine grids



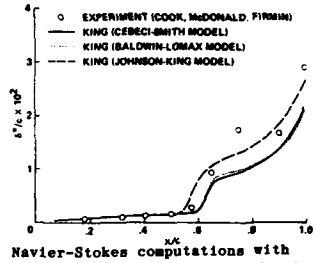
Navier-Stokes computations with turbulence model variation due to King.[10]



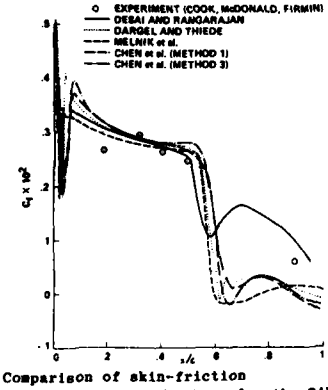
Comparison of upper-surface boundary layer displacement thickness for the RAE 2822 airfoil, M_∞=0.75 (uncorrected), α=3.19° (uncorrected), Re_c=6.2x10^6, case 87. a)Computations utilizing inviscid-plus-boundary-layer methods



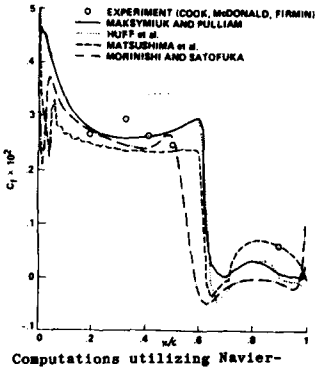
Computations utilizing Navier-Stokes methods on fine grids



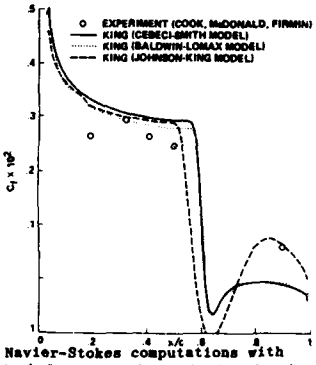
Navier-Stokes computations with turbulence model variation due to King.[10]



Comparison of skin-friction coefficient distributions for the RAE 2822 airfoil upper surface, M_∞=0.75 (uncorrected), α=3.19° (uncorrected), Re_c=6.2x10^6, case 88. a)Computations utilizing inviscid-plus-boundary-layer methods



Computations utilizing Navier-Stokes methods



Navier-Stokes computations with turbulence model variation due to King.[10]

Fig. 5.6, begin. Navier-Stokes calculations and experiments for transonic flow with shock-induced separation, AIAA Viscous Transonic Airfoil Workshop

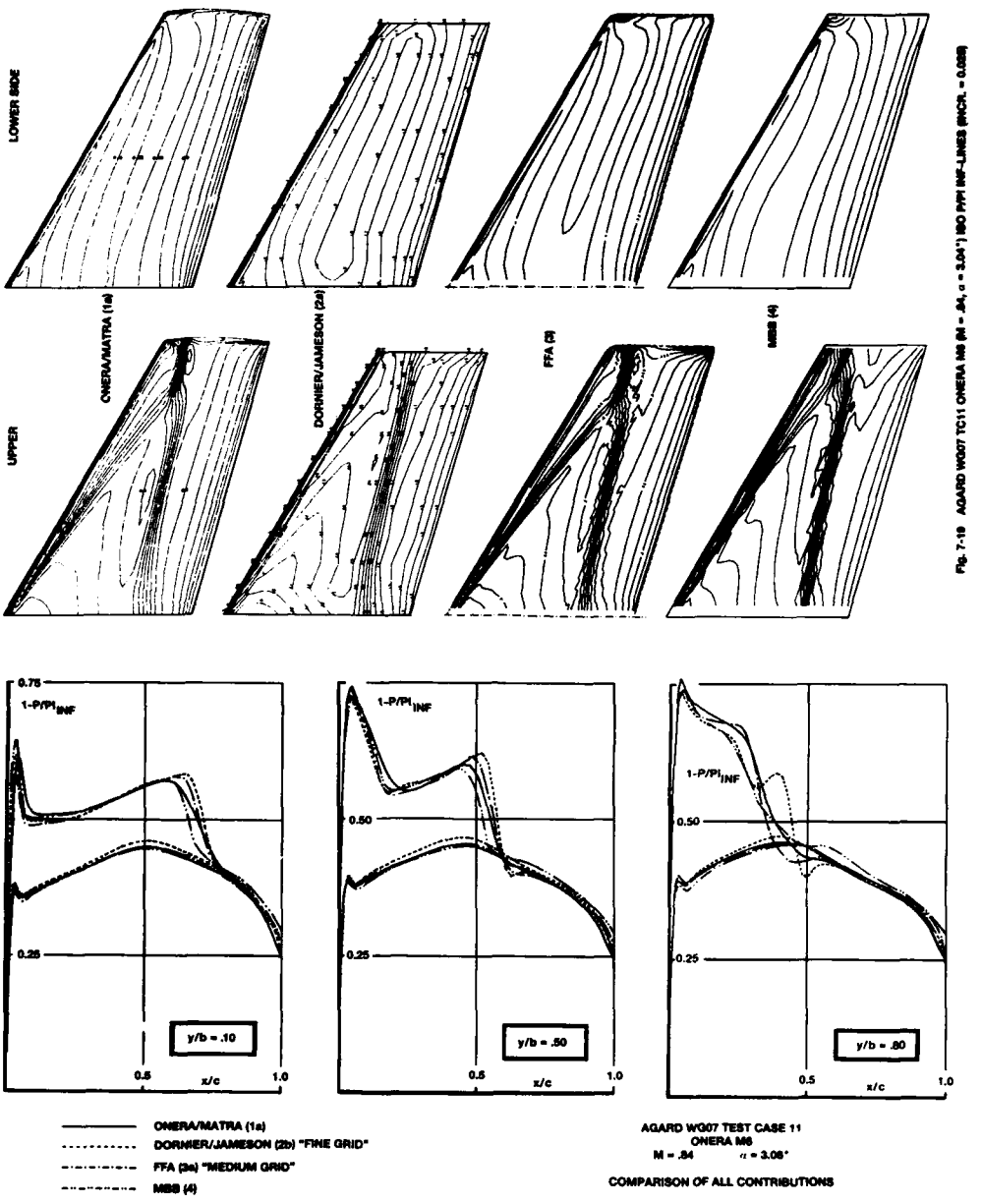
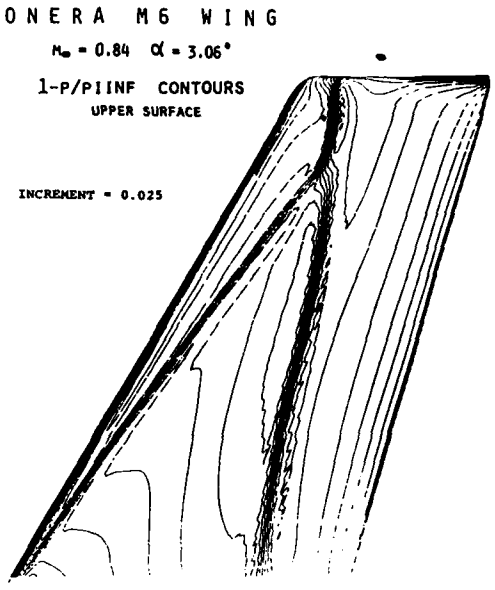
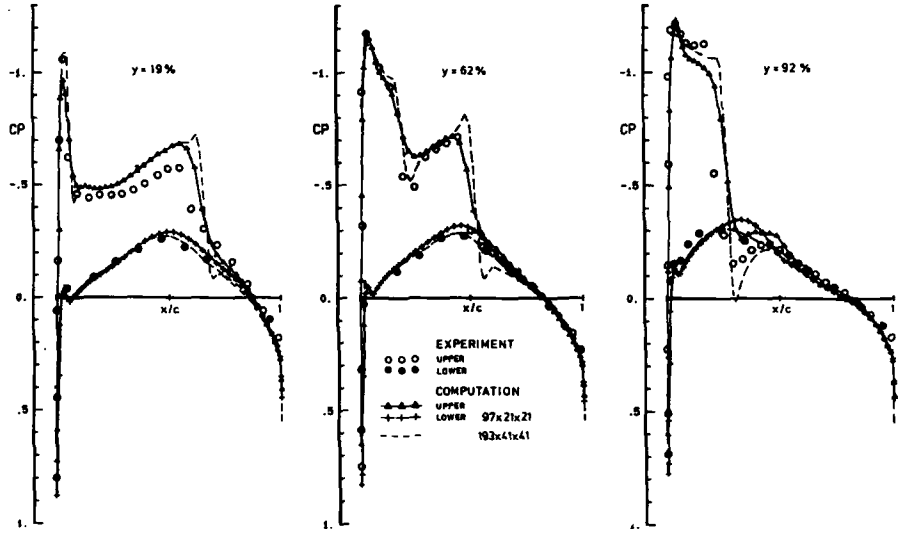


Fig. 7-18 AGARD WG07 TC11 ONERA M6 (M = .84, α = 3.04°) ISO P/PI INF-LINES INCR. = 0.020

Fig. 5.7 Pressure distributions on ONERA M6 wing, transonic Euler flows, AGARD report



Contours of computed 1-P/PIINF plotted on the upper surface of the M6 wing. M_∞=0.84 α=3.06 deg. Contour increment 0.025.



Comparison of measured and computed c_p in three chordwise sections of the M6 wing. M_∞=0.84 α=3.06

Fig. 5.8 Experimental and computed pressure distributions on ONERA M6 wing, medium and fine grids, AGARD report

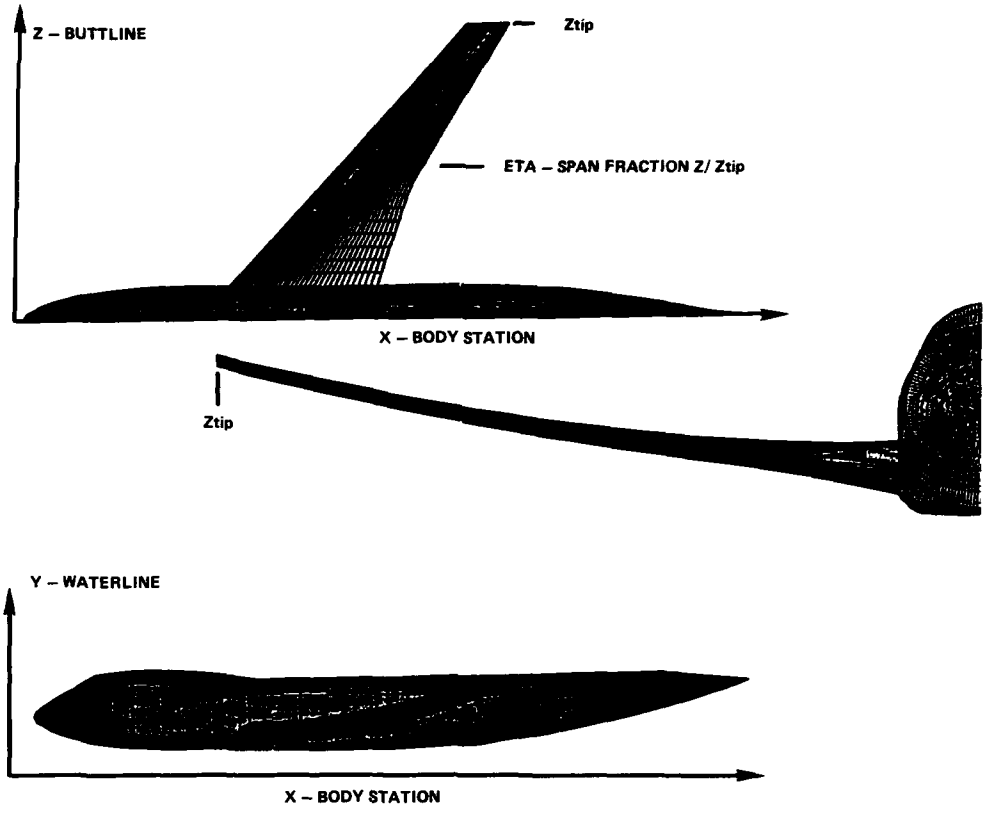


Fig. 5.9, begin. Boeing 747-200 wing-body for test case 3 of AIAA Euler Solvers Workshop

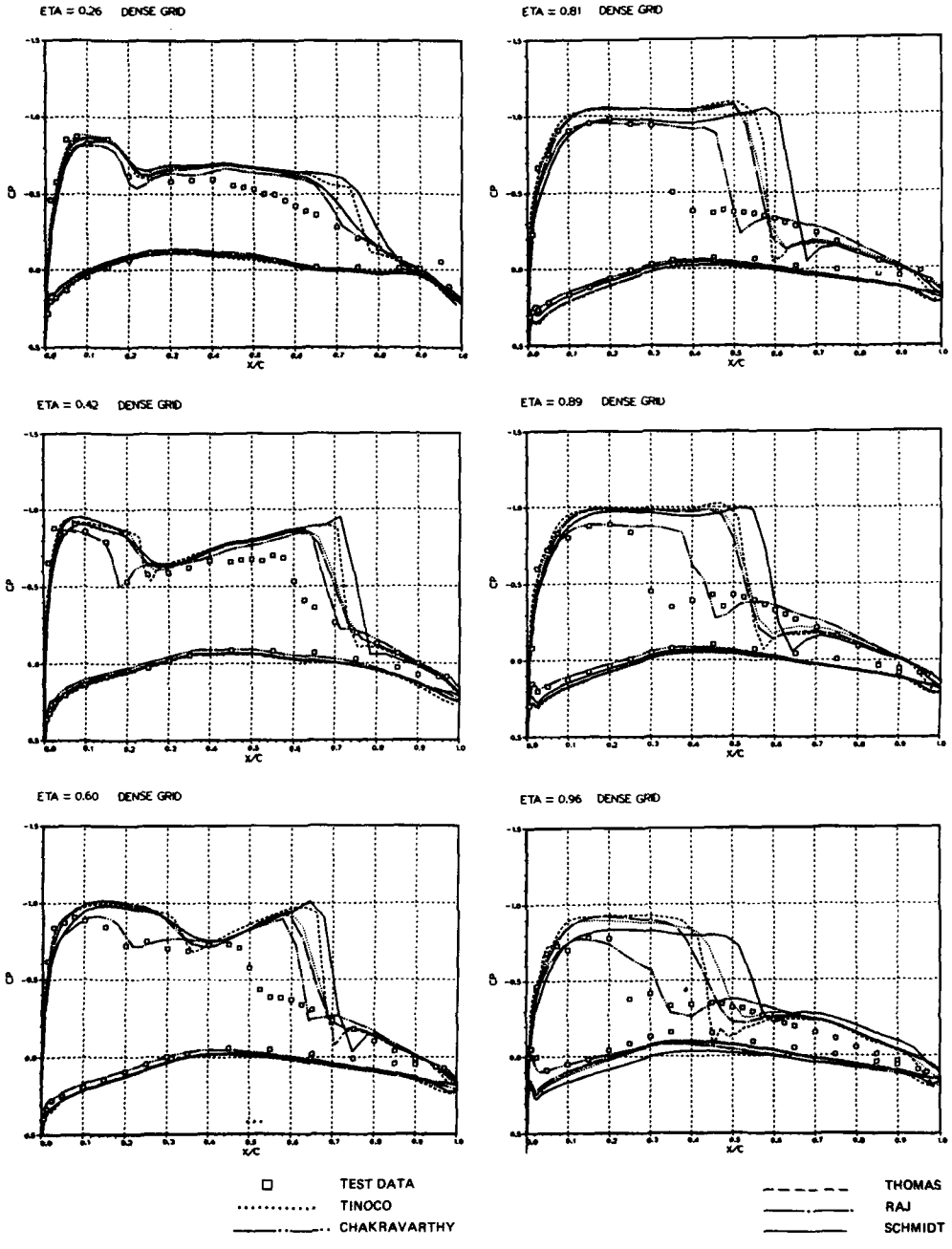
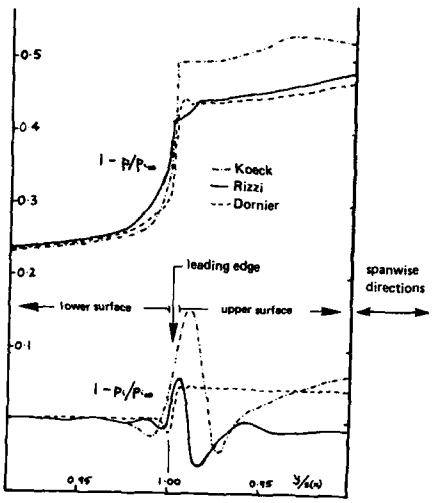
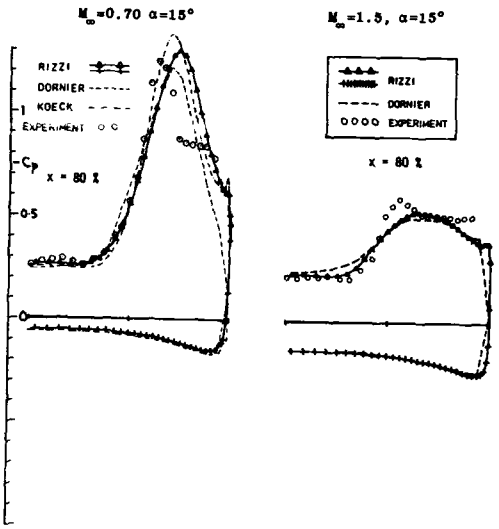


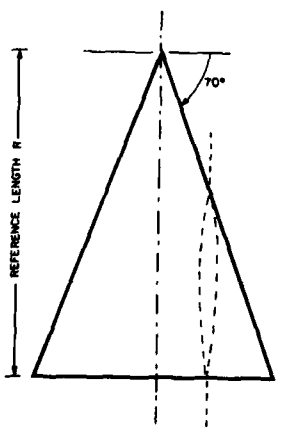
Fig. 5.9, end. Test case 3 of AIAA Euler Solvers Workshop, Boeing 747-200 wing-body, $M = 0.86$, $C_L = 0.43$, $Re = 4.6$ M



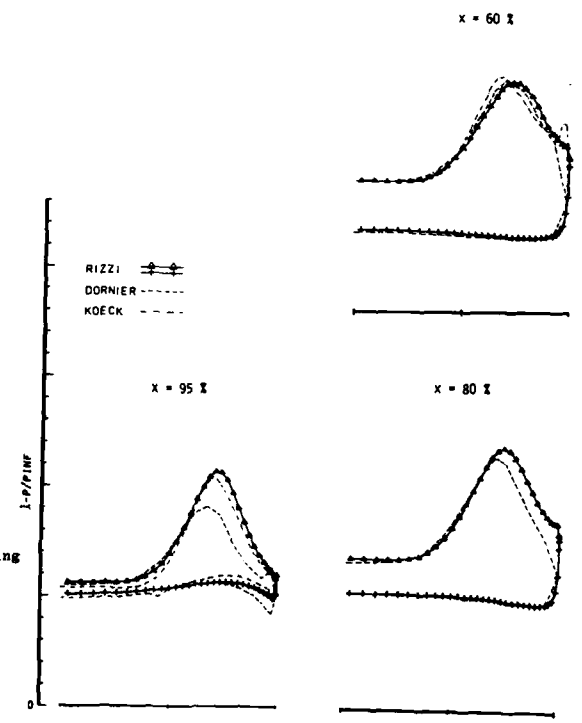
Variation of static and total pressure near leading edge at x/c=0.6, case 15, M=0.7, α≈15°.



Calculated and measured pressure coefficients for cases 15 and 14, at x/c=0.8.



Test cases 14 and 15. Dillner wing



Comparative plot for case 15, static pressure, M=0.7, α=15°

Fig. 5.10 Comparison of distributions (computed, experimental) on the Dillner delta wing at α = 15°, M = 0.7 and 1.5, AGARD report

WIND TUNNEL EXPERIMENTS ON AEROFOIL MODELS FOR THE ASSESSMENT OF COMPUTATIONAL FLOW METHODS

by

P. R. Ashill, D. J. Weeks and J. L. Fulker
Ministry of Defence (Procurement Executive)
Royal Aircraft Establishment
Bedford MK41 6AE England

SUMMARY

This paper describes wind tunnel experiments on two aerofoil models (one unswept and the other of sweep 25°) at high subsonic speeds and for Reynolds numbers up to about 20×10^6. Both models had detachable trailing edges for studying flows with differing rear-pressure distributions and used a method for fixing transition which gave precise control of the disturbance to the boundary layer. Following a discussion of the measurement and correction procedures, comparisons are presented between the data and CFD methods: these comparisons reveal the importance for the accurate prediction of the flow over advanced aerofoils of including effects in the modelling of the shear layers which become significant as separation is approached.

NOTATION

c	aerofoil chord	x	distance along aerofoil chord from leading edge
C_D	drag coefficient	α	angle of incidence
C_{D_S}	notional drag coefficient per surface, $= C_D/2$	θ	boundary-layer momentum thickness
C_L	lift coefficient	Λ	angle of sweep
C_m	pitching moment coefficient, referred to 1/4 chord	ν	kinematic viscosity
C_p	static-pressure coefficient		
M	corrected, free-stream Mach number	SUFFIXES	
R	Reynolds number based on c	2	equivalent flow over unswept aerofoil
R_L	unit Reynolds number	v,w,f,F	viscous, wave, skin friction and boundary-layer pressure components
t	aerofoil maximum thickness		
U	corrected free-stream speed	∞	far downstream

1 INTRODUCTION

The further development of Computational Fluid Dynamic (CFD) methods for calculating transonic wing flows requires high-quality data from carefully-conducted wind-tunnel experiments. These experiments should reflect current wing-design standards and provide information in sufficient detail to allow CFD methods to be validated. Thus special care is needed to determine accurately the boundary conditions of the flow in the wind tunnel. This implies accurate inspection of the model geometry and a knowledge of the way it distorts under aerodynamic load. Tunnel-wall boundary conditions should be determined either for direct use in CFD methods which represent tunnel walls or in the correction of the data to 'free air' conditions. As well, the flow in the empty tunnel should be appropriately calibrated over the range of conditions of the experiment. Special efforts should be made to ensure that boundary-layer transition is properly fixed with minimum disturbance. Excessive disturbance can result in the downstream development of the boundary layer being adversely affected and a significant spurious drag[1], particularly for modern, rear-loaded wings.

This paper describes two experiments for the validation of CFD methods, both being performed at high subsonic speeds and over a wide range of Reynolds number in the 8ft x 8ft Wind Tunnel at RAE Bedford. In the first, the model comprised an unswept cylinder with interchangeable rear sections of differing camber and base thickness. The second experiment, made on a swept-panel wing of sweep, 25°, typical of subsonic aircraft, complemented the first by allowing analogous flows over swept-wing sections to be studied. The main object of this experiment was to provide data for the assessment of CFD predictions of differences in drag between swept-wing sections.

The experiments are described, in turn, in sections 2 and 3 where details are given of the techniques used to ensure high-quality data. In both experiments, boundary-layer transition was fixed by the air-injection method, a technique which is particularly

suitable for CFD validation since it permits precise control of the disturbance to the boundary layer. Descriptions are given of the methods used to correct the data for comparison with CFD methods for 'free air' flows. These corrections include those for tunnel-wall constraint and for the effect of aeroelastic distortion of the aerofoil model. A novel feature of the swept-panel model is the use of wing thickness alone to generate the desired pressure distribution, and, as shown in section 3, this technique offers several practical advantages.

In order to illustrate the use of the data for the validation of CFD, comparisons are described between calculation and measurement in section 5. The CFD methods assessed are briefly described in section 4; all are based on the viscous version of the Garabedian and Korn method[2] developed at RAE[3] (VGK): this method is of the viscous/inviscid interaction type and it utilizes a potential-flow algorithm for the inviscid flow. Hence the CFD codes assessed here are less advanced than many other codes to be described in this Conference. Nevertheless, as shown in section 5, the most highly-developed of the codes considered in this paper, BVGK[4], provides a standard of prediction which the more modern methods will have, at least, to equal before they are accepted as design tools.

2 AEROFOIL MODEL

2.1 Model, instrumentation and test details

The model spanned the working section and was of chord, c, 0.635 m giving an aspect ratio 3.84 and a chord to working-section height ratio 0.26. Model incidence was adjusted by a mechanism outside the working section and adjacent to one end of the model span. The other end of the model was free to rotate in a bearing (to avoid the complication of a following mechanism) thus allowing the model to twist under aerodynamic load. This aspect is considered in section 2.4.

Special efforts were made to seal the two ends of the model.

Provision was made to change the model aft of 65% chord to allow sections of differing rear camber or base thickness to be tested (Fig 1). All the sections are of 14% thickness/chord ratio with significant rear camber and are illustrated in Fig 2. Sections referred to as 'convex' are a family with adverse pressure gradients on the aft 40-50% chord of the upper surface which increase monotonically with chordwise distance (except close to the trailing edge where boundary-layer displacement effects become significant). In order of increasing tendency towards rear separation on the upper surface, the sections with sharp trailing edges are RAE 5225, 5229 and 5230. The design requirement for RAE 5225 is the attainment of shock-free flow at a lift coefficient $C_L = 0.6$, a free-stream Mach number $M = 0.734$ and chord Reynolds number $R = 20 \times 10^6$ with transition at 5% chord on both surfaces. At this condition, the boundary layer on the upper surface is calculated to be close to separation near the trailing edge and thus boundary layer effects are expected to be marked at lower Reynolds number. RAE 5230 is shaped so that at the design condition of RAE 5225 it has similar tendencies towards rear separation on the upper surface as RAE 5225 has at $R = 6 \times 10^6$.

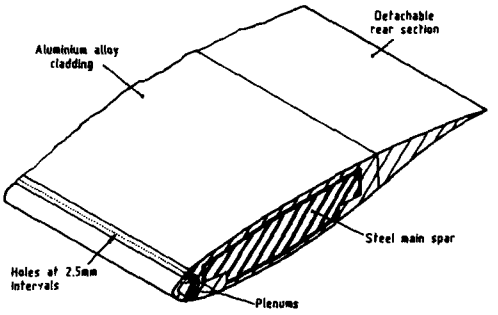


Fig. 1 Isometric view of model showing air-injection system

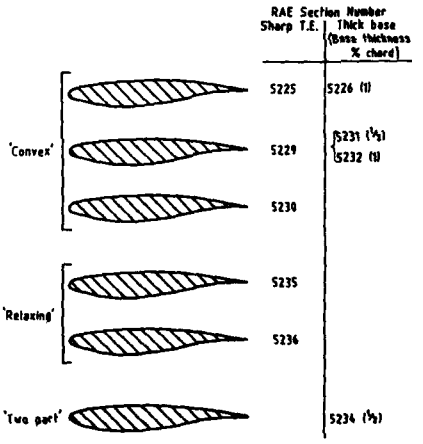


Fig. 2 Aerofoil sections studied

As shown in Fig 2, 'convex' sections with blunt bases, RAE 5226, 5231 and 5232, are derived from the sections RAE 5225 and 5229, the base bluntness being provided without altering the camber.

As the name implies, the 'relaxing' sections have pressure distributions with monotonically-decreasing adverse pressure-gradient with chordwise distance over the aft 30% chord of the upper surface. The 'two-part' section RAE 5234 has a pressure distribution which is in two parts over the rear 30% chord of the upper surface, with a mild-adverse pressure-gradient between 60 and 90% chord followed by a rapid rise in pressure to the trailing edge.

Inspection of the models revealed a high standard of surface finish (0.1-0.2 μm) and that manufacturing errors in the ordinates are small, being typically of order 0.1 mm (0.00015 × chord). The effects of these errors on pressure distribution and drag are discussed in sections 4 and 5.

The tests were made for Mach numbers between 0.5 and 0.75 and at $R = 6 \times 10^6$ and 20×10^6, approximately. Measurements included surface static-pressures on the model and on the working section roof and floor together with total and static pressures in the wake. Approximately 50 static pressure tappings, drilled normal to the surface of the model and of diameter 0.5 mm, were provided on the centre line of the model. In addition, a limited number of pressure tappings were drilled at lines about one chord either side of the centre line in order to provide a check on the two-dimensionality of the flow. A total of 24 static pressure tappings in the working section roof and floor, within a distance of one working-section height both upstream and downstream of the model centre of rotation, were used to determine wall-induced velocities (section 2.4). A wake rake for the measurement of drag, comprising 91 pitot tubes with one static tube at either extremity was placed in the vertical plane of symmetry 2.08 chords downstream of the model trailing edge.

The 'convex' section RAE 5225 was chosen for a more detailed investigation of the flow. On this section, measurements were made of mean-flow profiles in the boundary layers both at the trailing edge and in the region between 57 and 80% chord on the lower surface. Details of the probes and the measurement techniques are given in Ref 5 together with mean-flow data.

2.2 Air-injection technique

As noted in the Introduction, the air-injection technique[6] was used to fix boundary-layer transition, the scheme being shown in Fig 1. On either surface of the model, air was bled into the boundary layers by an independent supply through a row of holes of 0.33 mm diameter drilled normal to the surface at intervals of 2.5 mm along the span at 5% chord. As well as providing precise control of the level of disturbance to the boundary layer, the method offered other advantages as follows:

(a) Above a critical air-injection mass flow, considered to correspond to transition being fixed, no further increase in drag with mass flow was observed[6] within the range of air mass flows tested, suggesting that the spurious drag associated with transition fixing is avoided.

(b) With transition fixed, good agreement was obtained between drag polars measured on the section RAE 5225 in two separate test series[5], the differences in drag coefficient at a given lift being less than 0.0002. This may be taken as evidence of the reliability and consistency of the air-injection method as well as of the other experimental procedures (see section 2.5).

Further details of the technique, including its use to identify scale-sensitive features of flows over the aerofoil section RAE 5225, are given in Ref 6.

2.3 Determination of drag

Drag was determined from the momentum deficit in the wake far downstream of the model. This deficit was inferred from wake-rake measurements of total and static pressures by using the formula of Ref 7 together with an estimate of the static pressure far downstream. Calculations by classical wall-interference theory[8] suggested that a satisfactory value for this pressure could be derived from the mean of the static pressures measured at the tappings in the roof and floor adjacent to the leading edge of the wake rake.

On the basis of data from initial tests using an alternative wake rake with several static tubes in the wake, the static pressure was assumed to vary linearly with distance across the wake.

Limited checks were made of the spanwise variations of the wake flow for the section RAE 5225 by rotating the wake rake about its roll axis through the wake. Only shock-free flows were studied but tests were made at both $R = 6 \times 10^6$ and 20×10^6. Typical spanwise variations of total head with the rake horizontal ($\phi = 0$) and local drag coefficient are shown in Fig 3 which indicates that the change in drag coefficient relative to the centre-line value is small in the region of measurement.

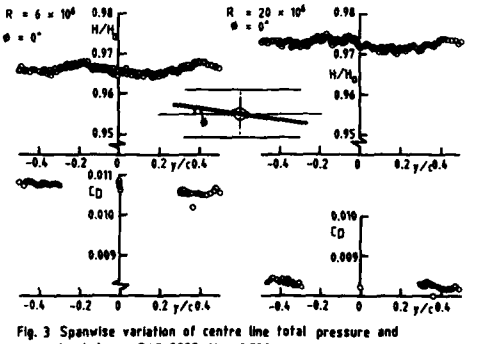


Fig. 3 Spanwise variation of centre line total pressure and local drag, RAE 5225, M = 0.735

2.4 Corrections to data

Corrections have been applied to the data for tunnel wall interference, aeroelastic distortion of the model and static-hole errors.

Tunnel-wall interference corrections were calculated using a procedure which has been described in detail before[9,10]. The method is based on Green's theorem for the velocity potential, applied to a surface neighbouring the tunnel walls, and uses the fact that the normal component of velocity of the inviscid flow at the surface is accurately defined for solid-wall tunnels. The streamwise velocity components at the surface are inferred from the static-pressure measurements made on the roof and floor. No assumptions are needed about the flow near the model.

Blockage increment in Mach number is found to vary slowly along the aerofoil chord, the maximum variation about the mean being approximately 0.0003 at $M = 0.73$ and $C_L = 0.6$ for all sections. Therefore the mean value has been used to define the correction to Mach number. By contrast, wall-induced upwash can vary significantly near the model, depending on model lift, and so a correction to model incidence alone is inadequate. In the assessment of CFD methods for 'free-air' flows about aerofoils (section 5), allowance is made for the variation by a camber correction, using the analogy between flow curvature and camber suggested by linear theory. Although the method may only be justified for subcritical flows, unpublished calculations by M. P. Carr (ARA Bedford) suggest that the method is applicable to transonic flows. His calculations were made using a non-aligned mesh method for solving full-potential flows over aerofoils, both in the tunnel and in free-air, and they show considerable improvement in agreement between pressure distributions in the two cases if the camber correction is applied in the free-air calculation.

The influence on the tunnel flow of the streamwise growth of the wall boundary layers in the absence of the model and the effect on the wall static-pressure measurements of hole imperfections and non-zero diameter is catered for by the tunnel calibration, details of which are given in Ref 11. The secondary effect of the mutual interaction between the wall boundary layers and the model as well as the images beyond the walls is ignored; this is done on the basis of calculation for the roof and floor boundary layers[9] and by noting that the wall boundary layer is thin and the model is of relatively large aspect ratio in the case of the sidewall boundary layers.

The effect on centre-line incidence of aeroelastic twist, referred to in section 2.1, was deduced from a prior static-calibration and by using values of aerodynamic pitching-moment inferred from the measurements of static pressure on the model centre line. Since the model was free to rotate about one end, the centre-line incidence was accompanied by a twist which, over the central 50% span, was about half the change in centre-line incidence. Typical results for the correction to centre-line incidence are shown in Fig 4 where they are combined with the correction for wall interference to give the resultant correction to incidence.

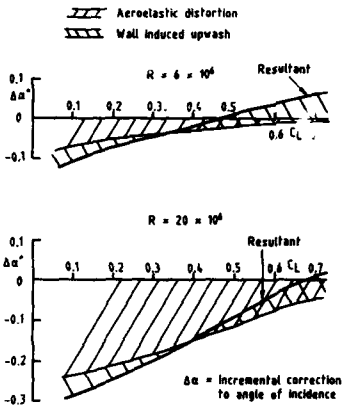


Fig. 4 Effect of static aeroelastic distortion and tunnel wall induced upwash on angle of incidence at model centre line, RAE 5225, M = 0.735

Corrections for non-zero hole diameter have been made to static pressures measured on the model with tappings which, it will be recalled, were of 0.5 mm diameter. These corrections have been calculated using Shaw's correlation[12] for hole depths between 1.5 and 6 diameters, adapted to allow for compressibility[13], and combined with boundary-layer data calculated by BVGK. Chordwise distributions of the corrections are shown in Fig 5 for RAE 5225 at $M = 0.735$ and $C_L \approx 0.4$. Over most of the chord, the corrections do not differ greatly between the two surfaces mainly because the local skin friction coefficients predicted by BVGK at a given chordwise position on either surface are similar. Hence the effect on integrated quantities is small. At $R = 6 \times 10^6$ the correction is barely discernible to plotting accuracy over the aft 60% chord (section 5.1) but is significant at $R = 20 \times 10^6$.

Corrections of similar order to those shown in Fig 5 have been made to the data of the swept panel model using BVGK, as before, but with allowance for sweep as described in section 4.1.

2.5 Accuracy of aerofoil model tests

An assessment of the effect of various sources of error[5] suggests that static pressure and drag coefficients are accurate to within ±0.002 and ±0.0001, respectively.

A high standard of repeatability was achieved in the measurement of pressure between, as well as within, test series, static pressure and drag coefficients being repeatable to within ±0.001 and ±0.0001.

3 SWEPT PANEL MODEL

3.1 Model, instrumentation and test details

The model comprised a cylindrical wing, of aspect ratio 4 approximately and sweep back $\Lambda = 25°$, mounted in a mid position on a symmetrical half-body from a sidewall of the working section (Fig 6). Since the main aim of the experiment was to provide data for the study of differences in drag between swept-wing sections, a precise simulation of infinite yawed-wing flows was not considered necessary. The requirement adopted was that the flow should be sectionally uniform between 40 and 70% span (ie within about one wing chord). In order to achieve this aim, the half body was shaped in the vicinity of the wing and a small, axisymmetric body was fitted to the wingtip (Fig 6).

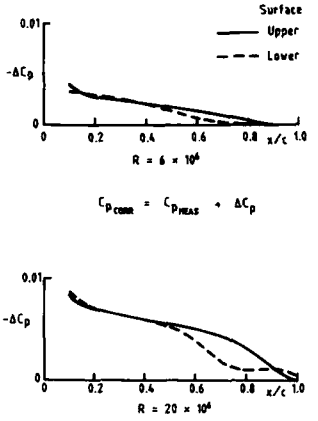


Fig. 5 Calculated correction to surface static pressure coefficients for static hole size, RAE 5225, $C_L \approx 0.4$, $M = 0.735$

An important feature of the model is that the required pressure-gradients over the rear 50% chord of the wing were generated by wing thickness only, ie the wing was uncambered and tested at zero lift. This approach offered the following advantages:

(a) The design aim of uniform flow across part of the wing span was not compromised by tunnel-wall lift interference, aeroelastic distortion of the wing and trailing vorticity in the wake.

(b) Since the wing was not subject to bending or torsion, it could be made from aluminium alloy, saving on cost and time of manufacture.

(c) The body shaping required was simple since it was symmetric about the wing chord plane.

Different trailing-edge sections could be fitted aft of a line 0.256 m downstream of the wing leading edge, ie at approximately 55% chord. Five different rear-sections were studied, each related through calculated boundary-layer characteristics[14] to one surface of a rear section of the unswept aerofoil model, and the relationship is shown in Fig 7. Except for RAE 5241, the surface of the related aerofoil section is the upper. Section 5241 provides flows analogous to those found on the lower surface of the unswept aerofoil section RAE 5225 at low lift and high Mach number.

The basic wing and the trailing edges were inspected before testing and the errors in the ordinates were found to be of the order of 0.01% chord.

Static pressures were measured on the wing at a number of positions across the span, the station with the largest number of tappings being at 55% span. This station, which was used for the assessment of the CFD codes, had 35 tappings on the upper surface and 10 on the lower, the latter set being used to establish the required zero-lift condition. All the tappings were drilled normal to the wing surface and were of 0.5 mm diameter. Details of the locations of the tappings are given in Ref 14.

Measurements of total and static pressures were made in the wake with a rake of pitot and static tubes located at 66% span and about one chord downstream of the wing trailing edge at that station. For the main series of tests, the rake was of different design to that used with the unswept aerofoil model, with the pitot tubes spaced at about half the pitch of that of the aerofoil rake.

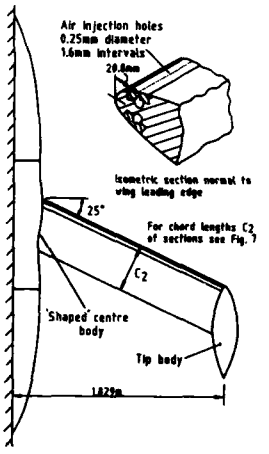


Fig. 6 Swept panel model

Two series of tests[5] were performed, the first concerned mainly with proving the air-injection system and the second devoted to the main task of studying the flow over the various aerofoil sections with transition fixed. In the main series, tests were performed at Mach numbers between 0.6 and 0.85 for the unit Reynolds number $R_L = 14.4 \times 10^6$/m and within the range 0.7–0.85 for $R_L = 31.2 \times 10^6$/m.

Boundary-layer transition was fixed on both surfaces by the air-injection method at the position shown in Fig 6, ie at about 5% chord. The holes were drilled normal to the surface, as with the unswept aerofoil model, but were of 0.25 mm diameter, at 1.6 mm pitch and were supplied by a common feed.

3.2 Determination of sectional drag

Sectional drag was inferred from the rake measurements in the same way as for the unswept aerofoil model but with two detailed differences. This method is valid only for two-dimensional, planar flows; however, calculations by a CFD method for infinite yawed-wings (SWVGK, section 4.2) indicates that the cross-flow at the rake is small (typically less than 3°), and, as will be shown later, the flow is uniform across the span in the region of the rake. The differences mentioned above are in the determination of the static pressure both at the rake and far downstream. The static pressure within the wake was obtained from a weighted average of the four static-pressure measurements on the rake, the weighting being biased towards the two readings nearest the centre line. This weighting was based on data from traverses of the static tubes through the wake using the technique described below. Static pressure far downstream was assumed to be given by the rake mean value. Again, calculations by SWVGK of the streamwise variation of static pressure in the wake suggest that this is a satisfactory approximation.

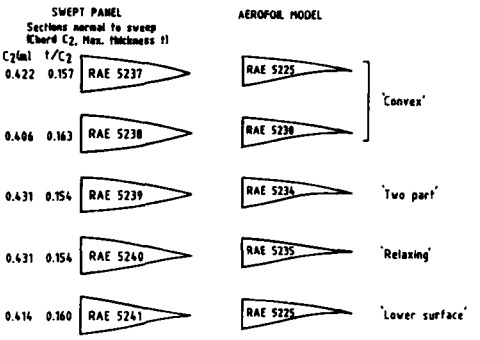


Fig. 7 Swept panel and related aerofoil model sections

The approximations described above should be viewed against the main aim of the experiment which, it will be recalled, was to study differences in the drag of various wing sections.

Checks on the spanwise uniformity of the flow included:

(i) Oil-flow tests on a pilot model of approximately 3/8th scale* in the 3ft × 3ft Wind Tunnel, RAE Bedford with the same transition trip positions and for the same Mach-number range as for the present model but at R = 2.5 × 10^6;

(ii) studies of the measured static-pressure distributions on the wing and boundary-layer parameters inferred from them;

(iii) measurements of the spanwise variation of sectional drag obtained by rotating the rake about its axis through the wake.

The oil-flow tests suggest that the limiting-streamline direction changes slowly along the wing generators except within about 1/4 chord of either end of the wing for Mach numbers up to about 0.8. The second check involved calculating the boundary-layer parameters at the wing trailing edge using the measured pressure distributions. Two calculation methods were used, one for infinite yawed-wings and the other for fully three-dimensional flows, and the results for all the aerofoil sections at M = 0.81 (presented in Ref 14) show that the flow is uniform, with boundary-layer displacement thickness changing by less that 3% in the interval 40-70% span. Further confirmation of flow uniformity is provided by isobar plots, an example of which is given in Fig 8 together with the corresponding spanwise variation of drag which is seen to be small in the interval 55-70% span.

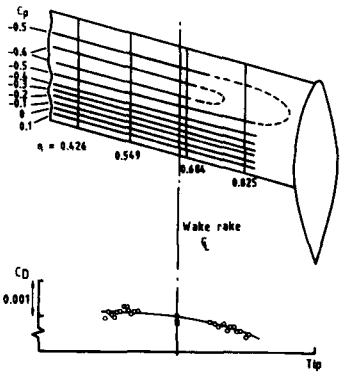


Fig. 8 Isobars on upper surface and spanwise variation of drag, RAE 5237, M = 0.811, R_L = 14.4 × 10^6/m

3.3 Corrections to Mach number

In order to correct the data for comparison with CFD methods for 'free-air' flows about infinite yawed-wings, it was necessary to allow for two effects on the streamwise flow.

The more obvious of the effects is the usual blockage constraint for half models mounted from one wall (ie for the remaining three walls). In the absence of detailed pressure measurements on the walls, this correction was determined using a technique which

* In order to ensure that these oil flows were representative of those on the 'full scale' model at R = 7 × 10^6, the aerofoil section of the pilot model was designed to have boundary-layer characteristics close to the trailing edge similar to those of the present model with the section RAE 5237.

is standard for subsonic tests in the 8ft × 8ft Wind Tunnel. In this method, linear theory is used to calculate (a) the effect of the model and its images on velocity increments at two points on the roof and corresponding points on the floor, in both cases on the tunnel centre line and close to the model centre of volume, and (b) the blockage increment at a reference point on the model. The ratio of the blockage increment to the arithmetic mean of the increments in (a) is combined with the mean of the measured changes in static pressure at the four points relative to those in the empty tunnel to infer the blockage at the model. Since the method uses wall-pressure measurements in the region of the model, with linear theory merely providing a ratio, the technique is considered to be accurate for the flows studied on the swept-panel model. Evidence to support this view is given in Ref 9 where blockage calculated by the method is compared with that determined by the potentially more-accurate theory of section 2.4 for aerofoil flows.

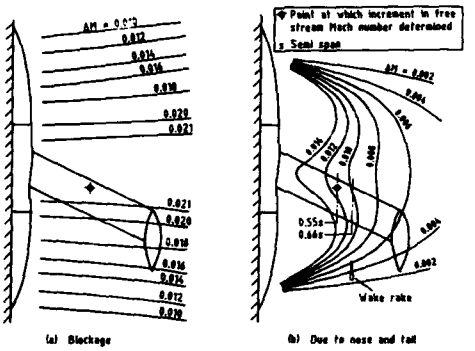


Fig. 9 Lines of constant Mach number increment, M = 0.8

The reference point at which the blockage was calculated is illustrated in Fig 9 which also indicates that blockage increment in Mach number, calculated by linear theory, varies slowly over the region of interest for M = 0.8.

A second correction is needed for end effects of the model not represented in CFD methods for infinite yawed-wings. The effects of the wing tip and root in the region of interest are counteracted by the tip body and the shaping of the half body, as shown in section 3.2. However, there remains the effect of the nose and tail of the half body and their reflections in the adjacent sidewall: the resulting Mach-number increment varies slowly over the wing and thus a correction for the effect may be made to free-stream Mach number. The correction has been calculated using a panel method[15] and results for lines of constant Mach number increment are shown in Fig 9 where the change in this increment along the chord is seen to be small at the measurement station 55% span. The incremental correction to Mach number calculated for the reference point (Fig 9) at M = 0.8 is 0.011.

Further justification for these procedures is given in section 5.2 where calculated and measured pressure distributions are compared.

3.4 Repeatability of measurements

Since the aim of this experiment was to measure differences rather than absolute values of drag, the emphasis was on achieving a high standard of repeatability. This was made possible by the consistency of the air-injection method and also by minimising excursions of tunnel total-pressure during each scan of the wake rake. By this means, sectional drag coefficient was repeated to within ±0.00015. Static-pressure coefficient was repeatable to within ±0.001.

4 CFD METHODS

In this section a brief description is given of the CFD methods for unswept and swept aerofoils assessed in this paper.

4.1 VGK

The viscous version of the Garabedian and Korn method (VGK)[3] was developed to calculate viscous, transonic flows over unswept aerofoil sections. Based on the viscous/inviscid interaction technique, VGK uses a modified form of the full-potential algorithm of Ref 2 for the inviscid flow and integral methods to calculate the shear layers. Thwaites method[16], extended to allow for compressibility[17], is used for the laminar layers, and the turbulent layers are computed by the lag-entrainment method[18]. Displacement effects of the shear layers are represented by wall transpiration, and allowance is made for the effect of flow curvature in the wake as well as on the calculation of the 'wall' static pressures in the real viscous flow.

The modification to the method of Ref 2 is in the representation of the shock, the non-conservative difference scheme in the original method being replaced by a 'quasi-conservative' operator[3]. In this way a better representation is possible of the shock pressure-rise as well as of shock position. The new scheme requires a 'quasi-conservative difference' parameter to be specified, and this parameter is usually found by matching the shock pressure-rise in a related inviscid flow to that of a Rankine-Hugoniot shock (see section 4.4).

VGK and its derivatives, to be described later, calculate drag by two methods:

(i) The direct process of integrating the streamwise components of pressure and skin-friction forces around the section, and

(ii) application of the momentum theorem to the far field.

In this paper, method (ii) is preferred because it is less sensitive to discretisation errors than the other method[19]. Thus drag coefficient is determined using the expression

$$C_D = C_{D_V} + C_{D_W} ,$$

where

$$C_{D_V} = 2\theta_\infty/c$$

is the viscous drag coefficient and θ_∞ is the momentum thickness of the viscous wake far downstream. Wave drag coefficient, C_{D_W}, is calculated by the subroutine MACHCONT[20]. The underlying theory of this method is described in Refs 19 and 20, and mention need only be made of the assumptions used that (a) the local flow is normal to the shock and (b) the flow downstream of the shock is adiabatic and isentropic. The former assumption is reasonable for inviscid flows where the shock intersects the aerofoil along a normal to the surface but in real flows the shock interacts with the boundary layer in such a way that the shock is oblique. This implies that MACHCONT overestimates wave drag, in general, and evidence to support this view is provided in section 5.1.

In calculations for swept-wing sections (section 5.2), sweep is allowed for as follows: on an infinite yawed-wing the inviscid part of the flow is two-dimensional in planes that are perpendicular to both the wing leading edge and chord plane. Thus the inviscid flow is inferred from an equivalent two-dimensional flow, defined by the suffix 2, at the free stream Mach number

$$M_2 = M \cos \Lambda$$

about the aerofoil section normal to the leading edge and with appropriate boundary conditions on the aerofoil and in the wake. The static-pressure coefficients of the two flows are related by [2].

$$C_p = C_{p_2} \cos^2 \Lambda . \qquad (1)$$

The more subtle effects of sweep on the shear layers are catered for approximately by a suitable choice of chord Reynolds number. Following Ref 22, the equivalent Reynolds number, R_e, is considered to be based on streamwise chord, c, and the component of free-stream speed normal to the leading edge, or

$$Re = U_2 c/\nu .$$

Referring to Eq.(1) and noting the relationship between the non-dimensional thickness of the two sections

$$t/c = (t/c_2) \cos \Lambda ,$$

it follows that pressure-drag coefficients, including wave-drag coefficient, are related by

$$C_{D_W} = (C_{D_W})_2 \cos^3 \Lambda \qquad (2)$$

Likewise the viscous-drag coefficient may be expressed as

$$C_{D_V} = (C_{D_F})_2 \cos^3 \Lambda + C_{D_f} , \qquad (3)$$

where suffixes F and f refer to boundary-layer pressure (or form) and skin-friction components. An approximate relationship between skin-friction drag coefficients for wings with transition close to the leading edge (as in the present case) is derived in Ref 14 as follows:

$$C_{D_f} = (C_{D_f})_2 \cos^{1/5} \Lambda .$$

Thus noting that $C_{D_F} = C_{D_V} - C_{D_f}$, Eq.(3) may be rewritten as:

$$C_{D_V} = \{(C_{D_V})_2 - (C_{D_f})_2\} \cos^3 \Lambda + (C_{D_f})_2 \cos^{1/5} \Lambda . \qquad (4)$$

Comparison between the drags predicted by this method and by a version of VGK representing cross-flow effects in the shear layers (SWVGK, section 4.2) suggests that Eq.(4) is accurate for sweep angles below about 30°. Evidence showing that this statement applies to the present swept-wing sections is provided in section 5.2.

4.2 SWVGK

SWVGK, short for swept version of VGK, is based on VGK but, as noted above, represents cross-flow effects in the shear layers. The method for the laminar layers is adapted using Cooke's small cross-flow approximation[23] while the lag-entrainment method is

replaced by the entrainment integral-method of Smith for infinite yawed-wings[24], extended to incorporate the effects of 'lag' on the entrainment equation in the way described in Ref 25.

Viscous drag is determined from principles of mass and momentum conservation in the wake[26].

4.3 BVGK

This version of VGK[4] includes 'higher-order' effects which become increasingly important as flow separation is approached. These include (a) flow curvature as it affects the streamwise momentum-integral equation[27], the matching between the viscous and inviscid flows[27], and the turbulence structure[18], and (b) Reynolds normal stresses in the streamwise momentum integral equation[27]. As well, corrections are made to allow for the effects of low Reynolds number (mainly on skin friction) and a shape-parameter relationship is used which is more suitable for flows with separation than that of the lag-entrainment method. On the basis of a study by Preston[28] of turbulent boundary-layers on flat plates, a correction is also made to increase local Reynolds number based on boundary-layer momentum thickness just downstream of transition to 320 if it falls below this value. Finally, the turbulent shear-layer equations are integrated by an inverse method which is computationally more efficient than the normal 'direct' method of VGK for flows approaching separation.

Sweep is allowed for approximately in the way described in section 4.1 for VGK, and hence this correction does not include the effect on turbulence structure of the non-linear interaction between flow curvature and cross flow observed by Baskaran et al[29].

4.4 Details of calculations

In all the calculations, the 'artificial viscosity' and 'quasi-conservative difference' parameters are set at 0.8 and 0.25 respectively, and the calculations are performed to a high degree of numerical convergence in 'fine' (160 × 31) grid, except where indicated. A value of 0.25 gives approximately the correct (Rankine-Hugoniot) shock pressure rise in related inviscid flows.

For a number of flows over both wind tunnel models, it has been shown[5] that the air-injection system effectively fixes transition at the lines of air holes. Thus transition is taken to be at these lines in the calculations.

Nominal ordinates of the sections are used in the calculations rather than the inspected ordinates. As already indicated in sections 2 and 3, the errors in the ordinates are small. On the other hand, the associated errors in static pressure can be significant where they occur close to sonic conditions. Estimated corrections to the (measured) pressures based on calculations by BVGK are shown on pressure distributions to be presented in section 5.

5 COMPARISONS BETWEEN MEASUREMENT AND CFD

5.1 Aerofoils

VGK provides reasonable predictions of pressure distribution for attached flows[9]. However, where separation is approached or occurs, VGK is less satisfactory. This is illustrated in Fig 10a-d which show calculated and measured pressure distributions for the sections RAE 5225 and 5230 ('convex'), RAE 5234 ('two part') and RAE 5235 ('relaxing').

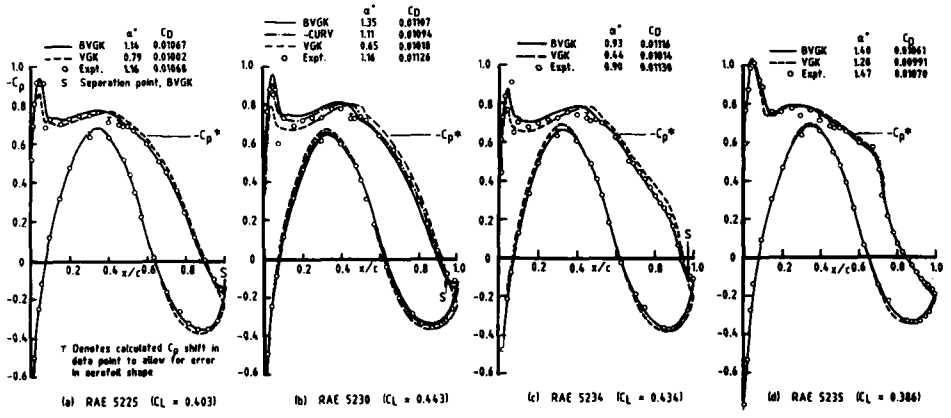


Fig. 10 a - d Calculated and measured pressure distributions
$C_L \triangleq 0.40$, M = 0.735, R = 6 × 10^6

The comparisons are made at M = 0.735, R = 6 × 10^6 and for a lift coefficient (≈0.4) at which the flows are shock free. The calculated values of incidence (to achieve the required lift) and drag coefficient are compared with the measured values in the figures. For the three cases with separation calculated by BVGK to occur upstream of the trailing edge, BVGK gives significantly better predictions of pressure distributions, incidence and drag than does VGK. The differences between the two predictions of pressure distributions are less evident for the one attached flow, RAE 5235; however, even in this case, BVGK's predictions of incidence and drag are much closer to the measured values than those of VGK. Overall, the agreement between the predictions by BVGK and measurement of drag is particularly encouraging. Less satisfactory is the tendency for BVGK to underestimate the suctions on the upper surface of the rear half of RAE 5230. This discrepancy is traced[4] to the inadequacy of the allowance in BVGK for the effect on turbulence structure of flow curvature in cases with separation occurring some distance upstream of the trailing edge (ie > 2% chord). In such cases, it is better to ignore this correction as shown in Fig 10b where the modified method is referred to as -CURV.

Fig 11a-d show corresponding comparisons for flows with shock waves on the upper surface (C_L ≈ 0.6). As before, BVGK gives better predictions of pressure distributions and incidence than does VGK, and, for the flow with the largest region of rear separation, RAE 5230, further improvement in agreement with measurement is achieved if the curvature correction noted above is neglected. Estimates of drag by BVGK are also closer to measurement than those of VGK for all sections except for RAE 5235, on the upper surface of which there is a relatively strong shock at C_L = 0.6. In this case BVGK overestimates drag coefficient by 0.0009. Possible reasons are discussed later.

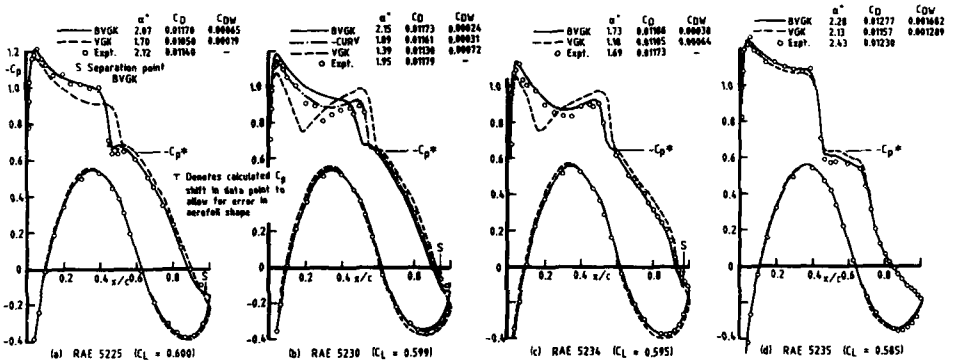


Fig. 11 a - d Calculated and measured pressure distributions
$C_L \triangleq 0.6$, M = 0.736, R = 6 × 10^6

Calculated and measured overall section forces and pitching moments for the aerofoils of Figs 10 and 11 are compared in Fig 12 for M ≈ 0.735* and the Reynolds numbers 6 × 10^6 and 20 × 10^6. Fig 12 confirms the improved accuracy of BVGK compared with that of VGK and shows that drag predictions by BVGK are in generally good agreement with measurement where shock waves may be considered either absent or weak, typically for C_L between 0.2 and an upper limit between 0.5 and 0.6 depending on section. For this class of flows, BVGK estimates with reasonable accuracy the change in drag, at a given lift, both with Reynolds number and section shape. However, where wave drag is a significant proportion of the total drag, BVGK overestimates drag. A possible explanation, already noted in section 4.1, is that the field method used to calculate wave drag, MACHCONT, assumes that the local flow is normal to the shock and consequently overestimates the wave drag for real viscous flows. However, the calculated wave drag is also affected indirectly by the tendency for BVGK to underestimate the rear loading for flows with significant rear separation (notably RAE 5230). In order to compensate for this loss of lift, BVGK requires a somewhat higher incidence than that measured with the consequence that the strength of the upper-surface shock is overestimated by the method. Some improvement in agreement between the calculated and measured drags of RAE 5230 at high lift is obtained if the curvature correction to turbulence structure is ignored as shown in Fig 12.

Further comparisons between calculation and measurement are given in Ref 4 including pressure distributions and drag for the 'relaxing' section RAE 5236 as well as boundary-layer thicknesses and skin friction for the 'convex' section RAE 5225.

---

* In the tests corrected Mach number was allowed to change slightly with incidence; however, all the calculations have been made at the appropriate Mach number.

5.2 Swept wing sections

Pressure distributions of the five swept-wing sections are shown in Fig 13 for M = 0.811 (M_2 = 0.735) and R = 7 × 10^6, or more precisely at a unit Reynolds number 14.4 × 10^6/m. Measurements are compared with predictions by VGK, BVGK (both corrected for sweep in the way described in section 4.1) and SWVGK. Calculations by all three methods are in good agreement with measurement over the forward 40% chord where the displacement effect of the shear layers is small and the CFD methods should thus be accurate, indicating that the Mach-number corrections (section 3.4) are satisfactory.

Of the three methods, BVGK gives the closest estimate of the pressures over the aft 10–20% chord, especially for the sections with separations predicted by BVGK. However, predictions by BVGK of pressures on the aft 20% chord of the 'lower surface' section RAE 5241 are not in good agreement with measurement, probably because cross-flow and other three-dimensional effects[29] in the shear layers are not properly represented. SWVGK, which includes cross-flow effects, does not represent effects included in BVGK and shown in section 5.1 to be important for unswept aerofoils with rear separation. On the other hand, this flow has a relatively large region of separation (approximately 10% chord in length) and thus is perhaps of less interest to wing designers than are the other four.

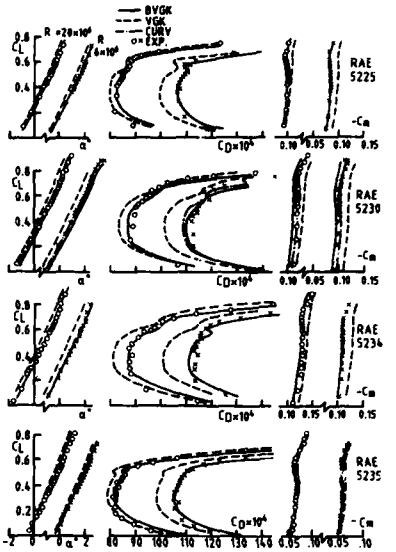


Fig. 12 Lift, drag and pitching moment curves, M ≙ 0.735 R = 6 × 10^6 & 20 × 10^6 (17.7 × 10^6 RAE 5230)

For the analysis of drag a 'notional drag coefficient per surface' is defined, $C_{D_S} = C_D/2$. The section RAE 5237 (the less extreme of the two 'convex' sections in terms of rear pressure-gradient, Fig 13) is used as the datum for the study of the effect on drag of changes in section shape. Measurements and predictions of C_{D_S} for this section are compared in Fig 14 for the two Reynolds numbers 7 × 10^6 and 15 × 10^6 over the range of (corrected) Mach numbers tested. All three methods are in reasonable accord with measurement at Mach numbers of 0.7 and below, where the flows are attached, suggesting that the test technique is basically sound and that RAE 5237 is a suitable choice as a datum section. At Mach numbers between 0.7 and 0.8 closest agreement with measurement is provided by BVGK.

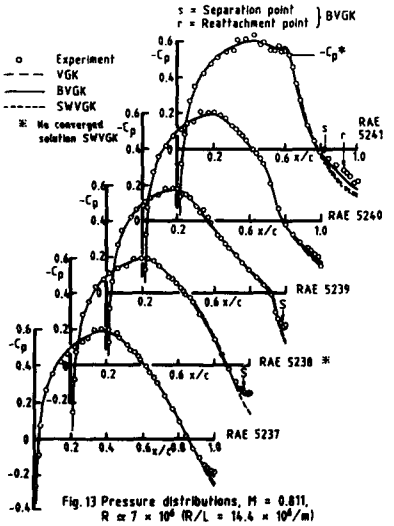


Fig. 13 Pressure distributions, M = 0.811, R ≈ 7 × 10^6 (R/L = 14.4 × 10^6/m)

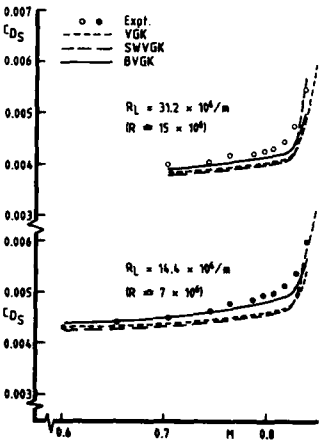


Fig. 14 Notional drag per surface RAE 5237

Fig 15a-d show corresponding plots of increments in C_{D_S}, relative to that of RAE 5237, for the four remaining sections. Two main points may be made about these comparisons: the first is that the predictions by VGK and SWVGK of the drag increments and the drag of the datum section RAE 5237 (Fig 14) are in good agreement. This suggests that

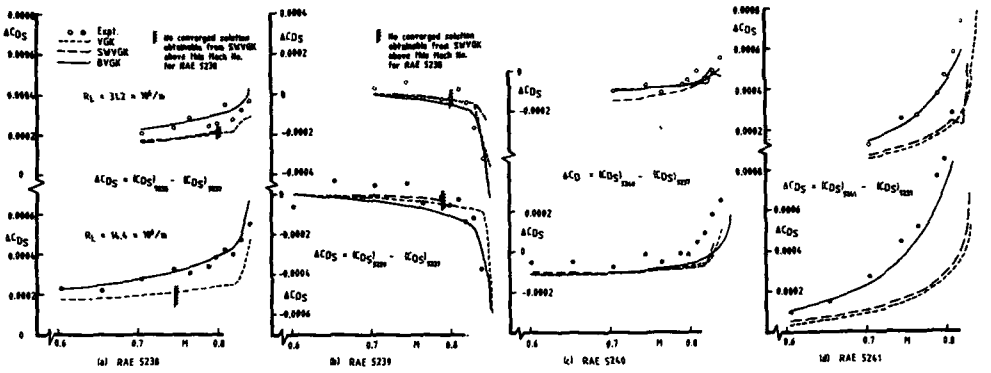


Fig. 15 a - d Notional drag per surface relative to that of RAE 5237

the simple sweep-correction applied to both VGK and BVGK is adequate for the swept-wing sections tested. The second observation is that the best agreement with measurement, overall, is obtained with BVGK which predicts the increments ΔC_{D_S} to better than about 0.0001. The improvement in agreement over the other methods is particularly evident for the 'convex' section RAE 5238 and the 'lower surface' section RAE 5241. Both these sections have long reaches of adverse pressure gradient over the aft 50% chord, with, in each case, separation predicted (by BVGK) to occur upstream of the trailing edge at $M = 0.81$, $R = 7 \times 10^6$ (Fig 13).

The effect on drag of changing unit Reynolds number from 31×10^6/m to 14×10^6/m is illustrated for each of the sections in Fig 16a-e. Again BVGK is seen to give the closest agreement with measurement of the three CFD methods, especially for the sections RAE 5238 and 5241.

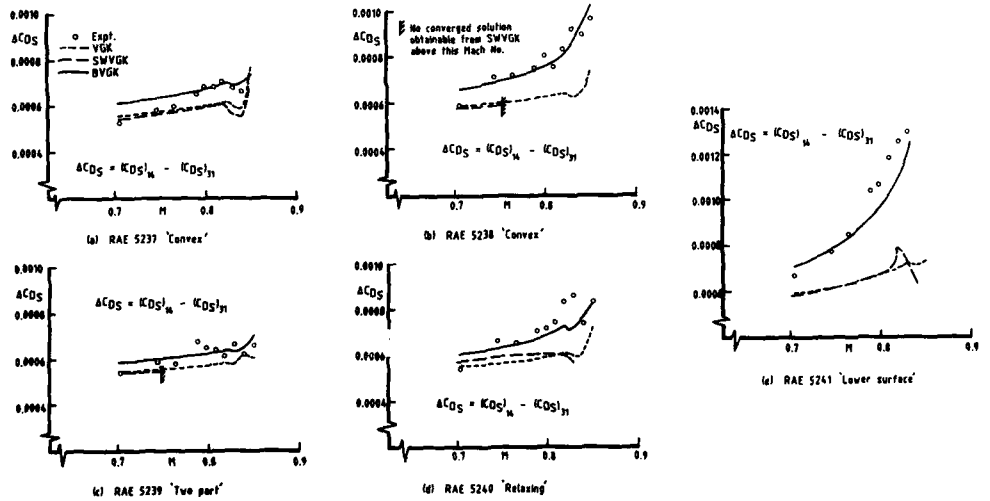


Fig. 16 a - e Differences between notional drag per surface at two Reynolds Numbers, $R_L = 31.3 \times 10^6$/m and 14.4×10^6/m

Figs 14-16 taken together indicate that effects included in BVGK and found to be important in flows on unswept aerofoils approaching separation, have a similar significance for swept wings of modest sweep.

6 CONCLUSIONS

Two experiments have been described which are suitable for validating CFD methods for transonic flows over aerofoils. The first experiment was performed on an unswept aerofoil model with various trailing-edge sections of differing rear-camber and base thickness and the second simulated analogous flows over a panel wing of 25° sweep. In

both experiments, care was taken to minimise experimental error from various sources, including wall interference and aeroelastic distortion, and to ensure that the initial and boundary conditions of the flows were accurately defined.

Data from the experiments have been used to assess a number of CFD methods for aerofoils, including VGK and modified versions of this method, BVGK and SWVGK. The main conclusions of the comparisons between calculations by these methods and measurement are as follows:

(1) Unswept aerofoils

(i) BVGK predicts pressure distributions and drag that are generally to a high standard of accuracy and a significant improvement over those of VGK.

(ii) Estimates by BVGK of the change in drag with section shape and Reynolds number are in close agreement with measurement.

(iii) BVGK, with the field method MACHCONT used to determine wave drag, overestimates drag for flows with shock waves. However, for flows with significant rear separation, as defined in section 5.1, some improvement in agreement with measurement is obtained if the curvature correction to turbulence structure is omitted.

(2) Swept wing sections

(i) BVGK, corrected for sweep in a simple way, predicts accurately the pressure distribution of all the sections except the 'lower-surface' section, and also the effect on drag of section shape and Reynolds number.

(ii) The simple sweep-correction applied to drag estimates by BVGK is justified, to some extent, by the good agreement between the drag predictions by VGK with the same correction and those of SWVGK.

The investigation as a whole has demonstrated the importance of including effects in the modelling of the shear layers which become important as separation is approached.

REFERENCES

1 J. F. Nash, P. Bradshaw. The magnification of roughness drag by pressure gradients. 1967, Journal R Ae S, 71, pp 44-46.

2 P. R. Garabedian, D. G. Korn. Analysis of transonic airfoils. 1971, Comm Pure App. Math, XXIV, pp 841-851.

3 M. R. Collyer, R. C. Lock. Prediction of viscous effects in steady transonic flow past an aerofoil. 1979, Aero Qu 30, (3) pp 485-505.

4 P. R. Ashill, R. F. Wood, D. J. Weeks. An improved, semi-inverse version of the viscous Garabedian and Korn method (VGK). 1987, RAE Technical Report 87002.

5 P. R. Ashill, D. J. Weeks. Measurements of the flow over aerofoils of advanced design. RAE Technical Report in preparation.

6 P. R. Ashill, J. L. Fulker, D. J. Weeks. The air-injection method of fixing boundary-layer transition and investigating scale effects. 1987, The Aeronautical Journal 91, pp 214-224.

7 C. N. H. Lock, W. F. Hilton, S. Goldstein. Determination of profile drag at high speeds by a pitot traverse method. 1940, ARC R&M 1971.

8 H. C. Garner, E. W. E. Rogers, W. E. A. Acum, E. C. Maskell. Subsonic wind tunnel wall corrections. 1966, AGARDograph 109.

9 P. R. Ashill, D. J. Weeks. A method for determining wall-interference corrections in solid wall tunnels from measurements of static pressure at the walls. 1982, AGARD-CP-335, Paper 1.

10 P. R. Ashill, R. F. A. Keating. Calculation of tunnel wall interference from wall-pressure measurements. 1985, RAE Technical Report 85086.

11 D. Isaacs. Calibration of the RAE Bedford 8ft × 8ft Wind Tunnel at subsonic speeds, including a discussion of the correction to the measured pressure distribution to allow for the direct and blockage effects due to the calibration probe shape. 1969, ARC R&M 3583.

12 R. Shaw. The influence of hole dimensions on static pressure measurements. 1960, Journal of Fluid Mechanics, 7, pp 550-564.

13 L. Gaudet. Humidity and scale effect on static pressures measured on the walls of a large supersonic wind tunnel. 1965, RAE Technical Report 65074.

14 P. R. Ashill, J. L. Fulker, R. F. Wood. On the sectional drag and pressure distributions of swept wing aerofoil sections. RAE Technical Report in preparation.

15 H. W. M. Hoeijmakers. A panel method for the determination of the aerodynamic characteristis of complex configurations in linearised subsonic or supersonic flow. Part I Description and application, Part II Evaluation of aerodynamic influence coefficients, Part III Description of computer code NLRAERO. 1980, NLR TR 80124u.

16 B. Thwaites. Approximate calculation of the laminar boundary layer. 1949, Aero Qu, 1 245.

17 K. Stewartson. Correlated compressible and incompressible boundary layers. 1949, Proc Roy Soc Lond, A200, pp 84-100.

18 J. E. Green, D. J. Weeks, J. W. F. Brooman. Prediction of turbulent boundary layers and wakes in compressible flow by a lag entrainment method. 1973, ARC R&M 3791.

19 R. C. Lock. Prediction of the drag of wings at subsonic speeds by viscous/inviscid interaction techniques. 1985, AGARD-R-723, Paper 10.

20 C. M. Billing, A. J. Bocci. The MACHCONT method for calculating the wave drag of a 2-D aerofoil. 1986, ARA Memorandum 272.

21 B. G. J. Thompson, G. A. Carr-Hill, M. Ralph. The prediction of boundary-layer behaviour and profile drag for infinite yawed wings. 1973, RAE Technical Report 73090.

22 P. H. Cook, M. A. McDonald, M. C. P. Firmin. Wind tunnel measurements of the mean flow in the turbulent boundary layer and wake in the region of the trailing edge of a swept wing at subsonic speeds. 1979, RAE Technical Report 79062.

23 J. C. Cooke. Boundary layers over infinite yawed wings. 1960, Aero Qu, 11 pp 333-347.

24 P. D. Smith. A calculation method for the turbulent boundary layer on an infinite wing in compressible adiabatic flow. 1972. RAE Technical Report 729193.

25 P. R. Ashill, P. D. Smith. An integral method for calculating the effects on turbulent boundary-layer development of sweep and taper. 1985., The Aeronautical Journal 89, (882), pp 43-54.

26 J. C. Cooke. The drag of infinite swept wings with an Addendum. 1969, ARC CP 1040.

27 L. F. East. A representation of second-order boundary layer effects in the momentum integral equation and in viscous-inviscid interaction. 1981, RAE Technical Report 81002.

28 J. H. Preston. Minimum Reynolds number for a turbulent boundary layer and the selection of a transition device. 1957, Journal of Fluid Mechanics, Vol 3, Part IV, pp 373-384.

29 V. Baskaran, Y. M. Pontikis, P. Bradshaw. Experimental investigation of a three-dimensional boundary layer on an 'infinite' swept convex wing. 1987, Imperial College of Science and Technology unpublished Technical Report.

Acknowledgments

The efforts of Mrs N. E. Rycroft and Mr G. L. Riddle in preparing the figures and assistance with CFD calculations by Miss C. J. Betts and Mr M. J. Simmons are gratefully acknowledged.

Copyright © Controller HMSO London 1988

PARAMETRIC STUDY OF GRID SIZE, TIME STEP, AND TURBULENCE MODELING ON NAVIER-STOKES COMPUTATIONS OVER AIRFOILS

by
Christopher L. Rumsey
W. Kyle Anderson
NASA Langley Research Center
Mail Stop 128
Hampton, VA 23665
USA

SUMMARY

An upwind-biased implicit approximate factorization algorithm is applied to several steady and unsteady turbulent flows. The thin-layer form of the compressible Navier-Stokes equations is used. Numerical aspects of the solutions are investigated, including grid and time step effects. Both the flux-vector splitting and flux-difference splitting methods are used to determine fluxes, and the results are compared. Flux-difference splitting predicts results more accurately than flux-vector splitting on a given mesh size, but, in its present implementation, is more severely limited by the maximum CFL number for unsteady time-accurate flows. Physical aspects of the computations are also examined. An equilibrium turbulent boundary layer model computes generally better steady and unsteady results than a nonequilibrium model when there is little to no boundary layer separation. Conversely, when a significant region of separation exists, the nonequilibrium model performs in better agreement with experiment.

NOMENCLATURE

G,H	inviscid fluxes
H_v	viscous fluxes
I	identity matrix
J	transformation Jacobian
L	reference length, taken as chord, c
Pr	Prandtl number, taken at 0.72
Q	conservation variables
R	distance outward from body
T	temperature
U,V	contravariant velocities
a	speed of sound
c_d	total drag coefficient
c_{df}	skin friction drag coefficient
c_{dp}	pressure drag coefficient
c_f	skin friction coefficient
c_ℓ	lift coefficient
c_m	moment coefficient about $\frac{1}{4}$ c, positive nose up
c_p	pressure coefficient
e^p	total energy, nondimensionalized by $\tilde{\rho}_\infty \tilde{a}_\infty^2$
k	reduced frequency, $\tilde{\omega}\tilde{L}/\tilde{q}_\infty$
p	pressure, nondimensionalized by $\tilde{\rho}_\infty \tilde{a}_\infty^2$
q	total velocity, nondimensionalized by $\tilde{a}_\infty$
q_{x_i}	heat flux terms
t	time, nondimensionalized by $\tilde{L}/\tilde{a}_\infty$
u,v	Cartesian velocities in x and y directions, nondimensionalized by $\tilde{a}_\infty$
x,y	Cartesian coordinates
y^+	inner wall similarity variable
Δt	time step
α	angle of attack
γ	ratio of specific heats, taken at 1.4
η,ζ	general curvilinear coordinates
κ	parameter controlling spatial difference-scheme type
λ	coefficient of bulk viscosity
μ	coefficient of molecular viscosity
ρ	density, nondimensionalized by $\tilde{\rho}_\infty$
$\tau_{x_i x_j}$	viscous shear stress terms
ϕ	time-accuracy parameter
ω	frequency

Subscripts:

e	edge
t	denotes differentiation in time
x,y	denotes differentiation in x and y directions, respectively
η,ζ	denotes differentiation in η and ζ directions, respectively
∞	denotes conditions at infinity

Superscripts:

n	denotes time level
$\hat{}$	denotes quantities in generalized coordinates
$\tilde{}$	denotes dimensional quantities

INTRODUCTION

The accurate computations of both steady and unsteady flows over airfoils are an important aspect of the aircraft design and performance evaluation process. However, practical considerations limit the accuracy that can be attained. Present-day computer speed and storage limitations restrict researchers, at best, to the use of the Reynolds-averaged Navier-Stokes equations for practical 2-D airfoil or 3-D wing problems. Therefore, some type of turbulence model must be employed for turbulent flow computations. Even with this restriction, for high Reynolds number flow computations, it is impractical to employ a fine enough streamwise grid to resolve the (usually small) viscous terms assocated with derivatives along the body. Therefore, the thin-layer approximation to the Reynolds averaged Navier-Stokes equations is generally used, and only gridpoints normal to the body are densely clustered.

In addition to the unavoidable errors inherent in the use of approximations to the Navier-Stokes equations, any numerical method introduces other types of error. In time-accurate solutions, for example, any implicit scheme that does not use Newton's method or some other form of sub-iterations introduces linearization error into the solution. Additionally, factorization error results from the use of approximate factorization on the left-hand side of the Navier-Stokes equations. Most importantly, however, are discretization errors, present in both time-accurate and non-time-accurate flow computations, associated with the use of finite grid sizes and/or time steps. This type of error can be assessed by successive grid and time step refinements. In fact, it is very important to perform a detailed parametric study using a given computational fluid dynamics code for a particular class of problem at least once. The discretization error bounds determined can then serve as a guide to the accuracy of the solutions of similar problems.

The present paper describes parametric studies for two types of turbulent flow: flow over airfoils at constant angle-of-attack as well as unsteady flow over airfoils in pitch. For the steady cases, a study of the variation in the solution with grid spacing, grid extent, and turbulence model is given. For the unsteady cases, an additional study of the effect of time step size is included. Also, two different methods for evaluating fluxes at the cell faces are examined. These methods are termed flux-vector splitting (FVS) and flux-difference splitting (FDS), respectively, and are described in the text.

GOVERNING EQUATIONS

The thin-layer approximation to the Navier-Stokes equations is used in the present analysis. Therefore, only viscous derivatives in the direction normal to the wall (ζ) are retained. The equations are written in generalized coordinates and conservation form:

$$\frac{\partial}{\partial t}(\hat{Q}) + \frac{\partial}{\partial \eta}(\hat{G}) + \frac{\partial}{\partial \zeta}(\hat{H} - \hat{H}_v) = 0 \tag{1}$$

$$\hat{Q} = \frac{Q}{J} = \frac{1}{J}\begin{Bmatrix} \rho \\ \rho u \\ \rho v \\ e \end{Bmatrix} \tag{2}$$

$$\hat{G} = \frac{1}{J}\begin{Bmatrix} \rho U \\ \rho U u + \eta_x p \\ \rho U v + \eta_y p \\ (e+p)U - \eta_t p \end{Bmatrix} \tag{3}$$

$$\hat{H} = \frac{1}{J}\begin{Bmatrix} \rho V \\ \rho V u + \zeta_x p \\ \rho V v + \zeta_y p \\ (e+p)V - \zeta_t p \end{Bmatrix} \tag{4}$$

$$\hat{H}_v = \frac{1}{J}\begin{Bmatrix} 0 \\ \zeta_x \tau_{xx} + \zeta_y \tau_{xy} \\ \zeta_x \tau_{xy} + \zeta_y \tau_{yy} \\ \zeta_x b_x + \zeta_y b_y \end{Bmatrix} \tag{5}$$

$$\begin{aligned} U &= \eta_x u + \eta_y v + \eta_t \\ V &= \zeta_x u + \zeta_y v + \zeta_t \end{aligned} \tag{6}$$

$$p = (\gamma - 1)[e - \rho(u^2 + v^2)/2] \tag{7}$$

The variables η and ζ correspond to the coordinates parallel and normal to the body surface, respectively. The terms η_t and ζ_t represent the mesh velocity, and are zero for flow over a non-moving body. Q

represents density, momentum, and total energy per unit volume. The Jacobian of the transformation is J, defined as:

$$J = \frac{\partial(\eta,\zeta)}{\partial(x,y)} \tag{8}$$

The equations are nondimensionalized by the freestream density $\tilde{\rho}_\infty$ and soundspeed $\tilde{a}_\infty$. The shear stress and heat flux terms are defined in tensor notation as:

$$\tau_{x_i x_j} = \frac{M_\infty}{Re_L}\left[\mu\left(\frac{\partial u_i}{\partial x_j} + \frac{\partial u_j}{\partial x_i}\right) + \lambda \frac{\partial u_k}{\partial x_k}\delta_{ij}\right] \tag{9}$$

$$q_{x_i} = -\left[\frac{M_\infty}{Re_L Pr(\gamma-1)}\right]\frac{\partial(a^2)}{\partial x_i} \tag{10}$$

$$Re_L = \frac{\tilde{\rho}_\infty \tilde{q}_\infty \tilde{L}}{\tilde{\mu}_\infty} \qquad M_\infty = \frac{\tilde{q}_\infty}{\tilde{a}_\infty} \tag{11}$$

In (5), b_{x_i} is defined as:

$$b_{x_i} = u_j \tau_{x_i x_j} - q_{x_i} \tag{12}$$

Stokes hypothesis for bulk viscosity, $\lambda + 2\mu/3 = 0$, and Sutherland's law for molecular viscosity,

$$\mu = \tilde{\mu}/\tilde{\mu}_\infty = (\tilde{T}/\tilde{T}_\infty)^{3/2}\left[(\tilde{T}_\infty + \tilde{c})/(\tilde{T} + \tilde{c})\right] \tag{13}$$

are used, with $\tilde{T}_\infty$ = freestream temperature = 460°R, and $\tilde{c}$ = Sutherland's constant = 198.6°R.

NUMERICAL METHOD

The linearized, backward-time approximation for the two-dimensional equations is given in delta form as:

$$\left[\frac{I(1+\phi)}{J\Delta t} + \delta_\eta \frac{\partial \hat{G}}{\partial Q} + \delta_\zeta\left(\frac{\partial \hat{H}}{\partial Q} - \frac{\partial \hat{H}_v}{\partial Q}\right)\right]\Delta Q = -L(Q^n) \tag{14}$$

where $L(Q^n)$ is given by:

$$L(Q^n) = \delta_\eta \hat{G} + \delta_\zeta(\hat{H} - \hat{H}_v) - \frac{\phi}{J\Delta t}\Delta Q^{n-1} \tag{15}$$

If $\phi = 0$, the scheme is first-order accurate in time, while if $\phi = 1/2$, the scheme is temporarily second-order accurate.

The flux-vector splitting (FVS) method extended for dynamic meshes in reference 1 is used to split the fluxes into forward and backward contributions according to the signs of the eigenvalues of the Jacobian matrices. For example, $\delta_\eta \hat{G}$ in (15) at a cell centered at point i (holding the j index constant) can be written:

$$\left[\delta_\eta \hat{G}\right]_i = \hat{G}_{i+1/2} - \hat{G}_{i-1/2} = \left[\hat{G}^+(Q^-_{i+1/2}) + \hat{G}^-(Q^+_{i+1/2})\right] - \left[\hat{G}^+(Q^-_{i-1/2}) + \hat{G}^-(Q^+_{i-1/2})\right] \tag{16}$$

$Q^\pm$ denotes state variables on cell interfaces determined from upwind-biased interpolations of the conserved variables.

Flux-difference splitting (FDS), developed by Roe[2], can also be used to determine fluxes on the faces. In this case, the example in (16) would be written:

$$\left[\delta_\eta \hat{G}\right]_i = \hat{G}_{i+1/2} - \hat{G}_{i-1/2} \tag{17}$$

where, for example

$$\hat{G}_{i+1/2} = 1/2\left[\hat{G}(Q^-_{i+1/2}) + \hat{G}(Q^+_{i+1/2}) - |\bar{A}|_{i+1/2}(Q^+_{i+1/2} - Q^-_{i+1/2})\right] \tag{18}$$

and

$$|\bar{A}|_{i+1/2} = \bar{T}_{i+1/2}|\bar{\Lambda}|_{i+1/2}\bar{T}^{-1}_{i+1/2} \tag{19}$$

where A is the Jacobian of $\hat{G}$, Λ is the matrix of eigenvalues of A, and T and T^{-1} are the matrices of right and left eigenvectors, respectively. The overbars in (18) and (19) denote Roe-averaged quantities. See reference 2 for details.

State variables for both FVS and FDS are obtained on the interfaces via upwind-biased interpolation of the conserved variables.

$$Q^{-}_{i+1/2} = Q_i + \{1/4[(1-\kappa)\Delta_- + (1+\kappa)\Delta_+]\}_i \tag{20a}$$

$$Q^{+}_{i+1/2} = Q_{i+1} - \{1/4[(1-\kappa)\Delta_+ + (1+\kappa)\Delta_-]\}_{i+1} \tag{20b}$$

where

$$\Delta_+ = Q_{i+1} - Q_i \qquad \Delta_- = Q_i - Q_{i-1} \tag{21}$$

The parameter $\kappa \in [-1,1]$ forms a family of difference schemes: $\kappa = -1$ corresponds to second-order fully-upwind differencing, $\kappa = 1/3$ to third-order upwind-biased differencing, and $\kappa = 1$ to central differencing.

When flux-limiting is desired to eliminate oscillations in shock regions, particularly for the upwind-biased scheme, a **min-mod** limiter is used. Flux-limited interpolations are identical in form to (20a) and (20b), except that Δ_+ and Δ_- are replaced with $\bar{\Delta}_+$ and $\bar{\Delta}_-$, respectively, where:

$$\begin{aligned} \bar{\Delta}_+ &= \max[0,\min(\Delta_+ \mathrm{sgn}\Delta_-,\ \beta\Delta_- \mathrm{sgn}\Delta_+)]\mathrm{sgn}\Delta_+ \\ \bar{\Delta}_- &= \max[0,\min(\Delta_- \mathrm{sgn}\Delta_+,\ \beta\Delta_+ \mathrm{sgn}\Delta_-)]\mathrm{sgn}\Delta_- \end{aligned} \tag{22}$$

$$\beta = \frac{(3-\kappa)}{(1-\kappa)} \tag{23}$$

Equation (14) is spatially factored and solved in a series of sweeps through the mesh.

$$\left[\frac{I(1+\phi)}{J\Delta t} + \delta_\eta \frac{\partial \hat{G}}{\partial Q}\right]\Delta Q^* = -L(Q^n) \tag{24a}$$

$$\left[\frac{I(1+\phi)}{J\Delta t} + \delta_\zeta\left(\frac{\partial \hat{H}}{\partial Q} - \frac{\partial \hat{H}_v}{\partial Q}\right)\right]\Delta Q = \left(\frac{I(1+\phi)}{J\Delta t}\right)\Delta Q^* \tag{24b}$$

$$Q^{n+1} = Q^n + \Delta Q \tag{24c}$$

The implicit spatial derivatives of the convective and pressure terms are spatially first-order accurate, resulting block tridiagonal inversions for each sweep. For example, the left-hand side of (24a) is a block banded matrix with the following structure for the ith row:

$$\left[\ \ldots,0,-A^{+}_{i-1/2},\ \left(A^{+}_{i+1/2} - A^{-}_{i-1/2} + \frac{I(1+\phi)}{J\Delta t}\right),\ A^{-}_{i+1/2},0,\ldots\ \right] \tag{25}$$

where, for FVS, A^+ and A^- are the true Jacobians of $\hat{G}^+$ and $\hat{G}^-$ evaluated at cell centers:

$$A^{+}_{i+1/2} = \left[\frac{\partial \hat{G}^+}{\partial Q}\right]_i \qquad A^{-}_{i+1/2} = \left[\frac{\partial \hat{G}^-}{\partial Q}\right]_{i+1} \tag{26}$$

For FDS, the true Jacobians are more difficult and hence more expensive to compute, so the following approximation is used in the present analysis:

$$A^{+}_{i+1/2} = \frac{A_i + |\bar{A}|_{i+1/2}}{2} \qquad A^{-}_{i+1/2} = \frac{A_{i+1} - |\bar{A}|_{i+1/2}}{2} \tag{27}$$

where the overbars in (27) denote Roe-averaged quantities.

Two different turbulence models are studied, and their results are compared. Both the equilibrium, algebraic, eddy-viscosity model of Baldwin and Lomax[3] and the nonequilibrium half-equation model of Johnson and King[4] solve for an effective turbulent viscosity μ_t, which is incorporated into the laminar Navier-Stokes equations. The Johnson-King model performs streamwise integration of an ordinary differential equation in order to obtain values for the maximum shear stress along the body.

Boundary conditions are applied explicitly. In the farfield, a quasi-one-dimensional characteristic analysis is used to determine boundary data, and a point vortex representation for induced velocities on the outer boundary is included for steady flow solutions.[5] On the body, no-slip and adiabatic wall conditions are used, along with a zero normal pressure gradient assumption.

The present computational algorithm is highly vectorized for use on either the CYBER 205 or the CRAY 2 computers. Computational speed averages approximately 16μs/gridpt/iteration, and the main memory required in words is about 260 x (meshsize). About half of this memory allocation is associated with saving the Jacobian matrices, which are recomputed only once every set number of iterations. This procedure results in increased computational speed with no discernible effect on either steady or unsteady results, provided that the number of iterations to update is small in comparison with the number of iterations over which large changes take place in the unsteady flowfield. A further increase in computational speed is obtained for turbulent cases by updating the effective turbulent viscosity in a similar fashion. In the present analysis, the Jacobians and turbulence quantities are updated every 20 iterations.

STEADY FLOW RESULTS

A summary of the steady-state cases analyzed is presented in Tables 1 and 2. Most of these cases were studied previously in Rumsey et al.[6] When started from uniform freestream conditions, a typical airfoil case using approximately 26,000 gridpoints converges to a steady-state solution in about 3000 to 4000 iterations, or about 20 to 30 minutes of CPU time on either the CYBER 205 or CRAY 2 computers.

Grid Sensitivity Study

The grid sensitivity study was performed for the steady results on an NACA 0012 airfoil at M_∞=0.7 , α=1.49°, and Re=9 million. Table 1 lists the conditions and results. This corresponds to one of the experimental test cases of Harris.[7] The Baldwin-Lomax turbulence model is employed for all results in this section, with transition location specified at 5 percent of the chord.

A 265x101 C-mesh was developed for the NACA 0012 airfoil with 180 points on the airfoil, a maximum grid extent of R_{max}=15c, and a minimum spacing normal to the wall of ΔR_{min}=2.06x10^{-4}c. This minimum spacing allows for at least three points in the laminar sub-layer of the turbulent boundary layer. For the conditions of M_∞=0.7, α=1.49°, and Re=9 million, this yields a y^+ value of about 0.6 one gridpoint off the wall at x/c=0.5. The near-field of this grid is shown in figure 1.

In order to perform a grid extent study, the 265x101 mesh with R_{max}=15c was both shortened and extended, keeping an identical grid distribution and minimum spacing in the interior of the grid. The resulting grids are: a 251x85 mesh with R_{max}=5c, a 279x117 mesh with R_{max}=30c, and a 289x125 mesh with R_{max}=45c. The code was run using the third-order upwind-biased scheme (κ = 1/3) with the min-mod flux limiter employed. Figures 2(a) and (b) show lift and drag coefficient as a function of R_{max} for both FVS and FDS methods using the farfield point vortex boundary condition, as well as the FDS method using no point vortex. The experimental results of Harris are also included. When the point vortex boundary condition is used, lift and drag for both FVS and FDS methods remain essentially unchanged over the range of R_{max} examined. In fact, results using FDS on a grid with R_{max}=30c are identical to results for R_{max}=15c. In other words, errors in global properties such as lift and drag associated with the use of grids of finite extent for this problem are nearly eliminated through the use of the point vortex boundary condition. Therefore, for the grid density study described below, in which grids with R_{max}=15c are used, these types of errors need not be considered. Notice, in figures 2(a) and (b), that the FDS result without the point vortex is approaching the FDS result with the point vortex as R_{max} is increased. For R_{max}=45c, both lift and drag are within about one percent of their values on a mesh of infinite extent.

For the grid density study, four grid sizes with an outer boundary extent of R_{max}=15c were used: the 265x101 grid described earlier, a 211x81 grid with 142 points on the airfoil and ΔR_{min}=2.58x10^{-4}c, a 169x65 grid with 116 points on the airfoil and ΔR_{min}=3.23x10^{-4}c, and an 85x33 grid with 58 points on the airfoil and ΔR_{min}=6.46x10^{-4}c. Again, using the κ = 1/3 scheme with the flux-limiter, both FVS and FDS methods were run on the four grids. Global properties of lift and drag coefficient are plotted in figures 3(a) and 3(b), respectively, as a function of the inverse of the meshsize. The experimental result of Harris is also plotted. The lift and drag coefficients for both FVS and FDS methods can be extrapolated to values of about 0.259 and .0077, respectively, for a mesh of infinite density. This lift value is higher than experiment by about 7 percent, and the drag value is low by about 3 percent. On the finest 265x101 mesh, lift is predicted to within 0.15 percent of its value on an infinite mesh by FDS, and to within 0.35 percent by FVS. Drag is within 1.6 percent for FDS and 2.8 percent for FVS.

For boundary-layer flows, FDS has been found to give a more accurate representation of the viscous layer than FVS for a given number of gridpoints.[8] The present results are consistent with this observation. As seen in figures 3(a) and (b), there is less variation in lift and drag with meshsize for FDS than for FVS. Figure 4(a) shows boundary layer profiles at two upper surface locations using FVS on both the finest (265x101) and coarsest (85x33) grids. There is a significant underprediction of the velocities in the profile by the coarsest mesh, particularly near the "knee" of the profile. However, as shown in figure 4(b), FDS results on the coarsest mesh are very similar to results on the finest mesh.

It should be noted that, for a typical airfoil problem such as the one investigated here, large differences between FVS and FDS only manifest themselves on very coarse meshes such as the 85x33 mesh. The finer the mesh, the less differences are seen not only in global properties such as lift and drag, but in boundary layer profiles, skin-friction coefficients, and flowfield contours as well. This is expected, since the solutions using both methods should be identical in the limit of infinite mesh size.

All of the steady results in the following section on turbulence model comparison are obtained using FVS and second order upwind spatial differencing (κ = -1). The differences between second and third-order spatial differencing using FVS are shown as a function of meshsize in figures 5(a) and (b). As expected, third-order upwind-biasing yields more accurate lift and drag values on a given mesh than second-order fully

upwind, and results extrapolate to the same values on infinitely dense grids. Since a fine 265x101 mesh is used for all of the results in the next section, the errors introduced as a result of using second-order spatial accuracy as opposed to higher-order accuracy is expected to be very small. In this case, the second-order method on the 265x101 mesh predicts lift to within 2.2 percent of its value extrapolated on an infinite mesh (compared with 0.3 percent for third-order). Drag is within 3.5 percent (compared with 2.8 percent for third-order).

Turbulence Model Study

The second-order fully upwind scheme ($\kappa = -1$) was used to compute several transonic viscous flows over airfoils using both the Baldwin-Lomax and Johnson-King turbulence models. In all cases, a 265x101 C-mesh was employed, with R_{max}=15c and ΔR_{min}=2.06x10^{-6}c. Results are compiled in Table 2. Most of these cases were used as standard test cases for the Viscous Transonic Airfoil Workshop held in 1987, and reported by Holst.[9] Coakley[10] compared several different turbulence models, including Baldwin-Lomax and Johnson-King. He found the Johnson-King model to do generally better than Baldwin-Lomax for airfoil flows with significant regions of boundary layer separation.

First, the NACA 0012 airfoil case from the grid sensitivity study was examined using the two turbulence models. Pressure coefficients and upper surface skin friction coefficients are shown in figures 6(a) and (b). The pressure coefficients from the two turbulence models are similar and generally agree with the experiment of Harris except near the suction peak. The Johnson-King model predicts lift and drag coefficients of 0.2397 and 0.00789, as opposed to 0.2533 and 0.00797 for Baldwin-Lomax. Slight differences are also seen in the skin friction. Johnson-King yields slightly lower friction values over most of the airfoil upper surface. Notice that although the streamwise grid spacing is fairly fine at the trailing edge (about 0.010c), the skin friction values at the last couple of gridpoints near the trailing edge rise. This behavior is numerical in nature, caused by the natural dissipation of the scheme. Although not shown, further refinement of the grid at the trailing edge or use of a higher-order spatial scheme (such as $\kappa = 1/3$) help to alleviate this problem.

Further results for the NACA 0012 airfoil at two different conditions are given. Figures 7(a) and (b) show pressure coefficients and skin friction coefficients at M_∞=0.55, α=8.34°, and Re=9 million. The Johnson-King model gives a shock slightly forward of the Baldwin-Lomax model result. Both turbulence models show a small amount of separation (about 5%c) downstream of the shock and again near the trailing edge. Results for the NACA 0012 airfoil at M=0.799, α=2.26° and Re=9 million are shown in figures 8(a) and (b). In this case, a fairly strong shock near the mid chord tends to separate the boundary layer. In fact, the Johnson-King model predicts a separated region extending about 38 percent of the chord behind the shock, with separation again near the trailing edge. This model does a better job than the Baldwin-Lomax model in predicting the location of the upper surface shock for this case. The reason for the disagreement of the Johnson-King pressures with experiment on the lower surface for this case is not known. All of the results shown here for the NACA 0012 airfoil agree well with the results of Coakley in reference 10, for both turbulence models.

Three more steady-state cases were run using both turbulence models. Results are shown for the RAE 2822 airfoil, and are compared to the experimental results of Cook et al.[11] Transition location for all cases is assumed to be at 3 percent of the chord. Lift and drag coefficients are tabulated in Table 2. The angles-of-attack used in the computations were obtained by applying the wall interference corrections suggested in reference 11. Again, all results obtained for the RAE 2822 airfoil using both turbulence models agree qualitatively with Coakley's results in reference 10.

Results for RAE Case 6 (as designated in reference 11), at M_∞=0.725, α=2.54°, Re=6.5 million are shown in figures 9(a) through (d) in plots of pressure coefficient, skin friction coefficient, displacement thickness, and velocity profiles, respectively. Baldwin-Lomax does generally better for this case than Johnson-King, particularly in the prediction of the shock location. Notice that the computed lower pressures do not match experiment, indicating that perhaps a Mach number correction or a further angle-of-attack correction is necessary. This case has very little shock-induced separation predicted by Baldwin-Lomax, and none predicted by Johnson-King. In front of the shock, skin friction coefficient levels are underpredicted by Johnson-King, although displacement thicknesses and the velocity profile at x/c=0.319 agree with Baldwin-Lomax and experiment. Aft of the shock, skin friction and displacement thickness values predicted by Johnson-King are generally higher than those predicted by Baldwin-Lomax.

Figures 10(a) through (d) show results for RAE Case 9, at M_∞=0.73, α=2.79°, and Re=6.5 million. Again, there is little or no shock-induced separation for this case, and the Baldwin-Lomax model correctly predicts the shock location in comparison with experiment while Johnson-King predicts the shock too far upstream. Skin friction, displacement thickness, and velocity profile trends for both turbulence models are similar in nature to RAE Case 6.

Finally, RAE Case 10, at M_∞=0.750, α=2.81°, and Re=6.2 million, is shown in figures 11(a) through (d). In this case, Baldwin-Lomax fails to capture the shock location accurately while Johnson-King does. Both turbulence models predict a significant region of separation behind the shock (extending about 20 percent of the chord). The Johnson-King model yields displacement thicknesses aft of the shock in better agreement with experiment and does slightly better to predict the boundary layer profiles at two stations downstream of the shock.

UNSTEADY FLOW RESULTS

Most of the unsteady results analyzed in the present study were studied previously by Rumsey and Anderson,[12] and represent an airfoil undergoing a sinusoidal pitching motion about its quarter chord. The angle-of-attack of the airfoil at any time is given by the equation:

$$\alpha(t) = \alpha_0 + \alpha_1 \sin(M_\infty k t)$$

Computations are started impulsively from freestream, and are continued until the cyclic variation of the lift is periodic in time. The farfield point-vortex boundary condition is not utilized for unsteady flows.

Grid and Time Step Sensitivity Study

An extensive computational study is presented for the NACA 0012 airfoil in sinusoidal pitch, corresponding with AGARD Case 3 from Landon.[13] Effects of grid extent, grid density, spatial accuracy, time step, and temporal accuracy are examined for their effect on the unsteady solution. Additionally, solutions using FVS and FDS are compared. The conditons are: M_∞=0.6, α_0=4.86°, α_1=2.44°, Re=4.8 million, and k=0.1620. Unless otherwise noted, all computations for this case are carried out using FVS with first-order accuracy in time (ϕ = 0), third-order accuracy in space (κ = 1/3), and flux-limiting employed. Also, the flow over the airfoil is assumed to be fully turbulent (transition location = 0%), and is solved using the Baldwin-Lomax turbulence model.

In order to study the effect of outer boundary extent on the solution, a 129x49 grid with R_{max}=15c has been shortened and extended to yield grids with R_{max}=5c (123x41) and R_{max}=30c (137x57), respectively, keeping an identical distribution in the interior of the grid. Minimum normal spacing at the wall is 4.37×10^{-6}c and there are 88 points on the airfoil. Results are obtained using a time step of Δt=0.05. Figures 12(a) and (b) show lift and moment coefficients as a function of angle-of-attack. The curves are followed in a counterclockwise sense; i.e., increasing alpha is represented on the lower portions of the plots. Results show that increasing grid extend from 5c to 30c increases both lift and moment throughout the cycle. The solution is less sensitive to changes past R_{max}=15c, indicating that 15 chords is adequate for the computations presented. The lift coefficients throughout the cycle agree well with experiment for both the R_{max}=15c and R_{max}=30c grids. Moment coefficients, however, are generally low in comparison with experiment.

For the grid density study, three grid sizes were used. The finest is a 257x97 C-mesh, with R_{max}=15c and Δs_{min}=2.15×10^{-6}c. The two coarser meshes were formed by subsequently deleting every other mesh line from the finer mesh, yielding a 129x49 mesh (used above in the grid extent study) and a 65x25 mesh. The time step used is 0.01 for the finest mesh and 0.05 for the two coarser meshes, resulting in approximately 6464 and 1293 iterations per pitching cycle, respectively. The effect of using different time steps on the solution is discussed below.

Figures 13(a) and (b) show lift and moment coefficients as functions of angle-of-attack for the three mesh sizes. The 65x25 mesh underpredicts lift throughout the cycle, while both the 129x49 and 257x97 meshes give results in close agreement with each other and with experiment. All three grids predict moments which are low compared with experiment, but the two finer meshes produce similar results and give higher values than the coarse mesh over most of the cycle.

The two finest mesh solutions are compared with experimental pressure coefficients at various points in the cycle in figures 14(a) through (e). Results are given at the following angles-of-attack: 5.95°+ , 6.97°+ , 6.57°+ , 5.11°+ , and 2.43°+ . The + symbol indicates that the angle-of-attack is increasing and + indicates decreasing. As can be seen in figures 14(a) through (d), when a shock is present, the finest mesh yields slightly more negative pressure coefficients upstream and in the region of the shock, in better agreement with experiment. The two meshes give nearly identical results at other locations on the airfoil. Computations show the greatest disagreement with experiment at α = 5.11°+and α = 2.43°+(figures 14(d) and (e)). However, the computations at these two angles-of-attack also show higher pressures over the entire lower surface in comparison with experiment, indicating that perhaps an angle-of-attack correction is necessary.

Figures 15(a) and (b) show the effect of right-hand side spatial accuracy on the solution using a 129x49 grid and a time step of 0.05. Third-order upwing-biasing (κ = 1/3) gives higher lift and moment values than the second-order fully-upwind method (κ = -1), in generally better agreement with the finer mesh solution (in figures 13(a) and (b)) and with experiment.

The effect of time step on the solution using the 129x49 grid has been assessed. Results are nearly identical for time steps of 0.1, 0.05, and 0.025, corresponding to 646, 1293, and 2586 steps per cycle, respectively. Results are shown in a plot of c_l vs. t in figure 16. The maximum lift coefficient varies slightly from 0.89 to 0.90 as the time step decreases from 0.1 to 0.025. Although not shown, moment coefficients and pressure coefficients are also nearly identical for the three time steps. For this grid size, the maximum CFL number (occurring near the body where the mesh is finest) is about 16000, 32000, and 64000 for time steps of 0.025, 0.05, and 0.1, respectively. Although not shown, increasing the temporal order of accuracy from first to second-order has virtually no effect on the solution for a 129x49 grid using a time step of 0.05. This study indicates that, for this case, a time step of 0.1 (corresponding to 646 steps per cycle) on a 129x49 grid using κ = 1/3 and ϕ = 0 is sufficient to produce accurate results with respect to discretization error.

FDS was also used to obtain a solution to this problem on the 129x49 grid. In this case, however, it was necessary to lower the time step by a factor of about 10 (to Δt = 0.005). The reason for this is believed to be the high maximum CFL numbers (of order 10000) in combination with the use of approximate linearizations of the fluxes on the left-hand side of the equations of motion. FVS uses exact left-hand side linearizations. Comparisons between FVS and FDS are given in figure 17(a) through (c). Figures 17(a) and (b) show the lift and moment coefficients to be in good agreement for both methods. At an angle-of-attack of 6.57°+, FVS and FDS both give nearly identical pressure coefficients, as shown in figure 7(c). Similar results are obtained at other times in the cycle.

Turbulence Model Study

Although the Baldwin-Lomax and the Johnson-King turbulence models were originally developed for the computation of steady flows, both are employed in the present study for unsteady flows. All computations are carried out using FVS, and are first-order accurate in time, with a time step of Δt=0.01.

The effect of turbulence model is assessed for the same NACA 0012 airfoil case from reference 13 investigated in the Grid and Time Step Sensitivity Study Section. Results are shown in figures 18(a) through (c). For this case, third-order upwind-biasing ($\kappa = 1/3$) is used. Solutions using the Baldwin-Lomax turbulence model are shown with transition location at the leading edge as well as at 3 percent chord. Results are nearly identical for the two cases. The Johnson-King turbulence model, with transition set at 3%c, produces lift values which are lower than both Baldwin-Lomax and experiment, particularly at the high end of the cycle when the angle-of-attack is decreasing. The Johnson-King model tends to predict slightly lower shock strengths as well as shock locations further forward from the Baldwin-Lomax solution, resulting in lower lift values. An example at $\alpha = 6.57°$+ is shown in figure 18(b). This is consistent with the behavior of the Johnson-King model for steady transonic flows with little to no boundary layer separation. Although not shown, the present sinusoidal pitch case exhibits only a small region of shock-induced separation, extending at most about 5%c behind the shock, at any of the angles-of-attack displayed in figures 14(a) through (d). Figure 18(c) shows that the Johnson-King model yields higher moment values than Baldwin-Lomax, in better agreement with experiment over most of the cycle.

Since the Johnson-King turbulence model tends to predict results more accurately than Baldwin-Lomax for flows with large regions of separation, a NACA 64(A)-010 airfoil case tested experimentally by Davis[14] was chosen at the conditions M_∞=0.8, α_o=4.0°, α_1=1.0°, Re=12 million, and k=0.4. A 265x101 mesh with R_{max}=15c and ΔR_{min}=2.06x10^{-4}c was employed, with transition location assumed at 0.05c. Although not shown, the Johnson-King model yields a large separated region extending from the shock all the way to the trailing edge at the two times examined during the pitching cycle of this case. Using the second-order fully upwind method ($\kappa = -1$), the two turbulence models predict significantly different results, as shown in figures 19(a) through (d). Lift and moment coefficients as a function of angle-of-attack are shown in figures 19(a) and (b), respectively. No experimental data for lift and moment was available for comparison. In these figures, lift is traced clockwise (higher lift values for increasing alpha), and moment is traced counterclockwise. The Johnson-King model predicts significantly lower lifts and higher moments than Baldwin-Lomax.

Figures 19(c) and (d) show pressure coefficients at two times during the pitching cycle using the two turbulence models in comparison with experimental upper surface pressures. Note that the experiment was carried out at a slightly lower Mach number of 0.789. Small oscillations in the computed pressure coefficients are believed to be caused by non-smoothness in the airfoil surface representation of the grid. It is believed, however, that the general character of the results are not effected. Johnson-King predicts the shock location in better agreement with experiment than Baldwin-Lomax at both α=3.0° and α=5.0°. Again, this result is consistent with the conclusions for steady flows with a significant region of boundary layer separation.

CONCLUDING REMARKS

The present method has been used to solve the thin-layer Navier-Stokes equations. Numerical and physical aspects of both steady and unsteady turbulent flows have been studied for several different airfoils, and results have been compared with experiment.

The numerical study for the steady NACA 0012 airfoil case indicates the following:

1. Lift is computed to within 1 percent and drag to within 3 percent of its extrapolated value on an infinite mesh using third-order spatial differencing on a 265x101 grid with an outer boundary extent of 15c.

2. FVS and FDS yield identical results in the limit of infinite mesh size, but FDS is more accurate on a given mesh size.

The numerical study for the unsteady NACA 0012 airfoil case indicates:

1. Accurate results (with respect to discretization error) are obtained for this case using third-order spatial differencing and first-order time differencing on a 129x49 mesh, with an outer boundary extent of 15c and a time step of 0.1, corresponding to 646 time steps per cycle.

2. FVS and FDS yield similar results on a 129x49 mesh, although FDS in its present form is more severely limited by the maximum CFL number.

The physical aspects of the solutions have also been investigated. In general, for both steady and unsteady flows, an equilibrium, zero-equation turbulence model tends to predict pressure and force coefficients more accurately in comparison with experiment than a nonequilibrium, half-equation model when there is little to no boundary layer separation. Conversely, when a significant region of separation exists, the nonequilibrium model performs in better agreement with experiment.

REFERENCES

1. Anderson, W., Thomas, J., and Rumsey, C., "Extension and Applications of Flux-Vector Splitting to Unsteady Calculations on Dynamic Meshes," AIAA Paper 87-1152-CP, 1987.

2. Roe, P., "Approximate Riemann Solvers, Parameter Vectors, and Difference Schemes," **Journal of Computational Physics**," Vol. 43, 1981, pp. 357-372.

3. Baldwin, B. and Lomax, H., "Thin Layer Approximation and Algebraic Model for Separated Turbulent Flows," AIAA Paper 78-257, 1978.

4. Johnson, D., "Predictions of Transonic Separated Flow with an Eddy-Viscosity/Reynolds-Shear-Stress Closure Model," AIAA Paper 85-1683, 1985.

5. Thomas, J. and Salas, M., "Far-Field Boundary Conditions for Transonic Lifting Solutions to the Euler Equations," AIAA Paper 85-0020, 1985.

6. Rumsey, C., Taylor, S., Thomas, J., and Anderson, W., "Application of an Upwind Navier-Stokes Code to Two-Dimensional Transonic Airfoil Flow," AIAA Paper 87-0413, 1987.

7. Harris, C., "Two-Dimensional Aerodynamic Characteristics of the NACA 0012 Airfoil in the Langley 8-Foot Transonic Pressure Tunnel," NASA TM-81927, 1981.

8. Van Leer, B., Thomas, J., Roe, P., and Newsome, R., "A Comparison of Numerical Flux Formulas for the Euler and Navier-Stokes Equations," AIAA Paper 87-1104, 1987.

9. Holst, T., "Viscous Transonic Airfoil Workshop Compendium of Results," AIAA Paper 87-1460, 1987.

10. Coakley, T., "Numerical Simulation of Viscous Transonic Airfoil Flows," AIAA Paper 87-0416, 1987.

11. Cook, P., McDonald, M., and Firmin, M., "Airfoil RAE 2822 - Pressure Distributions, and Boundary Layer Wake Measurements," AGARD AR-138, Paper A6, 1979.

12. Rumsey, C., and Anderson, W., "Some Numerical and Physical Aspects of Unsteady Navier-Stokes Computations Over Airfoils Using Dynamic Meshes," AIAA Paper 88-0329, 1988.

13. Landon, R., "NACA 0012. Oscillatory and Transient Pitching," **Compendium of Unsteady Aerodynamic Measurement**, AGARD-R-702, 1982.

14. Davis, S., "Data Set 2, NACA 64A010 (NASA Ames Model) Oscillatory Pitching," **Compendium of Unsteady Aerodynamic Measurement**, AGARD-R-702, 1982.

Table 1 Steady Flow Computations for Grid Sensitivity Study, NACA 0012 Airfoil, $M_\infty = 0.7$, $\alpha = 1.49°$, Re = 9 million

GRID	R_{max}/c	TYPE	κ	PV*	c_ℓ	c_{dp}	c_{df}	c_d
265x101	15	FVS	1/3	Yes	0.2581	0.00238	0.00554	0.00792
		FVS	-1	Yes	0.2533	0.00250	0.00547	0.00797
		FDS	1/3	Yes	0.2594	0.00228	0.00554	0.00782
		FDS	1/3	No	0.2476	0.00255	0.00555	0.00810
211x81	15	FVS	1/3	Yes	0.2579	0.00256	0.00552	0.00808
		FVS	-1	Yes	0.2520	0.00275	0.00546	0.00821
		FDS	1/3	Yes	0.2597	0.00239	0.00548	0.00787
169x65	15	FVS	1/3	Yes	0.2577	0.00282	0.00549	0.00831
		FVS	-1	Yes	0.2507	0.00323	0.00550	0.00873
		FDS	1/3	Yes	0.2604	0.00256	0.00536	0.00792
85x33	15	FVS	1/3	Yes	0.2529	0.00681	0.00583	0.01264
		FVS	-1	Yes	0.2395	0.00907	0.00664	0.01571
		FDS	1/3	Yes	0.2594	0.00496	0.00443	0.00939
251x85	5	FVS	1/3	Yes	0.2577	0.00243	0.00554	0.00797
		FDS	1/3	Yes	0.2592	0.00233	0.00554	0.00787
		FDS	1/3	No	0.2297	0.00296	0.00556	0.00852
279x117	30	FVS	1/3	Yes	0.2583	0.00238	0.00554	0.00792
		FDS	1/3	Yes	0.2594	0.00228	0.00554	0.00782
		FDS	1/3	No	0.2544	0.00238	0.00552	0.00790
289x125	45	FDS	1/3	No	0.2560	0.00235	0.00553	0.00788

* PV indicates point-vortex farfield boundary condition

Table 2 Steady Flow Computations for Turbulence Model Study, 265x101 mesh, R_{max} = 15c, FVS, κ = -1

AIRFOIL	M_∞	Re x 10^{-6}	METHOD	α	c_ℓ	c_{dp}	c_{df}	c_d
NACA 0012	0.700	9.0	Experiment	1.86	0.241			0.0079
			B-L*	1.49	0.2533	0.00250	0.00547	0.00797
			J-K	1.49	0.2397	0.00263	0.00526	0.00789
NACA 0012	*0.550*	*9.0*	*Experiment*	*9.86*	*0.983*			*0.0253*
			B-L	8.34	0.9990	0.03251	0.00376	0.03327
			J-K	8.34	0.9171	0.03023	0.00395	0.03418
NACA 0012	0.799	9.0	Experiment	2.86	0.390			0.0331
			B-L	2.26	0.4923	0.04024	0.00493	0.04517
			J-K	2.26	0.3001	0.02979	0.00393	0.03372
RAE 2822 (Case 6)	0.725	6.5	Experiment	2.92	0.743			0.0127
			B-L	2.54	0.8183	0.00813	0.00543	0.01356
			J-K	2.54	0.7406	0.00659	0.00542	0.01201
RAE 2822 *(Case 9)*	0.730	6.5	Experiment	3.19	0.803			0.0168
			B-L	*2.79*	*0.8649*	*0.01314*	*0.00525*	*0.01839*
			J-K	2.79	0.7879	0.01044	0.00528	0.01572
RAE 2822 (Case 10)	0.750	6.2	Experiment	3.19	0.743			0.0242
			B-L	2.81	0.8629	0.02466	0.00517	0.02983
			J-K	2.81	0.7543	0.01951	0.00477	0.02428

* B-L indicates Baldwin-Lomax turbulence model
J-K indicates Johnson-King turbulence model

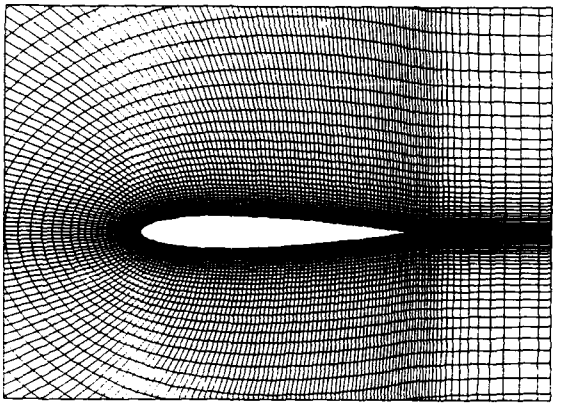
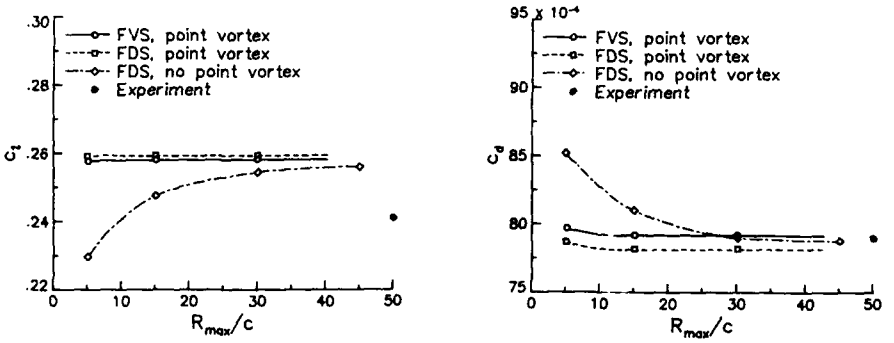
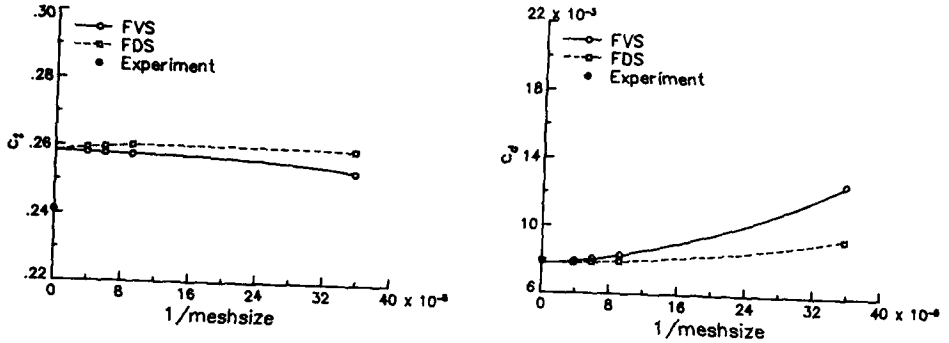


Figure 1 265x101 C-mesh for NACA 0012 airfoil (near-field)



a) lift coefficients b) drag coefficients

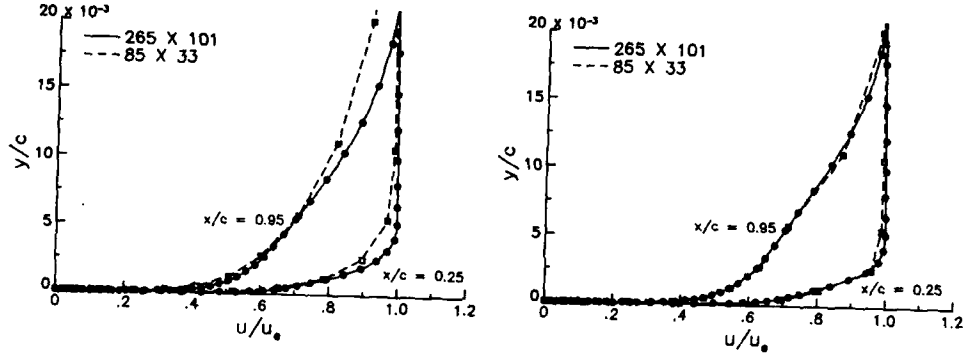
Figure 2 Grid extent study, NACA 0012 airfoil, M_∞=0.7, α=1.49°, Re=9 million



a) lift coefficients

b) drag coefficients

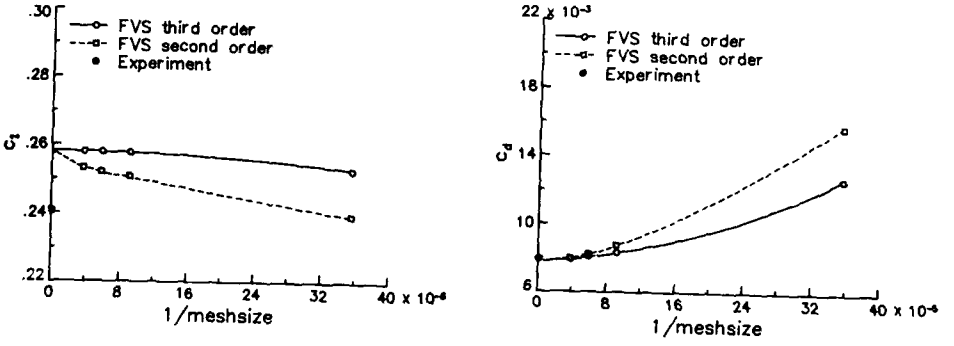
Figure 3 Grid density study, NACA 0012 airfoil, M_∞=0.7, α=1.49°, Re=9 million, R_{max}=15c



a) FVS

b) FDS

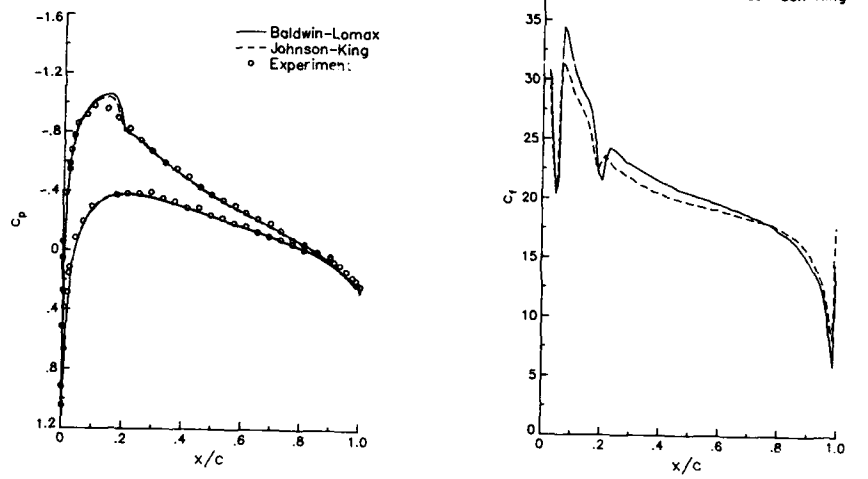
Figure 4 Upper surface velocity profiles, NACA 0012 airfoil, M_∞=0.7, α=1.49°, Re=9 million, R_{max}=15c



a) lift coefficients

b) drag coefficients

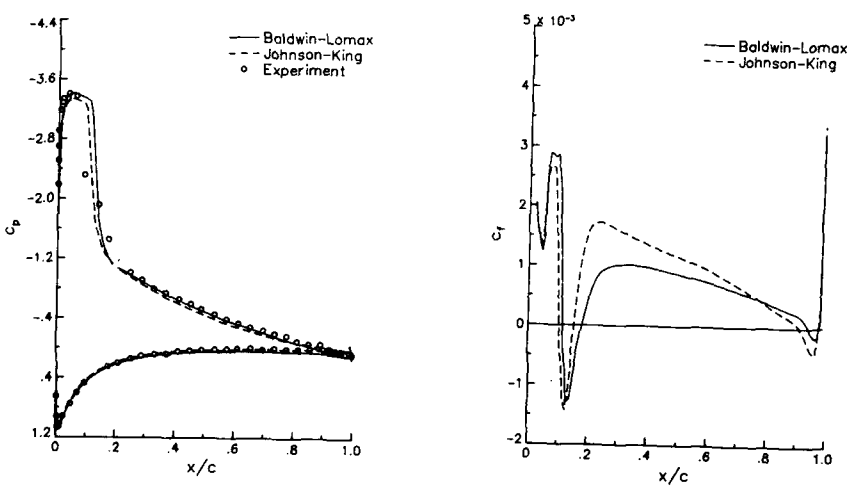
Figure 5 Spatial accuracy study, NACA 0012 airfoil, M_∞=0.7, α=1.49°, Re=9 million, R_{max}=15c



a) pressure coefficients

b) upper surface skin friction coefficients

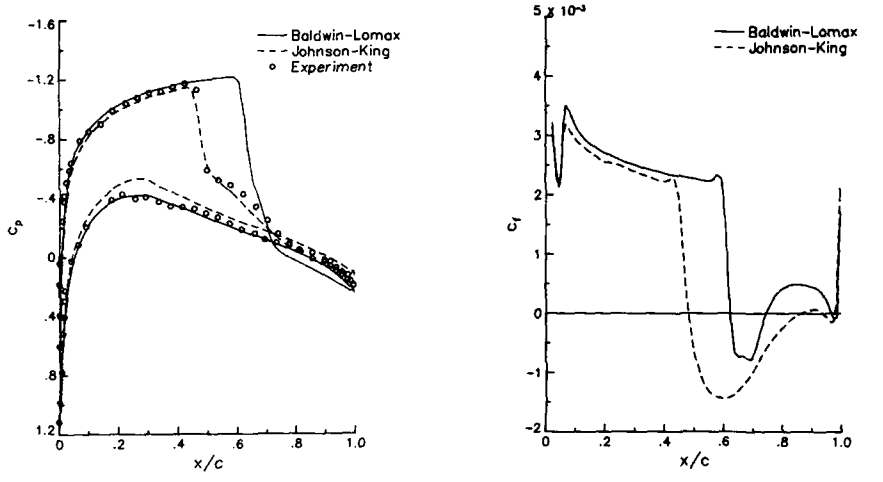
Figure 6 NACA 0012 airfoil, M_∞=0.7, α=1.49°, Re=9 million



a) pressure coefficients

b) upper surface skin friction coefficients

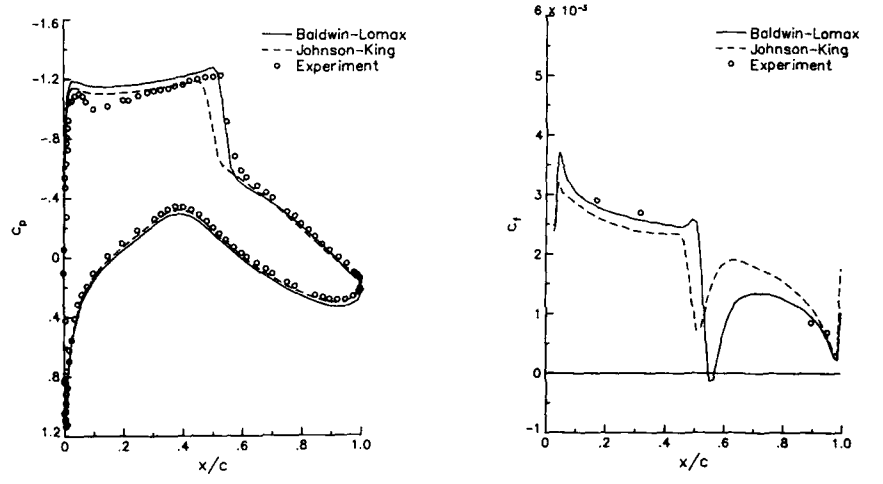
Figure 7 NACA 0012 airfoil, M_∞=0.55, α=8.34°, Re=9 million



a) pressure coefficients

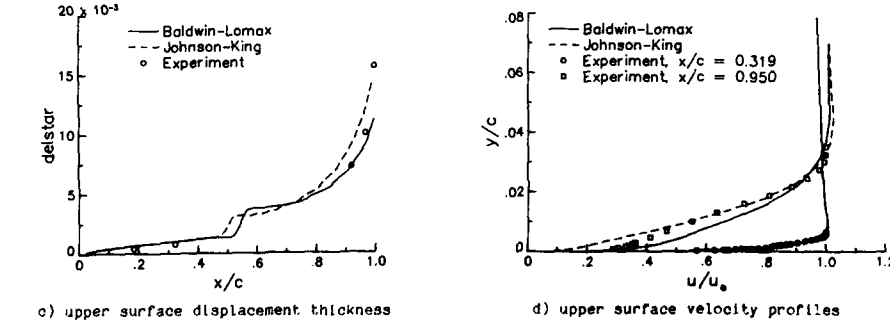
b) upper surface skin friction coefficients

Figure 8 NACA 0012 airfoil, M_∞=0.799, α=2.26°, Re=9 million



a) pressure coefficients

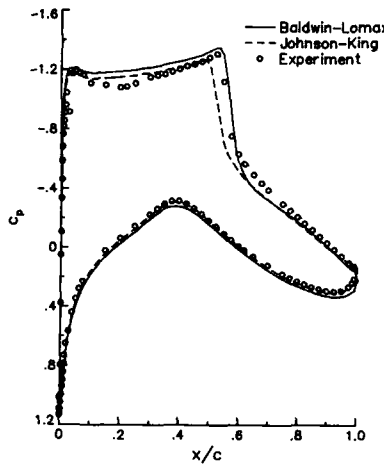
b) upper surface skin friction coefficients



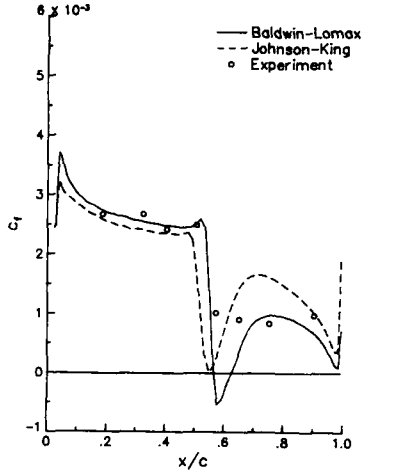
c) upper surface displacement thickness

d) upper surface velocity profiles

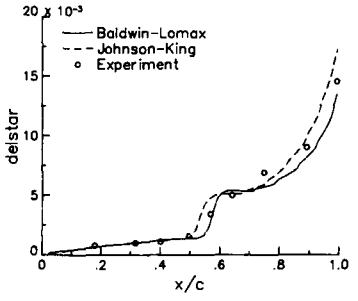
Figure 9 RAE 2822 airfoil, M_∞=0.725, α=2.54°, Re=6.5 million (Case 6)



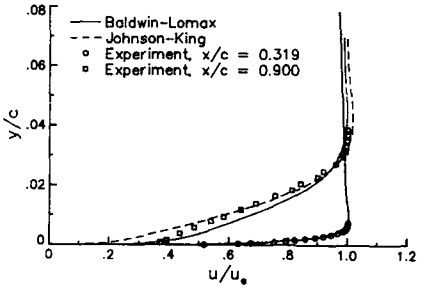
a) pressure coefficients



b) upper surface skin friction coefficients

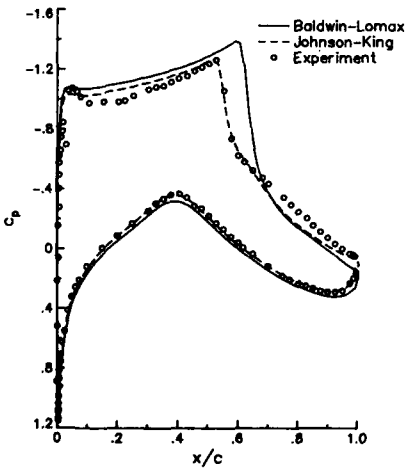


c) upper surface displacement thickness

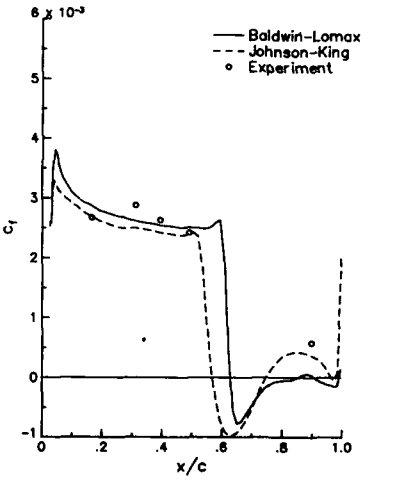


d) upper surface velocity profiles

Figure 10 RAE 2822 airfoil, M_∞=0.730, α=2.79°, Re=6.5 million (Case 9)

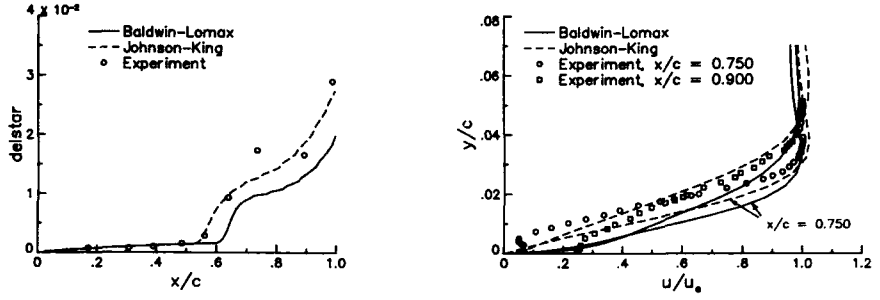


a) pressure coefficients



b) upper surface skin friction coefficients

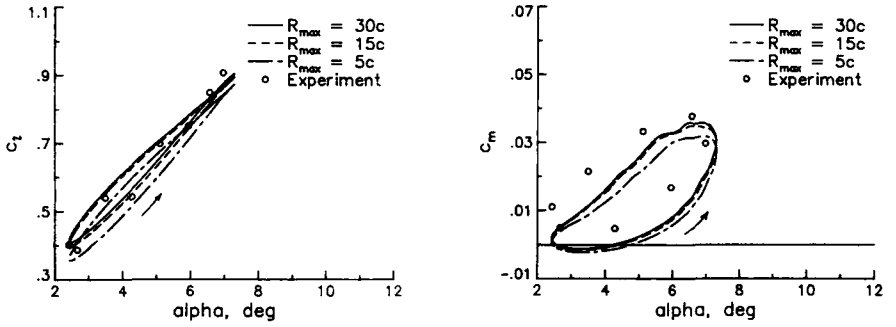
Figure 11 RAE 2822 airfoil, M_∞=0.750, α=2.81°, Re=6.2 million (Case 10)



c) upper surface displacement thickness

d) upper surface velocity profiles

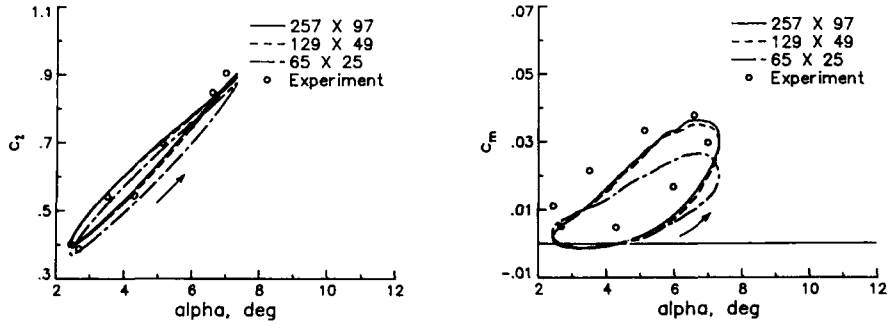
Figure 11 (continued)



a) lift coefficients

b) moment coefficients

Figure 12 Grid extent study, NACA 0012 airfoil, M_∞=0.6, α_o=4.86°, α_1=2.44°, Re=4.8 million, k=0.1620



a) lift coefficients

b) moment coefficients

Figure 13 Grid density study, NACA 0012 airfoil, M_∞=0.6, α_o=4.86°, α_1=2.44°, Re=4.8 million, k=0.1620, R_{max}=15c

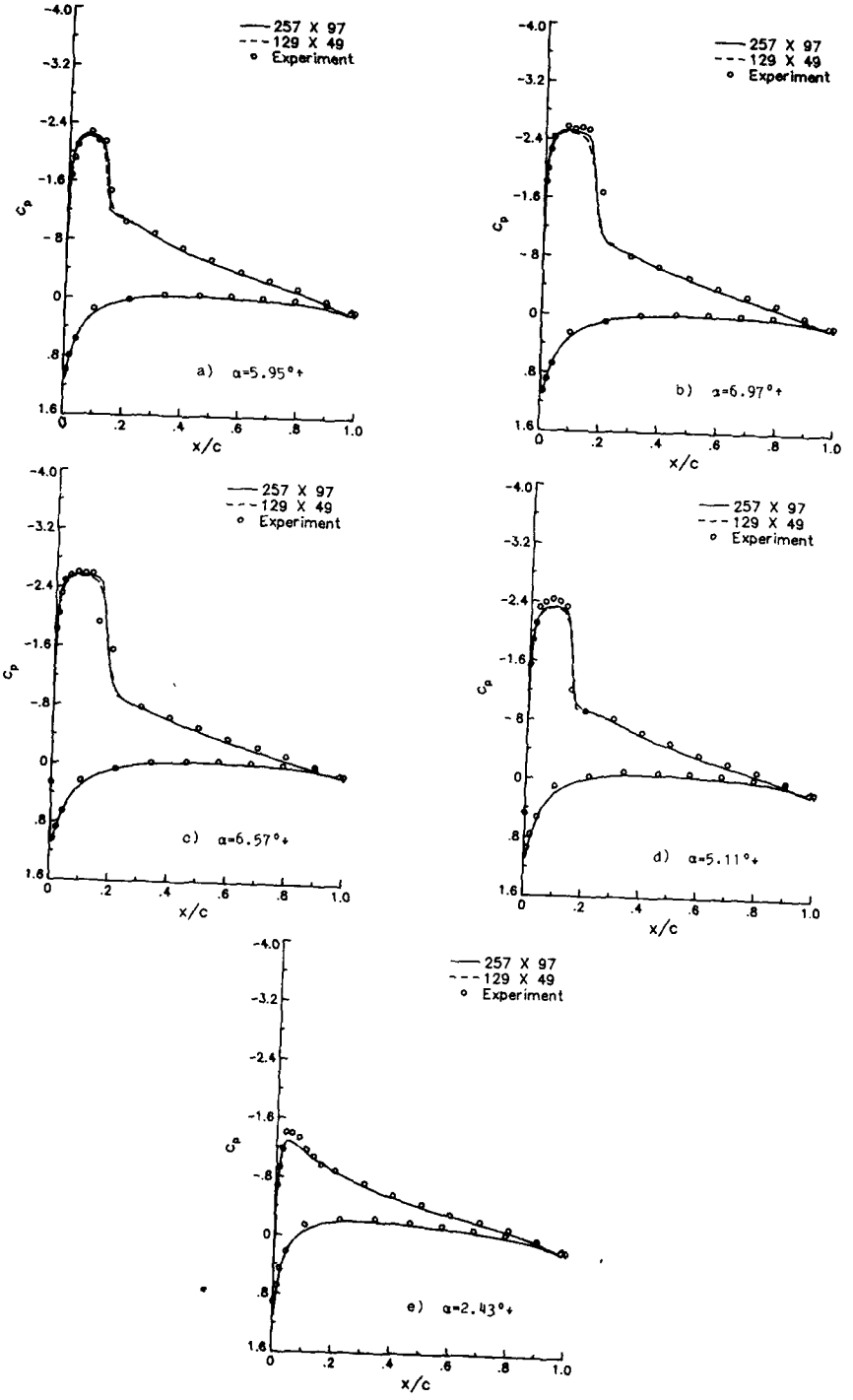
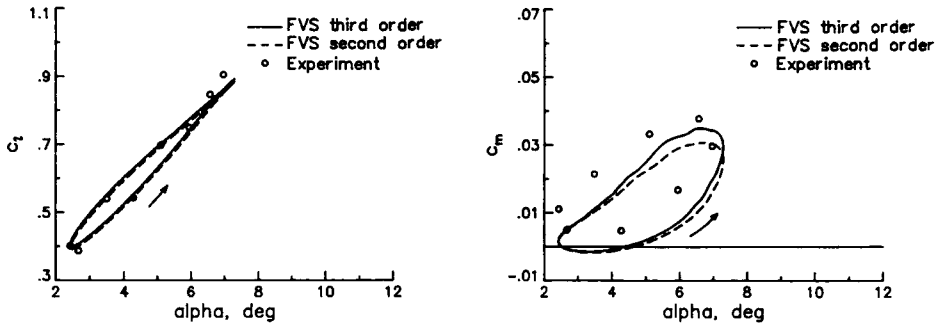


Figure 14 Pressure coefficients, NACA 0012 airfoil, M_∞=0.6, α_0=4.86°, α_1=2.44°, Re=4.8 million, k=0.1620, R_{max}=15c



a) lift coefficients

b) moment coefficients

Figure 15 Spatial accu[illegible], NACA 0012 airfoil, M_∞=0.[illegible]°, α_1=2.44°, Re=4.8 million, k[illegible]20, 129x49 grid, R_{max}=15c

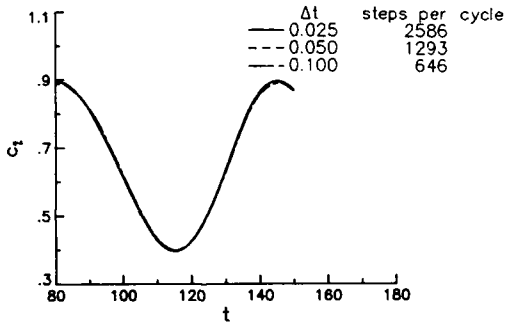
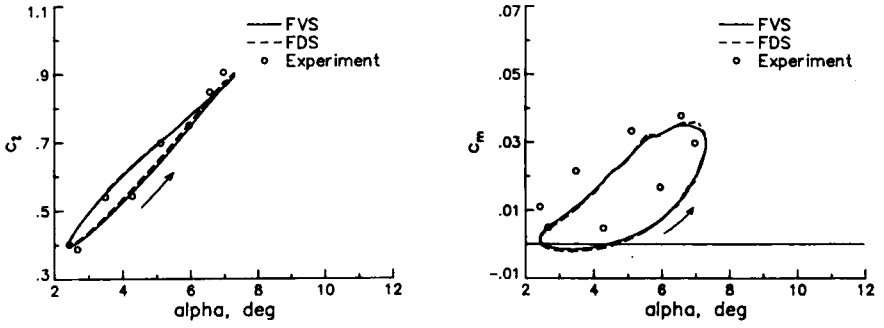


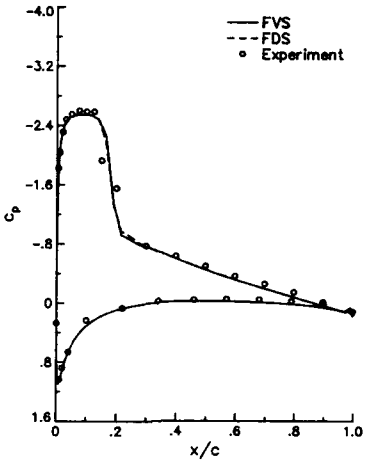
Figure 16 Time step study, NACA 0012 airfoil, M_∞=0.6, α_∞=4.86°, α_1=2.44°, Re=4.8 million, k=0.1620, 129x49 grid, R_{max}=15c.



a) lift coefficients

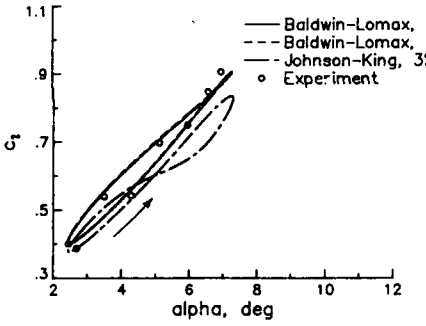
b) moment coefficients

Figure 17 Comparison of flux methods, NACA 0012 airfoil, M_∞=0.6, α_∞=4.86°, α_1=2.44°, Re=4.8 million, k=0.1620, 129x49 grid, R_{max}=15c.

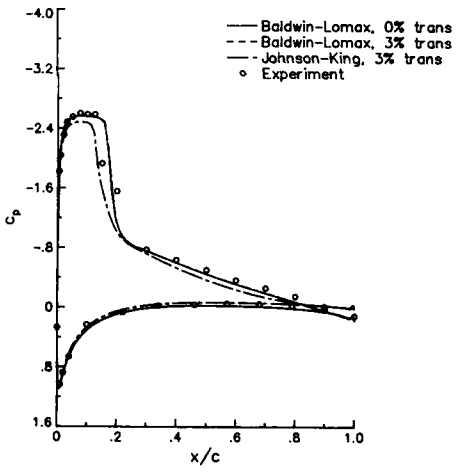


c) pressure coefficients, α=6.57°↓

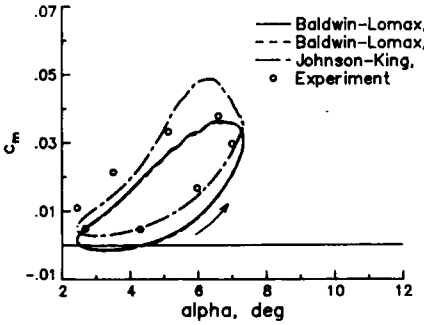
Figure 17 (continued)



a) lift coefficients

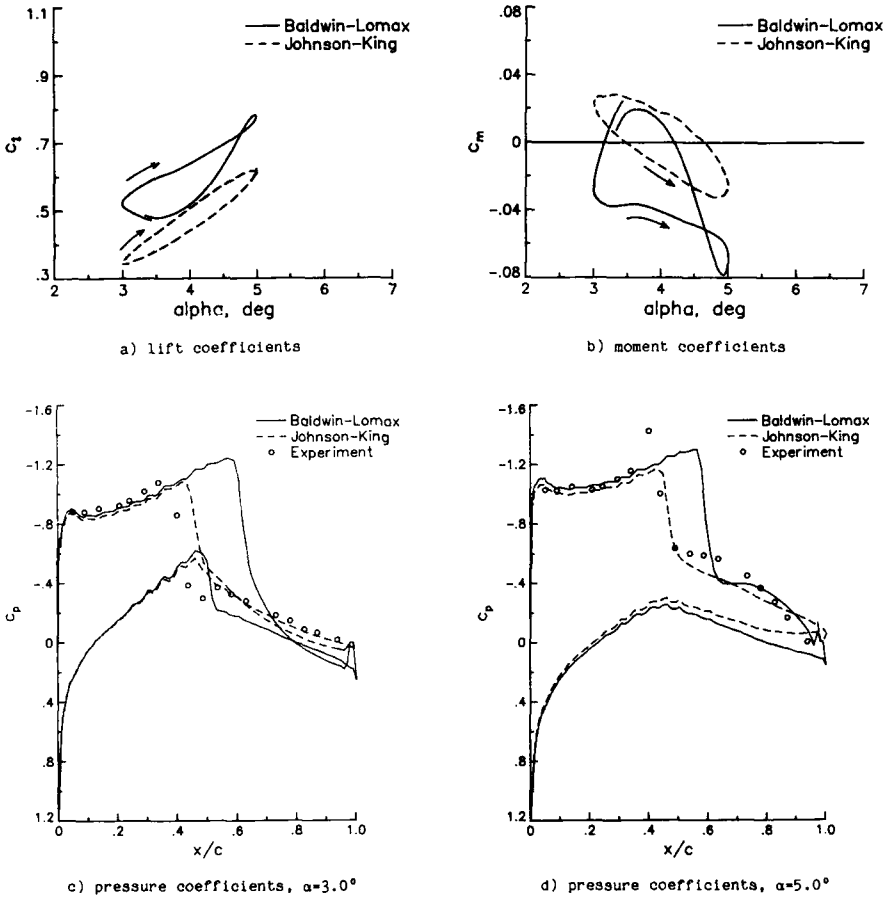


b) pressure coefficients, α=6.57°↓



c) moment coefficients

Figure 18 Turbulence model study, NACA 0012 airfoil, M_∞=0.6, α_0=4.86°, α_1=2.44°, Re=4.8 million, k=0.1620, 257x97 grid, R_{max}=15c



a) lift coefficients

b) moment coefficients

c) pressure coefficients, α=3.0°

d) pressure coefficients, α=5.0°

Figure 19 Turbulence model study, NACA 64(A)-010 airfoil (NASA Ames Model), M_∞=0.8, α_o=4.0°, α_1=1.0° , Re=12 million, k=0.40, 265x101 grid, R_{max}=15c

ON THE VALIDATION OF A CODE AND A TURBULENCE MODEL APPROPRIATE TO CIRCULAR CONTROL AIRFOILS

by

J.R.Viegas and M.W.Rubesin
NASA Ames Research Center
Moffett Field, CA 94035, USA

and

R.W.MacCormack
Stanford University
Stanford, CA 94035, USA

ABSTRACT

A computer code for calculating flow about a circulation control airfoil within a wind tunnel test section has been developed. This code is being validated for eventual use as an aid to design such airfoils. The concept of code validation being used is explained. The initial stages of the process have been accomplished. The present code has been applied to a low-subsonic, two-dimensional flow about a circulation control airfoil for which extensive data exist. Two basic turbulence models and variants thereof have been successfully introduced into the algorithm, the Baldwin-Lomax algebraic and the Jones-Launder two-equation models of turbulence. The variants include adding a history of the jet development for the algebraic model and adding streamwise curvature effects for both models. Numerical difficulties and difficulties in the validation process are discussed. Turbulence model and code improvements to proceed with the validation process are also discussed.

INTRODUCTION

Code Validation Process

The requirement of validating codes for computational fluid dynamics (CFD) has taken on increased emphasis is recent times. The primary reason for this is that the field of CFD has matured to the point that now it can be considered one of the major tools available to the aircraft designer, namely, an addition and complement to experimental data from wind tunnel and flight tests. However, in order for codes to be used with confidence, designers must know the accuracies and limitations of such a code. The process of establishing these code characteristics has come to be known as code validation.

To the authors, the validation process means developing a computer code whose results agree with the principal aerodynamic data from one or more experiments. These data are the usual force and moment coefficients and visualizations of the flow fields. It is required, however, that the experiments be those with known accuracies and unambiguously defined boundary conditions surrounding the test section, including information on the turbulence intensity and scale at the upstream station. The experiments should also cover a range of variables, such as configurations, Reynolds numbers, Mach number, jet momentum coefficients, etc., that envelop those of the proposed application.

Advances in the development of supercomputers and computational codes have permitted computations, at reasonable costs, of flow field configurations having a complexity approaching that of complete aircraft, when the computations are restricted to inviscid flow. For more realistic physical modeling, configurations such as wing-body combinations can be solved. These advances reflect the considerable improvements that have occurred in techniques for the generation of computational meshes and in solution algorithms in recent years. Currently, there are no inherent limitations on the numerical accuracy that can be achieved with these CFD codes other than their computational expense introduced by additional mesh points and the use of higher order solution techniques. There is a practical limit, however, to which numerical accuracy needs to be driven because all the codes contain certain errors that result from the approximate "physics" which has been introduced into them. For example, panel methods and Euler codes ignore viscous effects and Reynolds averaged Navier-Stokes codes contain only approximate statistical turbulence models. An intelligent use of computer codes has to give consideration to the specific accuracy needs of the designer and, concomitantly, requires an assessment of the errors introduced in the codes by the approximations to the "physics" contained in the codes. Requiring numerical accuracies to be much more stringent than those inherent in the physical aspects of a code is economically unwise and not beneficial to the designer. Thus, the establishment of the magnitude of the errors introduced by various physical approximations over a range of flow variables and configurations is critical to the code validation process. The validation process also serves to uncover lower order logic errors and/or "bugs" that often creep into very large and complex codes and produce subtle, but significant, numerical errors in the results.

In this paper, the initial stages of a validation process are demonstrated with a code that is being developed to compute the performance of circulation control airfoils, where lift is augmented by a surface jet flowing tangentially over the airfoil's blunt trailing edge. The jet adheres to the surface of the airfoil through the Coanda effect. From a turbulence modeling viewpoint the flow over a circulation control airfoil is exceedingly complex, containing such features as surface jets and free shear layers where the jet and and the upper boundary layer merge. Each of these regions experience the complicating effects of both high streamwise curvature and adverse pressure gradients. In addition, boundary-layer separation occurs somewhere within the Coanda region where the jet can no longer move forward against an adverse surface pressure gradient. All these effects combine to introduce large pressure gradients normal to the

airfoil surface and recirculation regions, both of which require flow-field solutions to be solved in the Navier-Stokes mode. This paper first describes the development of a computer code that solves the Reynolds-averaged Navier-Stokes equations about the trailing-edge region of a circulation control airfoil in free air. This same code is then extended to apply to an entire airfoil within a wind tunnel test section by including the presence of upper and lower walls. It is this latter arrangement that makes this code particularly suitable for calibration and, ultimately, verification. The code verification process, both in its numerical accuracy and in its turbulence model, can be performed with much less ambiguity because the code can duplicate the wall effects of wind tunnel experiments, provided the flow remains essentially two dimensional. A particularly important experiment such as this has recently been conducted and reported in Ref. 1. Parts of the data of this experiment are used in this paper as standards against which to calibrate the performance of the code with a variety of turbulence models and to suggest the improvements needed in the best of the models. The remaining parts of the available data, that is, the aerodynamic force data over extensive ranges of jet mass flow rates and angles of attack, will be used subsequently to validate the code with the most appropriate turbulence model identified in this initial calibration process.

Computation Method

The computational code employed here uses an extension of the Gauss-Seidel relaxation method proposed by MacCormack in 1985 (Ref. 2). This is an implicit, finite volume method that uses flux splitting. The extensions involve the introduction of second-order space accuracy for the flux-splitting technique and an improved treatment of source terms contained in advanced turbulence models that reinforces the diagonal dominance of their implicit representation and accounts analytically for each of the source contributions (Ref. 3). The resulting code is robust, receptive to different turbulence models, and can use complex mesh arrangements. The acceptability of complex meshes allows the introduction of the wind tunnel walls into the problem, which is critical to the concept of code validation because it allows, in principle, accounting for wind tunnel interference in an unambiguous manner. The code is known to be efficient for flows at transonic and supersonic speeds, but is somewhat slower at the speeds considered here. The latter is a disadvantage in the current work where the improvement of turbulence models requires testing with many repeated runs; however, the ultimate goal of this study is the design of circulation control airfoils operating in transonic flow and for this the code should be effective.

Earlier Results

The earliest application of this code (Ref. 4) was to the experiment of Ref. 5. To save computer time, without sacrificing resolution, the Navier-Stokes computational zone was confined to the immediate region of the trailing edge. The conditions at the boundaries of the zone were estimated from a limited number of velocity measurements, educated guesses of the jet conditions corresponding to the measured mass flow rate, and estimates of total pressures, total temperatures, and flow angles along incoming boundaries and static pressures at outflow boundaries. Subsequently, an analytical potential flow solution for an elliptic cross section airfoil was used to provide the flow angles at the inflow boundaries and static pressures at the outflow boundaries. These boundary conditions and the potential flow solution provided the solution in which the Navier-Stokes zone was immeshed. This surrounding solution will be called the "ambient" solution in the descriptions that follow. Only algebraic models of turbulence (Refs. 6 and 7) and variants required to account for the jet boundary-layer mixing and curvature were used in these calculations. These variants will be described later in the section of this paper entitled Turbulence Modeling. It was found that the computed results were very sensitive to the particular turbulence model employed and to small changes in the estimates of the boundary conditions.

To obtain a firmer understanding of the use of a local Navier-Stokes zone (NS zone) at the trailing edge of a circulation control airfoil, comparisons were next made with the wind tunnel data of Ref. 8. The ambient solution used in this case was provided by the Navier-Stokes computations of Ref. 9. The outer boundary of these computations extended away from the airfoil to distances well beyond the wind tunnel walls, and the effect of the tunnel walls were accommodated by using corrected angles of attack as recommended by the experimentalists. The turbulence model employed in the calculations of Ref. 9 was the Baldwin-Lomax model, but with modifications to account for the intense streamwise curvature in the trailing-edge region of the airfoils. A coefficient in the curvature correction term was altered for each stream velocity and trailing-edge configuration to achieve agreement in lift and surface pressure coefficients with the experimental data (Ref. 8). Thus, the method of Ref. 9 could not be considered predictive in that the "calibration constant" varied from case to case. It was these inadequacies that added an impetus to the current work.

To compute the details of the flow in the trailing-edge region of the airfoil tested in Ref. 8, the local NS zone was imbedded in the ambient solution supplied by the complete Navier-Stokes solution (Ref. 9) as is shown in Fig. 1. The complete Navier-Stokes computation of Ref. 9 was used to define the boundary conditions on the local zone as described previously. On the upstream boundaries these involve the total pressure, total temperature, and flow angles (also the turbulence kinetic energy and dissipation rate if needed by the turbulence model) in the stream and in the jet. The downstream boundary conditions are determined from the static pressure distribution of the ambient solution along the circular boundary. With these boundary conditions there is no assurance that the stream angles on the outflow boundary of the local NS zone would agree with those of the ambient solution at the same location unless the two solution techniques are compatible. To permit focusing on numerical compatibility, an identical turbulence model, Baldwin-Lomax plus curvature correction, was employed in the local zone as was used in the calibrated ambient solution. The test of the compatibility between the two solutions was to adjust the mass

flow rate of the jet entering the local NS zone until the stream angles within the zone at the exit boundary agreed with those of the ambient solution. Note that the mass flow and momentum flow rates in the jet are small compared to those of the inlet or exit boundary, so that changes in the jet conditions from those consistent with the experiment or the ambient calculation of Ref. 9 should not introduce serious mismatches in the conditions at the exit boundary. For the test case of Mach number equal to 0.3, zero geometric angle of attack, a circular trailing edge, and $C_\mu = 0.0322$ of Ref. 8, it was found that a reduction of about 10% from the actual jet mass flow rate entering the local computation zone in the ambient solution yielded the agreement in out-flowing streamlines shown in Fig. 2. Here the closely spaced streamlines are from the local zone calculation and the sparse streamlines from the base ambient solution. Thus, the matching procedure, as well as innate differences between the current code and that of Ref. 9, resulted in uncertainties of about 10% in jet mass flow rate required to produce a given lift.

Figure 3 shows a comparison of the experimental pressure coefficients in the Coanda region with the corresponding computed values from the ambient solution code and the immeshed local Navier-Stokes code with the same turbulence model as was used in the ambient solution code and with two additional models. The experimental data from Ref. 8 are designated with open circles, whereas the computed results are shown as solid lines. Figure 3(a) shows this comparison with the computed results of Ref. 9, when the basic turbulence model (Ref. 7) is modified by the calibrated streamwise curvature correction. The agreement in the pressure coefficients is quite good, when consideration is given to the comparatively large spacing between the pressure taps. Figure 3(b) shows a comparison of the data with the computed results of imbedded code calculation, using the same turbulence model as in the ambient calculation, but with 10% less mass flow in the jet. The agreement with the experimental data is almost identical with that of the ambient solution shown in Fig. 3(a). Figure 3 also shows the effect of the turbulence model calibration recommended in Ref. 9. This can be seen in the comparison between Figs. 3(b) and 3(c), where the calibrated curvature correction was removed from the imbedded flow calculation, but with the adjusted mass flow rate of the jet still retained. Removing the curvature correction degrades the accuracy of the computed values. Finally, Fig. 3(d) shows computations with a two-equation model (Ref. 10) without any curvature correction, but with the experimental mass flow rate. These results are also poorer than the case with the "calibrated" reduced mass flow (Fig. 3(b)).

Current Approach

The work just described served to give credence to the current numerical method and suggested continuing its use in developing a turbulence model that did not require alterations for each test condition for the circulation control airfoil. To develop such a turbulence model requires guidance from careful and rather complete experiments, that include measurements of the flow field as well as surface pressure and/or overall forces. Fortunately, an experiment such as this exists (Ref. 1) although it is restricted to fairly low free-stream speeds. The experimenters did not, however, measure profiles of the local flow conditions at the entrance to the wind tunnel test section, and this omission is a cause of concern as will be explained later in this paper. The wind tunnel model in this experiment was large enough to allow some resolution of flow field quantities necessary to define the conditions of the exiting jet and to aid in assessing the performance of the turbulence model. The large size of the model, however, introduced wind-tunnel-wall interference; the tunnel walls were only a few chords away from the wind tunnel model. The experimenters were conscious of the possibility of wind tunnel interference and took care to define the static pressures along the upper and lower walls of the wind tunnel. Thus, to be able to use these data to calibrate codes, guide turbulence modeling and, subsequently, verify the code-model combination, it is necessary to eliminate the uncertainties introduced by the wind tunnel walls by including their presence into the calculation. Since the spiral mesh in the code of Ref. 9 could not do this readily, and also could not accept higher order models easily, it was decided to expand the code developed here from one of a local zone to a complete one that encompasses the entire airfoil and the wind tunnel walls.

CODE DEVELOPMENT

Computation Grid

The grid selected for computing the flow of Ref. 1 is shown in Fig. 4. This grid is generally an O-mesh contoured to fit between the tunnel walls and the airfoil and extends upstream and downstream to the limits of the wall surface pressure measurements. The grid shown contains 126 nodal points in the circumferential direction and 80 in the "radial" direction. This grid can be readily altered locally if more resolution is needed. A unique feature of this grid applied to the circulation control airfoil is that mesh grid lines that emerge from the jet and and its lip are allowed to pass forward under the airfoil and then collapse to a singular point at the airfoil leading edge. Details of this mesh in the vicinity of the jet and over the entire trailing edge, or Coanda region, are shown in Figs. 5 and 6. The mesh stretches and shrinks in the outward direction from the body, guided by the need to define the jet region adequately. In the jet, the mesh stretches away from both walls symmetrically. In the mesh shown, 32 points are used to resolve the jet and the jet lip. The mesh behind the jet lip is also stretched, inwardly from the lip surfaces, but is presently fairly coarse, containing 12 points in the mesh shown. It proved to be adequate to assure mesh independent solutions. The mesh contains 48 points stretched from the top surface of the jet lip to the tunnel wall above the jet. Throughout the remainder of the control volume, the mesh stretching described above for the plane of the jet exit is made proportional to the distance from the body to the outside boundaries. Additional test computations were performed with the mesh dimensioned numbers diminished by a factor of 0.7 in both the direction between the airfoil and the

walls and in the circumferential direction. It was found that the results were insignificantly different. It is believed, therefore, that the results shown in this paper are essentially mesh independent.

Boundary Conditions

As previously mentioned, it had been found in the earlier study, Ref. 4, that the computational results for flow about the trailing edge of a circulation control airfoil were very sensitive to the boundary conditions employed. It is felt that this same sensitivity prevails in calculations over the full airfoil, especially when the effects of the tunnel walls are included in the calculations. The flow of Ref. 1 was chosen for this study because it presented the most detailed data available for circulation control airfoil code validation. However, even this well documented experiment contains regions along the boundaries where more complete data would be desired. In the present study, care is exercised to represent the boundary conditions as accurately as possible and with reasonable approximations often substituting for missing information.

No-slip and adiabatic boundary conditions are used on the surface of the airfoil. Slip flow and adiabatic boundary conditions are used on the wind tunnel walls. Subsonic boundary conditions based on the method of characteristics are used at all inflow and outflow boundaries. At the upstream boundary of the control volume, $x/c = -2$, the total pressure, total temperature, and the flow angle are specified. In a complex subsonic flow such as this the influence of the circulation can extend far upstream and downstream of the airfoil. There is evidence in the data of Ref. 1 that this might also be true for this case. Under such conditions, a distribution of total pressure, total temperature, and flow angle would need to be specified everywhere along the upstream boundary to accurately represent the flow entering control volume. For the turbulent field equations, distributions of the kinetic energy and the energy dissipation rate also need to be specified. The latter quantity is extremely difficult to measure, however, profiles of the more easily measured quantities were also not provided in Ref. 1 at this inflow boundary. Thus for the present computations the total pressure and total temperature were taken as constants corresponding to the stagnation chamber conditions for the experiment of Ref. 1. For the low jet momentum case, the pressure on the upper and lower tunnel walls were nearly equal and, consequently, the velocity was assumed to be horizontal along this inflow boundary. For the higher jet momentum case, where the upper and lower wall static pressures were clearly different, the flow angle angle distribution on the boundary was estimated from a solution of the low-blowing case at a station closer to the leading edge of the airfoil where similar pressure differences existed between the walls. The kinetic energy and the associated energy dissipation rate were assumed constant at values that might correspond to the outer edge of an equilibrium boundary layer at the tunnel test conditions.

At the downstream, or outflow, subsonic boundary, only a precise specification of the static pressure distribution is needed to obtain a solution. The experiment did not provide a pressure distribution in the flow field at this boundary, but the equal tunnel-surface-pressure data at the upper and lower walls at this location suggest that a constant pressure corresponding to their measured values would be reasonable for use on the entire outflow boundary.

At the jet entrance boundary, distributions of the total enthalpy, the mass flux, and the flow angle distributions were specified. These values were estimated from the velocity profiles and flow angles that were provided by the laser doppler velocimeter (LDV) data in the vicinity of the jet exit, as well as from the total jet plenum conditions and the jet mass flow rate. This specification enabled an exact duplication of the jet momentum coefficient, a key parameter in the calibration of circulation control airfoil performance. The kinetic energy and energy dissipation rate distributions in the jet were assumed to be constants equal to the estimated values in the free stream at the entrance to the tunnel test section. This assumption and possible consequences are discussed more fully in the next section.

The computations were initiated by assuming no flow throughout the control volume and applying the tunnel total conditions at the entrance and tunnel static pressure at the exit. The jet is gradually introduced by controlling the mass flow rate. From this gentle start the flow relaxes smoothly, but sometimes with a persistent, but damped oscillation, to convergence.

Turbulence Modeling

Although it is known (Ref. 11) that full second-order, Reynolds-stress turbulence modeling captures the anisotropies and related reduction of skin friction that develop over convex curved surfaces such as exist at the trailing edge of a circulation control airfoil, this level of modeling is currently too costly in terms of algorithm derivation and computer run times to be considered at the current stage of development of the present computer code. Consequently, the turbulence models used in this study employ the simplifying concept of an eddy viscosity.

The basic turbulence models that were used here fall into two categories. The first is an algebraic model, developed by Baldwin-Lomax (Ref. 7). The second is the two-equation model, developed by Jones and Launder (Ref 10). As these models are most appropriate for ordinary attached boundary layers, variations of each of these models were also employed to account for the history of the development of the free shear layer between the jet and the upper surface boundary layer for the case of the algebraic model, as described later, and/or for the extreme streamwise curvature of the trailing and leading edges in both models.

The LDV data of Ref. 1 indicate that the boundary layers approaching the trailing edge region on both the upper and lower surfaces of the airfoil are turbulent. The experimentors tripped the boundary layer

at $x/c = 0.075$ on the lower surface, and suggest that transition to turbulence also occurred on the upper surface very close to the leading edge. For these reasons, the turbulence was assumed to occur from the leading edge for the algebraic models. For the two-equation model, transition to turbulence occurs automatically when free-stream turbulence is introduced, although the location and extent of transition is not necessarily physically correct. For this model, the calculations indicate transition is complete by $x/c = 0.05$ on the upper surface, but as late as $x/c = 0.4$ on the lower surface. It is expected, however, that this late transition on the lower surface will have only a secondary influence the overall behavior of the circulation control jet.

Recall that the Baldwin-Lomax model, which is divided into two zones, treats the inner zone with the van Driest form of the mixing length, which increases monotonically with distance from the surface. The extent of the inner zone is determined by the location of the point where the product of the distance from the surface and the absolute value of the local mean vorticity first becomes a maximum. The size of the eddy viscosity over much of the boundary layer is established by the value of the eddy viscosity at this point. In the region over the trailing edge where the presence of the jet is still distinct, this maximum occurs very close to the surface, well below the point of maximum velocity in the jet. Since the total jet height in the experiment of Ref. 1 is only approximately 5% of the upper-surface boundary-layer thickness at the lip of the jet, it is seen that the Baldwin-Lomax model applied to the jet boundary layer interaction largely ignores the much larger scales of the entrained boundary layer. Thus, the eddy viscosity in the free-interaction zone between the surface jet and the boundary layer as given by the Baldwin-Lomax model can be expected to be too low, which limits mixing with the free shear layer and in turn permits the surface jet to maintain larger velocities as it moves around the trailing edge; however, the eddy viscosities near the surface, below the position of the maximum velocity in the jet are scaled properly. When combined with the faster moving jet, these proper eddy viscosities allow separation to occur farther downstream.

To assess the importance of this apparent deficiency of the Baldwin-Lomax model, the basic model was modified to account for the distribution of the eddy viscosities within the jet at its exit and the boundary layer above the jet lip. Within the jet, these eddy viscosities were established by assuming the jet to behave as two boundary layers separated by an inviscid core. This assumption was found to be consistent with the total mass flow rate of the jet and the laser doppler velocities as measured in the experiment of Ref. 1. In the top surface boundary layer at the lip of the jet exit, the eddy viscosities were established as part of the overall computation process. To account for the "history" of the jet development, these eddy viscosities at the jet exit station were then blended with the local eddy viscosity given by the Baldwin-Lomax model through a linear weighting function that gave full weight to the upstream values at the jet exit and full weight to the Baldwin-Lomax model at the trailing edge. No attempt was made to optimize the length of the region of blending. The process was used only to gain some insight into the effects of the apparent shortcomings of applying the Baldwin-Lomax model to the present problem. Corrections for the effects of streamwise curvature were made as recommended in Ref. 9.

With the two-equation model, the interaction of the jet and boundary layer proceeds as part of the overall solution process. In contrast to the mixing length model, no new modeling in the jet-boundary layer interaction zone was required. It was necessary, however, to define boundary conditions for the kinetic energy and energy dissipation rate at the exit plane of the jet. The laser doppler data of Ref. 1 show rather intense turbulent kinetic energy emerging from the jet, however, no consistent way could be found to estimate the corresponding kinetic energy dissipation rate at the jet exit. To permit proceeding with the solution of the two-equation model, it was decided to bypass the problem of arbitrarily assigning dissipation rates to the measured kinetic energies by merely assuming that the values of the kinetic energy and dissipation rate at the jet exit were the same as was estimated at the inflow boundary of the wind tunnel test section. Although this appears to be a rather poor assumption, it is not believed that it introduces serious error in the solutions because it was noticed that both the kinetic energy and dissipation rates increased very rapidly downstream of the jet exit to values consistent with those that occur within shear layers. Future studies will examine the sensitivity of the solutions to altered assumptions regarding the turbulence conditions at the jet exit.

To account for the intense streamwise curvature in the Coanda region, the methods of modifying the two-equation model for curvature recommended in Ref. 12 were adopted here. In this method the coefficient in the destruction term of the dissipation equation is modified by a correction factor equal to one minus a curvature coefficient times a Richardson number. The modeling coefficient accounting for curvature was set equal to the recommended value of 0.2. The radius of curvature employed in the Richardson number was set equal to that of the surface of the model, not local values along the streamlines. This was done for expediency; however, it is not believed to introduce serious error because those regions where the tangential jet plays its most important role are quite close to the body surface. Because the streamwise curvature terms are meant to be perturbations to uncorrected models of turbulence, the curvature correction factor was restricted to values between 0.25 and 1.75.

RESULTS

Test Conditions

The computations shown in this paper apply to the experimental conditions of Ref. 1 where both flow field velocities and surface pressures were measured. In particular, computed results are presented for the following:

Test section conditions:
- Velocity, U = 42.50 m/s
- Chord Reynolds number = 10^6
- Free-stream Mach number = 0.121
- Total temperature = 303.2 K
- Total pressure = 98952.0 N/m^2

Model conditions:
- Chord of airfoil, c = 0.382 m
- Angle of attack = 0°
- Dimensionless jet height, h/c = 0.002
- $U_{jet}/U_{free\ stream}$ = 3.44 and 5.69
- Jet momentum coefficient, C_μ = 0.03 and 0.1

Although Ref. 1 contains airfoil surface pressure data over a range of angles of attack from -5° to +5°, and includes jet momentum coefficients up to about 0.4, the computations shown here were confined to those just indicated because it was under these conditions that LDV measurements were made in the trailing-edge region. These velocity measurements were used in the computations to define the mean flow conditions at the jet exit, and as standards for comparison with the computed results. Of course, in the final validation process of the computer code with its best turbulence model, the entire range of the test conditions of Ref. 1 should be computed and the results compared with the surface pressure data, lift, drag, and pitching moments.

Example of Flow Field Results

Figures 7 through 9 show examples of the flow fields computed about the circulation control airfoil in the wind tunnel test section. This group of computations is based on the unmodified Baldwin-Lomax model and apply to the lower jet momentum coefficient equal to 0.03. Figure 7 shows the streamlines about the airfoil within the entire test section. The overall effect of the circulation control jet is evident in the downwash shown at the trailing edge and in the upwash at the leading edge that is induced by the circulation that has been created. It is significant that a larger proportion of the wind tunnel airflow passes over the airfoil than underneath, and is an indication that wind tunnel wall interference is likely to be important in these experiments.

It should be noted that the plotting routine used here has difficulty in accounting for the presence of the jet in evaluating the absolute numerical values of the streamlines because of a local new source of mass. Accordingly, the lines shown should be considered to be streaklines. The specific numbers on the lines are not proper stream function values and are used here merely as line identifiers. The anomalous behavior can be seen in the enlarged figures as stagnation lines that do not meet the surface of the airfoil or those that are inconsistent with the velocity vectors near the trailing edge. Farther from the airfoil surface the streaklines agree quite well with the corresponding velocity vector fields.

The details of the flow field in the leading-edge region are shown in the expanded plots of Fig. 8, where (a) shows the streamlines and (b) shows the velocity vector field. The latter figure indicates that the stagnation point occurs at about 2% of chord on the lower surface of the airfoil. The velocities passing over the leading edge to the upper surface are much larger than the free stream values and suggest considerable leading edge suction. There is no evidence of a leading-edge separation bubble on the upper surface.

Similar detailed flow field results are shown at the trailing edge in Fig. 9. On Fig. 9(a), the streamline labeled 0.00, away from the surface of the body, is approximately the lower bound of the free-stream air passing over the top of the airfoil. It shows that the trailing edge jet hugging the surface is effective in inducing considerable downwash at the trailing edge. The presence of the jet is very evident in Fig. 9(b), and it can be seen to exist well around the trailing edge. It should be noted, however, that the jet has separated from the surface a short distance ahead of the trailing edge. This cannot be seen clearly from the figure, but is detected in the calculated skin friction directions.

Comparative Turbulence Model Performance

Figure 10 and Table 1 show the computed predictions of the the lift coefficients in comparison with the experimental results of Ref. 1. The lift data were obtained in Ref. 1 from integration of the experimental pressure distributions about the airfoil. The calculated lift was computed in a similar way from the local calculated surface pressures. For this paper, most of the airfoil computations were performed for the jet momentum coefficient equal to 0.03, with just one case shown for C_μ = 0.1. Recall these were the jet conditions where laser doppler measurements were made of the trailing edge flow field in addition to surface pressure measurements on the model. The turbulence models indicated here were described in a previous section.

It is observed from the figure and the table that the basic Baldwin-Lomax turbulence model yields results that are approximately 50% higher than the data at each value of the jet momentum coefficient. Including the effect of the jet history causes the lift to rise. The reason for this is that the jet at its exit, as assumed in the calculations, possesses quite a low value of eddy viscosity relative to that which the Baldwin-Lomax model would predict for the stations downstream of the jet exit. Consequently, the weighting procedure adopted to account for the jet history lowers the eddy viscosities in the free

shear layer between the jet and the overlaying boundary layer. The result of this is to reduce the mixing and, hence, the retardation of the jet and to allow it to move farther around the Coanda region. Alternatively, the near wall eddy viscosities are not affected much by the jet history weighting. The combined effect of less jet retardation and similar eddy viscosities in the vicinity of the wall cause the point of separation to move farther around the trailing edge, which in turn, contributes to the increased lift. It is interesting that the Jones-Launder model yields essentially the same results, which indicates that the history effects that are inherent in the two-equation model were fortuitously approximated with the weighting procedure adopted here for the Baldwin-Lomax algebraic model.

The effect of the curvature correction in the algebraic mouel is to reduce the lift. With the value of the curvature correction coefficient, C_c, introduced in Ref. 9 set equal to 8.0, it is found that the lift is still about 37% higher than the experimental value at $C_\mu = 0.03$. The reason for the reduction of lift introduced by the curvature correction is that it reduces the eddy viscosity between the maximum velocity in the jet and the wall, while generally increasing the eddy viscosity in the interaction zone between the jet and the exterior flow. Thus, the jet is retarded more by the external flow and increasingly susceptible to separation. These effects combine to move the separation point towards the jet exit and result in a reduction of the overall lift. To approach the experimental data by reducing the lift even more, some runs were made with the code with values of $C_c = 10.0$ and 12. It was found that the increment of reducing the lift diminished and that some periodic oscillations were introduced into the solution. Also, these values of C_c are an order of magnitude larger than those required in Ref. 9 to achieve agreement with the data of Ref. 8. It is believed that the difference in the way the two codes behaved in their comparisons with the different experiments was primarily the result of the freedom enjoyed in Ref. 9 of also being able to adjust the angle of attack. Because of inherent weaknesses of the Baldwin-Lomax model's ability to handle the complexities of this flow, we did not pursue this matter further at this time.

The last modification made to the Baldwin-Lomax model was to combine the effects of jet history and curvature. As expected, the effects tended to cancel and resulted in values of lift close to that of the original Baldwin-Lomax model. The Jones-Launder two-equation model, corrected for curvature as in Ref. 12, also yields results that are quite similar to those of the original Baldwin-Lomax model, or its variants that contain curvature corrections. This conclusion is not unique to the circulation control airfoil, but has also been demonstrated in the computation of transonic airfoils without curvature corrections (Ref 13). For a circulation airfoil, then, the only advantage of using the Jones-Launder two-equation model is its ability to account for the jet history without additional modeling assumptions. It is known that the performance of the Jones-Launder model can be improved considerably, and procedures for doing this are listed later in the description of the future directions this code validation process may take.

The streamline patterns in the trailing edge region of the circulation control airfoil corresponding to the different variants of the Baldwin-Lomax model are shown in Fig. 11. These are in agreement with the explanations given above for the behavior of the lift, and can be seen best by comparing the positions of the streamline labeled 0.01 in Figs. 11(a) to 11(c). With reference to Fig. 11(a), corresponding to the basic Baldwin-Lomax model, the streamlines in Fig. 11(b), including the effects of jet history, show a decided movement clockwise around the trailing edge which is reflected in increased lift. The curvature correction alone, Fig. 11(c) shows a counter-clockwise movement relative to Fig. 11(a). Finally, the combined effects of jet history and curvature corrections, as shown in Fig. 11(d), bring the streamline pattern almost back to its original form (Fig. 11(a)).

Figure 12 shows the flow field in the trailing-edge region corresponding to the smaller jet-mass coefficient, $C_\mu = 0.03$, when the basic Jones-Launder two-equation model is used. As expected from the comparisons of the results for lift, the stream pattern shown in Fig. 12(a) is virtually identical with that of Fig. 11(b), corresponding to the Baldwin-Lomax model with jet history. The vector plot (Fig. 12(b)) shows separation to occur on the surface of the airfoil just beyond the trailing edge in a clockwise direction. It is remarkable how large a "dead water region" (i.e., very low velocity) exists just below the trailing edge. The relatively large spacing between the streamlines labeled 0.000 and 0.016 on Fig. 12(a) are also indicative of this.

A comparison of Figs. 12(a) and 12(c) shows the effect of the curvature correction on the Jones-Launder model on the streamline pattern in the trailing-edge zone. Near the surface, the curvature correction introduces a decided counter-clockwise motion to the flow field. In addition, there is significantly less downwash in the far field. The vector fields, shown in Figs. 12(b) and 12(d), support these observations and give more detail of the jet behavior near the surface. The identity of the jet remains evident to farther clockwise positions without the curvature correction. This flow pattern behavior is consistent with an increase in the jet-free stream mixing and a significant reduction in the lift as a result of the curvature correction.

Figure 13 shows the streamline pattern around the entire airfoil corresponding to the basic Baldwin-Lomax model for the two values of jet momentum coefficient used here. Figure 13(a) is a blowup of the streamline pattern shown earlier in Fig. 7 for $C_\mu = 0.03$. Figure 13(b), corresponding to $C_\mu = 0.1$, shows how dramatically the flow under the entire airfoil is affected by the increase in the jet momentum coefficient. The air exiting the jet is seen to circulated about the airfoil. The air that originally passes over the upper surface of the airfoil is thrown forward under the airfoil to about 20% chord by the circulation control jet. The complexities of this flow certainly tax the bases of the Baldwin-Lomax model, the only one used to date for this flow condition.

Figure 14 shows a comparison of the computed and measured trailing-edge mean streamline patterns for both values of the jet momentum coefficient. The computations shown in these figures are based on the Baldwin-Lomax model, without modifications. Figure 14(a) is a more detailed version of Fig. 11(a), corresponding to a value of jet momentum coefficient, $C_\mu = 0.03$. Figure 14(b) is the corresponding figure for $C_\mu = 0.1$. Figures 14(c) and 14(d) show the experimental results from Ref. 1 for the same pair of values of jet momentum coefficient. Recall, now, that the experimental lift produced by the value of $C_\mu = 0.03$ is much less than that corresponding to the computation for the same value of C_μ. The experimental lift for $C_\mu = 0.1$ also is much less than the computed lift; however, it is above the computed lift for the case of $C_\mu = 0.03$, see Table 1. The patterns of the flow fields in Figs. 14(a), (b), and (d) are generally consistent with these observations. The experimental flow pattern for $C_\mu = 0.1$, except for exhibiting some waviness, generally lies between the two computed patterns. Some features appear in the streamline pattern of Fig. 14(c) that are inconsistent with the lift behavior. Although in the immediate vicinity of the surface, the experimental streamlines turn less clockwise than the computed values shown in Fig. 14(a), consistent with the relative lifts, the experimental flow pattern away from the surface indicates more downwash than does the computation. Why this is not reflected in more experimental lift is not clear at this time and will require further study and interaction with the experimentors, as will the anomalous results shown in the next figure.

Figure 15 shows comparisons of the measured pressure coefficients on the upper and lower surfaces of the airfoil in comparison with some of the computations. Figure 15(a) compares the experimental data (circular symbols), with computed results (solid lines) based on the Baldwin-Lomax model containing corrections for curvature for the same values of jet momentum coefficient, $C_\mu = 0.03$. Figure 15(d) shows a similar comparison for the Jones-Launder model, with curvature correction. These alternative model comparisons are virtually identical. The oscillations in the computed quantities on the upper surface near the leading edge are believed to have resulted from the first-order curve-fitting procedure employed to interpolate between the wind tunnel model coordinates in setting up the airfoil surface coordinates for the computation mesh. It is not believed that these oscillations seriously impair the global results or the conclusions that can be drawn therefrom. The larger computed lift, noted earlier, is shown by the larger area between the upper and lower lines than exhibited by the area bounded by the experimental points. In addition, it is shown here that a large part of the increased lift evident in the computed results occurs over the forward portion of the airfoil. The computed drag and pitching moments also will differ considerably from the measured values because of this behavior.

The cause of the large leading-edge suction pressure shown in the computations and absent in the data is critical to our understanding of the directions future turbulence modeling modifications should take for this class of flow. Towards this end, it was decided to compare computations with data at the same lift, accomplished by comparing with experimental data at a higher jet momentum coefficient that provides the proper lift. From Fig. 10 it is seen that such a match exists with the computations of the Baldwin-Lomax model with jet history or the basic Jones-Launder model with $C_\mu = 0.03$ and the experimental data at $C_\mu = 0.62$. The comparisons of pressure coefficients from these computations and the experimental data are shown in Figs. 15(b) and 15(c). First, it is striking how closely the results for the two turbulence models agree in these figures. In each figure, the apparent area between the computed lines now agrees more closely with the area between the groups of data points. As in Fig. 15(a), but to a lesser extent, on the upper surface, the computed pressure coefficient shows more of a suction peak in the vicinity of the leading edge than is exhibited by the data. At the trailing edge, less suction is generated. It is clear that an improvement in the turbulence model that would achieve the correct suction peak in the trailing-edge region, at the proper or matched lift, would be helpful in reducing the leading edge suction peak. This interplay of the behavior of the leading-edge and trailing-edge flow regions was not evident in the earlier work (Refs. 8 and 9). In the calculations of Ref. 9, "wind tunnel corrections" to the actual geometric angle of attack, as recommended by the experimenters of Ref. 8, were introduced simultaneously with turbulence model changes to improve the pressure coefficient behavior in the leading edge region. In the current work, with the inclusion of the wind tunnel walls in the calculations, in principle one should not be justified in modifying geometrically established angles of attack. The burden should be on the improvement of the turbulence model so that results, to the accuracy required by the user, are attained when ambiguities in the boundary conditions are minimized or assessed. For example, Fig. 16 shows the calculated upper and lower wind tunnel wall static pressure coefficients corresponding to the case where $C_\mu = 0.03$ with the Jones-Launder turbulence model and some representative experimental measurements. The differences in the pressure coefficients at the upstream boundary indicate the extent of the upstream influence on the flow caused by the circulation. Recall that only the total pressure was assigned at this boundary and these static pressure differences developed as part of the solution. Differences between the measured and calculated static pressures at this station would suggest that the assumption of zero angle of flow for the incoming streamlines, employed in the calculations with $C_\mu = 0.0$, may have introduced some error. This is an example where more complete documentation (i.e., stream angles at the entrance to the test section) would have eliminated some degree of uncertainty in the calculations.

Before leaving this section, it should be mentioned that none of the solutions described were easily obtained. The algorithm, developed for compressible flows, seemed to be taxed by the complex low subsonic flow studied here. Even though the algorithm is robust (in that once debugged, it could be operated with very large time steps or CFL numbers, as befitting a good implicit code) there was a problem obtaining quick convergence for the circulation control airfoil at all the conditions studied. During the relaxation process from an initial flow condition towards a new steady state, the solution would oscillate very slowly with no apparent physically based characteristic frequency. The oscillation was related more to

the number of iterations, as seen by comparisons at different values of CFL number. The magnitude of the oscillations sometimes seemed dependent on the size of the CFL number. On some occasions, the oscillations persisted indefinitely. The solution behaved as if the feedback between the various boundaries made the equation set very stiff. The overall lift was the aerodynamic parameter focused upon, and for the solutions present, this parameter converged to within 1%, even in the presence of oscillations. The number of iterations required to attain this convergence level could be from several hundreds to a few thousand. The larger number of iteration counts was required when the jet momentum coefficient was the low value of $C_\mu = 0.03$. At the higher value of $C_\mu = 0.1$, the convergence rate of a few hundred iterations is very respectable. Currently the code is unvectorized and computations cost 10 to 15 sec/iteration on a Cray XMP for the algebraic and two-equation turbulence models, respectively. Increased computational efficiency, while not critical, is certainly worth pursuing to enhance the code's efficiency at the lower free stream speeds and lower jet momentum coefficients.

Although the 1% oscillation in lift, the overall flow pattern, and the friction drag indicated the solutions had achieved an acceptable level of convergence, other aerodynamic parameters such as the pitching moment or the pressure drag, because of their dependence on relatively small differences between large quantities, continued to show disproportionately large oscillations. It is expected that improving the numerical fit to the body shape and grid about the leading edge of the airfoil will reduce the raggedness of the surface pressure in this region shown in Fig. 15. The improved grid may also reduce the range of the oscillation of the higher order aerodynamic parameters.

CONCLUDING REMARKS

This paper presents the early stages in a program to calibrate and validate a computer code being developed to compute the performance of circulation control airfoils. The opportunity to attempt this validation process arose because of 1) the availability of new data from an experiment that included mean flow and turbulence measurements in addition to model surface pressure data (Ref. 1), and 2) the development of a computer code that could account for the presence of a model within wind tunnel walls, with the latter experiencing slip flow conditions. The code is currently two-dimensional, requiring the model to be an airfoil, and only accounts for the upper and lower wind tunnel walls. The computer code is also capable of accepting different kinds of turbulence models, both algebraic or those based on auxiliary field equations for turbulence quantities. Finally, the code, which is known to be economical for high-speed compressible flows (Ref. 2) has proven to be only marginally economical for this low-speed flow condition at the lower jet momentum coefficient. Under these conditions, the code presently is useful only as a research tool when enough mesh points are employed to provide numerical results that are mesh independent.

Inclusion of the wind tunnel walls in the calculations was expected to eliminate some of the uncertainties introduced by empirical wind tunnel wall "corrections" and to place the burden squarely on the turbulence models to achieve an agreement between computations and experimental data, provided adequate boundary condition data are known for the incoming and outflowing boundaries of the test section. The present computed results, which show higher suction pressures at the leading edge and less downwash beyond the trailing edge than indicated in the experimental data, even when total lift is matched to the experimental results, are indicative of a negative effective angle of attack. The cause of this anomalous behavior is not known at this time, but could result from an induced three-dimensional effect that was not detected in the experiment and could not be generated by the present two-dimensional flow code.

Despite these aforementioned uncertainties regarding the effects of undefined conditions on the test section boundaries and the apparent residual angle of attack, even in the presence of the computed wall effects, and the relatively uneconomical behavior of the compressible flow code applied to low speeds, the current study provided several positive results regarding the process of validating a code for the design of circulation control airfoils. Some of these are as follows:

1. Computations applying turbulence models that are used commonly in Navier-Stokes codes, namely, the Baldwin-Lomax algebraic model and variants to account for curvature and the history of jet merging with the external flow field or the Jones-Launder k-epsilon model with corrections for streamwise curvature, show little difference between each other and both provide good qualitative descriptions of the flow fields about the circulation control airfoil.

2. The code proved to be readily adaptable to higher order turbulence modeling, and the cost penalty of running the two-equation model relative to the zero equation model was only an increase of 50%.

3. The code converged sufficiently rapidly if the initial conditions were a previous solution at somewhat different flow conditions or with a different turbulence model. It was also noticed that convergence occurred quite rapidly at the high value of the jet momentum coefficient. These characteristics should be useful in parametric studies involved in the ultimate validation process under low-speed conditions.

4. The code is written in a generalized coordinate frame. This feature allowed generation of the mesh involving the airfoil and wind tunnel wall to be very direct, and should be easily adapted to include geometric angles of attack. This will be needed to investigate the apparent angle of

attack evident in the experimental data and to allow covering the range of angle of attack measured in Ref. 1.

5. For the limited cases computed to date, the turbulence models employed indicate quantitative results that, for given jet mass coefficients, show values of lift that are approximately 50% too high at both values of jet mass flow that have been computed. This suggests that the code could possibly be "calibrated", but such a task requires computation at other test conditions to confirm the concept.

With these results, decisions have to made how to proceed in advancing the validation of this code. Should one try to calibrate the code over the entire range of conditions for which experimental data exists, even though it is apparent that the calibration may involve large, and possibly non-uniform, adjustments to the computed results? Or should one try to first eliminate the uncertainties in the boundary conditions through consultation with the experimenters and then improve an existing turbulence model, or obtain a new turbulence model, to yield values of all the aerodynamic coefficients that are close and consistent with trends of a limited set of experimental data? This second approach, if successful, could enable one to proceed with confidence with the validation process over the ranges for which the circulation control airfoil has been tested.

The authors agree with the latter of these two philosophies, but are aware of the difficulties in advancing a turbulence model to flow conditions that are large extrapolations beyond the conditions of the fundamental fluid dynamic experiments upon which the current models utilized here were based. In the present example, such experiments involved surface jets on planar or curved surfaces, and free shear layers between surface jets and boundary layers; however, the radii of surface curvature and pressure gradients were orders of magnitude less influential than those which exist in the trailing edge of a circulation airfoil. Thus, it is not surprising that the models employed in the present paper were not adequate for design.

The authors are continuing to develop the computer code. In the near future, the following numerical and turbulence modeling modifications will be tried:

1. Close attention will be placed on obtaining a smooth body contour at the leading edge to eliminate this as source of numerical problems.

2. Numerical algorithm improvement for low-speed conditions is still warranted and is being pursued.

3. Sensitivity studies will be conducted with variations in the stream angles entering the test section and with small changes in the angle of attack. (The reasonableness of the magnitudes of the quantities used in the sensitivity studies will be checked through consultation with the authors of Ref. 1.)

4. Sensitivity studies with the Jones-Launder model plus curvature will be conducted to test the need for defining the turbulence, in scale and intensity, at the exit plane of the jet.

5. Wall functions will be introduced to the Jones-Launder model. These were found to help the Jones-Launder model in transonic flows (Ref. 14) and in subsonic deadwater regions (Ref. 15).

6. The Jones-Launder model will be modified to account for the effects of streamwise curvature by reinterpreting the kinetic energy equation to account for anisotropy in a manner similar to what was done in Ref. 11.

7. The Jones-Launder model will be modified to relax the eddy viscosity concept through the use of Rodi's algebraic stress model (Ref. 16).

8. Full Reynolds stress modeling will be introduced in the manner of Ref. 3.

At present it is not clear what level of modeling will lead to results that are reasonably accurate and characteristic of the behavior of changes in the data with alterations in the flow conditions to warrant fine tuning through calibration. Success here, will lead to testing the code over the entire range of conditions of the experiment of Ref. 1 and for a new experiment being conducted at the NASA Ames Research Center that will extend the data, similar to that obtained in Ref. 1, to a circulation control airfoil within a transonic flow.

Although Ref. 1 was well written, it was found during the computations described here that occasions arose when consultation was required with the authors of that paper to clarify some of the experimental conditions. The excellent cooperation given by these experimentalists was extremely beneficial to the current work and is a demonstration of the strong need for close cooperation between experimentalists and code validators that should be a continuing process for future studies.

REFERENCES

1. Novak, C. J., Cornelius, K. C., and Roads, R. K., "Experimental Investigations of the Circular Wall Jet on a Circulation Control Airfoil," AIAA-87-0155, AIAA 25th Aerospace Sciences Meeting, Reno, Nevada, January 12-15, 1987.

2. MacCormack, R. W., "Current Status of Numerical Solutions of the Navier-Stokes Equations," AIAA-85-0032, AIAA 23rd Aerospace Sciences Meeting, Reno, Nevada, January 14-17, 1985.

3. HaMinh, H, Kollmann, W., and Vandromme, D., "Implicit Treatment of Multi-Equation Turbulence Models for Compressible Flows, "Final Report for Contract NASA-NCC2-186, University of California, Davis, Calif., 1987.

4. Viegas, J. R., Rubesin, M. W., and MacCormack, R. W., "Navier-Stokes Calculations and Turbulence Modeling in the Trailing Edge Region of a Circulation Control Airfoil," Circulation Control Workshop, NASA Ames Research Center, Feb. 19-21, 1986.

5. Spaid, F. W. and Keener, E. R., "Boundary Layer and Wake Measurements on a Swept, Circulation Control Wing," Circulation Control Workshop, NASA Ames Research Center, Feb. 19-21, 1986.

6. Cebeci, T. and Smith, A. M. O., Analysis of Turbulent Boundary Layers, Academic Press, New York, 1974.

7. Baldwin, B. and Lomax, H., "Thin-Layer approximation and Algebraic Model for Separated Turbulent Flows," AIAA-78-257, 1978.

8. Abramson, J. and Rogers, E. O., "High-Speed Characteristics of Circulation Control Airfoils," AIAA-83-0265, AIAA 21st Aerospace Sciences Meeting, Reno, Nevada, January 10-13, 1983.

9. Pulliam, T. H., Jesperson, D. C., and Barth, T. J., "Navier-Stokes Computations for Circulation Controlled Airfoils," AIAA-85-1587, AIAA 18th Fluid Dynamics and Plasmadynamics and Lasers Conference, Cincinnati, Ohio, July 16-18, 1985.

10. Jones, W. P. and Launder, B. E., "The Prediction of Laminarization with a Two-Equation Model of Turbulence," International Developments in Heat Transfer, Vol. 15, 1972, pp. 303-314.

11. Wilcox, D. C. and Rubesin, M. W., "Progress in Turbulence Modeling for Complex Flow Fields Including Effects of Compressibility, NASA Technical Paper 1517, April 1980.

12. Launder, B. E., Priddin, C. H., and Sharma, B. I., "The Calculation of Turbulent Boundary Layers on Spinning and Curved Surfaces," Transactions of the ASME, Journal of Fluids Engineering, pp. 231-239, March, 1977.

13. Rubesin, M. W. and Viegas, J. R., "Turbulence and Modeling in Transonic Flow," Transonic Symposium, Theory, Application, and Experiment, NASA Langley Research Center, Hampton, Virginia, April 19-21, 1988.

14. Viegas, J. R , Rubesin, M. W., and Horstman, C. C., "On the Use of Wall Functions as Boundary Conditions for Two-Dimensional Separated Compressible Flows," AIAA-85-0180, AIAA 23rd Aerospace Sciences Meeting, Reno, Nevada, January 14-17, 1985.

15. Chen, H. C. and Patel, V. C., "Practical Near-Wall Turbulence Models for Complex Flows Including Separation," AIAA-87-1300, AIAA 19th Fluid Dynamics, Plasma Dynamics and Lasers Conference, Honolulu, Hawaii, June 8-10, 1987.

16. Rodi, W., "A New Algebraic Relation for Calculating the Reynolds Stresses," ZAMM, Vol. 56, 1976.

ACKNOWLEDGMENT

The authors wish to acknowledge the excellent cooperation provided by the staff of the Advanced Flight Sciences Department of the Lockheed-Georgia Corporation, in particular, Mr. C. J. Novak, in providing unpublished wind tunnel data of the experiment described in Reference 1.

R. W. MacCormack acknowledges the support by NASA Ames Research Center, through Joint Research Interchange No. NCA 2-40.

TABLE 1

COMPARISON OF EXPERIMENTAL AND COMPUTED LIFT COEFFICIENTS

SOURCE	JET MOM. COEFFICIENT, C_μ	LIFT COEFFICIENT, C_L	ERROR, %
EXPERIMENT	0.03	1.50	
COMPUTATIONS			
BALDWIN-LOMAX (BL)	0.03	2.26	+51
BL + HISTORY	0.03	2.51	+67
BL + CURVATURE CC = 8.0	0.03	2.06	+37
BL + CURVATURE + HISTORY	0.03	2.24	+49
JONES-LAUNDER (JL)	0.03	2.54	+69
JL + CURVATURE	0.03	2.08	+39
EXPERIMENT	0.10	3.58	
COMPUTATIONS			
BL	0.10	5.30	+48

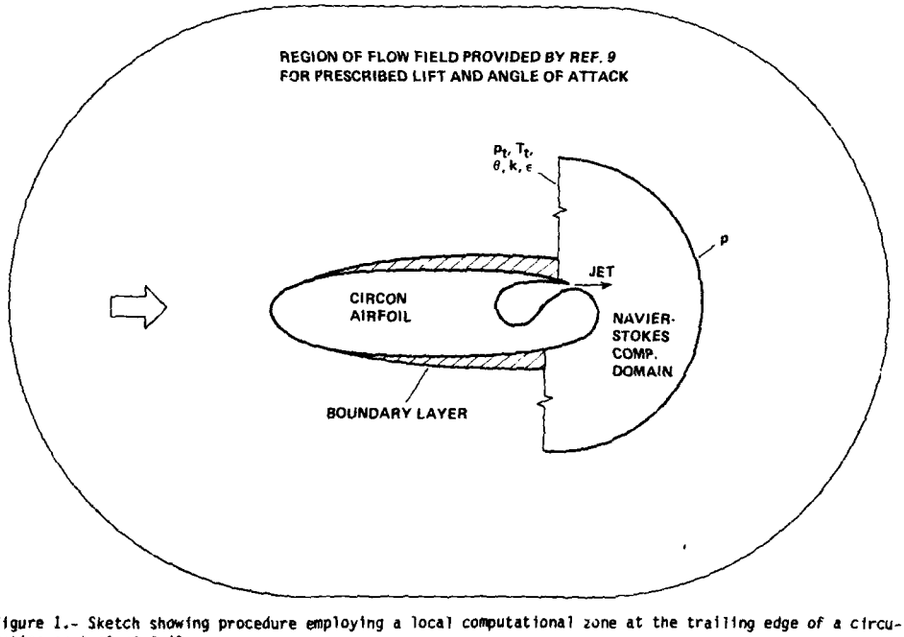


Figure 1.- Sketch showing procedure employing a local computational zone at the trailing edge of a circulation control airfoil.

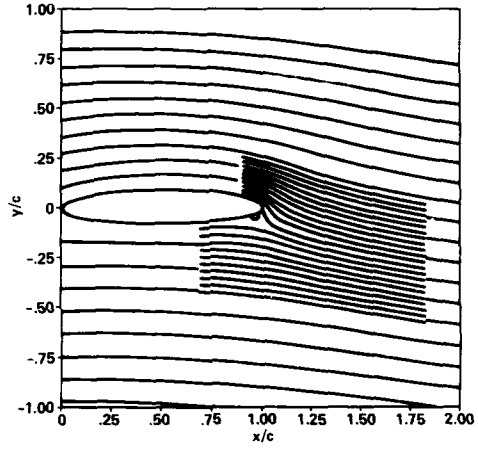


Figure 2.- Overlay of streamlines from local zone calculation onto those of ambient calculation of reference 9.

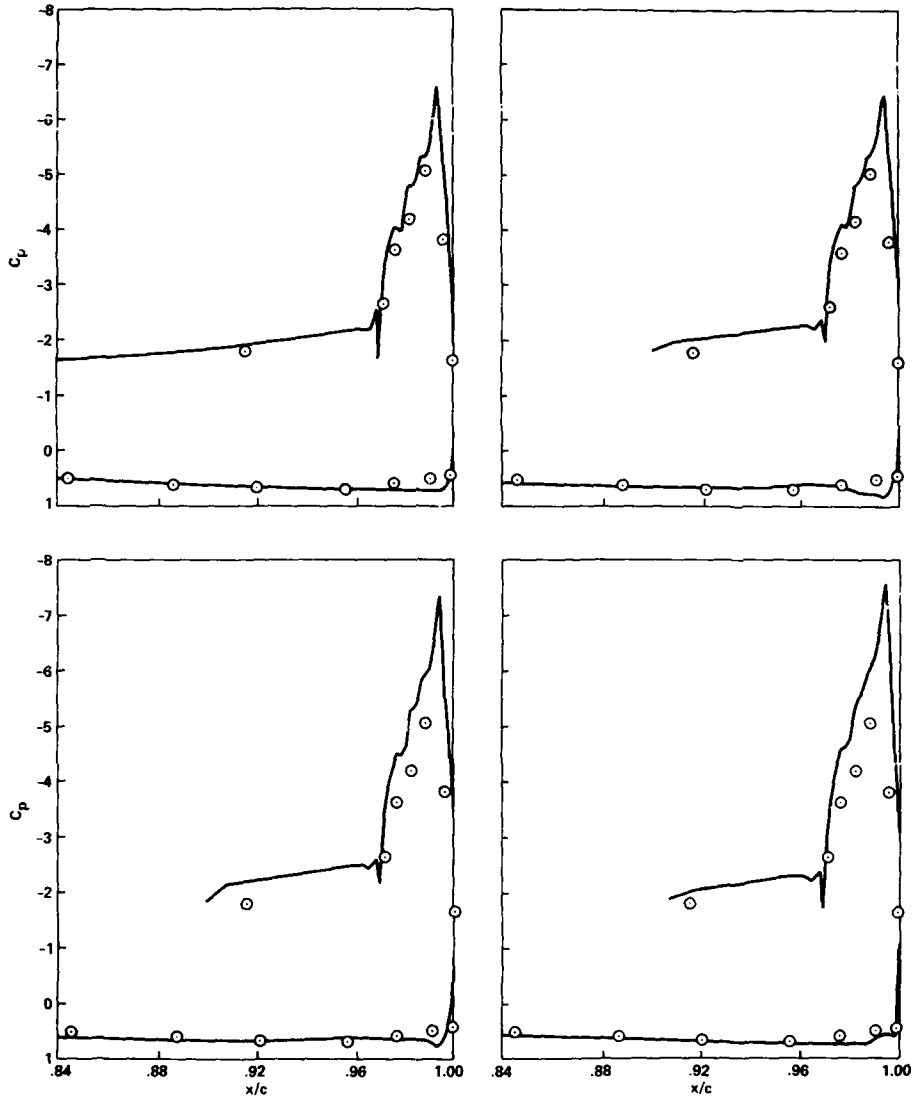


Figure 3.- Surface pressure coefficients on the trailing edge of the circulation control airfoil of reference 8. a) Full field solution of reference 9, Baldwin-Lomax turbulence model plus curvature correction. b) Local Navier-Stokes solution, Baldwin-Lomax turbulence model plus curvature correction. c) Local Navier-Stokes solution, Baldwin-Lomax turbulence model, no curvature correction. d) Local Navier-Stokes solution, Jones-Launder turbulence model, no curvature correction.

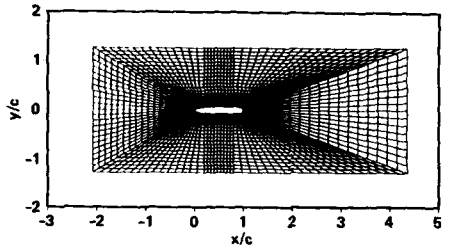


Figure 4.- Grid used for full airfoil/test section computation.

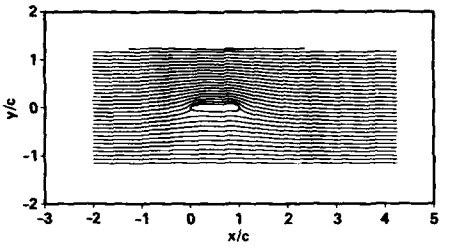


Figure 7.- Stream function of flow field in test section with circulation control airfoil. Baldwin-Lomax turbulence model; C_μ = 0.03.

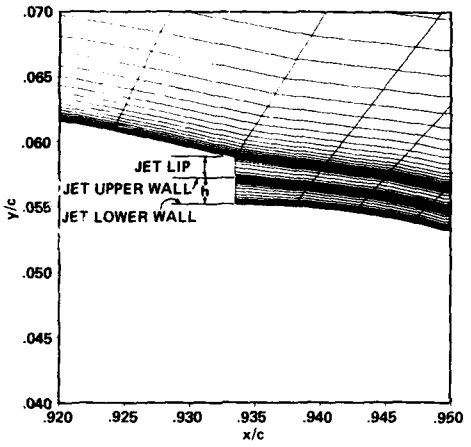
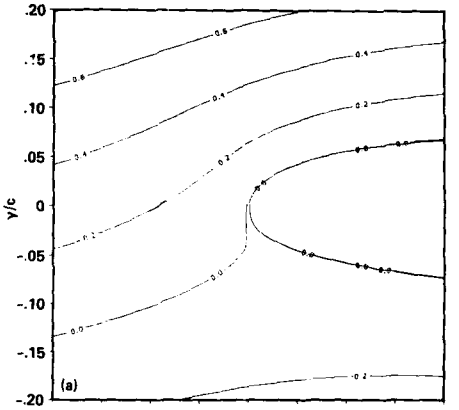


Figure 5.- Grid detail near jet exit; h/c = 0.002.



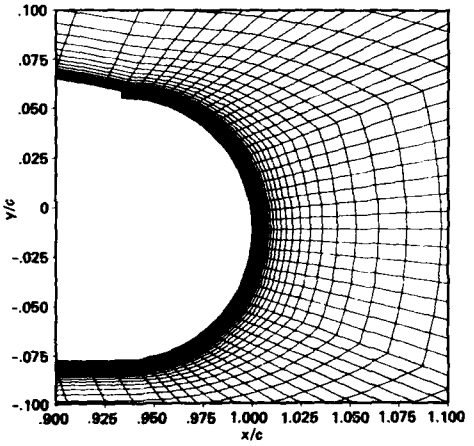


Figure 6.- Grid detail over entire trailing edge.

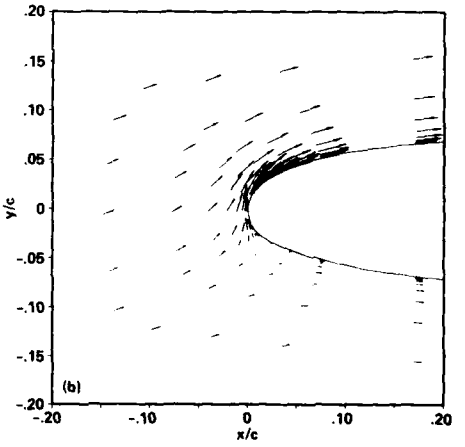


Figure 8.- Stream function and vector field near leading edge of circulation control airfoil. Baldwin-Lomax turbulence model; C_μ = 0.03. a) Stream function. b) Vector field.

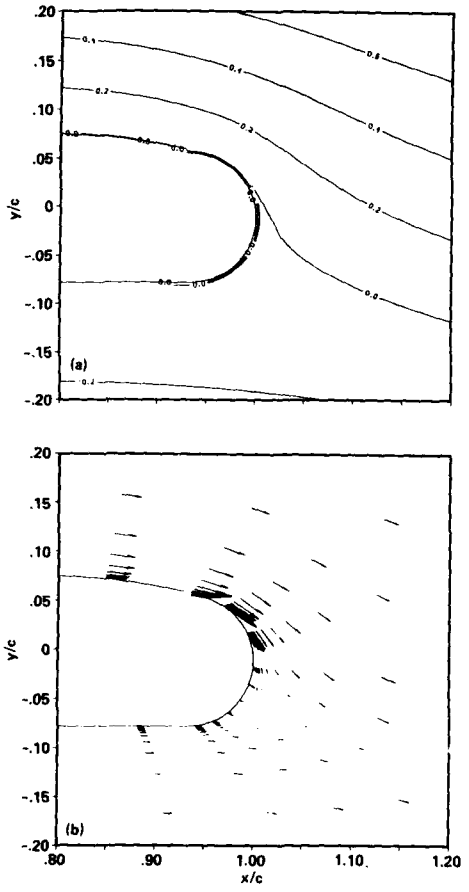


Figure 9.- Stream function and vector field near trailing edge of circulation control airfoil. Baldwin-Lomax turbulence model; C_μ = 0.03. a) Stream function. b) Vector field.

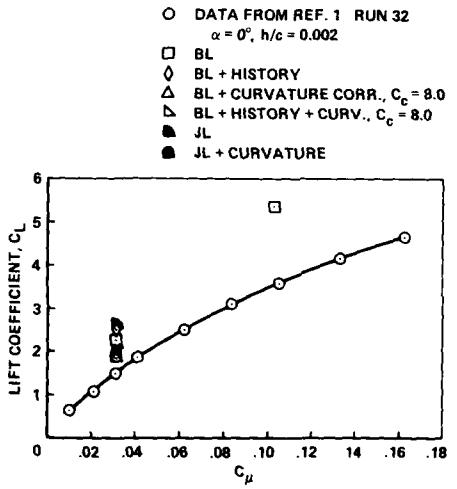


Figure 10.- Sectional lift coefficient as function of jet momentum coefficient. Angle of attack = 0.

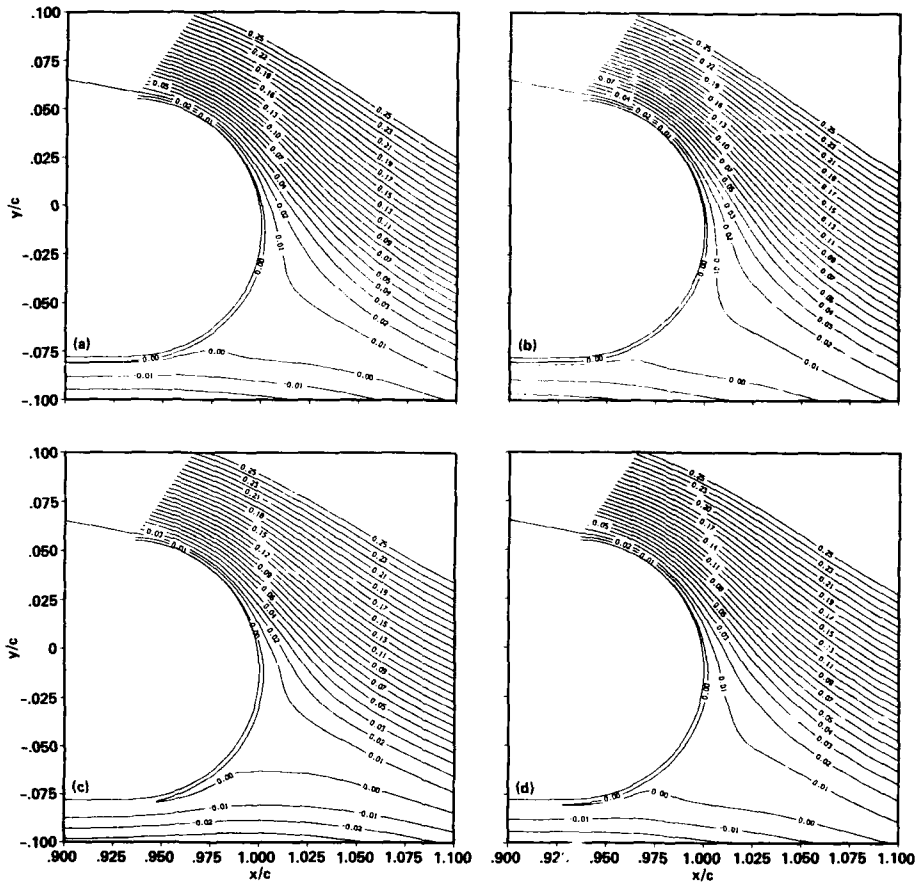


Figure 11.- Stream function corresponding to different turbulence models in the trailing edge region of the circulation control airfoil; C_μ = 0.03. a) Baldwin-Lomax turbulence model. b) Baldwin-Lomax turbulence model plus jet history. c) Baldwin-Lomax turbulence model plus curvature correction. d) Baldwin-Lomax turbulence model plus jet history and curvature correction.

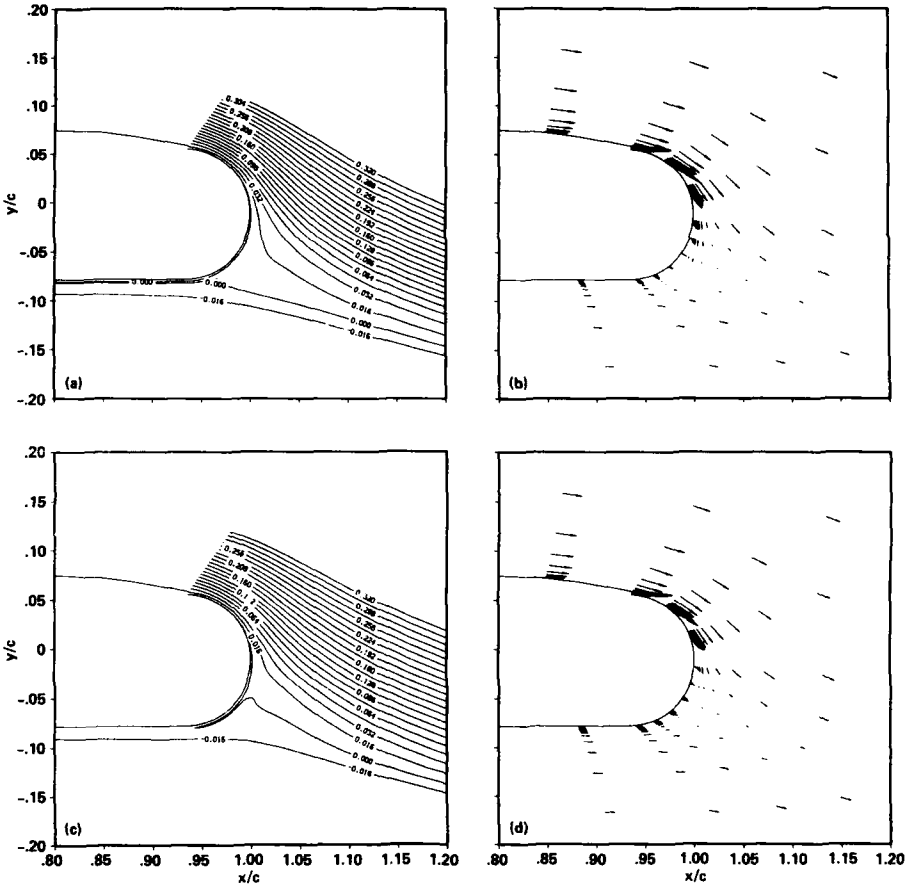


Figure 12.- Stream function and vector field in the trailing-edge region of circulation control airfoil; C_μ = 0.03. a) Stream function, Jones-Launder turbulence model. b) Vector field, Jones-Launder turbulence model. c) Stream function, Jones-Launder turbulence model plus curvature correction. d) Vector field, Jones-Launder turbulence model plus curvature correction.

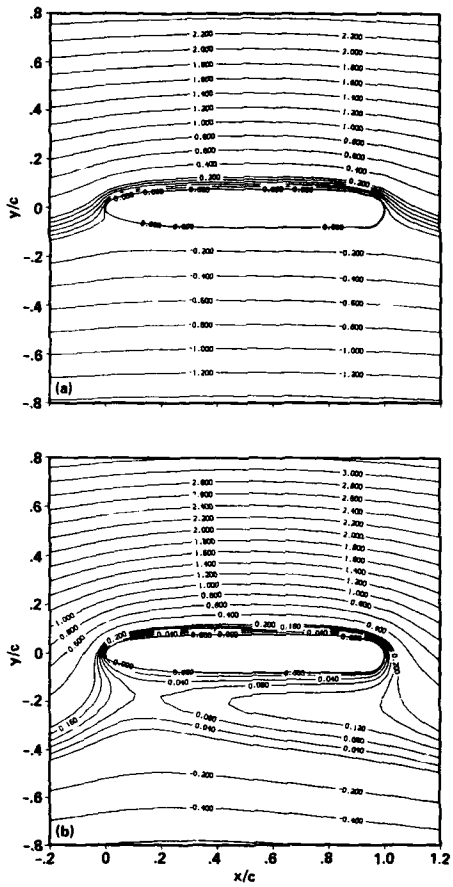


Figure 13.- Comparison of test section stream functions corresponding to two jet mass momentum coefficients. a) C_μ = 0.03. b) C_μ = 0.10.

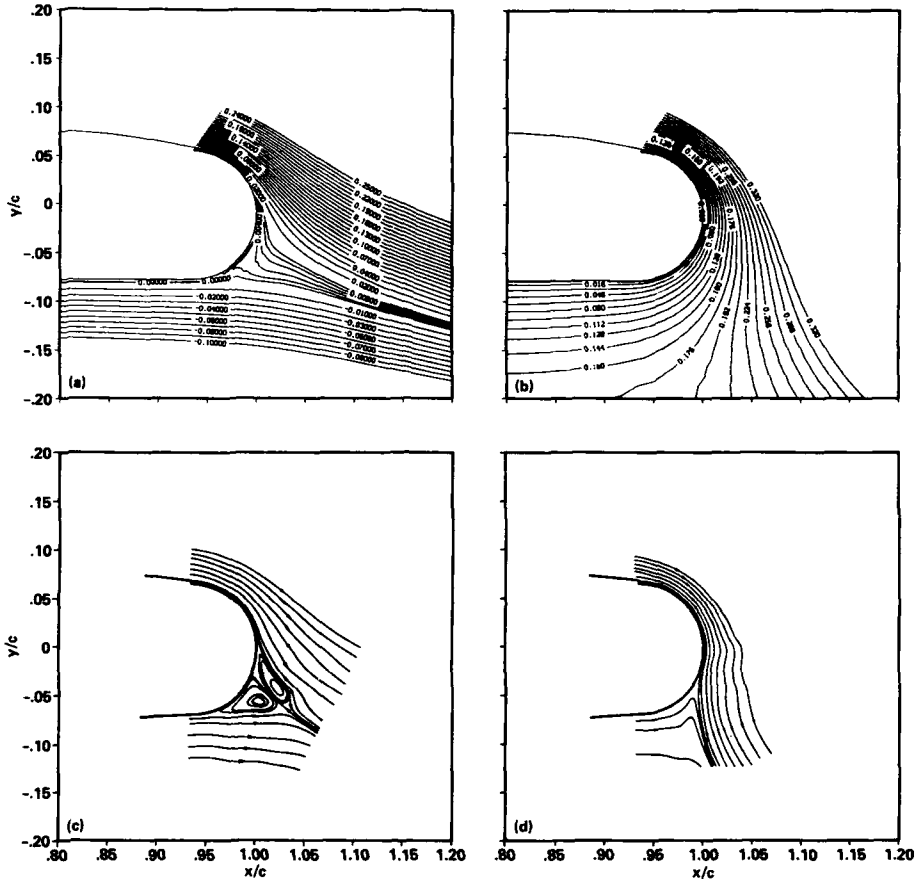


Figure 14.- Comparison of computed and measured streamlines in the trailing-edge region. a) Computed, C_μ = 0.03. b) Computed, C_μ = 0.10. c) Experimental, C_μ = 0.03. d) Experimental, C_μ = 0.10.

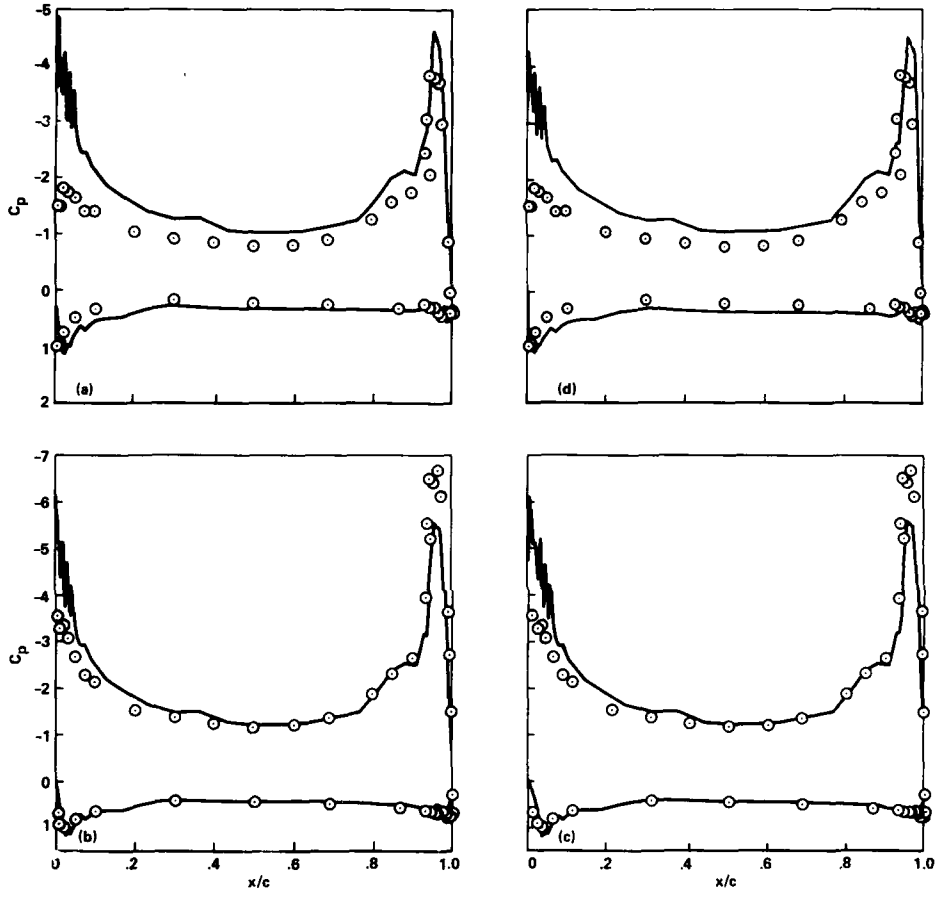


Figure 15.- Pressure coefficient distribution of the upper and lower surfaces of the airfoil. a) Baldwin-Lomax turbulence model plus curvature correction, with jet momentum coefficient matched to the experimental value. b) Baldwin-Lomax turbulence model plus jet history, with total lift matched to the experimental value. c) Jones-Launder turbulence model, with total lift matched to the experimental value. d) Jones-Launder turbulence model corrected for curvature, with jet momentum coefficient matched to the experimental value.

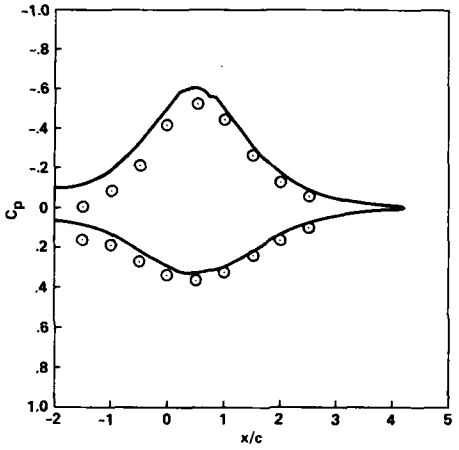


Figure 16.- Comparison of computed and measured pressure coefficients on the upper and lower wind tunnel walls for the Jones-Launder model with lift matched to the experimental value.

COMPARATIVE STUDY OF CALCULATION PROCEDURES FOR VISCOUS FLOWS AROUND AIRFOILS IN THE TRANSONIC REGIME

H.W. Stock, W. Haase, H. Echtle

Dornier GmbH
D-7990 Friedrichshafen 1, Federal Republic of Germany

ABSTRACT

Comparative studies for the evaluation of flows around airfoils will be presented. This problem is solved in two different ways. Flows are computed by

1. a finite volume Navier-Stokes method,
2. an iterative calculation procedure using a finite volume method to solve the full potential equation for the inviscid flow and an inverse integral boundary layer method for the viscous part.

Using the Navier-Stokes method, two different algebraic turbulence models are investigated. First the Baldwin-Lomax model is applied followed by the Cebeci-Smith model - in combination with a recently developed approach to evaluate the turbulent length scales in Navier-Stokes methods.

Concerning the problem of the computation of shock wave boundary layer interaction regions, a numerical study is performed using the finite volume Navier-Stokes method. The influence of mesh refinement - in the surface normal and tangential direction - with respect to the prediction quality is studied.

Two different airfoils - the RAE 2822 and the DoAL3 airfoil - will be investigated and compared to experimental findings.

LIST OF SYMBOLS

c	Chord length
c_D	Drag coefficient
c_f	Skin friction coefficient
c_L	Lift coefficient
c_p	Pressure coefficient
H_{in}	Incompressible form parameter
n	Mesh points in the boundary layer
q	Geometrical stretching factor
Re_C	Reynolds number based on chord length
U	Wall parallel velocity component
u_τ	Friction velocity
x	Chordwise direction
y	Wall normal direction
y^+	Law of the wall coordinate
α	Angle of attack
δ	Boundary layer thickness
δ^*	Displacement thickness
μ	Dynamic viscosity
ν	Kinematic viscosity
ρ	Density
τ	Shear stress
θ	Momentum loss thickness

Subscripts

e	Outer edge of the boundary layer
w	Wall
1	First meshsize at the wall

INTRODUCTION

A close connection between the experimental and computational developments is necessary to finally produce reliable computational methods. The insight in physical aspects gained from critical experiments should be represented by adequate models in the code development work. The aim is to get computational methods with an ensured validity in a carefully determined range of applicability if compared to appropriate experiments. This situation of code validation can only be achieved if the accuracy and limitations of both the experiments and the computational methods are known over a specified range of well understood physical parameters.

In the present paper two different approaches are considered to compute the transonic flow around airfoils. One approach contains a method, solving the time averaged Navier-Stokes equations, the other approach solves the full potential equation, coupled iteratively to an inverse boundary layer method via the outflow concept. The numerical results

are compared to an experiment with a shock-wave boundary layer interaction, which is expected to be an adequate experiment of a transonic profile flow. Windtunnel corrections for the effective angle of attack of the model are given. A second experiment is a fairly recent one where no shocks are present in the flow field and no windtunnel corrections are supplied.

The influence of mesh density, mesh adaption and the applied turbulence models on the Navier-Stokes solutions will be presented. Furthermore, for flows with no extensive flow separation, it is shown that the coupled potential and boundary layer computation approach is comparable to the results of the Navier-Stokes code.

SHORT DESCRIPTION OF THE COMPUTATIONAL METHODS

The Navier-Stokes method

The numerical method to solve the Navier-Stokes equations for compressible flows in full conservation form is a finite volume method according to Ref. 1. Rewriting the governing equations in integral form and dividing the computational domain into quadrilateral cells, a system of ordinary differential equations is obtained by applying the integral equations to each cell separately. The set of ordinary differential equations in time is solved by means of an explicit 3-stage Runge-Kutta-type time-stepping method. To control an odd-even decoupling, a blended second and fourth order filter is introduced. Due to the fact that only the steady state is of interest the difference equations are solved by a local time stepping approach based on the maximum allowable time step for each cell (CFL number = 1.8). Introducing the residual averaging approach[2], i.e. collecting the information from residuals implicitly, leads to a higher CFL number which has been chosen to be 3.5 in all calculations. The viscous terms are treated using central differences throughout the domain and one-sided formulas at the surface.

The steady state is defined to be reached if all force coefficients do not vary more than 0.05% and for transonic flow problems the total number of supersonic points remains constant within a monitoring sequence of 30 iterations. Typically an error norm reduction (L2-norm of $\partial\rho/\partial\tau$) of approximately four decades will then be obtained.

The coupled potential and boundary layer method

The inviscid flow is computed using the multigrid procedure of Jameson[3] for the solution of the full potential equation. The laminar boundary layer part is calculated by the two-dimensional version of an integral method for three-dimensional flows[4]. The turbulent flow is evaluated using the inverse integral method of Ref. 5. No transitional boundary layer calculation is performed, the method switches at the transition point from the laminar method directly to the fully turbulent method. The coupling between the inviscid and viscous part is done by means of the outflow concept.

Influence of the turbulence model and mesh adaption

The main objective in developing turbulence models is to specify closure conditions in which the unknown Reynolds stresses of turbulence are related to known mean flow properties. The relation is established either analytically (zero equation model) or through differential equations for the transport quantities of turbulence (one- or two equation models).

The turbulence models which are commonly used are not well advanced[6] as they are essentially developed for attached boundary layers and simple shear flows. For boundary layer computations, the algebraic eddy viscosity model of Cebeci-Smith[7] has found a broad application. For the computation of non-complex flows solving the Navier-Stokes equations it would be advantageous to use the Cebeci-Smith model. Unfortunately, this model can not be applied directly as the edge of the viscous layer is not known a priori. The latter quantity however, is needed for the formulation of the eddy viscosity in the outer layer in the Cebeci-Smith model.

The Baldwin-Lomax[8] algebraic turbulence model, developed in 1978 and patterned after Cebeci-Smith, is suitable for Navier-Stokes methods circumventing the difficulty of determining the outer edge of the viscous layer by the formulation of an alternative expression. Since then, the Baldwin-Lomax model has been widely used in its original form or slightly modified to take history effects into account[9].

Recently, a method has been presented[10] which allows the evaluation of the turbulent length scale in Navier-Stokes methods. The advantage of the new turbulent length scale computation is twofold. Firstly, the Cebeci-Smith model can be applied directly and secondly an adapted mesh can be established during the course of iterations based on the knowledge of the shear layer thickness δ. Hence, it is possible to ensure a constant desired mesh point number inside the viscous layer from the leading edge of the airfoil down to the wake, producing a controlled resolution in this area. Additionally, during the iteration, the wake centerline is equally well adapted to the numerically evaluated streamline leaving the trailing edge of the airfoil.

The total number of mesh points inside the viscous layer was chosen to n = 25 for the first test case. These points are aligned in the wall normal direction or - in the wake - nearly normal to the wake centerline. For wall layers, the height of the first volume adjacent to the wall is chosen so that the value y^+ for the considered volume center satisfies the condition

$$y_1^+ = \frac{y_1 |u_\tau|}{\nu_w} = 1$$

With respect to the volume heights, a geometrical stretching is used across the viscous layer with a constant ratio q of neighbouring volume heights:

$$\frac{\delta}{y_1} = \frac{1 - q^n}{1 - q}$$

with

$$\delta = y_1(1 + q + q^2 + ... + q^{n-1})$$

Knowing δ and u_e at each airfoil station the stretching factor q can be determined. The mesh in the wake is constructed by taking the lower or upper side mesh at the trailing edge and replacing the trailing edge δ by the local value of δ in the wake. The mesh in the inviscid region is generated by simple stretching functions.

In order to update the mesh during the course of iterations the computed quantities δ and u_e on the airfoil and in the wake are smoothed by use of a Shuman filter. The present updating of the mesh delivers a redistribution in a normal direction along the airfoil and the wake centerline.

RESULTS

RAE 2822 airfoil (case 9)

Fig. 1 gives an example of the mesh updating for the RAE 2822 airfoil, case 9. In the upper part of fig. 1 the initial mesh in the vicinity of the airfoil is presented. In the middle of fig. 1 the first 25 volumes adjacent to the wall were omitted. The finally (three times) updated mesh is given in the lower part of fig. 1. The empty space between airfoil/wake and the first mesh line parallel to airfoil and wake represents the calculated viscous layer thickness and consists of the desired 25 volumes normal to wall and wake centerline. As can be seen, the present updating already carries some of the computed flow features, i.e. the rapid growth of the viscous layer approaching the trailing edge as well as the nicely detectable shock wave boundary layer interaction zone.

The transonic flow around the RAE 2822 airfoil[11] was calculated at a Mach number M = 0.73, a Reynolds number based on the chord length of $Re_c = 6.5 \times 10^6$ and at a corrected[11] angle of attack $\alpha = 2.79°$. Three different computational results are given in figures 2 - 4.

First the flow was computed using the Cebeci-Smith model together with the new turbulent length scale calculation and the adapted mesh (298 x 70 mesh points, 204 on the airfoil) given in the lower part of fig. 1. The second calculation uses the Baldwin-Lomax model in the initial mesh (mesh point numbers as in the adapted mesh) and the third computation has been performed again with the Baldwin-Lomax model but in the adapted mesh. It should be kept in mind, that the third calculation is only given for comparison, as the Baldwin-Lomax model does not give any information about the viscous layer thickness. All three calculations were done with a small filter value, keeping the numerical viscosity down and thus tolerating only small oscillations in the solution.

Fig. 2 gives the pressure distribution compared to the measurements. The calculations are almost indistinguishable except in the shock location and the pressure plateau on the suction surface. They do not predict sufficiently well the small suction peak in the nose region of the upper surface. A possible explanation may be the fact that the largest differences between the design and the actual airfoil contour are located in that region (the design contour was used for all computations). Furthermore, the compression of the flow in the shock region is overpredicted, which is certainly due to the deficiencies of the turbulence models in strong interaction regions. Fig. 3 shows the boundary layer type results $\delta^* \cdot \theta$, H_{in} and c_f. These results using the Baldwin-Lomax model could only be obtained by analyzing the final converged flow field data with the turbulent length scale determination[10].

The best agreement with the measured data is found with the Cebeci-Smith model together with the turbulent length scale calculation[10]. Especially upstream the shock the Baldwin-Lomax model clearly underpredicts the displacement and momentum loss thickness. This situation is ameliorated by the use of the adapted mesh. In the shock region the incompressible shape parameter H_{in} is clearly overpredicted and the subsequent relaxation of H_{in} is not seen in the experiment due to the lack of an interaction turbulence model. The corresponding underprediction of δ^* in the region downstream of the shock is responsible for an overestimation of the compression in that region. see fig. 2.

The calculated and measured velocity profiles at different x/c stations are presented in fig. 4. Here again the results of the Cebeci-Smith model (together with the turbulent length scale determination) are visibly in better agreement with the measurement. Upstream the shock and in the trailing edge region the prediction is fairly acceptable and the lower side trailing edge flow is also better predicted.

Influence of mesh density

In order to investigate the situation whether an increased mesh density may ameliorate the prediction in the shock wave boundary layer interaction region, 1024 x 128 mesh points were used in the computation. Here again, the Cebeci-Smith model together with the new turbulent length scale calculation was used. Fig. 5 demonstrates that the pressure distribution is almost unchanged with respect to the more coarse mesh, see fig. 2. Similarily, the predicted boundary layer values remained unchanged. Hence, there is a certain upper boundary of the mesh density above which the prediction quality is not ameliorated.

Computation of drag and lift polars

Recently, the DoAL3 airfoil was investigated in a transonic wind tunnel for free transition conditions[12]. Table 1 gives the measured transition locations on the upper and lower surface of the airfoil. The Mach number was $M = 0.48$ and the Reynolds number based on the chord length 3.2×10^6. Figures 6 and 7 compare the measured and computed pressure distributions for various angles of attack, using the Navier-Stokes code and the above mentioned modelling of turbulence. The mesh consisted of 298 x 70 mesh points.

In the computation, separation was detected on the upper surface of the airfoil for angles of attack $\alpha \geq 3°$. Fig. 8 gives the separation location as a function of the angle of attack. At $\alpha = 10°$, 40% of the suction surface showed separated flow. Additionally, in fig. 9 Mach number contours for $\alpha = 0°$ and $\alpha = 9°$ are given. The large separated region for $\alpha = 9°$ can clearly be seen.

The comparison of measured and calculated lift and drag polars is presented in figures 10 and 11. The transition from laminar to turbulent flow was fixed in the computations corresponding to the measured values, see table 1. The laminar bucket is fairly well represented and agrees well with the c_L range of the measurements for which the drag is clearly reduced due to the presence of large portions of laminar flow on the profile. The level of the drag in the laminar bucket is slightly overpredicted by the computations. The deviation in the lift polar, especially for $dc_L/d\alpha$, fig.10, may be due to the uncorrected wind tunnel data. On the other hand, the maximum lift is very well predicted.

The coupled potential and boundary layer method compared to measurements and Navier-Stokes results

For the coupled potential and boundary layer method figures 12 and 13 give the results for the RAE 2822 profile, case 9. In order to fit the experimentally given lift the original angle of attack (2.79°) was modified to 2.56°. The prediction quality of the pressure distribution, fig. 12, and the boundary layer properties, fig.13, is slightly worse compared to the difference between the measurements and the Navier-Stokes results.

In the last two figures, 14 and 15, the flow around the DoAL3 profile at low lift is compared to measurements and Navier-Stokes predictions. The pressure distribution is almost identical to the experiments for both methods, but the prediction of the skin friction in the laminar part of the flow is visibly different. The Navier-Stokes method predicts a higher level of wall shear, the reason is not yet well understood. In both methods the calculation switches from the laminar to the turbulent calculation without a transition model. A sudden jump in c_f occours in the boundary layer code. In the Navier-Stokes method the apparent turbulent shear is added to the laminar shear starting at the location of transition. Therefore, the skin friction distribution in the Navier-Stokes code does not exhibit a sudden jump, due to the fact that the laminar velocity profiles at the wall are gradually modified into turbulent ones by the addition of the apparent turbulent shear.

CONCLUSIONS

It is shown for Navier-Stokes calculations of transonic airfoil flows that the application of the Cebeci-Smith turbulence model together with the new turbulence length scale determination produces in adapted meshes a better prediction quality than the Baldwin-Lomax model for which a mesh adaption of the type shown is not feasible. Furthermore, computations with free transition, where the transition location is prescribed based on the experimental data, are in a good agreement with measurements of pressure distributions and lift and drag coefficients. The c_L range of the laminar bucket is well predicted, but the drag is slightly overpredicted. The measured maximum lift however, is represented well by the computations.

For flows which do not exhibit extensive separated regions, the potential theory coupled to an inverse boundary layer method shows a fair agreement between measurements and Navier-Stokes calculations.

ACKNOWLEDGMENT

The authors are greatful to the NLR for the allowance to run the very fine mesh cases on their NEC-SX2 computer and especially to M. Schuurmans and G. Huizing for their patience and assistance.

REFERENCES

[1]Haase, W., Wagner, B., Jameson, A., "Development of a Navier-Stokes Method Based on a Finite Volume Technique for the Unsteady Euler Equations," Notes on Numerical Fluid Mechanics, Vol. 7, p. 99-107, Vieweg Verlag (1983)

[2]Jameson, A., Schmidt, W., "Some Recent Developments in Numerical Methods for Transonic Flows," Computer Methods in Applied Mechanics and Engineering 51, p. 467-493 (1985)

[3]Jameson, A., "Acceleration of Transonic Potential Flow Calculations on Arbitrary Meshes by the Multiple Grid Method," AIAA-Paper 79-1458 (1979)

[4]Stock, H.W., Horton, H.P., "Ein Integralverfahren zur Berechnung dreidimensionaler, laminarer, kompressibler, adiabater Grenzschichten," Z. Flugwiss. und Weltraumforschung, Vol. 9, p. 101-110 (1985)

[5]Stock, H.W., "An Inverse Boundary Layer Method for Turbulent Flows on Infinite Swept Wings," Z. Flugwiss. und Weltraumforschung, Vol. 12, p. 51-62 (1988)

[6]Marvin, J.G., "Turbulence Modeling for Computational Aerodynamics," AIAA-Paper 82-164 (1982)

[7]Cebeci, T., Smith, A.M.O., "Analysis of Turbulent Boundary Layers," Academic Press (1974)

[8]Baldwin, B.S., Lomax, H., "Thin Layer Approximation and Algebraic Model for Separated Turbulent Flows," AIAA-Paper 78-257 (1978)

[9]Visbal, M. Knight, D., "Evaluation of the Baldwin-Lomax Turbulence Model for Two-Dimensional Shock Wave Boundary Layer Interactions," AIAA-Paper 83-1697 (1983)

[10]Stock, H.W., Haase, W., "The Determination of Turbulent Length Scales in Algebraic Turbulence Models for Attached and Slightly Separated Flows Using Navier-Stokes Methods," AIAA Paper 87-1302 (1987)

[11]Cook, P. H., McDonald M. A., Firmin, M. C. P., "Aerofoil RAE 2822 - Pressure Distributions, and Boundary Layer and Wake Measurements", AGARD-AR-138, (1979)

[12]Lück, H., "Windkanalmessung mit dem 2-D Profilmodell DoAL3 bei der DFVLR Braunschweig", Dornier AV Nr. BF40-59/87 (1987)

Table 1

α	Upper Surface	Lower Surface
deg	x/c	x/c
-2.0	0.55	0.64
-1.0	0.55	0.64
0.0	0.55	0.64
0.5	0.55	0.64
1.0	0.17	0.64
3.0	0.05	0.64
5.0	0.00	0.68
7.0	0.00	0.68
8.0	0.00	0.68
9.0	0.00	0.68
10.0	0.00	0.68

FIGURES

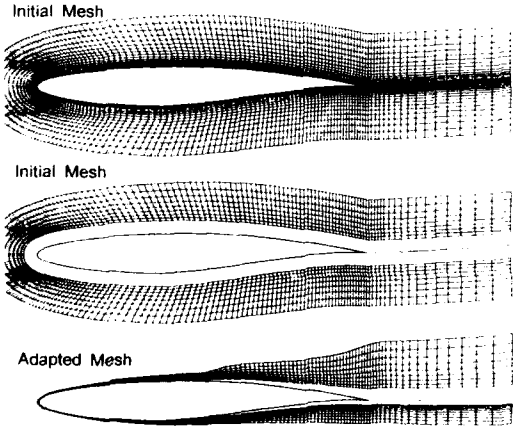


Fig. 1: Initial and adpated mesh for the RAE 2822 airfoil[11], case 9, (298 × 70 mesh points)

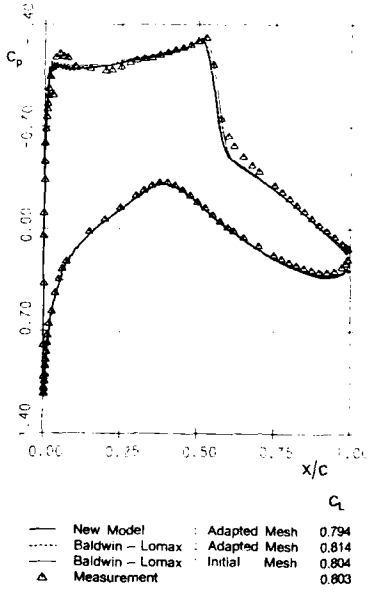


Fig. 2: Measured[11] and calculated (Navier-Stokes) pressure distribution for the RAE 2822 airfoil, case 9, for $M = 0.73$, $\alpha = 2.79°$ and $Re_C = 6.5 \times 10^6$ (298 × 70 mesh points)

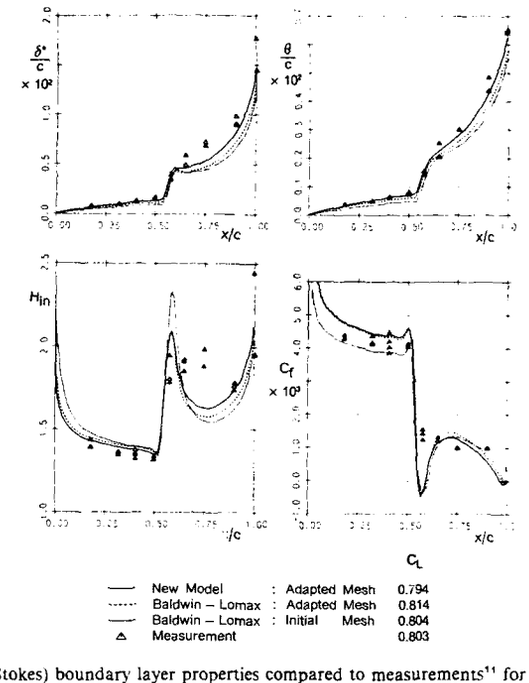


Fig. 3: Calculated (Navier-Stokes) boundary layer properties compared to measurements[11] for the RAE 2822 airfoil, case 9, for $M = 0.73$, $\alpha = 2.79°$ and $Re_c = 6.5 \times 10^6$ (298 × 70 mesh points)

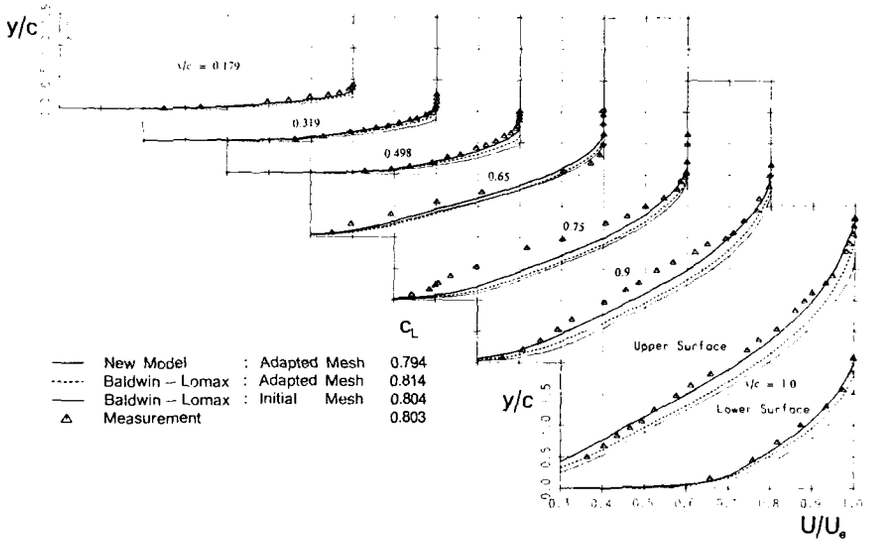


Fig. 4: Velocity profiles on the upper surface and the trailing edge for the RAE 2822 airfoil, case 9, for $M = 0.73$, $\alpha = 2.79°$ and $Re_c = 6.5 \times 10^6$ (298 × 70 mesh points)

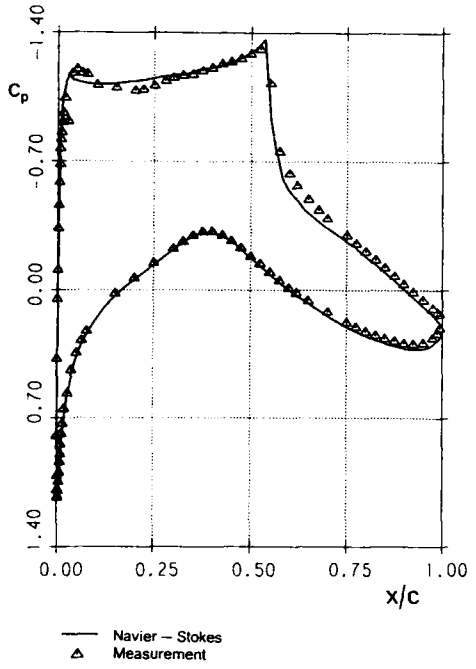


Fig. 5: Measured[11] and calculated (Navier-Stokes) pressure distribution for the RAE 2822 airfoil, case 9, for $M = 0.73$, $\alpha = 2.79°$ and $Re_c = 6.5 \times 10^6$ (1024 × 128 mesh points)

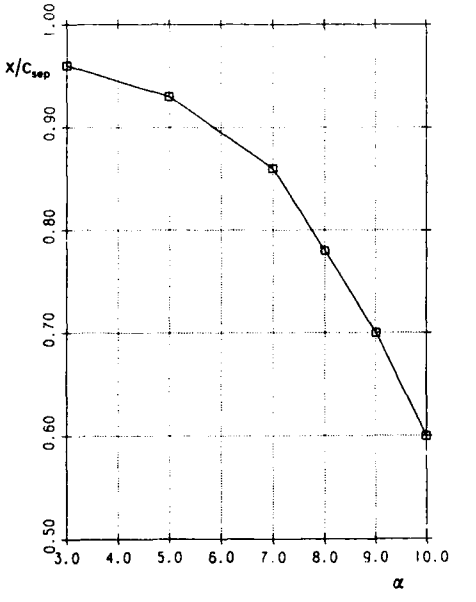


Fig. 8: Separation point motion on the suction surface of the DoAL3 airfoil as a function of the angle of attack - calculated by Navier-Stokes method for $M = 0.48$ and $Re_c = 3.23 \times 10^6$

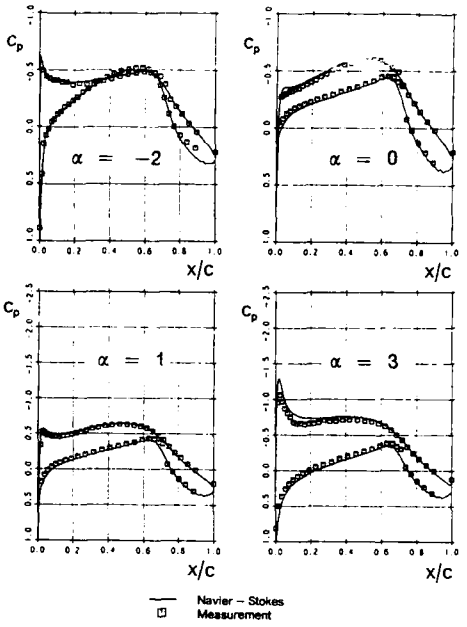


Fig. 6: Pressure distribution for the DoAL3 airfoil for $M = 0.48$ and $Re_c = 3.23 \times 10^6$ as a function of the angle of attack

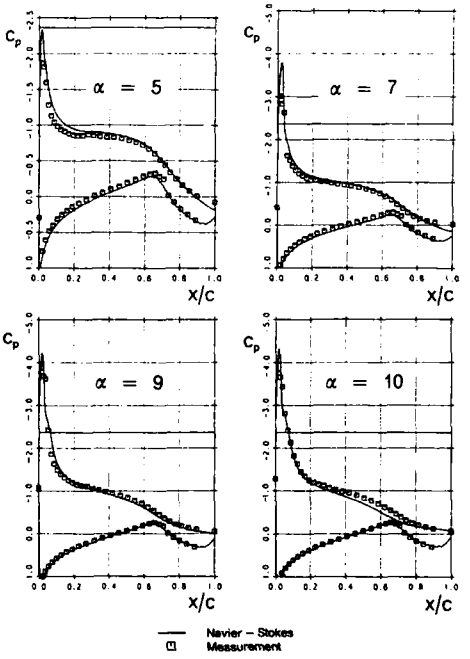


Fig. 7: Pressure distribution for the DoAL3 airfoil for $M = 0.48$ and $Re_c = 3.23 \times 10^6$ as a function of the angle of attack

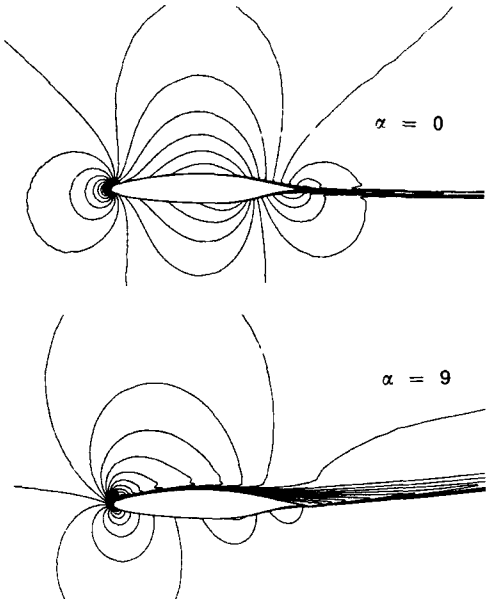


Fig. 9: Mach number contours for the DoAL3 airfoil - calculated by the Navier-Stokes method for $M = 0.48$ and $Re_c = 3.23 \times 10^6$

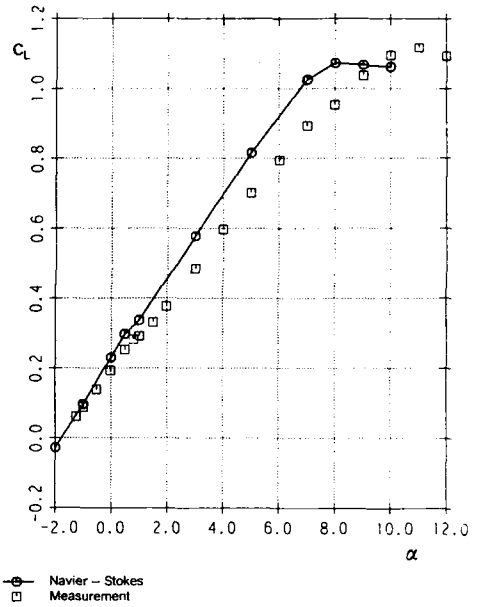


Fig. 10: Lift polar for the DoAL3 airfoil for $M = 0.48$ and $Re_c = 3.23 \times 10^6$

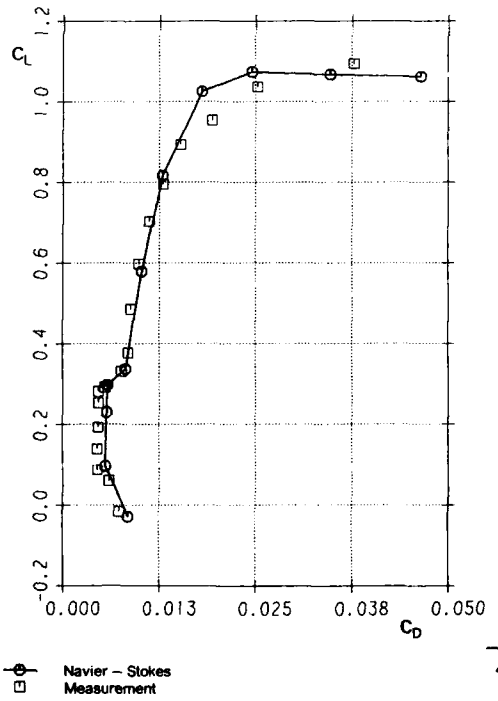


Fig. 11: Drag polar for the DoAL3 airfoil for $M = 0.48$ and $Re_c = 3.23 \times 10^6$

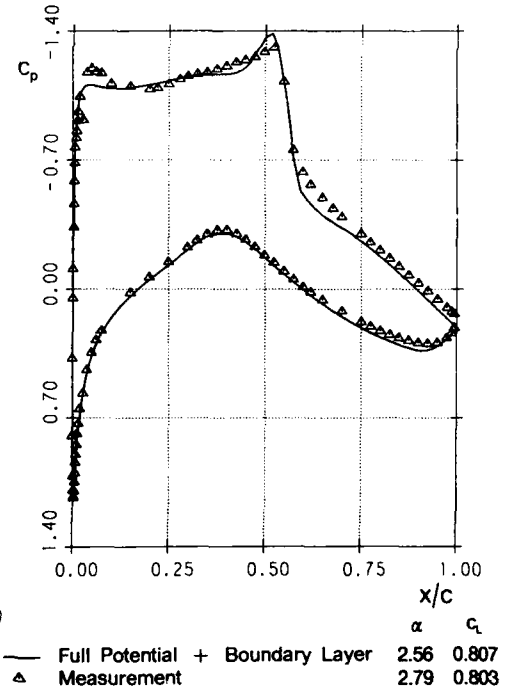


Fig. 12: Measured[11] and calculated pressure distribution for the RAE 2822 airfoil, case 9, for $M = 0.73$ and $Re_c = 6.5 \times 10^6$

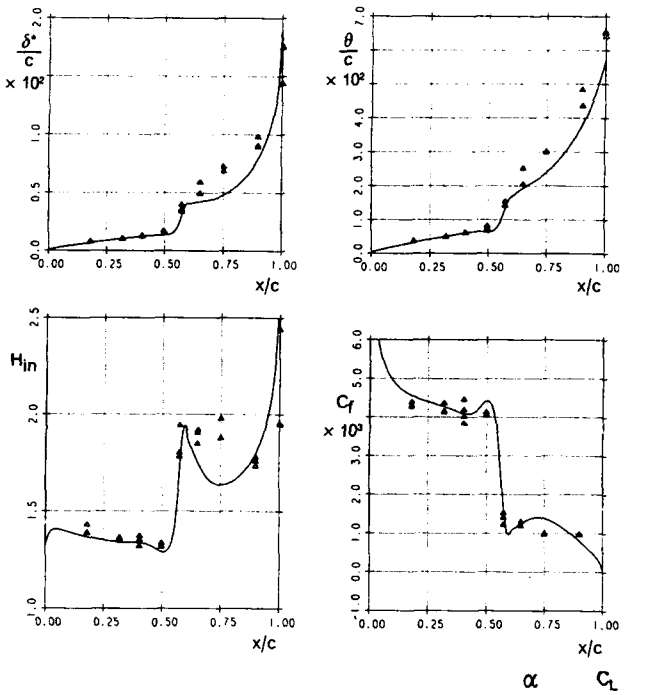


Fig. 13: Calculated boundary layer properties compared to measurements[11] for the RAE 2822 airfoil, case 9, for $M = 0.73$ and $Re_c = 6.5 \times 10^6$

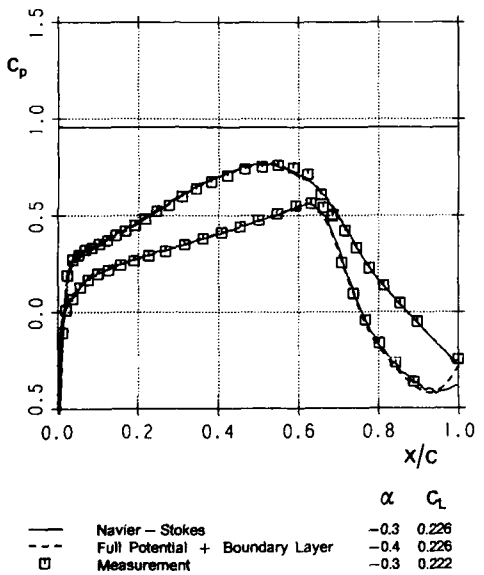


Fig. 14: Computed pressure distribution for the DoAL3 airfoil compared to measurements for $M = 0.48$ and $Re_c = 3.23 \times 10^6$

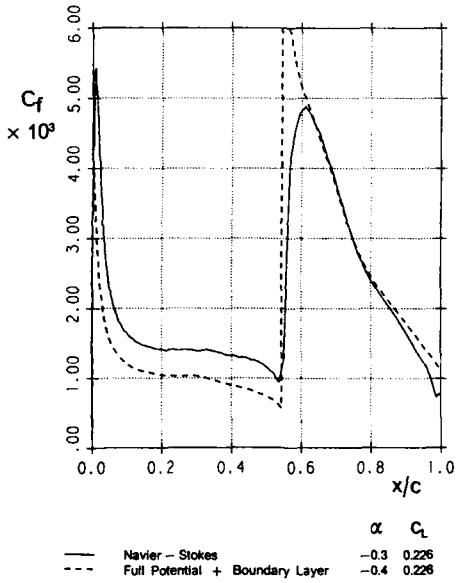


Fig. 15: Skin friction distribution on the suction surface of the DoAL3 airfoil for $M = 0.48$ and $Re_c = 3.23 \times 10^6$

NUMERICAL SOLUTION OF COMPRESSIBLE NAVIER-STOKES FLOWS

F. Bassi*, F. Grasso**, M. Savini***

* Universita' di Catania, Istituto di Macchine, via A. Doria 6, 95125 Catania, Italia

** Universita' di Roma "La Sapienza", Dip. di Mecc. e Aeronautica, via Eudossiana 18, 00184 Roma, Italia

*** CNR/CNPM, Viale Baracca 69, 20068 Peschiera Borromeo (Mi), Italia

SUMMARY

Here is presented and fully described a mesh embedding technique for increasing the accuracy of Navier Stokes computations of compressible flows. The method proposed is quite robust and the results obtained applying it to transonic airfoils computations are in fairly good agreement with the experiments and with computations made by other authors using much finer meshes. Thus this technique allows to compute solutions of such flows for practical use even on small computers.

INTRODUCTION

Several papers, dealing with the development of algorithms for the solution of viscous compressible flows, have recently appeared, and workshops have been organized for validation purposes [1-5]. The main conclusions that can be drawn from such flourishing activities are:

1) the most important errors associated with Navier-Stokes (NS) solvers are mainly numerical, and are due to grid topology and mesh refinement;
2) the inability to simulate very complex flows, such as strongly separated flows, is generally due to the lack of adequate physical submodels.

The present paper deals with the development of a robust NS solver for compressible flows [2-5]. The objective of this work is to show that accurate solutions can indeed be obtained on rather coarse meshes when an adaptive mesh embedding technique is used. The technique here presented exploits a local multigrid strategy to embed finer meshes onto the original (base) grid so as to improve the accuracy only in the regions of high gradients where greater accuracy is indeed required. Embedded cells are generated by halving on a cell by cell basis the mesh spacing both in x and y directions. In previous works [4-5] these authors have used only one level of grid embedding. In the present work the formulation has been generalized to handle any number of grid embedding so as to be able to perform computations on very coarse base grids. However numerical tests carried out by the authors have shown that it is not worth to use more than two such levels to achieve good solution accuracy. To increase the computational efficiency a multigrid technique on the base grid is also implemented. To show the effectiveness of method, computations of flows around Rae2822 and Jones airfoils are presented and results compared with experiments and/or other numerical results reported in Ref. [1].

The NS solver together with the mesh embedding technique is described in the next sections and numerical results are finally discussed.

GOVERNING EQUATIONS

The governing equations are the Reynolds-averaged compressible NS equations. Following Reynolds all variables are decomposed in a mean and a fluctuating part, and then averaging is performed. The equations for the mean flow variables are

$$\frac{\partial}{\partial t}\int_V W\,dV = -\oint_{dV}(F_E - F_V)\cdot\vec{n}\,dS \qquad (1)$$

where W, F_E, F_V are respectively the vector unknown, the inviscid (Euler type) flux and the viscous one, defined as:

$$W = [\rho, \rho\vec{u}, \rho E]^T$$

$$F_E = \left[\rho\vec{u}, \rho\vec{u}\vec{u} + p, \rho\vec{u}\left(E + \frac{p}{\rho}\right)\right]^T$$

$$F_V = [0, \vec{\sigma}, -(\vec{q} - \vec{u}\cdot\vec{\sigma})]^T$$

and

$$p = (\gamma - 1)\rho\left(E - \frac{1}{2}(u^2 + v^2)\right)$$

$$\vec{\sigma} = \vec{\sigma}_l + \vec{\sigma}_t$$

$$\vec{q} = \vec{q}_l + \vec{q}_t$$

where the subscripts *l* and *t* stand for laminar and turbulent contributions.

The constitutive equations for the viscous laminar terms are:

$$\vec{\sigma}_l = \mu_l\left(\left(\nabla\vec{u} + \nabla\vec{u}^T\right) - \frac{2}{3}\nabla\cdot\vec{u}\vec{U}\right) \tag{2}$$

$$\vec{q}_l = -\frac{\gamma}{Pr_l}\mu_l\nabla e \tag{3}$$

$$\mu_l = \mu_\infty\left(\frac{T}{T_\infty}\right) \tag{4}$$

Note that Chapman-Rubesin approximation for μ_l is here used for the sake of simplicity.

The closure problem, i.e. the constitutive equations for the additional terms due to turbulence, is solved by use of the two layer algebraic Baldwin-Lomax (BL) model [6], modified to avoid unphysically small values of the turbulent viscosity near separation or reattachment, where ambiguities arise in the determination of the length scale [7].

The constitutive equations for σ_t and q_t are formally the same as the laminar counterpart whereby the laminar diffusion coefficients are replaced by the turbulent ones.

The BL model assumes the existence of an inner and outer region. Prandtl-Van Driest formulation is employed in the inner region yielding

$$\mu_t = \rho(.4YD)^2|\omega|$$

where Y is the distance normal to the wall, $|\omega|$ is the magnitude of the vorticity, and D is the Van Driest damping factor:

$$D = \left[1 - \exp\left(-Y^+/26\right)\right]$$

$$Y^+ = Y\rho_w\frac{u_\tau}{\mu_{t_w}}$$

u_τ is the friction velocity, defined as

$$u_\tau = \sqrt{\tau_w/\rho_w}$$

In the original BL model τ_w is the local shear stress. In the present use of the model a "local" average value (τ) of τ_w is assumed, that partially takes into account for the history of the boundary layer development, and τ_w is replaced by τ defined as

$$\tau(x) = \frac{1}{L(x)}\int^{L(x)}\tau_w(x)dx$$

where x stands for the curvilinear coordinate along the body. The turbulent viscosity is obtained as

$$\mu_t = 2.68\cdot 10^{-2}\rho F_W F_K$$

where F_W and F_K are respectively the outer function and Klebanoff intermittency factor, given by

$$F_W = \min\left(Y_{max}F_{max}, .25Y_{max}\left(u_{max} - u_{min}\right)^2/F_{max}\right)$$

$$F_K = \left[1 + 5.5\left(.3\frac{Y}{Y_{max}}\right)^6\right]^{-1}$$

and

$$F_{max} = \max(YD|\omega|)$$

Observe that near separation F may be double peaked and consequently ambiguities may arise in the definition of Y_{max}, F_{max} [6-8]. A remedy to this has been proposed by Visbal and Knight [8] that obtain Y_{max}, F_{max} from the extremum farthest from the wall. However results with such a modification do not show dramatic changes in the solution and it has not been used in the present work.

NUMERICAL SOLUTION

The basic algorithm for solving the system of governing equations is a finite volume explicit three-stage Runge-Kutta algorithm, with symmetric discretization of both the inviscid and viscous terms [2,3,9]. The solution is advanced in time as follows:

$$W^{(0)} = W^{n}$$

$$W^{(k)} = W^{(0)} + \alpha_k \frac{\Delta t}{V}\left[-\left(F_E^{(k-1)} - F_V^{(0)} - F_{AD}^{(0)}\right)\cdot \vec{n}\Delta S\right]^{\wedge} \qquad k = 1,3 \tag{5}$$

$$W^{n+1} = W^{(3)}$$

where $\alpha_1 = \alpha_2 = .6$; $\alpha_3 = 1$.
Note that the symbol $^{\wedge}$ in Eqn (5) refers to the discretized form of the terms appearing in the square brackets.

A cell centered formulation is used and the numerical Euler flux F_E at the control surfaces is evaluated as the average of the fluxes defined at centers of the cells sharing the interface; e.g. between the cells (i,j) and (i+1,j) one has:

$$F_E^{\wedge} = \frac{1}{2}\left[F_E(W_{i,j}) + F_E(W_{i+1,j})\right] \tag{6}$$

Eqn. (6) ensures that consistency and conservation are guaranteed.

Vertex variables are used to compute the numerical viscous fluxes so as to achieve greater computational efficiency and accuracy, and central differencing is used. As for F_{AD} the same formulas proposed by Jameson have been used.

Adaptive Mesh Embedding

Adaptive techniques such as dynamic clustering, zonal method and grid embedding are generally the most suitable for reducing numerical errors.

In the first technique, grid points are moved toward regions where higher resolution is required [10], so as to achieve greater accuracy for a fixed computational cost. However the accuracy of the results may even deteriorate due to the topological properties of the adapted grid.

In the zonal approach the computational domain is divided into subdomains, and different grids are used in the different regions [11]. The technique is best suited for complex three-dimensional problems, however conservation properties of the algorithm can be destroyed at zonal interfaces.

In adaptive mesh embedding the solution accuracy is enhanced by local mesh enrichment [4,5,12-15]. The new grid points are organized either in a single fine grid or in fine grid patches embedded in the coarse grid. This process can be repeated by generating finer and finer meshes so as to achieve a fixed accuracy at low cost.

Adaptive mesh embedding technique has mainly been used for inviscid flows [12-15]. We have applied it to viscous flows [4,5].

In the present work the fine grid points are organized in patches and the devised strategy provides for the possibility of having a coarse, a fine and a finer grid, having found that generating further levels violates the following golden rule: " the amount of computational work should be proportional to the amount of real physical changes in the computed solution " [16]. Grids belonging to different levels are kept independently in a tree-like structure, each one with its own solution vector. Grid communication is achieved via a complex data structure that is discussed later.

Embedding is performed on a cell by cell basis, i.e. cells are refined if and only if it is needed. Several criteria for mesh refinement may be devised based on: first (and/or second) derivatives of thermodynamic variables; truncation error estimates; adaptive dissipative fluxes, etc. The best choice is problem dependent. Our a posteriori experience is that use of first derivative of pressure leads to a satisfactory embedding for viscous transonic airfoil computations.

For computational efficiency, the turbulent viscosity on the embedded grids is computed by interpolating a turbulent viscosity evaluated on the lowest level grid. However the vorticity that enters in the BL formulas, that define such a viscosity, is computed using the vorticity of the highest level grid.

The computed solution is obtained in three phases.

Phase I

Let G_0 be the starting (base) computational grid, where 0 indicates the lowest level (level-0). In this phase the solution ${}_0W$ on G_0 is obtained via Eqn. (5).

Phase II

Eqn. (5) is solved until quasi convergence is reached. Then an adaptation criterion is checked and a higher level (level-1) of embedded grid is introduced as follows.

Let f, f^* and F be respectively the modulus of pressure gradient multiplied by a linear dimension of the cell, its average value over the entire domain, and the cumulative distribution function (*i.e. the fractional number of* points having a refinement parameter f/f^* greater than a threshold value T).

Once F is constructed, the mesh is adapted: all cells belonging to G_0 where the adaptation criterion is not satisfied are flagged, and four embedded fine cells are created for each flagged coarse cell. Then the fine cells are organized in grid patches and the level-1 grid (G_1) defined.

Initialization

The solution vector ${}_1W$ associated to G_1 is initialized by interpolation of the lower level solution ${}_0W$.

In the present work a high order interpolation polynomial belonging to the family of Legendre polynomials is used [8,16]. For example referring to Fig. 1, the value ${}_1W_a$ (a stands for cell index belonging to G_1) is initialized according to:

$$
\begin{aligned}
{}_0DWI &= \frac{\left({}_0W_{i+1,j} - {}_0W_{i-1,j}\right)}{2} \\
{}_0DWJ &= \frac{\left({}_0W_{i,j+1} - {}_0W_{i,j-1}\right)}{2} \\
{}_0D2WI &= {}_0W_{i+1,j} - 2\,{}_0W_{i,j} + {}_0W_{i-1,j} \\
{}_0D2WJ &= {}_0W_{i,j+1} - 2\,{}_0W_{i,j} + {}_0W_{i,j-1} \\
{}_0D2WIJ &= \frac{\left({}_0W_{i+1,j+1} - {}_0W_{i,j+1} - {}_0W_{i+1,j-1} + {}_0W_{i-1,j-1}\right)}{4} \\
{}_1W_a &= {}_0W_{i,j} + \frac{1}{4}\left(-{}_0DWI - {}_0DWJ\right) + \frac{1}{16}\left[{}_0D2WIJ - \frac{\left({}_0D2WI + {}_0D2WJ\right)}{6}\right]
\end{aligned}
\tag{7}
$$

Level-1 grid solution

Thereafter time integration is performed advancing first ${}_1W$ solution by solving an equation similar to Eqn. (5).

$$
\begin{aligned}
{}_1W^{(0)} &= {}_0W^n \\
{}_1W^{(k)} &= {}_1W^{(0)} + \alpha_k\left(\frac{{}_1\Delta t}{{}_1V}\right)\left[-\left({}_1F_E^{(k-1)} - {}_1F_V^{(0)} - {}_1F_{AD}^{(0)}\right)\cdot {}_1\left(\vec{n}\Delta S\right)\right]^{\wedge} \qquad k = 1,3 \\
{}_1W^{n+1} &= {}_1W^{(3)}
\end{aligned}
\tag{8}
$$

Injection

In the regions of adaptation the fine grid solution ${}_1W$ is injected onto the lower level grid. For example, referring to Fig. 1, for the cell (i,j) of G_0, volume weighted average yields:

$${}_0W_{i,j} = \frac{\left[{}_1(V\cdot W)_a + {}_1(V\cdot W)_b + {}_1(V\cdot W)_c + {}_1(V\cdot W)_d\right]}{{}_0V_{i,j}} \tag{9}$$

Level-0 grid solution

In this phase the solution on G_0 is advanced as in Phase I. However in the regions of adaptation, for all cells underlying level-1 cells, by exploiting multigrid strategy, the residuals collected from the embedded cells (belonging to the higher-level grid, G_1 in this case) are transferred onto G_0 via a forcing function that is added to Eqn. (5). For example for the cell (i,j) of Fig. 1, one has:

$$
\begin{aligned}
{}_0W^{(0)} &= {}_0W^n \\
{}_0W^{(k)} &= {}_0W^{(0)} + \alpha_k\left(\frac{{}_0\Delta t}{{}_0V}\right)\left[\left[-\left({}_0F_E^{(k-1)} - {}_0F_V^{(0)} - {}_0F_{AD}^{(0)}\right)\cdot {}_0\left(\vec{n}\Delta S\right)\right]^{\wedge}\right. \\
&\quad \left. + \sum_{a,b,c,d} {}_1R^{n+1} - {}_0R^{(0)}\right] \qquad k = 1,3 \\
{}_0W^{n+1} &= {}_0W^{(3)}
\end{aligned}
\tag{10}
$$

where R represents the residual of Eqn. (5)

Level-1 grid correction

Once ${}_0W^{n+1}$ is computed, on the G_1 patches overlaying G_0 the embedded grid solution ${}_1W$ is updated by distributing the lower-level grid residuals. For example at cell a of grid G_1 use of bilinear interpolation yields:

$$
\begin{aligned}
{}_1W_a = {}_1W_a &+ .5625\left({}_0W^{n+1}_{i,j} - {}_0W^{n}_{i,j}\right) \\
&+ .1875\left({}_0W^{n+1}_{i-1,j} - {}_0W^{n}_{i-1,j}\right) \\
&+ .1875\left({}_0W^{n+1}_{i,j-1} - {}_0W^{n}_{i,j-1}\right) \\
&+ .0625\left({}_0W^{n+1}_{i-1,j-1} - {}_0W^{n}_{i-1,j-1}\right)
\end{aligned} \tag{11}
$$

Interface treatment

Embedded grids introduce boundaries which are internal to the computational domain and which require a correct choice of boundary conditions to ensure conservation, accuracy and stability. Two approaches are generally implemented when a cell centered formulation is used.

Allmaras and Baron [15] concentrate on finding an accurate and stable definition of interface fluxes by interpolating coarse and fine grid fluxes, and they reach the conclusion that stability can be achieved at the expenses of accuracy. Berger [12] solves the problem by first defining fine grid boundary conditions by using bilinear interpolation, and then enforcing conservation by transfering the fine grid fluxes on the coarse cell.

In the present work an approach similar to that of Refs. [4,5,7] is employed. For computational efficiency fictitious embedded cells are generated along the boundary of the adaptation regions, i.e. in the proximity of the interfaces between grids of different levels. Correct coupling of grids at interfaces requires an accurate definition of these fictitious values. The same polynomial used for the embedded grid initialization is employed.

To retain accuracy and the shock capturing property of the scheme, conservation must be enforced at the interface between cells belonging to different levels. For example, referring to Fig. 2, at each stage we impose:

$$
{}_0F_{i+1/2} = \frac{1}{2}\left({}_1F_D + {}_1F_c\right) + \frac{1}{2}\left({}_1F_B + {}_1F_a\right) \tag{12}
$$

where F stands for any of the numerical fluxes of Eqn. (5). Eqn. (12) shows that the fictitious values (uppercase subscript refers to fictitious cells) affect directly conservation.

Phase III

In the presence of a finer level (level-2) of embedded grids, the solution proceeds in a manner similar to that described in Phase II.

At the end of Phase II the adaptation criterion is verified and grid patches of the G_2 family are constructed. The hierarchical ordering of the grids requires that the solution be computed moving from the highest level (level-2) down to the intermediate (level-1) and then to the lowest one (level-0). The computational strategy in this phase is as decribed previously.

Data Structure

As mentioned above the different grids (standard and embedded ones) are organized in a tree-like structure. Hence two matrices of pointers are needed to answer the existency question of each cell: who and where am I ?. Thus pointers are needed to establish relationships between each grid (belonging to a certain level), and the ones above and below it. However most of the information comes from the same level (evaluation of fluxes, variables, etc.).

To minimize the overhead every grid level is made out of stripes in logical space, as depicted in Fig. 3. Two pointers are associated to each cell giving its position as one sweeps in the i and/or j direction. To compute efficiently the viscous fluxes, two more pointers are needed that give the position of each vertex. Computation can so proceeds as on the lowest level grid using a series of fast unconditional do-loops. The total amount of storage requirement is only slightly increased since halfword integers are used for the matrices of pointers. The overhead that one must pay amounts to an increase of CPU time of about 15% when comparing the CPU time of the present approach and that of the multigrid solution on a domain containing N cells, where

$$
N = \sum_l N_l
$$

N_l being the number of cells of level l that do not contain cells of level $l+1$ type. Note that this is a rather small penalty in computational time; i.e. the algorithm of grid communication via pointers is very efficient. On the other hand there is a tremendous saving with respect to a multigrid solution on the highest level grid.

The implemented data structure achieves high performance on a scalar machine; moreover the pointers introduced for fast index addressing can easily exploit vectorization. However on a vector computer there may still be a penalty due to the large number of load/store operations needed.

Multigrid

In the present work the efficiency of the method is further increased by implementing on the lowest level grid a multigrid technique [2,3,9].

RESULTS

The objective of this work is to evaluate the robustness and reliabilty of the proposed grid embedding technique by applying it to compute viscous transonic flows around Rae2822 and Jones airfoils.

For all test cases a C-mesh is used, and the standard grid is obtained by solving the incompressible flow equations with an efficient multigrid solver [4]. All computations have been performed on rather coarse meshes with either one or two levels of embedding: the total number (N_c) of coarse cells is 5-10 times less than that used by other authors [1]. The minimum distance from the wall is a critical parameter for adequate treatment of leading and trailing edges, and for the shock/boundary layer interaction at the foot of the shock: oscillations leading to instabilities may arise if $Y^+ > 10$. In the computations the coarse grid has been generated by satisfying $Y^+ < 10$. Positioning the far field at a distance of approximately 10 chords has been found to yield lift coefficients independent of far field location. The threshold value of the adaptation criterion has been selected so as to get at most $N_c/4$ embedded cells. The interface flux treatment and high order interpolation for obtaining embedded grid boundary values have yielded results that do not depend on the topological properties of the embedded grids, and no oscillations have been observed in the proximity of fictitious cells boundaries.

A typical run takes approximately 3000 cycles for obtaining a nearly-converged solution on the coarse grid (70x28) and 1000 cycles with embedding; this amounts to 90 minutes of CPU time on a IBM 3090.

Note that for graphical representation the solution is always represented on the coarse grid, which causes solution discontinuities to look slightly spreaded.

Rae2822 airfoil

Computations on the Rae2822 airfoil have been carried out using a 70x28 coarse mesh to show that as long as the grid is sufficiently refined in the normal direction along the airfoil and wake, accurate results can be still obtained with adaptive mesh embedding. All the results are shown in Figs. 4. The results with one level of embedding show a substantial improvement over the coarse grid solution. A second level of embedding does show a more detailed flow structure. However lift and drag coefficients as well as separation do not change much. No separation is predicted on the coarse grid and the shock moves toward the trailing edge. Separation is predicted with one level of embedding at $x/c = .62$. Some discrepancies are noticeable in the position of the shock on the upper surface as the comparison of the computed and measured C_p indicate: this is mainly due to inadequacies of the turbulence model [1]. With two levels of embedding the main differences are on the more detailed resolution of the shock, as the Mach contours indicate.

Jones airfoil

To investigate the aerodynamic properties of the airfoil four different angles of attack have been selected (α = 0°, 2°, 4°, 6°) as proposed for the Viscous Transonic Airfoil Workshop. The computations have been performed on a 70x28 coarse grid. On account of the conclusions reached in the Rae2822 study, one level of grid embedding has been judged to be sufficient to obtain aerodynamic coefficients and flow features within engineering accuracy. All results are plotted in Figs. 5-9.

The computed values of C_L vs α and C_L vs C_D fall on the curves reported in Ref. [1]. The case $\alpha = 6°$ has not been plotted since the solution did not reach a steady state, most likely on account of the fact that the profile stalls around 6°, as also shown in Ref. [1], and that the shock position is not stable. However the coarseness of the 70x28 grid with one level of mesh embedding may be also responsible for enhancing the instability of the results.

CONCLUSIONS

An accurate efficient finite volume algorithm with adaptive grid embedding has been applied to solve transonic turbulent flows around airfoils. A local multigrid strategy is exploited for the treatment of embedded grids. The multigrid strategy in the regions of adaptation is used as a mean for enhancing the accuracy of the coarse grid solution. Furthermore a multigrid algorithm is implemented on the lowest level grid to increase the convergence rate. High order interpolation is needed to set boundary conditions at grid interfaces. The method is shown to be robust and reliable even in the presence of abrupt mesh refinement in regions of high gradients.

REFERENCES

[1] Holst, T.L., AIAA paper no. 87-1460, 1987.
[2] Grasso, F., Jameson, A., Martinelli, L., Vieweg Verlag, Lecture Notes on Numerical Fluid Mechanics, 18, 1986.
[3] Martinelli, L., Jameson, L., Grasso, F., AIAA paper no 86-0208, 1986.
[4] Bassi, F., Grasso, F., Savini, M., Springer Verlag, Lecture Notes in Physics, 264, 1986.
[5] Bassi, F., Grasso, F., Savini, M., Vieweg Verlag, Lecture Notes on Numerical Fluid Mechanics, 20, 1988.
[6] Baldwin, B., and Lomax, H., AIAA paper no. 78-257, 1978.
[7] Bassi, F., Grasso, F., Savini, M., IX AIDAA Congress, Palermo, Italy, October 1987.
[8] Visbal. M., and Knight, D.., AIAA J., 22, 7, 1984, pp 921-927.
[9] Jameson, A., Schimdt, W., Turkel, E., AIAA paper no. 81-1259, 1981.
[10] Dwyer, H.A., AIAA J., 22, 12, 1984, pp 1705-1712.
[11] Rai, M.M., AIAA paper no. 85-0488, 1985.
[12] Berger, M.J., Von Karman Institute, Lecture Series 1987-04, 1987.
[13] Berger, M.J., Jameson, A., AIAA J., 23, 4, 1985, pp 561-568.
[14] Dannenhoffer, J.F., Baron, J.R., AIAA paper no. 86-0495, 1986.
[15] Allmaras, S.R., Baron, J.R., AIAA paper no. 86-0509, 1986.
[16] Brandt, A., Von Karman Institute, Lecture Series 1984-04, 1984.
[17] van Leer, B., J. of Comp. Phys., 23, 1977, pp 276-299.

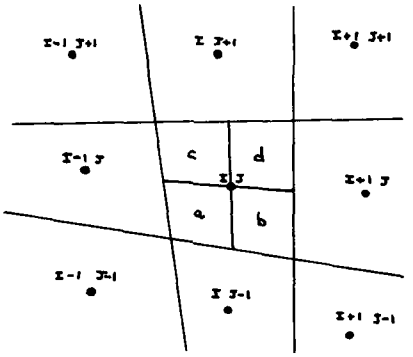


Fig.1 - Level-0 and level-1 grid arrangement

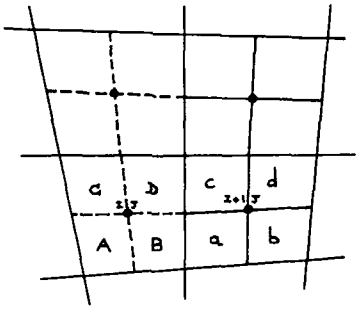
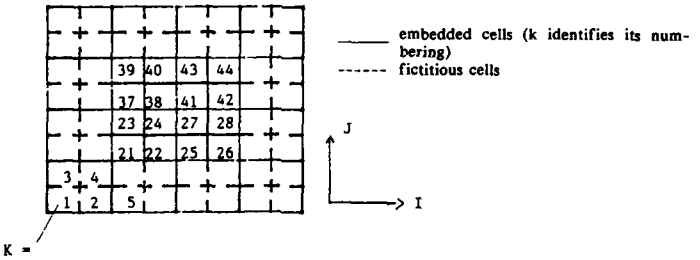
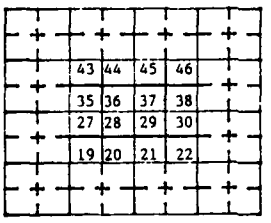


Fig.2 - Real and fictitious level-1 cells





Embedded cell addressing for the i-sweep

KI(19) = 21 it yields the K of the 19th embedded cell when sweeping in i

KOI(1) = 19 it yields the first index of the embedded cells marching from left to right

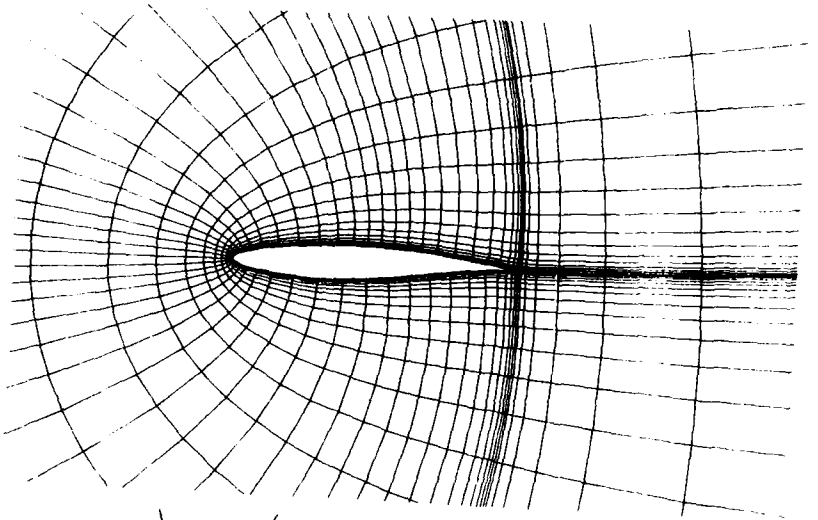
KII(1) = 22 it yields the last ...

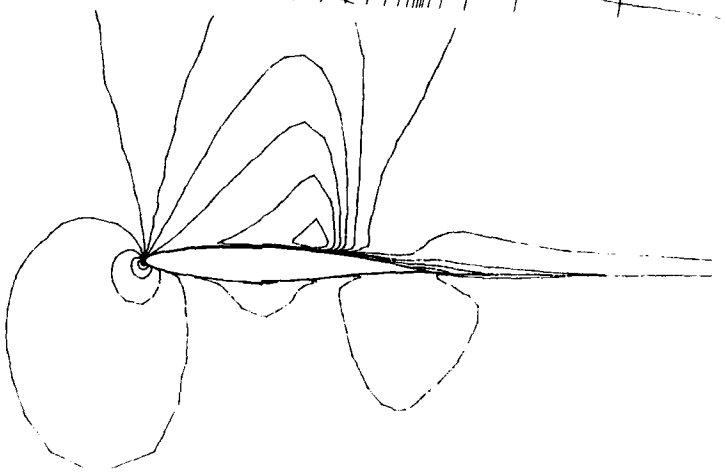
KOI(2) = 27

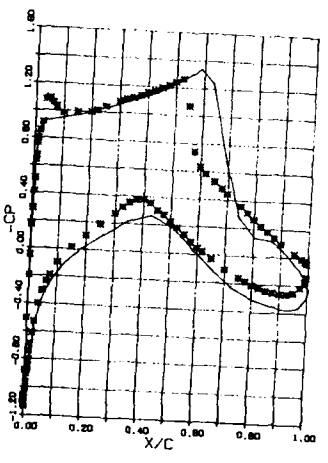
KII(2) = 30

Similarly for the j sweep

Fig.3 - Data structure







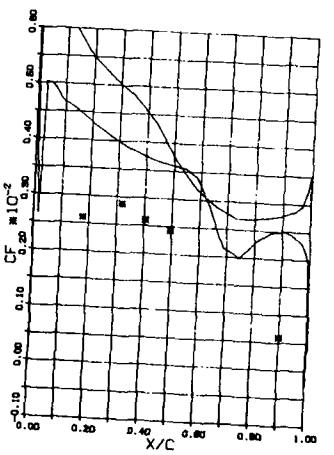
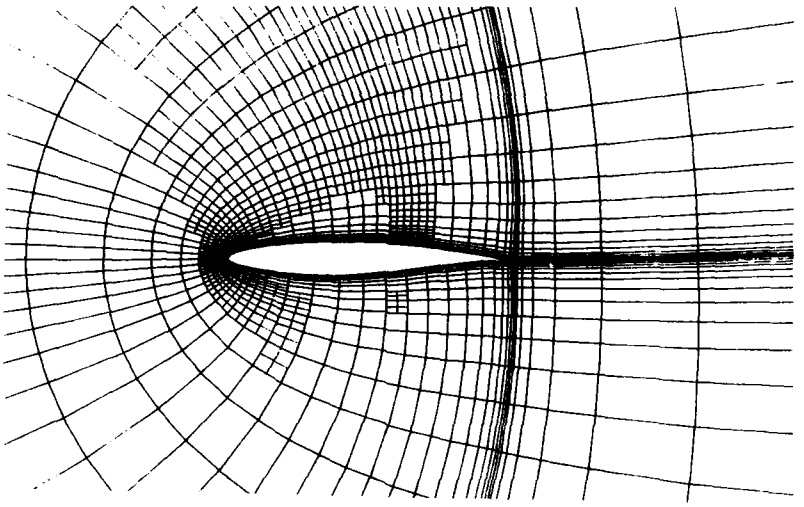
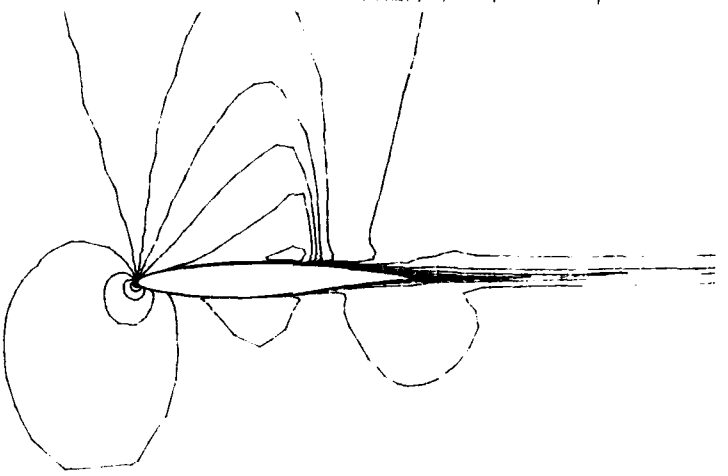
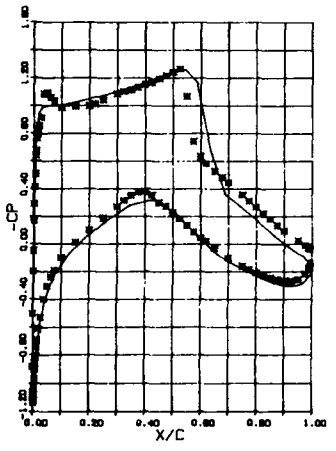


Fig.4.1 - Rae2822 (*l*-0): grid, iso-M, C_p, C_f







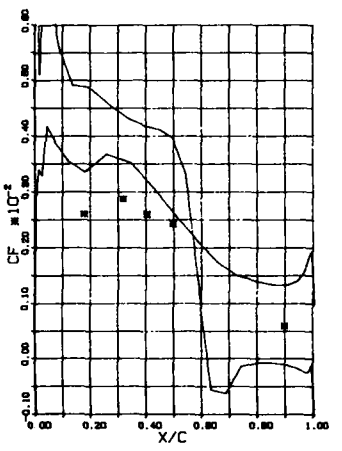


Fig.4.2 - Rae2822 (*l*-1): grid, iso-M, C_p, C_f

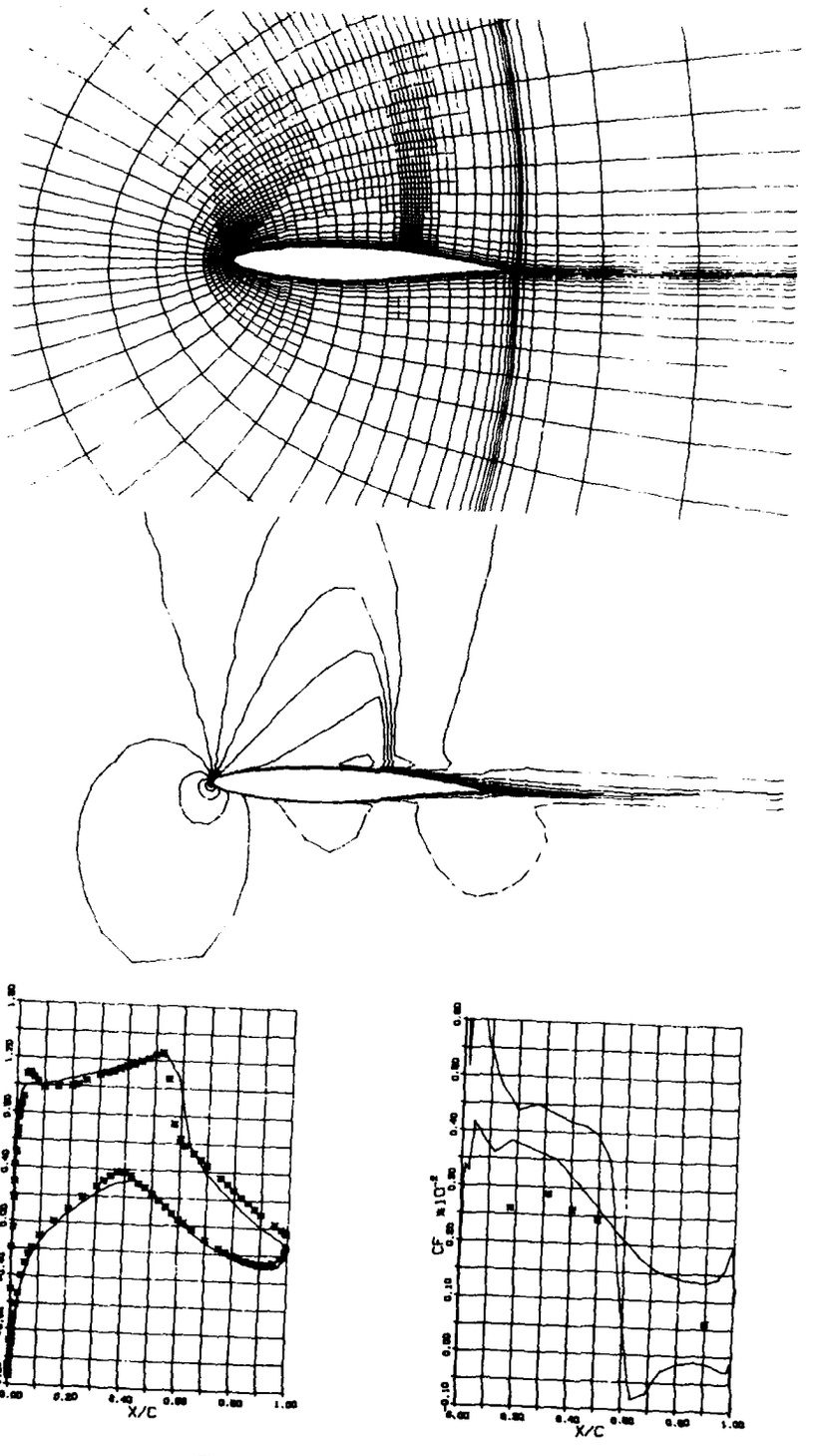
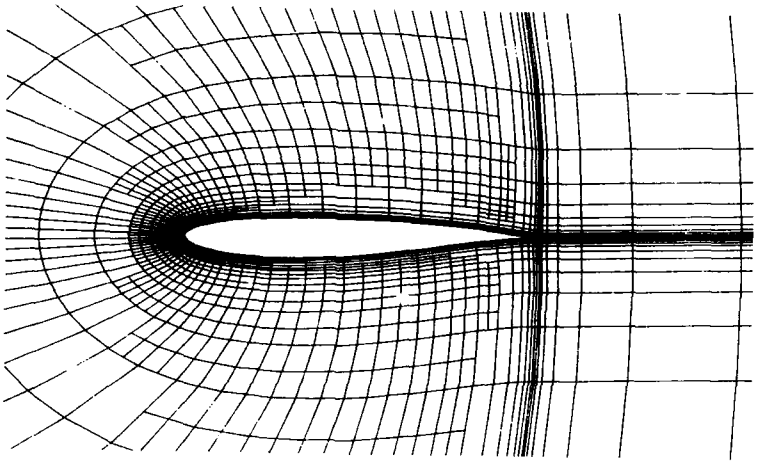
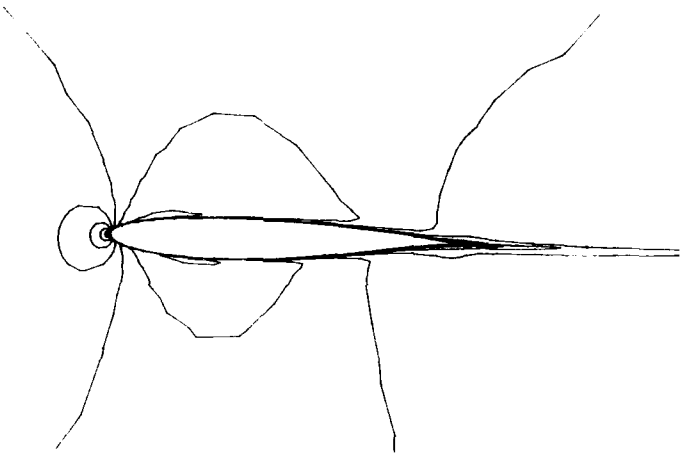
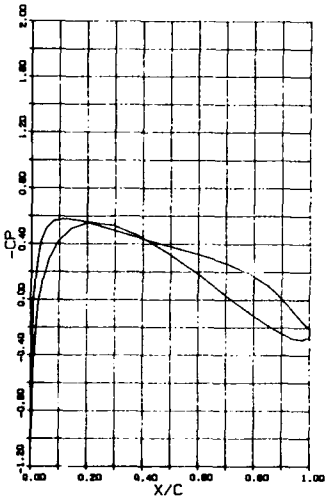


Fig.4.3 - Rae2822 (*l*-2): grid, iso-M, C_p, C_f







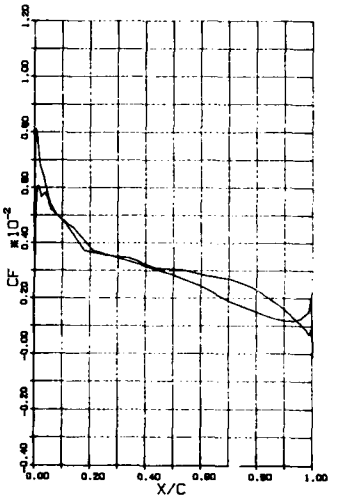


Fig.5 - Jones ($\alpha \approx 0°$): grid, iso-M, C_p, C_f

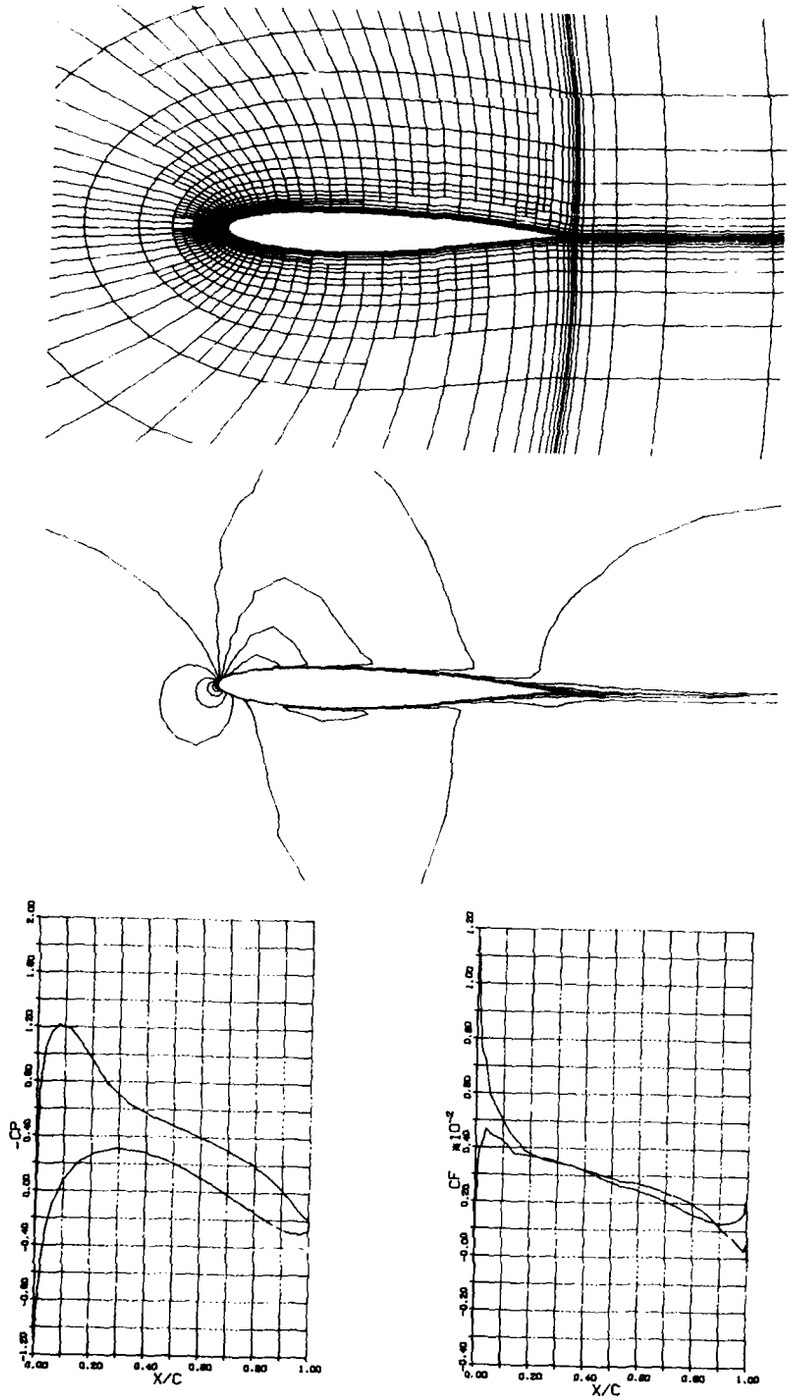
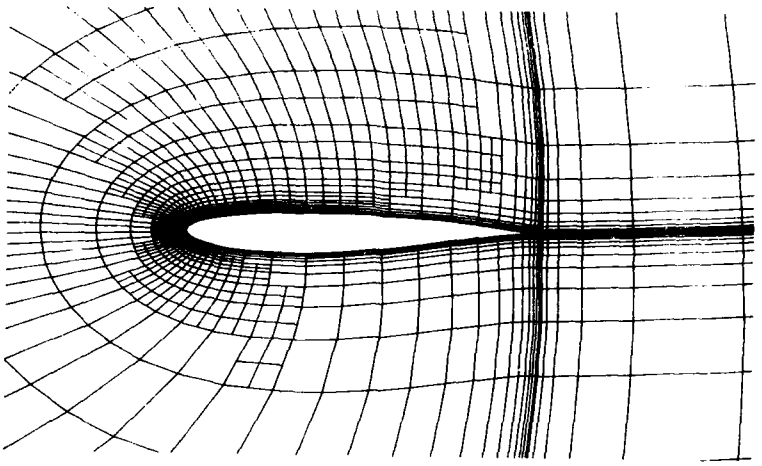
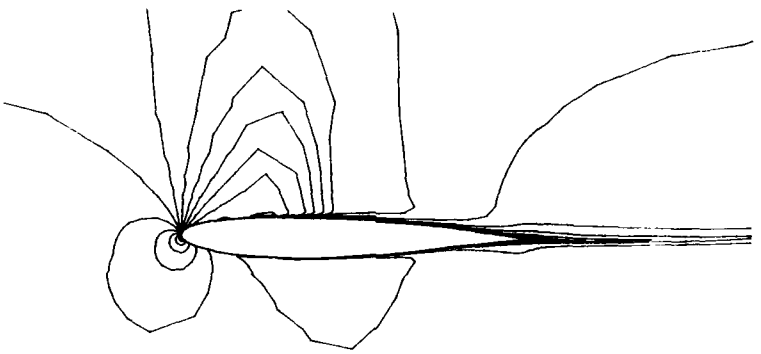
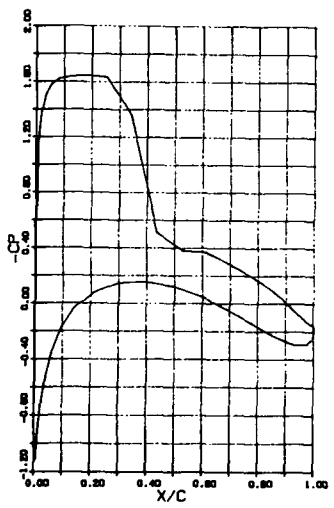


Fig.6 - Jones (α = 2°): grid, *iso*-M, C_p, C_f







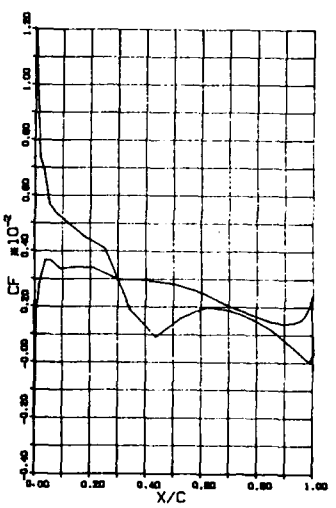


Fig.7 - Jones (α = 4°): grid, iso-M, C_p, C_f

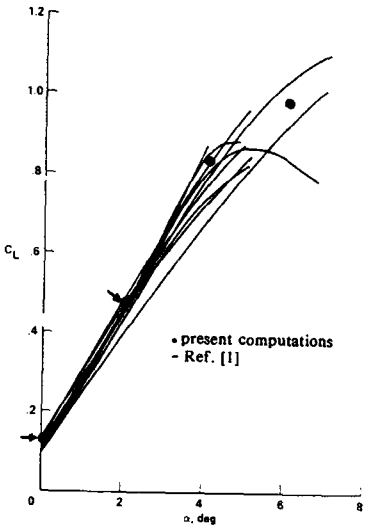


Fig.8 - Jones: C_L vs α

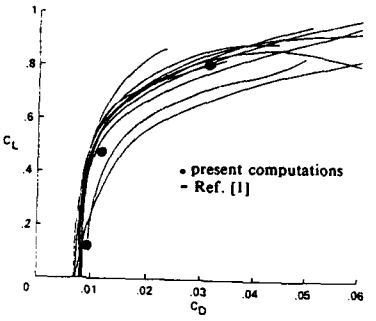


Fig.9 - Jones: C_L vs C_D

Table 1

Rae2822 airfoil: M = .75 Re = $6.2 \cdot 10^6$ α = 2.7°

Ref.	C_L	C_D*	Grid
exp. [1]	.743	242	
[5]	.762	247	100x28 *l*-1+
present	.875	417	70x28
"	.786	268	70x28 *l*-1+
"	.780	259	70x28 *l*-2+
Coackley	.859	298	240x60
King	.813	279	249x49
Haase	.793	281	298x70
Pulliam	.838	289	369x65

* in drag counts (1 count = .0001)
\+ levels of embedded grids

Table 2

Jones airfoil: M = .70 Re = $9 \cdot 10^6$

α	C_L	C_D*	Grid
0°	.131	98	70x28 *l*-1+
2°	.474	116	70x28 *l*-1+
4°	.801	313	70x28 *l*-1+
6°	.973**	700**	70x28 *l*-1+

* in drag counts (1 count = .0001)
** averaged values
\+ levels of embedded grids

THE INTERNATIONAL VORTEX FLOW EXPERIMENT

by
A. Elsenaar (NLR, Amsterdam, The Netherlands),
L. Hjelmberg (FFA, Bromma, Sweden),
K. Bütefisch (DFVLR, Göttingen, FRG) and
W.J. Bannink (Delft, University of Technology, The Netherlands)

SUMMARY

Experimental results of the "International Vortex Flow Experiment" are presented. In this joint program the vortex flow development on a 65 deg delta wing has been studied for Mach numbers between 0.4 and 4. The experimental results include pressure and force measurements, surface flow visualizations and flow field surveys. The influence of leading edge shape (sharp or rounded), a decrease in leading edge sweep (to 55 deg), the addition of a canard wing and yaw effects have been measured and analysed in some detail as far as vortex development, shock wave formation and vortex break-down are concerned. Particular attention has been given to experimental details that affect the comparison with theory. Some specific test cases for computer code validation are recommended.

1. INTRODUCTION

During the last decade the numerical solution of the Euler and Navier-Stokes equations has become within reach. A whole new class of flows with complicated flow structures can now, in principle, be simulated on a computer. The calculation of flows with embedded shocks and free vortices is a challenging perspective. The transonic flow over a delta wing represents an ideal test case: this flow is characterized by a leading edge vortex and by shock waves whereas viscous effects, that still require empirical modeling in the computations, are believed to be confined to small regions. Delta wings have been studied extensively for subsonic and supersonic flow conditions, but experimental results in the transonic flow regime are limited. To fill in this need, FFA, NLR, AFWAL, DFVLR, MBB, DORNIER and the Technical Universities of Delft (DUT) and Braunschweig started in 1983 a joint experimental and theoretical program known as "The International Vortex Flow Experiment on Euler Code Validation". This program rapidly picked up momentum. A delta wing configuration was defined at the end of 1983. First wind tunnel tests were made in November 1984 followed by more tests at NLR, DFVLR, FFA and DUT. A rather complete account of this joint program can be found in the proceedings of a Symposium held in Stockholm in October 1986 (ref.1). The present paper summarizes the scope of the experimental program. In the paper it will be attempted to highlight a number of physical aspects of the flow from an analysis of the experimental results. The analysis is neither complete nor conclusive. In fact we are just starting to understand some of the observed flow phenomena. In a separate paper by Wagner, Das and Sacher (ref.2) some results of calculations for this test case will be presented.

2. THE EXPERIMENTAL PROGRAM

2.1 Models and facilities

Quite early in this joint program, the participants agreed on a common model geometry. Based on this design four different wind tunnel models have been constructed and subsequently tested in five different wind tunnels (Table 1 and 2): a small pilot model made and tested at DUT, a much larger model made by AFWAL and tested at NLR in the transonic (HST) and supersonic (SST) wind tunnels and two models of intermediate size made by MBB and FFA respectively and both tested in the DFVLR (TWG) and FFA (S4) transonic wind tunnels. All models had a delta wing with 65 deg sweep except for the FFA model with a sweep angle of 55 deg (fig.1). The geometry of these models resulted from a compromise between different requirements from CFD and from industry and practical considerations as regards to windtunnel testing. A high sweep angle (65 deg or more) favours the formation of a strong leading-edge vortex but most contemporary fighter designs exhibit smaller sweep angles. For that reason two model configurations were selected with sweep angles of 55 and 65 deg respectively. The majority of the tests, however, was carried out on the 65 deg configuration. The wing had a simple geometry: the planform of a cropped delta wing (for finite thickness in the tip region), a constant airfoil section in streamwise direction for all wing stations (a modified NACA 64A005 profile), no twist or camber. Due to this choice the spanwise wing sections (fig.2) are not at all similar, yielding a far from conical geometry. The wing was mounted on a body that accommodated scanivalves for pressure measurements and/or a balance. The location of the wing on top of the fuselage allowed good accessibility for LDV flow field surveys over the wing upper surface. The body did not protrude upstream of the wing apex, but the nose could be extended to support a canard wing with 60 deg sweep at a fixed location in the plane of the main wing. For Euler code validation a sharp leading edge was foreseen originally with a shape defined by replacing the NACA profile contour between the nose and the 40% chord location with a bi-convex circular arc. FFA and the industry favoured a more realistic rounded leading edge with a leading edge radius of 0.7% of the local chord. Therefore it was decided to make the nose section of the wing exchangeable and to include a rounded and even a drooped leading edge shape in the plans. This turned out to be very fruitful because some of the effects of viscosity on vortex formation could so be illustrated. The three different leading edge shapes were only investigated on the AFWAL model (NLR measurements). The MBB and FFA models had a rounded leading edge. Pressures could be measured at three spanwise pressure rows at 30, 60 and 80% of the root chord, with additional streamwise sections on the smaller models. No pressures were measured on the canard wing. The DUT pilot model finally had the same basic planform (65 deg sweep) but a flat upper surface, a sharp leading edge and a different body shape. It was the first model to be manufactured, based on an early configuration design with a body protruding upstream of the wing apex.

2.2 Test programmes and experimental techniques

In the tables 3 to 5 a summary is presented of all wind tunnel tests. The force and pressure measurements (table 3) constitute a unique set of data for a wide range of test conditions from subsonic to supersonic speeds, with and without side slip and for various Reynolds numbers. The larger part of the data is related to the 65 deg rounded leading edge configuration. From thereon a systematic assessment can

be made of the effects of configuration changes due to:
- different leading edge shapes (sharp, rounded and drooped).
- a change in sweep angle to 55 deg.
- the addition of a canard wing.

Force and pressure data have been taken at small (1 degree) incidence increments. Surface flow visualizations (oil flow) have only been made for a limited range of test conditions (table 4). The most complete set of surface flow pictures is available from the tests made at DUT (65 deg sharp leading edge but slightly different model geometry) and at FFA (55 deg, rounded leading edge). At NLR and DFVLR visu test have only been made for flow conditions selected to illustrate a particular flow phenomenon in support of the interpretation of the pressure measurements. The laser sheet technique has been used by DFVLR to visualize the primary and secondary separations and subsequent vortex development for conditions with and without a canard at a Mach number of .85. An image processing system was used to enhance the contrast (fig.3). This technique provided information on the location of vortex cores and on vortex break down. Flowfield surveys, even more time consuming than oil flow visualizations, have been carried out for a Mach number of .85 (table 5). DUT employed a spherical 5-hole pressure probe (with a diameter of 1.5 mm) and FFA used a conical 7-hole probe (3.0 mm diameter). The flow field measurements at DFVLR were carried out with a three-component laser anemometer in a back scatter arrangement. The measuring volume was 0.1 mm in diameter and 0.5 mm long. Artificial seeding was used to obtain a data rate of 200 samples per second with an integration time of 10 seconds. For further details the reader is referred to ref. 3, 4, 5 and 30-38).

2.3 Experimental aspects affecting the comparison with theory

Boundary layer transition and Reynolds number.

In the comparison with theory, especially Euler codes, the importance of viscous effects has to be assessed. This can be accomplished experimentally by a variation of Reynolds number or by boundary layer manipulation (boundary layer tripping). A comparison of results obtained with the sharp and the rounded leading edge provides another indication on the role of viscosity in primary vortex formation as will be discussed in section 3.2. Viscous effects on primary separation will be less important for a sharp leading edge. For that reason this configuration is to be preferred for a comparison with results from Euler codes (see section 4). For a primary separation starting from a rounded leading edge, the state of the boundary layer (laminar or turbulent) and the Reynolds number can be important. The attachment line boundary layer at the wing leading edge and prior to vortex formation, was most likely turbulent due to leading edge contamination in the HST tests (see ref.6). This is less clear at the lowest Reynolds number of the TWG tests. Figure 4 and 5 illustrate how an increase in Reynolds number delays the formation of the primary vortex. As soon as the vortex is developped, the effect of Reynolds number appears to be small. The characteristics of the boundary layer are known to have a strong effect on secondary separation. Results of theoretical calculations (ref.6) for the 65 deg delta wing illustrate that the level and location of the vortex induced suction peak critically depends on the location of the secondary separation line. A turbulent boundary layer delays the secondary separation and therefore reduces its effect on the pressure distribution. In reference 6 it is made plausible that the boundary layer over the larger part of the wing surface is turbulent for a chord Reynolds number above 9 million. This was verified in the HST with an acenaphthene test. A comparison of overall forces and pressure distributions with and without a boundary layer trip did not show significant differences (ref.7). Furthermore the secondary separation line did not show the kinks that are often indicative of laminar-turbulent transition. For these reasons it was decided to do all tests with free transition. It is however possible that differences in pressure distribution between the TWG and HST results at high incidences (fig.10) are related to differences in viscous effects due to Reynolds number or the state of the boundary layer.

Resolution in the leading edge region.

The width of the pressure peak at the (rounded) leading edge prior to vortex formation scales with the local nose radius. Hence a decrease in the absolute width of the leading edge suction peak can be expected from apex to wing tip. Since the pressure holes are located at constant fractions of the local semi-span, the resolution in pressure distribution will not be constant along the leading edge. The lack in pressure resolution will be most pronounced near the wing tip (see fig.2). Therefore the experimental suction peak levels can be misleading. This is illustrated in figure 6: calculations for attached flow conditions (a panel method) show an increase in peak pressure from apex to wing tip whereas this trend is not observed in the measurements due to the lack of pressure resolution.

Body influence.

From a computational point of view it might be more convenient to calculate the isolated wing. In this respect it is important to have some indication of the influence of the body. Although the supporting body does not extend upstream of the wing apex, its size is such that the overall flow development might have been affected. To estimate this effect, a few panel method (ref.7) and Euler (ref.8) calculations have been made for conditions with attached flow. These calculations indicate that the effect is confined to a region upstream of the first pressure station (30% chord) for transonic and low supersonic flow (fig.7). At higher supersonic flow conditions the shape of the body determines the curvature of the bow shock near the model nose. This will certainly affect the flow near the apex (ref.7).

Wind tunnel wall and support interference.

For the HST tests the model size is such that wall interference effects can be neglected (blockage .4%, wing surface relative to test section area 5%). Since the pressures on the (slotted) upper and lower and (closed) side walls have also been measured, an indirect assessment of possible interference effects can be made by comparing the computed far field pressures with the measured pressures for identical free stream conditions (see fig.8 for a typical experimental result). Although the MBB and FFA models are slightly larger with respect to the respective test sections, the interference effects are believed to be still negligible. In the NLR tests the model was supported by a straight sting from the rear of the model, ensuring negligible sting interference effects. In the FFA tests an ordinary cranked model support sting was used. During the DFVLR tests a special bend sting was used with a variable position relative to the model (to locate the model in the center of the test section for the LDV measurements). It was verified that a change in sting position did not affect the results.

2.4 A limited comparison of different test results

Force and pressure measurements.

The force and pressure results of the DFVLR and NLR wind tunnel tests can be compared for the configuration with the rounded leading edge. Note that not only the tunnels are different but also the models are of different scale. Some typical results are presented in the figures 9, 10 and 11 taken from ref.9. The overall forces and moments show a good agreement (fig.9). Good agreement is also found in the pressure distributions at lower incidences (apart from an apparent Reynolds number effect; see fig.4 and 5) but at higher incidences differences can be observed over the outboard part of the wing (fig.10). This is to be explained partly from a better pressure resolution on the AFWAL model, but differences due to viscous effects will also be of importance. At a Mach number of 1.2 the agreement is again satisfactory (fig.11).

Flow field surveys.

A detailed comparison of the results of the flow field surveys is awaiting further analysis. A preliminary qualitative comparison is presented in figure 12 where vector plots of cross flow velocities are shown for the DFVLR LDV measurements and the FFA pressure probe surveys. The agreement is quite satisfactory apart from some discrepancies underneath the vortex.

3. CHARACTERISTICS OF THE FLOW FIELD

3.1 Shocks and primary vortex formation: a tentative classification

The flow on the upper surface of a delta wing can, depending on angle of attack (α_∞) and free-stream Mach number (Ma_∞), either be attached, separated or partly attached, partly separated. When separation occurs, the detaching free shear layer rolls up into a vortex. In downstream direction vorticity is continuously fed into the vortex core, which increases both in strength and in cross-sectional dimension. When the free-stream Mach number is sufficiently high, shocks will develop in the flow field. In some cases the shock itself might induce separation and the development of a vortex. The occurence of separation, shock waves and vortices can be used for the identification and classification of distinct types of flow as done originally by Stanbrook & Squire (ref.10). They drew attention to the analogy between the two-dimensional flow over an airfoil and the flow over a delta wing. The connecting parameters are a normal Mach number Ma_N and a normal angle of attack α_N defined by (Λ = leading edge sweep):

$$Ma_N = Ma_\infty . \cos\Lambda . \sqrt{1 + \sin^2\alpha_\infty \tan^2\Lambda}$$

$$\alpha_N = \tan^{-1}(\tan\alpha_\infty / \cos\Lambda)$$

A similar tentative classification for the present 65 deg delta wing the rounded leading edge is presented in figure 13. Since the flow is not conical, only the results for the wing station at 60% root chord have been used. The original Stanbrook & Squire boundary for a sharp leading edge has been indicated as a reference. This latter boundary separates the separated (low Ma_N) from attached (high Ma_N) flow conditions. The existence of attached flow at high Mach numbers is analogous to what can be found on two-dimensional airfoils around Mach=1 and beyond. Further extensions of the original classification have been made by Squire (ref.11), Szodruch & Peake (ref.12), Miller & Wood (ref.13) and Seshadri & Narayan (ref.14). Within the present test boundary, and as far as primary separation is concerned, four flow regimes can be distinguished for the rounded leading edge configuration. They are indicated schematically in figure 13. This figure has been deduced from an analysis of the pressure distributions at X/c_R=.6 in combination with the available surface flow visualizations. The separation boundaries are derived from a break in the C_p versus α development of the pressure hole nearest to the leading edge as indicated in figure 5. The interpretation is increasingly difficult at higher Mach numbers (because of sparse flow visualizations) and that part of the diagram is more uncertain. One should further realize that the flow is not conical in the neighbourhood of the separation boundaries as discussed before. Separation and subsequent vortex formation generally starts at the wing tip and moves with increasing incidence in the direction of the apex. The International Vortex Flow Experiment originated from an interest in transonic flow. Therefore, we will be concerned mainly with flow conditions to the left of the Stanbrook & Squire boundary. What is the physical mechanism that characterizes the boundaries between different flow regimes?

In an attempt to answer this question the two-dimensional analogy is taken as a starting point. The inviscid flow in the leading edge region of a swept wing can be derived from the flow over a two-dimensional airfoil with the so called "infinite swept wing approximation". It is assumed that the flow variation along the leading edge (from apex to tip) is small compared with the variation in a direction perpendicular to the leading edge. The flow velocity can then locally be obtained by adding to the two-dimensional velocity field (for a two-dimensional free stream Mach number $Ma_N = Ma_\infty . \cos\Lambda$) a constant velocity component in the direction along the leading edge ($U_\infty . \sin\Lambda$). This approximation is only valid for attached flow close to the leading edge. In figure 14a the experimental pressure distribution in spanwise direction for a subsonic flow condition (Ma_∞=0.4) is compared with the results of theoretical calculations: a three-dimensional subsonic panel method and a two-dimensional transonic flow method (the inviscid BGK method, transformed into a spanwise pressure distribution with the "infinite swept wing approximation" using the modified NACA profile section). Since the equivalent two-dimensional angle of attack is not known a priori (due to three-dimensional effects) the two-dimensional calculations have been made for a range of incidences. The good correspondence in pressure distribution between theory and experiment illustrates the applicability of the "infinite swept wing approximation". The agreement is obviously lost at 12° incidence when the experimental pressure distribution indicates the beginning of vortex formation. In this subsonic case the primary vortex formation is caused by boundary layer separation in the steep pressure gradient inboard of the suction peak.

The results of similar calculations for a transonic condition (Ma_∞=.85) are presented in figure 14b. The experimental pressure distributions for α_∞=2° and 4° agree reasonably well with the results of the transformed two-dimensional calculations. At α_∞=6° the experimental pressure distribution shows signs of vortex formation. The two-dimensional transonic flow calculations at higher incidences indicate the formation of a shock wave. The shock strength (defined by the local Mach number component perpendicular to the leading edge) is sufficient to cause shock induced boundary layer separation. Studies on shock wave

boundary layer interaction (ref. 15, 16) indicate that incipient separation occurs when the local shock Mach number is about 1.3. Similar results (not shown here) have been obtained for the other two pressure sections. Therefore, it is suggested that at a sufficiently high free stream Mach number, primary vortex formation is caused by shock induced boundary layer separation near the leading edge. It should be remarked here that the calculated shock wave is not apparent in the measured pressure distribution. This is partly due to the lack of pressure resolution in the leading edge region. It is also possible that the thickening of the boundary layer due to the shock wave boundary layer interaction masks a clear footprint of the shock or that a single shock disappears as soon as the flow has separated. The situation appears to be analogous to the flow development on two-dimensional airfoils near maximum lift where subsonic pressure gradient separation changes into shock induced separation when the free stream Mach number is sufficiently high (see ref.17).

The two-dimensional transonic calculations as presented in figure 14b indicate that the shock wave moves away from the leading edge at higher incidences. In the real viscous flow this shock wave movement is not realized because of shock induced separation. But at higher free stream Mach numbers a shock wave movement away from the leading edge is possible for shock Mach numbers lower than 1.3, although at lower incidences. This is illustrated in figure 15 where the calculated shock wave strength and position (relative to the local nose radius) is presented. These calculations have been made for the two-dimensional airfoil section (at Ma_N and α_N) whereas also the corresponding infinite swept wing conditions (Ma_∞ and α_∞) have been indicated. This figure helps to explain the rapid fall in the angle of attack for vortex formation with increasing Mach number up to a free stream Mach number of about 1.7 ($Ma_N \approx .7$) (fig.13). Beyond a free stream Mach number of 1.7 the shock wave can move inboard without causing shock induced separation.

The oil flow pictures support this view of the flow development with increasing Mach number. At Mach=.85 (fig.16) the separation is shock induced near the leading edge. At Mach=1.72 (fig.17) a very small region of attached flow is visible near the leading edge indicating a small supersonic plateau, followed by a shock strong enough to cause primary separation. This region has grown substantially at Mach=2.18 (Ma_N=.92; fig.18,23). In this analysis the "infinite swept wing approximation" has been used to establish the conditions for the formation of an extended supersonic plateau near the leading edge. When the shock has moved away from the leading edge the analogy is no longer applicable. For a two-dimensional airfoil the position of the shock follows from a match between the upstream (supersonic) and downstream (subsonic) conditions (ref.18). For the delta wing configuration the latter condition has to be replaced by the condition that follows from a flow direction imposed by the plane of symmetry of the wing.

At still higher Mach numbers, with a supersonic leading edge (Ma_N>1) the shock is also at a more inboard location. Only when this shock is sufficiently strong (at higher incidences) it will cause separation and primary vortex formation (fig.13 and 24).

This tentative analysis suggests a continuous change from subsonic to supersonic flow conditions where shocks and shock induced separations are of prime importance for the distinction between the various flow regimes. It should finally be remarked that some features of this flow development with increasing Mach number in the transonic regime have already been observed on the 65 deg delta wings investigated by Squire, Jones and Stanbrook in 1963 (ref.19).

3.2 The effect of leading edge shape

In the NLR tests the shape of the leading edge could be changed from sharp to rounded (in the latter case with or without additional droop). For some test conditions the pressure distributions are almost identical for the two leading edge shapes. For other conditions significant differences are present. This can be understood from the flow classification as discussed in the previous section. For the sharp leading edge the flow is separated along the entire leading edge at conditions to the left of the Stanbrook & Squire boundary (fig.13). For the rounded leading edge the flow can either be attached, partly attached/separated or fully separated depending on the leading edge geometry, Reynolds number, Mach number and incidence. Where the two regions of separated flow in the Ma_N-α_N plane overlap, the pressure distributions are almost identical (see e.g. fig.22): the leading edge can then be considered to be "aerodynamically sharp". Large differences can of course be observed when the flow is still attached with the rounded and separated with the sharp leading edge (fig.20). Figure 21 shows the intermediate case with part span leading edge separation and vortex formation: with the rounded leading edge the flow near the apex of the wing is still attached and the vortex is less developed and more outboard as compared with the sharp leading edge configuration. The strength and position of the vortex depends on the location of the primary separation position along the leading edge and is therefore influenced by the leading edge shape. This is somewhat analogous to the effect of Reynolds number on vortex formation as discussed before (section 2.3; fig.4 and 5) in the sense that in that case the separation position depends on the Reynolds number for a fixed geometry. Similar effects of the leading edge shape have been reported in ref.19 where the flow development on a 65 deg wing with a sharp and a rounded (.27% chord leading edge radius) leading edge has been analysed.

When the leading edge is supersonic (Ma_N>1), far to the right of the Stanbrook & Squire boundary, the pressure distributions are approximately determined by the local surface slope. Hence differences between the two leading edge configurations are primarily expected in the leading edge region as figure 24 indicates. The topology of the flow field for the two leading edge shapes, either with a shock or with shock induced separation is very similar in these cases.

At a lower free stream Mach number and near the Stanbrook & Squire boundary, a large difference in pressure distribution and flow topology can be observed in some cases like Mach=2.18 at α=8° as a typical example (see fig.23). With a rounded leading edge the flow is attached in the leading edge region, most likely followed by a shock further inboard that induces primary separation. With the sharp leading edge the large pressure gradient (or shock) in the nose region causes primary separation at the leading edge. The corresponding oil flow patterns are shown in the figures 18 and 19.

The drooped leading edge was only investigated for the Mach numbers .4 and .85. The results are very similar to those with the rounded leading edge. Only the incidence for which vortex formation occurs shifts to higher values.

3.3 Other shocks in the flow field

At transonic Mach numbers shocks near the wing leading edge play an important role in the process of primary vortex formation as discussed in section 3.1. Are there shocks at other locations in the flow

field at transonic free-stream conditions? Figure 25 shows the cross-flow velocities as measured in the TWG at DFVLR with LDV at a Mach number of .85 and an incidence of 20°. A supersonic pocket (in terms of the cross-flow velocity, the velocity component perpendicular to a conical ray) can be observed above the vortex. It has been suggested (see e.g. ref.20) that this supersonic region is terminated by a shock. However, the existence of such a supersonic pocket is a necessary, but not a sufficient condition for the formation of a shock wave. Shock waves can only occur when the Mach number component in a direction perpendicular to the isobar surface exceeds a value of 1 (ref.28). Since the isobar surfaces above the vortex are approximately aligned with the local flow direction, this situation is not likely to occur when the cross-flow velocities are barely supersonic. However, shocks at this location have been observed at much higher free stream Mach numbers (see e.g. ref.13).

At transonic conditions shock wave formation is more likely to occur underneath the vortex core (ref.21,22 and 23). The LDV measurements (fig.25) do not show sufficient detail in that region but there are arguments to support the view that such a shock exists. The isobar surfaces underneath the vortex core have to be perpendicular to the wing surface and the flow in that region will be approximately parallel to the wing surface. These conditions are favourable for the cross-flow Mach number component perpendicular to the local isobar to exceed a value of 1. Calculations by Houtman from DUT confirm this. Assuming conical flow and constant total pressure, the measured pressure distribution (i.e. the one shown in fig.26) can be integrated starting from the attachment line to find the cross-flow Mach number on the wing surface. The results of this calculation (fig.27) indicate supersonic cross flow beyond 11° incidence. A shock wave is then likely when the flow has to decelerate in outboard direction. This shock, if sufficiently strong, will cause shock induced boundary layer separation, followed by the formation of a secondary vortex as indicated in figure 26. In figure 28 the corresponding oil flow pattern is shown. It is of interest to note here that with the formation of shocks total pressure losses are introduced that might accumulate near the vortex core. For that reason it is likely that total pressure losses are no longer confined to small regions near the core (see e.g. Hall, ref.24) or near the rolled up shear layer, but that they can be more diffuse at transonic and supersonic conditions. The total pressure losses as measured by DUT (fig.29 from ref.3; note that these tests have been made for a sharp leading edge configuration) are significantly increased at a higher incidence. This is most likely due to the increased vortex strength since the cross flow shock is still relatively weak at this condition. But it is likely that shock induced total pressure losses will be more important at higher free stream Mach numbers. It is of interest to note here that numerical experiments with Euler and Navier-Stokes methods by Kandil et al (ref.29) show strikingly similar phenomena as discussed in this and the previous sections.

Another typical transonic flow phenomenon can be observed near the wing symmetry plane at higher incidences. Near the apex the flow is accelerated to supersonic speeds. Near the trailing edge the flow has to re-adjust itself to free-stream subsonic conditions. Isobars in the trailing edge region of the delta wing will be approximately parallel to the trailing edge and perpendicular to the plane of symmetry. Hence it is likely that the supersonic flow in the plane of symmetry will be decelerated through a shock wave. A shock wave was observed in the wind tunnel tests for sharp and rounded leading edges (see e.g. fig.30) and also measured by Bannink and Houtman with pressure probes (ref.3) in the plane of symmetry. In the LDV measurements of DFVLR (ref.5), presented in figure 31, such a shock can also be observed (note that in this figure the free-stream velocity has been subtracted to accentuate the change in flow direction). A similar shock was already observed in 1960 by *Elle* (ref.25). This shock is somewhat analogous to the shock that terminates the supersonic region on a two-dimensional airfoil and will therefore be named "terminating shock". A complete reconstruction of the three-dimensional flow field in this region has not been possible yet and there are some open questions. Why is this shock not visible in the surface oil flow pattern (fig.28)? What is the spatial extent of the shock and how is it connected with the supersonic regions and shocks above, below or even in the vortex? Hypotheses have been made (see ref.3 and 26) but the situation is far from understood at present.

The terminating shock might play an important role in combination with vortex break down. At subsonic speeds vortex break down and its upstream movement with increasing angle of attack, has a very gradual effect on the pressure distribution. It has been observed for a 65 deg uncropped flat delta wing with a sharp leading edge, that the break down point reaches the trailing edge at an incidence of about 20° (ref.27) almost independent of Reynolds number. In the present experiment direct measurements of vortex break down have not been made at Mach=.4. However, for the rounded leading edge wing, the suction peak underneath the vortex at the wing stations x/c_R=.6 and .8 reverses its trend with increasing incidence at 23°, indicating a possible effect of vortex break down. At Mach=.85 and at 21° incidence a very abrupt loss of lift is observed (see also fig. 36). At the same instant the terminating shock jumps discontinuously to a 30% root chord location (fig. 30). Also at Mach=.85 vortex break down has been observed with the laser sheet technique in the TWG. Figure 32, derived from these measurements, shows a sudden increase in vortex area around x/c_R=.4 and .7 for α=25° at the approximate shock locations (see fig.30). These results suggest a particular type of interaction between vortex break down and the transonic flow field when supersonic flow or shocks are present. This interesting phenomenon is dicussed in more detail by Bannink in Appendix A.

In summary a tentative view of the possible shock wave locations at transonic conditions as discussed before is presented in figure 33.

3.4 The effect of a change in leading edge sweep

The results of the tests made at FFA on the 55 deg delta wing (rounded leading edge) can be compared with those of the 65 deg wing to assess the effect of a decrease in leading edge sweep. Also extensive flow field surveys from FFA are available for both sweep angles at Mach=.85, α=10° (ref. 4, 38). Vector plots of the cross flow velocities at 80% root chord are presented in the figures 34 and 35. The position of the vortex relative to the wing is rather similar but the magnitude of the cross flow velocities near the vortex core is appreciable higher for the 65 deg wing. More information can be obtained from the pressure distributions and the integrated local lift coefficients at 30, 60 and 80% root chord. Such a comparison (fig.36) reveals rather significant differences. For the 65 deg wing the local lift values show a steady increase with incidence up to 21° where vortex break down causes an abrupt loss of lift at the most downstream stations. But for the 55 deg swept wing configuration the local lift values show a break at much lower incidences. An analysis of the pressure distributions makes it clear that the flow development in the latter case is much more complicated. A global view of some pertinent features of the flow over the two wings is presented in figure 37 in a x-α diagram. In this diagram the non-conical aspects of the flow are accentuated by presenting some typical boundaries as a function of incidence and its location along the model axis (percentage of root chord). These figures have been deduced by plotting

the local pressures as a function of incidence. Onset of leading edge separation is defined as the break in the c_p-α curve for the pressure hole closest to the leading edge (see e.g. fig.5). The vortex break down position follows from the local development of the pressure peak underneath the vortex. A comparison of the two figures shows that the onset of leading edge separation has shifted to lower values of incidence and developes more rapidly along the leading edge for the lowest sweep angle. This is the final outcome of different trends. A smaller sweep angle reduces the normal angle of attack α_N (delaying separation) but increases the normal Mach number Ma_N (hastening separation). Moreover, since both wings have the same streamwise basic airfoil shape, the airfoil sections in a direction normal to the leading edge will be effectively thinner for the 55 deg wing (this is even more pronounced for the spanwise sections; see fig.38). This will also favour early separation. For flat and sharp edged delta wings at subsonic speeds, vortex break down is strongly influenced by leading edge sweep (ref.27): a change in sweep angle from 65° to 55° halves the angle of attack for vortex break down. The pressure distributions suggest that vortex break down occurs at about 8°. Measurements of the total pressure losses by FFA (depicted in a rather crude way in figure 38) also indicate a much larger region of total pressure losses for the 55 deg wing and the downstream wing stations. The schlieren pictures (see ref.37) for this case show complicated shock wave patterns over the first 50% of the root chord. It might even be the case, although speculative at present, that a more classical "subsonic" vortex break down starts at low incidence (α=8°) followed by a "transonic" flow break down (causing abrupt shock wave movements) at higher incidences. Although much more analysis is required it is clear from the presented results that the flow over the 55 deg delta wing is far more complex than the flow over the 65 deg wing.

3.5 Canard effects

To conclude the discussion on the characteristics of the flow field some typical results of the effect of the canard will be presented. The figures 34 and 35 show the dominant effect of the canard vortex on the flow field above the wing at Mach=.85 and α=10° for the 55 and 65 deg wings. The effect of the canard however is not always favourable. For the 65 deg wing the canard reduces the local lift values (fig.39) up to 23° angle of attack. (Note that results for the sharp leading edge configuration have been presented; for this configuration vortex break down occurs at 23° incidence instead of 21° for the rounded leading edge; fig.36.) From thereon the effect is favourable for the downstream stations due to the suppression (?) of the abrupt vortex break down. For the 55 deg wing on the contrary, where vortex break down has occurred at much lower incidence, the canard effect is favourable over almost the entire incidence range (fig.40). An other illustration of the moderating effect of the canard is shown in figure 41 where some results of the side slip measurements are presented. The rolling moment of the 65 deg wing (sharp leading edge) shows discontinuities at Mach=.85 and higher incidences that are probably related to vortex break down effects on one of the wing halves. This effect is not present at a Mach number of .4. Also the addition of a canard wing suppresses the discontinuities at Mach=.85. These examples suggest that the canard wing has a moderating effect on the flow development. It "reorganizes" the flow field when the vortex has already broken down. But there appears to be little room for improvement if well organized flow is present as is the case for the 65 deg wing up to 20° incidence.

4. RECOMMENDED TEST CASES

The experimental results of the International Vortex Flow Experiment constitute a wealth of information for the validation of computational methods. The participants in this program selected four "recommended test cases" for the configuration with 65 deg sweep and a sharp leading edge:

case 1: Mach=0.4 , α = 15°
case 2: Mach= .85, α = 10°
case 3: Mach= .85, α = 20°
case 4: Mach=1.2 , α = 10°

These cases have been chosen primarily for comparison with Euler methods since viscous effects in the leading edge region (e.g. a Reynolds number dependence) are expected to be small. The secondary separation effects are likely to be small as well for the cases 1 and 2. Case 3 is especially interesting from the point of view of shock wave development: underneath the vortex and in the plane of symmetry near the trailing edge (see section 3.3). These test cases are well documented as far as the pressure distributions are concerned but flow field measurements and oil flow patterns are not available (see table 3, 4 and 5). Some indication of the flow field might be obtained from the tests made by DUT, though for a slightly different geometry (table 1).

The rounded leading edge configuration is of great interest for comparison with Navier Stokes methods. The 65 deg sweep configuration at 10° incidence is by far the best documented test case: numerous results are available from NLR, DFVLR and FFA tests, including detailed flow field surveys. This is a difficult test case, however, since the flow is still partly attached near the wing apex (see e.g. fig.16, 21 and 37), requiring detailed viscous modeling in the leading edge region (see the discussion in section 3.1). The pressure distribution for this case is markedly different from the results obtained with the sharp leading edge (see fig.21). Differences between the sharp and the rounded leading edge configurations are much smaller for the other 3 cases (case 1,3 and 4; see e.g. fig.22) as discussed in section 3.2.

Of course, many other test cases might have been selected and it is to be expected that the continuing experimental analysis and additional measurements will reveal other flow conditions with interesting features. Some suggestions are made here for further Euler and/or Navier Stokes calculations:

case 5: 65 deg sweep, rounded L.E., Mach=.85, α=25°, showing the effect of vortex break down with accompaning shock wave movement relative to case 3 (fig.30, 32, 36);
case 6: 55 deg sweep, rounded L.E., Mach=.85, α=10°, showing the effect of leading edge sweep; this case has a rather complicated flow field where vortex break down has already taken place (fig.35-38);
case 7: 65 deg, rounded L.E. with canard, M=.85, α=10° a relatively simple case to investigate the canard effect (fig.34);
case 8: 55 deg, rounded L.E., with canard, M=.85, α=10°, showing a very strong canard effect in a more complicated flow field (fig.35, 40);

case 9 and 10: 65 deg, rounded respectively sharp L.E., Mach=2.18, α=8°, showing the effect of leading edge shape for an almost supersonic leading edge (fig.18, 19, 23);
case 11:65 deg, rounded L.E., Mach=3.0, α=10°, showing an inboard shock with (most likely) primary vortex formation for a supersonic leading edge condition (fig.24).

The test reports with the available information can be obtained from the respective institutes upon request (ref.30-38).

ACKNOWLEDGEMENTS

This paper resulted from a very stimulating co-operation with colleagues from AFWAL, DFVLR, FFA, NLR, MBB-München, Dornier and the Technical Universities of Delft and Braunschweig. Many people contributed in this program and the authors would like to express their thankfulness in particular to Mr. Buter from AFWAL (for his contribution in model design and construction at the start of the program), Dr. Hartmann, Mr. Pszolla and Dr. Pallek of DFVLR (for additional analysis), Mr. Hoeijmakers and Boersen from NLR (for critically reading the manuscript) and last but not least Dr. Drougge for his devotion to this joint program.

LIST OF REFERENCES

1. A. Elsenaar, G. Eriksson — Proceedings of the Symposium on the "International Vortex Flow Experiment on Euler Code Validation"; Stockholm, October 1-3, 1986 (published by FFA).

2. B. Wagner, A. Das, P. Sacher — Status of CFD Validation on the Vortex Flow Experiment, AGARD Symposium on "Validation of Computational Fluid Dynamics", Lisbon, May 2-5, 1988.

3. E.M. Houtman, W.J. Bannink — Experimental Investigation of the Transonic Flow at the Leeward Side of a Delta Wing at High Incidence, Delft University of Technology, Faculty of Aerospace Engineering, Report LR-518 (1987).

4. L. Hjelmberg — Test on a 55° and 65° Delta Wing at FFA (in ref.1)

5. K.A. Bütefisch, D. Pallek, J. Reichmuth — Flow Field Study on a 65° Delta Wing (in ref.1).

6. A.C. de Bruin, H.W.M. Hoeijmakers — Computation of the Three-Dimensional Boundary Layer Transition and Separation on a 65 Deg Swept Delta Wing at 20 Deg Angle of Attack (in ref.1).

7. S.J. Boersen, A. Elsenaar — Tests on the AFWAL 65° Delta Wing at NLR: A Study of Vortex Flow Development between Mach=.4 and 4 (in ref.1).

8. T. Berglind, G. Drougge, P. Eliasson — The influence of the leading edge geometry on the wave drag for a 65° delta wing at low supersonic speed and small angles of attack, FFA Report 141, 1988.

9. K. Hartmann — Force and Pressure Measurements Including Surface Flow Visualizations on a Cropped Delta Wing (in ref.1).

10. A. Stanbrook, L.C. Squire — Possible Types of Flow at Swept Leading Edges, Aeronautical Quarterly, Vol 15, Part 1, p.72, 1964.

11. L.C. Squire — Leading-edge separations and cross-flow shocks on delta wings, AIAA Journal, Vol.23, No.3, March 1985.

12. J.G. Szodruch, D.J. Peake — Leeward Flow Over Delta Wings at Supersonic Speeds, NASA TM-1187 (1980).

13. D.S. Miller, R.M. Wood — Lee-side flow over delta wings at supersonic speeds, NASA TR 2430, June 1985.

14. S.N. Seshadri, K.Y. Narayan — Lee-Surface Flow Over Delta Wings at Supersonic Speeds, National Aeronautical Laboratory, Bangalore, TM AE 8610 (1986).

15. J. Delery, J.G. Marvin — Turbulent Shock Wave Boundary Layer Interaction, AGARDograph No.280 (1985).

16. X. Liu, L.C. Squire — An investigation of shock/boundary layer interactions on curved surfaces at transonic speeds, J. Fluid Mech., Vol 187, pp. 467-486 (1988).

17. L.R. Wootton — Effect of compressibility on maximum lift coefficient of aerofoils at subsonic airspeeds, Journal of the Royal Aeronautical Society, Vol.71 (1967).

18. C.S. Sinnott, J. Osborne — Review and extension of transonic aerofoil theory, ARC R&M 3156 (1961).

19. L.C. Squire, J.G. Jones, A. Stanbrook — An experimental investigation of the characteristics of some plane and cambered 65° delta wings at Mach-Numbers from 0.7 to 2.0, ARC R&M No.3305 (1963).

20. K.F. Schrader, G.A. Reynolds, C.J. Novak — Effects of Mach number and Reynolds Number on Leading-Edge Vortices at High Angle of Attack, AIAA paper 88-0122.

21. Y. Brocard, V. Schmitt — Interaction aerodynamique entre un canard proche et une aile en flèche en écoulement transsonique, ONERA TP 1980-34, 1980.

22. J.M. Muylaert — Vortex bursting on slender delta wings in transonic flow and its influence on missile aerodynamic characteristics, Jahrestagung DGLR, Aachen, 12-14 May 1981.

23. G. Vorropoulos, J.F. Wendt — Laser Velocimetry Study of Compressibility Effects on the Flow Field of a Delta Wing, AGARD CP 342, Paper 9, 1983.

24. M.G. Hall — A theory for the core of a leading edge vortex, Journal of Fluid Mech. 11 (1961).

25. B.J. Elle — On the Breakdown at High Incidence of the Leading Edge Vortices on Delta Wings, J Royal Aer. Soc. Vol.64 (1960).

26. E.P. Sutton — Some observations of the Flow over a Delta-Winged Model with 55-deg Leading-Edge Sweep, at Mach number between 0.4 and 1.8, R&M No. 3190 (1960).

27. W.H. Wentz, D.L. Kohlman — Vortex breakdown on slender sharp edged wings, Journal of Aircraft, Vol.8, No.3 (1971).

28. W.G. Bickley — Critical conditions for compressible flow, ARC R&M No.2330 (1950).

29. O.A. Kandil, A.H. Chuang, J.M. Shifflette — Finite Volume Euler and Navier-Stokes Solvers for Three-Dimensional and Conical Vortex Flows over Delta Wings, AIAA-87-0041 (1987).

30. R.H.C.M. Hirdes — US/European Vortex Flow Experiment; Test Report of Wind Tunnel Measurements on the 65° Wing in the NLR High Speed Wind Tunnel HST, NLR TR 85046 L, 1985.

31. S.J. Boersen — US/European Vortex Flow Experiment; Test Report of Wind Tunnel Measurements on a 65° Delta Wing in the NLR Supersonic Facility SST, NLR TR 86117 L.

32. K. Hartmann — US/European Transonic Vortex Flow Experiment - Plots of Force Measurements - Photos of Flow Visualizations -, DFVLR IB 222-85 A 36, August 1985.

33. K. Hartmann — US/European Transonic Vortex Flow Experiment - Data Lists of Force Measurements -, DFVLR IB 222-86 A03, February 1986.

34. K. Hartmann — US/European Transonic Vortex Flow Experiment. - Plots of Pressure Measurements -, DFVLR IB 222-86 A 23, June 1986.

35. K. Hartmann — US/European Transonic Vortex Flow Experiment. - Data Lists of Pressure Measurements -, DFVLR IB 222-86 A 26, June 1986.

36. K.A. Bütefisch, D. Pallek, K.-H. Sauerland — International Vortex Flow Experiment - Results of Three Component LDA Measurements on a 65° Delta Wing, DFVLR IB 222-87 A 34 (1987).

37. L. Hjelmberg — International Vortex Flow Experiment on Euler Code Validation. Force and pressure measurements on a 55° Delta Wing. (To be published in 1988 as a FFA TN with supplements).

38. L. Hjelmberg — International Vortex Flow Experiment on Euler Code Validation. Flow Field Measurements with 7-hole probes above a 55° and a 65° Delta Wing. (To be published in 1988 as a FFA TN with supplements).

TABLE 1
MODEL CHARACTERISTICS

MODEL	Λ_{LE} (°)	b (m)	C_{ROOT} (m)	CANARD MOUNTING POSSIBLE	REMARKS
AFWAL	65	.476	.600	YES	Combined Forces & Pressures (X/C_R=.3,.6,.8)
MBB	65	.333	.420	YES	Forces or Pressures (x/c_R=.3,.6,.8; $y/\frac{1}{2}b$=.55)
FFA	55	.410	.345	YES	Combined Forces & Pressures (x/c_R=.3,.6,.8; $y/\frac{1}{2}b$=.20,.50,.85)
DELFT	65	.095	.120	NO	Flat Upper Surface; Nose Protruding in Front of Apex; No Pressure Holes

TABLE 2
WIND TUNNEL CHARACTERISTICS

TUNNEL	TYPE	TEST SECTION DIMENSIONS (m^2)	MACH-RANGE	WALL CONFIGURATION
NLR-HST	CONT.	1.6 x 2	M<1.3	Slotted Upper & Lower Wall
NLR-SST	BLOW DOWN	1.2 x 1.2	1.3<M<4.0	Closed
DFVLR-TWG	CONT.	1 x 1	.4<M<2.2	Perforated*
FFA-S4	BLOW DOWN	.92 x .90	.5<M<1.2	Slotted Upper & Lower Wall
		.92 x 1.15	M=1.31/1.42/1.71/1.93	Closed
DUT-TST27	BLOW DOWN	.28 x .255	0.55<M<0.85	Closed

* At time of tests

TABLE 3
SUMMARY OF FORCE AND PRESSURE MEASUREMENTS

TEST BY	MODEL	TUNNEL	CONFIGURATION Λ 55°	Λ 65°	L.E. SHARP	L.E. ROUNDED	L.E. DROOPED	CANARD OFF	CANARD ON	TEST CONDITIONS MACH	α (°)	β (°)	Re x 10^{-6}	TYPE OF MEASUREMENTS
NLR	AFWAL	HST	-	X	X	X	X	-	X	.4	-1(1)25	0	9	F&P
"	"	"	-	X	X	-	-	X		"	10,16(2)24	-5(2½)5	"	"
DFVLR	MBB	TWG	-	X	-	X	-	X		.5	0(2)22	0	4.5	F&P
FFA	FFA	S4	X	-	-	X	-	X		"	-1(1)24	0	3.3	
NLR	AFWAL	HST	-	X	X	X	X	-			-1(1)25	0	9	F&P
DFVLR	MBB	TWG	-	X	-	X	-	X		.7	0(2)22	0	4.5	"
FFA	FFA	S4	X	-	-	X	-	X			-1(1)24	0	4.2	"
NLR	AFWAL	HST	-	X	X	X	X	-			-1(1)25	0	9	F&P
"	"	"	-	X	X	-	-	X			10,16(2)24	-5(2½)5	"	"
"	"	"	-	X	-	X	-	-			-1(1)25	0	13	F&P
DFVLR	MBB	TWG	-	X	-	X	-	X			0(2)22	0	4.5	"
"	"	"	-	X	-	X	-	-		.85	0(2)22	0	2.4	"
"	"	"	-	X	-	X	-	-			0(2)12	0	7	"
"	"	"	-	X	-	X	-	-			25	0	4.5	"
FFA	FFA	S4	X	-	-	X	-	X			1(1)24	0	4.6	F&P
"	"	"	X	-	-	X	-	X			12(2)18	-5(1)5	"	F&P
NLR	AFWAL	HST	-	X	X	X	X	-			-1(1)10	0	7	F&P
DFVLR	MBB	TWG	-	X	-	X	-	X		1.2	0(2)8+	0	4.5	F&P
FFA	FFA	S4	X	-	-	X	-	X			-1(1)12	0	5.1	F&P
NLR	AFWAL	SST	-	X	X	X	-	X		~1.3	0(~2)12	0	~15	F&P
"	"	"	-	X	X	X	-	X		~1.7	0(~2)14	0	~15	"
"	"	"	-	X	X	X	-	X		~2.2	0(~2)10	0	~18	"
"	"	"	-	X	X	X	-	X		~3.0	0(~2)10	0	~28	"
"	"	"	-	X	X	X	-	X		~3.9	0(~2)6	0	~42	"

\+ plus some extra conditions

TABLE 4
SUMMARY OF VISUALIZATIONS

TEST BY	MODEL	TUNNEL	CONFIGURATION Λ 55°	65°	L.E. SHARP	ROUNDED	DROOPED	CANARD OFF	ON	TEST CONDITIONS MACH	α (°)	β (°)	Re x 10^{-6}	TYPE OF MEASUREMENTS
FFA	FFA	S4	X	-	-	X	-	X	X	.5	0(5)25+	0	3.3	Oil Flow & Schlieren
DELFT	DELFT	TST-27	-	X	FLAT			X	-	.55	5(5)20	0	1.5-3.6	Oil Flow & Schlieren
FFA	FFA	S4	X	-	-	X	-	X	X	.7	0(5)25+	0	4.2	Oil Flow & Schlieren
DELFT	DELFT	TST-27	-	X	FLAT			X	-	.7	5(5)20	0	1.8-4.2	Oil Flow & Schlieren
NLR	AFWAL	HST	-	X	-	X	-	X	-		5,10,20	0	9	Oil Flow
"	"	"	-	X	-	X	-	X	-		10,20	0	9	Acenaphtene
"	"	"	-	X	-	X	-	X	-		10(5)25	0	9	Schlieren
DFVLR	MBB	TWG	-	X	-	X	-	X	-		25	0	4.5	Oil Flow
"	"	"	-	X	-	X	-	-	X	.85	15,20,25	0	4.5	Oil Flow
"	"	"	-	X	-	X	-	X	-		20,25	0	4.5	Laser Sheet
"	"	"	-	X	-	X	-	-	X		10,15,20	0	4.5	Laser Sheet
FFA	FFA	S4	X	-	-	X	-	X	X		0(5)25+	0	4.6	Oil Flow & Schlieren
DELFT	DELFT	TST-27	-	X	FLAT			X	-		5(5)20+	0	2.0-4.7	Oil Flow & Schlieren
FFA	FFA	S4	X	-	-	X	-	X	X	1.2	0(5)15+	0	5.1	Oil Flow & Schlieren
NLR	AFWAL	HST	-	X	-	X	-	X	-	1.32	10	0	15.2	Oil Flow & Schlieren
			-	X	-	X	-	X	-	1.72	4,7.9	0	15.2	" "
			-	X	X	X	-	X	-	2.18	8	0	18.7	" "

TABLE 5
SUMMARY OF FIELD MEASUREMENTS

TEST BY	MODEL	TUNNEL	CONFIGURATION Λ 55°	65°	L.E. SHARP	ROUNDED	DROOPED	CANARD OFF	ON	TEST CONDITIONS MACH	α (°)	β (°)	Re x 10^{-6}	TYPE OF MEASUREMENTS/ STATIONS(x/c)
DFVLR	MBB	TWG	-	X	-	X	-	X	-		10	0	4.5	LDA(.6/.8)
											20	0		" (.6/.8/SP)
											25	0		" (.8)
FFA	FFA	S4	X	-	-	X	-	X	X	.85	10	0	4.6	PP(.3/.6/.8/.95)+
"	MBB	S4	-	X	-	X	-	X	X		10	0	5.6	PP(.3/.6/.8/.95)+
DELFT	DELFT	TST-27	-	X	FLAT			X	-		10,20	0	"	PP(.3/.6/1.0/SP)

NOTE LDA = Laser Doppler Anemometry
PP = Pressure Probe
SP = Plane of Symmetry
+ = Plus some extra conditions

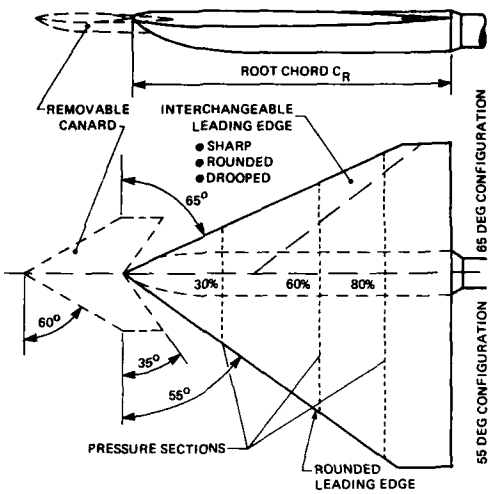


Fig. 1 Geometry of 55 and 65 deg wings

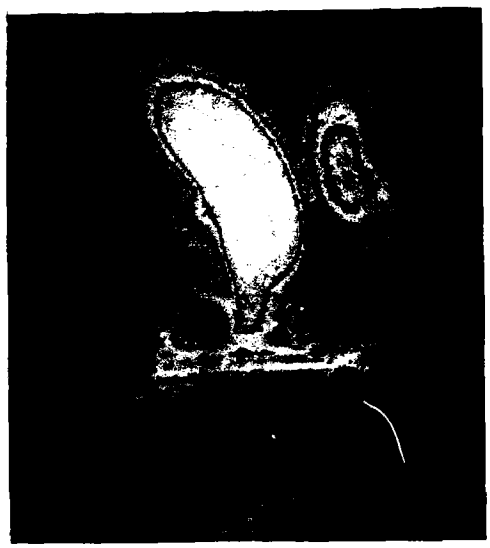


Fig. 3 Example of laser sheet technique (65 deg wing, DFVLR measurements)

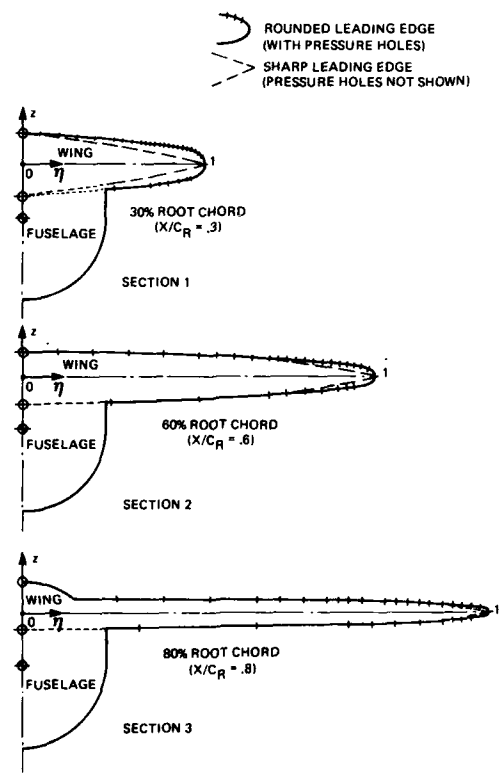


Fig. 2 Spanwise pressure sections (65 deg wing)

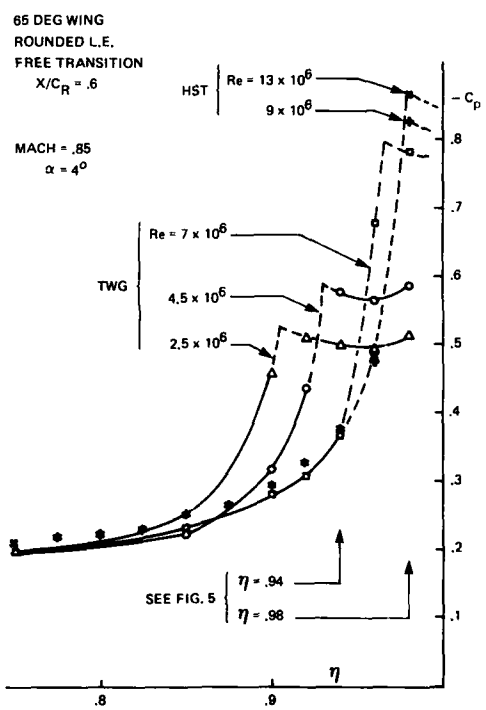


Fig. 4 Influence of Reynolds number on pressure distribution near vortex formation (tentative)

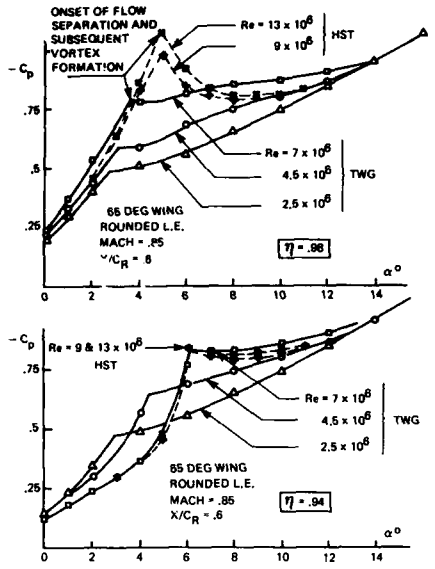


Fig. 5 Influence of Reynolds number on vortex formation (tentative)

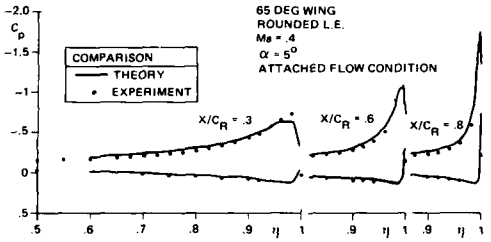


Fig. 6 Illustration of lack of experimental pressure resolution in leading edge region

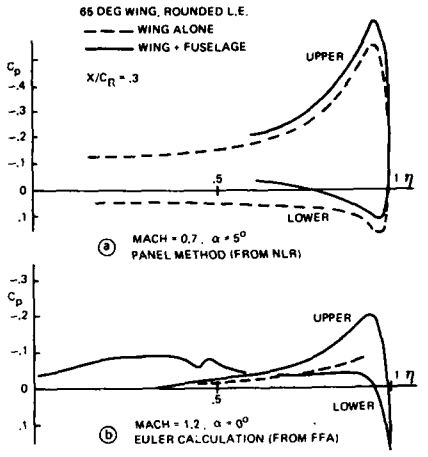


Fig. 7 Calculated body influence on first pressure station (attached flow)

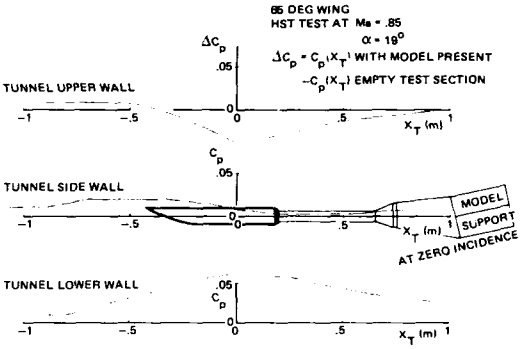


Fig. 8 Wall pressure distributions (NLR tests)

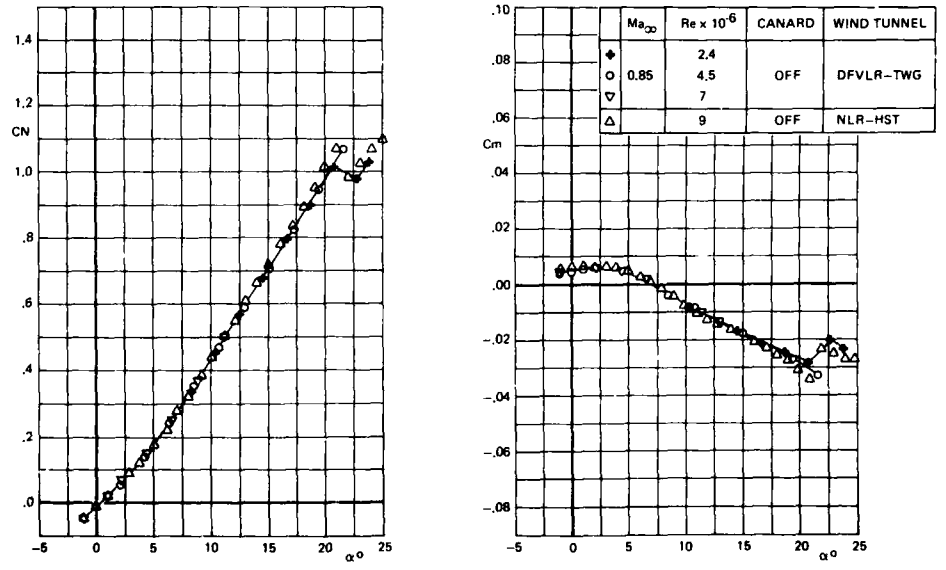


Fig. 9 Comparison of NLR (HST) and DFVLR (TWG) balance measurements (65 deg wing; rounded L.E.)

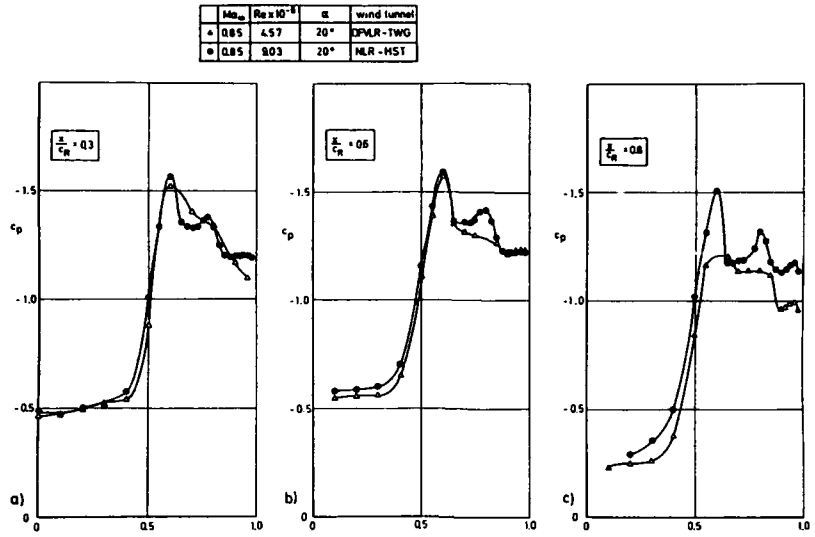


Fig. 10 Comparison of upper surface pressure distributions from NLR (HST) and DFVLR (TWG) tests (rounded leading edge; 65 deg wing)

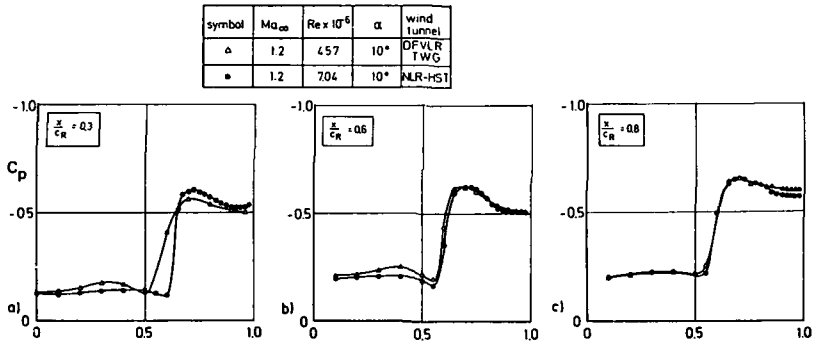


Fig. 11 Comparison of upper surface pressure distributions from NLR (HST) and DFVLR (TWG) tests (rounded leading edge; 65 deg wing)

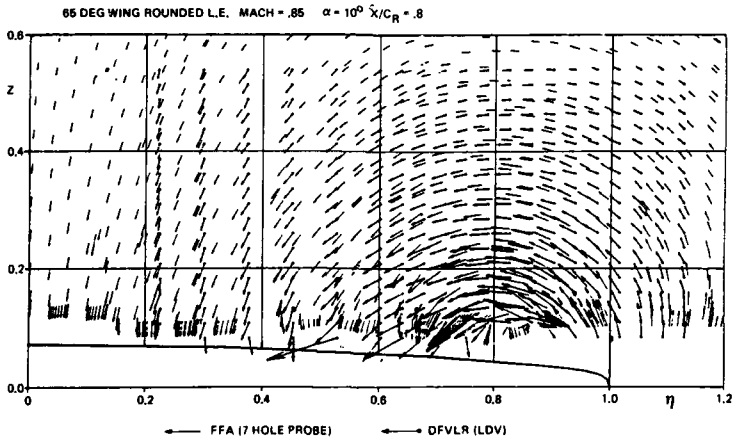


Fig. 12 Comparison of FFA (7-hole probe) and DFVLR (LDV) flow field measurements - cross flow velocities at $X/C_R = .8$

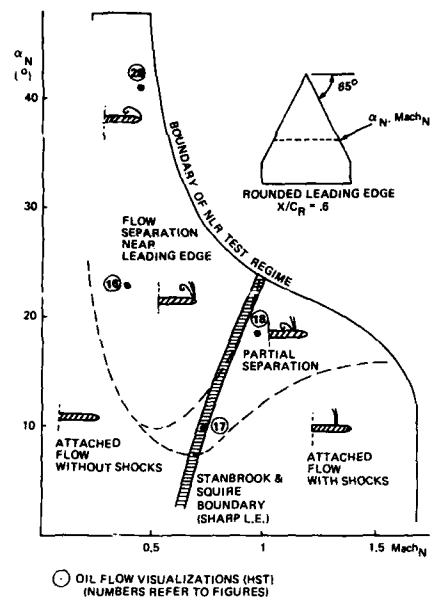


Fig. 13 Tentative flow classification (65 deg delta wing, rounded L.E., X/C_R=.6)

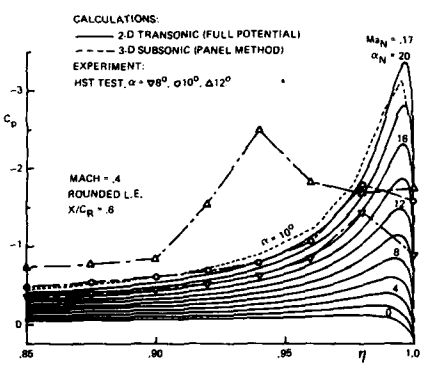


Fig. 14a Two-dimensional analogy in leading edge region; subsonic condition

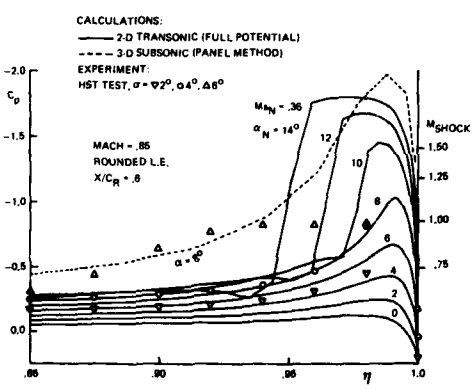


Fig. 14b Two-dimensional analogy in leading edge region; transonic condition illustrating shock wave formation

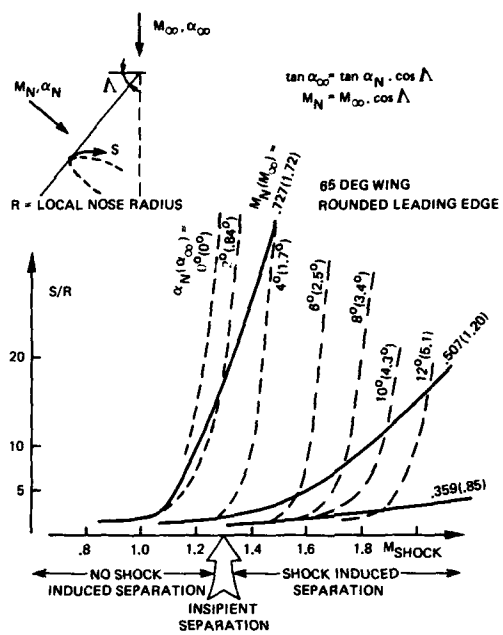
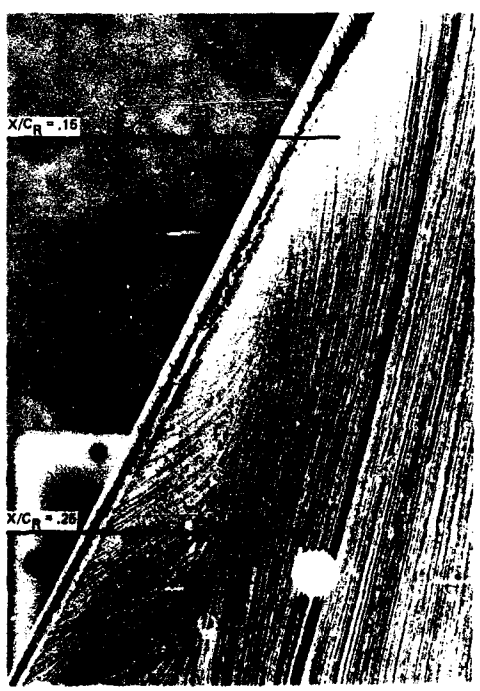
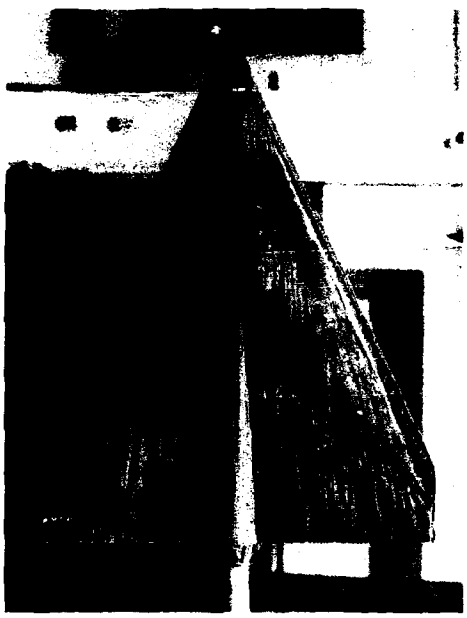


Fig. 15 Calculated shock wave movement as a function of shock wave strength (using infinite swept wing approximation in combination with 2-D inviscid full potential method)



65 DEG WING, ROUNDED L.E., M_∞ = .85, α = 10°

Fig. 16 Oil flow visualization (NLR tests) Detail of vortex formation



65 DEG WING, ROUNDED L.E., Ma = 1.72, $\alpha = 4^{o}$

Fig. 17 Oil flow visualization (NLR tests)
Attached flow and shock induced primary vortex formation close to leading edge



65 DEG WING, ROUNDED L.E., Ma = 2.18, $\alpha = 8^{o}$

Fig. 18 Oil flow visualization (NLR tests)
Flow attached at leading edge and shock induced vortex formation further inboard



65 DEG WING, SHARP L.E., Ma = 2.18, $\alpha = 8^{o}$

Fig. 19 Oil flow visualization (NLR tests)
Flow separated at sharp leading edge

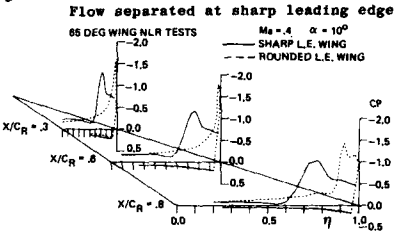


Fig. 20 Effect of leading edge shape on pressure distribution (subsonic condition)

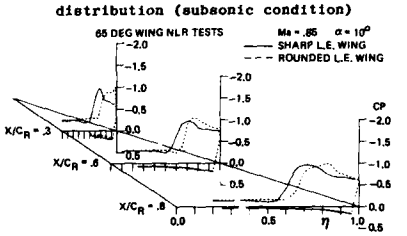


Fig. 21 Effect of leading edge shape on pressure distribution (transonic condition, moderate incidence)

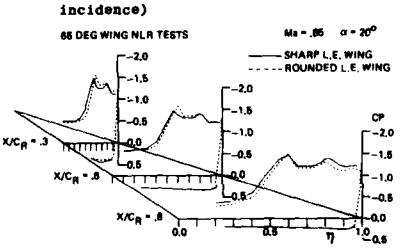


Fig. 22 Effect of leading edge shape on pressure distribution (transonic condition, high incidence)

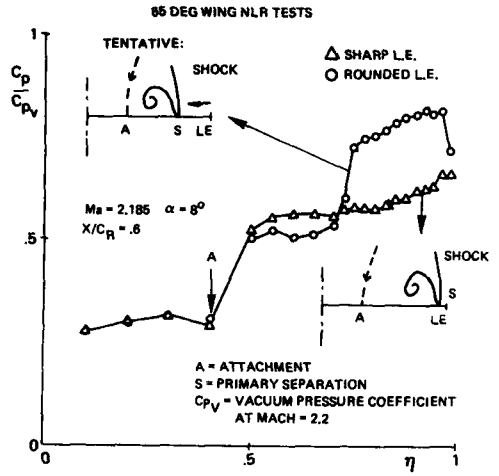


Fig. 23 Effect of leading edge shape on pressure distribution (supersonic condition, subsonic leading edge)

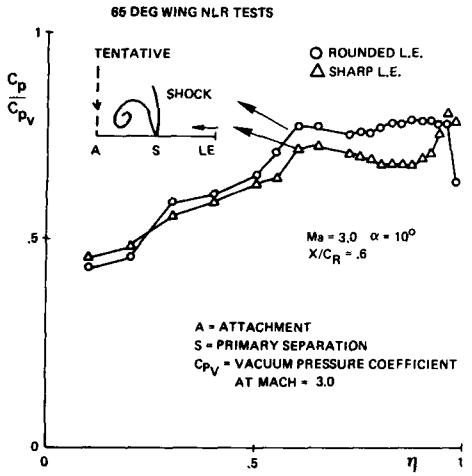
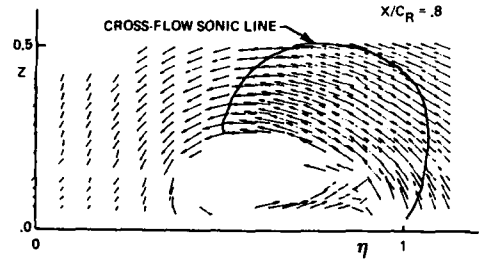


Fig. 24 Effect of leading edge shape on pressure distribution (supersonic condition, supersonic leading edge)



65 DEG WING, ROUNDED L.E., MACH = .85 α = 20°

Fig. 25 Cross flow velocity vectors (LDV measurements, DFVLR)

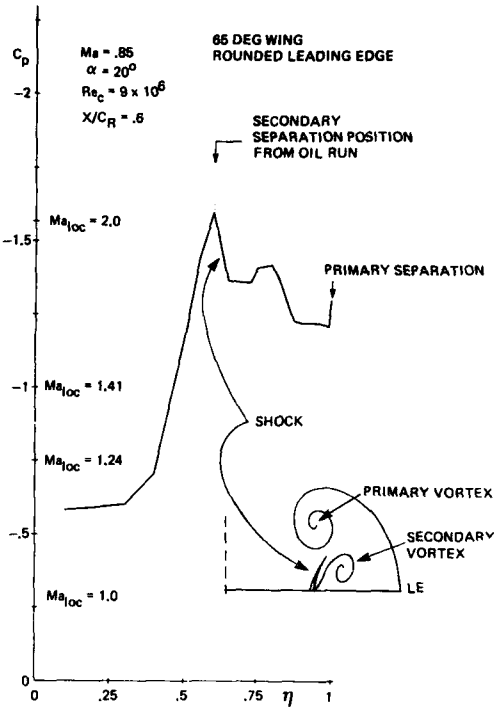


Fig. 26 Pressure distribution with secondary shock induced separation (tentative, NLR tests)

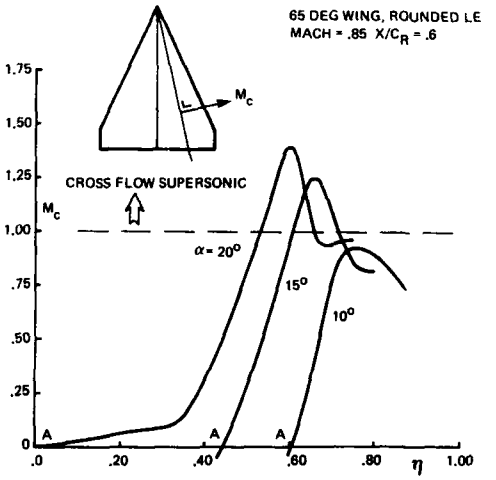


Fig. 27 Calculated surface cross flow Mach numbers from measured pressure distributions (according to Houtman)



65 DEG WING, ROUNDED L.E., MACH = .85, $\alpha = 20^{o}$

Fig. 28 Oil flow visualization (NLR tests, taken during run)

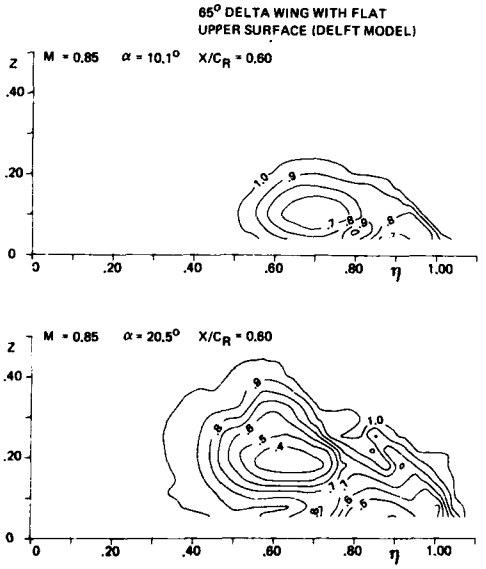
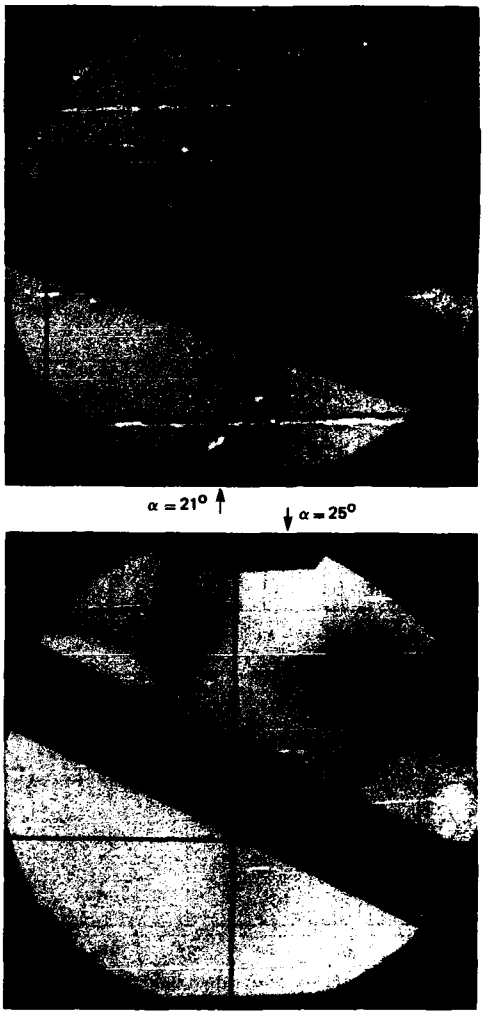
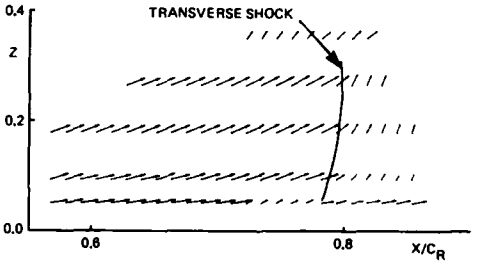


Fig. 29 Total pressure losses measured with 5-hole probe (DUT tests)



65 DEG WING, ROUNDED L.E., MACH = .85

Fig. 30 Schlieren view showing shock wave movement related to vortex break down (NLR tests)



65 DEG WING ROUNDED L.E., MACH = .85, $\alpha = 20^{o}$
NOTE: MEAN FLOW COMPONENT SUBSTRACTED

Fig. 31 Velocity vectors in plane of symmetry indicating terminating shock (LDV measurements, DFVLR)

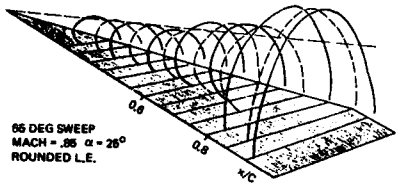


Fig. 32 Cross-sectional area of the vortex at Mach=.85, α=25° indicating vortex break down (laser sheet measurements in TWG)

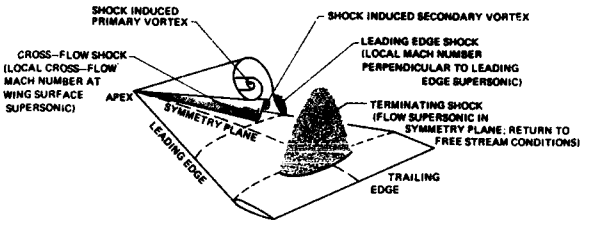


Fig. 33 Shock wave formation on a delta wing at transonic conditions (tentative)

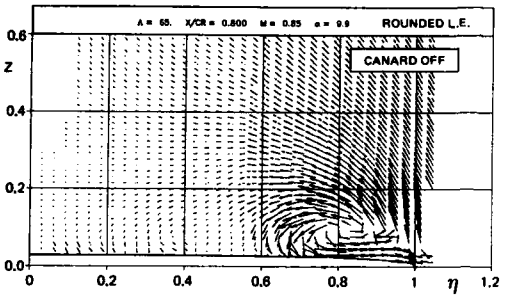


Fig. 34 Cross flow velocities from 7-hole probe measurements (65 deg wing, FFA tests)

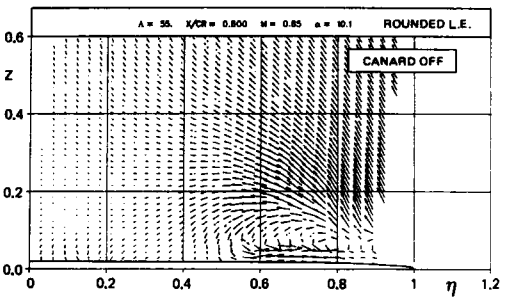


Fig. 35 Cross-flow velocities from 7-hole probe measurements (55 deg wing, FFA tests)

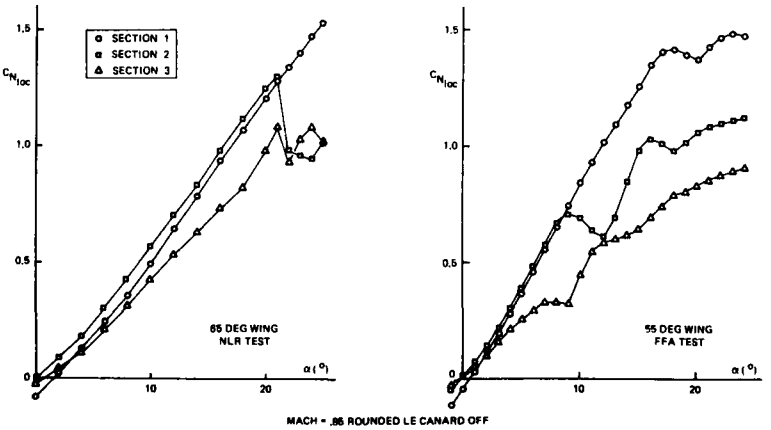


Fig. 36 Sectional normal force development illustrating effect of wing sweep

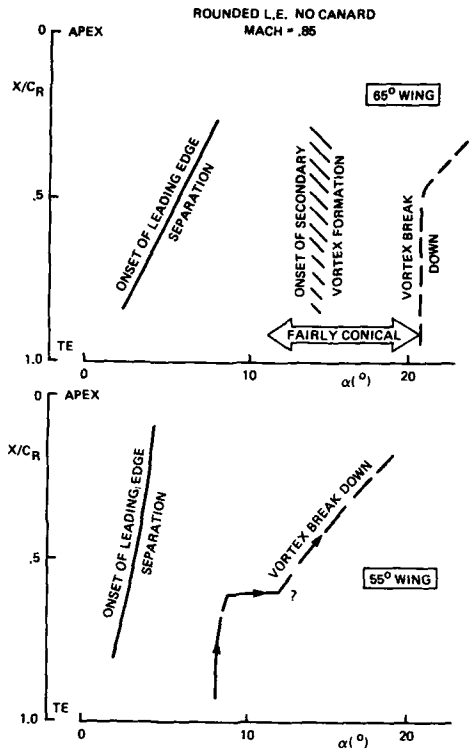


Fig. 37 Tentative flow development deduced from pressure distributions

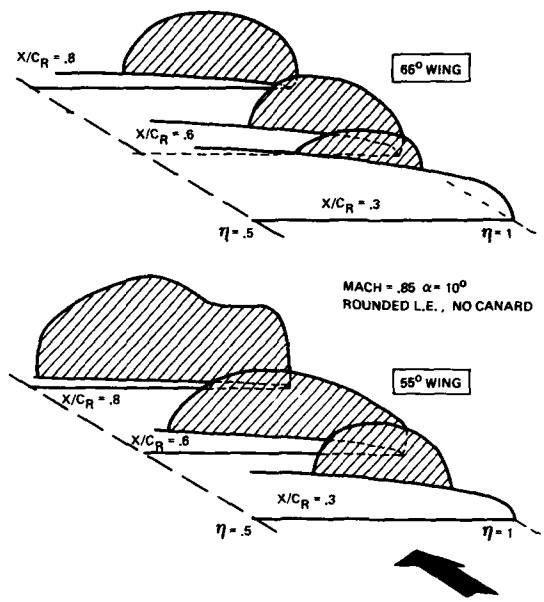


Fig. 38 Approximate regions of more than 5% total pressure loss (deduced from FFA-tests)

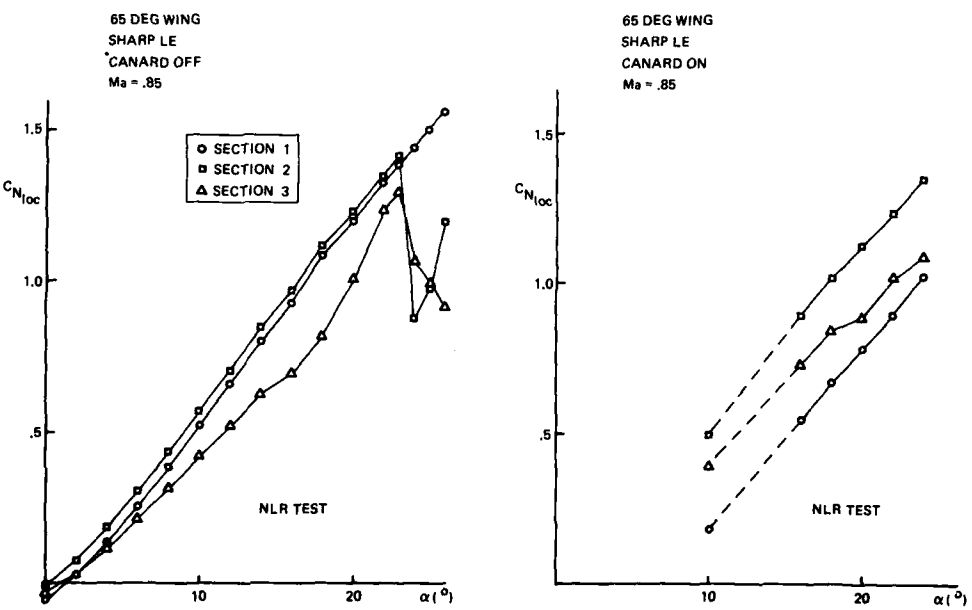


Fig. 39 Variation of sectional normal force coefficient at Mach=.85 for canard-off and canard-on configuration (65 deg wing, NLR tests)

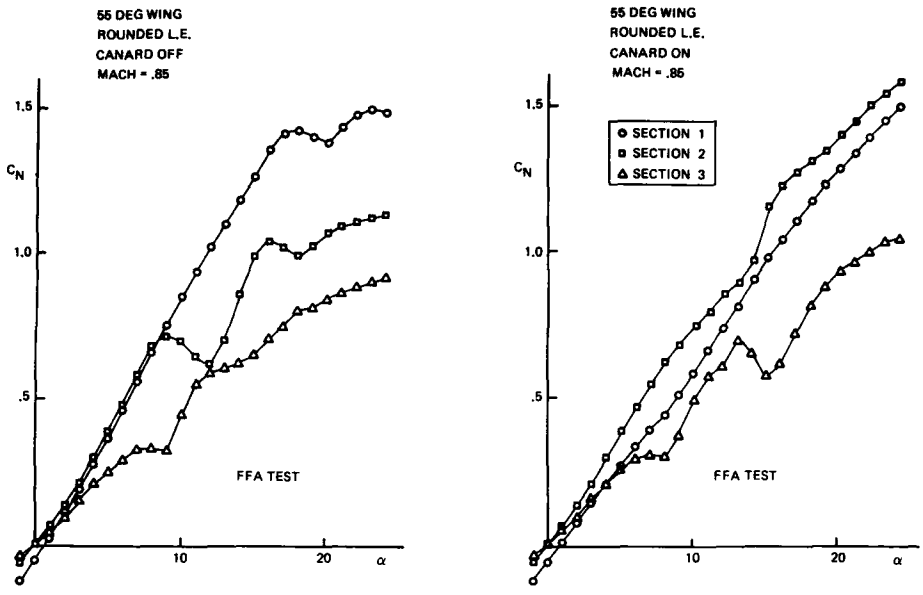


Fig. 40 Variation of sectional normal force coefficient at M=0.85 for canard-off and canard-on configuration (55 deg wing, FFA tests)

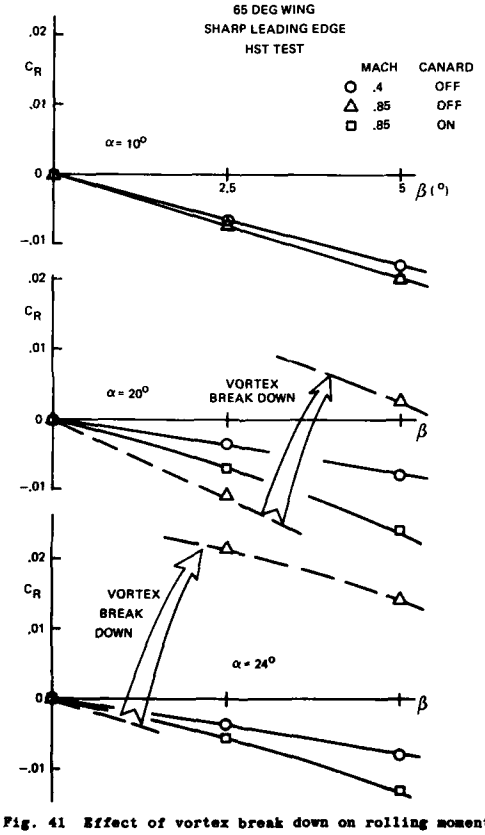


Fig. 41 Effect of vortex break down on rolling moment (tentative)

Appendix

SOME RECENT RESULTS ON VORTEX BURSTING ON A DELTA WING AT HIGH SUBSONIC SPEEDS

W.J. Bannink, Aerospace Engineering, Delft University of Technology, The Netherlands

1. INTRODUCTION

Vortex bursting may be described as the breaking down of a regular structured rapidly swirling flow into a flow where the swirling rate has decreased abruptly or has disappeared leaving almost no vortex structure but rather a highly turbulent motion. The original vortex core has expanded suddenly and the axial flow deceleration may be such as to cause even reverse flow. In delta wing aerodynamics vortex bursting is usually said to have started when the bursting point lies just above the trailing edge of the wing. The angle of attack at which this occurs is called the critical angle of attack. The bursting point moves upstream when the angle of attack is increased. The location of this point is dependent on a combination of several quantities: leading edge sweep, angle of attack, Mach number and Reynolds number. However, the dependence on the Reynolds number seems not to be very convincing, see for example the collected results obtained in different flow regimes in all kinds of wind tunnels and water tunnels, given in Ref. A1.

It is not our intention here to give a discussion or to review all the existing literature on the subject. For that purpose we refer to the appropriate texts, e.g. section IV of Ref. A2. An exception will be made for those references we believe to be directly related to the present investigations.

Experiments in the transonic flow regime (refs. A3,A4,A5) have shown that in these flows vortex bursting starts at lower angles of attack than in low speed flow. Also it is observed that an increase of the angle of attack above the critical value causes the bursting point to move abruptly upstream in contrast to low speeds where the process is much more gradual. The present results confirm these observations. They probably lift also a tip of the veil on the problem whether a shock (see Ref. A6) causes an early and abrupt vortex bursting or vice versa.

2. EXPERIMENTAL SET-UP

The experiments (Ref. A7) have been performed in the Transonic-Supersonic Wind tunnel (test section 280mmx253 mm) of the Delft University of Technology, Faculty of Aerospace Engineering. The tests were made at free stream Mach numbers of 0.6 (0.05) 0.9. The geometry of the model differed slightly from that used in the International Vortex Flow Experiment. It was a triangular sharp-edged planar wing without cropping at the tips. Its leading edge sweep was the same as for the Vortex Flow Experiment model: 65°. The model had a rootchord of 120 mm and was provided with several rows of pressure taps: 12 along the rootchord from 30%-92%; 14 in spanwise direction from 0-92.5% local span at 70% chord position; a grid of spanwise rows between 65% and 90% chord of 4-5 taps. The angles of attack ranged from 5°-22° and the Reynolds numbers based on the rootchord was 3-3.6 million depending on the free stream Mach number.

3. DISCUSSION OF RESULTS

In order to analyse the way the pressure distributions are affected at angles of attack close to the critical angle, spanwise (X/C_r=0.70) and rootchord pressure distributions are plotted in two series: at constant angle of attack ($18° < \alpha < 20°$) for different Mach numbers (Figs. A1,A2) and at constant Mach number M_∞=0.85 for three angles of attack close around the critical value (Figs. A3,A4). Below the critical angle of attack (in this case ≈ 18.5°) the pressure distribution along the rootchord shows a gradual, almost linear compression towards the trailing edge at free stream Mach numbers $M_\infty < 0.8$ (Ref. A7). In Schlieren pictures taken at α=15° in the experiments of Ref. A7 shocks were observed in the flow field at free stream Mach numbers of M_∞=0.85 and 0.9 at approximately X/C_r=0.60 and 0.85, respectively.

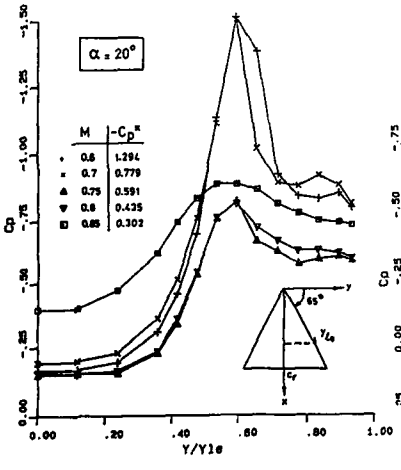


Fig. A1 Spanwise pressure distribution at X/c_r = 0.70

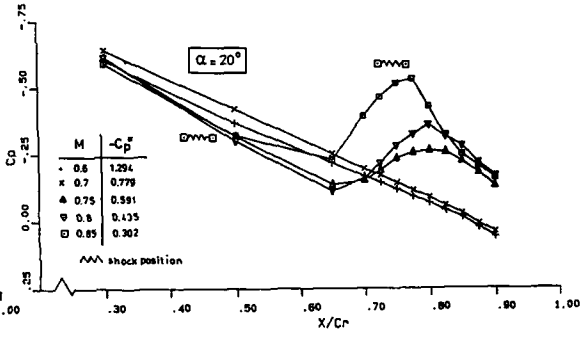


Fig. A2 Pressure distribution along rootchord

Fig. A1 shows for M_∞=0.75, 0.8 and 0.85 the typical spanwise pressure distribution observed down stream of a burst vortex: the suction peak has disappeared completely. Along the rootchord (Fig. A2) we see the marching upstream of the bursting point location. Where at M_∞=0.7 no bursting takes place, the bursting point at M_∞=0.75 and higher is located well upstream of the trailing edge. In the latter case a region of considerable expansion is seen in Schlieren pictures downstream of X/C_r=0.65. Combining these observations with the pressures of Fig. A2 we learn that the expansion is felt in the symmetry plane of the wing. Due to the bursting process the vortex increases in size and becomes disorganized resulting in a region of low velocity. This region forms a converging boundary for the flow along the center part of the wing. The converging channel effect will cause the subsonic flow to accelerate. Further downstream an aerodynamic sonic throat may be formed and the flow is accelerated to supersonic speeds eventually terminated by a shock wave (M_∞=0.85); a shock is observed at X/C_r=0.45 in Schlieren pictures. The pressure distributions obtained at M_∞=0.75, 0.8 and 0.85 show a similar trend when vortex bursting has occurred, as is seen in Fig. A2. However, at M_∞=0.7 and 0.75 no shock waves were observed in Schlieren pictures. At M_∞=0.85 two successive shocks with an expansion zone between were detected. The shock positions are indicated in Fig. A2. A tentative conclusion could be that the second (down-stream shock) is generated by the burst vortex and not vice versa. Another novelty in the bursting process as compared to low speed results is the abruptness of forward movement of the bursting point with increasing Mach number. In the small Mach number range from 0.7 to 0.75 the bursting point moves from the trailing edge (or downstream of it) to about 65% rootchord, to stay there at least up to M_∞=0.85.

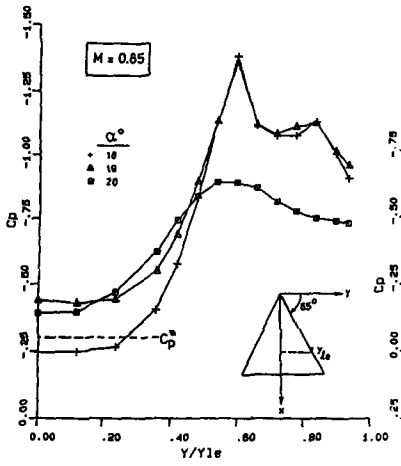


Fig. A3 Spanwise pressure distribution at $^X/_{C_r}$=0.70

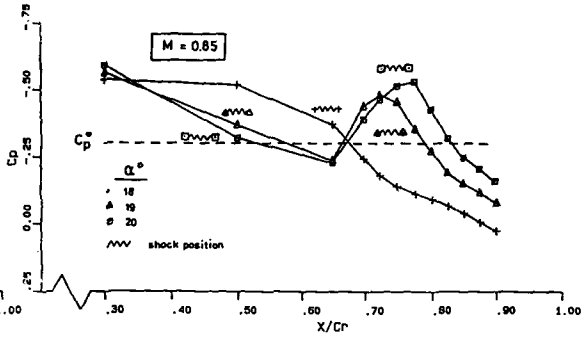


Fig. A4 Pressure distribution along rootchord

From Fig. A3 it is evident that at α between 18° and 19° the vortex bursting has its influence on the 0.70 chord position and the bursting has reached this position at α=20°, because then the suction peak is completely distorted. Note that at α=19° the pressure distribution along the rootchord suggests vortex burst, see Fig. A4 (compare with Fig. A2), whereas the spanwise distribution at X/C_r=0.70 depicted in Fig. A3 looks more like the case of a regular structured vortex. The coinciding spanwise distributions at α=18° and 19° indicate, however, that bursting is near. The discrepancy is probably due to asymmetric bursting, as is suggested by the oilflow pictures (Figs. A6 and A7). Also some port side pressure measurements support this point of view (Ref. A7). It is clear that the flow changes drastically within a fraction of a degree; it is not a matter of a gradual movement of the bursting point. To study the phenomenon in more detail the resolution of pressure orifices should be more dense than in the present investigation, so that between X/C_r=0.3 and 0.7 a more refined pressure distribution can be obtained. In view of the occurring shock waves it is in the present situation centainly not allowed to simply connect the data points lacated far from each other.

The oil flow patterns of Figs. A5-A7 allow a closer definition of the angle of attack at which the vortex burst suddenly appears above the wing than the preceeding figures do; this angle is found between 18.3° and 18.5°. The pattern of Fig. A5 is obtained just prior to vortex bursting. At 18.5° (Fig. A6) only the starboard vortex is burst, whereas at α=19° (Fig. A7) this has happened for both vortices. The asymmetric bursting of leading edge vortices above delta wings has been observed earlier (Refs. A3,A4) and it is assumed to be generated by small imperfections in free stream flow conditions or by imperfections in model and support. Due to slight unsteadiness in the flow or backlash in the model system the asymmetric bursting is not necessarily similar in cases which are nominally the same (Ref. A7).



Fig. A5 Oil flow pattern; M=0.85, α=18.3°

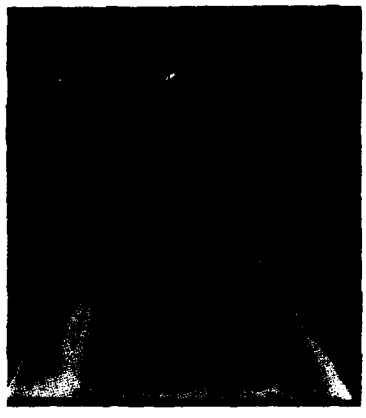


Fig. A6 Oil flow pattern; M=0.85, α=18.5°

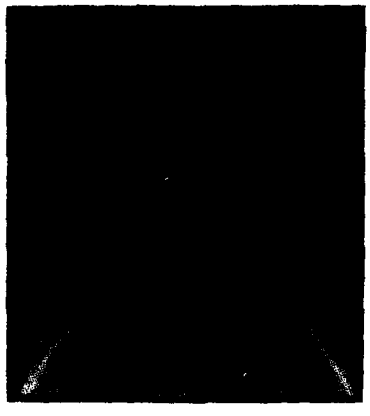


Fig. A7 Oil flow pattern, M=0.85, α=19°

Finally it should be mentioned that the present measurements have indicated that a description of a more complete flow model is very difficult. The presence and shape of shocks cannot be detected sufficiently accurate by surface pressure measurements and Schlieren photography. It also appeared that the vortex bursting phenomenon reveals a rather chaotic character. One is never sure whether the same kind of bursting happens again, whether it occurs at the same side of the wing or that it starts at the same critical angle of attack. However, the present remarks on the general description about the influence of M_∞, the difference with low speed results, the influence of the bursting process on the pressure distributions and the generation of additional shock waves may be maintained.

4. REFERENCES

A1. Skow, A.M. and Erickson, G.E., Modern Fighter Aircraft Design for High-Angle-of Attack Maneuvring, AGARD-LS-121, item 4, 1982.

A2. Aerodynamics of Vortical Type Flows in Three Dimensions, AGARD Conference Proceedings No. 342, 1983.

A3. Muylaert, J.M., Effect of Compressibility on Vortex Bursting on Slender Delta Wings, VKI Project Report 1980-21, 1980.

A4. Stahl, W., Zum Einfluss eines Strakes auf das Strömungsfeld eines Deltaflügels (AR=2) bei Schallnahen Geschwindigkeiten, DLR-Mitt. 73-04, 1973.

A5. Wentz, W.H. and Kohlman, D.L., Wind Tunnel Investigation of Vortex Breakdown on Slender Sharp-Edged Wings, NASA CR 98731, 1968.

A6. Houtman, E.M. and Bannink, W.J., Experimental Investigation of the Transonic Flow at the Leeward Side of a Delta Wing at High Incidence, Delft University of Technology, Faculty of Aerospace Engineering, Report LR-518, 1987.

A7. Ottochian, S.P., Bannink, W.J. and Houtman, E.M., Investigation of the Vortex Flow Over a Sharp-Edged Delta Wing in the Transonic Speed Regime, Delft University of Technology, Faculty of Aerospace Engineering, To be published, 1988.

STATUS OF CFD VALIDATION ON THE VORTEX FLOW EXPERIMENT

by

B.Wagner and S.M.Hitzel
Dornier GmbH
B.F. 10
Postfach 1420
D-7990 Friedrichshafen, 1

M.A.Schmatz and W.Schwarz
MBB – UF

and

A.Hilgenstock and S.Scherr
DFVLR
Federal Republic of Germany

SUMMARY

The vortex flow phenomena developing at highly swept wings by leading-edge separation are of great interest for fighter and missile aerodynamics. While panel methods are already known for more than one decade to model satisfactorily the roll-up of the corresponding vortex sheets at subsonic speed, Euler methods became available in the early 80-ties for predicting these effects also in the transonic and supersonic speed ranges. Subsequent trials to validate such transonic vortex flow computations revealed the experimental data basis to be very poor for high speeds and, in consequence, the "International Vortex Flow Experiment on Euler Code Validation" has been set up. More recently also three-dimensional Navier-Stokes codes could be applied in order to clarify the role of viscous effects and to investigate in detail the neglect of those in the Euler solutions. This paper presents a survey on the Euler code validation based on the Symposium on the IVFE in 1986 and gives additional insight into some related Euler and Navier-Stokes work done in West-Germany more recently.

1. INTRODUCTION

The formation of stable vortex-systems above highly swept wings in consequence of leading-edge separation is a very important aerodynamic phenomenon for fighter and missile configurations as well as for supersonic transports. High speed designs often exhibit rather sharp leading edges causing this type of separation already at low incidence. Although mostly being avoided at cruise conditions this vortex flow can be of considerable importance in manoeuvering flight. Depending on the wing's sweep and the angle-of-attack a sudden change of the vortex structure - the so called vortex-breakdown - can affect the force and moment behaviour significantly. In sideslip conditions the lateral stability behaviour often is not understood looking only on overall forces and moments measured. Very complex flow structures can emerge, which will become even more complicated if the vortex-system of a canard (or a forebody) interacts with the main wing.

Since the leading edge vortex flow phenomenon first has been detected [1] in 1947 by WILSON and LOVELL many trials were made to understand the details of the vortex flow fields either experimentally or by corresponding theoretical approaches. The SAAB-Viggen design is known first having made a favourable use of vortex flow interference at a close-coupled canard configuration in subsonic flow whose aerodynamics had been optimized in a series of wind tunnel experiments [2]. An overview on early computational approaches is given in reference 3. These approaches are characterized by modelling the vortices and the vorticity layers using the formulations of the subsonic potential flow theory and searching iteratively for equilibrium positions of the nonlinear vortex-system. First some methods for conical flow were developed, later the corresponding basic ideas were transferred successfully to three-dimensional panel-methods including such of higher order type [4]. Also extensions of this work to linearised supersonic flow and to transonic nonlinear potential flow are known.

A great success were the first Euler solutions shown in the early eighties which exhibited leading edge vortex flows automatically without any special modelling conditions for separation. According to HELMHOLTZ [5] such type of separation may occur at sharp-edged bodies without the need of viscous effects. Although the numerical mechanism creating the flow separation was not fully understood in detail, the solutions showed a surprisingly good agreement with measured surface pressure distributions at high incidences in all speed ranges (sub-, tran- and supersonic flow). Of course, only the primary separation - being rather independent of the Reynolds number - can be calculated correctly by solving the Euler equations while viscous effects such as the secondary vortices underneath the leading-edge vortices cannot be predicted. Those secondary vortices shift the positions of the primary vortices inboard due to displacement effects. In those early trials [3] also vortex breakdown was predicted, showing obviously many flowfield effects typical for this phenomenon.

A first comparison between different numerical solutions and experimental results has been made in the report of the AGARD-FDP Working Group 07 [6]. This comparison revealed considerable differences between different computational results mainly due to mesh topology and resolution and possibly also due to the numerical schemes used.

Furthermore it had been recognized up to the 1983 AGARD-FDP symposium on vortical type flows [7] that the experimental data base was poor especially at higher speeds containing only force-measurements and a few included surface-pressures. Also this work was not in systematic order to judge detailed effects as e.g. the influence of leading edge radii on the numerical solutions. Hence, the way was cleared to define a joint multi-national vortex flow experiment, the history and the details of which is given in another paper at the present conference [8].

This experiment has been set up for the purpose of "Euler code validation" and this dedication up to now seems to be a rather unique case in the relation of experiments and computations. The configuration investigated and the experimental techniques including flowfield measurements have been selected on purpose in joint meetings by experimental and numerical specialists. Also the actual test conditions have been specified jointly by the thorough discussion on the expected physical behaviour of the flow considered.

2. REVIEW ON THE COMPUTATIONS AT THE SYMPOSIUM ON "INTERNATIONAL VORTEX FLOW EXPERIMENT ON EULER CODE VALIDATION"

Fall 1986 a symposium in Stockholm, Sweden, was organized by the FFA in order to publish an overview on the experimental results of the IVFE as well as the related computational work [9] and to provide a fruitful discussion between many experimental and numerical specialists on the observed physical phenomena and their computational simulation. From the computational point of view the following aspects were of highest importance during this meeting:

- The difference between the round and sharp leading edge cases in the different speed ranges, including the phenomenon of part span leading edge vortices which occur at low up to medium angles-of-attack. This part span separation is favoured by round leading-edges at low subsonic speeds.
- The formation of shock waves in transonic vortical flows, including shocks in chordwise directions as well as cross flow shocks.
- The detailed flow structure of vortex breakdown and the possible mechanisms of it.
- The reasons of the high total-pressure losses in the vortex core, which seem to be almost independent of numerical details but heavily dependent of the free stream conditions for a given geometry. The bulk of the losses obviously is not convected from the leading egde to the vortex core in the numerical solution but is formed in the vortex core.
- The possibilities of improvements in the numerical results by solving the time averaged Navier-Stokes equations instead of the Euler equations.

HIRSCHEL [10] gave a very good insight into the 3-D production and the containment of the vorticity in Euler methods by a modern numerical approach. While VON KARMAN [11] describes the vorticity being produced either by viscous effects and/or the nonviscous separation from aerodynamically sharp edges HIRSCHEL distinguishes with respect to the free vortex sheets behind a lifting wing a so called kinematically inactive part which vanishes in the limit $Re \rightarrow \infty$ from the so called kinematically active part. The main direction of the latter coincides in the limit with the main stream direction thus forming longitudinal vortices. Therefore the kinematically inactive part may be reduced to the local influence of friction on the wing while the other kinematically active part represents the vorticity responsible for the 3-D longitudinal vortex flow. The local viscous influence corresponds to a 2-D wake-defect in viscous 2-D profile investigations. In 3-D Euler approaches where no viscous effects are simulated, the so called kinematically inactive part nevertheless may occur due to numerical effects.

Although the formation of vorticity at wing edges has thus been been proved successfully for an Euler solution at a low Mach number on a high aspect ratio trapezoidal wing with a low leading edge sweep, it is difficult to explain the high total-pressure losses in the vortex core of a low aspect ratio delta wing at high incidence. Although high losses are observed close to the leading edges they are small compared with those being found in vortex cores. No significant convection of leading edge losses to the core could be reported. As stated explicitely by Murman [12] the strength of the total-pressure losses in the core essentially depend on the wing's geometry and the flow conditions but not on details of the numerical codes employed. No significant effect, e.g. of the so called artifical viscosity parameters and the meshes, was found. As SMITH [13] stated in his overview of the IVFE the total-pressure losses seem not to have considerable influence on the outcome of the Euler simulations. Only one important question remained open whether the losses will change considerably by intense mesh refinements within the vortex core or by accounting for the viscous effects in the core together with sufficient resolution.

Also in general for a couple of flow cases the different solutions shown at the IVFE symposium look quite similar. Especially the results of KUMAR [14], HITZEL [15] and SIRBAUGH [16] came close to each other essentially using the same numerical approach on the sharp edged wing configuration. However, as SACHER [17] turned out, essential discrepancies exist between the different numerical results - also in comparison with the experiments - in the case of round leading-edge and lower angles-of-attack, which may be of considerable importance for fighter manoeuvering.

Obviously, the simulation of the leading edge separation becomes very sensitive to geometric, numerical and compressibility effects, especially at medium and low angle-of-attack. Very different results were achieved with respect to the spanwise position of separation onset leading to quite different spanwise extensions of the vortex flow region. These effects were supposed to depend strongly on the mesh resolution at the leading edge and on the numerical viscosity effects. Thus in low subsonic flow the separation at round leading edges even can be avoided in Euler solutions by thorough numerical treatment, although the experimental results already show separation along the entire leading edge. In transonic flow the separation seems to be triggered by compressibility effects at rather low incidences already.

Even sharp leading edge simulation sometimes resulted in part span separations at lower angles-of-attack because it suffered from the often used C-H-mesh topology of the wing, which does not provide sufficient geometrical resolution at the wing's apex. At transonic speeds the differences which were observed in subsonic flow between round and sharp leading edge solutions diminished (see also the experimental results [8]).

Considering the part span vortex separation from round edged wings most authors suggested possible improvements by solving the Navier-Stokes equations instead of the Euler equations. However the only Navier-Stokes solution [18] available was a first trial in a rather coarse mesh therefore not exhibiting significant improvements compared to Euler solutions.

Finally it has to be mentioned that several authors (e.g. reference 14, 15, 16 and 19) simulating high angle-of-attack cases found flowfield structures in their solutions which correspond to the features of vortex breakdown. As measured they show the abrupt widening of the vortex structure and reversed axial flow within the vortex core as already had been presented by HITZEL and WAGNER [20] for an arrow wing configuration at very high angle-of-attack. Although the mechanisms of this breakdown phenomenon is not completely understood, the capability of Euler solutions to predict vortex breakdown appears to be rather obvious. The computed breakdown cases exhibited changes of total lift and pitching moment very similar to the experimental results. Details of the corresponding flowfields have been discussed by several authors. Unfortunately the evaluation of the vortex breakdown field measurements were in an early status [21], thus preventing the comparison between numerical simulation and experiment for these cases.

The discussion of shock wave formations in the 3-D flows and their interaction with the vortex flow especially with vortex burst at that time was based more on presumptions rather than on conclusive observations (see e.g. [16]).

3. RECENT EULER RESULTS

This chapter is dedicated to recent experiences on Euler simulations and their results. The corresponding work at DORNIER is discussed first, then the Euler work done at MBB is presented while the DFVLR Euler-work is shown third. All calculations have been performed for the wing alone.

The finite volume approach to solve the time-dependent Euler-equations in an expicit time-stepping procedure of Runge-Kutta type as described by JAMESON and SCHMIDT [22] was used at DORNIER. The cell centered formulation corresponds to a central difference scheme and provides second order accuracy in space if sufficently homogeneous meshes are used. The 3-D version has been further developed by LEICHER [23] and coupled with a block-stuctured approach. Using this version and combining it with a new mesh generator HITZEL [24] evaluated the sharp edge delta wing of the Vortex Flow Experiment. DORNIER - while having produced quite satisfying results [15] for the sharp edged delta wing at high angle-of-attack - at first was interested in the problem of the wrong onset of part span vortices at medium angle-of-attack mentioned above. The previous computational C-H-mesh topology was suspected to provide a very bad resolution at the apex of the delta wing. Consequently the mesh topology was changed to a more appropriate H-O-mesh topology as depicted in figure 1. Usually a so called fine mesh containing more than 270.000 computational volumes was employed there. 80 volumes in chordwise direction and 32 in spanwise direction on the wing's upper and lower surface, while 32 volumes exist in vertical direction. In front of the wing 20 volumes were distributed in I-direction, while 32 volumes in I-direction formed the wake region.

The change of the topology had a striking effect on the computational results. As can be seen from figure 2 in isobars for the Mach = 0.85, $\alpha = 10°$ case on the wing surface the part span vortex pattern disappeared. A single leading edge vortex from the apex up to the trailing edge can be traced. Of course the same result must be possible in a C-H-mesh topology. However a C-H-mesh required more than 1.000.000 mesh volumes to provide the same details of the flow e.g. for the isobars as shown in figure 2. Thus a H-O-mesh has been found to be superior to the C-H-mesh topology with respect to both numerical efficiency and mesh resolution.

Figure 3 once more shows the difference of the mesh topologies for the Mach = 0.85, $\alpha = 10°$ in the Cp-distribution of selected cross-section cuts. The H-O-results are in very good agreement with the experimental results of the NLR [25] keeping in mind that the neglect of viscous secondary vortices - basically having a displacement effect on the primary leading edge vortex-system - must shift the vortex position a little bit outboard and results usually also in slightly higher suction-peaks. Similar agreement as shown was also achieved for all other angle-of-attack Mach number cases computed.

In order to provide some insight into the effects of the compressibility figure 4 is presented. It depicts the isobars of 10° angle-of-attack cases at different Mach numbers. The higher the Mach number the lower the upstream influence of the trailing edge, the more conical the flow looks like. Also the suction-peaks become lower, since compressibility effects may lower the leading-edge vortex influence. The Mach numbers induced on the wing can be considerable higher than the free-stream Mach number. This holds for subsonic, transonic as well as supersonic speeds.

Figure 5 shows the isobars on the wing's surface at different angle-of-attack. Figure 6 gives a summary and a survey of the flow-field at Mach = 0.85 and 10° angle-of-attack. It shows the isobars on the wing surface and the total-pressure losses at the same cross-section cuts as the isoMach contours. Within the vortex the Mach numbers are considerably higher than the free-stream Mach number. Apart from vortex-breakdown conditions, the pattern of the isobars, iso-Mach contours and total-pressure losses are rather typical for all other Mach number and angle-of-attack cases. More detailed results also of other flow-conditions are provided in reference 24.

Mesh refinements always produced slighly higher lift coefficients than those measured in the experiments. The higher values compared to the experimental results may be due to the neglect of viscous effects since secondary vortices are not being treated by Euler methods. On the other hand, a purely compressible vortex [26] shows a velocity profile in the vortex core which may differ from viscous cores.

Vortex-breakdown is of major interest and thus a lot of work was dedicated to this flow phenomenon. Here only one case at Mach = 0.85, $\alpha = 24°$ is shown (fig. 7). The calculations revealed a very complex transonic vortex-breakdown flowfield, which contains some features also found in the experimental work [8]. On and above the wing's front part the results are very similar to those in figure 6 with regard to all variables. In the rear part of the wing all variables differ considerably, showing a typical breakdown flowfield. The bubble of reversed flow as indicated above the delta wing starboard side is well represented by very low Mach numbers in the rear part. The isobar pattern shows traces of a quite complex shock-system connected with the vortex-breakdown flowfield. Within this shock-system a center-line shock and a vortex-breakdown shock may be distinguished as depicted above the wing starboard surface. Reference 24 shows more details also for subsonic cases and for the superfine meshes which captured also some instationary effects qualitatively.

At MBB SCHWARZ concentrated on the examination of the influence of different grids close to the leading-edge of the round-edged wing configuration at Mach = 0.85, $\alpha = 10°$. Both C-H-mesh and H-H-mesh topologies were employed. In contrast to the above H-O-mesh the latter H-H-mesh was oriented along the wing leading edge such that the wing surface resolution is the same as in the C-H-mesh topology (fig. 8). The grids were constructed by using either algebraic or elliptic methods based on the solution of the Poisson equations [27].

The Euler code which was employed for these calculations is the EUFLEX code developed at MBB by A. EBERLE [28]. This is a finite volume sheme which uses an upwinding method based on a GODUNOV type averaging procedure for the evaluation of the fluxes at the cell faces [28]. For homogeneous meshes it is third order accurate except at shocks or boundaries where it reduces to first order accuracy. Explicit as well as implicit time relaxation procedures can be used.

All calculations at MBB [29] were performed in four different grids containing approximately 260.000 computational volumes. The wing surface was formed by 60 volumes in lenghtwise and 22 volumes in spanwise direction. This discretization of the wing was kept the same for both mesh-types as well as the number of volumes in normal direction and the positions of the farfield boundaries relative to the wing. The main difference was the resolution of the leading-edge in the C-H-topology as well as in the H-H-mesh (fig. 8). Depending on the grid resolution and the grid volume aspect ratios the separation of leading edge vortices may differ considerably. Figure 9 and figure 10 show very different pattern of separations. While the results of the round-edged Euler-case in figure 9 corresponding to the case (a) in figure 11 is in quite good agreement with experiments figure 10 shows no separation at all due to its mesh. In the latter case total-pressure losses as a consequence of the very bad resolution and the very high aspect ratios of the computational volumes locally cause a very high numerical dissipation which shifts possible separations further downstream. In the very extreme case shown here, no separation at all may occur. Figure 11 gives a survey of the Cp-distributions of the different meshes involved in the investigations described together with a comparison to the experimental results. In the results a distinct vortex already was measured at the wing's apex ahead X/C = 0.3. The difference in the Euler-results also may be caused by the bad resolution of the apex region of the wing by the meshes employed here.

The DFVLR-Braunschweig also contributed to the Euler-results. Some first results were produced with the Euler solver CATS. This program is a cell-centered finite volume code based on the algorithm of JAMESON, TURKEL und SCHMIDT. Calulations were performed for the wing with sharp and round leading edges on algebraically created meshes with an O-O topology. Results were obtained on successively refined meshes for Mach numbers of 0.4 and 0.85 for various angles-of-attack. Refinements of the mesh appears always to produce a higher lift coefficient than the experimental value (Fig. 12). The same was experienced by other investigators [24]. However the finer the meshes the smaller the increase in those derivatives indicating an asymptotic approach towards a higher but finite value. Figure 12 shows some DFVLR results which also indicated some vortex-breakdown effects in the lift versus angle-of-attack diagram.

The DFVLR used two different versions of their code. The second version CEVCATS is a cell-vertex method in which it is guaranteed that the discretization error is at worst first order with the mesh spacing. This ensures that the difference of the solution from the exact. inviscid solution goes to zero as the mesh spacing goes to zero. The trend of increasing lift is smaller within the CEVCATS method than in the cell-centered sheme (fig. 13). Current investigations include further comparison of results from the CATS and CEVCATS codes.

4. RECENT NAVIER-STOKES RESULTS

Most recent Navier-Stokes results on the Vortex Flow Experiment were performed at MBB and the DFVLR-Göttingen for the wing alone configuration.

SCHMATZ at MBB applied the NSFLEX code, a Navier-Stokes solver using characterstic flux extrapolation to the round-edge version of the Vortex Flow Experiment delta wing. The basic equations are the time dependent Reynolds-averaged compressible Navier-Stokes equations and the fundamental feature of the solution method is a GODUNOV type averaging procedure based on an eigenvalue analysis of the inviscid equations in a finite volume approach. The method is based on an eigenvalue analysis of the inviscid equations by means of which the inviscid fluxes are evaluated at the volume faces which separate sets of constant flow variables on either side. The sum of the flux differences is approximated via a third-order spatial characteristic flux extrapolation scheme for the inviscid fluxes. using sensor functions to detect nonmonotoneous behaviour of the flow such as shocks. Here the scheme is reduced to first-order accuracy. In those aspects the code corresponds to the Euler code mentioned above. The viscous fluxes are formed by central differences at each volume's faces. The unfactored implicit equations are solved by a Newton method whose relaxation is performed with a point Gauss-Seidel technique with the red-black strategy due to vectorization. It was found that the red-black relaxation does not hamper convergence at all. The underlying Euler method was proved to produce highly accurate results for a wide range of Mach numbers. Turbulent eddy viscosity is calculated using the simple algebraic mixing length model of BALDWIN and LOMAX.

Figure 14 shows the finite volume C-H-grid of the delta wing. The total amount of cells employed was 277.400. 146 volumes were used in I-direction, 50 volumes in spanwise direction and 38 normal to the wing.

MBB selected the Mach = 0.85, $\alpha = 10°$ case at Reynolds = 9.000.000 [29]. The laminar-turbulent transition was fixed as in the experiment [30]. The skin friction pattern in figure 15 indicates the separation at the leading edge. The comparison of the Cp-distribution of the computed results and the experiment in cross-section cuts shows reasonable agreement in the rear part of the wing. The other two cross-section exhibit differences. No proper vortex is calculated at all at X/C = 0.3, while the experiment shows a distinct influence of a leading edge vortex. These severe differences probably are due to mesh problems discussed. Test calculations in finer grids are under progress.

The DFVLR-Göttingen Navier-Stokes method [31] employes a cell centered finite volume approach of JAMESON type in connection with a Runge-Kutta four-stage method exhibiting basically second order accuracy in space. The block-structured code was used to integrate the laminar equations for the Mach = 0.85, $\alpha = 10°$ flow around the sharp-edged delta wing. The Reynolds number was chosen to be 10^6.

The topology selected was of H-H-mesh type as shown in figure 16. Results were obtained in 3 different grids which contained 1.000.000 - 2.000.000 mesh-points of grid resolution. A typical grid consisting of 1.000.000 volumes used 50*50 points on the wings upper side. 40 volumes were used in normal direction, while another 40 volumes were positioned in front of the wing as well as in its wake. Finally 50 volumes in spanwise direction formed the computational domain from the wing tip to the farfield boundary. At the wing tip an O-H-mesh topology filled the gap formed by the wing upper and lower surface in the space between the tip and the far-field. Figure 17 shows some typical chordwise cuts in the mesh. The mesh was produced by an algebraic grid generator.

Figure 18 gives a comparison of the experimental Cp-distributions with the numerical Navier-Stokes results. Again as in the MBB-results the solution is in good agreement in the wing's most rear cross-section cut of the wing. However the flow ahead is not simulated properly. Some discrepancy on the wing's lower side may be due to the neglect of the support-fuselage of the wind-tunnel model (as in the previously discussed Euler and Navier-Stokes simulations), however the differences on the upper side can not be explained by those effects. The problems especially at $X/C = 0.3$ also may be attributed to mesh-resolution problems as discussed with the other Euler and Navier-Stokes solutions mentioned already.

The differences at $X/C = 0.6$ may be due the difference of turbulent and laminar flows. While the experiment is turbulent the numerical simulation is laminar. Laminar conditions produce much larger secondary vortices than turbulent flows. This results in a more intense displacement effect of the secondary vortex on the leading edge vortex position. Being shifted more inboards and further above the wing its suction-peak declines in the laminar case. The quite strong laminar secondary vortex also causes an additional suction-peak. Both together, the leading-edge and secondary vortex system now cause a saddle point in the primary suction-peak of the leading edge vortex. This is not possible in a turbulent case since the turbulent secondary vortices are much smaller and have almost no effect on the leading edge vortex position.

Considering these effects also at $X/C = 0.8$ the good agreement there can not be explained since the computational laminar result very well follows the turbulent experimental pressure distributions. A refined mesh in normal direction (80 volumes) and an increased numerical dissipation inside the boundary layer finally established a laminar behaviour at $X/C = 0.8$ also (fig. 19). Possibly the simulation of turbulent effects may improve those results.

The figure 20 shows a comparison of the skin-friction of both mesh refinements mentioned. The reattachment lines of the primary vortices of both are in good agreement with each other in the front and and in the middle part of the wing. For the finer mesh the secondary vortices reattachment lines are only a little bit more inboard. However the skin-friction pattern inbetween the two reattachment lines differs considerably in both cases. The MBB results never showed such a complicated flow-field in the turbulent simulation. The skin-friction pattern inbetween the wing centerline and the leading edge vortex reattachment line looks rather strange.

Latest turbulent results at the same flow conditions at Reynolds $= 9*10^6$ show a quite good agreement of the pressure distribution in the cross-sections $X/C = 0.6$ and $X/C = 0.8$ (fig. 21). The suction peaks are simulated as in the experiment regarding the position and the peak magnitudes. The front cut $X/C = 0.3$ still shows significant differences probably due to the mesh's resolution in the apex region. Qualitatively the influence of the turbulent secondary vortices is predicted as known from experiments and mentioned above. The skin-friction lines for the turbulent case (fig. 22) confirm the findings in the pressure distributions. The secondary vortex is much smaller, while the primary vortex hardly changes it's position. The mesh used for these calculations contained 40 * 40 volumes on the wing surfaces and 40 volumes normal to the wing.

5. CONCLUSIONS

Since the first Euler solutions have been achieved for leading edge vortex flows on slender highly swept wings in the early eighties considerable progress has been made up to now. While the judgement of the early solutions suffered from the poor experimental data basis available at that time for the compressible speed range, the situation has essentially been improved by performing the detailed measurements of the International Vortex Flow Experiment. Reasonable agreement has been gained between calculations and experiments with respect to overall forces and pressure distributions if suitable numerical codes together with thoroughly designed meshes are applied. Although the mechanisms of the high total pressure losses in the vortex core and of the vortex breakdown are not completely understood, different Euler codes have been proved to predict very similar results corresponding to the experiments surprisingly well. The formation of shock waves and their interaction with vortex breakdown have been analysed in more detail.

Navier-Stokes solutions have been shown to be slightly superior predicting viscous effects at the surface where fine mesh resolutions are used. However, no conclusions can be drawn with respect to the viscosity influence within the flowfields since sufficient mesh resolutions have not been used there. Further detailed work is needed in order to validate the codes for more complicated flow cases as e.g. the wing-fuselage configuration in sideslip and in presence of a canard. Also detailed comparisons should be made as soon as possible between the calculated and the measured flowfields, the latter now being available from the International Vortex Flow Experiment.

References

[1] Wilson J.A., Lovell J.C., "Full Scale Investigation of the Maximum Lift and Flow Characteristics of an Airplane Having Approximately Triangular Plan Form", NACA Research Memorandum No. L6K20, 1947

[2] Behrbohm H., "Basic Low Speed Aerodynamics of the Short-Coupled Canard Configuration o Small Aspect Ratio", SAAB TN60, 1965

[3] Hitzel S.M., Schmidt W., " Slender Wings with Leading-Edge Vortex Separation - A Challenge for Panel-Methods and Euler-solvers", Journal of Aircraft, Volume 21, 1984, pp 751-759,
former AIAA paper 83-262, Reno, 1983

[4] Johnson F.T., Lu P., Tinoco E.N., Epton M.A., "An Improved Panel Method for the Solution of Three-Dimensional Leading-Edge Vortex Flows", Volume I - Theory Document, NASA CR-3278, 1980

[5] Helmholtz H., "Über die Integrale der hydrodynamischen Gleichungen welche den Wirbelbewegungen entsprechen", Journal für die reine und angewandte Mathematik, Band 55, Heft 1, 1858, pp 41

[6] Smith J.H.B., "Numerical Solutions for the 3-D Cases - Delta Wings", AGARD AR-211, Test Cases for Inviscid Flow Field Methods, 1985, pp 8-1 - 8-94

[7] " Aerodynamics of Vortical Type Flows in Three Dimensions", AGARD conference proceedings No. 342, Rotterdam, Netherlands, April 1983

[8] Elsenaar A., Hjelmberg L., Bütefisch K., Bannink W.J., "The International Vortex Flow Experiment", AGARD Symposium on Validation of Computational Fluid Dynamics, Libon, Portugal, 2-5 May, 1988

[9] Proceedings of the International Vortex Flow Experiment on Euler Code Validation, Stockholm, Sweden, edited by Elsenaar A., NLR, 1986

[10] Hirschel E.H., Rizzi A., "The Mechanism of Vorticity Creation in Euler Solutions for Lifting Wings", Proceedings of the International Vortex Flow Experiment on Euler Code Validation, Stockholm, Sweden, 1986, pp 127-162

[11] von Karman T., "Theory of Lift", Aerodynamics, McGraw-Hill Paperback, Cornell University Press, 1954, pp 25-55

[12] Murman E.M., "An Overview of Research on Vortex Flows in the U.S.A.", Joint US/European Vortex Flow Symposium, Stockholm Sweden, Oct. 1986

[13] Smith J.H.B., "Overview of the Symposium", Proceedings of the International Vortex Flow Experiment on Euler Code Validation, Stockholm, Sweden, 1986, pp 357-361

[14] Kumar A., Das A., "Numerical Solutions of Flow Fields Around Delta Wings Using Euler Equation Method", Proceedings of the International Vortex Flow Experiment on Euler Code Validation, Stockholm, Sweden, 1986, pp 175-186

[15] Hitzel S.M., Wagner B., Leicher S., "Euler-Simulation of the Vortex Flow Experiment - A Critical Consideration", Proceedings of the International Vortex Flow Experiment on Euler Code Validation, Stockholm, Sweden, 1986, pp 281-288

[16] Sirbaugh J.R., "Euler Analysis of the AFWAL 65° Delta Wing", Proceedings of the International Vortex Flow Experiment on Euler Code Validation, Stockholm, Sweden, 1986, pp 245-264

[17] Sacher P.W., "Computational Results for the Euler Wing", Joint US/European Vortex Flow Symposium, Stockholm Sweden, Oct. 1986

[18] Müller B., Rizzi A., "Navier-Stokes Simulation of Laminar Flow Over the 65° Round Leading-Edge Delta Wing at Mach = 0.85 and α = 10°", Proceedings of the International Vortex Flow Experiment on Euler Code Validation, Stockholm, Sweden, 1986, pp 269-280

[19] Rizzi A., Drougge G., Purcell C.J., "Euler Simulation of Shed Vortex Flows over the 65° Delta Wings", Proceedings of the International Vortex Flow Experiment on Euler Code Validation, Stockholm, Sweden, 1986, pp 289-344

[20] Hitzel S.M., Wagner W., "Untersuchungen der dreidimensionalen Vorderkantenablösung an schlanken Flügeln mittels einer Euler-Zeitschrittmethode", 4. DGLR-Symposium on separated flows, Göttingen, 10-12 October, 1983

[21] Bütefisch K.A., Pallek D., Reichmuth J., "Flow Field Study on a 65° Delta Wing", Proceedings of the International Vortex Flow Experiment on Euler Code Validation, Stockholm, Sweden, 1986, pp 269-280

[22] Jameson A., Schmidt W., " Some Recent Development in Numerical Methods for Transonic Flows", Computational Methods in Applied Mechanics and Engineering 51, 1985, pp 467-493

[23] Leicher S., "Numerical Solution of Internal and External Inviscid and Viscous 3-D Flow Fields, AGARD Applications of Computational Fluid Dynamics in Aeronautics 14, Aix-en-provence France, 1986

[24] Hitzel S.M., "Wing Vortex-Flows Up Into Vortex-Breakdown", AIAA paper 88-2518 to be presented at the 6th Applied Aerodynamics Conference, Williamsburg Virginia, June 1988

[25] Boersen S.J., Elsenaar A, "Test of the AFWAL 65° Delta Wing at NLR: A Study of the Vortex Flow Development between Mach = 0.4 and 4.0. Proceedings of the International Vortex Flow Experiment on Euler Code Validation, Stockholm, Sweden, 1986, pp 23-36

[26] Brown S., "The Compressible Inviscid Leading Edge Vortex", Journal of Fluid Mechanics, Volume 22, part 1, 1965, pp 17-32

[27] Schwarz W., "Elliptic Grid Generation System for Three-Dimensional Configurations Using Poisson's Equation", in Proc. 1st Intern. Conf. on Numerical Grid Generation in CFD, J. Häuser, C. Taylor (eds.), Pineridge Press, Swansea, 1986, pp 341-352

[28] Eberle A., "3-D Euler Calculations Using Characteristic Flux Extrapolation", AIAA paper 85-0119, 1985

[29] Schwarz W., Schmatz M.A., "Euler and Navier-Stokes Calculations for the Vortex Flow Experiment - Interim Report", MBB report MBB-FE122-AERO-MT799, 17. 2. 1988

[30] Schmatz M.A., Brenneis A., Eberle A., "Verfication of an Implicit Relaxation Method for Steady and Unsteady Viscous and Inviscid Flow Problems", AGARD Symposium on Validation of Computational Fluid Dynamics, Lisbon, 1988

[31] Schwamborn D., "Simulation of the DFVLR F5-Wing Experiment Using a Block Structured Explicit Navier-Stokes Method", to be published in Proceedings fo an International Workshop, Vieweg Series "Notes on Numerical Fluid Mechanics", Vieweg 1988

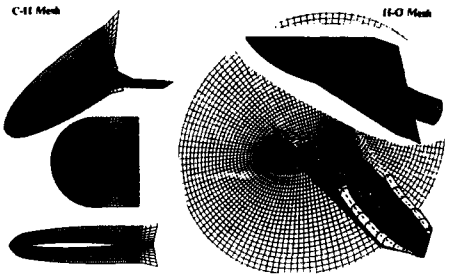


Fig. 1: Computational mesh and surface grid of the Vortex Flow Experiment delta wing [24]

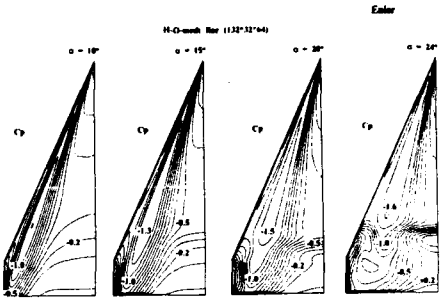


Fig. 5: Isobars on the delta wing at Mach = 0.85 [24]

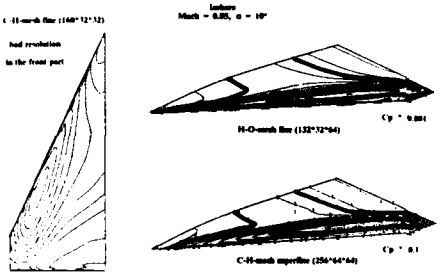


Fig. 2: Comparison of isobars in different mesh topologies [24]

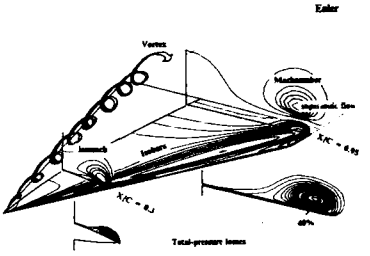


Fig. 6: Flow structure above the delta wing at Mach = 0.85, α = 10° [24]

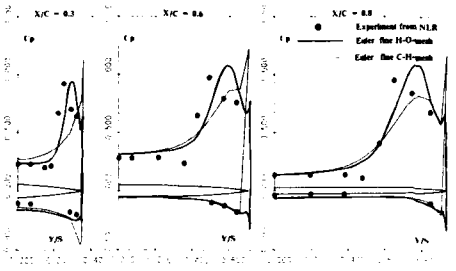


Fig. 3: Cp-distribution in cross-flow cuts at Mach = 0.85, α = 10° [24]

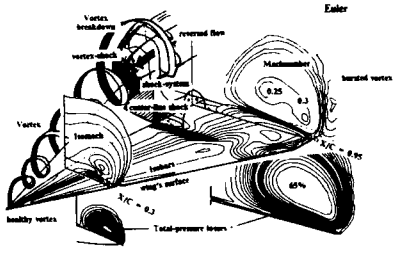


Fig. 7: Flow structure above the delta wing at Mach = 0.85, α = 24° [24]

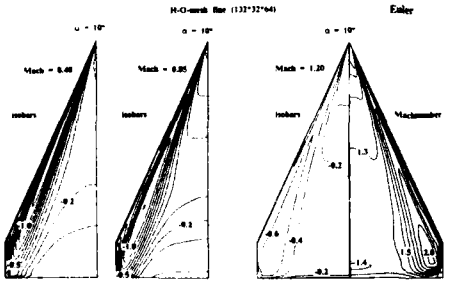


Fig. 4: The delta wing at different Mach numbers [24]

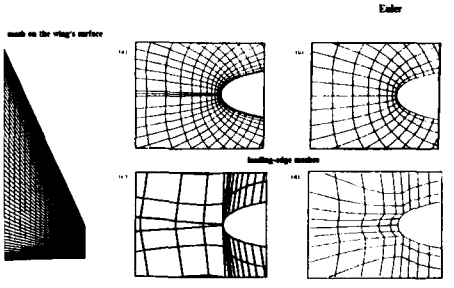


Fig. 8: Meshes along the leading edge of the round edged wing [29]

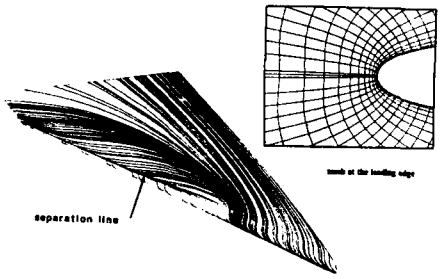


Fig. 9: Surface streamlines of an Euler result for the round edged delta wing at Mach = 0.85, α = 10° [29]

Mesh Size	Cell-centered Algorithm		Cell-vertex Algorithm	
	c_r	c_d	c_r	c_d
48 x 12 x 24	0.7783	0.2661	0.8336	0.2879
96 x 24 x 48	0.9672	0.3353	0.9280	0.3180
128 x 48 x 96	1.0271	0.3547		

Lift and drag coefficients for the VFE delta wing, $M_\infty = 0.4$, $\alpha = 20°$

Fig. 13: Lift-coefficients for the delta wing depending on mesh-size and algorithm by the DFVLR Braunschweig

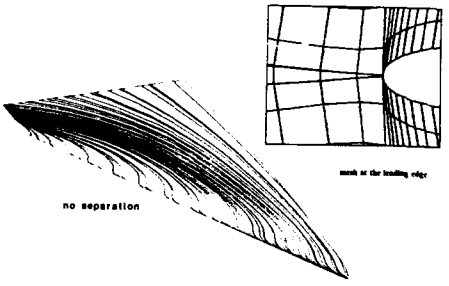


Fig. 10: Surface streamlines of an Euler result for the round edged delta wing at Mach = 0.85, α = 10° [29]

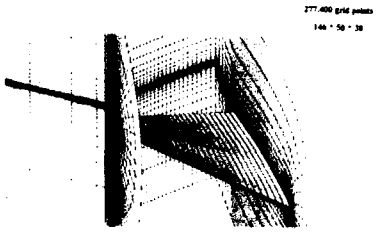


Fig. 14: Navier-Stokes mesh [29]

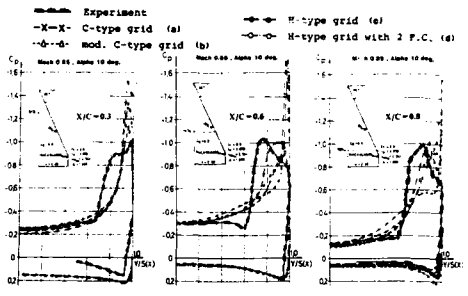


Fig. 11: Cp-distribution by Euler at Mach = 0.85, α = 10° [29]

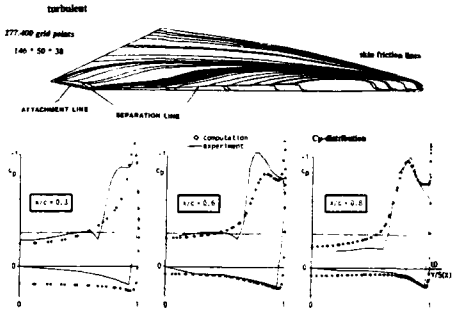


Fig. 15: Navier-Stokes results at Mach = 0.85, α = 10° [29]

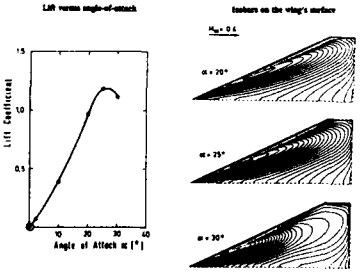


Fig. 12: Euler results on the sharp edged delta wing by the DFVLR Braunschweig

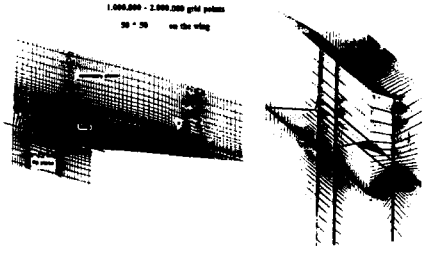


Fig. 16: Navier-Stokes mesh by the DFVLR Göttingen

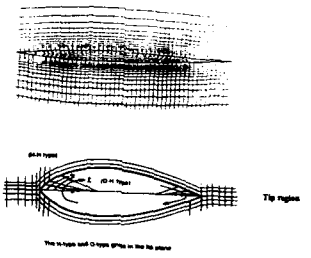


Fig. 17: Some chordwise cut
of the Navier-Stokes mesh
by the DFVLR Göttingen

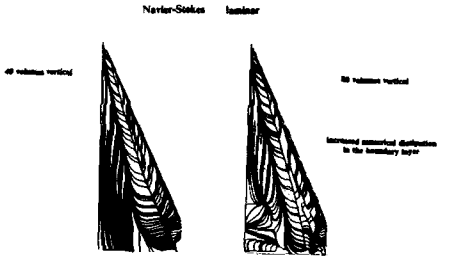


Fig. 20: Surface skin friction lines at
Mach = 0.85, α = 10°
by the DFVLR Göttingen

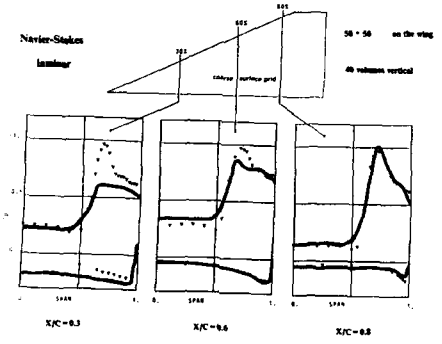


Fig. 18: Cp-distribution in cross-sections
at Mach = 0.85, α = 10°
by the DFVLR Göttingen

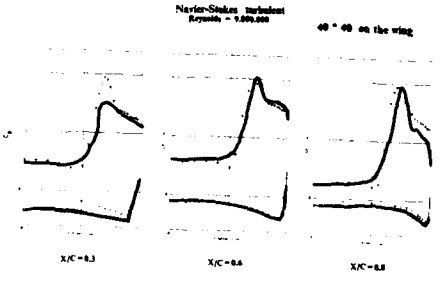


Fig. 21: Cp-distribution in cross-sections
at Mach = 0.85, α = 10°
by the DFVLR Göttingen

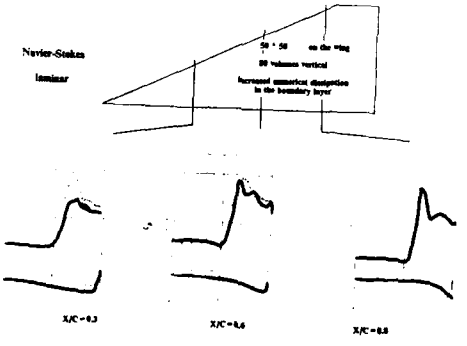


Fig. 19: Cp-distribution in cross-sections
at Mach = 0.85, α = 10°
by the DFVLR Göttingen

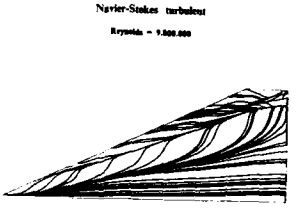


Fig. 22: Surface skin friction lines at
Mach = 0.85, α = 10°
by the DFVLR Göttingen

Flow Field Surveys of Leading Edge Vortex Flows

by

T. T. Ng and R. C. Nelson
Department of Aerospace and Mechanical Engineering
University of Notre Dame
Notre Dame, IN 46556

and

F. M. Payne
Boeing Commercial Airplane Company
Seattle, WA 98124
USA

Summary

The phenomenon of vortex breakdown over slender delta wings is examined experimentally. Measurements of leading edge vortex structures were obtained using both flow visualization and detailed wake surveys using either a seven-hole pressure probe or a laser Doppler anemometer. The structure of the leading edge vortex on a family of delta wings is presented. The delta wing models were sharp-edge flat plates having leading edge sweep angles of 70°, 75°, 80°, and 85°. These models were tested at angles of attack of 10°, 20°, 30° and 40° in a Reynolds number range of 8.5×10^4 to 6.4×10^5.

Specifically data is presented on vortex trajectories, wake surveys, and swirl angles before and after vortex breakdown. In addition the effect of Reynolds number on the vortex surveys is discussed. The data presented in this paper represents a portion of a large experimental data base that should be of value to the development and validation of computational models of leading edge vortices.

List of Symbols

C_{P_t}	Total pressure coefficient, $(P_{t_1} - P_s) / Q$
C	Root chord length
P_s	Freestream static pressure
P_{t_1}	Local total pressure
Q	Freestream dynamic pressure
R_e	Reynolds number, UC/v
s	Local semi span
U	Freestream velocity
u	Velocity component parallel with wing chord
w	Velocity component normal to wing surface
X	Distance from apex parallel with wing chord
Y	Lateral distance from wing root chord

Introduction

One of the most interesting aspects of leading edge vortices is the phenomenon known as vortex breakdown. As the wing angle of attack is increased, vortex breakdown will eventually reach the wing. Vortex breakdown refers to the sudden change in the structure of the vortex. Prior to vortex breakdown, the vortex is a tightly rolled spiralling motion. The vortex core axial velocity can be greater than three times the freestream velocity. However, at breakdown the core flow stagnates, the circumferential velocity decreases and the core size increases. All this occurs over a very short distance.

Figure 1 shows flow visualization photographs that illustrate the change in the vortex structure when breakdown occurs. The two photographs were taken for an 85° leading edge sweep, sharp-edge delta wing. The vortices are visualized by marking the flow with kerosene smoke. The first photograph is illuminated with flood lights and the second photograph shows several cross flow planes of the vortices using a laser light sheet (Ref. 1).

a) Flood lamp b) Laser light sheet

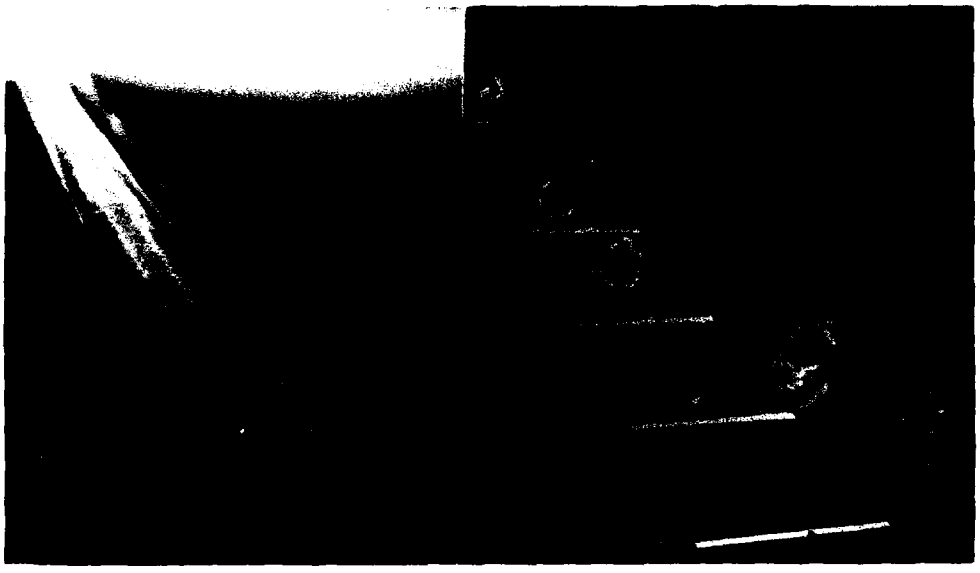


Figure 1. Visualization of leading edge vortices on a sharp-edge delta wing at $\alpha = 40°$.

Despite the growing list of theoretical and experimental investigations of vortex breakdown, there is still no consensus on the primary mechanisms governing the breakdown phenomenon. In addition, many numerical simulations of vortex breakdown on wings are being developed following different approaches and with differing levels of sophistication. All of these require experimental data to check the accuracy of the solution.

Most of the experimental data related to vortex breakdown to date has been obtained in vortex tube experiments. Investigations on delta wings have been generally limited to flow visualization, force balance and surface pressure studies. Quantitative measurements in the vortex flowfield are relatively rare. Only a handful of investigators have attempted multi-hole probe measurements on delta wings. These include Earnshaw (Ref. 2), Hummel (Ref. 3,4), Sforza (Ref. 5,6), Verhaagen (Ref. 7) and Kjelgaard, Sellers and Weston (Ref. 8). Of these, only Hummel looked at vortex breakdown. The majority of the above investigations dealt with only one model at a single angle of attack. Furthermore, all of the wings in the above studies had sweep angles between 75° and 80°.

The available laser Doppler anemometer data is even more scarce. An extensive literature search turned up only three studies reporting LDA measurements on delta wings. These were Chigier (Ref. 9), Anders (Ref. 10), and Vorropoulos and Wendt (Ref. 11).

Clearly, there is a great need for experimental measurements of the vortical flowfield on delta wings, particularly at critical (near breakdown) angles of attack, both for comparison with theory and for comparison with vortex tube experimental results. If measurements are to be taken using a physical probe, the question of probe interference in this type of flow must also be addressed. For the past four years a series of experiments have been conducted in the Aerospace Laboratory at the University of Notre Dame. The objective of these experiments was to develop a detailed data base on the structure of the leading edge vortices for a family of flat plate delta wings at low subsonic speeds. Flow field surveys using both laser doppler anemometry and a seven-hole pressure probe were obtained over an angle of attack range that included vortex breakdown.

Some of the results from this study have been published by Payne, Ng, Nelson and Schiff (Ref. 1), Payne, Ng and Nelson (Ref. 12) and Payne, Ng and Nelson (Ref. 13). The purpose of this paper will be to summarize the findings of the previous investigations as well as including new information from Payne (Ref. 14). The detailed structural

information included in this paper should prove to be invaluable to both theoretical and numerical studies of vortex breakdown.

Experimental Apparatus

Experimental Equipment

Laser Doppler anemometer (LDA) measurements were obtained using a TSI single component system described in Payne et al (Ref. 12). The setup had an estimated measurement probe length of 1 mm and thickness of about 0.14 mm. A single beam frequency shifter was incorporated.

Total pressure, dynamic pressure, and flow angle measurements were taken using a seven-hole probe (SHP). The SHP had a nose diameter of 2.8 mm (0.109 in.) and a nose length of 15.5 cm (6.1 in.). A 90° right elbow connected the nose to a 4.6 mm (0.18 in.) diameter stem.

The SHP was calibrated to pitch and yaw angles of +/-60°, at 5° increments, following the method of Gallington (Ref. 16). The flow angle measurements had a standard deviation of 0.5° at low angles (less than 30°) with a maximum error of 1.0°, and a standard deviation of 0.6° at high angles with a maximum error of 3.5°. The total pressure and dynamic pressure measurements had a standard deviation of 1.0% of the freestream values at low angles with a maximum error of 4.0%, and a standard deviation of 1.5% at high angles with a maximum error of 6.4%.

The experiment was conducted in a subsonic indraft tunnel. The tunnel has a 24:1 contraction inlet and a 182 cm long test section with a 61 x 61 cm square cross section. The freestream turbulence level in the test section is less than 0.1%. For additional information on wind tunnel and experimental equipment the reader is referred to Payne (Ref. 14).

Model

Four thin, sharp-edged delta wings were used in this study. The models each had a root chord of 16 in (406.4mm) and were 1/4 of an inch (6.4mm) thick with sweep angles of 70°, 75°, 80°, and 85°. The leading edge was beveled with a 25° angle so that a sharp-edge was formed on the upper side of the model. The models used in the flow visualization tests, which were run at low speeds, were made of plexiglas and were sting mounted to a support system that provided very little interference to the flow. At speeds higher than about 25 ft/s (7.6 m/s) the plexiglas models were found to bend in the chordwise direction which resulted in reverse camber and a higher than indicated angle of attack. To alleviate this problem a second set of models was constructed identical to the first except that they were constructed of aluminum plate. These models were mounted on a strut connected to the lower surface of the model and were used in all subsequent flow visualization tests and the LDA and SHP wake survey experiments. All models were painted flat black for contrast against the white smoke.

Results

Detailed Velocity Surveys

Detailed velocity distribution of the leading edge vortex field have been obtained by Payne (Ref. 14) and Iwanski (Ref. 15) using laser Doppler anemomentry. Payne made single traverses through the vortex core at several axial locations along two sharp-edged, flat plate delta wings for angle of attack of 10°, 20°, 30°, and 40°. The wings had leading edge sweep angles of 70° and 85° and thickness to chord ratios of t/c = 0.016. Recently Iwanski (Ref. 15) studied the flow field above a sharp-edge delta wing having a leading edge sweep of 70° and t/c = 0.063 for 30° angle of attack. Iwanski conducted detailed wake surveys of the velocity components parallel and normal to the wing's surface at various positions along the wing. The grid surveys included spanwise traverses at 14 vertical positions at the various survey planes along the wing.

Figure 2 is a sketch showing the approximate positions of the survey planes relative to the vortex breakdown. In interpreting these data one should keep in mind the breakdown position is not stationary. The spanwise variation of the parallel and normal velocity components through the leading edge vortex above a sharp-edge delta wing having a leading edge sweep of 70° is shown in Figures 3 and 4 for various chordwise positions along the wing.

In Figure 3a upstream of the breakdown (x/c = 0.412 and 0.448) the parallel velocity component within the vortex is similar to a jet-like flow. The peak parallel velocity occurs at the center of the vortex and is approximately three times the freestream velocity. The jet-like region is approximately 0.5 semi-span wide. The first indication that vortex breakdown is about to occur is the deceleration of the core flow at (x/c = 0.484). After breakdown (x/c > 0.521) a wake-like velocity defect appears in the parallel velocity profile. The wake defect region is approximately 0.3 of a semi-span wide at x/c = 0.521 and broadens with increasing distance downstream. This velocity profile is consistent with the flow visualization results which show a bubble type breakdown.

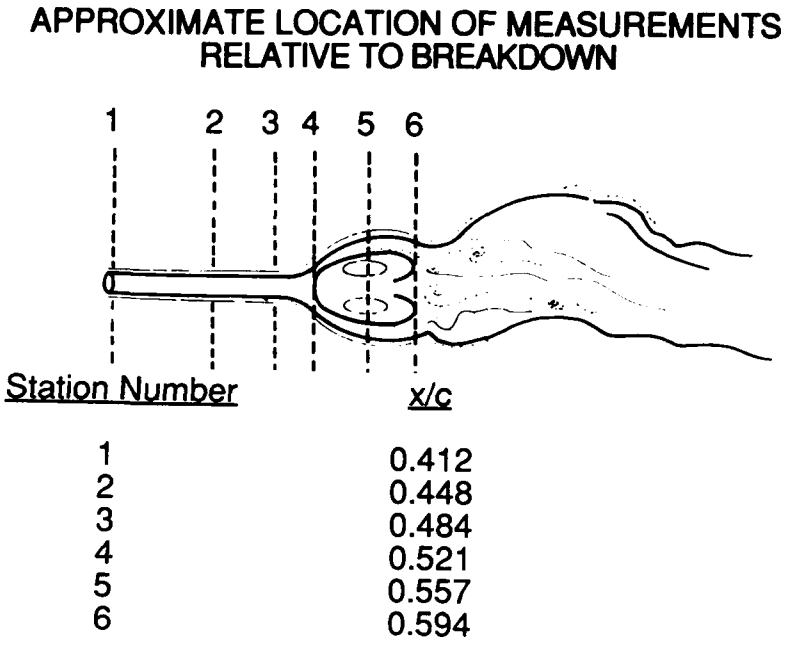


Figure 2. Relative position of wake surveys to vortex breakdown position.

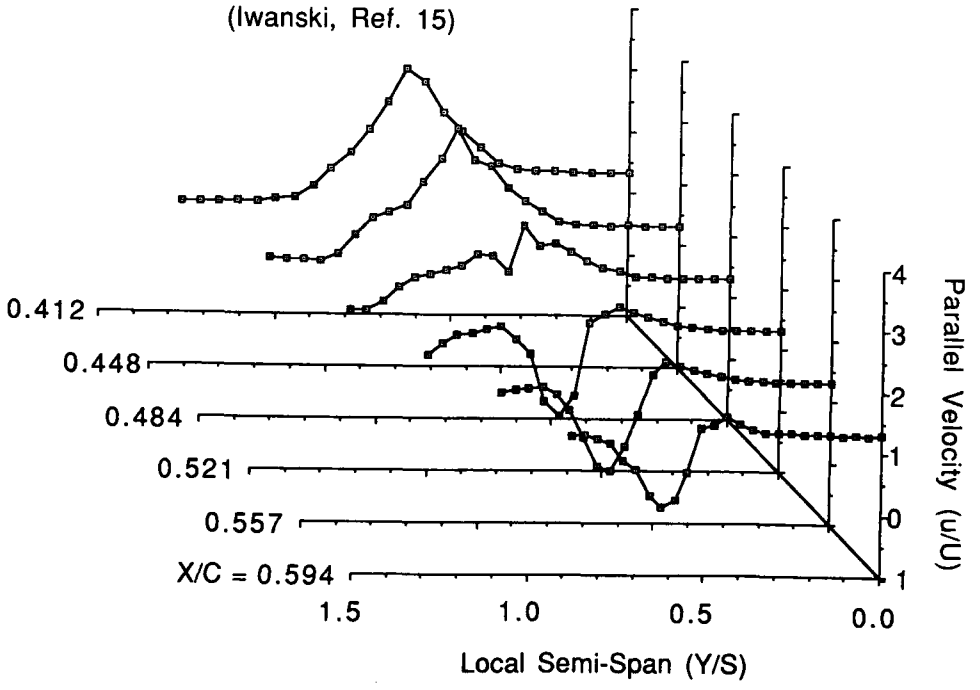


Figure 3a. Non-dimensional parallel velocity component (Λ_{LE} = 70°, t/c = 0.063, (R_e = 150,000, α = 30°).

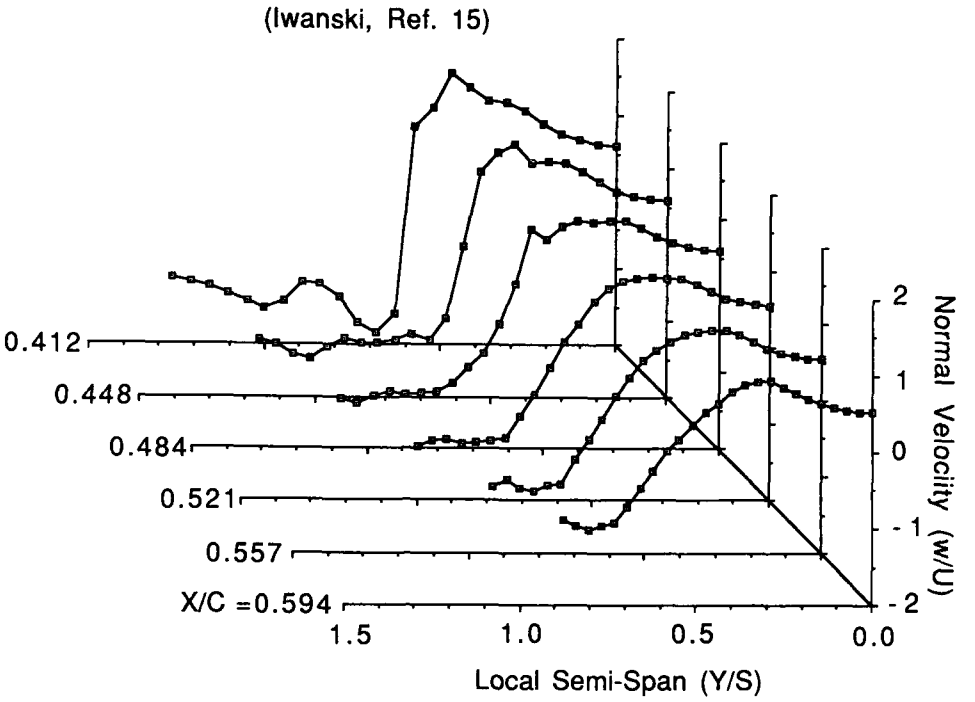


Figure 3b. Nondimensionalized normal velocity component (Λ_{LE} = 70°, t/c = 0.063, R_e = 150,000, α = 30°).

The normal velocity component is shown in Figure 3b. The peak normal velocity prior to breakdown is approximately 1.5 times the freestream velocity and after breakdown it is approximately equal to the freestream. Before breakdown the subcore region is small as indicated by the steep velocity gradient. However, after breakdown there is a reduction in the normal velocity component and a rapid diffusion of the subcore. The subcore region expands from approximately 20% of the local semi-span before breakdown to nearly 50% of the local semi-span after breakdown (x/c = 0.594).

Vortex trajectories

The vertical height of the vortex above each model was determined from a flow visualization experiment. Smoke was entrained into the vortex cores making them visible. The center of the core could be identified by a dark region void of smoke. The seven-hole probe was lowered at the center plane of the model (y/s = 0.0) until it was (visually) aligned with the dark zone on the vortex axis. The height of the vortex could then be read off the computer terminal controlling the probe. Since the probe was at the center of the model and not actually in the vortex there was no interference and the height of the vortex was determined.

With the vertical height of the vortex known from the above experiments, a set of single, spanwise traverses was made with the SHP on each model from y/s = 0.0 to 1.2 at the measured height of the vortex center. These measurements were made at chordwise stations (x/c) of 0.167, 0.333, 0.500, 0.667, and 0.833, and for angles of attack of 10°, 20°, 30° and 40°. After the data was reduced, the spanwise position of the vortex could be determined by noting the location where the normal velocity crossed over from a negative to a positive value.

In general, the vortex height above the model increased with angle of attack and the spanwise location was approximately constant with angle of attack. The nondimensional vertical and spanwise location was also relatively constant with chordwise position. The absolute accuracy of the vortex position measurements was estimated to be about 2 to 5 millimeters and is the same for the four models tested. In terms of percent of local semi-span the error is therefore smallest on the 70° wing and greatest on the 85° wing.

There was some concern that the presence of the probe might cause a change in the spanwise position of the vortex. In fact, it was determined from the wake surveys that the probe would "push" the vortex slightly in the direction of the probe movement. The amount of displacement was small amounting to +/- 1mm or about 3% of the local semi-span on the 70° wing at x/c = 0.500 or about 10% of the local semi-span on the 85° wing at x/c = 0.500. To investigate this question further the spanwise position of the vortices on each wing at 30° angle of attack was determined from longitudinal cross section laser sheet photographs. A comparison of the spanwise locations determined both from the probe measurements and from the flow visualization photographs is presented in Figures 4a-4d. There is good agreement between the two methods on all except for the 85° wing. On this wing (Figure 4d) the difference between the two methods is about 20 percent of the semi-span at x/c = 0.333. It should be noted, however, that 20% of the semi-span at this station on the 85° wing amounts to 2.34 millimeters which is less than one probe diameter. For this reason it was extremely difficult to make accurate measurements with respect to spanwise position on the 85° wing.

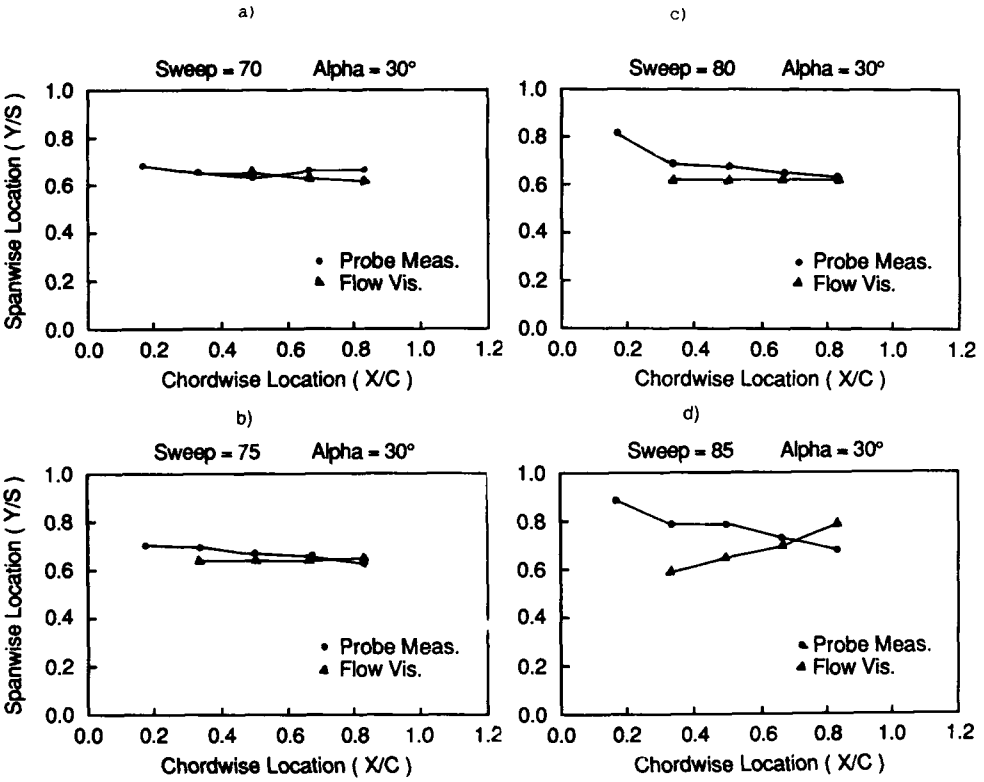


Figure 4. Comparison of methods for determining vortex core location.

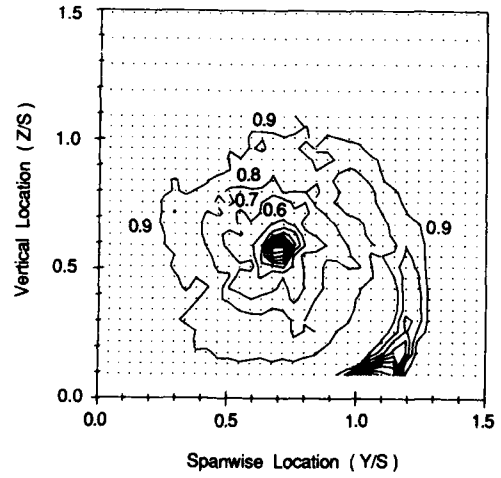
Reynolds Number Effects

To investigate the influence of Reynolds number, wake surveys were made on the 85° wing at 20° angle of attack at x/c = 0.833 for freestream velocities of 30 ft/s, 50 ft/s, and 75 ft/s. In terms of chord Reynolds number these velocities correspond to 2.54×10^5, 4.24×10^5, and 6.36×10^5 respectively.

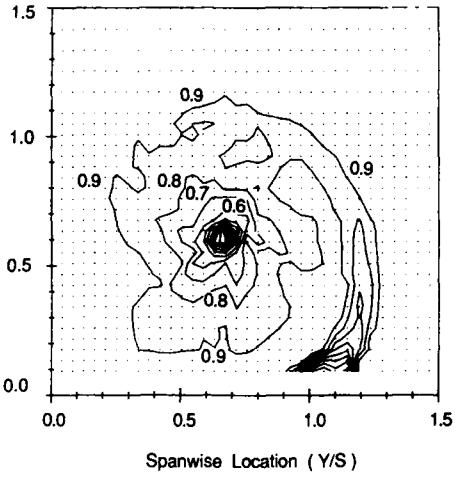
The wake survey plots for these tests are presented in Figures 5a-5c (total pressure coefficient), and 6a-6c (velocity component parallel to the wing surface). There was little or no change in the spanwise and vertical position of the vortex with increasing Reynolds number. However, a reduction in minimum total pressure coefficient was measured as well as an increase in maximum parallel velocity ratio. The maximum nondimensional parallel velocity increased 12% from u/U = 1.49 at $Re_c = 2.5 \times 10^5$ to u/U = 1.67 at $Re_c = 6.36 \times 10^5$. A similar result was reported by Werle (Ref. 17) in experiments with a 75° delta wing at 35° angle of attack. Werle found that the maximum core velocity increased 16% from u/U = 2.45 to u/U = 2.85 when the Reynolds number was increased from 2×10^4 to 4×10^4.

Kjelgaard, et al (Ref. 8), studied the flow past a 75° sweep delta wing at 20.5° angle of attack at Reynolds numbers of 0.5 x 10^6 to 2.0 x 10^6. Pitot pressure surveys and two types of flow visualization were conducted. Kjelgaard found that the vortex core location is relatively insensitive to Reynolds number in the range tested. In Figure 7, Kjelgaard's results are compared with the vortex core locations from the present study which were obtained at a Reynolds number of 2.5 x 10^5 . The comparison shows that the change in vortex location with Reynolds number in the range 2.5 x 10^5 to 2.0 x 10^6 is small.

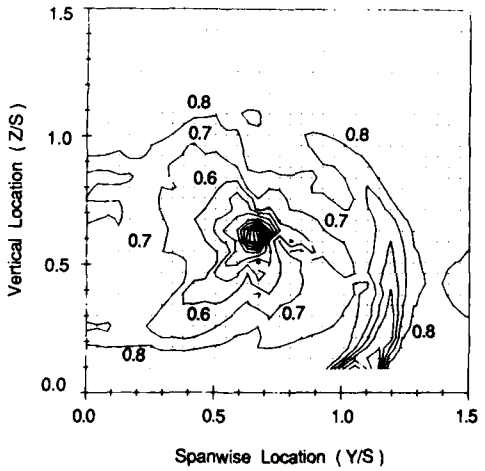
Kjelgaard also found that the maximum total pressure deficit in the vortex core was independent of Reynolds number in the range 0.5 x 10^6 to 2.0 x 10^6. Contours of pitot pressure deficit divided by freestream dynamic pressure are presented in Kjelgaard's paper with a maximum value greater than 4.5 in the core at x/c = 0.500. If the minimum total pressure coefficient in the corresponding wake survey of the present study is converted to total pressure deficit divided by dynamic pressure, a value of 2.72 is obtained at x/c = 0.500 for the 75° wing at 20° angle of attack and a Reynolds number of 2.5 x 10^5. The large difference in total pressure deficit between the two studies can at least partially be attributed to Reynolds number effects since a significant change in core total pressure was noted in the present study on the 85° wing at 20° angle of attack over a similar Reynolds number range of 2.5 x 10^5 to 6.4 x 10^5. In addition, the Kjelgaard results were obtained with a boundary layer probe aligned with the freestream and so was not capable of measuring the true total pressure.



a) U = 30 ft/sec. (9.1 m/sec)



b) U = 50 ft/sec. (15.2 m/sec)



c) U = 75 ft/sec. (22.9 m/sec)

Contour Increment = 0.10

Minimum Pressure Coefficient and Location

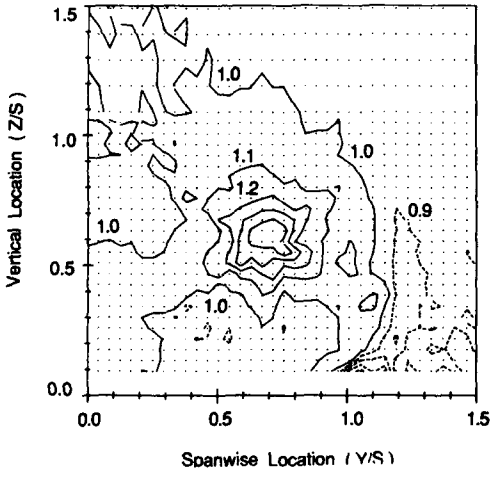
	U(ft/sec) 30 (9.1)	50 (15.2)	(m/sec) 75 (22.9)
$C_{P_{min}}$	-0.04	-0.17	-0.40
Z/s	0.59	0.63	0.63
Y/s	0.67	0.67	0.67

Figure 5. Contours of total pressure coefficient (Λ_{LE} = 85°, α = 20°, x/c = 0.833).

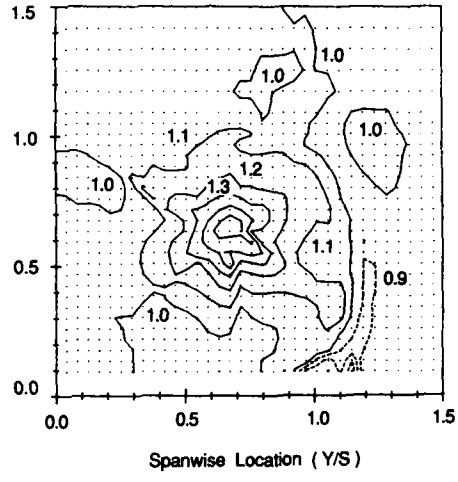
It is interesting to note that the shape of the total pressure contours in the present study changed with increasing Reynolds number. At 30 ft/s ($Re_c = 2.5 \times 10^5$) the contours were essentially round as in Figure 5a. However, as the freestream velocity was increased to 75 ft/s ($Re_c = 6.4 \times 10^5$), the contours took on a more asymmetric elliptic shape and a large gap develops in the feeding sheet above, and slightly outboard of, the vortex core where the total pressure recovers to near the freestream value as shown in Figure 5c. This gap is also evident in the total pressure deficit contours of Kjelgaard at $Re_c = 1.0 \times 10^6$.

In summary, the Werle tests ($2 \times 10^4 < Re_c < 4 \times 10^4$) (Ref. 17), the present tests ($2.5 \times 10^5 < Re_c < 6.4 \times 10^5$), and the Kjelgaard study ($5.0 \times 10^5 < Re_c < 2.0 \times 10^6$) (Ref. 8), indicate that there is little Reynolds number effect on vortex core location in the range 2.5×10^5 to 2.0×10^6 and little or no effect on core total pressure in the range 5.0×10^5 to 2.0×10^6, but there is significant Reynolds number effect on core total pressure and maximum velocity at Reynolds numbers below 5.0×10^5.

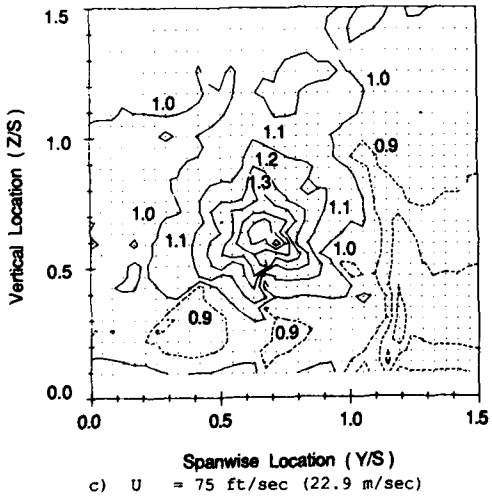
Another matter related to Reynolds number is the question of whether or not a particular form of breakdown is favored at high Reynolds numbers. It is often mentioned in the literature that the spiral form seems to be more prevalent in wind tunnel tests and on aircraft in flight. However, the source of this information is rarely identified. In fact, most wind tunnel and flight test studies report only under what conditions a breakdown was observed and do not attempt to identify the type.



a) U = 30 ft/sec (9.1 m/sec)



b) U = 50 ft/sec (15.2 m/sec)



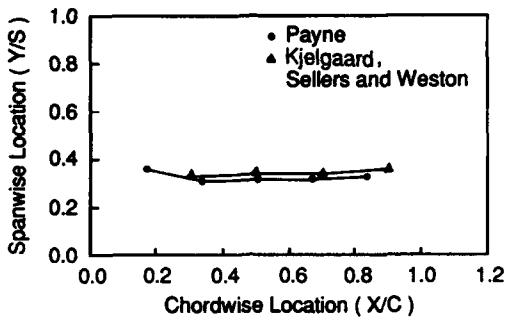
c) U = 75 ft/sec (22.9 m/sec)

Maximum u/U and Position

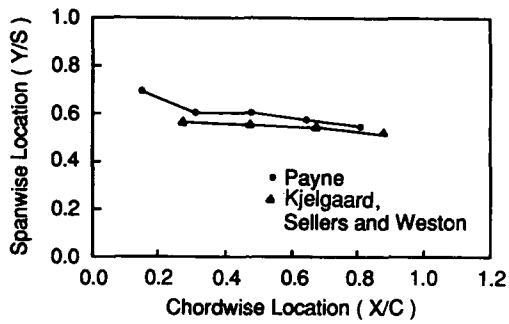
	U(ft/sec) 30 (9.1)	50 (15.2)	(m/sec) 75 (22.9)
u/U	-0.17	-1.56	-0.67
Z/s	0.63	0.67	0.59
Y/s	0.67	0.67	0.71

Contour Increment = 0.1

Figure 6. Contours of nondimensional parallel velocity ($\Lambda_{LE} = 85°$, $\alpha = 20°$, x/c = 0.833).



a) Vertical position



b) Spanwise position.

Figure 7. Comparison of vortex core locations on 75° delta wing at 20° angle of attack.

A survey of the literature revealed very few studies in which the breakdown form was identified on delta wings or related configurations. The great majority of cases in which the form was identified was in water tunnel experiments. Lambourne and Bryer (Ref. 18) identified both a spiral and bubble type breakdown on a delta wing in a water tunnel study at a chord Reynolds number of approximately 1.1×10^4. Lowson (Ref. 19) reported both spiral and bubble forms in a water tunnel test on a delta wing at $Re_c = 3.0 \times 10^4$ and Anderson (Ref. 20) saw both forms in water tunnel tests of delta wings at $Re_c = 3.0 \times 10^4$ to 5.7×10^4.

Wind tunnel studies in which the breakdown form is identified are even more scarce. The flow visualization results presented in this study at $Re_c = 8.5 \times 10^4$ indicate the presence of both forms of breakdown. Cunningham (1985) reported a spiral type breakdown on a cranked delta wing with $Re_c = 5 \times 10^5$ and Wentz (1971) reported a "coiling core" associated with breakdown on a delta wing with a smooth upper surface at $Re_c = 1.0 \times 10^6$. When distributed roughness was added to the surface of the wing in Wentz's experiment the coiling pattern did not appear, possibly indicating that the breakdown form was now a bubble.

Vortex tube experiments have shown that the breakdown type is a function of tube Reynolds number and swirl angle. Presumably then, both the bubble and spiral forms are possible at any Reynolds number and which will occur is configuration dependent. It has also been shown that the spiral is the milder form of breakdown. It is possible that this form is more commonly observed on aircraft simply because most aerodynamic configurations in use today are designed to operate in flow regimes conducive to a mild breakdown.

Swirl Angle

The helix or swirl angle in a vortex is defined as $\phi = \arctan(w/u)$, where w is the circumferential velocity and u is the axial velocity. In an isolated vortex, the swirl angle is zero on the vortex axis and increases in the radial direction to a maximum at the outer edge of the viscous subcore before decreasing to zero with increasing distance from the axis. In a leading edge vortex, the maximum swirl angle may occur near the leading edge where the axial flow may be relatively slow compared with the circumferential component. However, it is the swirl angle at the edge of the viscous subcore which is important and it is usually this value which is referred to as the maximum swirl angle.

It has been shown by Hall (Ref. 23) that the combination of axial and rotational motions in a vortex gives it a highly responsive character. There is a strong interaction between the different flow components which results in marked responsiveness of the vortex to changes in the surrounding flow. A small change in axial velocity along the outside of a vortex results in a more pronounced change in velocity along the axis with the magnitude of the effect being dependent on the swirl angle. The larger the value of swirl the greater the effect.

As the angle of attack of a delta wing is increased the vortex becomes stronger and the swirl angle increases. The chordwise pressure gradient also becomes more adverse. The increasing pressure is communicated to the vortex axis which causes the axial flow in the core to decelerate. According to the various breakdown theories, the core flow will eventually either stagnate or establish the conditions at which a critical transition can take place which permits disturbance waves to propagate upstream. In either case the result is vortex breakdown.

Some authors have suggested that there is a critical swirl angle which will result in breakdown. Criteria have been developed following various approaches. Based on a theoretical analysis, Squire (Ref. 24) formulated a condition for the appearance of standing waves in an inviscid vortex and concluded that the swirl angle is the only characteristic parameter determining whether breakdown will occur and, depending on the upstream swirl velocity distribution, the critical swirl angle would fall in the range 45.0° to 50.2°. Ludwieg (Ref. 25) applied a stability criterion to the profiles of leading edge vortex flows obtained theoretically and found that the flow becomes unstable if the swirl angle exceeds 48.0°.

Several authors have computed the maximum swirl angle which will occur before breakdown with numerical solutions of the equations of motion. Bossel (Ref. 26) obtained a solution for vortex flow including breakdown by reducing the Navier-Stokes equations to three different approximating systems in four distinct regions of a vortex having large swirl. Bossel computed a maximum swirl angle for breakdown of 62.5°. Grabowski (Ref. 27) obtained numerical solutions of the full steady axisymmetric Navier-Stokes equations for breakdown in an unconfined viscous vortex for Reynolds numbers up to 200. Based on the calculations the swirl angles corresponding to solutions exhibiting stagnation on the axis varied between about 44° and 51°.

The maximum swirl angle upstream of breakdown has been measured in vortex tube experiments by several authors. Harvey (Ref. 28) measured a maximum angle of 50.5° upstream of a bubble type breakdown using a smoke flow visualization technique. Kirkpatrick (Ref. 29) measured a maximum swirl angle of 49.5° upstream of a breakdown using a small pressure probe. Sarpkaya (Ref. 30) obtained the velocity profiles upstream of several forms of breakdown with a laser Doppler anemometer and calculated the maximum swirl angles. Sarpkaya found that the swirl angle distribution was a function of the breakdown form. For spiral breakdown the maximum swirl angle varied from about 38° to 55° depending on the intensity of the circulation. For the axisymmetric (bubble) form the maximum angle was about 50°. In a similar experiment, Garg, et al (Ref. 31) obtained LDA measurements upstream of the spiral and bubble forms of breakdown and determined the swirl angles. Garg also found that the maximum swirl angle was a function of breakdown form. The maximum angle upstream of a spiral type breakdown was found to be in the range 43.8° to 46.0°, whereas the maximum angle upstream of a bubble type breakdown was in the range 49.7° to 52.2°.

Hummel (Ref. 3) was the only author found to have measured the swirl angle upstream of breakdown in a vortex on a delta wing. Hummel obtained five-hole probe measurements upstream of breakdown on a 79° sweep delta wing at 31° angle of attack and found the maximum swirl angle was 53.0°.

The reported differences in maximum swirl angle measured upstream of breakdown make it unlikely that the occurrence of breakdown could be predicted as a function of swirl angle alone. The fact that the bubble and spiral forms of breakdown have been shown to occur with different ranges of swirl angle shows that other factors are important. Nevertheless, swirl angle is a significant parameter and it has been shown that breakdown will not occur unless the swirl angle exceeds about 40°. Above that angle the occurrence and type of breakdown is apparently a function of swirl angle, pressure gradient and vortex Reynolds number as has been shown in vortex tube experiments.

The swirl angle distribution at six stations in the vicinity of vortex breakdown on the 85° delta wing at 40° angle of attack was calculated from the LDA velocity profiles. The six stations are x/c = 0.550, 0.600, 0.650, 0.675, 0.700, and 0.750. For convenience, the swirl angle was approximated in the calculations by using the ratio of normal to parallel velocities (with respect to the wing) instead of the ratio of axial to circumferential velocities (with respect to the vortex). The resulting distributions of swirl angle are presented in Figures 8a to 8f.

If the location of vortex breakdown is defined as the point at which the core flow stagnates, then the measurements at x/c = 0.600 may be considered "upstream of breakdown". A deceleration of the core flow is occurring at that location, however the flow has not yet completely stagnated. The maximum swirl angle at the edge of the subcore upstream of breakdown would, therefore, be about 44° from Figure 8b. As shown in Figures 8c to 8f the swirl angle in the breakdown region reaches almost 90°. The changes in sign of the swirl angle in the subcore region are due both to the reversal of parallel velocity and to the cross over of normal velocity from one side of the vortex to the other.

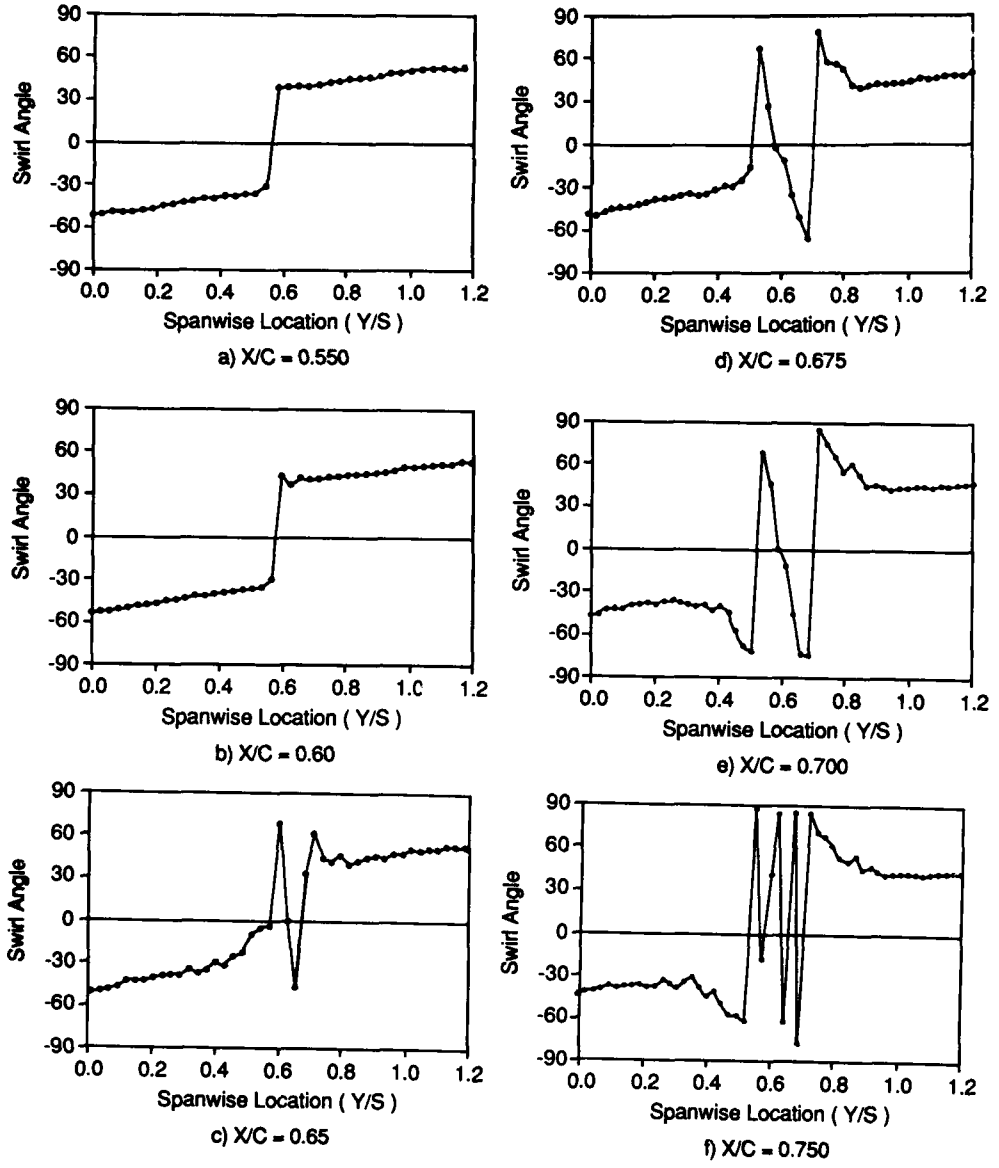


Figure 8. Swirl angle distribution.

Concluding Remarks

The structure of the leading edge vortex on a family of delta wings was studied using flow visualization, laser Doppler velocimetry, and a seven-hole probe. Vortex trajectories, Reynolds number effect, and swirl angles before and after vortex breakdown were investigated. Detailed velocity and pressure surveys reveal details of the leading edge vortex structure before and after breakdown. The information obtained in this study represent a large quantitative data base which should be valuable for computational models of leading edge vortices.

REFERENCES

1. Payne, F.M., Ng, T.T., Nelson, R.C., and Schiff, L.B., "Visualization and Wake Surveys of the Vortical Flow over a Delta Wing , to appear in AIAA Journal, January 1988.

2. Earnshaw, P.B., "An Experimental Investigation of the Structure of a Leading-Edge Vortex", R.A.E. Tech. Note No. Aero. 2740, March 1961.

3. Hummel, D., "Research on Vortex Breakdown on Slender Delta Wings", Zeitschrift fur Flugwissenshaften, 13, 5, Aircraft Research Association Ltd., Bedford Library Translation No. 12., May 1965.

4. Hummel, D., "On the Vortex Formation Over a Slender Wing At Large Angles of Incidence", AGARD-CP-247, Oct. 1978.

5. Sforza, P. M., Stasi, W. Pazienza, J., and Smorto, M., "Flow Measurements in Leading Edge Vortices", AIAA-77-11, January 1977.

6. Sforza, P. M., and Smorto, M. J., "Streamwise Developement of the Flow over a Delta Wing", AIAA-80-0200, January 1980.

7. Verhaagen, N.G., and Kruisbrink, A.C., "The Entrainment Effect of a Leading Edge Vortex", AIAA-85-1584, July 1985.

8. Kjelgaard, S.O., Sellers, W.L., and Weston R.P., "The Flowfield Over A 75 Degree Swept Delta Wing at 20.5 Degrees Angle Of Attack", AIAA-86-1775, June 1986.

9. Chigier, N.A., "Measurement of Vortex Breakdown Over a Delta Wing Using a Laser Anemometer", Nielson Engineering, NEAR TR 62, June 1974.

10. Anders, K., "LDV Measurements of the Velocity Field of a Leading Edge Vortex Over A Delta Wing Before and After Vortex Breakdown", Von Karmen Inst. Tech. Note 142, March 1982.

11. Vorropoulos, G., and Wendt, J.F., "Preliminary Results of LDV Surveys in the Compressible Leading Edge Vortex of a Delta Wing", Von Karman Inst., Tech. Note 137, Aug. 1982.

12. Payne, F.M., Ng, T.T., and Nelson, R.C., "Experimental Study of the Velocity Field on a Delta Wing", AIAA Paper 87-1231, June 1987.

13. Payne, F.M., Ng, T.T., and Nelson, R.C., "Seven-Hole Probe Measurement of Leading Edge Vortex Flow", to be published in the Experiments in Fluids.

14. Payne, F.M., "The Structure of Leading Edge Vortex Flows Including Vortex Breakdown", Ph.D. Dissertation, University of Notre Dame, Notre Dame, Indiana, 1987.

15. Iwanski, K. P., "An Investigation of the Vortex Flow Over a Delta Wing With and Without External Jet Blowing", Masters Thesis, University of Notre Dame, Notre Dame, Indiana, 1988.

16. Gallington, R. W., "Measurement of Very Large Flow Angles With Non-Nulling Seven-Hole Probes", USAF-TR-80-17, 1980.

17. Werle, H., "On Vortex Bursting", ONERA-NT 175, 1971.

18. Lambourne, N.C., and Bryer, D.W., "The Bursting of Leading-Edge Vortices - Some Observations and Discussion of the Phenomenon", A.R.C., R.& M. No. 3282, April 1961.

19. Lowson, M.V., "Some Experiments with Vortex Breakdown", J. of the Royal Aero. Soc., Vol. 68, May 1964.

20. Anderson, W.V., Beran, P.S., and McCann, M.K., "Vortex Breakdown Over Delta Wings", Grad. Aero Lab., California Inst. Tech., Pasadena, CA, May 1983.

21. Cunningham, A.M., "Vortex Flow Hysteresis", NASA-CP-2416, No. 11, Oct. 1985.

22. Wentz, W.H., and Kohlman, D.L., "Vortex Breakdown on Slender Sharp-Edged Wings", J. Aircraft, Vol. 8, No. 3, March 1971.

23. Hall, M.G., "Vortex Breakdown", Ann. Rev. Fluid Mech., Vol. 4, 1972.

24. Squire, H.B., Imperial College, London, Dep. of Aero. Rept. No. 102, 1960.

25. Ludwieg H., "Zur Erklarung der Instabilitat der uber angestellten Deltaflugeln auftretenden freien Wirkbelkerne", Z. Flugw. 10., 1962.

26. Bossel, H.H., "Stagnation Criterion for Vortex Flows", AIAA Journal, Vol. 6, No. 6, June 1968.

27. Grabowski, W.J., and Berger, S.A., "Solutions of the Navier-Stokes Equations for Vortex Breakdown", J. Fluid Mech., Vol. 75, 1976.

28. Harvey, J.K., "Some Observations of the Vortex Breakdown Phenomena", J. Fluid Mech., Vol. 14, 1962.

29. Kirkpatrick, D.L.I. "Experimental Investigation of the Breakdown of a Vortex in a Tube", Aeronautical Research Council Current Papers, May 1964.

30. Sarpkaya, T., "On Stationary and Travelling Vortex Breakdowns", J. Fluid Mech., Vol. 45, Part 3, 1971(a).

31. Garg, A.K., and Leibovich, S., "Spectral Characteristics of Vortex Breakdown Flowfields", Phys. of Fluids, Vol. 22, No. 11, Nov. 1979.

Acknowledgments

This research was supported by NASA Ames Research Center, Moffett Field, CA, under grant number NAG-2-258 and the University of Notre Dame, Notre Dame, IN.

A THEORETICAL AND EXPERIMENTAL EVALUATION OF A NUMERICAL METHOD FOR CALCULATING SUPERSONIC FLOWS OVER WING-BODY CONFIGURATIONS

by

J. L. Fulker and P. R. Ashill
Royal Aircraft Establishment, Bedford, MK44 6AE, UK

SUMMARY

A method of solving the Euler equations is described and is applied to the calculation of supersonic flows over two wing-body configurations typical of present day combat aircraft. A 'multiblock' method is used to generate body-conforming grids for the complex three-dimensional geometries of the configurations and the flow equations are solved by applying time-stepping to a finite-volume algorithm. An assessment is made of the theoretically predicted flows, by demonstrating the effect on the solution of some of the important features of the CFD method. Results are given for a series of careful wind-tunnel tests on models of similar geometry, and comparisons between calculated and measured results are shown.

LIST OF SYMBOLS

A	axial force, defined positive downstream
AR	wing aspect ratio
$\bar{c}$	geometric mean chord of wing
c_o	wing root chord
C_A	axial force coefficient, $A/\frac{1}{2}\gamma p_\infty M_\infty^2 S$
$C_A(x)$	local axial-force coefficient
C_D	drag coefficient, $D/\frac{1}{2}\gamma p_\infty M_\infty^2 S$
C_L	lift coefficient, $L/\frac{1}{2}\gamma p_\infty M_\infty^2 S$
C_M	pitching moment coefficient, $M/\frac{1}{2}\gamma p_\infty M_\infty^2 S\bar{c}$
C_N	normal force coefficient, $N/\frac{1}{2}\gamma p_\infty M_\infty^2 S$
$C_N(x)$	local normal-force coefficient
C_p	static pressure coefficient
D	drag
L	overall lift
M	overall pitching moment; positive nose up and relative to the datum point shown in Fig 4
M_∞	free-stream Mach number
N	normal force
p_∞	pressure far upstream
$R_{\bar{c}}$	Reynolds number based on wing geometric mean chord
S	gross wing planform area (Fig 4)
s	semi-span of wing
t	time
x, y, z	right-handed Cartesian coordinate system, x positive downstream with origin as shown in Fig 4
α	angle of incidence
Δ	incremental part of
η	non-dimensional spanwise distance, y/s
ρ	density
$\bar{\rho}$	mean density ratio

SUFFIXES

NET	net wing
W	wing alone
o	zero lift

1 INTRODUCTION

Rapid advances in computer technology in recent years allied with improved flow algorithms means that flow calculations for realistic aircraft configurations can be contemplated. However the aim of Computational Fluid Dynamics (CFD) to solve the full equations of motion over a complex configuration such as shown in Fig 1 is not achievable at present and some simplifications have to be made either to the flow equations or the configuration or both.

A significant step in the direction of modelling complex flows over realistic configurations is provided by the Euler-Multiblock code developed jointly by British Aerospace, Filton and the Aircraft Research Association, Bedford. In principle, Euler solvers are able to represent changes in flow quantities across shock waves and the multiblock technique can provide grids for relatively complex configurations such as those shown in Fig 2, taken from Ref 1. As the name suggests, the multiblock scheme divides the flow field into a series of blocks within which grids are generated conforming to the

neighbouring aircraft surface and between which they are continuous. A finite-volume algorithm for solving the Euler equations, based on that of Ref 2, is adapted for use in the context of the multiblock scheme.

Before the Euler-Multiblock scheme can be used routinely for performance prediction and design, it must be validated rigorously for a wide range of configurations. The results presented are a validation of the method for two wing-body combat-aircraft configurations intended for efficient 4g manoeuvre at $M_\infty = 1.6$ at the tropopause. Both configurations have quasi-delta wings of 4% thickness/chord ratio and 60° leading-edge sweep but with differing cambers. The assessment of the method is based on a study of the sensitivity of the results to the numerical approximations and comparisons of the solutions with measurements from a series of carefully-controlled wind-tunnel tests.

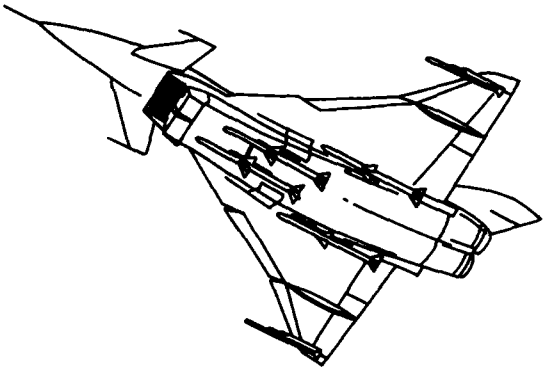


Fig. 1 The ultimate goal for CFD ?

The paper is divided into two halves. In the first half, a description of the method in section 2 is followed by a discussion of the evaluation of the numerical approximations in section 3.

The second half commences in section 4 with a description of the wind-tunnel tests, continues with a discussion of comparisons between predictions of wing pressure distributions and overall forces, and draws conclusions from the study in section 6.

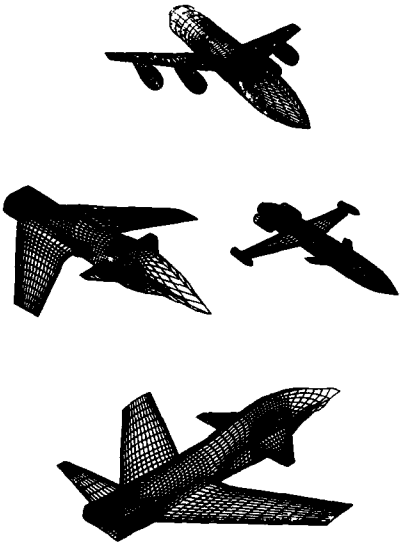


Fig.2 Typical surface grids for a variety of aircraft configurations from Ref. 1

2 EULER-MULTIBLOCK SYSTEM

The multiblock system evaluated in this paper[1,4] employs body-conforming grids for complex three-dimensional geometries and combines this with a finite-volume flow algorithm for solving the Euler equations. The entire flow-field between the configuration surface and a far-field boundary is divided into a set of blocks within which the grid systems conform to the boundary surfaces and between which the grids are continuous. The blocks fill the entire flow field with no voids or overlaps. Each block is topologically equivalent to a cuboid and can thus be mapped into a unit cube in the computational space.

Block boundaries coinciding with the surfaces of the configuration or an outer boundary have a grid imposed upon them by a surface-grid generator as shown in Figs 2 and 3. All other block boundaries are purely notional, having no physical significance.

The position of points in the field are determined by the solutions of the three-dimensional elliptic grid-generation equations and, in a similar manner to the development of the surface grid, the equations are solved iteratively using a point over-relaxation scheme.

The block-structured flow-algorithm for solving the Euler equations uses a scheme described by Jameson et al[2], which applies time-stepping to a finite volume algorithm. In order to achieve satisfactory levels of convergence, residual smoothing is employed[5]. By smoothing the residuals, the restriction on the time step imposed by the Courant-Friedrichs-Levy (CFL) condition is relaxed.

A modified formulation of the artificial-dissipation model[6] has been employed as this improves the definition of predicted pressure peaks and shock waves and results in closer agreement between prediction and measurement.

3 EVALUATION OF THE NUMERICAL APPROXIMATIONS

In assessing the method, the sensitivity of the solution for the flow over the configuration shown in Fig 4 (wing A described in more detail later) to changes in various parameters has been determined for $M_\infty = 1.6$. Spanwise pressure distributions are compared at positions defined in terms of axial distance from the virtual apex of the wing, x/c_0. All of the calculations use the same residual smoothing and artificial-dissipation parameters and no enthalpy damping[2]. The only changes made to improve the quality of the results have been in the grid generation scheme.

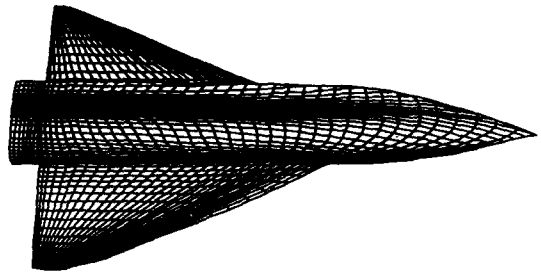


Fig. 3 Typical surface grid for the present configuration

3.1 BLOCK TOPOLOGY

The subdivision of the flow domain into blocks enables grid structures (topologies), to be constructed which are compatible with each component of the configuration. The grid is constructed using combinations of the three basic building units, O-grid, C-grid and H-grid around the configuration. O-grids have the attraction that they are computationally efficient[7], requiring fewer grid points to represent the solution in the same volume, but they are difficult to construct around some geometric surfaces. C-grids are less efficient than O-grids but they are structurally suited to wing sections and wakes. H-grids are the least efficient but topologically simplest in that the structure is created by perturbation of a Cartesian mesh. Three different topologies have been assessed for the wing-body configuration of interest. The grid types used to construct the three topologies are given in the following Table.

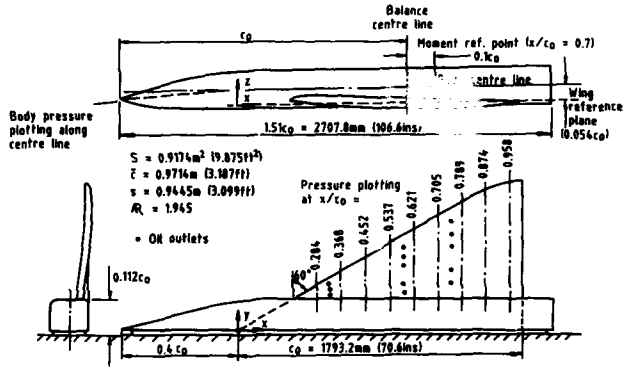


Fig.4 General layout of model showing pressure plotting locations

Topology	Structure Around Chordwise Section of Wing	Structure Around Spanwise Section of Wing	Structure Around Body Cross-Section	Structure Around Axial Sections of Forebody	Number of Blocks
A	'C'	'H'	'H'	'C'	24
B	'C'	'H'	'O'	'C'	42
C	'C'	'H'	'O'	'H'	106

Topology A is the classic 'squashed-body' grid obtained from a single block mapping between computational and physical space, and serves as a test case for investigating the component adaptive grid structures denoted by topologies B and C. Topologies B and C both have O-grids enclosing the body in planes normal to the body axis but differ in the axial grids used for the forebody.

Block subdivisions were chosen such that the three topologies have approximately the same number of grid cells. The surface grid on the wing for topology A has 14 cells across the span at each section of the wing and 39 cells along each chord, ie a total of 14 x 39 = 546 cells. Owing to the efficiency of the O-grid structure around the body, however, topologies B and C have more grid points in the spanwise direction on the wing surface and therefore have 18 by 39 grids. This grid will be referred to as the 'coarse' grid in later discussion of topology C. The differences between the topologies are shown in Figs 5 and 6. Fig 5 compares plan views of the grid structures and indicates that topology A can be thought of as a set of two-dimensional grids stacked spanwise with some perturbation of the spanwise coordinate to allow for the body. Topology B has a singular line in the field, S , at the junction of five blocks. Topology C overcomes this feature with two singular lines, forward, above and below the leading edge (not shown here). Since the flow algorithm is based on a 'cell-centred' scheme, singular lines do not affect the solution directly. However, their presence influences the general quality of the grid. Nevertheless, it is considered that the singular lines are far enough away from the configuration so as not to affect the solution on the surface.

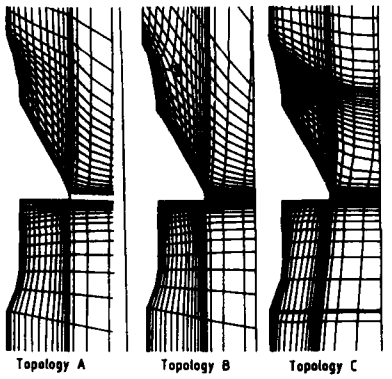
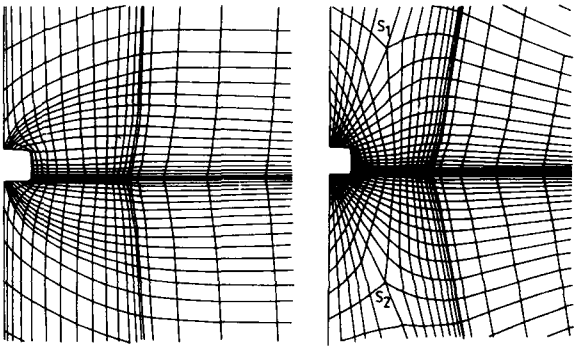


Fig.5 Plan views of field grids in vicinity of the configuration for various topologies



(a) Topology A (b) Topologies B and C

Fig.6 Cross sections of field grids showing differing grid structures for various topologies

Fig 6a and b are views of coordinate-surfaces at approximately-constant axial positions which show the differences between the grid structures around the body. In topology A the grid cells near the body are larger than would be considered ideal and are highly skewed relative to the body surface. Distinct advantages can be seen for the O-grid structure around the body in topologies B and C, with none of the apparent weaknesses of topology A. However, this is at the expense of two singular lines, S_1 , and S_2 in the field, although there is no evidence that they affect the solution on the surface.

Pressure distributions calculated for the various topologies are shown in Fig 7. It can be seen that changes in block structure have little effect on wing spanwise pressure distributions. This is to be expected since the topologies differ only in the grid structure around the body. However, topology C predicts slightly different suction levels around the leading edge compared with the other topologies and this is considered in more detail later. Topologies B and C which were specifically designed to model the flow near the body appear to yield pressures in this region which differ little from those of topology A. This illustrates the 'robustness' of the flow solver.

3.2 GRID DENSITY

The effect of varying the grid density on the surface is shown in Fig 8 for topology C. The 'coarse' grid in Fig 8 is the same as was used in the previous section, that is 18 cells in the spanwise direction and 39 in the chordwise direction on the exposed wing whereas the 'fine' grid is 34 x 69, approximately doubling the number of cells in both directions, increasing the number of blocks by a factor of 5 and not surprisingly quadrupling the computing time.

The 'fine' grid has a tendency to predict higher suction levels over the outboard portion of the upper surface of the wing and to improve the definition of the shock. However, it is doubtful if, for this flow condition, the small refinements to the pressure

distributions warrant the extra complexity and greater computing time.

Attention is drawn in both Figs 7 and 8 to waves in the upper-surface pressure distributions inboard of the pressure rise region. Increasing the grid density appears to reduce the wave length of the undulations, suggesting that they are due to discretisation errors.

Consideration of the effect of grid density on the calculated values of drag and on the fine detail in the pressure distributions near the leading edge are considered in section 3.4.

3.3 CONVERGENCE HISTORY

Although the topologies A, B and C are different in detail, close to the wing there are a number of similarities in the grid structure and quality. It is perhaps not surprising, therefore, that the convergence rates of the three topologies are similar as shown in Fig 9 which illustrates the variation in the average rate of change of density or residual with number of time steps. For a CFL number of 2 both the residual and the rate at which it decays with time step (residual decay rate) are little changed between topologies, while increasing the CFL number to 4 has little effect on the residual. Moreover, the residual decay rate is such that, if it were deemed necessary, a continued significant decrease in residual could be expected if the computation was executed for more than 1000 cycles.

Fig 10 shows spanwise pressure distributions at a typical streamwise position for varying numbers of time steps. Larger differences can be seen between the cases for 50 and 100 time steps than between cases for 100 and 150 time steps. However, for numbers of time steps greater than 150 the pressure distributions are indistinguishable to 3 significant figures in C_p (as are the local and overall forces coefficients). Thus, if the aim of the calculation is to produce accurate surface-pressure distributions, there would appear to be no reason to carry out more than 200 time steps even though the mean residual, as shown in Fig 9, is still significant.

3.4 EFFECT OF TOPOLOGY AND GRID SIZE ON CALCULATED OVERALL FORCES

Consideration of the effect of topology and grid size in the previous sections has shown that the solution is relatively insensitive to these parameters if gauged by differences in the calculated pressure distributions. An additional and important consideration for the aircraft designer is the effect on overall forces. The Table below gives values of the overall force and pitching moment coefficients of the net or exposed wing based on gross wing area for $\alpha = 5.32°$ $M_\infty = 1.605$ and overall configuration $C_L = 0.2$.

It is evident that topologies A and B are in close agreement whereas topology C gives a similar value of drag, $C_{D_{NET}}$, but a lower value of lift, $C_{L_{NET}}$ and a higher value of pitching moment, $C_{M_{NET}}$. Since drag is of special interest, the effect of topology on the drag polar is assessed in order to gain a clearer picture of the differences in drag obtained

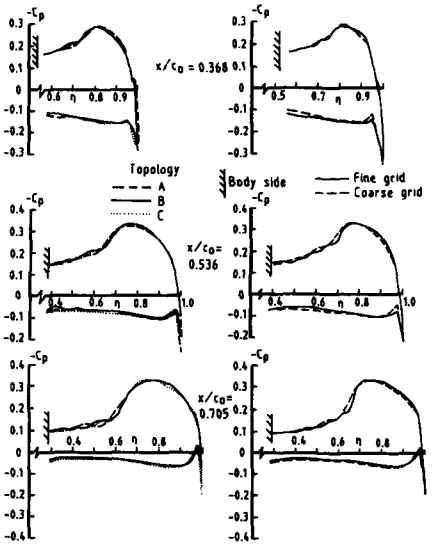


Fig.7 Comparison of spanwise pressure distributions for various topologies, $M_\infty = 1.605$, $\alpha = 5.3°$

Fig.8 Comparison of spanwise pressure distributions for 2 grid densities, $M_\infty = 1.605$, $\alpha = 5.3°$

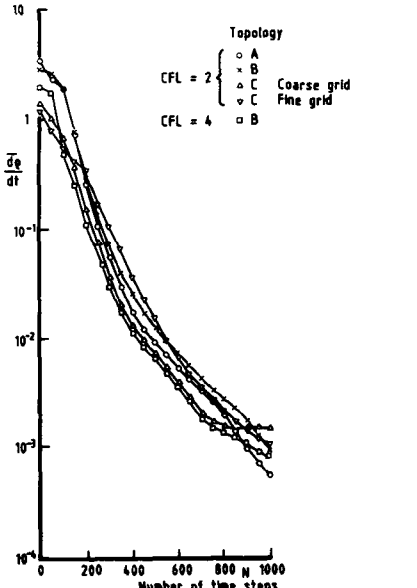


Fig.9 Convergence histories for various topologies

Topology	$C_{L_{NET}}$	$C_{D_{NET}}$	$C_{A_{NET}}$	$C_{M_{NET}}$
A	0.1427	0.01170	-0.00150	0.00683
B 'Coarse'	0.1427	0.01173	-0.00155	0.00658
C	0.1395	0.01174	-0.00120	0.00919
C 'Fine'	0.1387	0.01180	-0.00106	0.00829

(Fig 11). To resolve the drag differences in detail, a drag term KC_L^2 (K = 0.3738) has been removed, such that the variation of residual drag with lift is small. Fig 11 reveals that the predicted values of drag using topologies A and B are in close agreement while topology C yields somewhat higher values, and is dependent on grid density. Reasons for these differences have yet to be established.

In an attempt to understand the possible sources of these discrepancies, it is instructive to examine the pressure distributions close to the leading edge in detail. Fig 12 shows pressure distributions (plotted in the form C_p against $\sqrt{(1-\eta)}$ to highlight the effect of pressures in the leading-edge region) at two, typical axial-stations for the various topologies. Also included are the equivalent experimental data, which are used as a basis for judging the relative merits of the different topologies. Boundary-layer displacement effects are expected to be insignificant close to the leading edge where the pressure gradient is favourable and the boundary layer is thin. Therefore the predictions by the (inviscid) calculation method may be expected to be accurate in this region. Fig 12 indicates that topology C is less satisfactory than the other two topologies in that it underestimates the suctions near the leading edge. This loss of suction on a vital forward-facing surface is entirely consistent with the axial force values in the Table above, the differences between which are of the same magnitude as the differences in $C_{D_{NET}}$ at a given value of $C_{L_{NET}}$ exhibited in Fig 11. At the present, it is not clear whether the different solutions obtained using topology C are due to the grid generation or with the Euler solver. Since the grid structure around the wing for topology C is identical to those of A and B, it is surprising that the 'coarse' topology C cannot resolve the pressure distributions to the same detail. Investigations are continuing to resolve this anomaly.

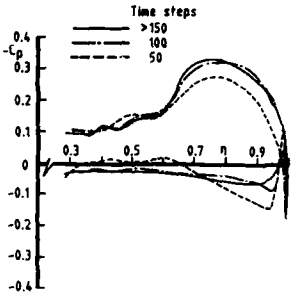


Fig.10 Comparison of spanwise pressure distributions for varying numbers of time steps, M_∞ = 1.605, α = 5.3°, x/c_0 = 0.705

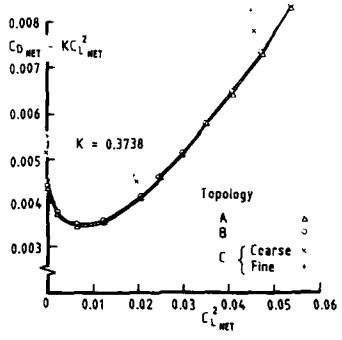


Fig.11 Variation of net wing drag with net wing lift for various topologies and grid densities, M_∞ = 1.605

4 DESCRIPTION OF EXPERIMENTS

Tests have been made on two wings at supersonic speeds in the 8ft × 8ft Wind Tunnel, RAE Bedford. The wings form part of a large half-model mounted on the sidewall of the wind tunnel, the layout of the models in the wind tunnel being illustrated in Fig 4. The use of large half-models gave a high chordal Reynolds number and permitted detailed flow measurements. Additionally, by using a large wing, the desired model accuracy was easier to achieve with conventional machine tolerances. This is particularly important in the highly-curved region of the leading edge which controls the development of the flow on the upper surface.

Both wings were mounted low on a common body which is cylindrical and essentially rectangular in cross section where the wing joins the body. Further upstream, the body becomes circular in cross section as the nose is approached. Each wing has the same quasi-delta planform of inboard leading-edge sweep Λ = 60° and has a 4% thickness distribution.

Wing A has a warp distribution based on that of an earlier design which was studied as part of an extensive programme of research on slender wings suitable for supersonic transport aircraft. Designed using linearised theory[8], the original wing was of leading-edge sweep 71° and was warped in such a way that the leading edges are attachment lines at a lift coefficient of 0.05 and at a cruise Mach number of 2.2. Chordwise and spanwise loadings were chosen with the dual aims of achieving low lift-dependent drag and of being trimmed at the cruise lift coefficient of 0.1. The present wing is related to the original wing insofar as the shape of the camber surface has been retained at each axial

station but it has been scaled to match the lower sweep of the new wing. According to linear theory, the new wing should have attached flow at the leading edge at a lift coefficient of approximately 0.1 and a Mach number of 1.5. This lift coefficient is much less than the required design value of $C_L = 0.3$ (4g manoeuvre, $M_\infty = 1.6$ at the tropopause). Therefore, in order to achieve increased lift by increasing incidence while maintaining attached flow at the leading edge, the thickness distribution chosen has rounded leading edges.

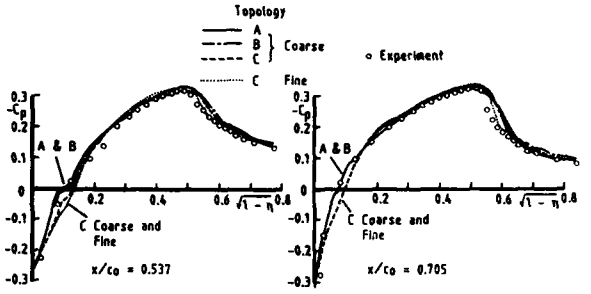


Fig.12 Typical detailed pressure distributions for various topologies, $\alpha = 5.32°$, $M_\infty = 1.605$

Wing B is of conical camber, designed using the COREL[9] full-potential method to be free of cross-flow shocks at $M_\infty = 1.6$ and $C_L = 0.4$. This results in a camber surface which is entirely different in character from that of wing A as shown in Fig 13. (Wing design using the COREL code and the subsequent wind-tunnel tests have been conducted in a collaborative RAE-NASA research program.)

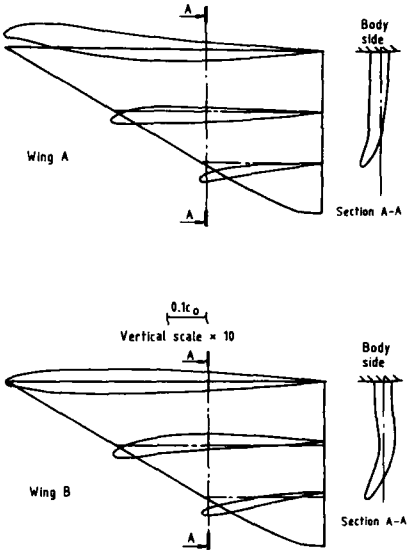


Fig.13 Comparison of typical streamwise and spanwise wing sections for Wings A & B

Each wing was machined from a single piece of high-tensile steel and, together with the body was attached by a block within the body to a strain-gauge balance mounted outside the tunnel. The centre-line of the body was offset approximately 25 mm from the tunnel sidewall to minimise interference between the model and the sidewall boundary layer. Inspection of the models revealed a high standard of surface finish (0.1 to 0.2 μm) and that manufacturing errors in the ordinates are small being typically of order 0.1 mm (0.00006 × root chord) except close to the trailing edge on wing A which deformed slightly during manufacture.

The wings were pressure-plotted at nine streamwise stations and the body was equipped with pressure tappings on the side along the centre line.

The tunnel has good control of stagnation pressure, temperature and humidity down to a frost point of -40°C. The correction to nominal Mach-number was obtained directly from the tunnel calibration and for the conditions studied increases Mach number by 0.005. The various tunnel and reference pressures were measured by individual self-balancing capsule manometers, which have a very stable zero and calibration. The manometers recording stagnation pressure have a resolution of 0.34 mbar and those recording wall static pressures 0.17 mbar. Tunnel total-temperature was controlled to minimise balance temperature excursions during a run. Frost point was maintained below -30°C.

The overall forces acting on the model were measured with a five-component, strain gauge balance. A study of the errors in the calibration of the balance and of the measurement of free-stream dynamic pressure suggests that overall-force coefficients are potentially accurate to within the following limits:

$$\Delta C_N = \pm 0.001 C_N \pm 0.00005,$$
$$\Delta C_M = \pm 0.001 C_M \pm 0.0001,$$
$$\Delta C_A = \pm 0.001 C_A \pm 0.00005.$$

However, repeatability was generally outside the range of the figures quoted above for overall accuracy, being as shown below.

$$\Delta C_N = \pm 0.0001$$
$$\Delta C_M = \pm 0.00005$$
$$\Delta C_A = \pm 0.0001$$

Measurements of flow pitch angle indicate that the error in angle of incidence is small and probably within the range ±0.02°.

Model pressures were measured by nine 48-way pressure switches each with transducers having a working range of ±1.7 bar. Calibration of the transducers was effected during each scan, using tunnel total and static pressures as known datum conditions. Overall accuracy of pressure coefficients, allowing for uncertainties in transducer calibration and dynamic and static pressures, is estimated to be ±(0.001 C_p - 0.0005) at the test conditions. The repeatability of the measurements of pressure was within this range.

The tests on both wings were performed at a unit Reynolds number 4 × 10^6/ft (13.1 × 10^6/m) corresponding to a Reynolds number based on geometric mean chord $R_{\bar{c}}$ = 12.7 × 10^6 and at the free-stream Mach numbers 1.405, 1.606 and 1.805.

Tests were also carried out on the body alone at similar conditions as an aid to the drag analysis (section 5).

Boundary-layer transition was fixed by narrow bands of sparsely-distributed ballotini, cemented to the model by epoxy resin. On each surface of the wing the band was 25.4 mm from the leading edge in plan view and was 5.08 mm wide. On the body the band was 12.7 mm wide and was located 101.6 mm along the body surface downstream of the nose. The grade of ballotini used had diameters between 0.21 mm and 0.25 mm.

5 COMPARISONS BETWEEN EXPERIMENTAL AND COMPUTED RESULTS

Comparisons between calculation, using topology B, and measurement of spanwise pressure distributions are shown in Figs 14 and 15.

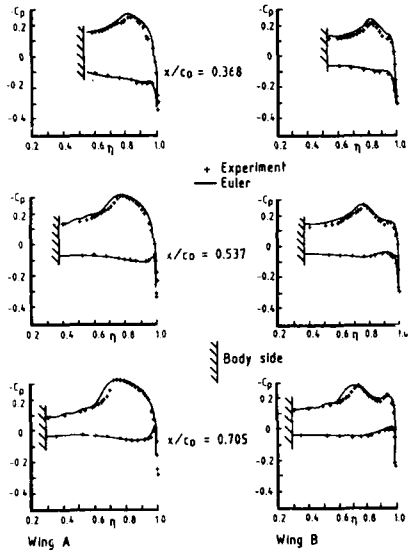


Fig.14 Comparison of spanwise pressure distributions experiment and Euler, M_∞ = 1.605, C_L ≈ 0.2

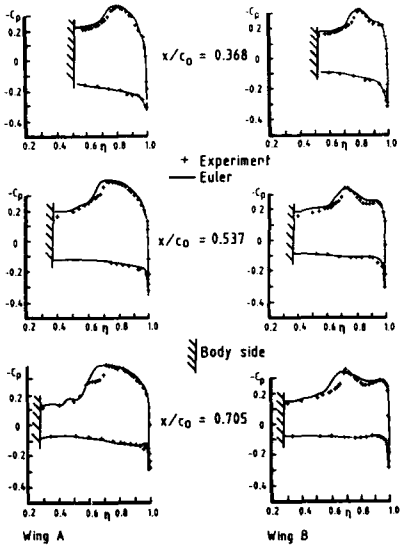


Fig.15 Comparison of spanwise pressure distributions experiment and Euler, M_∞ = 1.605, C_L ≈ 0.30

At an overall lift coefficient of approximately 0.2 (Fig 14) the agreement can be seen to be good on both wings except at the station x/c_0 = 0.705 in the region of the cross-flow shock wave on the upper surface, station x/c_0 = 0.705 being typical of the rear 30% chord. Further forward at stations x/c_0 = 0.368 and 0.537 the pressure distributions appear to be shockfree. Such good agreement between wind-tunnel measurement and (inviscid) calculations is attributable to the fact that the local flow is supersonic and boundary layer effects do not influence upstream pressure distributions.

At an overall lift coefficient of approximately 0.3, Fig 15, the shock wave has increased in strength and, for wing A, there are clear indications of shock-induced separation at x/c_0 = 0.705; however, the agreement between theory and experiment is still good outboard of the shock. Further forward, shocks are now apparent at stations x/c_0 = 0.368 and 0.537 and the agreement is good except in the vicinity of the shock wave. Figs 14 and 15 show that the calculation method is able to represent the different character of the leading-edge pressure distribution of wings A and B, indicating that the method is potentially useful as a tool for designing wings for manoeuvre at supersonic speeds.

Fig 16 shows normal and axial force coefficients for the net wing obtained by integrating calculated and measured pressures at a selection of axial positions. Again the agreement between calculation and measurement is good, which, for the cases discussed previously, is not surprising bearing in mind the quality of agreement between measured and calculated pressure distributions. Fig 16 also demonstrates that the good agreement between theory and experiment is not restricted to angles of incidence close to those of Figs 14 and 15.

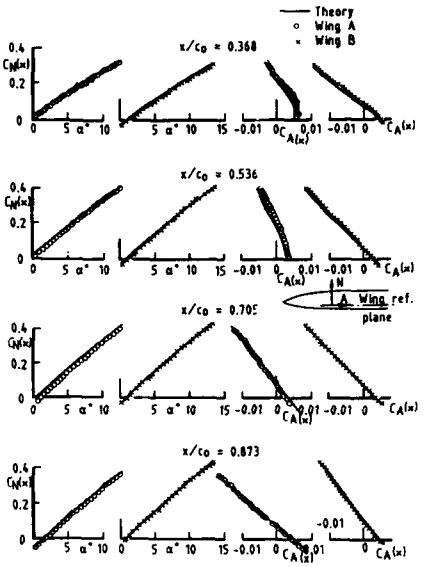


Fig.16 Normal and axial forces : comparison between theory and experiment, M_∞ = 1.605

A comparison of overall forces is shown in Figs 17 and 18. In order to eliminate extraneous effects such as those induced by the boundary-layer diverter between the body and the tunnel side-wall, overall forces measured on the body alone have been subtracted from those of the wing-body at each angle of incidence to give a notional wing-along force (in the presence of the body). These forces include those arising from the 'carry-over' effect of the wing on the body but exclude those on the forebody which are unaffected by the wing. In order to allow for the influence of the wing on the base flow, the measured drag of the notional wing-alone has been corrected using the Euler-Multiblock method to determine the change in mean base-pressure coefficient.

In the calculation method, the assumption is made that the forces on the cylindrical surface of the body-alone are zero in accordance with slender-body theory. Therefore, by analogy with the procedure used in the analysis of measured forces, the notional wing-alone forces are calculated by integrating the pressures on the wing and body appropriately from the junction of the wing leading-edge and the body to the wing trailing edge.

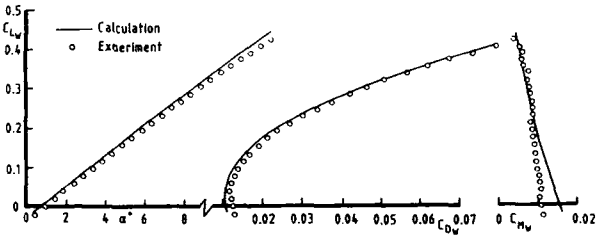


Fig.17 Overall lift, drag and pitching moment variations : comparison between theory and experiment, M_∞ = 1.605, Wing A

It can be seen that the agreement between measured and calculated values of lift is fairly good at low lift (C_{L_W} < 0.2 for wing A and C_{L_W} < 0.3 for wing B). At higher values of lift coefficient, the CFD method overestimates the value of lift coefficient. The surface pressure distributions for lift coefficients within this range (Fig 15) suggest that this can be explained by the predicted level of upper-surface suctions generally being higher than those measured inboard of the cross-flow shock. This, in turn, can be explained by the lack of representation in the calculation method of separation at the cross-flow shock. Observations using laser-illuminated vapour screens support this, showing shock-induced separation over the rear of the wing for C_L > 0.2 for wing A and C_L > 0.3 for wing B.

The comparisons of drag are most encouraging. The calculated drag contains an allowance for skin-friction drag, calculated assuming that the exposed wing is a flat plate of the same planform area and neglecting the effect of incidence. At M_∞ = 1.6, this increases the calculated drag coefficient by 0.0054. One possible cause for the discrepancy at low lift (C_{L_W} < 0.1) is separation of the flow from the lower surface.

Comparisons between measured and calculated pressure distributions near the trailing edge show that the leading edge suction has collapsed indicating flow separation on the lower surface. Another possibility is the inability of the theoretical method to resolve the lower-surface suction 'peaks' sufficiently accurately. At moderate lift (0.2 < C_{L_W} < 0.3) the agreement is good as would be expected since in this region the calculation method provides generally good predictions of the pressure distributions, Fig 14. For high values of lift coefficient (C_{L_W} > 0.3) the theory displays a tendency to overestimate the

drag coefficient in the case of wing B. Reasons for this are not known but it is interesting that Pittman[10] noted a similar discrepancy between calculations using a full-potential method and measurement on a wing designed for manoeuvre at $C_L = 0.4$, $M_\infty = 1.6$.

In the case of pitching moment, which is notoriously difficult to predict accurately, the level of agreement is not good. However, this is considered again later.

An important objective of CFD methods must be to predict changes in pressure distributions and overall forces resulting from small differences between geometries or wing designs. Fig 19a shows the variation of the difference in wing drag between wings A and B with lift, as observed in the experiment and as calculated. At low lift coefficients the agreement is good bearing in mind the comments made previously but, for values of C_{L_W} above 0.2, the measured difference increases with lift relative to that of the calculated difference. This discrepancy can best be understood by writing the drag difference as

$$\Delta C_{D_W} \simeq \Delta C_{A_W} + C_{L_W} \Delta\alpha \quad .$$

Fig 19b shows that although calculation and measurement of ΔC_{A_W} are not in complete agreement for some, at present, unexplained reason, the trends of ΔC_{A_W} with C_{L_W} are at least similar. Thus the discrepancy between calculated and measured drag at a given lift may be attributed to errors in the estimate of incidence at a given lift coefficient. Fig 17 shows that this may be explained by the greater tendency for the calculation method to underestimate the angle of incidence for a given lift of wing A than for wing B at lift coefficients above 0.2. This in turn may be linked to the inability of the CFD method to model shock-induced separation as described earlier.

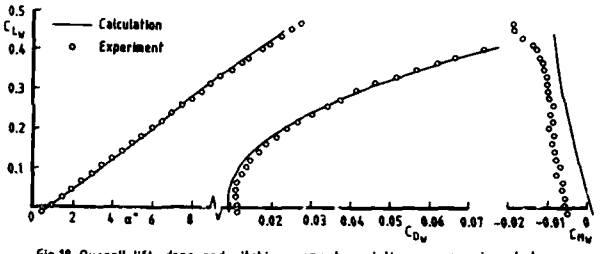


Fig.18 Overall lift, drag and pitching moment variations : comparison between theory and experiment, $M_\infty = 1.605$, Wing B

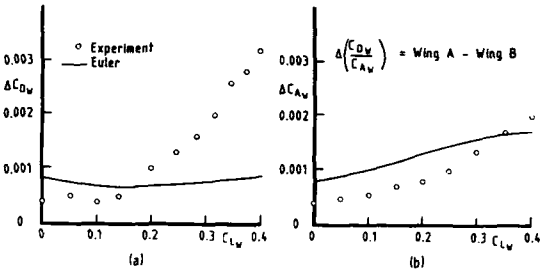


Fig.19 Difference in wing drag and axial force between Wings A and B as predicted and measured, $M_\infty = 1.605$

Although the absolute levels of pitching moment are not predicted well by the theory (possibly because of the assumption concerning the absence of forces on the cylindrical surface of the body alone in the calculation) the differences in zero-lift pitching moment between the two wings is estimated reasonably well, the value from experiment being $\Delta C_{M_o} = 0.0165$ and from calculation $\Delta C_{M_o} = 0.0145$.

6 CONCLUSIONS

A multiblock grid-generation scheme coupled to an algorithm for solving the Euler equations has been evaluated for wing-body configurations suitable for combat aircraft at supersonic speeds. The flow predictions have been shown to be insensitive to grid topology, or grid structure, as judged by comparisons of overall features of pressure distributions. However, one topology is found to predict values of overall drag significantly different from those predicted by the other two. It is seen that this is due to the suction near the leading edge being smaller than for the other two, which are in reasonable agreement with experiment.

Convergence has been shown to occur within 200 time steps as judged from pressure distributions even though at this stage the residual is still significant.

Comparisons between predictions by the CFD method and measurement of pressure distributions as well as local and overall forces from a carefully-controlled experiment show good agreement except where separation of the flow on the wing is observed. The CFD

method has demonstrated its robustness for the calculation of supersonic flows and provides a significant step towards the ultimate aim of being able to solve the full equations of motion over complex configurations.

REFERENCES

1 N. P. Weatherill, J. A. Shaw, C. R. Forsey and K. E. Rose. A discussion on a mesh generation technique applicable to complex geometries. AGARD Symposium on Applications of Computational Fluid Dynamics in Aeronautics, Aix-en-Provence, France, April 1986, AGARD CP 412, Paper 2.

2 A. Jameson, W. Schmidt and E. Turkel. Numerical solutions of the Euler equations by finite volume methods using Runge-Kutta time stepping schemes. AIAA Paper 81-1259, 1981.

3 N. P. Weatherill and C. R. Forsey. Grid generation and flow calculations for aircraft geometries. J. Aircraft, Vol 22, No.10, October 1985, pp 855-860.

4 J. A. Shaw, C. R. Forsey, N. P. Weatherill and K. E. Rose. A block structured mesh generation technique for aerodynamic geometries. Proceedings of the First International Conference on Numerical Grid Generation in Computation Fluid Dynamics. Landshut, West Germany, July 1986, Published by Pineridge Press.

5 A. Jameson and T. J. Baker. Solution of the Euler equations for complex configurations. AIAA Paper 83-1929, 1983.

6 N. P. Weatherill and J. A. Shaw. Inviscid flowfield predictions for wing-body geometries using a multiblock approach. ARA Memo 270, June 1986.

7 L. E. Eriksson. Generation of boundary-conforming grids around wing-body configurations using transfinite interpolation. AIAA Journal, Vol 20, No.10, pp 1313-1320, October 1982.

8 J. H. B. Smith, J. A. Beasley, D. Short and F. Walkden. The calculation of the warp to produce a given load and pressure due to a given thickness on thin slender wings in supersonic flow. ARC R&M 3471, 1967.

9 W. H. Mason and B. S. Rosen. The COREL and W12SC3 computer programs for supersonic wing design and analysis. NASA CR-3676, 1983.

10 J. L. Pittman. Experimental flowfield visualization of a high alpha wing at Mach 1.62. J. Aircraft, Vol 24, No.5, pp 335-341, May 1987.

ACKNOWLEDGEMENTS

The authors are grateful to the Aircraft Research Association, Bedford (ARA) and British Aerospace, Filton for the use of the Euler-Multiblock code to compute the results presented. In particular, we wish to thank Mr J A Shaw (ARA) for his help and guidance in preparing this paper, Mrs I M Gaudet for her development of the experimental data reduction software and to Mr M J Simmons for his assistance in the design of the wings and conduct of the experiments.

Copyright © Controller HMSO London 1988

THE DFVLR-F5 WING EXPERIMENT
-Towards the Validation of the Numerical Simulation of Transonic Viscous Wing Flows -

by
W. Kordulla, D. Schwamborn and H. Sobieczky
DFVLR SM-TS, Bunsenstr. 10, D-3400 Göttingen, FRG

SUMMARY

A major step towards the rigorous validation of Navier-Stokes codes for the simulation of the transonic flow past transport-type wings is being described. The basis for this is the DFVLR-F5 wing experiment which has been designed to allow the analytical formulation of a boundary value problem. This requires the determination of flow conditions on the entire surface of the prescribed control volume. The experiment led to the organisation of a workshop selected results of which are presented. These show *considerable scatter the sources of which can not be defined very well because there are too many* possible ones, and the salient ingredients are too diverse. Some of the difficulties are illustrated by results of additional computations. Both, experimentalists as well as computational aerodynamicists, have to do more work to achieve a successful validation.

1. INTRODUCTION

The development of faster and faster supercomputers (currently with vector architecture) with ever increasing main or dedicated external memory (e.g. with 256 million words storage capacity) together with the development of more and more efficient numerical schemes enable the numerical simulation of increasingly complicated flow fields. Thus, the flow fields about simplified but still fairly complete aircraft configurations have been simulated by numerically integrating the Navier-Stokes equations in the transonic or hypersonic flow regime, see e.g. [1,2,3,4]. The proceedings of two recent AGARD Conferences [5,6] give evidence of the potential power of numerical flow simulation methods. In spite of such major achievements there is some doubt in the usefulness of the results in terms of e.g. boundary layer properties. This is due to the lack of local grid resolution as well as to the missing appropriate physical models, e.g. for transition and turbulence.

One of the essential tasks of the computational aerodynamicist is the validation of his method as is the case for any code developer. For this purpose a dedicated experiment is required which provides the conditions needed to perform the numerical simulation in a unique manner. In transonic flow with subsonic free stream Mach number the flow simulation is determined by prescribing appropriate boundary conditions. In general, these conditions are not furnished in experiments.

There have been several workshops in which code validation was an important topic. Two recent *dedicated workshops are, in particular, worthwhile to be mentioned. One concerns the simulation of* laminar, low Reynolds number two-dimensional transonic flows past profiles and through a nozzle with two throats [7]. In spite of the fact that any trouble due to turbulence model is avoided there is considerable scatter for the airfoil flow predictions which seems to be partly due to the influence of the formulation of the far field boundary conditions and the used computational grids, while excellent agreement *is achieved for the nozzle flow simulations. The other workshop deals with the numerical simulation of* turbulent transonic flows past airfoils [8]. Again appreciable scatter can be observed for the computational results.

This paper reports on first steps towards the validation of aerodynamic Navier-Stokes solutions in the transonic flow regime for transport-type wings in three dimensions. First the basis, the DFVLR-F5 wing experiment, is described which allows to define a boundary value problem. Next, the simulation of the corresponding flow field is discussed based on an explicit block structured Runge-Kutta time-stepping scheme for the Navier-Stokes equations. Finally, selected results are presented from the international workshop based on the DFVLR-F5 wing experiment.

2. THE DFVLR-F5 WING EXPERIMENT AND THE BOUNDARY VALUE PROBLEM

The DFVLR-F5 wing experiment [9,10,11] is - to authors' knowledge - unique in the sense that the measurement of pressure is not restricted to the wing surface with the sole purpose of recognizing *aerodynamic characteristics of the wing in question. In addition, flow field measurements have been* carried out in wind tunnel cross sections ahead and aft of the wing. These planes together with the closed wind tunnel walls allow to form a control volume of simple shape. Note that the slotted wind tunnel walls have been closed in order to have well defined no-slip boundary conditions there. These can be supplemented by the assumption of an adiabatic wall which is a good approximation because the *used wind tunnel is of the continuously running type. In addition, the boundary-layer assumption is* usually used to determine the wall pressure which is certainly a good approximation for the flow on plane surfaces. The figures 1 and 2 illustrate the wing position in the wind tunnel and in the control volume. Note that the downstream boundary is fairly close to the trailing edge of the wing, see figure 2. The wing is attached to a splitter plate which can be turned to achieve an angle of attack of the wing with *respect to the oncoming flow. The purpose of the splitter plate is to generate a new boundary layer such* that the wing is not drowned in the thick boundary layer on the wind tunnel walls (roughly 90 mm) [...].

The wall boundary layer is flowing between splitter plate and tunnel wall, influenced, in addition, by suction, see figure 2. Thus, a smooth flow past the leading edge of the splitter plate is established [9,12], resulting in nice flow profiles in the entrance plane of the control volume which is located about 10 mm aft of that leading edge (figure 2). Note that the flow is being tripped immediately behind the leading edge.

The surface of the control volume including that one of the wing is given in analytical form with only a few parameters by Socieczky [10] so that any wanted surface discretization can be achieved. The selection of the aerodynamic configuration for the test case was motivated by keeping some of the practical considerations but allowing also for some simplifications. High aspect ratio wings exhibit large regions with quasi-2D swept wing flow where profile design methodology can be applied. Special interest is attached to section pressure distributions which allow to maintain laminar flow. The main part of the wing of aspect ratio 9 is defined based on an airfoil designed to be shock free at a free stream Mach number of 0.78. With a leading edge sweep angle of 20° a free flight Mach number of about 0.82 is expected. Severe rear loading, which is typical for modern supercritical profile shapes, is lacking because of symmetric cross sections. A substantial portion of the flow is expected to remain laminar. An extreme fairing at the wing - splitter plate junction prevents the generation of a horse shoe vortex and thus avoids the associated root flow problems. This corresponds to the fillets designed by the aerodynamicist at the wing - fuselage junction of realistic aircrafts.

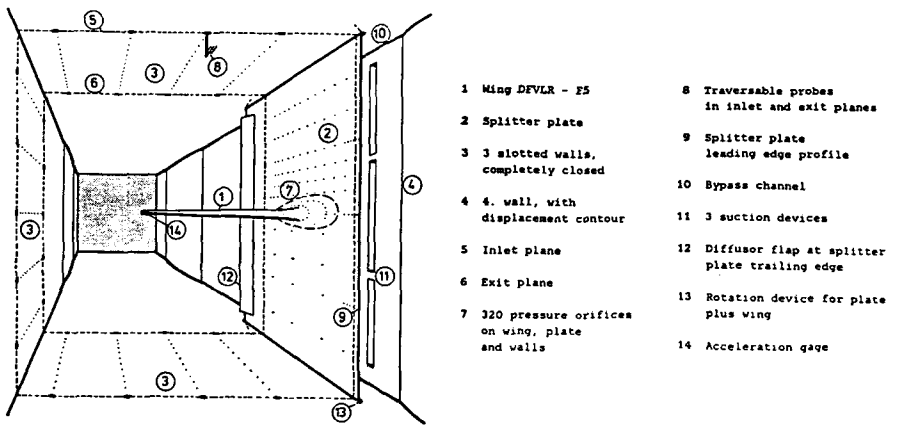


Fig. 1: Sketch of the wing position in the wind tunnel (streamwise view).

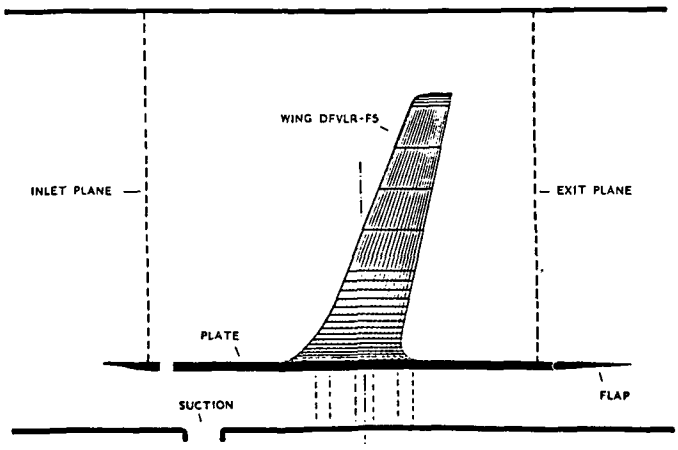


Fig. 2: Sketch of the wing position within the control volume (planform view) to scale.

In order to define uniquely the flow problem with subsonic flow in the entrance and in the exit planes appropriate boundary conditions are required at those locations. According to the theory of characteristics 4 boundary conditions must be prescribed at the entrance plane and one at the exit plane. The remaining boundary conditions have to be obtained using data from the interior of the computational domain. Therefore, complete profiles have been measured in the entrance and exit planes, see the traversing paths in figure 3. The resolution of the flowfield depends, of course, on the possible positions of the probes restricted by the construction of the tunnel and by the time available for measurements.

For the inlet plane the complete measured profiles in modelized, analytical form were available to the participants of the workshop so that each participant could continue to use his favourite variables and boundary condition formulations [9,10,11]. In the exit plane only the pressure distribution was furnished in an approximate analytical form. Note that the third author assumed that the conditions in the entrance and exit planes do not depend considerably on the angle of attack of the wing [10]. While this is a sufficiently safe assumption in the entrance plane, it may cause trouble when applied to the exit plane because of the proximity of that plane to the trailing edge of the wing, see figure 2. In order to perform the numerical simulation of the flow on the wing the location of the line of transition is needed. Because of the lack of time with respect to the measurements, only a quick look at the line of transition was possible based on the acenaphtene evaporization technique. Thus only a rough estimate was obtained, with transition wedges emanating from taps due to open pressure tubes, and modelled in [10], see also [9,11] and figure 4. In future experiments a cleaner definition will be needed.

The flow conditions for the experiments are characterized by the Reynolds number per meter of 10^7 (or $Re = 3.6 \cdot 10^6$ based on the root chord) and by a representative Mach number of 0.82 on the tunnel centerline ahead of the control volume. The angles of attack were 0° and 2° with full measurements.

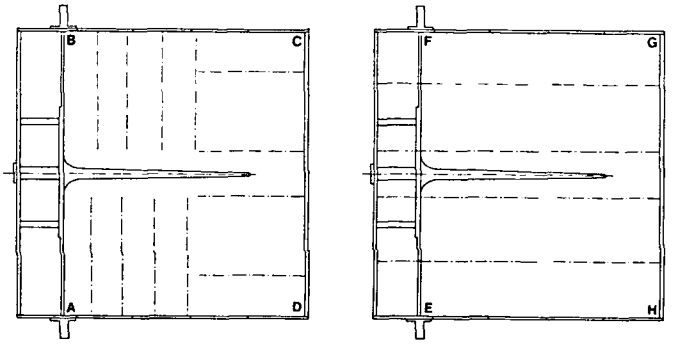


Fig. 3: Entrance (ABCD) and exit (EFGH) planes of the control volume with probe traversing paths. Upstream view.

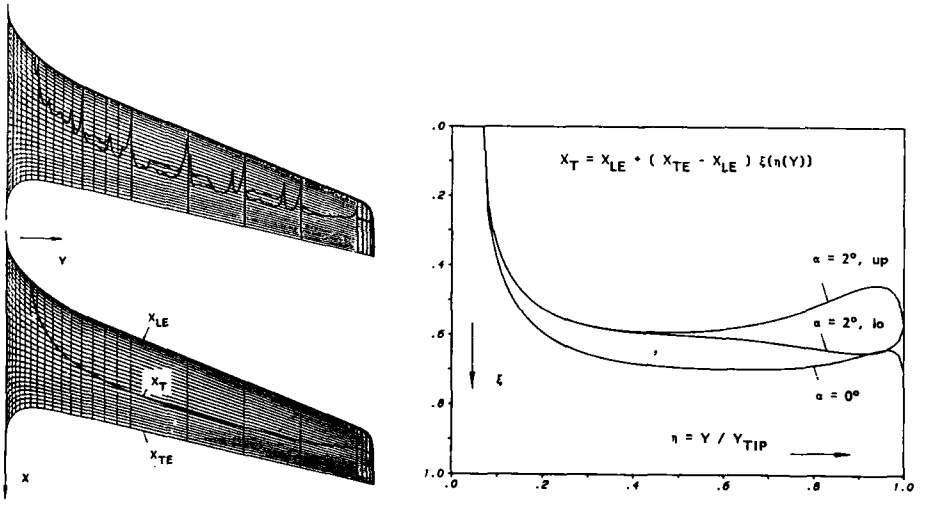


Fig. 4: Analytical model for transition lines derived from acenaphtene visualization.

Notice, that the majority of the pressure taps were installed on the upper surface of the wing. Only three pressure taps are located on the lower surface for control purpose in the non-lifting cases. Thus, for lifting flow with an angle α of incidence the measurements were actually carried out for α = 2° and -2°. And the agreement of the three pressure values with the corresponding curves indicates the accuracy of the measurements. For the workshop it was desired to have computed the complete wind tunnel flow within the prescribed control volume based on Navier-Stokes solutions. Since this requires considerable computational work it was also permitted to simulate the flow past the DFVLR-F5 wing in free air.

Fourteen persons from France, Germany, Japan, Sweden and the USA participated in the international workshop based on the DFVLR-F5 experiment [11]. Table 1 summarizes the test cases and table 2 names the groups contributing to the evaluation.

Table 1: Summary of the test cases*)

Notation	Wind tunnel	Angle of attack α [°]	-	Free-stream Machnumber
A1	Yes	0	Desired	-
A2	Yes	2	Desired	-
B1	No	0	Desired	0.82
B2	No	2	Desired	0.82
B3	No	5	Optional	0.82
B4	No	8	Optional	0.82

*) Re/m = 10 000 000; transition lines given, adiabatic surfaces; boundary conditions for cases A1 and A2 are given in entrance (flow profiles) and exit (pressure only) planes.

Table 2: Summary of the participants providing data on tape and a filled-in questionnaire

Participant	Affiliation	Test Cases Done
Chaderjian	NASA, Ames Research Center, USA	A1, A2, B1 to B4
Lindeberg, Rizzi, Müller	FFA, Sweden	B1, B2
Obayashi, Fujii, Gavali	NAL, Japan / Amdahl, USA	A1, A2, B1 to B4
Schmatz	MBB, FRG	A2
Schwamborn	DFVLR, Göttingen, FRG	A1, A2, B1, B2
Vatsa, Wedan	NASA, Langley Research Center, USA	A1, A2, B1, B2

3. THE SIMULATION OF THE DFVLR-F5 WING FLOW WITH AN EXPLICIT TIME-STEPPING NAVIER-STOKES METHOD

3.1 DESCRIPTION OF THE METHOD

The complete time dependent Navier-Stokes equations are used in integral form: A finite volume discretization in space results in a set of ordinary differential equations which is integrated with the help of a Runge-Kutta time stepping scheme [13,14]. The scheme is based on a cell centered formulation, i.e. the variables are constant within each cell of the mesh and placed in the middle of the cell. The fluxes across the cell faces are averaged from neighboring cells which is equivalent to central differencing and makes the use of artificial diffusion necessary. The damping terms incorporated into the discretized equations are the usual blend of second and fourth order differences [13] except that a weighting function

$$\min\,(1, |\bar{V}|)/\sqrt{1+\varepsilon} \qquad (1)$$

is employed. This weighting function is used to avoid that the artificial diffusion becomes too large in the viscous near-wall regions. In the laminar sublayer where the (dimensionless) eddy viscosity ε is small, the dimensionless velocity $|\bar{V}|$ is utilized to reduce the artificial diffusion, whereas farther outside or in the wake, where $|\bar{V}|$ is already too large, the eddy viscosity is employed for this purpose. Note that the well-known turbulence model of Baldwin and Lomax is used.

A local coordinate transformation is used [15] to approximate the derivatives in the physical diffusion terms. Since we are, in general, only interested in steady state solutions, we accelerate the convergence of the linearized four-stage Runge-Kutta scheme with the help of local time stepping. In order to save computation time the artificial and physical diffusion terms are only updated once per time step resulting in a reduction of the execution time of more than 50 percent.

A set of appropriate boundary conditions is needed to have a well-posed problem. At the wing

surface the no-slip and the adiabatic wall conditions are used. The pressure is derived from the assumption of a zero pressure gradient normal to the wall which is justified for the very small step sizes normal to the wall used in Navier-Stokes calculations for turbulent flows. For the free air cases the wing is assumed to emanate from a plane of symmetry with corresponding symmetry conditions. The same condition is applied along all wind tunnel walls, because we handle all tunnel walls as inviscid and the boundary conditions for inviscid walls become identical to symmetry conditions taking into account that these walls are flat. At the far field boundary (in the free air cases) we use one-dimensional Riemann invariants normal to the boundary. For the tunnel cases similar conditions are used at the inflow boundary, where velocity, pressure and temperature are known from the experiment. In the exit plane only the pressure distribution is given from the experiment, and an extrapolation of four variables (namely $\rho, \rho u, \rho v, \rho w$) and a non-reflecting boundary condition for the pressure [16] are employed.

The method uses a block structured approach, i.e. the computational domain is divided in a number of subdomains called blocks, such that only the data for one block have to be in the central memory of the computer at a time. The advantages of this approach are that solutions for large-size grids can be obtained using only a relatively small amount of central memory, and, furthermore, that it is very flexible regarding the handling of complex geometries (e.g. with multiple connected domains). The flexibility is enhanced by the segmentation of the block faces, which allows for the use of different types of boundary conditions and of different neighboring blocks at each block face. For the information transport between blocks each block has a layer of dummy cells around it, which correspond to inner cells of the respective neighbor. The blocks are handled one after the other computing one or a few time steps at a time. After the data of a block have been stored into the memory all dummy cells are updated before the calculation within that block starts. Since the boundary conditions are also fullfilled using the dummy cells, the algorithm for all cells within the block is the same and the number of segments on the block faces has no influence on the calculation.

Up to now the meshes are hand-tailored with respect to the block structure, because an algebraic grid generator is used that handles global C-O or C-H meshes about wings and wing-body combinations [17]. This mesh generation is based on simple analytical functions describing connections between two given points in space. Some of these functions allow for additional requirements like prescribed tangents or curvature at one or both end points, or for exponential clustering of points along the connecting curve. This approach is very fast, but it requires considerable checking to avoid intersections of grid lines, in particular in very dense meshes for Navier-Stokes calculations.

For the flow about the wing alone the mesh consists of 200x40x48 cells in chordwise, spanwise and surface normal direction, respectively, see a view of the grid close to the wing in figure 5. There are 160x40 cells on the wing surface and the first step size normal to the wing surface is about $\approx 2.5 \cdot 10^{-5}$ root chords. Where the boundary layer is turbulent this is equivalent to $z^+ \approx 2$ in the first cell center off the wall. The far field is about 6 root chords away from the wing.

Since the wing has a blunt trailing edge, the grid generator yields a mesh with a slit in the wake of the wing. Some test calculations habe been made using the mesh with the slit, but ignoring its width in the code or using a mesh without slit by pinching the trailing edge of the wing. Since there were no important differences in the solutions, it is assumed that the solution is not much dependent on the way the trailing egde is treated, because the slit width is only 0.5 percent of the local chord length.

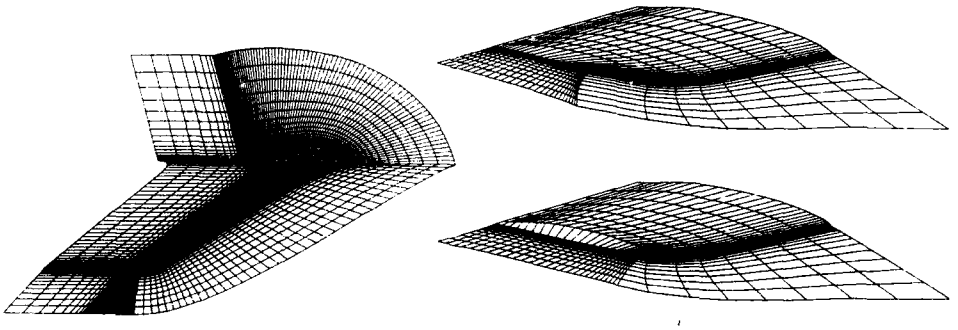


Fig. 5: C-O mesh near the wing.

Fig.6a/b: Detail of the mesh near the wing tip, improved version at the bottom (b).

Due to the surface grid generator supplied to the workshop participants, the mesh on the wing is composed of lines of constant span and lines of constant chord. Together with the strong curvature of the leading edge at the wing tip this leads to a three dimensional mesh near the tip as is shown in figure 6a. Since there are twice as many lines on the wing surface in the actual computational grid, the situation is much worse in the tip region and results in severe convergence problems. These are overcome by

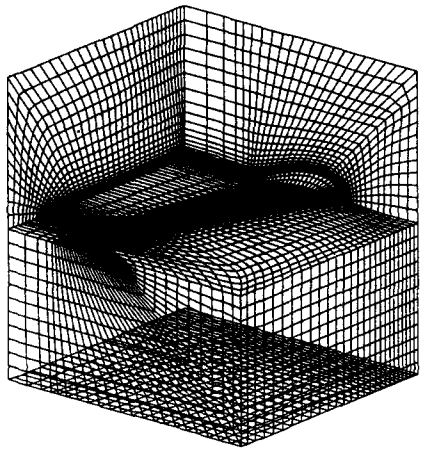


Fig. 7: C-O mesh for the wing in the wind tunnel case; only every third line in chordwise and every second line in surface normal direction are shown.

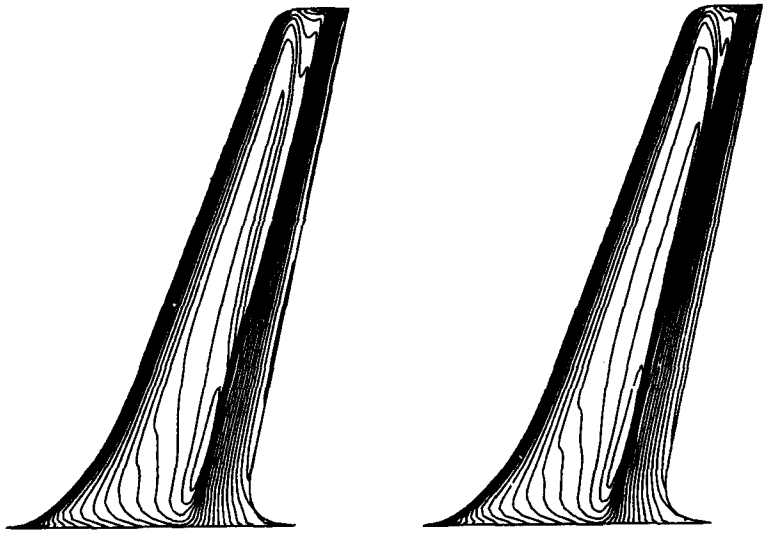


Fig. 8: Isobars on the wing surface for $\alpha = 0°$ in free air and in the wind tunnel (right).

extending the outmost line of constant span along the leading edge, such that it is no longer a line of constant span but changes neither the last profile nor the planform of the wing. The resulting grid in the tip region is given in figure 6b and the comparison with figure 6a shows that the skewness of the mesh is now substantially reduced.

For the calculation of the wing in the wind tunnel a 200x40x34 cells mesh is used with 160x40 cells on the wing surface (figure 7). For the angle of attack case two further meshes are employed, where the only difference between the first and second grid is a different stretching of the cells in the direction normal to the wall resulting in a better resolution within the boundary layer. The influence of the resolution in the two surface tangential directions is investigated with the third, coarser grid using only 160x26x34 cells with 120x26 cells on the wing surface.

Thus we are able to get at least some information about the influence of the grid on the solution. For the tunnel cases the first step size normal to the wing (Δz) is proportional to the local chord over most of the span. The smallest ratio Δz /chord is $4 \cdot 10^{-5}$ at the leading edge with an increase in chordwise direction such that the value at the trailing edge is about 3 times that at the leading edge. This first step size in the surface normal direction is used for all grids.

3.2 RESULTS

In this chapter some of the results for the DFVLR-F5 wing are presented in terms of pressure distributions and skin friction lines, and the influence of the grid and of the numerical dissipation on the solution are shown. As already mentioned computed results are discussed for the free air cases and for the wind tunnel case, however with inviscid tunnel walls and splitter plate. It is not yet clear how much the solution near the wing is changed by the accumulated viscous effects at the tunnel walls.

Because of the lack of an appropriate transition model the transition location obtained in the experiment is used, even for the free air calculations. Note that a switching function is employed to increase the eddy viscosity from zero at the given transition line to its full value over a distance of about 4 percent of the local chord length. The reason for this are difficulties in converging some cases when fully turbulent flow is assumed from one cell to the other.

Figure 8 shows pressure contours on the wing surface for the non-lifting flow in free air and in the wind tunnel, respectively. There is a weak shock extending over the main part of the wing at about 70 percent chord, which is also found in the comparison with the experimental c_p-distribution in figure 9. The agreement is quite good near the root section up to about 10 percent of the half span for both cases with some larger discrepancies for the windtunnel case. Over the main part of the wing, however, an over-expansion is found to develop in the numerical results in comparison with the experiment, and the shock location is calculated upstream of the experimentally observed one. In the free air case the over-expansion is strongest near section 4 (figure 9) and vanishes at mid span, but even farther outboard the weak shock (or recompression) is still located upstream of the experimental position (e.g. section 7). For the windtunnel case the over-expansion is stronger and extends over most of the span. Near the tip (section 9) the agreement between experiment and computation becomes again better for both cases.

The skin friction line pattern obtained from the integration of the wall shear stress is presented in figure 10 for non-lifting flow. For the free air solution a broken separation line is formed at the foot of the

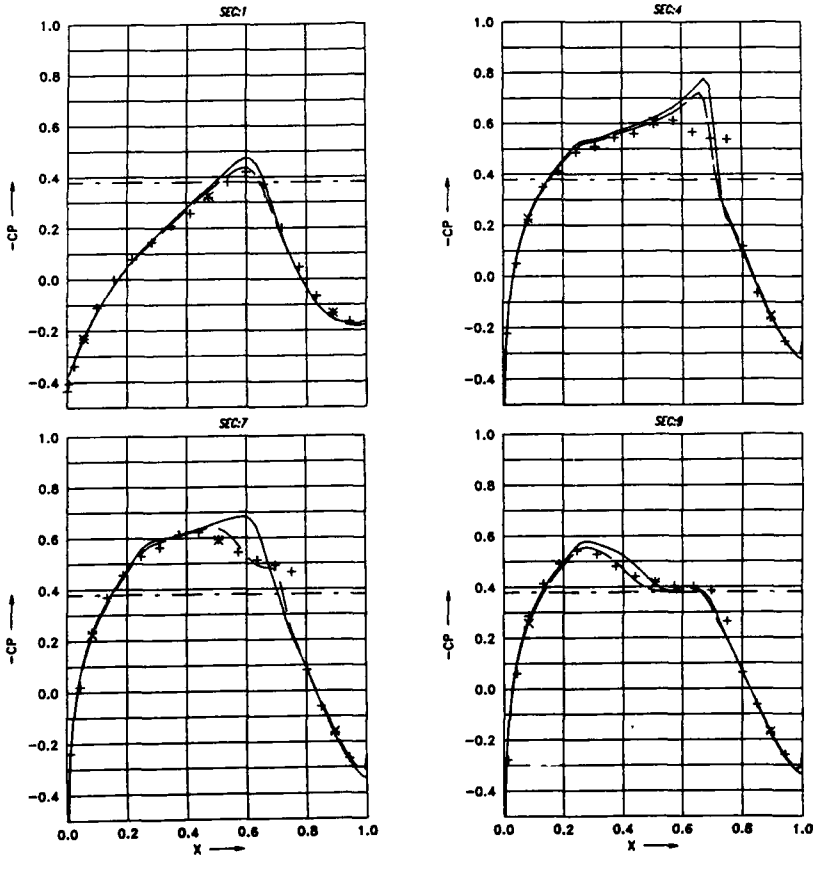


Fig. 9: c_p-distribution at four span stations (α = 0°): solid line: wind tunnel, broken line: free air. Sections 1, 4, 7 and 9 are at 0.1, 20.5, 64.6 and 95.4 percent span. Symbols denote experimental data [9].

shock. The separation is laminar with turbulent reattachment. Since the transition line is immediately behind the separation line, a small change in the transition location in upstream direction or in the way transition is modelled results in the vanishing of separation. Another small separated flow region, where the flow is fully turbulent, is found near the fairing at the trailing edge. In the wind tunnel case the overall picture is the same, only the separation at the shock is stronger, and the shape of the second separation line has changed a bit.

Starting the calculation for the free air flow at $\alpha = 2°$ with the converged non-lifting flow solution resulted in some convergence problem because the solution exhibited unsteadyness in the root trailing edge region. The pressure distribution for this case is shown in figure 11a. This problem could be overcome by omitting initially the velocity in the weighting function in equation (1). The resulting pressure contours and skin friction line pattern are shown in figures 11b and 12a, respectively. Once the solution was sufficiently converged (figure 11) the original weighting function was used, and the solution converged again. The difference in pressure was so small that it is not visible, but at least some differences

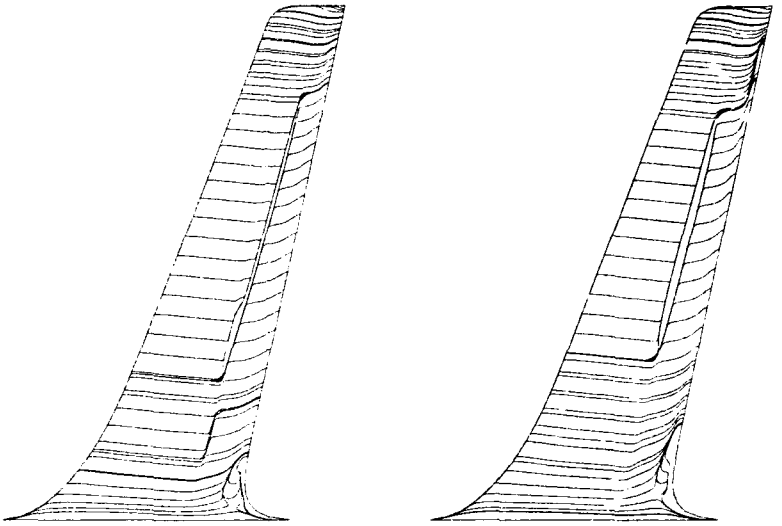


Fig. 10: Skin friction line pattern on the upper wing surface ($\alpha = 0°$). Free air (left) and wind tunnel (right).

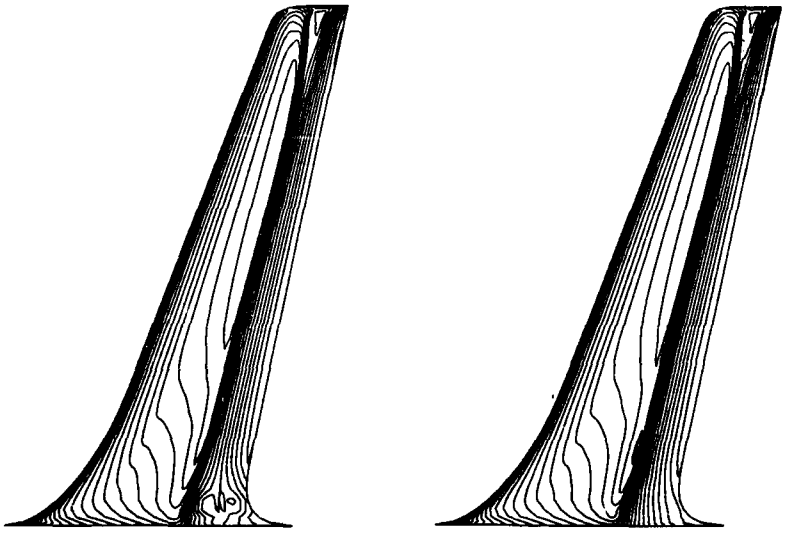


Fig. 11: Pressure contours on the wing surface at $\alpha = 2°$ (free air): a) not converging (left) and b) converged (right).

are found regarding the topology of the skin friction line pattern near the fairing (figure 12b). Although the numerical damping has no large influence on the steady state pressure distribution, it seems to have a substantial influence on the convergence and on the shear stress, and the general question arises whether different solutions are found depending only on how the artificial viscosity is handled.

Comparing the predicted c_p-distribution with the experimental one (figure 13), we find again an astonishingly good agreement near the root section. Away from the root, where the shock becomes stronger (figure 11b), the results exhibit a typical over-expansion which extends over most of the wing. The shock position agrees better with the experiments than for $\alpha = 0°$, and on the lower surface the value of the pressure minimum is obtained almost correctly, but the recompression starts too early and is not as strong as in the experiment. The flow pattern at $\alpha = 2°$ (figure 12b) is similar to the case with $\alpha = 0°$, except that the turbulent separation induced by the shock is now more pronounced especially at the outboard half of the wing. The separated flow area near the trailing edge and the fairing has grown with the angle of attack. The streamlines at the lower surface are not shown here since there is no separation.

For the wind tunnel case with an angle of attack of $\alpha = 2°$ we obtain solutions on different meshes, as already mentioned above. The first calculation is made for the 200x40x34 mesh. The only difference between the second and the first grid is that the resolution in the boundary layer is increased, i.e. starting with the same first step size the stretching of the grid normal to the wall is less. Looking at the resulting pressure distribution for both cases we find very little difference, such that we show only the c_p-distribution and isobars for the solution on the first grid in figures 13 and 14. Comparing this solution with the corresponding free air case (figures 13 and 11b) we find the same tendency as in the zero incidence case, namely that the pressure minimum is too pronounced in the wind tunnel case. The solutions at incidence exhibit almost the right shock position compared with the experiment, but the experimental pressure distribution seems to indicate a separation in front of the shock which is not found in the computed results. On the lower surface of the wing another discrepancy is found regarding the position and width of the recompression zone, which are almost the same in the free air and wind tunnel calculation, but show a much steeper recompression in the experiment.

Although there is almost no difference in the pressure distribution for the two grids, we find some - at least quantitatively - in the skin friction line pattern shown in figures 14 and 15a for the first and second mesh, respectively. The global structure seems to be the same in both cases, but there is a higher ratio of the shear stress components in spanwise and chordwise direction within the separated flow region for the mesh with stronger stretching. In a further calculation with the second mesh we halved the coefficient for artificial damping (fourth order) to see the influence of numerical diffusion. The result yields almost the same pressure distribution, and the effect on the skin friction line pattern (figure 15b) shows the same tendency as with the increased resolution, i.e. the ratio between chordwise and spanwise shear stress is increased further. In comparison with the free air flow at $\alpha = 2°$ we find for both grids a larger separated flow region behind the shock whereas the separation structure near the fairing close to the trailing edge has become much smaller now.

The third, coarser mesh with 160x26x34 cells is used to examine the influence of the resolution tangential to the wing surface. The corresponding c_p-distribution is given in figure 16. The comparison

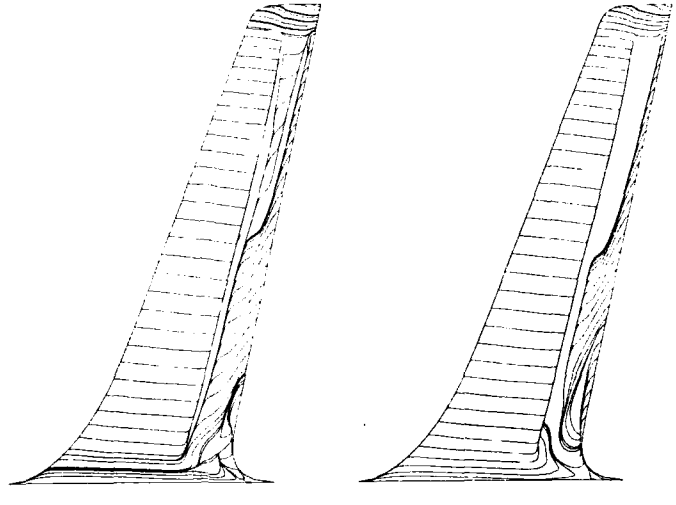


Fig. 12: Skin friction line pattern on the upper wing surface for $\alpha = 2°$ (free air, 200x40x48 cells): a) more damping in boundary layer (left), b) original damping (right).

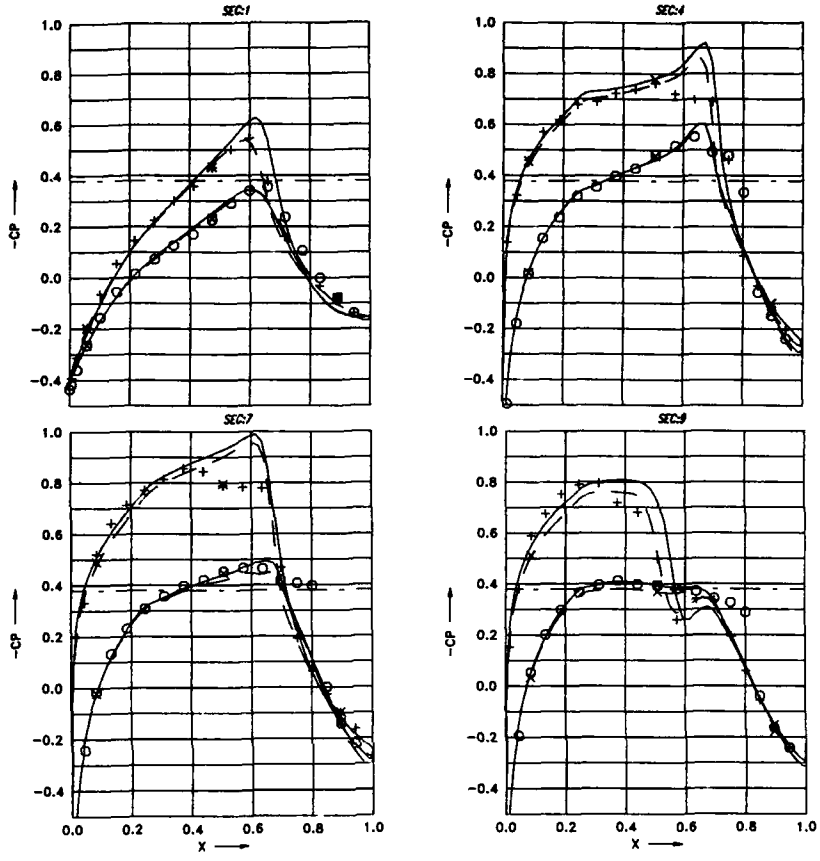


Fig. 13: c_p-distribution at four span stations (α = 2°): solid line: wind tunnel, broken line: free air. Symbols denote experimental data [9].

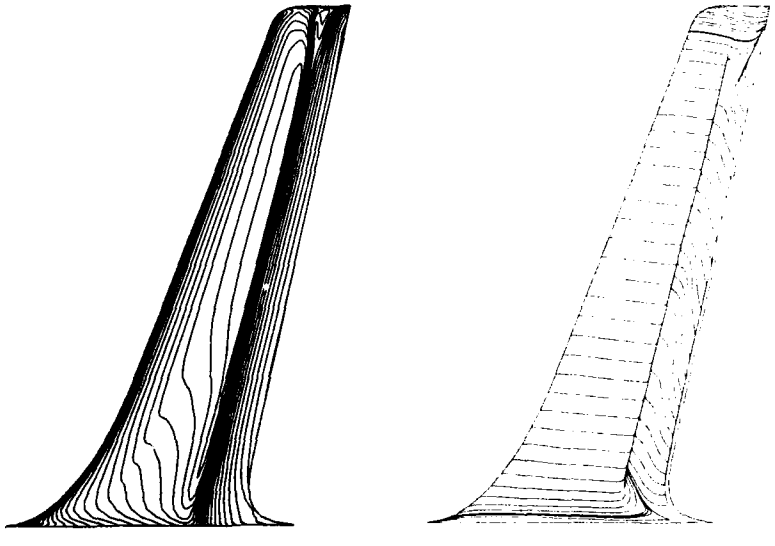


Fig. 14: Pressure contours and skin friction line patterns (right) on the upper wing surface for the wind tunnel case for α = 2° (200x40x34 cells).

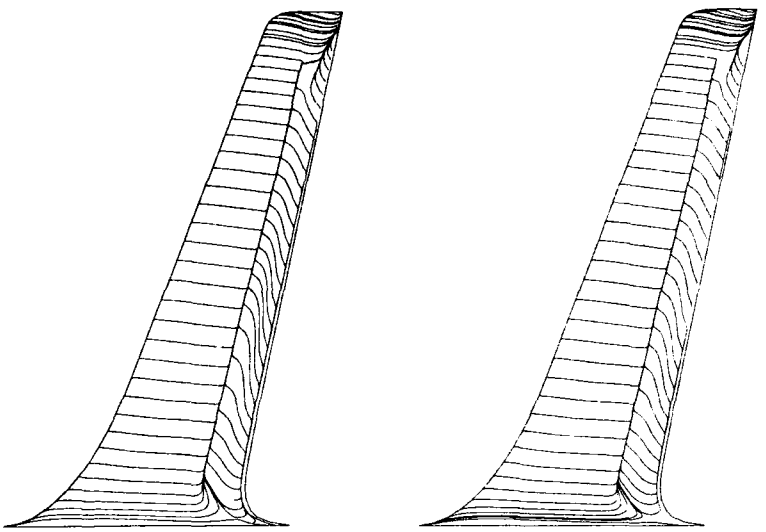


Fig. 15: Skin friction line pattern on the upper wing surface (200x40x34 cells, smoother grid near surface). Wind tunnel case for $\alpha = 2°$: a) damping as for the solution in figure 14 (left) and b) with reduced damping (right).

with the finer mesh (figure 13) shows that there is only some difference on the suction side regarding the pressure plateau and the location of the recompression near the tip. Since there exist no large spanwise gradients over the main part of the wing we state that mainly the chordwise resolution is important in that region and that this resolution seems to be still sufficient with the coarse mesh except maybe in the vicinity of the shock.

Near the splitter plate (section 1, 0.1 percent span) a further discrepancy is observed at the leading edge. Since the chordwise resolution of the mesh is sufficient to predict the stronger leading edge gradients farther outboard, the spanwise resolution near the root seems to be responsible. Taking the results at section 2 and 3 (1.2 and 8.5 percent span) in figure 17 into account, we find a strong spanwise pressure gradient especially in the vicinity of the leading edge that is due to the extreme curvature of the fairing. Obviously the curvature in spanwise direction is no longer sufficiently resolved by the coarse spanwise mesh. In fact, we use the same function to distribute the cross sections along the span for both meshes such that the local mesh density drops everywhere by the same factor. Changing this appropriately would probably result in a better solution with the same number of cells.

The influence of the formulation of the boundary conditions on the solutions is indicated next. Two different versions of the used non-reflecting pressure condition [16] at the wind tunnel exit plane were employed. Allowing the exit pressure to evolve freely, as was done in the case just discussed, results always in a pressure distribution in the exit plane with only small but two-dimensional gradients within that plane. But in the experiment a relatively strong spanwise pressure gradient is found in the vicinity of the splitter plate that is due to the flap at the end of the splitter plate, somewhat outside of the computational domain.

In order to simulate the experimentally observed pressure distribution at the exit a formulation of the non-reflecting pressure condition is used which gives the wanted pressure once convergence is obtained. This results in a certain acceleration of the flow, especially in the vicinity of the wing and the splitter plate, which in turn increases the discrepancy between numerical result and experiment with respect to the value of the pressure minimum. The corresponding results are not shown here because the other features of the pressure distribution (e.g. shock position) are mainly unchanged. However, an unsteadiness of the flow seems to develop at least in the lifting case, after the pressure at the exit has reached the prescribed distribution if the computation is only continued for a sufficiently long time. If the boundary layer on the wind tunnel walls was simulated, the situation might be different in that the mass flow is less and the boundary layer may act as a cushion which reduces the pressure variation.

In the following we give some information about the computation itself. The CPU time per cell and time step is about $2.4 \cdot 10^{-5}$ seconds on the CRAY-XMP 216, and the required central memory using 43 words per cell is 5.6 MWords for the largest block, which could be easily reduced to about 80 percent if we would recompute some of the data every time we use them. The maximum use of the dedicated Solid-State Storage Device (SSD) is 12.2 MWords for the 200x40x34 mesh. This number could also be reduced to roughly 6 MWords, if we would optimize the storage. At this time the storage of the block data is done on two files at alternating time steps. The number of time steps to achieve convergence is about 4000 in the wind tunnel cases (fine mesh) and about 6000 for the free air cases. As convergence criterion we use the drop of the L_2 and the L_∞ norm of the residual by about 3 orders of magnitude as well as the convergence of the force coefficients in terms of the first 2 to 3 digits.

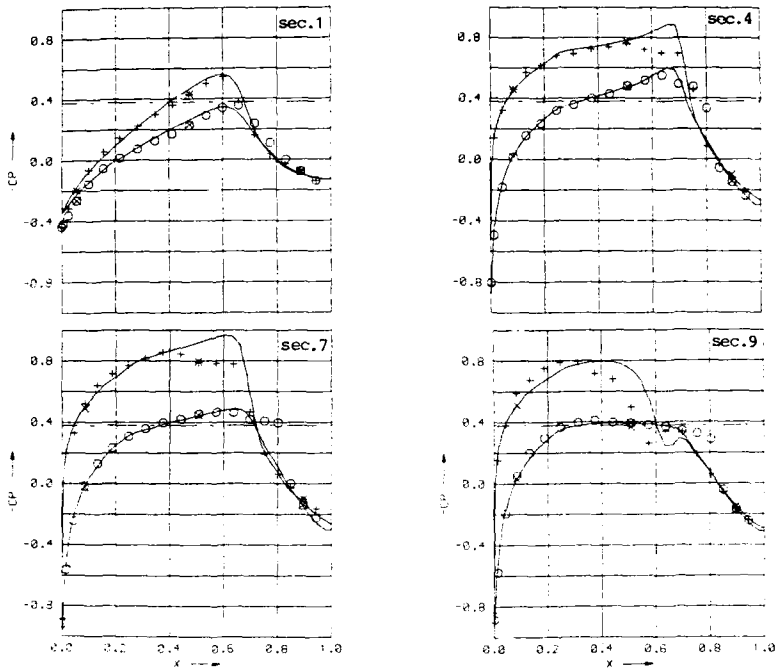


Fig. 16: c_p-distribution for the wind tunnel case for $\alpha = 2°$ (160x26x34 mesh).

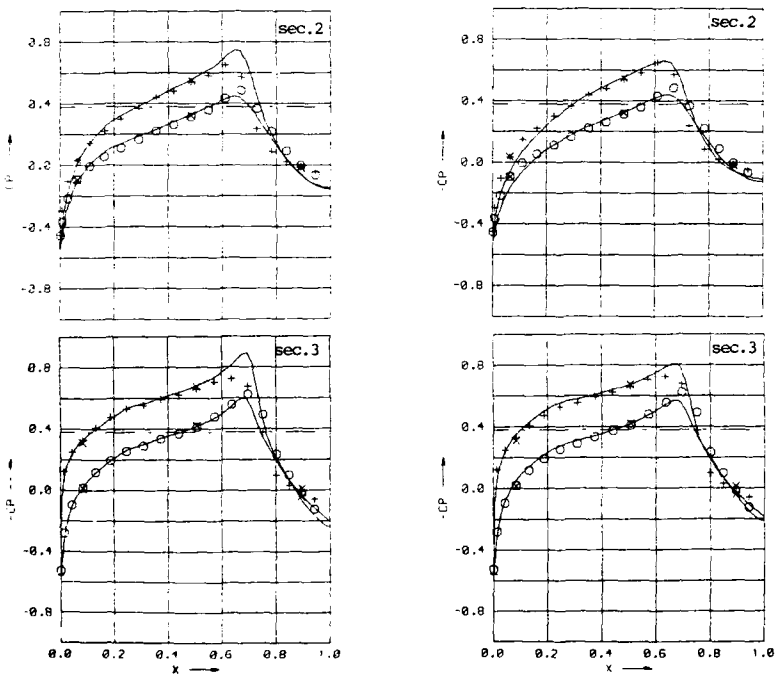


Fig. 17: Comparison of the c_p-distribution for the grid with 200x40x34 cells (left) and with 160x26x34 cells (right) at two sections in the region of the fairing. Wind tunnel case.

4. SELECTED RESULTS OF THE DFVLR-F5 WORKSHOP

4.1 CRUCIAL ISSUES

Some crucial issues of the numerical simulations of the flow past the DFVLR-F5 wing in the wind tunnel have been mentioned earlier. One such issues concerns the modelling of transition and turbulence. Provided that the line of transition is well defined, it turns out that - in the case of scalar eddy viscosity models - the way of switching on the model may be important. This is in particular the case if the positions of the transition line and of the shock are close to each other. According to the findings of Chaderjian [18] who investigated the influence of the length of the blending region, there is no sense in having a blending region over more than five mesh cells in computational space because the solution would not change any more. The position of the blending region with respect to the line of transition may, however, be of some influence (see [19]). There is, of course, also the unresolved problem of the modelling of turbulent viscous interactions, e.g. with respect to the interaction of the boundary layers of the splitter plate and wing, or the wake flow and the boundary layer on the splitter plate, or near the wing tip. It is practically impossible to achieve such an appropriate modelling with a scalar turbulence model. There is, however, some hope that the corresponding effects on the major portions of the wing is negligible. The pressure distribution on the wing near the root section e.g. can be predicted well by assuming no wall at all (see figures 9,13 and 17).

Another crucial issue concerns the treatment of the wind tunnel walls as inviscid. This leads to rectangular flow profiles in the entrance plane of the control volume with increased mass flow as compared with the experimental flow situation. Thus the usefulness of experimental boundary conditions is put in jeopardy because the measured pressure distribution in the exit plane will no longer be compatible with the entrance conditions. Three out of the five groups, see table 1, tackling the wind tunnel problem assumed, however, inviscid walls.

The accuracy of the modelling of the measured pressures in the exit plane is a controversial topic. It was mentioned earlier that in [10] the conditions in the exit plane are assumed independent of the angle of attack. The proximity of that plane with respect to the trailing edge of the wing requires, however, a very accurate determination of the pressure distribution. Some people even think that one should not prescribe the pressure because it would not be accurate enough, but use an integral quantity such as the mass flow. In fact, in the evaluation report [19] it is shown that there exists some discrepancy between upper and lower wall c_p-distributions such that the pressure distribution seems to be two-dimensional in the exit plane instead of one-dimensional as it was prescribed for the test cases. The dependence on the angle of attack seems to be less severe without knowing its influence on the numerical simulation, see also the discussion in paragraph 3.2.

In the wind tunnel test cases an appropriate modelling of the thin, turbulent boundary layer on the splitter plate requires an extremely fine mesh next to the surface. If then a global mesh approach is maintained as is the case with all participants but one, one would encounter serious difficulties at the wing - splitter plate junction because of the large skewness of the grid lines. The remedy is to generate a zonal grid system, see e.g. [19], which could be handled in principle, by at least two of the participants who use block structured solvers. None of the participants attempted to use such a zonal grid because of the large computational effort involved. One could, of course, argue as well - after knowing the results - that the appropriate consideration of the boundary layer on the splitter plate is not very important because the inviscid-wall simulations obtain excellent results in the immediate neighborhood of the splitter plate.

4.2 SELECTED RESULTS

Eight individuals and groups participated in the workshop by presenting results of their flow simulations. Six of those furnished raw data on magnetic tape and returned filled-in questionnaires, see table 2 [11]. Thus all data are evaluated based on the same graphic software package. Because, to date, only pressure measurements have been carried out in the DFVLR-F5 wing experiment computed chordwise c_p-distributions on the wing surface are shown in figures 18 and 19 in comparison with experimentally observed data. In figure 20 the results for the lifting free air test case B2, see table 1, are displayed for four sections at 0.1, 20.5, 49.2 and 95.4 percent of span. It is surprising how well Schwamborn's free air data agree with the wind tunnel data especially in the immediate neighborhood of the splitter plate, see also chapter 3.2. Note that Schwamborn's data are arbitrarily used for direct comparison with the experimental data because of the convenience for the evaluator. The comparison of all results with each other reveals some scatter, and an over-expansion where the experimentalists suggest laminar flow separation. The reasons for the scatter are not yet singled out because the approaches are too diverse including the grid which is known to influence the solution considerably if it is not chosen appropriately, see also 3.2. This situation is not much different when the numerical simulation is restricted owing to the presence of wind tunnel walls. Figure 19 gives an impression for the corresponding lifting case, again. Without knowing exactly the reasons it is observed that the solutions based on the consideration of viscous wind tunnel walls do not exhibit better results than the remaining solutions. Note that some of the participants have changed somewhat the shape of the wing next to the root section (e.g. the extreme fairing by reducing the local chord). Remember, in particular, that those approaches which attempt to take into consideration the thin turbulent boundary layer on the splitter plate may experience difficulties due to the fairing and the associated skewness of the grid surfaces.

In order to give an impression of the scatter in terms of boundary layer properties such as the skin

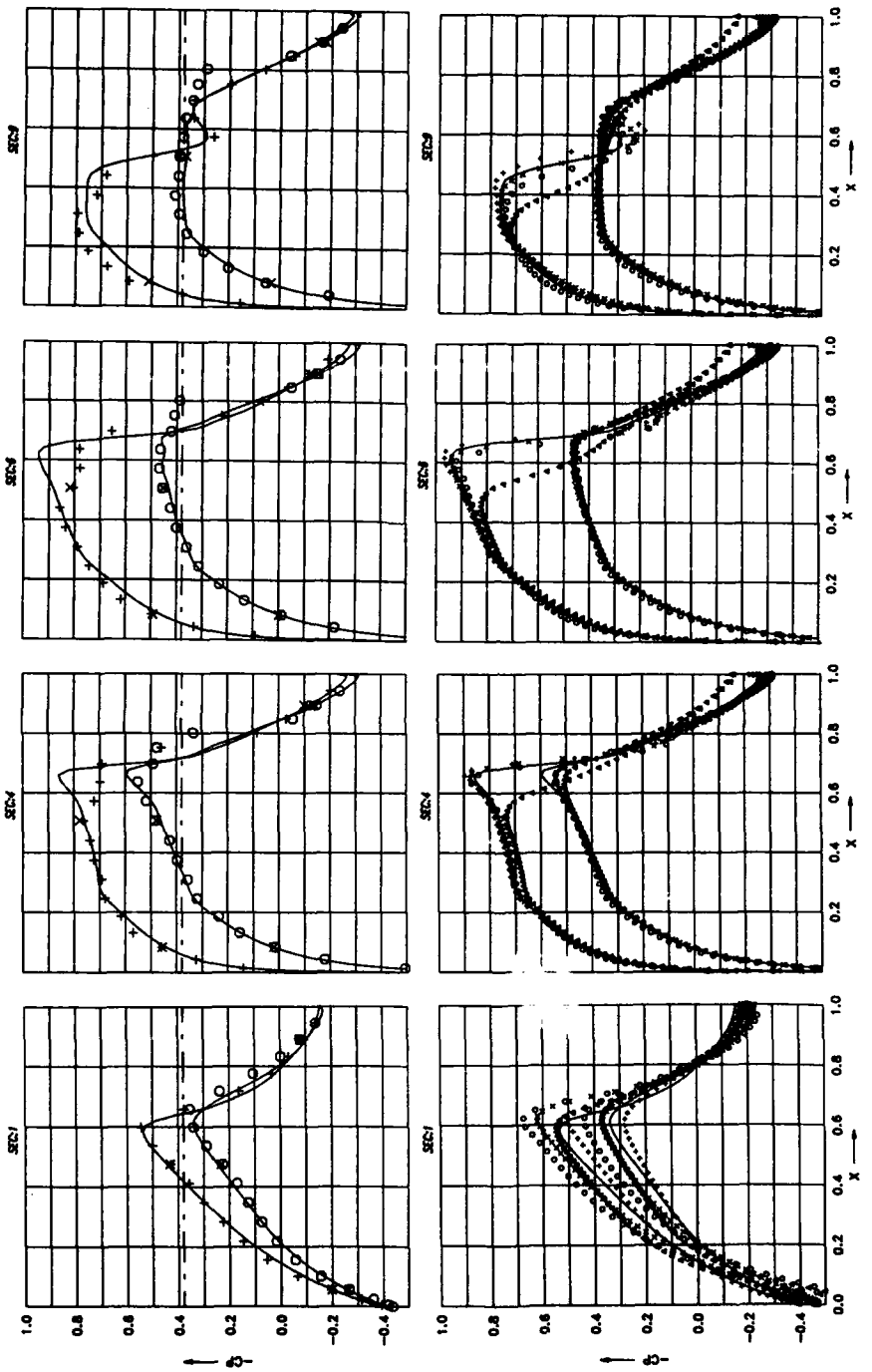


Fig. 18: Comparison of c_p-distributions for the free air test case ($\alpha = 2°$). The sections 1, 4, 6 and 9 correspond to 0.1, 20.5, 49.2 and 95.4 percent span. Top row: symbols denote the experimental data in the wind tunnel. Bottom row: symbols denote predicted values: o Chaderjian, x Lindeberg et al., Δ Obayashi et al., + Vatsa/Wedan. Solid lines are Schwamborn's data.

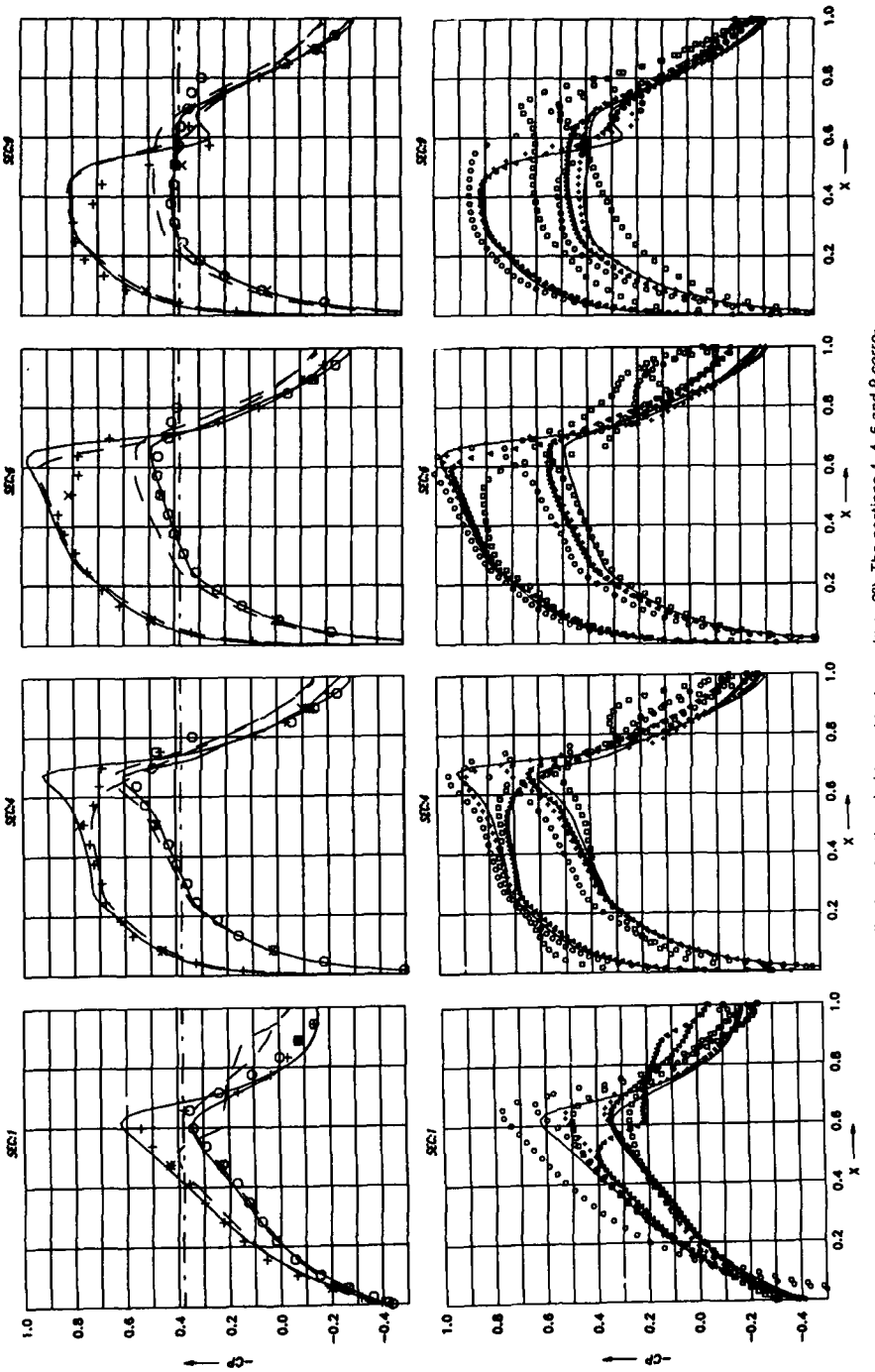


Fig. 19: Comparison of c_p-distributions for the wind tunnel test case ($\alpha \approx 2°$). The sections 1, 4, 6 and 9 correspond to 0.1, 20.5, 49.2 and 95.4 percent span. Top row: symbols denote the experimental data, broken line the prediction of Obayashi et al. (viscous tunnel walls). Bottom row: symbols denote predicted values: o Chaderjian, Δ Obayashi et al., □ Schmatz (viscous walls), + Vatsa/Wedan. Solid lines are Schwamborn's data.

friction lines which are much more sensitive to the quality of the solution than pressure distributions, the corresponding patterns on the upper wing surface are shown in figure 20. The examples chosen compare the situation for the wind tunnel test case with the free air test case for $\alpha = 2°$. Owing to the lack of flow visualization the theoretical patterns can only be compared with each other. Generally, the flow separates at the foot of the shock. Note that the pattern on the lower surface is not exciting at all. The pattern in the case with viscous splitter plate indicates spiralling flow near the trailing edge close to the splitter plate, see figure 20, although this needs to be checked by a streamline integration in space. The larger over-expansions in the wind tunnel simulations, visible in the c_p-plots in figure 19, is reflected in the skin friction line patterns as well leading to stronger shocks and to a less complicated separation line pattern on the major portion of the span.

The purpose of Navier-Stokes simulations is to predict the correct lift and drag of aerodynamic configurations which to date cannot be achieved routinely even for simple shapes. Figure 21 displays the communicated values for the lift coefficient versus the angle of attack and also versus the drag coefficient. The scatter of the data is obvious. Because of the half-model technology used in the experiment force measurements are not available to compare with. Note that the discrepancies between the results of different authors is larger, in particular with respect to the drag values, than the differences regarding the influence of the wind tunnel walls.

For a completer presentation of the results of the participants in comparing form see [19]. The major conclusion from the workshop is that the experiments need to be continued and that the computors should do one mandatory test case as is described at the end of the following concluding remarks.

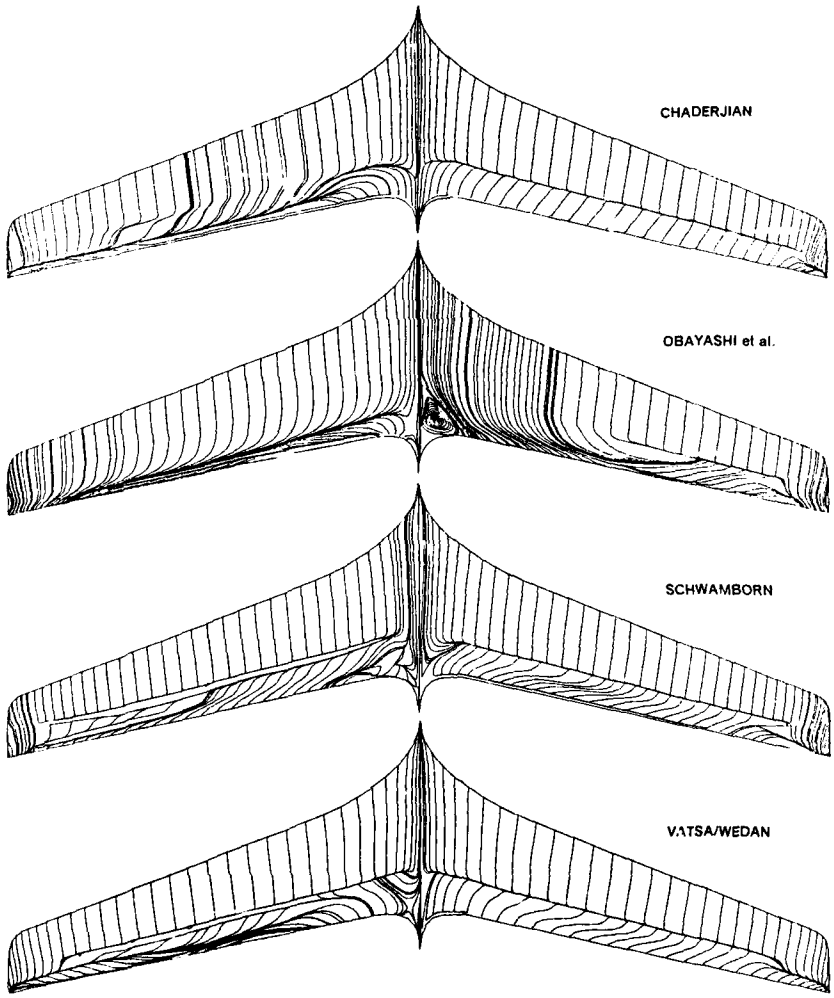


Fig. 20: Display of theoretical skin friction line patterns on the upper surface of the DFVLR-F5 wing: wind tunnel simulations (right) versus free air computations (left). $\alpha = 2°$.

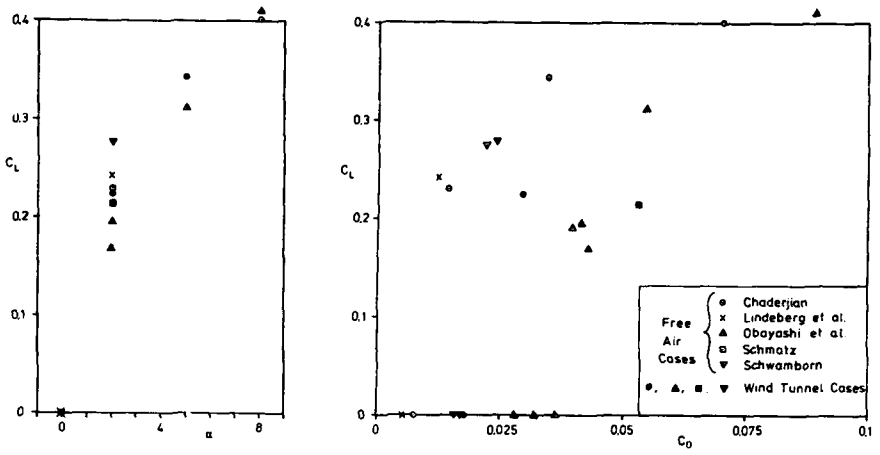


Fig. 21: Plots of the lift coefficient C_L versus the angle of attack α (left) and of C_L versus the drag coefficient C_D (right). Symbols denote predicted values: open symbols free air and filled symbols wind tunnel computations.

5. CONCLUDING REMARKS

The DFVLR-F5 wing experiment and the subsequent international workshop as one step towards the validation of Navier-Stokes codes have been described. The experiment is a dedicated one because the experimentally obtained data allow for an analytic description of the boundary value problem for a defined control volume. The latter is given by the closed wind tunnel walls, the splitter plate with the attached wing, and the entrance and exit planes. The experiment is unique in the sense that, for the first time, the flow field has been measured in the entrance and exit planes, in addition to the usual determination of the pressure on the wing surface for aerodynamic purposes.

Although the configuration of the wing is considered rather simple because of the symmetric cross section and the small angle of attack (0°, 2°), the numerical simulation of the corresponding flow is quite a challenge for the computational aerodynamicist. Some of the crucial issues of the simulation with respect to the modelling of transition and turbulence, the generation of a suitable grid and the analytic modelling of the experimentally observed pressure distribution in the exit plane have been discussed.

Results have been presented obtained with a finite volume Runge-Kutta time-stepping solver of the Navier-Stokes equations. The computations were carried out for a block structured global C-O mesh, although a zonal grid is preferable with different topologies adapted to the local geometry in an efficient way. In this approach the walls were treated as inviscid stream surfaces. The results illustrate the influence of grids of different sizes where the distribution in wall-normal direction near the wall is smoother, or where the resolution in surface-tangential direction is changed. This includes also the influence of intelligent gridding near the tip on convergence. It is illustrated that a coarse grid for which a solution is correspondingly less expensive to obtain and to use may produce as good results as a finer mesh. The influence of the given one dimensional downstream pressure distribution is also discussed. By allowing that pressure distribution to evolve it is reported to change with the angle of attack of the wing, and to be two dimensional. The influence of the artificial diffusion terms on the solution is considered as well.

The comparison of the chordwise pressure distributions show that the computed free air as well as the wind tunnel results (note that the wind tunnel walls and the splitter plate are treated inviscidly) compare quite favorably with the measured values. This is in particular the case near the splitter plate which can only be explained by the extremely smooth fairing and hence negligible interaction effects. The main difference between free air and wind tunnel results concerns the over-expansion which is larger in the case with wind tunnel restriction. Note that the experimentalists interprete laminar separation ahead of the shock location. This could not be found in the computations.

Finally selected results were shown from the international workshop with the simulation of the measured DFVLR-F5 wing flows as test cases. Two of the participants considered viscous wind tunnel walls. The corresponding results in terms of the chordwise pressure distributions on the wing were not at all better than the remaining results. In fact, comparing all pressure distributions with each other a large scatter of the data is observed, mainly with respect to the lifting flow cases. The sources for this are not well understood because of the many possible reasons and of the difference in the salient ingredients of the used schemes, including the grids. This scatter is enlarged concerning the skin friction line pattern because the latter is a more sensitive quantity than pressure. Unfortunately, to date only pressure measurements are available such that the skin friction line pattern can only be compared with each other.

Because the DFVLR-F5 wing experiment is considered only a first step towards the validation of aerodynamic computer codes in three dimensions it is intended to be continued with the experiences learnt during the workshop in mind. First, the measurement as well as the analytic modelling of the flow properties in the entrance and, in particular, exit plane will be considered with special care. The determination of viscous-flow quantities such as skin friction lines or velocity profiles with non-intrusive devices is indispensable. Furthermore, a clean definition of the transition line is needed as well. With respect to the numerical simulation in another workshop it is considered extremely useful to have one mandatory case for everybody with the same salient ingredients. This would include the grid, the formulation of the boundary conditions, the use of a (scalar) turbulence model with its treatment in critical regions such as wing - body junction, wake - surface boundary layer interaction or tip flow. The way of blending in the turbulence model and the position of the blending zone relative to the transition line needs also to be specified. Thus a good comparison could be achieved for the efficiency and quality of the involved schemes. There would be room to show the improvements due to the individual treatment and tuning kits in additional test cases.

6. REFERENCES

[1] Miyakawa, J.; Takanashi, S.; Fujii, K.; Amano, K: "Searching the Horizon of Navier-Stokes Simulation of Transonic Aircraft". AIAA Paper 87-0524, 1987.

[2] Reznick, S.G.; Flores, J.: "Strake-Generated Vortex Interactions for a Fighter-Like Configuration". AIAA Paper 87-0589, 1987.

[3] Shang, J.S.; Scherr, S.J.: "Navier-Stokes Solution of the Flow Field Around a Complete Aircraft". AIAA Paper 85-1509-CP, 1985.

[4] Candler, G.V.; MacCormack, R.W.: "Hypersonic Flow Past 3-D Configurations". AIAA Paper 87-0480, 1987.

[5] - : "Applications of Computational Fluid Dynamics in Aeronautics". AGARD CP-412, 1986.

[6] - : "Aerodynamics of Hypersonic Lifting Vehicles". AGARD CP-428, 1987.

[7] Bristeau, M.O.; Glowinski, R.; Periaux, J.; Viviand, H. (eds): "Numerical Simulation of Compressible Navier-Stokes Flows". A GAMM-Workshop. Notes on Numerical Fluid Mechanics, Vol. 18, Vieweg Verlag, Braunschweig, 1987.

[8] Holst, T.L.: "Viscous Transonic Airfoil Workshop - Compendium of Results". AIAA Paper 87-1460, 1987.

[9] Sobieczky, H.; Hefer, G.; Tusche, S.: "DFVLR-F5 Test Wing Experiment for Computational Aerodynamics". AIAA 87-2485-CP, 1987.

[10] Sobieczky, H.: "DFVLR-F5 Test Wing Configuration for Computational and Experimental Aerodynamics: Wing Surface Generator Code, Control Surface and Boundary Conditions". DFVLR IB 221-87 A 01, 1987.

[11] Kordulla, W.(ed.): "Numerical Simulation of the Transonic DFVLR-F5 Wing Experiment". Proceedings of the international workshop "Num. Simulation of Compr. Viscous-Flow Aerodynamics", Sept. 30 - Oct. 2, 1987, Göttingen, FRG. To appear in Vieweg Series Notes on Numerical Fluid Mechanics, 1988.

[12] Hefer, G.; Sobieczky, H.; Tusche, S.: "Verbesserung der Halbmodelltechnik im Transsonischen Windkanal Göttingen". Jahrbuch der DGLR 1987, Bd. II, 87-083.

[13] Jameson, A.; Schmidt, W.; Turkel, E.: "Numerical Solution of the Euler Equations by Finite Volume Methods Using Runge-Kutta Time-Stepping Schemes". AIAA Paper 81-1259, 1981.

[14] Schwamborn, D.: "Simulation of the DFVLR-F5 Wing Experiment Using a Block Structured Explicit Navier-Stokes Method", in [11].

[15] Deiwert, G.S.: "Numerical Simulation of the High Reynolds Number Transonic Flows". AIAA J. 13 (1980), pp. 1354-1359.

[16] Rudy, D.M.; Strickwerda, J.C.: "A Nonreflecting Outflow Boundary Condition for Subsonic Navier-Stokes Calculations". Computational Physics 36 (1980), pp. 55-70.

[17] Sobieczky, H.: "Geometry Generation for Transonic Design". In: Recent Advances in Numerical Methods in Fluids, Vol. 4, Ed. W.G. Habashi, Swansea: Pineridge Press, 1985.

[18] Chaderjian, N.: "Navier-Stokes Simulation of Transonic Wing Flow Fields Using a Zonal Grid Approach", in [11].

[19] Kordulla, W.: "Evaluation of the Workshop", in [11].

ACCURATE SOLUTIONS, PARAMETER STUDIES, AND COMPARISONS FOR THE EULER AND POTENTIAL FLOW EQUATIONS

by

W.Kyle Anderson and John T.Batina
NASA Langley Research Center
Hampton, VA 23665-5225, USA

ABSTRACT

Parameter studies are conducted using the Euler and potential flow equation models for steady and unsteady flows in both two and three dimensions. The Euler code is an implicit, upwind, finite volume code which uses the Van Leer method of flux-vector-splitting which has been recently extended for use on dynamic meshes and maintains all the properties of the original splitting. The potential flow code is an implicit, finite difference method for solving the transonic small-disturbance (TSD) equations and incorporates both entropy and vorticity corrections into the solution procedure thereby extending its applicability into regimes where shock strength normally precludes its use. Parameter studies resulting in benchmark type calculations include the effects of spatial and temporal refinement, spatial order of accuracy, far field boundary conditions for steady flow, frequency of oscillation, and the use of subiterations at each time step to reduce linearization and factorization errors. Comparisons between Euler and potential flow results are made as well as with experimental data where available.

INTRODUCTION

Considerable progress has been made over the past two decades on developing computational fluid dynamics (CFD) methods for steady and unsteady flow analysis. Two recent surveys which summarize much of this progress are given in Refs. 1 and 2. Jameson,[1] for example, has discussed successes and challenges in computational aerodynamics with emphasis on steady flow applications. Edwards and Thomas,[2] have reviewed computational methods for unsteady transonic flows with emphasis on applications to aeroelastic analysis and flutter prediction. Applications of CFD methods have become relatively commonplace in recent years, for a wide range of fluid flow problems. These applications have met with varying degrees of success, however, due to various deficiencies in the numerical modeling. These deficiencies include: an insufficient number of grid points to resolve the physics of the flow, an insufficient grid extent for external flow problems, too large of a time step to accurately capture the unsteadiness of the flow, and inaccurate boundary conditions, to name but a few. Consequently, the methods require further evaluation by performing detailed studies to assess the influence of each parameter in the numerical modeling on the solution. Through such studies, the accuracy and hence applicability of the methods may be determined.

Because of increased computer speed and memory available on current supercomputers, it is now timely to pursue such validation studies. Therefore, the purpose of the present paper is to report some results of such a study, performed using the Euler equations and the transonic small-disturbance (TSD) potential equation. Descriptions of the governing equations and numerical methods of solution are given first. Parameter studies for steady flow applications are presented next which show the effects of grid density, spatial accuracy, and far field boundary conditions. Parameter studies for unsteady flow applications are also presented which show the effects of reduced frequency, time step size, and the use of performing subiterations to minimize linearization and factorization errors in the time-accurate calculations. Comparisons of the TSD solutions with the Euler solutions are given to assess the applicability of the TSD potential flow method. In the TSD solutions, entropy and vorticity effects are accounted for to more accurately treat cases with strong shock waves. Finally, the results are validated by making comparisons with available experimental steady and unsteady data.

COMPUTATIONAL PROCEDURES

In this section, the computational procedures are described including the governing equations and the numerical method of solution for both the Euler equations and the transonic small-disturbance equation.

Euler Code

Governing Equations

The governing equations are the time-dependent equations of ideal gas dynamics, i.e. the Euler equations, which express the conservation of mass, momentum, and energy for an inviscid gas. The equations are written in generalized coordinates and conservation form:

$$\frac{\partial \hat{Q}}{\partial t} + \frac{\partial \hat{F}}{\partial \xi} + \frac{\partial \hat{G}}{\partial \eta} + \frac{\partial \hat{H}}{\partial \zeta} = 0 \tag{1}$$

where

$$\hat{Q} = \frac{Q}{J} = \frac{1}{J}\begin{bmatrix} \rho \\ \rho u \\ \rho v \\ \rho w \\ e \end{bmatrix} \tag{2}$$

$$\hat{F} = \frac{1}{J}\begin{bmatrix} \rho U \\ \rho U u + \xi_x p \\ \rho U v + \xi_y p \\ \rho U w + \xi_z p \\ (e+p)U - \xi_t p \end{bmatrix} \tag{3}$$

$$\hat{G} = \frac{1}{J}\begin{bmatrix} \rho V \\ \rho V u + \eta_x p \\ \rho V v + \eta_y p \\ \rho V w + \eta_z p \\ (e+p)V - \eta_t p \end{bmatrix} \tag{4}$$

$$\hat{H} = \frac{1}{J}\begin{bmatrix} \rho W \\ \rho W u + \varsigma_x p \\ \rho W v + \varsigma_y p \\ \rho W w + \varsigma_z P \\ (e+p)W - \varsigma_t p \end{bmatrix} \tag{5}$$

$$\begin{aligned} U &= \xi_x u + \xi_y v + \xi_z w + \xi_t \\ V &= \eta_x u + \eta_y v + \eta_z w + \eta_t \\ W &= \varsigma_x u + \varsigma_y v + \varsigma_z w + \varsigma_t \end{aligned} \tag{6}$$

$$p = (\gamma - 1)[e - \rho(u^2 + v^2 + w^2)/2] \tag{7}$$

The variables ξ and η correspond to the coordinates parallel and normal to the body surface, respectively, while ς corresponds to the spanwise direction for three dimensional flow. Q represents density, momentum, and total energy per unit volume. The Jacobian of the transformation, J, is defined as:

$$J = \frac{\partial(\xi, \eta, \varsigma)}{\partial(x, y, z)} \tag{8}$$

The equations are nondimensionalized by the freestream density $\tilde{\rho}_\infty$ and soundspeed $\tilde{a}_\infty$.

Numerical Method

The Euler code used in the present study is the CFL3D code developed in the Analytical Methods Branch at NASA Langley Research Center.[3,4] This is an implicit, finite volume, upwind-differencing code in which the spatial derivatives of the fluxes are split into forward and backward contributions using flux-vector splitting so that type dependent differencing can be utilized. The flux-vector splitting method used is that of Van Leer,[5,6] which has been recently extended for use on dynamic meshes.[4] It is continuously differentiable at eigenvalue sign changes and allows shocks to be captured with at most two interior zones. In practice, only one zone is usually observed.

Although flux-vector splitting is used in the current study, the code also incorporates the flux-difference approach of Roe.[6] The code can be used for steady and unsteady flows using either the Euler or Navier Stokes equations and can handle very general geometries since it allows for block structured and embedded grids.

The starting point for the time advancement algorithm is the backward Euler time differencing scheme:

$$R(Q^{n+1}) = 0 \tag{9}$$

where $R(Q^{n+1})$ is given by:

$$\left[\delta_\xi \hat{F} + \delta_\eta \hat{G} + \delta_\varsigma \hat{H}\right]^{n+1} + \left[\frac{(1+\phi)}{J\Delta t} Q^{n+1} - \frac{(1+2\phi)}{J\Delta t} Q^n + \frac{\phi}{J\Delta t} Q^{n-1}\right] = 0 \tag{10}$$

If $\phi = 0$, the scheme is first–order accurate in time, while if $\phi = 1/2$, the scheme is temporally second–order accurate.

The flux–vector splitting (FVS) method extended for dynamic meshes in Ref. 4 is used to split the fluxes into forward and backward contributions according to the signs of the eigenvalues of the Jacobian matrices. For example, $\delta_\xi \hat{F}$ in Eq. (10) at a cell centered at point i (holding the j and k indices constant) can be written:

$$\begin{aligned} \left[\delta_\xi \hat{F}\right]_i &\equiv \left[\delta_\xi^- \hat{F}^+ + \delta_\xi^+ \hat{F}^-\right]_i \\ &= \left[\hat{F}^+(Q^-_{i+1/2}) + \hat{F}^-(Q^+_{i+1/2})\right] - \\ &\quad \left[\hat{F}^+(Q^-_{i-1/2}) + \hat{F}^-(Q^+_{i-1/2})\right] \end{aligned} \tag{11}$$

The equations for $\widehat{F}^{\pm}$ for a moving mesh can be found in Ref. 4. $Q^{\pm}$ denotes state variables on cell interfaces determined from upwind-biased interpolations of the conserved variables.

$$Q^{-}_{i+1/2} = Q_i + \left\{\frac{1}{4}[(1-\kappa)\Delta_- + (1+\kappa)\Delta_+]\right\}_i \tag{12a}$$

$$Q^{+}_{i+1/2} = Q_{i+1} - \left\{\frac{1}{4}[(1-\kappa)\Delta_+ + (1+\kappa)\Delta_-]\right\}_{i+1} \tag{12b}$$

where

$$\Delta_+ = Q_{i+1} - Q_i \qquad \Delta_- = Q_i - Q_{i-1} \tag{13}$$

The parameter $\kappa \in [-1, 1]$ forms a family of difference schemes[5]: $\kappa = -1$ corresponds to second-order fully-upwind differencing, $\kappa = 0$ to Fromms scheme, and $\kappa = 1/3$ to third-order upwind-biased differencing.

When flux-limiting is desired to eliminate oscillations in shock regions, a *min-mod* limiter is used. Flux-limited interpolations are identical in form to Eqs. (12a) and (12b), except that Δ_+ and Δ_- are replaced with $\overline{\Delta}_+$ and $\overline{\Delta}_-$, respectively, where:

$$\begin{aligned} \overline{\Delta}_+ &= \max\left[0, \min(\Delta_+ \mathrm{sgn}\Delta_-, \beta\Delta_- \mathrm{sgn}\Delta_+)\right]\mathrm{sgn}\Delta_+ \\ \overline{\Delta}_- &= \max\left[0, \min(\Delta_- \mathrm{sgn}\Delta_+, \beta\Delta_+ \mathrm{sgn}\Delta_-)\right]\mathrm{sgn}\Delta_- \end{aligned} \tag{14}$$

$$\beta = \frac{(3-\kappa)}{(1-\kappa)} \tag{15}$$

Equation (9) is a nonlinear equation which can be solved iteratively using a Newton linearization as

$$\frac{\partial R}{\partial Q}(Q^{\ell+1} - Q^{\ell}) = -R(Q^{\ell}) \tag{16}$$

Here, ℓ is a sequence of iterates so that at convergence $Q^{\ell+1} = Q^{\ell} = Q^{n+1}$. The solution of Eq. (16) at each time step is generally not feasible, however, since it requires the solution of a large banded matrix. The solution is therefore obtained with a spatially-split approximate factorization, in which the implicit operator is split into a sequence of easily invertible equations. The three-dimensional algorithm is implemented in three steps as:

$$\begin{aligned} &\left[\frac{I(1+\phi)}{J\Delta t} + \delta^-_\xi \frac{\partial \widehat{F}^+}{\partial Q} + \delta^+_\xi \frac{\partial \widehat{F}^-}{\partial Q}\right]\Delta Q^* = -R(Q^{\ell}) \\ &\left[\frac{I(1+\phi)}{J\Delta t} + \delta^-_\eta \frac{\partial \widehat{G}^+}{\partial Q} + \delta^+_\eta \frac{\partial \widehat{G}^-}{\partial Q}\right]\Delta Q^{**} = \left(\frac{1+\phi}{J\Delta t}\right)\Delta Q^* \\ &\left[\frac{I(1+\phi)}{J\Delta t} + \delta^-_\zeta \frac{\partial \widehat{H}^+}{\partial Q} + \delta^+_\zeta \frac{\partial \widehat{H}^-}{\partial Q}\right]\Delta Q^{\ell} = \left(\frac{1+\phi}{J\Delta t}\right)\Delta Q^{**} \\ &Q^{\ell+1} = Q^{\ell} + \Delta Q^{\ell} \end{aligned} \tag{17}$$

For time accurate calculations, successive iterations of Eq. (17) can be used at each time step in order to minimize factorization and linearization errors.

For steady state calculations, only one iteration of Eq. (17) is used at each step. In addition, the convergence rate is accelerated using a local time stepping procedure and the FAS multigrid scheme.[3] The implicit spatial derivatives of the convective and pressure terms are spatially first-order accurate, resulting in block tridiagonal inversions for each sweep. The algorithm is completely vectorizable since the operations in each of the spatial directions can be vectorized over the remaining two.

At each time step boundary conditions are applied explicitly. In the far field, a quasi-one-dimensional characteristic analysis is used to determine boundary data, while on the body, pressure and density are extrapolated from the interior and no flow is allowed through the surface.

Potential Code

Governing Equations

In the potential flow calculations, the flow is assumed to be governed by the general frequency, modified TSD potential equation which may be written in conservation law form as

$$\frac{\partial f_0}{\partial t} + \frac{\partial f_1}{\partial x} + \frac{\partial f_2}{\partial y} + \frac{\partial f_3}{\partial z} = 0 \tag{18}$$

where

$$\begin{aligned} f_0 &= -A\phi_t - B\phi_x \\ f_1 &= E\phi_x + F{\phi_x}^2 + G{\phi_y}^2 \\ f_2 &= \phi_y + H\phi_x\phi_y \\ f_3 &= \phi_z \end{aligned} \tag{19}$$

The coefficients A, B, and E are defined as

$$A = M_\infty^2 \qquad B = 2M_\infty^2 \qquad E = 1 - M_\infty^2 \tag{20}$$

Several choices are available for the coefficients F, G, and H depending upon the assumptions used in deriving the TSD equation. The coefficients herein are defined as

$$F = -\frac{1}{2}(\gamma+1)M_\infty^2 \quad G = \frac{1}{2}(\gamma-3)M_\infty^2 \quad H = -(\gamma-1)M_\infty^2 \tag{21}$$

The lifting surface is modeled by imposing the following boundary conditions:

$$Flow \quad tangency : {\phi_z}^{\pm} = {f_x}^{\pm} + f_t \tag{22a}$$

$$Trailing \quad wake : \Gamma_t + \Gamma_x = 0 \qquad and \qquad \Delta\phi_z = 0 \tag{22b}$$

where $\Delta(\ )$ represents the jump in $(\ )$ across the wake. The flow-tangency condition is imposed along the mean plane of the lifting surface. In Eq. (22a) the plus and minus superscripts indicate the upper and lower surfaces of the mean plane, respectively. The wake is assumed to be a planar extension from the trailing edge to the downstream boundary of the finite-difference grid.

Entropy effects are included in the TSD solution[7] by replacing the streamwise flux f_1 (Eq. (19)) in the TSD equation by an alternative flux given by

$$f_1 = (\gamma+1)M_\infty^2 R(V\overline{V} - \frac{1}{2}V^2) + G{\phi_y}^2 \tag{23}$$

where

$$R = \left[\frac{2 + (\gamma-1)M_\infty^2}{(\gamma+1)M_\infty^2}\right]^{\frac{1}{2}} \tag{24a}$$

$$V = \left[\frac{(1+R)\phi_x}{1+\phi_x+R}\right] \tag{24b}$$

$$\overline{V} = \left[\frac{R^2-1}{2R}\right] \tag{24c}$$

The first term of this new flux was derived by an asymptotic expansion of the Euler equations including the effects of shock-generated entropy. This analysis shows that Eq. (23) is accurate to at least $O({\phi_x}^3)$ in the expanded Euler equations.

Vorticity effects are included in the TSD solution[7] by writing the velocity vector as the sum of potential and rotational components according to

$$\vec{V} = \nabla\Phi - \frac{1}{\gamma-1}\frac{s}{c_v}\nabla^{\omega} \tag{25}$$

In Eq. (25), the first term on the right-hand side is the gradient of a scalar potential Φ and the second term involves the product of the entropy s and the gradient of a Clebsch variable Ψ. The function Ψ is a measure of the stretching and rotating of vortex filaments associated with entropy variation.[8] For the applications of interest in the present work, the rotational part of the velocity vector is assumed to occur only in the region downstream of shock waves. Further assuming that the entropy convects with the freestream speed and that the shock curvature is negligible implies that

$$\frac{\partial \Psi}{\partial x} = \frac{1}{\gamma M_\infty^2}, \qquad \frac{\partial \Psi}{\partial y} = 0, \qquad \frac{\partial \Psi}{\partial z} = 0 \tag{26}$$

as shown in Ref. 8. These assumptions eliminate the variable Ψ from the formulation leaving only the entropy to be determined throughout the flow field. In a steady flow, entropy is constant along streamlines and changes only through shock waves. The entropy jump is computed along shocks using the Rankine-Hugoniot relation

$$\frac{s}{c_v} = ln\frac{(\gamma+1){u_1}^2 - (\gamma-1)R^2}{(\gamma+1)R^2 - (\gamma-1){u_1}^2} - \gamma ln\frac{{u_1}^2}{R^2} \tag{27}$$

where

$$u_1 = 1 + \phi_x - u_s \tag{28}$$

In Eq.(28), u_1 is the flow speed upstream of the shock and u_s is the shock speed. Then, for simplicity, the grid lines are assumed to approximate the streamlines of the flow, which is consistent with the small-disturbance approximation. The entropy is either convected downstream along the grid lines according to

$$\frac{\partial s}{\partial t} + \frac{\partial s}{\partial x} = 0 \tag{29}$$

for unsteady applications, or is held constant along the grid lines for steady applications.

The modified velocity vector in turn modifies the TSD equation because the streamwise disturbance speed $u = \phi_x$ is now given by

$$u = \phi_x - \frac{1}{\gamma(\gamma-1)M_\infty^2}\frac{s}{c_v} \tag{30}$$

The new TSD equation has the same conservation law form as Eq. (18) with the new fluxes defined by simply replacing ϕ_x by the modified speed given by Eq. (30).

Numerical Method

The potential flow code used in the present study is the CAP-TSD code developed in the Unsteady Aerodynamics Branch at NASA Langley Research Center.[9,10] The code uses a time-accurate approximate factorization (AF) algorithm similar to that described previously for the Euler equations, for the solution of the TSD equation.[11,12] The AF algorithm consists of a Newton linearization procedure coupled with an internal iteration technique. For unsteady flow calculations, the solution procedure involves two steps. First, a time linearization step is performed to determine an estimate of the potential field. Second, internal iterations are performed to minimize linearization and factorization errors. Specifically, the TSD equation (Eq. (18)) is written in general form as

$$R(\phi^{n+1}) = 0 \tag{31}$$

where ϕ^{n+1} represents the unknown potential field at time level (n+1). The solution to Eq. (31) is then given by the Newton linearization of Eq. (31) about ϕ^ℓ

$$R(\phi^\ell) + \left(\frac{\partial R}{\partial \phi}\right)_{\phi=\phi^\ell}\Delta\phi = 0 \tag{32}$$

In Eq. (32), ϕ^ℓ is the currently available value of ϕ^{n+1} and $\Delta\phi = \phi^{\ell+1} - \phi^\ell$. During convergence of the iteration procedure, $\Delta\phi$ will approach zero so that the solution will be given by $\phi^{n+1} = \phi^\ell$. In general, only one or two iterations are required to obtain acceptable convergence.

The AF algorithm is formulated by first approximating the time derivative terms (ϕ_{tt} and ϕ_{xt} terms) by second-order accurate finite-difference formulae. The TSD equation is rewritten by substituting $\phi = \phi^\ell + \Delta\phi$ and neglecting squares of derivatives of $\Delta\phi$ which is equivalent to applying Eq. (32) term by term. The resulting equation is then rearranged and the left-hand side is approximately factored into a triple product of operators yielding

$$L_\xi L_\eta L_\varsigma \Delta\phi = -\sigma R(\phi^\ell, \phi^n, \phi^{n-1}, \phi^{n-2}) \tag{33}$$

where

$$\begin{aligned} L_\xi &= 1 + \frac{3B}{4A}\xi_x \Delta t \frac{\partial}{\partial \xi} - \xi_x \frac{\Delta t^2}{2A}\frac{\partial}{\partial \xi} F_1 \frac{\partial}{\partial \xi} \\ L_\eta &= 1 - \xi_x \frac{\Delta t^2}{2A}\frac{\partial}{\partial \eta} F_2 \frac{\partial}{\partial \eta} \\ L_\varsigma &= 1 - \xi_x \frac{\Delta t^2}{2A}\frac{\partial}{\partial \varsigma} F_3 \frac{\partial}{\partial \varsigma} \end{aligned} \tag{34}$$

The equations for the spatial fluxes F_1, F_2, F_3, and the residual R are given in Ref 11. In Eq. (33) σ is a relaxation parameter which is normally set equal to 1.0. To accelerate convergence to steady-state, the residual R may be over-relaxed using $\sigma > 1$. Equation (33) is solved using three sweeps through the grid by sequentially applying the operators L_ξ, L_η, and L_ς as

$$\begin{aligned} \xi - sweep &: L_\xi \Delta\phi^* = -\sigma R \\ \eta - sweep &: \quad L_\eta \Delta\phi^{**} = \Delta\phi^* \\ \varsigma - sweep &: L_\varsigma \Delta\phi = \Delta\phi^{**} \end{aligned} \tag{35}$$

Further details of the algorithm development and solution procedure may be found in Refs. 11 and 12.

The CAP-TSD code can be used for aerodynamic and aeroelastic analysis of complete aircraft configurations with arbitrary combinations of lifting surfaces and bodies including canard, wing, tail, control surfaces, tip launchers, pylons, fuselage, stores, and nacelles. The code has the option of half-span modeling for symmetric cases or full-span modeling to allow the treatment of anti-symmetric mode shapes, fuselage yaw, or unsymmetric configurations such as an oblique wing or unsymmetric wing stores.

TWO–DIMENSIONAL RESULTS

For two-dimensional study, the NACA 0012 airfoil was selected for analysis because of the simplicity of the geometry and the availability of experimental unsteady data.[13] Steady-state calculations were performed for the airfoil at $M_\infty = 0.8$ and $\alpha_0 = 1.25°$. These conditions correspond to an AGARD test case for inviscid flow methods,[14] and have been studied by numerous researchers. Unsteady calculations were performed for the airfoil pitching harmonically about the quarter chord with an amplitude of $\alpha_1 = 2.51°$ and a reduced frequency of k=0.1628 ($k = \frac{\omega c}{u}$) at $M_\infty = 0.755$ and $\alpha_0 = 0.016°$. These calculations are compared with the experimental unsteady data of Ref. 13.

Steady Flow

The effects of grid density were determined first, using the Euler code, by examining the force and moment coefficients as well as the pressure distribution as the grid was systematically refined. For this study, three C-type grids were considered. The finest grid was a 257 × 65 mesh with 257 points along the surface and wake, with 176 points on the airfoil surface and 65 points approximately normal to the surface. The coarsest grid was constructed by deleting every other mesh line from the finest grid resulting in a 129 × 33 mesh with 88 points on the airfoil. An intermediate 193 × 41 mesh was also used which had 112 points on the airfoil. For all of the grids, the outer boundary radius was fixed at approximately 20 chordlengths.

The effects of grid density on the lift, moment, and drag coefficients are shown in Fig. 1. The results are plotted as coefficient versus 1/(total number of grid points) for three values of κ, which controls the spatial accuracy of the upwind FVS scheme. The calculations included a point vortex representation for the airfoil to account for the induced velocities in the far field due to circulation (lift). As the grid density was increased the values of the lift, moment, and drag coefficients extrapolate to 0.3606, -0.0395, and 0.0229, respectively, for all values of κ. With the third-order upwind-biased scheme ($\kappa = 1/3$), the lift and moment coefficients are relatively insensitive to grid density as shown in the upper part of Fig. 1. The solution obtained using Fromm's scheme ($\kappa = 0$) shows slightly more variation in these coefficients as the grid density is decreased. The second-order fully upwind scheme ($\kappa = -1$) exhibits the largest change between the fine and coarse grid solutions. For the drag coefficient, all three schemes yield approximately the same results. With the third-order upwind-biased scheme, the lift and drag coefficients on the 257 × 65 mesh differ from the extrapolated values by 0.04 percent and 1.38 percent, respectively. On the 193 × 41 mesh the values of lift and drag differ by 0.10 percent and 3.9 percent of the extrapolated values. For both the fine and the medium grids, the moment coefficient is within 0.1 percent of the value extrapolated for infinite mesh density. On the 129 × 33 mesh, the lift, moment, and drag coefficients show a 0.175 percent, 0.58 percent, and 6.8 percent difference from the extrapolated values, respectively.

The effects of grid density on the pressure distribution are shown in the top third of Fig. 2. These results were obtained using the third-order scheme for the three grids previously described. The pressure distributions computed using the three grids are almost identical with only slight differences near the upper and lower surface shocks.

The effect of including the point vortex induced velocities in the far field boundary conditions on the solution is shown in the center of Fig. 2. The calculations were performed using the 193×41 grid and results were obtained both with and without including the point vortex. The resulting pressure distributions are very similar with small differences occurring only near the shocks. The effect on the force and moment coefficients, however, is more significant. For example, the lift coefficient decreases from the previously reported value of 0.3606, computed with the point vortex, to a value of 0.3428 computed without it. It is noted that in Ref. 15, Euler solutions for airfoils were obtained which were virtually independent of the outer boundary extent when the point vortex velocities were included in the far field boundary condition.

Finally, a comparison between Euler and TSD potential flow pressure distributions for this case is presented in the lower third of Fig. 2. Both sets of results were obtained by neglecting the vortex induced velocities in the far field. The Euler calculation was performed using the 193×41 grid. The TSD calculation was performed on a Cartesian grid which was derived from the Euler grid by using the distribution of points along the airfoil projected to the mean plane and using the (approximately) vertical distribution of points at the trailing edge. As shown in Fig. 2, the two solutions are in very good agreement, with the main differences occuring in the regions of the shocks. The shocks are slightly sharper in the Euler solution, which has only one interior point in each of the shocks, in comparison with the TSD solution. Furthermore, this case is a very challenging one for the TSD code since it is normally regarded as being outside the range of applicability of TSD potential theory. The good agreement is attributable to the inclusion of entropy and vorticity effects as demonstrated in Ref. 7.

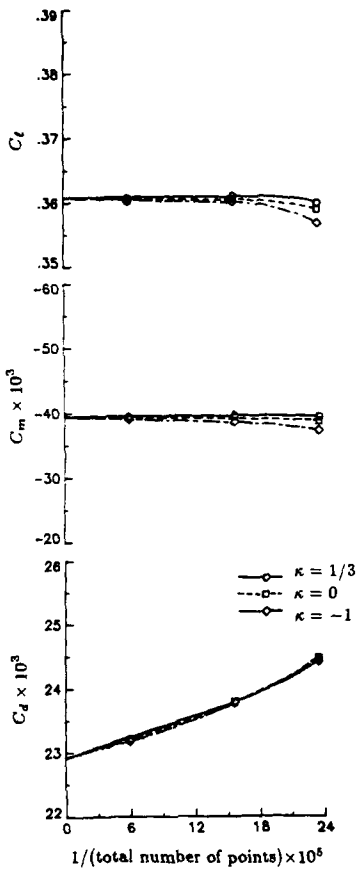


Figure 1. Effects of grid density and spatial accuracy on the force and moment coefficients for the NACA 0012 airfoil at $M_\infty = 0.8$ and $\alpha_0 = 1.25°$ computed using the CFL3D code.

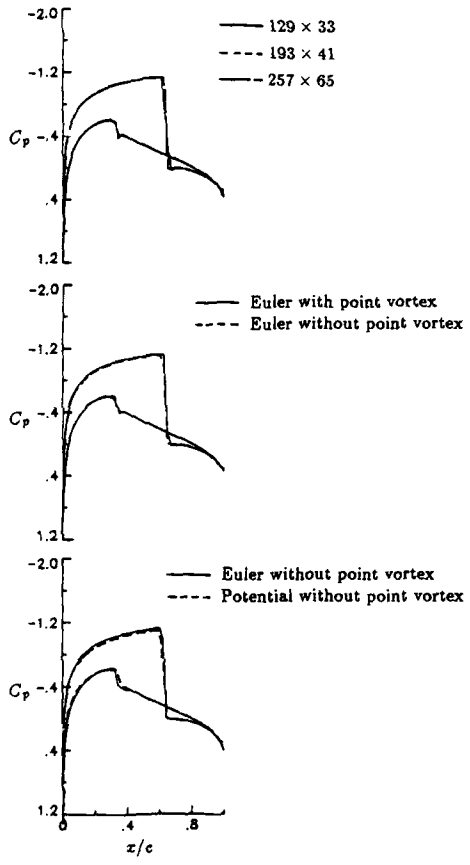


Figure 2. Effects of grid density and far field boundary conditions on the pressure distribution for the NACA 0012 airfoil at $M_\infty = 0.8$ and $\alpha_0 = 1.25°$.

Unsteady Flow

Results were obtained for the pitching NACA 0012 airfoil using both the Euler and potential codes. The Euler results were obtained using the 193 × 41 grid and the third-order upwind-biased scheme ($\kappa = 1/3$). The grid for the potential flow calculations was derived from the Euler grid as described previously. For both Euler and TSD, the results were obtained using second-order time accuracy and two subiterations at each time step, unless otherwise noted. Furthermore, the Euler and TSD solutions did not use the point vortex far field boundary condition since the steady-state lift is nearly zero for this case.

Calculated instantaneous pressure distributions at eight points in time during a cycle of motion are shown in Fig. 3 for comparison with each other as well as with the experimental data. In each pressure plot, the instantaneous angle of attack is noted. Both sets of calculations were performed using 1000 steps per cycle of motion to ensure temporal convergence. During the first part of the cycle, there is a shock wave on the upper surface of the airfoil and the flow over the lower surface is predominately subcritical. During the latter part of the cycle, the flow about the upper surface is subcritical and a shock forms along the lower surface. The pressure distributions indicate that the shock position oscillates over approximately 25 percent of the chord, and in general, that the two sets of calculated results compare well with the data with notable exceptions near the shocks. Furthermore, the shock from the potential solutions is generally located slightly downstream of the Euler shock. This result is somewhat surprising given the near perfect agreement in shock location for the steady case shown in Fig. 2.

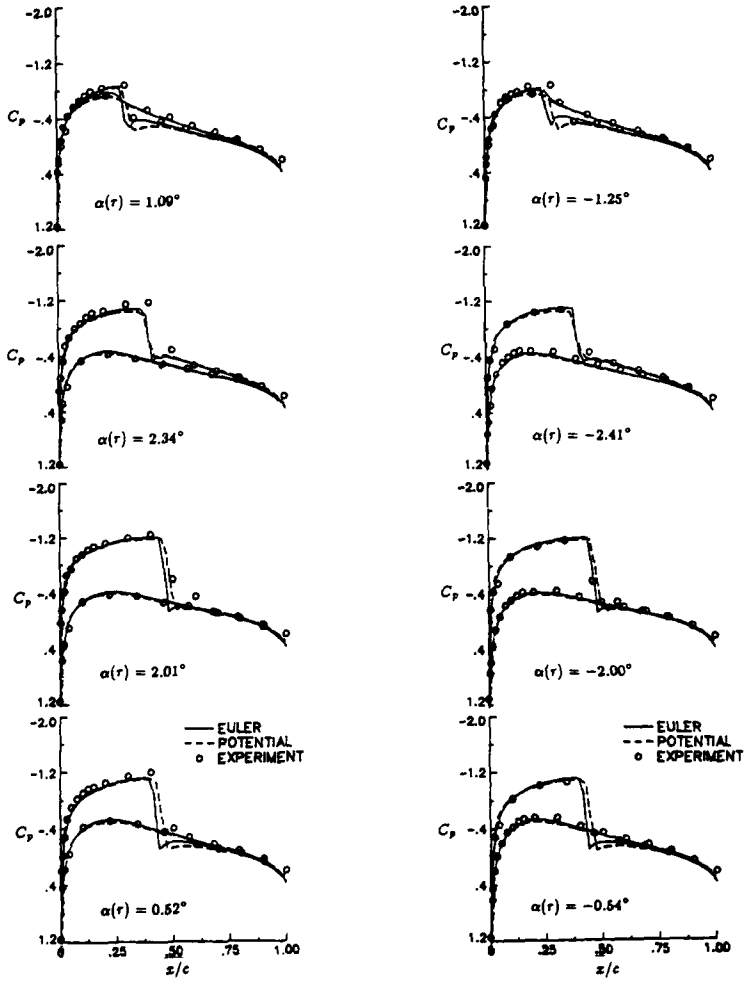


Figure 3. Comparison of instantaneous pressure distributions for the NACA 0012 airfoil at $M_\infty = 0.755, \alpha_0 = 0.016°, \alpha_1 = 2.51°$, and k = 0.1628.

Effects of reduced frequency on the first harmonic components of the upper surface pressure distributions are shown in Fig. 4. The results are presented as real and imaginary parts of the first harmonic of the pressure coefficient, normalized by the amplitude of motion. Potential flow results were obtained using 1000 steps per cycle of motion for k=0.1628, 0.3256, 0.6512, and 1.3024. Euler results for k=0.1628 were also obtained using 1000 steps per cycle while 500 steps per cycle were used for the other three frequencies. Comparisons between Euler and potential solutions are presented for all four values of k. Experimental data is available at k=0.1628 to assess the accuracy of the calculations. As shown in Fig. 4, the two sets of calculations agree equally well across the frequency range considered and are also in good agreement at k=0.1628 with the experimental unsteady pressure data.

Effects of time-step size were also investigated by obtaining results for a wide range of Δt using both the Euler and potential codes. These results are partly summarized in Fig. 5 in the form of lift and moment coefficients versus the instantaneous angle of attack during a cycle of motion, for the four values of k that were considered previously. Euler results are shown in Fig. 5(a); TSD potential results are shown in Fig. 5(b). The calculations were performed with as many as 1000 steps per cycle and with as few as 25. In each case, two subiterations were used at each time step. The Euler and TSD coefficients are generally very similar due to the similarity in the pressure distributions already shown. At k=0.1628, the Euler and TSD coefficients compare reasonably well with each other and with the experimental data. At the higher reduced frequencies, however, small differences between the two sets of results are apparennt. For example, at k=1.3024 the phase lag in the Euler lift coefficient is less than that in the TSD lift coefficient. Also at k=0.6512 and 1.3024, the TSD moment coefficients have a slightly greater magnitude in comparison with the Euler moment coefficients. Furthermore, the results indicate that generally much less than 1000 steps per cycle of motion were required to obtain temporally converged solutions depending on the reduced frequency. At the higher k-values, fewer steps per cycle of motion were required. At the lower frequencies, a larger number of steps were required to accurately resolve the unsteadiness of the flow. When too few steps per cycle were used, small differences appear in the lift and moment coefficients. The differences in the moment coefficients are slightly larger than the differences in the lift coefficients. These differences occur because of numerical oscillations which form near shock waves as shown in Fig. 6, computed using the Euler code. These oscillations are a further indication of an insufficient resolution of the solution in time.

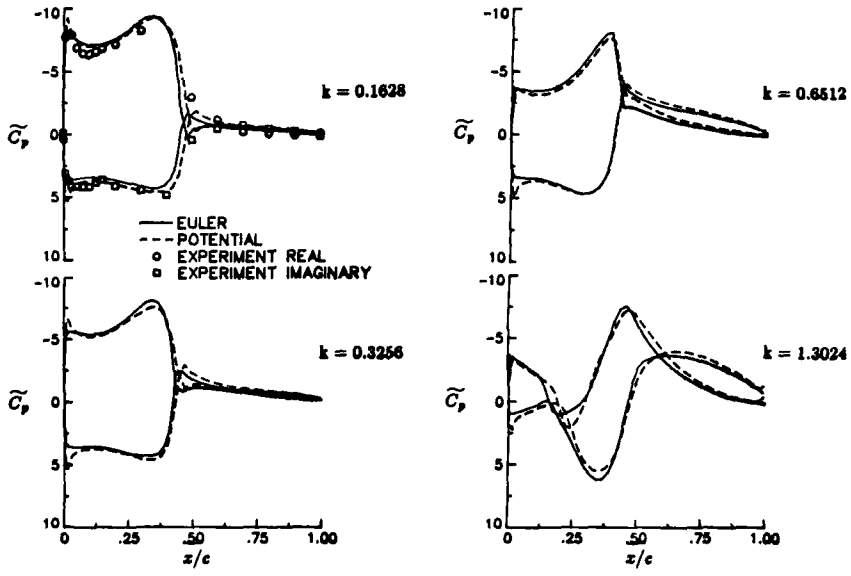
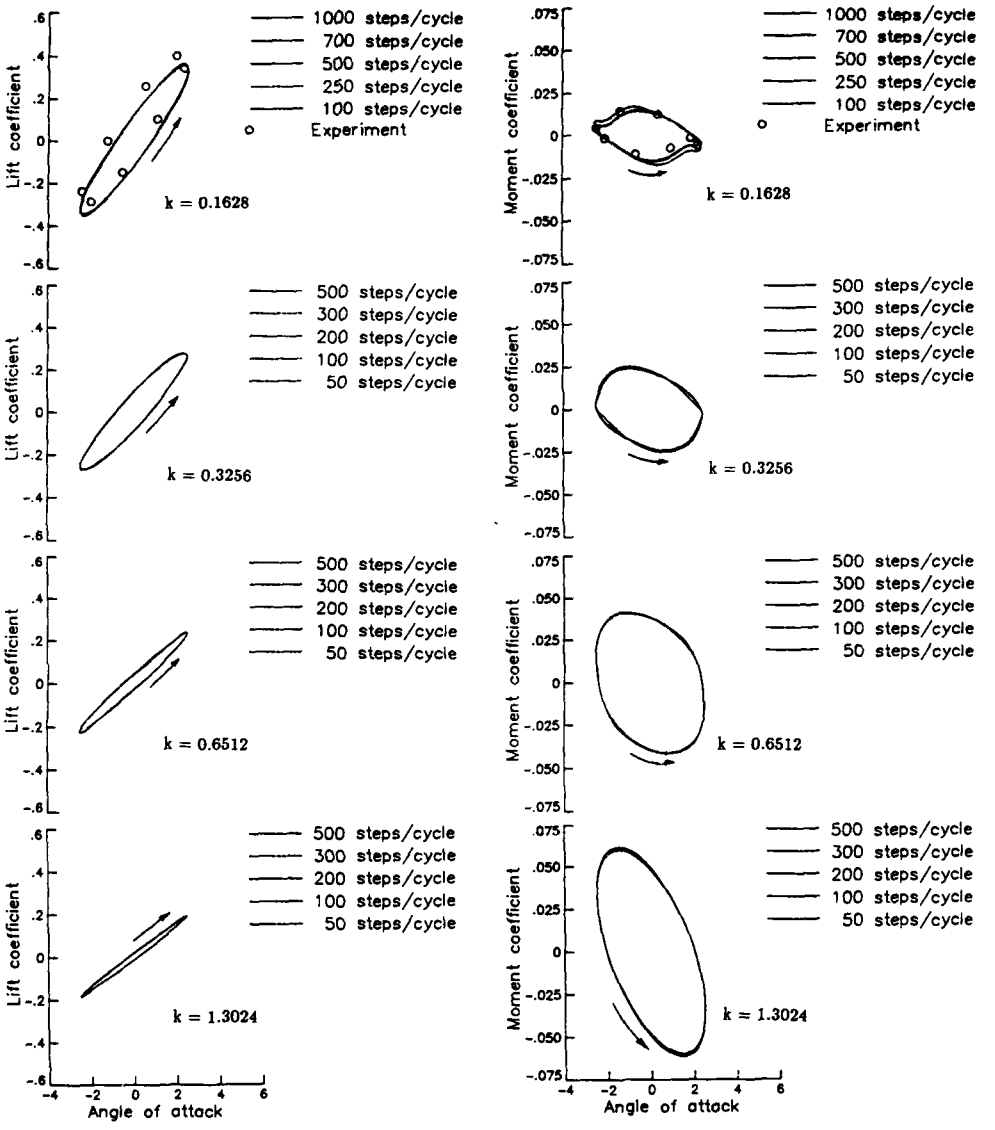
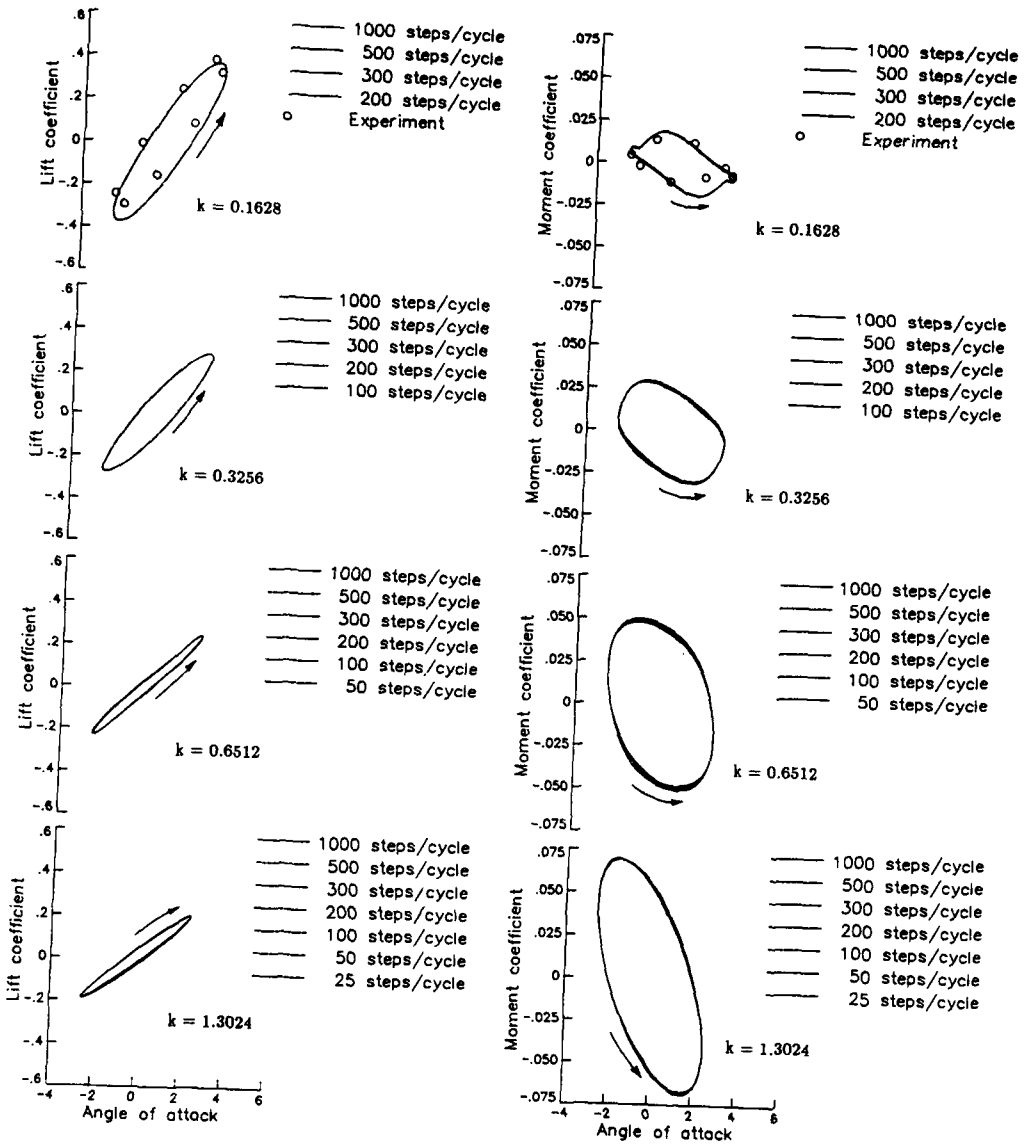


Figure 4. Effects of reduced frequency on first harmonic components of the upper surface pressure distributions for the NACA 0012 airfoil at $M_\infty = 0.755$, $\alpha_0 = 0.016°$, and $\alpha_1 = 2.51°$.



(a) Euler.

Figure 5. Effects of time-step size and reduced frequency on the lift and moment coefficients versus instantaneous angle of attack for the NACA 0012 airfoil at $M_\infty = 0.755, \alpha_0 = 0.016°$, and $\alpha_1 = 2.51°$.



(b) Potential.

Figure 5. Concluded.

To examine this effect more closely, the average total variation of the pressure coefficients over a cycle of motion was computed using the Euler code for various numbers of steps per cycle of motion. The average total variation (TV_a) over a cycle was defined by

$$TV_a = \frac{1}{N}\Sigma_n\Sigma_i(\mid c_p(i+1) - c_p(i) \mid) \tag{36}$$

where N is the total number of steps per cycle and the summations Σ_i and Σ_n are over the number of grid points on the surface of the airfoil and over the number of time steps in the cycle, respectively. Since the total variation gives an indication of how much the pressure increases and decreases over the airfoil, numerical oscillations in the solution can be detected by a higher average total variation over a cycle of motion. Figure 7 shows the average total variation versus the number of steps per cycle for three values of reduced frequency. As the number of points per cycle is increased, the average total variation asymptotes to a particular value indicating that sufficient temporal convergence has been achieved. The number of steps per cycle required to adequately resolve the flow unsteadiness increases as the reduced frequency decreases. It is important to note however that although fewer time steps per cycle are required as the reduced frequency is increased, the actual time step required decreases. For example, from Fig. 7 it is seen that for a reduced frequency of 0.1628, good results can be expected with 300 steps per cycle corresponding to a time step of approximately 0.17. For a reduced frequency of 1.3024, a time step of this size yields less than 50 points in the cycle which is clearly seen in Fig. 7 to be insufficient. This result is not surprising since the higher frequency case should require smaller time steps to resolve the physics of the flow.

Finally, the effects of performing subiterations at each time step on the Euler solutions were investigated as shown in Fig. 8. The pressure distributions were obtained with and without subiterations using 1000 steps per cycle of motion. As shown in the figure, the results obtained without using subiterations are slightly different in the shock region from those obtained with two subiterations at each time step. If the number of steps per cycle is increased to 1700, then Fig. 9 shows that the pressure distribution obtained without subiterations agrees closely to the previous results obtained using two subiterations. The influence of the subiterations is therefore to decrease the number of steps required to sufficiently resolve a cycle of motion. This gain, however, may be offset by the additional work required at each step.

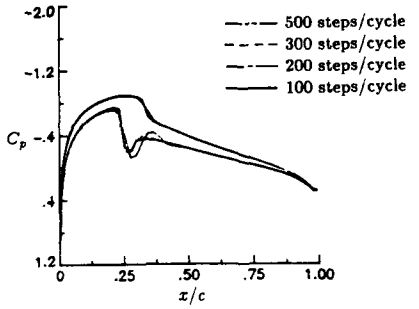


Figure 6. Effect of step size on the instantaneous pressure distribution for the NACA 0012 airfoil at $M_\infty = 0.755$, $\alpha_0 = 0.016°$, $\alpha_1 = 2.51°$, and k = 0.3256.

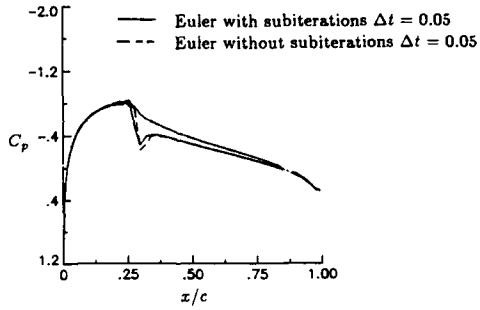


Figure 8. Effect of performing subiterations on the instantaneous pressure distribution at $\alpha(\tau) = -1.25°$.

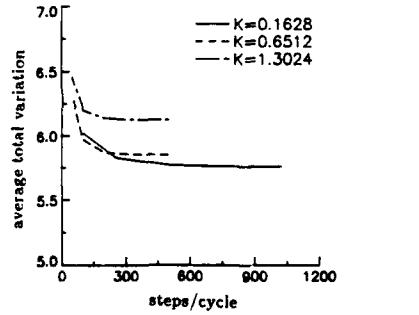


Figure 7. Average total variation versus the number of steps per cycle for three values of reduced frequency for the NACA 0012 airfoil.

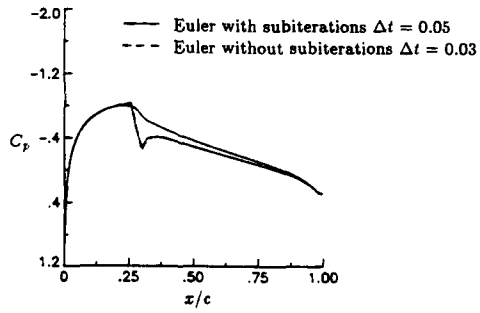


Figure 9. Instantaneous pressure distributions which illustrate the comparison between using a small step size with no subiterations and using a larger step size with subiterations.

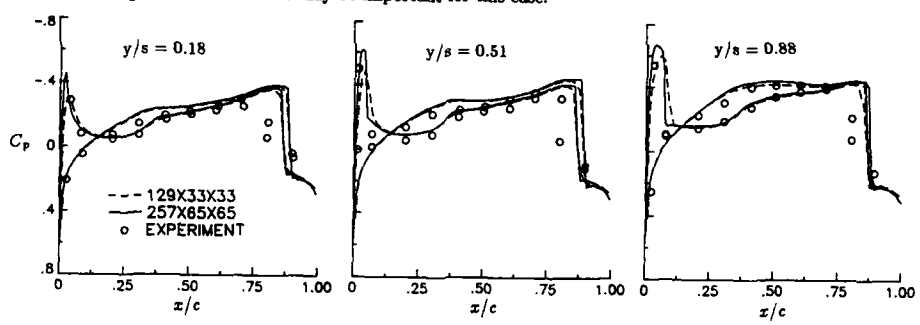
THREE–DIMENSIONAL RESULTS

For three-dimensional study, the F-5 fighter wing was selected for analysis because of the availability of both steady and unsteady data to assess the accuracy of the calculations. The F-5 wing has a panel aspect ratio of 1.58, a leading edge sweep angle of 31.9°, and a taper ratio of 0.28. The airfoil section is a modified NACA 65A004.8 airfoil which has a drooped nose and is symmetric aft of 40 percent chord. The calculations are compared with the experimental pressure data from an F-5 wing model tested by Tijdeman, et al.[16] Steady calculations were performed at $M_\infty = 0.95$ and 0.90, for the wing at zero degrees angle of attack; conditions which have also been studied by other researchers. Unsteady calculations were performed at $M_\infty = 0.9$ for the wing pitching harmonically about a line perpendicular to the root midchord. The amplitude of motion was selected as $\alpha_1 = 0.109°$ and the reduced frequency (based on root chord) was k=0.274 for comparison with the experimental pressure data of Ref. 16. It is noted that the amplitude is very small which may influence the accuracy of the experimental data and that the wing model had some small aeroelastic deformation which was not accounted for in the calculations.

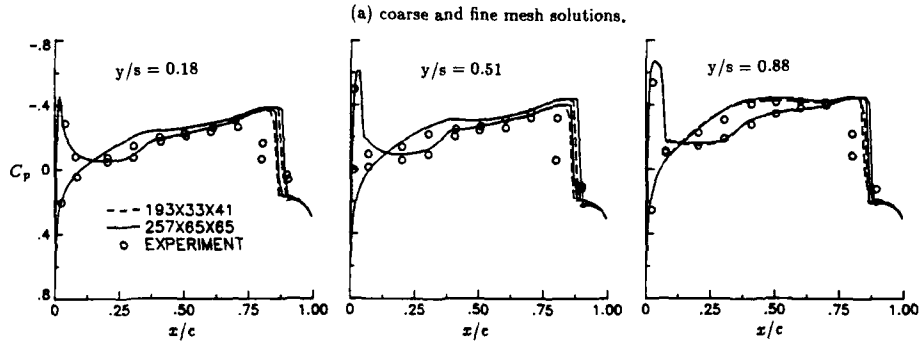
Steady Flow

Similar to the NACA 0012 airfoil study, the effects of grid density on the steady pressure distributions of the F-5 wing at $M_\infty = 0.95$ were determined using the Euler code. Three successively finer grids were used and the pressure distributions are compared with each other as well as with the experimental data. The finest grid is a $257 \times 65 \times 65$ mesh which has 176 points on the wing surface in the streamwise direction, 65 points normal to the surface, and 65 points in the spanwise direction with 33 spanwise points on the wing. A medium grid consisted of a $193 \times 33 \times 41$ mesh with 112 points on the wing surface in the streamwise direction, 33 points normal to the surface, and 20 points on the wing in the spanwise direction. The coarsest grid, which was a $129 \times 33 \times 33$ mesh, was constructed by deleting every other mesh line from the finest grid.

Figure 10(a) shows steady pressure distributions obtained using the $129 \times 33 \times 33$ (coarse) and $257 \times 65 \times 65$ (fine) grids at three span stations of y/s=0.18, 0.51, and 0.88, where y is the direction along the span and s is the span of the wing. The two sets of calculated results agree fairly well with each other except along the upper surface near the leading edge which indicates that the $129 \times 33 \times 33$ grid is too coarse and that grid refinement is necessary. Solutions obtained using the $193 \times 33 \times 41$ (medium) and $257 \times 65 \times 65$ (fine) grids are compared in Fig. 10(b). At each of the three span stations, the calculated pressure distributions agree closely with one another at all points on the wing surface including the leading edge region. This indicates that both grids provide adequate grid resolution and that the results would not change appreciably by the addition of more grid points. Therefore, the $193 \times 33 \times 41$ grid is adequate for obtaining spatially converged solutions for the F-5 wing at these conditions. Furthermore, the calculated pressures agree with the experimental data in regions away from the shocks. The computed shocks, however, lie aft of the experimental shock locations indicating that viscous effects may be important for this case.



(a) coarse and fine mesh solutions.



(b) medium and fine mesh solutions.

Figure 10. Effect of grid density on the steady pressure distributions for the F-5 wing at $M_\infty = 0.95$ and $\alpha_0 = 0.0°$ computed using the CFL3D code.

Steady pressure distributions obtained using both Euler and TSD are compared with the experimental data in Fig. 11 for the F-5 wing at $M_\infty = 0.90$. The grid used for the Euler calculation was the 193 x 33 x 41 mesh. For the potential flow calculations, the grid was constructed in a similar manner as was done for the NACA 0012 airfoil. For all three span stations along the wing, the agreement between the Euler and potential flow results is excellent on the lower surface of the wing including the leading edge suction peak. Along the upper surface of the wing, there is a mild shock wave that is similarly predicted by the Euler and potential codes, although the potential flow results show slightly more negative pressures upstream of the shock than the Euler results. The two sets of calculated results generally compare well with the experimental data especially along the lower surface of the wing. The data, however, does not indicate the presence of the mild shock wave on the upper surface at y/s=0.18 and 0.51 which is predicted by the calculations.

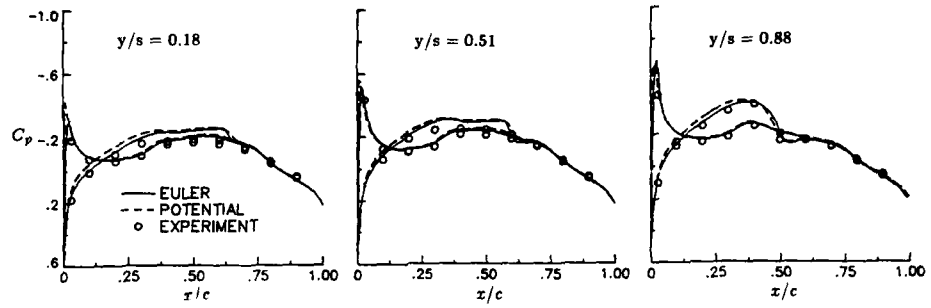
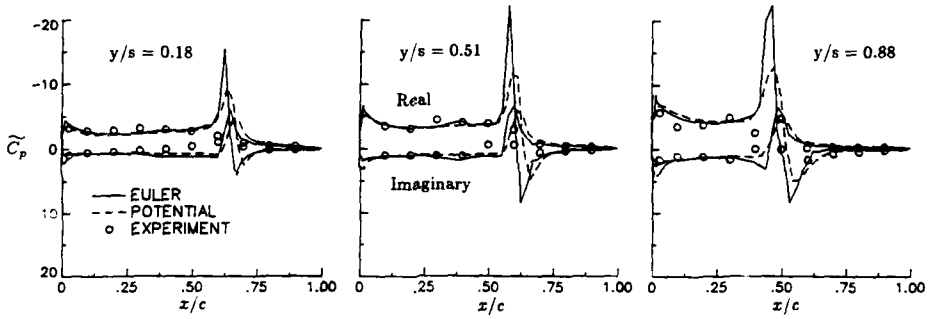
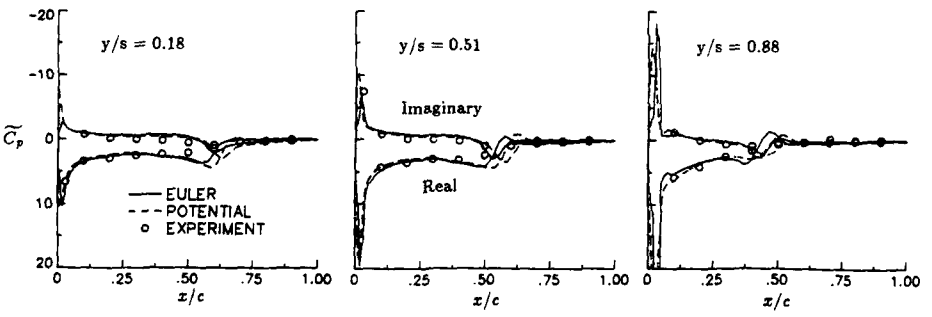


Figure 11. Comparison of steady pressure distributions for the F-5 wing at $M_\infty = 0.9$ and $\alpha_0 = 0.0°$.



(a) upper surface.



(b) lower surface.

Figure 12. Comparison of first harmonic components of the pressure distribution for the F-5 wing at $M_\infty = 0.9, \alpha_0 = 0.0°, \alpha_1 = 0.109°$, and k = 0.274.

Unsteady Flow

Results were obtained for the pitching F-5 wing using both the Euler and potential codes. The Euler calculations were performed using first order time accuracy, no subiterations, and slightly more than 1000 steps per cycle of motion. The potential flow calculations were performed using second-order time accuracy, two subiterations at each time step, and 300 steps per cycle of motion. Figure 12 shows the real and imaginary components of the unsteady pressure distributions at the same three span stations as the steady results of Fig. 11. Unsteady pressures along the upper surface are shown in Fig. 12(a); unsteady pressures along the lower surface are shown in Fig. 12(b). On the upper surface there is a shock pulse in the calculated pressure distributions near 50-60 percent chord which is produced by the motion of the shock wave. The experimental data does not show a shock pulse in the pressures at the two inboard stations because of the absence of the steady shock as discussed above. On the lower surface there are positive and negative spikes in the real and imaginary pressure distributions, respectively, which are much more pronounced in the outboard region of the wing. These spikes are produced by an embedded region of supersonic flow, as indicated by the lower surface leading edge suction peaks shown previously in Fig. 11. In general, the two sets of calculated pressures agree well except near the upper surface shock pulse and in the midchord region along the lower surface. These differences may be attributed to the sharper shock capturing ability of the Euler code in comparison with that from the TSD code. Also, comparisons with the experimental data are qualitatively good for both the Euler and potential results. Further work is required to sort out the differences between the two sets of calculations, however, and additional correlations with experimental data are necessary to validate both codes.

CONCLUDING REMARKS

A code validation study has been presented involving the CFL3D Euler code and the CAP-TSD transonic small-disturbance code for both steady and unsteady applications. The purpose of the evaluation was to determine the accuracy and applicability of the methods by performing detailed studies to assess the influence of several parameters in the numerical modeling of the solution. Two-dimensional parameter studies for steady flow applications were conducted to determine the effects of grid density, spatial accuracy, and far field boundary conditions. The case considered was a NACA 0012 airfoil at a freestream Mach number of 0.8 and an angle of attack of 1.25 degrees. It was found that as the grid was refined, the third-order upwind biased calculation showed less sensitivity than either of the two second-order methods as expected. The values of the lift and drag coefficients on the finest grid (257×65) differ from the values obtained by extrapolation to infinite mesh size by 0.04 percent and 1.38 percent, respectively. The lift and drag on the medium mesh (193×41) differ by 0.10 and 3.9 percent, respectively. For both the fine and medium meshes, the moment coefficient is within 0.1 percent of the extrapolated value. The effect of including a point vortex representation for the airfoil to account for the induced velocities in the far field boundary conditions exhibited only small changes in the pressure distribution which when integrated over the chord, results in approximately a five percent change in the lift coefficient. For three-dimensional steady flow, a grid refinement study using the Euler equations was conducted on the F-5 fighter wing at $M_\infty = 0.95$ and $\alpha_0 = 0.0°$ using three grids with approximately one million, two-hundred fifty-thousand, and one-hundred forty-thousand mesh points, respectively. It was found that the finest grid and the medium grid resulted in essentially identical results. Comparisons between the Euler and potential flow calculations were made for both two–and three–dimensional cases. For the cases considered, the comparisons were very good.

Unsteady calculations were also performed for forced sinusoidal pitching motion to determine the effects of reduced frequency, time step size, and subiterations performed to minimize linearization and factorization errors. It was determined that fewer time steps per cycle were required to resolve the flow field as the frequency of oscillation was increased. In addition, the influence of using subiterations at each time step is to decrease the number of steps required to sufficiently resolve a cycle of motion. Comparisons for two–and three–dimensional cases between Euler and potential flow calculations were generally good except in the immediate vicinity of the shocks where the potential flow shocks were often located slightly aft of the Euler shocks. This result was somewhat surprising given the excellent agreement between the Euler and TSD calculations for steady flow where the shocks were much stonger.

To asses the applicability of the TSD code, comparisons with Euler calculations for both steady and unsteady flows have been made. The generally favorable agreement between the Euler and TSD calculations indicates that TSD calculations incorporating both entropy and vorticity corrections can be expected to yield results comparable to Euler calculations for problems similar to those considered in the current study. In addition, for TSD calculations, the grid remains fixed for calculating both steady and unsteady flows so that computations over complex configurations are relatively straightforward. Similar calculations with the Euler equations are often complicated by difficult grid generation and by the fact that for unsteady calculations on moving meshes, new grids must be computed at each time step. Also, since the solution of the three dimensional Euler equations involves five unknowns at each grid point, the computer time required for the Euler calculations is much higher than that required by the solution of the TSD equation. For the Euler code used in the present study, the computational rate for three-dimensional calculations was approximately 60×10^{-6} seconds/grid point/iteration while the TSD code required only 5×10^{-6} seconds/grid point/iteration. Both the Euler and TSD calculations were done on a CRAY-2 supercomputer at the National Aerodynamic Simulator facility located at NASA Ames Research Center.

REFERENCES

1. Jameson, A., "Successes and Challenges in Computational Aerodynamics," AIAA 87-1184, January 1987.
2. Edwards, J. W., and Thomas, J. L., "Computational Methods for Unsteady Transonic Flows," AIAA 87-0107, January 1987.
3. Anderson, W. K., Implicit Multigrid Algorithms for the Three-Dimensional Flux Split Euler Equations. PhD. Dissertation, Mississippi State University, August 1986.
4. Anderson, W. K., Thomas, J. L., and Rumsey, C. L., "Extension and Applications of Flux-Vector Splitting to Unsteady Calculations on Dynamic Meshes," AIAA 87-1152-CP, 1987.
5. Anderson, W. K., Thomas, J. L., and Van Leer, B.,"A Comparison of Finite Volume Flux Vector Splittings for the Euler Equations," AIAA Journal, Vol. 24, No. 9, September 1986, pp. 1453-1460.
6. Van Leer, B., Thomas, J. L., Roe, P., and Newsome, R., "A Comparison of Numerical Flux Formulas for the Euler and Navier-Stokes Equations," AIAA 87-1104-CP, 1987.
7. Batina, J.T., "Unsteady Transonic Small-Disturbance Theory Including Entropy and Vorticity Effects," AIAA 88-2278, April 1988.
8. Dang, T.Q., and Chen, L. T., "An Euler Correction Method for Two- and Three-Dimensional Transonic Flows," AIAA 87-0522, January 1987.
9. Batina, J. T., Seidel, D. A., Bland, S. R., and Bennett, R. M., "Unsteady Transonic Flow Calculations for Realistic Aircraft Configurations," AIAA 87-0850, April 1987.
10. Batina, J. T., Seidel, D. A., Bennett, R. M., Cunningham, H. J., and Bland, S. R., "Steady and Unsteady Transonic Small Disturbance Analysis of Realistic Aircraft Configurations," Transonic Symposium, NASA Langley Research Center, Hampton, Virginia, April 1988.
11. Batina, J. T., "An Efficient Algorithm for Solution of the Unsteady Transonic Small Disturbance Equation," AIAA 87-0109, January 1987.
12. Batina, J. T., "Unsteady Transonic Algorithm Improvements for Realistic Aircraft Applications," AIAA 88-0105, January 1988.
13. Landon, R. H., "NACA 0012 Oscillatory and Transient Pitching," Data Set 3 in AGARD-R-702, Compendium of Unsteady Aerodynamic Measurements, August 1982.
14. Yoshihara, H., "Test Cases for Inviscid Flow Field Methods," AGARD-AR-211, May 1985.
15. Thomas, J. L., and Salas, M. D., "Far-Field Boundary Conditions for Transonic Lifting Solutions to the Euler Equations," AIAA Journal, Vol. 24, No. 7, July 1986, pp 1074-1080.
16. Tijdeman, H., Van Nunen, J. W. G., Kraan, A. N., Persoon, A. S., Poestkoke, R., Roos, R., Schippers, P., and Siebert, C. M.,: "Transonic Wind Tunnel Tests on an Oscillating Wing with External Stores," AFFDL-TR-78-194, December 1978.

VERIFICATION OF AN IMPLICIT RELAXATION METHOD FOR STEADY AND UNSTEADY VISCOUS AND INVISCID FLOW PROBLEMS

M.A. SCHMATZ, A. BRENNEIS, A. EBERLE
MESSERSCHMITT-BÖLKOW-BLOHM GmbH,
FE122, Postfach 80 11 60
D - 8000 München 80, FRG

SUMMARY

Described is a three-dimensional Navier-Stokes code (NSFLEX) and an unsteady Euler code (INFLEX3). The fundamental feature of both methods is a Godunov type averaging procedure based on an eigenvalue analysis of the inviscid equations for the calculation of the inviscid fluxes. Up to third-order accuracy in space is employed for the flux calculation. The unfactored implicit equations are solved in time-dependent form by a Newton method. Relaxation is performed with a point Gauss-Seidel technique. Both codes are highly vectorized. Because the codes are finite-volume schemes, they are flexible in handling complex geometries. In PART I the NSFLEX code is applied to steady viscous two-dimensional airfoil and three-dimensional delta wing flows at transonic Mach numbers including vortices. The method compares very well with the experiment. The vortex flow simulation demonstrates that the solution is not very grid dependent. Some problems still exist for these separated flow cases and are regarded to be due to the turbulence model used. In PART II the INFLEX3 method is applied to the unsteady Euler equations in order to predict time-accurate, unsteady, subsonic and transonic flows about three-dimensional configurations oscillating in the flow. Numerical results are given for a rectangular supercritical wing and the so-called LANN-wing. Comparisons show good agreement with experiments for a wide range of Mach numbers. Viscous effects, especially at the rear part of the wing, explain some deviations from the experiment.

1. INTRODUCTION

Advances in the production of higher speed and larger memory computing facilities have made possible the development of new computational aerodynamics methods. Both, the solution of the steady Navier-Stokes equations and the unsteady Euler equations for complex three-dimensional configurations make great demand upon the above mentioned features.

A three-dimensional unsteady Euler code and a steady Navier-Stokes code were developed based on a well proven steady inviscid Euler method [1,2]. The viscous method [3,4] is called **NSFLEX**, which is an acronym for Navier-Stokes solver using characteristic flux extrapolation. The inviscid unsteady method [5] uses the same flux extrapolation and therefore is called **INFLEX3**. The fundamental feature of the method is a Godunov type averaging procedure based on an eigenvalue analysis of the inviscid equations by means of which the inviscid fluxes are evaluated at the finite volume faces which separate constant sets of flow variables on either side. The sum of the flux differences is approximated via a third-order spatial characteristic flux extrapolation scheme for the inviscid fluxes, using sensor functions to detect nonmonotonuous behaviour of the flow variables such as shocks, where the scheme reduces to first-order accuracy. Third-order accuracy is employed to reduce the inherent numerical viscosity of the inviscid flux discretisation. Viscous fluxes are constructed by central differences at each cell face. The unfactored implicit equations are solved in time-dependent form by a Newton method following [6]. Relaxation is performed with a point Gauss-Seidel technique with red-black strategy due to vectorization. It was found that red-black relaxation does not hamper convergence at all. The underlying Euler method was proven to produce highly accurate results for a wide range of Mach numbers [7]. Because the codes are finite-volume schemes, they are flexible in handling complex geometries.

In **PART I** of this paper the NSFLEX code, developed by SCHMATZ, is applied to steady viscous two-dimensional airfoil and three-dimensional wing flows at transonic Mach numbers. The equations solved are the Reynolds-averaged Navier-Stokes equations. The method has been applied successfully to many airfoils and recently to an aircraft-type 'wing in a wind tunnel' flow problem [3]. In this paper two airfoil calculations demonstrate the large influence of the turbulence model on the prediction of drag and even of the pressure distribution. Two simulations of the flow past a fighter-type delta wing are shown and compared with each other and with the experiment. The computation problems are:

- typical transonic airfoil,
- delta wing with round leading edge (RLE),
- delta wing with sharp leading edge (SLE).

The airfoil calculations are performed at two different angles of attack (α=2.1° and α=4.5°). The Mach number is M_∞=0.73 and the Reynolds number is Re=6,100,000. For the round leading edge delta wing (RLE) case a solution on a fine grid (783,522 volumes) and on a coarse grid (270,100 volumes) was performed. The sharp leading edge case (SLE) was simulated with 938,952 cells. The grid topology is of C-H-type. Freestream conditions are: M_∞=0.85, α=10°, Re=9,000,000 for both cases. Laminar-turbulent transition is fixed and the standard Baldwin & Lomax turbulence [8] model is used to calculate the turbulent eddy viscosity. These simple geometry test cases are used to verify the Navier-Stokes method and to assess the number of grid points necessary for complex geometry viscous flow

simulations. The two-dimensional test cases demonstrate the necessity to improve the turbulence models for separated flows.

In **PART II** the INFLEX3 code, developed by BRENNEIS, is applied to the unsteady Euler equations in order to predict time-accurate, unsteady, subsonic and transonic flows about three-dimensional configurations. The wings are considered as rigid and oscillate in the flow. Therefore aeroelastic deformations are not included to keep the calculation simple. Note that the method is not restricted to rigid body motion. The numerical method, called INFLEX3, is an extension to three dimensions of the two-dimensional code INFLEX2. The experiences and theoretical investigations made with INFLEX2 were employed and are summarized in [5]. The code permits the computation of important non-linear flow phenomena, such as irregular shock wave motion, occuring under certain transonic flow conditions. Numerical results were obtained for:

- rectangular supercritical wing (RSW),
- LANN-wing.

Comparisons with experiments [9,10,11] and other computations [12] are given. The goal is to evaluate the accuracy, efficiency and range of applicability of the code and to get the necessary insight for further improvements.

2. GOVERNING EQUATIONS

The basic equations are the time dependent Reynolds-averaged compressible Navier-Stokes equations. Conservation laws are used with body-fitted arbitrary coordinates ξ, η, ζ with cartesian velocity components u, v, w:

$$U_t + E_\xi + F_\eta + G_\zeta = 0 \ , \tag{1}$$

where : $U = J\ (\rho, \rho u, \rho v, \rho w, e)^T$

Fluxes normal to ξ=const., η=const., ζ=const. faces are:

$$E = J\ (\tilde{E}\ \xi_x + \tilde{F}\ \xi_y + \tilde{G}\ \xi_z) \ , \tag{2a}$$

$$F = J\ (\tilde{E}\ \eta_x + \tilde{F}\ \eta_y + \tilde{G}\ \eta_z) \ , \tag{2b}$$

$$G = J\ (\tilde{E}\ \zeta_x + \tilde{F}\ \zeta_y + \tilde{G}\ \zeta_z) \ . \tag{2c}$$

The cartesian fluxes therein are:

$$\tilde{E} = \begin{bmatrix} \rho(u-\dot{x}) \\ \rho u(u-\dot{x}) - \sigma_{xx} \\ \rho v(u-\dot{x}) - \sigma_{xy} \\ \rho w(u-\dot{x}) - \sigma_{xz} \\ e(u-\dot{x}) - \sigma_{xx}u - \sigma_{xy}v - \sigma_{xz}w + q_x \end{bmatrix} , \tag{3a}$$

$$\tilde{F} = \begin{bmatrix} \rho(v-\dot{y}) \\ \rho u(v-\dot{y}) - \sigma_{yx} \\ \rho v(v-\dot{y}) - \sigma_{yy} \\ \rho w(v-\dot{y}) - \sigma_{yz} \\ e(v-\dot{y}) - \sigma_{yy}v - \sigma_{yx}u - \sigma_{yz}w + q_y \end{bmatrix} , \tag{3b}$$

$$\tilde{G} = \begin{bmatrix} \rho(w-\dot{z}) \\ \rho u(w-\dot{z}) - \sigma_{zx} \\ \rho v(w-\dot{z}) - \sigma_{zy} \\ \rho w(w-\dot{z}) - \sigma_{zz} \\ e(w-\dot{z}) - \sigma_{zz}w - \sigma_{zx}u - \sigma_{zy}v + q_z \end{bmatrix} . \tag{3c}$$

σ is the stress tensor and q the heat flux vector. The indices ξ,η,ζ,x,y,z denote partial derivatives with respect to ξ, η, ζ or x, y, z except for the stress tensor σ and the heat flux vector q. For inviscid calculations diffusive terms are set to zero. J is the Jacobian of the inverse mapping and $\dot{x}$, $\dot{y}$ and $\dot{z}$ are the appropriate velocity components of the moving cell. Effective transport coefficients are introduced with the Boussinesq approximation in case of Navier-Stokes equations.

3. NUMERICAL METHOD

To solve equation (1) an implicit procedure is developed which allows time steps with CFL >> 1. The first-order in time discretized implicit form of (1)

$$\frac{U^{n+1} - U^n}{\Delta t} + E_\xi^{n+1} + F_\eta^{n+1} + G_\zeta^{n+1} = 0 \tag{4}$$

is not directly solvable for the dependent variables U^{n+1} by virtue of its nonlinearity. Therefore a sequence of approximations denoted by U^μ such that

$$\lim_{\mu>1} U^\mu \longrightarrow U^{n+1} \tag{5}$$

is constructed.

Linearizing the fluxes

$$E^{\mu+1} = E^\mu + \frac{\partial E^\mu}{\partial U} \Delta U^{\mu+1} , \tag{6a}$$

$$F^{\mu+1} = F^\mu + \frac{\partial F^\mu}{\partial U} \Delta U^{\mu+1} , \tag{6b}$$

$$G^{\mu+1} = G^\mu + \frac{\partial G^\mu}{\partial U} \Delta U^{\mu+1} \tag{6c}$$

around the subiteration state μ, a non-linear Newton method for $U^{\mu+1}$ can easily be given:

$$\frac{\Delta U}{\Delta t} + (A^\mu \Delta U)_\xi + (B^\mu \Delta U)_\eta + (C^\mu \Delta U)_\zeta = \frac{U^n - U^\mu}{\Delta t} - (E_\xi + F_\eta + G_\zeta)^\mu = \text{RHS} . \tag{7}$$

A, B, and C are the Jacobians of the fluxes E, F, and G. μ is the non-linear subiteration count. $\Delta U = U^{\mu+1} - U^\mu$ is the variation of the solution vector ΔU in time and therefore the update is

$$U^{\mu+1} = U^\mu + \Delta U. \tag{8}$$

Because it is well known that for three-dimensional calculations approximate factorisation leads to tremendous time step restrictions, here Eq. (7) is solved using a relaxation technique with special care to vectorization. To construct a relaxation method it is necessary to have a diagonal dominant system of equations. Upwind differencing of the inviscid flux vectors is the natural way to reach a diagonal dominant system. Special attention is taken on using a true representation of the fluxes (RHS) in the left-hand-side Jacobians. For the fluxes used in the present scheme this property is inherent for the Jacobians of the inviscid fluxes [2,3]. The viscous Jacobian is represented approximately by the thin-layer terms in all three directions [3]. Several two- and three-dimensional applications prove that it is not necessary to use the full viscous Jacobian. For inviscid flux calculations a linear locally one-dimensional Riemann solver (Godunov-type differencing) is employed at the finite-volume faces which guarantees the homogeneous property of the Euler fluxes. Diffusive fluxes at the cell faces are built with central differences second-order accurate in space. With the divergence of the characteristically extrapolated fluxes on the right-hand-side (RHS), Eq. (7) has to be solved approximately at every time step. A point Gauss-Seidel technique is used. The implicit equation is discretized for point Gauss-Seidel iteration. The Gauss-Seidel subiteration count is indicated by an upper index ν.

At every i,j,k location the variation in time can be calculated from:

$$\text{DIAG}^\mu_{i,j,k} \; \Delta U^{\nu+1}_{i,j,k} = \omega \; \text{RHS}^\mu_{i,j,k} + \text{ODIAG}_{i,j,k}. \tag{9}$$

DIAG^μ is a 5*5 matrix of the sum of the eigenvalue splitted inviscid and the viscous thin-layer Jacobians with ΔU as factor together with $I/\Delta t$. The term $I/\Delta t$ strengthens diagonal dominance and therefore stability and is necessary in unsteady calculations to get time-accurate solutions. The divergence of the fluxes RHS^μ and matrix DIAG^μ rest at iteration level μ during ν-iteration. The term ODIAG is a function of the i,j,k neighbouring ΔU vectors:

$$\text{ODIAG} = f(\Delta U_{i+1,j,k}, \Delta U_{i-1,j,k}, \Delta U_{i,j+1,k}, \Delta U_{i,j-1,k}, \Delta U_{i,j,k+1}, \Delta U_{i,j,k-1}) , \tag{10}$$

where the actual ΔU vectors of the ν-subiteration are taken. ω is an underrelaxation parameter compensating errors of different spatial order of accuracy on RHS and LHS. By application of the so-called checkerboard scheme, in which points are devided into black and red ones, a high rate of vectorization is achieved.

4. PART I : STEADY VISCOUS FLOW SIMULATION (NSFLEX)

4.1 DETAILS OF THE NUMERICAL METHOD

The governing equations are the Reynolds-averaged Navier-Stokes equations (Eqs. (1,2,3) of Chapter 2). Since steady flow is of interest only,the grid velocity components dx/dt, dy/dt, dz/dt are set equal to zero in Eq. (3). The basis of the computational method is explained in Chapter 3. As it is not necessary for steady flow simulations to be time consistent here a linear Newton method is used instead of a non-linear one (Eq. (7):

$$\frac{\Delta U}{\Delta t} + (A^n \Delta U)_\xi + (B^n \Delta U)_\eta + (C^n \Delta U)_\zeta = -(E_\xi + F_\eta + G_\zeta)^n = RHS \ . \qquad (11)$$

NSFLEX was also tested with a non-linear Newton method in two and three dimensions. It was found that the non-linear method generates less waves and smoothes low frequency errors faster than the linear one. To reduce the memory requirements for the steady state simulation, nevertheless, the linear method is used, especially in the three-dimensional code. Note that both the divergence of the fluxes (RHS) and the Jacobians of the fluxes rest at time level n during the Gauss-Seidel relaxation. The left-hand-side differences are build by second-order upwind differences. Therefore higher under relaxation factors ω can be used in Eq. (9). With first-order upwind differences ω is 0.3, whereas second-order upwind allows ω to reach 0.6 depending on the smoothness of the grid. As the time step Δt is just a remedy to enforce diagonal dominance in steady flow calculations, here a local time step is used depending on the maximum spectral radius of the inviscid Jacobians:

$$\Delta t = CFL/(\max|\lambda_{i,j,k}| + 2k(\xi_x^2+\xi_y^2+\xi_z^2+\eta_x^2+\eta_y^2+\eta_z^2+\zeta_x^2+\zeta_y^2+\zeta_z^2)) . \qquad (12)$$

The CFL number is typically between 150 and 200, k is the heat conductivity coefficient of the cell. Note that the CFL number is restricted by the degree of smoothness of the grid, too. With this method typically 800 to 1000 time steps are necessary to reach asymptotically the steady state solution. Three ν Gauss-Seidel subiteration sweeps are performed at every time step. For inviscid flow simulations two ν sweeps are sufficient to reach a fast and stable residual drive, but for visous solutions the smallness of the cells makes it necessary to converge the subiterations more. In two-dimensional tests it was found that by doubling the subiteration number ν from 3 to 6, the number of time steps n could be reduced by a factor of 2. Note that the cpu-time needed is the same.

Boundary conditions are applied both on the right-hand-side and on the left-hand-side (LHS). For the inviscid fluxes characteristic boundary conditions found from one-dimensional Riemann solutions at the wall and at free surfaces are inherent in the code. In addition for viscous fluxes no slip and adiabatic conditions at solid bodies are used. Note that as inviscid and viscous fluxes are handled separately a zero pressure gradient condition is not necessary. To avoid the manipulation of the LHS terms simple inviscid and viscous boundary conditions are prescribed on ΔU in phantom cell rows. As the configuration moves in freestream no special care must be taken on the freestream condition stored in a phantom cell row. The code extracts automatically such information which is unalterable from characteristic theory. The same holds at the exit plane.

The computations were performed on three different super computers (SIEMENS VP200, CRAY XMP, CRAY 2) and on scalar computer (IBM 3090). In the code the geometry (x,y,z), the solution vector (ρ,ρu, ρv,ρw,e), the divergence of the flux vectors (fρ,fρu,fρv,fρw,fe), the change of the solution vector ($\Delta\rho$, $\Delta\rho$u,$\Delta\rho$v,$\Delta\rho$w,Δe), the eddy viscosity and a switching function have to be stored. This means that the words to store in core are 20 times the number of grid points. Single precision with 32 bits per word is used for the round leading edge delta wing simulation, whereas it was found to be necessary to compute the sharp leading edge cases with 64 bits per word, since the mesh size gets too small at the leading edge, there. The code is fully vectorized. A speed-up factor of 25 compared with a scalar mode run was observed on the SIEMENS VP200. It is interesting to note, that the turbulence model after hand vectorization gives the highest speed-up factor of all subroutines.

More details of the computational method can be found in [3].

4.2 APPLICATIONS

4.2.1 TWO-DIMENSIONAL VISCOUS FLOW (AIRFOIL)

At first typical two-dimensional transonic airfoil simulations are shown to validate the NSFLEX method both for attached and separated flows. Two angle of attack cases are discussed: α=2.1° and α=4.5°. The freestream Mach number is M_∞=0.73, the Reynolds number is Re=6,000,000 and transition is fixed on the upper and on the lower side, respectively, at 7 per cent of the chord length as in the experiment for both cases. In Fig. 4.1 a part of the C-type grid used with 248 times 49 cells is shown. In Fig. 4.2 (α=2.1°) the computed pressure distribution compares very well with the experimental one. Note that the nominal angle of attack of α=2.5° is reduced to α=2.1° to match the lift since wind tunnel effects occur in the experiment. In Fig. 4.3 the iso-Mach lines demonstrate the smoothness of the solution. In Tab. 4.1 the computed aerodynamic forces are compared with the experiment. The pitching moment compares very well, the computed drag coefficient is about 12 per cent overpredicted. Note that the coefficients are found from integrating the pressure and the friction forces on the surface and little errors in the pressure, especially at

the nose, influence the prediction of drag very strongly.

The second case is a separated one with an angle of attack of α=4.5°. Here the aerodynamic forces (Tab. 4.1) compare very well with the experiment, but the pressure distribution does not (Fig. 4.4) albeit the lift is predicted as in the experiment. As one sees in the pressure distribution (Fig. 4.4) and especially in the iso-Mach lines (Fig. 4.5), the flow separates behind the shock both in the experiment and in the computation. As found by other authors, too, the pressure distribution is very strongly influenced by the turbulence model for separated flows [13]. Here the standard turbulence model of Baldwin & Lomax [8] is used. With this model, the shock strength is overpredicted and the shock position is too far downstream [13]. To overcome this lack, work is under progress to substitute the Baldwin & Lomax model in the NSFLEX code or to improve it for separated flow cases. The model of Johnson & King seems to improve this situation [13], but up to now it is restricted to two-dimensional flows. As the NSFLEX code mainly has to be applied to three-dimensional flows, the standard Baldwin & Lomax model is used due to its simplicity compared with transport equation models. But one should keep in mind that especially for separated transonic flows the error introduced by the turbulence model is large and the pressure distribution does not compare very well with the experiment. Whether the same strong dependency as in two dimensions exists in three dimensions is not obvious up to now. But the experiences made in the 'wing in a wind tunnel' workshop [3] indicate this trend.

4.2.2 THREE-DIMENSIONAL VISCOUS FLOW (DELTA WING)

To verify the three-dimensional version of NSFLEX and to assess the capacity of the method, here simulations of the flow past a fighter-type delta wing are shown. The test geometry is the 65° swept delta wing proposed for the 'International Vortex Flow Experiment on Euler Code Validation'. The experimental data are given by the NLR for the present cases. Note that the experiment was performed with a body on the lower side of the wing and the computations with a clean delta wing. Therefore the agreement with the experiment can not be perfect since there are wing body interferences in the experiment. Two different geometrical shapes are considered here: delta wing with round leading edge (RLE) and delta wing with sharp leading edge (SLE). Freestream conditions are: M_∞=0.85, Re=9,000,000, α=10° for both cases. Laminar-turbulent transition is fixed as in the experiment at 11 per cent of root chord length. The standard Baldwin & Lomax turbulence model [8] is used. For the round leading edge delta (RLE) wing case a solution on a coarse grid (RLE1: 270,100 volumes) and on a fine grid (RLE2: 783,522 volumes) was performed. The sharp leading edge case (SLE) was simulated with 938,952 cells (SLE). In Fig. 4.6 the C-H-type grid topology is shown. The special features of the three cases RLE1, RLE2, SLE are summarized in Tab. 4.2.

To visualize the different number of grid points, especially in the round leading edge cases, the surface grid and the grid in the symmetry plane are shown in Fig. 4.7. In Fig. 4.8 the pressure coefficients at the stations x/c(root)=0.3, 0.6, 0.8 are compared with the experiment. The agreement of computation and experiment is very well at the downstream cuts 0.6 and 0.8 but poor at the x/c(root)=0.3 cut for the round leading edge case. Due to the existence of a body on the lower side of the wing in the experiment, the agreement especially for the x/c(root)=0.3 cut cannot be good on the lower side. The same holds for the fine grid solution (Fig. 4.8b). The solution seems not to be very grid dependent since it is nearly the same for the round leading edge cases as can be seen in Fig. 4.8 and in the isobar pictures of Fig 4.9, too. In Fig. 4.10 the reason for the poor agreement at the x/c(root)=0.3 cut can be seen. Flow separates just behind this cut from the leading edge, whereas in the experiment the flow separates from the whole leading edge. This behaviour of the computations seems to depend on the turbulence model as can be seen in the skin friction pattern (Fig. 4.10a,b). The lines converge in front of the transition line (x/c(root)=0.11) and diverge just behind it again. The convergence of the skin friction lines indicate the separation line a short distance downstream of the leading edge. Together with Fig. 4.11, where the three-dimensional streamlines are plotted for the RLE1 case, the topology of the flowfield can be seen. A vortex separates from the leading edge. One small secondary separation region can be seen in the wing tip region. But no secondary separation is found on the main part of the wing for this turbulent solution, as for example was observed for a laminar Navier-Stokes simulation [14]. Note that the solution is not very dependent on the number of grid points within the observed range (270,100 and 783,522). That the turbulence model influences this secondary separation effects, seems to be obvious, but cannot be assessed up to now. Note also that in the turbulence model the first peak of F(z) is selected for the computation of the turbulent eddy viscosity since there is a first maximum of z_{max} and a second one for separated flows. By using the second z_{max}, the turbulent viscosity would be incorrectly overpredicted [15].

For the sharp leading edge case (SLE) the figures indicate that the flow separates from the whole leading edge. Especially in Fig. 4.10 the skin friction pattern shows the topology. The flow leaves the surface at the leading edge, and in contrast to the round leading edge cases the pressure distribution compares better with the experiment at the x/c(root)=0.3 cut. The pressure distribution is given in Fig. 4.8. It seems to be in better agreement with the experiment than in the round leading edge cases. Note that the solution for this case is not as far converged to the steady state solution as the RLE cases due to computational costs. For this case 600 time steps were performed, whereas the round leading edge cases were run about 1000 time steps. The isobars in Fig. 4.9 indicate the differences between round and sharp leading edge solutions. Again no secondary vortices can be found. Whether this is due to the turbulence model or not has to be decided later.

4.3 CONCLUSIONS

The Navier-Stokes solver NSFLEX has been verified for two- and three-dimensional transonic flow problems for separated and attached flows, respectively. As can be studied in two dimensions, the turbulence model influences the solution very strongly if separation is significant. The attached flow simulation comapares very well with the experiment. Even the aerodynamic forces do so, too. The vortex flow simulation demonstrates the capacity of the three-dimensional code. The solution is not very grid dependent. For the round leading edge cases the solution is nearly the same with a fine grid and a coarse grid discretisation. Problems seem to occur with the turbulence model, see also [3]. Here some more investigation is necessary, especially for separated flows. Another problem is the large computer time needed for this viscous flow simulations. To reduce computer time a zonal approach is under development to couple an equivalent inviscid flow together with a boundary-layer solution in regions of weak viscous-inviscid interaction and a Navier-Stokes solution in regions of strong viscous interaction [4,16,17]. Another work under progress is to expand the validity of NSFLEX to hypersonic flow conditions.

5. PART II : UNSTEADY INVISCID FLOW SIMULATION (INFLEX3)

5.1 NUMERICAL DETAILS

For the treatment of real unsteady problems and the application of the relaxation method two necessary assumptions have to be introduced. First, the computation of the unsteady evolution must be done with an uniform time step Δt in the whole computational domain. This global time step is defined from a fixed CFL-number:

$$\Delta t \leq \Delta t_{max} = \min_{i,j,k} \left(\frac{J \, CFL}{\lambda_{max}} \right)_{i,j,k} , \tag{13}$$

where λ_{max} is the maximal Eigenvalue of the cell i,j,k. Secondly, it is necessary to fully converge the subiterations between two time steps. Converging ΔU to zero on the LHS of Eq. (7), on the RHS remains the implicit formulation of Eq. (4) with $\mu \rightarrow n+1$. In contrast to time-asymptotic solution methods, a linear Newton method without subiterations μ, having the advantage of less memory needs, cannot be used. Note that only the application of the non-linear Newton method as formulated in Eq. (7) leads to a time consistent unsteady solution.

5.2 BOUNDARY CONDITIONS

The computation of inviscid flow requires the solid body to be stream surface. This means that the normal mass flux across the boundary must be zero. The so-called no-through flow condition for the finite solid body element moved with $\dot{x}$, $\dot{y}$ and $\dot{z}$ reads:

$$\rho(u-\dot{x})\xi_x + \rho(v-\dot{y})\xi_y + \rho(w-\dot{z})\xi_z = 0 . \tag{14}$$

In the farfield nonreflecting boundary conditions are inherent in the code to avoid reflections of waves from there.

5.3 GRID GENERATION

The mesh used is of type H-H with fixed farfield frame and is generated using Poisson equation [18]. The fourth-order (biharmonic) system

$$\nabla^4 x^i = 0 \quad (i=1,2,3) \tag{15}$$

is implemented as a set of three second-order equations (Poisson and Laplace equation):

$$x_{\xi\xi} + x_{\eta\eta} + x_{\zeta\zeta} = P , \tag{16a}$$

$$y_{\xi\xi} + y_{\eta\eta} + y_{\zeta\zeta} = Q , \tag{16b}$$

$$z_{\xi\xi} + z_{\eta\eta} + z_{\zeta\zeta} = R , \tag{16c}$$

with:

$$P_{\xi\xi} + P_{\eta\eta} + P_{\zeta\zeta} = 0 , \tag{17a}$$

$$Q_{\xi\xi} + Q_{\eta\eta} + Q_{\zeta\zeta} = 0 , \tag{17b}$$

$$R_{\xi\xi} + R_{\eta\eta} + R_{\zeta\zeta} = 0 . \tag{17c}$$

The linear algebraic equations in the physical space (Eq. (16) and (17)) are discretized by central differences and are solved with point Gauss-Seidel iterations. The resulting grid with grid points $(x,y,z)_{i,j,k}$ and source terms $(P,Q,R)_{i,j,k}$ is stored. After each time step in the flowfield computation the wing surface is moved and the mesh is de-

formed, rearranged by one to two grid iterations. To speed up the grid generation method red-black iteration is used as in the Euler method.

5.4 APPLICATIONS AND VALIDATION

The relaxation scheme was tested on a rectangular supercritical wing (RSW) [9] with an aspect ratio of 4 and on a typical transport-aircraft type supercritical wing with an aspect ratio of 7.92 known as the LANN-wing [10,11]. Experiments for these configurations were done at the NASA-Langley Research Center (RSW-wing) and at the NLR facilities (LANN-wing). Both wings perform rigid solid body pitching oscillations about axis normal to the root wing section. Due to the harmonically varying angle of attack

$$\alpha_{(t)} = \alpha_0 + \mathrm{Re}(\alpha_1 e^{i\omega t}) = \alpha_0 + \alpha_1 \cos(\omega t) , \tag{18}$$

the unsteady flow analysis is made with the Fourier analysis. α_0 is the mean angle of attack, α_1 the amplitude of oscillation. The harmonic analysis of the surface pressure coefficient is

$$c_{p(x/c,t)} = c_{p_m(x/c,t)} + \sum_{n=1}^{\infty} \mathrm{Re}[(c^n_{p,\alpha_1(x/c,t)})\ \alpha_1 e^{in\omega t}] , \tag{19}$$

where $c_{p_m(x/c,t)}$ is the mean value of the local surface pressure coefficient and $[c^n_{p,\alpha_1(x/c,t)}]$ the n-th complex component of the local unsteady pressure coefficient per radian. The real (in-phase) and imaginary (out-of phase) value of c^n_{p,α_1} can be expressed as

$$\mathrm{Re}[c^n_{p,\alpha_1(x/c)}] = (c^n_p/\alpha_1) \cos\phi_n \tag{20a}$$

and

$$\mathrm{Im}[c^n_{p,\alpha_1(x/c)}] = (c^n_p/\alpha_1) \sin\phi_n , \tag{20b}$$

with the n-th harmonic unsteady pressure c^n_p and the n-th harmonic phase shift ϕ_n between angle of attack and pressure response. In the computation three Fourier harmonics are calculated. The reduced frequency k, which is the important similarity parameter for unsteady flow is defined as

$$k = \frac{\omega\, c}{2U_\infty} . \tag{21}$$

c is either the chord lenth of the root c_r or the mean aerodynamic chord length $c_{\bar{A}C}$ and U_∞ the freestream velocity. All calculations were started with parallel flow and were carried out for two or three cycles to ensure that the surface pressure repeat from cycle to cycle. As the wave propagation is inverse proportional to frequency and as the reduced frequency was low in most of the test cases examined, two cycles were enough to establish the periodic regime in the vicinity of the wing. Taking into account the two-dimensional experiences of [5] the calculations were done with 100 time steps per cycle (Δt/ cycle). Except for the subsonic test case of the RSW-wing all computations were carried out on the SIEMENS VP200 vector computer.

Rectangular Supercritical Wing

The planform with the four spanwise sections for the pressure evaluation and the surface mesh are shown in Fig. 5.1. The airfoil, Fig. 5.2, is a 12 percent thick (t/c=0.12) supercritical shape with a two-dimensional design Mach number of 0.8 and design lift coefficient of 0.6. The design values of the airfoil geometry are taken from [19] and the wing tip is formed by connecting the lower and upper surface with semicircular arcs. The pitching axis is located at 46 percent of the chord. The location of the wing in the computational domain can be seen in Fig. 5.3. The computational test cases are listed in Tab. 5.1.

The case 1 with a freestream Mach number of 0.700 and a reduced frequency of k=0.178 was calculated on the IBM 3090 without vector facility. A coarse grid with 69*30*34 points was used, which had 74 nodes on the airfoil (37 above and 37 below) at each of the 17 span stations. The CFL-number was 120, corresponding to about 110 Δt/cycle. Calculations done with an explicit code and a CFL-number of 0.4 showed exactly the same results as the implicit one. The ratio of the specific heats γ was equal to 1.131 (Freon) like in the measurements [9].

In Fig. 5.4 the computed mean surface pressure distributions are compared with experimental steady results. The comparisons are good over most of the wing both on the upper and the lower surface. The suction peak at the leading edge is very well predicted by the present method at all spanwise stations. Especially, note the behaviour at the most

outboard section towards the trailing edge. Only the mid-chord region on the upper surface deviates somewhat from the measurements. The real and imaginary parts of the first harmonic analysis are plotted in Fig. 5.5 and Fig. 5.6. Both the in-phase and out-of phase components on the upper surface and on the lower surface are in best agreement with the experimental data everywhere. Fig. 5.7 and Fig. 5.8 show the comparison of the present solution with the results from XTRAN3S [12] (a non-linear transonic small disturbance code), RHOIV [12,20] (a linear lifting surface Kernel function) and the measured data. The resulting pressure magnitude of the upper and lower surface, Fig. 5.7, computed by INFLEX3 agrees very well with the experiment over the whole wing. At the leading edge, XTRAN3S shows an overpredicting oscillating behaviour at the inboard station and an underpredicting behaviour at the outboard stations. The RHOIV results, presented for 0.31, 0.59 and 0.811 fractional span stations are underestimated in the forward half of the wing. The leading edge shock, of course, is not predicted by the linear theory. With exception of the XTRAN3S result at the most inboard station the phase agreement is good over the forward two-thirds of the chords for the three computational methods. Towards the trailing-edge the results by XTRAN3S and RHOIV deviate considerably, whereas the INFLEX3 result represents the decreasing phase qualitatively well. The discrepancy shown may be attributed to viscous effects, starting to influence the flow near the trailing edge.

The numerical results of the second test case were obtained on a refined grid (88*32*50 points). The number of the chordwise-points on the half wing was rised from 37 to 50 for better reproduction of the blunt nose. Fig. 5.9 shows the mean pressure distribution obtained by INFLEX3 and the measured data for a freestream Mach number of 0.804 and a mean angle of attack of 0.06 degree using the original design values of the airfoil geometry from [19]. The oscillations in the mean pressure distribution, Fig. 5.9, which also occur in the real and imaginary part (not shown here), are due to poor geometry definition and can be eliminated by smoothing the wing surface, Fig. 5.10. The curvature behaviour of the upper and the lower surface of the original airfoil and the smoothed airfoil geometry are shown in Fig. 5.11. In Fig. 5.10 the good reproduction of the suction peak at the leading edge and the lower surface pressure distribution can be seen. Poorer agreement is achieved on the upper surface with shocks further aft than in the experiment. This suggests that viscous effects are significant for this supercritical wing and Mach number. The unsteady results for the second test case with a reduced frequency k=0.155 and an oscillation amplitude α_1=1.086 degrees are shown in Fig. 5.12 and Fig. 5.13. The real and imaginary part are well predicted on the lower surface by the present method. On the upper surface they agree better by moving from the inboard to the outboard stations. The peak of the shock near the trailing edge observed in the inboard stations 0.311 and 0.590 vanishes towards the wing tip.

LANN-Wing

Details of the planform with the location of the six spanwise sections for the pressure evaluation and the surface mesh of the wing tip are shown in Fig. 5.14. The airfoil geometry of the 12 percent thick supercritical root and wing tip section, Fig. 5.15, are taken from [21]. Sections lying between the root and wing tip are linearly interpolated. The wing tip is formed by semicircular arcs like for the RSW-wing. The pitching axis is located at 62.1 percent of the root chord from the wing apex and the reduced frequency is based on the mean aerodynamic chord. The location of the wing in the computational domain is shown in Fig. 5.16. The calculations were performed on a grid with 80*38*46 points. Each of the 18 span stations is represented by 100 nodes, 50 on the upper and 50 on the lower surface. Tab. 5.2 lists the computational test cases refered to the standard AGARD cases [10].

The results of CT2, M=0.77, k=0.080, α_0=0.6 and α_1=0.25 degree are shown in Fig. 5.17 to Fig. 5.19. The mean pressure distribution of INFLEX3 correlates very well with the experimental data [10]. Only a slight overprediction on the upper surface behind the shock is observed. The in-phase and out-of phase components agree very well, too, both on the upper and on the lower surface.

In Fig. 5.20 to Fig. 5.22 the results for the design cruise condition, named CT5 (M=0.82, k=0.076, α_0=0.6 and α_1=0.25 degree), are plotted and compared. The mean pressure distribution, the real and imaginary part on the lower surface are in good agreement with experiment. On the upper surface the leading edge suction peak of the mean pressure distribution is exactly represented at all fractional sections. A shift of the shock location aft of the experimental shock position and an overprediction of the shock strength, indicating noticeable viscous effects, is observed. The in-phase and out-of phase components in front of the shock are well reproduced. Due to the downstream shift of the shock location the peak in the in-phase and out-of phase components is shifted downwards, too. With exception of this and the overprediction of the shock strength the unsteady pressures are well predicted by the present method. In order to show that unsteady pressures of higher order than one are negligible small in comparison with the first-order components they are included and compared with the measured data, Fig. 5.23 and Fig. 5.24. The experimental pressure data have to be handled with care because at many locations they are equal to zero in the data set of [10].

Finally the test case CT5 was repeated with twice the pitching oscillation frequency of 48 Hz instead of 24 Hz. The unsteady results of this test case, CT8, are compared with the experiment in Fig. 5.25 and Fig. 5.26. Here, again, the observation made for CT5 holds: Exact reproduction of the real and imaginary pressure coefficients on the lower surface, and good correlation on the upper surface up to the shock, which is shifted aft of the experimental one and overpredicted. Comparing the unsteady results from CT5 (Fig. 5.21 and Fig. 5.22) and CT8 (Fig. 5.25 and Fig. 5.26) the decrease of the in-phase and the

increase of the out-of phase component by rising of the oscillation frequency can be observed.

5.5 CONCLUSIONS

The unsteady Euler code INFLEX3 was applied to a rectangular (RSW-wing) and to a typical transport-type wing, called the LANN-wing. Both have 12 percent thick supercritical airfoil sections and performed rigid body pitching oscillations about an axis normal to the root wing section. The mean pressure distribution and the unsteady pressures were compared with experimental data and results of other computations to validate the present analytical code.

The numerical results of INFLEX3 agreed very well with the measured data at a Mach number of 0.7 and 0.77 for the RSW-wing and the LANN-wing respectively. INFLEX3 showed better agreement than XTRAN3S and RHOIV with experiment at all fractional sections. At higher Mach numbers, 0.804 for the RSW-wing and 0.82 for the LANN-wing (the cruise design condition), INFLEX3 represented very well the mean pressure distribution and the in-phase and out-of phase components on the lower surface and on the upper surface up to the shock. The shock pressure jump is overpredicted and located aft of the experimental shock position. This is due to the absence of viscosity in the Euler solver. Currently, investigations are under progress for the evaluation of viscous-inviscid interactions by coupling the unsteady Euler solution with a boundary layer solution [22].

6. FINAL CONCLUSIONS

The extension of the well-proven steady Euler equations solver EUFLEX [1,7] to steady viscous flows (PART I : NSFLEX) and to time-consistent unsteady inviscid flows (PART II : INFLEX3) is demonstrated here. Both methods compare well with the experiment. Some lacks in the viscous method are due to the turbulence model, especially for separated flows. The methods are fully vectorized and run on different super computers very efficiently.

Acknowledgement: The authors want to thank E. Schnepf from SIEMENS vector processor systems, U. Harms from the IABG supercomputing center and U. Küster from the Rechenzentrum Universität Stuttgart for their help in vectorization and computer system management.

7. REFERENCES

[1] Eberle, A.: 3D Euler calculations using characteristic flux extrapolation. AIAA-paper 85-0119, 1985.

[2] Eberle, A., Schmatz, M.A., Schaefer, O.: High-order solutions of the Euler equations by characteristic flux averaging. ICAS-paper 86-1.3.1, 1986.

[3] Schmatz, M.A.: Three-dimensional viscous flow simulations using an implicit relaxation scheme. In: Kordulla, W.(ed.): Numerical simulation of compressible viscous flow aerodynamics. Notes on Numerical Fluid Mechanics. Vieweg, Braunschweig- Wiesbaden, 1988.

[4] Schmatz, M.A.: Simulation of viscous flows by zonal solutions of the Euler, boundary-layer and Navier-Stokes equations. Zeitschrift für Flugwissenschaften und Weltraumforschung (Journal of Flight Science and Space Research), Vol. 11, 1987, pp. 281-290.

[5] Brenneis, A., Eberle, A.: Unsteady transonic flows past airfoils using a fast implicit Godunov type Euler solver. In: Deville, M.(ed): Proceedings of the 7th GAMM-Conf. Num. Meth. Fl. Mechanics. Notes on Numerical Fluid Mechanics, Vieweg, Braunschweig-Wiesbaden, 1988.

[6] Chakravarthy, S.R.: Relaxation methods for unfactored implicit upwind schemes. AIAA-paper 84-0165, 1984.

[7] Eberle, A.: Characteristic flux averaging approach to the solution of Euler's equations. VKI lecture series, Computational fluid dynamics, 1987-04, 1987.

[8] Baldwin, B.S., Lomax, H.: Thin layer approximation and algebraic model for separted turbulent flow. AIAA-paper 78-257, 1987.

[9] Ricketts, R.H., Sanford, M.C., Watson, J.J., Seidel, D.A.: Subsonic and transonic unsteady- and steady-pressure measurements on a rectangular supercritical wing oscillated in pitch. NASA TM 85765, Part I and II, 1984.

[10] Zwaan, R.J.: LANN-wing. Pitching oscillation. Data set 9, AGARD-R-702, 1982.

[11] Horsten, J.J., den Boer, R.G., Zwaan, R.J.: Unsteady transonic pressure measurements on a semi-span wind tunnel model of a transport-type supercritical wing (LANN model). AFWAL-TR-83-3039, Part I and II, 1983.

[12] Ricketts, R.H., Sanford, M.C., Watson, J.J., Seidel, D.A.: Transonic pressure distributions on a rectangular supercritical wing oscillating in pitch. AIAA-paper, 83-0923, 1983.

[13] King, L.S.: A comparison of turbulence closure models for transonic flows about airfoils. AIAA-paper 87-0418, 1987.

[14] Müller, B., Rizzi, A.: Navier-Stokes computation of transonic vortices over a round leading edge delta wing. AIAA-paper, 87-1227, 1987.

[15] Panaras, A.G., Steger, J.L.: A thin-layer Navier-Stokes solution of the flow about a prolate spheroid. Zeitschrift für Flugwissenschaften und Weltraumforschung (Journal of Flight Science and Space Research), Vol. 12, 1988.

[16] Wanie, K.M., Schmatz, M.A., Monnoyer, F.: A close coupling procedure for zonal solutions of the Navier-Stokes, Euler and boundary-layer equations. Zeitschrift für Flugwissenschaften und Weltraumforschung (Journal of Flight Science and Space Research), Vol. 11, 1987, pp. 347-359.

[17] Schmatz, M.A., Monnoyer, F., Wanie, K.M., Hirschel, E.H.: Zonal solutions of three-dimensional viscous flow problems. IUTAM, Symposium Transsonicum, 1988.

[18] Schwarz, W.: Elliptic grid generation system for three-dimensional configurations using Poisson's equation. 1st Int. Conf. Num. Grid Generation in Comp. Fluid Dyn., Pineridge Press, 1986.

[19] Ricketts, R.H., Sanford, M.C., Watson, J.J., Seidel, D.A.: Geometric and structural properties of a rectangular supercritical wing oscillated in pitch for measurement of unsteady transonic pressure distributions. NASA TM 85673, 1983.

[20] Redman, M.C., Rowe, W.S.: Prediction of unsteady aerodynamic loadings caused by leading edge and trailing edge control surface motions in subsonic compressible flow - computer program description, NASA CR 132634, 1975.

[21] Bland, S.R.: AGARD three-dimensional aeroelastic configurations, AGARD-AR-167, 1982.

[22] Monnoyer, F.: Calculation of 3D attached viscous flows on general configurations with second-order boundary layer theory. To be published in 1988.

Tab. 4.1 Comparison of viscous airfoil simulations (NSFLEX) for a typical transonic airfoil

M_∞ = 0.73, Re = 6,000,000, x_t/c = 0.07 (Baldwin&Lomax), grid : 248 * 49 cells								
α	2.1° (experimental α=2.5°)				4.5° (experimental α=4.5°)			
	A E R O D Y N A M I C F O R C E S							
	computation			experiment	computation			experiment
	pressure	viscous	total		pressure	viscous	total	
c_L	.6896	-.000082	.6895	.7000	.9541	-.000066	.9541	.936
c_D	.01288	.00566	.01857	.0160	.05332	.00458	.0579	.0565
c_M			-.0828	-.0827			-.0802	-.0983

Tab. 4.2 Verification of viscous delta wing flow simulations (NSFLEX)

M_∞ = 0.85, Re = 9,000,000, xt/c(root) = 0.11, α=10°, grid : C-H type			
case	RLE1	RLE2	SLE
cells in ξ - wing (upper) - wake (upper)	146 47 26	158 53 26	162 53 28
cells in η - wing - off tip	50 38 12	87 68 19	92 70 12
cells in ζ	37	57	63
total	270,100	783,522	938,952

Tab. 5.1 Test cases for the Rectangular Supercritical Wing (INFLEX3)

Case	M	α_0 [deg]	α_1 [deg]	f [Hz]	$k=\omega c_r/2U$	Δt/cycle
1	0.700	2.00	1.000	10.0	0.178	110
2	0.804	0.06	1.086	10.0	0.155	100

Tab. 5.2 AGARD test cases for the LANN-Wing (INFLEX3)

Case	M	α_0 [deg]	α_1 [deg]	f [Hz]	$k=\omega c_{AC}/2U$	Δt/cycle
CT2	0.77	0.6	0.25	24.0	0.080	100
CT5	0.82	0.6	0.25	24.0	0.076	100
CT8	0.82	0.6	0.25	48.0	0.151	100

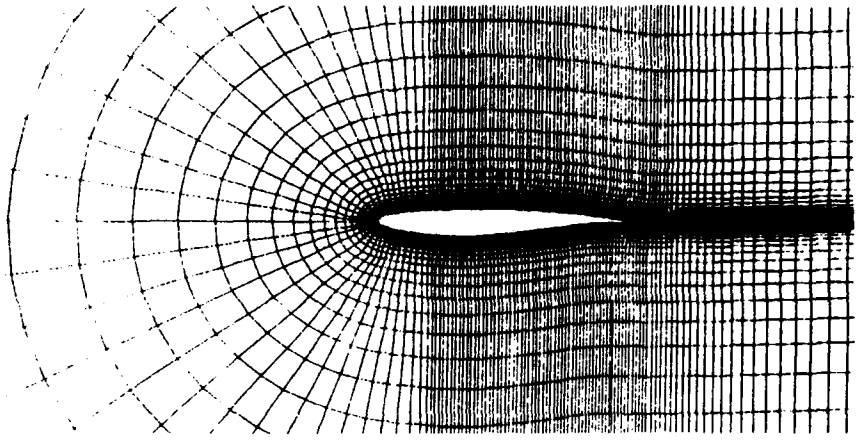


Fig. 4.1 Grid for viscous simulations (248*49 cells)

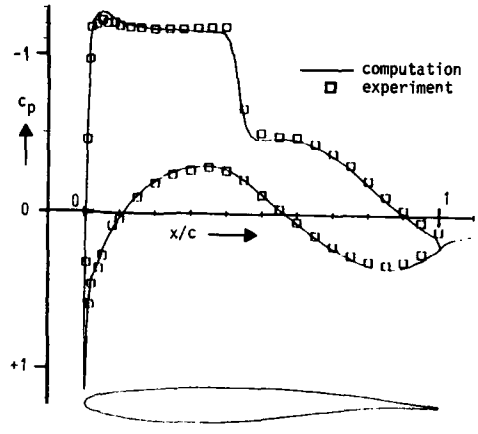


Fig. 4.2 Pressure distribution
(M_∞=0.73, α=2.1°, Re=6*10^6)

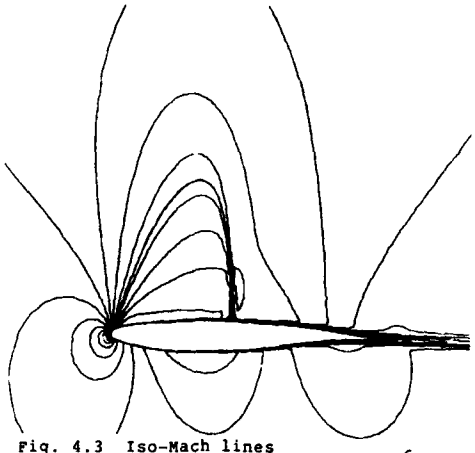


Fig. 4.3 Iso-Mach lines
(M_∞=0.73, α=2.1°, Re=6*10^6)

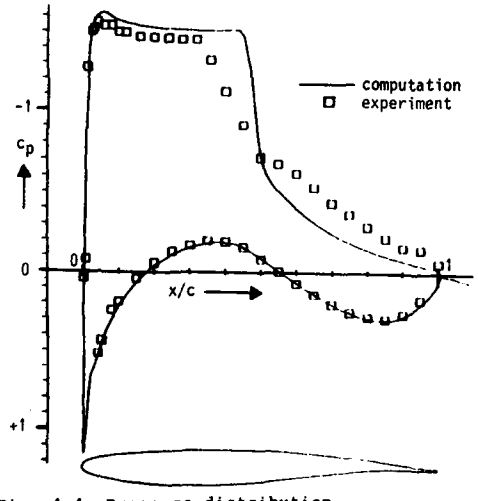


Fig. 4.4 Pressure distribution
(M_∞=0.73, α=4.5°, Re=6*10^6)

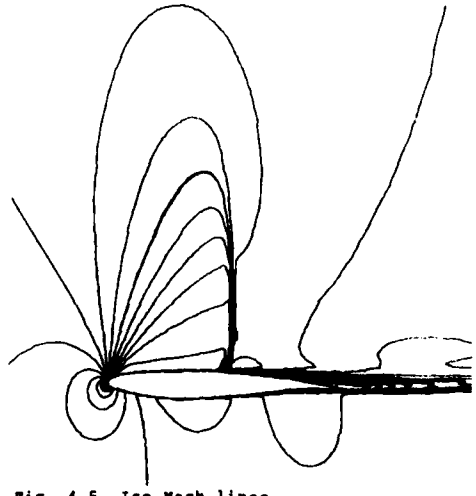


Fig. 4.5 Iso-Mach lines
(M_∞=0.73, α=4.5°, Re=6*10^6)

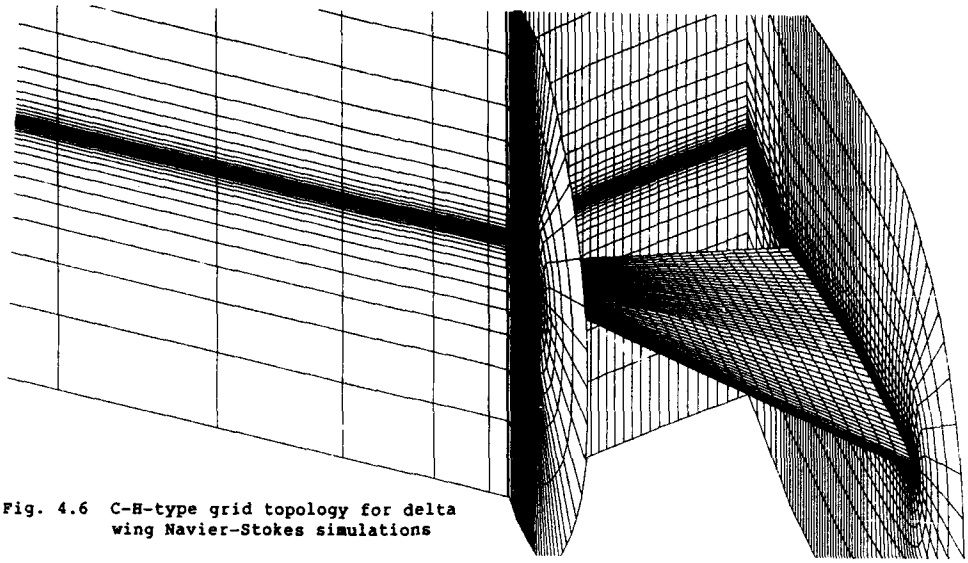


Fig. 4.6 C-H-type grid topology for delta wing Navier-Stokes simulations

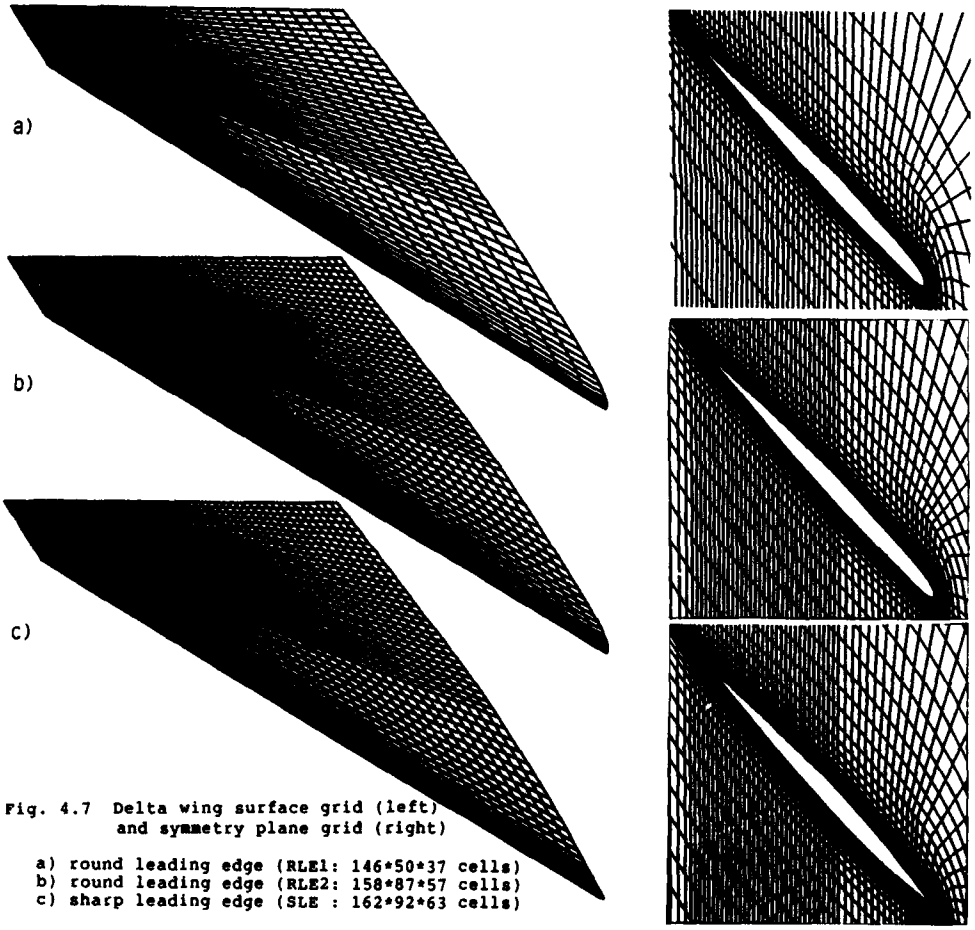


Fig. 4.7 Delta wing surface grid (left) and symmetry plane grid (right)

a) round leading edge (RLE1: 146*50*37 cells)
b) round leading edge (RLE2: 158*87*57 cells)
c) sharp leading edge (SLE : 162*92*63 cells)

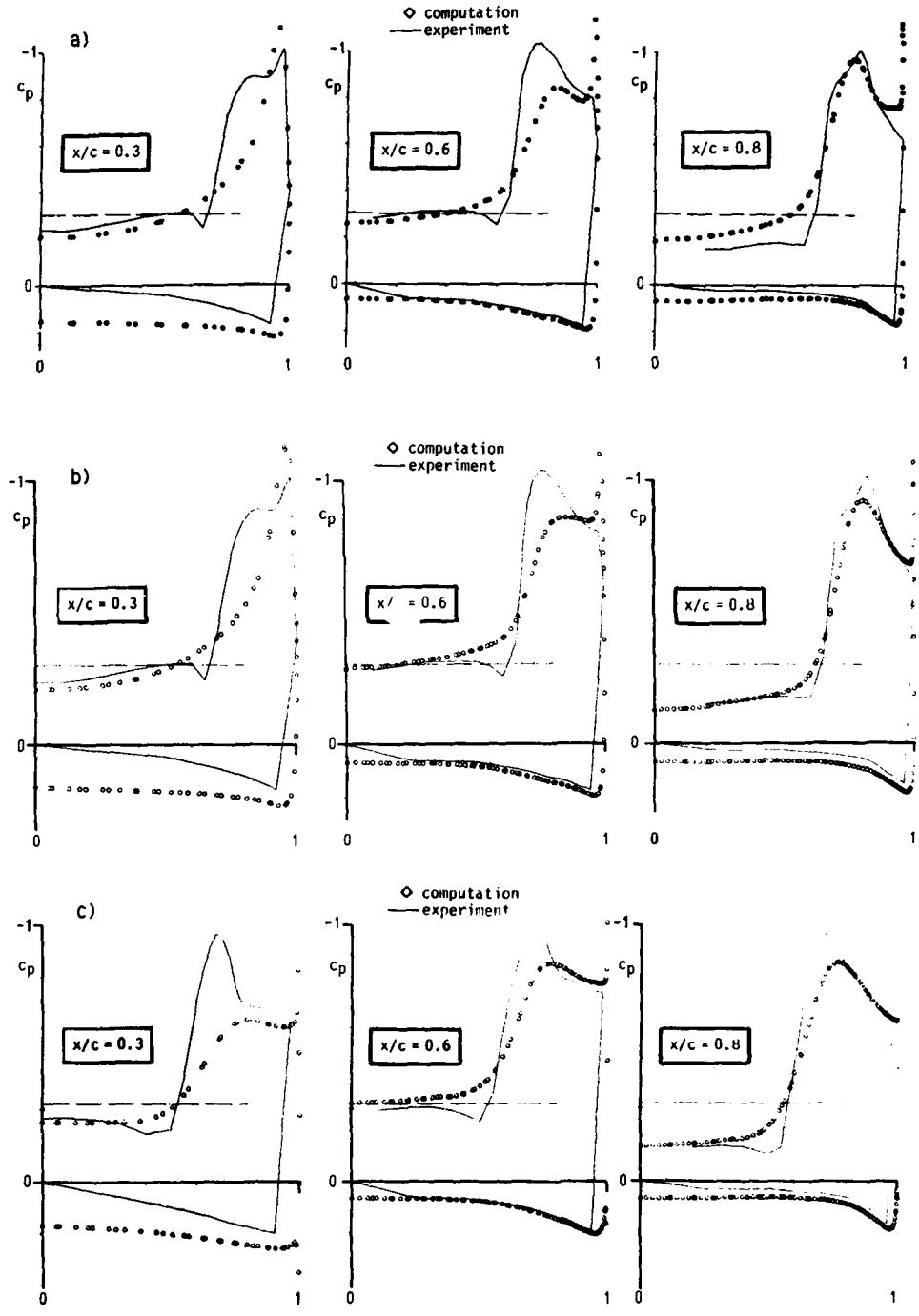


Fig. 4.8 Delta wing pressure distribution (M_∞=0.85, Re=9,000,000, α=10°) at x/c cuts
a) round leading edge (RLE1: 146*50*37 cells)
b) round leading edge (RLE2: 158*87*57 cells)
c) sharp leading edge (SLE : 162*92*63 cells)

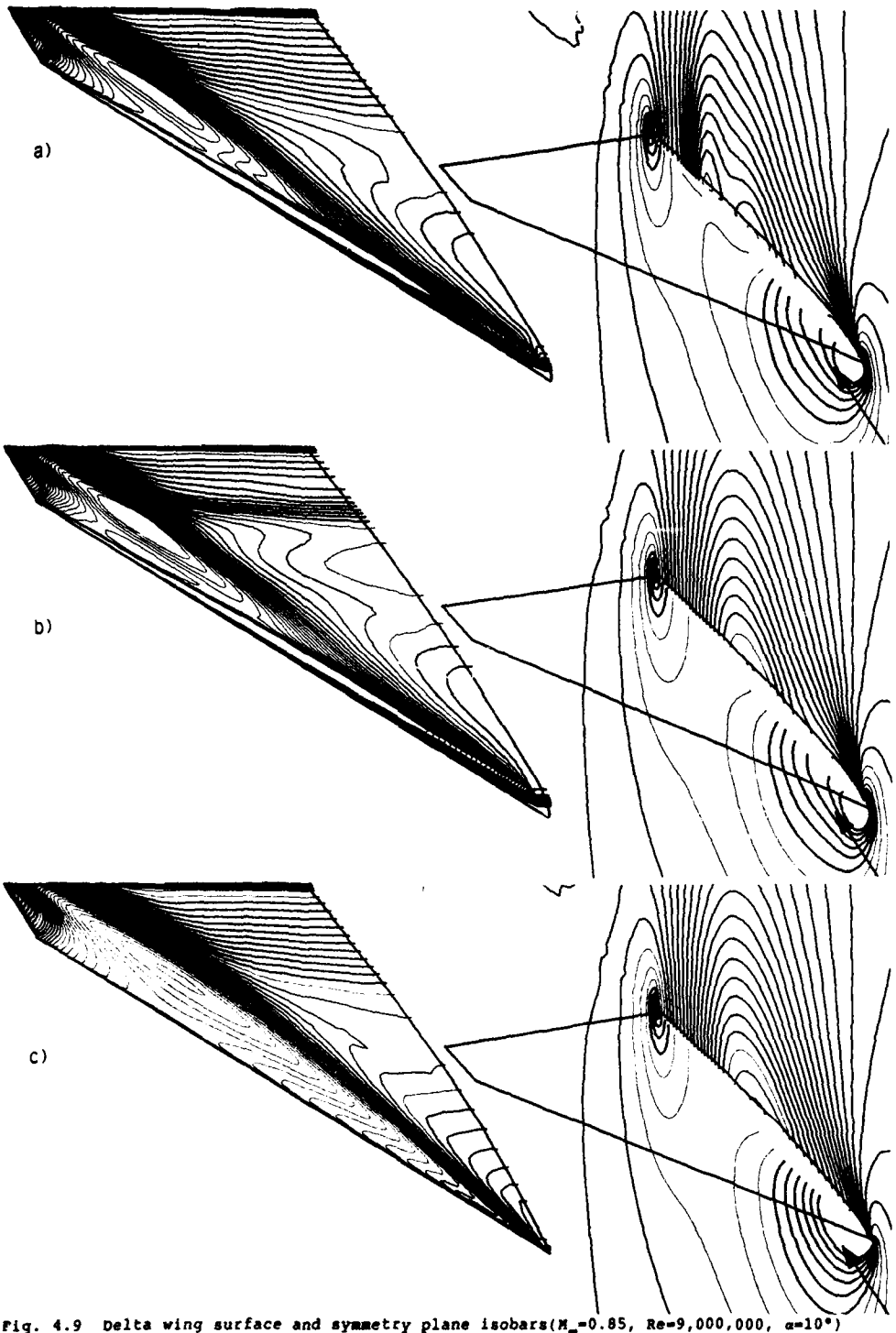


Fig. 4.9 Delta wing surface and symmetry plane isobars(M_∞=0.85, Re=9,000,000, α=10°)
a) round leading edge (RLE1: 146*50*37 cells)
b) round leading edge (RLE2: 158*87*57 cells)
c) sharp leading edge (SLE : 162*92*63 cells)

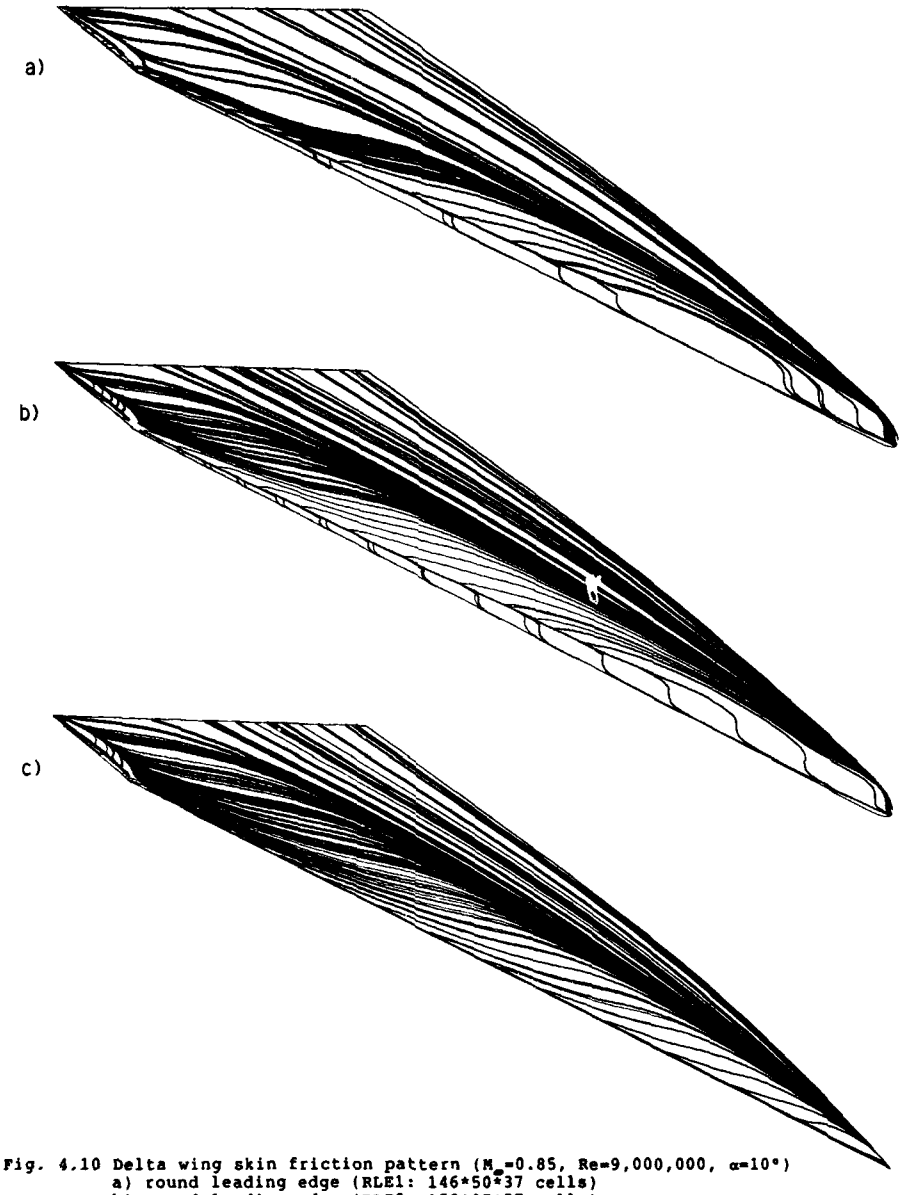


Fig. 4.10 Delta wing skin friction pattern (M_∞=0.85, Re=9,000,000, α=10°)
a) round leading edge (RLE1: 146*50*37 cells)
b) round leading edge (RLE2: 158*87*57 cells)
c) sharp leading edge (SLE : 162*92*63 cells)



Fig. 4.11 Round leading edge delta wing streamlines (RLE1)

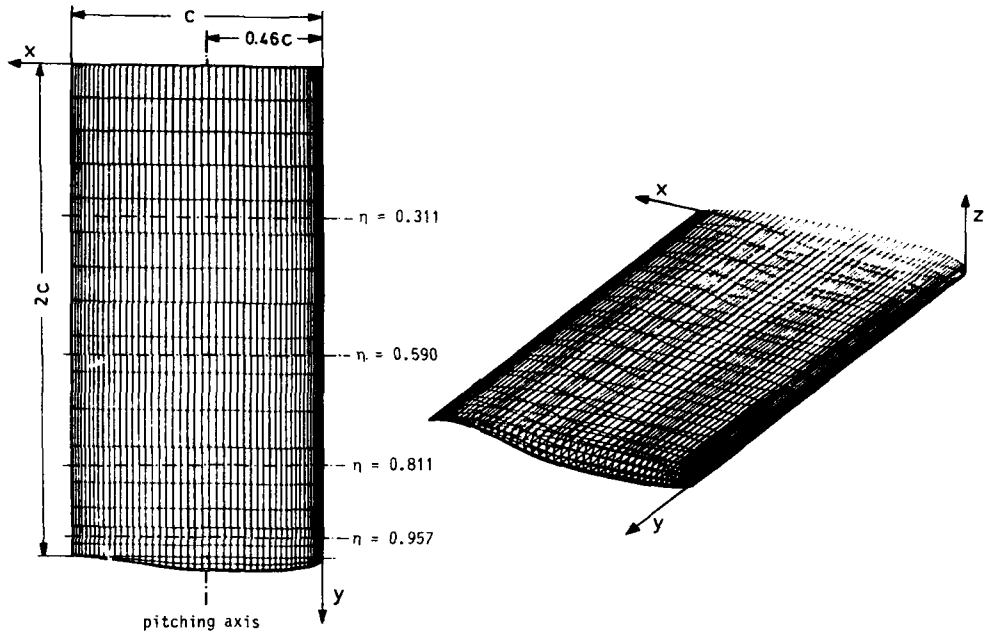


Fig. 5.1 Planform and surface mesh of the rectangular supercritical wing

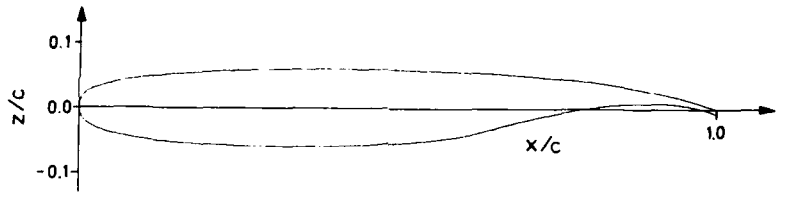


Fig. 5.2 Airfoil shape of the rectangular supercritical wing

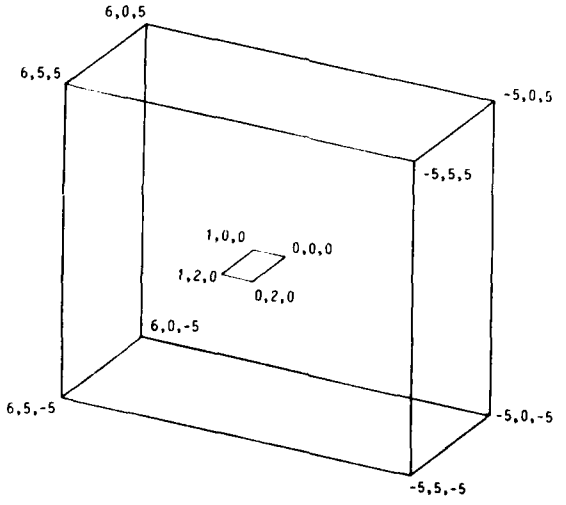


Fig. 5.3 Location of the rectangular supercritical wing in the computational domain

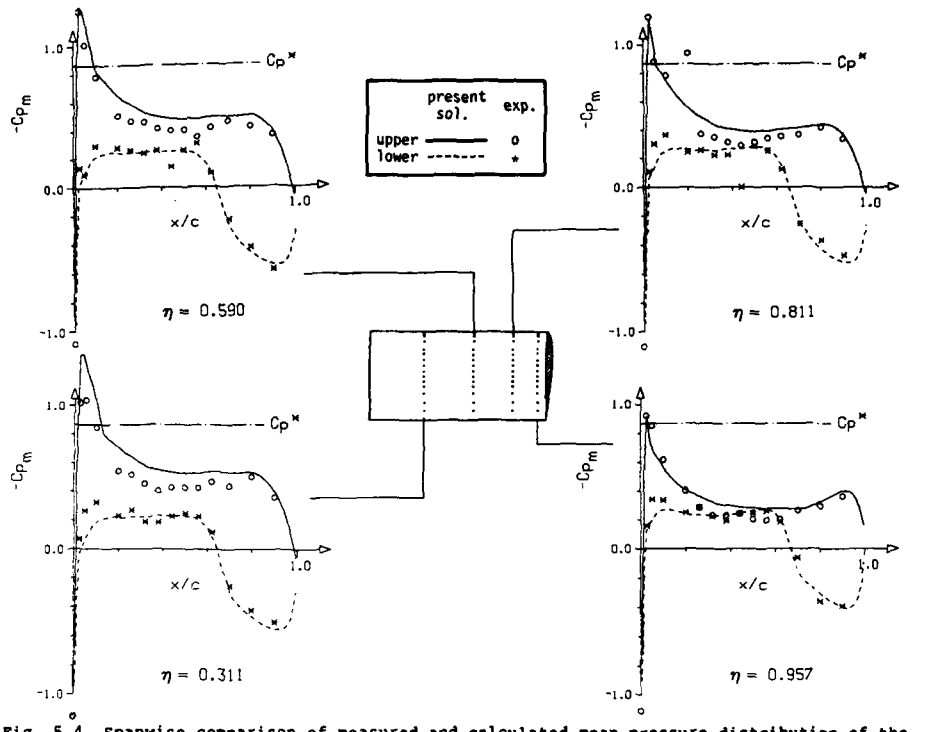


Fig. 5.4 Spanwise comparison of measured and calculated mean pressure distribution of the RSW-wing. Case 1: M=0.700, α_0=2.0 deg, α_1=1.0 deg, k=0.178

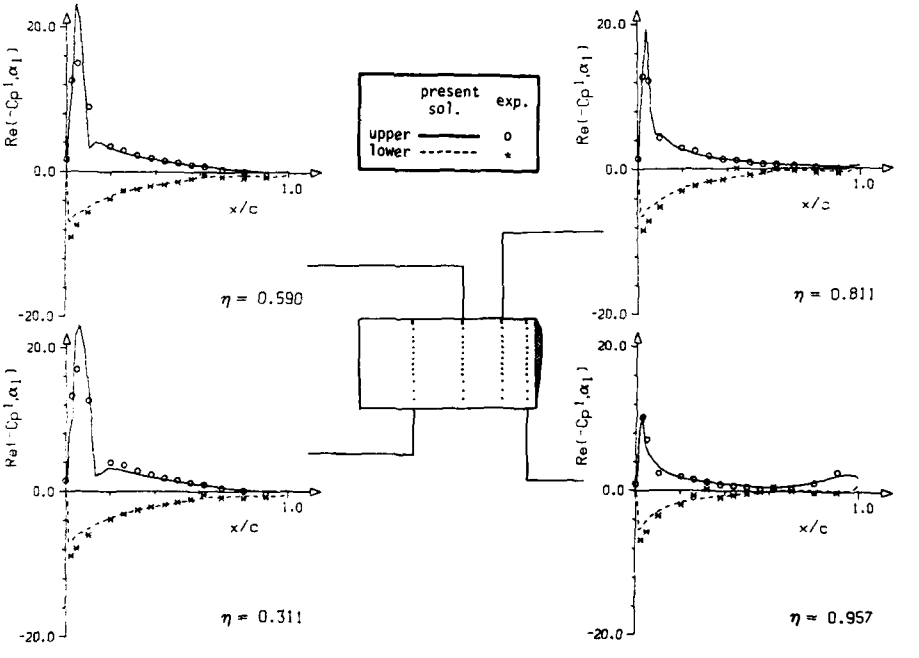


Fig. 5.5 Spanwise comparison of measured and calculated in-phase pressure distribution of the RSW-wing. Case 1: M=0.700, α_0=2.0 deg, α_1=1.0 deg, k=0.178

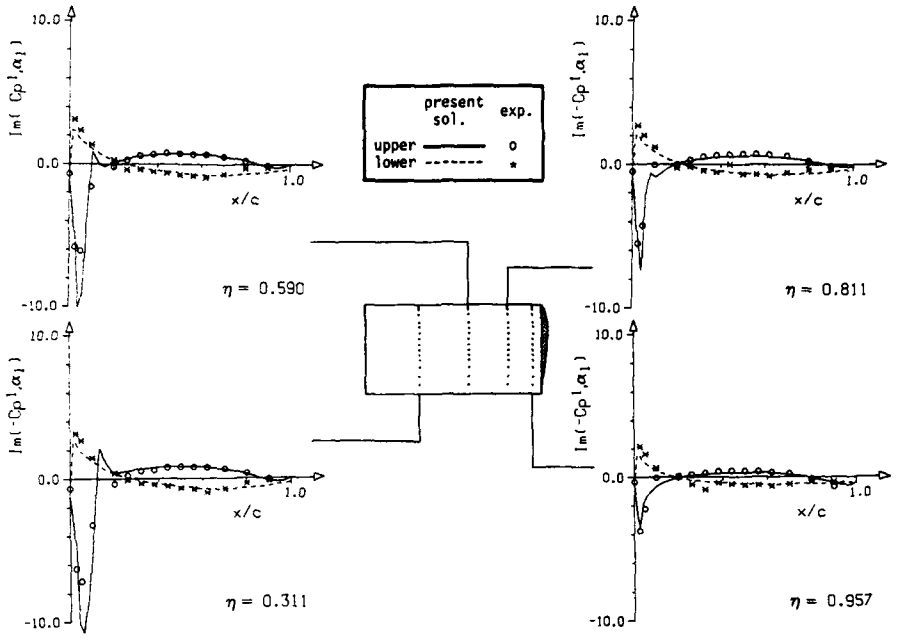


Fig. 5.6 Spanwise comparison of measured and calculated out-of phase pressure distribution of the RSW-wing. Case 1: M=0.700, α_0=2.0 deg, α_1=1.0 deg, k=0.178

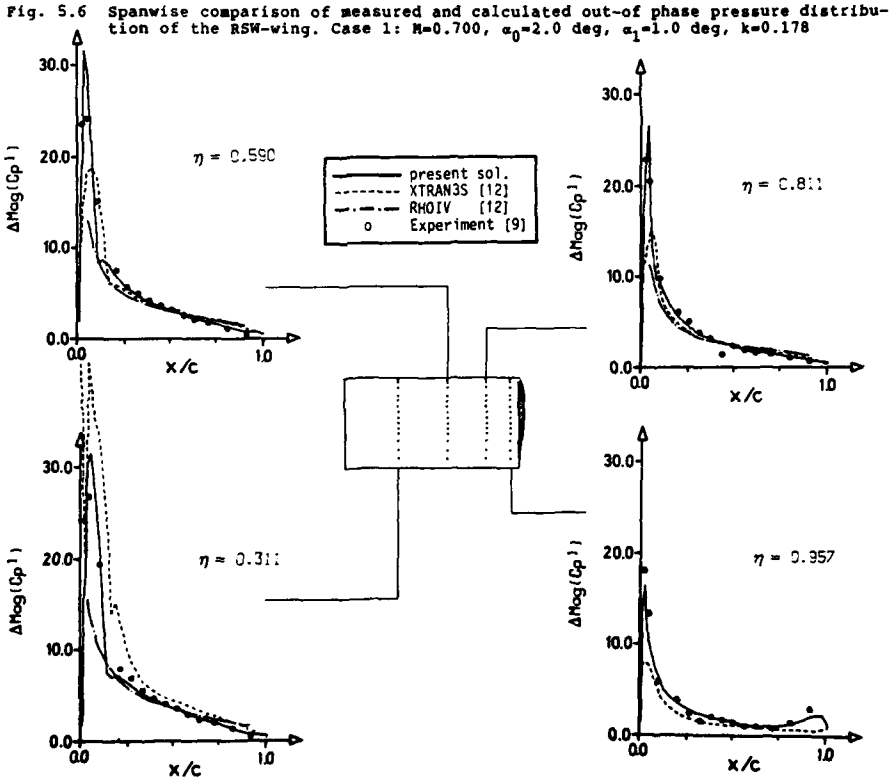


Fig. 5.7 Spanwise comparison of measured and calculated magnitude of the unsteady pressure distribution. Case 1: M=0.700, α_0=2.0 deg, α_1=1.0 deg, k=0.178

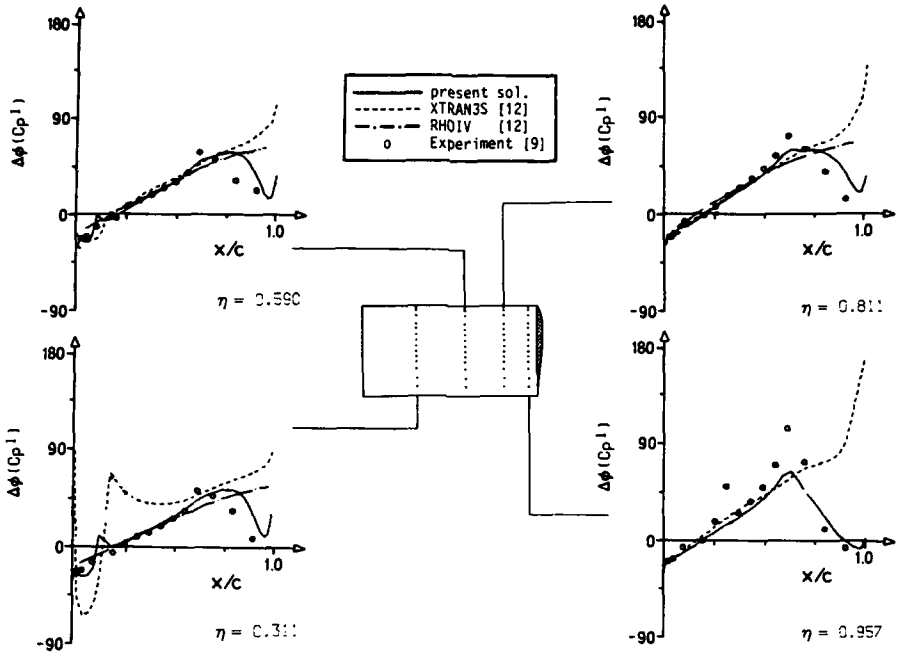


Fig. 5.8 Spanwise comparison of measured and calculated phase of the unsteady pressure distribution. Case 1: M=0.700, α_0=2.0 deg, α_1=1.0 deg, k=0.178

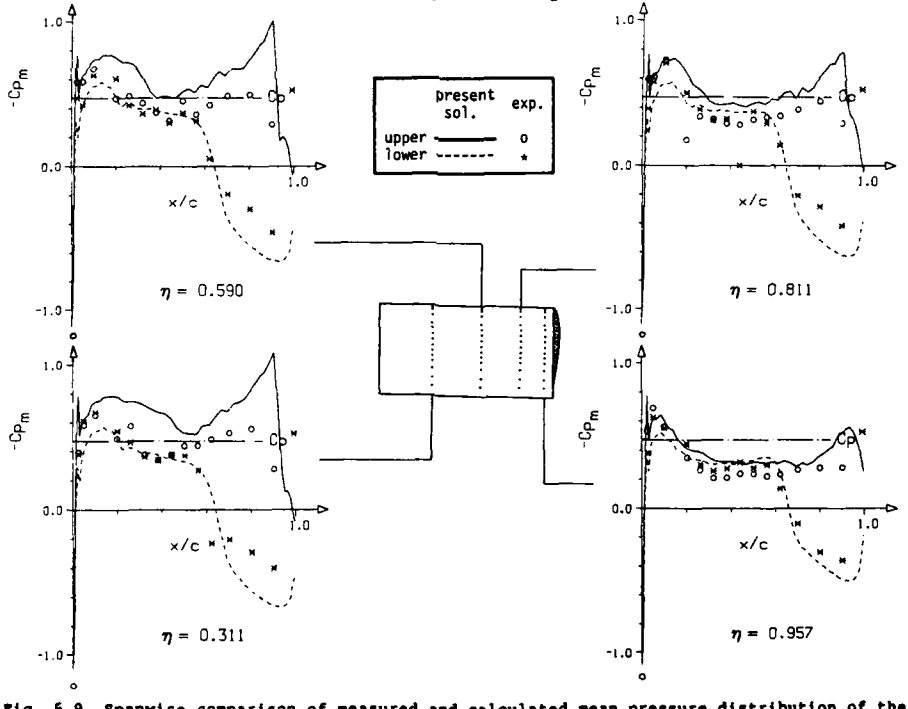


Fig. 5.9 Spanwise comparison of measured and calculated mean pressure distribution of the RSW-wing without smoothing the airfoil geometry. Case 2: M=0.804, α_0=0.06 deg, α_1=1.086 deg, k=0.155

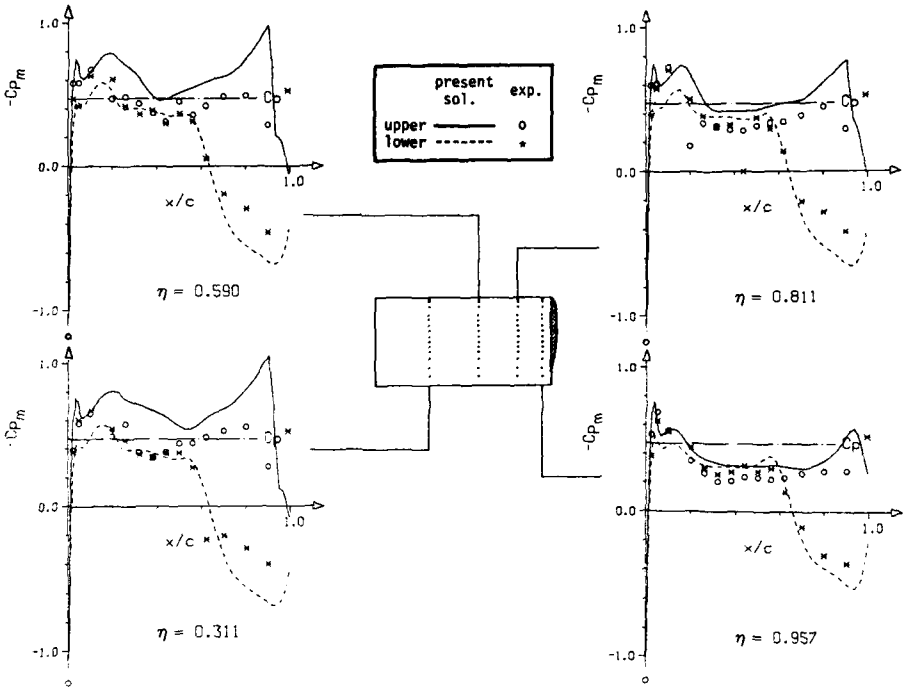
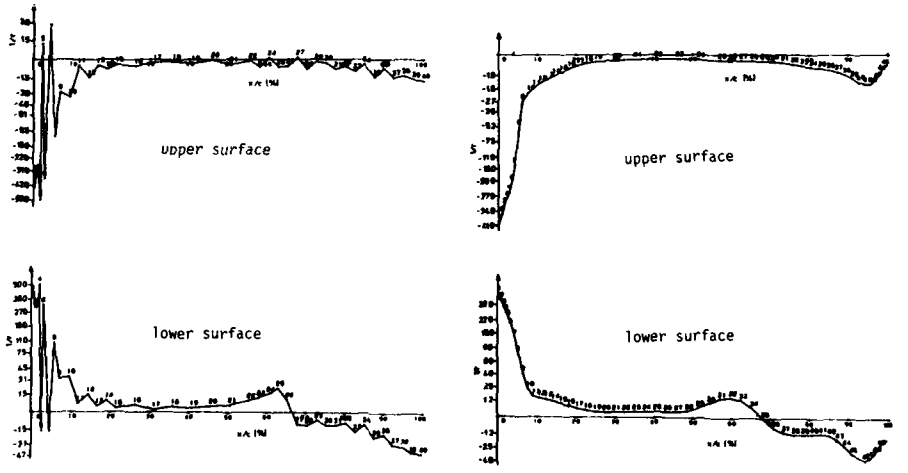


Fig. 5.10 Spanwise comparison of measured and calculated mean pressure distribution of the RSW-wing with smoothed airfoil geometry. Case 2: M=0.804, α_0=0.06 deg, α_i=1.086 deg, k=0.155



a) original design values

b) smoothed airfoil geometry

Fig. 5.11 Curvature behaviour of the RSW-wing airfoil geometry

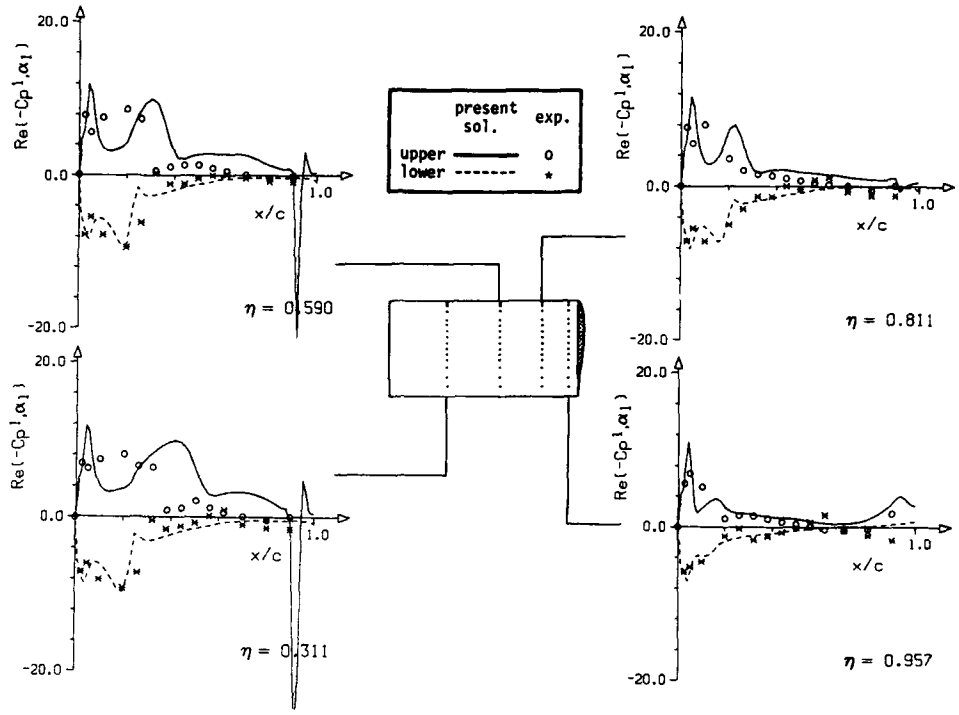


Fig. 5.12 Spanwise comparison of measured and calculated in-phase pressure distribution of the RSW-wing. Case 2: M=0.804, α_0=0.06 deg, α_1=1.086 deg, k=0.155

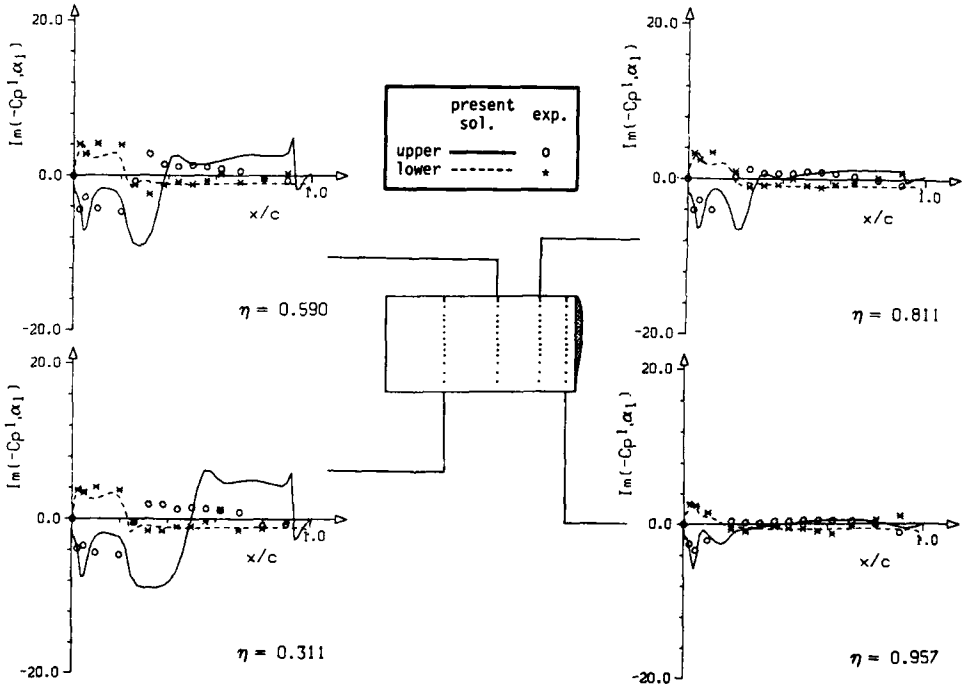


Fig. 5.13 Spanwise comparison of measured and calculated out-of phase pressure distribution of the RSW-wing. Case 2: M=0.804, α_0=0.06 deg, α_1=1.086 deg, k=0.155

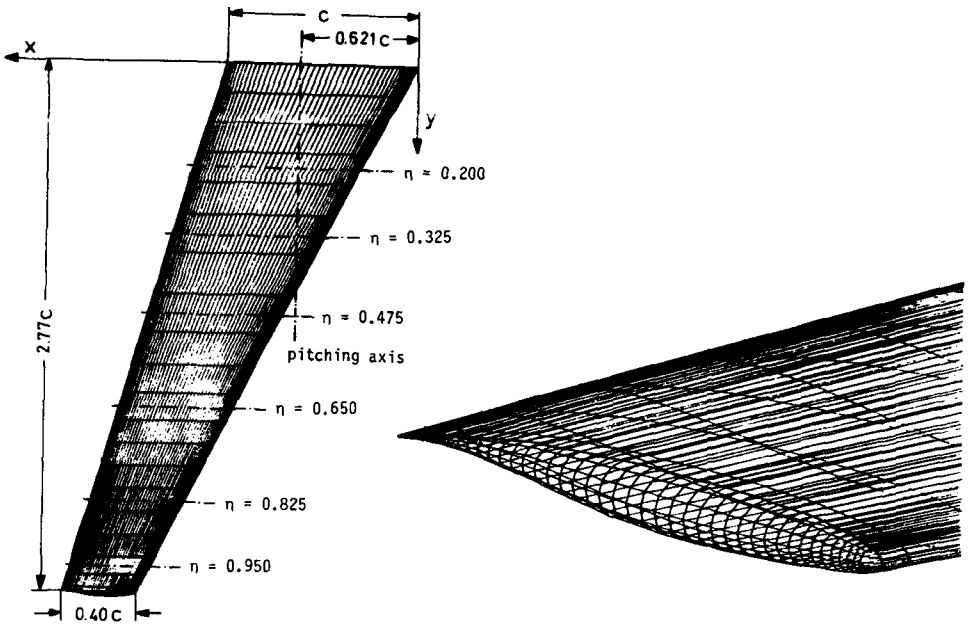


Fig. 5.14 Planform and wing tip surface mesh of the LANN-wing

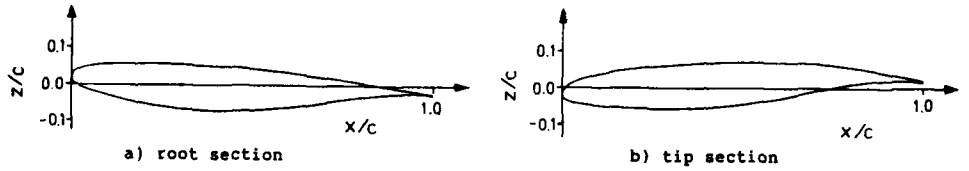


Fig. 5.15 Airfoil shape of the LANN-wing

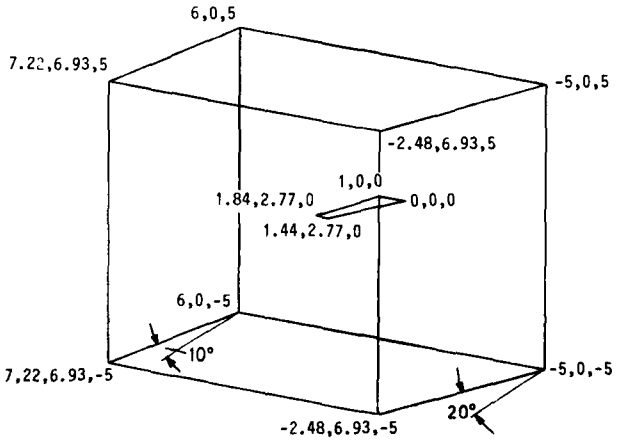


Fig. 5.16 Location of the LANN-wing in the computational domain

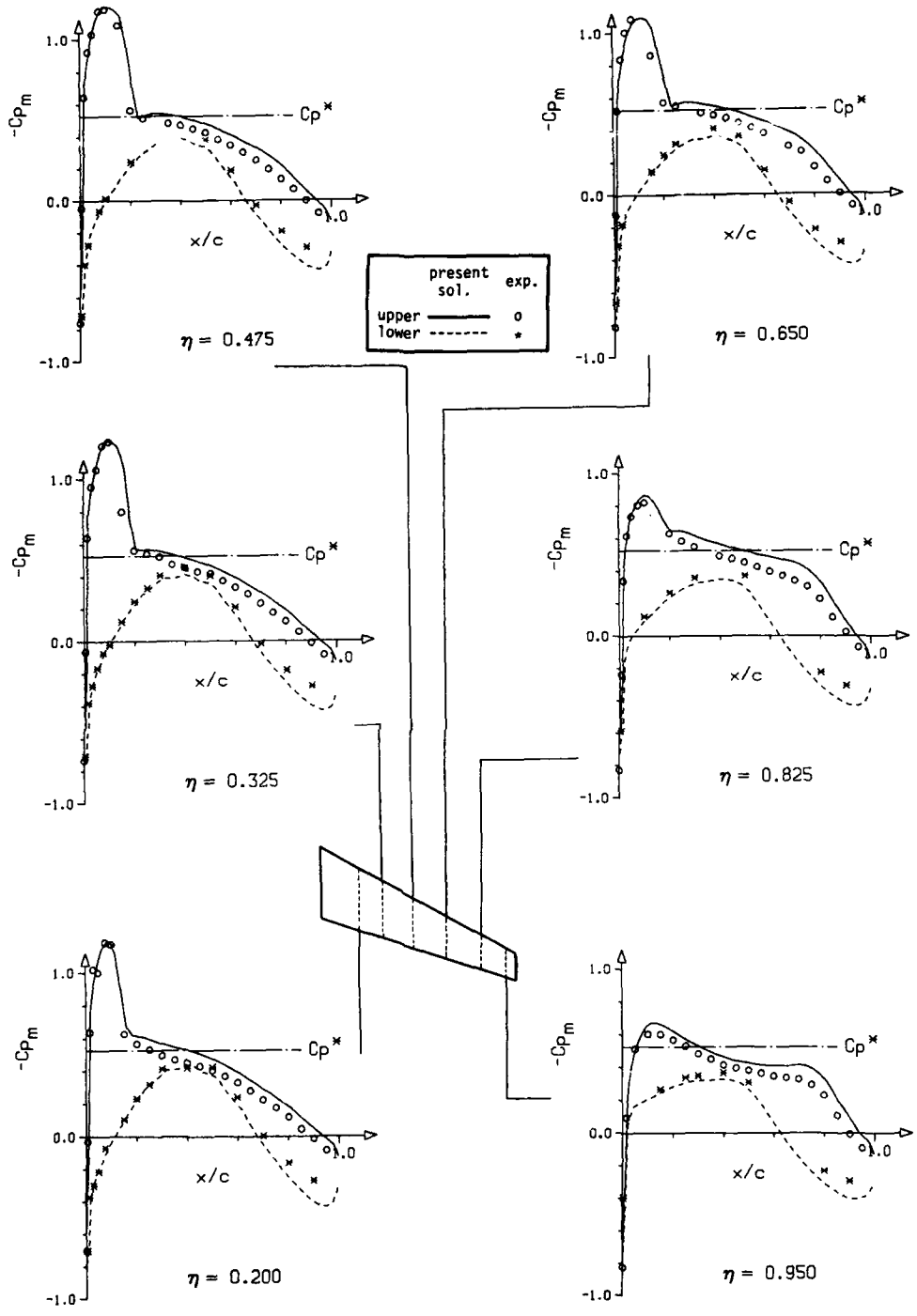


Fig. 5.17 Spanwise comparison of measured and calculated mean pressure distribution of the LANN-wing. Case CT2: M=0.77, α_0=0.6 deg, α_1=0.25 deg, k=0.080

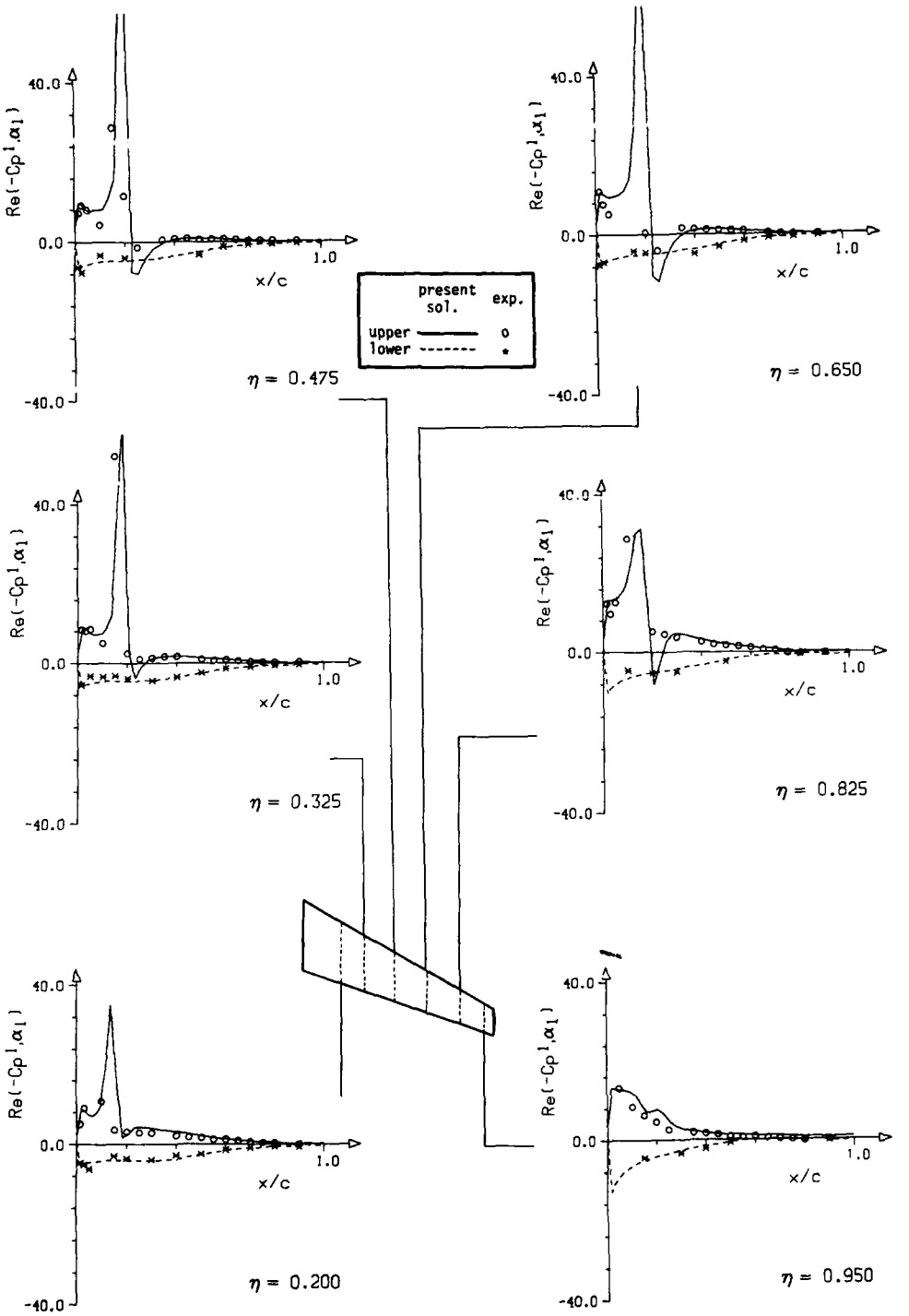


Fig. 5.18 Spanwise comparison of measured and calculated in-phase pressure distribution of the LANN-wing. Case CT2: M=0.77, α_0=0.6 deg, α_1=0.25 deg, k=0.080

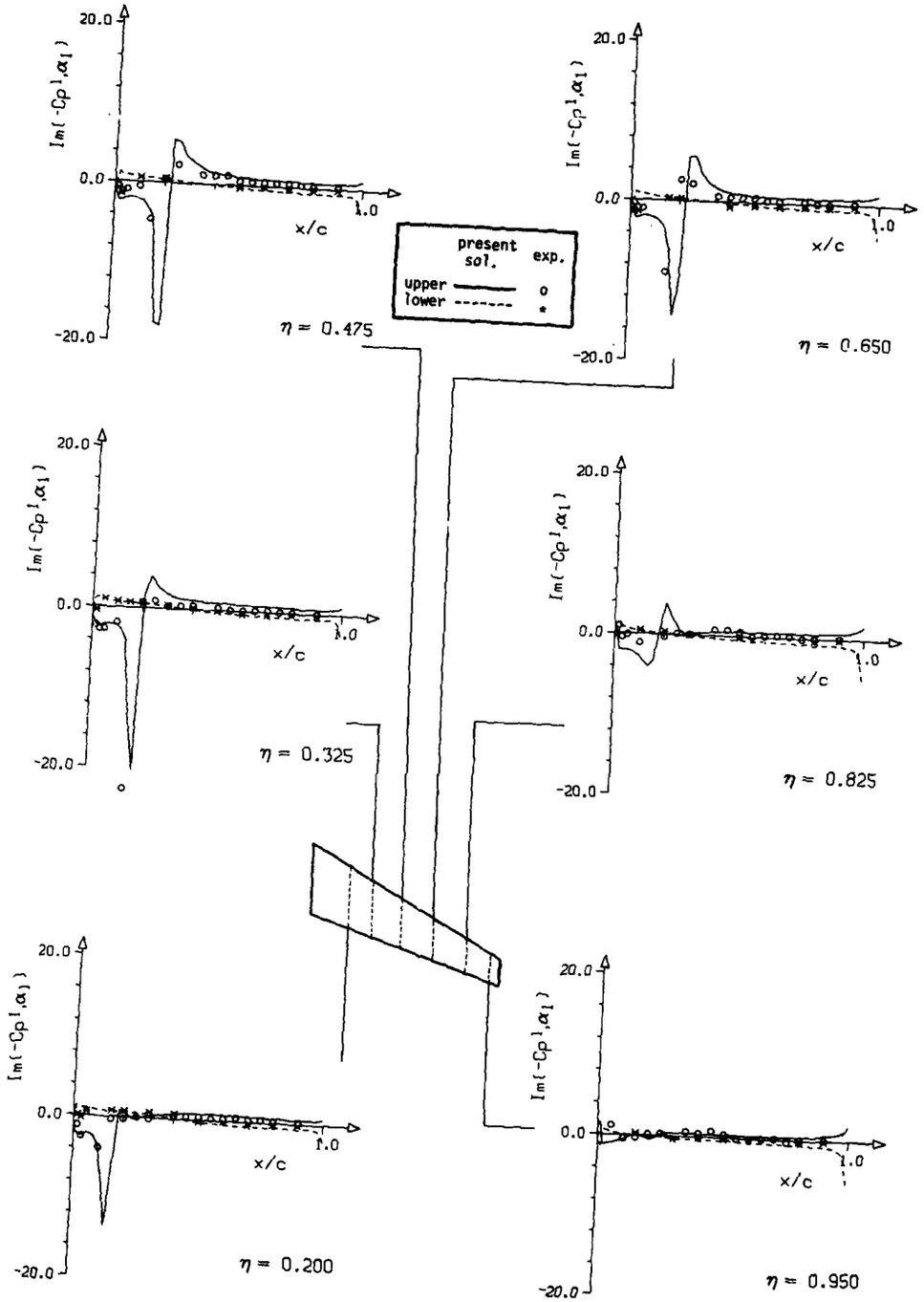


Fig. 5.19 Spanwise comparison of measured and calculated out-of phase pressure distribution of the LANN-wing. Case CT2: M=0.77, α_0=0.6 deg, α_1=0.25 deg, k=0.080

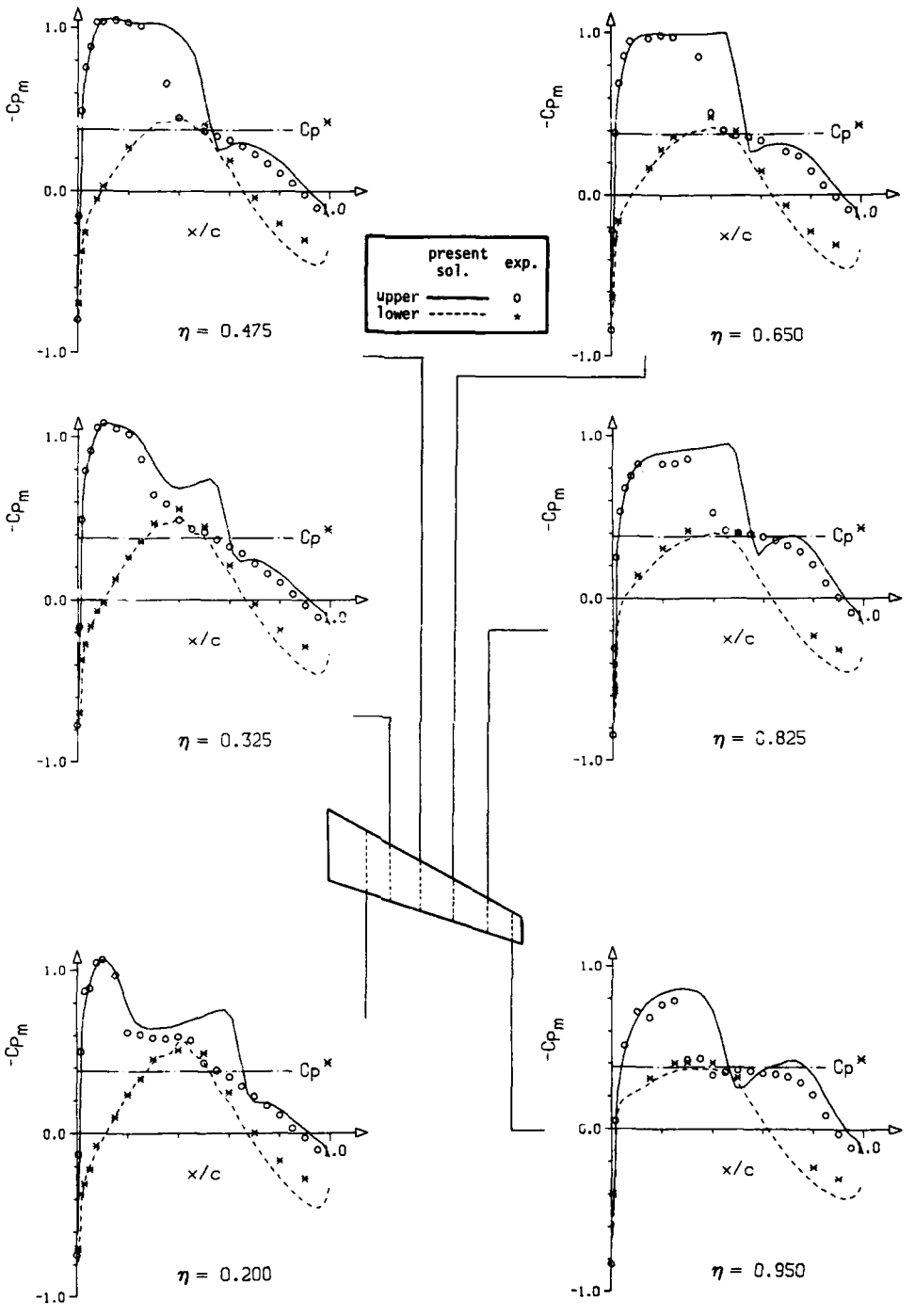


Fig. 5.20 Spanwise comparison of measured and calculated mean pressure distribution of the LANN-wing. Case CT5: M=0.82, α_0=0.6 deg, α_1=0.25 deg, k=0.076

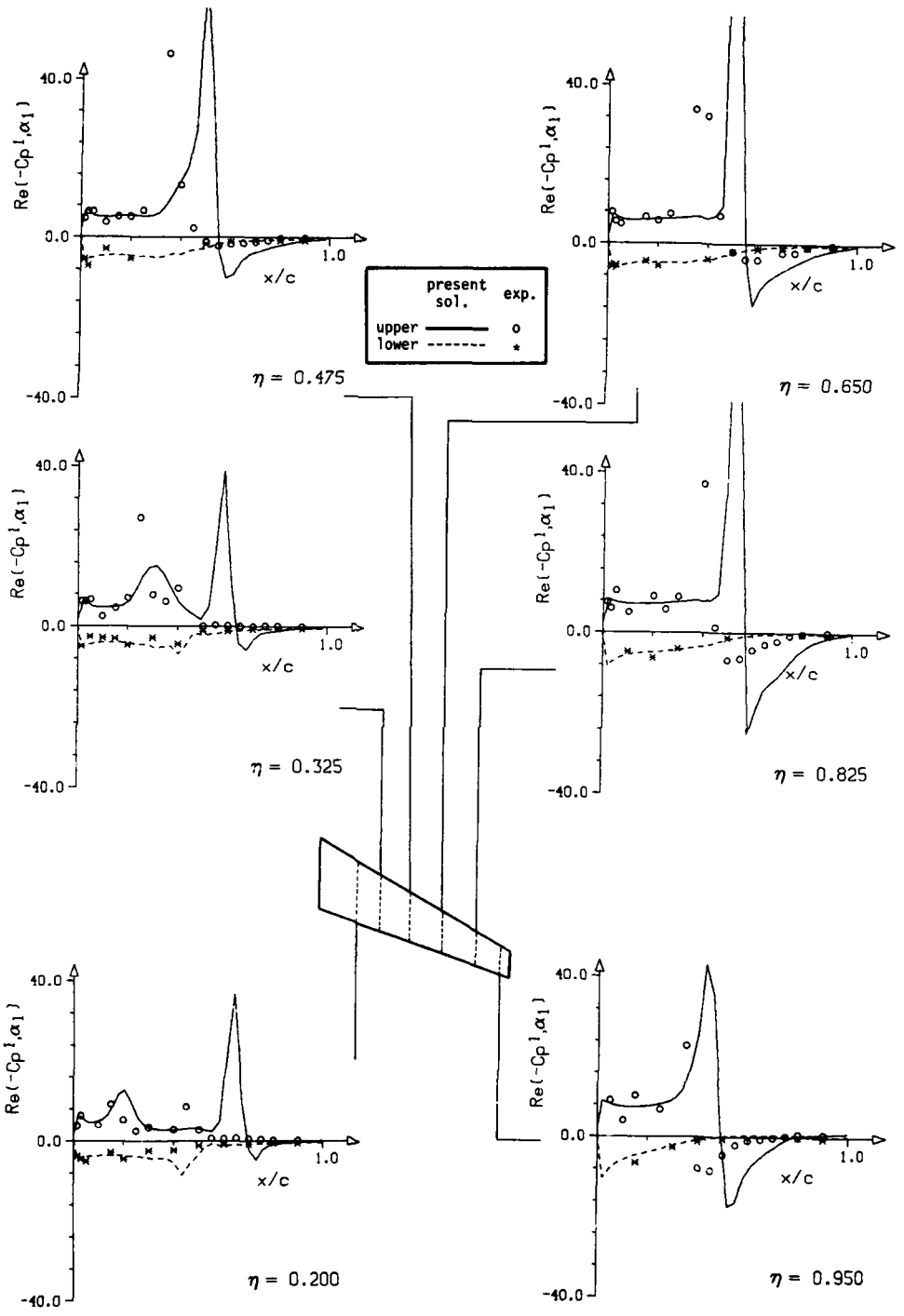


Fig. 5.21 Spanwise comparison of measured and calculated in-phase pressure distribution of the LANN-wing. Case CT5: M=0.82, α_0=0.6 deg, α_1=0.25 deg, k=0.076

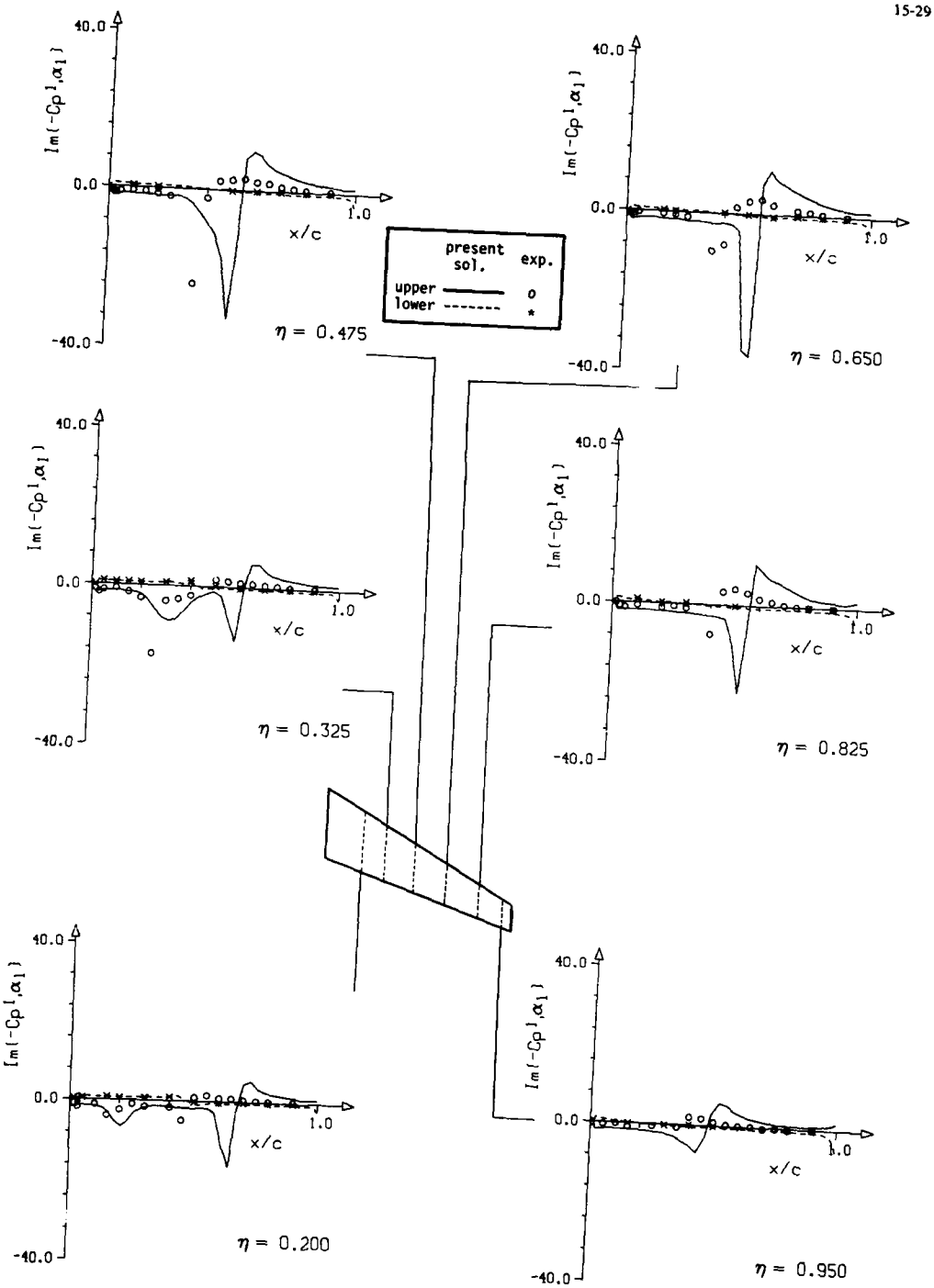


Fig. 5.22 Spanwise comparison of measured and calculated out-of phase pressure distribution of the LANN-wing. Case CT5: M=0.82, α_0=0.6 deg, α_1=0.25 deg, k=0.076

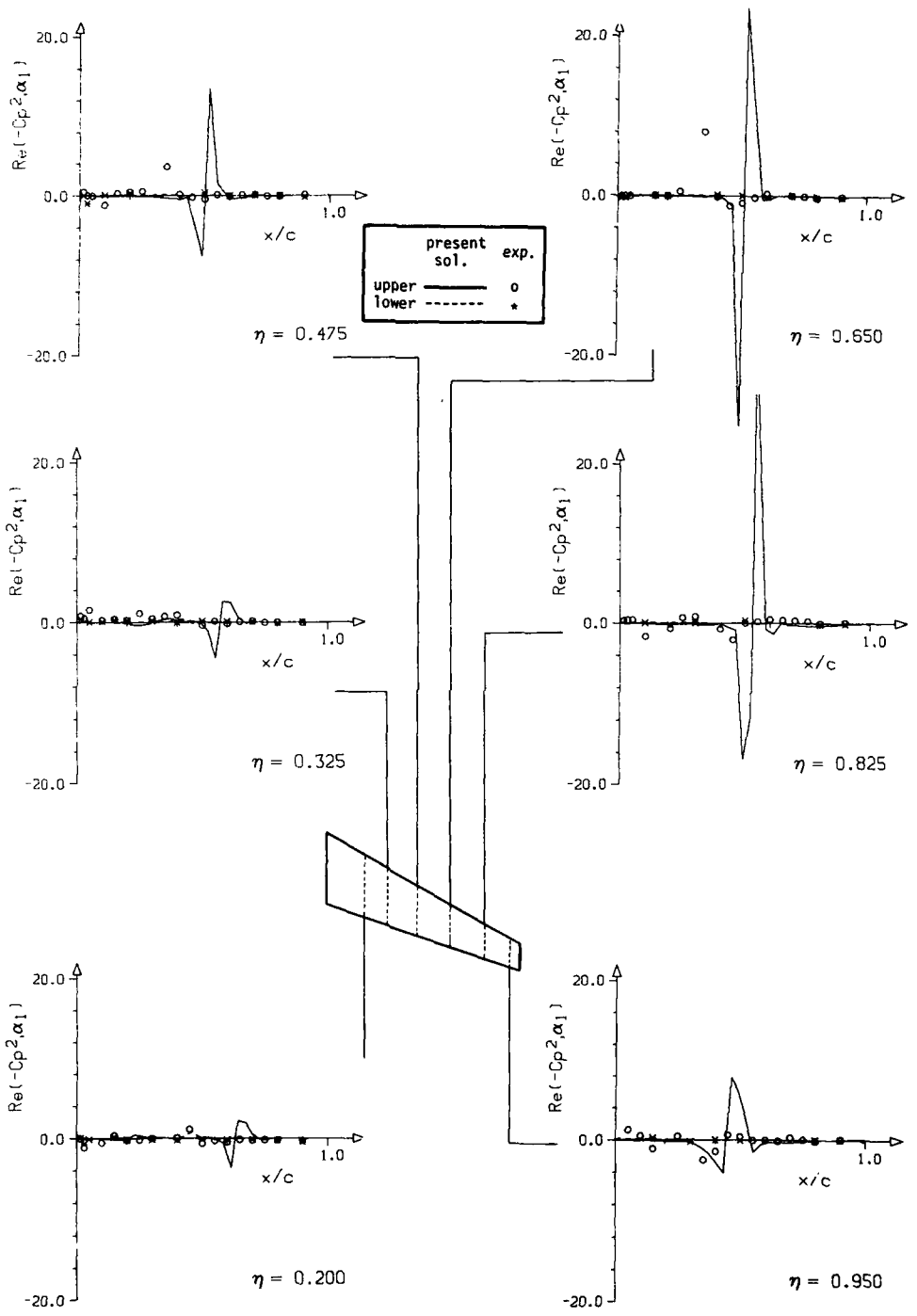


Fig. 5.23 Spanwise comparison of measured and calculated second-order in-phase pressure distribution of the LANN-wing. Case CT5: M=0.82, α_0=0.6 deg, α_1=0.25 deg, k=0.076

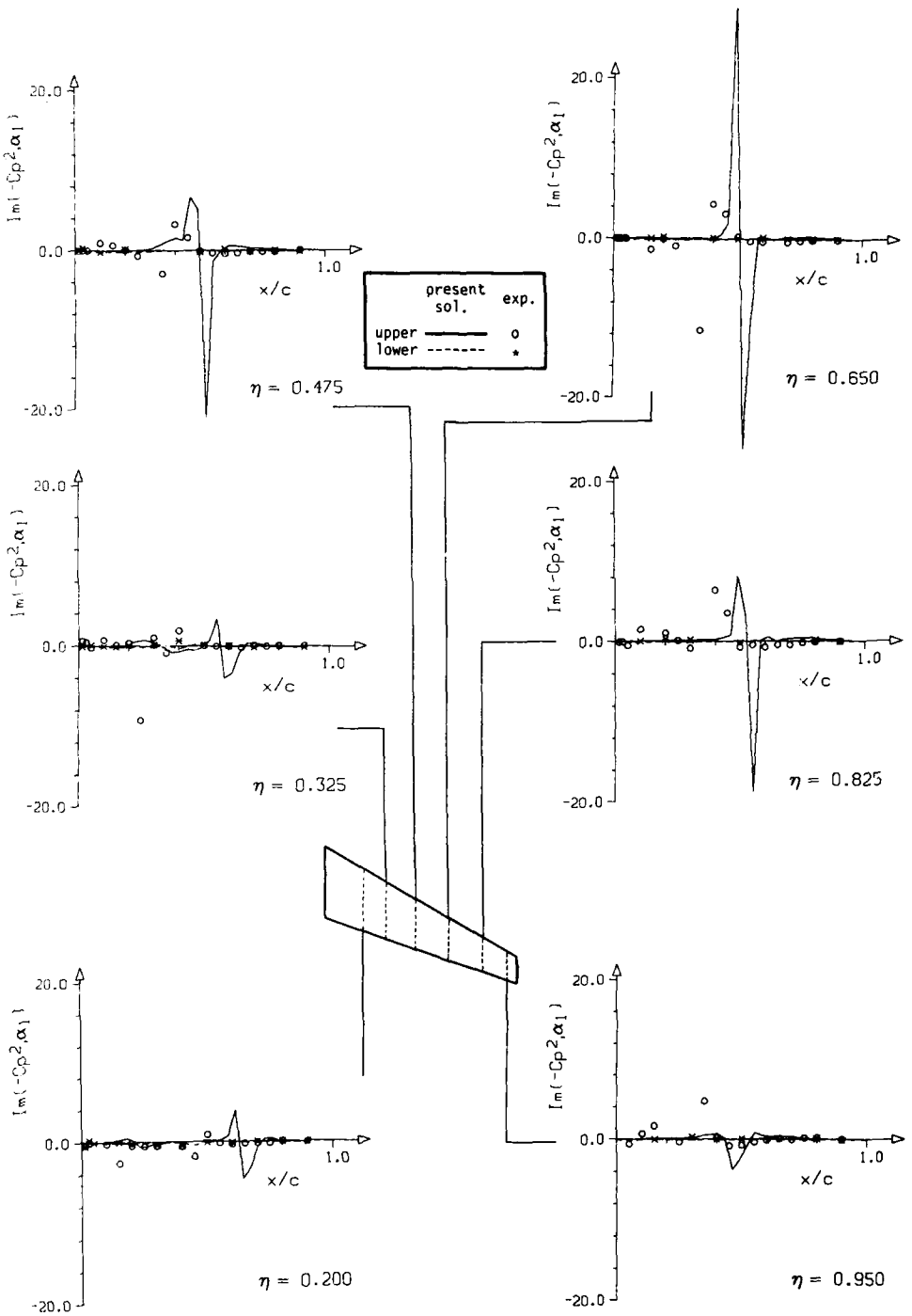


Fig. 5.24 Spanwise comparison of measured and calculated second-order out-of phase pressure distribution of the LANN-wing. Case CT5: M=0.82, α_0=0.6 deg, α_1=0.25 deg, k=0.076

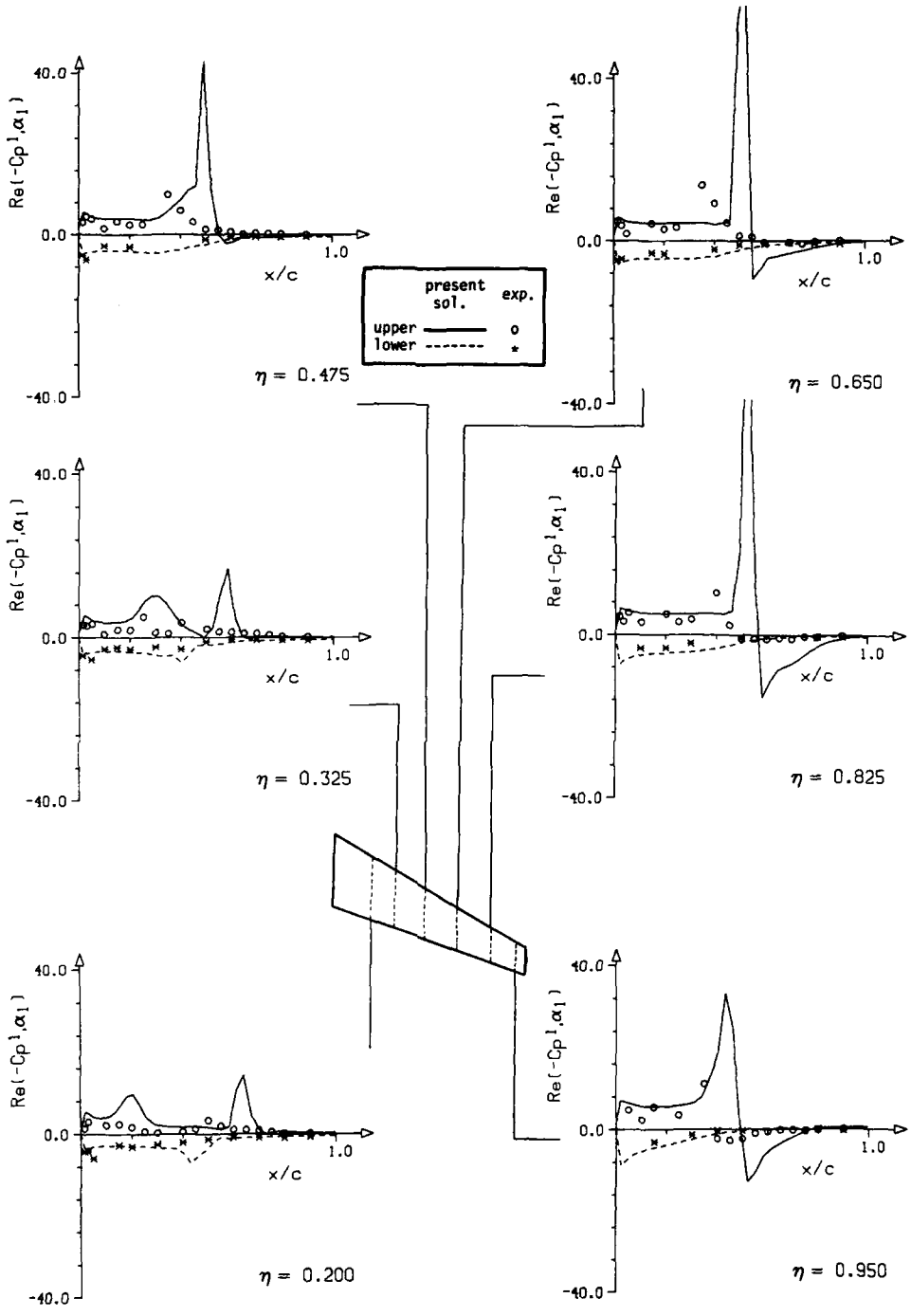


Fig. 5.25 Spanwise comparison of measured and calculated in-phase pressure distribution of the LANN-wing. Case CT8: M=0.82, α_0=0.6 deg, α_1=0.25 deg, k=0.151

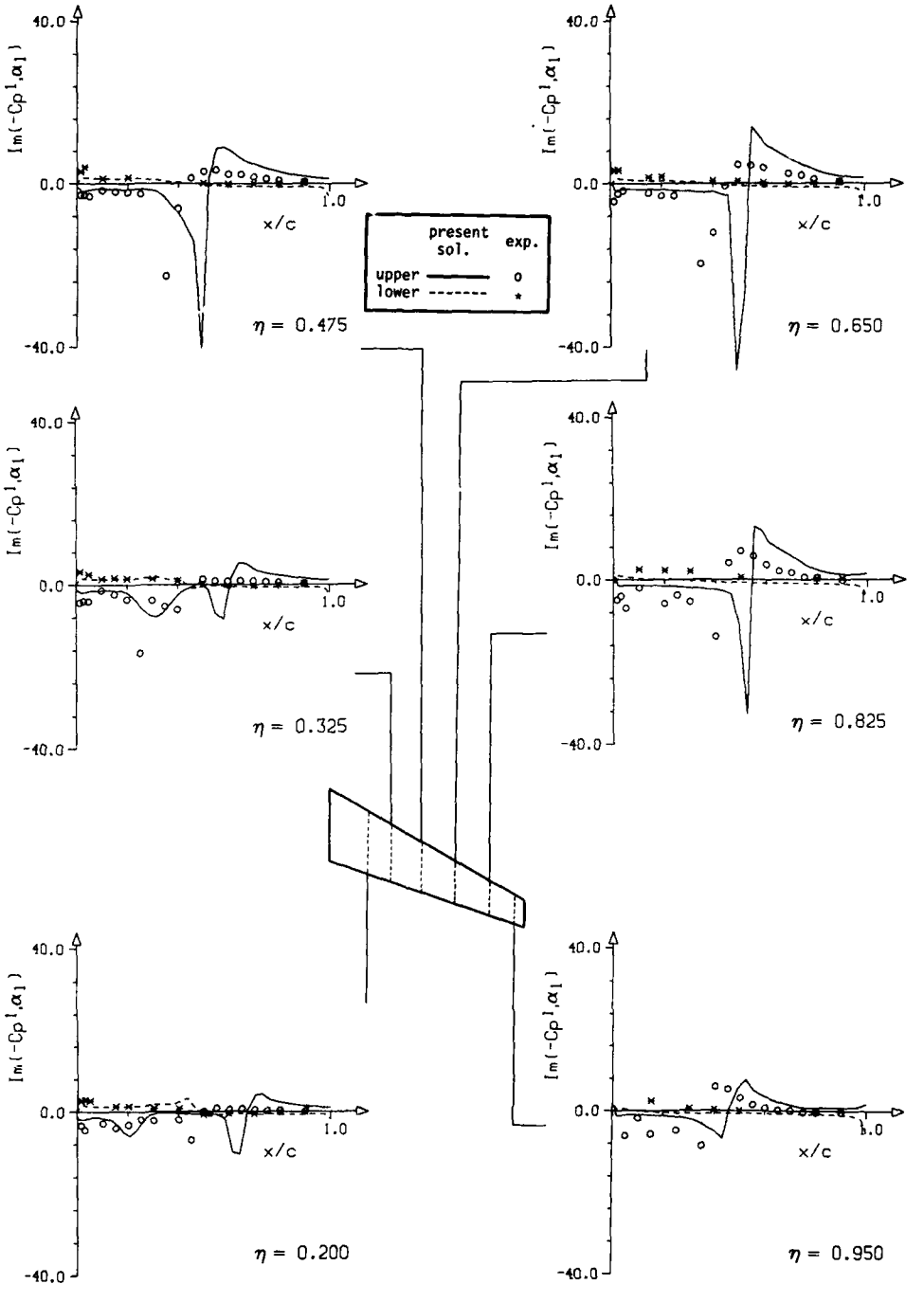


Fig. 5.26 Spanwise comparison of measured and calculated out-of phase pressure distribution of the LANN-wing. Case CT8: M=0.82, α_0=0.6 deg, α_1=0.25 deg, k=0.151

FIABILITE ET VALIDITE DES CODES DE C.F.D. COMPARAISON AU VOL ET A LA SOUFFLERIE

par

G. HECKMANN
Chef de Service
Division des Etudes Avancées
AVIONS MARCEL DASSAULT-BREGUET AVIATION
78, Quai Marcel Dassault
92214 SAINT-CLOUD

1. INTRODUCTION

Le développement des codes informatiques de C.F.D. est dû principalement aux progrès considérables des méthodes de résolution des équations de la mécanique des fluides et à l'accroissement de la taille et de la puissance des ordinateurs. L'utilisation de tels codes entre de plus en plus dans la définition des avions en parallèle et en complément de la soufflerie. Alors que cette dernière permet de tester une maquette continûment en fonction du nombre de Mach, de l'incidence, etc..., le calcul donne la possibilité de comparer de nombreuses formes dans un nombre réduit de cas de vol.

Il s'avère donc absolument indispensable de veiller à une réelle qualité informatique donc de tester ces codes par des comparaisons avec des expériences de base et avec des essais en soufflerie et surtout en vol. Il est aussi fondamental de connaître les limites de validité, les possibilités et le coût de ces nouveaux outils. Quelquefois ceux-ci ne donnent que la variation et non la valeur absolue des grandeurs étudiées mais cela peut être suffisant lors de comparaisons.

Les résultats doivent aussi être indépendants de l'utilisateur ce qui, a priori, semble évident mais ne l'est pas toujours en réalité. La fiabilité dépend aussi d'un usage continu et dans des cas très variés afin de vérifier à tout instant que l'ensemble du programme calcule correctement. Comme une soufflerie qui doit fonctionner sans longues périodes d'arrêt pour être opérationnelle, les codes de calcul industriels doivent être utilisés très souvent pour rester eux aussi fiables et opérationnels.

2. ROBUSTESSE ET FIABILITE

A) Les codes et la discrétisation

La complexité des codes aérodynamique est décomposée grâce à des codes de différents niveaux (fig. 1) qui traduisent plus ou moins bien la compressibilité ou la viscosité du fluide.

La résolution d'un système d'équation aux dérivées partielles entraîne la discrétisation de l'espace de travail. En général, les concepteurs de codes et de méthodes numériques utilisent des cas géométriquement simples pour mettre au point leurs outils de calcul. Il est très important de se rendre compte rapidement de la robustesse des algorithmes vis-à-vis des maillages qui sont toujours loin d'être idéaux : les éléments peuvent être allongés ou aplatis voire tordus ; la taille et la forme varient quelquefois rapidement d'une maille à la voisine.

La méthode de calcul impose un type de maillage. Le cas le plus simple est celui des méthodes intégrales qui ne travaillent que sur la peau de l'avion : la discrétisation est alors aisément contrôlable donc modifiable à la main.

Les méthodes de types différences finies ou volumes finis correspondent à des maillages structurés : seuls des espaces simples peuvent être traités et les possibilités de sous maillage local sont limitées.

Le maillage volumique, par exemple, celui de l'entrée d'air d'un avion d'arme avec la manche à air, les pièges à couche limite et les prélèvements, le fuselage, la casquette de protection entraîne un maillage extrêmement difficile car il est nécessaire de représenter correctement le rayon de courbure de la lèvre ou celui du bord d'attaque de la voilure (fig. 2). La discrétisation ne peut se faire uniquement avec des hexaèdres non dégénérés et les méthodes par éléments finis semblent s'imposer.

Il en est de même avec toutes les combinaisons tridimentionnnelles : arrière-corps d'un avion d'arme bimoteur ou fuselage arrière d'un avion civil trimoteur de type FALCON 50 ou 900.

B) Réglages numériques

Souvent de nombreux paramètres de réglage sont nécessaires pour assurer la convergence des algorithmes. Sans entrer dans le détail, l'accès à ces diverses valeurs doit être formellement interdit à tout utilisateur autre que le concepteur lui-même, ne serait-ce que pour une bonne reproductibilité des calculs à plusieurs mois de distance lors de l'industrialisation du programme. Le concepteur doit trouver pour ces paramètres, soit des valeurs données fixées une fois pour toute, soit des règles du jeu de définition totalement incluses dans le code.

La convergence d'une solution est, en général, ératique (fig. 3) ceci peut être dû au processus lui-même qui n'est pas monotone ou à la technique de multigrille ou de sous maillage.

Les codes qui nécessitent pour leur fonctionnement correct différents réglages présentent trois inconvénients majeurs :

- la solution est unique et alors il faut plusieurs itérations longues et coûteuses en délai et en temps de calcul donc inutilisables industriellement,
- la solution n'est pas unique, dans ce cas, le résultat dépend des réglages, toute comparaison et toute conclusion deviennent aléatoires et subjectives,
- la qualité de la comparaison avec d'autres résultats numériques ou avec l'expérience est fonction des paramètres, il faut admettre que ce sont surtout les réglages qui induisent les bons recoupements et alors le code ne présente qu'un intérêt très limité.

C) Unicité de la solution

Quelquefois la solution physique n'est pas unique : lors de l'initialisation du processus de convergence, il faut être sûr d'obtenir le résultat souhaité et non une autre solution comme l'écoulement supercritique dans les prises d'air.

Dans d'autres cas, c'est la discrétisation qui entraîne la multiplicité des solutions et alors deux problèmes se posent :

- l'existence de solutions multiples,
- le tri de ces solutions.

D) Comparaison et optimisation

Le processus de calcul et d'optimisation de forme conduit à une suite de calculs dont l'enchaînement est automatique ou non. Dans le processus direct, une forme géométrique donnée est calculée, de même que la maquette de soufflerie est bien définie. Dans le cas d'itérations automatiques, la forme doit dépendre d'un petit nombre de paramètres géométriques, le problème consiste alors à minimiser une fonction coût par itérations en faisant varier chacun des paramètres dans des limites permises. La difficulté principale réside alors dans l'unicité du minimum.

Pour que les comparaisons soient valables, il faut éviter toute intervention subjective comme les réglages ci-dessus. Les discrétisations doivent être le plus homogènes possible quant au nombre, à la forme et la disposition des éléments car tous les codes sont sensibles plus ou moins au maillage. En ce qui concerne les calculs itératifs, il faut se méfier des critères de convergence qui conditionnent l'arrêt du programme et qui dépendent souvent de la taille et de la forme des mailles même si l'on prend des précautions lors du choix de ces critères.

L'existence de discontinuités dans le champ aérodynamique ondes de choc, sillages..., impose un sous maillage local : il n'est pas logique car coûteux de mailler finement tout l'espace ; les variations brutales doivent être cependant prises en compte par un resserrement local des points (fig. 4). On remarque que le sous maillage améliore la vitesse de la convergence sans doute parce que le phénomène physique est mieux respecté.

3. FIABILITE INFORMATIQUE

A) Portabilité

Un code industriel représente un investissement coûteux en années de travail et en temps de calcul pour la mise au point. Il doit "vivre" très longtemps pour justifier son existence donc supporter l'évolution des logiciels de base et des matériels, aussi et surtout les inéluctables changements humains. Ceci impose une programmation claire à laquelle il faut quelquefois sacrifier la place occupée en mémoire voire le temps de calcul : il faut donc penser aux inévitables corrections et modifications futures qui seront effectuées par les auteurs eux-mêmes mais qui auront oublié certaines astuces ou souvent par d'autres personnes.

Quelquefois, il est nécessaire de rassembler en un seul code deux ou plusieurs éléments écrits séparément : sans entrer dans les détails, certaines règles doivent être respectées, par exemple, en FORTRAN le nom des sous programmes et celui des COMMON qui peuvent interférer et doivent satisfaire à des règles intangibles sous risque d'erreurs difficilement détectables.

B) Documentation

Il est évident que des commentaires clairs et nombreux doivent agrémenter la programmation : ceci n'est souvent qu'un voeu pieux car lors de l'écriture du code tout est dans la tête du programmeur qui ne prend pas le temps de documenter sa programmation car souvent il n'en voit pas l'intérêt immédiat. Ces exigences sont à rapprocher des problèmes de portabilité.

Les notes documentaires ou d'utilisation, qui quelquefois accompagnent le code, finissent par être obsolètes par manque d'un suivi coûteux. Il est alors nettement préférable d'ajouter tous les commentaires à la programmation car la mise à jour est plus aisée.

C) Entretien des codes

L'entretien d'un code est un travail souvent fastidieux et sans fin mais absolument indispensable au niveau industriel : il existe, en effet, un fossé très large entre un code de recherche et un code opérationnel. Ce dernier doit être en état de fonctionner à tout instant et le départ d'un responsable ne doit jamais affecter la maintenance de logiciel. Il faut plusieurs années pour mettre au point l'environnement d'un code de calcul qui doit fonctionner correctement pour les multiples raisons indiquées ci-dessus.

D) Bases de données

Les fichiers utilisés pour stocker les diverses informations seront à la fois pratiques à gérer et aisés à répertorier car l'optimisation d'un avion conduit à traiter un très grand nombre de variantes de formes, chacune composée de dizaines voire de centaines de sous-éléments. Les cas de calculs, les maillages différents et les nombreux codes qui traitent l'information risquent de conduire à une confusion générale sans une organisation très sérieuse des informations donc des bases de données.

Tout ce qui est nécessaire à l'identification du calcul devra figurer dans les fichiers afin d'apparaître sur tout document, listing, courbe ou toute autre visualisation. Toute information ajoutée par la suite à la main peut être sujette à erreur donc à contestation, de plus elle disparaîtra avec le document et ne pourra plus jamais être retrouvée.

E) Comparaison des résultats et "release"

Souvent le résultat de calcul peut être critiqué en tant que valeur absolue alors que ses variations avec les formes d'avion sont parfaitement correctes. Une comparaison est d'autant plus sûre que le même code a été utilisé par la même personne ou la même équipe ; il est donc indispensable de repérer tout programme exécutable par un numéro de "release" voire une date de mise en service qui identifie parfaitement l'outil utilisé. Ceci est une évidence pour un code commercialisé mais les équipes de chercheurs n'en voient pas toujours l'utilité.

Dans le doute, il est nécessaire de recalculer voire de remailler des formes géométriques de base ou des itérations précédentes afin de comparer des résultats valablement. Même si ce genre de façon d'opérer peut sembler coûteux, c'est une nécessité dictée par la sagesse : il existera toujours des erreurs dans les codes de CFD, mettons néanmoins toutes les chances de notre côté.

F) Détection et repérage des erreurs

L'utilisation d'un code industriel impose une correction donc une détection et une identification très rapide des erreurs car le temps est une des contraintes industrielles. Il est aussi très important de faire avoisiner les utilisateurs et les concepteurs de programmes pour améliorer les délais d'intervention et afin que ces derniers soient bien conscients des problèmes particuliers posés par les calculs industriels.

Un code constitué de dizaines de milliers d'instructions, dont un nombre non négligeable de tests, ne pourra jamais être garanti sans erreur de type informatique (comme une simple faute de frappe) car il est impossible de tester tous les cas de figures possibles surtout si le code contient de nombreux tests logiques. Certaines routines peuvent contenir un certain nombre de "DATA" dont il est extrêmement difficile de vérifier l'exactitude. Il est indispensable si le déroulement ne semble pas correct de pouvoir extraire les données nécessaires à la détection et à la compréhension des erreurs surtout si les calculs qui ont conduit à l'imperfection sont longs donc difficiles à reconstituer. Dans certains cas, les conditions initiales sont inconnues, par exemple, si l'erreur est due à la non initialisation d'une variable.

4. TRAITEMENT DES DONNEES

A) Les différents types de données

La première règle fondamentale, certes évidente mais cependant difficile à faire respecter, est simplement que toute information doit être stockée dans le fichier afin de pouvoir servir ultérieurement comme critère de choix ou comme paramètre de caractérisation du calcul.

La surface géométrique, définie dans la base de données géométrique, sert de plus à communiquer avec les autres utilisateurs au niveau de la définition des avions, par exemple, les bureaux d'études. La création de la base de données géométriques est toujours conversationnelle car il est indispensable de visualiser tous les éléments lors de leur définition.

Cette géométrie continue est discrétisée sous forme d'un maillage de peau puis d'espace si nécessaire adapté au code de calcul :

- la peau seulement si singularités,
- l'espace structuré si différences ou volumes finis,
- l'espace non structuré si éléments finis.

Le fichier résultant contient la topologie de définition des éléments, les coordonnées des points et le vecteur unitaire normal localement à la surface. Il est important d'y adjoindre des informations supplémentaires comme les types de conditions aux limites et de différencier les surfaces limites, par exemple, pour intégrer la pression sur des parties d'avion pour obtenir les efforts locaux.

B) Interactivité et reproductibilité

Alors qu'avec les mêmes conditions initiales un code conduit aux mêmes résultats, il est évident que l'intervention humaine dans le mode conversationnel entraîne une certaine subjectivité donc des variations qui peuvent être très importantes. Ces écarts sont encore amplifiés par l'intervention de personnes différentes. Il est important de faire exécuter par le même ingénieur les préparations de calcul qui donneront lieu ultérieurement à des comparaisons.

5. VALIDATION EN SOUFFLERIE

A) Processus de validation

Les méthodes mises au point sont d'abord testées par comparaison avec des expériences de base. Ce sont, en général, des calculs effectués sur des cas géométriquement simples : corps de révolution, cônes, sphères... Quelquefois, une solution analytique existe. Les expériences spécifiques sont demandées aux laboratoires équipés en conséquence. A ce stade seul le coeur du programme est mis au point et pas encore toute l'intendance indispensable.

B) Les essais en soufflerie

Les possibilités de mesures en soufflerie sont extrêmement nombreuses :

- pesées et résultats globaux,
- mesure de la pression locale,
- mesure de la température locale,
- mesures par jauges de contraintes pour évaluer les efforts locaux,
- mesures dans la couche limite et les sillages...

Les visualisations permettent de comprendre les phénomènes voire de recouper le traitement par imagerie des calculs :

- strioscopies,
- plans lasers,
- visualisation par infrarouge,
- visualisation pariétale par acénaphtène,
- visualisation pariétale par injection de fluides colorés...

D'autres techniques peuvent être employées comme les fils de laine collés sur la peau de l'avion pour visualiser la direction de la vitesse pariétale ou la fumée pour l'écoulement spatial.

C) Comparaisons calcul-soufflerie : pressions

Le cas le plus simple est celui des pressions sur un profil de voilure (fig. 5). Les résultats sur le profil courant sont en général très bons. En ce qui concerne l'extrémité ou l'emplanture de la voilure, il peut y avoir des écarts dus aux effets tridimensionnels importants. La modélisation correcte du fuselage et des karmans de raccordement est très importante (fig. 6). Dans les cas difficiles, la discrétisation est importante, c'est le cas figure 7 sur le profil situé à 95 % d'une voilure.

Le problème est plus complexe quand il s'agit de l'écoulement sur les mâts qui supportent les nacelles moteur du FALCON 20G par exemple (fig. 8). Le couloir délimité par la nacelle, le fuselage et le mât est très sensible en transsonique à la présence de la voilure, donc à la portance et finalement à l'incidence, le maillage nécessaire est très délicat à réaliser.

Les pressions sur le fuselage avant d'avions d'arme sont bien représentées par le calcul à condition de bien choisir les méthodes de calcul :

- en subsonique une simple méthode à potentiel suffit,
- en supersonique, dans les cas ou le choc de tête est attaché, le potentiel linéarisé donne une solution correcte,
- en transsonique le potentiel complet n'est pas toujours suffisant et il faut recourir aux équations d'Euler surtout en cas de chocs dans l'écoulement.

Dans tous les cas, il y a intérêt à épaissir le volume de l'avion de l'épaisseur de déplacement de la couche limite et à recommencer le calcul de fluide parfait sur cette nouvelle forme (fig. 9).

Au voisinage des entrées d'air, il est indispensable de modéliser correctement la prise, la manche et de bien imposer le débit moteur. En subsonique, l'équation au potentiel suffit ; mais il est toujours préférable d'y adjoindre les effets de couche limite, dans tous les autres cas, l'utilisation des équations d'Euler s'avère absolument indispensable.

D) Visualisations

Les visualisations pariétales de l'ALPHA JET sont comparables aux calculs de couche limite (fig. 10) notamment en ce qui concerne la position du décollement. Ces calculs ont été effectués d'abord en fluide parfait, écoulement à potentiel ; le champ aérodynamique ainsi défini a permis le calcul visqueux dans la couche limite.

Les strioscopies de soufflerie peuvent être comparées à la détection par le calcul des gradients locaux de pression ; à débit de moteur équivalent, les deux visualisations sont parfaitement comparables (fig. 11, 12 et 13). Ce calcul a été exécuté grâce à un code aux différences finies à maillage topologiquement axisymétrique.

E) Champs de vitesse

La direction du champ de vitesse local peut être matérialisée sur la peau par divers types de bouillie, des fluides colorés ou des fils de laine ; il est alors simple de comparer ces directions avec la visualisation locale du champ calculé sauf dans le cas de décollements ou celui d'interactions couche limite-onde de choc importantes, les recoupements sont bons. La figure 14 montre la comparaison entre des mesures clinométriques et le calcul, à Mach = 0,8 (code utilisant les singularités) et à Mach = 1,3 (différences finies).

6. VALIDATION EN VOL

A) Les essais en vol

Le juge final est bien sûr l'essai en vol. Les installations sont coûteuses certaines mesures sont effectuées lors d'essais non spécifiques. Les difficultés résident dans l'identification précise des conditions d'essai : nombre de Mach, incidence, dérapage, paramètres atmosphériques (pression, température, vitesse et direction du vent...). Fort heureusement le suivi télématique et les divers capteurs et sondes ont fait de gros progrès. De plus, le vol est rarement stationnaire au moment précis où ont lieu les mesures : accélération ou virage.

La détermination de la traînée dépend de la connaissance de la poussée du moteur donc des caractéristiques et du point de fonctionnement de celui-ci. Comme cela a déjà été vu en soufflerie, le débit du moteur influe sur les caractéristiques des entrées d'air et des arrière-corps donc sur leur fonctionnement ainsi que sur leur voisinage.

B) Les mesures locales, les pressions

La mesure de pressions est très intéressante si les conditions de vol sont bien définies ; les prises peuvent être réparties sur un profil (fig. 15 et 16). Les conclusions sont similaires à celles de la soufflerie et les recoupements sont excellents entre calcul et vol. La position de la transition a été filmée par caméra infrarouge lors de l'étude en vol de profils laminaires et elle correspond parfaitement au calcul effectué préalablement.

Mais les mesures les plus intéressantes sont effectuées dans les parties géométriquement plus complexes.

Autour des entrées d'air d'un avion militaire en vol supersonique, les pressions sont conditionnées par le choc qui se trouve en amont de la prise donc par le débit, un petit décollement peut avoir lieu sur la lèvre. La comparaison des résultats de vol avec divers calculs montre que pour obtenir de bons recoupements, il faut y mettre le prix tant sur la sophistication de la méthode que sur la finesse du maillage donc sur le temps de calcul (fig. 17). Le nombre de prises de pression est très faible, il faut de nombreux recoupements si les phénomènes non continus doivent être analysés.

Dans le piège à couche limite, la pression est en plus déterminée par le débit de prélèvement, dans ce cas la connaissance de sa valeur est indispensable pour exécuter les calculs de recoupement (fig. 18).

C) La traînée

La traînée d'un avion peut se décomposer comme suit :

- traînée induite par la portance,
- frottement, forme et décollements,
- onde (si vol supersonique),
- entrée d'air,
- arrière-corps,
- divers (bosses, sondes diverses, antennes, ventilations...).

Comme nous l'avons vu plus haut, l'obtention de la valeur de la traînée est un problème très difficile en vol comme par le calcul. Le premier écueil réside dans la définition de cette grandeur notamment en ce qui concerne l'arrière-corps et l'entrée d'air : la différence poussée-traînée est connue avec la précision des mesures en vol mais la répartition en motoriste et avionneur est très délicate. Il importe d'abord de connaître la poussée du moteur à partir des paramètres mesurés en vol. Ensuite, il faut définir clairement ce qu'est la traînée de l'entrée d'air.

La traînée de l'arrière-corps ne peut être évaluée correctement que si l'on a une bonne évaluation des pressions sur l'arrière du fuselage, sur les volets mobiles du moteur et et les divers culots. Le recoupement, outre les conditions de vol, exige la connaissance de la géométrie (position des parties mobiles par exemple), des différents débits de moteur et de ventilation avec leurs conditions génératrices respectives (pression et température notamment).

En général, que ce soit en vol ou par le calcul, la valeur de la traînée est connue à quelque pour-cent près ; la précision est bien sûre meilleure pour un avion civil en croisière que pour un avion d'arme à grande incidence mais les contraintes ne sont pas du tout les mêmes (fig. 19).

7. VOL ET SOUFFLERIE

Les comparaisons entre essais en vol et en soufflerie montrent souvent des écarts non négligeables. Indépendamment de la précision des mesures et de la détermination des différents paramètres, il reste des difficultés avec :

- les effets de paroi jamais complètement corrigés,
- les effets de turbulence différents en soufflerie et en vol,
- les effets de taille (nombre de Reynolds),
- les interactions des supports des maquettes,
- la non conformité des détails entre avion et maquette :
  - imperfections de la peau,
  - les bosses, sondes, antennes, etc...,
  - les fentes,
  - toutes les discontinuités mécaniques,
  - les déformations sous charge.

Le cas idéal lors de l'identification d'une forme d'avion consiste à restituer par le calcul les essais de soufflerie et à retranscrire en vol en tenant compte de toutes les remarques ci-dessus (fig. 20).

Dans le cas de conditions de vol hypersonique, le calcul est absolument indispensable : le passage de la soufflerie au vol ne peut se faire directement notamment à cause des problèmes thermiques dont les conditions sont trop différentes (fig. 21).

8. CONCLUSION

Les comparaisons entre calculs, d'une part, essais en soufflerie et vol, d'autre part, sont indispensables pour valider les codes qui servent de plus en plus à définir les formes aérodynamiques des avions. La première difficulté est la connaissance des conditions d'essais, surtout en vol, et celle de tous les paramètres géométriques (parties mobiles) et aérodynamiques.

La validation des méthodes n'est pas suffisante car elle ne peut couvrir tous les aléas possibles. Il faut donc veiller à la robustesse des codes à leur portabilité et à la fiabilité informatique en général.

La chance des AMD-BA est d'avoir un grand choix de types d'avions civils FALCON 500 ou 900, militaires MIRAGE F1 - MIRAGE 2000 - RAFALE, HERMES dont les domaines de vol couvrent de larges plages de nombre de Mach, incidence, altitude, nombre de Reynolds..., dont les formes sont très variées (flèches de bord d'attaque, allongement, et épaisseur de voilure, nez arrondi ou pointu...) pour valider les codes de calculs aérodynamiques dans un très large domaine.

Les codes de calcul correctement testés, dont on connait bien les caractéristiques, la qualité des résultats et les limites de validité, permettent aujourd'hui d'optimiser les avions de demain en parallèle avec les essais de soufflerie et de façon parfaitement complémentaire. De plus, le calcul permet de mieux analyser donc de mieux comprendre les phénomènes liés à l'aérodynamique en soufflerie et surtout en vol.

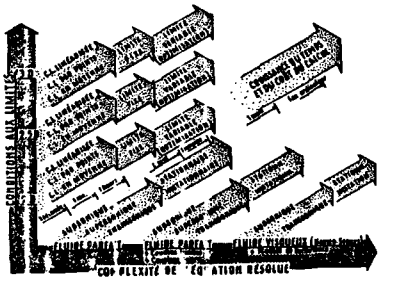
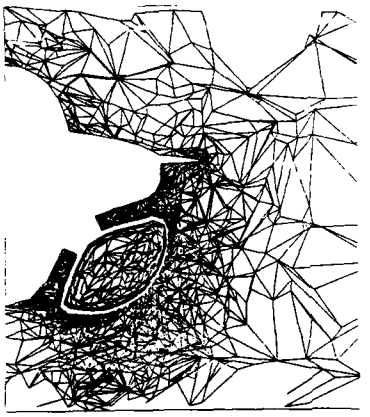


Fig. 1 : Complexité de l'aérodynamique



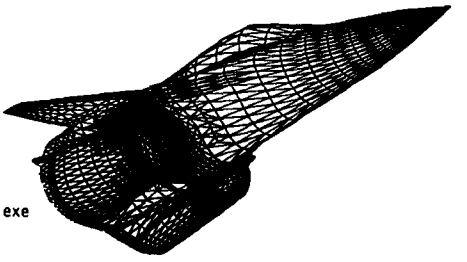


Fig. 2 : Discrétisation d'un cas complexe
La peau
Coupe dans le fluide

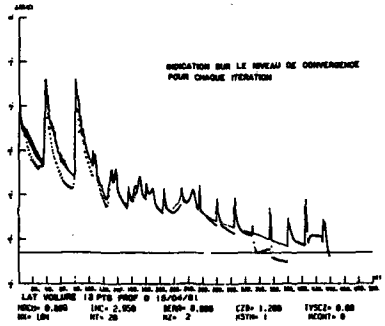


Fig. 3 : Exemple de courbe de convergence

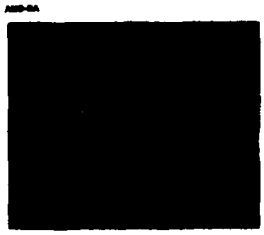


Fig. 4 : Raffinement du maillage

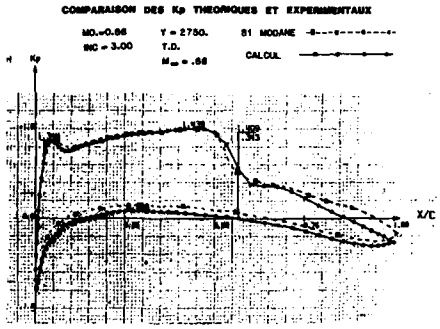


Fig. 5 : Comparaison sur un profil

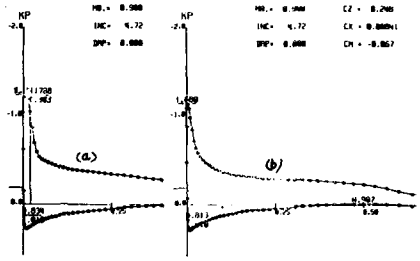


Fig. 6 : Effet du Karman sur les pressions
Simulation du Karman (b)
Aile sans fuselage (a)

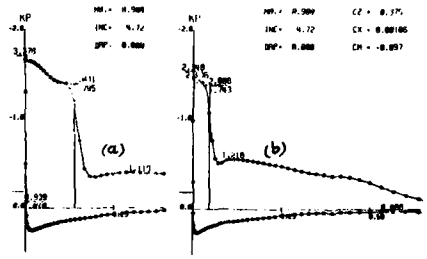


Fig. 7 : Effet de discrétisations : profil à 95 %
Sans profil à 98 % (a)
Avec profil à 98 % (b)

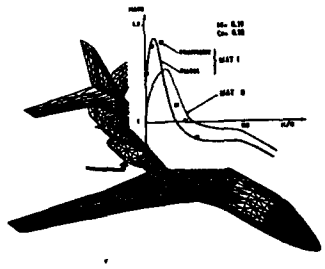


Fig. 8 : Pressions sur un mât du Falcon

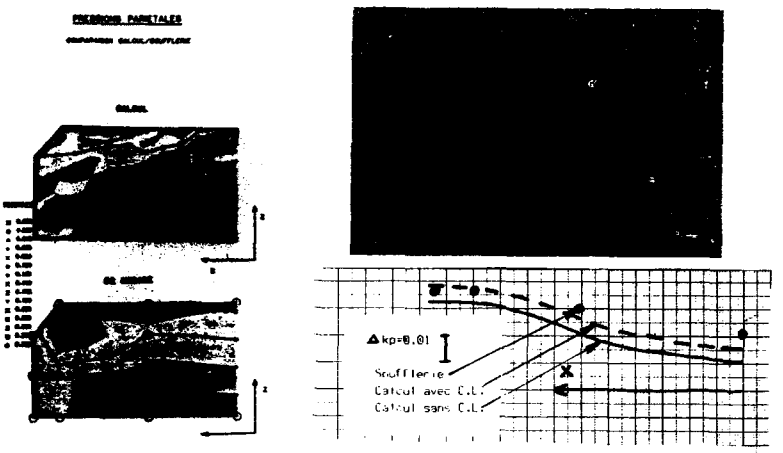


Fig. 9 : Pression sur l'avant du Rafale

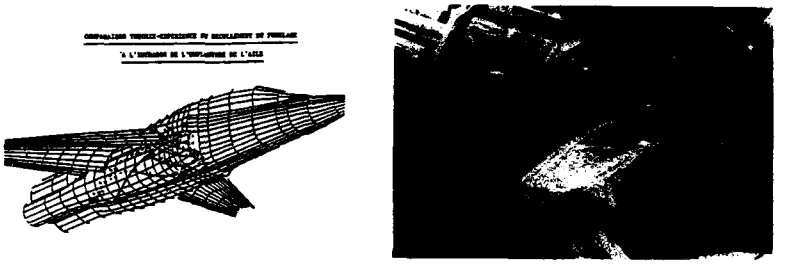


Fig. 10 : Décollement sur le fuselage de l'Alpha-Jet

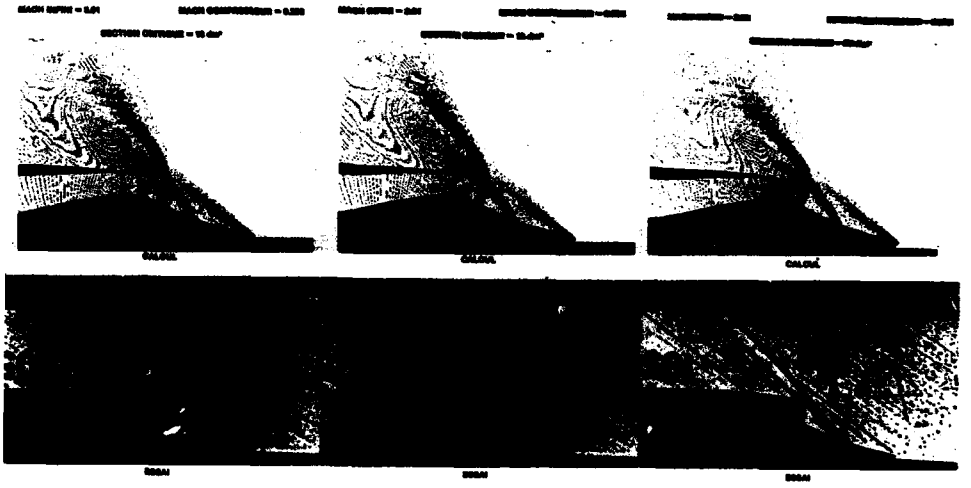


Fig. 11 : Prise d'air supersonique

Fig. 13 : Prise d'air supersonique

Fig. 12 : Prise d'air supersonique

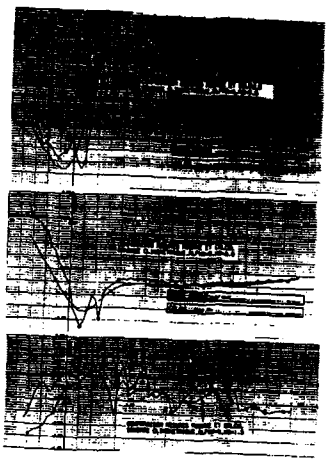


Fig. 14 : Sondages clinométriques

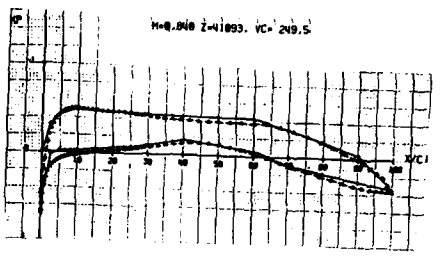


Fig. 15 : Pression sur un profil en vol

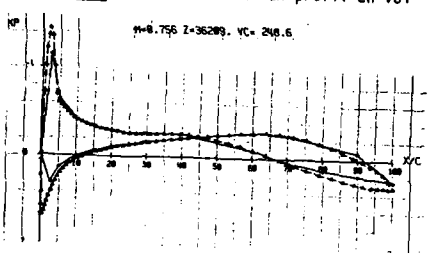


Fig. 16 : Pression sur un profil en vol

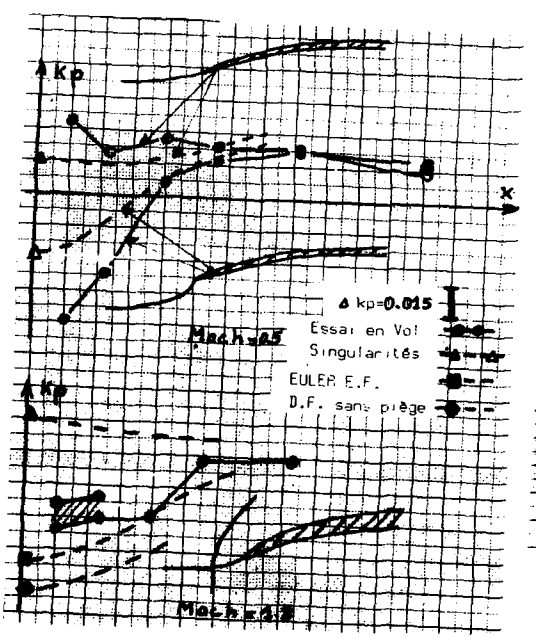


Fig. 17 : Pression sur la lèvre d'entrée d'air

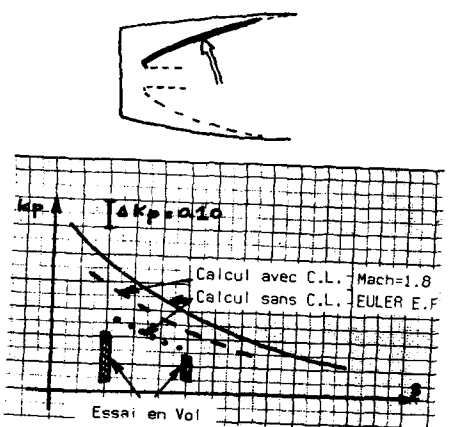


Fig. 18 : Pression dans le piège

Traînée: avion d'arme en vol supersonique

Trainee induite. dépend de CZ

Traînée à CZ=0 (en % de celle-ci)

Frottement.....	18 à 25 %
Onde.....	40 à 60 %
Entrées d'air...	7 à 20 %
Arrière corps...	-5 à 10 %
Divers.....	10 à 15 %

Traînée des emports

Fig. 19 : Décomposition de la traînée



Fig. 21 : L'hypersonique : HERMES

Essai en soufflerie

- Echelle de la maquette
- Conditions d'essai (MACH, densité, pression...
- Enthalpie totale
- Impuretés, état chimique du fluide
- Equilibre et temps de réaction chimique
- Temps d'essai

Calcul en condition de soufflerie

- Recoupement en veine vide
- Recherche des impuretés
- Itérations sur les conditions mal connues

Calcul en condition de vol

- Echelle du vol
- Enthalpie, MACH, densité, pression...
- Réactions chimiques

Apres le VOL, restitution de celui-ci.

Fig. 20 : De la soufflerie au vol par le calcul

DECOLLEMENT SUR OBSTACLES DE TYPE ELLIPSOIDE EXPERIENCES DE VALIDATION ET MODELISATION

Par
D. BARBERIS
B. CHANETZ
Office National d'Etudes et de Recherches Aérospatiales (ONERA)
B.P. N° 72 - 92322 CHATILLON CEDEX (France)

RESUME

Dans le but de mieux comprendre la physique des phénomènes de décollement et de fournir des cas tests bien documentés permettant de valider les modèles théoriques, des mesures pariétales (pressions, visualisations par enduit visqueux), des explorations du champ aérodynamique au moyen de sondes de pression anémoclinométriques et d'un vélocimètre laser tridirectionnel ont été réalisées sur des obstacles arrondis de forme simple. La structure des enroulements tourbillonnaires et des couches limites au voisinage du plan de symétrie extrados ont été caractérisées. Les expériences ont, en particulier, servi à discuter et à valider une méthode de calcul de la couche limite tridimensionnelle. La formulation inverse a permis d'étendre les calculs dans la région décollée. Pour la couche limite, au voisinage du plan de symétrie, la confrontation des résultats expérimentaux et des calculs pour les propriétés turbulentes, a mis en évidence les insuffisances du modèle de turbulence utilisé.

ABSTRACT

In the aim of understanding three dimensional separation phenomenon and obtaining detailed experimental data for the development and calibration of numerical models, wall measurements (pressures, surface flow visualizations by viscous coating), flow field measurements with pressure probes and three directional laser doppler velocimeter were carried out on blunt bodies of simple form. Vortex flows and boundary layers near the plane of symmetry were investigated. Experimental data have been used for the validation of a numerical method for three dimensional boundary layers. The inverse mode allows the continuation of the calculation beyond the separation line. Differences observed between theoritical and experimental results on turbulent quantities indicate some insufficiencies of the turbulence model used.

NOTATIONS UTILISEES

Symboles

A_i : demi axes de l'ellipsoïde
C_f : coefficient de frottement pariétal
K_p : coefficient de pression statique $K_p = p-p_o/q_o$
L : longueur de référence
p : pression statique
p_o : pression statique de référence
q_o : pression dynamique de référence $q_o = 1/2\ \rho V_o^2$
R_e : nombre de Reynolds de référence $(V_o L/\nu)$
V^i : composantes contravariantes de la vitesse
V_o : vitesse infinie amont
X^i : coordonnées d'un point de la surface
$XG^{i'}$: coordonnées d'un point du repère cartésien associé à la maquette
α : angle d'incidence
Γ^i_{jk} : coefficients de Christofell
Δ_i : épaisseurs de déplacement
μ : coefficient de viscosité
μ_t : coefficient de viscosité turbulente
ν : viscosité cinématique
ρ : masse spécifique
ω^i : composantes du vecteur tourbillon

Indices

i=1et2 : pour les composantes situées dans un plan parallèle à la surface
i=3 : pour la composante normale à la surface

1 - INTRODUCTION

Le présent travail se rattache à une étude fondamentale sur le décollement turbulent tridimensionnel dans le cas où la séparation se produit sur une surface régulière à grand rayon de courbure. Le phénomène est analysé en considérant des corps du type ellipsoïde qui présentent l'avantage d'une certaine simplicité de forme facilitant la modélisation tout en modulant convenablement l'écoulement autour de fuselage

d'avions ou d'hélicoptères. Le décollement sur de tels obstacles est un phénomène le plus souvent nuisible, car source de traînée supplémentaire, d'instabilités, de vibrations et de bruits. Il est donc important de pouvoir prédire la séparation, ce qui implique la mise au point de méthodes de calcul de la couche limite sur un obstacle tridimensionnel.

Dans le développement de ces méthodes de calcul, l'apport expérimental joue bien évidemment un rôle capital, non seulement en tant qu'élément de validation de la théorie, mais aussi comme support à la bonne compréhension physique des phénomènes, indispensable à une saine interprétation des observations et à l'élaboration des modèles théoriques.

En effet, si en bidimensionnel, le critère de décollement est l'annulation du frottement pariétal et l'apparition d'un écoulement de retour sur les profils de vitesse, la situation est beaucoup plus complexe pour les écoulements tridimensionnels où un décollement peut prendre naissance sans annulation du frottement à la paroi.

Un progrès considérable dans la compréhension physique des écoulements tridimensionnels a été apporté par les travaux de LEGENDRE [1, 2] et de LIGHTHILL [3] qui s'appuient, en grande partie, sur les travaux de POINCARE consacrés aux points singuliers des équations différentielles [4].

En particulier, on introduit en tridimensionnel la notion fondamentale de ligne de courant limite ou ligne de frottement, qui se définit comme la position limite d'une ligne de courant quand sa distance à la paroi tend vers zéro. Raisonnant sur les lignes de frottement, il est alors possible d'introduire des singularités en nombre réduit qui permettent, comme l'a montré LEGENDRE, d'interpréter la plupart des observations expérimentales.

Le calcul exact du comportement de l'écoulement au voisinage d'un point singulier ou d'une ligne de séparation, définie comme ligne de convergence des lignes de courant pariétales, conduit à des difficultés qui ne sont pas encore totalement maîtrisées. Les rares résultats dont on dispose ont été obtenus en résolvant localement les équations de Navier-Stokes au moyen de techniques de développement en série [5, 6].

Dans ces conditions, l'étude du processus de séparation (ou décollement), avec la prévision corrélative des propriétés de l'écoulement à la naissance d'une nappe tourbillonnaire, peut avantageusement faire appel à une approche plus simple reposant sur la résolution des équations de la couche limite en mode inverse.

Depuis les travaux de GOLDSTEIN [7] il est bien connu que le calcul d'une couche limite bidimensionnelle en mode direct (c'est-à-dire devant satisfaire à une répartition de vitesse externe donnée) devient instable à l'approche d'un décollement en raison de l'existence d'une singularité au point où le frottement pariétal s'annule. Toutefois, en procédant en mode inverse, c'est-à-dire en imposant comme condition une propriété liée au développement de la couche limite (épaisseur de déplacement ou frottement pariétal, par exemple), il est possible de poursuivre le calcul sans encombre au-delà du point de décollement [8-10].

En tridimensionnel, des difficultés numériques apparaissent également à l'approche d'une ligne de séparation lorsque le calcul est conduit en mode direct. Ce problème a été analysé par COUSTEIX et HOUDEVILLE [11] qui ont par la même occasion montré que le mode inverse, appliqué par eux à une méthode intégrale permettait de franchir une ligne de séparation.

Les travaux ultérieurs de FORMERY [12] et de BARBERIS [13] ont conduit au développement d'une méthode aux différences finies résolvant les équations de la couche limite turbulente tridimensionnelle aussi bien en mode direct qu'en mode inverse.

La présente communication fait le point sur un ensemble de travaux récents ayant comme double but :

i - de fournir un ensemble de données expérimentales permettant d'améliorer la compréhension physique du phénomène de décollement en écoulement tridimensionnel et de valider les codes de calcul des écoulements tourbillonnaires existant ou en cours de développement,

ii - de valider les méthodes de prévision du décollement sur surface à courbure régulière dans le cadre d'une approche du type couche limite avec modèle de turbulence.

Les expériences ont été exécutées en écoulement incompressible sur des maquettes de forme simple se prêtant facilement à une représentation analytique, ce qui facilite l'exécution des calculs. Nous examinerons d'abord les propriétés du système tourbillonnaire qui prend naissance à partir des lignes de séparation sur un ellipsoïde cylindre aplati. Nous montrerons que l'approche couche limite inverse permet de prédire les lignes de séparation ainsi que les caractéristiques de l'écoulement au voisinage immédiat de ces lignes. La seconde partie de la communication sera consacrée à une étude détaillée de la couche limite tridimensionnelle dans le plan de symétrie d'un ellipsoïde-cylindre de révolution.

Différents auteurs [14, 15] ont montré l'intérêt de l'étude d'un tel écoulement qui se situe à un niveau de complexité compris entre un écoulement purement bidimensionnel car pouvant être calculé indépendamment du reste de l'écoulement et un écoulement purement tridimensionnel. Il permet donc de tester à moindres frais les programmes de calculs tridimensionnels, les expériences servant alors plus spécialement à valider des modèles de turbulence.

2 - CHAMP TOURBILLONNAIRE ASSOCIE AU DECOLLEMENT SUR UN ELLIPSOIDE-CYLINDRE APLATI

2.1 - Etude expérimentale

2.1.1 - Conditions et moyens d'essais

La maquette utilisée, dont la longueur totale est de 1830 mm, est représentée schématiquement figure 1. Elle est constituée de deux parties de forme géométrique simple : la partie avant est un demi-ellipsoide aplati de demi-axes A1 = 800 mm, A2 = 400 mm, A3 = 230 mm ; la portion aval est un cylindre dont la section est une ellipse de demi-axes A2 et A3. La maquette se termine par un culot plan incliné à 45°, ce qui permet de fixer le décollement aval le long d'une arête et d'éviter ainsi les instabilités éventuelles résultant d'un décollement sur une partie arrière fuselée.

Les visualisations pariétales ont été obtenues en revêtant la maquette d'une bouillie blanche composée d'un mélange d'huile de parafine, d'oxyde de titane et d'acide oléique.

Certaines mesures au sein du fluide, comportant la détermination de la pression et de la vitesse, ont été réalisées à la sonde de pression anémoclinométrique à 5 trous. L'explorateur portant la sonde est fixé en aval du culot de la maquette, comme on le voit figure 2a. Il permet des mouvements selon les trois axes XG^1', XG^2', XG^3', liés à la maquette, définis figure 1.

Les explorations des champs de vitesse moyenne et fluctuante ont été effectuées au moyen d'un vélocimètre laser tridirectionnel mis au point par la Direction de la Physique Générale de l'ONERA [16]. Il s'agit d'un appareil mesurant simultanément les trois composantes du vecteur vitesse. En raison de l'obstruction créée par la maquette, le vélocimètre laser fonctionnait ici en rétro-diffusion, c'est-à-dire que les ensembles émission et réception étaient situés d'un même côté de la maquette, comme on le voit sur la photographie de la figure 2b. Afin d'obtenir des cadences d'acquisition suffisamment élevées près du centre des tourbillons où les particules tendent à être centrifugées, l'écoulement était ensemencé par de la fumée d'encens émise au moyen d'une canne placée à la sortie du collecteur.

2.1.2 - Présentation des résultats

2.1.2.1 - Propriétés de l'écoulement pariétal

La plupart des résultats présentés ici ont été obtenus pour une vitesse amont V_∞ de 50 m/s, à laquelle correspond un nombre de Reynolds, calculé avec la longueur de la maquette L = 1,6 m, valant $5{,}6.10^6$. La transition se produisant dans la région du nez pour ces conditions, la couche limite était turbulente dans la zone où les enroulements tourbillonnaires résultant du décollement se développent pleinement.

L'apparition du décollement avec formation de structures tourbillonnaires enroulées peut d'abord être caractérisée par l'examen de propriétés pariétales, à savoir répartitions de pression (voir SCHMITT et CHANETZ [17], CHANETZ [18], CHANETZ et DELERY [35]) et spectre des lignes de frottement pariétal.

Les visualisations par enduit visqueux présentées figure 3 ont été obtenues pour des vitesses V_∞ = 50 m/s (figure 3a), V_∞ = 70 m/s (figure 3b et 3c) et sont relatives à des incidences croissant de 10° à 30°. Chaque figure donne une vue de l'extrados (côté sous le vent) et une vue de côté. Comme on le sait, moyennant certaines précautions, les lignes d'accumulation du produit visqueux peuvent être assimilées avec un bon degré de confiance aux lignes de frottement pariétal. L'interprétation rationnelle du spectre de ces lignes constitue un préalable indispensable à la compréhension de la structure des écoulements tridimensionnels décollés.

Quand l'incidence est de 10°, le noeud d'attachement à la pointe de la maquette est légèrement déplacé vers l'intrados. Il est l'origine de toutes les lignes de frottement pariétales qui enveloppent la maquette en s'écoulant de l'intrados vers l'extrados. Sur la vue de côté, ces lignes présentent une inflexion, plus accentuée sur la partie cylindrique de la maquette. A l'extrados, le spectre pariétal est remarquablement symétrique avec convergence très progressive des lignes de courant pariétales en direction du plan de symétrie vertical. Pour cette incidence, aucune ligne de séparation n'est détectée sur la surface de l'obstacle (la région du culot étant exclue de cette analyse). L'absence de séparation a été confirmée par un calcul de couche limite (BARBERIS et CHANETZ [19]). Quand α devient égal à 20° (voir figure 3b), on observe un phénomène remarquable sur le dernier tiers de la maquette, côté extrados. De part et d'autre du plan de symétrie, dans une région voisine des bords latéraux de l'obstacle, les lignes de frottement pariétal s'infléchissent rapidement et convergent en "enveloppant" une courbe commune. Comme nous l'avons signalé dans l'introduction, un tel comportement des lignes pariétales est typique de la formation d'un décollement donnant naissance à un enroulement tourbillonnaire bien organisé.

Pour une incidence supérieure α = 30° (voir figure 3c), les lignes de frottement pariétal divergent rapidement depuis le plan de symétrie vertical qui contient la ligne d'attachement (A1) et convergent en direction d'une ligne de séparation (S2). En outre, les lignes de frottement en provenance de l'intrados tendent vers une autre ligne de séparation située près du bord latéral de la maquette. Cette ligne (S1) est associée au décollement primaire qui donne naissance au tourbillon le plus intense.

La ligne de séparation secondaire (S2) correspond au décollement du fluide qui, près de la paroi, s'écoule depuis le plan de symétrie extrados en direction du bord de la maquette. Ainsi (S2) est à l'origine d'un tourbillon secondaire situé au-dessous du tourbillon primaire. La structure du champ extérieur sera précisée, dans ce qui suit, grâce aux explorations au vélocimètre laser et à la sonde de pression. Entre les deux lignes de séparation (S1) et (S2), existe une ligne d'attachement (A2), peu visible sur les photographies reproduites ici mais parfaitement observable lors des essais en soufflerie. La présence de cette ligne est d'ailleurs nécessaire pour des raisons topologiques évidentes.

D'une manière générale, les visualisations pariétales confirment la bonne symétrie de l'écoulement à dérapage nul. Elles montrent qu'un décollement avec des lignes de séparation bien identifiables est déjà

présent pour $\alpha = 20°$. Les deux enroulements tourbillonnaires principaux sont nettement écartés l'un de l'autre, ce qui est une garantie de stabilité pour de tels écoulements.

2.1.2.2 - Organisation du champ externe

Le champ externe, côté extrados, a été analysé en détail pour une incidence α de 30° et une vitesse V_0 égale à 50 m/s, conditions conduisant à la formation de décollements avec tourbillons bien organisés, comme le laissent prévoir les spectres pariétaux.

La zone de formation des enroulements tourbillonnaires, c'est-à-dire en fait la région où un mouvement tourbillonnaire commence à pouvoir être discerné par les procédés d'investigation employés, a d'abord été explorée au moyen d'une sonde de pression anémoclinométrique à cinq trous. La sonde permettait en effet de s'approcher plus près de la paroi (environ 3 mm) que le vélocimètre laser dont les optiques de réception étaient éblouies par la surface de la maquette dès que la distance du volume de mesure à cette dernière était inférieure à 15 mm.

Ainsi, 11 secteurs contenus dans des plans perpendiculaires à l'axe longitudinal OXG^1' de la maquette ont été explorés entre les abscisses $XG^1' = 800$ mm et $XG^1' = 1000$ mm, soit une distance de 200 mm en aval de la jonction ellipsoïde-cylindre (voir figure 4). Nous allons examiner les propriétés du champ dans cette région en considérant l'écoulement moyen projeté dans les plans d'exploration, c'est-à-dire le champ de la composante du vecteur vitesse contenue dans des plans perpendiculaires à OXG^1'. La figure 4 indique les domaines du champ externe explorés à la sonde 5 trous et au vélocimètre laser.

La figure 5 montre l'évolution du champ de vecteur vitesse pour les quatre abscisses $XG^1' = 880$ mm, 920 mm, 960 mm, 1000 mm. Dans chaque section, la zone explorée est une portion de couronne de largeur 55 mm comprise entre les positions angulaires $\varphi = 109°$ et $\varphi = 170°$. Chaque profil comprend 23 points de mesure espacés de h = 2,5 mm, le premier point étant distant de 3 mm de la paroi. Les tracés mettent en évidence le mouvement de contournement de la maquette avec ralentissement progressif à l'approche du plan de symétrie vertical. On y distingue aussi l'amorce d'un mouvement tourbillonnaire intéressant une couche relativement mince au contact de la paroi. Les résultats suivants sont relatifs aux sections dont les abscisses vont de $XG^1' = 1000$ mm à $XG^1' = 1600$ mm.

Cette partie de l'écoulement a été explorée au vélocimètre laser tridirectionnel, si bien que la zone très proche de la paroi n'a pu être sondée pour les raisons signalées plus haut. Toutefois, dans cette partie du champ, le système tourbillonnaire principal est suffisamment détaché de la surface pour que les mesures effectuées en donnent une image précise.

Les champs de la composante de vitesse projetée dans des plans perpendiculaires à l'axe OXG^1', d'abscisse $XG^1' = 1120$ mm, 1280 mm, 1440 mm et 1540 mm sont représentés figure 6. La surface explorée est ici une couronne de largeur égale à 50 mm comprise entre $\varphi = 109°$ et $\varphi = 135°$ et contenant 21 lignes d'exploration espacées de 2,5 mm. Pour l'ensemble de ces explorations, le tourbillon principal, qui est maintenant bien détaché de la paroi, apparaît distinctement. On remarque aussi l'amorce du mouvement d'enroulement qui va constituer le tourbillon secondaire, le centre de rotation associé à ce tourbillon étant trop proche de la paroi pour apparaître dans le champ exploré. Cependant, à partir d'une trajectographie dans le champ de vitesse et en s'appuyant sur les visualisations pariétales, qui donnent avec précision les positions des lignes de séparation et d'attachement sur la surface de la maquette, il est possible d'établir un tracé quantitativement correct des lignes de courant du mouvement transversal (voir figure 7). Les points singuliers apparaissant dans ces tracés, effectués pour les quatre plans considérés, sont les deux foyers $\mathcal{F}_1$ et $\mathcal{F}_2$, les demi-cols $\mathcal{C}_3$ et $\mathcal{C}_4$, traces des lignes de séparation (S_1) et (S_2), et le demi-col $\mathcal{C}_5$ correspondant à la ligne d'attachement (A_3). Apparaissent aussi le col $\mathcal{C}_1$ situé au sein de l'écoulement et le demi-col $\mathcal{C}_2$, trace de la ligne d'attachement contenue dans le plan de symétrie.

La figure 8 donne une représentation de l'écoulement transversal autour de l'ensemble de la maquette pour la section située à $XG^1' = 1280$ mm, le tracé des lignes de courant côté intrados étant évidemment hypothétique. On peut ainsi dénombrer, 4 foyers, 1 col et 8 demi-cols (sur la surface de la maquette). Sachant que topologiquement un foyer est équivalent à un noeud, les points singuliers ainsi représentés satisfont bien la relation suivante déduite des travaux de POINCARE [4].

I noeuds + 1/2 I demi-noeuds - I cols + 1/2 I demi-cols = -1

soit dans le cas présent : 4 - 1 - 4 = -1.

Les résultats obtenus révèlent une organisation bien définie du système tourbillonnaire associé au décollement se produisant pour l'incidence de 30°. La figure 9 offre une vue en perspective montrant l'écoulement dans une certain nombre de plans transversaux à laquelle est associée une représentation schématique du spectre des lignes de frottement pariétal. Jusqu'à une abscisse un peu supérieure à 1120 mm, les tourbillons primaire et secondaire sont contenus dans une couche mince au contact de la paroi ; la structure de l'écoulement dissipatif est alors peu différente de celle d'une couche limite classique. Ce n'est qu'au-delà de $XG^1' = 1120$ mm que les deux tourbillons se détachent franchement de la paroi pour constituer le système tourbillonnaire bien organisé associé à un décollement franc en écoulement tridimensionnel. A cette évolution correspond un changement net du spectre pariétal, les lignes de séparation et d'attachement devenant bien identifiables, alors qu'auparavant elles se distinguaient difficilement des autres lignes de frottement pariétal.

2.2 - Modélisation du phénomène de séparation en écoulement 3D

2.2.1 - Méthode de calcul

2.2.1.1 - Equations générales

Les équations sont écrites dans une base covariante locale $(\vec{E_1}, \vec{E_2}, \vec{E_3})$ associées aux coordonnées curvilignes X^1, X^2 étant la distance normale à la surface (S) de l'obstacle et X^1, X^2 des coordonnées

curvilignes générales du point courant P sur (S). Alors $\vec{E_1}$ et $\vec{E_2}$ sont parallèles au plan tangent à (S) en P et $\vec{E_3}$ est le vecteur unitaire normal à (S) en P (figure 10).

En mode inverse, la pression étant inconnue, il est commode de l'éliminer en dérivant les équations de quantité de mouvement par rapport à X^3 ; dans le cadre des approximations de couche limite, le vecteur tourbillon $\vec{\Omega}$ a pour composantes contravariantes dans le plan tangent à (S) en P (pour plus de détails voir [20]).

$$\omega^1 = -\frac{1}{\sqrt{G}}\frac{\partial V^2}{\partial X^3} \; ; \; \omega^2 = \frac{1}{\sqrt{G}}\frac{\partial V^1}{\partial X^3}$$

Les équations de quantités de mouvement s'écrivent alors suivant $\vec{E_1}$:

$$V^1\frac{\partial \omega^2}{\partial X^1} + V^2\frac{\partial \omega^2}{\partial X^2} + V^3\frac{\partial \omega^2}{\partial X^3} - \frac{\partial V^2}{\partial X^2}\omega^2 - \frac{\partial V^1}{\partial X^2}\omega^1$$

$$+2(\Gamma_{1\,1}^{1}\,V^1 + \Gamma_{1\,2}^{1}\,V^2)\,\omega^2 - 2\,(\Gamma_{2\,2}^{1}\,V^2 + \Gamma_{1\,2}^{1}\,V^1)\,\omega^1 = \frac{1}{\rho}\frac{\partial^2}{(\partial X^3)^2}\,((\mu+\mu_t)\,\omega^2)$$

suivant $\vec{E_2}$

$$V^1\frac{\partial \omega^1}{\partial X^1} + V^2\frac{\partial \omega^1}{\partial X^2} + V^3\frac{\partial \omega^1}{\partial X^3} - \frac{\partial V^1}{\partial X^1}\omega^1 - \frac{\partial V^2}{\partial X^1}\omega^2$$

$$-2(\Gamma_{1\,2}^{2}\,V^1 + \Gamma_{1\,2}^{2}\,V^2)\,\omega^2 + 2\,(\Gamma_{2\,2}^{2}\,V^2 + \Gamma_{1\,2}^{2}\,V^1)\,\omega^1 = \frac{1}{\rho}\frac{\partial^2}{(\partial X^3)^2}\,((\mu+\mu_t)\,\omega^1)$$

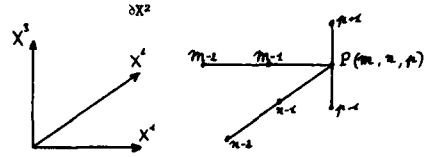
où V^i $i = 1,3$ représentent les composantes contravariantes de la vitesse $\vec{V} = V^i\,\vec{E_i}$, μ la viscosité moléculaire, μ_t la viscosité turbulente, $\Gamma_{i\,k}^{j}$ représentent les coefficients de Christoffel.
Avec comme conditions aux limites

$X^3 = 0 \qquad V^1 = V^2 = 0$
$X^3 \to +\infty \qquad \omega^1 = \omega^2 = 0$

Pour le plan de symétrie une nouvelle variable est introduite $\varphi = \frac{\partial V^2}{\partial X^2}$ qui permet de tenir compte des particularités de ce type d'écoulement [20].

2.2.1.2 - Résolution du système discrétisé

La molécule de calcul adoptée est la suivante :



Les dérivées selon X^1 et X^2 sont évaluées en p à l'aide d'un schéma retardé d'ordre 2, la dérivée selon X^3 est évaluée par un schéma centré. Le maillage est à pas variable dans les trois directions X^1, X^2, X^3. Le système obtenu est résolu par un algorithme de double balayage (pour plus de détails voir [20]).

Le calcul est stabilisé dans les zones où l'une des deux composantes de la vitesse devient négative à l'aide de l'approximation FLARE [21] qui consiste à annuler le terme de convection correspondant à la direction suivant laquelle la vitesse change de signe.

2.2.1.3 - Transition et modèle de turbulence

Le calcul de la couche limite sur une maquette du type ellipsoïde comporte en réalité trois régions correspondant aux régimes laminaire, transitionnel et turbulent. Dans les résultats présentés ici la zone de transition n'est pas déterminée numériquement mais est fixée à partir des résultats expérimentaux (visualisations à l'acénapthène, mesures du frottement pariétal). On distingue alors seulement deux régions : entre le point d'arrêt qui marque le début du calcul et une ligne AB déterminée expérimentalement l'écoulement est laminaire, en aval de AB, il est turbulent.

La première étape du travail étant le développement d'une méthode de calcul numérique adaptée à des géométries complexes, un modèle simple de turbulence a été utilisé.

Il s'agit d'une extension au tridimensionnel de la loi de longueur de mélange proposée par MICHEL et al. [22].

On fait d'abord une hypothèse de viscosité turbulente isotrope en posant :

$$\tau_{t\,x^1} = -\rho\,\overline{V^{1\prime}V^{3\prime}} = \mu_t\,\frac{\partial V^1}{\partial X^3} \qquad \tau_{t\,x^2} = -\rho\,\overline{V^{2\prime}V^{3\prime}} = \mu_t\,\frac{\partial V^2}{\partial X^3}$$

Suivant COUSTEIX [23], μ_t est exprimé par la relation :

$$\mu_t = \rho F^2 f^2 \sqrt{G_{1\,1}\,(\frac{\partial V^1}{\partial X^3})^2 + G_{2\,2}\,(\frac{\partial V_2}{\partial X^3})^2 + 2\,G_{1\,2}\,\frac{\partial V^1}{\partial X^3}\,\frac{\partial V^2}{\partial X^3}}$$

Dans cette relation :

$$F = 1 - \exp\left[-\frac{f}{26\,k\,\mu}\sqrt{\rho\,\tau^s}\right]$$

$$f = 0{,}085\,\delta\,\tanh\left(\frac{k}{0{,}085}\,\frac{X^3}{\delta}\right) \quad \text{avec } k = 0{,}41$$

τ^* est le module du vecteur frottement global physique, c'est-à-dire :

$$\tau^* = \sqrt{G_{11}\ (\tau_{x1})^2 + G_{22}\ (\tau_{x2})^2 + 2\ G_{12}\ \tau_{x1}\ \tau_{x2}}$$

2.2.2 - Comparaison aux expériences

2.2.2.1 - Première application : Ellipsoïde de Révolution du DFVLR

Le premier cas test retenu est relatif à l'écoulement autour d'un ellipsoïde de révolution allongé de rapport de demi-axes 1/6. Cette maquette de grandes dimensions (longueur du grand axe égale à 2,4 m) a été employée au DFVLR pour de nombreuses expériences comportant, en particulier, des mesures de pression et de frottement à la paroi par films chauds [24, 25]. Des visualisations ont en outre été effectuées pour définir le spectre des lignes de courant pariétales. La transition est localisée à partir des mesures de frottement. Une étude expérimentale de l'écoulement autour de cette maquette a aussi fait l'objet d'une coopération ONERA-DFVLR [26, 27].

Mode direct

La figure 11 montre une comparaison entre les visualisations pariétales réalisées à l'aide d'une bouillie, les lignes de courant pariétales déterminées à partir des mesures de frottement faites par le DFVLR [28] et les lignes de courant pariétales calculées. L'accord entre les différents résultats est correct pour la partie arrière de l'ellipsoïde, malgré l'utilisation d'un modèle de turbulence simple et d'une distribution de vitesse extérieure déduite d'une solution potentielle. Cependant, on note l'existence sur la partie avant de l'ellipsoïde d'une zone de convergence des lignes de courant pariétales déterminées à partir des mesures de frottement qui n'est mise en évidence ni par les visualisations, ni par le calcul. Il est permis de penser que cette zone, qui se trouve dans la partie transitionnelle de l'écoulement, ne peut être calculée avec précision qu'avec une modélisation correcte du passage laminaire-turbulent.

Des sondages de la couche limite à l'aide d'une sonde trois trous ont été effectués par le DFVLR dans deux plans normaux au grand axe de l'ellipsoïde. Les mesures sont comparées au calcul sur la figure 12. Pour la section située à $XG^1{}' = 1536$ mm le calcul se déroule sans difficultés du plan de symétrie intrados au plan de symétrie extrados. En revanche, pour la section à $XG^1{}' = 1704$ mm, qui se trouve dans une zone où les lignes de frottement pariétal convergent fortement, des difficultés numériques apparaissent pour un angle φ, mesuré à partir de l'indrados, supérieur à 140°.

Mode inverse

Pour tenter d'améliorer les résultats sur la partie arrière de l'ellipsoïde un calcul inverse a été exécuté en utilisant comme données le frottement pariétal mesuré. La partie avant de l'ellipsoïde est calculée en mode direct puis, pour une abscisse donnée, le programme est commuté sur le mode inverse. La figure 13 montre les résultats pour les calculs effectués en mode inverse. Comme pour le mode direct, une comparaison a été réalisée entre les profils de vitesse calculés et mesurés (figure 14).

Pour la section à $XG^1{}' = 1536$ mm les résultats sont moins bons que ceux donnés par le calcul en mode direct, sans doute en raison du manque de précision des valeurs du frottement pariétal mesurées, introduites comme données.

En revanche, pour la section située à $XG^1{}' = 1704$ mm, le calcul se déroule sans difficultés numériques jusqu'au plan de symétrie extrados, le mode inverse permettant donc dans ce cas de franchir une zone de convergence des lignes de frottement pariétal.

2.2.2.2. Deuxième application. Ellipsoïde Cylindre Aplati (ECA)

Ne disposant pas encore de renseignements suffisants sur la structure de la couche limite (frottement pariétal, épaisseurs de déplacement), les exploitations relatives à l'ECA ont été uniquement effectuées en mode direct.

Dans ce genre d'application, le champ de vitesse à la frontière de la couche limite est déterminé, soit par une solution analytique, soit à partir des distributions de pression pariétale mesurée.

A faible incidence ($\alpha = 10°$), voir figure 15, on observe un bon accord entre les lignes de courant pariétales calculées et les visualisations par enduit visqueux. Dans ce cas, aucune formation de ligne de séparation n'est détectée.

La figure 16 présente les résultats relatifs à l'incidence $\alpha = 30°$. Le calcul met en évidence un décollement laminaire près du nez de la maquette, côté extrados. Ce décollement local est également observable sur les visualisations où il se manifeste par une accumulation d'enduit. En fait, comme il est fréquent lorsque le nombre de Reynolds est suffisamment élevé, un tel décollement provoque une transition brutale de l'écoulement, ce qui est confirmé par la visualisation par produit sublimant présentée sur la figure 16.

Ainsi, en accord avec ce qui est observé sur les ogives à grande incidence [29], on distingue sur l'ECA deux types de décollement : l'un se situe sur la partie avant de la maquette et correspond à un bulbe de transition laminaire-turbulent ; l'autre se produit dans la zone turbulente et est à l'origine des enroulements tourbillonnaires principaux.

3 - DEVELOPPEMENT DE LA COUCHE LIMITE TRIDIMENSIONNELLE

3.1 - Conditions et moyens d'essais

La maquette utilisée pour cette étude, a une forme et des dimensions données figure 17. La partie avant est un demi ellipsoïde de révolution de demi-axes : A1 = 800 mm et A2 = A3 = 200 mm, la partie arrière

est un cylindre terminé par un culot plan incliné à 45° par rapport à l'axe longitudinal de la maquette. La photographie de la figure 18 montre la maquette installée dans la veine d'essai de la soufflerie F2 du Centre du Fauga-Mauzac. Le support permet la mise en incidence de la maquette depuis $\alpha = 0°$ jusqu'à $\alpha = 40°$.

Les propriétés de l'écoulement pariétal ont été mises en évidence par mesures de pression, au moyen de 287 orifices, et par visualisations : enduit visqueux mettant en évidence le spectre des lignes de courant pariétales (ou ligne de frottement) et acénaphtène donnant la position de la transition laminaire-turbulent. Les positions des prises de pression dans dix sections numérotées de 1 à 10 sont précisées sur la figure 17.

Les mesures de la couche limite dans le plan de symétrie extrados ont été réalisées à l'aide de 2 systèmes de vélocimétrie laser. Les premières expériences ont été effectuées avec un système de vélocimétrie laser bidirectionnelle (voir figure 19) en réalisant des mesures strictement dans le plan de symétrie où la composante transversale de la vitesse est théoriquement nulle.

L'introduction récente d'une troisième composante dans le système a permis la mesure simultanée des trois composantes du vecteur vitesse. Les figures 20 et 21 présentent un schéma de principe et une photo du vélocimètre laser tridirectionnel [30]. Le vélocimètre fonctionnait en diffusion avant, les optiques d'émission et de réception sont placées de part et d'autre de la veine d'expérience. L'angle formé entre le faisceau violet et les faisceaux bleu et vert est de 79°.

3.2 - Présentation des résultats

3.1.1 - Ecoulement pariétal

La figure 22 montre le spectre pariétal et les distributions circonférentielles du coefficient de pression Kp dans quelques sections significatives pour l'incidence $\alpha = 20°$ et la vitesse amont $V_\infty = 70$ m/s. A l'extrados et sur la moitié arrière du corps, les lignes de courant pariétales qui divergent depuis la ligne d'attachement située dans le plan de symétrie vertical sont fortement défléchies. Elles présentent une inflexion et viennent "envelopper" ce qui constitue une ligne de séparation. Corrélativement à la formation des lignes de séparation, les répartitions de Kp mettent en évidence l'apparition d'une zone dépressionnaire très localisée, bien visible à l'extrados pour les sections les plus aval, spécialement celle située à $XG^{1'} = 1440$ mm.

3.1.2 - Sondages dans le plan de symétrie extrados

Au cours de ces essais, qui doivent servir à la validation de modèles de turbulence, une attention toute particulière a été portée à la qualité des mesures, c'est-à-dire à leur précision et à leur fiabilité.

Les sondages de la couche limite ont été réalisés pour différentes abscisses dans le plan de symétrie, côté extrados ($\varphi = 180°$), mais aussi pour des plans voisins du plan de symétrie ($\varphi = 175$, 170 et 165°). Les positions de ces sondages sont indiquées figure 23.

Tous ces essais ont été exécutés pour une incidence de 20° et pour une vitesse à l'infini amont égale à 50 m/s.

La fidélité des mesures a été examinée pour la position d'exploration située la plus en aval ($XG^{1'} = 1050$ mm) et pour les deux normales $\varphi = 180°$ et $\varphi = 170°$. Comme le montre la figure 24, on note un très bon accord entre les résultats des deux séries de mesures pour ce qui concerne les trois composantes de la vitesse moyenne. La figure 25 présente une comparaison des résultats relatifs aux corrélations turbulentes. Malgré un bon accord sur la grandeur $\overline{V^{1'}V^{3'}}$, des différences sensibles ainsi qu'une certaine dispersion affectent la mesure de la corrélation $\overline{V^{2'}V^{3'}}$. Ce défaut de qualité résulte d'un manque de précision dans la détermination de la composante transversale V^2 qui n'est pas mesurée directement mais qui est déduite d'une composition de composantes dans un plan horizontal déterminées selon les directions de visée du vélocimètre laser (voir plus haut).

Les figures 26 à 29 regroupent l'ensemble des résultats obtenus au moyen de la vélocimétrie laser 3D. Considérant la figure 27, on note que la composante transversale de vitesse V^2 n'est pas strictement nulle dans le plan de symétrie ($\varphi = 180°$). Toutefois, l'écart est faible, la valeur maximale de V^2 n'excédant pas 2 m/s (soit $V^2_{max} \simeq 0{,}04\ V_\infty$). Ces différences par rapport à zéro sont vraisemblablement dues à un léger dérapage de la maquette.

Si l'on considère les résultats dans les plans méridiens voisins ($\varphi = 175$, 170 et 165°), on constate que l'écoulement converge vers le plan de symétrie loin de la paroi et en diverge au voisinage de celle-ci. Les profils de vitesse pour φ 175, 170 et 165° permettent de déterminer la dérivée $\partial V^2/\partial\varphi$ qui caractérise les écoulements dans un plan de symétrie et les distingue ainsi d'un écoulement strictement bidimensionnel.

L'amorce du tourbillon induit par le décollement peut être décelée en considérant les distributions de la composante de vitesse normale V^3 représentées figure 28 et plus particulièrement celles relatives à la méridienne $\varphi = 165°$. Pour les sections situées à $XG^{1'} = 650$; 750 et 850 mm, l'hypothèse classique de couche limite ($V^3 \simeq o$) est vérifiée près de la paroi. Puis lorsque la composante transversale de la vitesse V^2 croit au voisinage de la paroi, la composante verticale de la vitesse V^3 devient négative, les hypothèses de couche limite ne sont donc plus valables dans cette zone. Le déficit de vitesse observé sur les profils de la composante longitudinale V^1 pour les sections $XG^{1'} = 950$ et 1050 mm et $\varphi = 170°$ et 165° a déjà été observé par d'autres auteurs pour ce type d'écoulement [31] et est causé par le fort cisaillement de la couche limite. La figure 29 présente les profils obtenus pour la grandeur $\overline{V^{1'}V^{3'}}$. On note une plus grande dispersion des résultats que pour les grandeurs moyennes. On observe, pour les couches limites dont les profils de vitesse moyenne longitudinale V^1 présentent une forme en S, un deuxième pic de la tension de cisaillement à une certaine distance de la paroi.

3.3 - Modélisation de la couche limite dans le plan de symétrie

3.3.1 - Cas test de l'Ellipsoïde de Révolution du DFVLR

Des explorations de la couche limite ont été réalisées dans la soufflerie S2 Ch de Chalais-Meudon à l'aide de la vélocimétrie laser dans le plan de symétrie, côté extrados. La maquette était placée à 10° d'incidence dans un écoulement dont la vitesse amont était de 45 m/s.

La figure 30 présente une comparaison entre les résultats des calculs en mode direct et des profils mesurés. Pour ces calculs, le champ de vitesse extérieur a été déterminé à partir de formules analytiques. Les différences constatées sur les profils de vitesse entre le calcul et l'expérience sont attribuables en grande partie aux insuffisances du modèle de turbulence utilisé.

La figure 31 présente les évolutions du frottement pariétal. On constate pour la configuration considérée un accord presque parfait entre le calcul et l'expérience dans la partie laminaire de l'écoulement. Cependant si des différences entre les résultats théoriques et expérimentaux existent pour la partie turbulente, les évolutions reproduisent assez fidèlement l'expérience. En particulier, contrairement aux résultats de SCHNEIDER et ZHU [32] l'augmentation du coefficient de frottement à l'extrados de la partie arrière de l'ellipsoïde est bien prédite.

3.3.2 - Ellipsoïde Cylindre de Révolution

Pour les calculs en mode direct il est nécessaire de connaître le champ des vitesses à l'extérieur de la couche limite. Ce dernier est ici déterminé en exploitant un programme résolvant les équations d'Euler à partir du champ des pressions pariétales [33]. De cette manière il est possible d'utiliser le champ des pressions obtenu expérimentalement. Les figures 32 et 33 présentent une comparaison entre les résultats expérimentaux et des calculs résolvant les équations de plan de symétrie sur l'ellipsoïde cylindre de révolution placé à 20° d'incidence dans un écoulement dont la vitesse amont est de 50 m/s. Les résultats indiquent l'inadaptation du modèle de turbulence à ce type d'écoulement, ce qui ne permet pas de décrire correctement l'évolution de la grandeur $\overline{v^1 v^3}$. Il semble nécessaire de tenir compte de l'influence de la convergence et de la divergence de l'écoulement sur les propriétés de la turbulence [34]. Actuellement cette influence n'est prise en compte que sur les grandeurs moyennes au moyen d'une équation de transport pour la variable $\varphi = \frac{\partial V^2}{\partial X^2}$

4 - CONCLUSION

Les conditions de formation du décollement sur un obstacle tridimensionnel régulier ont été étudiées expérimentalement sur des maquettes de forme ellipsoïdale.

Une première série d'expériences a été exécutée sur un corps en forme d'Ellipsoïde-Cylindre Aplati. Elles ont permis de caractériser finement la structure de l'écoulement pariétal pour des incidences croissantes de la maquette. En particulier, les lignes de séparation ont été soigneusement repérées. L'écoulement externe et plus spécialement les tourbillons se formant à grande incidence ont été explorés en utilisant des sondes de pression anémoclinométriques à 5 trous ainsi que la vélocimétrie laser à trois composantes. Ces mesures ont permis de caractériser finement la région initiale de formation des enroulements tourbillonnaires.

Le phénomène de formation des lignes de séparation est modélisé en résolvant les équations de la couche limite tridimensionnelle incompressible par une méthode aux différences finies qui s'applique à des obstacles de forme quelconque. Les résultats obtenus avec un modèle de turbulence algébrique sont en assez bon accord avec l'expérience. Les traits principaux de l'écoulement, notamment la forme des lignes de séparation, sont correctement prédits. Quand la séparation intervient, le mode inverse permet de poursuivre le calcul dans la région décollée.

Le comportement de la couche limite a été plus spécialement examiné en considérant une deuxième maquette en forme d'Ellipsoïde-Cylindre de Révolution. Des sondage au vélocimètre laser à trois composantes ont été pratiqués dans le plan de symétrie extrados ainsi qu'à son voisinage. Les propriétés moyennes et turbulentes de la couche limite ont ainsi pu être définies avec précision.

Des calculs de couche limite ont alors mis en évidence des insuffisances du modèle de turbulence utilisé qui ne prend pas en compte certains aspects physiques propres à ce type d'écoulement.

REFERENCES

[1] - LEGENDRE R.
Lignes de courant d'un écoulement permanent, décollement et séparation. La Recherche Aérospatiale N° 1977-6, pp. 327-335.

[2] - LEGENDRE R.
Séparation de l'écoulement laminaire tridimensionnel. La Recherche Aéronautique N° 54 (novembre décembre 1956).

[3] - LIGHTHILL J.
Attachment and separation in three dimensional flow. Laminar boundary Layer. Oxford University Press (1963).

[4] - POINCARE H.
Les points singuliers des équations différentielles. C.R. Académie des Sciences 13.2.1892 et Oeuvres Complètes (volume 1).

[5] - PERRY A.E., CHONG M.S.
Local solutions of the Navier-Stokes equations in separated flows. Third Symposium on Numerical and Physical Aspects of Aerodynamics Flows, Long Beach, Californie (1985).

[6] - DALLMANN U.
Topological structures of three-dimensional vortex flow separation. AIAA-83-1935 (1983).

[7] - GOLDSTEIN S.
On laminar boundary-layer flow near a position of separation. The Quarterly Journal of Mechanics and Applied Mathematics, Vol. 1, Part 1 (1948), pp. 43-69.

[8] - CHATHERALL D., MANGLER K.W.
The integration of the two-dimensional laminar boundary-layer equations past the point of vanishing skin friction. JFM, Vol. 26, Part 1 (1966), pp. 163-182.

[9] - CARTER J.E.
Inverse solutions for laminar boundary-layer flows with separation and reattachment. NASA TR-R-447 (1975).

[10] - DELERY J., MARVIN J.G.
Turbulent shock-wave/boundary-layer interaction. AGARDograph N° 280 (1986).

[11] - COUSTEIX J., HOUDEVILLE R.
Singularities in three-dimensional boundary-layer calculations and separation phenomena. AIAA Journal, Vol. 19, n° 8 (1981).

[12] - FORMERY M.
Méthode aux différences finies pour le calcul en modes inverses de la couche limite turbulente tridimensionnelle. ONERA NT 1982-6 (1982).

[13] - BARBERIS D.
Calcul de la couche limite tridimensionnelle en modes direct ou inverse sur des obstacles quelconques. La Recherche Aérospatiale, Année 1986, N° 3, mai-juin pp. 169-195.

[14] - WANG K.C.
Three-dimensional boundary layer near the plane of symmetry of a spheroid at incidence. JFM (1970), vol. 43, part 1, pp. 187-209.

[15] - PATEL V.C., BAEK J.H.
Boundary layers in planes of symmetry, Part I : Experiments in turbulent flow". AIAA Journal, vol. 25, N° 4, April 1987, pp. 550-559.

[16] - BOUTIER A., d'HUMIERES Ch., SOULEVANT D.
Three dimensional laser velocimetry : a review. 2nd International Symposium on "Applications of Laser Anemometry to Fluid Mechanics", Lisbonne, 2-4 Juillet 1984.

[17] - SCHMITT R.L., CHANETZ B.P.
Experimental Investigation of Three Dimensional Separation on an Ellipsoid-Cylinder Body at Incidence, AIAA Paper 85-1686, AIAA 18th Fluid Dyn. and Plasma Dyn. and Lasers Conference, Cincinatti, 16-18 July 1985.

[18] - CHANETZ B.
Contribution à l'étude du décollement tridimensionnel en écoulement turbulent incompressible. Thèse de Doctorat, septembre 1986, Université Lyon I.

[19] - BARBERIS D., CHANETZ B.
Décollement en écoulement incompressible tridimensionnel. Expériences de validation et modélisation. 23ème Colloque d'Aérodynamique Appliquée, Aussois, France, 12-14 novembre 1986.

[20] - BARBERIS D.
Méthode aux différences finies pour le calcul en modes direct et inverse de la couche limite sur un obstacle quelconque. ONERA RT N° 15/7252 AN 030A (1986).

[21] - REYHNER T.A., FLUGGE-LOTZ I.
The interaction of a shock-wave with a laminar boundary layer. International Journal of Non-Linear Mechanics, vol. 3, N° 2 (1968), pp. 173-199.

[22] - MICHEL R., QUEMARD C., DURANT R.
Application d'un schéma de longueur de mélange à l'étude des couches limites turbulentes d'équilibre. ONERA NT 154 (1969).

[23] - COUSTEIX J.
Analyse théorique et moyens de prévision de la couche limite turbulente tridimensionnelle. Thèse de Doctorat, Université Paris VI (février 1974).

[24] - KREPLIN H.- P., MEIER H.U., MAIER A.
Wind tunnel model and measuring techniques for the investigation of three-dimensional Turbulent boundary layers. AIAA paper 78-781, 1978.

[25] - KREPLIN H.- P., VOLLMERS H., MEIER H.U.
Experimental determination of wall shear stress vectors on an inclined prolate spheroid. Proc. 5th US/FRG DEA Meeting AFFDL-TR-80-3088, pp. 315-332-1980.

[26] - RAYNAL J.C., CASSOUDESALLE D.
Essais dans la soufflerie F1 d'un ellipsoïde de révolution DFVLR. Deuxième série d'essais (avril 1983). Document interne ONERA non publié.

[27] - COPONET D., SOULEVANT D.
Etude, par vélocimétrie laser, de la couche limite sur un ellipsoïde de révolution allongé du DFVLR. Document interne ONERA non publié.

[28] - MEIER H.U.
Communication privée.

[29] - POLL D.I.A.
On the effects of boundary-layer transition on a cylindrical afterbody at incidence in low-speed flow. Aeronautical Journal. Octobre 1985, pp. 315-327, 1985.

[30] - AFCHAIN D.
Présentation du vélocimètre laser tridirectionnel de la soufflerie F2 (document à paraître).

[31] - RAMAPRIAN B.R., PATEL V.C. CHOI D.H.
Mean flow measurements in the three dimensional boundary layer over a body of revolution at incidence. J.F.M. (1981), vol 103, pp. 479-504.

[32] - SCHNEIDER G.R. ZHU Z.
The calculation of incompressible three-dimensional laminar and turbulent boundary layers in the plane of symmetry of a prolate spheroid at incidence. DFVLR-FB 82-16-1982.

[33] - GLEYZES C. COUSTEIX J.
Calcul des lignes de courant à partir des pressions pariétales sur un corps fuselé. La Recherche Aérospatiale N° 3, 1984, pp. 223-231.

[34] - PATEL V.C., BAEK J.H.
Boundary layers in planes of symmetry, Part II : Calculations for laminar and turbulent flows. AIAA Journal, vol. 25, N° 6, June 1987, pp. 812-818.

[35] - CHANETZ B., DELERY J.
Etude expérimentale du décollement turbulent sur un ellipsoïde-cylindre aplati, à paraitre dans la Recherche Aérospatiale, 1988.

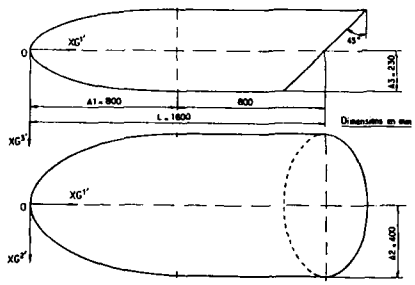


Fig. 1 _ DEFINITION DE LA MAQUETTE EN FORME D'ELLIPSOIDE CYLINDRE APLATI



Fig. 2 _ MONTAGE DE LA MAQUETTE DANS LA SOUFFLERIE S2Ch
a _ EN PRESENCE DE L'EXPLORATEUR DE PRESSION
b _ EN PRESENCE DU VELOCIMETRE LASER A 3 COMPOSANTES

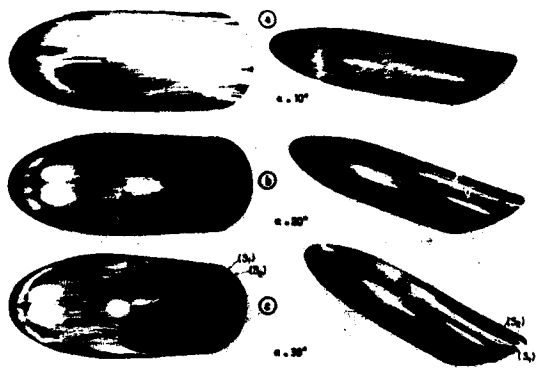


Fig. 3 _ EVOLUTION DU SPECTRE PARIETAL EN FONCTION DE L'INCIDENCE

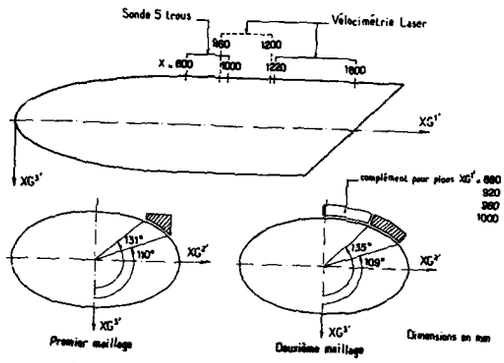


Fig. 4 - DOMAINE DE MESURES DANS LE CHAMP EXTERNE

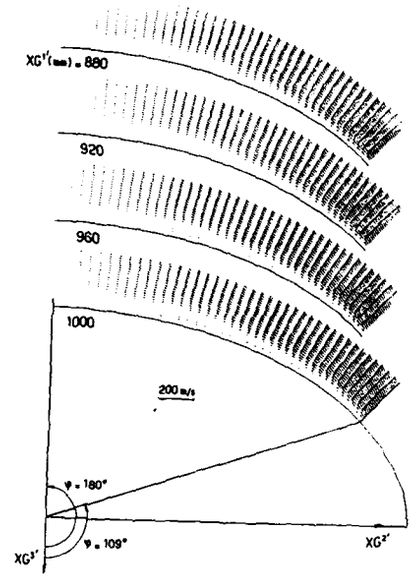


Fig. 5 - CHAMP DE LA COMPOSANTE DE VITESSE TRANSVERSALE DANS LES SECTIONS AMONT - $V_0 = 50$ m/s $\alpha = 30°$

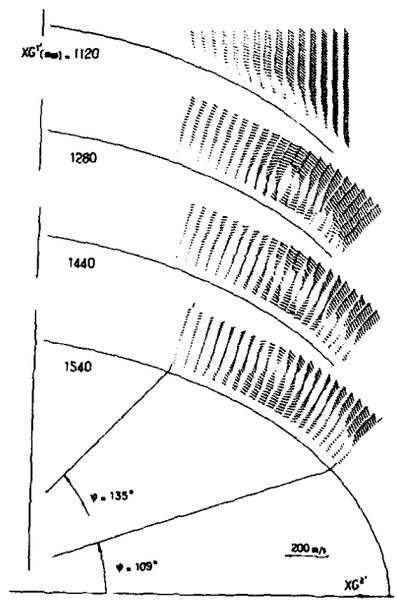


Fig. 6 - CHAMP DE LA COMPOSANTE DE VITESSE TRANSVERSALE DANS LES SECTIONS AVAL - $V_0 = 50$ m/s $\alpha = 30°$

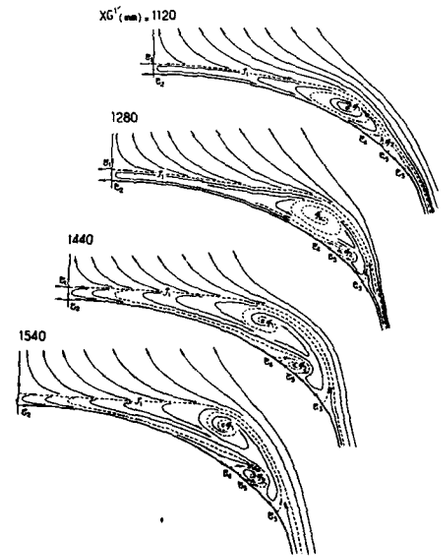


Fig. 7 - LIGNES DE COURANT DE L'ÉCOULEMENT TRANSVERSAL DANS LES SECTIONS AVAL - $V_0 = 50$ m/s $\alpha = 30°$

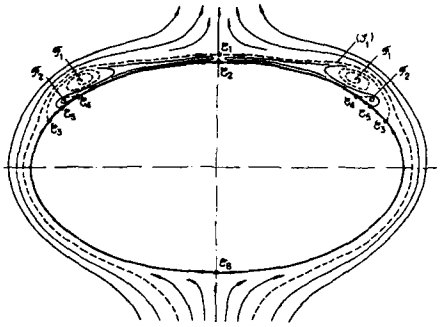


Fig. 8 _ LIGNES DE COURANT DE L'ECOULEMENT TRANSVERSAL POUR L'ENSEMBLE DU CHAMP _ $XG' = 1280$ mm $V_0 = 50$ m/s $\alpha = 30°$

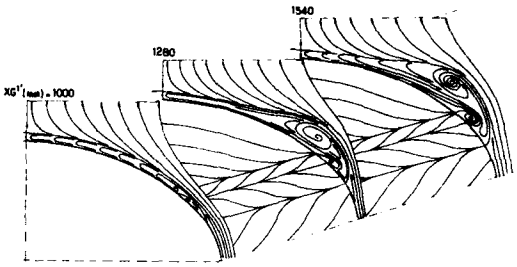


Fig. 9 _ REPRESENTATION EN PERSPECTIVE DU CHAMP TRANSVERSAL

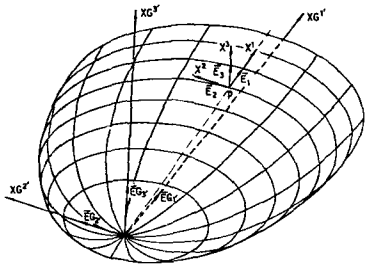


Fig. 10 _ DEFINITION DES SYSTEMES DE COORDONNEES

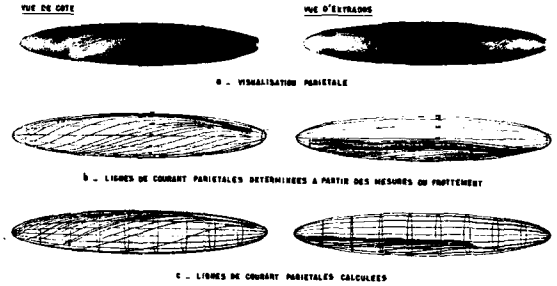


Fig. 11 _ COUCHE LIMITE SUR L'ELLIPSOIDE DFVLR
$\alpha = 10°$ $V_0 = 45$ m/s $Re = 7{,}2 \times 10^6$

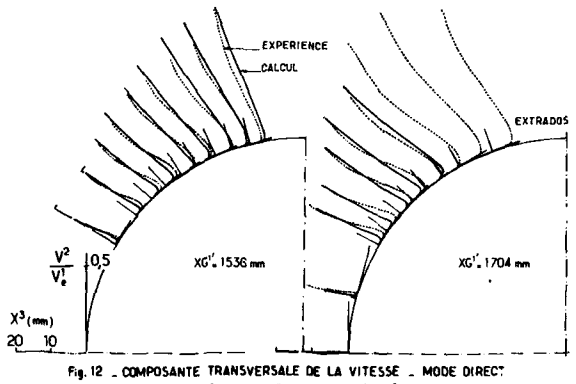
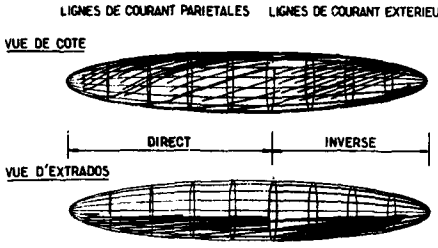


Fig. 12 _ COMPOSANTE TRANSVERSALE DE LA VITESSE _ MODE DIRECT
$\alpha = 10°$ $V_0 = 45$ m/s $Re = 7{,}2 \times 10^6$



RESULTATS

$\alpha = 10°$ $V_0 = 45$ m/s $R_e = 7{,}2 \times 10^6$

Fig. 13 _ COUCHE LIMITE SUR L'ELLIPSOIDE OFVLR

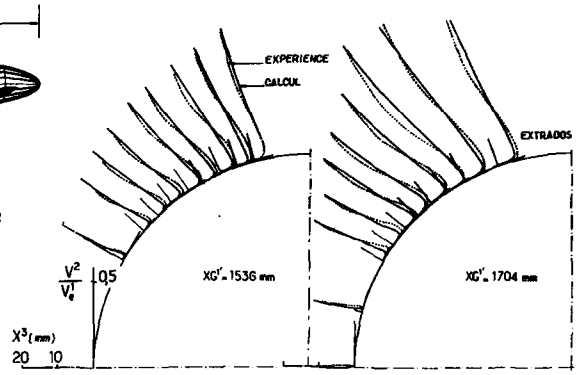


Fig. 14 _ COMPOSANTE TRANSVERSALE DE LA VITESSE _ MODE INVERSE

$\alpha = 10°$ $V_0 = 45$ m/s $R_e = 7{,}2 \times 10^6$

a _ Vue de côté



VISUALISATION PARIETALE

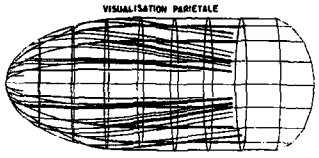


LIGNES DE COURANT PARIETALES CALCULEES

b _ Vue d'extrados



VISUALISATION PARIETALE



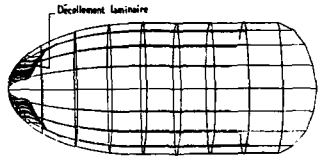
LIGNES DE COURANT PARIETALES CALCULEES

Fig. 15 _ COUCHE LIMITE SUR L'ECA

$\alpha = 10°$ $V_0 = 50$ m/s $R_e = 5{,}6 \times 10^6$



VISUALISATION PARIETALE



LIGNES DE COURANT PARIETALES CALCULEES

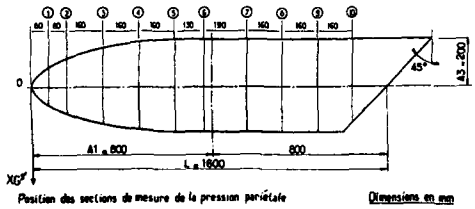


VISUALISATION DE LA LIGNE DE TRANSITION PAR PRODUIT SUBLIMANT (ACENAPHTENE)

Fig. 16 _ COUCHE LIMITE SUR L'ECA

$\alpha = 30°$ $V_0 = 50$ m/s $R_e = 5{,}6 \times 10^6$

VUES D'EXTRADOS



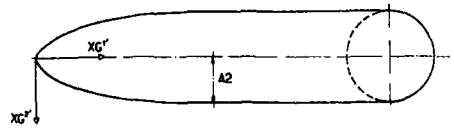


Fig. 17 _ ELLIPSOIDE CYLINDRE DE REVOLUTION (ECR)

DEFINITION DE LA MAQUETTE



Fig. 18 - MONTAGE DE LA MAQUETTE ECR
DANS LA SOUFFLERIE F2

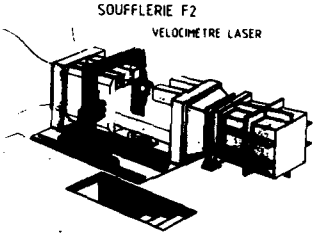


Fig. 19 - VELOCIMETRIE LASER 2D DANS LA SOUFFLERIE F2



Fig. 21 - INSTALLATION DU BANC LASER 3D
DANS LA SOUFFLERIE F2

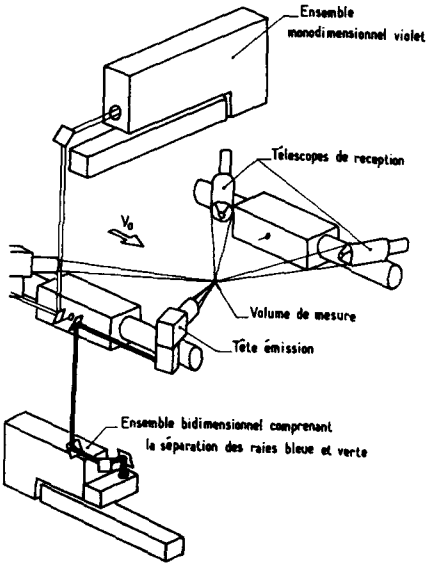


Fig. 20 - SCHEMA DE LA PARTIE OPTIQUE
DU VELOCIMETRE LASER TRIDIRECTIONNEL

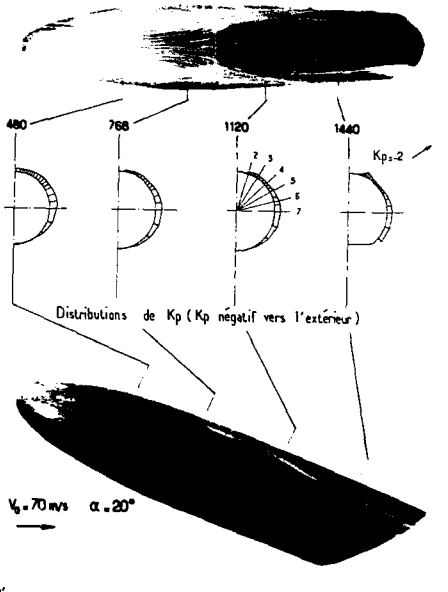


Fig. 22 - ELLIPSOIDE CYLINDRE DE REVOLUTION
VISUALISATION DE L'ECOULEMENT PARIETAL
POUR L'INCIDENCE ETUDIEE AU VELOCIMETRE LASER

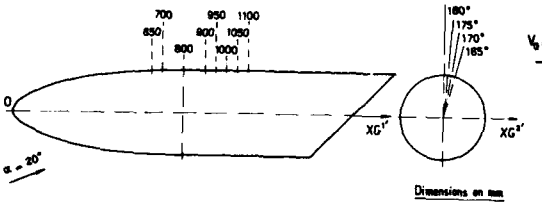


Fig. 23 - POSITION DES EXPLORATIONS DE LA COUCHE LIMITE
SUR L'ELLIPSOIDE CYLINDRE DE REVOLUTION

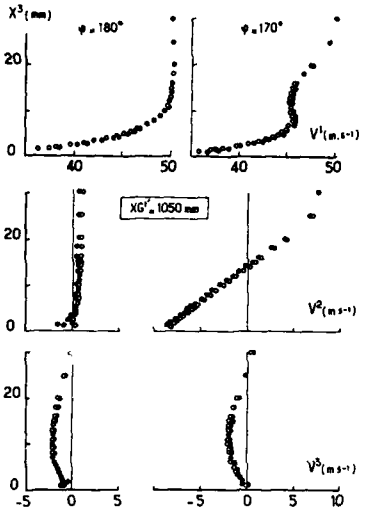


Fig. 24 _ FIDELITE DES RESULTATS
OBTENUS PAR VELOCIMETRIE LASER 3D

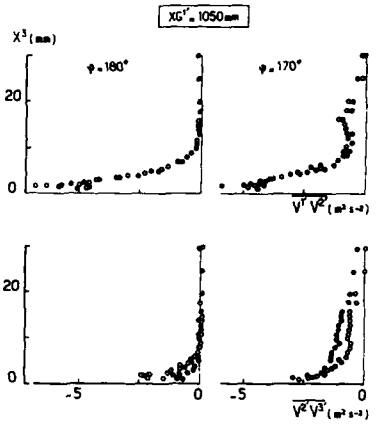


Fig. 25 _ FIDELITE DES RESULTATS
OBTENUS PAR VELOCIMETRIE LASER 3D

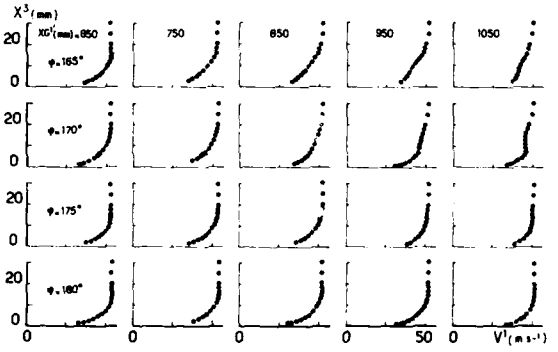


Fig 26 _ RESULTATS VELOCIMETRIE LASER 3D _ V¹

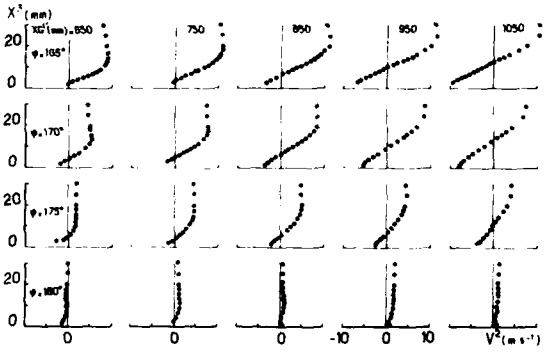


Fig 27 _ RESULTATS VELOCIMETRIE LASER 3D _ V²

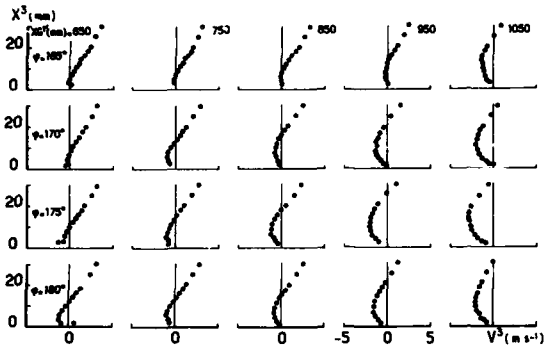


Fig. 28 - RESULTATS VELOCIMETRIE LASER 3D - V^3

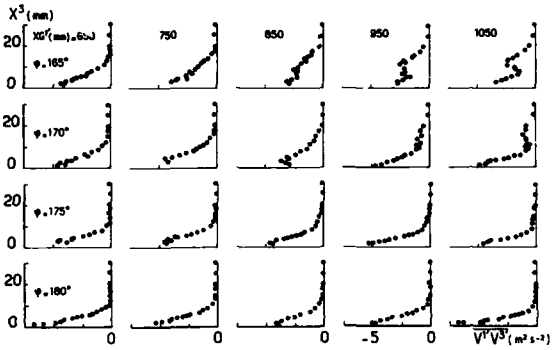


Fig. 29 - RESULTATS VELOCIMETRIE LASER 3D - $\overline{V'V^3}$

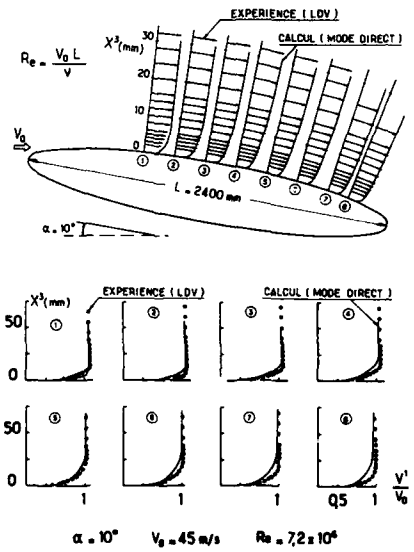


Fig. 30 - PROFILS DE VITESSE MOYENNE LONGITUDINALE
DANS LE PLAN DE SYMETRIE DE L'ELLIPSOIDE DFVLR

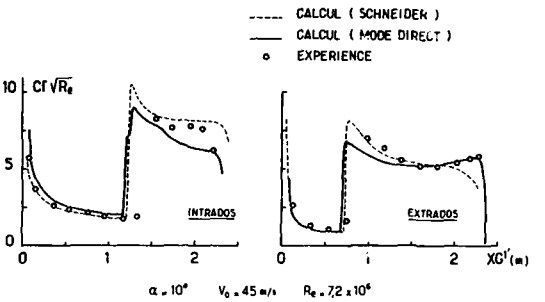


Fig. 31 _ COEFFICIENT DE FROTTEMENT PARIETAL
DANS LE PLAN DE SYMETRIE DE L'ELLIPSOIDE DFVLR

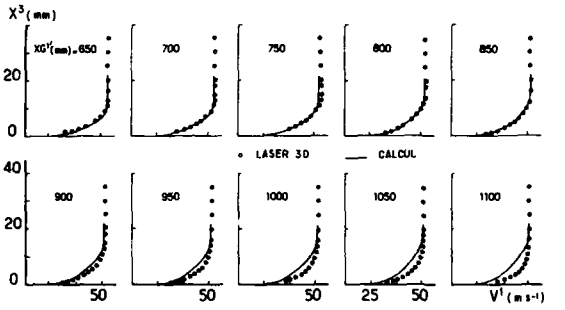


Fig. 32 _ ECR _ $\alpha = 20°$ $V_0 = 50\ m/s$
PLAN DE SYMETRIE _ COMPOSANTE LONGITUDINALE DE LA VITESSE

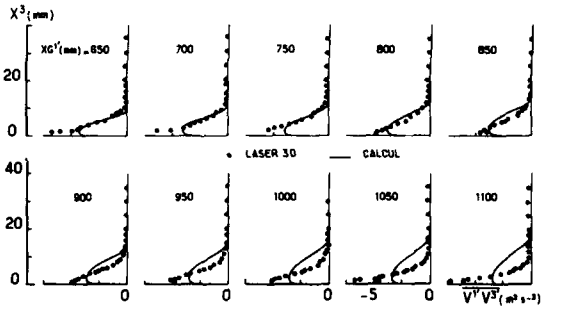


Fig. 33 _ ECR _ $\alpha = 20°$ $V_0 = 50\ m/s$
PLAN DE SYMETRIE _ TURBULENCE $\overline{V^1V^3}$

ACCURACY STUDY OF TRANSONIC FLOW COMPUTATIONS FOR THREE DIMENSIONAL WINGS

by

M P Carr
Chairman, GARTEUR Action AD(AG05)
Aircraft Research Association Limited
Manton Lane, Bedford, UK, MK41 7PF

SUMMARY

GARTEUR Action Group AD(AG05) has undertaken an investigation of ten flowfield methods. Calculations of inviscid flow over the DFVLR F4 wing for two conditions have been analysed and the work repo ted. The main results and conclusions of the Action Group are presented.

1 INTRODUCTION

Computational Fluid Dynamics (CFD) is being used increasingly in the prediction of aerodynamic flows. An area of particular interest is that of transonic flow over external aircraft configurations and a number of methods and computer codes have been developed to predict flows for this specific problem. In particular, although there is much work in progress in dealing with more general aircraft configurations or attempting to model the full physics of the flows, the developed computer codes in everyday use are less ambitious in their aims. They are generally based on inviscid flows, sometimes with interactive boundary layer models, either solving the Euler equations or even the more limiting potential equation with geometry restricted to wing-alone and wing-body configurations. Nevertheless, these codes have proved and are continuing to prove extremely useful in the aerodynamic analysis and design of, for example, civil transport aircraft.

As a prelude to using these CFD codes in aerodynamic analysis and design it is necessary to assess their accuracy. A number of computer codes had been used to calculate the flow over the DFVLR F4 wing within GARTEUR Action Group AD(AG-01) which had been set up primarily to produce an experimental data base for the F4 wing-body configuration. The theoretical results were most disappointing with significant differences between the methods. A number of reasons were suggested for the computational differences, the major ones being connected with the difficulties involved in solving non-linear flow field equations, namely ensuring convergence of the iterative techniques and providing an adequate computing grid on which to solve the discretised equations. Therefore a new GARTEUR Action Group AD(AG-05) was set up to investigate the detailed differences between various flow field methods. The geometry was the DFVLR F4 wing at two flow conditions, one subsonic (M_∞ = 0.3, α = 0.84°) and one transonic (M_∞ = 0.75, α = 0.84°) and results from ten methods submitted for consideration. These are inviscid flowfield methods based on the non-conservative potential, conservative potential and Euler equations. The list of methods is given in table 1 with their main features detailed in tables 2 and 3. Studies have been made of the convergence characteristics and sensitivity to grid refinement and grid extent as well as items such as the treatment of trailing edge and wake flows. These studies have been reported in GARTEUR TP30.

This paper presents a selection of the results from these studies together with discussion and conclusions of the most significant items. This includes details of the methods, general considerations regarding realistic expectations from the comparisons, comparisons of convergence rates, pressure distributions, overall lift and drag coefficients and spanwise lift distributions.

2 SUMMARY OF METHODS

The methods and resulting computer codes cover a development [illegible]d of about a decade and are based either on the potential or Euler equations. They the[illegible]nclude codes which have been in production use for a number of years and codes wh[illegible]ecently developed or indeed in the development stage. For this exercise all codes were [illegible] at 31 December 1985 so that clearly there will be more advanced versions of some of these codes in existance now. However it is considered that most of the conclusions from this exercise are still valid. A summary of the main features of the methods is given in tables 2 and 3. The methods employ a range of computational grids and flow solvers apart from the division between Euler and Potential equations. Thus a brief description of these variations is appropriate.

2.1 Codes based on the Potential Equation

All such codes used in the present exercise are based on solutions of the full potential equation, which in conservation form is:

$$\frac{\partial}{\partial x}\left[\rho\frac{\partial \Phi}{\partial x}\right] + \frac{\partial}{\partial y}\left[\rho\frac{\partial \Phi}{\partial y}\right] + \frac{\partial}{\partial z}\left[\rho\frac{\partial \Phi}{\partial z}\right] = 0 \qquad (2.1)$$

This equation is solved numerically at each node of a computational grid by replacing it with a discrete approximation and solving the resulting set of non-linear algebraic equations by some iterative technique.

All methods have an H grid in the spanwise direction, but O, C and H grids are all used around the wing sections. The non-conservative methods (NC) all employ a finite difference (FD) formulation but the various fully conservative (FC) methods employ the full range of finite difference, finite volume

(FV) and finite element (FE) approximations. Although table 2 gives overall details of the methods a few additional points regarding some of the methods are worth noting

1. In the ONERAFD method, the grid is offset half a grid interval from the wing and wake surfaces to facilitate application of the boundary conditions.

2. In the DFVLRFL method, the spanwise grid lines are not aligned with the trailing edge and hence, values at the nearest point to the trailing edge at each spanwise grid station are used for the Kutta condition and when integrating to obtain forces.

3. In the ARACONS method, the control parameter for the PC scheme is chosen to give results equivalent to an FC scheme (in Jameson's quasi-conservative sense).

4. In the NLR method, the smoothing used at each multigrid level (4 levels are used) is a combination of an implicit upper/lower (ILU) decomposition and the strongly implicit procedure (SIP).

5. In the ONERAFE method, the outer boundary condition is applied as a Neumann condition everywhere except at the inflow boundary. Also in the ONERAFE method, both the wing tip and the wing trailing edge geometry are modified. The wing tip is modified by slightly extending the planform and closing the tip down to zero thickness. Zero normal flow is applied on this tip extension and zero circulation is imposed around the new (zero thickness) tip section. The trailing edge is modified to produce a zero trailing edge thickness by subtracting a parabolic modification from both the upper and lower surface coordinates, from the leading edge to the trailing edge, at each spanwise station. This changes the sections's thickness distribution but leaves the camber unchanged.

6. In the AS method, the wing trailing edge geometry is modified and an additional boundary condition imposed at the wing tip. The trailing edge is modified to produce a zero trailing edge thickness by subtracting a parabolic modification from both the upper and lower surface coordinates, between 70% local chord and the trailing edge, at each spanwise station. This leaves the first 70% of a section unchanged but changes both the thickness and camber over the last 30% chord. At the wing tip the geometry is not modified but zero flow is imposed normal to the tip in the spanwise direction.

2.2 Codes Based on the Euler Equations

All such codes used in the present exercise are based on solutions of the full Euler equations:

$$\frac{\partial}{\partial t}\begin{bmatrix}\rho\\ \rho u\\ \rho v\\ \rho w\\ \rho E\end{bmatrix} + \frac{\partial}{\partial x}\begin{bmatrix}\rho u\\ \rho u^2 + p\\ \rho uv\\ \rho uw\\ \rho uH\end{bmatrix} + \frac{\partial}{\partial y}\begin{bmatrix}\rho v\\ \rho uv\\ \rho v^2 + p\\ \rho vw\\ \rho vH\end{bmatrix} + \frac{\partial}{\partial z}\begin{bmatrix}\rho w\\ \rho uw\\ \rho vw\\ \rho w^2 + p\\ \rho wH\end{bmatrix} = 0 \qquad (2.2)$$

rather than the reduced steady state set with the energy equation omitted. Although there are many ways to solve the Euler equations, all the codes in the present study are closely based on the method of Jameson et al (ref.16) and hence only differ in the computational grid, the convergence acceleration techniques and various fine details.

Thus all methods have a C-H grid, use a FV discretisation and employ a Runge-Kutta integration technique. Table 3 summarises the main features but the following points are worthy of note.

1. In the BAE method, the normal momentum equation used for surface pressure extrapolations has been modified as suggested by Boeing researchers.

2. In the DFVLREU method, a special treatment for the dissipation terms near solid boundaries has been used to yield small total pressure losses near such surfaces.

3 EXPECTATIONS

Before discussing the results it is necessary to consider what one should expect. There are two classes of differences between the methods, modelling and numerics.

3.1 Modelling differences

As long as the flow is everywhere subsonic, the main source of differences between results (viz. shock waves) is eliminated and therefore differences can be expected to be small.

The true shape of a fully relaxed (rolled-up) vortex sheet is such that the velocity normal to the vortex sheet is zero and the pressure across the vortex sheet is continuous. Then the direction in which the vortex sheet leaves the trailing edge is normally either along the upper surface or along the lower surface (Mangler-Smith ref.13). Modelling of the trailing edge flows is generally referred to as the implementation of the Kutta condition.

The potential methods and the Euler methods differ in their basic assumptions with respect to the treatment of the vortex sheet that leaves the trailing edge of the wing and the implementation of the Kutta condition. This consequently affects the lift.

With the potential methods vortex sheet roll-up is not modelled. Instead, the position of the

trailing vortices of which the vortex sheet is composed is estimated (or more usually imposed by the computational grid) and it is generally required that either the mass flow or the normal velocity is continuous across the vortex sheet. The Kutta condition is defined by the vortex sheet leaving the trailing edge in the direction of the bisector of the trailing edge angle. It follows, that the estimated position of the vortex sheet in the immediate vicinity of the trailing edge is the same for all methods. It is well known that differences in estimated position of the trailing vortices, and of the vortex sheet, further away from the trailing edge have hardly any influence on the pressure distribution on the wing. Therefore, from the modelling point of view, differences between the pressure distributions as obtained by all potential methods are most likely caused by differences in the implementation of the Kutta condition. Hopefully these differences are small; but even then the results are not in agreement with the Mangler-Smith criterion.

With the Euler methods used, vortex sheet roll-up is formally modelled and no Kutta condition is implemented. This implies that, from the modelling point of view, there is no reason for differences between the pressure distributions as obtained by all Euler methods used; also the results are, at least in principle, in agreement with the Mangler-Smith criterion.

In transonic flow shockwaves almost always occur. Since the shock relations for the full potential equation in full conservation form and for the Euler equations in full conservation form (the Rankine-Hugoniot relations) are notably different, they admit shockwaves of different strengths. Generally speaking, Rankine-Hugoniot shocks are weaker than potential shocks for the same upstream flow conditions. In most cases this results in a more upstream position of strong supersonic/subsonic shocks in the case of the Euler equations, and consequently in a lower lift. Naturally the strength and position of weak supersonic/supersonic shocks is affected also; however, the effect of this is difficult to predict.

Also the Rankine-Hugoniot shock relations imply a loss of total pressure associated with an entropy production. In many cases this effect will be counteractive to the subsonic trailing edge behaviour of the vortex sheet as predicted by the Mangler-Smith criterion. With the Euler methods used, these effects are in principle taken into account because vortex sheet roll-up is formally modelled and no Kutta condition is implemented. In potential flow there is no entropy production and, as in the subsonic case, the vortex sheet leaves the trailing edge along the trailing edge angle bisector in the potential flow methods.

3.2 Numerical differences

In practical calculations there are always discrepancies between the results of different methods. Very often these discrepancies are greater than is to be expected from the viewpoint of flow modelling. This is caused by numerical inaccuracies within the framework of each individual method, due to lack of convergence, insufficient mesh density, a too small mesh extent, or even deficiencies.

Assessment of non-converged results is almost impossible so that only converged results should be considered.

For routine calculations of three dimensional flows, a major difficulty is being able to use a sufficient number of mesh points. This can lead to insufficient mesh density. Numerical inaccuracies due to this are directly related to details of the discretisation such as conservation, artificial viscosity, freestream consistancy, order of accuracy, boundary condition implementation, mesh distribution and wing tip treatment. For a properly constructed (ie consistent) method these inaccuracies must vanish in the limit of an infinite number of mesh cells. For subsonic flow potential methods can satisfy this requirement but Euler methods must capture the vortex sheet and this can be difficult thus producing problems near the trailing edge and so affecting lift. Euler methods are also susceptable to spurious entropy production. In transonic flow with non-conservative potential methods there is no quarantee of convergence towards a unique solution in the limit of vanishing mesh size. Experience has shown, however, that non-conservative potential methods produce weaker shocks further upstream resulting in lower lift.

With an infinite mesh extent the mapping onto computational space should take proper care of the asymptotic flow field solution. With a finite mesh extent the far field boundary condition is an approximation for a finite number of mesh cells but improves as the computational domain gets larger.

Numerical deficiencies occur in a method whenever, in the practical case of a finite number of mesh cells, differences in the details of the discretisation heavily influence the quality of the solution as compared to the solution in the limit of an infinite number of mesh cells. In particular the mesh distribution can have such influence, notably if the mesh stretches too fast towards the far field boundary. Another difficult factor can be the treatment of the wing tip in the case of O-H, C-H, or H-H topology meshes, where the mesh is generally not boundary conforming to the wing tip. In such cases, the mesh locally degenerates in the limit of zero spacing between spanwise gridplanes.

3.3 Conclusions

Assuming all methods are properly constructed, the above discussion indicates the following conclusions, provided that the mesh extent used is large enough (automatically satisfied for DFVLRFL and ARA), and the number of mesh cells is sufficient.

1. Except for the AS-method, where the O-H topology mesh is boundary conforming to the wing tip, all methods employ a O-H, C-H or H-H topology mesh implying local mesh degeneration in the limit of zero spacing between spanwise gridplanes. Hence, discrepancies between the pressure distributions of all methods close to the wing tip should not be given too much attention.

2. In the subsonic case, all potential methods used can be expected to produce almost the same pressure distribution on the wing, except close to the wing tip. The (small) differences between

the methods can be attributed to differences in the implementation of the Kutta condition. Note in particular, that the flow in the vicinity of the trailing edge is generally not in agreement with the (subsonic) Mangler-Smith criterion; this consequently affects the spanwise lift distribution.

3. For the transonic case conclusion 2 is valid for conservative methods but not for non-conservative methods.

4. In the transonic case, non-conservative potential methods can be expected to produce lower lift than conservative potential methods.

5. Both in the subsonic case and in the transonic case, all Euler methods used can be expected to produce almost the same pressure distribution on the wing, except close to the wing tip. The (small) differences between the methods can (probably) be attributed to differences in the quality of vortex sheet capture in the immediate vicinity of the trailing edge and to differences in spurious entropy production. Because the (subsonic) Mangler-Smith criterion and its transonic generalisation is formally modelled, the above mentioned differences can have their effect on the spanwise lift distribution.

6. In the subsonic case, potential methods and Euler methods cannot be expected to produce the same spanwise lift distribution (Kutta condition, Mangler-Smith criterion).

7. In the transonic case, conservative potential methods can be expected to produce higher lift than Euler methods.

The above conclusions in fact pertain to the practical limit of an infinite number of mesh cells and an infinite mesh extent. They are therefore strongly based on modelling differences and on those numerical differences which have a direct effect on the modelling differences (notably vortex sheet capture near the trailing edge and spurious entropy production in case of Euler methods, and type of artificial viscosity in case of non-conservative potential methods). However, when differences between methods are apparently larger than can be expected on the basis of these conclusions, this must be caused either by numerical inaccuracies (due to an insufficient mesh density or a too small mesh extent), or a form of numerical deficiency. The most likely causes are then lack of freestream consistency, an improper mesh distribution (notably a too fast stretching towards the far field boundary), a too small mesh extent, or even combinations of these.

4 RESULTS

Although there were only two flow conditions the investigation into varying various parameters produced a large amount of data, overall well over 100 calculations were performed. The list of 'selected solutions' is given in table 4 and this paper is primarily limited to those. In particular it is not possible to cover the detailed discussions of the Action Group and only a selection of the results together with the conclusions is presented. The F4 wing planform is shown in figure 1.

4.1 Subsonic Case

The flow condition considered was $M_\infty = 0.3$, $\alpha = 0.84$. Figure 2 shows plots of the C_L convergence histories of all methods which are all acceptably converged. It is interesting to note the wide variation in the number of iterations of the various methods. The general tendency is that more recently developed codes are more efficient, e.g. NLR and DORNIER.

Figure 3 shows the global lift and drag coefficients. These tend to increase when going from potential non-conservative methods to potential conservative methods, and subsequently to Euler methods; this behaviour reflects in the global pressure drag coefficient as indeed it should. The average discrepancy between the global lift coefficients obtained by the potential non-conservative and conservative methods used is surprisingly large. No significance can be attributed to the average difference in global lift coefficient as obtained by the potential and Euler methods used since they employ different trailing edge treatments.

The investigation of effect of mesh density was not conclusive due probably to the general inability to use sufficient mesh cells on a mesh of sufficiently large extent. However it appeared that for a given mesh extent, the conservative methods used (potential as well as Euler) are less sensitive to variations in the mesh density than the non-conservative potential methods; the probable cause is mass-leakage with the non-conservative potential methods. This implies that potential non-conservative methods require in principle more mesh cells than potential conservative methods. Extrapolation of C_L to an infinite number of mesh cells reduces the variation in the various groups and the difference between the non-conservative and conservative methods is reduced on average as shown in figure 4. However the potential non-conservative C_L values are still significantly lower than the potential conservative C_L values.

Figure 5 shows the spanwise lift distribution. In each of the three classes of methods used, the mutual agreement between the spanwise lift distributions obtained is acceptable on the inner 80% of the span; however, the average discrepancies between the spanwise lift distributions as obtained by each class of methods are substantial; these discrepancies are smallest inboard of the kink section, possibly because there the direction in which the trailing vortices leave the trailing edge is best in agreement with the assumption made by all the potential methods used; differences in spanwise lift distributions on the outer 20% span as obtained by all methods, should be disregarded in drawing conclusions. However note the final comparison in figure 5 which shows the effect of a H-O mesh due to Radespiel (Ref.17) on the loading near the tip. Thus the overestimation of the lift in the tip region as observed for the Euler methods used seems to be caused by the usage of C-H topology meshes which inadequately model the wing tip with respect to vortex sheet roll-up.

In retrospect the investigation into the effect of mesh extent was not sufficiently controlled so that no conclusions could be drawn. However this does illustrate the difficulties of being able to use enough mesh cells with computing constraints. Figure 6 shows the pressure distributions at three spanwise stations; root, kink and tip: η=0.067, η=0.324, η=0.821 (see figure 1). Though the present investigation has not led to the ultimate subsonic solution for potential and Euler flow, it can be said that all methods give qualitatively the same pressure distribution in a fairly narrow band, and as such prove their engineering value in predicting relative changes in response to changes in wing geometry. Note that since this exercise the AS method has been changed and the trailing edge problem removed.

4.2 Transonic Case

The chosen condition was M_∞ = 0.75, α = 0.84°. Figure 7 shows plots of the C_L convergence histories. Although most are acceptably converged ONERAFD, ARACONS and AS are questionable and this should be taken into consideration in the following discussion. The number of iterations is in general higher than that required for the subsonic case as would be expected. Since for flows with shock waves the three classes of method are expected to produce significantly different results they must be considered separately. Figure 8 shows the global lift and drag coefficients and figure 9 the same extrapolated to a infinite number of grid points. Figure 10 shows the spanwise lift distributions, and figures 11 to 14 the pressure distributions.

For the non conservative potential methods the fact that the DFVLRFL pressures have a shock as much as 10% chord aft of those of the other methods is reflected in the spanwise lift distribution and overall C_L. This discrepancy probably illustrates the problems of the non-conservative methods in not conserving mass and momentum across the shock. The other major difference in the DFVLRFL method is the pressures near the trailing edge due to a relatively coarse mesh in that region. Further calculations on a refined mesh improved the agreement near the trailing edge but had little effect on the shock strength and location. A more recent ONERAFD calculation using fewer mesh points (the same number as for the subsonic case) produced a result of acceptable convergence. This gave an C_L = 0.851, ie closer to ARA, with no significant change in pressure distribution.

The agreement between the conservative full potential methods is disappointing but it should be noted that this class constitutes the broadest of those under study not only in the number of contributers but also with respect to the range of numerical techniques and solution algorithms. Also only two methods (NLR, ONERAFE) were fully converged and the overall C_L extrapolated to an infinite number of mesh cells for these two methods are closer. The prime observation is that the results fall into two sets for both spanwise lift and pressure distribution (NLR,AS and ONERAFE, ARACONS). The only feature that would place the methods into these two sets is a different implementation of the Kutta condition; NLR and AS maintain continuity of normal mass flow across the vortex sheet rather than continuity of normal velocity. All other features are contradictory. However a more recent ONERAFE calculation with greater extent in the y, z directions (with smoother stretching) and more points normal to the wing produced a result with the shock wave moved downstream nearer to NLR and AS.

The Euler methods all derive from the cell centred finite volume scheme due to Jameson et al, differences between the flow code are outlined. Hence, any differences in the results can be expected to be attributable to detailed differences in the implementation of the method or to differences in the mesh systems used. The mesh densities and extents used by the Euler contributors are to be found in table 4. BAE used an algebraic grid generator based on the sheared parabolic co-ordinate transformation due to Jameson and the resulting mesh has rather large cells in the vicinity of the trailing edge and consequently poor resolution of the flow field in that region.
DORNIER used very fine meshes generated by solving a set of elliptic partial differential equations to define the spatial grid. Careful use of the mesh control parameters results in a smooth mesh with a near-constant cell height normal to the surface. The DFVLREU meshes were derived from those of DORNIER by removing every other mesh surface in the normal and spanwise directions.
The further aft shock and the corresponding increase in spanwise lift of DORNIER is presumably due to the finer mesh. The change in wing tip loading produced by the H-O mesh is similar to the subsonic case but the difference betweenb DORNIER and the other methods must be due to difference of detail in the implementation of the flow algorithm. As with the other clauses of methods extrapolating to an infinite number of mesh cells brings the overall coefficients closer together. Finally a worrying feature of all Euler results is the generation of spurious entropy.

5 CONCLUSIONS

The main theme that comes out of this exercise is that performing controlled numerical experiments for three dimensional flows is difficult. Most methods still require large amounts of computer time and even though the exercise was limited to two flow conditions, the number of options was still large. Also the majority of the methods have been developed independently with different mesh topologies and changes in mesh size and mesh extent are effected in different ways with different codes. More particularly, significant development times are required for 3-D codes, even for wing-alone, and it is not feasible to define specific meshes to combine with each individual's flow solver as it is for exercises in two dimensions. Moreover the intention of the exercise was to evaluate existing codes which were being, or were about to be, used in routine aerodynamic analysis and design exercises. Finally there is, in general, no such thing as a final code or method and most of the codes contributing to this comparison were and are, evolving so that in many cases we have a 'snapshot' of an establishment's capability at a given time.

However, despite these problems a number of clear conclusions can be drawn:

1. Though the present investigation has not led to the ultimate subsonic solutions using potential and Euler flow models, it can be said that all methods give qualitatively the same pressure distribution in a fairly narrow band, and as such prove their engineering value in predicting

relative changes in response to changes in wing geometry. However, when absolute values for lift and drag are required, more effort is required in carefully balancing the mesh extent, the mesh density distribution, the number of mesh cells, and the convergence.

2. Wing tip treatment is important and appears inadequate in many codes. In particular the overestimation of the lift in the tip region, as observed for the Euler methods used, seems to be caused by the usage of C-H topology meshes which inadequately model the wing tip with respect to vortex sheet roll-up.

3. For a given mesh extent, the conservative methods used (potential as well as Euler) are less sensitive to variations in the mesh density than the non-conservative potential methods. The probable cause is mass-leakage with the non-conservative potential methods; this implies that potential non-conservative methods require in principle more mesh cells than potential conservative methods.

4. For the transonic case the variation of shock position within each class is disappointing. Although this is perhaps not unexpected for the non-conservative potential codes with no mass conservation, better agreement between the conservative potential codes had been expected. Although the agreement was better for the Euler codes, it was still slightly disappointing considering that all codes are based on the same original method.

5. Generally, there is a tendency to use too few mesh points and perhaps not consider the position of the far field boundary sufficiently. Whilst there is always the problem with three dimensional calculations of computer time and memory limitations, more attention to detail in these areas is recommended.

6. Despite the qualifications above, the potential results show a significant improvement on those obtained during the AD(AG01) exercise. The conservative potential methods will continue to be used particularly for transport aircraft applications, including wing design where inverse methods can play an important role. However, the Euler results are sufficiently encouraging to indicate that most future work will be based on the Euler equations leading eventually to full Navier-Stokes solutions.

6 REFERENCES

1. J.Th.Van der Kolk, J.W.Slooff. A Comparison of Computational and Experimental Results for the Transonic Flow around the DFVLR-F4 Wing-Body Configuration. NLR TR 83127. GARTEUR/TP-012. October 1982.

2. C.R.Forsey, M.P.Carr. The Calculation of transonic Flow over Three-Dimensional Swept Wings using the Exact Potential Equation. DGLR Symposium 'Transonic Configurations' Bad Harzburg, June 1978.

3. A.Jameson, D.A.Caughey. Numerical Calculation of the Transonic Flow past a Swept Wing. ERDA Report COO-3077-140, New York Univ., 1987.

4. N.Kroll. Mathematische Beschreibung Konvergenzbeschleunigung und Vektorisierung des Programms FLO222 zur Berechnung transsonischer Stromungen um Tragflügel endicher Spannweite. DFVLR-IB 1983.

5. J.J.Chattot, C.Coulombeix, C.Tome. Calculs d'Ecoulements Transsoniques autour d'Ailes. La Recherche Aerospatiale n° 1978-4, pp. 143-159,1978. (English translation ESA - TT - 561).

6. J. Van der Vooren, A.J.Van der Wees, J.H.Meelker. MATRICS, Transonic Potential Flow Calculations about Transport Aircraft. AGARD Conference 'Applications of Computational Fluid Dynamics in Aeronautics', Aix-en-Provence, April 1986.

7. A.J. Van Der Wees. FAS Multigrid employing ILU/SIP Smoothing: a Robust Fast Solver for 3D Transonic Potential Flow. 2nd European Conference on Multigrid Methods, Cologne, October 1985.

8. Y.Vigneron, T.Lejal. Calculation of Transonic Flow around an Aircraft Configuration with Motorized Nacelle. ICAS Paper Number 84-2.10.2, Toulouse, September 1984.

9. M. Bredif. Finite Element Calculation of Potential Flow around Wings. 9th International Congress on Numerical Methods in Fluid Dynamics, Saclay, June 1984

10. R.Radespiel, N.Kroll. Progress in the Development of an Efficient Finite Volume Code for the Three-Dimensional Euler Equations. DFVLR-FB 85-31, 1985.

11. S.Leicher. Numerical Simulation of Internal and External Inviscid and Viscous 3-D Flow Fields. AGARD 58th Meeting on Applications of Computational Fluid Dynamics in Aeronautics, 7-10 April 1986. Aix-En-Provence, France.

12. R.H.Doe, T.W.Brown, A.Pagano. The Development of practical Euler Methods for Aerodynamic Design. 15th Congress of the International Council of the Aeronautical Sciences, London, September 1986. ICAS-86-1.4.2 1986.

13. K.W.Mangler, J.H.B. Smith. Behaviour of the Vortex Sheet at the Trailing Edge of a Lifting Wing. RAE Technical Report 69049, March 1969.

14. E.B.Klunker. Contribution to Methods for Calculating the Flow about Thin Lifting Wings at Transonic Speeds-Analytic Expressions for the Far Field. NASA TN D-6530, November 1971.

15. H.A.Sytsma, B.L.Hewitt, P.E.Rubbert. A Comparison of Panel Methods for Subsonic Flow Computation. AGARDograph No.241, February 1979.

16. A.Jameson, W.Schmidt, E.Turkel, Numerical Solutions of the Euler equations by Finite Volume Methods using Runge-Kutta Time-Stepping Schemes. AIAA-81-1259. 1981

17 R.Radespiel. Efficient Solution of Three-Dimensional Euler Equations Using Embedded Grids. ICAS-86-1.3.3 1986.

7 ACKNOWLEDGEMENTS

The report of GARTEUR AD(AG05) from which this paper is derived is the result of significant contributions of all members of the Action Group together with a number of additional participants. Those involved were Mr.J.Bousquet Aerospatiale, Mr.M.Bredif MATRA (formerly with ONERA), Mr.D.Destarac ONERA, Mr.R.H.Doe British Aerospace, Mr.C.R.Forsey ARA, Mr.S.Leicher Dornier, Dr.R.Radespiel DFVLR, Mr.J.W.Sloof NLR, Mr. J.van der Vooren NLR, Mr.Y.Vigneron Aerospatiale, Mr.G.Wichmann DFVLR. I am grateful to them all.

ARA	ARA potential non-conservative
DFVLRFL	DFVLR potential non-conservative
ONERAFD	ONERA finite difference potential non-conservative
ARACONS	ARA potential, conservative
NLR	NLR potential conservative (MATRICS)
AS	AEROSPATIALE potential conservative
ONERAFE	ONERA finite element potential conservative
DFVLREU	DFVLR Euler
DORNIER	DORNIER Euler
BAE	BRITISH AEROSPACE Euler

TABLE 1 METHODS NOMENCLATURE

METHOD	MESH TOPOLOGY	MESH EXTENT	GENERATION METHOD	DISCRE-TISATION	ARTIFICIAL VISCOSITY	CONSERVATION	ITERATIVE SCHEME	MESH REFINEMENT	REFERENCES
ARA	O-H	Infinite	Conformal transformation	FD	Rotated differences	NC	SLOR	3 levels	2
DFVLRFL	C-H	Infinite	Conformal transformation + shearing	FD	Rotated differences	NC	SLOR + Richardson extra-polation	3 levels	3,4
ONERAFD	C-H	Finite	Conformal transformation + shearing	FD	Rotated differences	NC	SLOR	3 levels	5
ARACONS	O-H	Infinite	Conformal transformation	FD	Rotated differences	PC (run as FC)	SLOR	3 levels	2
NLR	C-H	Finite	Conformal transformation + shearing	FV	Flux splitting	PC	FAS multi grid + ILU/SIP smoothing	3 levels	6,7
AS	O-H (O except) (near t.e)	Finite	Elliptic p.d.e.	FE	Retarded density	PC	Fixed point iteration + non-linear conjugate gradient	1 level	8
ONERAFE	H-H	Finite	Algebraic (transfinite) interpolation)	FE	Retarded density	PC	Fixed point iteration + conjugate gradient pre-conditioned by incomplete Cholesky factorisation (ICCG)	1 level	9

TABLE 2 DETAILS OF POTENTIAL METHODS

METHOD	MESH TOPOLOGY	MESH EXTENT	GENERATION METHOD	DISCRE-TISATION	DISSIPATION	TIME INTEGRATION	CONVERGENCE ACCELERATION	MESH REFINEMENT	REFERENCES
DFLRRU	C-H	Finite	Elliptic p.d.e.	FV	2nd + 4th order differences	5 stage Runge-Kutta	Local time stepping,+ enthalpy damping + residual smoothing	3 levels	10
DORNIER	C-H	Finite	Elliptic p.d.e.	FV	2nd + 4th order differences	3 stage Runge-Kutta	Local time stepping + enthalpy damping + residual smoothing + multigrid	3 levels	11
BAE	C-H	Finite	Conformal transfora-ation + shearing	FV	2nd + 4th order differences	4 stage Runge-Kutta	Local time stepping + enthalpy damping	1 level	12

TABLE 3 DETAILS OF EULER METHODS

METHOD	CASE	GRID	EXTENT (multiple of semi-span)
ARA	S	161x37x21	
ARA	T	161x37x41	
DFVLRFL	S	225x41x41	
DFVLRFL	T	225x41x41	
ONERAFD	S	290x34x44	10x4x18
ONERAFD	T	338x47x50	10x4x18
ARACONS	T	161x37x21	
NLR	S	176x32x32	4.9x3.2x9.9
NLR	T	176x56x32	12.3x5x24.5
AS	S	49695	6x8x6
AS	T	49695	6x8x6
ONERAFE	S	274x33x21	10x4x8
ONERAFE	T	274x33x21	10x4x8
DFVLRRU	S	225x41x33	3x2.5x3
DFVLRRU	T	225x41x33	3x2.5x3
DORNIER	S	225x81x66	3x2.5x3
DORNIER	T	225x81x66	3x2.5x3
BAE	S	193x41x41	4.1x3.6x7.7
BAE	T	193x41x41	4.1x3.6x7.7

TABLE 4 SELECTED SOLUTIONS

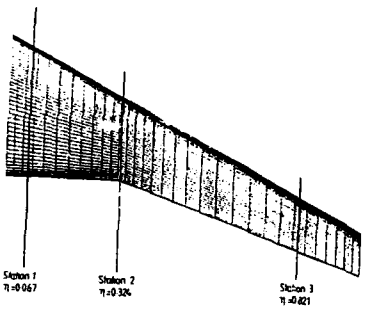


Fig. 1 DFVLR F4 Wing Planform

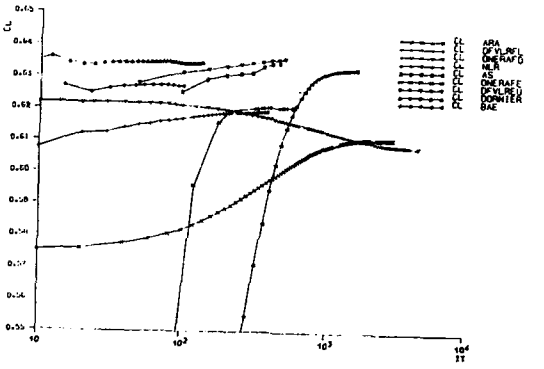


Fig. 2 Convergence of CL(it) Transonic case

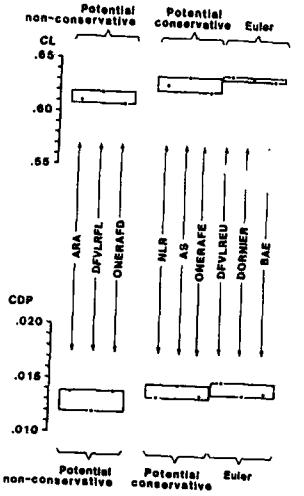


Fig. 3 Global coefficients Subsonic case

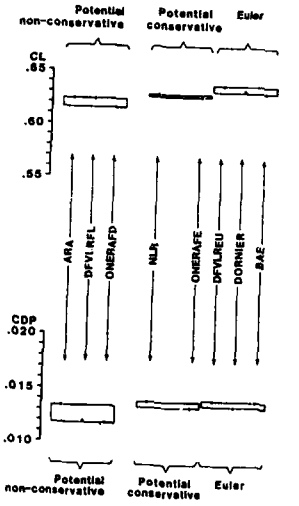


Fig. 4 Global coefficients (extrapolated to an infinite number of grid points) Subsonic case

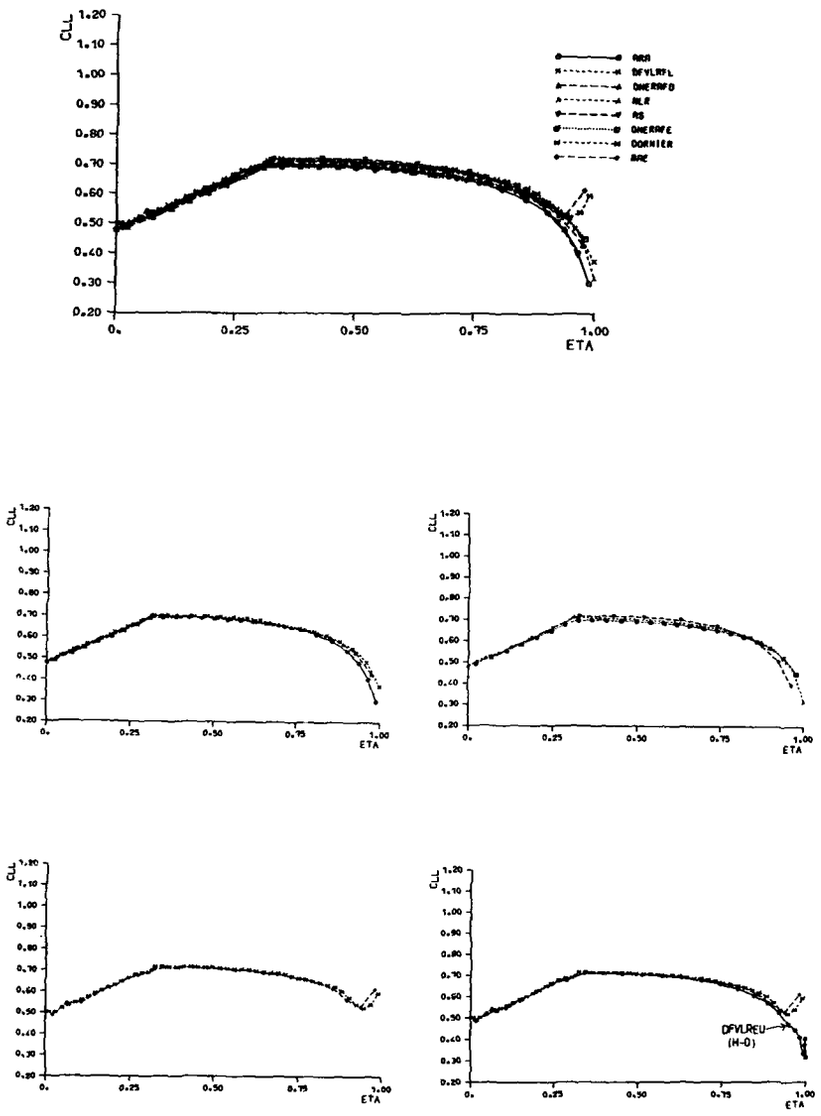


Fig. 5 Local lift coefficients – Subsonic case

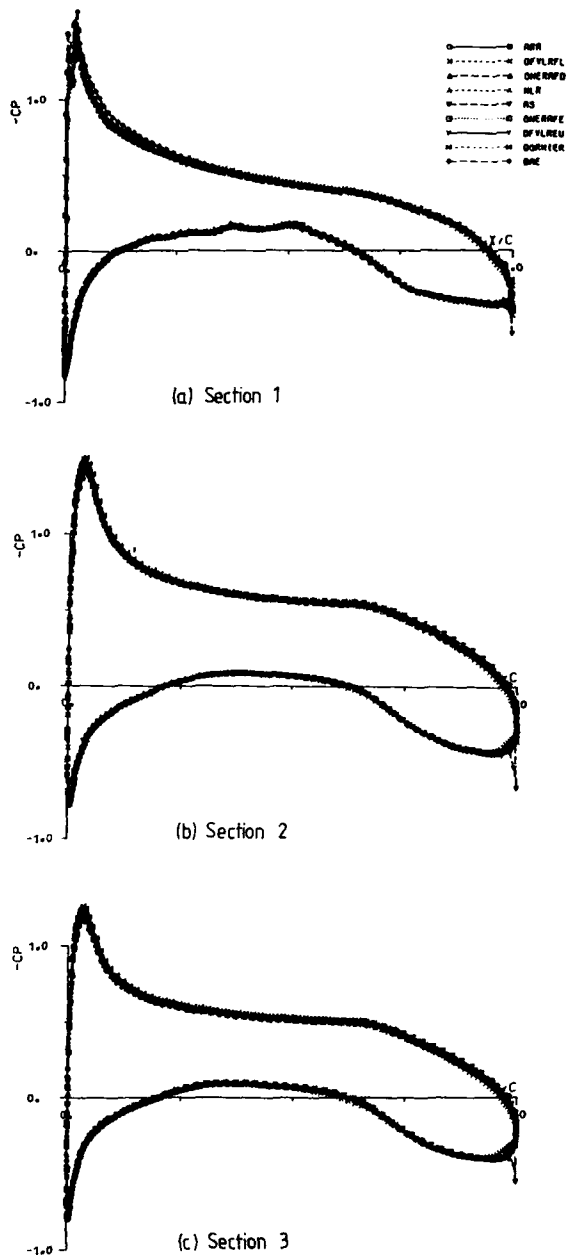


Fig. 6 Pressure distributions: comparison of all methods
Subsonic case

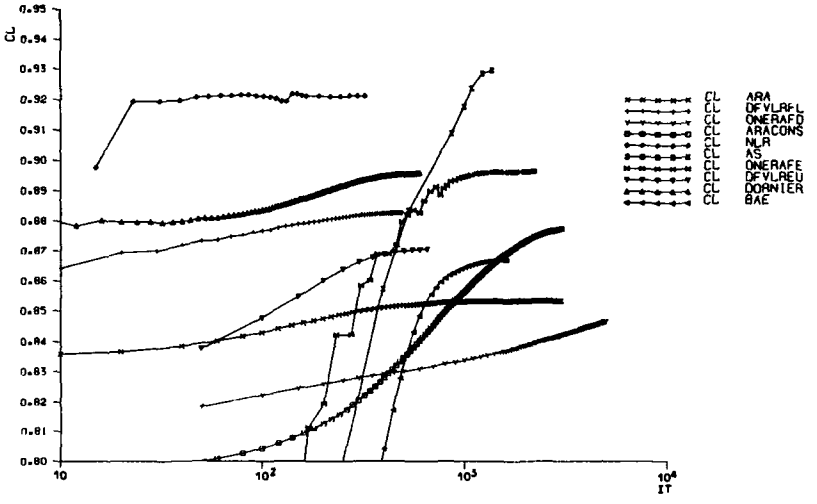


Fig. 7 Convergence of CL(it)
Transonic case

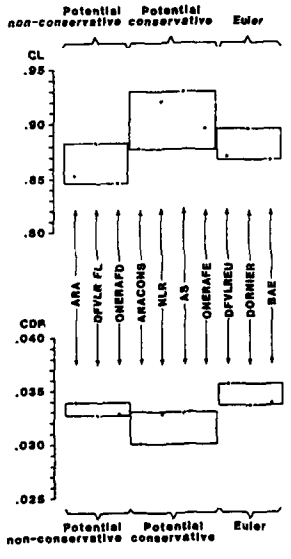


Fig. 8 Global coefficients
Transonic case

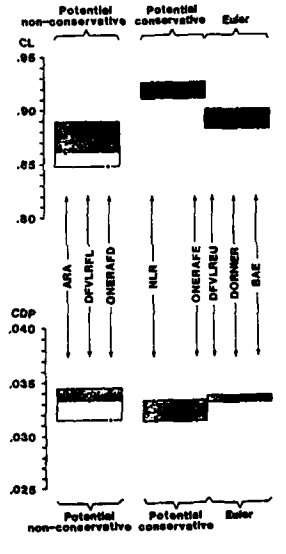


Fig. 9 Global coefficients
(extrapolated to an infinite number of grid points)
Transonic case

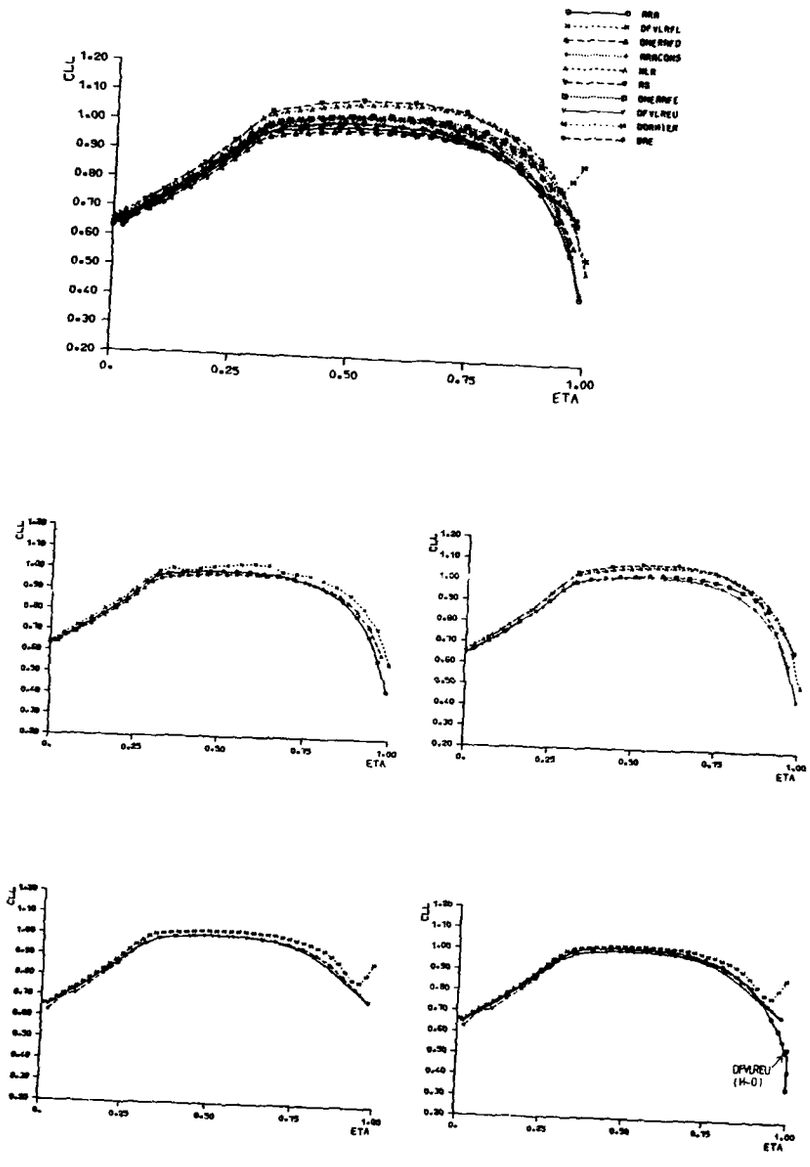


Fig. 10 Local lift coefficients – Transonic case

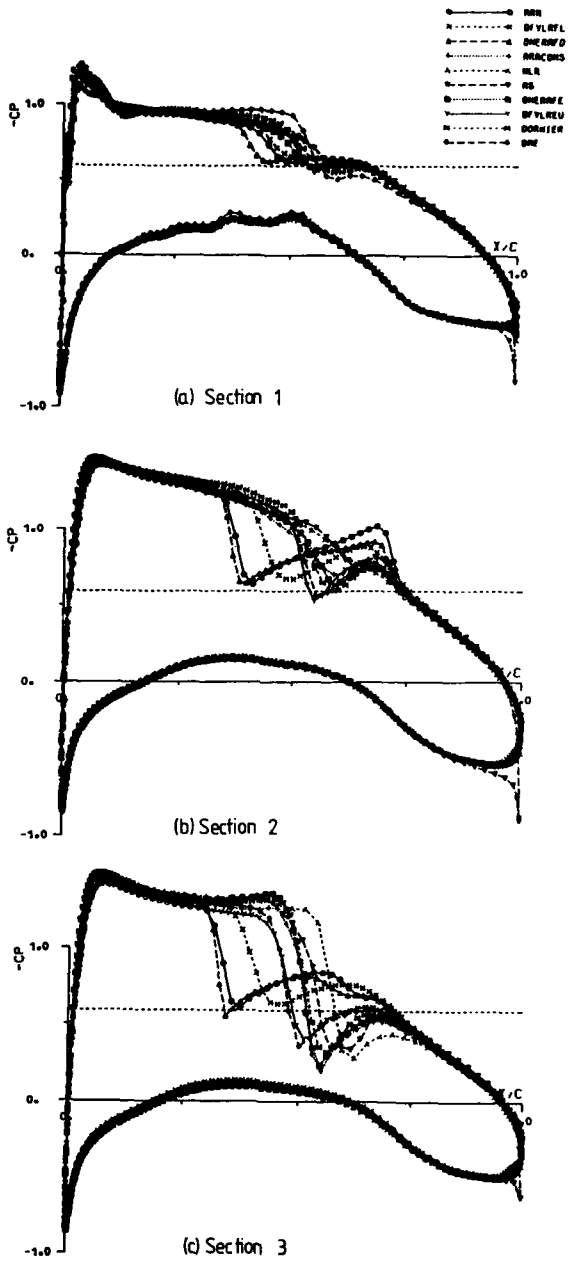


Fig.11 Pressure distributions: comparison of all methods
Transonic case

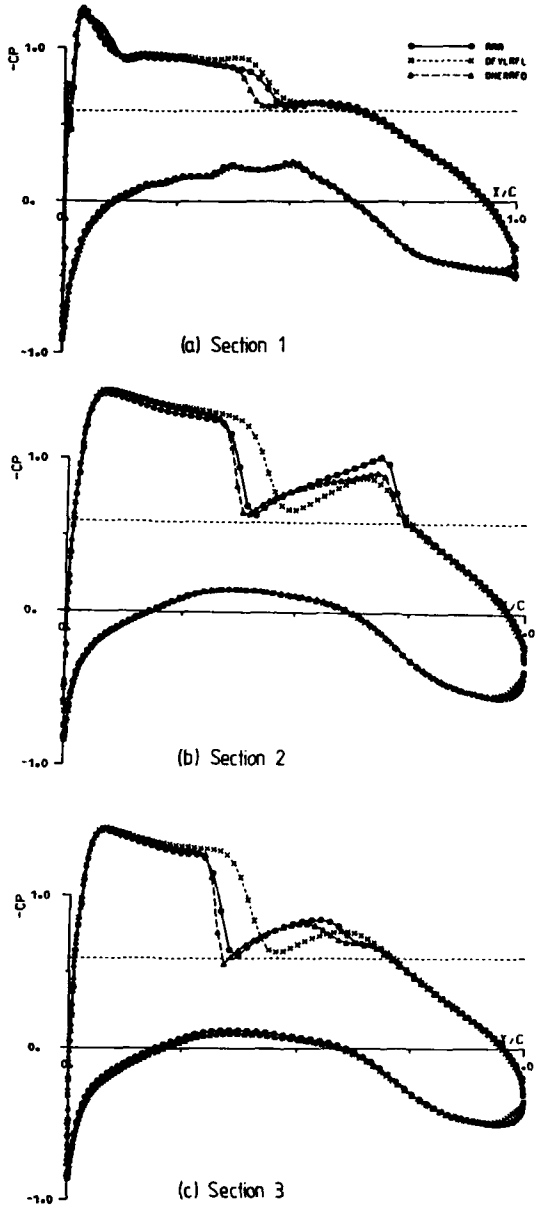


Fig. 12 Pressure distributions:
comparison of Potential Non-Conservative methods
Transonic case

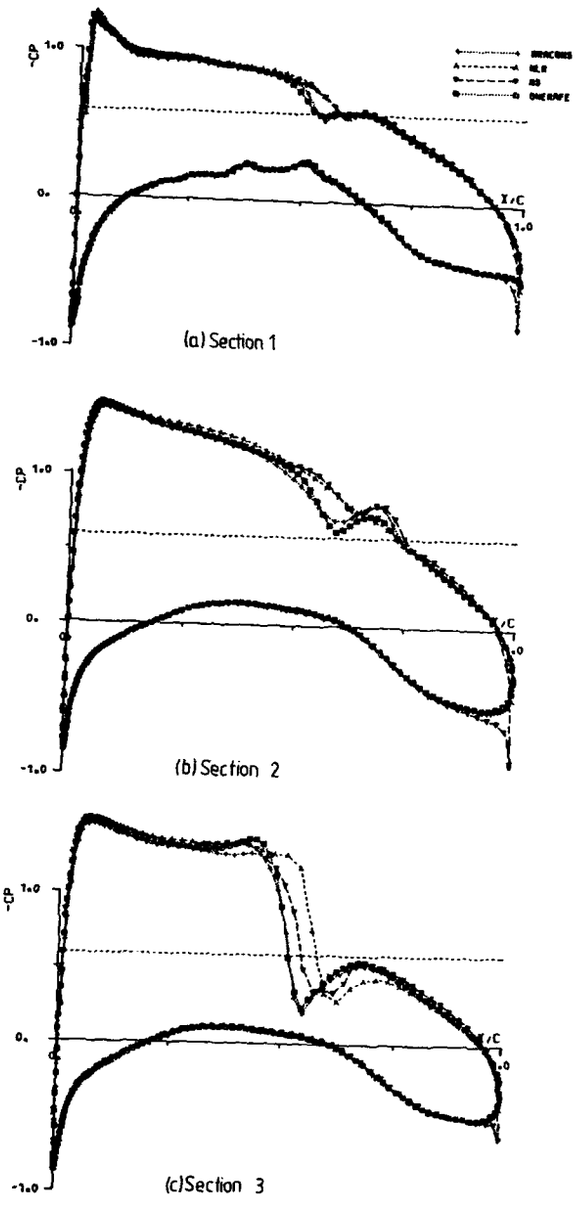
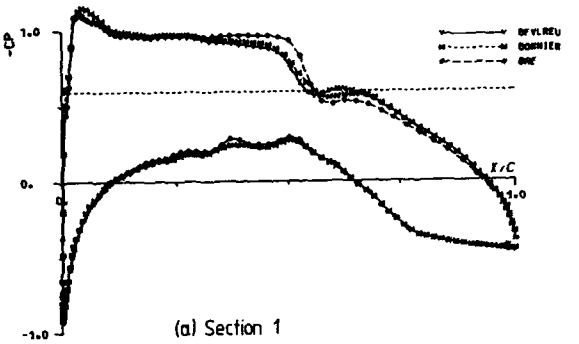
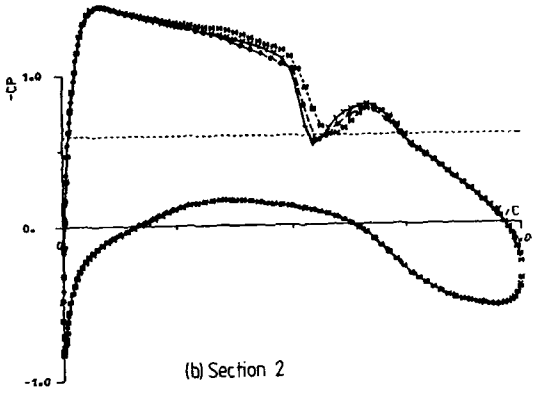


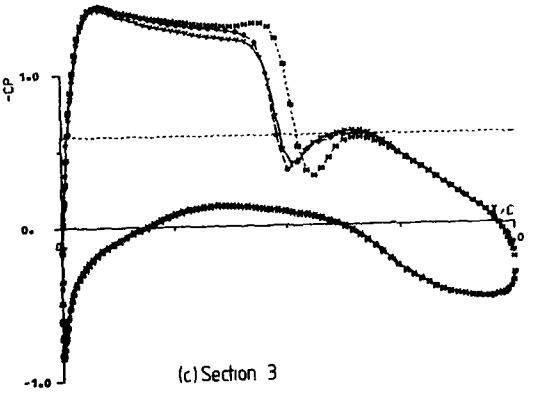
Fig. 13 Pressure distributions:
Comparison of Potential Conservative methods
Transonic case



(a) Section 1



(b) Section 2



(c) Section 3

Fig. 14 Pressure distributions:
Comparison of Euler methods
Transonic case

CFD applications in design and analysis of the Fokker 50 and Fokker 100.

N. Voogt
W.J.A. Mol
J. Stout
D.F. Volkers

Fokker Aircraft B.V.
Aerodynamics and Aeroelasticity Dept.
P.O. Box 7600
1117 ZJ Schiphol
Holland

SUMMARY

Aerodynamic computational codes have been used and validated extensively during the aerodynamic development phases of the Fokker 50 and Fokker 100 aircraft projects. Validations were made against windtunnel tests as well as flight measurements. A description is given of the methods on which the codes are based and applications are discussed in areas of intake aerodynamics, low-speed high-lift flow and transonic flow.

1. INTRODUCTION

Computational aerodynamics plays an increasingly important role in aerodynamic design and analytical support of windtunnel and flight testing. Two major types of application can be distinguished. The first one is the aerodynamic analysis of given geometric shapes - using direct methods - with applications ranging from prediction of overall aerodynamic coefficients for simplified configurations to elaborate computation of complex flow fields around realistic configurations. The second type of application lies in design and optimization where aerodynamic flow codes are used to compute geometric shapes either for required flow fields - through inverse methods - or for required properties by means of optimization methods. The combination of both types of application can be fully exploited by using them complementary to windtunnel testing. In this way design cycle times can be reduced as well as possible development risks.

Two equally important factors are essential for optimal application of CFD codes in a project engineering environment: a sufficient confidence level in the codes and the availability of a hardware/software infrastructure in which they are embedded. The latter should ensure routine applications with short turn around times and requires adequate pre- and postprocessing facilities. The level of confidence has to be accumulated over many applications and validations against experiments.

During the development phases of the Fokker 50 and Fokker 100 projects many aerodynamic codes have been applied for configuration design and off-design analysis and comparisons with windtunnel experiments could be made. Flight measurements leading to type certification of both aircraft in 1987 provided unique opportunities to validate some of the codes at full-scale Reynolds numbers.

After discussing the codes which were used, the paper describes a number of test-theory comparisons in application areas such as intake aerodynamics, low-speed high-lift and transonic aerodynamics.

2. AERODYNAMIC ANALYSIS CODES USED

In the present paper only analysis applications will be described i.e. codes which compute flow fields about given configurations.
Within the scope of the paper the codes will be divided into three categories:

- Those for low-speed, high-lift flow cases about single or multi-component airfoils.
- Potential flow solvers for subcritical flow cases about complex geometric configurations.
- Potential flow solvers for transonic flow cases about wing-body combinations.

In the first category methods for inviscid flow computation are coupled with boundary layer methods. Usually the coupling is such that a weak interaction is assumed between inviscid potential flow and boundary layer. In such computations a procedure is followed in which the inviscid velocity distribution and boundary layer displacement thickness are computed in an iterative sequence. This procedure however is limited to attached flow because a direct computation is used for the boundary layer in which pressure is prescribed and this computation breaks down when flow separation occurs.
For computation of viscous flow near maximum lift about single airfoils a region of separated flow has to be incorporated and a different approach is required to account for strong viscous-inviscid interaction such that a simultaneous solution of inviscid flow and boundary layer is obtained. In the present paper results will be presented which are based on such an approach. Herein an inviscid low frequency transonic small perturbation method is coupled with Green's lag-entrainment method for steady turbulent boundary layers (Ref. 1). It appears that the code can be successfully applied to compute maximum lift for single airfoils at subsonic flow conditions.

For multi-component airfoils flow computation near maximum lift also requires a strong interaction coupling procedure. In this case the interaction coupling is between the potential flow computed by means of an incompressible panel method and the wake of the main component which is subjected to an adverse pressure gradient created by a downstream component such as a deflected flap (Ref. 2).
The amplification of the displacement thickness of the wake resulting from this off-the-surface pressure recovery may lead to a substantial interaction between wake and inviscid flow. For computations near maximum lift it is essential to take this interaction into account.

The second category is the domain of the panel methods (Ref. 3).
These surface singularity methods have been in development since the mid sixties and are extensively and routinely applied to solve subcritical flow problems. Because only a surface discretization is required very complex configurations can be modeled on which the panel density is adjustable to the desired accuracy. Basically panel methods are restricted to linear potential flow and subsonic compressibility effects are taken into account by modifying the incompressible solution.
At present three types of panel method are being used at Fokker, each of them in different areas of application.

* A non-planar lifting surface code is used primarily for design studies where only limited geometric information is available or required (fig. 1a). The effects of variations in geometric parameters such as planform shape, flap span and flap deflection, etc. can be investigated in terms of overall aerodynamic coefficients.

* The NLR panel method is used for more detailed analysis of aerodynamic interference and therefore requires a more detailed geometric specification (fig. 1b). The method can be described as a first order singularity method with Neumann boundary conditions. Special features are the inclusion of semi-empirical compressibility terms and a fast iterative method of solution. As a result of this the CPU-time for a realistic configuration with 1500 panels on one half of a symmetric configuration is only 7 minutes on a VAX 8650. The method can be considered as a general purpose subsonic aerodynamic "workhorse" and has been used as such at Fokker over the last 12 years.

* The third panel method is a first version of a higher order singularity method in development at NLR with Dirichlet boundary conditions. It was recently evaluated specifically for duct flow aerodynamics. The method eliminates the failure of the older panel methods to solve duct flow problems, which are connected to leakage resulting from numerical errors created by flat source panels inside a duct. In terms of input generation the higher order singularity method is the most time consuming as it requires a more regular panel distribution (fig. 1c).

Finally the last category of analysis codes is based on methods which analyse three-dimensional transonic flow fields about wing-fuselage configurations. Two different codes are in use at Fokker, both solving the transonic full potential equations.
The basis of the first one is the well-known and widely used FLO-22 wing code of Jameson and Caughey (*Ref.* 4). It has been modified and extended to simulate fuselage cross-flow effects. For this simulation the NLR panel method is used to compute a normal velocity distribution in a plane near the side of the body. This is specified as a boundary condition to FLO-22. The code *XFLO-22* (Ref. 5) is embedded in a pre- and postprocessing system together with a 3-D laminar/turbulent boundary layer code BOLA (Ref. 6) for drag evaluation and prediction of buffet onset. Its main operational advantage is the ease of input generation as well as the very modest computation time, which amounts to 10 CPU minutes on an IBM 3090 for a standard computational grid of the order of 150.000 grid points.

The other code is a first version of MATRICS, a transonic flow solver in development at NLR on the basis of full potential theory and the finite volume concept (Ref. 7). The first version is capable of handling wing-fuselage configurations but eventually its application will be extended to flows about fuselage-wing-nacelle configurations also including boundary layer interaction.

3. APPLICATION AREAS

Most of the aerodynamic codes mentioned above have been applied extensively during the development phases of the new Fokker 50 and Fokker 100 projects.
The Fokker 50 (figure 2) is a twin engined aircraft for short to medium range operations carrying 50 passengers. It is powered by two turboprop engines each driving a six-bladed propeller.
Much of the aerodynamic development work was connected with the design of the new engine nacelle and intake ducts for engine and oil cooler. Figure 3 illustrates the very complex geometry of the external nacelle surface and the even more complex internal duct. In order to protect the engine from foreign object damage the intake duct is bifurcated; the inertia of solid objects carries them through a bypass duct while the main airflow follows the engine inlet duct which is wrapped around the propeller shaft. In this application panel methods were used to analyse external and internal flow fields and to predict ice accretion.

The Fokker 100 (figure 4) is a twin-jet-engined aircraft for short to medium range operations which can carry 107 passengers. Compared with the F28 from which it is derived it has an advanced flight management system, high bypass ratio engines and improved aerodynamics.
The wing was designed by extending and modifying leading and trailing edges as well as the tip area of the F28 wing.
The aerodynamic optimization process quickly converged by combining codes for 2-D transonic design, 3-D transonic analysis and 2-D low-speed, high-lift analysis with windtunnel experiments in an iterative cycle. Panel methods were used to guide the design process of the stubwing-nacelle configuration on the rear fuselage. In the next section test-theory comparisons are described for 2-D low-speed high-lift flow, high-subsonic flow about the rear fuselage and for transonic flow.

In these comparisons also in-flight wing pressure measurements are involved which were made on one of the Fokker 100 prototypes for structural load verification purposes. As shown in figure 5 measuring belts were fixed at 5 spanwise locations. Pressures measured by differential pressure transducers mounted in scanivalves were continuously recorded during flight.
For each specified test condition pressures were measured over a period of 40 seconds. Appropriate pressure distributions were selected on the basis of least variation in angle of attack and Mach number during a measuring cycle. Corrections were made to account for time-lag in the pressure tubes.

4. CODE EVALUATION

The examples used in the evaluation of the various codes cover the following subjects:
For the Fokker 50
- computation of pressures inside the intake duct
- prediction of ice accretion around the oil cooler intake

For the Fokker 100
- prediction of maximum lift for single and multi-component airfoils
- prediction of drag for a multi-component airfoil
- prediction of wing lift distribution at a high-lift condition
- computation of wing pressures at a high-lift condition
- computation of stubwing pressures in high-subsonic flow
- computation of wing pressures in transonic flow
- prediction of buffet-onset boundary

4.1 FOKKER 50 INTAKE DUCTS

The first application is the computation of the pressure distribution inside the complex intake duct which was shown in figure 3. Windtunnel measurements of the pressure distribution at the central cross-section of the duct were used to evaluate a first version of a new panel method which was developed at NLR. Pressures have been measured in the main- and bypass duct at a low Mach number, M = .25. A velocity ratio of 0.8 was simulated at the engine inlet face with the propeller removed. Computations were made for two widely different flow conditions in the bypass duct; in one case a velocity ratio of 1.06 was simulated whereas in the other case the flow was restricted such that the velocity ratio is only 0.09. The configuration is represented by 2100 flat panels of which 1700 inside the duct. A higher order composite source/doublet distribution is used on the surface and the required velocity ratios are specified in the exit plane.
The comparison of computed and measured pressures shown in figure 6 illustrates the capability of the method to handle complicated duct flow cases.

The second application concerns the smaller intake for the oil cooler located on the lower surface of the nacelle. The objective of the computations was to predict droplet impingement and resulting ice accretion. For such a prediction methods for streamline and particle tracing are used which compute required velocity vectors at each integration point of the compu' ' flow field.
Empiricism plays an important role in determining particle motion in (potential) flow fields: it is applied in the particle drag force determined by the Stokes factor and in modeling particle bouncing against a wall. The prediction of droplet impingement around the nacelle and intakes was done by making 2-D computations at the central cross-section. It can be argued that results of such 2-D computations are conservative in comparison with 3-D results because the captured streamtubes can diffuse in more than one direction. The flow solver used in the computations is a panel method in which velocity ratios are prescribed in control planes located in the intake ducts.

The computation was made to simulate a condition with a free-stream velocity of 100 m/sec and velocity ratios for engine and oil cooler of .54 and .1 respectively.
Computed streamlines and droplet trajectories are shown in figure 7 for droplets of $30*10^{-6}$ m diameter. The result indicates that droplets are impinging on the spinner, the inside and outside lip of the engine intake duct and on the leading edge of the oil cooler intake.

Windtunnel experiments in icing conditions confirmed the prediction of ice accretion inside the engine intake duct with spikes growing upstream in the direction of the computed impingement lines (figure 8).
Flight tests confirmed the computational results near the oil cooler intake and showed that spiky accretion occurs around the intake lip outer surface but it leaves the highlight free for air entering the intake (figure 9). The photograph also shows runback ice which results from de-icing at the leading edge of the engine intake duct.

4.2 FOKKER 100: PREDICTION OF LOW-SPEED, HIGH-LIFT FLOW

4.2.1 SINGLE AIRFOILS

Prediction of aerodynamic characteristics at low-speed, high-lift flow conditions has been given much emphasis during the aerodynamic development of the Fokker 100.
The basis is formed by prediction of maximum lift for single airfoils. As explained in section 2 the necessity to take separated flow regions into account for such predictions requires a strong viscous-inviscid interaction approach.
The capability to predict maximum lift at low speed has been evaluated for a code which is based upon such an approach. It was originally developed to compute viscous transonic flow in steady and unsteady motion and can take regions of separated flow into account (Ref. 1). A first evaluation revealed that the code could well be used to predict maximum lift for those cases where trailing edge stall was the limiting mechanism but not for cases with leading edge stall or for thin airfoil stall.

The reason behind this is that the underlying inviscid flow solver is based upon transonic small perturbation theory and therefore fails to predict correct suction peak levels at high angles of attack. In order to be able to compute minimum pressures a full potential flow solver has been included in the computational procedure. It makes use of the computed boundary layer displacement thickness.
At the same time an empirical criterion for leading edge stall has been implemented based on experimental data and comprising minimum pressure, nose radius and Reynolds number.

The computational procedure presently used for the prediction of maximum lift is shown in figure 10. Both the section liftcoefficient and the minimum pressure are computed as functions of angle of attack. Maximum lift is reached either when the minimum pressure exceeds the critical value or when trailing edge stall occurs whichever comes first.
Maximum lift has been predicted for a large number of airfoils including some Fokker 100 sections. Thickness-chord ratios ranged from 9 to 21 percent. A correlation has been made between computed and measured maximum lift values for Mach numbers of the order of M = .2 and Reynolds numbers between $1.5*10^6$ and $12*10^6$. Of all cases nearly 50 percent experienced trailing edge stall. The correlation is shown in figure 11 and illustrates that with the exception of three airfoils the difference between predicted and measured maximum lift is within a margin of 0.1. This relatively small margin provides sufficient engineering accuracy and allows the prediction method to be used in design studies.

4.2.2 MULTI-COMPONENT AIRFOILS

In high-lift flow about multi-component airfoils the turbulent wake originating from the trailing edge of the main component plays an important role. It flows into a region of higher pressure caused by the downstream component. High-lift characteristics of multi-component airfoils are predicted by means of a code which models strong interaction between the turbulent wake and the potential flow (Ref. 2).
The code has the following limitations:

- compressibility effects are neglected
- flow separation is not modeled although its occurrence is predicted
- merging of wake and boundary layer is not modeled

For slatted configurations these limitations may necessitate inclusion of empirical criteria for prediction of maximum lift.
The code has been validated against many experiments and proved to be very valuable in predicting maximum lift.

One example is a double-slotted flap system used on the Fokker 100 which was tested at low Mach number and a Reynolds number of 3 million. Figure 12 shows computed and measured lift as a function of angle of attack. The computation overestimates lift because local separation occurs on the flap. This local separation causes a lift loss which can be estimated by an inviscid potential flow code. In this code free streamlines are computed starting from the predicted separation point and the trailing edge and which contain the separated flow region (figure 12). The lift loss is then estimated from the difference in lift computed for the original configuration and the one which includes the separated flow. When the original results are corrected for the lift loss estimated at each angle of attack the agreement with the measured lift is very much improved. For the lower liftcoefficients the larger difference can be attributed to uncertainties in the location of boundary layer transition.
Although not at the same angle of attack - due to the limitations as mentioned before - maximum lift is very well predicted.

Apart from that the code is also capable of showing details of the physics behind the stall mechanism. In this case as well as in a number of the other evaluated cases the code predicts an abrupt stall which is a result of flow reversal in the wake of the main component. This is illustrated in figure 13 which shows the development of the wake near maximum lift. The wake displacement thickness grows rapidly when maximum lift is approached. The wake can no longer stand the adverse pressure gradient and prevents a further increase of circulation.

The inclusion of the turbulent wake modeling also improves the prediction of viscous drag. The viscous wake is computed sufficiently far downstream - usually 7 chordlengths - and drag is computed from the momentum deficit. A comparison of computed and measured drag as a function of lift is shown in figure 14 for a single slotted high-lift system. From the windtunnel measurements drag was obtained by averaging the data of 4 wake rakes. Maximum deviation from mean values is about 8 drag counts.
The correlation between computed and measured drag is rather good and shows an increasing underprediction of drag to about 30 counts at 90 percent of maximum lift.
At lower liftcoefficients a good comparison can not be made because of uncertainties in transition location. Transition was left free in computation and experiment and could not easily be established. This is clearly illustrated in fig. 14 by the type of pressure distribution on the main component computed at such a condition.

4.2.3 THREE-DIMENSIONAL HIGH-LIFT FLOW

For prediction of overall characteristics in 3-D high-lift conditions a lifting surface code is applied. It requires very simple geometric modeling and the effect of wing thickness is neglected. In cases of highly deflected part-span flap systems on which some flow separation will occur empiricism is required in defining an effective flap deflection angle. Empiricism is also required in modeling of the trailing wake system. It is usually observed that predictions from lifting surface methods compare rather well with experimental data. The reason is that the effects of wing thickness and viscosity, which are both neglected, cancel each other in most cases.

The code used at Fokker has been evaluated for a number of configurations with part-span high-lift devices. A typical example is shown in figure 15 for the Fokker 100 with the flap system 42 degrees deflected. In the computation a deflection of 38 degrees has been used to compute the spanwise liftdistribution. Comparison with the liftdistribution measured in the windtunnel at the same angle of attack illustrates the capability of the method and its value for design studies.

The prediction of a three-dimensional wing pressure distribution in a similar condition is much more complicated. Because in-flight measured wing pressures were available the correlation was investigated between these data and pressures converted from 2-D computations.
A wing section with a double-slotted deflected flap at 52 percent semi-span was scaled up by taking the inverted cosine of the quarter chord sweep angle. For this quasi 2-D section viscous computations were made using the code as described in section 4.2.2. Computed pressures were converted to 3-D flow conditions by the squared cosine of the quarter chord sweep angle. The predicted deformation of the flap system at the proper flight condition was simulated in the computations and the liftcoefficient was closely matched to the lift measured in flight. A comparison between measured and computed pressures in figure 16 shows a remarkable overall agreement and illustrates the good two-dimensionality of the flow.

4.3 FOKKER 100 HIGH-SPEED FLOW

A first application is at the lower end of this flow regime and concerns computation in high-subsonic flow about the rear fuselage. For such computations interference between fuselage, engine nacelle and stubwing as well as the downwash from the wing must be taken into account. For these flow problems panel methods can be applied successfully as long as the flow is subcritical.

The stubwing between fuselage and nacelle has been designed by combining results of 2-D design methods with 3-D panel methods. Figure 17 shows the typical cross-section and computed pressures on upper and lower surface at a Mach number of .72 and 1 degree of incidence. Comparison with measured pressures at the same condition in the windtunnel shows a generally good correlation on the upper surface with a deviation near the trailing edge as a result of viscous effects. In order to obtain a good correlation on the lower surface it was essential to include the windtunnel model support in the computation.
As shown in figure 17 the model support increases the lower surface pressures with $\Delta C_p = 0.1$ whereas the upper surface pressure level remains unchanged.

The second application is the prediction of buffet onset and includes the associated capability of transonic flow codes to predict high-speed off-design conditions.
The transonic wing-body code XFLO-22 (Ref. 5) has been used extensively during the aerodynamic development of the Fokker 100. It is based on a non-conservative finite difference method and body influence is simulated by a panel method. In this version the trailing edge flow is tangent to the lower surface. Many validations have shown that this type of modeling apparently compensates for the absence of viscous effects. When comparing computed results with windtunnel measurements the characters of the pressure distributions usually agree but the computed shock location is further downstream than in the experiment. Such comparisons have indicated th t XFLO22 results could be representative for higher, full-scale Reynolds numbers.

In-flight wing pressure measurements on one of the Fokker 100 prototypes provided the opportunity to verify this assumption. For a number of subsonic, transonic design and off-design conditions comparisons have been made between flight measurement and computation. In all these cases wing deformation resulting from torsion and bending was taken into account. An example of the surprisingly good correlation that has been obtained is shown in figure 18. It concerns a comparison for an off-design condition at M = .78 for wing stations close to the fuselage and at mid semi-span. The result for the inner wing station illustrates that body influence is well represented in the code.
Also shown is a comparison with windtunnel measurements at the same free-stream condition for the same lift. The effects of Reynolds number in terms of shock location and trailing edge pressures are clearly illustrated. The results seem to indicate that at low Reynolds numbers viscous effects somewhat weaken the shocks on the inner wing.

In figure 19 a comparison is made between measured pressures and computed results from a first version of MATRICS, a finite volume wing-body code (Ref. 7). The computational grid used on the wing for these computations was similar to the grid used in XFLO22. Unlike the XFLO22 grid the MATRICS grid has a proper body representation. The code was used in non-conservative mode for the same flow condition. The computed pressure distribution is similar to the result of XFLO22 although the shocks are less well predicted.

The capability of the XFLO22 code has been used to predict the buffet onset boundary for the Fokker 100. An empirical criterion is applied which correlates local Mach number and momentum thickness just ahead of the shock with buffet onset. Momentum thickness is computed by a boundary layer code for the pressure distribution resulting from XFLO22. The accuracy of the prediction is determined by the selection of the extent of the wing span on which the criterion is exceeded. This amounts in practice to deviations of the order of 0.02 in liftcoefficient. This deviation is less than what is usually found from flight test results which are obtained by pilot comment.
A comparison of buffet onset boundaries obtained from computations, windtunnel experiments and flight tests (converted to tail-off values) is shown in figure 20. It illustrates the effect of Reynolds number as well as the capabilities of XFLO22.

The XFLO22 system was also applied to the prediction of compressibility drag. Postprocessing was used to predict induced-, viscous- and wave drag contributions. These results played a role in the extrapolation procedure for aircraft drag prediction.
In-flight measurements largely confirmed the compressibility drag prediction and showed that overall drag performance was better than predicted.

5. CONCLUDING REMARKS

In the present paper validation of CFD codes have been presented for areas which are of major importance for a successful aerodynamic design. Some conclusions can be drawn:

- empirical rules and criteria must be added to CFD codes for the solution of many practical flow problems.
- computations can reveal details which could not be obtained otherwise.
- simple methods for prediction of overall characteristics must be used complementary to methods for computation of complex flow details.

Although at present many flow problems can not yet be handled by CFD, the results show that in combination with windtunnel testing it plays a vitally important role in the aerodynamic development process.

6. REFERENCES

1. R. Houwink: Computation of separated subsonic and transonic flow about airfoils in unsteady motion NLR MP 84094 U, 1984.

2. B. Oskam, D.J. Laan and D.F. Volkers: Recent advances in computational methods to solve the high-lift multi-component airfoil problem, NLR MP 84042 U, 1982.

3. H.W.M. Hoeijmakers: Panel methods in aerodynamics; some highlights, NLR MP 87028 U, 1987.

4. A. Jameson and D.A. Caughey: Numerical calculations of transonic flow past a swept wing, ERDA Report COO-3077-140, Courant Institute, NYU, 1977.

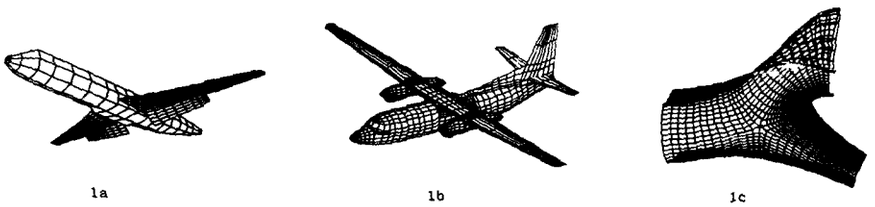
5. J. van der Vooren, J. Th. van der Kolk and J.W. Slooff: A system for the numerical simulation of sub- and transonic viscous attached flows around wing-body configurations, NLR MP 82019 U, 1982.

6. J.P.F. Lindhout, G. Moek, E. de Boer and B. van den Berg: A method of the calculation of 3-D boundary layers on practical wing configurations, NLR MP 79003 U, 1979.

7. J. van der Vooren, A.J. van der Wees and J.H. Meelker: MATRICS, transonic potential flow calculations about transport aircraft, NLR MP 86019 U, 1986.

ACKNOWLEDGEMENTS

The authors wish to thank Prof. E. Obert of Fokker for his support in the development of the CFD capabilities, Messrs. G.J. Schipholt and J.L. Kuijvenhoven for their contribution in the computations and last but not least the many colleagues from NLR who contributed to the development of most of the CFD codes.



1a 1b 1c

FIG. 1. PANEL METHOD MODELING SCHEMES.



FIG. 2. FOKKER 50 PROTOTYPE.

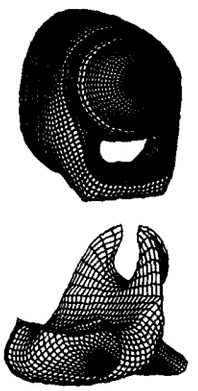


FIG. 3. FOKKER 50 NACELLE AND INTAKE DUCT MODELING.



FIG. 4. FOKKER 100 PROTOTYPE.



FIG. 5. PRESSURE MEASURING BELTS ON FOKKER 100 WING.

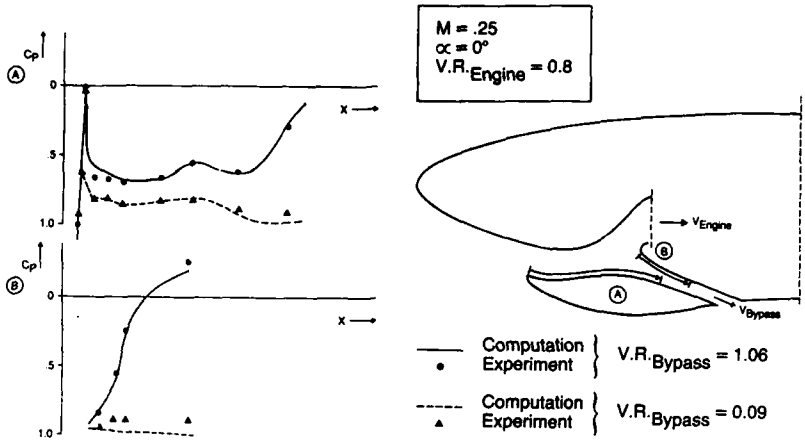


FIG. 6. COMPUTED AND MEASURED PRESSURES INSIDE FOKKER 50 INTAKE DUCT.

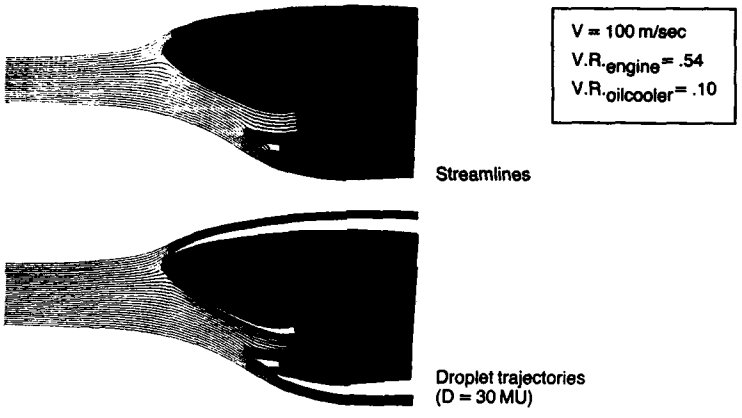


FIG. 7. COMPUTED STREAMLINES AND DROPLET TRAJECTORIES.



FIG. 8. ICE ACCRETION MEASURED INSIDE FOKKER 50 INTAKE DUCT.



FIG. 9. IN-FLIGHT MEASURED ACCRETION OF ICE ON FOKKER 50 NACELLE.

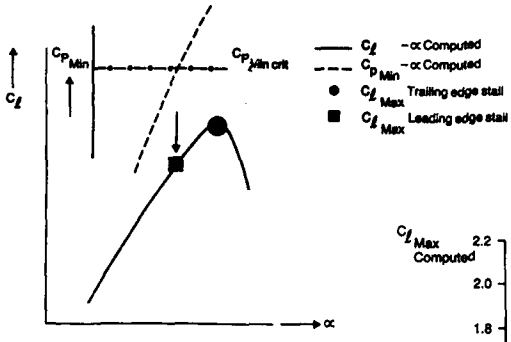


FIG. 10. COMPUTATIONAL PROCEDURE FOR PREDICTION OF SINGLE-AIRFOIL MAXIMUM LIFT.

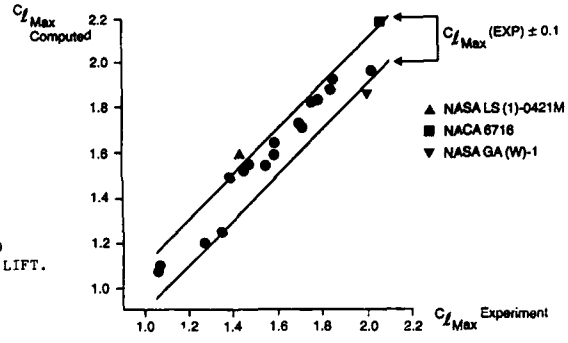


FIG. 11. CORRELATION OF COMPUTED AND MEASURED LOW-SPEED MAXIMUM LIFT.

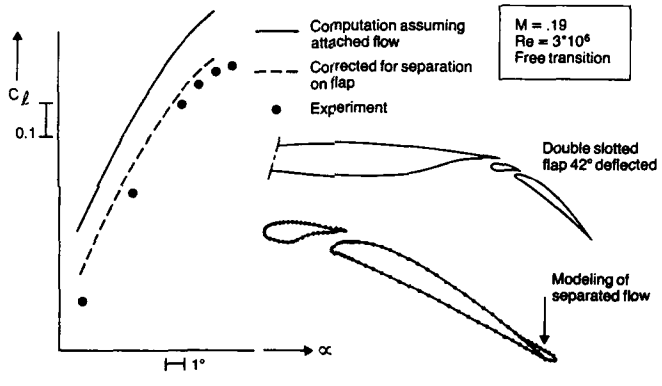


FIG. 12. MAXIMUM LIFT COMPUTATION FOR FOKKER 100 HIGH-LIFT SYSTEM.

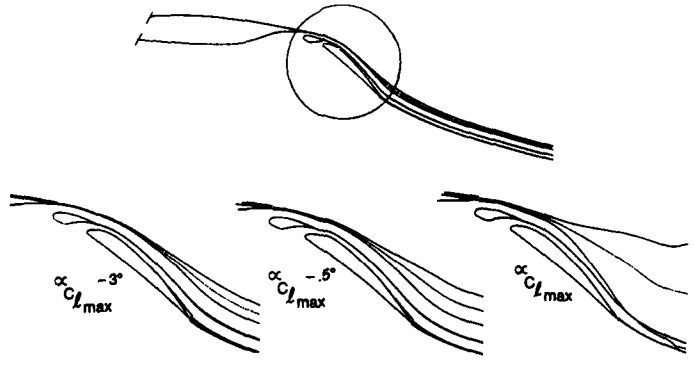


FIG. 13. WAKE DEVELOPMENT NEAR MAXIMUM LIFT.

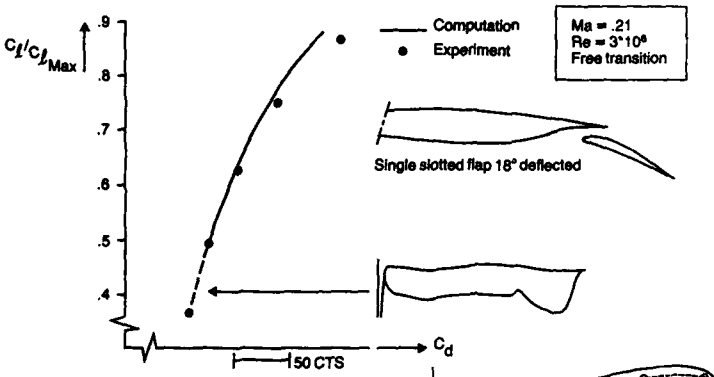


FIG. 14. DRAG COMPUTATION FOR FOKKER 100 HIGH-LIFT SYSTEM.

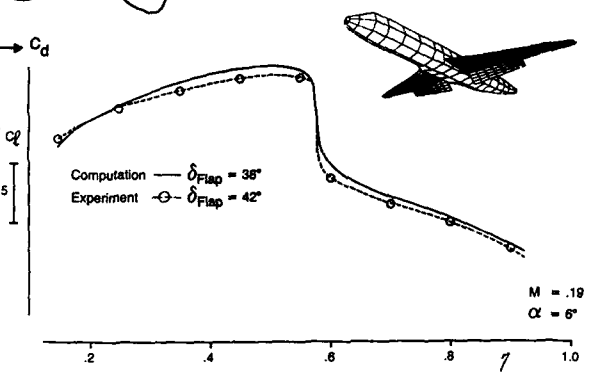


FIG. 15. COMPUTATION OF SPANWISE LIFT-DISTRIBUTION ON FOKKER 100.

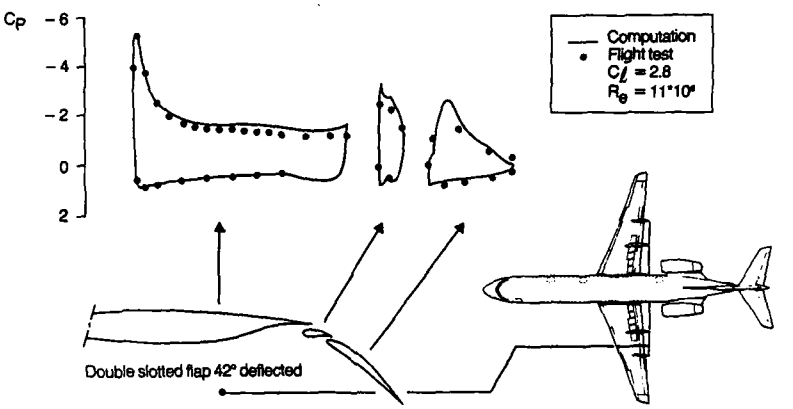


FIG. 16. COMPARISON OF COMPUTED AND MEASURED WING PRESSURES.

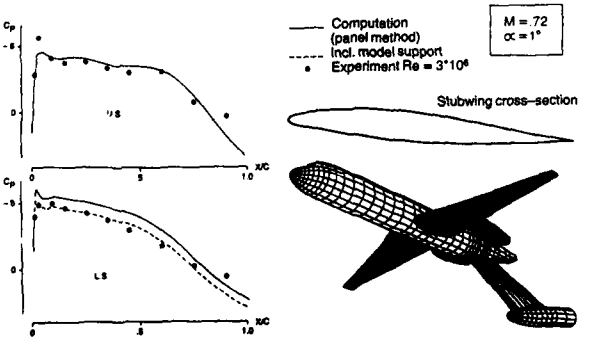


FIG. 17. COMPUTED AND MEASURED STUBWING PRESSURES.

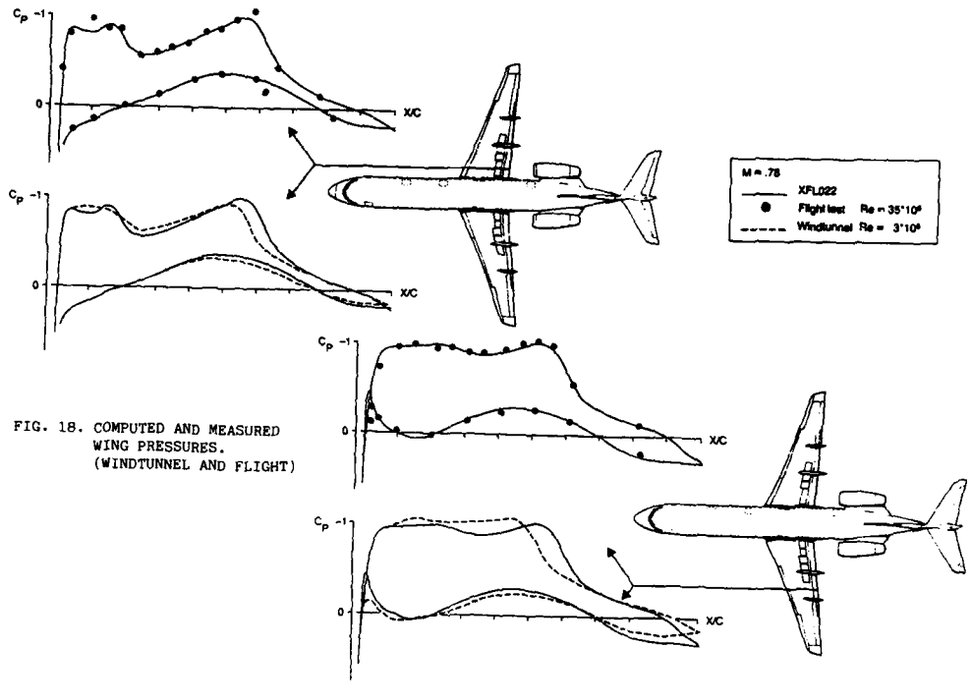


FIG. 18. COMPUTED AND MEASURED WING PRESSURES. (WINDTUNNEL AND FLIGHT)

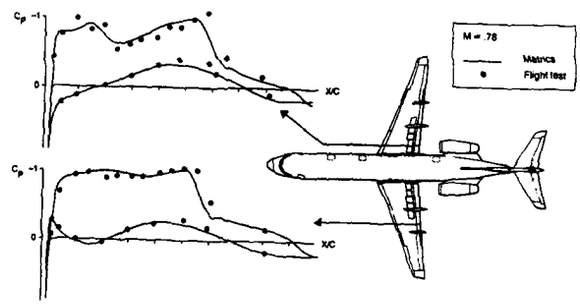


FIG. 19. COMPUTED AND MEASURED WING PRESSURES.

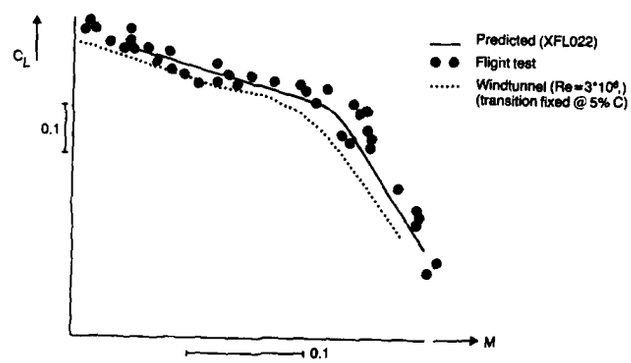


FIG. 20. COMPARISON OF BUFFET ONSET BOUNDARIES.

EXPERIMENTAL PROGRAM FOR REAL GAS FLOW CODE VALIDATION AT NASA AMES RESEARCH CENTER

by

George S. Deiwert, Anthony W. Strawa, Surendra P. Sharma, and Chul Park
Aerothermodynamics Branch
NASA Ames Research Center, Moffett Field, California 94035 USA

SUMMARY

The experimental program for validating real gas hypersonic flow codes at NASA Ames Research Center is described. Ground-based test facilities used include ballistic ranges, shock tubes and shock tunnels, arc jet facilities and heated-air hypersonic wind tunnels. Also included are large-scale computer systems for kinetic theory simulations and benchmark code solutions. Flight tests consist of the Aeroassist Flight Experiment, the Space Shuttle, Project Fire 2, and planetary probes such as Galileo, Pioneer Venus, and PAET.

INTRODUCTION

Computational fluid dynamics involves the numerical solution of the equations of motion which describe the conservation of mass, momentum, and energy. The most general forms of these equations are the compressible Navier-Stokes equations for continuum flight regimes and the Boltzmann equation for rarefied flight regimes. Many continuum flow fields have been well simulated for a variety of shapes and flow conditions where strong viscous/inviscid interactions and/or flow separation are important by advancing these equations in time until a steady state is asymptotically achieved. When there is no flow reversal and the flow in the streamwise direction is supersonic, these equations can be simplified by neglecting the streamwise viscous terms. The solution to these simplified equations, referred to as the parabolized Navier-Stokes equations, can be found by efficient streamwise marching techniques. Further simplification can be achieved, when viscous/inviscid interactions are weak, by decoupling the viscous and inviscid dominated regions from one another and simulating the regions separately in an iterative manner. Here the inviscid Navier-Stokes equations, termed the Euler equations, are solved in the inviscid region away from body surfaces. Near the body surface, the viscous dominated boundary layer equations are solved. A fourth simplification which can be used for strong viscous/inviscid interactions is the viscous shock layer approximation. This method is used for the stagnation region of hypersonic blunt bodies between the bow shock and the body surface.

Real gas effects include thermochemical nonequilibrium, where finite rate processes for chemical and energy exchange phenomena occur, and radiative transport is a coupled process. To account for chemical reactions, conservation equations for each chemical species must be added to the flow-field equation set. There are five flow-field equations (one continuity, three momentum, and one energy equation). For dissociating and ionizing air, there are typically 11 species (N_2, O_2, N, O, NO, O^+, N^+, NO^+,N_2^+, O_2^+, and e^-). The inclusion of conservation equations for each of these species nearly triples the number of equations to be solved. When there are combustion processes or gas/surface interactions or ablation products, the number of species increases dramatically. To account for thermal nonequilibrium and radiative transport, there are additional energy equations to describe the energy exchange between the various energy modes (such as translational, rotational, vibrational, and electronic). To further complicate the analysis, the range of time scales involved in thermochemical processes is many orders of magnitude wider than the mean flow time scale. This is the single most complicating factor in computational aerothermodynamics. Coupled radiative transport results in a system of integrodifferential equations which are exceedingly difficult to solve. Simplifying assumptions (such as either optical transparency, or gray gas, or tangent slab models) are generally used to reduce this level of complexity. Many varieties of simplifications are used to alleviate problems associated with widely disparate time scales and are discussed briefly next.

Many flows can be adequately approximated by assuming an equilibrium real gas. Here all the reaction rates are assumed to be fast enough so that the gas is everywhere in local equilibrium, and the thermochemical state of the gas can be defined solely by the local temperature and pressure. Reactions are allowed to occur and effect the solution only through the equation of state of the equilibrium gas mixture. This is a good approximation for higher-pressure, lower-altitude cases, and it can be used for a major portion of the analysis of such vehicles as hypersonic aircraft which fly in the sensible part of the atmosphere. In the other extreme, reactions are sometimes so slow that the gas can be considered frozen in a particular chemical state. This phenomenon frequently occurs in regions of rapid expansion such as in jets or base regions of body shapes, but the frozen gas model can sometimes be used behind compressive shocks as well.

When finite rate chemical reactions are important, they can often be considered to be in thermal equilibrium. That is, the energy modes of the species equilibrate very rapidly compared to the chemical rate processes. Even with this simplification the chemical rate time scales vary over an extremely wide range, resulting in a "stiff" behavior of the complete equation set and adding to the difficulty in solving the flow field and species equations in a fully coupled manner. In these cases the species equations are often effectively uncoupled from the flow-field equations and solved separately in a "loosely" coupled manner, often by a different (usually implicit) numerical technique. To validate these real gas codes, both ground- based and flight experiments are necessary to assess the effects of chemical kinetics, high enthalpy, low density, and scale.

In the past, ground-based test facilities (such as shock tubes, arc jets, and ballistic ranges) were used, in coujunction with engineering design and analysis codes, to achieve closure on designs of such vehicles as Apollo, the Space Shuttle, and the Galileo probe. Ground-based test facilities can provide valuable insight for the design and understanding of aerospace vehicles but cannot simulate all of the conditions (combinations of scale, altitude, and velocity) that will be encountered in planned missions of the future. Today, these facilities are being used to provide validation data for real gas flow codes which are, in turn, used to simulate actual flight conditions. Photographs of some of these facilities are shown in Fig. 1. The simulation capability of these facilities as a function of length Reynolds number, flight velocity, and enthalpy is shown in Fig. 2. The facilities represented in this figure are: (1) The Hypersonic Free-Flight Aerodynamic Facility (HFFAF), a countercurrent ballistic range which can also be operated as a Mach 7 shock tunnel with sting mounted models, and as a ballistic free-flight range with a quiescent gas;, (2) the Electric Arc Shock Tube (EAST) Facility; (3) the 60-MW Interaction Heating Facility; and (4) the 3.5-Foot Hypersonic Wind Tunnel (HWT). Also shown are the flight regimes for the Space Shuttle and for the Aeroassist Flight Experiment (AFE). Indicated in the figure are regimes where various real gas phenomena become important, such as slip-flow and free-molecular-flow regimes, the dissociation of oxygen and nitrogen, and

ionization. Superimposed are trajectories of typical hypersonic aerospace vehicles including the Space Shuttle, boost glide vehicle (BGV), a transatmospheric vehicle (TAV), and an aeroassisted orbital transfer vehicle (AOTV).

The operating characteristics of each of the test facilities, how each relates to the flight regimes of various aerospace vehicles, the type of data each can produce with appropriate instrumentation, and how each can be used for code validation, are covered in this paper. Both ground-based tests and flight tests can provide valuable data to validate computational methods. The computational methods can then, in turn, be used to extrapolate our understanding and analysis into regimes not covered by existing facilities.

A summary of the experimental activity and its relationship to the validation of real gas flow codes is shown in Table 1. Here the flow codes have been summarized by six generic classes: (1) perfect gas hypersonic upwind codes, (2) real gas upwind codes, (3) real gas nozzle/plume codes, (4) hydrogen-air combustion codes, (5) multi-temperature thermochemical nonequilibium codes, and (6) hypersonic transition and boundary layer codes. A discussion of this activity follows in the next section, and is identified by each experimental facility.

EXPERIMENTAL PROGRAM

Ballistic Range Tests

Ballistic ranges can be used to achieve flight velocities where real gas effects are important. They offer an advantage over other hypersonic facilities in that the free-stream conditions are known and there are no model supports to cause interference, particularly in the base region. This simplifies boundary and initial conditions used in computations and eliminates one source of ambiguity between computational and experimental results.

Two ballistic range facilities at Ames Research Center support hypersonic research: The Hypersonic Free-Flight Aerodynamic Facility (HFFAF), and the Pressurized Ballistic Range (PBR). These two facilities compliment each other, each having specific advantages for certain types of tests. Together, they allow testing of a variety of models over a wide range of density, speed, and Reynolds number. Each facility and associated experiments is described briefly.

Hypersonic Free-Flight Aerodynamic Facility (HFFAF). A photograph and schematic of the HFFAF are shown in Fig. 3. The free-flight test section is 23 m long and has 16 orthogonal spark shadowgraph stations evenly spaced (1.52 m) over its length. Kerr-cell shutters are used to produce a sharp model and flow-field image on the film. Four deformable-piston, light-gas guns, having bore diameters of 0.71, 1.27, 2.54, and 3.81 cm, are available for launching the model into free flight. Each of these guns can operate to muzzle velocities of about 9 km/sec. A shock tunnel to provide a countercurrent flow capability is currently being reactivated.

Tests in this facility can be conducted from as high as 1 atm to as low as about 0.02 Torr, and in nontoxic gases other than air, such as CO_2, H_2, He, Kr, and Xe. The details of the operating characteristics of this facility are described in detail in Ref. 1, and are summarized in Table 2.

Pressurized Ballistic Range. The PBR consists of a large cylindrical test section 3 m in diameter and 62 m long, which can be pressurized or evacuated to achieve the desired Reynolds number for the model size and velocity. The model is launched from a light-gas gun located at one end on the test section, and travels in free flight down its length. Data are collected along the flight path of the model by orthogonal, direct-shadowgraph systems located at 24 stations irregularly spaced over its length between 2.1 m to 4.2 m intervals. All of the optics are internal to the tank, which imposes a limit on the maximum velocity of the model because of fogging problems when the gas radiates. Many tests in this facility are conducted with powder-gas guns rather than with deformable-piston light-gas guns. A schematic of the facility is contained in Fig. 4. The advantages of this facility over HFFAF are threefold: long model trajectory, ambient pressures up to about 6 atm and highly detailed shadowgraphs. The operating characteristics of this facility are summarized in Table 3.

Slender Cone Drag Tests. Experiments have been conducted on sharp 5° and 10° half-angle cones at a Mach number of approximately 15 in the two ranges. The 5° data was recently acquired in the HFFAF, while the 10° data obtained in the PBR has been reported in Ref. 2. Drag coefficients have been obtained using both a linearized data reduction routine as well as a more sophisticated 6-degree-of-freedom data reduction routine, which can identify the effects of angle of attack and velocity on the total drag. Results of the two methods are consistent. Drag coefficients are compared with the results of a real gas computation and with ideal gas results. At the conditions of the experiments, skin friction drag makes up a significant portion of the total drag and can be affected by chemistry.

The effects of real gas chemistry on the drag of sharp, slender cones appear as an increase in the skin friction. In the case of the 10° cone at a Reynolds number of 400,000, about 40% of the total drag is due to skin friction.

Figs. 5 and 6 show shadowgraphs obtained for the 10° and 5° cones in free flight at the ballistic ranges. The computed shock angles compare well with the measured angles. Fig. 7 is a comparison of computed and measured drag coefficient for the 10° cone at a Reynolds number of 0.4×10^6 and Mach number of 15. The rms residual of the best fit for the trajectory of the 10° cone was 0.1 inches. The measurement accuracy for any ballistic range data is a function of the model size and shape, the clarity of photographs, and the skill of the film reader. Included in the figure are computed values of drag coefficient from ideal gas[3] and real gas[4] parabolized Navier-Stokes (PNS) codes and the ideal gas pressure drag value from Sims.[5] The pressure drag contributes about 40% of the total drag at zero angle of attack. The real gas drag coefficient is slightly higher than the ideal gas value although the computation agrees very well with the experiment for this case. Generally the computational results fall below the experimental values. Comparable agreement was found between computation and experiment for the more recently acquired 5° cone data.

During the course of comparing the computer solutions with experimental results, we made several observations relating to code calibration and validation. When comparing absolute values, such as drag coefficient, all sources of experimental, as well as computational, error must be evaluated. For example, since drag is sensitive to Reynolds number, the measurement accuracy of that number as well as that of other input parameters should be evaluated. In one case a 10% change in calculated Reynolds number resulted in a 6.5% change in the drag coefficient. This is outside of the experimental error range and could make comparison between theory and experiment meaningless. Since all initial and boundary conditions used in a computation cannot or have not been measured, code sensitivity to these conditions should be explored. All sources of error in the experimental data should be documented. The sensitivity of the computer code to grid size and shape, and to initial and boundary conditions, should be well documented. This is especially true when people other than the code developers are running the code.

Finally, while aerodynamic coefficients give a gross indication that a computer code can properly simulate a flow field, detailed flow-field quantities (such as density, temperature, and species concentration) must be measured if problems within the computational solution are to be identified and corrected. These kinds of measurements are difficult to obtain in the ballistic range. Modern diagnostic techniques are now available, however, that make such measurements feasible. At the present time a laser holographic system is being installed in the HFFAF which will permit the determination of the density field from interferogram fringe patterns. Techniques to determine model wall temperature are also being studied, such as temperature sensitive paints, infrared photography, and telemetered data. These additional data will permit code validations as well as calibration by the drag data discussed above.

Galileo Tests. The ballistic ranges have also supported all of the United States' probe missions to other planets. These include the 1976 Viking mission to Mars and the 1978 Pioneer Venus mission. Currently, tests are being conducted on the Galileo probe. The Galileo spacecraft will be launched in the near future and will arrive at Jupiter 2 years later. The probe will make in situ measurements as it descends through the Jovian atmosphere prior to its eventual destruction caused by extreme external pressures.

Although the probe aerodynamics were needed initially for design purposes, more accurate aerodynamics are needed in support of the Atmosphere Structure Experiment carried on board the probe. This experiment is designed to determine the state properties (i.e., density, pressure, temperature) of an unknown planetary atmosphere as functions of altitude from measurements made during the entry and descent of a probe. The experiment consists of a three-axis accelerometer, plus pressure and temperature sensors. During the high-speed portion of the trajectory, from an entry velocity above 47 km/sec to sonic speed, direct measurements are impractical and accelerometers are used to determine the state properties. This requires the precise knowledge of the probe aerodynamics, in particular the vehicle drag and lift coefficients as functions of Mach number and Reynolds number. The aerodynamic characteristics plus the measured decelerations allow the probe attitude to be determined and the atmospheric density to be deduced. Integration of the density gives the pressure, and the temperature is deduced from the equation of state (given the molecular weight, which is measured by another onboard experiment). The ballistic range facilities are well suited to providing the accurate aerodynamic data over a wide range of conditions.

A typical shadowgraph of a Galileo model in flight obtained in HFFAF is shown in Fig. 8. The screw on the model base is for attachment to its sabot prior to launch. The vertical wires are plumb lines for reference, and the irregular markings are imperfections in the facility windows caused by past debris impacts.

Low-Reynolds-Number Tests. Tests are also being conducted to precisely define the drag characteristics of the Galileo probe at Reynolds numbers, based on model diameter, of about 500 to 250. Obtaining drag data at these low Reynolds numbers is important because the drag coefficient is expected to increase markedly as the slip-flow and free-molecule-flow regimes are approached. This dramatic increase in drag coefficient occurs below a Reynolds number of about 1000.

The importance of obtaining drag data at various Reynolds numbers is shown in Fig. 9. Shown are Pioneer Venus data[6] down to a Reynolds number of about 250. The drag coefficient increases continuously below a Reynolds number of 1 million, but the increase becomes most dramatic below 1000.

AOTV Tests. Ballistic range tests have been conducted for two AOTV configurations: a symmetric and a raked-elliptic-cone configuration. These tests were conducted to: 1) provide experimental aerodynamic data and good flow-field definition against which computational aerodynamicists could validate their computer codes, 2) define bow shock wave shape and shock standoff distance, 3) investigate flow impingement on the afterbody, 4) compare the aerodynamics of several configurations, 5) investigate how minor changes in corner geometry affect the flow field, 6) determine the trim angle of attack of a trimmed vehicle.

A shadowgraph for the symmetric configuration[6] is shown in Fig. 10 and for the raked elliptic cone[6] in Fig. 11. These flow visualizations along with drag data from these tests are used for computer code calibration. With the newer holographic techniques, density data can also be used for code validation.

Other Tests. Simple shapes (such as sharp and blunt cones, bi-cones, and blunt bodies) are used in the ballistic ranges and sting mounted in shock tubes and tunnels to study the effect of real gas properties. Real gas thermodynamic and transport properties and finite rate chemical reactions have a pronounced effect on shock and Mach wave positions and shapes, emitted radiation, and aerodynamic drag. A detailed survey of simulation and diagnostic techniques used for these studies was presented by Sharma and Park.[7]

Transition Studies. In the past, transition studies were made in the HFFAF. Shadowgraph data on models launched in the range clearly show transition onset (e.g., Ref. 8), and measurements of total drag show the effect of low density in increasing drag coefficient. These transition studies will be continued on slender cone, bi-cone, and tri-cone shapes as well as on slender bodies.

Shock Tunnel

The 16-in. combustion driven shock tunnel, which provides the counterflow capability for the ballistic range, consists of a 23-m long, 43-cm diam driver section followed by an 26-m long, 30-cm diam driven section. It is capable of producing enthalpies corresponding to flight at Mach 15 and, because of the long, large diameter driver and driven sections, can produce a run time typically of 25 msec when operated at tailored-interface conditions. The flow from the shock tube is expanded through a Mach 7 axisymmetric nozzle through a test section which is 27 m long and 1 m across. The operating characteristics of this facility have been summarized in Table 2, and are described in detail in Ref. 1.

Hypersonic Boundary Layer Studies. Hypersonic boundary layer studies can be made in the HFFAF shock tunnel. The tunnel length of 27 m results in Reynolds numbers as high as 80×10^6. Tunnel wall boundary layer surveys can determine species, density, and velocity distributions and surface measurements can determine pressure, temperature, and heat flux.

Nozzle/Plume Experiments. Real gas nozzle/plume flow-field experiments are being designed for the Mach 7 shock tunnel. Detailed flow-field measurements including velocity, density, and species distributions will define plume structures as will shadowgraphs and holograms. Surface pressure, heat flux, and streamlines will define the nozzle flow. Momentum loss measurements will be made where possible to determine performance characteristics. By loading the driven section with hydrogen-air mixtures it will be possible to simulate hypersonic air-breathing propulsion systems. Both nozzle expansion studies (with hydrogen-air combustion products) and combustor process studies are being planned. New optical diagnostic instrumentation will permit the measurement of species and temperature distributions, which will be critical for code validation purposes.

Arcjets/Combustion Experiments

Hydrogen-air combustion processes are studied in the 20-MW Panel Test Facility where an oblique detonation wave will be established in a supersonic stream consisting of a mixture of hydrogen and air. This experiment and preliminary computations are described by Cambier et al.[9,10] and Adelman et al.[11]

The 20-MW arc-jet facility consists of an arc heater supplied continuously with high-pressure air. The arc chamber can be pressurized to 10 atm. Air leaving the arc heater passes through a semi-elliptical nozzle with an exit area ratio of 36. A schematic of the test configuration is shown in Fig. 12. Enthalpies can range from 5 to 35 MJ/kg and air flow is variable from 0.05 to 0.68 kg/s. Nominal test conditions for the oblique detonation wave engine (ODWE) experiment correspond to maximum pressure and minimum current. Upgrading of the facility from 10 atm stagnation pressure to 40 atm is now in progress. This higher pressure will allow a closer simulation of the conditions expected at the inlet of a supersonic combustor. A five-stage steam ejector pump maintains test cell pressures down to 13 Torr.

The analysis of the ODWE has many levels of sophisticaion ranging from one-dimensional, steady, perfect gas flow to two-dimensional, viscous, shock capturing codes with finite rate chemistry. These codes are used to guide an experimental program aimed at proving the existence of oblique detonation waves and their use in supersonic combustors. The codes can, in turn, be validated by the resulting experimental data.

Proof-of-concept studies of the ODWE are designed to experimentally create and stabilize oblique detonation waves. The NASA Ames arc-jet hypersonic wind tunnel facilities can simulate combustor inlet conditions of Mach number and enthalpy. However, they cannot currently reproduce the expected pressures. Therefore it was necessary to determine if the low pressures would prevent the establishment of a detonation wave. This verification was carried out in several ways. The simplest method utilized a one-dimensional, steady flow, finite rate chemistry program [9] which calculated ignition delays and combustion behavior behind a 30° oblique shock wave.

The results of these calculations, which are shown in Fig. 13, demonstrate the strong dependence of ignition delay and combustion rate on pressure and temperature. As temperature and pressure are increased, combustion occurs closer to the oblique wave. However, this program does not simulate any coupling between heat release and wave angle, so the question remains whether a detonation has been created. Some estimates of coupling can be made by generating characteristics in the combustion zone and determining their intersections with the shock. If these characteristics do not intersect the shock within the bounds of the combustion chamber, then there is not enough coupling to be classified as a detonation. Instead, there is shock-induced combustion.

For the nominal experimental conditions, the gas exits the nozzle at Mach 4.6 at a pressure of 0.016 atm and a temperature of 840 K. Combustion behind a 30° oblique wave takes about 0.5 msec corresponding to a distance normal to the shock of approximately 5 cm. The closest characteristics originating from the combustion front would intersect the oblique shock at a point about 20 cm normal to the base of the wedge. This distance would correspond approximately to the height of the test section. Raising the pressure by a factor of 5 shortens the distance to about 0.7 centimeters. Characteristics would then start to intersect the oblique wave at a point 3.5 cm vertically above the base of the wedge. This coupling should create a detonation. Indeed, more sophisticated analyses employing fully coupled computational fluid dynamics and finite rate chemistry codes have shown the existence of a detonation under these conditions.[9]

The oblique waves will be created by a water-cooled wedge located approximately 1 ft downstream of the struts in the test section. Optical access is provided by 30-cm windows on either side of the test section, and a schlieren system will provide photographic records of the wave angle with and without fuel. Pressure and temperature transducers on the wedge will be used to measure the state of combustion behind the oblique wave.

Shock Tube Experiments

Shock tubes are unique in producing homogeneous high-temperature gas samples heated to an enthalpy and pressure calculable and selectable from the state of the undisturbed gas and measured shock velocity.

The electrical discharge heats either hydrogen or helium to a temperature of about 8000 K for hydrogen, and about 20,000 K for helium, without causing melting or ablation of the materials because the discharge time is very short. The maximum temperatures are set by the onset of ionization and accompanying energy loss by radiation. Compared to other heating methods, such as combustion, electrical heater, or adiabatic compression by a piston, the electrical arc-driven shock tube operating on this principle produces the highest shock speed.

The Electric Arc Shock Tube (EAST) Facility at Ames consists of one driver system and two parallel-driven tubes. One is a 10-cm i.d. tube 12 m in length, and the other is a 60-cm i.d. tube 21 m in length, both made of stainless steel. The driver can be operated in two configurations: 1) a 17.7-cm conical drive configuration with a 10.16-cm i.d. exit, and 2) a variable length (34 - 137 cm) 10-cm i.d. cylindrical configuration. The length of the cylindrical drivers can be varied by using a Lexan filler plug. A schematic of the facility is shown in Fig. 14.

Energy to the driver is supplied by a 1.24 megajoule 40 kV capacitor energy storage system. The 6-tier capacitor bank has 220 capacitors. By using different combinations of series-parallel connections, the capacitance of the bank can be varied from 861.3 μF to its maximum value of 6,126 μF. A diaphragm made of Mylar 0.35 to 0.50 mm in thickness separates the driver gas from the driven gas. It is ruptured because of the rise in pressure within the driver during the time the capacitor discharges.

The 24-inch EAST facility operates at pressures between 7 and 30 μm of mercury to simulate flight altitudes between 68 to 81 km. Test firings show that: (1) shock velocities in excess of 13 km/sec are achieved at densities equivalent to altitudes of 80 km, (2) the hot driver gas emits radiation in the same pattern as observed in previous higher density, slower shock speed tests, and (3) the driver gas does not radiate at unanticipated spectral frequencies. The 4-in. EAST facility operates at initial pressures between 0.1 and 760 Torr. Nonequilibrium real gas effects in N_2 and O_2 can be simulated by operating it at initial pressures between 0.1 and 3 Torr with shock velocities ranging from 4 to 12 km/sec. With certain modifications these facilities will be able to produce spectrally clean test gases, which will be used to perform basic experimental investigations on thermo-chemical nonequilibrium with particular emphasis on vibrational energy excitation and nonequilibrium. A description of proposed tests and instrumentation is given by Sharma and Park.[7]

A total of 760 runs have been made to date. Of these, the conditions of 75 runs are shown in Fig. 15. These runs can be classified into three different categories: (1) air or a gas of similar molecular weight (argon, carbon dioxide) as the test gas in the 10-cm tube, (2) air or a gas of similar molecular weight as the test gas in the 60-cm tube, and (3) hydrogen as the test gas in the 10-cm tube. These three classes of operations occupy different regions in the velocity-pressure plot in Fig. 15. Test times for these runs range from 2 μsec to 20 μsec corresponding to flight speeds of 40 km/sec to 6 km/sec respectively.

In order to study chemical kinetics at low densities, emission, absorption, and scattering spectroscopic techniques are used. For accurate and reliable measurement, the test gas produced must be spectroscopically clean. For this reason the spectra of the test gas produced in the shock tubes were analysed using 99.99% pure nitrogen. The spectra of test gas, Fig. 16, were recorded in an aluminum tube and consist of vibrational bands from molecular species, CN, N_2, N_2^+, NO, and O_2^+. No iron or chromium lines are identifiable in the spectra. The peak at about 3883 Å is caused by the compounding of the (0,0) band of the CN violet system with band head at 3883 Å and the (0,0) band of the first negative band of N_2^+ with band head at 3914.4 Å. The carbon element in the CN molecules is believed to have originated from the carbon dioxide and hydrocarbons contained in the test gas, vacuum pump oil vapors, and the Mylar diaphragm. Near the red end of the spectra, the first negative bands of O_2^+ with a band head at 5631.9 Å are seen. The oxygen molecules are believed to have originated mostly from the test gas. The presence of O_2 also explains the NO-β bands with band heads at 3207, 3043 and 2754 Å in the ultraviolet region. Overall, the spectrum is dominated by the molecular bands of N_2^+. The present finding agrees with the results of the tests conducted at AVCO.[12] Two wavelength uv absorption spectroscopy (1100 Å - 1800 Å) will be used to measure the ground state number density and vibrational temperature in N_2 and O_2. Using gated diode arrays, emission spectra of the gases will be recorded in the spectral range of 2000 Å - 9000 Å. A detailed discussion of the measurements is given by Sharma and Park.[7] Solutions obtained by Park,[13] using a two-temperature gas model, are compared with this AVCO emission data in Fig. 17. These AVCO tests also will be repeated in the EAST facility.

3.5-Foot HWT Experiments

Hypersonic perfect gas code validation experiments consist of complete flow-field measurements about simple generic TAV configurations in the 3.5-Foot HWT. Data includes surface pressure, heat flux and streamline patterns (oil flow), shadowgraphs, and laser Doppler velocimetry (LDV) and pitot probe flow-field surveys. The free-stream Mach number is varied between 5 and 14, length Reynolds numbers between 1 and 25 million, and altitudes up to 210,000 ft. Fig. 18 shows an elliptic cross section, delta planform all-body hypersonic aircraft model, sting mounted in the test section, currently under investigation. Shown in Fig. 19 is a shadowgraph for a Mach 7.4 free stream. The angle of incidence is 15 degrees and the length Reynolds number is 15 x 10^6. Clearly discernible is the windward shock and the expansion fan emanating from the forebody/afterbody junction.

The Ames 3.5-Foot HWT is a closed-circuit, blowdown-type tunnel with a pebble-bed heater to heat the air to prevent liquefaction and with axisymmetric contoured nozzles to achieve the test Mach numbers. The tunnel is equipped with a model quick-insert mechanism for moving models (transit time as short as 0.5 sec) into and out of the air stream.

The test conditions for this ongoing study will include nominal free-stream Mach numbers of 5, 7, and 10 (the Mach 14 nozzle being redesigned); free-stream Reynolds numbers, based on model length of 3 ft, from 1.5 × 10^6 to 25 × 10^6 (laminar to turbulent flows); and model angles of attack of 0°, 5°, 10°, and 15° (attached and separated flows). For the complete investigation, flow-visualization data (shadowgraphs and surface oil-flow patterns), surface pressures, surface heat transfer, and flow-field surveys (probes and laser velocimetry) will be obtained for the all-body model both without and with control surfaces. The surveys by LDV are contingent upon the development of an LDV system for the 3.5-Foot HWT. A study in this facility has demonstrated that LDV capability can be used therein.

FLIGHT EXPERIMENTS

Aeroassist Flight Experiment

A forthcoming NASA flight experiment called the Aeroassist Flight Experiment (AFE) is planned for early in the next decade. Ames Research Center will participate in this experiment by constructing a large base of radiometric data for high-altitude, high velocity thermochemically nonequilibrated flow conditions. The AFE will be carried to orbit by the Space Shuttle and then deployed for the atmospheric data pass. Accelerated by an 18,000-lb thrust solid rocket motor, the vehicle will enter the atmosphere at nearly 10 km/sec and then experience approximately 500 sec of aerodynamic deceleration, during which a variety of flight data, including radiative and convective heating rates, will be gathered. The vehicle will exit the atmosphere at orbital speed and be recovered by the Shuttle Orbiter for return to Earth for postflight evaluation. As a preliminary to the design of a radiometer for this experiment, an approximate method for predicting both equilibrium and nonequilibrium radiative surface fluxes has been developed.[14] Spectral results for one trajectory state, a velocity of 10 km/sec at an altitude of 85 km, are shown in Fig. 20, where the spectral surface flux at a distance of 20.9 cm behind the shock front is plotted as a function of wavelength in the spectral region from 0.2 to 2.0 μm. An inspection of the figure reveals that the spectrum appears to be composed of a background continuum with a color temperature in the range of 7,000 K to 8,000 K (based on a flux maximum in the vicinity of 0.4 μm) on which is superimposed a complex structure of molecular bands and broadened atomic lines. The radiation calculation included 11 species (O_2, N_2, NO, O, N, N^+, O^+, N_2^+, NO^+, O_2^+, and e^-); some of the more apparent band-heads and lines from these species are identified in the figure. These results, and others like them, are used to develop the instrument parameters for the three different types of radiometers proposed for the experiment.

RAM-C Experiments

During the late 1960s three experimental probes were flown into the atmosphere at approximately satellite speed.[15–17] These probes, which were called the RAM-C tests, were sphere-cone configurations with a 0.1524-m nose radius, 9° cone half-angle, and a total length of 1.295 m. They were instrumented to measure electron number densities in the flow field. The second test, RAM-C II, is of particular interest because no ablation products were produced. This probe had a beryllium heat-sink nose cap and a Teflon-coated afterbody. Electron number densities were measured at four axial locations using microwave reflectometers and in the boundary layer using an electrostatic rake.

Computations were performed to replicate the RAM-C II tests at altitudes of 61, 71, and 31 km. This altitude range approximately spans a region of near-thermo-chemical equilibrium at 61 km to strong nonequilibrium at 81 km. The wall temperature was fixed at 1500 K, which is an approximation to the experimental wall temperature which is unknown. The wall was assumed to be fully non-catalytic which is also an approximation to the RAM-C II test. In each case the free-stream velocity was 7650 m/s.

The computations[18] were performed on body-fitted meshes with 35 points axially along the sphere-cone and 50 points in the flow field normal to the body. Figure 21 shows a typical mesh used for one of the test cases. The computations were performed using shock-capturing for all cases.

Each case was computed using two different chemical models. One set of results was obtained considering five chemical species (N_2, O_2, NO, N, and O), and three vibrational temperatures (*i.e.*, one vibrational temperature per diatomic species). There are a total

of eleven coupled equations to be solved. The number density of electrons may be approximated with the use of the quasi-steady-state (QSS) assumption. A second set of results was computed for this gas with NO ionized. In this case there are seven species (N_2, O_2, NO, NO^+, N, O, and e^-), four vibrational temperatures, and the electron temperature, for a total of fifteen equations to be solved. The purpose of performing both sets of calculations is to compare the effects of the electrons on the flow field.

The computed results are first compared to the peak electron number density measured axially along the body at each altitude. These results are presented in Figs. 22 to 24. They show that the electron number density is highest at the nose and falls off rapidly around the shoulder of the body. The QSS approximation and the nonequilibrium approach follow this trend, but the latter method predicts the data much better. The QSS technique works best at lower altitudes because the flow field is closer to equilibrium for these cases. Conversely, the agreement between the experiment and the nonequilibrium results is best for the higher, nonequilibrium cases. The differences between the two computed results indicate the nature of a nonequilibrium flow field. As the gas expands around the shoulder of the sphere-cone, the translational temperature falls rapidly. The fluid carries with it a large number of electrons that have been produced near the nose but have not yet recombined. Thus, although the local temperature is relatively low, the number of electrons remains high in the shoulder region. This effect is captured by the seven-species solution. However, if we assume that the reaction producing the electrons is governed by the local temperature as in the QSS approach, we predict too few electrons.

Figure 25 compares the computed results using the seven-species model to the measured electron number density near the body surface at $x/r_n = 8.10$ for altitudes of 71 km and 81 km. The results are approximately the right magnitude but do not show the correct behavior near the wall. This problem is likely caused by the uncertainty in wall boundary conditions. The surface of the probe was probably catalytic for the electron-ion recombination reaction and thus would cause a lessening of the electron number density near the wall. This wall effect is not currently included in the calculations. Alternatively, the fixed-wall temperature used in the calculations may be too high which would produce an excessive number of electrons near the wall.

The electron number densities computed using the seven-species gas model are in good agreement with the RAM-C II flight experiment. The use of a QSS assumption to derive the electron density from the five-species model predicts the correct trend. However, this approach yields results that are typically at least an order of magnitude in error, especially in highly nonequilibrium cases. The computations also indicate that the heat transfer to the body in the nose region is about 50% greater for a reacting gas than for a perfect gas. The heat transfer results also show that for the cases studied, the flow field is adequately described by the five-species model unless an accurate representation of the electron density distribution is required. The vibrational state of the flow field may be approximated with only one vibrational temperature.

These results and others not discussed here demonstrate that the models used for the translation-vibration and electron-vibration energy exchange mechanisms are inadequate in the regime of the test cases. Further research is required to improve these models for high temperatures so that the vibrational and electron temperatures may be computed correctly.

Other Flight Experiments

Other flight experiments include the Fire 2[19] project where radiative emission power was measured at the stagnation point during the flight, and the PAET[20] flight where the radiation intensity in several narrow wavelength channels was measured at the stagnation point of a spherical nose re-entry body. Comparisons between each of these flight experiments and computed results by Park[21] (in which a two-temperature thermochemical nonequilbrium model for dissociating and ionizing air was used) are shown in Figs. 26 and 27, respectively.

RAREFIED FLOWS

Direct simulation Monte Carlo calculations are being used to study and validate nonequilibrium thermodynamic and transport models, slip-flow codes, and modified Navier-Stokes codes designed to accommodate the breakdown of the Stokes hypothesis. New algorithms based on kinetic theory concepts are also being studied and evaluated.

CONCLUDING REMARKS

The experimental program for validating real-gas hypersonic flow codes at NASA Ames has been described. Ground- based test facilities include ballistic ranges, shock tubes and shock tunnels, arc jet facilities and heated-air hypersonic wind tunnels. Flight test facilities consist of the Aeroassist Flight Experiment, the Space Shuttle, project Fire 2, and planetary probes such as Galileo, Pioneer Venus, and PAET. While any single experiment is not sufficient to validate a given code, the experimental program described herein, taken in total, should provide data over a broad range of conditions. Real gas computer flow codes which account for finite rate chemical reactions and thermal nonequilibrium can then, in part, be validated and calibrated by comparisons with data from the experiments identified in this program.

REFERENCES

1. Ballistic Range Technology. AGARDograph No. 138 (ed. Canning, T.N., Seiff, A., and James C.S.).

2. Intrieri, P. F., Kirk, D. K., Chapman, G. T., and Terry, J. E., "Ballistic Range Tests of Ablating and Nonablating Slender Cones," AIAA J., Vol. 8, No. 3, Mar. 1970, pp 558-564.

3. Lawrence, S. L., Chaussee, D. S., and Tannehill, J. C., "Application of an Upwind Algorithm to the PNS Equations," AIAA Paper 87-1112, Honolulu, HI, June 1987.

4. Prahbu, D.K, Tannehill, J.C., and Marvin J.G., "A New PNS Code for Three-Dimensional Chemically Reacting Flows," AIAA Paper 87-1472, Honolulu, HI, June 1987.

5. Sims, J.L., "Tables for Supersonic Flow around Right Circular Cones at Zero Angle of Attack," NASA SP-3004, 1964.

6. Intrieri, P.F. and Kirk, D.B., "High-Speed Aerodynamics of Several Blunt-Cone Configurations," AIAA Paper 86-0300, Reno, NV, Jan. 1986.

7. Sharma, S.P. and Park, C., "A Survey of Simulation and Diagnostic Techniques for Hypersonic Nonequilibrium Flows," AIAA Paper 87-0406, Reno, NV, Jan. 1987.

8. James, C. S., "Observations of Turbulent-Burst Geometry and Growth in Supersonic Flow," NACA TN 4235, Apr. 1958.

9. Cambier, J-L., Adelman, H. G., and Menees, G. P., "Numerical Simulations of Oblique Detonations in Supersonic Combustion Chambers," 8th International Symposium on Air-Breathing Engines, June 1987, Cincinnati, OH, also submitted to the AIAA Journal of Propulsion and Power.

10. Cambier, J-L., Adelman, H. G., and Menees, G. P., "Numerical Simulations of an Oblique Detonation Engine," AIAA Paper 88-0063, Reno, NV, Jan. 1988.

11. Adelman, H. G. and Menees, G. P., "Analytical and Experimental Validation of the Oblique Detonation Engine Concept," AIAA Paper 88-0063, Reno, NV., Jan. 1988.

12. Camm, J.C. and Rose, P.H., "Electric Shock Tube for High Velocity Simulation," AVCO Everett Research Laboratory, Research Report No. 136, July 1962.

13. Park, C., "Assessment of Two-Temperature Kinetic Model for Dissociating and Weakly Ionizing Nitrogen," AIAA Paper 86-1347, Boston , MA, June 1986.

14. Davy, W.C., Park, C., Arnold, J.O., and Balakrishnan, A., "Radiometer Experiment for the Aeroassist Flight Experiment," AIAA Paper 85-0967, Williamsburg, VA, June 1985.

15. Akey, N. D. and Cross, A. E., "Radio Blackout Alleviation and Plasma Diagnostic Results From a 25,000 Foot per Second Blunt-Body Reentry," *NASA TN D-5615*, Feb. 1970.

16. Grantham, W. L., "Flight Results of 25,000 Foot per Second Reentry Experiment Using Microwave Reflectometers to Measure Plasma Electron Density and Standoff Distance," *NASA TN D-6062*, Dec. 1970.

17. Jones, W. L., Jr. and Cross, A. E., "Electrostatic Probe Measurements of Plasma Parameters for Two Reentry Flight Experiments at 25,000 Feet per Second," *NASA TN D-6617*, Feb. 1972.

18. Candler, G. and MacCormack, R., "The Computation of Hypersonic Ionized Flows in Chemical and Thermal Nonequilibrium," AIAA Paper 88-0511, Reno, NV, Jan. 1988.

19. Cauchon, D. L.,"Radiative Heating Results from the Fire 2 Flight Experiment in a Reentry Velocity of 11.4 Kilometers per Second," NASA TM-X 1402, 1967.

20. Whiting, E. E., Arnold, J. O., Page, W. A., and Reynolds, R. M., "Composition of the Earth's Atmosphere by Shock-layer Radiometry During the PAET Entry Probe Experiment," J. Quantitative Spectroscopy and Radiative Transfer, Vol. 9, Sept. 1973, pp. 837-859.

21. Park, C., "Assessment of Two-Temperature Kinetic Model for Ionizing Air," AIAA Paper 87-1574, June 1987.

TABLE 1. HYPERSONIC FLOW CODE VALIDATION ACTIVITY

Code	Validation activity	Facility
Perfect gas	Generic TAV configurations	3.5 ft HWT
	AOTV configurations	Pressurized ballistic range
Real gas	Cones and blunt bodies	HFFAF (ballistic range)
	Blunt body shock layer	Shock tubes
	Benchmark codes	CCF and NAS
Nozzle/plume	Multi-nozzle perfect gas	3.5 ft HWT
	Semi-direct connect test	HFFAF (16 in. shock tunnel)
Combustion	Oblique detonation wave	20 MW arcjet
Thermochemical Nonequilibrium	Shock tube data	E.A.S.T.
	Shock layer data	HFFAF and 60 MW arcjet
	Flight experiment	AFE
Boundary layer	Tunnel wall boundary layer	HFFAF (16 in. shock tunnel)
	Transition on cones	HFFAF (ballistic range)

TABLE 2. AMES RESEARCH CENTER HYPERSONIC FACILITIES HYPERSONIC FREE FLIGHT FACILITY TEST CONDITIONS

• Stream	
– Mach number	7 (or still air)
– Static pressure	0.005 to 2 atm
– Enthalpy, max.	3000 Btu/lb
• Reynolds number	80,000,000 ft^{-1}
• Model	
– Velocity, max.	30,000 ft/sec
– Acceleration, max.	1,500,000 g
– size, max.	37 mm diam
– Weight, max.	45 g
• Instrumented range section	
– Diameter	3.5 ft
– Length	75 ft
– Number of stations	16

TABLE 3. AMES RESEARCH CENTER HYPERSONIC FACILITIES PRESSURIZED BALLISTIC RANGE TEST CONDITIONS

• Static range conditions	
– Gas composition	Air
– Pressure	0.1 to 1 atm
– Temperature	Ambient
• Reynolds number, max.	40,000,000 ft^{-1}
• Model	
– Velocity, max.	11,000 ft;sec
– Acceleration, max.	1,000,000 g
– Size, max	57 mm diam
– Weight, max.	100 g
• Instrumented range section	
– Length	203 ft
– Size, max.	20 in. wide X 20–60 in. high
– Number of stations	24

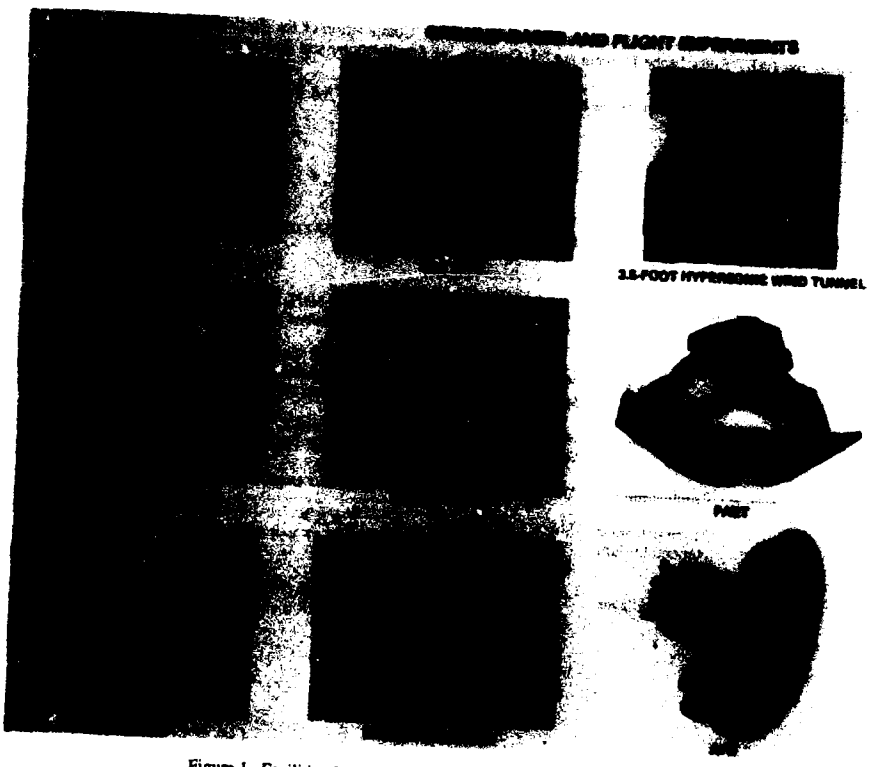


Figure 1 Facilities for studies in hypersonics and entry technology.

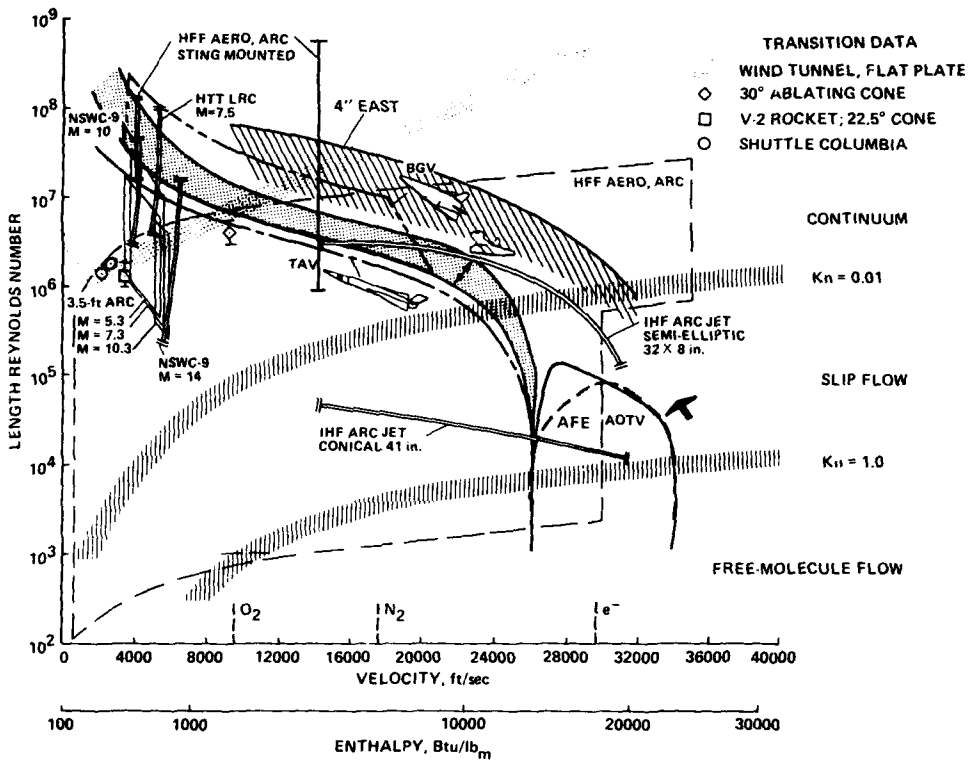


Figure 2 Flight domain simulation capability.

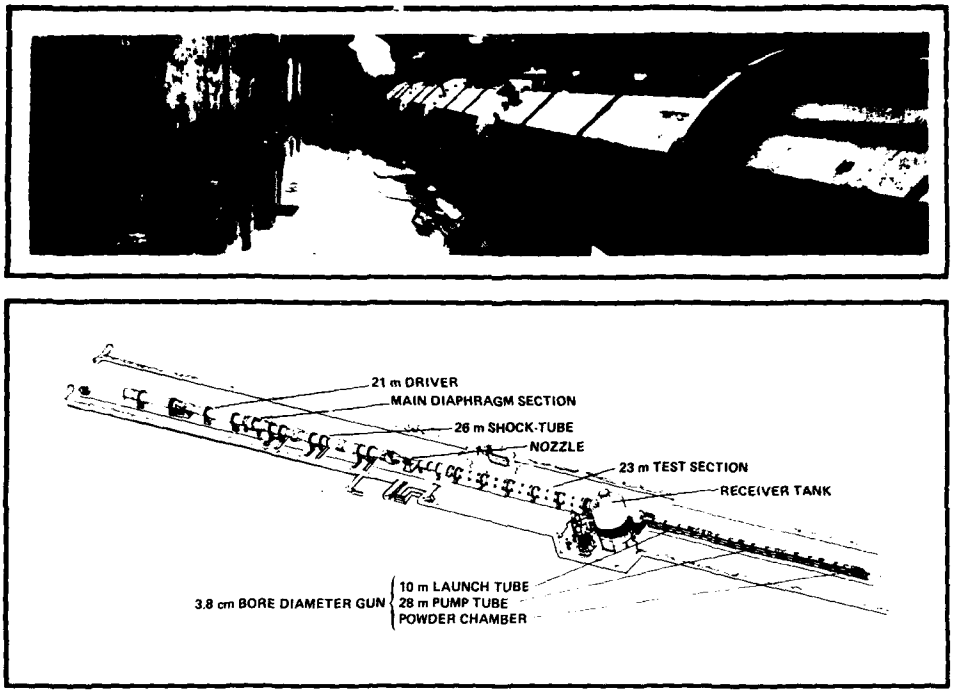


Figure 3 Hypersonic Free Flight Aerodynamic Facility.

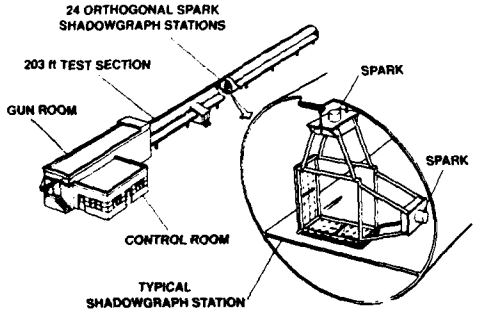


Figure 4 Pressurized ballistic range.



Figure 5 Shadowgraph of 10° cone at Mach 15.

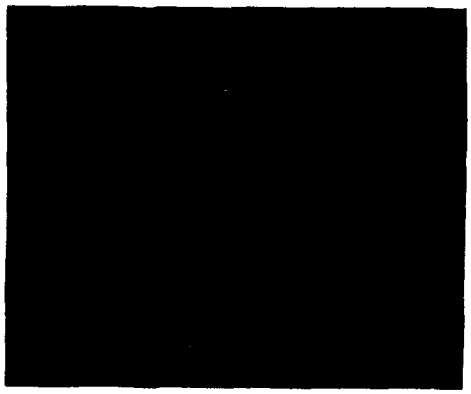


Figure 6 Shadowgraph of 5° cone at Mach 15.

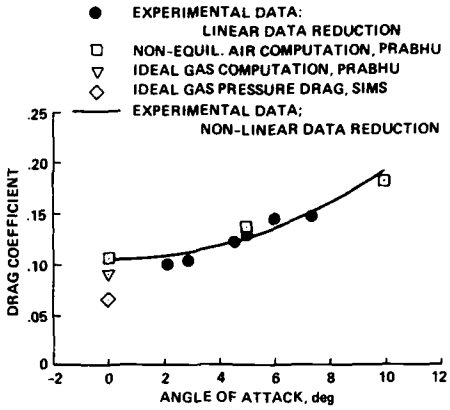


Figure 7 Drag data for 10° cone.



Figure 8 Shadowgraph of Galileo Probe. $M_\infty = 14$, $Re_d = 100{,}000$.

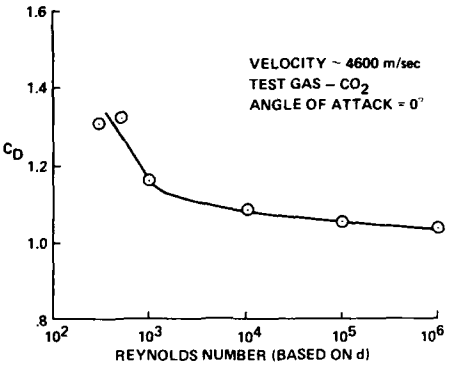


Figure 9 Effect of Reynolds number on drag characteristics of Pioneer Venus.

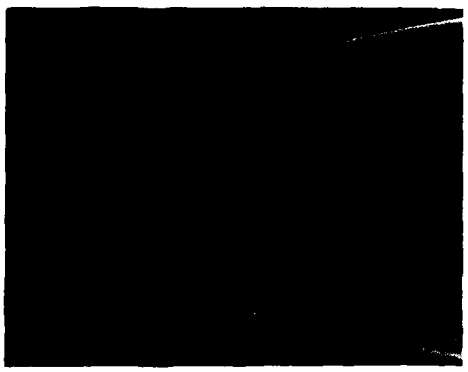


Figure 10 Shadowgraph of symmetric AOTV (Ref. 6).

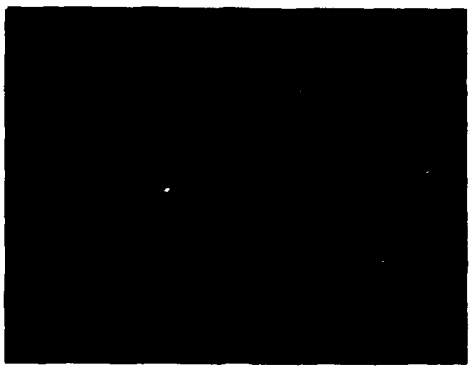


Figure 11 Shadowgraph of the raked elliptic cone (Ref. 6).

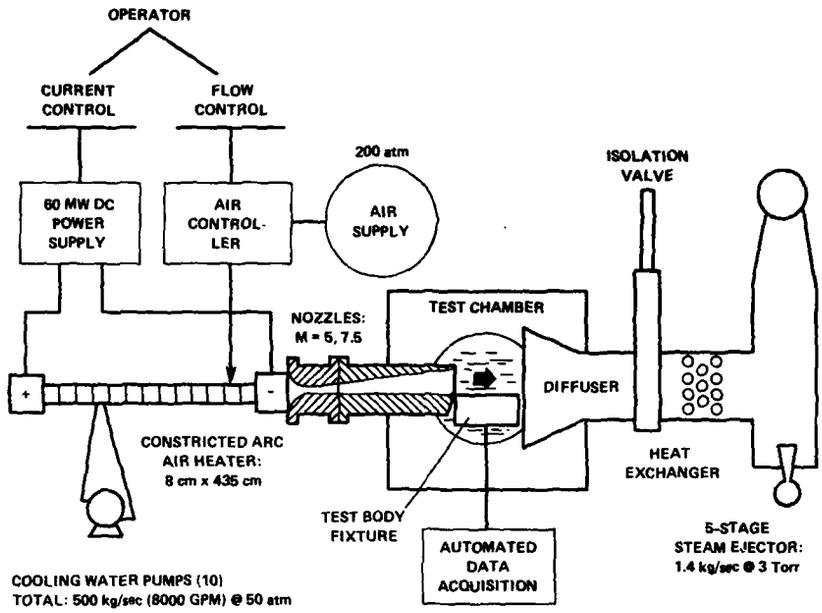


Figure 12 Schematic of interaction heating arcjet facility.

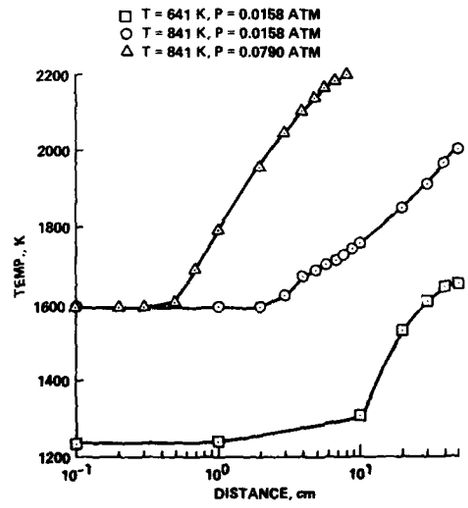


Figure 13 Computed combustion progress behind a 30° oblique shock wave.

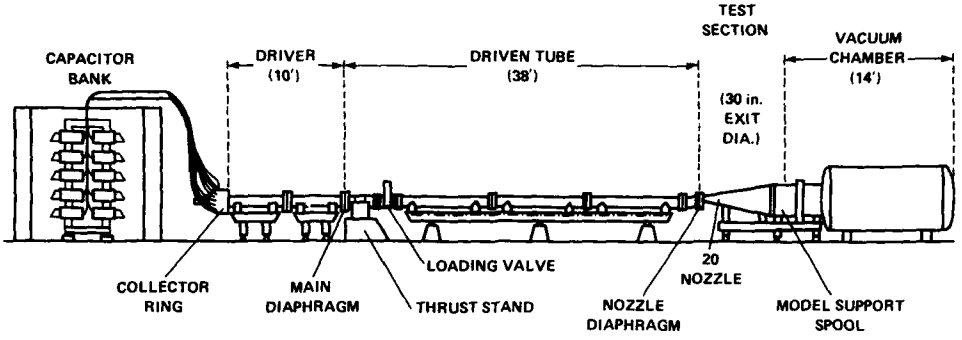


Figure 14 Schematic of Electric Arc-Shock Tube (EAST) Facility.

TUBE, cm	DRIVER GAS	DRIVEN GAS	DRIVER
▽ 10	He	AIR	30-in.
□ 60	He	AIR	30-in.
□ 10	H_2	H_2	54-in.
○ 10	H_2	H_2	CONICAL
◿ 10	He	Kr	54-in.
◺ 10	He	H_2/Ne	54-in.
□ 10	H_2	AIR	CONICAL

TUBE, cm	DRIVER GAS	DRIVEN GAS	DRIVER
○ 10	He	AIR	CONICAL
△ 60	He	AIR	CONICAL
◇ 10	N_2	AIR	CONICAL
△ 10	He	Ar	CONICAL
◇ 10	He	CO_2	CONICAL
⌂ 10	He	AIR	54-in.

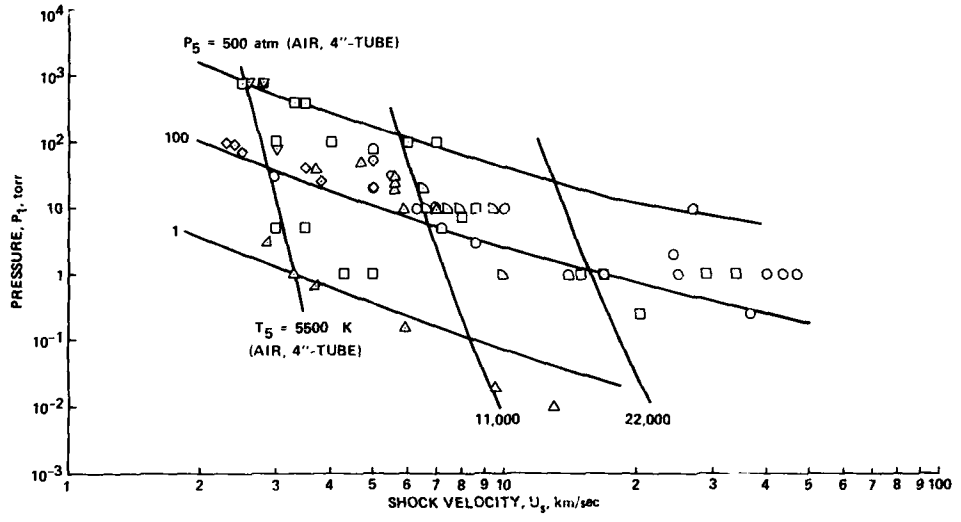


Figure 15 Measured shock velocity vs initial driven-tube charging pressure P_1.

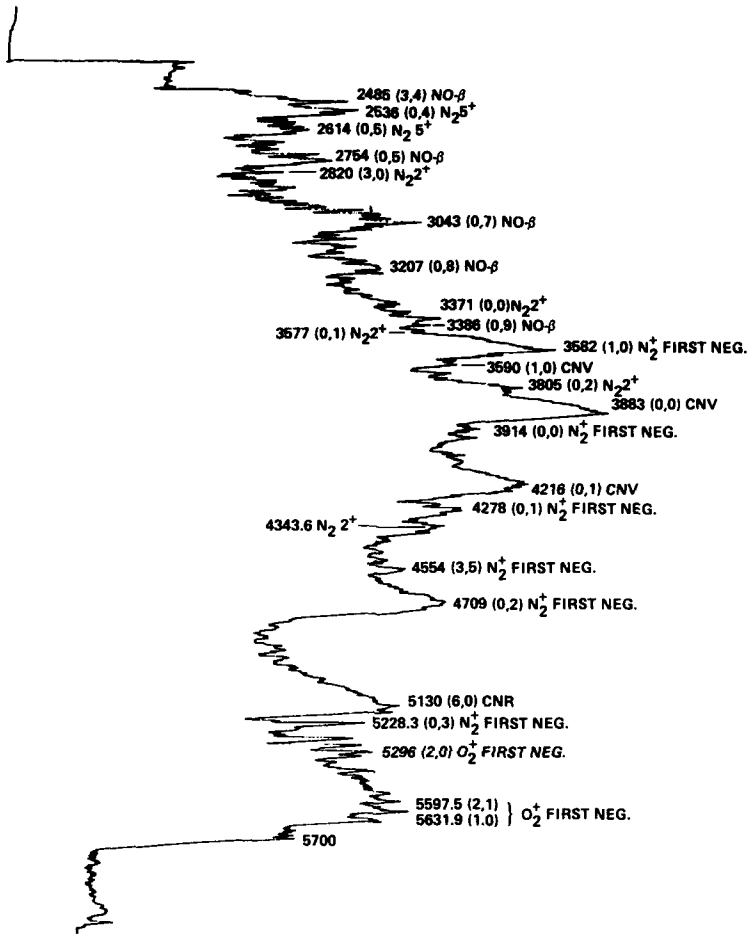


Figure 16 Emission spectra produced in the 10-cm driven aluminum tube. Initial drive pressure = 0.1 torr, shock velocity = 10.3 km/sec.

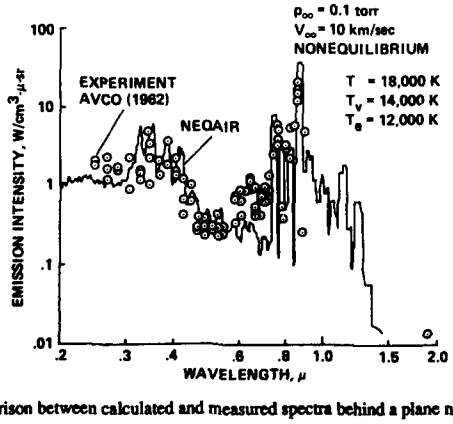


Figure 17 Comparison between calculated and measured spectra behind a plane normal shock wave.



Figure 18 Generic all-body hypersonic aerospace plane model. 75° half-angle delta with elliptic cross section.

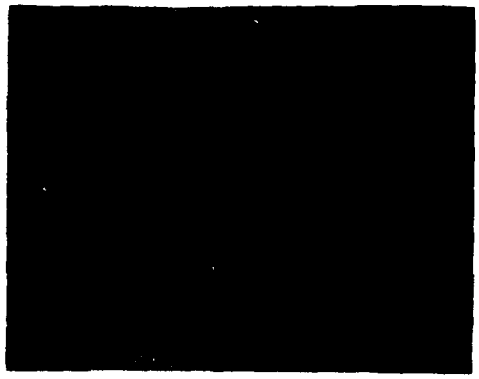


Figure 19 All-body model shadowgraph. $\alpha = 15°$, M = 7.4 half-angle delta with elliptic cross section.

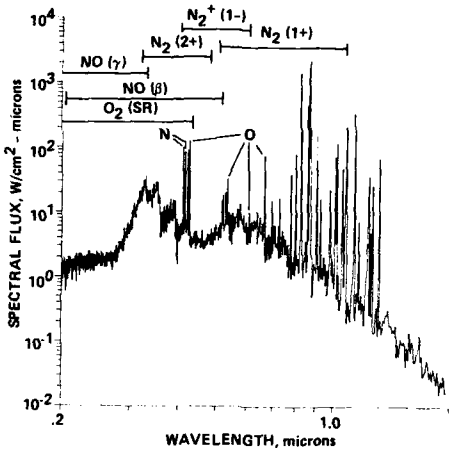


Figure 20 Nonequilibrium-flow spectral flux: shock-layer depth = 20.9 cm.

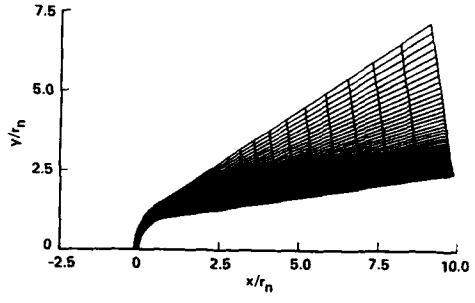


Figure 21 Computational grid for RAM-C.

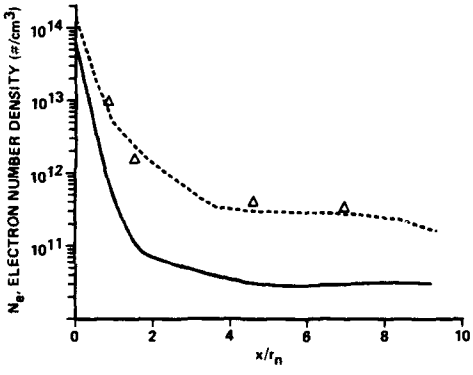


Figure 22 Comparison of peak electron number density. 61 km alt., $M = 23.9$.

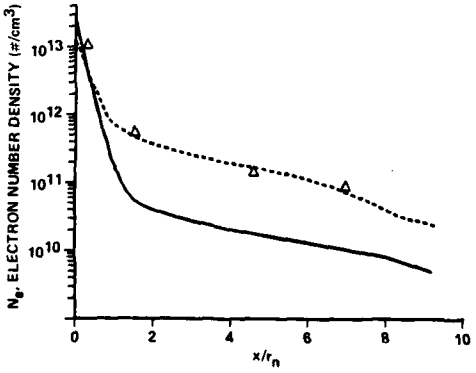


Figure 23 Comparison of peak electron number density. 71 km alt., $M = 23.9$.

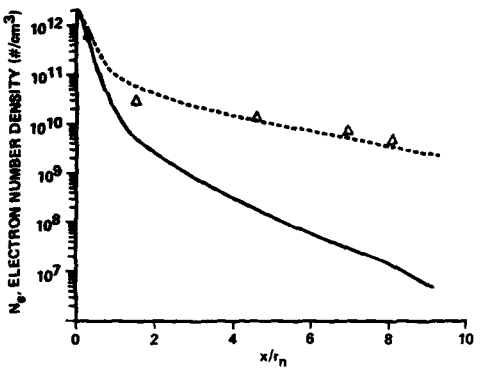


Figure 24 Comparison of peak electron number density. 81 km alt., M = 28.3.

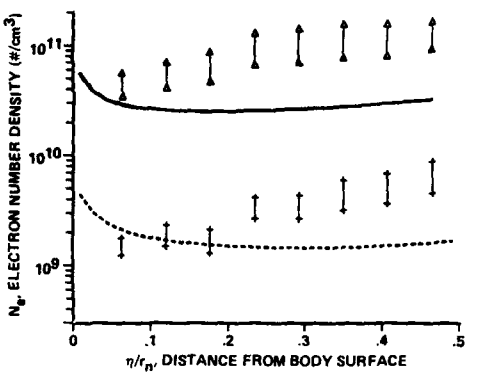


Figure 25 Comparison of electron number density distribution at $x/r_n = 8.1$.

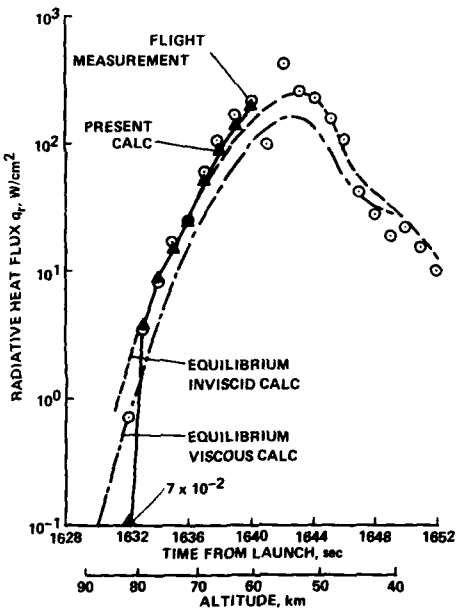


Figure 26 Comparison between calculated and measured stagnation-point radiative heat fluxes for Fire 2.

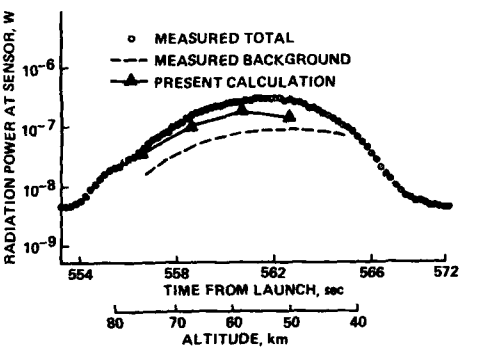


Figure 27 Comparison between calculated and measured radiation intensities at 391 nm in PAET experiment.

CALCULS TRIDIMENSIONNELS DE L'INTERACTION D'UN JET LATERAL AVEC UN ECOULEMENT SUPERSONIQUE EXTERNE

par
M. DORMIEUX
AEROSPATIALE-Division Engins Tactiques
2 à 18, rue Béranger-92320 CHATILLON (FRANCE)

C. MAHE
Office National d'Etudes et de Recherches Aérospatiales (ONERA)
29, avenue de la Division Leclerc-92320 CHATILLON (FRANCE)

RESUME

Les forts niveaux de manoeuvrabilité et les faibles temps de réponse requis pour certains missiles tactiques ont conduit au développement de nouveaux concepts de pilotage, parmi lesquels figure le pilotage par force directe créée par un jet latéral au voisinage du centre de gravité.

Pour sa part, AEROSPATIALE a adopté ce dernier concept pour certains de ses prochains missiles. Toutefois, la création d'un jet latéral sur un engin pose le problème de l'interaction aérodynamique de ce jet sur le missile. Dans le cadre du développement des applications du pilotage par jet, AEROSPATIALE étudie, en étroite collaboration avec l'ONERA, les phénomènes aérodynamiques liés au jet latéral et en particulier les interactions du jet sur un missile.

A ces fins, des calculs tridimensionnels des interactions d'un jet latéral avec un écoulement supersonique externe ont été réalisés au moyen du code numérique Euler FLU3C. L'objet de cette communication est de présenter certaines des validations réalisées.

ABSTRACT

High manoeuvrability levels and short response time required for some tactical missiles have lead to the development of new concepts for control systems among which direct thrust vector control generated by a lateral jet in the vicinity of the center of gravity.

AEROSPATIALE has chosen such a concept for some of its future missiles. However, generation of a transverse jet on a missile raises the problem of the aerodynamic interactions of this jet on the missile. Within the framework of the development of lateral jet control applications, AEROSPATIALE has been investigating, with the collaboration of ONERA, aerodynamic phenomena connected with lateral jet interactions.

For this purpose, three dimensional computations of lateral jet interactions with an external supersonic stream have been achieved by means of the FLU3C Euler solver. The purpose of this paper is to present some of the validations achieved.

1. INTRODUCTION

L'amélioration des systèmes d'armes antichars passe par une meilleure adaptation au tir en confinement et une bonne manoeuvrabilité à très basse vitesse. La capacité antimissile des nouveaux systèmes d'armes antiaériennes nécessite pour le missile défenseur une forte manoeuvrabilité et un temps de réponse très court, y compris à très haute altitude.

Parallèlement à l'amélioration du guidage et du pilotage aérodynamique, le pilotage en force directe par jets latéraux constitue une solution à ces objectifs. Pour réaliser ce pilotage, des tuyères sont placées au voisinage du centre de gravité de l'engin, d'où le nom de pilotage en force. Dans le cas de missiles antimissiles, un pilotage aérodynamique classique lui est associé; ce pilotage mixte rend possible la création de facteurs de charge élevés et conduit à de faibles temps de réponse [1] et [2]. Par ailleurs, la force créée étant d'origine propulsive, elle ne dépend ni de la vitesse de l'engin, ni de la densité de l'air, autrement dit de l'altitude.

Pour sa part, AEROSPATIALE a adopté ce concept pour certains de ses prochains missiles (fig.1).

La présence d'un ou plusieurs jets latéraux sur un missile, réglables en direction et en intensité, pose le problème

des interactions aérodynamiques sur la paroi au voisinage de la tuyère -on parle d'interactions proches-, mais aussi sur les ailes ou empennages situés en aval -on parle d'interactions lointaines- (fig.2). Il s'agit alors de prévoir les caractéristiques aérodynamiques du missile ainsi piloté.

Dans le cadre du développement de ces applications du pilotage par jet, AEROSPATIALE a étudié, en étroite collaboration avec l'ONERA, les phénomènes aérodynamiques liés au jet latéral et en particulier l'influence des interactions du jet sur le missile. Les moyens mis en oeuvre pour mener cette étude ont été de deux types, des essais en soufflerie [3], et des calculs théoriques.

Les essais en soufflerie

Il s'agit soit d'essais sous la responsabilité de l'ONERA (acquisition d'une connaissance des phénomènes, constitution d'une base de données...), soit d'essais liés à des projets ou avant-projets d'AEROSPATIALE (missile antimissile ASTER, missile antichar ERYX...)

Les calculs théoriques

Deux sortes de méthodes sont utilisées, les méthodes semi-empiriques et les méthodes numériques. Les premières supposent la connaissance de l'écoulement dans un plan en aval de la tuyère; elles permettent d'évaluer les interactions lointaines. Les secondes résolvent les équations de la mécanique des fluides, ici les équations d'Euler qui traduisent une modélisation de type fluide parfait; elles permettent d'évaluer l'ensemble des interactions proches et lointaines.

L'objet de cette communication est de présenter des validations réalisées au moyen du code numérique Euler FLU3C, concernant des calculs tridimensionnels des interactions d'un jet latéral avec un écoulement supersonique externe.

Deux validations à caractère fondamental sont d'abord exposées. Les comparaisons calcul/essai portent sur les phénomènes associés au jet (choc détaché, disque de Mach...), et différentes grandeurs aérodynamiques (pression d'arrêt, coefficient de pression, vecteurs vitesse...).

Deux validations à caractère industriel sont ensuite présentées. Elles sont relatives à la configuration d'un missile générique utilisé à l'ONERA, et à celle du missile antimissile ASTER développé par AEROSPATIALE. Les comparaisons calcul/essai portent sur des caractéristiques aérodynamiques globales (coefficient de force normale, position du centre de poussée).

2. PHENOMENES AERODYNAMIQUES

Considérons le cas d'un jet émergeant verticalement d'une plaque plane dans un écoulement supersonique.
Les figures 3 et 4 fournissent une description de la plupart des phénomènes aérodynamiques. En sortie de tuyère, le jet constitue un obstacle qui perturbe l'écoulement supersonique externe. Cette perturbation se traduit par :

- un choc détaché juste en amont de la tuyère,
- un choc en "λ" dû à l'interaction entre ce choc et la couche limite,
- deux zones de recirculation, l'une de décollement en amont de la tuyère, l'autre de recollement en aval.

L'écoulement externe courbe le jet et le contourne. De ce fait, on observe en aval de la tuyère:

- l'apparition d'un choc secondaire,
- la formation d'une trombe ascensionnelle sous le jet,
- une zone à caractère fortement rotationnel traduisant d'importants cisaillements.

Au fur et à mesure que l'on de déplace vers l'aval:

- la hauteur du jet augmente,
- le choc secondaire s'élève,
- deux tourbillons contrarotatifs se forment, puis gagnent en hauteur et en largeur tout en se diffusant.

Comme cela a été mentionné au paragraphe précédent, ces nombreux phénomènes peuvent être rangés en deux classes:

- les interactions proches (figure 5),
- les interactions lointaines (figure 6).

3. CODE FLU3C

Le code FLU3C a été développé à l'ONERA, en collaboration avec AEROSPATIALE, qui en outre, en a effectué l'industrialisation.

Du fait des fortes discontinuités existant dans l'écoulement, le choix de la méthode numérique s'est porté sur les schémas décentrés dont les développements depuis quelques années ont permis d'améliorer la robustesse et la précision [4]. Comme cela a été dit au paragraphe 1, une modélisation du type fluide parfait a été retenue. Le code de calcul résout les équations d'Euler instationnaires tridimensionnelles. Le schéma numérique et la mise en oeuvre du code sont décrits

précisément en [5]. La mise en oeuvre est présentée ci-dessous de façon succincte.

La mise en oeuvre

Le calcul est effectué sur un seul domaine. Les conditions aux limites sont prises en compte au moyen de "fenêtres" définies sur les frontières de ce domaine. Cette technique a permis d'imposer facilement la condition limite dans la section de sortie de tuyère (fenêtre) située à la paroi (frontière).

Le code est vectorisé sur le CRAY et la gestion des entrées/sorties fait appel à un stockage plan par plan qui permet d'occuper peu de place en mémoire centrale. La recherche d'une solution stationnaire nécessite pour chaque itération en temps, d'amener successivement en mémoire centrale chacun des plans et impose donc un nombre important d'entrées/sorties. Le calcul d'une solution stationnaire utilise une technique d'accélération de convergence par pas de temps local.

Une version du programme a été développée pour résoudre les problèmes où il existe une direction de l'espace selon laquelle l'écoulement est supersonique. Cette version utilise une technique dite de pseudo-marche en espace. Elle consiste à faire converger la solution dans le temps plan par plan. De cette façon, chaque plan est appelé une et une seule fois en mémoire centrale. Il en résulte une forte diminution des entrées/sorties et une accélération sensible de la convergence.

Le maillage tridimensionnel de calcul est constitué de maillages bidimensionnels successifs. Cette technique permet de traiter un nombre important de configurations.

4. COMPARAISONS CALCUL/ESSAI

Les validations effectuées sont de deux types: fondamental d'une part, industriel d'autre part. Il est important de noter ici que pour toutes les validations présentées, le jet est de même nature que l'écoulement principal (gaz froid).

4.1. LES VALIDATIONS A CARACTERE FONDAMENTAL

Elles concernent deux configurations, la première de type plaque plane, la seconde de type fuselage.

4.1.1. LA PLAQUE PLANE

La figure 7 précise les caractéristiques du montage en soufflerie et du maillage de calcul. La configuration et les conditions aérodynamiques sont les suivantes:

- une plaque plane (plan XY),
- un écoulement externe supersonique dont le nombre de Mach est égal à 2,
- une tuyère de section de sortie rectangulaire située dans le plan de la plaque,
- un jet émergeant verticalement de la tuyère à Mach 2,5 et de pression génératrice environ 14 fois supérieure à celle de l'écoulement externe.

Les essais effectués à la soufflerie de Chalais-Meudon S5Ch, ont permis de réaliser:

- des strioscopies,
- des mesures de pression à la paroi le long de l'axe X passant par le centre de la section de sortie de la tuyère,
- des sondages dans un plan transverse en aval de la tuyère.

Le calcul a été effectué sur le demi-domaine $Y \geq 0$. Le maillage total comprend environ 700000 points. Ce maillage très dense a été retenu afin de déterminer avec précision les phénomènes que le calcul est capable de restituer. Les conditions de sortie de la tuyère sont définies sur 175 points.

La figure 8 fournit les lignes isobares issues du calcul dans le plan de symétrie de l'écoulement, le plan de la plaque et un plan transverse situé loin en aval de la tuyère. Sur cette figure, on observe:

- le choc détaché,
- le choc secondaire,
- les surpressions et dépressions qui apparaissent au voisinage de la tuyère,
- le disque de Mach,
- une onde incidente créée au voisinage du disque de Mach, qui correspond à une zone de légère surpression.

La figure 9 présente les lignes iso-Mach calculées dans le plan de symétrie de l'écoulement. On a reporté sur ce tracé le lieu du choc détaché obtenu par strioscopie lors de l'essai. On note la bonne capture du choc détaché par le code FLU3C, sauf à la paroi où se produit une interaction choc/couche limite non prise en compte par la modélisation fluide parfait utilisée par le code. On retrouve sur ce tracé certains des phénomènes cités précédemment. On note en particulier une zone de très fortes survitesses apparaissant dans le jet en sortie de tuyère, suivie d'une chute des vitesses allant jusqu'à la formation d'une poche subsonique.

La figure 10 illustre les évolutions du coefficient de pression le long de l'axe X de la plaque, obtenus par l'essai et

le calcul. Dans les zones de recirculation -en amont et en aval de la tuyère-, le calcul ne traduit pas l'évolution du coefficient de pression, ce qui s'explique par l'absence de modélisation des phénomènes de couche limite. En revanche, la zone de recompression progressive est à peu près correctement captée. La surpression liée à l'onde incidente l'est aussi, mais elle est positionnée trop en aval.

Les figures 11 à 14 présentent respectivement les lignes isobares, isopression d'arrêt, isorotationnelles et les vecteurs vitesse, dans un plan transverse situé 17,5.Ds (Ds diamètre moyen de la section de sortie de tuyère) en aval de la tuyère. Précisons que toutes les valeurs d'essai au voisinage de la paroi ne sont pas des mesures, mais résultent d'extrapolations.

La position du choc secondaire est à peu près retrouvée sur les lignes isobares (fig.11). En revanche la zone de dépression captée par le calcul est trop haute et trop intense.

Pour les résultats relatifs aux pressions d'arrêt (fig. 12), on note une profonde divergence entre l'essai et le calcul. D'après l'essai, à cette distance de la tuyère, le jet a complètement éclaté et ne se repère plus que par la ligne de pression d'arrêt égale à celle de l'écoulement externe amont. En revanche, le calcul fournit des pressions d'arrêt quatre fois supérieures. La forme du jet diffère également. Le calcul ne rend donc pas compte de la diffusion du jet.

La forme, la position et l'intensité de la zone rotationnelle (fig.13) ne sont pas reproduites de manière satisfaisante par le calcul.

La figure 14 présente l'évolution des vecteurs vitesse transverse dans ce même plan. La correspondance est meilleure. Le calcul surestime la hauteur des tourbillons et l'intensité des vecteurs vitesse transverse. En revanche, la forme des tourbillons et la position du choc secondaire sont bien restituées.

Le calcul très imparfait des interactions lointaines appelle une remarque. Etant donnée la très grande finesse du maillage utilisé dans tout le sillage du jet, on peut penser que dans cette région, la solution calculée est assez proche de la solution exacte des équations d'Euler. Dans ces conditions, la non prise en compte des termes de viscosité dans le modèle fluide parfait peut expliquer les divergences entre essai et calcul.

4. 1. 2. LE FUSELAGE

La figure 15 présente les caractéristiques du montage en soufflerie et du maillage de calcul. La configuration et les conditions aérodynamiques sont les suivantes:

- un ensemble ogive + cylindre placé à une incidence nulle dans un écoulement externe à Mach 2,
- un jet émerge d'une tuyère circulaire dont la section de sortie est située à 6,5.D en aval de la pointe avant (D étant le diamètre du fuselage),
- en sortie de tuyère, le jet est caractérisé par un nombre de Mach égal à 2,5, une pression d'arrêt 28 fois supérieure à celle de l'écoulement externe amont, et une inclinaison vers l'aval de 30° par rapport à la normale à l'axe engin.

Les essais effectués à la soufflerie de Modane S2Ma ont fourni des sondages dans trois plans transverses en aval de la tuyère.

Le calcul a été effectué sur un demi-domaine. Le maillage total comprend 190000 points. Les conditions de sortie de la tuyère sont définies sur 153 points. Le temps CPU nécessité par ce calcul est de 1 heure sur CRAY XMP.

Les figures 16 à 18 présentent les lignes isobares dans les plans transverses situés respectivement à 1,5.D, 3,5.D et 6,5.D en aval de la tuyère (D diamètre du fuselage). D'une façon générale, on note une bonne correspondance entre calcul et essai:

- dans le premier plan, le calcul capte correctement le choc primaire, la poche d'écoulement dépressionnaire, le choc secondaire,
- plus en aval, le calcul restitue bien les chocs primaire et secondaire, à peu près la poche dépressionnaire (un peu trop haute et trop intense),
- à 6,5.D de la tuyère, le choc primaire est situé en dehors du domaine de sondage; en ce qui concerne le choc secondaire et la poche dépressionnaire, les résultats demeurent corrects.

Les figures 19 à 21 présentent les vecteurs vitesse transverse dans les mêmes plans. A nouveau, il y a une bonne correspondance entre calcul et essai, excepté dans le deuxième plan où la hauteur des tourbillons obtenus par le calcul est trop élevée. On observe très bien la trace du choc primaire dans le premier plan et le développement des tourbillons sur l'ensemble des trois plans.

Le calcul des interactions lointaines donne de meilleurs résultats pour cette validation que pour la précédente. Bien qu'il soit difficile de les comparer (plaque plane: inclinaison du jet nulle par rapport à la verticale - fuselage: inclinaison du jet de 30° par rapport à la normale à l'axe engin), on peut remarquer que la seconde utilise un maillage beaucoup moins dense que la première. La diffusion numérique augmentant avec le relâchement du maillage, celle-ci est alors plus importante dans le deuxième calcul et peut expliquer en partie cette différence.

Les validations suivantes concernent l'évaluation des coefficients globaux d'un missile piloté par jet latéral.

4. 2. VALIDATIONS A CARACTERE INDUSTRIEL

Elles concernent deux configurations de missile, la maquette "ONERA" et le missile ASTER.

4. 2. 1. LA MAQUETTE "ONERA"

La figure 22 présente les principales caractéristiques de cette validation. La configuration et les conditions aérodynamiques sont les suivantes:

- un missile constitué d'un ensemble ogive + cylindre, et équipé de quatre ailes calées soit en "+", soit en "X",
- la maquette est placée dans un écoulement externe amont à Mach 2 pour différentes incidences,
- lors de la simulation du pilotage en force, le jet sort à Mach 2,5 d'une tuyère située à l'intrados du fuselage, un calibre en amont de l'apex des ailes.

Les essais réalisés à la soufflerie de Modane S3Ma ont consisté en des pesées de voilures en présence et en absence de jet.

Les calculs ont été effectués avec un maillage total de 380000 points. Les temps CPU sur CRAY XMP nécessités par ces calculs ont été de 30 minutes en absence de jet et de 70 minutes en présence de jet, cet écart s'expliquant par l'impossibilité d'utiliser la méthode de pseudo-marche en espace dans la zone proche de la tuyère, du fait de la présence d'une poche subsonique.

La figure 23 présente des résultats de calcul uniquement. Il s'agit des répartitions de pression sur la maquette à 8° d'incidence en présence ou non du jet. D'après le calcul, on note que les interactions de jet sont importantes. Pour le cas avec jet on distingue, la trace du choc détaché en amont de la tuyère, et une importante zone de dépression en aval de celle-ci.

Les figures 24 et 25 illustrent les variations du coefficient de force normale en fonction de l'incidence, respectivement d'une aile horizontale (les ailes étant calées en "+"), et d'une aile sous le vent (les ailes étant calées en "X"). Le calcul restitue assez bien l'évolution du coefficient de force normale, et en particulier, l'écart à incidence donnée entre valeurs avec et sans jet.

4. 2. 2. LE MISSILE ASTER

La figure 26 présente cette validation. La configuration et les conditions aérodynamiques sont les suivantes:

- un fuselage muni de quatre nageoires et de quatre gouvernes coplanaires calées en "+", et terminé par un rétreint,
- le nombre de Mach de l'écoulement externe amont est égal à 2, et l'incidence est égale à 12°,
- lors de la simulation du pilotage en force, un jet sort du bord marginal de la nageoire inférieure.

Les essais effectués à la soufflerie de Modane S2Ma ont fourni des strioscopies et les efforts globaux sur le missile en présence et en absence de jet.

Les calculs ont été effectués avec un maillage total d'environ 300000 points. Les temps CPU sur CRAY XMP nécessités par ces calculs sont de 35 minutes dans le cas sans jet, et de 1 heure 45 minutes dans le cas avec jet. Cet écart s'explique comme pour la validation précédente par l'impossibilité d'utiliser la technique de pseudo-marche en espace dans la zone proche de la tuyère.

Les répartitions de pression calculées à la paroi de l'ASTER avec et sans jet (fig.27) mettent bien en évidence les interactions de jet (trace du choc détaché en amont de la tuyère, zones de surpression et de dépression).

La figure 28 présente dans le cas avec jet la répartition de pression à la paroi de l'ASTER et les lignes isobares dans un plan transverse situé juste en aval de la tuyère. Cette coupe témoigne de la complexité de l'écoulement: outre les interactions dues au jet (choc primaire, zones de surpression et de dépression), on y distingue également l'effet d'incidence (tourbillons marginaux aux extrémités des ailes horizontales).

L'augmentation de l'altitude se traduit par une baisse de la pression externe et conduit à un éclatement du jet plus important. Les conséquences sur la forme et la position du choc primaire sont illustrées par les strioscopies de la figure 29: le choc se redresse et se déplace vers l'amont. On observe une bonne correspondance entre calcul et essai.

Le tableau de la figure 30 donne les erreurs relatives sur les coefficients aérodynamiques prédits par le calcul. L'erreur sur le coefficient de force normale est nettement inférieure à 10% et celle sur la position du centre de poussée au quart de calibre.

Ces résultats particulièrement satisfaisants sont meilleurs que ceux obtenus dans la validation précédente relative à la maquette "ONERA". Cela peut s'expliquer par le fait que l'influence des interactions de jet sur l'ASTER est nettement plus faible, de part sa géométrie (la tuyère est implantée dans le bord marginal de la nageoire).

5. CONCLUSION

D'un point de vue fondamental, on constate que certains phénomènes sont bien captés par le calcul (choc détaché, disque de Mach), d'autres le sont moins bien (position et intensité des tourbillons, diffusion du jet), d'autres enfin ne le sont pas du tout du fait de la modélisation fluide parfait (décollement en amont de la tuyère, recollement en aval de la tuyère).

D'un point de vue industriel, les interactions sont bien calculées par le code FLU3C dans le cas d'un jet froid, ce qui fait de ce code un outil précieux au stade des avant-projets et projets.

Pour l'avenir, on peut citer trois grands axes de développement: le maillage adaptatif, la simulation de la viscosité et la simulation des effets thermiques (jet chaud).

REFERENCES

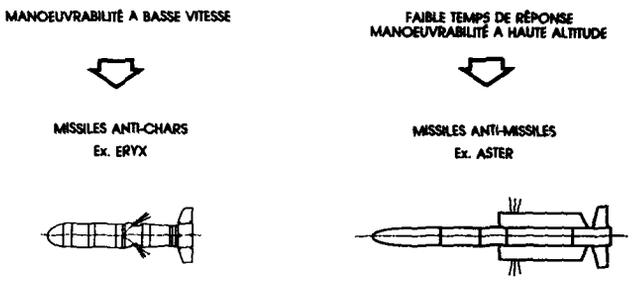
[1] - G. Selince. Un Nouveau Concept de Pilotage des Missiles. Application aux Sol-air. AGARD LS n°135, 1984.

[2] - B. Lazure, Pif-Paf Control of Tactical Missiles. AGARD FMP - Stability and Control of Tactical Missile Systems - ANKARA, May 1988 (classifié).

[3] - M. Leplat, P. Champigny, M. Robert. Interactions Aérodynamiques de Jets Transversaux sur Missiles. AGARD-CP n° 431, 1987 (classifié).

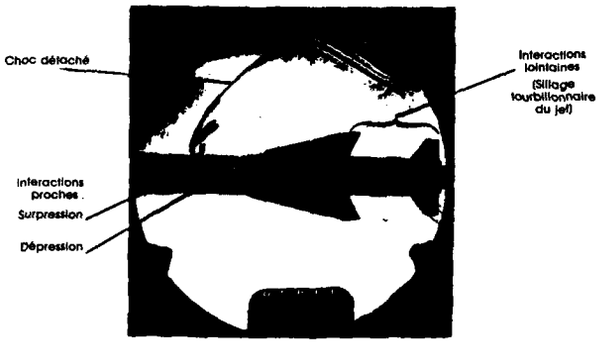
[4] - M. Borrel, J.L. Montagné. Numerical Study of a Non-Centered Scheme with Application to Aerodynamics. AIAA paper n° 85-1497-CP, 1985.

[5] - M. Borrel, J.L. Montagné, J. Diet, Ph. Guillen, J. Lordon. Méthode de Calcul d'Ecoulements autour de Missiles Tactiques à l'aide d'un Schéma Décentré. La Recherche Aérospatiale 1988-2.



APPLICATIONS DU PILOTAGE PAR JETS LATÉRAUX A L'AEROSPATIALE

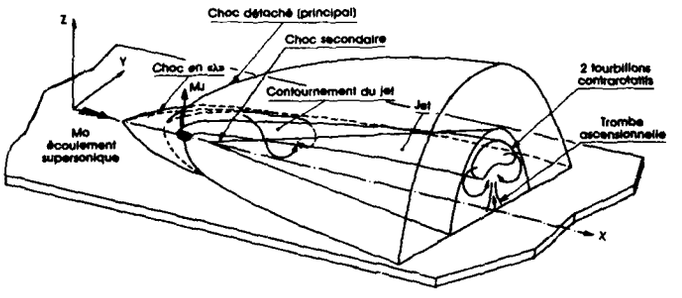
Fig. 1



STRIOSCOPIE

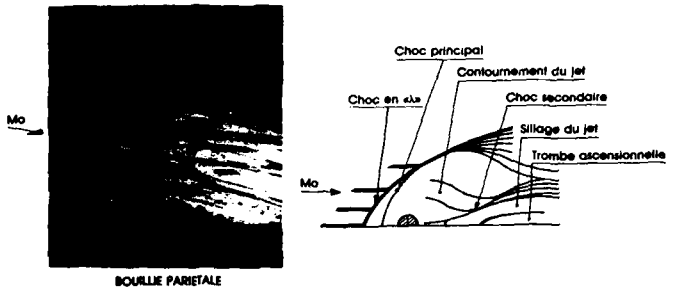
PILOTAGE PAR JETS LATERAUX
INTERACTIONS JET-ECOULEMENT

Fig. 2



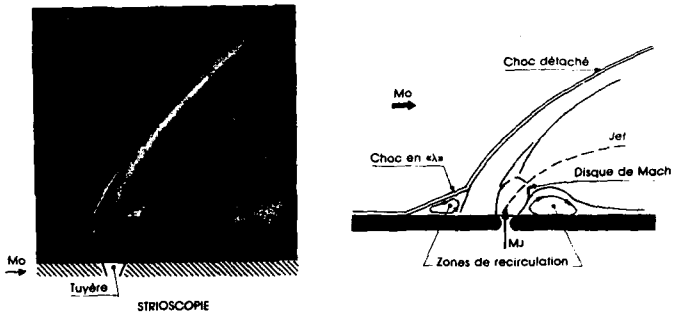
DESCRIPTION TRIDIMENSIONNELLE DE L'ECOULEMENT

Fig. 3



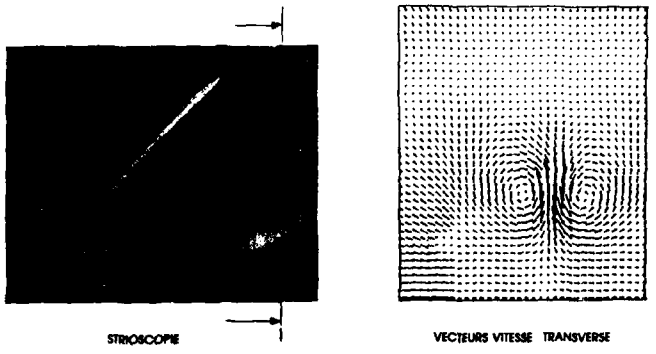
DESCRIPTION DE L'ECOULEMENT PARIETAL

Fig. 4



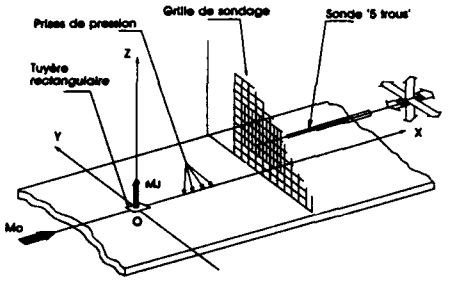
INTERACTIONS PROCHES

Fig. 5



INTERACTIONS LOINTAINES

Fig. 6



ESSAI

- Strioscopie
- Pressions pariétales
- Sondage dans un plan X = cte

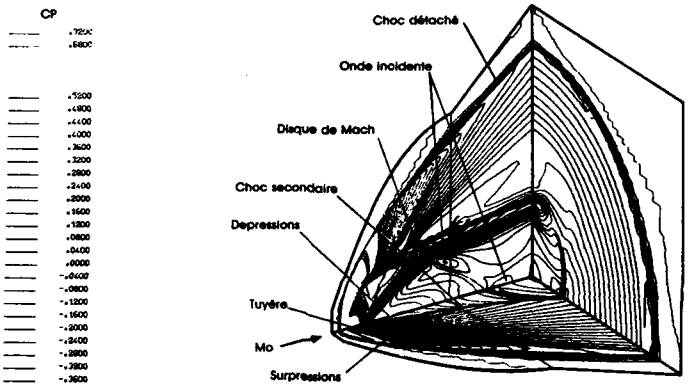
CALCUL

- Demi-domaine Y ≥ 0
- Maillage de 135 x 70 x 75 points
- 175 points dans la section de sortie de la tuyère

VALIDATION FONDAMENTALE : PLAQUE PLANE

Mo = 2 MJ = 2.5 PIJ/PIO = 14.3

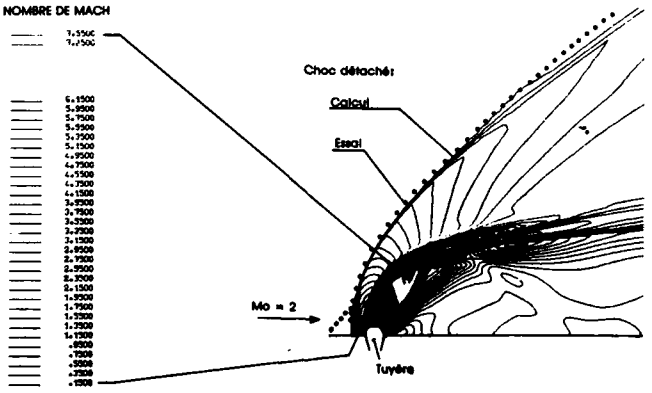
Fig. 7



PLAQUE PLANE (Mo = 2 – MJ = 2.5 – PIJ/PIO = 14.3)

LIGNES ISOBARES – CALCUL FLU3C

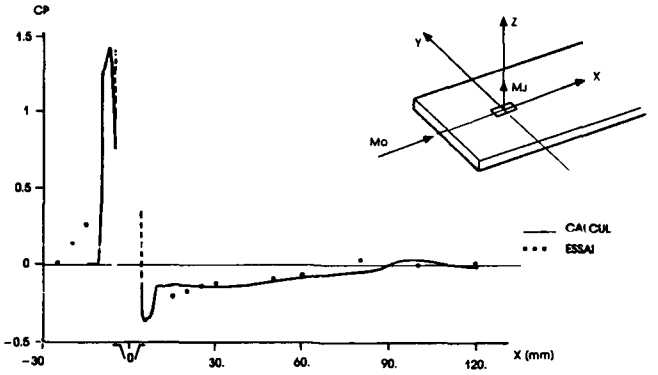
Fig. 8



PLAQUE PLANE (Mo = 2 – MJ = 2.5 – PIJ/PIO = 14.3)

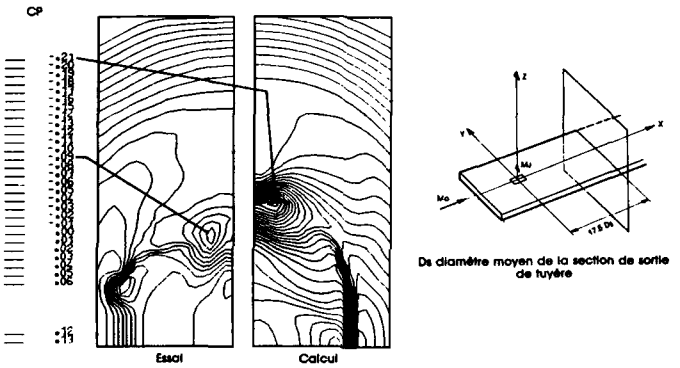
LIGNES ISO–MACH DANS LE PLAN DE SYMETRIE – CALCUL FLU3C

Fig. 9



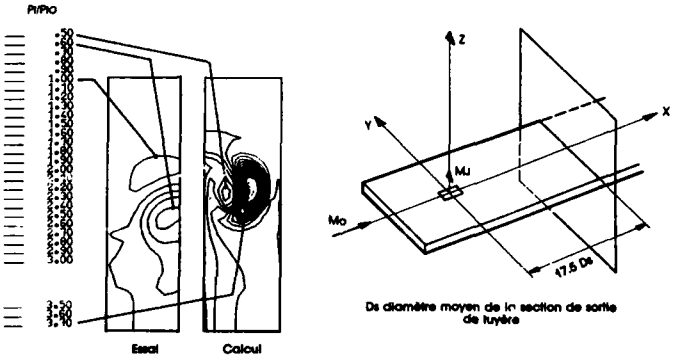
PLAQUE PLANE (Mo = 2 – MJ = 2.5 – PtJ/Pto = 14.3)
COEFFICIENT DE PRESSION PARIETALE SELON X

Fig. 10



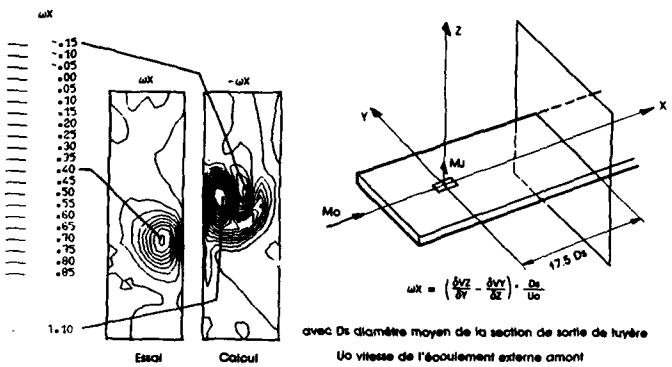
PLAQUE PLANE (Mo = 2 – MJ = 2.5 – PtJ/Pto = 14.3)
LIGNES ISOBARES DANS LE PLAN TRANSVERSE 17.5 Ds
EN AVAL DE LA TUYERE

Fig. 11



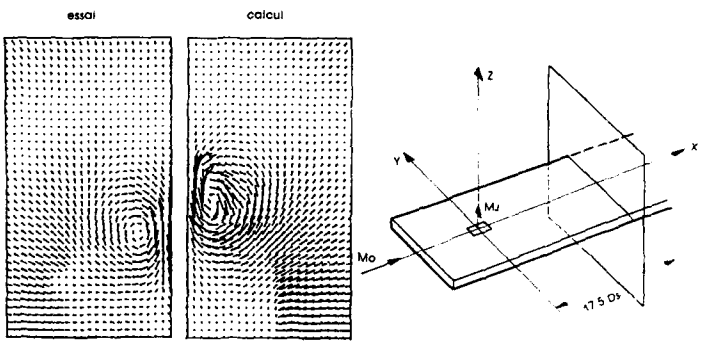
PLAQUE PLANE (Mo = 2 – MJ = 2.5 – PtJ/Pto = 14.3)
LIGNES ISOPRESSION D'ARRET DANS LE PLAN TRANSVERSE 17.5 Ds
EN AVAL DE LA TUYERE

Fig. 12



PLAQUE PLANE (Mo = 2 – MJ = 2.5 – PIJ/PIO = 14.3)
LIGNES ISOROTATIONNELLES DANS LE PLAN TRANSVERSE 17.5 Ds
EN AVAL DE LA TUYERE

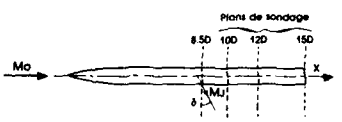
Fig. 13



PLAQUE PLANE (Mo = 2 – MJ = 2.5 – PIJ/PIO = 14.3)
VECTEURS VITESSE DANS LE PLAN TRANSVERSE 17.5 Ds EN AVAL DE LA TUYERE

Fig. 14





ESSAI

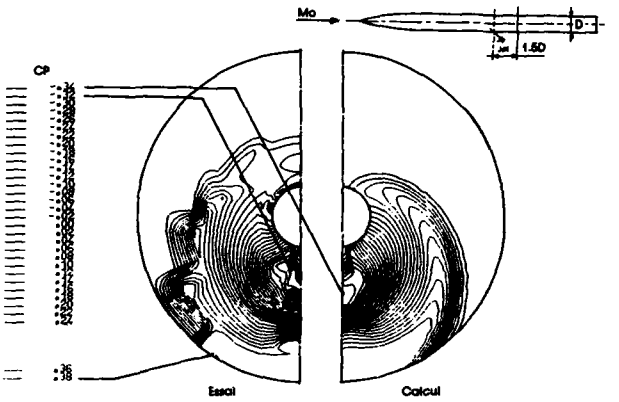
– Sondage dans 3 plans X = cte

CALCUL

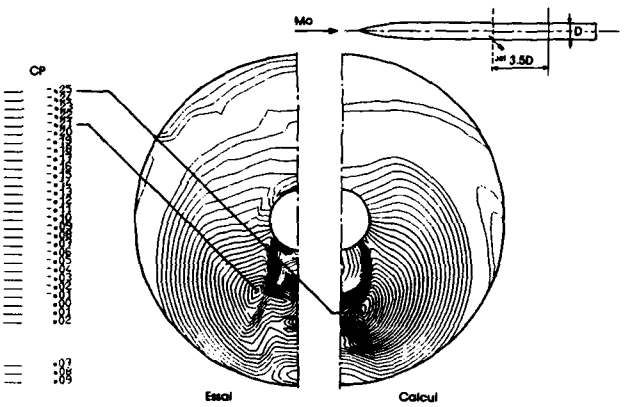
– Demi-domaine
– Maillage de 190 000 points
– 153 points dans la section de sortie de tuyère
– 1 heure CPU sur CRAY XMP

VALIDATION FONDAMENTALE : FUSELAGE
α = 0° Mo = 2 MJ = 2.5 δ = 30° PIJ/PIO = 28

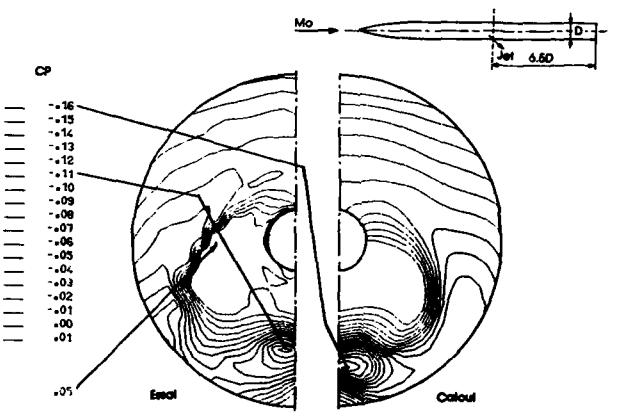
Fig. 15



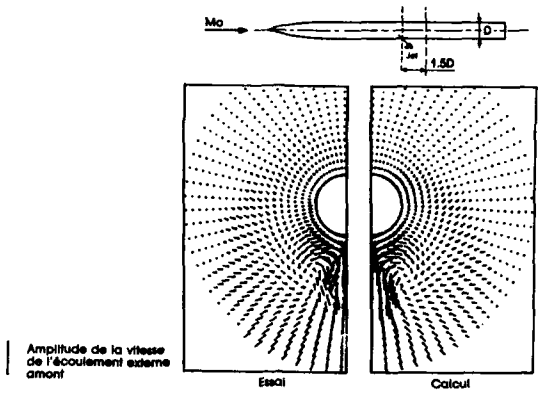
FUSELAGE (Mo = 2 – MJ = 2.5 – PtJ/Pto = 28)
LIGNES ISOBARES DANS LE PLAN TRANSVERSE 1.5D EN AVAL DE LA TUYERE
Fig. 16



FUSELAGE (Mo = 2 – MJ = 2.5 – PtJ/Pto = 28)
LIGNES ISOBARES DANS LE PLAN TRANSVERSE 3.5D EN AVAL DE LA TUYERE
Fig. 17

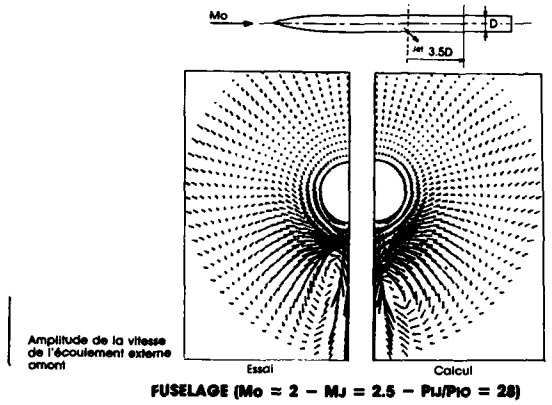


FUSELAGE (Mo = 2 – MJ = 2.5 – PtJ/Pto = 28)
LIGNES ISOBARES DANS LE PLAN TRANSVERSE 6.5D EN AVAL DE LA TUYERE
Fig. 18



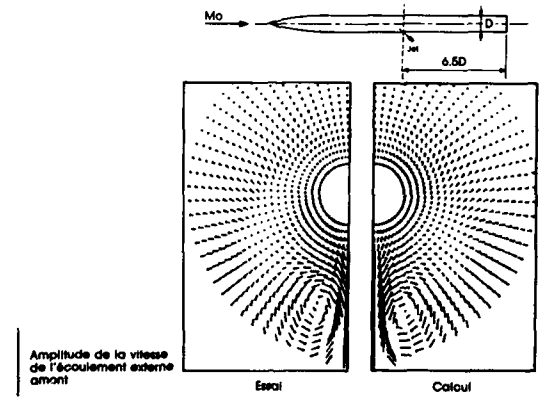
FUSELAGE (Mo = 2 – MJ = 2.5 – PtJ/Pto = 28)
VECTEURS VITESSE DANS LE PLAN TRANSVERSE 1.5D EN AVAL DE LA TUYERE

Fig. 19



FUSELAGE (Mo = 2 – MJ = 2.5 – PtJ/Pto = 28)
VECTEURS VITESSE DANS LE PLAN TRANSVERSE 3.5D EN AVAL DE LA TUYERE

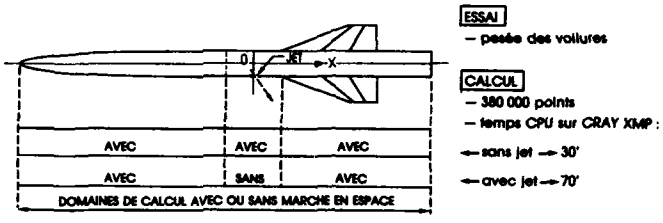
Fig. 20



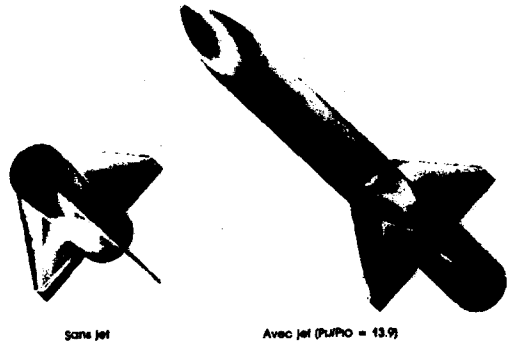
FUSELAGE (Mo = 2 – MJ = 2.5 – PtJ/Pto = 28)
VECTEURS VITESSE DANS LE PLAN TRANSVERSE 6.5D EN AVAL DE LA TUYERE

Fig. 21

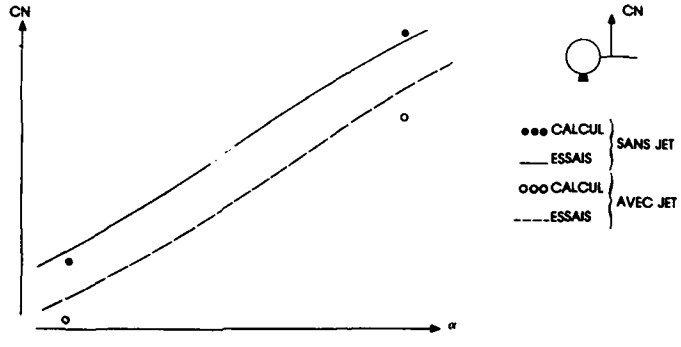
2 CONFIGURATIONS D'AILES CRUCIFORMES : AILES EN +, AILES EN X



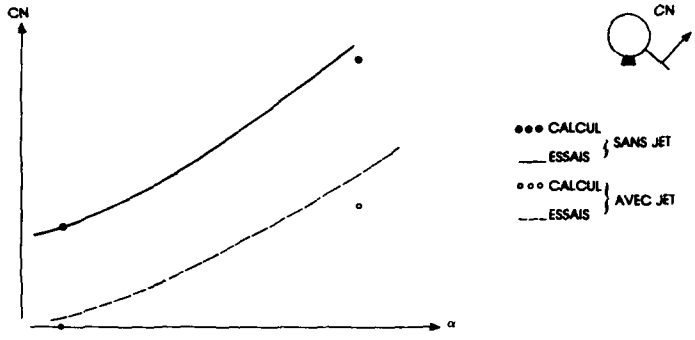
VALIDATION INDUSTRIELLE : MAQUETTE "ONERA"
Mo = 2 MJ = 2.5 PtJ/Pto = 13.9
Fig. 22



MAQUETTE «ONERA» (AILES EN X – Mo = 2 – α = 8°)
REPARTITION DE PRESSION – CALCUL FLU3C
Fig. 23

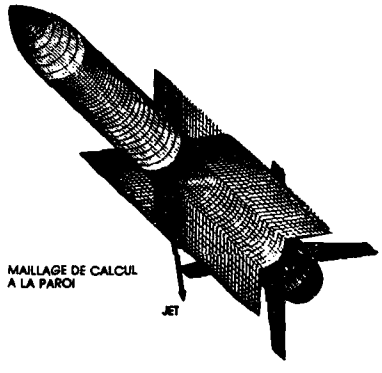


MAQUETTE "ONERA" (AILES EN + – Mo = 2)
COEFFICIENT DE FORCE NORMALE D'UNE AILE HORIZONTALE
Fig. 24



MAQUETTE "ONERA" (AILES EN X — Mo = 2)
COEFFICIENT DE FORCE NORMALE D'UNE AILE INFÉRIEURE

Fig. 25



ESSAI
- Strioscopies
- Pesées globales

CALCUL
- 300 000 points
- Temps CPU sur CRAY XMP :
  Sans Jet — 35'
  Avec Jet — 1 h 45'

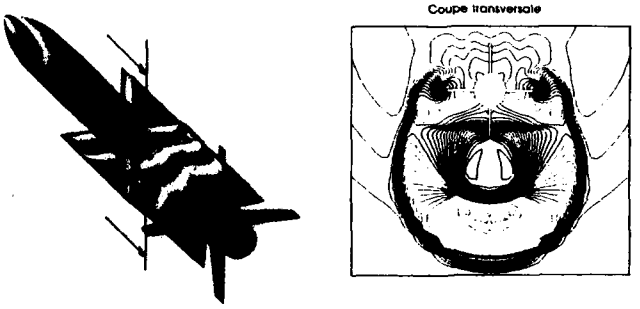
VALIDATION INDUSTRIELLE : MISSILE ASTER
Mo = 2 α = 12°

Fig. 26



MISSILE ASTER (Mo = 2 — α = 12°)
REPARTITION DE PRESSION — CALCUL FLU3C

Fig. 27



MISSILE ASTER (Mo = 2 – α = 12° - AVEC JET)
REPARTITION DE PRESSION – CALCUL FLU3C

Fig. 28



Strioscopie – altitude = 0 m

Strioscopie – altitude >> 0 m

MISSILE ASTER (Mo = 2 – α = 12° - AVEC JET)
POSITION DU CHOC DETACHE – COMPARAISON CALCUL FLU3C/ESSAI

Fig. 29

	SANS JET LATÉRAL	AVEC JET LATÉRAL	
		ALTITUDE = 0 m	ALTITUDE >> 0 m
$\frac{\Delta CN}{CN}$	7 %	4 %	4 %
$\frac{\Delta Xcp}{D}$	0,23	0,14	0,10

D diamètre du missile

MISSILE ASTER (Mo = 2 – α = 12°)
ERREURS RELATIVES SUR LES COEFFICIENTS AERODYNAMIQUES PREDITS PAR LE CODE FLU3C

Fig. 30

NUMERICAL SIMULATION OF SEPARATED SUPERSONIC FLOWS AROUND TACTICAL MISSILE BODIES

by

Philippe Guillen * and Jérôme Lordon **

aerospatiale - Division Engins Tactiques
2, rue Béranger - 92320 Chatillon - France

ABSTRACT

Beyond four or five degrees of incidence, vortices develop on the leeside of tactical missile fuselages. This paper presents the validation of a numerical approach to simulate these separated flows. In this approach the flow is computed by solving the Euler equations and separation is forced by a local treatment (Kutta condition like) on the body of the missile, near the supposed location of the separation line, which has to be known. This local treatment has been implemented in two different Euler solvers. Results are presented for various configurations and different aerodynamic conditions. The influence of several parameters has been investigated. Finally some calculations show the interest of the method to evaluate the vortical flow interaction with wings.

1. INTRODUCTION

The main difficulty occuring in the numerical simulation of flows around tactical missiles is due to their highly nonlinear behaviour. The two main effects are the presence of shocks and the development of vortices. The theoretical model which takes into account all these physical effects is constitued by the Navier-Stokes set of equations which is yet too costly to be solved with the present time computers, and some aspects of which, like turbulence modeling still belongs to fundamental research.

The use of the perfect fluid models, which neglect viscous effects and which are constitued by the Euler equations is quite interesting for the following reasons:

- their CPU cost is reasonable and so they can be used in an industrial way, espescially for supersonic cases
- perfect fluid solutions admit shocks and vortices.

If the shocks captured are quite similar to the experimental ones, this is not true for vortices; two aspects are to be considered:

-the origin of vortex sheet
-the development of this sheet into the flow.

Concerning the vortex sheet origin, two practical cases may be encountered:

- separation on sharp edges. In this case the numerical solution of the Euler equations exhibits a rotational structure on the leeside which is very close to the experimental one. The origin of this entropy creation by numerical schemes still remains an open problem
- separation on smooth bodies. As soon as incidence is beyond four or five degrees, vortices develop on the leeside of tactical missile fuselages. The numerical solution can incidently present rotational phenomena due to the capture of a curved shock but this separated flow is in general different from the real one. To simulate a more realistic separation we have developped a local treatment on the surface so as to create a vortex sheet from separation line data.

The aim of this paper is to validate this approach which enhances the simulation of vortex flows around smooth bodies with an Euler method. The treatment has been implemented in two very different numerical codes. This allows us to make differences between what may come from the physical modelling and what is relevant to the numerical scheme used to solve the Euler equations.

After a brief overview of general results obtained by several authors on separated flows with an Euler model in part 2, and the description of the two numerical methods used in part 3, comparisons are made with experimental results concerning both the global aerodynamic coefficients and experimental flowfield details.

* :Engineer in theoretical aerodynamics group,
Presently at ONERA (29, avenue de la Division Leclerc - 92320 Chatillon - France)
** :Engineer in theoretical aerodynamics group.

2. PHYSICAL AND NUMERICAL CONSIDERATIONS

The prediction of aerodynamic characteristics for supersonic tactical missile configurations has been greatly improved these last years by the massive use of Euler solvers, see for instance Wardlaw et al [1], Borrel et al [2]. Nevertheless much care is required when analysing the computed results in depth. It appears that for high incidences the main part of the nonlinear lift is due to the development of separated flows over lifting surfaces such as wings and tails. Figure 1 shows the isobar contours on the surface and in a crossflow plane for the ASTER missile calculated with an Euler method. Clearly, vortices are captured. This phenomenon has been vastly investigated both experimentally and numerically.

Many authors, Powell et al [3], Rizzi and Murman [4] among others have shown that the gross features of the flow over sharp edged wings were quite well captured with an Euler model. From a theoretical point of view the simulation of separated flows by these equations is not clear. They admit solutions with rotational flow, the critical point is how to generate it. A natural way of creating an entropy increase (or a total pressure loss) is to capture a curved shock but this appears not to be the main reason for Euler computations around wings.

For smooth configurations, Newsome [5] has shown that Euler modeling of separated flows over an elliptic wing was not consistent, in particular it was grid dependent: separation occured near the edge for coarse grids and disappeared for fine ones. These results seem to condemn definitely any Euler computation for separated flows. In fact, for practical engineering purposes, it appears not to be true since for sharp edge wings the separation occurs experimentally at the leading edge as well as in most Euler computations. It appears also that the global lift coefficient is well predicted.

If some confidence has been acquired for the calculation of sharp edge wing configurations, the same is not true for flows over smooth slender bodies. The main reason for the discrepancy is the developpement of a vortex sheet on the leeside which is not properly modelled with the perfect fluid assumption. This is shown on figure 2 where experimental and computational results for isobars and crossflow velocity field, respectively, are presented in a crossflow plane of an ogive-cylinder body configuration at Mach 2 and 15 degrees of incidence. A small vortex is developped behind a strong leeside shock in the computational results but it is quite clear that its strength is about an order of magnitude lower than the experimental vortex; moreover there seems to be no shock in the experiment. A remedy suggested and used by several authors, Baltakis et al [6], Marconi [7], consists in modifying locally the flow near the supposed location of the separation line. This approach has a practical engineering interest as 3D Navier-Stokes solvers can't yet be considered as everyday tools. The datz of the separation line can be obtained empirically from experimental data base or may be calculated, for critical cases, with a 3D boundary layer code such as the ones of Cousteix [8], or Lazareff and Le Balleur [9,10].

3. NUMERICAL METHODS

3.1 GOVERNING EQUATIONS

Two numerical methods quite different have been used to solve the 3D Euler equations which can be written in their unsteady form:

$$W_t + F_x + G_y + H_z = 0 \qquad (1)$$

where:

$$W=\begin{bmatrix}\rho\\ \rho u\\ \rho v\\ \rho w\\ e\end{bmatrix} \quad F=\begin{bmatrix}\rho u\\ p+\rho u^2\\ \rho uv\\ \rho uw\\ (e+p)u\end{bmatrix} \quad G=\begin{bmatrix}\rho v\\ \rho uv\\ p+\rho v^2\\ \rho vw\\ (e+p)v\end{bmatrix} \quad H=\begin{bmatrix}\rho w\\ \rho uw\\ \rho vw\\ p+\rho w^2\\ (e+p)w\end{bmatrix}$$

ρ is the density; u,v,w the cartesian components of the speed and e the total energy per unit volume. Pressure p is given by the state equation of a polytropic gas:

$$p = (\gamma - 1)\ (e - \frac{1}{2}\rho\ (u^2+v^2+w^2) \qquad (2)$$

3.2 SPACE MARCHING METHOD – SUP CODE

3.2.1 HYPOTHESIS

For steady supersonic flows in one direction, say x, one may consider the steady system:

$$F_x + G_y + H_z = 0$$

which is hyperbolic with respect to the x variable and thus can be solved in a space marching manner along the x axis by computing plane by plane x= constant. Similar methods have been derived by Wardlaw [1] or Arlinger [11].

The flow being steady the energy equation may be integrated to:

$$H_T = \frac{\gamma}{(\gamma - 1)} \frac{p}{\rho} + \frac{u^2+v^2+w^2}{2} \qquad (3)$$

where H_T is the stagnation enthalpy, which is constant if the upstream field is uniform. With this simplification the system may be conveniently written in conservative form :

$$div(F_i)=0 \qquad \text{for } i=1,4$$

$$\begin{cases} F1 = \rho U \\ F2 = \rho uU + pE_1 \\ F3 = \rho vU + pE_2 \\ F4 = \rho wU + pE_3 \end{cases} \qquad (4)$$

where U is the speed vector and E1,E2,E3 the cartesian space unit vectors.

3.2.2 SHOCK FITTING AND GRIDDING

For supersonic flows around slender bodies the flowfield is not modified outside the frontal shock which is fitted by the present numerical method. In each calculation plane x a mesh is constructed between the trace of the body and the trace of the bow shock. The first stage to achieve computing a new plane x + dx is to make an estimation of the position of the shock in this plane. This is made by using the Rankine-Hugoniot relations with a predicor corrector scheme.

3.2.3 MARCHING ALGORITHM

The variables are advanced from plane x to plane x+dx by applying the mass and momentum equations on an elementary volume such as the one drawn on fig3. Denoting the surface vectors as indicated in fig.3 the fluxes in the x+dx plane $F_{k,l}(x+dx)$ are deduced from the values in the x plane by the following Mac Cormack type algorithm:

predictor: $\underline{F}_{k,l}.S4 = F_{k,l}.S1 + F_{k-1,l}.S2 - F_{k,l}.S5 + F_{k,l-1}.S3 - F_{k,l}.S6$

corrector: $F_{k,l}(x+dx).S4 = .5\,(\underline{F}_{k,l}.S1 + F_{k,l}.S1 - \underline{F}_{k,l}.S2 + \underline{F}_{k+1,l}.S5 - \underline{F}_{k,l}.S3 + \underline{F}_{k,l+1}.S6)$

where Fj,k is the value of the fluxes of equations (2) for the mean value of the p,u,v,w variables on the S1 surface. Knowing the flux values Fi.S = gi for i=1 to 4 p,u,v,w can be deduced:

with:

$$p=(G.S - \Delta)/((\gamma+1)S^2) \quad \text{and} \quad U=(G - pS)/g1$$

$$\Delta 2=(G.S)2 - (\gamma 2 - 1).(2.HT.g12 - G2).S2 \qquad G=\begin{bmatrix} g2 \\ g3 \\ g4 \end{bmatrix}$$

This scheme is explicit and a CFL criterion has to be respected, limiting the space step.

3.2.4 BOUNDARY CONDITIONS

On the wall, a slip condition is applied. The flux contribution on the wall surface is then reduced to the pressure force. An extrapolated value from the flow pressure field is not sufficient for stability reasons. It is necessary to use the compatibility relations obtained by discretising the quasi-linear system of Euler equations. The relation expressing an information coming from inside the body is replaced by the slip condition. The technique used is thoroughly described in [1] and the reader is referred to it for a more detailed description.

3.2.5 VISCOSITY

To stabilise nonlinear effects due to strong shocks it is necessary to add some dissipation applied to the flux vectors in the field and to pressure, entropy, and speed component belonging to the x plane on the body. Following relations were used:

$$F_{k,l}=F_{k,l}+\mu.(t_{k+1/2,l}.(F_{k+1,l}-F_{k,l}) - t_{k-1/2,l}.(F_{k,l}-F_{k-1,l})) + \lambda.(t_{k,l+1/2}.(F_{k,l+1}-F_{k,l}) - t_{k,l-1/2}.(F_{k,l}-F_{k,l-1}))$$

where $t_{k+1/2,l}=|P_{k+1,l}-P_{k,l}|/(P_{k+1,l}+P_{k,l})$ $\quad t_{k,l+1/2}=|P_{k,l+1}-P_{k,l}|/(P_{k,l+1}+P_{k,l})$

μ et λ are constants generally of the order of .1

3.3 TIME MARCHING METHOD - FLU3C CODE

This numerical method is accurately described in [2], only a brief synopsis of the essential features is given below. The unsteady Euler equations are used (time marching). A finite volume is employed so that the variables W are evaluated at the nodes of grid with a ijk structure. By averaging Eq (1) over control volume V surrounding each node, one easily obtains the time evolution of W through the flux balance formula:

$$W_{ijk}^{n+1} = W_{ijk}^{n} - \frac{\Delta t}{vol(V)} \int_{dV} F.N dS$$

where N stands for the outward unit vector normal to each face of the control volume and F the vector of fluxes. The numerical fluxes F.N across control volume boundaries are evaluated explicitly at time level t^n using the flux-vector splitting technique introduced by Van Leer [12] :

$$F.N = F^{+}(W^{+}) + F^{-}(W^{-})$$

where W^{+} and W^{-} are the values of conservative variables on both sides of the interface.

This upwind differencing splitting technique enables us to compute complex flows with strong discontinuities. The second order of accuracy in time and in space is achieved using the MUSCL approach which expresses the values of W in each control volume in terms of linear distributions by introducing slopes around the averaged quantities. These non constant distributions enable us to evaluate an intermediate solution $W^{n+1/2}$ (predictor) and then the numerical fluxes at the middle of the interfaces. In order to avoid numerical oscillations across discontinuities, a TVD correction is made whenever it is necessary, and therefore, near the extrema, the scheme reduces to first order spatial accuracy.

The boundary conditions are taken into account using a compatibility relation technique [13]. The scheme, being explicit, is stable if the time step Δt satisfies a CFL like condition.

In the steady flows computed below, a local time stepping technique has been used. The steady state solution is reached by iterating in time until convergence. When the flow is supersonic almost everywhere in one direction, a space marching strategy has been developped. It consists in iterating in time plane by plane, using only the upstream information, according to the supersonic nature of the flow. This numerical procedure does not imply any CFL like condition in space, it has been used for most applications presented in this paper.

The frontal shock is captured and not fitted, the grid is constructed before the computation and is not adapted.

FLU3C code is convenient because:

- it does not need any additionnal numerical viscosity for stability
- it can compute both subsonic and supersonic flows
- the marching technique allows industrial supersonic calculations
- it can handle complex geometry configurations
- it is robust and easy to use.

3.4 TREATMENT OF SEPARATION

The procedure used consists in initiating the vortex sheet by making the speed vector on the surface of the body parallel to the separation line. The directions of the speed vectors of the two grid points between which separation occurs are modified in each plane normal to the missile axis.

Let Ψ be the ratio $\frac{T.U}{|U|}$ where T is the unit vector tangent to the fuselage in the plane orthogonal to its axis at the separation point, the separation line being known we have $\Psi=\Psi_s=\frac{T.D}{|D|}$. If the separation point is between grid points k and k+1 , Ψ is modified at these two points by interpolating linearly according to the polar angle ϕ:

$$\Psi_k=\Psi_{k-1} + (\phi_k-\phi_{k-1})\frac{(\Psi_s-\Psi_{k-1})}{(\phi_s-\phi_{k-1})} \quad ; \quad \Psi_{k+1}=\Psi_{k+2} + (\phi_{k+1}-\phi_{k+2})\frac{(\Psi_s-\Psi_{k+2})}{(\phi_s-\phi_{k+2})}$$

To avoid oscillations, entropy, pressure and total enthalpy for FLU3C at points k and k+1 are determined by a linear interpolation between k-1 and k+2. The speed vector modulus $|U|$ is then deduced from the energy equation.

4 VALIDATION OF THE METHODS

First, we will discuss the influence of some parameters on the numerical results, and after different comparisons between computations and experiments showing how the method developped herein can improve the Euler calculation of separated flows on smooth surfaces will be presented.

4.1 INFLUENCE OF SOME PARAMETERS

The configurations used for the tests are:
- body#1 = 2D circular ogive + 11D cylinder [1]
- body#2 = 3D circular ogive + 7D cylinder [14]
- body#3 = 3D parabolic ogive + 12D cylinder (ONERA Experiments)
- body#4 = 3D cubic ogive + 10D cylinder [15]

D is the body diameter.

We used different separation lines defined by the polar angle $\phi s(x)$ ($\phi s=+\Pi/2$ <=> leeside):
- line#1 : ϕs = Wardlaw expression: $\phi s = 2.23 * ((X/D - 1.5) * \tan(\alpha))^{-0.23} - \Pi/2$
- line#2 : ϕs = -5 degrees; when Wardlaw expression is valid
- line#3 : ϕs = Wardlaw expression-20 degrees
- line#4 : ϕs = Wardlaw expression-40 degrees
- line#5 : ϕs = 0

Subscript * used below with the line number means that separation is forced only after ogive-cylinder junction.

4.1.1 INFLUENCE OF THE EULER METHOD

For the body #1 we present the results given by three different Euler methods at Mach 3, incidence 15 degrees and separation line #1: SUP, FLU3C and SWINT [1] that uses a similar technique to force separation. The agreement is very good for:
- the parietal pressure in the last section (fig. 4)
- the local normal force coefficient (fig. 5)
- the abscissa of the center of pressure (fig. 6)
- the global forces coefficients (CA and CN are axial and normal forces coefficients; Xcp is the center of pressure abscissa):

Method	CA	CN	Xcp/D
FLU3C	0.200	2.31	5.63
SUP	0.198	2.21	5.51
SWINT	0.193	2.26	5.61

body #1 - M=3 - α=15° separation line #1

For the body #2 at Mach 1.98, incidence 15 degrees and separation line #2 the agreement is not so good as presented below.

Method	CA	CN	Xcp/D
FLU3C	0.0925	1.83	4.55
SUP	0.0897	1.57	4.09

body #2 - M=1.98 - α=15° separation line #2

This will be analysed later.

4.1.2 INFLUENCE OF THE NUMERICAL VISCOSITY

Unlike FLU3C, the SUP code uses an artificial viscosity model to stabilise the solution. We have studied the influence of the amount of dissipation (coefficient Cdis=λ=μ in the viscosity expressions § 3.2.5) on the results.

For the body #1 at Mach 3, incidence 15 degrees and separation line #1 the influence is very weak for the parietal pressure in the last section (fig. 7) as well as for global forces coefficients:

Method	Cdis	CN	Xcp/D
SUP	0.2	2.21	5.50
SUP	0.4	2.21	5.51
SUP	0.8	2.21	5.52
FLU3C	XX	2.31	5.63

body #1 - M=3 - α=15° - separation line #1

As already seen, FLU3C and SUP results are close to each other.

For the body #2 at Mach 1.98, incidence 15 degrees and separation line #2 the dissipation influence is more important for the parietal pressure in the last section (see fig. 8). When the coefficient of dissipation decreases the pressure distribution on the leeside calculated with SUP closer to the FLU3C results. The wind side pressure is not modified. This influence do not affect the global force coefficients.

The difference between FLU3C and SUP at the wind side comes from the low value of ϕs (see §4.1.3).

Method	Cdis	CN	Xcp/D
SUP	0.2	1.60	4.16
SUP	0.4	1.57	4.09
SUP	0.8	1.57	4.07
FLU3C	XX	1.83	4.55

body #2 - M=1.98 - α=15° - separation line #2

For the body #3 at Mach 2, incidence 10 degrees and separation line #2* the influence of the dissipation is even more important on the force distribution over the fuselage as can be seen below:

Method	Cdis	CN	Xcp/D
SUP	0.2	0.910	5.69
SUP	0.7	0.852	5.11
SUP	1.5	0.885	5.22

body #3 - M=2 - α=10° - separation line #3*

4.1.3 INFLUENCE OF THE SEPARATION LINE

Many experimental parameters (Mach number, incidence, Reynolds number, freestream turbulence...) can modify the separation line position and its knowledge is quite a difficult subject to grasp. The attempts to derive an empirical expression from measured datas were not very successfull. So it is important to know the influence of its location on the calculations.

For the body #1 at Mach 3 and incidence 15 degrees the influence of the separation line is weak:

Method	Sep. L.	CN	Xcp/D
SUP	#1*	2.20	5.78
SUP	#3*	2.24	5.83
SUP	#4*	2.32	5.95

body #1 - M=3 - α=15° - Cdis=0.2

For the body #2 at Mach 1.98 and incidence 15 degrees the influence is more important for FLU3C. Figure 9 gives the local normal force coefficient.

Method	Sep. L.	CN	Xcp/D
FLU3C	no	1.51	3.83
FLU3C	#1	1.63	4.06
FLU3C	#2	1.83	4.55
FLU3C	#3	1.77	4.36
SUP	#2	1.57	4.09
SUP	#3	1.56	4.01

body #2 - M=1.98 - α=15° - Cdis=0.4(for SUP)

For the body #3 at Mach 2 and incidence 10 degrees the influence is even more important on the force distribution over the fuselage.

Method	Sep. L.	CN	Xcp/D
SUP	#1*	0.644	3.29
SUP	#3*	0.852	5.11
SUP	#4*	1.119	6.36

body #3 - M=2 - α=10° - Cdis=0.7

When the separation angle ϕs is too low, the parietal pressure is not very good at the windside with FLU3C, unlike with SUP. This can be seen on figure 8 with line#2 (ϕs=-5°). With a constant ϕs $\neq$ 0 degrees, we obtain fig.10 for the parietal pressure in the last section. The agreement between SUP and FLU3C for the windside is much better (the difference for the leeside has already been analysed in §4.1.2).

For the global force coefficients, the difference between SUP and FLU3C results has been divided by two.

4.1.4 COMMENTS

The test cases presented seem to belong to two groups depending on the crossflow Mach number:
- at Mach 3 and 15 degrees incidence the computed flow is not influenced by the amount of artificial viscosity and the position of the separation line has few effect.
- at Mach 2, 15 degrees incidence and even more at 10 degrees the artificial viscosity has strong effects and the separation line is a critical datum. The numerical method may have an influence too, depending on the separation line position.

When the separation angle ϕs is too low, the parietal pressure at the windside calculated with FLU3C is not very good.

The grid cells size influence has also been investigated. No practical effect on the results has been found. The vortex location is the same with a fine or a coarse grid.

4.2 COMPARISON WITH EXPERIMENTS

4.2.1 BODY#2 AT MACH 1.98 AND 15 DEGREES INCIDENCE (PRESSURE, NORMAL FORCE, CENTER OF PRESSURE)

Figures 11 and 12 present comparisons of SUP and FLU3C results with experimental values [14] for body #2 at Mach 2 and 15 degrees incidence (parietal coefficient of pressure in the last section and local normal force coefficient, respectively). The separation line used for the calculation is line #5 ($\phi s = 0$) and for SUP Cdis=0.8 .

Pressure calculated by SUP is close to the measured one. For FLU3C we find the same characteristic as seen before: the pressure is too low at the leeside under the vortex.

For normal force coefficient, a difference between the experiments and the calculated results appears on the cylinder. A better estimation of the separation line might improve the results. Nevertheless, the error on the global force coefficient is acceptable (less than 9%) and the abscissa of the center of pressure is well predicted by SUP (4.05 D for 4.10 D) and reasonable for FLU3C (4.33 D)

4.2.2 CROSS-FLOW RESULTS (PRESSURE, VELOCITY)

Experiments have been carried on at ONERA S2Ma wind tunnel test facilities to know the flow around a 15D ogive-cylinder body with a 3D circular ogive (body#3), in some cross-flow planes located at 10,12 and 15 diameters from the apex. The aerodynamic variables were measured by means of 5 hole probes, at 10*73 locations in each plane. Comparisons are made hereafter for some of these planes at two aerodynamic freestream conditions, with FLU3C computations. The separation line used is the line #1.

➜ MACH= 2, INCIDENCE = 15 DEGREES

On Fig 13 and 14 are shown respectively the isobar and iso total-pressure contours in the crossflow planes. Two results are presented:

-the computed results with the #1 separation line
-the experimental results

For the static pressure, the contours represent the ratio of static pressure over the freestream pressure. There is a contour every 0.05 ratio from 0.30 to 1.75. For the total pressure, the contours represent the ratio of total pressure over the freestream total pressure. There is a contour every 0.15 ratio from 0.50 to 0.95. Fig 15 shows a comparison in the last plane for the velocity vectors together with the iso total pressure contours. From these figures one can notice that the general shape of the separated flow is similar for computed and experimental results. The height of the vortex relative to the distance to the apex seems to be correctly predicted. But great discrepancies occur on the levels in the center of the vortices, thus the total pressure in the experimental vortex is overestimated by the computation. There are differences in the static pressure levels too. In the regions outside the viscous core and the boundary layer, good agreement is observed.

➜ MACH=3, INCIDENCE = 15 DEGREES

Figures 16, 17 and 18 correspond to figures 13, 14 and 15 presented above with a different freestream Mach number. As for Mach 2, the same features can be noticed: similar vortex shape and height but different pressure levels in its core, good agreement outside.

The discrepancies in the center of the vortex might come from its viscous nature not modelised by our perfect fluid model.

➜ SEPARATION TREATMENT EFFECTS

Figures 19 and 20 show, for both cases, the parietal pressure on the body versus the polar angle in the last crossflow plane with and without separation treatment, respectively. Forced separation limits the lower (Φ_w=0) and upper (Φ_w+Π/2) pressure bounds. The global coefficients obtained are indicated below. For Mach 3 the separation treatment does not seem to be necessary for evaluating the global forces. The same fact is not true for the other case.

Method	Sep. L.	CN	Xcp/D
FLU3C	#1	1.959	5.407
FLU3C	no	1.727	4.796

body #3 - M=2 - α=15°

Method	Sep. L.	CN	Xcp/D
FLU3C	#1	2.531	6.690
FLU3C	no	2.528	6.695

body #3 - M=3 - α=15°

4.2.3 VARIATION OF THE ANGLE OF ATTACK (NORMAL FORCE, CENTER OF PRESSURE)

This configuration consists of body #4. Figure 21 presents the comparison between SUP calculations and the measurements made at RAE [15] for the normal force coefficient and the center of pressure versus the angle of attack. The numerical results are excellent even at incidence 20 degrees. The linear extrapolation of the normal force coefficient from its value at incidence 4 degrees shows the high non-linearity of the flow at great incidence.

4.2.4 BODY-TAIL RESULTS (VORTEX INTERACTION)

The configuration used to study vortex interaction is the following:
- 3D parabolic ogive + 12D cylinder + tail (see fig.22)

For supersonic flows, measurements were made at ONERA facilities at Mach 2 with several total incidence αt and roll angle Φr values. We have made calcultations for
- Φr = ±45° (X position) and αt = 10 and 20 degrees
- Φr = 0 degrees ; αt=20 degrees

We have compared the coefficient of the force normal to the wing and the center of pressure abscissa on the wing calculated by FLU3C, with and without separation, to experimental values:

- CNw = the coeffient of the force normal to the wing
- Xcpw = center of pressure of the force normal to the wing abscissa
subscript "c" means calculated value
subscript "e" means experimental value
Φr is the roll angle
c is the length of the tail root chord.

Φr	CNwc	(CNwc-CNwe)/CNwe	Xcpwc/c	(Xcpwc-Xcpwe)/c
+Π/4	0.382	+58%	54.6%	- 2.4%
- Π/4	0.404	+ 4%	55.1%	+0.7%

Comparison with experiment - FLU3C without separation - M=2 - αt=10°

Φr	CNwc	(CNwc-CNwe)/CNwe	Xcpwc/c	(Xcpwc-Xcpwe)/c
+Π/4	0.270	+12%	60.0%	+3.0%
- Π/4	0.390	+ 1%	55.3%	+0.8%

Comparison with experiment - FLU3C with separation - M=2 - αt=10°

Φr	CNwc	(CNwc-CNwe)/CNwe	Xcpwc/c	(Xcpwc-Xcpwe)/c
+Π/4	0.324	+53%	60.8%	-2.8%
0	0.834	+ 7%	56,5%	+1.4%
- Π/4	0.768	+ 0%	55.1%	- 0.8%

Comparison with experiment - FLU3C without separation - M=2 - αt=20°

Φr	CNwc	(CNwc-CNwe)/CNwe	Xcpwc/c	(Xcpwc-Xcpwe)/c
+Π/4	0.247	+16%	66,9%	+3.3%
0	0.800	+ 3%	56,4%	+1.3%
- Π/4	0.768	+ 0%	55.1%	- 0.8%

Comparison with experiment - FLU3C with separation - M=2 - αt=20°

When the tail is near the vortex, the values of CNw are more accurately predicted with the forced separation technique at both incidence 10 and 20 degrees. The agreement becomes adequate for practical applications.

As the tail goes away from the vortex ($\Phi r=0°$ or $\Phi r= -45°$) the influence decreases and is well restituted by calculations. As expected, for the wind side tails there is no influence of the vortex.
The position of the center of pressure moves 5% of the root chord towards the apex when separation is forced.

With forced separation, the lift on the cylinder increases but the lift on the tail decreases so the sum stay nearly constant as well as the global center of pressure. Thus, the influence of forced separation on the global force coefficients is not very important for the cases studied here.
The results for the body alone (ogive+cylinder) are presented here:

Separation	CNb	Xcpb/D
free	0.580	1.92
forced	0.833	4.67

FLU3C - body alone - M=2 - α=10°

Separation	CNb	Xcpb/D
free	3.65	6.16
forced	3.78	6.23

FLU3C - body alone - M=2 - α=20°

We find the same trends as explained in §4.1.4 . It is interesting to note that at incidence 20 degrees the forced separation has very few effects on the global force for the body alone but strong ones on the wing loads.

Figure 23 shows parietal pressures on the body surface and total pressure contour slices in several crossflow planes that exhibit the development of the vortices in the field that interact with tails.
This Mach 2 case, a difficult one for calculations, especially at 10 degrees incidence, is a good example of a practical engineering application of the study presented herein.

5 CONCLUSION

After this study on the simulation of separated supersonic flows over slender bodies the main conclusions are:

- two kinds of separated flows of different nature can be distinguished:
  - ➢ for rather high crossflow Mach numbers (e.g. Mach number 3 and incidence of 15 degrees) the computed results for smooth bodies seem independant of most parameters: numerical method, numerical viscosity, position of separation line. The global forces computed with and without treatment are even very close to each other
  - ➢ for less high crossflow Mach numbers, the computed results depend strongly on the latter parameters. In particular the separation line data is critical.

- there is a need for detailed experimental studies which would concern parietal, flowfield and separation line measurements. Generally, the three aspects are never treated together which makes comparisons and numerical methods validations difficult. This will be even more useful with the development of Navier Stokes codes

However the use of a separation treatment, even if not always accurate for the body alone, gives much more precise results than no treatment at all when interaction takes place. For example, the evaluation of external vortical flow interaction with tails located at the end of a fuselage is greatly improved when one takes into account forced separated vortices. The prediction of inflow characteristics of air breathing missiles and induced rolling moments (which is an important problem for tactical missiles at high incidence) should be improved in the same way.

ACKNOWLEDGEMENTS:

This work has been carried out with the support of the Direction des Recherches Etudes et Techniques (DRET).

REFERENCES

[1] A.B.Wardlaw, F.B. Baltakis, J.M. Solomon, L.B. Hackerman: An Inviscid Computational Method for Tactical Missile Configurations. -NSWC TR 81 -457 (1981)
[2] M. Borrel, J.L. Montagné, J. Diet, Ph. Guillen, J. Lordon: Méthode de Calcul d'Ecoulements autour de Missiles Tactiques à l'aide d'un Schéma Décentré. La Recherche Aérospatiale 1988-2.
[3] K.G. Powell, E.M. Murman, R.M. Wood, D.S. Miller: A Comparison of Experimental and Numerical Results for Delta Wings with Vortex Flaps. AIAA paper 86-1840-CP

[4] E.M. Murman, A. Rizzi: Applications of Euler Equations to Sharp Edge Delta Wings with Leading Edge Vortices. AGARD CP 412.
[5] R.W. Newsome: A Comparison of Euler and Navier-Stokes Solutions for Supersonic Flow Over a Conical Delta Wing. AIAA paper 85-0111
[6] F.P. Baltakis, A.B. Wardlaw, J.M. Allen: Leeside Crossflow Modeling in Euler Space-Marching Computations. NSWC TR 86-342
[7] F. Marconi: On the Prediction of Highly Vortical Flows Using an Euler Equation Model. AFOSR TR 86-2073
[8] J. Cousteix Three Dimensional Boundary Layers. Introduction to Calculation Methods. AGARD-R-741
[9] J.C. Le Balleur, M. Lazareff: A Multi-Zonal Marching Integral Method for 3D Boundary-Layer with Viscous Inviscid Interaction. ONERA TP 1984-67
[10] M. Lazareff, J.C. Le Balleur: Calculs d'Ecoulements Tridimensionnels par interaction visqueux-non visqueux utilisant la méthode MZM. ONERA TP 1986-29.
[11) B.G. Arlinger: Computation of Supersonic Flows around Three Dimensional Wings. ICAS-82_6.1.3
[12] B. van Leer: Flux Vector Splitting for the Euler Equations. Lecture Notes in Physics, vol.70, pp 507-512,1982
[13] H. Viviand J.P. Veuillot: Méthodes Pseudo-Instationnaires pour le Calcul d'Ecoulement Transsonique. ONERA TP 1978-4
[14] W. Perkins, H. Jorgensen: Comparison of Theoretical Normal Force Distributions on an Ogive-Cylinder Body at Mach Number 1.98. NACA TN 3716
[15] W. K. Osborne: Guided Weapons Aerodynamic Study. Tests on a Body Alone, and in Combination with Delta-Wings. RAE TR-65109 1965

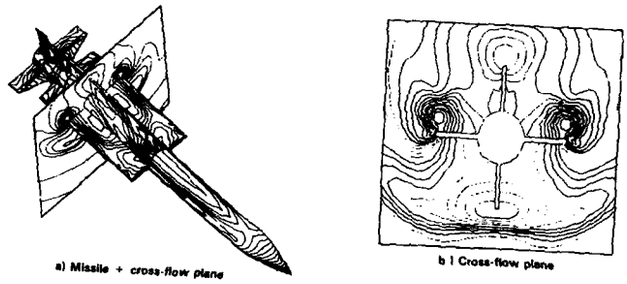


Fig 1: PRESSURE CONTOURS - ASTER MISSILE, M=2.5, INCIDENCE =10 DEGS

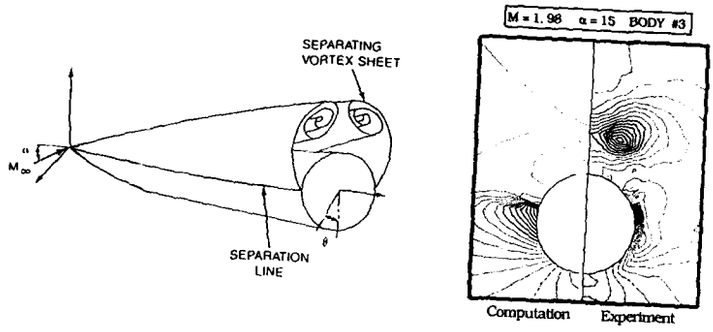


Fig 2: - SKETCH OF 3D FLOW -
COMPUTED AND EXPERIMENTAL PRESSURE IN A CROSSFLOW PLANE

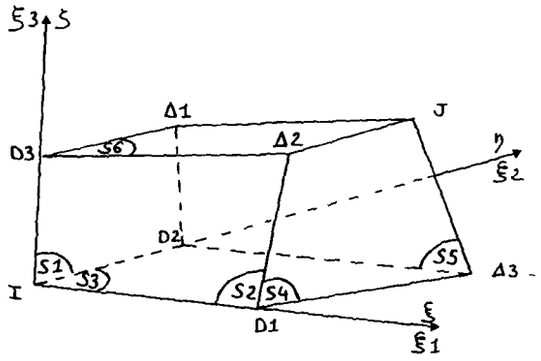


Fig 3 : FINITE VOLUME DISCRETISATION

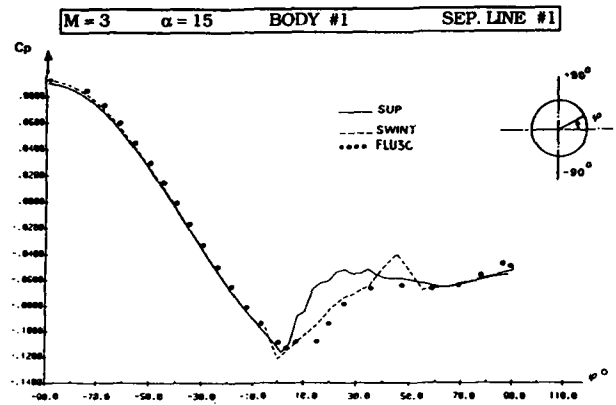


Fig 4 : COMPARISON OF COMPUTED PARIETAL PRESSURE COEFFICIENTS AT X = 13 D, FOR THREE EULER CODES

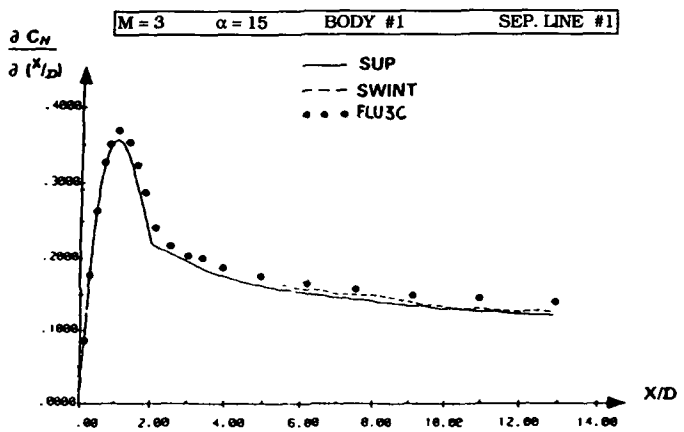


Fig 5 : COMPUTED LOCAL NORMAL FORCE COEFFICIENT FOR THREE EULER CODES

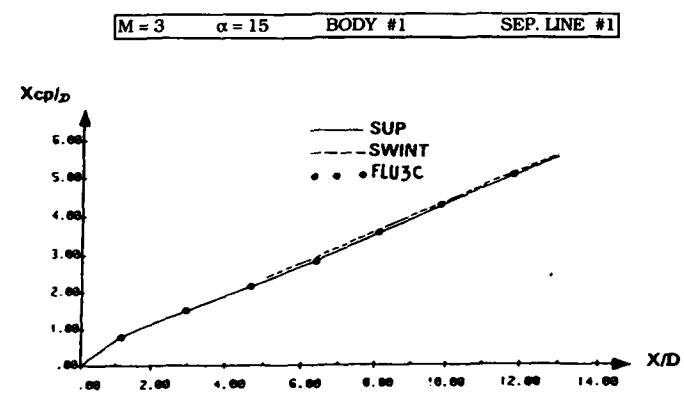


Fig 6 : COMPUTED LOCAL CENTER OF PRESSURE FOR THREE EULER CODES

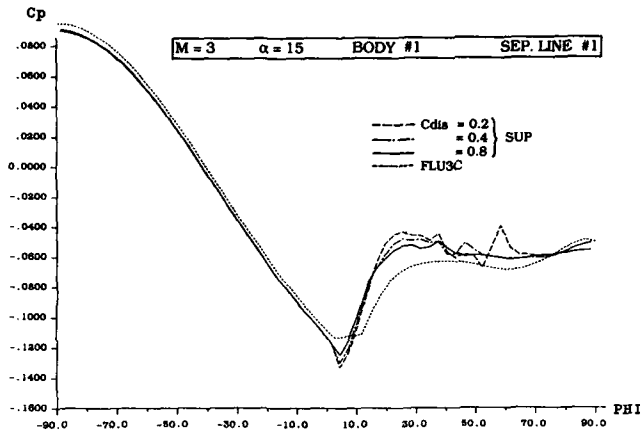


Fig 7 : INFLUENCE OF NUMERICAL VISCOSITY ON PARIETAL PRESSURE COEFFICIENTS AT M = 3, X = 13 D

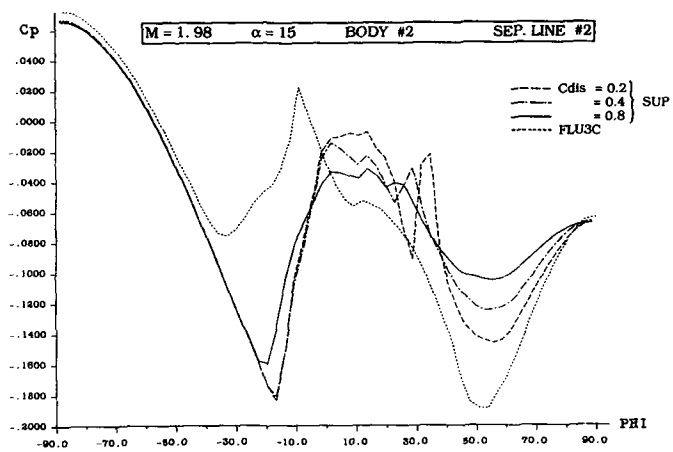


Fig 8 : INFLUENCE OF NUMERICAL VISCOSITY ON PARIETAL PRESSURE COEFFICIENTS AT M = 1.98 , X = 13 D

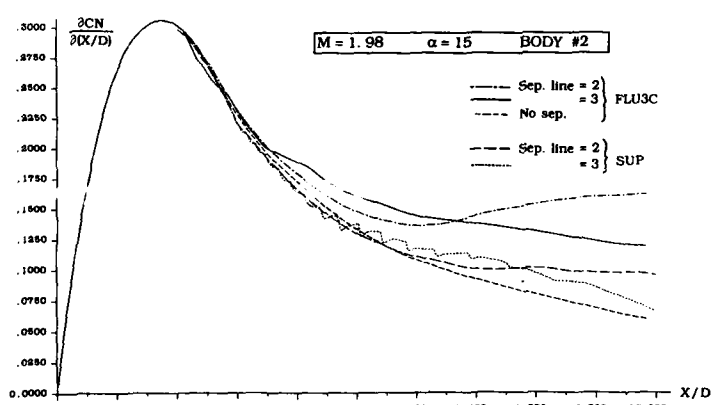


Fig 9 : INFLUENCE OF THE SEPARATION LINE ON THE LOCAL NORMAL FORCE COEFFICIENTS

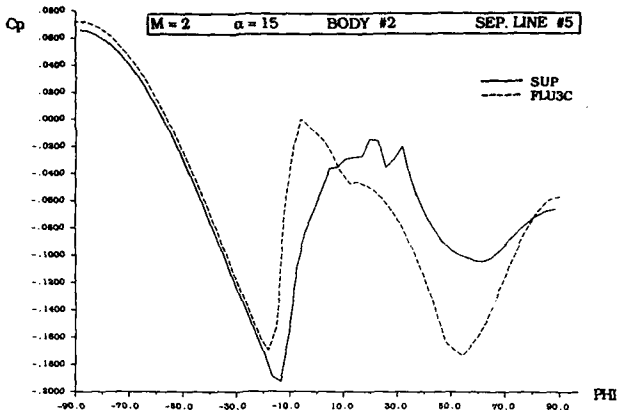


Fig 10 : PARIETAL PRESSURE COEFFICIENTS AT X= 10D FOR SUP AND FLU3C CODES

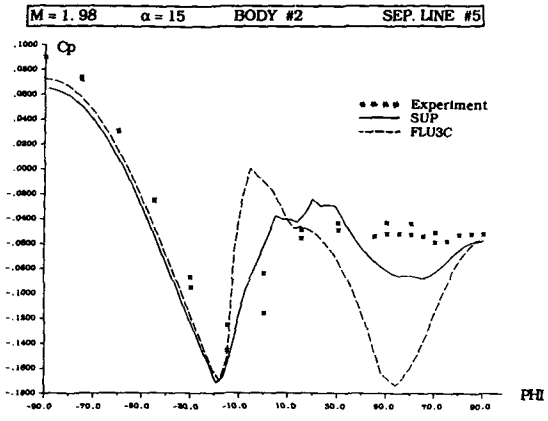


Fig 11 : COMPUTED AND EXPERIMENTAL PARIETAL PRESSURE COEFFICIENTS AT X= 10D

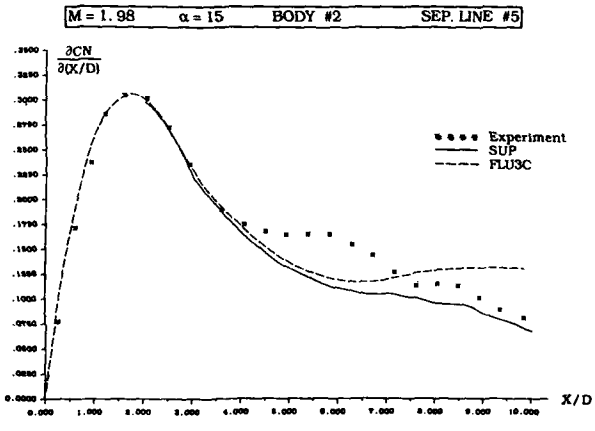


Fig 12 : COMPUTED AND EXPERIMENTAL LOCAL NORMAL FORCES

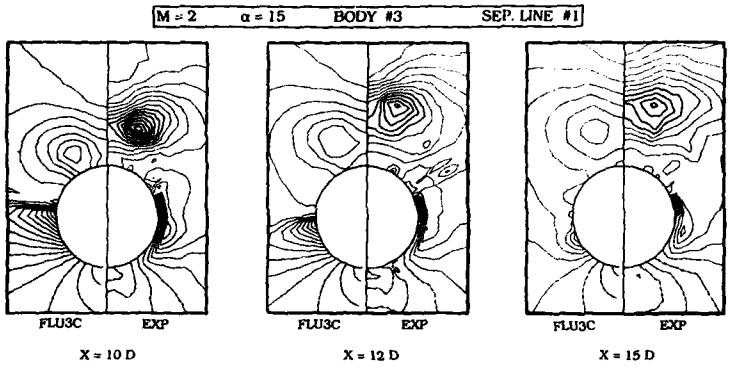


Fig 13 : COMPUTED AND EXPERIMENTAL PRESSURE CONTOURS IN CROSSFLOW PLANES

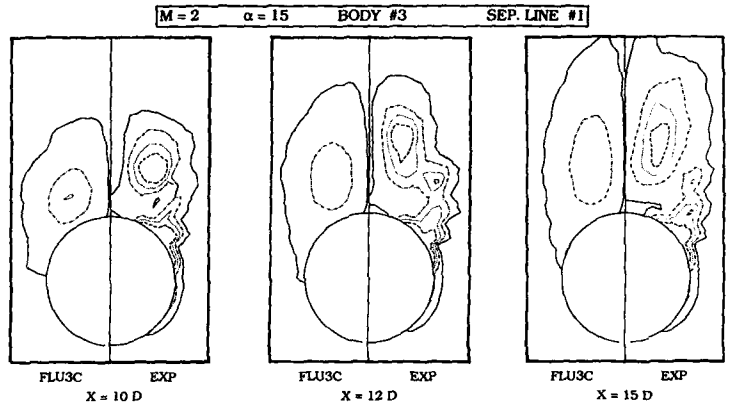


Fig 14 : COMPUTED AND EXPERIMENTAL TOTAL PRESSURE CONTOURS IN CROSSFLOW PLANES

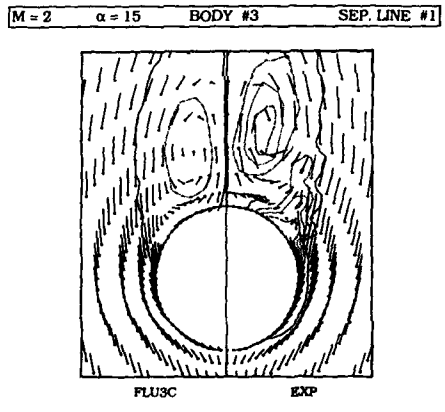


Fig 15 : COMPUTED AND EXPERIMENTAL TOTAL PRESSURE CONTOURS AND VELOCITY FIELD AT X = 15 D

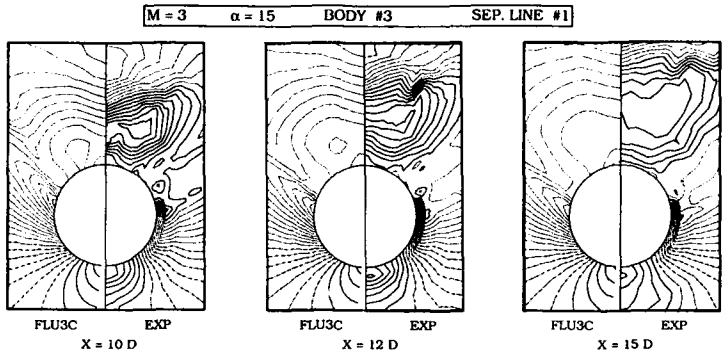


Fig 16 : COMPUTED AND EXPERIMENTAL PRESSURE CONTOURS IN CROSSFLOW PLANES

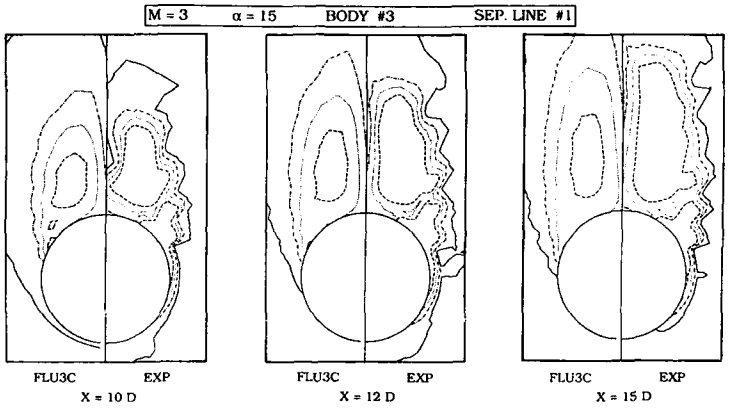


Fig 17 : COMPUTED AND EXPERIMENTAL TOTAL PRESSURE CONTOURS IN CROSSFLOW PLANES

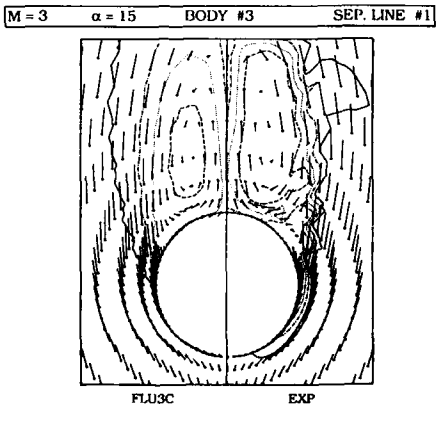


Fig 18 : COMPUTED AND EXPERIMENTAL TOTAL PRESSURE CONTOURS AND VELOCITY FIELD AT X = 15 D

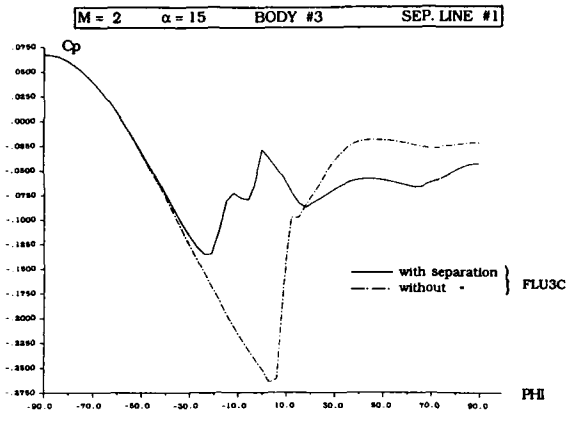


Fig 19 : COMPARISON OF COMPUTED PARIETAL PRESSURES AT X = 15 D WITH AND WITHOUT SEPARATION TREATMENT

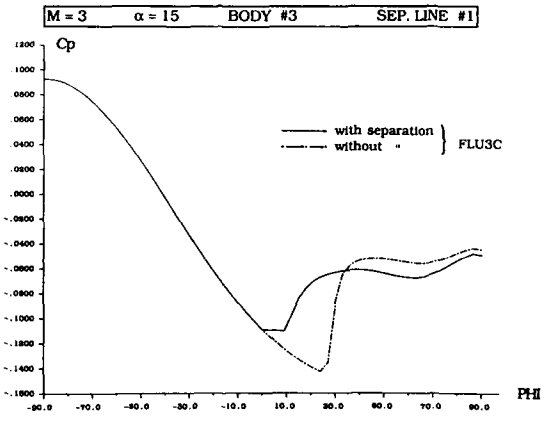


Fig 20 : COMPARISON OF COMPUTED PARIETAL PRESSURES AT X = 15 D WITH AND WITHOUT SEPARATION TREATMENT

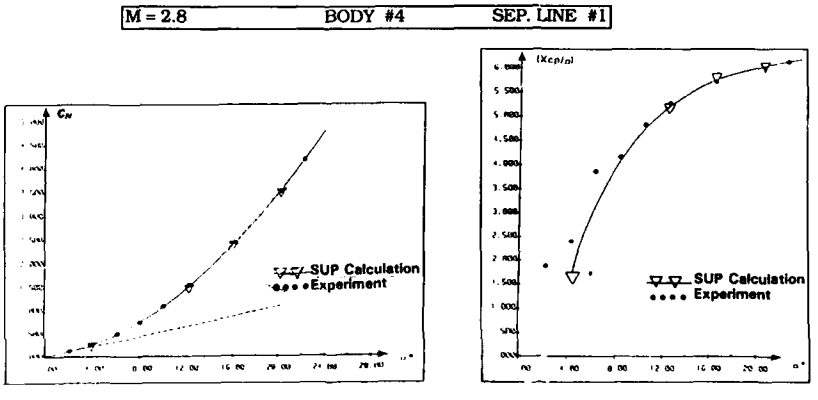
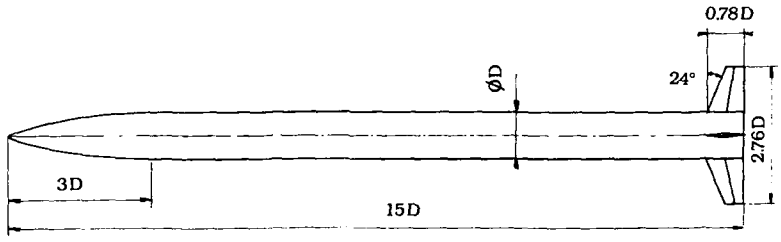


Fig 21 : COMPUTED AND EXPERIMENTAL LOCAL NORMAL FORCE AND CENTER OF PRESSURE VERSUS INCIDENCE



thickness ratio: 0.08

Fig 22 : BODY-TAIL CONFIGURATION

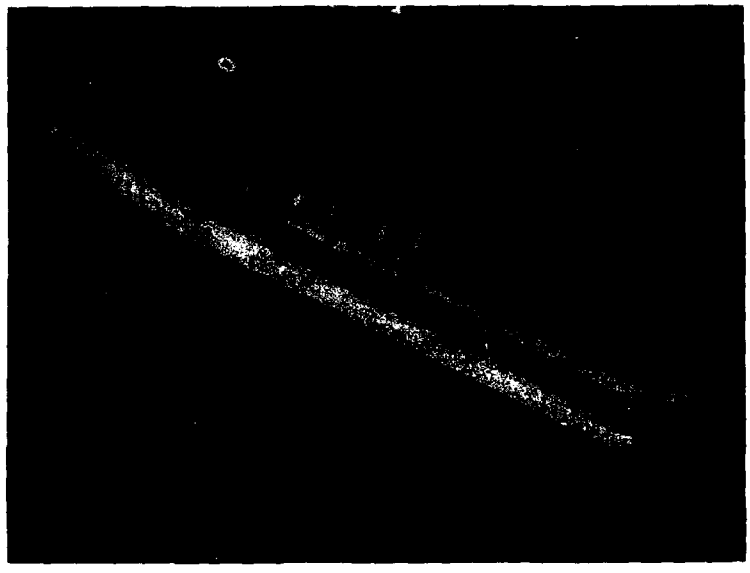


Fig 23 : FLU3C BODY-TAIL RESULTS : -PRESSURE ON THE BODY
-TOTAL PRESSURE IN CROSSFLOW PLANES

DEVELOPMENT AND APPLICATION OF A WEAPONS MULTIBLOCK SUITE

P.A. Shepherd and G.R. Tod
Aerodynamics and Performance Department
Dynamics Division
British Aerospace PLC
P.O. Box 5, FPC67
Filton
Bristol BS12 7QW
ENGLAND

Summary

A Multiblock Euler capability for use on Weapons in the Project environment is described, with comparisons between predicted and experimental data being given for a number of Weapon related problems.

The present Jameson flow code is shown to produce good agreement with experiment in most cases, covering a wide range of Mach number and incidence. The limitations of the code for more general Weapon applications, where viscous effects dominate, is also clear.

Extension of the existing flow solver to higher Mach number and the modelling of viscous phenomena, will form the subject of further development.

1. INTRODUCTION

This paper outlines a Multiblock Euler capability, developed for the prediction of transonic flow around complex missile configurations. The Suite of codes described, grew from a need to bridge the gap in Mach Number between existing subsonic panel methods (e.g. [1]) and space-marching Euler codes (e.g. [2]), the latter of which typically become effective for most practical configurations above Mach 2. It was also recognised that space-marching codes failed whenever a subsonic patch was encountered, and that this problem could only be addressed with recourse to a time-marching scheme.

Of particular importance was the need to develop a method for use within the Project environment. Here the emphasis is on ease and versatility of application, perhaps by staff not specialised in CFD. Such requirements are often deemed burdensome to the researcher, but to the Project Aerodynamicist they are as important as knowing that the flow code has been properly validated.

The direction for flow code development drew from experience of an explicit Jameson scheme within the British Aerospace, Civil Aircraft Division, applied to transonic flow around axisymmetric bodies [3]. Following initial familiarisation, i became clear that a far more general capability could be realised if advantage were taken of the algorithm's obvious suitability to Multiblocking. This involves sub-dividing the flow domain into blocks which are topologically equivalent to a cube, with six faces which either correspond to components of the missile surface; specify free stream conditions remote from the missile; or permit flow between adjacent blocks. A three-dimensional mesh is generated within each block, so tailoring the overall grid to local features of the configuration and flow field (Note that the overall grid is structured, with continuous grid lines across block boundaries).

Early work at Aircraft Research Association Ltd., on algebraic grid generation within a Multiblock framework [4], suggested this to be a useful approach for Weapons, particularly when considering the more conventional missile designs (e.g. cruciform body-wing-control). Algebraic methods are considerably cheaper than solving partial-differential equations for the grid, but the user does need to provide significantly more input data. This problem has been largely overcome however, by developing an interactive pre-processor which defines both the block structure and geometry. Thus, Project Aerodynamicists can now consider quite complex configurations, requiring in excess of a hundred blocks, with the minimum of tuition and effort.

In the following sections an overview of the Suite is given, highlighting present capabilities and deficiencies. Attention then turns to preliminary validation of the Euler flow code: predictions being compared with experiment for a number of Weapon related problems. The paper concludes with a discussion of future areas for development.

2. SUITE OVERVIEW

2.1 General

Figure 1 shows the packages contained within the Suite and their interrelation.

The aforementioned interactive code which defines the block structure (termed "topology data") and geometry, is MBGEOM. It provides topology information for the flow code, MBCORE1, and specifies the outline and grid distribution for each block in physical (cartesian) space, for the algebraic grid generator, MBGRID.

Two other pre-processors, MBVBLK and MBRBLK, provide for "reblocking". This permits a sequence of adjacent blocks to be joined for treatment as one by the flow code (see figure 2). MBCORE1 also accommodates the presence of any "fin patches" after reblocking. This facility reduces the number of internal boundary conditions and increases vector length, which has brought reductions in run time by a factor of two.

There are three post-processors within the Suite. Surface data can be written from the flow code for analysis within MBSURF. Data for all or isolated surface components (e.g. body, fin1, fin2, etc.) can either be interpolated for direct plotting against experiment; be displayed in terms of three-dimensional shaded views; or be integrated for overall or distributive forces and moments. Contour, vector or grid plots of the field data is provided by MBPLOT, while MBPRNT permits selected field data to be formatted as line-printer output.

Facilities also exist (though not shown on figure 1) to extract plot data from large files stored on a remote supercomputer; interface post-processors with space-marching Euler codes; and form single-block C- and H-grids over bodies of revolution by conformal mapping.

A detailed account of each code and its operation is given in reference [5].

2.2 Interactive Topology and Geometry Specification

The block structure is constructed by working with a three-dimensional view in a representative "topological" space, which may be either cylindrical-polar (being the most appropriate for axi-symmetric designs) or cartesian (for say, rectangular intakes). A "current" block is first displayed by MBGEOM, on to which others of similar shape are built. One always builds from the current block, which appears outlined in red, with local grid directions (I,J,K) shown by other colours (see figure 3, axes being labelled in the absence of colour). A command "I+4" builds four blocks in I, "K-2" builds two in negative K, and so on. New blocks appear outlined in black, but the current block can then be moved to any one of them. The overall topology is formed by a series of these build-and-move operations. With each build, the adjacent block and face numbers are recorded, as is the relative orientation of adjacent block faces.

Further options exist while working in topological space. These permit flow between remote faces (which may physically be joined); separate faces between which flow is initially assumed (note that faces which are or become coincident while building are automatically assumed to have flow between them); change block shape to better represent the physical configuration; and temporarily remove blocks from view for clarity. The user also specifies outstanding boundary conditions and assigns physical (cartesian) coordinates to block corner-points, while in topological space (MBGEOM highlights each face or point in turn that requires input).

With the block structure and corner-points wholly or partly defined, the user can opt to specify the remaining geometric data in either topological or physical space. This includes the type of line between corner-points (straight, circular arc, ellipse, line-fit, etc.); the number of grid points per line; and their distribution (via trigonometric, power-law or geometric progression "stretching" functions). Input is simplified by using "generic labels" which MBGEOM assigns to lines which must have the same number of grid points (by virtue of the grid being continuous across block boundaries). There are considerably fewer labels than lines.

Selected face grids can also be drawn from within MBGEOM, to check user-input and refine grid point distribution before writing data for the flow code and grid generator.

The largest drawback with MBGEOM is that blocks, once built, can not as yet be deleted. The problem is off-set however, by the ability to save and restart at any time.

2.3 Grid Generation

With grid points positioned on the twelve lines forming the edge of each block, the six face grids and then the internal three-dimensional mesh, can be generated by transfinite interpolation [6,7,8]. MBGRID performs this task for each block in turn, but can also arrange for particular face grids to be written for external modification or read for inclusion in the field grid (having been generated by user-written software or a CAD package).

It is often preferable to interpolate between boundary data stored in cylindrical-polar coordinates, when dealing with bodies of revolution. This is an option within MBGRID, but additional checks are required to ensure that intrinsic functions return consistent face-corner theta values, should one or more corner have zero radius on conversion from the cartesian coordinates supplied by MBGEOM.

Transfinite interpolation has been found to be a cheap and efficient means of grid generation. Grid orthogonality can be improved in the field by moving corner-points (which can be done using the screen cross-wires from within MBGEOM), while cell aspect-ratio is easily controlled by changing the stretching functions and/or number of cells. This process can however reduce to one of trial and error, but techniques which could be used to improve an initially interpolated grid (or initial set of block corner-points) are now being reported in the literature [9,10].

2.4 The Multiblock Euler Flow Code

The flow solution is advanced through each time step, block by block, using the explicit four stage Runge Kutta scheme of Jameson et al [11]. The flux divergence for mass, momentum and energy over each finite volume is found by centre-differencing: the dependent variables being stored at each cell centre.

The scheme employs fourth-order artificial viscosity to prevent odd/even point decoupling in regions of smooth flow. These terms are multiplied by a coefficient $\kappa^{(4)}$, whose value derives from stability criteria [12]. Second-order terms are also introduced, but are confined to regions of steep pressure gradient (i.e. across shocks). These suppress oscillations which otherwise occur in the absence of some treatment for molecular diffusion, found in reality. Implementation is such that fourth-order terms are omitted when the second-order become significant. Second-order terms are multiplied by the coefficient $\kappa^{(2)}$. Typical values for $\kappa^{(2)}$ and $\kappa^{(4)}$ are 1/4 and 1/256 respectively, as quoted in [11].

In section 3, the level of artificial viscosity is described in terms of the input parameters VIS2 ($= \kappa^{(2)}$) and VIS4 ($=64\ \kappa^{(4)}$). The aforementioned typical values $\kappa^{(2)}$ and $\kappa^{(4)}$ are thus obtained when VIS2 and VIS4 are both 0.25. Throughout this work however, VIS2 has been set to unity, with acceptable smearing of shocks for practical purposes. More significantly, we will see that VIS4 has had to be changed for convergence at higher Mach number.

Local time-stepping and enthalpy damping are two techniques used to accelerate convergence toward the steady state. The former sets the maximum time step at each cell that can be supported by the local stability bound (expressed via the Courant, Friedrichs and Lewy criterion, with an optimum CFL number of 2.8 for the present four stage scheme), while the latter makes use of stagnation enthalpy being constant in steady flow with a uniform free stream, to damp oscillations arising in the conservation equations during convergence. Both techniques are again described in [11]. With the present flow code, enthalpy damping is proportional to an input paramater, HM, of typical value 0.05. We will see that this also requires modification at high Mach number.

A more recent addition to the flow code has been implicit residual smoothing [13,14], which is now being assessed as a further means of improving the rate of convergence. It has currently proved useful in reducing flow code sensitivity to particular grids during early iteration, and is here only used for the body-fin configuration reported in section 3.

Initial conditions are assumed to be free stream throughout. The local free stream velocity component, normal to the far-field boundary, is used to determine whether an inflow or outflow is to be specified for a cell. If supersonic, halo cells retain free stream values for inflow, but are updated by adjacent internal values for outflow. Halos for subsonic inflow and outflow derive from a characteristic analysis on the boundary normal, based upon values at the previous time level. A no-normal-flow condition is prescribed at solid walls, while the orientation of adjacent block faces is handled by appropriate reordering of data on transfer into halos. Block faces can also be defined as symmetry planes.

Apart from the obvious limitation to cases not dominated by viscous effects, the largest restriction on the flow code is currently one of storage, as all data must be held in core. An asychronous input/output version is however being written, which will permit finer grid studies and application to more complex configurations.

3. PRESENTATION AND DISCUSSION OF RESULTS

The following test cases formed part of a presentation to the Second Meeting of the Technical Cooperation Programme (TTCP, WTP-2, KTA-9 for Weapons in isolation), at the Royal Aircraft Establishment, Bedford, in July 1987. Full results are given in [15].

All predictions were performed between 180° symmetry planes (configurations being at incidence), without reblocking. Grid sizes are quoted in terms of NIxNJxNKxNBLOCKS, where NI, NJ and NK are the number of grid points in the axial, radial and circumferential directions for the finest block. All runs were performed on a Cray 1S supercomputer.

3.1 Simple Tangent Ogive

Results for a tangent ogive at Mach 1.6 and incidences between 0° and 12°, are compared with the experimental data of Landrum [16,17]. Figure 4 defines the configuration and shows the axial stations used for comparison with surface pressure data. A single-block H-grid was generated for this case by conformal mapping, an example of which is given in figure 5. Note that for H-grids, the block face on the body surface extends forward of the nose, to become the centre-line. The flow algorithm is thus not affected by cell-face areas becoming zero.

Figure 6 shows variation of normal force and pitching moment with incidence. Both agree well with experiment and show grid independence with twelve (uniformly distributed) cells in the circumferential direction. Reported accuracy for the experimental data at Mach 1.6 is ±0.063 and ±0.011 for Cn and Cm respectively.

Comparisons with surface pressure coefficient at each axial station are given in figure 7: findings at 8° being typical of those at other incidences. Measurements are quoted as accurate to 0.007 (presumably ±, to comply with slightly larger variations observed at 0°). Twelve cells in the circumferential direction are again sufficient for grid independence. Moreover, predicted and measured trends agree favourably, though there is a general tendency to under-predict in the absence of any boundary layer representation.

Convergence was obtained using the standard input parameters (CFL=2.8, VIS2=1.0, VIS4=0.25 and HM=0.05) within 1000 iterations, which took 11 minutes on the Cray 1S for a 60x30x12 grid.

3.2 AFATL Bomb/Sting Configuration

Figure 8 gives dimensions and surface pressure locations for a sting-mounted bomb design. Details of the experiments performed are given in reference [18], though unfortunately the data is not available for publication. The conclusions to be drawn from the predictions are however worthy of note.

Five blocks were used for this case, each being bounded by the 180° symmetry plane. The blocks were positioned ahead of and over the nose; along the cylindrical mid-section; over the boat-tail; and on the sting. A typical grid is shown in figure 9. Comparisons with surface pressure data were made at three axial stations: on the nose; half way along the cylindrical mid-section; and toward the rear of the boat-tail. The data considered was for 4° incidence, at Mach 0.6, 0.95 and 1.2.

Results were generally good over the nose and cylindrical mid-section at all Mach numbers. The tendency to under-predict was again evident, being perhaps most noticeable on the leeside of the nose at Mach 0.6. Mid-section experimental data at Mach 1.2 suggested that separation had occurred, for which there is currently no treatment within the flow code. Results at both axial stations were shown to be independent of the grid with fifteen (uniformly distributed) cells in the circumferential direction.

Results over the boat-tail were particularly interesting. At Mach 0.95, viscous effects produced a near uniform profile in experimental data, which could not be modelled by the Euler solver. Some variation due to grid size was also evident. Comparison was also poor at Mach 1.2, where the Euler code was unable to model shock/boundary-layer effects at the boat-tail/sting junction. A shock was correctly predicted at the junction (as shown by the pressure contours in figure 10), but an inviscid code was clearly found to be inadequate for predicting surface pressure in this region of the flow.

Typical run times for a 25x20x15x5 grid were 20 minutes for convergence within 1000 iterations. The standard input parameters were again used throughout.

3.3 AFWAL (2.5:1) Elliptic Body

Figures 11 and 12 show the dimensions and typical grid for an elliptic body: the force, moment and surface pressure data for which is given in references [19,20], for Mach 2.0 and 5.0 at incidences between 0° and 4°. Data is also reported at Mach 0.55, but is not here compared with predictions. Four blocks were used to model the configuration: two over the nose from -90° to 0° and 0° to +90°; and two over an assumed afterbody of constant elliptic cross-section. Note that points are now clustered in the circumferential direction, to better represent the increased curvature of the ellipse and associated details of the flow.

Comparisons between predicted and measured normal force and pitching moment at Mach 2.0 and 5.0, are given in figure 13. Agreement for Cn is good at both Mach numbers and for each incidence considered. The trend for Cm is however slightly under-predicted at Mach 2.0 and over-predicted at Mach 5.0. None of the plots show a difference in predictions on the two grids tried.

Figures 14 and 15 compare predicted and measured surface pressure coefficient at three axial stations, for Mach 2.0 and 5.0 respectively. Agreement is particularly good at Mach 5.0, which also shows (and may be related to) a small cross-flow shock at x=3.2", which would have "forced" separation to occur in the inviscid solution. The inability to model the boundary layer, consistently leads to under-prediction on the windward and leeward surfaces.

Various changes to the standard input parameters were required for convergence at each Mach number (there being no subsequent change with incidence), viz:

Mach	CFL	VIS2	VIS4	HM
0.55	1.50	1.00	0.25	0.05
2.00	1.00	1.00	0.35	0.025
5.00	0.45	1.00	0.50	0.00

We see a significant reduction in CFL with Mach number, with the standard 2.8 value not even being applicable at Mach 0.55 for this configuration. It was also necessary to increase VIS4 and reduce HM at higher Mach number. The effect of increasing VIS4 would be to raise the level of background diffusion applied throughout the flow field. In doing so, fourth-order artificial viscosity is effectively being used to approach the "numerical diffusion" associated with upwind schemes. The potential for using such terms to extend centre-differenced schemes to high speed flow is thus a topic of future interest.

Figure 16 shows the typical convergence history at each Mach number, in terms of the log of the sum of rms residual mass for each block. The plot for Mach 2.0 shows that although predictions have agreed favourably with experiment, there is still scope for refining the input parameters. The Mach 5.0 plot is however most encouraging: despite the reduced CFL, it attains better convergence after 1000 iterations than the lower Mach number runs.

A typical run time for the 40x30x15x4 grid over 1500 iterations, was 32 minutes.

3.4 RAE Cruciform Body-Control Configuration

Figure 17 shows a finned configuration for which force and moment data was supplied by RAE [21]. Sixteen blocks were used, ten to define the missile in-board of the fin tips, with six defining the far-field. Note that two blocks were required over each of the twin-panelled fins, faces of which collapsed on to a line (circular-arc) between adjacent fin tips. Figure 18 shows a typical grid, which is of C-type around the slightly blunted nose. The grid is clustered circumferentially to improve resolution near fin surfaces; and axially for detail around the fins and nose/body junction.

Pressure contours on the symmetry plane at Mach 1.45 and 8° incidence are shown in figure 19.

We will consider two test cases, both at 8° incidence, the experimental force and moment data for which is as follows:

Mach	Cn	Cm
0.70	1.2884	-11.3040
1.45	1.4792	-12.6981

Predicted values for each case using three different grids were:

Mach	grid	Cn	Cm
0.70	15x15x15x16	1.3766 (6.8)	-12.6055 (11.5)
0.70	20x20x15x16	1.3796 (7.1)	-12.6486 (11.9)
0.70	25x20x15x16	1.3877 (7.7)	-12.7419 (12.7)
1.45	15x15x15x16	1.4526 (1.8)	-12.9121 (1.7)
1.45	20x20x15x16	1.4565 (1.5)	-12.9773 (2.2)
1.45	25x20x15x16	1.4666 (0.8)	-13.0919 (3.1)

Values shown in brackets are percentage error compared with the experimental data.

Predictions are particularly good at the higher Mach number, being to within 1% for Cn on the finer grid. The slight increase in Cm error with further grid refinement is of concern, but 3% error on the fine grid is nonetheless encouraging. It is at Mach 0.7, that the most significant error is observed. From calculations performed using a semi-empirical data base however [22], it would appear that the error is largely attributable to contributions from vortex lift, the necessary viscous mechanisms for which are not modelled in the present Euler code.

The requirement that all data be stored in core has limited the study of finer grids, but this problem is being addressed. Convergence was obtained at both Mach numbers using the standard input parameters, albeit with CFL=2.0, but residual smoothing was found necessary to avoid the failure of some cases during early iteration (which probably reflects inadequate grid resolution). Storage for the finest grid was 1.6Mwords, with convergence being obtained within 1000 iterations (taking 60 minutes on the Cray 1S).

To date this configuration has been successfully run to 14° incidence. Runs above this would be impractical without some treatment of flow separation from the body.

4. AREAS FOR FUTURE DEVELOPMENT

We have mentioned aspects of topology and grid generation that need improvement, but flow code development is the main area for future work. The role of artificial viscosity in extending application to higher Mach number warrants investigation, as does the question of introducing a model for flow separation. A model to define the separation streamline in accordance with experimental data, is to be incorporated during 1988 [23].

In the longer term, the ability to effect a Navier-Stokes solution in all or any block will be required for Weapon applications. Reference [24,25,26] suggest some useful directions for research in this respect.

5. CONCLUSIONS

A Multiblock Euler capability has been developed as a practical tool for use within the Project environment. Complex missile designs, well beyond the scope of those shown within this paper, can be addressed by Project Aerodynamicists with the minimum of tuition and effort.

There is however, significant scope for further flow code development, to extend applicability to higher Mach number and cases where viscous effects become dominant.

ACKNOWLEDGEMENTS

The authors would like to acknowledge the support of the Procurement Executive, Ministry of Defence, in funding some of this work. In addition, our thanks go to Messrs R.H. Doe and A. Pagano of BAe Civil Aircraft Division, Bristol and Mr. J. Hodges of Ae4 Division, RAE Bedford, for their continued help and encouragement. We would also like to acknowledge the help of Dr. K. Rose of Aircraft Research Association Ltd., for his initial support on algebraic grid generation.

REFERENCES

1. Petrie J.A.H, "User guide for the SPARV panel program (release 7)", BAe Military Aircraft Division, Brough, YAD 3382, Issue 5, December 1985.

2. Wardlaw A.B. (Jr), Hackerman L.B. and Baltakis F.P, "An invicid computational method for supersonic missile type bodies - program description and user's guide", NSWC TR 81-459 (1981).

3. Hookway Y, "User notes for flow code EJ50", Report B59R/EULA/530/12962, BAe Civil Aircraft Division, Bristol.

4. Private communication with Dr. K. Rose, Aircraft Research Association Ltd., Bedford, England.

5. Shepherd P.A. and Tod G.R, "The Weapons Multiblock Suite (WMS): A user guide for all programs", JS10910, March 1988.

6. Eriksson L.E, "Generation of boundary-conforming grids around wing-body configurations by transfinite interpolation", AIAA Journal, Vol. 20, No. 10, pp1313-1320, 1982.

7. Eriksson L.E, "Transfinite mesh generation and computer-aided analysis of mesh effects", Doctoral Thesis, Department of Computer Science, Uppsala University, 1984.

8. Thompson J.F, "Composite grid generation for general 3-D regions", International Conference on Numerical Grid Generation in Computational Fluid Dyunamics, Landshut, 1986.

9. Kennon S.R. and Dulikravich G.S, "Generation of computational grids using optimization", AIAA Journal, Vol. 24, No. 7, July 1986, pp1069-1073.

10. Thompson J.F, Notes on grid generation presented at the AIAA/VKI Seminar on "Navier-Stokes Flow Simulations", September 1986.

11. Jameson A, Schmidt W and Turkel E, "Numerical solution of the Euler equations by finite volume methods using Runge-Kutta time stepping schemes", AIAA-81-1259.

12. Jameson A, "A non-oscillatory shock capturing scheme using flux limited dissipation", Princeton University, MAE Report 1653, 1987.

13. Private communication with Mr. R.H. Doe, BAe C. il Aircraft Division, Filton, Bristol.

14. Jameson A and Baker T.J, "Solution of the Euler equations for complex configurations", Proc. AIAA 6th CFD Conference, Danvers, pp293-302.

15. Shepherd P.A, BAe Dynamics Division, Ref: 389/PAS/87109

16. Landrum E.J, "Wind-tunnel pressure data at Mach numbers from 1.6 to 4.63 for a series of bodies of revolution at angles of attack from -4° to 60°", NASA TM X-3558, 1977.

17. Landrum E.J. and Babb C.D, "Wind-tunnel force and flow-visualization data at Mach numbers from 1.6 to 4.63 for a series of bodies of revolution at angles of attack from -4° to 60°", NASA TM 78813, 1979.

18. Cottrel D.E. and Lijewski E, AIAA-87-0519.

19. "Pressure test of three elliptical body configurations at Mach numbers from 1.5 to 5.0", AFWAL TM 84236.

20. "A static force test of three elliptical body configurations at Mach numbers from 1.5 to 5.0", AFWAL TM 84199.

21. Data supplied through Mr. J. Hodges, Ae4 Division, Royal Aircraft Establishment, Bedford.

22. Bizon S.A, "A userguide to the aerodynamic prediction computer program 'ABACUS' (Issue 8)", Aerodynamic Information Note: AIN 85/2, BAe Sowerby Research Centre, Bristol, April 1985.

23. Kwong C.M, Myring D.F. and Livesey J.L, "Euler calculations with a separation model of flow around a missile at high alpha", Department of Aeronautical and Mechanical Engineering, University of Salford.

24. Haase W, Wagner B, Jameson A and Schmidt W, "Development of a Navier-Stokes method based on finite volume techniques for solving the time-dependent Euler equations", 5th GAMM Conference on Numerical Methods in Fluid Mechanics, Rome, Italy, 1983.

25. Swanson R.C. and Turkel E, "A multistage time-stepping scheme for the Navier-Stokes equations", NASA-CR-172527.

26. Kordulla W, "Integration of the Navier-Stokes equations in finite volume formulation", von Karmann Institute of Fluid Dynamics, Lecture Series 1987-04.

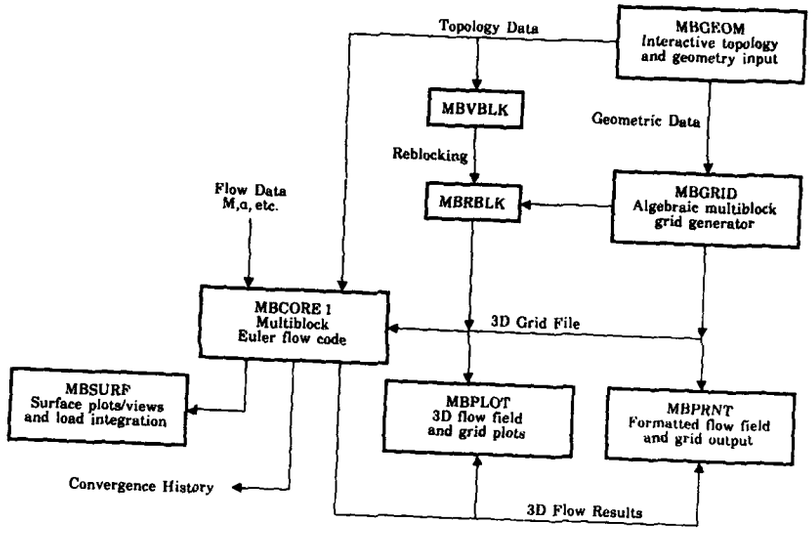


Figure 1: Schematic of the Weapons Multiblock Suite

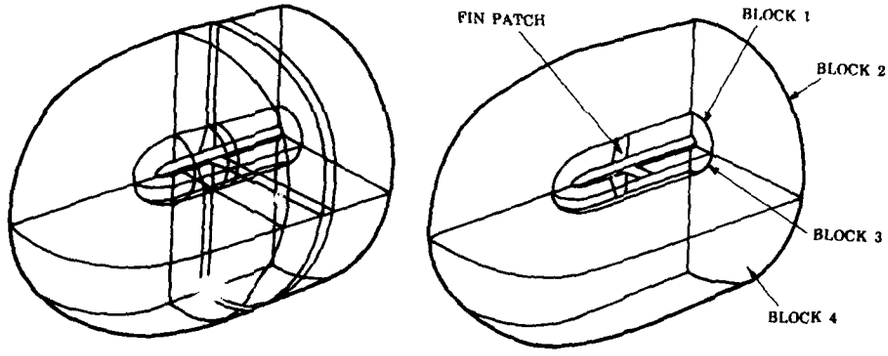
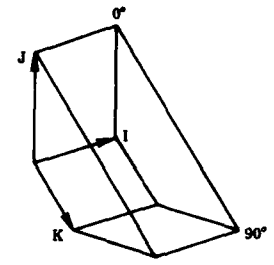
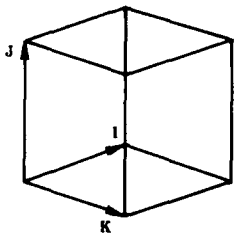


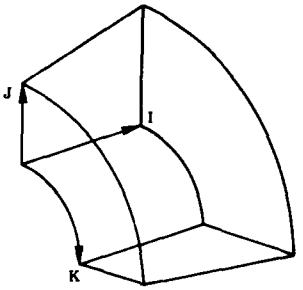
Figure 2: An example of reblocking a grid. Four blocks are constructed by merging those from MBGRID in the *axial direction*. Note that two of the new blocks require 'fin patches' on some faces



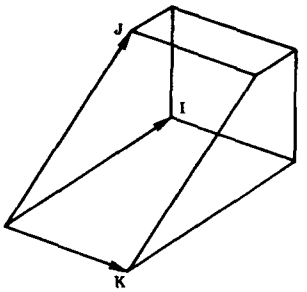
Current Block Outline
(Cylinderical-polar topological space)



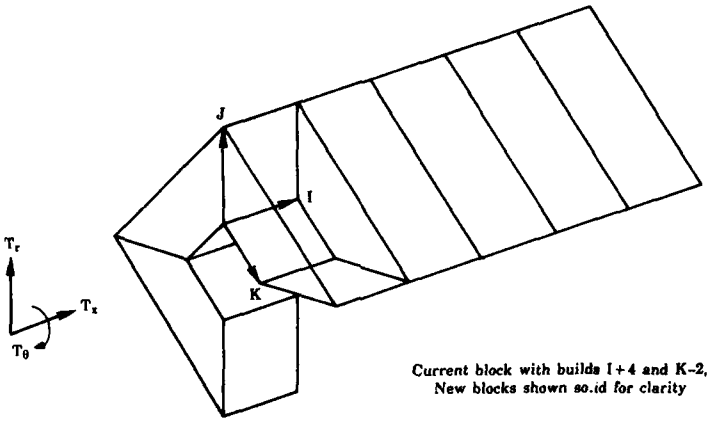
Current Block Outline
(Cartesian topological space)



Example Physical Outline



Example Physical Outline



Current block with builds I+4 and K-2,
New blocks shown so.id for clarity

Figure 3: Principles of building a topology

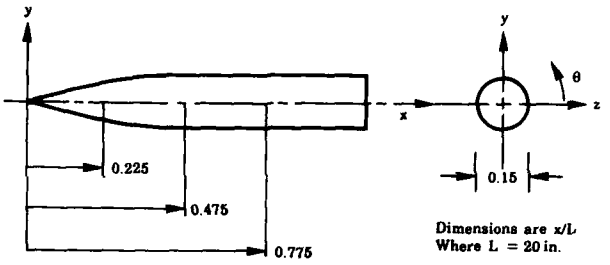


Figure 4: Tangent ogive showing axial stations for surface pressure data

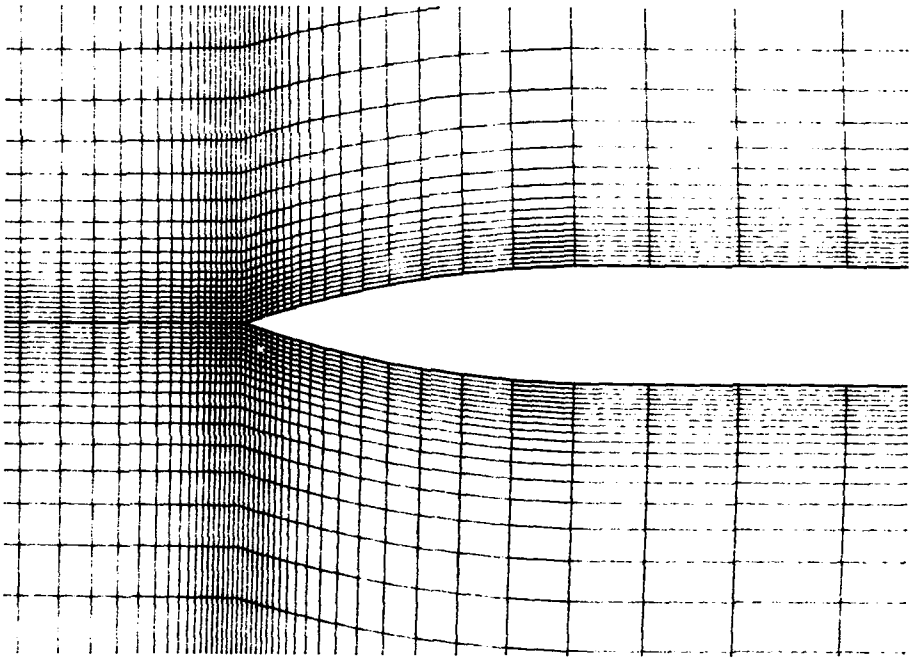


Figure 5: Typical H-grid for tangent ogive, generated by conformal-mapping in a single block

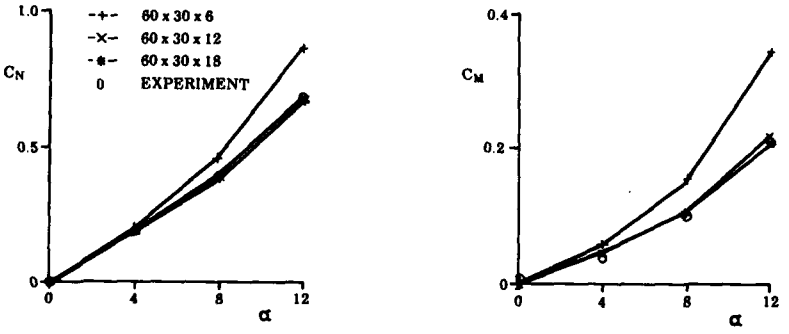


Figure 6: Variation of normal force and pitching moment with incidence for the tangent ogive at Mach 1.6

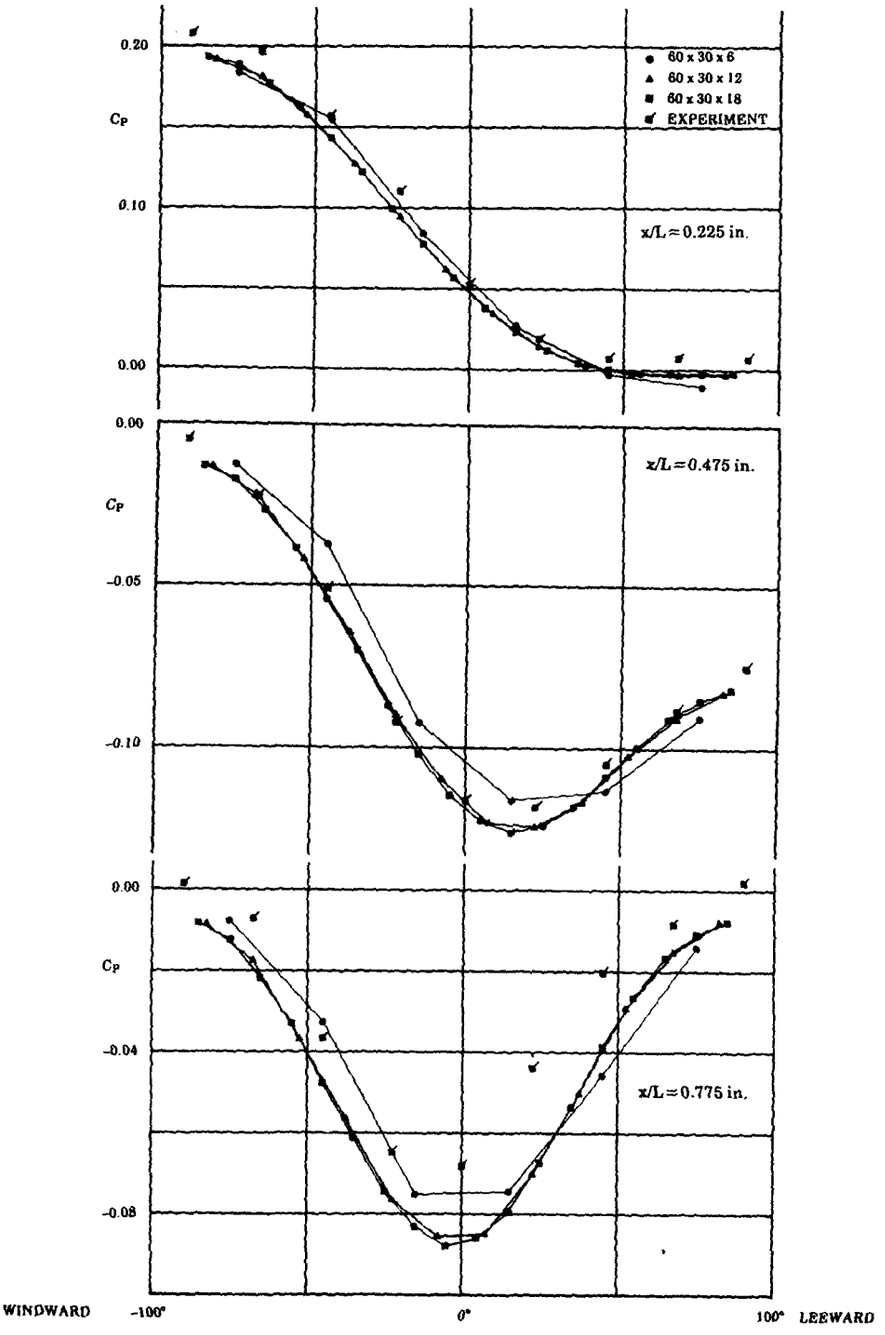


Figure 7: Circumferential variation of pressure coefficient for the tangent ogive at Mach 1.6 and 5° incidence

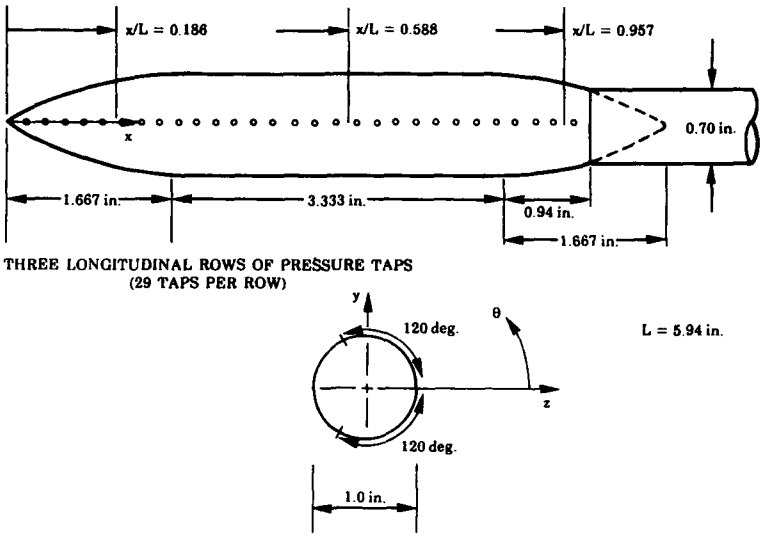


Figure 8: AFATL bomb/sting configuration showing axial stations for surface pressure data

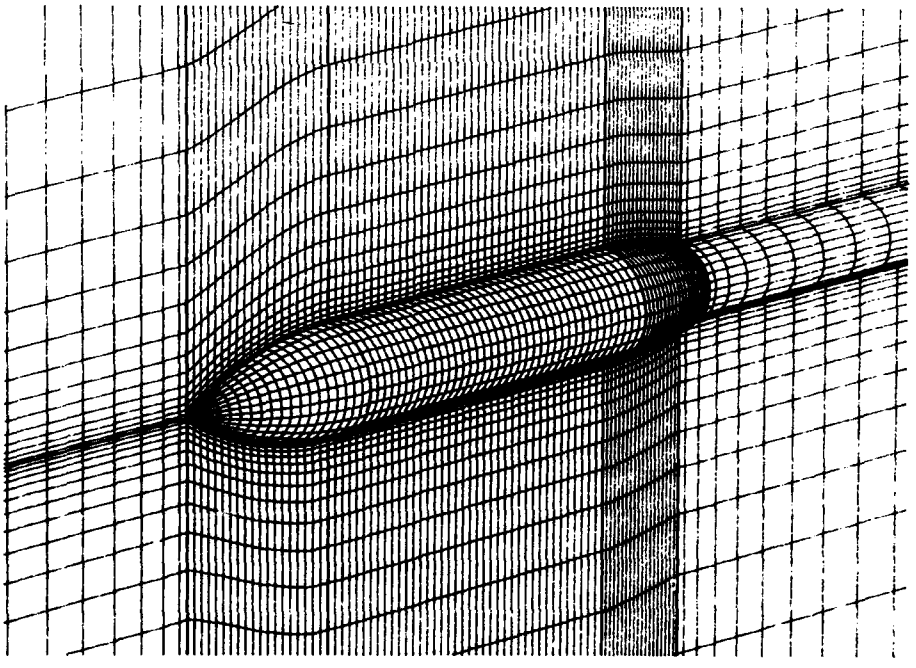


Figure 9: Perspective view of typical five-block grid for the AFATL bomb/sting configuration

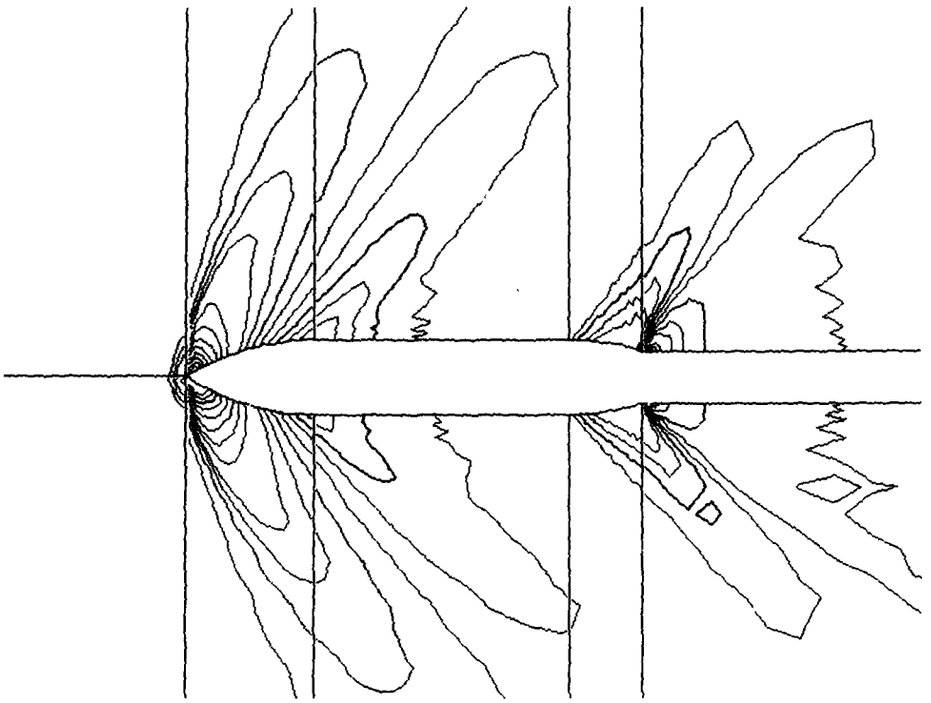


Figure 10: Symmetry-plane pressure contours for the bomb/sting, Mach 1.2 at 4° incidence

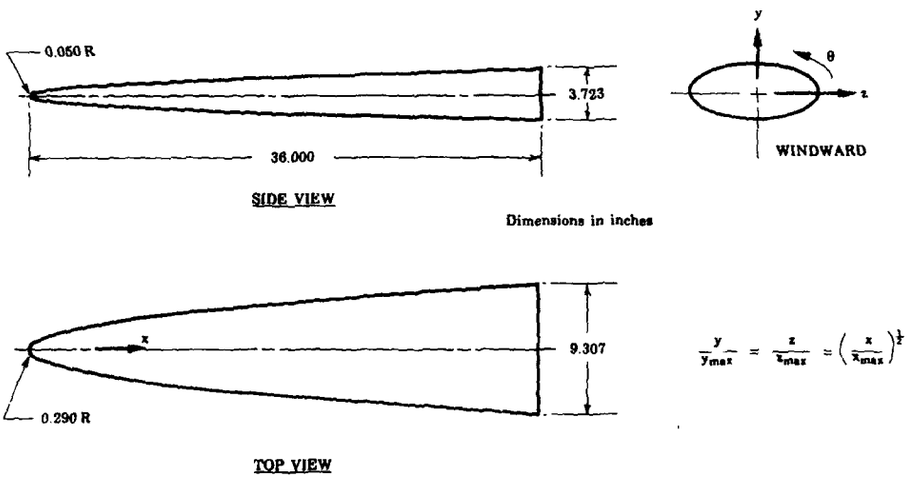


Figure 11: AFWAL (2.5:1) elliptic-body configuration

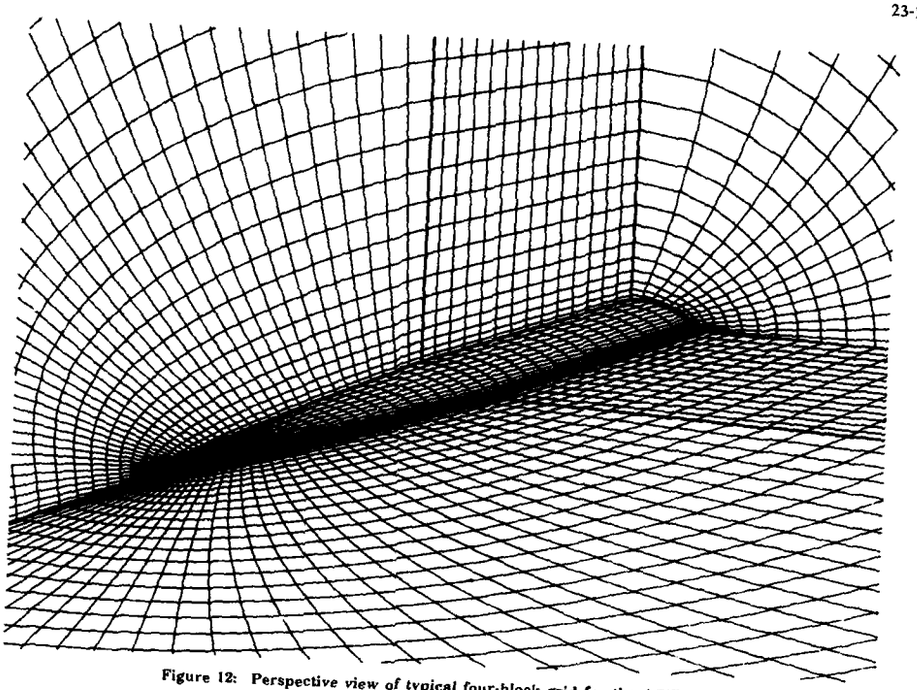


Figure 12: Perspective view of typical four-block grid for the AFWAL elliptic body (only leeward blocks shown)

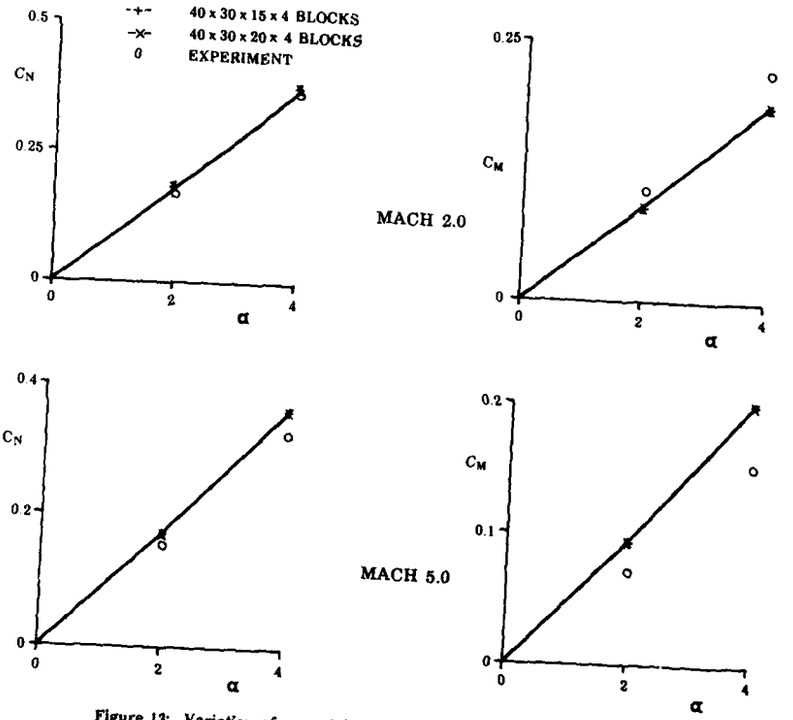


Figure 13: Variation of normal force and pitching moment with incidence for the elliptic body

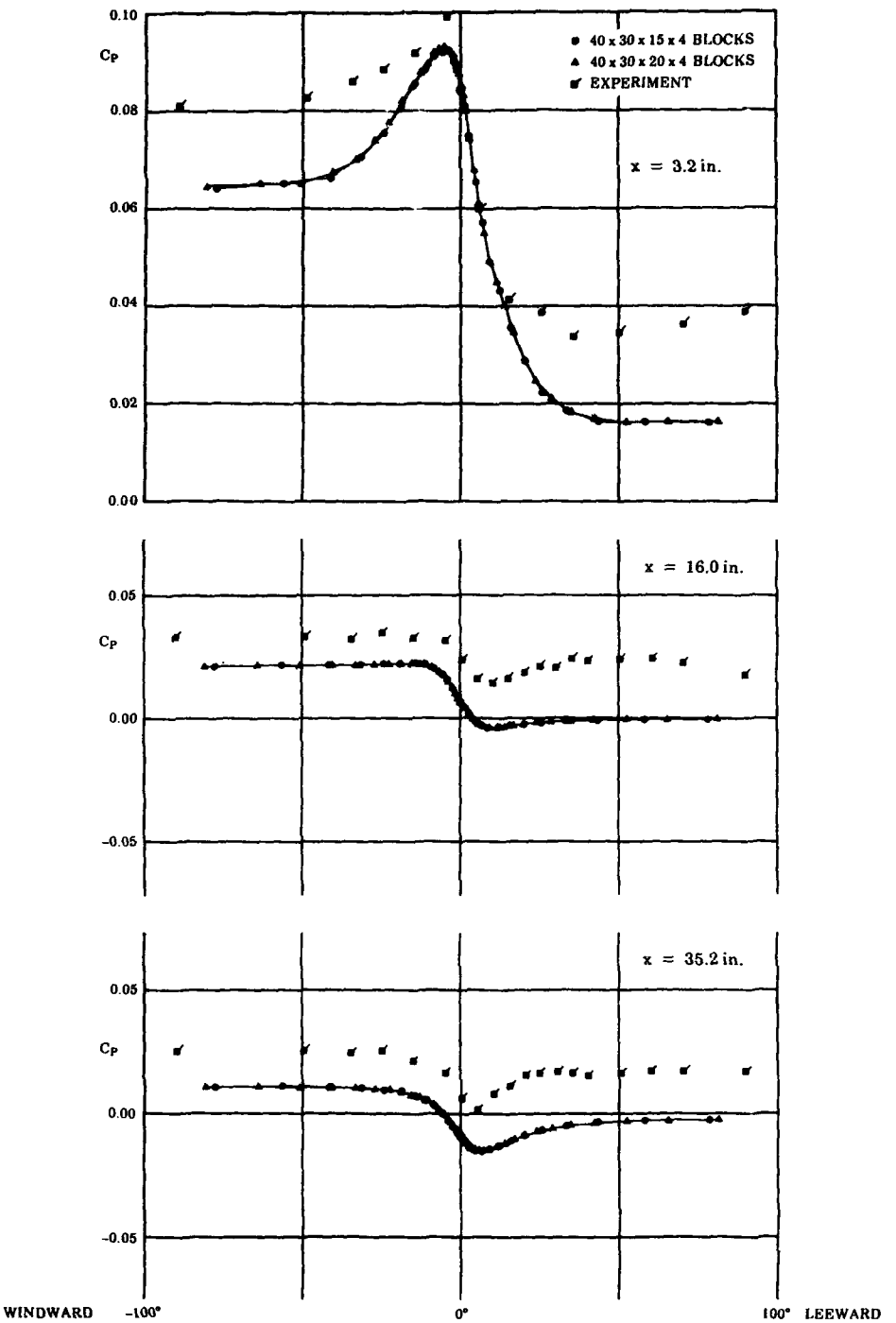


Figure 14: Circumferential variation of pressure coefficient for the elliptic body at Mach 2 and 2° incidence

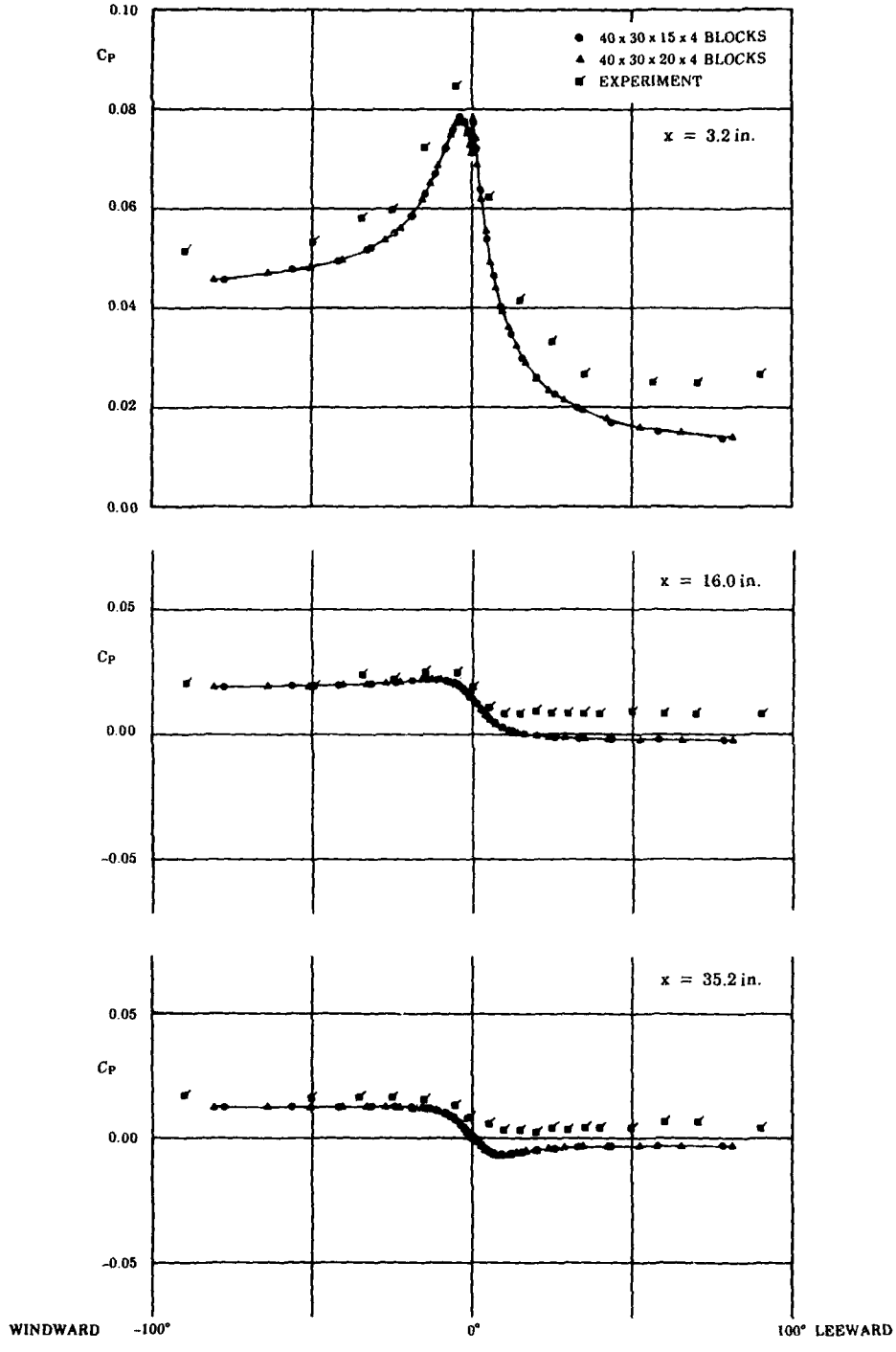


Figure 15: Circumferential variation of pressure coefficient for the elliptic body at Mach 5 and 2° incidence

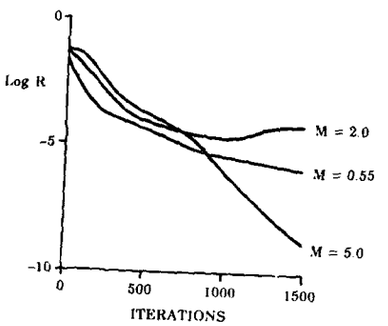
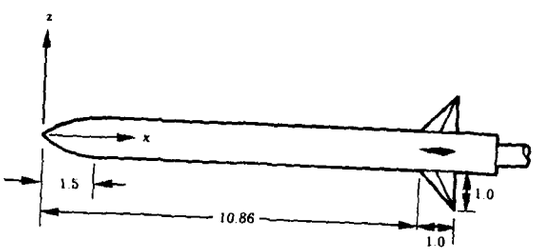
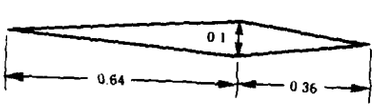


Figure 16: *Elliptic body convergence history at 2° incidence and varying Mach number*



TANGENT OGIVE NOSE WITH BLUNTED TIP (Radius 0 05)

All dimensions in calibres



FIN ROOT SECTION (Enlarged)

Figure 17: *RAE model 2073 (BICCIR) body-fin configuration*

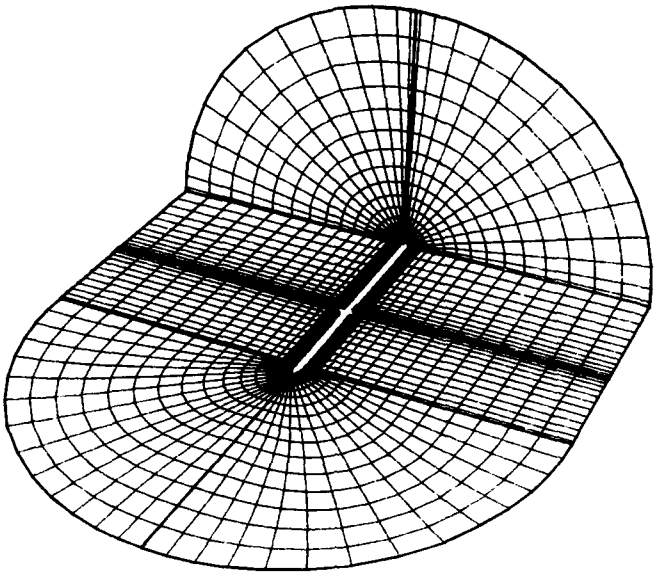


Figure 18: Perspective view of typical body-fin grid

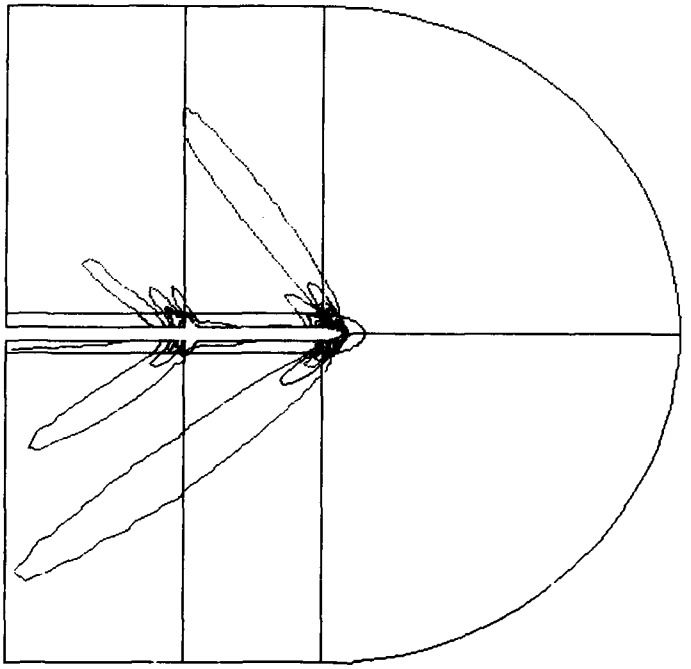


Figure 19: Symmetry-plane pressure contours for body-fin configuration at Mach 1.45 and 8° incidence

ARCJET VALIDATION OF SURFACE CATALYCITY USING A VISCOUS SHOCK-LAYER APPROACH

by

Allen D.Zwan, Richard S.Crooks and Walter J.Whatley
General Dynamics Convair Division
PO Box 85357
San Diego, CA 92138, USA

ABSTRACT

A two-dimensional planar, viscous shock layer code was developed to analyze surface catalytic effects on small, leading edge test specimens in an arcjet environment. An arcjet test was performed to generate validation data for the newly developed code. The test program consisted of testing leading edge test specimens with radii of 0.10, 0.25, and 0.35 inches. Test specimens of each radius were coated with silicon carbide, silicon monoxide, or nickel. The code predicted the surface recombination rates for silicon carbide and nickel coatings. These rates agree well with other values found in similar literature.

NOMENCLATURE

A_{eff}	Effective nozzle exit area (neglecting boundary layer)
h_1, h_2, h_3	Shape factors for general orthogonal coordinate system
h_N	Enthalpy of dissociation of nitrogen
h_O	Enthalpy of dissociation of oxygen
p	Pressure
R_n	Nose radius
R_{sh}	Radius of shock from axis
T	Temperature
u,v,w	Velocity components, u*/U ,v*/U ,w*/U
V	Velocity
α	Atom mass fraction
$\varkappa_s$	Body curvature in the streamwise direction, = R_n
ξ, η, ζ	Normalized surface-oriented coordinates
ρ	Density

Subscripts

N	Nitrogen
O	Oxygen
sh	Conditions behind the bow shock
w	Wall conditions
T	Total conditions
∞	Dimensional freestream conditions

Superscripts

$\bar{(\ )}$	Normalized variable
*	Dimensional variable

INTRODUCTION

In 1986, General Dynamics Convair Division conducted a material test program[1] at the NASA Ames Arcjet Facility to evaluate coated carbon-carbon wing leading edge test specimens. During the test, heat flux inferred from thermocouple measurements indicated a strong catalytic surface effect on heat transfer due to the nonequilibrium state of the test environment. Because the test was primarily a materials and coating evaluation, the data generated was inadequate to determine catalytic properties of the various coatings. Furthermore, a detailed finite rate analysis of the two-dimensional geometries tested required the development of a new analytical CFD tool for data reduction.

To analyze the arcjet's complex chemically reactive flowfield, the Two-Dimensional Viscous Shock-Layer code (VSL2D) was developed. A follow-on test program[2] conducted in 1987 provided data to help determine the catalytic properties of candidate carbon-carbon coating materials using the VSL2D program. Both the arcjet test program and the ensuing development and validation of the VSL2D program are discussed.

ARCJET TEST PROGRAM

The arcjet test program was divided into three major areas: catalycity, instrumentation, and heat conduction. This paper discusses the catalytic objectives of the test. Fourteen test runs were completed during which three leading edge radii and three surface coatings were evaluated. Geometries of the test specimens were 0.10-, 0.25-, and 0.35-inch radii. The test specimens, end guards, and holding f[illegible] are illustrated in Figure 1. All specimens were initially coated with silicon carbide (SiC) through a chemical vapor deposition proce[illegible]. Specimens of each radii were subsequently coated with nickel (Ni) and silicon monoxide (SiO) by physical vapor deposition. Ni, SiC, and SiO were chosen as coatings that should exhibit highly catalytic, moderately catalytic, and low catalytic surface properties,[3] respectively. Test samples and end guards were machined from bulk, coating-grade graphite. Material properties of the substrate material were obtained from the vendor. In addition to the test specimens, a cold wall, two-dimensional calorimeter was developed with the same geometry as the 0.25-inch radius test specimens. The calorimeter was instrumented with two flux gauges: one coated with SiO in the same manner as the test specimens; the other remained uncoated. These were expected to provide cold wall data for two levels of accepted surface catalycity that would aid in the establishment of the arcjet free stream conditions. Useful data from this calorimeter was not obtained due to a mechanical failure of the calorimeter water-cooling system.

To maintain direct comparison to data from the materials test performed in the same facility in 1986, the same test conditions were used. Nominal test conditions of 62 psf stagnation pressure at an approximate stream enthalpy of 8,000 Btu/lbm were repeated. A second test condition with a lower enthalpy environment was added. The low test condition was selected to produce a leading edge

temperature of approximately 2,500F on the Ni-coated 0.25-inch-radius specimen. This temperature limit was chosen to ensure that the Ni coating remained below its melting point while preserving the nonequilibrium flowfield. Because the lower condition provided data for the Ni-coated specimens, this condition was analyzed, and the results are documented in this paper. Tests were run in a two-step mode. The low condition was held for approximately 400 seconds to achieve a steady-state material temperature condition. Arcjet

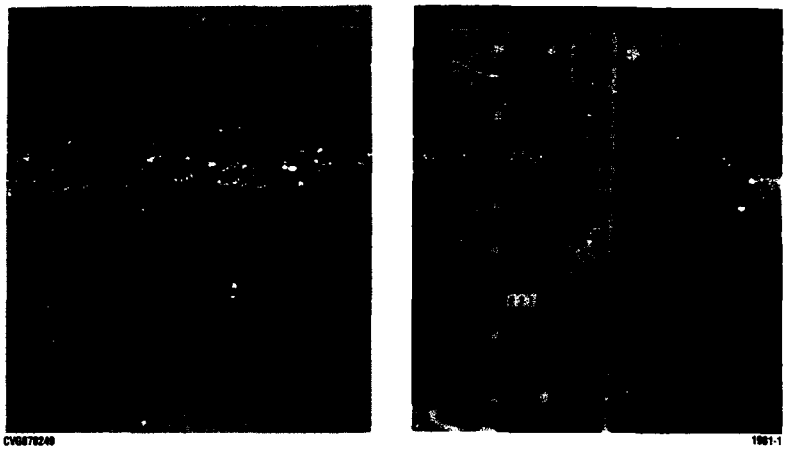


Figure 1. Leading edge test specimens and holding fixture.

settings were then adjusted to the higher condition for an additional 200 seconds to achieve the steady state for this higher enthalpy condition.

HEAT FLUX ANALYSIS

A two-inch-radius, hemispherical calorimeter was used to establish the test condition in the same manner as the previous materials test. The calorimeter was water cooled and measured heat flux directly using a constantan Gardon gauge. Temperature distribution of the test specimen was measured with embedded tungsten-rhenium thermocouples. In addition, two optical pyrometers were used to measure the surface temperature at three locations on the test specimen. One directly measured the relative intensity of photon energy of the surface, and the other, a tungsten wire pyrometer, matched the illuminescence of the wire to that of the leading edge. The physical location of the pyrometers in relation to the test specimens is shown in Figure 2.

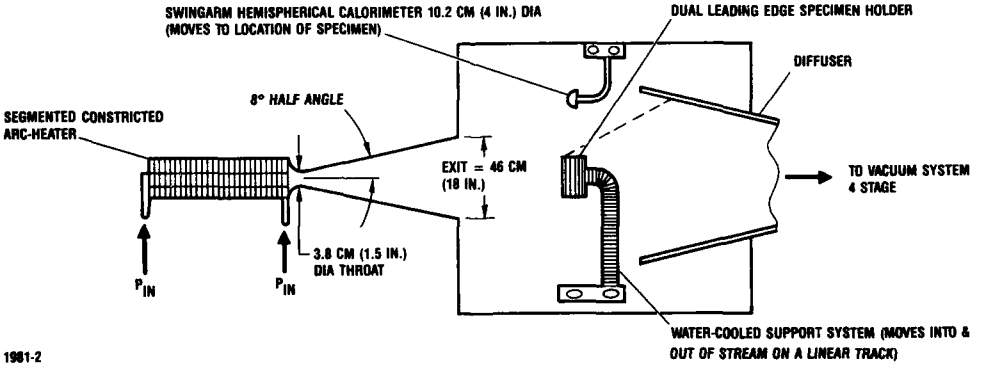


Figure 2. NASA Ames 20-MW arcjet facility.

An in-depth, three-dimensional thermal model of the complete fixture and specimen refined from the previous arcjet test was used to calculate the temperature profile throughout the geometry. Additional detail was added to the model at the stagnation point. The thermal model, thermocouple placements, and pyrometer reading locations for the individual specimen are shown in Figure 3. The pyrometer values were used to validate the thermal model by a comparison of the predicted surface temperatures using the embe thermocouple data and the optically measured surface temperatures. To simplify the analysis and reduce the extensive computational requirement of generating transient thermal analysis, the steady-state condition was used for the analysis. Curves of the imposed heat flux versus stagnation point surface temperature were generated using the thermal model for the steady-state condition (Figure 4). Due to the unique conduction path and external flowfield of each geometry, there are distinct curves for each radius. The trend of these curves indicate that as the geometries increase in relative size, the resulting curves will coalesce. This would be expected since the limiting case is the infinite radius or one-dimensional flat plate case.

ARCJET FLOWFIELD DETERMINATION

One of the most important criteria for analyzing shock-layer flow is confidence in the assumed freestream conditions. In the arcjet, the freestream condition is assumed to be the state of the flow immediately adjacent to the shock generated by the test specimen. This

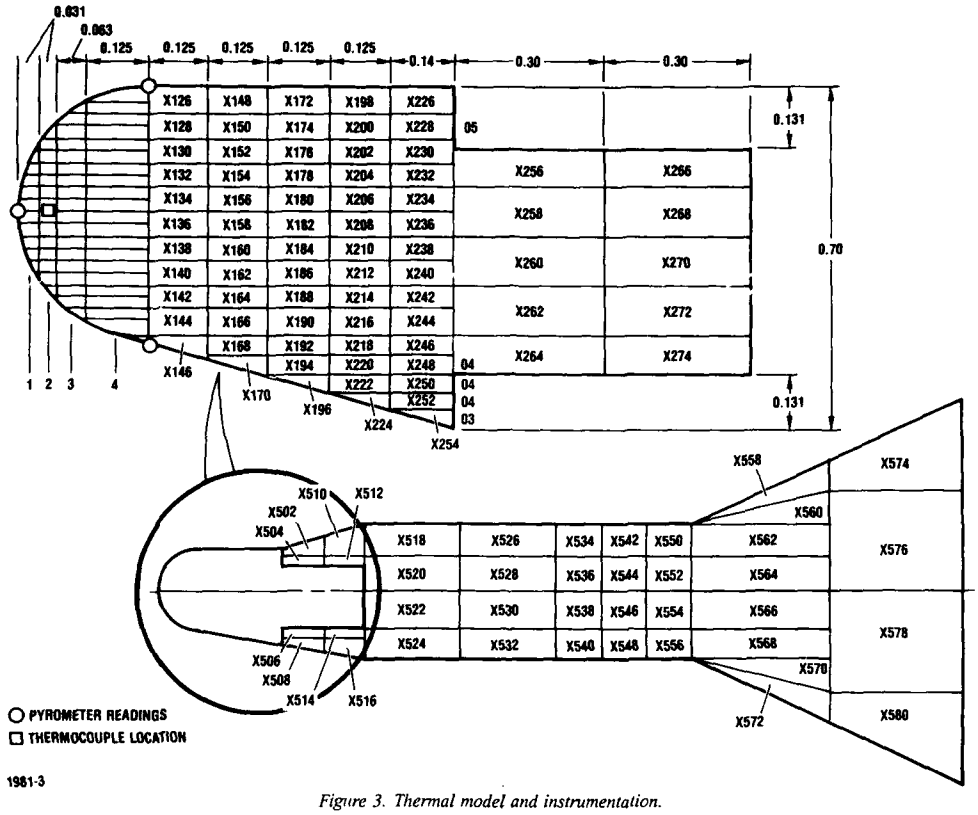


Figure 3. Thermal model and instrumentation.

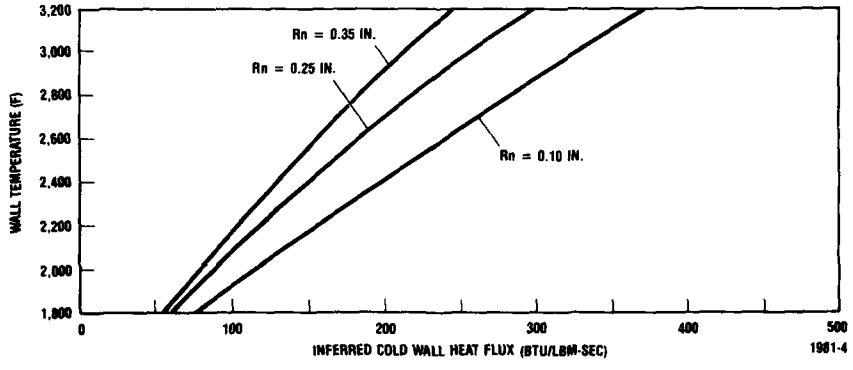


Figure 4. Cold wall heat flux vs. stagnation point surface temperature.

requires definition of the complex arcjet nozzle exit conditions. Currently there is no reliable measuring procedure to define these conditions, especially the chemical composition at the exit plane of high enthalpy arc streams. There have been attempts to model[4,5] the entire arc jet flow from the chamber to the nozzle exit using finite rate gas kinetics. These attempts have met with limited success. The approach used for defining the exit conditions was a combination of one of these arc flow programs, the NATA code,[5] and a method that solved the simple flow conservation equations. The NATA code was not used solely since it does not accurately characterize the flowfield chemistry[6] due to the assumption that the flow is in equilibrium in the reservoir.

Quantities measured in the arcjet experiment were stagnation pressure, exhaust chamber pressure, nozzle mass flow, and the temperature response of the test specimens. The NATA code was used to calculate the total enthalpy of the arcjet stream since small errors in the chemical composition should not affect the total enthalpy. The enthalpy was obtained by iterating on a total enthalpy value, which eventually resulted in predicted arcjet conditions that matched the measured quantities of stagnation pressure, exhaust chamber pressure, and nozzle mass flow. An added benefit of using the NATA code was the generation of the effective nozzle exit area based on

boundary layer calculations. With these calculated and measured quantities, the simplified flow equations for an inviscid stream tube were then solved.

Energy	$h_t = 1/2\ V_\infty^2 + 0.232\ h_o + \alpha_N\ h_N + C_p\ T_\infty$
Mass	$m = \rho_\infty\ V_\infty\ A_{eff}$
Momentum	$P_\infty = \rho\ V_\infty^2 + P_\infty$
Equation of State	$P_\infty = \rho_\infty\ R\ T_\infty$

The solution of the simultaneous equations determines the freestream quantities: temperature, density, velocity, and the atomic nitrogen mass fraction. Molecular oxygen is assumed to be fully dissociated at this arcjet condition. This assumption is also supported in the NATA solution. Furthermore, an assumption is made that the flow is frozen at the throat, which again is supported by the NATA solution. This assumption is generally accepted and has been indicated through analyses of many arcjet tests.[6]

The freestream values of velocity, pressure, gamma, and chemical composition are then used as the freestream conditions for the viscous shock-layer analysis using the VSL2D code.

SELECTION OF A CFD SOLUTION APPROACH

The analysis of the flowfield around the test specimens required a code capable of simulating the complex chemical gas phase and surface reactions that occur within the shock layer. The imposed ground rules for the development of such a code were:

1. Use an existing code for the core program,
2. Neglect surface material chemical interaction, and
3. Have the capability for:
   - Analysis of two-dimensional planar geometries
   - Computation of flowfields within arcjet environments
   - Finite rate gas phase kinetics
   - Finite rate surface recombination, and
   - Wall and/or shock slip.

A search of current computer programs that met most of the ground rules revealed two family of codes—the viscous shock layer (VSL) and finite rate boundary layer (BL) methods. The VSL equations are a subset of the Navier-Stokes equations, and in terms of complexity, fall between the parabolized Navier-Stokes (PNS) and boundary layer equations. The major advantage of the viscous shock layer equations is they remain hyperbolic-parabolic in both the streamwise and crossflow directions. Furthermore the VSL equations have the capability to compute the viscous flow in the subsonic blunt nose region by an iterative procedure determining the shock shape. The simplicity of the VSL method facilitated the addition of the finite rate gas phase chemistry.

At the test conditions of interest, the BL equations are less suited for the flow regime. At the low density, low Reynolds Number flows, the boundary layer is not thin and well defined. In fact, in most cases the boundary layer becomes a fully merged viscous layer. Figure 5 illustrates the limits of the shock Reynolds Number where the different flow regimes are present. In some boundary layer codes, particularly the BLIMPK code,[7] there is a shock layer option. However, this option still assumes the BL equations are applicable, thereby imposing a constant pressure across the entire shock layer and violating the physics of high curvature flow found in the nose region of small geometries. In addition, the BL method lacks the capability to simulate shock and/or wall slip. For these reasons, the boundary layer method was not used.

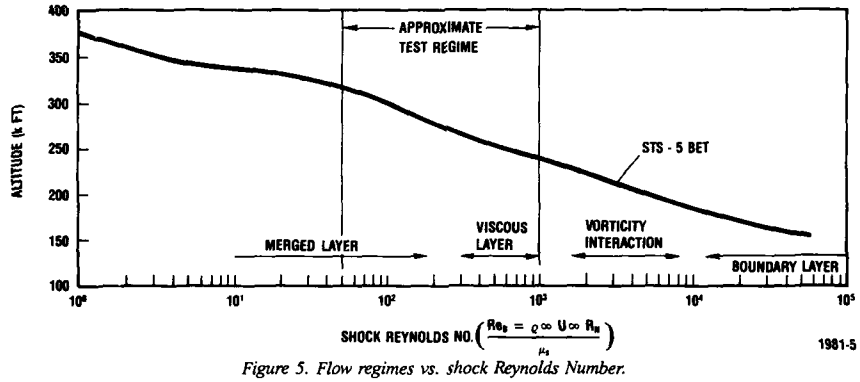


Figure 5. Flow regimes vs. shock Reynolds Number.

DEVELOPMENT OF THE VSL2D PROGRAM

There have been many viscous shock layer codes[8, 9, 10] developed to analyze various elementary three-dimensional geometries (i.e., hyperboloids, sphere cones, etc.). Analysis of the flowfield environment for this test required a two-dimensional planar analysis tool not currently available in the industry. Most of the methods were developed for nose tips and vehicle body analysis. The approach to developing such an analysis tool was to modify an existing three-dimensional VSL code to support two-dimensional planar analysis. The VSLNQ code[9] was used as the core program. This particular version was chosen because of General Dynamics Convair's recent code experience[11] and the successful Space Shuttle heating predictions (Figure 6). The program required modifications in the following areas:

1. Redefinition of the metrics and their derivatives
2. Derivation of the shock stand-off distance from flow equations
3. Derivation of the stagnation point velocity profile from the continuity equation
4. Developing an arbitrary two-dimensional shock shape module
5. Developing mass flow equations and convergence criteria
6. Developing/modifying finite rate surface kinetics module
7. Developing capability for highly dissociated free stream conditions

The following paragraphs define some of the flowfield equations derived for two-deminsional planar flow.

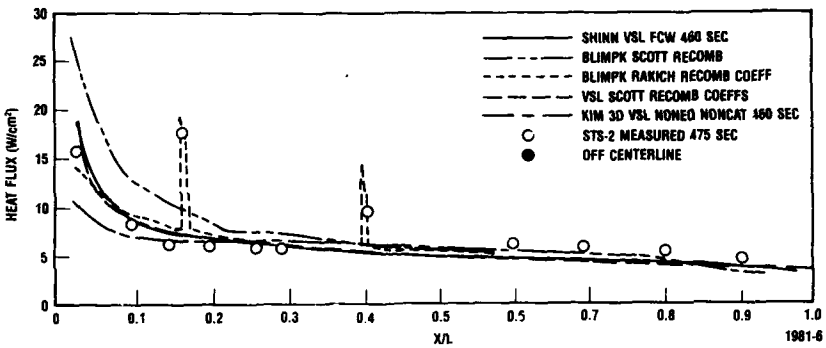


Figure 6. Comparison of calculated and measured Shuttle heat fluxes for STS-2, t=460 sec, V_{inf}=7.16 km/sec, and altitude of 74.7 km.

Shock Stand-off Distance (SSD) – The continuity equation is integrated from the body to the shock to obtain the shock stand-off distance. The continuity equation can be written as:

$$\frac{\partial}{\partial\xi}\left(\eta_{sh}\,\rho_{sh}\,u_{sh}\,\bar{\rho}\,\bar{u}\,h_3\right) - \frac{\partial}{\partial\eta}\left(\frac{\partial\eta_{sh}}{\partial\xi}\,\rho_{sh}\,u_{sh}\,\bar{\rho}\,\bar{u}\,h_3\right) + \frac{\partial}{\partial\eta}\,(h_1\,h_3\,\rho_{sh}\,\bar{\rho}\,\bar{v}) \tag{1}$$

$$-\frac{\partial}{\partial\eta}\left(\frac{\partial\eta_{sh}}{\partial\zeta}\,\eta\rho_{sh}\,\bar{\rho}wh_1\right) + \frac{\partial}{\partial\zeta}\left(\eta_{sh}\,\rho_{sh}\,\bar{\rho}\,wh_1\right) = 0$$

The terms involving the ζ derivative and the w component of velocity were removed, and the 2D equation is written as follows:

$$\frac{\partial}{\partial\xi}\,(\eta_{sh}\,\rho_{sh}u_{sh}\,\bar{\rho}\,\bar{u}) - \frac{\partial}{\partial\eta}\left(\frac{\partial\eta_{sh}}{\partial\xi}\,\eta\,\rho_{sh}\,u_{sh}\,\bar{\rho}\,\bar{u}\right) + \frac{\partial}{\partial\eta}\,(h_1\,\rho_{sh}\,\bar{\rho}\,v) \tag{2}$$

which is integrated with respect to η to give:

$$\left[h_1\,\rho_{sh}\,\bar{\rho}v - \frac{\partial\eta_{sh}}{\partial\xi}\,\eta\,\rho_{sh}\,u_{sh}\,\bar{\rho}\,\bar{u}\right]_0^1 + \int_0^1 \frac{\partial}{\partial\xi}\,(\eta_{sh}\,\rho_{sh}\,U_{sh}\,\bar{\rho}\,\bar{u})\,d\eta = 0 \tag{3}$$

Let $F = \rho_{sh}\,u_{sh}\int_0^1 \bar{\rho}\,\bar{u}\,d\eta$

$$\frac{\partial\,(F\eta_{sh})}{\partial\xi} = \frac{F\eta_{sh_i} - F\eta_{sh_{i-1}}}{\Delta\xi}$$

Then

$$\left[h_{1_{\eta=1}}\,\rho_{sh} - V_{sh}\,\frac{\partial\eta_{sh}}{\partial\xi}\,\rho_{sh}\,u_{sh} - h_{1_{\eta=0}}\,\rho_w\,v_w\right] + \frac{F\eta_{sh_i} - F\eta_{sh_{i-1}}}{\Delta\xi} = 0 \tag{4}$$

$$\text{Let } a = \rho_{sh}\,V_{sh}\,h_{1_{\eta=1}} - \frac{\partial\eta_{sh}}{\partial\xi}\,\rho_{sh}\,u_{sh} - \rho_w\,V_w \tag{5}$$

$$\eta_{sh} = \frac{-\frac{1}{2}\,\Delta\xi\,[a_i + a_{i-1}] + F\eta_{sh_{i-1}}}{F}$$

Stagnation Point SSD and Velocity Profile – At the blunt stagnation point, the ξ derivatives of the stand-off distance and the tangential shock velocity are zero, which creates a singularity when solving the flowfield equations. To treat this singularity, the following limits were applied to the continuity equation as ξ approaches zero:

$$r \to \xi.\,\cos\theta_s \to \xi.\,U_{sh} \to \xi\,\frac{\partial\,U_{sh}}{\partial\xi} \tag{6}$$

At ξ=0, $\frac{\partial\eta_{sh}}{\partial\xi}$=0, the continuity equation becomes:

$$\frac{\partial}{\partial\xi}\left(\eta_{sh}\,\rho_{sh}\,\xi\,\frac{\partial u_{sh}}{\partial\xi}\,\bar{\rho}\,\bar{u}\right) + \frac{\partial}{\partial\eta}\,(h_1\,\rho_{sh}\,v_{sh}\,\bar{\rho}\,\bar{v}) = 0$$

Using the relationship $\rho_{sh}\,V_{sh}$=-1 at the stagnation point and differentiating the first term with respect to ξ gives:

$$\frac{\partial}{\partial \eta}(h_1 \bar{\varrho} \bar{v}) = \eta_{sh}\, \varrho_{sh}\, \frac{\partial u_{sh}}{\partial \xi}\, \bar{\varrho}\, \bar{u} \tag{7}$$

$$h_1 \bar{\varrho}\, \bar{v} \Big|_0^1 = \frac{2\, \eta_{sh}\, \varrho_{sh}\, u_{sh}}{\Delta \xi} \int \bar{\varrho}\, \bar{u}\, d\eta$$

$$h_1 = \frac{2\, \eta_{sh}\, \varrho_{sh}\, u_{sh}}{\Delta \xi} \int \bar{\varrho}\, \bar{u}\, d\eta + \bar{\varrho}_w\, \bar{v}_w \tag{8}$$

$$h_1 = 1 + \kappa_s\, \eta$$

Where

$$\kappa_s^* = \frac{1}{R_n}\ ;\ \kappa_s = \kappa_s^* R_n \rightarrow \frac{R_n}{R_n} = 1 = \kappa_s$$

at the stagnation point.

Hence

$$1 + \eta = \frac{2\, \eta_{sh}\, \varrho_{sh}\, u_{sh}}{\Delta \xi} \int \bar{\varrho}\, \bar{u}\, d\eta + \bar{\varrho}_w\, \bar{v}_w \tag{9}$$

Let $F_1 = \varrho_{sh}\, u_{sh} \int_0^1 \bar{\varrho}\, \bar{u}\, d\eta$

$$\eta \left(\frac{2 F_1}{\Delta \xi} - 1 \right) + \bar{\varrho}_w\, \bar{v}_w - 1 = 0 \tag{10}$$

$$\eta = \frac{1 - \bar{\varrho}_w\, \bar{v}_w}{\left(\frac{2}{\Delta \xi} F_1 - 1 \right)} \tag{11}$$

Integrating Eq. 7 from 0 to η and rearranging terms gives the following expression for the stagnation normal velocity component.

$$h_1 \bar{\varrho}\, \bar{v} \Big|_0^\eta = \frac{2\, \eta_{sh}\, \varrho_{sh}\, u_{sh}}{\Delta \xi} \int_0^\eta \bar{\varrho}\, \bar{u}\, d\eta \tag{12}$$

Let $F_2 = \varrho_{sh}\, u_{sh} \int_0^\eta \bar{\varrho}\, \bar{u}\, d\eta$ and solve for $\bar{v}$:

$$\bar{v} = \frac{2\, \eta_{sh}\, F_2}{\Delta \xi\, \bar{\varrho}\, h_1} \tag{13}$$

The mass flow ratio was determined by integrating the mass flow across the shock layer at a given surface station then dividing by the mass flow that crossed the shock from the stagnation point to a plane perpendicular to the given surface station. The mass flow ratio is written as:

$$\text{Ratio} = \frac{\sum \varrho_s\, u_s \cdot \frac{(\varrho\,(2) + \varrho\,(1))}{2} \cdot \frac{(u\,(2) + u\,(1))}{2} \cdot [Y\,(2) - Y\,(1)]}{\varrho_\infty u_\infty R_{sh}} \tag{14}$$

Currently only the hyperbola geometry model is operational. The other two-dimensional model (a cylinder/wedge) has been developed but is not fully operational.

Code Verification – Results of a fully catalytic surface are shown in Figures 7 and 8 for a hyperbola with a 1.00-ft nose radius and an asymptotic angle of 20 degrees. The free stream conditions represent an altitude of 157,000 ft and velocity of 17,600 ft/sec. The selection of this flight condition was arbitrary with the constraint that it would produce a nonequilibrium flowfield in the VSL2D solution. Figure 7 illustrates the change in the initial shock shape, for the body shape shown, with each global iteration. The shock shape and location is initially the shape and location used for the three-dimensional case, thus causing the excessive iterations and resulting expansion of the shock. The resulting heat transfer distribution around the body is indicated in Figure 8, which shows individual magnitudes of the total, conductional, and diffusive components. There is a slight irregularity at the second step that is inherent in the numerics for this family of VSL codes. The Fay-Riddell[12] equilibrium solution with laminar swept wing theory prediction is also indicated on the figure and is in excellent agreement with the VSL2D prediction. Figure 9 shows the same calculation for a hyperbola nose radius of 0.5 inch. The code required approximately a 20% increase in computational time to reach the solution. This increase in time is directly related to the size of the geometry being analyzed due to the difficulty of resolving the large gradients found in this high curvature flow.

The results of the finite rate model are shown in Figure 10 for similar conditions. The figure shows the heat transfer distribution for a selected set of surface recombination rates. In this case the nitrogen and oxygen rates were set equal. The finite rate option for both the two- and three-dimensional geometries required a much tighter constraint on the convergence criteria when solving the flowfield and chemistry equations. Figure 11 illustrates the sensitivity of the constraint to the expected solution. The tightened constraints resulted in a measurable increase in computational time. Furthermore, the finite rate option affects the ability of full convergence on the global mass flow criteria.

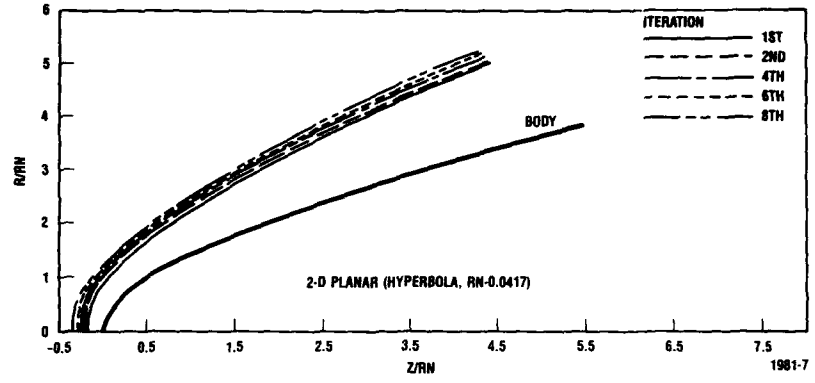


Figure 7. VSL2D shock shape convergence.

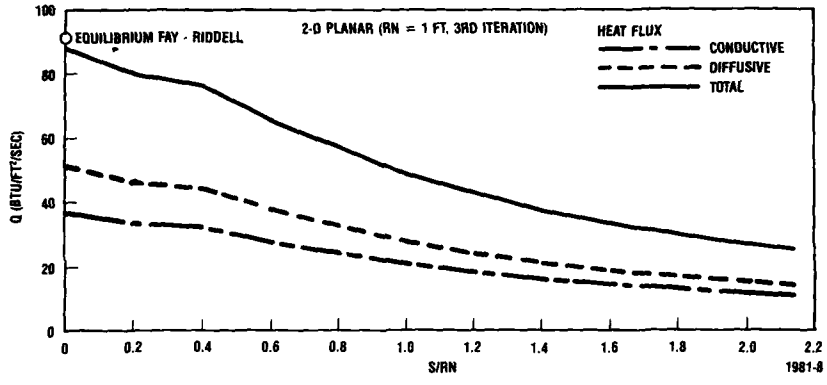


Figure 8. Heat transfer distribution for Rn= 1.0 ft.

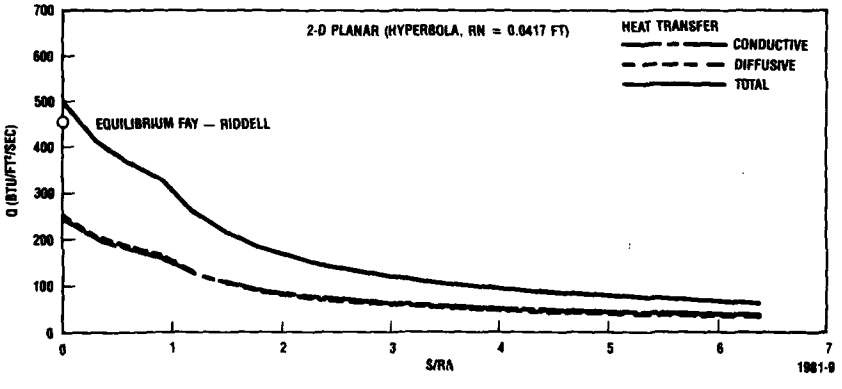


Figure 9. Heat transfer distribution for Rn= 0.047 ft.

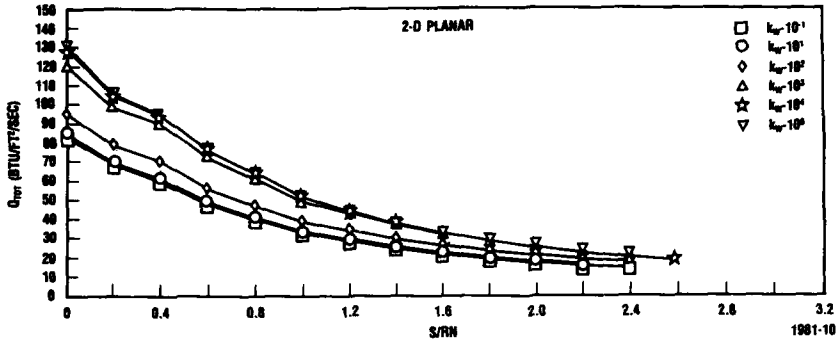


Figure 10. Heat transfer distribution for varying kW.

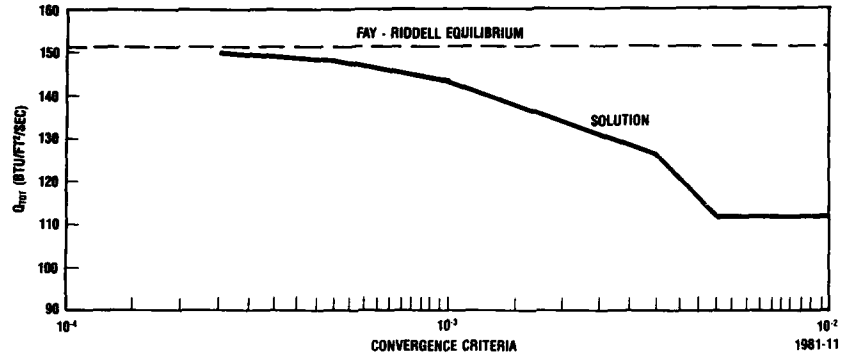


Figure 11. Convergence criteria's effect on solution.

EXPERIMENTAL RESULTS

The objectives of the test were to obtain data for validation of the VSL2D code and determine whether this approach provides a method for determining surface recombination rates of various coating materials. Since the tests were run in an air environment, the resulting recombination rates will be an effective "air" value. Therefore, the individual nitrogen and oxygen rates will be set equal to one another. The calorimeter was slowly swept across the arc stream to determine the heat flux profile in the vicinity of the test specimens. The sweep indicated a relatively constant heat flux across the test plane and is illustrated in Figure 12 along with the test specimen dimensions.

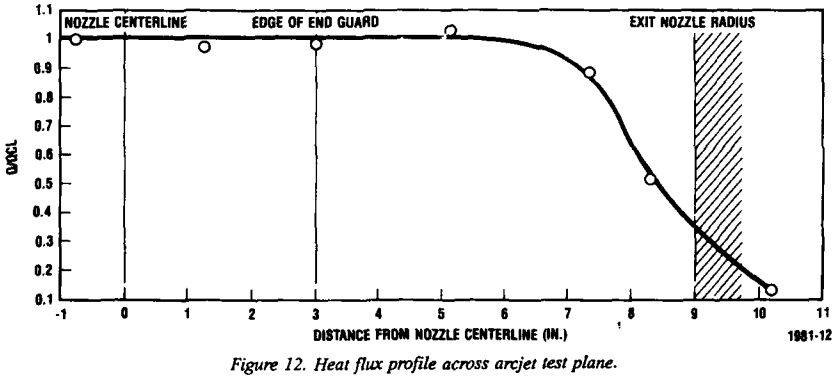


Figure 12. Heat flux profile across arcjet test plane.

Experimental Data – The measured test conditions were:

Mass Flow	0.095 lbm/sec
Stagnation pressure	26.5 psf
Chamber pressure	0.25 psf
Heat flux 4-in. Cal	88.5 Btu/lbm-sec

Based on these measured quantities, the NATA code solution resulted in a total enthalpy of 8,725 Btu/lbm. This value agrees well with

the simplified equilibrium Fay-Riddell value of 8,254 calculated from the measured flux on the four-inch calorimeter. The surface temperatures and the resulting inferred stagnation point heat flux are shown in Table 1 for each of the individual test specimens. Figure 13 illustrates the temperature response of the leading edge thermocouples for a Ni- and SiC-coated 0.10-inch radius test specimen. In most cases the steady-state conditions were achieved as indicated by the two distinct plateaus of the lower curve (SiC coating). This figure also illustrates the disintegration of the Ni coating on the specimen and is indicated by the drastic decrease in surface temperature during the initial temperature rise in the top curve. As the Ni disintegrates, the surface properties of the undercoating material (SiC) become dominant—thus the coalescence of the two curves. Figure 14 shows the actual flow fields generated during the tests of the three specimens with different radii. The photographs were not discrete enough to measure the shock stand-off distance but rather gave a general trend of the shock shapes. Also indicated in the figure is the Ni-coating effect on the heat transfer to the left test specimen, shown by the increased illuminescence of the specimen. This was seen until the Ni disentegrated, at which time both specimens appeared to have the same illuminescence. Because of the inability of the Ni-coated specimen to reach steady state at the low condition on the smaller geometries, only the 0.35-inch-radius specimen values were used. Figure 15 illustrates the thermal response of the 0.35-inch-radius, Ni-coated specimen. It is assumed that the peak is the steady state since the profile does not indicate any abrupt changes in the heat flux. This value was repeatable as indicated in Table 1. In general, the SiC- and SiO-coated specimens, regardless of radius size, responded with the typical temperature profile as seen in Figure 16 for a SiC-coated, 0.25-inch-radius specimen.

Table 1. Test specimen data.

			Left Specimen			Right Specimen		
Run No.	Rn (in.)	4-in. Cal	Coating	Wall Temperature (F)	Inferred Flux	Coating	Wall Temperature (F)	Inferred Flux
3	0.25	81.3	—	—	—	SiC	1,997	86
4	0.25	82.8	SiC	2,002	87	SiC	2,050	94
5	0.25	86.6	SiC	2,132	106	Ni	—	—
6	0.25	88.9	Ni	—	—	SiO	2,156	109
7	0.25	88.9	SiC	1,951	80	SiC	1,936	78
9	0.35	92.7	Ni	2,728	171	SiO	2,087	88
10	0.35	89.7	SiC	1,960	72	SiO	2,108	92
11	0.10	90.4	Ni	—	—	SiO	2,151	145
12	0.35	91.2	Ni	2,705	168	SiC	2,006	79
13	0.10	85.9	SiC	2,019	117	—	—	—
14	0.10	92.0	SiC	2,053	125	Ni	—	—
15	0.25	91.7	SiC	1,875	70	SiO	1,972	83

1981-13

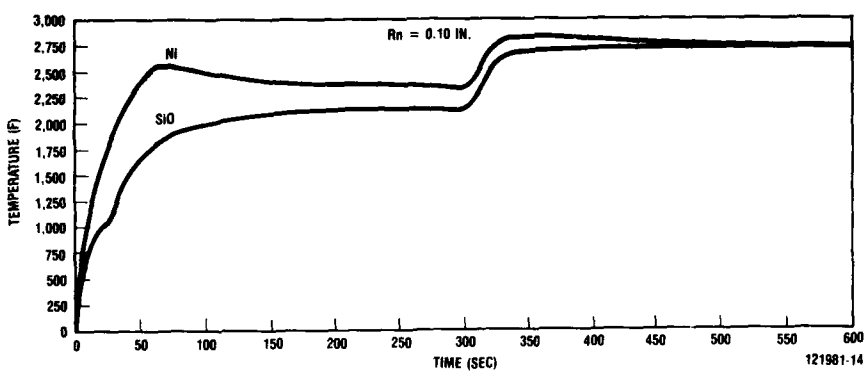


Figure 13. Specimen leading edge T/C response - Run = 11.

ANALYTICAL RESULTS

The arcjet exit conditions were defined using the previously described method. The following are the free stream conditions calculated for the low enthalpy environment:

Temperature	628.0R
Pressure	0.236 psf
Density	1.524E-07 slug/ft^3
Gamma	1.523
Velocity	12.656 ft/sec
$\propto$ N	0.262

An effective hyperbola nose radius and asymptotic angle were required to model the calorimeter. The asymptotic angle of 20 degrees was chosen due to the code's inability for robust solutions at smaller angles. The nose radius was obtained by iterating on a radius until the shock stand-off distance equaled the measured stand-off distance. The equivalent hyperbola and the predicted shock shape are shown in Figure 17 along with the calorimeter geometry and the measured shock. Using the VSL2D code with the three-dimensional option, an "S" curve was generated for predicting the surface heating of the hemispherical calorimeter (Figure 18). The intersection of the curve with the measured heat flux indicates a surface recombination rate of 840 cm/sec. This agrees well with values predicted from other tests.[13]

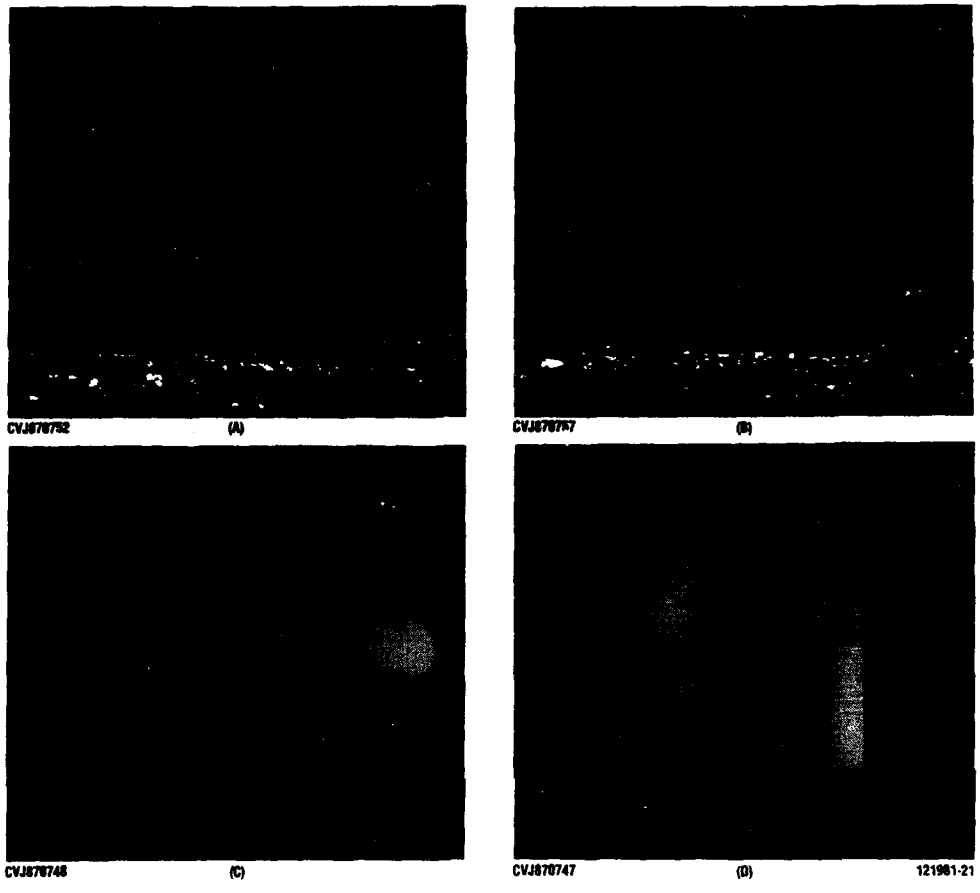


Figure 14. Flowfield visulization of the test specimens: a) Rn = .10 in., b) Rn = .25 in., c) Rn = .35 in., d) Ni coated

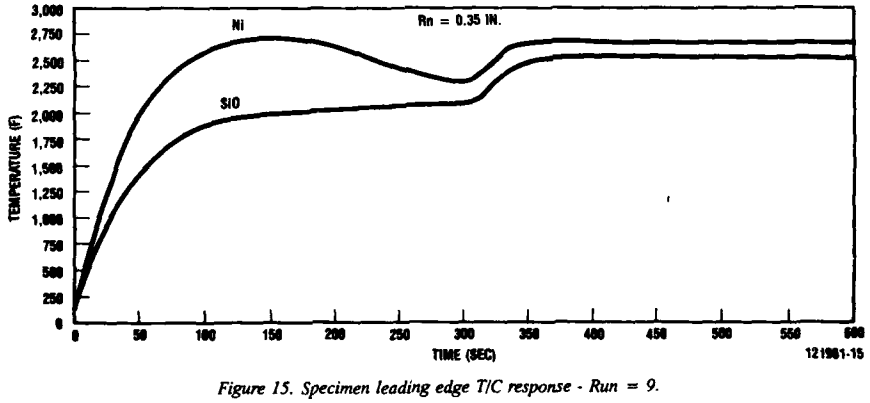


Figure 15. Specimen leading edge T/C response - Run = 9.

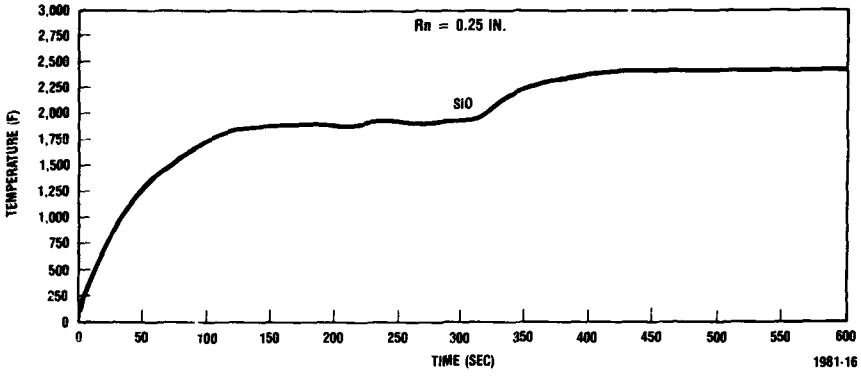


Figure 16. Specimen leading edge T/C response - Run = 7.

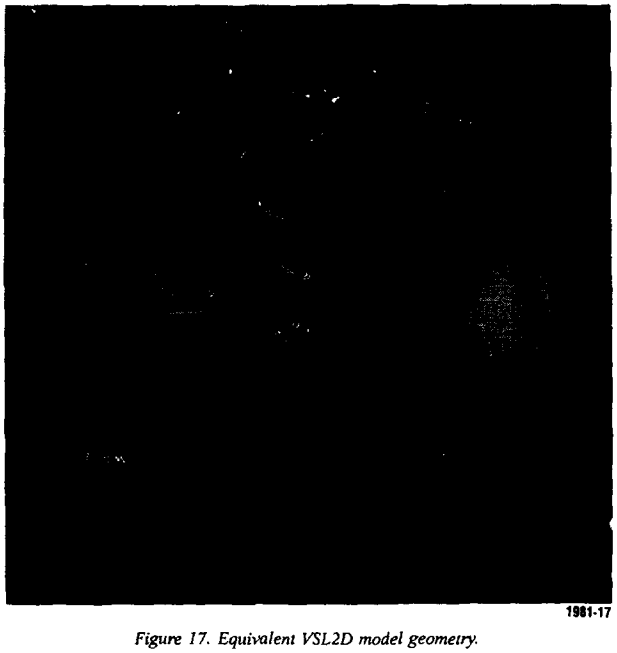


Figure 17. Equivalent VSL2D model geometry.

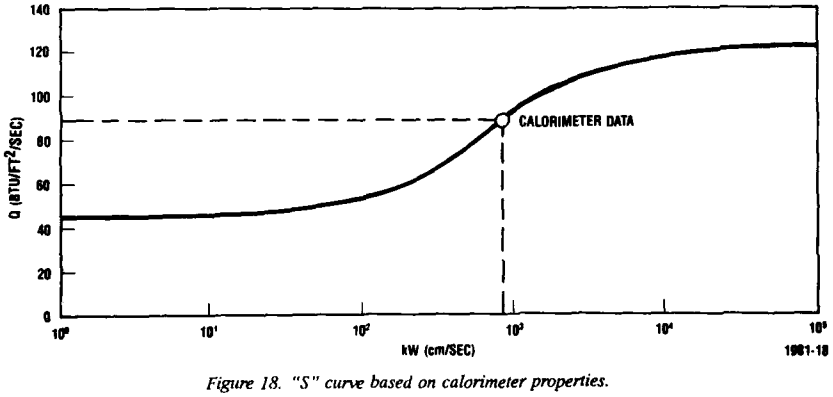


Figure 18. "S" curve based on calorimeter properties.

With further confidence in the exit conditions, an "S" curve was generated for both the 0.25- and 0.35-inch-radius specimens. The two curves are shown in Figure 19 with the upper curve being the 0.25-inch-radius case. The VSL2D code began indicating instability problems when the 0.10-inch-radius case was executed, hence this data was not used in the final results. From these "S" curves the surface recombination rates were extracted based on the calculated heat flux. These reaction rates were then plotted against the familiar inverse wall temperature parameter illustrated in Figure 20. The 0.25-inch data falls remarkably close together in a linear fashion as one would expect from previous tests and theory. The SiC- and SiO-coated specimens appear to exhibit the same surface properties even though SiO is known to exhibit lower catalytic surface properties. This is misleading since it is fairly certain the SiO coating either disintegrated or eroded at the beginning of the tests exposing the SiC undercoating. This was observed on the two-dimensional calorimeter where the Gardon gauge, which had the SiO coating, indicated the same inferred flux as the uncoated gauge. Visual inspection could find no trace of the SiO coating in the stagnation region. When the gauge was sprayed with a teflon-based spray, there was a significant drop in the inferred heat flux indicating the gauge was sensitive enough to measure the effects of a surface coating. The 0.35-inch data was limited with only two data points for each of the different surface coatings. The SiC and SiO data points fell just above the 0.25-inch data in the same linear fashion. This parallelism of the two sets of data might indicate some radius effect on the surface recombination rate. The Ni data is much higher and, as expected, at a much higher surface temperature.

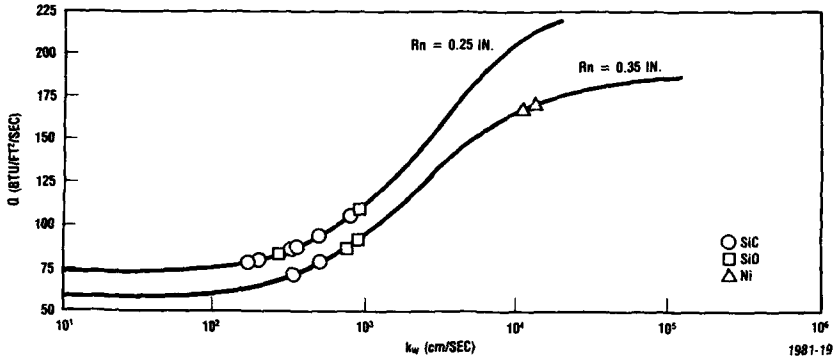


Figure 19. "S" curves for leading edge test specimens.

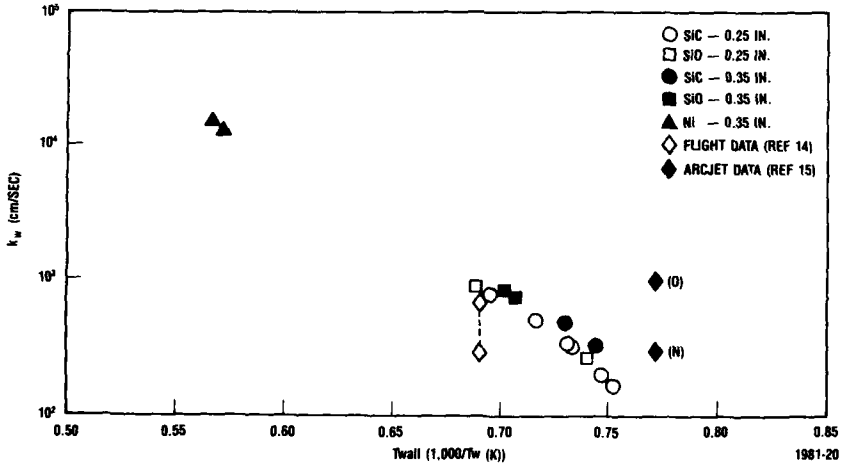


Figure 20. Predicted catalytic reaction rate constants.

Two sets of data on SiC were found for comparison: (1) values obtained from flight data and (2) data obtained from other arcjet tests. In general there is not a lot of available data for SiC recombination rates while there is much data for the RCG-type materials used on the Space Shuttle tiles. Since this is also a silicon-based material, it should exhibit surface properties similar to SiC, which was shown to be the case. To avoid confusion only, the SiC data is shown on Figure 20 for comparison. The flight data[14] indicates that a recombination rate of 300 to 700 cm/s RC for air matches the flight data depending on the solution method used. The data range is indicated with a dashed line. The upper values of this range follow the data generated in this experiment exceptionally well. The arc jet data[15] is in the form of individual recombination rates for oxygen and nitrogen and are indicated as such on the figure. The effective "air" value would fall between these two values, closer to the nitrogen value since the dissociation enthalpy of nitrogen is almost double that of oxygen. The placement of this effective value would again agree well with the data obtained from this test. There as no readily available Ni data for comparison in the temperature range tested. If the SiC data is extrapolated to the same wall temperature as that of the Ni, the recombination rate of the nickel is approximately three to four times greater than that of the SiC coatings. This increase appears to be reasonable when compared to the rates of the same type coatings at much cooler temperatures.

CONCLUSION

A viscous shock-layer code has been modified and used to analyze two-dimensional planar geometries. Concurrently, an experimental arcjet test program for validation of the new code was performed. The test program provided sufficient data for a first level validation. In addition the following conclusions were made in this study:

1. The viscous shock-layer approach is a very applicable tool for the analysis of two-dimensional planar flowfields. There are restrictions on the geometry size, which can be analyzed. For the test conditions, the code could not achieve acceptable solutions for nose radii below 0.20 inch.
2. The VSL2D code has shown it is a viable tool for analyzing and predicting catalytic surface recombination rates. The recombination rates generated were for "air," but the capability of analyzing individual rates of nitrogen and oxygen is available.
3. Finite rate surface reactions for the two-dimensional geometries dramatically increase the convergence criteria resulting in extensive computational requirements.
4. Silicon carbide coatings, as used on the Space Shuttle Orbiter nose cap and leading edges, are very effective in reducing atomic oxygen and nitrogen recombination at the surface, hence significantly reducing the peak temperatures to the immediate structure.
5. The loss of the SiO and some of the Ni coating data might have been prevented if thicker coatings had been applied. The coating thicknesses were approximately 0.4 micron and could easily have been a magnitude larger with little, if any, effect to the thermal model.
6. Finally, the two-dimensional viscous shock-layer code, VSL2D, has been shown to be a valuable tool for analyzing reacting flows over two-dimensional planar bodies in both hypersonic flight conditions and dissociated arcjet environments.

REFERENCES

1. Whatley, W.J., et al., "Hypersonic Leading Edge Materials and Coating Arcjet Test Program," GDC-ERR-86-701, General Dynamics Convair Division, Feb 1988.
2. Crooks, R.S., et al., "Final Test Report - Leading Edge Catalycity Test Program," GDC-ERR-87-503, General Dynamics Convair Division, Dec 1987.
3. Scott, C.D., "Measured Catalycities of Various Candidate Space Shuttle Thermal Protection System Coatings at Low Temperatures," NASA TN D 7113, Sep 1972.
4. Nicolet, W.E., et al., "Analytical and Design Study for a High Pressure, High Enthalpy Constricted Arc Heater," AEDC TR-75-47, July 1975.
5. Bade, W.L., and Yos, J.M., *The NATA Code - Theory and Analysis*, Vol. I, NASA CR-2547, June 1975.
6. Scott, C.D., "Catalytic Recombination of Nitrogen and Oxygen on High-Temperature Reusable Surface Insulation," AIAA Paper 80-1477, Presented at AIAA 15th Thermophysics Conference, Snomass, Colorado, July 14-16, 1980.
7. Tong, H., et al., "Nonequilibrium Chemistry Boundary Layer Integral Matrix Procedure," Aerotherm Rpt. 73-67, July 1973.
8. Moss, J. N., "Solutions for Reacting and Nonreacting Viscous Shock Layers with Multicomponent Diffusion and Mass Injection," PhD Dissertation, VPI, Blacksburg, Virginia, Oct 1971.
9. Lewis, C.H., Song, D.J., "VSLNQH: An Axisymmetric Viscous Shock-Layer Code for Nonequilibrium Finite Rate Chemically Reacting Viscous Flows Over Hyperboloid Geometries," VRA, Blacksburg, Virginia, Feb 1982.
10. Murray, A.L., "Three-Dimensional Fully Viscous Shock Layer Flows Over Sphere-Cones at High Angles of Attack," Engineer Report, VPI, Blacksburg, Virginia, Jan 1978.
11. Zwan, A.D., Shih, P.K., "Nonequilibrium Heating Analysis," Tech Report IRAD 111-1306-602, General Dynamics Convair Division, Dec 1986.
12. Fay, J., Riddell, F.R., "Theory of Stagnation Point Heat Transfer in Dissociated Air," *Journal of Aeronautical Sciences*, No. 2, Vol. 25, pp. 73-85.
13. Goulard, R.,"On Catalytic Recombination Rates in Hypersonic Stagnation Heat Transfer," *Jet Propulsion*, Vol. 28, Nov. 1958,pp 737-745.
14. Ting, P.C., et al., "Comparison of Viscous Shock Layer Reentry Heating Techniques for Orbiter Nose Cap," AIAA Paper 86-1350, Presented at AIAA/ASME 4th Joint Thermophysics and Heat Transfer Conference, Boston, Massachusetts, June 2-4, 1986.
15. Tong, H., et al., "Computational Procedure for Evaluation of Space Shuttle TPS Requirements," AIAA Paper 74-518, Palo Alto, California, June 1974.

CFD VALIDATION EXPERIMENTS FOR INTERNAL FLOWS

Louis A. Povinelli
National Aeronautics and Space Administration
Lewis Research Center
Cleveland, Ohio 44135 U.S.A.

SUMMARY

CFD validation experiments at NASA Lewis Research Center are described in this paper. The material presented summarizes the research in three areas: Inlets, Ducts and Nozzles; Turbomachinery; and Chemically Reacting Flows. The specific validation activities are concerned with shock-boundary layer interactions, vortex generator effects, large low speed centrifugal compressor measurements, transonic fan shock structure, rotor/stator kinetic energy distributions, stator wake shedding characteristics, boundary layer transition, multiphase flow and reacting shear layers. These experiments are intended to provide CFD validation data for the internal flow fields within aerospace propulsion system components.

INTRODUCTION

Internal fluid mechanics research at NASA Lewis is directed toward an improved understanding of the flow phenomena affecting aerospace propulsion systems, and the application of this knowledge in the formulation of accurate predictive codes. In order to achieve this objective, research is conducted which involves both detailed experimentation and analysis. A close coupling between the experimental and the code development work is a critical feature of this research. The insights gained from the experimental work are represented by mathematical models that form the basis for code development. The resulting codes are then tested by comparing them with appropriate experiments in order to ensure their validity and determine their applicable range. Subsequent improvements and refinements lead to validated numerical codes.

The definition of CFD code validation as used in this paper, is that adopted by the NASA Aeronautics Advisory Committee (Ref. 1); wherein a key item is the ability of a numerical code to accurately model the critical physics of the flow. In addition, validation may only occur when the accuracy and limitations of both the experimental data and the code's algorithm are known and understood over a range of specified parameters.

This paper is concerned with a number of experiments which are underway in order to provide validation information for internal flow codes, as well as to provide improved understanding of the flow physics. Previous publications by this author have addressed the assessment and validation for turbomachinery, inlet and ducting flows (Refs. 2 to 5). In this paper, those areas are addressed further along with chemically reacting flows. For each of the three subject areas, material will be presented on the experimental validation programs as well as the computational codes used.

INLETS, DUCTS AND NOZZLES FLOWS

The inlet, duct, and nozzle research is illustrated in Table I and includes experimental work in transition ducts, offset ducts, diffusers with vortex generators, inlet shock-boundary layer interactions, diffuser and nozzle jet mixing, inlet and diffuser boundary layer bleed and inlet/nozzle separation flow physics. The critical physics to be modeled (Table I) for these experiments are the phenomena associated with turbulence, boundary layer separation, vortex generation, bleed, transition, heat transfer and real gases effects. All of the research activity described above may be described according to three major classifications of flow phenomena: highly three-dimensional flow fields, shock boundary layer interactions and shear layer control. The importance of these three flow phenomena result from aircraft/propulsion requirements such as engine locations, thrust vectoring, maneuverability, high-Mach number flight, and shorter/lighter components. Specific elements of the research program are shown in Fig. 1 for each of the three flow field phenomena. Only two of the elements, however, will be presented here. The first is the shock boundary layer interaction phenomena which will be illustrated with a description of the normal shock research activity. The second, shear layer control, will be illustrated with vortex generator research. Additional information on these activities are described in Ref. 6.

Normal shock-boundary layer interaction. Figure 2 illustrates the nature of the normal shock interaction for two Mach numbers, 1.3 and 1.6. Schlieren photographs and oil streak photographs are shown for both Mach numbers. These data were obtained in the NASA Lewis 1-by-1-foot supersonic wind tunnel (Ref. 7). The Schlieren photographs show a view of the shock interaction, while the oil streaks illustrate the flow field details along the side wall. At both Mach numbers, the Schlieren photographs show the shock has a lamda structure near the boundary layer. The sidewall oil streaks reveal a major difference in the flow field for the two Mach numbers. At Mach 1.3 the flow remains uniform and passes through the shock with no major alteration. At Mach 1.6,

the adverse pressure gradient across the shock is strong enough to force the boundary layer to separate from the tunnel walls and to form the closed separation bubble shown in Fig. 2. Both the Mach 1.3 and 1.6 flow fields were surveyed in detail using nonintrusive laser anemometry. Results are shown in Fig. 3 for the Mach 1.6 case in two planes within the flow field. The top set of Mach contours illustrates the nature of the flow field in a cross plane downstream of the shock. The lower set of Mach contours shows the development of the flow field within a vertical plane passing through the centerline of the test section. The separated region in the vicinity of the initial interaction causes the actual flow area to contract downstream of the initial shock, leading to a reacceleration of the flow to supersonic Mach numbers. The flow then shocks down again, reaccelerates again due to the thickened boundary layer, and finally shocks down a final time. The lower portion of Fig. 3 is repeated as the lower portion of Fig. 4, namely the Mach contours measured with LV in a vertical plane passing through the centerline of the test section at Mach 1.6. The upper portion of Fig. 4 is a two-dimensional Navier-Stokes computation of the same flow field. Although the computation captures the initial features fairly well in the vicinity of the first shock, in the downstream region, none of the flow features is adequately replicated. This result is to be expected since the experimental data have shown the strong three-dimensionality of the flow. This comparison points out the need for three-dimensional computational methods for computing such flow fields. However, in the case of the Mach 1.3 flow, excellent agreement was obtained between experiments and computations. Again, this result is consistent with the experimentally observed two-dimensionality of the flow field. Additional insight and understanding of the experimental data were obtained through the use of computer graphics. The experimental data sets were modified to a format that was originally developed for presenting computational results. The three-dimensional data contours were then displayed and set into motion on the screen. A perspective may be gained much more quickly from these rotating images than can be obtained by looking at a series of two-dimensional or even three-dimensional plots.

Vortex generators in diffusing offset duct. Figure 5 illustrates a research model and facility that was used in an experiment to assess the performance of vortex generators in a 30° to -30° diffusing S duct (Ref. 8). The duct had a length-to-diameter ratio of 5.0, an offset-to-diameter ratio of 1.34, and an exit-to-inlet area of 1.51. Initial experiments with the duct identified the location of a separated flow region as shown by the surface oil streak photograph. Three pairs of vortex generators were then added to the duct surface just upstream of the separated region to control the separation. They were set at incidence angles of ±16° to form three pairs of counter rotating vortices. The azimuthal locations were at -38°, 0°, +38° as measured from the inside of the bend. The flow was turbulent with a Mach number of 0.6 and a Reynolds number (based on diameter) of 1.76×10^6. The initial boundary layer thickness was 0.1 times the initial duct radius. A comparison of total pressure contours at various locations down the length of the duct with the vortex generators in place is shown in Fig. 6. The experimental data were obtained by surveying the flow field with a total pressure probe. The computational results are from a three-dimensional parabolized Navier-Stokes code. The computations involve a method for modeling the streamwise vorticity due to the presence of the vortex generators and the decay of the vorticity. The computed total pressure contours are shown in the lower portion of Fig. 6, and the experimental data are shown in the upper portion. The comparisons show good agreement in all of the qualitative features, including the discrete effect of the three sets of vortex generators. Comparison of experimental and computational data for the duct without generators also showed good global agreement. In order to handle the region of separated flow in the absence of vortex generators, a flare approximation was used in the PNS code to march downstream of the separation bubble.

TURBOMACHINERY FLOWS

The second subject area is concerned with turbomachinery validation. Table II illustrates the program elements underway and includes Euler, Average-Passage, and Reynolds averaged steady and unsteady Navier-Stokes codes. The critical physics to be modeled include turbulence, boundary-layer transition, end wall and blade surface boundary layer interactions. Use of the unsteady Navier-Stokes approach reflects the fact that turbomachinery flow is fundamentally unsteady or time dependent, and may be further complicated by random disturbances.

Turbomachinery research at NASA Lewis currently involves a variety of computational and experimental approaches as shown in Fig. 7. On the far left of the computational approaches, the time accurate Navier-Stokes equations are capable of resolving all relevant time scales in turbomachinery flow. However, enormous computer power is required. In order to readily obtain solutions, a variety of averages are made, which result in a loss of information or resolution in the equations. It also introduces more unknowns and requires additional empirical data. As one moves to the left of the experimental path, increasing detail in the time domain is obtained, whereas moving to the right increases the averaging of temporal behavior. Current research at NASA Lewis focuses on the analytic range from the Reynolds averaged Navier-Stokes equations to the average passage equations. The experimental emphasis is on high response time resolved measurements and on laser anemometry measurements. Further information regarding these activities may be found in Ref. 9.

Large low speed centrifugal compressor. Centrifugal compressors feature large surface area and small exit-passage heights. Viscous flow effects, therefore, have a

major impact on the flowfield within these compressors. The inability to accurately predict and measure these flows contributes in large part to the inherently lower efficiency of centrifugal compressors relative to axial flow compressors. The large low-speed centrifugal compressor shown in the background of Fig. 8 has been designed specifically to provide flow modeling and viscous code validation data for centrifugal compressors. The impeller was designed to be aerodynamically similar to high performance, high speed centrifugal compressors such as the small 6:1 pressure ratio impeller shown in the photograph. The low speed impeller has a tip diameter of 50 in. and a rotational speed of 1950 rpm. Inlet and exit blade heights are 9 and 4.75 in., respectively. The large size and low speed of the new impeller generate viscous flow regions (such as blade and endwall boundary layers) and tip clearance flows which are large enough to measure in detail with laser anemometry. Figure 9 shows an overall view of the facility and 10 shows the rotor. Figure 11 shows the location and type of instrumentation currently being installed. It is anticipated that experimental data will be obtained during this year. Future plans include replacing the centrifugal rotor with a four stage axial compressor. A quasi-three-dimensional Navier-Stokes turbomachinery code has been developed and applied for the large low speed centrifugal analysis (Ref. 10). The code includes the effects of radius change, stream surface thickness and rotation. The unsteady Navier-Stokes equations are solved in finite difference form using an explicit Runge-Kutta algorithm with a spatially varying time step and multigrid convergence acceleration. The flow in the 6:1 pressure ratio centrifugal impeller has been calculated on a 161x33 grid. Relative Mach number contours in Fig. 12 show a supersonic bubble on the leading edge terminated by a shock. Rotational effects make the suction surface boundary layer thin, the pressure surface boundary layer thick, and they cause the wake to leave the trailing edge in a spiral. The calculations require about $3x10^6$ words of storage and 1.5 min of CPU time on a Cray X-MP. The flow in the new, large low-speed rig has also been calculated and is shown on the right. The ability to validate this and other codes in the large low-speed rig will generate confidence in the high speed calculations where validation may not be possible.

Transonic fan shock structure. A second example of the turbomachinery research is concerned with the shock behavior in a transonic fan. Current axial fan and compressor design systems do not account for the three-dimensionality of passage shocks. Figure 13 is an example of a high speed experiment to determine shock structure physics (Ref. 11). Shock locations determined from laser anemometry measurements are shown on blade-to-blade surfaces of revolution in the upper portion of the figure. Three different views of the same data, as displayed on a graphics workstation, are shown in the bottom portion of the figure. A significant spanwise lean of the shock surface is evident in these three-dimensional views.

Comparisons of the measured shock strength and location with an Euler code (Denton) are shown in Fig. 14 for two operating conditions; peak efficiency and near stall. The comparisons show that the spanwise location of the computed and measured sonic lines are in reasonable agreement over the range of operating conditions. A comparison of the measured and the idea shock strengths is shown in Figs. 14(b) and (c).

Compressor turbulent kinetic energy distribution. Measurements of the unsteady flowfield within a compressor stator operating downstream of a transonic fan rotor have been obtained using laser anemometry. Figure 15 shows a contour plot of the ensemble-averaged unresolved unsteadiness in the stator (includes unsteadiness due to both turbulence and vortex shedding) for one rotor/stator relative position. Areas of unresolved unsteadiness contain fluid which is in the rotor-blade wake. As the rotor blades rotate past the stator blades, the rotor wakes are convected through the stator row by the absolute flow velocity and, subsequently, chopped by the stator blades. Data obtained at additional times during the blade passing cycle have been used to produce a movie sequence which illustrates the ensemble-averaged wake dynamics and its effect on the stator flowfield. These data will be used in order to obtain closure modeling terms needed for turbomachinery codes.

Fan rotor vortex shedding. Karman vortex streets are known to exist in blunt body wakes over a wide flow regime. However, the existence of vortex streets in transonic fan and compressor blade wakes was not generally anticipated since these blades have thin trailing edges. Laser anemometer measurements obtained in the wake of a transonic fan blade indicated two distinct states of flow in the central portion of the wake (Ref. 12). This behavior is consistent with that which would be displayed by a Karman vortex street, see Fig. 16. A simple vortex street model was constructed in an attempt to explain the experimental measurements. The model qualitatively agreed with the bimodal character of the velocity measurements. The model was used to explain the highly unsteady nature of high response pressure measurements made in the same wake flowfield. This research typifies the manner in which advanced measurements coupled with modeling improve our understanding of complex flow phenomena.

Boundary layer transition. Boundary layer transition is a critical feature that needs to be modeled for each of the three general areas discussed in this paper. Transition plays an especially vital role in the gas-side heat transfer within turbomachinery as well as in high speed components. A fundamental experimental activity is underway which is investigating the nature of the transition mechanism. In particular, the differences in the classical boundary layer transition process and the bypass transition are being studied subject to variations in the external free stream turbulence level. Simultaneous hot wire and hot film measurements were made in a flat plate boundary layer tunnel. The transition location was determined by three methods which used

either the mean velocity profiles, the rms profiles or the intermittency measurements. By-pass transition was found to occur at freestream turbulence levels of 0.65 percent whereas the Tollmien-Schlicting path to transition was observed at 0.25 percent. Even though freestream disturbances varied only by a factor of ~2, the disturbances within the boundary layer vary by two orders of magnitude within the frequency range where linear stability theory would predict amplification.(Ref. 16).

Figure 17 shows a schematic of the tunnel used for the study as well as a carpet plot of the simultaneous hot film measurements along the flat plate surface. The progression and growth of turbulence along the surface can be readily observed. Continuing research will involve the investigation of wall heating effects.

CHEMICALLY REACTING FLOWS

The third subject area to be presented is that of chemically reacting flows. The relevant numerical codes are the steady and time accurate Reynolds averaged Navier-Stokes and Direct Numerical Simulation, as shown in Table III. In this category of flows, the critical physics to be modeled include turbulence-combustion interactions and chemical kinetics. The experimental activity involves multi-phase flows, phase interactions, planar reacting shear layers, radiation characteristics and shock tube measurements. Due to the complexity of the combustion process in propulsion devices, a stepwise approach is being taken in developing an improved understanding of the processes; see Fig. 18. Following this approach, the fluid mechanics of certain flows are studied in the absence of combustion; combustion chemistry is studied principally from the viewpoint of kinetics; and finally the interaction of the turbulence (fluid mechanics) and the chemistry becomes the focal point. Further information on these activities may be found in Ref. 13.

Multiphase flows. Particle laden jets were studied in order to assess the capability of current two-phase flow models (Ref. 14). An air jet containing solid glass beads (39 μm, Sauter mean diameter) discharged downward into a still environment. Particle laden jets with three swirl numbers were studied. Nonintrusive measurements of velocity were obtained with a two channel laser velocimeter. Particle size and velocity were measured with a phase/doppler particle anemometer. The gas phase was seeded with nominal 1 μm diameter aluminum oxide power to measure gas phase velocities. Figure 19 shows typical results. A contour plot of experimentally measured axial velocity of the gas phase (left side) and particle phase (right side) is illustrated. It is evident that, initially, the gas phase has a higher velocity than the particle phase. The particles are initially accelerated by the gas phase and then their velocity begins to decay. Because of their inertia, the rate of decay of axial velocity is slower for the particles than the gas. Also shown in Fig. 19 are predictions from the stochastic separated flow (SSF) model at 10 diameters downstream of the tube exit. This model tracks particle trajectories in the computed gas phase flowfield and allows momentum exchange between phases. The model also considers effects of gas-phase turbulence on particle trajectories. Predictions from the model show reasonable agreement with the data.

Turbulent reacting flow. A free shear layer experiment is currently underway in order to understand the coupling between fluid dynamics and combustion. The activity will also provide validation data. The experimental apparatus is shown in Fig. 20 and consists of two separate channels which merge into a combustion chamber with a splitter plate. The facility features continuous flow of air in one channel and hydrogen/nitrogen in the other. Mach numbers are limited to less than sonic. Upstream heating of air without contamination and high heat release in the combustion section are additional features of this experiment. Interactions between the combustion process and duct pressure oscillations will be principal foci for study.

Initial computations of the time-evolving shear layer without reaction have been carried out using a time accurate, two-dimensional shear layer code. This code employs a Navier-Stokes finite volume method with a two equation turbulence model. It has second order accuracy in both time and space. Figure 21 shows the computed vorticity contours for a shear layer at a Reynolds number of 1×10^5. Positive and negative vorticity contours originate at the boundary layers, specified at the inlet of the computational domain. Forcing is applied at a long wavelength, and smaller scale vorticities spontaneously develop as a result of the natural instability of the layer. These small scale vorticities cluster on the scale of the longer, forced wavelength. Small pockets of positive vorticity persist as remnants of the low speed boundary layer. The collective interaction of these small scale vortices, merging into larger scale structures, largely controls the dynamics of the shear layer. Further computational details are given in Ref. 15.

CONCLUDING REMARKS

The CFD validation activity at NASA Lewis is a balanced effort between the conduct of experimental research and the development of computational tools. The program has been briefly described by high-lighting research efforts in three areas; namely: Inlets, Ducts and Nozzles; Turbomachinery; and Chemically Reacting Flows. Much of the computational focus for the Inlets, Ducts and Nozzles has been on the development and validation of parabolized Navier-Stokes codes. In the future, more emphasis will be placed on three-dimensional Reynolds averaged Navier-Stokes methods. The experimental effort will continue to provide a fundamental understanding of the fluid flow physics,

to develop new and/or improved flow models, and to provide benchmark datasets for validation of both parabolized and Reynolds averaged Navier-Stokes methods.

In the turbomachinery area, the program encompasses a variety of computational and experimental approaches. Special emphasis is placed on the Reynolds averaged Navier-Stokes equations, the unsteady Euler equations and the average passage equations. The experimental emphasis is on high response time-resolved measurements and on measurements within rotating machinery blade passages.

Activity in chemical reacting flow research is focused on fluid mechanics, combustion chemistry and turbulence/combustion interaction. Emphasis is placed on Reynolds averaged Navier-Stokes solvers and Direct Numerical simulation. The experimental activity includes unsteady reacting flows, shock tube kinetics and multiphase flow phenomena.

In conclusion, it is noted that as numerical methods are improved and the ability to compute complex fluid physics is enhanced, it is critical that the users be aware of the code validity and limitations. These limitations can only be established by a careful, systematic evaluation of each numerical scheme. A coupled series of experiments must be conducted in close collaboration with the numerical approach in order to assess if the code can predict the critical physics. The exact nature of the measured surface and flow field quantities required is highly dependent on the problem under investigation, i.e., aerodynamics, heat transfer or reacting flows. The experiments in this paper are the type required for the CFD assessment and validation process.

REFERENCES

1. Bradley, R.G., et al: "Computational Fluid Dynamics Validation. Report prepared for NASA's Aeronautics Advisory Committee, Mar. 22, 1987.

2. Povinelli, L.A.: Assessment of Three-Dimensional Inviscid Codes and Loss Calculations for Turbine Aerodynamic Computations. Gas Turbines Power, vol. 107, no. 2, Apr. 1985, pp. 265-276. (NASA TM-83571).

3. Povinelli, L.A.: "Validation of Viscous and Inviscid Computational Methods for Turbomachinery Components. ASME Paper 86-GT-42, June 1986. (NASA TM-87193).

4. Povinelli, L.A.; and Towne, C.E.: Viscous Analyses for Flow Through Subsonic and Supersonic Intakes. Engine Response to Distorted Inflow Conditions, AGARD CP-400, AGARD, Nevilly-Sur-Seine, France, 1986, pp. 5-1 to 5-20. (NASA TM-88831).

5. Povinelli, L.A.; and Anderson, B.H.: Investigation of Mixing in a Turbofan Exhaust Duct, Part II: Computer Code Application and Verification. AIAA J., vol. 22, no. 4, Apr. 1984, pp. 518-525.

6. Abbott, J.M.; Anderson, B.H.; and Rice, E.J.: Inlets, Ducts and Nozzles. Aeropropulsion '87, NASA CP-10003, 1987.

7. Chriss, R.M., et al.: An LDA Investigation of Three-Dimensional Normal Shock-Boundary Layer Interactions in a Corner. AIAA Paper 87-1369, June 1987.

8. Kunik, W.G.: Application of a Computational Model for Vortex Generators in Subsonic Internal Flows. AIAA Paper 86-1458, June 1986. (NASA TM-87327).

9. Simoneau, R.J., et al: Turbomachinery. Aeropropulsion '87, NASA CP-10003, 1987.

10. Chima, R.V.: Explicit Multigrid Algorithm for Quasi-Three-Dimensional Viscous Flows in Turbomachinery. J. Propulsion Power, vol. 3, no. 5, Sept.-Oct. 1987, pp. 397-405.

11. Wood, J.R.; Strazisar, A.J.; and Simonyi, P.S.: Shock Structure Measured in a Transonic Fan Using Laser Anemometry. Transonic and Supersonic Phenomena in Turbomachines, AGARD CP-401, AGARD, Nevilly Sur-Seine, France, 1986.

12. Hathaway, M.D., et al.: Rotor Wake Characteristics of a Transonic Axial-Flow Fan. AIAA J., vol. 24, no. 11, Nov. 1986, pp. 1802-1810.

13. Mularz, E.J.; and Sockol, P.M.: Chemical Reacting Flows. Aeropropulsion '87, NASA CP-10003, 1987.

14. Bulzan, D.L.; Shuen, J.S.; and Faeth, G.M.: Particle-Laden Swirling Free Jets: Measurement and Prediction. AIAA Paper 87-0303, Jan. 1987. (NASA TM-88904).

15. Claus, R.W.; Huang, P.G.; and MacInnes, J.: "Time-Accurate Simulations of a Mixing Layer Forced at a Single Frequency. AIAA Paper 88-061, Jan. 1988.

16. Suder, K., O'Brien, J., and Reshotko, E.: "Experimental Study of Bypass Transition in a Boundary Layer", NASA CR, to be published 1988.

TABLE I. - INLET, DUCT AND NOZZLE CFD VALIDATION

Code and critical models requiring validation		Experimental program elements
CFD codes by class	Critical flow physics models	
Three-dimensional subsonic PNS	Turbulence Separation Vortex generation	Transition ducts Offset ducts Vortex generators
Three-dimensional subsonic/ hypersonic PNS	Turbulence Separation Real gas effects Boundary layer bleed Boundary layer transition	Shock-boundary layer interaction Boundary-layer bleed High temperature flow
Three-dimensional Navier-Stokes	Turbulence Real gas effects Boundary layer transition	Above experiments Separation flow physics Enhanced jet mixing

TABLE II. - TURBOMACHINERY CFD VALIDATION

Code and critical models requiring validation		Experimental program elements
CFD code by class	Flow physics models	
Steady Euler	End-wall boundary layer Blade surface boundary layer Shock boundary layer interaction	High-speed turbomachinery Low-speed turbomachinery Two-dimensional cascade Shock boundary layer interaction
Steady Navier-Stokes	Turbulence Boundary layer transition	Two-dimensional cascade Low-speed centrifugal Low-speed boundary layer Three-dimensional heat transfer Low-speed axial turbo-machinery
Passage-average Navier-Stokes	Turbulence Other closure models	Low-speed multistage High-speed multistage
Unsteady Navier-Stokes (rotor/stator)	Turbulence Boundary layer transition	Low speed turbomachinery High-speed turbomachinery

TABLE III. - CHEMICALLY REACTING FLOWS CFD VALIDATION

Code and critical models requiring validation		Experimental program element
CFD codes by class	Critical flow physics models	
Steady Navier-Stokes	Fuel spray Turbulence Turbulence/combustion Chemical kinetics interaction Radiation/soot formation	Multiphase flow research: phase interaction
Time accurate Navier-Stokes	Turbulence Turbulence/combustion interaction Chemical kinetics	Planar reacting shear layer: Turbulence/combustion interaction Soot/radiation characteristics
Direct numerical Simulation	Chemical kinetics	Shock tube chemical kinetics

- **HIGHLY 3D FLOW FIELDS**
  - **TRANSITION DUCTS**
  - **OFFSET DUCTS**
- **SHOCK-BOUNDARY-LAYER INTERACTIONS**
  - **NORMAL SHOCK-BOUNDARY LAYER**
  - **OBLIQUE SHOCK-BOUNDARY LAYER**
  - **GLANCING SIDEWALL SHOCK-BOUNDARY LAYER**
- **SHEAR LAYER CONTROL**
  - **VORTEX GENERATORS**
  - **BOUNDARY-LAYER BLEED**
  - **ENHANCED JET MIXING**

FIGURE 1. - INLETS, DUCTS, AND NOZZLES, FLOW PHENOMENA.

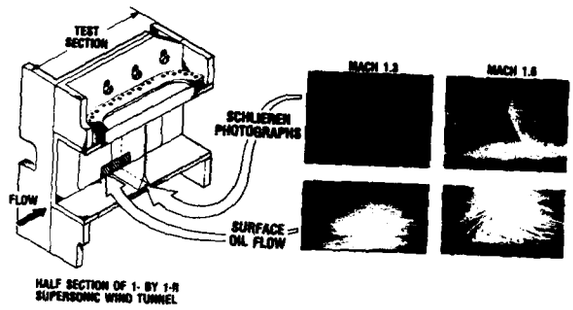


FIGURE 2. - NORMAL SHOCK-BOUNDARY-LAYER INTERACTION.

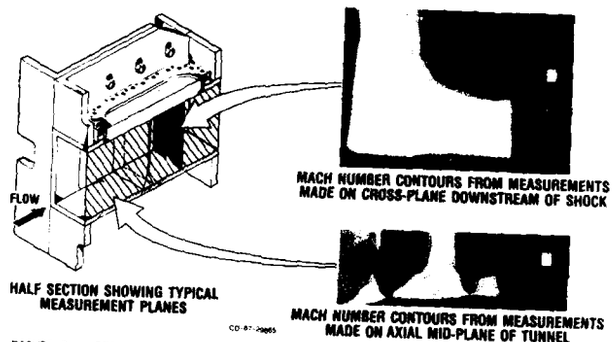


FIGURE 3. - RESULTS OF LASER ANEMOMETER MEASUREMENTS FOR NORMAL SHOCK-BOUNDARY LAYER INTERACTION AT MACH NUMBER 1.6.

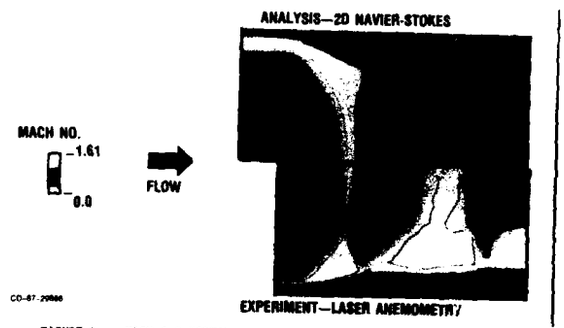


FIGURE 4. - MACH 1.6 NORMAL SHOCK WAVE BOUNDARY LAYER INTERACTION. COMPARISON OF LDV EXPERIMENT AND ANALYSIS.

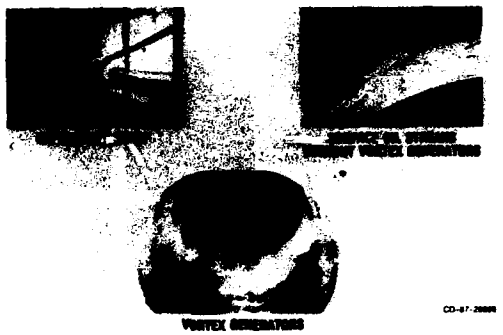


FIGURE 5. - VORTEX GENERATORS IN DIFFUSING OFFSET DUCT. L/D = 5.0; OFFSET/D = 1.34; A_{EXIT}/A_{INLET} = 1.50.

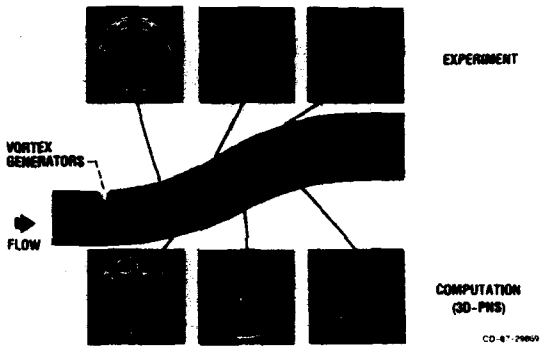


FIGURE 6. - VORTEX GENERATORS IN DIFFUSING OFFSET DUCT - COMPARISON OF ANALYSIS AND EXPERIMENT. TOTAL PRESSURE CONTOURS: M = 0.6.

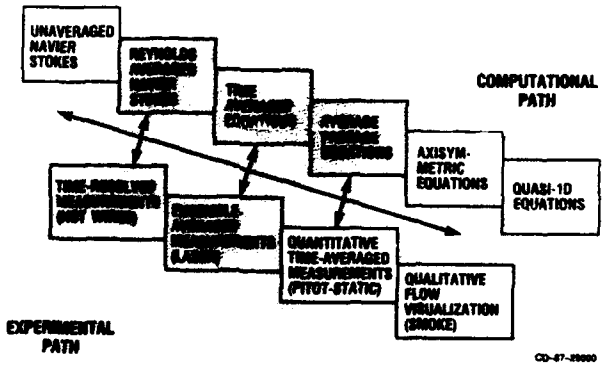


FIGURE 7. - POSITION OF THE TURBOMACHINERY PROGRAM ON COMPUTATIONAL AND EXPERIMENTAL PATHS.



FIGURE 8. - LARGE LOW-SPEED CENTRIFUGAL COMPRESSOR NEW FLOW PHYSICS AND CODE VALIDATION RIG.

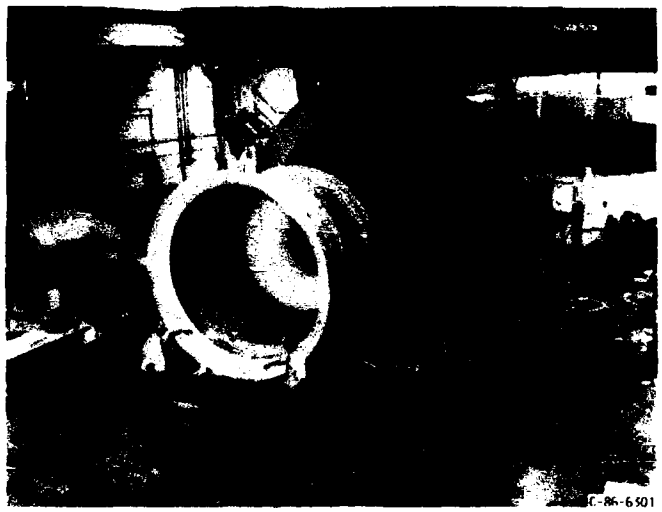


FIGURE 9. - LARGE LOW SPEED CENTRIFUGAL COMPRESSOR APPARATUS. PLENUM AND BELLMOUTH.



FIGURE 10. - LARGE LOW SPEED CENTRIFUGAL COMPRESSOR ROTOR.

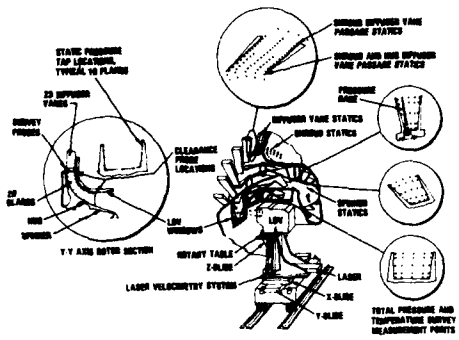


FIGURE 11. - LOW-SPEED CENTRIFUGAL COMPRESSOR INSTRUMENTATION.

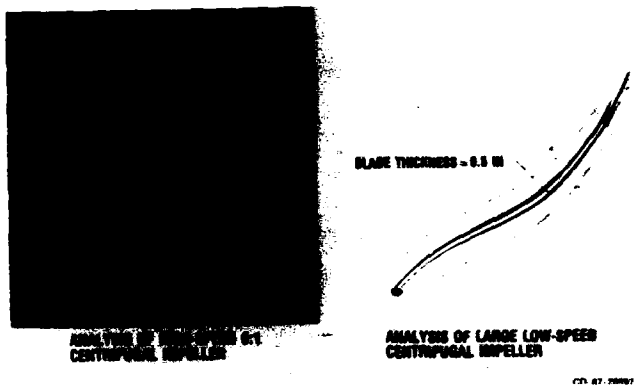


FIGURE 12. - QUASI-3D NAVIER-STOKES CODE FOR TURBOMACHINERY ANALYSIS.

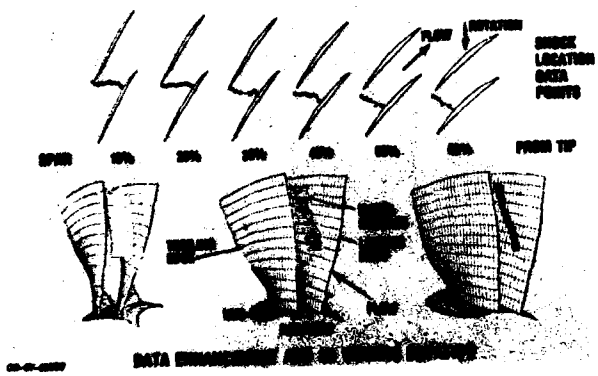
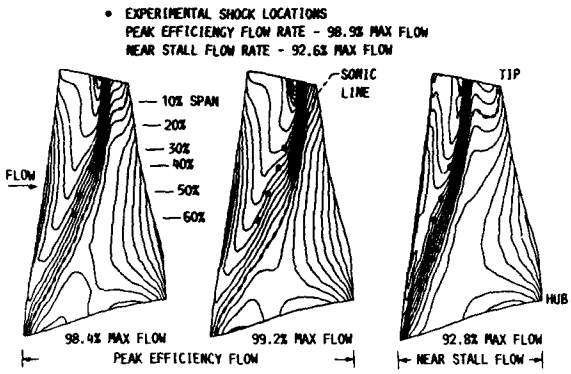
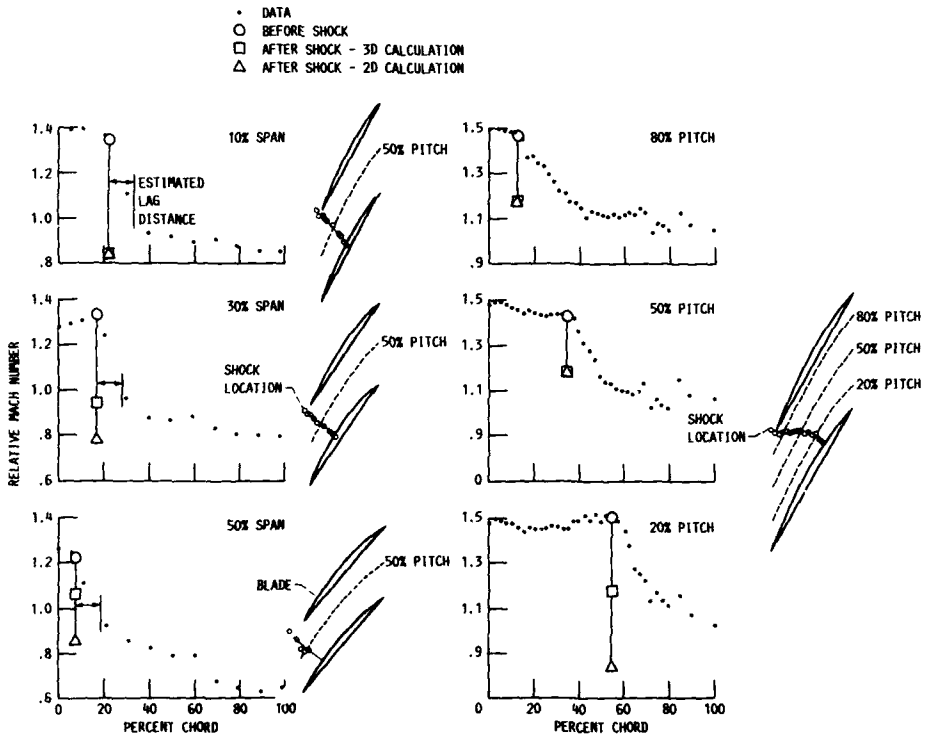


FIGURE 13. - MEASUREMENT OF 3D SHOCK STRUCTURE IN A TRANSONIC AXIAL-FLOW FAN.



(A) COMPARISON OF SHOCK LOCATIONS ON THE BLADE SUCTION SURFACE FOR PEAK EFFICIENCY AND NEAR STALL FLOW RATES WITH ISOMACH LINES FROM A 3D EULER CALCULATION.



(B) CHORDWISE PLOTS OF RELATIVE MACH NUMBER AT 50% PITCH FOR THE NEAR STALL FLOW RATE AT 10%, 30%, AND 50% SPAN.

(C) CHORDWISE PLOTS OF RELATIVE MACH NUMBER AT 10% SPAN FOR THE PEAK EFFICIENCY FLOW RATE AT 20%, 50%, AND 80% PITCH FROM THE SUCTION SURFACE.

FIGURE 14. - COMPARISON OF COMPUTATIONAL AND EXPERIMENTAL RESULTS FOR A TRANSONIC ROTOR.



FIGURE 15. - COMPRESSOR "TURBULENT" KINETIC ENERGY DISTRIBUTION. ONE FRAME FROM DATA MOVIE SHOWING THE PROGRESS OF A WAKE THROUGH A STATOR PASSAGE DOWNSTREAM OF THE ROTOR.

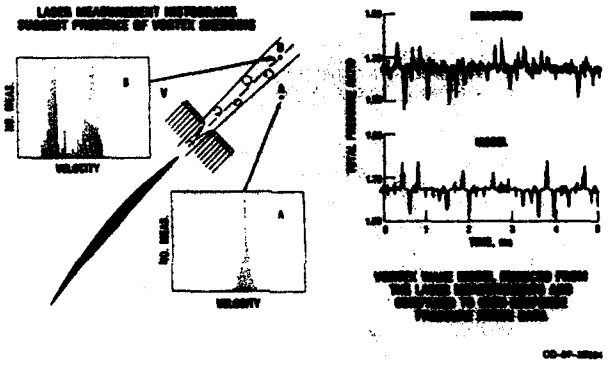


FIGURE 16. - FAN ROTOR VORTEX SHEDDING DEVELOPING MODELS TO EXPLAIN FLOW PHYSICS.

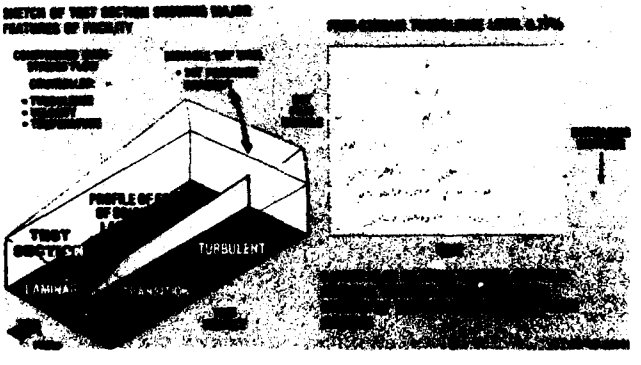


FIGURE 17. - BOUNDARY-LAYER TRANSITION RESEARCH - A STUDY OF INTERMITTENT BEHAVIOR.

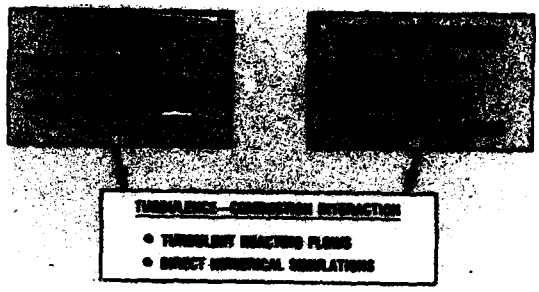


FIGURE 18. - CHEMICAL REACTING FLOWS.

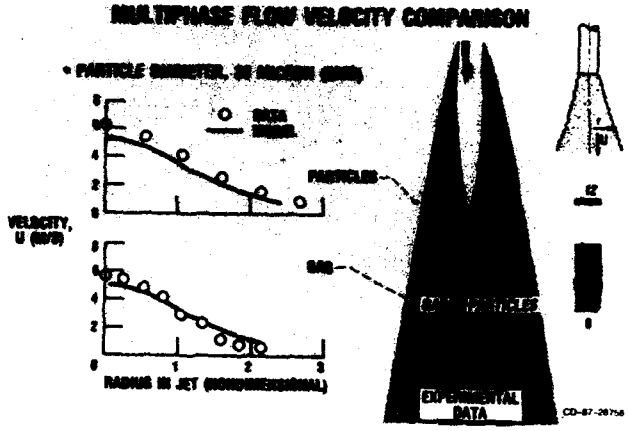


FIGURE 19. - MULTIPHASE FLOW VELOCITY COMPARISON.

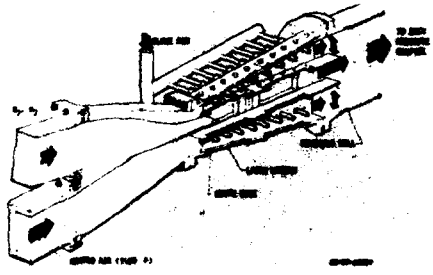


FIGURE 20. - PLANAR REACTING SHEAR LAYER TEST SECTION.

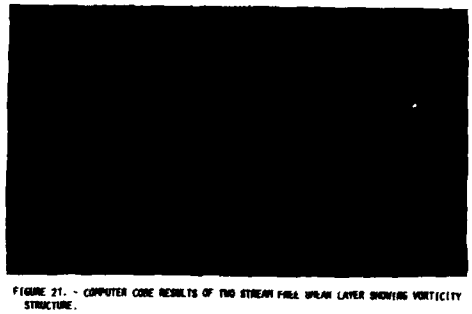


FIGURE 21. - COMPUTER CODE RESULTS OF TWO STREAM FREE SHEAR LAYER SHOWING VORTICITY STRUCTURE.

SOLUTION ON UNSTRUCTURED GRIDS FOR THE EULER- AND NAVIER-STOKES-EQUATIONS

by

W. Koschel, M. Lötzerich*, A. Vornberger

Institute for Jet Propulsion and Turbomachinery
Technical University of Aachen
Templergraben 55
D-5100 Aachen

*Aerodynamics Dept. BF30
Dornier GmbH
7990 Friedrichshafen
FRG

SUMMARY

An explicit Finite Element scheme based on a two step Taylor-Galerkin algorithm has been developed for solving the Euler- and Navier-Stokes Equations. The spatial discretisation is based on an unstructured Finite Element mesh. The adaptive grid refinement technique which is incorporated in the code allows a local refinement of the grid by mesh enrichment. For validation the method is applied to the simulation of the flow around a cylinder and a sphere, a regular shock reflection at a wall, the interaction of an oblique shock wave with a laminar boundary layer and the flow through a scramjet inlet and a turbine cascade. The computed results generally show a satisfying agreement with analytical solutions and experimental data.

NOMENCLATURE

C	mass matrix	ρ	density
C_{LM}	lumped mass matrix	τ	stress tensor
F	flux vector	μ	viscosity
N	shape function	Ω	computational domain
P	pressure		
R	residual	Subscripts	
t	time	i	number of nodal point
T	temperatur	j	number of direction (x,y,z)
u,v	components of velocity		
U	flow vector	Superscripts	
		n	time level

INTRODUCTION

The Finite Element Method has become a powerful tool in solving aerodynamic problems. The great flexibility of the FEM regarding the spatial discretisation offers attractive approaches to mesh generation for complex three-dimensional geometries. In addition the use of unstructured grids allows in a natural way the application of adaptive refinement strategies.

These advantages are counterbalanced so far by extra CPU-costs and significant higher storage requirements. However decreasing CPU-costs and enlarged main storage capacity on modern super computers are making the unstructured approach more and more attractive especially when applications around threedimensional complex shapes are considered. Following the research line of Löhner, Morgan et al. /1/, /2/ an explicit two step algorithm based on the Taylor-Galerkin formulation first introduced by Donea /3/ is used in this study for obtaining solutions to the Euler- and Navier-Stokes equations. In order to improve the convergence rate for steady state solutions a residual averaging and enthalpy damping technique as applied by A. Jameson and T.J. Baker in civil aircraft design /4/ is employed.

The adaptive grid refinement strategy /5/ implemented in the code is based on local error estimates and mesh enrichment. The objective of our study was to get some insight into the problems and capabilities related to the solution of the Euler- and Navier-Stokes equations on unstructured grids.

To validate the developed method and to demonstrate the achieved robustness flow problems belonging to quite different Mach and Reynolds number regimes were investigated.

NUMERICAL SCHEME

Governing Equations

The Navier-Stokes Equations governing compressible flow can be written in conservative form neglecting body forces and heat sources.

$$\frac{\partial U}{\partial t} + \frac{\partial F_j}{\partial x_j} = 0 \tag{1}$$

where

$$F_j = F_j^E - F_j^V$$

$$U = \begin{pmatrix} \rho \\ \rho u_j \\ \rho e \end{pmatrix} \quad F_j^E = \begin{pmatrix} \rho u_j \\ \rho u_i u_j + \delta_{ij} p \\ u_j(\rho e + p) \end{pmatrix} \quad F_j^V = \begin{pmatrix} 0 \\ \tau_{ij} \\ u_i \tau_{ij} + k\frac{\partial T}{\partial x_j} \end{pmatrix} \tag{2}$$

The summation convention is employed and the range of j depends upon the number of space dimensions. Fj^E represents the inviscid Euler part of the flux-vector whereas the viscous contributions are gathered in Fj^V. By input parameters the code can be forced to work with the inviscid or viscous equation set. In case of the viscous option a full approximation of the Reynolds' stress tensor is calculated.

Assuming a Newtonian fluid the stress tensor is proportional to the rate of strain and can be written using Stokes postulate as:

$$\tau_{ij} = \mu\left(\frac{\partial u_i}{\partial x_j} + \frac{\partial u_j}{\partial x_i}\right) - \frac{2}{3}\mu\delta_{ij}\frac{\partial u_i}{\partial x_i} \tag{3}$$

Sutherland's viscosity equation, the equation of state and the Prandtl number are specified to close the system of equations.

DISCRETISATION

After subdividing the domain respectively in triangular or tetrahederal Finite Elements with linear shape functions N_i ensuring C^0 continuity the set of equations can be expressed in a weighted residual formulation.

$$\int_\Omega \left(\frac{\partial U}{\partial t} + \frac{\partial F_j}{\partial x_j}\right) N_i \, d\Omega = 0 \tag{4}$$

Applying Gauss' divergence theorem inserting standard finite element approximations

$$\begin{aligned} U &= \sum N_i U_i \\ F &= \sum N_i F_i \end{aligned} \tag{5}$$

with $F_i = F(U_i)$

and replacing the time derivative by a type of Lax-Wendroff scheme yields

$$C\,\Delta U^{n+1} = \Delta t \int_\Omega F_j^{n+1/2} \frac{\partial N_i}{\partial x_j} \, d\Omega - \int_\Gamma F_j^{n+1/2} N_i n_j \, d\Gamma \tag{6}$$

with $\Delta U^{n+1} = U^{n+1} - U^n$

where n_1 corresponds to the outward normal unit vector on the boundary of the domain Ω and C represents the standard Finite Element mass matrix defined as:

$$C_{ij} = \int_\Omega N_i N_j \, d\Omega \tag{7}$$

For computational efficiency the integration of the fluxes in Eq. (6) is carried out in a two step scheme /6/. A Taylor series expansion truncated to first order and neglecting diffusion effects leads to:

$$\int_\Omega U_e^{n+1/2} P_e \, d\Omega = \int_\Omega U_i^n N_i \, d\Omega + \frac{\Delta t}{2} \int_\Omega F_j \frac{\partial N_i}{\partial x_j} \, d\Omega \tag{8}$$

where P_e denotes a piecewise constant shape function.

With this equation $U_e^{n+1/2}$ can be computed for each element explicitly. Using these values constant within each element the flux-vectors on the RHS of Eq. (6) are defined.

$$F_j^{n+1/2} = F_{ij}^{n+1/2} = F(U_e^{n+1/2}) \tag{9}$$

To obtain finally the following global equation system all integrations are exactly performed and the element matrices are assembled in an usual finite element way.

$$C\,\Delta U^{n+1} = \Delta t\, RHS \tag{10}$$

If the advantages of the constant mass matrix regarding transient solutions or shock capturing are desired Eq. (10) can be solved iteratively as the C-matrix is dominant on the diagonal by using the following scheme proposed by Donea and Giuliami /7/. Otherwise the diagonalized system is employed.

$$C_{LM}\Delta\Delta U_k^{n+1} = \Delta t\, RHS - \sum_e C\,\Delta U_{k-1}^{n+1}$$

$$\Delta U_k^{n+1} = \Delta U_{k-1}^{n+1} + \Delta\Delta U_k^{n+1} \tag{11}$$

$$1 \le k \le niter \qquad \Delta\Delta U_0^{n+1} = 0 \qquad C_{LMi} = \sum_j C_{ij}$$

where C_{LM}, the lumped mass matrix, represents the diagonalized mass matrix. Usually two or three iterations are sufficient.

ARTIFICAL VISCOSITY MODEL

To prevent oscillations in the vicinity of shocks and to stabilize the scheme artifical dissipation terms need to be added. Currently, the smoother consists of a second order difference term combined with a pressure switch similar to that discussed by Jameson /8/ and Morgan /9/. The Laplacian operator is approximated by summing over all edges meeting a node and using a Finite Element formulation to evaluate these operators in a conservative way, namely

$$D_i = \int_\Omega \Delta U_i\, d\Omega = \int_\Omega \sum_{k=1}^{n} (U_k - U_i)\, d\Omega \tag{12}$$

where n corresponds to the number of edges at node i. The pressure switch is calculated again as a sum over the edges

$$S_i = \frac{1}{Vol} \left| \int_\Omega \sum_{k=1}^{n} \frac{p_k - p_i}{p_k + p_i} d\Omega \right| \tag{13}$$

Finally smoothed nodal values can be calculated after each time step from:

$$U_s^{n+1} = U^{n+1} + \frac{1}{Vol} \int_\Omega \sum_{k=1}^{n} S_{ik} D_i\, d\Omega \tag{14}$$

where $S_{ik} = 0.5(S_i + S_k)$

The smoothing is globally conservative, the total contribution over the entire domain is zero. Due to the fact that no boundary conditions are used in evaluating the Laplacian operators slightly higher diffusion terms are calculated at the boundaries of the domain without adversely affecting the total solution.

BOUNDARY CONDITIONS

Fixed and interpolated Rieman invariants and linearized characteristic relations are used for specifying farfield, in and outflow boundary conditions. When simulating viscous flows the non-slip condition is employed and the flow is assumed to be adiabatic. To satisfy flow tangency in inviscid solutions, normal momentum is adjusted via a vector product of velocity and normal unit vector on the boundary. The non uniquely defined normal direction at each node is specified in such a way that global mass conservation is satisfied /10/.

$$n_j = \frac{\int_\Omega \frac{\partial N_i}{\partial x_j} d\Omega}{\left(\sum_j \left(\int_\Omega \frac{\partial N_i}{\partial x_j} d\Omega \right)^2 \right)^{1/2}} \tag{15}$$

CONVERGENCE ACCELERATION

Integration to steady state is performed with local time steps leading to a solution on a wharped time surface at a significant higher convergence rate. A method of increasing the maximum permissible time step is to stabilize the scheme by averaging the residuals /8/ with their neighbours. This is done in an implicit way, namely

$$\bar{R}_i + \epsilon \Delta \bar{R}_i = R_i \tag{16}$$

where ϵ is a small number (0.5). The Laplacian operator is computed by summing over the edges in the same way as described for the artifical viscosity terms. This leads to a diagonal dominant scheme for small ϵ which can be solved approximately by two Jacobi iterations. Furthermore, to damp high wave numbers in the energy equation enthalpy damping can be employed by input parameters. The improved convergence behaviour is documented later on.

STABILITY

Due to the explicit Euler time stepping the stability of the scheme is bounded by a local Courant number criterion which requires:

$$\Delta t \leq \frac{CFL\,\Delta h}{|u_i u_i|^{1/2} + a} \tag{17}$$

where a denotes the local speed of sound, and Δh is a representative element length, taken as the minimum height in each tetrahedron. The CFL-number is limited by the numerical scheme chosen. The transient scheme employing the iterative solution procedure, requires a CFL-number of 0.5 whereas for the diagonalized system values ranging from 0.8 to 0.9 and in combination with the residual averaging approach from 1.2 to 1.3 are appropriated.

DATA STRUCTURES

To minimize the number of operations the evaluation of the fluxes is computed looping over the elements. The most efficient way to carry out residual averaging and smoothing of the solution are loops over the edges. Therefore in a preprocessor a list of the edges is derived from the element list. Furthermore, to enable vectorisation elements and edges have to be reordered in groups in such a way, that data recurrences are avoided /11/.

MESH GENERATION

In recent years, there has been considerable improvement in the ability to generate unstructured grids over complex shapes. Among others, promising approaches are presented by Baker /12/ and Löhner /13/. Due to the fact that the investigations are concentrated on the flow solver a simple approach has been used for mesh generation. Starting from an already existing regular mesh the unstructured mesh is derived by subdividing regular mesh cells in an adequate number of tetrahedra. The step size defining the cells on the regular grid is prescribed by input parameters allowing a directional coarsening of the grid. Clearly this approach is not suited for complex shapes, however, in combination with the adaptive refinement strategy efficient meshes for all test cases are generated.

ADAPTIVE REFINEMENT STRATEGIES

In advection dominated flows local errors propagating through the domain may determinate the numerical accuracy obtained. Therefore it is desirable to control and bound local errors by adaptive refinement strategies. The solution of flow problems on unstructured grids offers the refinement of interesting flow features (shocks, boundary layers) by mesh enrichment. In all computations an error indicator is used based on a second derivative of a keyvariable, density or pressure, either evaluated via a variational statement or by summing differences over the edges as described in the artifical viscosity model. Using these second derivatives a dimensionless error indicator is calculated and in conjunction with a prescribed error bound each node is marked for refinement or unrefinement. Corresponding to the number of nodes, marked for refinement each element is subdivided in an adequate number of elements. A full discussion of the method is given in /5/.

The refinement process requires as much time as a few steps of the solution procedure.

COMPUTATIONAL RESULTS

For validation of the code, flow problems belonging to a wide range of Mach- and Reynolds number regimes were investigated.

In a first test the inviscid flow around a cylinder was considered. For the case of subsonic inviscid flow this geometry represents a very good possibility to check whether a numerical scheme is able to capture the flow phenomena of a potential solution.

In Fig. 1.a,b,c the unstructured grid, a plot of the isobars and the Machnumber distribution along the stagnation streamline are shown. The inviscid solution is in good agreement with the potential theory (Fig. 1.d). A total pressure loss of less than 0.3% and the well captured stagnation point regions are indicating a simulation free of errors introduced by numerical viscosity.

To validate the time accurracy of the code the viscous flow over a cylinder at Reynolds numbers 100 and 200 was simulated. The computation is performed on a grid of 4732 elements (Fig. 2.a), using the consistent mass formulation of the scheme. Three iterations are sufficient to solve the resulting equation system by the method proposed by Donea /7/.

The pressure and entropy distribution of a fully developed vortex street at a Reynolds number of 100 are shown in Fig. 2.b,c. A comparison between the calculated and measured /14/ Strouhal numbers is given in Fig. 2.d, confirming the high phase accuracy achieved using the consistent mass formulation.

To illustrate the advantages of mesh adaption numerical examples employing the refinement strategy described before are presented. The mesh and the solution obtained at different refinement levels in case of a regular shock reflection are shown in Fig. 3. The adapted mesh (three refinement levels) consists of 2902 grid points representing 12% of the points of a uniformly refined grid. In the case of a transonic nozzle flow the solution obtained after five refinement levels is presented in Fig. 4. The shock resolution is clearly improved in both cases indicating the potential offered by refinement strategies.

To demonstrate the capabilities of the refinement technique in a more complex flow situation the flow through a scramjet inlet at Ma = 5.0 is computed. The numerical solution (Fig. 5) is in good agreement with the results presented by Kumar /15/. Again adaption leads to an efficient mesh and the complex shock interactions are well resolved.

In the next case studied the refinement scheme is employed in the simulation of an oblique shock wave/boundary layer interaction. Three levels of refinement were allowed. In Fig. 6.a,b the adapted mesh and the density distribution as obtained by the numerical solution are shown. The velocity vectors representing the laminar separation bubble induced by the shock reflection are given in Fig. 6.c. The results of the numerical solution in terms of the pressure and skin friction distribution along the wall are compared in Fig. 6.d,e with the experimental data of Hakkinen /16/ indicating a correct capture of the flow features.

To demonstrate the capabilities of the adaptive grid refinement scheme in turbomachinery the flow through the turbine cascade is simulated at transonic conditions. In Fig. 7 the solution obtained at different refinement levels is given. The resolution of the shock is improved again in an efficient way.

To validate the code numerical results have been compared with available experimental data of a two dimensional MTU-turbine test case/17/.

The inviscid and viscous flow at a Reynolds number of 2×10^5 is simulated. At this Reynolds number in the experimental studies a laminar separation followed by turbulent reattachment is detected in the rear part of the suction side.

The mesh of 1521 grid points used for the inviscid solution is already given in Fig. 7. According to the flow features known a priori, the mesh is refined in the stagnation point region. Comparing experimental and numerical pressure distribution a good agreement for the attached flow regions can be stated (Fig. 8.a). The stagnation point regions are resolved well. To complement the results a plot of the calculated isobars is shown in Fig. 8.b.

Before discussing the results of the viscous solution it should be kept in mind that the flow is assumed to be purely laminar in spite of the laminar to turbulent transition indicated by the experimental data.

Therefore, although separation takes place at the right position a correct capture of the flow features near the separation bubble cannot be expected. This is confirmed by the pressure distribution (Fig. 9.a) indicating again a satisfying agreement for regions of attached flow. In contrast to the inviscid solution unsteady interactions in the separation bubble and in conjunction with the vortex street developing at the trailing edge are observed. Therfore, no convergence to steady state was achieved.

Nevertheless a satisfying agreement is found comparing the wake structure and loss distribution over one pitch in the exit plane with experimental data (Fig. 9.c). The overshoots in total pressure may be caused either by discretisation errors or the local time stepping scheme in the transient solution.

The use of the standard turbulence model of Baldwin and Lomax /18/ with the assumption of a regular grid in the boundary layer is under investigation.

To validate the 3-D version of the code the flow around a sphere is considered. In analogy to the flow around the cylinder in two dimensions a potential solution can be used to check the numerics. According to the experimental studies of Achenbach /19/ a viscous flow case with a Reynolds number of 162 000 is chosen, corresponding to purely laminar flow.

The unstructured grids for both flow cases were derived from spherical grid systems of 65x128x27 nodes. A minimum grid spacing in the normal direction of 2×10^{-4} diameters at the

sphere's surface was prescribed for the viscous flow case, whereas for the Euler solution tetrahedra with an aspect ratio aorund 2 were generated. On the sphere's surface the nodes are equally distributed.

To reduce the computational costs quite coarse meshes compared to the flow scales were derived for both flow cases, using the above described mesh generator. In addition a lateral symmetry condition which leads to a further reduction of the number of mesh points is employed in the viscous simulation. The final meshes consisting of 145 200 elements, 28 508 nodes for the inviscid and 188 624 elements, 34 587 nodes for the viscous flow case are shown in Fig. 10.

Due to the spherical nature of the meshes a singularity is present at the origin. This leads to small wiggles as well in the inviscid as in the viscous solution in the stagnation point regions, without affecting the solution elsewhere too much.

In Fig. 11.a the Cp-distribution of the inviscid simulation is compared with analytical solutions. The compressible approximation of Kaplan /20/ is valid for a critical Mach number of 0.573, whereas the second curve represents incompressible potential flow. In spite of the coarse mesh a satisfying agreement between analytical and numerical solution is obtained. The residual averaging approach discussed before leads to a significant improvement of the convergence at minimal extra costs (Fig. 11.b). The axisymmetric character of the flow is confirmed by plots of the isobars and the corresponding velocity vector field on the sphere's surface (Fig. 11.c,d).

In spite of the smooth shape of the sphere the viscous flow around such a geometry has a complex transient structure for the Reynolds number considered. A detailed description of the flow features is given in /21, 22, 23/ and therefore it will be not repeated here. The complex flow structure of the wake region is depicted in Fig. 12.a in terms of the velocity vector field in the symmetry plane.

To limit the computational work the viscous simulation was stopped after 6000 cycles although no quasi-periodical state was achieved. Due to the poor convergence behaviour of the explicit scheme in the viscous flow regions the L2-norm of the continuity equation is reduced only by two decades. Therefore and due to the low spatial resolution of the mesh the presented results should be considered as preliminary.

Nevertheless a comparison between experiment /19/ and theory in terms of the wall pressure distribution is presented in Fig. 12.b. To represent the not axisymmetric character of the solution the pressure distributions belonging to three different circumferential positions are plotted. Although the calculated pressure level in the separated region is slightly lower than in the experiment it can be stated that the agreement between numerical and experimental results is reasonable. On the other hand, to achieve these results in an efficient way either the basic scheme has to be combined with a multigrid method or an implicit phase has to be added.

CONCLUSIONS

For the validation of the unstructured mesh flow solver, problems within quite different Mach- and Reynolds Number regimes have been investigated. The obtained accurracy is competetive with those typical for structured mesh solvers.

The FEM's great flexibility regarding the mesh generation, allows the easy resolution of flow features known a priori. Further it can be seen from the numerical simulations, that the application of the adaptive grid refinement procedure improves greatly the quality of the numerical solution in an efficient way.

To accelerate the convergence to steady state, it appears desireable to combine the scheme with a multigrid method.

However, especially the pure FEM-treatment of large 3-D viscous flow problems may suffer from the higher operation count and storage requirements compared to a cell vertex scheme. While retaining the geometric flexibility of the FEM-code this lacking effiency can be improved by the combination of the cell vertex - and the FEM-scheme in a blockstructured approach.

REFERENCES

/1/ R. Löhner, K. Morgan, O.C. Zienkiewicz, An Adaptive Finite Element Procedure for Compressible High Speed Flows,
Computer Methods in Applied Mechanics and Engineering 1985

/2/ M. Lötzerich, Beitrag zur Strömungsberechnung in Turbomaschinen mit Hilfe der Methode der finiten Elemente,
Dissertation RWTH Aachen, July 1987

/3/ J. Donea, A Taylor-Galerkin Method for Convective Transportproblems, International Journal for Numerical Methods in Engineering, Vol 20 101-119 1984

/4/ A. Jameson, T.J. Baker, Euler Calculations for a Complete Aircraft, Preprint

/5/ R. Löhner, An Adaptive Finite Element Scheme for Transient Problems in CFD, Preprint

/6/ O.C. Zienkiewicz, K. Morgan, J. Peraire, M. Vahdati, R. Löhner, Finite Elements for Compressible Gas Flow and Similar Systems, 7th International Conference on Computing Methods in Applied Sciences and Engineering, December 1985

/7/ J. Donea, S. Giuliani, A Simple Method to Generate High Order Accurate Convection Operators for Explicit Schemes Based on Linear Finite Elements, Internat. J. Numerical Methods in Eng. 1, 63-79, 1981

/8/ D. Mavriplis, A. Jameson, Mulitgrid Solution of the Two-Dimensional Euler Equations on Unstructured Triangular Meshes, AIAA 25 th Aerospace Sciences Meeting, January 1987

/9/ K. Morgan, J. Peraire, Finite Element Methods for Compressible Flows, Lecture Series Programme Computational Fluid Dynamics, Von Karman Inst. for Fluid Dynamics, March 1987

/10/ J.T. Oden, P.T. Stroublis, P. Devloo, Adaptive Finite Element Methods for the Analysis of Inviscid Compressible Flow: Part 1. Fast Refinement/Unrefinement and Moving Mesh Methods for Unstructured Meshes, Comp. Meth. Appl. Mech. Eng. 59, 327-362, 1986

/11/ R. Löhner, K. Morgan, Finite Element Methods on Supercomputers: The Scatter Problem, Proc. NUMETA '85 Conf. (J. Middleton and G.pande eds.), 987-990, A.A. Balkeman, Rotterdam, 1985

/12/ T.J. Baker, Three Dimensional Mesh Generation by Triangulation of Arbitrary Point Sets, AIAA 8th CFD Conference, June 1987

/13/ R. Löhner, P. Parikh, Generation of Three-Dimensional Unstructured Grids by the Advancing-Front Method, AIAA 26th Aerospace Sciences Meeting, January 1988

/14/ H. Schlichting, Boundary-Layer Theory 1979

/15/ A. Kumar, O. Dominion, Numerical Analysis of the Scramjet Inlet Flow Field Using Two-Dimensional Navier-Stokes-Equations, AIAA 19th Aerospace Sciences Meeting, January 1981

/16/ R.J. Hakkinen, I. Greber, L. Trilling, S. Abarbanel, The Interaction of an Oblique Shock Wave with a Laminar Boundary Layer, NASA-Memorandum, March 1986

/17/ M. Lötzerich, A. Vornberger, Ch. Sautter, Die Berechnung von Gitterströmungen mit lokalen Ablösegebieten, DGLR-Fach-Symposium Strömung mit Ablösung, October 1986

/18/ B. Baldwin, H. Lomax, Thin-Layer Approximation and Algebraic Model for Separated Turbulent Flows, AIAA Paper 78-257

/19/ E. Achenbach, Experiments on the Flow Past Sphere's at Very High Reynolds Number, J. Fluid Mech., Vol 54, pp. 565-575, 1972

/20/ C. Kaplan, The Flow of a Compressible Fluid Past a Sphere National Advisory Committee for Aeronautics, Techn. Note 762

/21/ J.C. Strikwerda, Y. Nagel, Finite Difference Methods for Polar Coordinate Systems, NPC Technical Summary Report 2934

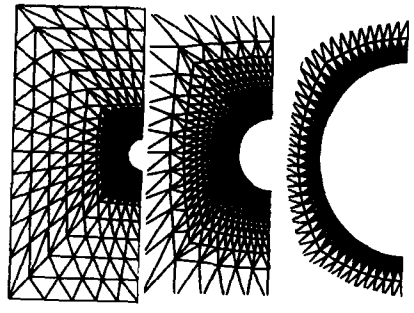
/22/ H. Rieger, J. Jameson, Solution of Steady 3D Compressible Euler- and Navier-Stokes-Equations by an Implicit Lu-Scheme, AIAA Paper 880619 Reno/Nevada, 11.-14. Jan., 1988

/23/ S. Taneda, Visual Observations of the Flow Past a Sphere at Reynolds between 10^4 and 10^6, J. Fluid. Mech., Vol. 85, 1978, pp. 187-192

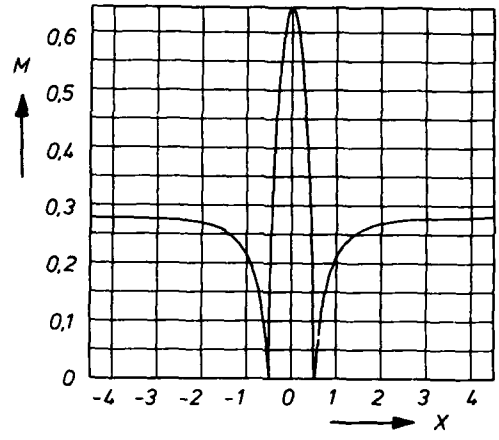
ACKNOWLEDGEMENTS

The financial support of this study by the Deutsche Forschungsgemeinschaft is gratefully acknowledged. The 3-D code was developed within the scope of a diploma thesis at Dornier Company.

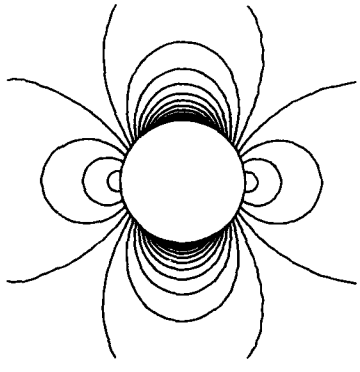
We would also like to thank Dr. J. Hourmouziadis, MTU München, for providing the turbine test data and some insight into the problems. Furthermore we would like to appreciate Ralf Tilch's contributions to the adaptive refinement scheme.



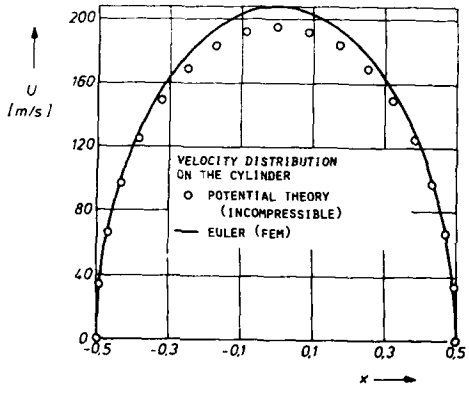
a)



b)



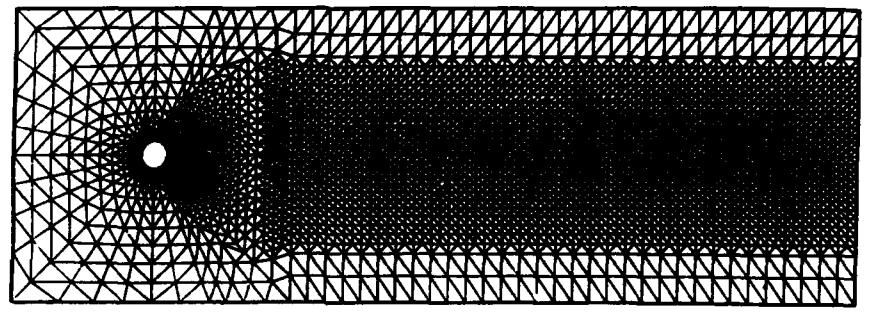
c)



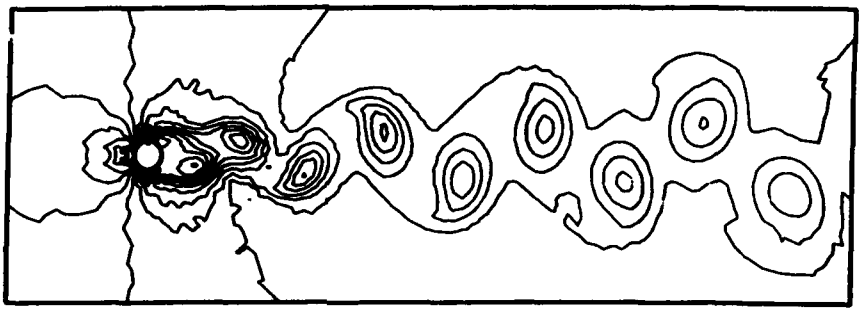
d)

Fig. 1 Flow around a cylinder, inviscid solution, a) Mesh, b) Isobars, c) Mach number distribution along stagnation streamline, d) Velocity distribution on the cylinder

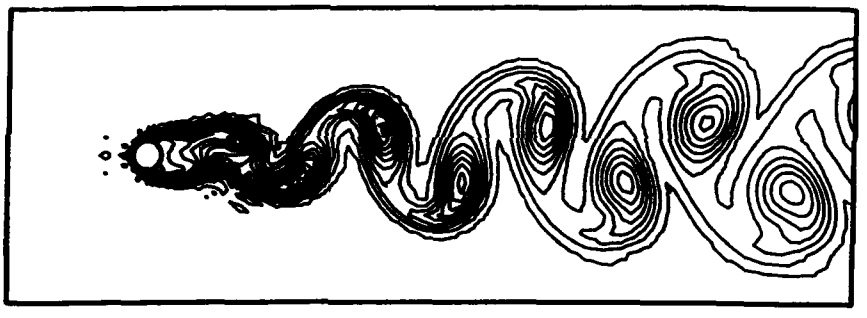
a)



b)



c)



d)

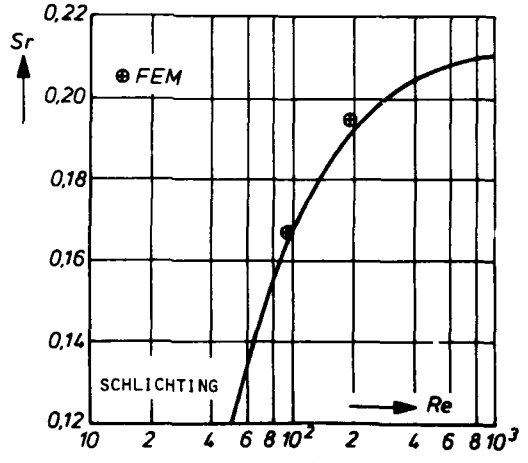
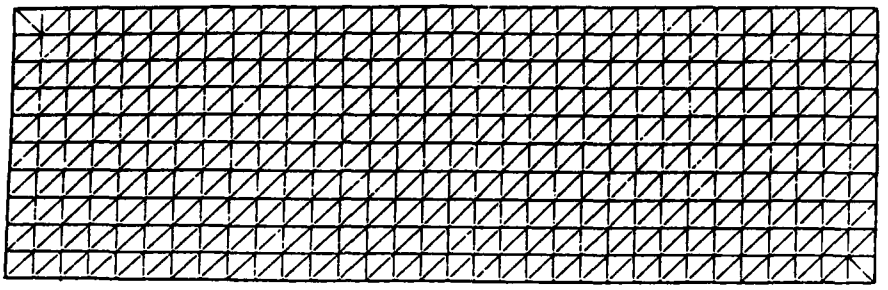
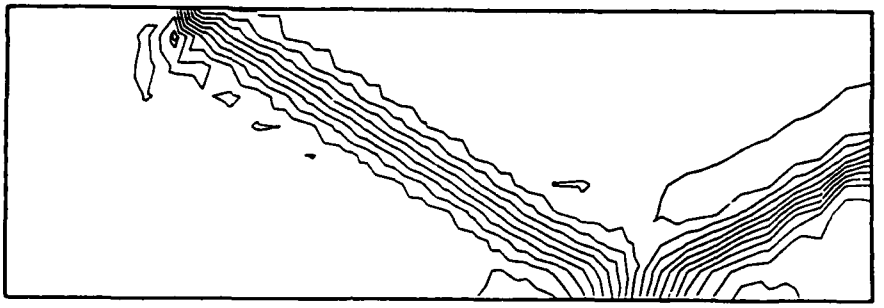


Fig. 2 Flow around a cylinder, viscous solution, a) Mesh, b) Pressure distribution, c) Entropy distribution, d) Strouhal number

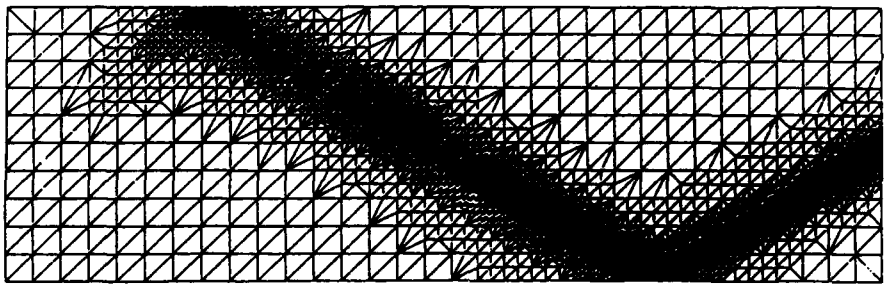
a)



b)



c)



d)

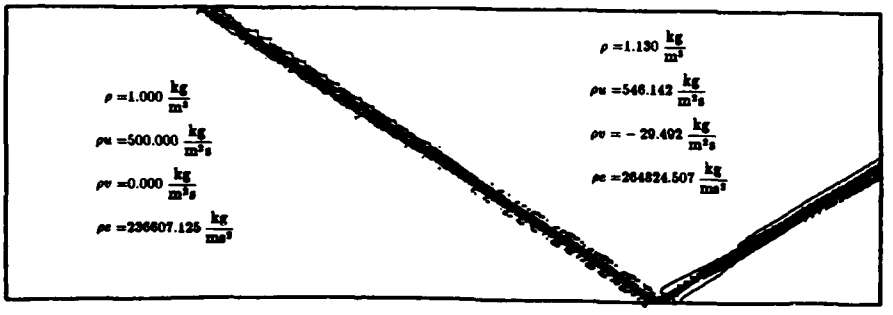
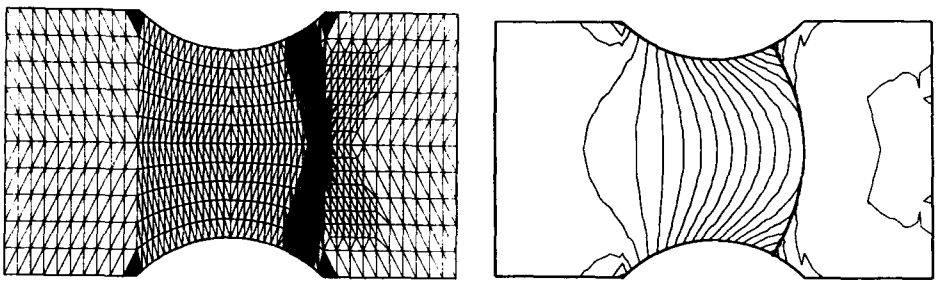
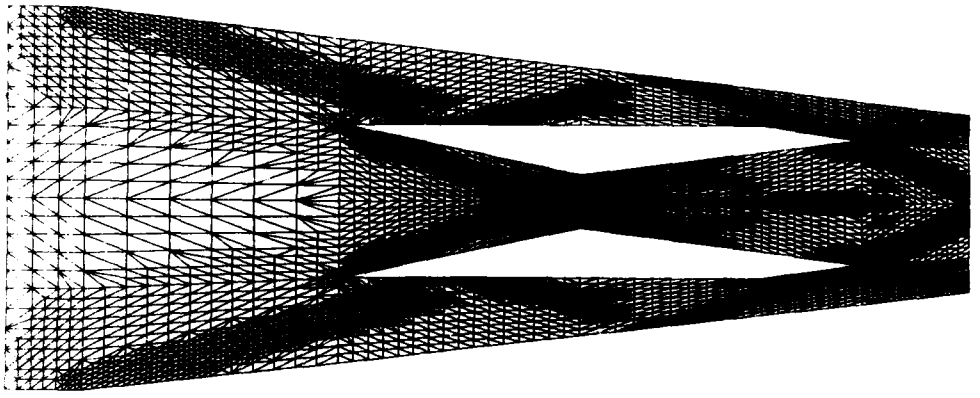


Fig. 3 Regular shock reflection at a wall, a) Initial mesh, b) Initial pressure distribution, c) Adapted mesh (3 refinement levels), d) Pressure distribution on adapted mesh

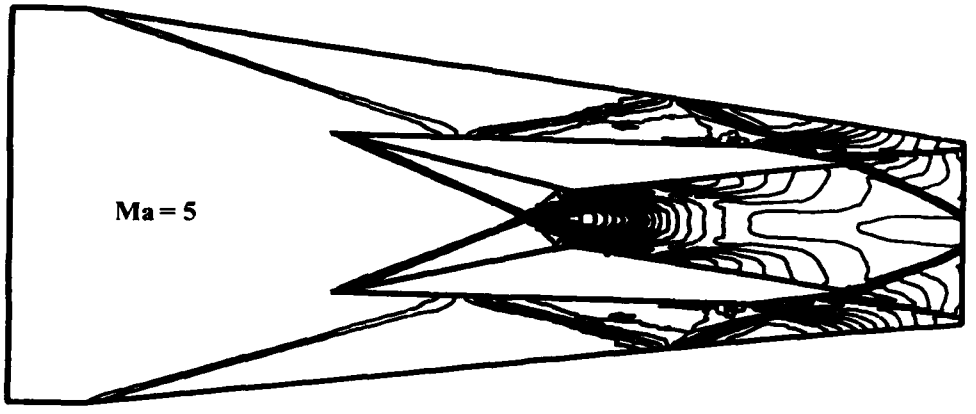


a) b)

Fig. 4 Transonic nozzle flow, Mach = 2, (5 refinement levels), a) Mesh, b) Pressure distribution

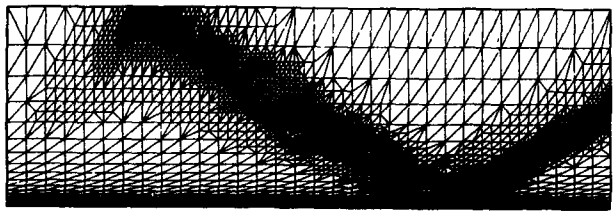


a)

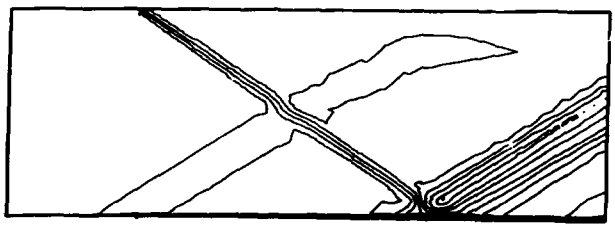


b)

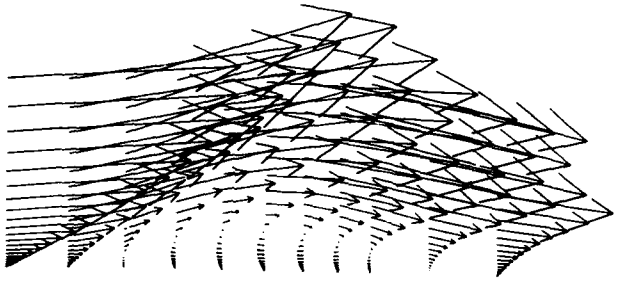
Fig. 5 Scramjet inlet flow, a) Adapted mesh (2 refinement levels), b) Pressure distribution $Ma_{in} = 5$



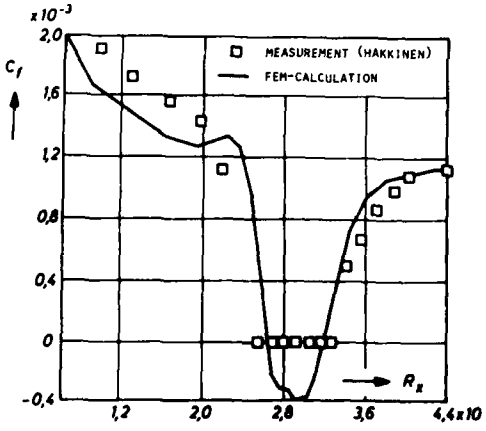
a)



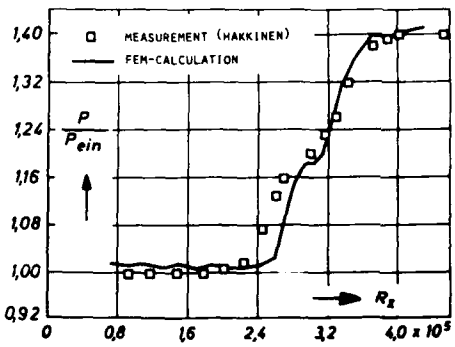
b)



c)



d)



e)

Fig. 6 Shock laminar boundary interaction, a) Mesh (4464 grid points), b) Densitiy distribution, c) Velocity vectors (stretched in y-direction), d) Wall friction distribution, e) Wall pressure distribution

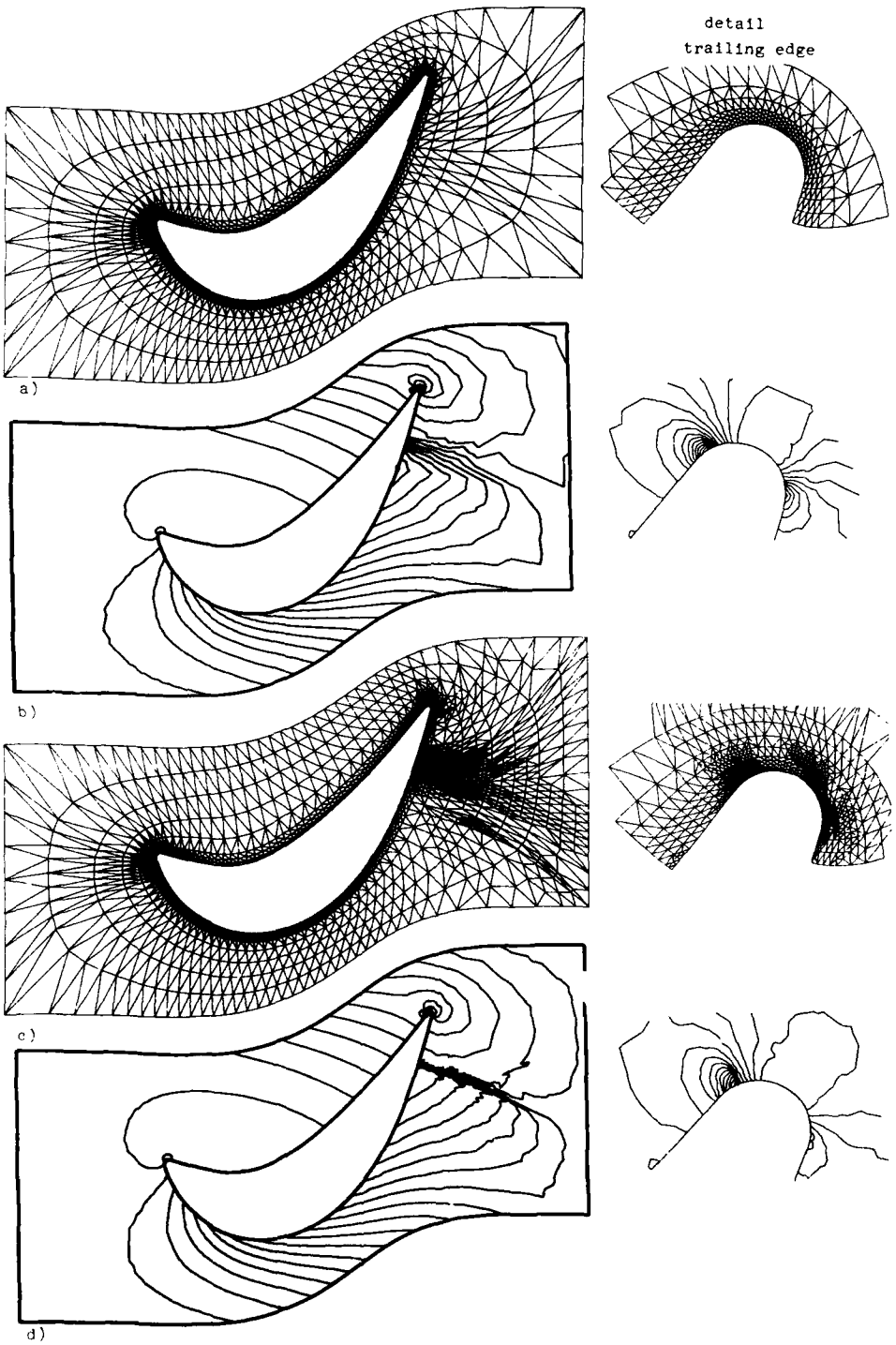


Fig. 7 Transonic turbine flow, a) Initial mesh, b) Initial pressure distribution, c) Adapted mesh (3 refinement levels), d) Pressure distribution on adapted mesh

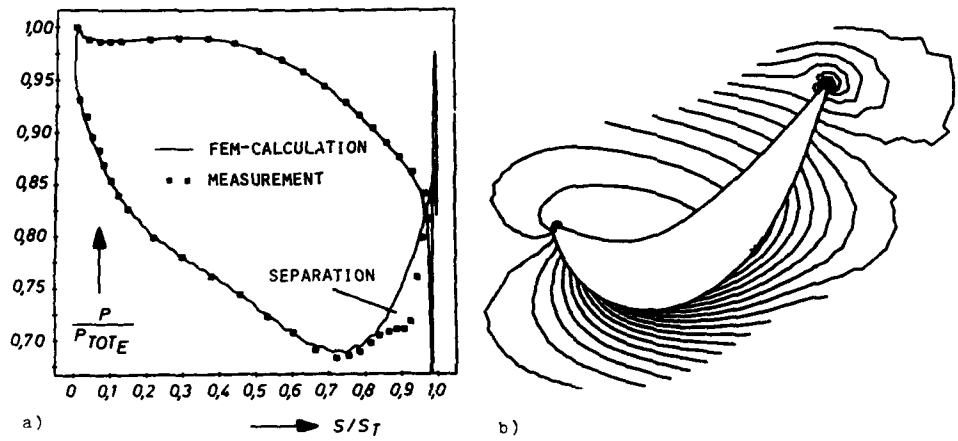
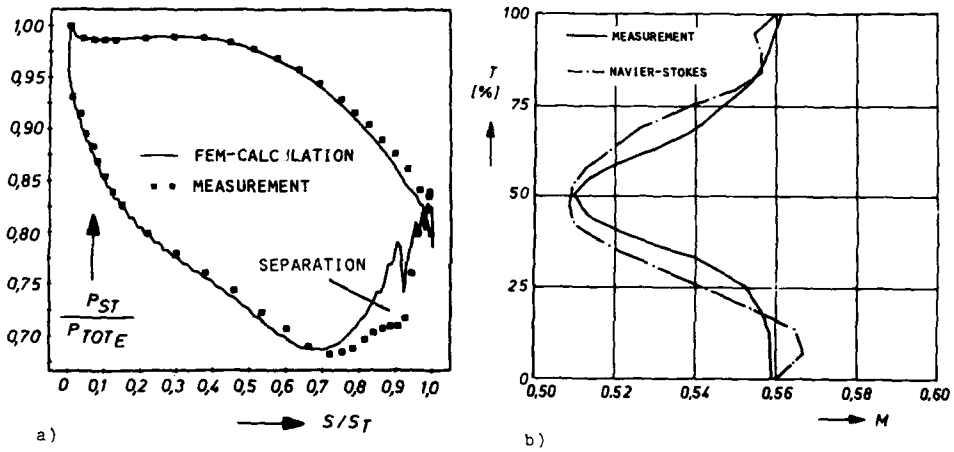


Fig. 8 Turbine flow, inviscid solution, a) Pressure distribution, b) Isobars



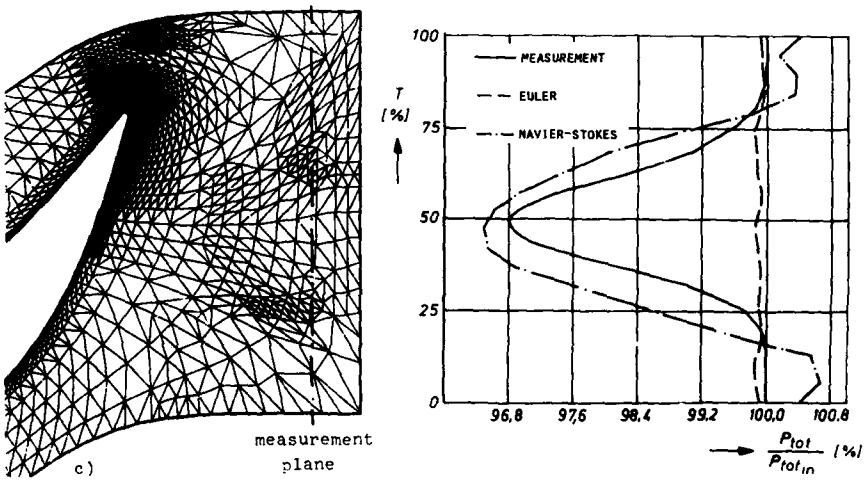
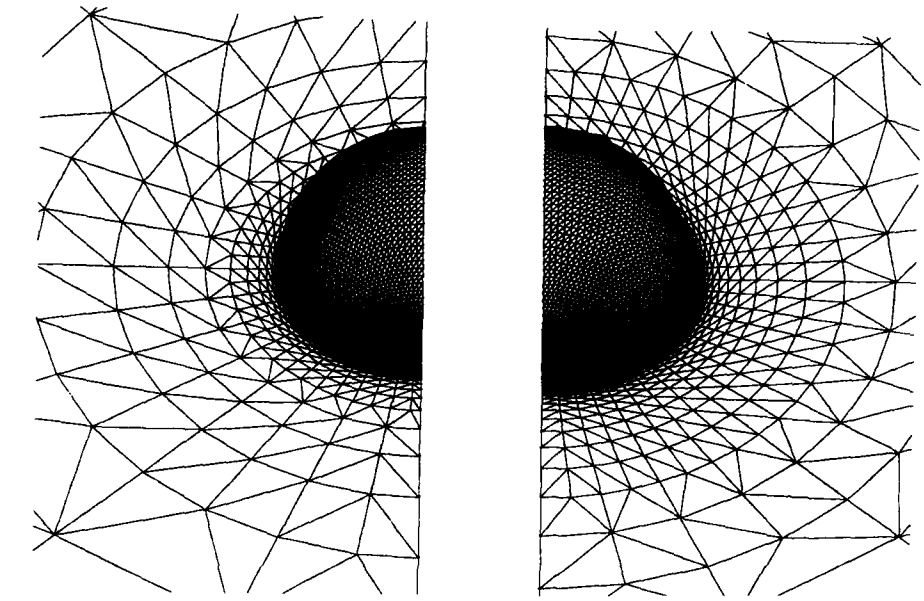
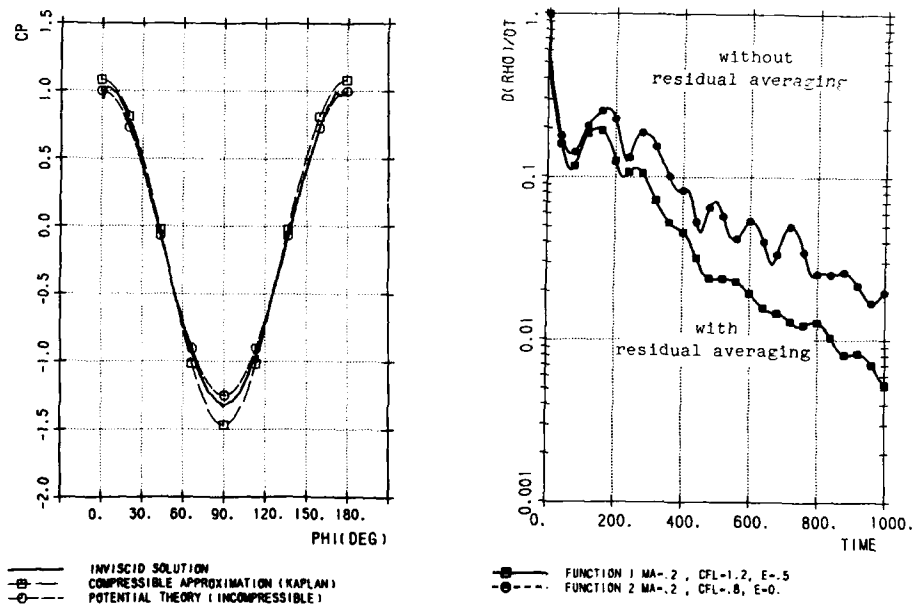


Fig. 9 Turbine flow, viscous and laminar solution, a) Pressure distribution, b)Mach number distribution over one pitch, c) Total pressure loss distribution over one pitch



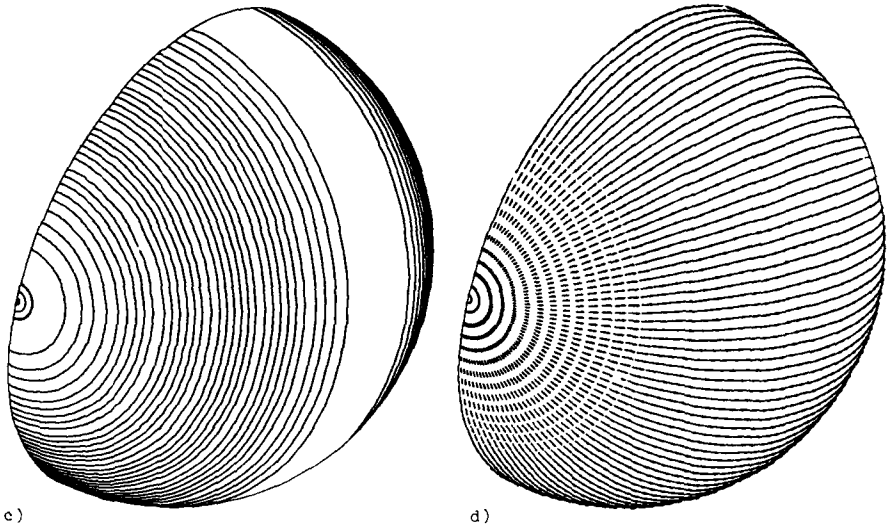
a) b)

Fig. 10 Flow around a sphere, a) Mesh (inviscid solution), b) Mesh (viscous solution)



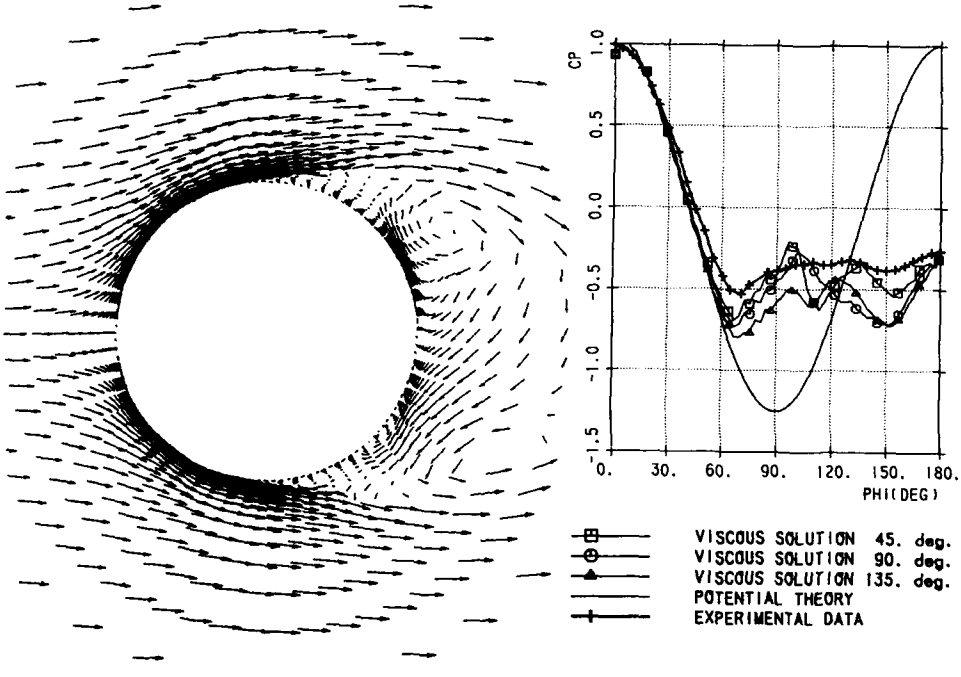
a) b)

Fig. 11 Flow around a sphere, inviscid solution, a) Cp-distribution on sphere's surface (Ma_{in} = 0.3), b) History plot of the L2-Norm of the continuity equation



c) d)

Fig. 11 Flow around a sphere, inviscid solution, c) Isobars on sphere's surface, d) Velocity Vectors on sphere's surface



a) b)

Fig. 12 Laminar flow around a sphere, viscous solution, Re = 162 000, a) Velocity vectors in symmetry plane, b) Cp-distribution on sphere's surface, (experimental data: Achenbach /19/)

VALIDATION OF AN EULER CODE FOR HYDRAULIC TURBINES[1]

F. Thibaud, A. Drotz, G.Sottas

Swiss Federal Institute of Technology (EPFL)
Hydraulic Machines and Fluid Mechanics Institute
CH-1015 Lausanne, Switzerland

Summary

Validation of a three dimensional internal incompressible stationary Euler flow solver has been performed. A finite volume discretization scheme with an explicit time integration is used. The influence of the numerical scheme parameters on the solution and on the convergence is extensively studied. The geometry on which the numerical and experimental comparisons are presented is the runner of an hydraulic Francis turbine. The difference between calculated and experimental integral values is less than 0.2%.

1. INTRODUCTION

Up to 5-10 years ago, the only flow calculation methods available for hydraulic machines were the potential methods. These methods could be easily developped, and in some cases it was possible to obtain with such an approximate approach a reasonable description of the flow in the machine, at least around the design point. With the arrival of supercomputers with large memory and computational speed capacity, the possibility to develop new and advanced numerical simulation procedures based on more realistic governing differential equations became available. This is desirable, especially since the flow in such machines is highly vortical, a flow phenomenon which cannot be captured with potential methods.

The flow simulation model presented in this paper is based on the Euler equations whereby a high Reynolds number flow is assumed. The model is otherwise complete such that Coriolis, centrifugal and gravitational forces are included and the vortical behaviour of the flow is captured.

At the Hydraulic Machines and Fluid Mechanics Institute (IMHEF) work has been in progress since 1982 on the development of an Euler solver for the calculation of internal incompressible three dimensional stationary flows ([1], [2], [3], [4]). These developments are based on a solver written by Rizzi and Eriksson applicable to external and compressible flows ([5]).

The studied geometry, the runner of a Francis turbine (Fig. 1), is very complex so that strong flow deviations and angular momentum changes in the blading generate secondary flow, which requires at least an Euler approach.

The code developped for this work is based on an explicit finite volume approach and has been fully vectorized to suit the particular architecture of a CRAY-1 and a CRAY-2 computer.

After a description of the numerical technique, the paper presents a detailed study of the influence on the computed solutions of four numerical parameters of the explicit method and a comparison between experimental and numerical results.

2. THEORETICAL ANALYSIS

2.1. Computational method

2.1.1. Governing equations

For a rotating coordinate system, the Euler equations for an incompressible flow can be written as

continuity equation :

$$\int_{\partial\Omega} w.n \, dS = 0 \qquad (2.1)$$

[1]This work has been partially sponsored by the "Commission d'Encouragement des Recherches Scientifiques" (CERS), the "Ateliers de Constructions Mécaniques de Vevey S.A." (ACMV) and Sulzer-Escher-Wyss Ltd. (SEW).

momentum equation :

$$\frac{\partial}{\partial t}\int_{\Omega} w\,\mathrm{dvol} + \int_{\partial\Omega} [\, w(w.n) + (p/\rho_0)n \,]\,\mathrm{dS} = \int_{\Omega} f\,\mathrm{dvol} \tag{2.2}$$

where ρ_0 is the constant density, w the relative velocity vector, p the pressure, n the outward unit vector normal to the surface $\partial\Omega$ of the volume Ω, and f the mass forces vector including the centrifugal, Coriolis and gravitational terms, i.e.

$$f = -\,\omega\wedge\omega\wedge r - 2\omega\wedge w - g \tag{2.3}$$

with ω the rotational velocity vector.

The equations (2.1) and (2.2) are written in integral form since a finite volume procedure will be used to solve them, see also section 2.1.2. It is widely known that hyperbolic flow problems can be solved efficiently using time marching methods. However equation (2.1) is not hyperbolic in time. For flow calculations in which only the steady state solution is of interest, Chorin [6] and Peyret [7] have shown that the continuity equation can be made hyperbolic in time by introducing an artificial time-dependent pressure term, and this equation may now be written as

$$\frac{\partial}{\partial t}\int_{\Omega} (p/\rho_0)\,\mathrm{dvol} + c^2\int_{\partial\Omega} w.n\,\mathrm{dS} = 0 \tag{2.4}$$

where c^2 is an arbitrary real parameter that has to be suitably selected to obtain convergence of the integration method.

The resulting system of equations (2.2), (2.4) has no physical meaning until the steady state is reached and, when this is the case, it reduces to the steady state solution of the original system of equations (2.1), (2.2). Consequently, we shall concentrate on the solution of the hyperbolic system (2.2), (2.4) which can be written in the form

$$\frac{\partial}{\partial t}\int_{\Omega} q\,\mathrm{dvol} + \int_{\partial\Omega} \mathcal{H}(q).n\,\mathrm{dS} = \int_{\Omega} \mathcal{F}\,\mathrm{dvol} \tag{2.5}$$

where

$$q = \begin{pmatrix} p/\rho_0 \\ u \\ v \\ w \end{pmatrix}, \quad \mathcal{H}(q).n = \begin{pmatrix} c^2 w.n \\ u\,w.n + (p/\rho_0)n.e_x \\ v\,w.n + (p/\rho_0)n.e_y \\ w\,w.n + (p/\rho_0)n.e_z \end{pmatrix}, \quad \mathcal{F} = \begin{pmatrix} 0 \\ f.e_x \\ f.e_y \\ f.e_z \end{pmatrix},$$

$$w = u e_x + v e_y + w e_z .$$

The quantity $\int_{\partial\Omega} \mathcal{H}(q).n\,\mathrm{dS}$ represents the sum of the net flux of q across the closed surface $\partial\Omega$ surrounding the volume Ω, and the pressure forces acting on $\partial\Omega$.

2.1.2. *Discretization and time integration*

The numerical procedure used has been developped by Rizzi and Eriksson [5] and is briefly outlined here.

Equation (2.5) can be locally applied to any volume Ω. This implies that it is valid for any quadrilateral cell Ω_{ijk} of the discretized computational domain (finite volume procedure). By using a scheme centered in the three parametric directions to spatially semi-discretize the hyperbolic system, (2.5) takes the form of the following differential equation

$$\frac{\partial}{\partial t} q_{ijk} = \mathcal{F}_{ijk} - \frac{1}{(\mathrm{Vol})_{ijk}}\,\delta\,[\,\mathcal{H}(q).S\,]_{ijk} = (\mathcal{F}_a(q))_{ijk} \tag{2.6}$$

where q and $\mathcal{F}$ are volumetric averages located at the center of the cell Ω_{ijk}, $\mathcal{H}(q).S$ is the non-linear corresponding flux evaluated on the cell surface S and $(\mathrm{Vol})_{ijk}$ is the volume of Ω_{ijk}.

For any function $\mathcal{G}$, the three dimensional central-difference operator δ is defined by

$$\delta G_{ijk} = (\delta_I + \delta_J + \delta_K)\, G_{ijk}$$

$$= (G_{i+1/2,j,k} - G_{i-1/2,j,k}) + (G_{i,j+1/2,k} - G_{i,j-1/2,k}) + (G_{i,j,k+1/2} - G_{i,j,k-1/2}). \quad (2.7)$$

Hence $\delta\,[\,\mathcal{H}(q).\mathcal{S}\,]_{ijk}$ expresses the net gain of flux and pressure forces into the cell and is fundamental to the conservation property.

Since q_{ijk} is located at the center of the cell and $\mathcal{H}(q).\mathcal{S}$ must be expressed at its surfaces, it is necessary to use some kind of interpolation procedure to evaluate $[\,\mathcal{H}(q).\mathcal{S}\,]_{ijk}$. This is done by computing the fluxes separately for each cell side and then averaging the results on each pair of opposite sides, i.e.

$$[\,\mathcal{H}(q).\mathcal{S}\,]_{ijk} = [\,\mu_I\, \mathcal{H}(q_{ijk})].\mathcal{S}_I + [\,\mu_J\, \mathcal{H}(q_{ijk})].\mathcal{S}_J + [\,\mu_K\, \mathcal{H}(q_{ijk})].\mathcal{S}_K \quad (2.8)$$

where μ is the averaging operator

$$\mu_I\, G_{ijk} = (G_{i+1/2,j,k} + G_{i-1/2,j,k})/2$$

and $\mathcal{S}_I$, $\mathcal{S}_J$ and $\mathcal{S}_K$ are the vector areas of the quadrilateral cell Ω_{ijk}.

The system (2.6) is integrated by the parametrized (θ) explicit three stage Runge-Kutta method with local time step (to accelerate the convergence to steady state). For the general differential equation

$$\frac{\partial}{\partial t}\, q = \mathcal{G}(q) \quad (2.9)$$

with initial value $q^{(0)}$ at time t_0, this scheme reads

$$k_1 = \mathcal{G}(q^{(0)})$$

$$k_2 = \mathcal{G}(q^{(0)} + \Delta t\, k_1)$$

$$k_3 = \mathcal{G}(q^{(0)} + \Delta t\,[(1-\theta)k_1 + \theta k_2])$$

$$q^{(1)} = q^{(0)} + \Delta t\,[(1-\theta)k_1 + \theta k_3] \quad (2.10)$$

The local time step satisfies a Courant-Friedrich-Lévy (CFL) type condition [8]

$$\Delta t_{ijk} \le \mathrm{CFL}\left[\frac{\mathrm{Vol}}{U + (U^2 + c^2 S^2)^{1/2}}\right]_{ijk} \quad (2.11)$$

where

$$U = |w\mathcal{S}_I| + |w\mathcal{S}_J| + |w\mathcal{S}_K|,$$

$$S = (|\mathcal{S}_I| + |\mathcal{S}_J| + |\mathcal{S}_K|).(|\mathcal{S}_I| + |\mathcal{S}_J| + |\mathcal{S}_K|)$$

with the convention $|a| = |a_x|\,e_x + |a_y|\,e_y + |a_z|\,e_z$.

The time integration process is terminated when the $c^{-2}\,\partial\,(\int_\Omega p/\rho_0\, \mathrm{dvol}\,)\,/\,\partial t$ term becomes small enough compared to $\int_{\partial\Omega} w.n\, dS$ so that the final solution satisfies the system (2.1), (2.2).

Due to the hyperbolic character of the equations, wave propagation plays an important role. It has been shown [5] that the truncation error of the above scheme is entirely dispersive and not dissipative. To prevent aliasing phenomena, a numerical filtering term is added to the advective terms of the Euler equations [5] :

$$\frac{\partial}{\partial t}\, q_{ijk} = (\mathcal{F}_a(q))_{ijk} + \gamma\,(\mathcal{F}_d(q))_{ijk} \quad (2.12)$$

This linear fourth order dissipative filtering term is controlled by the γ parameter.

2.1.3. The Francis turbine

The set of discretised equations (2.6) will be applied to calculate the flow in the interblade channel of the runner of a Francis hydraulic turbine (Fig. 1). In such a rotating machine the flow enters via the distributor, which consists of the spiral case, the stay vanes and the wicket gate (Fig 1). The distributor partially transforms the potential energy of the flow into kinetic energy. The remaining potential energy and the kinetic energy of the water is then transformed into rotational (mechanical) energy in the runner. Thereafter, the water enters the draft tube where the residual kinetic energy is partially transformed into pressure energy.

2.1.4. Computational domain

By assuming an axisymetric flow in the runner, it is possible to restrict the computational domain to one interblade channel (Fig. 2). Due to the geometrical complexity of this domain it is necessary to use a grid generation technique to describe the limiting surfaces correctly. A direct algebraic grid generation method of transfinite interpolation type is used to generate three dimensional meshes between arbitrary non-orthogonal limit surfaces [9, 10]. A limited number of parameters allow us to control the local grid density .

2.1.5. Boundary conditions

The boundary conditions to be prescribed depend on the physical nature of the bounding surfaces of the computational domain. On solid walls (blade sides, crown and band) the normal flux must be zero, i.e. the velocity vector must be tangential to the wall.

Fluid surfaces can be divided into two types, i.e. inlet-outlet and periodical surfaces (Fig 2). For periodic ones, the boundary conditions are imposed by using a periodicity condition, i.e. averaging the fluxes from both sides of the periodic surface. At the inlet, respectively at the outlet surface, it has been shown from the theory of characteristics that, for the hyperbolic system (2.5), three conditions, respectively one, have to be imposed. This mean that the velocity vector field has to be prescribed at the inlet whereas only the pressure can be given at the outlet.

2.1.6. Computational details

For a given mesh the calculation time is reduced by using a grid embedding technique. It consists in extracting a coarse grid out of a finer by dividing the number of cells in the three parametric directions by two. The solution obtained on the coarse grid is interpolated and then used as initial solution on the fine grid.

The calculations were performed on the Cray 1-S supercomputer of the Swiss Federal Institute of Technology (EPFL) in Lausanne (Switzerland) and on the Cray 2 supercomputer of the Ecole Polytechnique in Palaiseau (Paris, France).

2.2. Parametric studies

2.2.1. Preamble

The Euler code is tuned with four parameters. Two of these (θ and CFL) are purely numerical. The two others have in a certain sense a physical meaning : c^2 can be related to the "speed of sound", that is, the speed at which waves are travelling through the flow field; and γ can be interpreted as a "viscosity" because of its damping effect on the waves in the flow field.

2.2.2. Theoretical limitations

From the theory of linear equations, we know that :

- CFL should be about 1 ,
- the time integration order is 2 when $\theta = 1/2$ and 1 otherwise ,
- c^2 must be greater than $|w|^2$ to insure that the pressure waves dominate over the convection ones and that the system to be solved is less directionally dependant and better conditioned [8] ,
- γ should be as small as possible.

2.2.3. Numerical experimental studies

The major interest of this study is of course to get a converged solution which is not a trivial matter. On the basis of numerous runs of the Euler solver for different geometries (2D : isolated cylinder, pump geometries; 2D and 3D : isolated profile, cascade, S-duct, wicket gate; 3D : convergent nozzle, runner of Francis turbine), we have noticed that the optimal choice of parameters is changing with

- the geometry itself (simple or complex, 2D or 3D),
- the size of grid cells,
- the boundary conditions.

For the Francis runner, about 5700 parameter test runs have been performed. In these runs, CFL was ranging from 0.75 to 1.9, θ from 0.25 to 0.75, γ from 0.005 to 0.045 and c^2 from 4 to 200. Most of these runs were done on a mesh containing 512 cells ($17 \times 5 \times 9$ grid points), some of them were on a 4096 cells mesh ($33 \times 9 \times 17$ points) and a few of them were on a 32768 cells mesh ($65 \times 17 \times 33$ points). The convergence criterion used for these tests was : pressure residue less than 10^{-5}. In case of convergence, three comparison criteria were used :

- number of iterations required to reach convergence,
- relative difference between entrance and exit flowrate,
- relative error between measured and computed torque.

The results of these tests are reported in the next section.

2.2.4. Observations on numerical experiments

The major observations for each of the parameters are summarized here.

CFL

- The higher the CFL , the lower the number of iterations;
- the upper bound for CFL is decreasing together with the cell size and seems to tend to 1 for very fine grids (Fig. 3).

θ

- The higher the θ , the lower the number of iterations;
- the upper bound for θ is decreasing together with the cell size and seems to tend to $1/2$ for very fine grids (Fig. 3).

γ

- The higher the γ , the higher the error in computed mass flow rate at the exit;
- the lower bound for γ seems to be just under 1%;
- for increasing γ , the error on computed torque is first decreasing and afterwards increasing; the value of γ producing the lowest error depends on c^2.

c^2.

- The higher the c^2 , the higher the number of iterations;
- the lower bound for c^2 seems to be about 5;
- for increasing c^2 , the error on computed torque is first decreasing and afterwards increasing; the value of c^2 producing the lowest error depends on γ.

Cell size

- The smaller the cell size, the higher the number of iterations;
- the smaller the cell size, the smaller the difference between the mass flow rate at the entrance and the exit;
- the smaller the cell size, the smaller the difference between the measured and computed torque.

Table 1 summarizes our observations.

2.2.5. Conclusions

From the theory of linear equations and our experimental observations we have decided to fix

- CFL = 1,
- $\theta = 1/2$,
- $\gamma = 1\%$,

for all grids.

Moreover, because the lower bound for c^2 is locally determined by the condition $c^2 \leq \| w \|^2$, we have replaced the constant c^2 by

$$c^2 = \lambda \| w \|^2 \tag{2.12}$$

and fixed λ to 50, a figure which was based on our computational experience with this problem.

Further computations using the above mentioned values of the four parameters were performed on the Cray 2 using three new grids, the coarsest one containing 1080 cells ($19 \times 7 \times 11$ grid points), the middle one with 8640 cells ($37 \times 13 \times 21$ points) and the finest one with 69120 cells ($73 \times 25 \times 41$ points). Convergence was obtained immediately.

3. COMPARISON BETWEEN EXPERIMENT AND CALCULATIONS

3.1. Preamble

3.1.1. Experimental installations

The Hydraulic Machines and Fluid Mechanics Institute (IMHEF) has three universal experimental installations. Thea are equipped with high precision instrumentation. Their flexibility and adaptive possibilities allow for any kind of testing with hydraulic turbines or pumps in open or closed circuit. Its speciality is the acceptance tests, i.e. the construction of models and the determination of the hill chart of operating points (efficiency) of any kind of turbine. The importance of these hill charts comes from the fact that they enable to determine the best efficiency operating point of the turbine and they show how the turbine is dealing with "off design" operating conditions. The torque, the flow rate and the specific hydraulic energy is determined with an error less than 0.1%.

Velocity measurements are performed at the runner entrance and exit and at the draft tube entrance (Fig 4); these measurements are made using a 5 hole probe. By using the differential pressures between the holes of the probe we obtain (Fig 5):

- the velocity norm : $C_{(norm)}$ [-],
- the tangential velocity component : C_u [-],
- the axial velocity component : C_a [-],
- the meridional velocity component : C_m [-],
- the absolute flow angle : α [degrees].

These measurements are performed with a precision between 5 and 10%. They deliver average values over the circle described by the measurement point when it is viewed from the rotating runner.

3.1.2. Computational boundary conditions

The computational domain is starting just after the wicket gate (or guide vane) trailing edge. We have no velocity measurements at this location, so we have assumed a velocity profile based on experimental knowledge. It is fixed by using a parabolic shape of the profile with a vertical tangent at the roof of the guide vane, and by giving the ratio of the velocity norms at the roof and the bottom of the guide vane channel (Fig 4).

By using the measured flow rate and the geometrical characteristics of the wicket gate we can fix the velocity profile at the outlet of the wicket gate and, by adding to it the tangential velocity due to the rotation of the runner, we get the boundary condition, i.e. the relative velocity distribution at the inlet of the computational domain.

The computational domain terminates at the measurement axis placed at the draft tube entrance. As this measurement axis is perpendicular to the rotation axis of the turbine and placed quite far from the runner, the flow is nearly perpendicular to the measurement axis. Hence, the probe delivers the static pressure, which is used as boundary condition at the outlet of the computational domain.

3.1.3. Computational results

The numerical scheme used calculates the static pressure and the velocity components at the geometrical center of each cell of the mesh and the static pressure at the center of each elementary surface on solid walls [11].

From the static pressure distribution on both sides of the blade the global torque can be obtained.

As the computational grid is rotating with the runner and as the experimental measurements are averaged values, the computed velocity in the measurement points is obtained by the following procedure :

- the tangential velocity due to rotation is substracted from the computed velocity w to obtain the absolute velocity,
- the computed absolute velocity is interpolated on the portion of the circle described by the measurement point in the computational domain (by reference to the relative coordinate system),
- the interpolated values obtained on the circle are averaged (by reference to the relative angle) ,
- $C_{(norm)}$, C_u, C_a, C_m and α are computed.

3.1.4. The three selected operating points

Turbine designers mainly use two characteristic numbers to describe an installation

$$\varphi = \frac{\dot{V}/\pi}{NR^3}, \qquad \psi = \frac{gH}{R^2N^2/_2} \tag{3.1}$$

where $\dot{V}$ is the mass flow rate, R the reference radius, N the number of revolutions per second, g the gravitational constant and H the specific hydraulic energy. These two quantities are used to plot the hill chart of the efficiency.

The three selected operating points (o.p.) are specified by

- o.p. A : $\varphi_\wedge$ $\psi_\wedge$
- o.p. B : $\varphi_\wedge$ $0.85\,\psi_\wedge$
- o.p. C : $\varphi_\wedge$ $1.25\,\psi_\wedge$

where $\varphi_\wedge$ and $\psi_\wedge$ are the ones of best efficiency. They will be pointed out by using the relative flow rates

- o.p. A : optimum flow rate
- o.p. B : 6.61% below optimum flow rate
- o.p. C : 8.51% above optimum flow rate

3.2. Comparisons

The computations used in the comparisons shown below have been made using the grids described in section 2.2.5, i.e. the coarse grid with $19 \times 7 \times 11$ points, the middle one with $37 \times 13 \times 21$ points and the finest one with $73 \times 25 \times 41$ points.

3.2.1. Torque

Table 2 gives the comparisons between measured and computed torque.

3.2.2. Velocity components

Figures 6 to 8 present a selection of the results obtained for the five normalized quantities $C_{(norm)}$, C_u, C_a, C_m and α on the three measurement axis for the three operating points.

The relative errors of the measurements are fixed at 7.5% on all the components.

The abscissa is the normalized radius of the measurement points; the velocity components are normalized between 0 and 1.

3.3. Comments

3.3.1. General comments

A general overview of the results show a very good qualitative agreement between the computed and the experimental results. Furthermore, if we compare from a quantitative point of view the different set of results in the major portion of the flowfield, the difference between computed and experimental values is smaller than 7.5%.

From the results it is clear that the coarsest grid cannot be used for efficiency predictions, but the finest grids are adequate for turbine design purposes.

3.3.2. Hydraulic considerations

It is important to keep in mind the following points.

3.3.2.1. The conditions of the experiment

All the data have been obtained with 5 hole probes. However recent studies made by SEW on another Francis runner, comparing 5 hole probes and Laser-2-Focus (L2F) system measurements, show a better agreement between L2F data and computations with our code [12].

3.3.2.2. Simplifications made for the calculations

Since viscous effects are not taken into account in the Euler equations, boundary layer effects will lead to differences in computed and experimental results in some critical regions. These boundary layer effects are important especially at the outlet of the wicket gate, where we have supposed a parabolic profile. Strong 3-D boundary layer effects can be expected at this point due to the high curvature of the wall just after the bottom of the wicket gate.

3.3.2.3. The general flow behaviour when the flow rate changes

From a physical point of view, for low flow rates (inflow under the optimum) the flow in the runner tends to deviate toward the periphery of the runner. But for higher flow rates such that the inflow is over the optimum one, the flow is deviated toward the runner axis.

3.3.3. Results analysis

3.3.3.1. The torque

The with the finest grid calculated relative difference for the torque is very low, especially for the operating points A and C. However, for the o.p. B, the relative difference is more important. This can be explained by the fact that when the flow rates decrease a beginning of recirculation appears in this kind of turbines.

3.3.3.2. The velocity field

Consider next the three cases presented in Fig. 6 to 8.

o.p. A (Fig. 6)

The computed axial and meridional velocity (C_a, C_m), the computed norm of the velocity $C_{(norm)}$ and the computed absolute flow angle α are not in agreement with the experimental results in the region near the band, which confirm the observations made in 3.3.2.2.

o.p. B (Fig. 7)

We see that for maximum values of the radius along the measurements axis we have a discrepancy between experimental and numerical results. But the phenomena described in 3.3.2.2 and verified for the optimum flow rate (o.p. A) is convected along the band surface, because of the behaviour of the flow mentionned in section 3.3.2.3.

o.p. C (Fig. 8)

The velocity components are quite systematically underevaluated by the computations. The deviation of the flow towards the runner axis (see 3.3.2.3) tends to initiate the creation of a torch. This effect which modifies the flow field cannot be taken into account in our calculations and this explains the difference.

4. CONCLUSIONS

Our two industrial partners, the ACMV and SEW, are using this Euler solver with the aim to optimize the runner of Francis turbines. The results obtained are very promising for the future.

Acknowledgements

We would like to express our gratitude to CRAY Research France S.A. and CRAY Research Suisse S.A. for their help in optimizing the code and for allowing us the opportunity of running this code on the CRAY-2 of the CCVR at the Ecole Polytechnique in Palaiseau (Paris, France).

Many thanks are also due to P. Gamba, M. Eichenberg and M. Scherrer who helped us in running the tests or provided us with the graphical tools and to J. Vos for his help in improving the presentation of this paper.

Last but not least, we want to thank all our colleagues at IMHEF for providing the stimulating environment in which this work has been done, especially its director, Prof. I.L. Ryhming.

References

[1] L.E. Eriksson, A. Rizzi, J.P. Therre, *Numerical solution of the steady incompressible Euler equations applied to water turbines*, AIAA-84-2145.

[2] A. Saxer, H. Felici, C. Neury, I.L. Ryhming, *Euler flows in hydraulic turbines and ducts related to boundary conditions formulation*, to appear in the proceeding of the 7th GAMM conference on numerical methods in fluid mechanics.

[3] A. Saxer, H. Felici, *Etude numérique d'écoulements internes, incompressibles et stationnaires par les équations d'Euler*, report IMHEF/EPFL T-87-4 (1987).

[4] E. Goede, I.L. Ryhming, *3-D computation of the flow in a Francis runner*, Sulzer Technical Rewiev 69(1987), n° 4, 31-35, Sulzer Brothers Ltd, Winterthur, Switzerland.

[5] A. Rizzi, L.E. Eriksson, *Computation of flow around wings based on the Euler equations*, JFM 148(1984), 45-71.

[6] A.J. Chorin, *A numerical method for solving incompressible flow problems*, J. Comp. Phys. 2(1967), 12-26.

[7] R. Peyret, T. Taylor, *Computational methods for fluid flow*, Springer, New-York, 1982.

[8] A. Rizzi, L.E. Eriksson, *Computation of inviscid incompressible flow with rotation*, JFM 153(1985), 275-312.

[9] L.E. Eriksson, *Transfinite mesh generation and computer-aided analysis of mesh effect*, Doctoral Dissertation Upsala University, 1984.

[10] C. Neury, *3-D mesh generation for calculating flow through radial-axial turbines*, in Numerical grid generation in computational fluid dynamics, J. Häuser, C. Taylor Eds., Pineridge Press, Swansea, 1986, 387-398.

[11] A. Rizzi, *Numerical implementation of solid-body boundary conditions for the Euler equations*, ZAMM 58(1978), T301-T304.

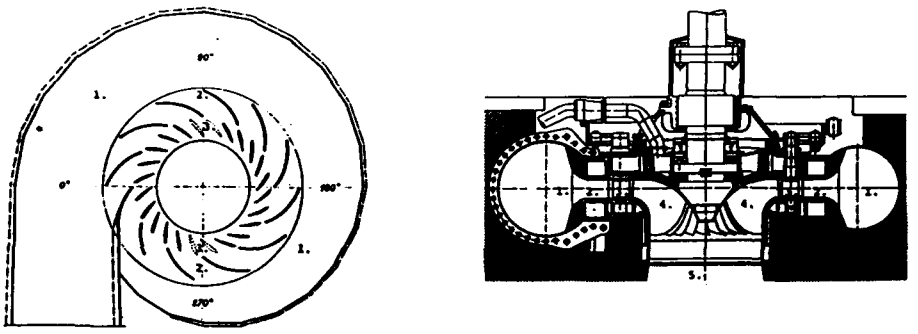
[12] E. Goede, R. Cuénod, P. Bachmann, *Theoretical and experimental investigation of the flow field around a Francis runner*, to appear in the proceeding of the 1988 symposium of the IAHR-AIRH.

	number of iterations	difference between entrance and exit flow rate	difference between computed and measured torque
CFL ↗	↘	—	—
θ ↗	↘	—	—
γ ↗	—	↗	↘ ↗
c^2 ↗	↗	—	↘ ↗
Cell size ↘	↗	↘	↘

Table 1. Influence of the parameters.

Operating point	A		B		C	
	Torque	Rel. difference	Torque	Rel. difference	Torque	Rel. difference
measurements	.03042	-.-	.03029	-.-	.03025	-.-
coarse grid	.03778	24.19%	.03321	9.28%	.03417	9.65%
middle grid	.03133	2.99%	.03136	3.09%	.03135	3.64%
fine grid	.03037	-0.16%	.02989	-1.32%	.03031	0.20%

Table 2. Comparisons between measured and computed torque.



Upper view Axial view

Figure 1. Francis turbine (1. spiral duct; 2. stay vanes; 3. wicket gate; 4. runner; 5. draft tube).

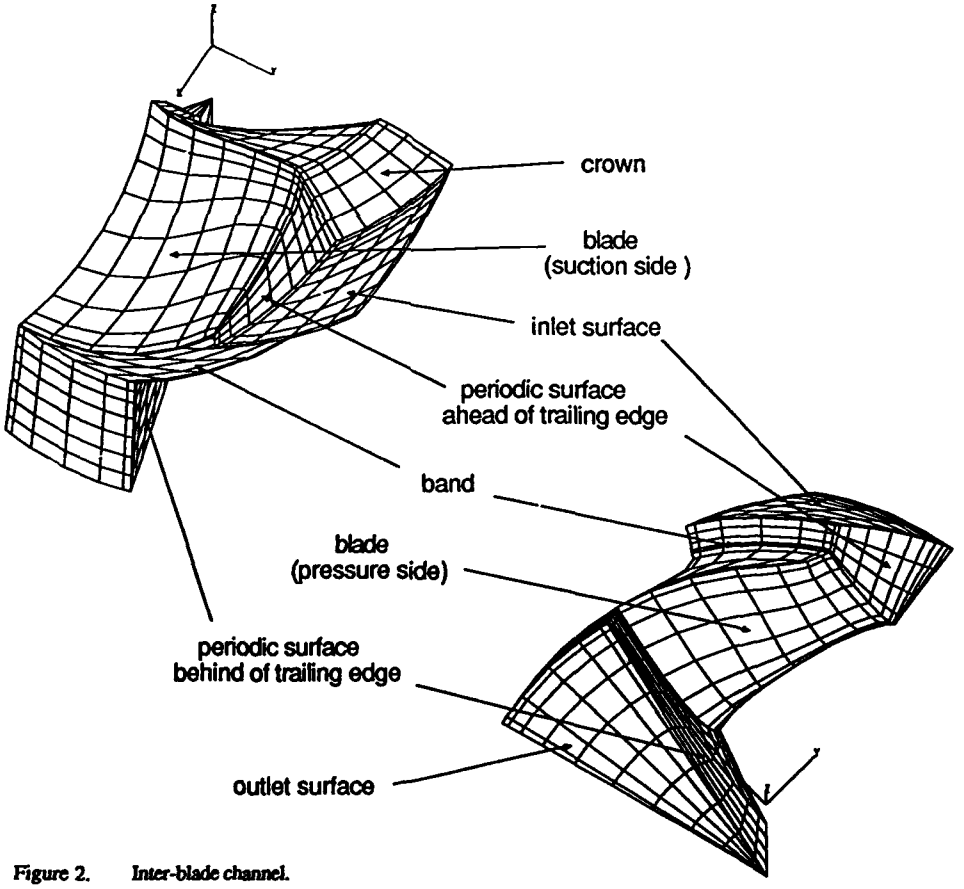


Figure 2. Inter-blade channel.

Figure 3. Area of convergence.

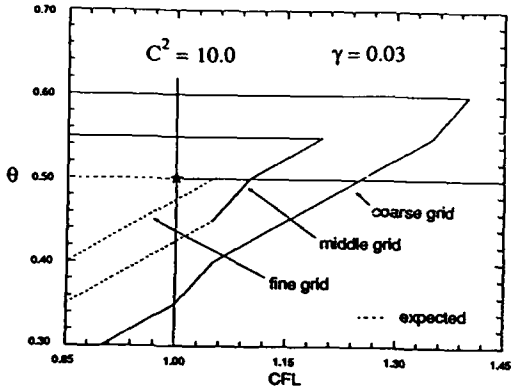


Figure 4. Meridional view of hydraulic channel with velocity profile at the entrance.

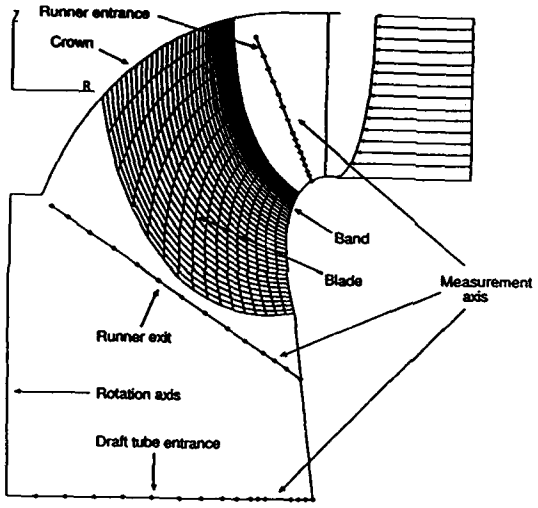
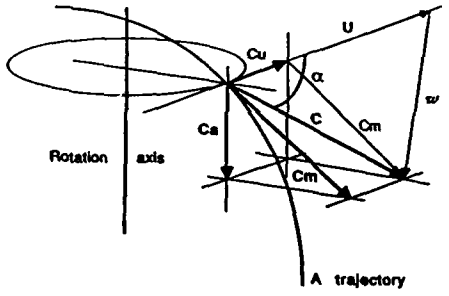


Figure 5. Velocity components.

C : absolute velocity norm
C_u : tangential velocity
C_m : meridional velocity
C_a : axial velocity
α : absolute flow angle
w : relative velocity
U : peripheral velocity



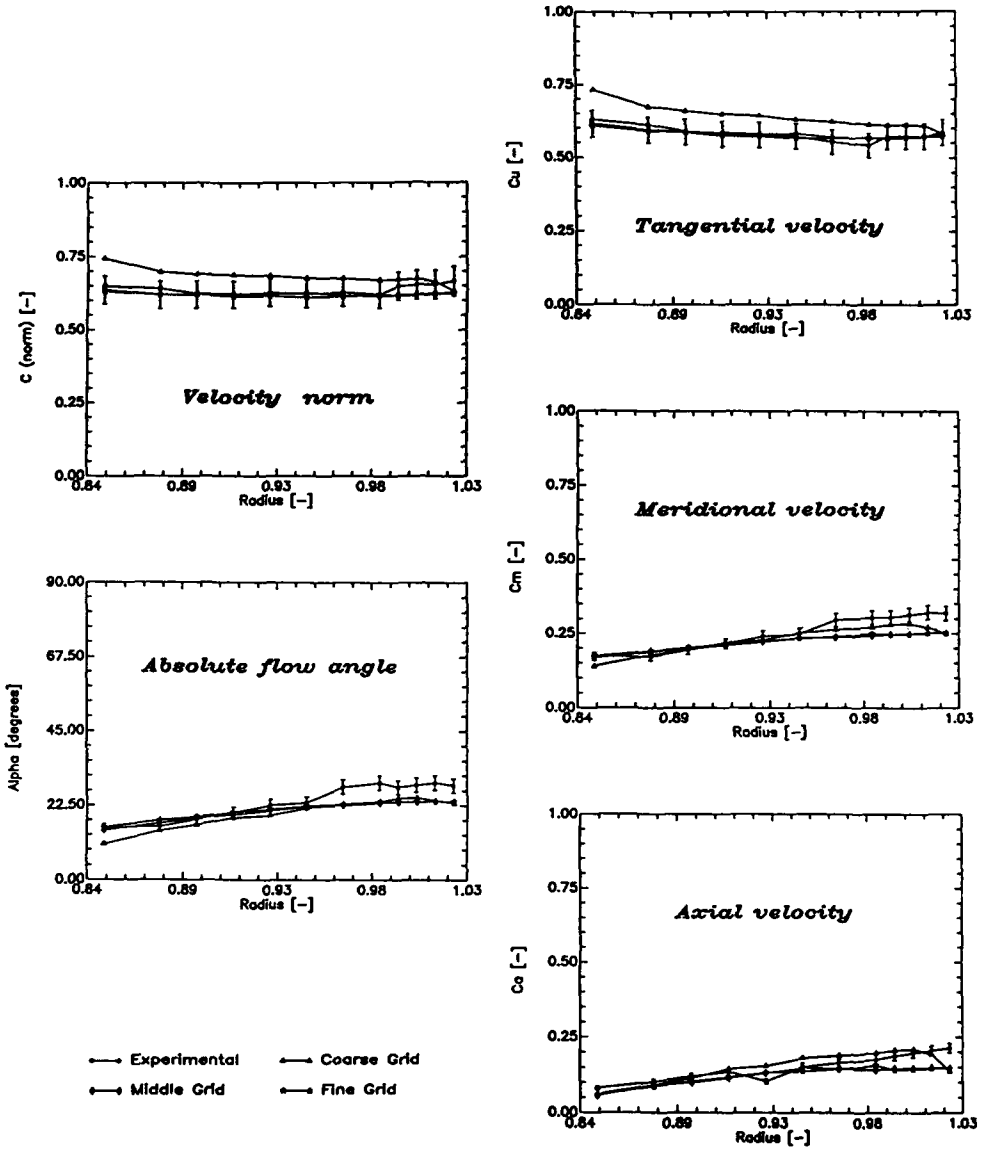


Figure 6. **Optimum flow rate (o.p. A); runner entrance.**

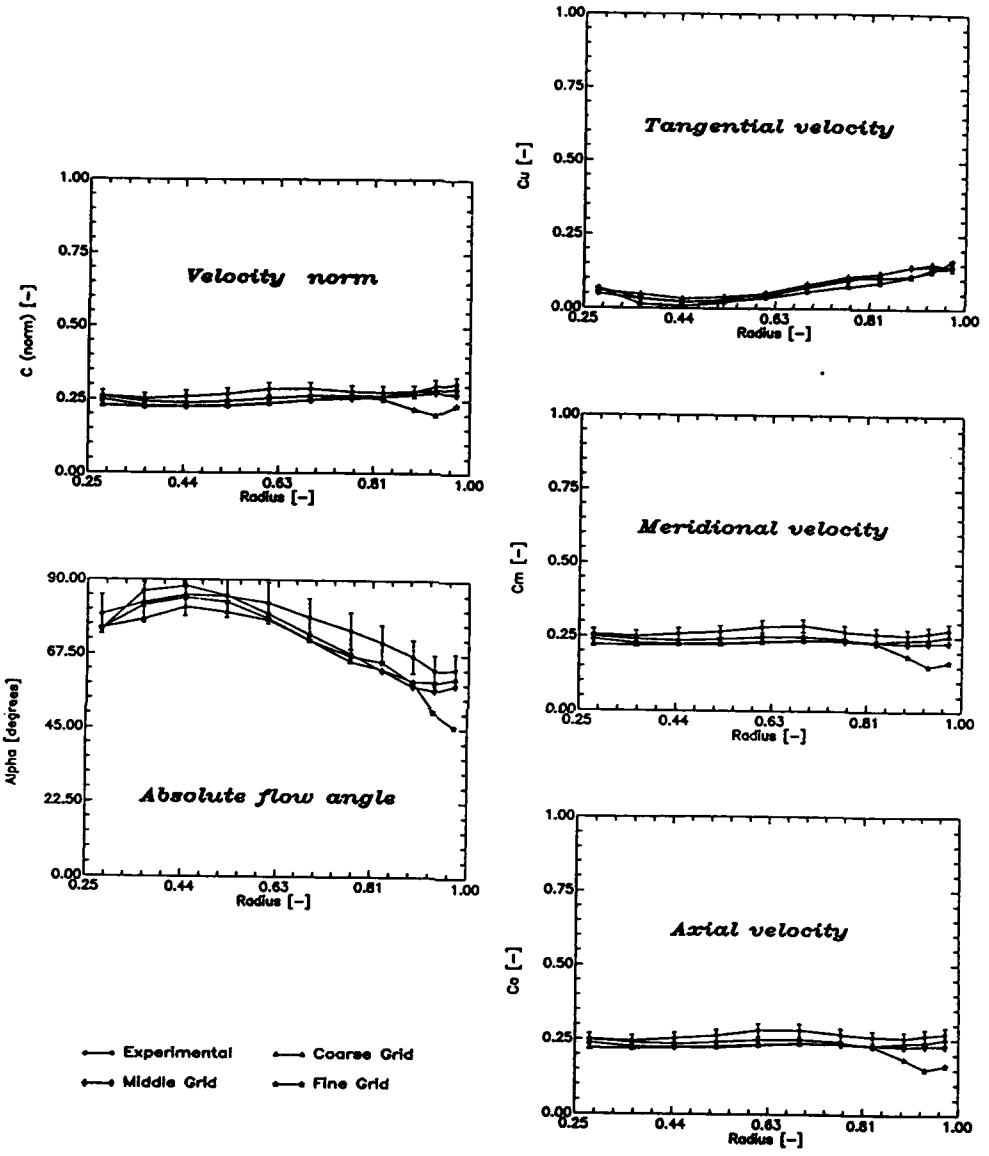


Figure 7. 6.61% below optimum flow rate (o.p. B); runner exit.

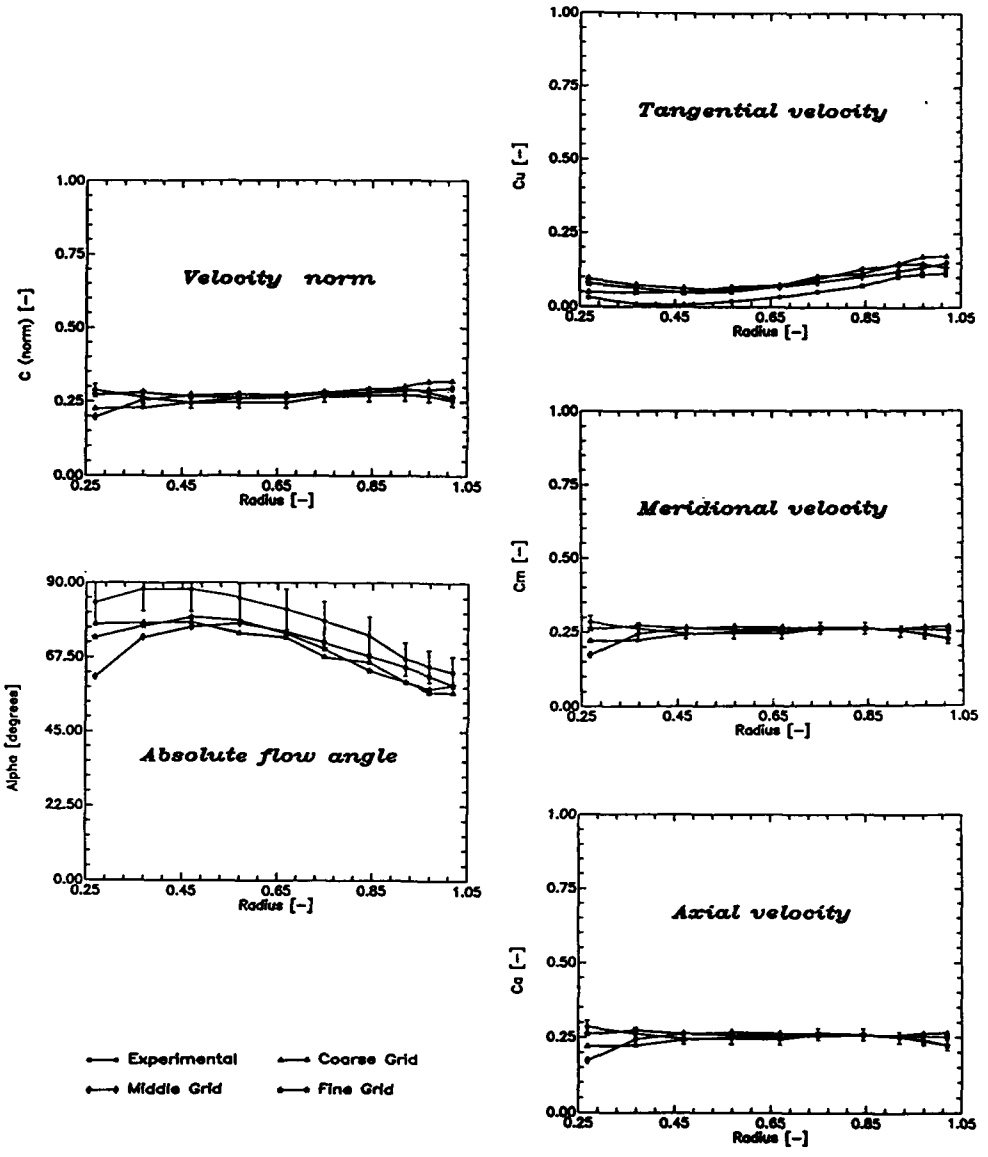


Figure 8. 8.51% above optimum flow rate (o.p. C); draft tube entrance.

COMPUTATIONAL TECHNIQUES AND VALIDATION OF 3D VISCOUS/TURBULENT CODES FOR INTERNAL FLOWS

B. Lakshminarayana, K. R. Kirtley and M. Warfield
Aerospace Engineering Department and Applied Research Laboratory
The Pennsylvania State University
University Park, PA 16802, USA

Summary

The computational techniques and codes developed for the prediction of three-dimensional turbulent flows in internal configurations and rotor passages are described. Detailed calibration and validation of the flow fields in 90° curved ducts, cascades, end wall flows and turbomachinery rotors are presented. Interpretation and comments on accuracy, level of agreement with various turbulence models and limitations of the codes are described. The single pass space-marching code is found to be efficient for curved duct and two-dimensional cascade flows. Multipass space marching, time marching and zonal methods are found to be accurate for complex situations. The efficiency and accuracy of a zonal technique, with considerable saving in computational time, is demonstrated.

Nomenclature

a	pressure relaxation coefficient (eqn. 5)
C_x	axial chord length
C	chord length
$c_\mu, c_{\mu 1}, c_{\mu 2}$ $c_{\mu 3}, c_{\mu 4}$	turbulence transport coefficient in k-ε model
C_p	pressure coefficient $2(p-p_{ref})/U^2_{ref}$
C_f	skin friction coefficient
D	duct width, diameter
$E,F,G,q,S,$ B,S_m	vectors in (eqn. 1)
$2h$	blade height
k	turbulence kinetic energy
p	static pressure
P	production of turbulence energy
Q	total velocity (relative velocity for a rotor)
R,R'	residuals
Re	Reynolds number
R_c	radius of curvature of duct
r	radius
S,N,R	streamwise, normal and binormal directions, normalized by blade chord for S,N, normalized by tip radius for R
S	cascade blade space/streamwise distance from leading edge
T,T'	mean and fluctuating temperature
$u,v,w,$	velocity in x,y,z directions (for curved duct see Fig. 2, for S duct see Fig. 3; For the definition of velocity components, u is the streamwise and v is the cross-flow velocity)
u_B	bulk velocity
U_s, U_n, U_R	relative velocity in S,N,R system for cascade endwall and rotor flows (U_s is the streamwise velocity, U_n is the velocity in blade-to-blade direction, U_R is the radial velocity)
u^*	friction velocity $\sqrt{\tau_{wall}/\rho}$
$\overline{u_i' u_j'}$	turbulent stresses
x,y,z	coordinate system (x is usually the streamwise direction, y is normal to the curved wall or cascade blade surface, z is the spanwise direction (see Figs. 2 and 3)
y_c	distance from wake center line
ξ,η,ζ	body fitted coordinate system (η is the boundary layer coordinate for cascade)
ε	turbulence dissipation
$\varepsilon_1, \varepsilon_2$	ellipticity parameters
β	pseudocompressibility parameter (eqn. 4)
δ	pressure relaxation parameter (eqn. 2)
ν, ν_t	kinematic, eddy viscosity
Ω	rotation rate
λ	stagger angle
ϕ	flow coefficient (axial velocity/blade tip speed)
ρ	density

Subscripts

1	inlet, first grid point
t,h	tip, hub
ref	reference; inlet velocity
e	edge velocity
ss, ps	suction, pressure surface

1. INTRODUCTION

Internal flows, such as the flow through straight and curved ducts, cascades, diffusors, nozzles, combustion chambers, turbomachinery stators and rotors are among the most complex flows encountered in practice. They are almost invariably three-dimensional and turbulent and are very frequently unsteady. In many instances (e.g., turbomachinery cascade and rotor), boundary conditions which are difficult to enforce are encountered. In addition, complex strain is encountered due to three-dimensionality, curvature and rotation effects. The governing equations are elliptic, parabolic, or hyperbolic depending on the flow variables and regions under consideration. It is not unusual to have regions where all three equation types are valid in the same passage. The system of equations governing this flow requires expensive iterative solution procedures which may become prohibitively expensive for application to full turbomachinery blade rows or coupled systems consisting of ducts, rotors, stators, etc.

Substantial progress has been made in resolving viscous internal flow through simple configurations or approximate flow in complex configurations. References 1 and 2 provide good reviews on these techniques. The next decade will see a major thrust in the development of efficient and accurate solution of multi-row turbomachinery (e.g., multistage) with three-dimensional turbulent flow and heat transfer.

The two levels of code verification are code calibration and code validation. Code calibration is carried out with some of the simplest flows and geometry for which exact analytical solutions or benchmark quality data are available. Examples of candidates for calibration are the laminar flow in a duct, cavity, or flow over a flat plate. This will enable decoupling of errors associated with the technique and the code from the inaccuracy of turbulence models, grids, etc. The next step is the calibration for turbulence models, grids etc., where well-documented turbulence data (e.g., turbulent flow on a flat plate with and without pressure gradient) is compared with the computation.

The code developer is now ready for the next level of check; namely, validation. This is carried out in more complex configurations that are representative of practical geometries. Examples of these are the flow through cascades of blades, curved ducts (convex and concave, S duct, etc.), transonic flows over an airfoil, wing body combinations, etc., for which accurate sets of data are available. The last stage is the prediction. This may include such state-of-the-art configurations as rotors (helicopter and turbomachinery), aircraft or components.

As described earlier, the major objective of this research is to develop original, efficient and accurate computational techniques and, most importantly, to calibrate and validate these codes as well as provide predictions for complex flows.

A need exists for efficient solution of the incompressible Navier-Stokes equations. Large classes of industrial, aerospace, marine and land flow devices have incompressible or nearly incompressible flow. The present effort has concentrated mainly on the computation of incompressible, turbulent and three-dimensional flows in internal flow passages, including turbomachinery.

2. GOVERNING EQUATIONS AND TURBULENCE MODELS

The governing equations for incompressible and rotating flows written in a vector form are

$$S_m \frac{\partial q}{\partial t} + \frac{\partial E}{\partial x} + \frac{\partial F}{\partial y} + \frac{\partial G}{\partial z} - \frac{1}{Re}(\nabla^2 q) = S$$

$$q = \begin{bmatrix} 0 \\ u \\ v \\ w \end{bmatrix}, \quad E = \begin{bmatrix} u \\ u^2 + p \\ uv \\ uw \end{bmatrix}, \quad F = \begin{bmatrix} v \\ uv \\ v^2 + p \\ vw \end{bmatrix}, \quad G = \begin{bmatrix} w \\ uw \\ vw \\ w^2 + p \end{bmatrix}$$

$$S = \begin{bmatrix} 0 \\ B_1 \\ B_2 \\ B_3 \end{bmatrix}, \quad B_i = [-2\varepsilon_{ijk}\Omega_j\Omega_k - \Omega_m x_m \Omega_i + \Omega_n \Omega_n x_i - \partial \overline{u_i' u_j'}/\partial x_j] \tag{1}$$

S_m = diag (0,1,1,1)
where u,v,w are velocities in the x,y,z directions, respectively (x being the dominant flow direction), i = 1, 2, and 3 represent x,y,z momentum equations, j,k,m,n are dummy indices. The Einstein summation convention is utilized. Coriolis force, centrifugal force and turbulence stresses are included in eqn. 1. For example, if the rotation is about the x axis ($\Omega_2 = \Omega_3 = 0$);

$$B_1 = 0 - \partial \overline{u_1' u_j'}/\partial x_j, \quad B_2 = \Omega^2 y + 2\Omega w - \partial \overline{u_2' u_j'}/\partial x_j, \quad B_3 = \Omega^2 z - 2\Omega v - \partial \overline{u_3' u_j'}/\partial x_j$$

If y (j=2) is the boundary layer coordinate, then j=2, i=1,2, and 3 are the only dominant shear stress and intensity terms in these equations.

Equation 1 is hyperbolic in time and can be solved using a time-marching algorithm. The Navier-Stokes equations can be simplified using realistic assumptions. For example, if the streamwise pressure gradient ($\partial p/\partial x$) and viscous diffusion (u_{xx}) terms are small, they may be neglected, and the resulting system is termed the parabolized Navier Stokes equations (PNS). If the u_{xx} is dropped and streamwise pressure gradient is treated elliptically, then the equations become the partially parabolized Navier-Stokes equations (PPNS). The simplified forms of the Navier Stokes equations are increasingly more efficient as terms are dropped; PNS requires more than one order of magnitude less computation time and less computer storage than the full Navier Stokes equations.

The techniques developed (or used) at Penn State can be generally classified as the single pass space-marching techniques, pseudocompressibility multipass space-marching technique, pseudocompressibility time-marching technique, and the zonal technique which is a combination of the first and the last techniques. As some of the boundary conditions and turbulence modeling are common for all these codes, they will be described first. Only the turbulent flow will be covered in this paper. In all the space-marching techniques, the steady flow is resolved neglecting time derivative in eqn. (1).

Turbulence Models

Internal flows cover a wide spectrum of geometry, starting from a simple duct to the complex three-dimensional rotor. It is neither desirable nor efficient to use the same model for all the flows. For example, in two-dimensional flows with a mild pressure gradient, both the algebraic eddy viscosity and the two equation model (k-ε) provide good predictions. In three-dimensional flows with curvature and rotation, it is necessary to resort to more complex and non-isotropic models such as Algebraic Reynolds Stress Models (ARSM). A review of various models available and their suitability to various situations is given in Ref. 3. All the lower and higher levels of turbulence models are incorporated in these codes. The Algebraic Eddy Viscosity Model (AEVM-BL) used by Baldwin and Lomax (4) is incorporated, as is the k-ε model used by Jones and Launder (5). In both these models the shear stress is represented by

$$-\overline{u_i' u_j'} = \nu_t \left(\frac{\partial u_i}{\partial x_j} + \frac{\partial u_j}{\partial x_i}\right) - \frac{2}{3}\delta_{ij} k$$

In the Algebraic Eddy Viscosity Model, ν_t is an empirical expression, while in the k-ε model it is related to the local k and ε given by $\nu_t = c_\mu k^2/\varepsilon$.

The Boussinesq assumption implies that the Reynolds stress tensor is aligned with the mean strain rate. Isotropic assumption implies that ν_t is independent of the direction. Here, a single value of ν_t is used to relate all the shear stresses. The Reynolds stress and Algebraic stress models rectify this deficiency and allow for more physics to be incorporated into the model. However, the solution of the full Reynolds stress equations are complex; hence the Algebraic Reynolds Stress Model (ARSM), becomes an efficient alternative. The ARSM equates the source terms in modelled Reynolds stress equations to the corresponding source terms in the turbulence kinetic energy equation (which implies that the ratio of the transport of Reynolds stress to the transport of turbulence kinetic energy is equal to $\frac{\overline{u_i' u_j'}}{k}$). This model was first proposed by Rodi (6) for stationary flows, but later extended by Galmes and Lakshminarayana (7) to rotating flows. Warfield and Lakshminarayana (8) manipulated these equations to derive values of c_μ which include the effect of three-dimensionality and rotation. Their equations are given by

$$-\overline{u'v'} = c_{\mu 1}\frac{k^2}{\varepsilon}\frac{\partial u}{\partial y}, \quad -\overline{u'w'} = c_{\mu 2}\frac{k^2}{\varepsilon}\frac{\partial u}{\partial z},$$

$$-\overline{v'w'} = c_{\mu 3}\frac{k^2}{\varepsilon}\frac{\partial v}{\partial z} + c_{\mu 4}\frac{k^2}{\varepsilon}\frac{\partial w}{\partial y}$$

$$\text{where } c_{\mu i} = f_i\left(\frac{P}{\varepsilon}, \frac{k\Omega_k}{\varepsilon}, \frac{\partial u_i/\partial x_j}{\Omega_k}, \frac{\partial u_i/\partial x_j}{\partial u_k/\partial x_m}\right), \; i = 1,2,3,4$$

Thus c_μ is a non-isotropic property dependent on the local flow field, rotation, production and dissipation; f_i is given in Ref. 8. Hence k-ε transport equations with a variable c_μ effectively incorporate many of the complex strain effects caused by the three-dimensionality and the rotation. In the calculation of vectorial c_μ in the current time or spatial step through the ARSM, the production terms are derived from the previous time or spatial step to avoid nonlinearity in the Algebraic turbulence stress equations.

Boundary Conditions

There are common elements in the boundary conditions employed in both the time-marching and space-marching techniques, but the implementation differs for internal flow problems. Four boundary conditions are considered.

(1) In surface boundaries, the velocities and the normal pressure gradient is zero. In many applications, especially a rotor, the grid resolution and thin boundary layers encountered make it

desirable to use a turbulent slip velocity. The slip velocity is based on the law of wall given by $\partial u/\partial y = u^*/\kappa y$, where u^* is the friction velocity, and κ is the Von Karman constant. In space marching, a two-point backward differencing is used for the pressure gradient condition in order to couple the odd-even points.

(2) Inlet conditions are generated from the available experimental data.

(3) Downstream boundary conditions differ depending on the technique used. For example, in single pass space marching, no downstream boundary condition is specified. In pseudocompressibility multipass techniques, only pressure is used as a boundary condition. In pseudocompressibility time marching, the pressure and velocity components were extrapolated while conserving the mass flow.

(4) In cascades and turbomachinery rotors, periodicity has to be enforced. In the time-marching code, the periodicity is enforced through the use of an implicit periodic matrix solver. In the pseudocompressibility space-marching technique, periodic conditions are applied to all variables in an explicit manner. Periodic nodes are treated as internal points, and averaging is used during the iterative matrix inversion process in the cross plane. Periodic conditions are applied to all variables, $u,v,w,p,k,\varepsilon,c_{\mu i}$, etc.

(5) In ducts with symmetrical inlet flow, the symmetry conditions have to be enforced. The gradients of pressure and streamwise velocity component in the transverse direction are set to zero. A two-point backward difference scheme is employed for these gradients both implicitly and explicitly.

In the case of the compressor rotor, the annulus wall was modelled as a moving wall (relative to the rotor) without the tip clearance, with the tangential velocity equal but opposite to the blade tip speed. The intention here is to capture the flow accurately away from the annulus walls on the blade surface, without resolving the tip.

Transformation of Equations and Grid Generation

For complex geometries, it is desirable to solve the governing equations on a generalized coordinate system. The following transformation is used to recast eqn. 1 in a body-fitted coordinate; $\xi = \xi(x,y,z)$, $\eta = \eta(x,y,z)$, $\zeta = \zeta(x,y,z)$.

The cartesian velocity components and the pressure are still dependent variables. However, the equation is now solved on a generalized coordinate system. The transformed equations in a rotating coordinate system are given in the Appendix of Ref. 9.

An algebraic grid generation technique is used since this technique is simple and efficient, especially for 3D configurations. The grid generation technique for a turbomachinery rotor will be briefly described, and those for curved ducts, s ducts and cascades are simple derivatives of the generalized case. The geometry of the blade passage, hub, annulus wall and blade profile is input to the cylindrical coordinate system (r,θ,z). First, a two-dimensional grid in the z-r plane is established giving cylindrical sheets of which two dimensional H grids in the blade to blade direction (θz plane) are established to follow the blade profiles through interpolation. Special care is taken to obtain a smooth grid which is periodic in θ. The H grid is well-suited for ducts, cascades, rotors or other configurations with sharp leading and trailing edges.

3. COMPUTATIONAL TECHNIQUES

As indicated earlier, it is inefficient to solve the full Navier Stokes equations, and inaccurate to solve only the parabolized equation for some turbomachinery and internal flows. Hence, there is a need to develop techniques to capture essential physics efficiently. With this objective in mind, the turbomachinery group at Penn State has developed several techniques and codes for prediction of internal flows. These techniques will be described briefly, and the reader is referred to quoted theses and papers for details. The main emphasis of this paper will be in validation, commenting on the accuracy of the grid, turbulence model, technique, and the effect of boundary conditions. The techniques and codes can be classified as follows.

(1) single pass space-marching technique (SPSALT)
(2) space-marching technique with a pressure solver (SALTPS)
(3) Multipass pseudocompressibility space-marching technique (MPSALT)
(4) pseudocompressibility time-marching technique (INS3DPSU)
(5) zonal technique (hybrid scheme incorporating techniques 1 and 4 (zonal 3D)

The abbreviations used for these codes are shown in parenthesis above. For example, SPSALT stands for single pass space-marching algorithm for laminar and turbulent flows, INS3DPSU is a code developed by Kwak et al. (10) at NASA Ames Research Center and modified (11) by Penn State University (PSU) to include a k-ε/ARSM turbulence model, convergence accelerators, and periodic boundary conditions for H grids.

In many internal flows of practical application (e.g. curved ducts, cascades, turbomachinery passages), a dominant flow direction can be identified and these flows can be predicted by marching along the dominant flow direction. In most subsonic flows, the streamwise pressure gradient is important, even though the streamwise diffusion term is small for thin unseparated shear layers. Many techniques have been developed to include the elliptic effects caused by these pressure gradients. No attempt will be made here to review the techniques developed by various investigations, as a detailed review can be found in Refs. 12 and 13. The problems of properly satisfying local continuity in the entire flow field through the iterations remain in the parabolic methods. A further drawback of some of these techniques is separation of the vector governing equation into individual scalar equations during the solution and use of an iterative scheme to couple the equations. In a flow field with strong secondary flow, the strong coupling between the pressure field and the transverse velocity field would slow the convergence. All the techniques and codes described in this paper solve these equations simultaneously; the methods differ in

the handling of pressure effects. These are described below. The time derivative terms of eqn. (1) are dropped in all the space marching techniques.

Govindan and Lakshminarayana (9) developed a space-marching technique to compute 3D viscous flow fields. The Navier-Stokes equations (eqn. 1) have been posed as an initial value problem by neglecting the streamwise diffusion term u_{xx} and treating the streamwise pressure gradient in E vector of eqn. 1 as a known source term. A non-iterative LBI scheme from Briley and McDonald (14) is used to solve the equations. Initially, the pressure is specified from an inviscid code. To conserve the global mass flow in computations, the mean streamwise pressure gradient is computed from the predicted velocity field and the corrected streamwise pressure gradient is computed for use at the next streamwise station. Since most of the results from this code are published (9, 15), these results will not be presented here. The reader is referred to Ref. 15 for accuracy of turbulence models (k-ε versus algebraic eddy viscosity), slip versus no-slip conditions, error due to grid resolution, etc.

Single Pass Space Marching Code (SPSALT)

The earlier technique (9) was developed for compressible flow, including the energy equation. The method was very sensitive to the specified pressure gradient, and difficulties were encountered at very low Mach numbers. This motivated the development of a new technique (16) specifically for incompressible flows. An eigenvalue analysis of eqn. 1 (two-dimensional form) for marching in the streamwise direction shows that two of the eigenvalues are imaginary. Such a situation precludes the use of single sweep space-marching method without uncoupling the pressure. Therefore the streamwise pressure was split into implicit and explicit parts, so that the vector E was split as follows:

$$E = E_{im} + E_{ex}$$

$$E_{imp} = \begin{bmatrix} u \\ u^2 - |\phi|\, p \\ uv \\ uw \end{bmatrix}, \qquad E_{exp} = \begin{bmatrix} 0 \\ |\phi|\, p + p \\ 0 \\ 0 \end{bmatrix} \tag{2}$$

Substitution of eqn. (2) in eqn. (1) makes the equation hyperbolic in space, (neglecting time derivative in eqn. (1)), enabling a streamwise integration. Reference 16 shows that ϕ should be small and negative; the introduction of $|\phi|$ changes the character of the equation from elliptic to hyperbolic. The numerical algorithm used is the same as that used earlier (9). This technique is very efficient and accurate provided the prescription of $\partial p/\partial x$ is accurate. In most situations in internal flows, cascades, and turbomachinery, the pressure distribution can be accurately specified (as it is mostly an inviscid phenomena) through the use of an efficient panel method code. Validation of this code was carried out for laminar and turbulent flows in a curved duct, cascade blade boundary layer and cascade end wall flows. Results from this code will be described later.

Space Marching Technique with a Pressure-Solver (SALTPS)

The SPSALT code was run without success in a multipass mode. Kirtley (13) has shown that the method is not stable in a multipass mode. If the prescribed or assumed pressure is not accurate, the calculated pressure may deviate considerably from the actual pressure. The elliptic effects are not captured, and the technique is therefore unstable. Hence, a Poisson solver for pressure was developed to capture the elliptic effects. For example, for two-dimensional flows, the pressure is given by

$$\nabla^2 p = 2\left[\frac{\partial u}{\partial x}\frac{\partial v}{\partial y} - \frac{\partial u}{\partial y}\frac{\partial v}{\partial x}\right] \tag{3}$$

This equation was solved using a standard line relaxation technique. No convergence accelerators were included. Details of this code are given in Ref. 17.

It should be emphasized here that even though a Poisson solver is used to correct the pressure, the technique solves all the equations (continuity and momentum) simultaneously and thus differs from the earlier parabolic marching techniques in which the equations are uncoupled and solved consecutively. The convergence, especially for flows with large pressure gradients, is likely to be slow in an uncoupled system. The transformed equations are marched in the ξ (streamwise) direction from the initial line using an assumed initial pressure field. For cascade flows, the inviscid pressure field was calculated from a panel code. After the domain was swept once, the computed velocity field was used in eqn. 3, which was iterated to convergence. This new pressure is then used again in eqn. 1 to update the velocity field. It was found that the change in the velocity field due to the updated pressure was very small. The velocity field was reasonably accurate after the first pass (from a prescribed accurate inviscid pressure), but the pressure had to be iterated to obtain accurate viscous corrections.

The SALTPS code was used mainly for two-dimensional viscous flow calculation. An attempt was made to develop a three-dimensional pressure solver, but the convergence was very slow; hence a new and more efficient technique described below was developed for 3D viscous flow. This is designated as a multipass space-marching technique which utilizes the pseudocompressibility technique and involves no separate pressure solver.

Multipass Space Marching Method (MPSALT)

In earlier parabolic-marching methods (Ref. 12), the continuity equation is satisfied only through an iterative process, and not directly. When the continuity and the momentum equations are solved in a coupled fashion, as in the methods described above, forward differencing of the streamwise pressure is sufficient to achieve a stable marching. Kirtley (13) has indicated that the pressure gradients cannot be

relaxed in order to achieve a stable multipass procedure without the use of auxiliary equations (e.g.,Poisson equation). Since the continuity equation is coupled to the momentum equation, some condition must be relaxed during computation in order to solve the complex flows. The only condition left to be relaxed in a practical way is the continuity equation. The method of pseudocompressibility developed by Chorin (18) is incorporated to yield a marching technique which is stable and convergent in a global iteration for complex geometries. Complete description of this technique is given in Ref. 13; a brief description follows.

Chorin's method, developed for incompressible flow, relaxes the continuity equation while keeping the equation coupled to the momentum equations. In this method, an artificial time derivative is added to the continuity equation as follows:

$$\frac{1}{\beta}\frac{\partial p}{\partial t} + \nabla \cdot \underline{V} = 0 \tag{4}$$

where $\underline{V}$ is the total velocity vector. This relaxes the continuity constraint during a time-marching integration of the Navier-Stokes equation. At convergence, the computed flow field is divergence-free and hence represents steady flow solution. Since it is a space-marching technique that is under consideration here, and no time derivatives are present, the continuity equation is written as

$$a(p^n - p^{n-1}) + \nabla \cdot \underline{V} = 0 \tag{5}$$

where n is a global iteration and a is analogous to $\frac{1}{\beta}\Delta t$ in Chorin's method.

Successive passes of the domain may be thought of as advancement in time. Substitution of eqn. 5 and eqn. 1 (with $S_m \neq 0$) results in the following changes in vectors E and F.

$$E = \begin{bmatrix} ap + u \\ u^2 + p \\ uv \\ uw \end{bmatrix}, \qquad S = \begin{bmatrix} a\,\partial_x p^n - p_i^n + p_i^{n-1} \\ B_1 \\ B_2 \\ B_3 \end{bmatrix} \tag{6}$$

Vectors q, F, G are the same as in eqn. 1. An eigenvalue analysis (13), as well as global stability analysis, has shown that forward marching with eqns. 1 and 4 is a stable solution technique and that the method will be convergent in a multipass mode.

Equation 1 with eqn. 5 was solved using the following iterative LBI scheme to reduce the effect of the splitting error in the computation. This error, unlike that for time marching methods, was multiplied by the streamwise change in the dependent vector Δq which does not tend to zero.

$$(L_\xi^\bullet + L_\eta^\bullet + L_\zeta^\bullet)(\Delta q^n - \Delta q^{n-1}) = R - (L_\xi^\bullet + L_\eta^\bullet + L_\zeta^\bullet)\Delta q^{n-1} = R'$$

L_ξ is the convection term in the marching direction (ξ) in the body-fitted coordinate system; L_η and L_ζ are the convection plus the diffusion terms in the transverse directions (η,ζ) in the body-fitted coordinate system. The following equations were solved.

$$(L_\xi^\bullet + L_\eta^\bullet)\,\Delta s^* = R'$$

$$(L_\xi^\bullet + L_\zeta^\bullet)\,\Delta s^n = L_\xi\,\Delta s^* \tag{7}$$

where $\Delta s^n = \Delta q^n - \Delta q^{n-1}$

The convergence is improved by including a relaxation parameter,

$$\Delta q^n = \Delta q^{n-1} + \omega \Delta s^n \tag{8}$$

Convergence of two orders of magnitude was generally achieved with $\omega = 0.8$. Once the convergence is achieved, the solution was advanced to the next streamwise station. Once the complete domain has been swept, the new pressure field was stored and used in the vectors for repeated passes of the domain. The global iterative procedure is terminated when the computed pressure no longer changed with iteration. The algorithm has been calibrated (13) for well-known laminar solutions, and the code is used to validate the turbulent data in an S duct, a curved 90° bend, cascade boundary blade layers and wakes, end wall flow and compressor rotor passage flow.

Pseudocompressibility Time Marching Code (INS3DPSU)

As mentioned earlier, this technique involves modifying the elliptic equations governing incompressible flows to hyperbolic equations by the introduction of time derivative in the continuity equation (eqn. 4). Substitution of eqn. 4 in eqn. 1 results in Chorin's formulation,

$q = (p/\beta, u, v, w)$, $S_m = \mathrm{diag}\,(1,0,0,0)$

$$S = \left(1/\beta\,\frac{\partial p^{n-1}}{\partial t}, B_1, B_2, B_3\right) \tag{9}$$

This introduces pressure waves of finite speed through the pseudocompressibility parameter β. Kwak et al. (10) utilized this technique and developed a code for three-dimensional viscous flow. Kwak et al. discussed the stability criteria for β, and suggested lower and upper bounds for β. The code, designated INS3D by Kwak et al. (10), has been modified by the Penn State group to include the periodic boundary conditions for H-grids and convergence acceleration via variable time step determined from a local CFLcondition. Their equations and code were modified to include vector S (rotation effects) and the turbulence modelling in eqn. 1. These modifications are described in Ref. 19. The code was utilized to predict the flow field in cascade blades, end walls and, most importantly, a compressor rotor. The solution technique used by Kwak et al. for the numerical integration of eqn. (1) is standard Euler implicit approximate factorization scheme, which reduces the three-dimensional equations to a form amenable to solution by block tridiagonal inversion methods. Both explicit and implicit smoothing were utilized to facilitate stability and convergence of the solution. The code has been validated against data available for internal flows.

Zonal Technique (ZONAL3D)

Complete solution of the full Navier-Stokes equation in all regions of flow is inefficient, expensive, and often unnecessary. For example, high Reynolds number viscous flows require resolution of thin viscous layers and an inviscid core. This situation often requires a large number of grid points in the viscous layer, which may not be possible with a Navier-Stokes method, due to storage and run-time limitations. Parabolized equations applied to the viscous layers, and Euler equations applied to the inviscid core, may result in a substantial decrease in computational time and storage. Even though the Navier-Stokes equations are universally valid, reduced forms are more appropriate and efficient in some regions. For example, many duct flows are parabolic or weakly elliptic, and downstream boundary conditions are difficult to apply. Many complex flows contain regions with natural elliptic and parabolic character. Flow over an aircraft, flow through a turbomachinery blade row and wakes are examples of such flows. Consider a turbomachinery blade row with an upstream annulus and downstream annulus. The parabolic solutions are appropriate upstream (say 1/3 to 1 chord) and downstream (including wake). The passage inside contains an inviscid region where the complete Euler equation is needed, and thin layers can be handled through parabolic or space-marching methods. This has motivated development of a zonal equation method. Warfield (19) has provided a critical review of these techniques. A schematic of the zonal technique developed (11) is shown in Fig. 1. The zonal equation method described in this paper involves solving the full Navier-Stokes equation in the elliptic zone using the INS3DPSU code described earlier, and the parabolized Navier-Stokes equation using SPSALT in the parabolic zone, with a buffer zone where ellipticity due to u_{xx} and p_x is changing from nearly zero to O(1) as an interactive boundary. The technique development and validation is described in Refs. 11 and 19 and the application is explained in this paper.

The quantification of ellipticity defined through parameters ε_1 and ε_2, is achieved before implementation of the zonal technique. For example, the ellipticity for a duct flow can be characterized as follows:

$$\varepsilon_1 = \frac{\partial p/\partial y \; u_{xx}^2}{\partial p/\partial x \; u_{yy}^2} \quad , \quad \varepsilon_2 = \frac{\partial p/\partial z \; u_{xx}^2}{\partial p/\partial x \; u_{zz}^2}$$

ε_1 and ε_2 go to zero in a purely parabolic flow, since $\partial p/\partial y \approx \partial p/\partial z \approx u_{xx} \approx 0$ for fully developed flow and u_{yy}, u_{zz}, and $\partial p/\partial x$ (which drives the flow) are non-zero. For more complex situations, such as those dominated by inviscid flow, one may need different characterization. Here ε_1 characterizes the ellipticity in the x direction, and ε_2 represents ellipticity in the z direction, y direction being the boundary layer coordinate.

The method first partially convergences the elliptic system (approximate 10% computation time) as shown in Fig. 1 is to derive an initial assumed pressure field for a single pass space-marching technique and to establish the elliptic and parabolic zones. The parameters ε_1 and ε_2 are used to establish boundaries. Since the single pass technique is sensitive to the assumed pressure field, it is very important to transmit the pressure information from the elliptic zone to the parabolic zone via a buffer zone. The pressure field is continually updated in the buffer zone and, if necessary, the parabolic zone is swept again (it then becomes a multipass) as shown in Fig. 1. The zonal 3D code was calibrated for a post and a bump in a duct; this is described in Refs. 11 and 19. Validation with the experimental data in a compressor rotor is described in the next section.

4. CALIBRATION OF CFD CODES

The most important step in developing a good code is the calibration of the results against a known exact solution or very accurate data in simple configurations with laminar or turbulent flow. Simple configurations are essential to discover the errors associated with grid and boundary conditions, and laminar flow is essential to avoid problems with the turbulence model. It is also important to test complex turbulence models against well-documented classical turbulence data such as those for a flat plate boundary layer. A list of codes used in this paper, as well as the calibration configuration/data/analysis used, is shown in Table 1.

5. VALIDATION OF CFD CODES

Six different configurations and eight sets of data have been chosen for validating the computer code/techniques described in this paper. These are listed in Table 2, including both the experimental and computational details. Several of these experiments were specifically designed to provide very accurate data for CFD validation. Among these are the data in 90° duct, S duct, and the cascade blade boundary layer. It is prohibitively expensive to run all codes for all configurations, hence only selective runs are made to check the ability of these codes to predict complex flows, accuracy of turbulence models, and accuracy of near-wall flow prediction.

Table 1

Data and Configurations Used for Code Calibration

Code	Square Straight Duct (Laminar) Ref. 20	90° Curved Duct (Laminar) Ref. 21	'S' Duct (Laminar) Ref. 22	Flat Plate (Turbulent) for Turbulence model Ref. 20	Cylinder Re = 40 Exact Numerical solution (Mehta - unpublished)	Post/Bump in a channel (Accurate NS Solution from INS3D	Backward Facing Step (Laminar & Turbulent) Refs. 23-24
Single pass Space Marching Code (SPSALT) (16)	X	X		X			X
Single pass Space Marching Code with Pressure Solver (SALTPS) (17)	X	X		X			X
Multipass Space Marching Code (MPSALT) (13)	X	X	X	X			
Pseudocompressibility Time Marching Code (INS3D) (10)	X				X INS3D		
Zonal Technique* (Zonal 3D) (19, 11)						X	

*Component codes have been validated for most cases.

Table 2

Validation Experiments (All Turbulent Flows)

	DATA				COMPUTATION					
Configuration & Reference	Geometry	Reynolds Number	Data Available	Accuracy	Code & Reference	Sweeps or Iteration	Turbulence Model	Grid x,y,z	Slip/ No Slip	Comp. Time IBM 3090
90° curved duct (21)	constant area; R_c/D = 2.3	Re_D=40,000	u,v,w	Good to Excellent	SPSALT(16)	1	AEVM-BL	180x41x47	No Slip	NA
S Duct (22)	Fig. 3	Re_D=40,000	u,v,w	Good to Excellent	MPSALT(13) a=30	80	AEVM-BL	47x25x21	No Slip	3332 secs.
Cascade Blade (25)	NACA65.410 α=10° λ=45° s/c=0.85	Re=310,000	u,p,p_o	Good to Fair	SPSALT(16)	1	AEVM-BL	139x49	Slip velocity	13 secs. (IBM 3081)
Boundary Layer (26)	DCA,β_1=55° λ=20.5°, s/c=0.46	500,000	$u,\overline{u'^2},\overline{v'^2}$	Good to Excellent	SALTPS(17)	300	AEVM-BL $k\varepsilon$	139x49	No Slip	122 secs. (IBM 3081)
Cascade wake (27)	DCA λ=20.77° s/c=0.6	588,000	$u,\overline{u'^2},\overline{v'^2}$	Good	MPSALT(13) (a=10)	30	AEVM-BL $k\varepsilon$	55x29x11	NAP	1055 secs.
					INS3D (19)	120	AEVM	55x29x11	NAP	400 secs.
Cascade	NACA65-12A_{10}^{10}	389,000	u,v,w,p_o,	Good	SPSALT(16)	1	AEVM-BL	50x21x21	No Slip	235 secs. (IBM 3081)
End Wall			p		INS3D(19)	120	AEVM-BL	50x21x21	No Slip	2772 secs. (IBM 3081)
Flow (28)					MPSALT(13)	50	AEVM/$k\varepsilon$	30x23x23	No Slip	1547 secs.
Compressor Rotor Design (29, 30)	r_h/r_t=0.5 r_t=.46m λ=22.5° to 45°	ϕ=0.56 R=400,000 (based on C,W_1) at midchord	$u,w,\overline{u'^2}$ $\overline{w'^2}$ p,p_o	Good	MPSALT(13)	100	AEVM	50x27x27	Slip	7100
Compressor Rotor Passage (Off-Design) (31, 32)	midradius C=13.45 cm S=10.4 cm λ=31.5°	ϕ=0.56 390,000	$u,w,\overline{u'^2}$ $\overline{w'^2},p,p_o$ (HW&LDV)	Good	INS3D(19)	200	ARSM/$k\varepsilon$	50x27x27	Slip for u,k,ε	1380 secs.
					Zonal 3D (19)	50 INS3D 1 Zonal	ARSM/$k\varepsilon$	50x27x27	No Slip for u and slip for $k\&\varepsilon$	432 secs.

NA - Not Available
NAP - Not applicable
*IBM 3090 and 3081 have different processors; 3090 is 2-3 times faster than 3081

90° Curved Duct (3D Flow)

The flow in a 90° turning duct is highly three dimensional, with substantial secondary flows due to the transverse pressure gradient. The algebraic eddy viscosity model was used in the SPSALT code to predict this flow (21). The assumed transverse pressure was approximated using a simplified radial equilibrium equation ($\partial p/\partial y = u^2/R$), and it was assumed to be constant in the streamwise (ξ) and spanwise (ζ) directions. The predictions are compared with the data at various locations in Fig. 2. A better agreement can probably be achieved through the use of a finer mesh. Secondary velocity predictions are good, especially near the surface. The overshoot in transverse velocity (v) profile for y/D = 0.1 is not predicted well; this is associated with the poor prediction of streamwise velocity profile. It is well-known in secondary flow theory that the transverse velocities (v) are caused by $\partial u/\partial z$ as well as by flow turning angle. Hence there is a close correlation between u and v velocity profiles. Any inaccuracy in u prediction will result in errors in v predictions. Nevertheless, this computation has revealed that the constant area curved duct flows can be efficiently handled by a single pass marching technique, which

requires over an order of magnitude less computation time than time marching or other iterative techniques.

Flow in an S-Shaped Duct (3D Flow)

The turbulent flow in an S-shaped duct was computed using the MPSALT code, as this case is characterized by strong transverse and streamwise pressure gradients. The results are compared with the data acquired by Taylor et al. (22); see Table 2 for details. The geometry is shown in Fig. 3. No assumed pressure was used as an initial condition and the inlet flow was determined using the SPSALT code in the straight inlet section. The Reynolds number (40,000) proved to be too low for successful application of the k-ε turbulence model, thus the algebraic eddy viscosity model (AEVM-BL) was used. Nearly two orders of magnitude reduction in pressure residuals were achieved after 80 global iterations.

At the initial measurement location, the computed streamwise velocity profiles compared very well with the experimental data (Ref. 13). Thus the inlet conditions, so important for space-marching methods, are accurately captured. At station 2, the computed streamwise flow does not compare well to the experimental data near the center of the duct (Fig. 4). Inspection of the profiles leads one to believe that there may be some computed mass surplus; however, the profiles very near the side walls were not measured and a conclusion can not be drawn. The computed mass flow did remain constant at convergence. The secondary flow at station 2 is predicted well (Fig. 4). The inviscid secondary flow is slightly overpredicted, yet the maximum flow turning in the end-wall viscous region is well-predicted. At station 4 (second bend of the duct), the computed streamwise and transverse velocity profiles compare well with the data (13). The computed streamwise velocity protiles at station 5 show excellent agreement near the side walls and reasonable agreement near the center of the duct (Fig. 5). The computed secondary flow profiles compare well to the experimental data except near the side walls, especially at Y/D = 0.9. Here the measured transverse velocity has an s-shaped profile, and reversal of secondary flow has occurred (compare Figs. 4 and 5). Capturing the reversed secondary flow represents a very severe test case for any code. Due to lack of adequate data very near the wall, no comment can be made with regard to accuracy of prediction near the walls. The computed transverse pressure gradient is well-predicted everywhere, while the bulk pressure drop is not well-predicted (see Fig. 6). With excellent agreement with the data for the laminar case for this same geometry (Ref. 13), the less than excellent prediction of the turbulent flow implicates the turbulence model. The value of the near-wall velocity gradient is strongly dependent upon the turbulence model. Good predictions of the skin friction in two dimensions have been achieved by many users of the Baldwin and Lomax (4) algebraic model. Therefore, simple extension of the two-dimensional model to three dimensions without regard for the actual physics of a three-dimensional boundary layer may be the reason for the reduced accuracy.

Cascade Blade Boundary Layer (2D Flow)

In order to evaluate the ability of these codes to predict a cascade boundary layer which is two dimensional, but is subjected to large adverse pressure gradient on the suction side, the flow in Peterson's (25) cascade was computed (Table 2).

A slip velocity, as well as inviscid pressure from a panel code, is used in predicting the flow from a single pass space-marching code (SPSALT). The computed boundary layer profiles show excellent agreement with the data, except at 60 percent chord length (Fig. 7). It is thus evident that the major viscous effects, including the blade boundary layer, can be captured using an inviscid panel code and a single pass marching code. It is also clear that a simple algebraic eddy viscosity model is adequate for this flow.

Separated Cascade Flow (2D Flow)

Some benchmark data on separated cascade flow was acquired by Deutsch and Zierke (26) for double circular arc blades (DCA) in a cascade (Table 2). Mean and fluctuating components of velocity were measured at various locations on the pressure and suction side and in the wake, using a laser doppler velocimeter. The flow was found to detach near the 80% chord location from the leading edge, and mean backflow velocities were measured even in the near-wake region. Therefore, this flow configuration is a good test case for SALTPS. The FLARE approximation was used in the separated zone.

Figure 8 shows the computed velocity profile for turbulent flow using the AEVM. For both the pressure and suction sides, the no-slip condition was used on the cascade blades. Up to the 53.6% chord location, the algebraic model does a good job of predicting the mean velocity profile. However, when the boundary layer detaches, computed at the 92.5% chord location, the mixing length hypothesis upon which the model was based breaks down and the prediction is poor. After four stations with backflow velocities, the solution diverged, and so the computation was not carried out into the wake region. For all of the attached profiles, the inviscid core was well-predicted, and no problems were encountered either near the leading edge of the cascade blades or at the detachment point.

The two-equation k-ε turbulence model was implemented in hope that the inclusion of 'history effects' would improve the prediction in and around the backflow region. The velocity profiles computed using the k-ε model are also given in Fig. 8. In the backflow region, the k-ε model gave much better results than the algebraic model but are still not good. The predicted detachment point was found to be .885c as compared to the actual point of .8c. The extent of the backflow region is slightly over-predicted as is the magnitude of the backflow velocities.

The blade pressure distribution is shown in Fig. 9. The prediction on the pressure side is very good. However, on the suction side the prediction is rather poor near the trailing edge. One can see that the detachment point is computed much farther downstream than the actual point. The over-predicted backflow velocities have also contributed to a poor pressure prediction by causing a drop in pressure rather than a leveling off as measured. The upstream effect of the separation is substantial, and the ability of SALTPS code to capture this effect is evident from the plot.

The above computation required only one sweep of the flow field. The Poisson equation for the pressure required 300 iterations to converge.

The technique is computationally efficient, and is a valuable tool for engineering analysis and design in industry. The results also indicate that neither the AEVM nor kε model is entirely suitable for predicting separated flows. However, the accuracy of the two models is almost identical for unseparated two dimensional boundary layers subject to a pressure gradient.

Compressor Cascade Wake Flow (2D)

This represents a free shear layer and is a good test case for validation of turbulence models. The MPSALT and INS3D codes were used to compute wake flows measured by Hobbs (27) using a hot film probe for the near wake and a five-hole probe for the far wake (Table 2). The inviscid pressure computed from the panel method was used as the initial pressure field to compute both the boundary layer and the wake development using MPSALT code. A no-slip condition was used on the blade surfaces, and the slip condition was applied on the end wall in an effort to achieve two-dimensionality.

The flow was computed with both the algebraic eddy viscosity model and the k-ε turbulence model. Comparison of the computed boundary layer profiles (x/C_x = -0.029) at the trailing edge and the wake profiles with the experimental data is given in Fig. 10. The boundary layer at the trailing edge is in good agreement with the data. The computed velocity profiles do not compare well with the experimental data near the wake centerline. The far wake is only adequately predicted. The wake centerline position is below the measured position and the wake spreading is less than measured. The wake spreading is a strong function of the turbulence and the adhoc approximations made in the algebraic turbulence model may contribute to the poor prediction.

The wake velocity profiles computed with the k-ε model in MPSALT code are also shown in Fig. 10. Again the boundary layer profiles are reasonably well predicted; however, the near wake profiles show the same lack of agreement with the centerline data as the computation with the algebraic model. In the far wake, the advantages of the k-ε model are clear, with excellent agreement between computation and the measurements. The wake centerline position, as well as the wake spreading, is accurately predicted even though the near-wake predictions were not as accurate. This leads one to believe that the far wake solution is not strongly influenced by the near wake. Overall, the prediction using the k-ε model is superior to the prediction using the algebraic model for all regions of the flow.

The predictions from the INS3D code, using the AEVM-model, is shown compared with the corresponding predictions (with the same turbulence model) and data in Fig. 10. The accuracy of the boundary layer prediction is equally good in both, but the inviscid velocities on the suction side are captured more accurately with the time-marching code. The prediction of the wake is comparable to that from the MPSALT code and suffers from the same deficiencies mentioned earlier. The wake centerline velocity and wake trajectory are not properly captured from either code with the AEVM turbulence model.

Cascade End Wall Flow (3D Flow)

The techniques described earlier (SPSALT, INS3D, MPSALT) were used to compute the three-dimensional turbulent flow in the end wall of a cascade (28) (Table 2). The inviscid pressure from a panel code is used as the assumed pressure in the SPSALT code, while no such assumed pressure is required for MPSALT and INS3D codes.

The space-marching method was effective in predicting the streamwise velocity profiles at each station, but the prediction is particularly good near the suction side stations (Fig 11). On the other hand, the profile computed by the time-marching method represents a very thin blade boundary layer y/s = 0.11 which contributes to a poor prediction there. Unfortunately, there is no experimental data near the blade/end wall corners to evaluate predictions in this region. The time-marching method is more successful in predicting the end-wall velocity profiles near the pressure side. Here the space-marching method is somewhat deficient.

A plot of the secondary velocity profile indicates that the time-marching method (INS3D) predicts the underturning of the flow in the outer reaches of the end-wall boundary layer better than the space-marching method (Fig. 11). The space-marching method performs better very near the end wall where the overturning of the flow is qualitatively better predicted. However, the magnitude of the peak of the overturning is not captured, especially farther downstream. Again the predictions show that the space-marching method performed better near the suction side, while the time-marching method performed better near the pressure side.

The time-marching solution required approximately 12 times as much computational effort as the space-marching technique. The space-marching code requires 1.5 Mb of storage while the time-marching code requires 3.6 Mb.

With respect to prediction accuracy, both techniques had their strong points, and showed better predictions for different parts of the flow field. Overall, the space-marching method appeared to have an edge in predicting this viscous flow. However, it must be noted that the grid used was more suitable for the space-marching method than for the time-marching method. Such a grid could not be used for a blunt leading edge airfoil, which precludes the use of the space-marching method. For the space-marching method, as long as the flow field at the preceding streamwise station is regular, the eddy viscosity field will be smooth and regular and lead to a successful computation. During the iteration process of the time-marching method, the flow field may not be regular, which can lead to a spurious eddy viscosity field. This can be destabilizing and must be handled very carefully when algebraic models are used. This problem appears to be most acute in flow regions containing interacting boundary layers.

The subject of smoothing is important when comparing these two techniques. The space-marching method includes no smoothing terms, while the time-marching method utilizes both explicit and implicit smoothing in the computation of the flow. The concurrent effects of smoothing and pseudocompressiblity in computing a large Reynolds number turbulent flow with the considered time-marching method are not easily defined; more applications of the technique to such cases will further elucidate this matter.

MPSALT code has also been validated against this data, and the agreement with the data is found to be excellent (see Table 2 for computational efficiency) even though the computational time is the same as time marching, but an order of magnitude more than the SPSALT.

These results provide an interesting dilemma. The Navier-Stokes solution is not necessarily the most accurate one, as error due to numerical technique, artificial dissipation and smoothing may compensate for the increased accuracy of the equations. The space-marching method provides good predictions. One word of caution. In turbine cascades, where large flow separation (end wall) and horseshoe vortices are encountered, the SPSALT technique failed to capture the elliptic effects associated with these features. For incompressible flow through cascades, without any end-wall separation, SPSALT code provides excellent predictions.

Flow in a Compressor Rotor Passage

One of the most complex internal flows is the flow in turbomachinery rotor passages. It is three-dimensional, turbulent and is subject to the influence of rotation and curvature. This is a very severe test case for 3D viscous codes. Comprehensive data on pressure, velocity field, including the blade boundary layers from hub to tip, leading to the trailing edge is available for the Penn State low-speed compressor (Table 2). The rotor blade boundary layer was acquired with a miniature rotating 'x' configuration probe, and the inviscid and end-wall flow data was acquired with either a laser doppler velocimeter or a rotating three-sensor hot wire probe. Two sets of data are available.

(1) The blade boundary layer, end-wall flow field and inviscid flow field in the entire flow passage and the wake is reported in Refs. 29 and 30 for design condition. This flow was computed using the MPSALT code. Details of computation and experimental data are listed in Table 2.

(2) The blade boundary layers and inviscid flow field, end wall flow in the entire rotor passage at the peak pressure rise coefficient (ϕ = 0.50), where the boundary layer growth is substantial. details of this data can be found in Refs. 31 and 32. This flow was computed using INS3D and zonal 3D codes.

In both cases, the flow is incompressible. For the design case (ϕ = 0.56), the MPSALT code used inviscid inlet conditions at the leading edge, and the initial inviscid pressure was generated by stacking multiple two-dimensional solutions from the panel method. Turbulent slip conditions were used on all the blade surfaces. Detailed comparisons are given in Ref. 33 and will not be repeated here. The suction surface boundary layers are predicted well, except near the tip regions. It is important to remember that the tip clearance effect has not been included in the computation and the measured data at this location may indeed include the interaction of the leakage jet with the blade boundary layer. The predictions are not as good on the pressure side, as the boundary layers are very thin (1-4 mm) and both measurements and computation are subject to error.

At the peak pressure rise coefficient (ϕ = 0.50) the blade boundary layers are approximately twice as thick as those at ϕ = 0.56. Hence the data is more accurate and comprehensive. This case was computed using both the INS3DPSU code and the zonal 3D code. Both techniques used the same grid, the same turbulence model and the same computer so that proper comparisons can be made.

The zonal method for this application consisted of an elliptic zone extending from the leading edge to the 25% chord location. The parabolic zone continued from the 25% chord location to the trailing edge. Both zones extended from blade to blade and from hub to tip. The wake was not computed for this flow coefficient. Only one sweep of the zonal method was utilized; the combination of zones with the elliptic zone upstream and the parabolic zone downstream reduces the need for multiple zonal sweeps due to the inability of the parabolic solution to influence the upstream elliptic solution.

A critical difference between the zonal and the benchmark predictions exists for this case. The benchmark time-marching solution (INS3DPSU) utilized turbulent slip velocity conditions on the blade surfaces, whereas the space-marching zone solution (SPSALT) utilized the no-slip condition. Otherwise, boundary conditions are unchanged. The prediction of the streamwise velocity on the suction side of the rotor blade is shown in Fig. 12. In this case, the INS3D solution shows quite good agreement with the data, especially near the trailing edge of the blade, while the zonal solution shows better agreement near the leading edge. The zonal solution consistently predicts a thinner boundary layer than the benchmark solution for both suction and pressure surfaces. In this case, the boundary layer edge velocity predicted by the zonal solution matches the data.

Radial velocity predictions on the suction side are shown in Fig. 13. The correct qualitative trends are predicted in both solutions, but the zonal solution is clearly superior in most chordwise and radial locations. The no-slip treatment and the lack of smoothing in the parabolic zone of the zonal solution increases the quality of the zonal prediction of radial flows. The benchmark solution gives inadequate definition of the radial flow profiles, missing all steep gradient regions and consistently underpredicting the maximum radial velocities near the wall. The mid-span radial flow prediction in the zonal case is particularly good, with both peak values and streamwise trends accurately predicted.

It should be remarked here that we do not imply that the INS3DPSU code, which was used as a benchmark solution, is less accurate than the zonal code. If no-slip conditions are used in the INS3DPSU code, it should provide as accurate results as did the zonal 3D code. But the smoothing in the INS3DPSU code should affect the solution near the wall to a greater extent with no-slip boundaries, giving poor boundary layer predictions.

The composite velocity predictions are shown in Fig. 14 for R = 0.75. The overall features of the flow field have been predicted by both solutions, with the best predictions occurring near the trailing edge. The overshoot of the boundary layer edge velocity on the pressure side for the zonal solution is one distinct feature which is readily apparent in the composite velocity plots. The prediction of the composite velocity is a very important result of a Navier-Stokes solution as it verifies the coupling effects of the viscous and inviscid flow features in establishing the overall pressure and velocity field. Both solutions have shown this capability.

The success of the zonal method (69% reduction in computer time) for this case, in both efficiency gain and in solution quality, makes it promising as a method for application to other complex turbulent flows where space-marching methods cannot be applied over the entire flow.

6. CONCLUDING REMARKS

We have demonstrated, through systematic calibration and validation, that simple and efficient techniques can be developed to predict internal flows. It is not necessary to use the full Navier-Stokes code for all situations. For incompressible flows, the classical methods available (e.g., the panel method for lifting body, inviscid analysis for turbomachinery flows) can be coupled with the space-marching methods to resolve the viscous layers. In situations where both transverse and streamwise pressure gradients are present, it is necessary to employ more accurate methods of capturing the pressure field.

The MPSALT technique, which utilizes the pseudocompressibility concept, is found to be accurate and unconditionally stable for a multipass global iteration procedure. Further refinement will require finer grid, modelling, and acceleration schemes such a multigrid technique.

The zonal equation method, which is an efficient method for resolving viscous flows in rotors, single stage and multistage turbomachinery, has been developed, calibrated and validated. This technique combines the efficiency of the space-marching technique and the accuracy of time iterative methods. The 69% savings in time for zonal compressor rotor flow solution was particularly impressive, as the solution compared better to the data than did the time-marching benchmark solution. The application of these techniques to multistage turbomachinery is promising. But the zonal technique needs improvement in the area of the adaptive buffer zones, and it could possibly include analytical solutions in some regions. The efficiency of this code is coupled to those of the component codes. The interaction of the zonal equation method with possible zonal turbulence modelling application and solution adaptive and/or zonal grid generation would provide a long-term goal of developing efficient techniques for all internal flows, including multistage turbomachinery, combustion flows, etc.

It has been demonstrated that the algebraic eddy viscosity model is adequate for two-dimensional flows with moderate streamwise pressure gradients. The model was not successful for 2D wake flows. The spreading of the wake centerline trajectory and the wake centerline velocity are strong functions of the turbulence. Hence, it is not surprising that the wake flows need more physically realistic models. The area which needs the most attention is the development of more accurate transition and turbulence models as well as the application of existing transition and turbulence models to the unique problems of turbomachinery.

The area that needs immediate attention is benchmark-quality data in complex internal flows such as turbine end wall flows and rotor flows. These measurements are not only complex, but very expensive. It is doubtful whether the same accuracy as benchmark-quality data (ducts, airfoils, bends) can be achieved in a rotor. New measurement techniques for resolving the wall layers, end wall flows and corner flows are essential before one can confidently establish the accuracy of these codes. A comprehensive data set should include not only three components of mean velocity, temperature, but also turbulence quantities such as $\overline{u_i' u_j'}$, $\overline{u_i' T'}$ spectrum, wall shear stress and heat transfer. Similarly, accurate data on transition and separation on a three-dimensional configuration is lacking.

ACKNOWLEDGMENTS

The research work on computation was sponsored by David Taylor Naval Ship Research and Development Center with Dr. D. Fuhs as the technical monitor, and NASA Lewis Research Center with Dr. P. Sockol as the technical monitor. Numerous discussions with Drs. P. Sockol and D. Fuhs are gratefully acknowledged. Drs. T. R. Govindan, M. Pouagare, and J. Gorski were responsible for the development of SPSALT and the earlier codes, and their assistance is gratefully acknowledged.

REFERENCES

1. McNally W. D. and Sockol P., "Computational Methods For Internal Flows With Emphasis on Turbomachinery," J. Fluids Engineering, 1981.

2. AGARD LS 140, "3 D Computational Techniques Applied To Internal Flows in Propulsion Systems", 1985.

3. Lakshminarayana B., "Turbulence Modelling for Complex Shear Flows," AIAA J., 24, 12, 1986, p. 1900.

4. Baldwin, B. S. and Lomax, H., "Thin Layer Approximation and Algebraic Model for Separated Turbulent Flows," AIAA 78-257, 1978.

5. Jones, W. P. and Launder, B.E., "The Calculation of Low-Reynolds Number Phenomena with a Two-Equation Model of Turbulence," J. Heat and Mass Transfer, Vol. 16, 1973, pp 1119-1130.

6. Rodi, W., "A New Algebraic Relation for Calculating the Reynolds Stresses," ZAMM, Vol. 56, 1976, pp 219-221.

7. Galmes, J. M. and Lakshminarayana, B., "Turbulence Modeling for Three-Dimensional Shear Flows over Curved Rotating Bodies," AIAA J., Vol. 22, No. 10, 1984, pp. 1420-1428.

8. Warfield, M. J. and Lakshminarayana, B., "Computation of Rotating Flow with an Algebraic Reynolds Stress Model," AIAA J., Vol. 25, 1987, pp 957.

9. Govindan T. R. and Lakshminarayana B., "A Space Marching Method for the Computation of Viscous Internal Flows," Computer & Fluids, Vol. 16, No. 1, 1988, pp 21-39.

10. Kwak, D. et al., "A Three-Dimensional Incompressible Navier-Stokes Flow Solver Using Primitive Variables," AIAA J., Vol. 24, No. 3, 1986, pp 390-398.

11. Warfield, M. J. and Lakshminarayana, B., "Calculation of a Three-Dimensional Locally Elliptic Flow with a Zonal Equation Method," AIAA-87-1141-CP, Proceedings of 8th Computational Fluid Dynamics Conference, Honolulu, Hawaii, June 1987.

12. Rubin, S., "A Review of Marching Procedures for PNS Equations," First Symposium Num. and Physical Aspects of Aerodynamic Flows, Springer Verlag, Long Beach, CA, p. 171, 1980.

13. Kirtley, K. R., "A Coupled Parabolic Marching Method for the Prediction of Three Dimensional Viscous Incompressible Turbomachinery Flows," Ph.D. Thesis, Department of Aerospace Engineering, The Pennsylvania State University, 1987.

14. Briley, W. R. and McDonald, H., "On the Structure and Use of Linearized Block Implicit Scheme," J. Comp. Physics, Vol. 34, 1980, pp. 54-73.

15. Gorski, J. J. et al., "Computation of Three Dimensional Turbulent Shear Flow in Corners," AIAA J., Vol. 21, No. 5, 1985, p. 685.

16. Pouagare, M. P. and Lakshminarayana, B., "A Space Marching Method for Viscous Incompressible Internal Flows," J. Comp. Phys., Vol. 64, No. 2, June 1986.

17. Kirtley, K. R., "Computation of Internal Incompressible Separated Flow Using a Space Marching Technique," M.S. Thesis, Department of Aerospace Engineering, The Pennsylvania State University, 1985.

18. Chorin, A. J., "A Numerical Method for Solving Incompressible Viscous Flow Problems," J. Comp. Phys., Vol. 2, 1967, pp. 12-26.

19. Warfield, M., "A Zonal Equation Method for Three Dimensional Locally Elliptic Laminar and Turbulent Flows," Ph.D. Thesis, Department of Aerospace Engineering, The Pennsylvania State University, 1987.

20. White, F., Viscous Fluid Flow, McGraw Hill, New York, 1974.

21. Taylor, A. M. K. P. et al., "Measurements of Laminar and Turbulent Flow in a Curved Duct with Thin Inlet Boundary Layers," NASA CR-3367, 1981.

22. Taylor, A. M. K. P. et al. "Developing Flow in S-Shaped Ducts, I-Square Cross-Section Duct," NASA CR-3550, 1982.

23. Durst, F. et al., "Low Reynolds Number Flow Over A Plane Symmetric Sudden Expansion," J. Fluid Mech., Vol. 64, 1974, p. 111.

24. Armaly, B. F. et al. "Experimental and Theoretical Investigation of Backward Facing Step Flow," J. Fluid Mech., Vol. 127, 1983, pp. 473-496.

25. Peterson, C. R., "Boundary Layer on an Airfoil in A Cascade," M.I.T. Gas Turbine Laboratory, Rep. No. 49, December 1958.

26. Deutsch, S. and Zierke, W. C., "The Measurement of Boundary Layers on a Compressor Cascade Blade," Part 1: A Unique Experimental Facility, ASME Paper 87-GT-248; Part 2: Suction Surface Boundary Layers; ASME Paper 87-GT-249; Part 3: Pressure Surface Boundary Layer and Near Wake, ASME Paper 87-GT-250, 1987 (to be published in J. Turbomachinery, 1988).

27. Hobbs, D. E., Wagner, J. H., Dannenhoffer, J. F., and Dring, R. P., "Experimental Investigation of Compressor Cascade Wakes," ASME Paper 82-GT-299.

28. Flot, R. and Papailiou, K., "Couches Limites et Effets D'Estremities Dans les Turbomachines," METRAFLU, contract DR.M.E 73/373, 1975.

29. Pouagare, M. et al., "An Experimental Study of the Compressor Rotor Blade Boundary Layer," ASME J. Engr. for Power, Vol. 107, 1985, pp. 364-373.

30. Pouagare, M. P., "Numerical and Experimental Investigation of Turbomachinery Rotor Flow Fields," Ph.D. Thesis, Department of Aerospace Engineering, The Pennsylvania State University, 1984.

31. Popovski, P. and Lakshminarayana, B., "Laser Anemometer Measurements in a Compressor Rotor Flow Field at Off-Design Conditions," AIAA J., Vol. 24, No. 8, 1986, pp. 1337-1345.

32. Lakshminarayana, B. and Popovski, P., "Three-Dimensional Boundary Layer on a Compressor Rotor Blade at Peak Pressure Rise Coefficient," J. Turbomachinery, Vol. 109, No.1, 1987, pp. 91-98.

33. Kirtley, K. R. and Lakshminarayana, B., "Computation of Three Dimensional Turbulent Turbomachinery Flows Using Coupled Parabolic-Marching Method," to be presented at the ASME 33rd Gas Turbine Conference, 1988.

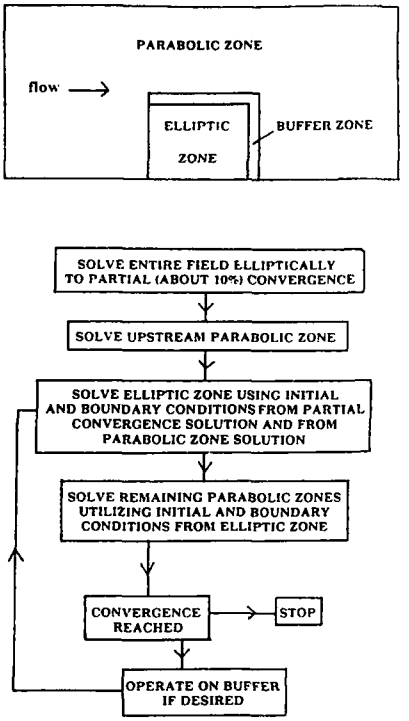


Fig. 1. The zonal equation method algorithm

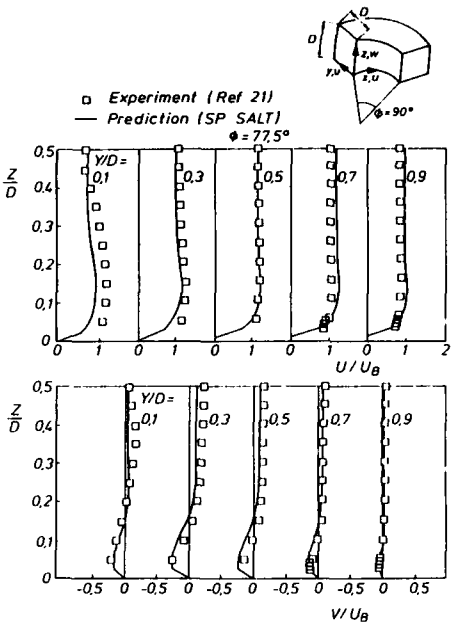


Fig. 2. Velocity profiles at ϕ = 77,5° for a 90° curved duct

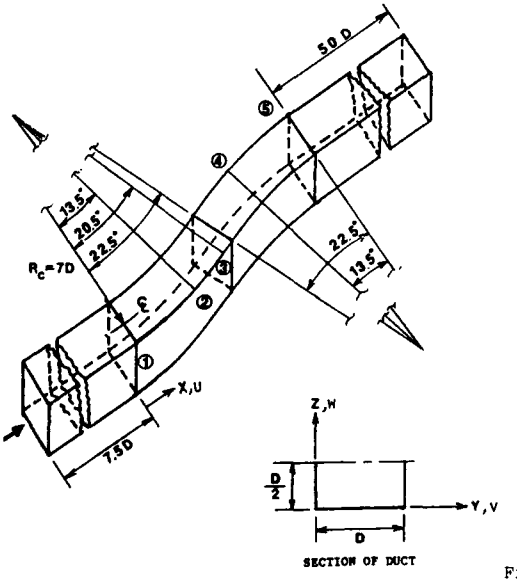


Fig. 3. Geometry of the S-shaped duct

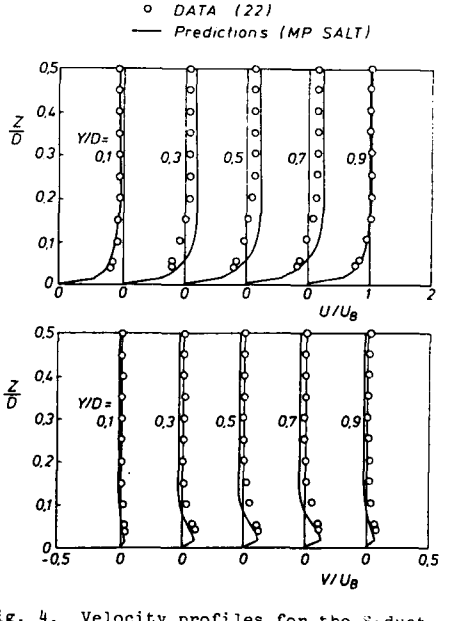


Fig. 4. Velocity profiles for the S-duct at Station 2 (see Fig. 3 for legend)

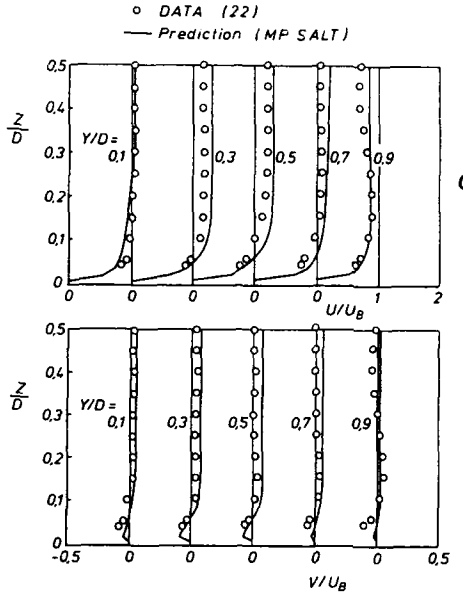


Fig. 5. Velocity profiles for the S-duct at Station 5 (see Fig. 3 for legend)

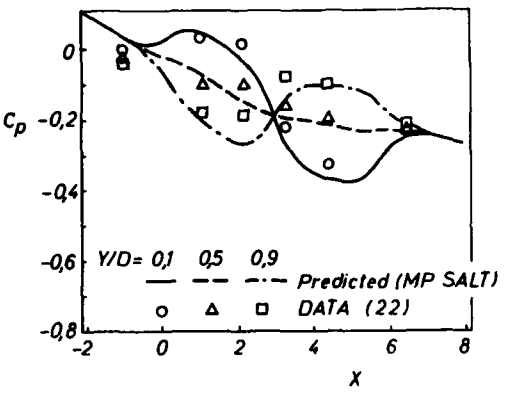


Fig. 6. Coefficient of pressure for the S-duct (see Fig. 3 for legend)

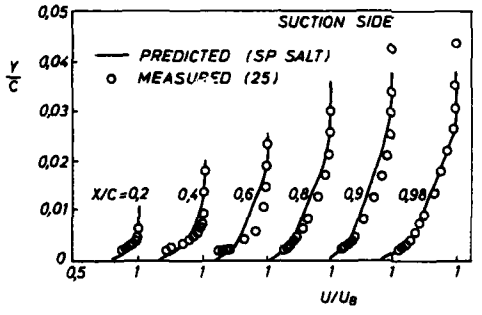


Fig. 7. Velocity profiles on suction side of Peterson's cascade

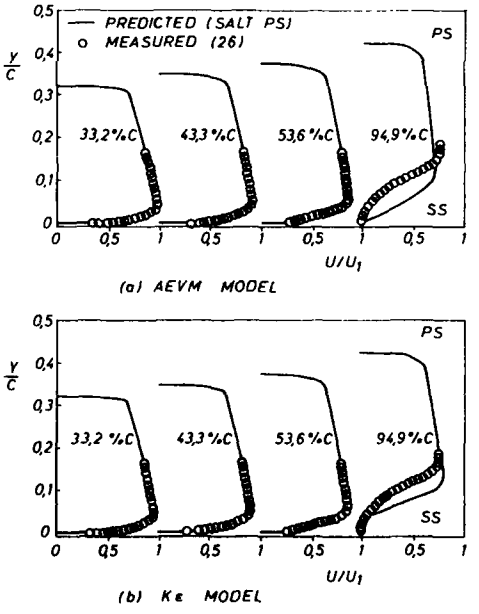


Fig. 8. Velocity profiles for DCA cascade Re = 500,000

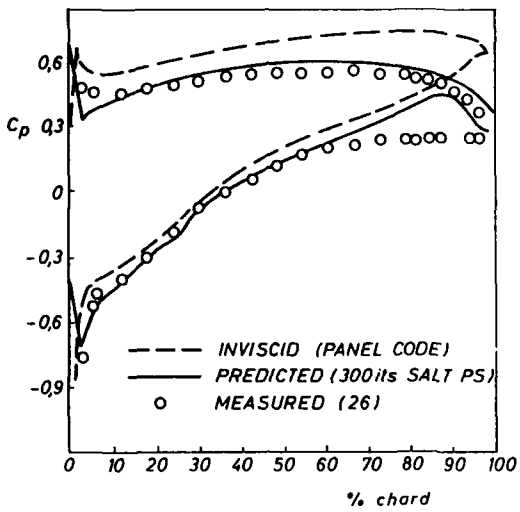


Fig. 9. Pressure distribution for DCA cascade

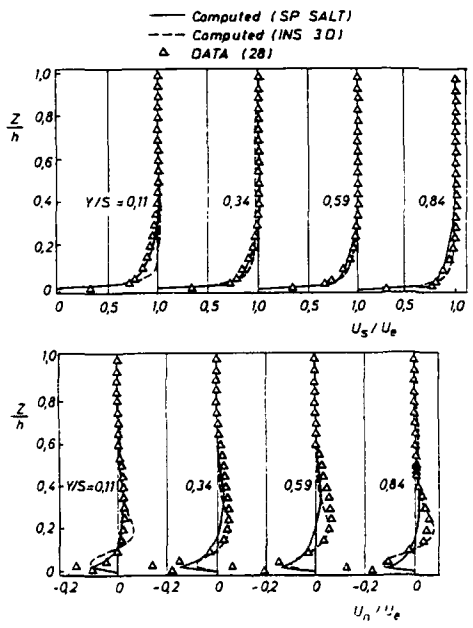


Fig. 11. End wall velocity profiles at 44% chord (y is the tangential distance from the suction surface)

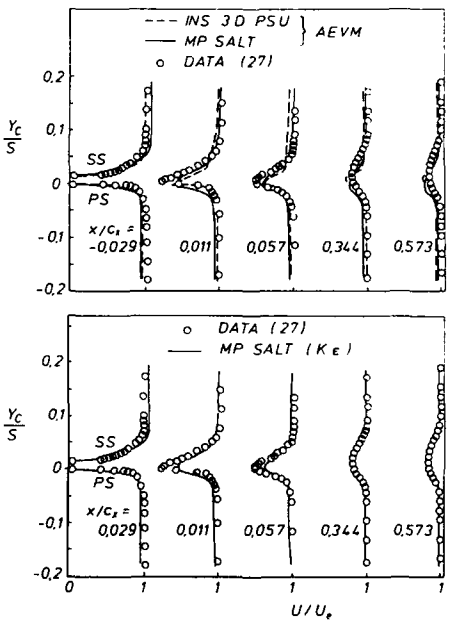


Fig. 10. Wake profiles for Hobbs cascade

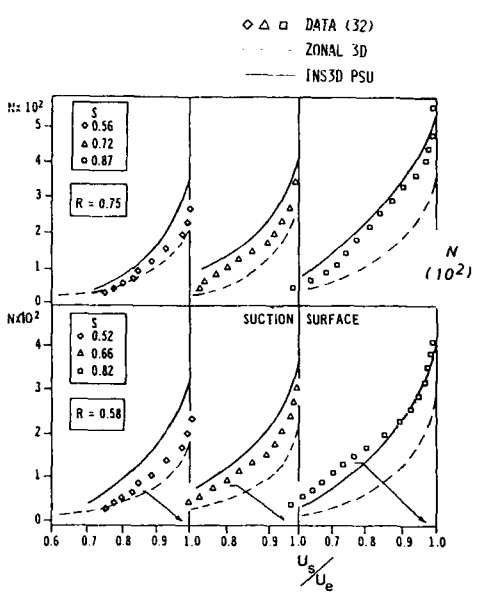


Fig. 12. Streamwise velocity profiles on suction surface of compressor rotor blade

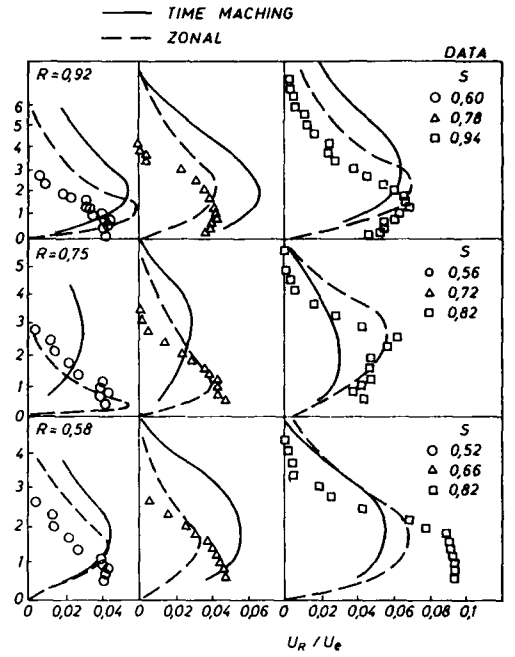


Fig. 13. Radial velocity profiles on suction surface of compressor rotor blade

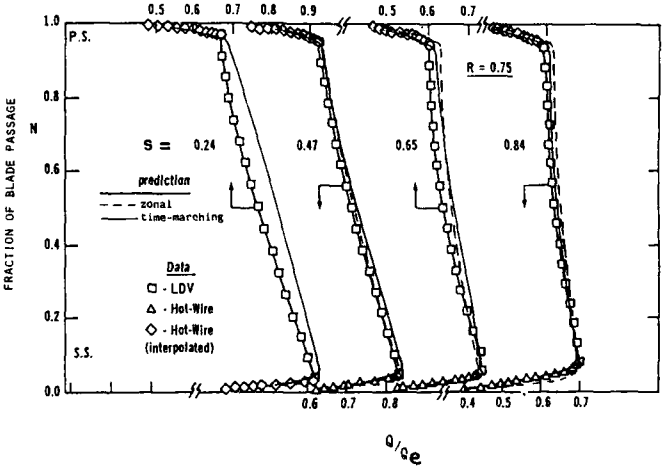


Fig. 14. Composite velocity profiles at R = 0.75 for a compressor rotor

VALIDATION A L'AIDE D'ESSAIS EN SOUFFLERIE DE CODES DE CALCUL DU CHAMP AERODYNAMIQUE DE ROTORS ET D'HELICES DANS DES CONDITIONS DE VOL VARIEES

par

C. Maresca, D. Favier, M. Nsi Mba et C. Barbi
Institut de Mécanique des Fluides, UM 34 CNRS
1, rue Honnorat, 13003 MARSEILLE (France)

RESUME

La validation de codes de calcul relatifs à l'aérodynamique de rotors d'hélicoptères et d'hélices a été effectuée pour différentes conditions de vol. La maquette de rotor d'hélicoptère a fait l'objet d'essais en vols stationnaire et d'avancement pour différents nombres de pales, pas généraux, vrillages de pales, formes d'extrémité... . La maquette d'hélice, quadripale, à vrillage non linéaire a été testée en régime de vol horizontal sur une gamme étendue de pas généraux et de paramètres d'avancement.

Les différents essais effectués, consistant en la mesure globale des charges aérodynamiques, et en la mesure locale du champ 3-D des vitesses induites, des trajectoires tourbillonnaires et des circulations le long des pales, ont permis de valider et d'améliorer les différents codes de calcul envisagés. Ceux-ci, basés sur un modèle de ligne portante simulant la pale, procèdent suivant une mise en équilibre du sillage, décomposé en un sillage proche et lointain. Les résultats numériques ont été confrontés aux valeurs expérimentales obtenues pour différents types de vols et différentes configurations de voilure.

NOTATIONS

A, B : coefficients de contraction des lignes tourbillonnaires marginales

a_o, a : conicité du rotor au point fixe et en vol d'avancement, deg.

b : nombre de pales ($b = 4$ pour l'hélice)

c : corde du profil d'une section de pale, m

C_b, t : cambrure locale et épaisseur des profils de pale d'hélice

C_L, C_D : coefficients de portance et de traînée des profils de pale

C_T : coefficient de traction du rotor : ($C_T = T/\rho\pi R^2 V_e^2$)

C_Q : coefficient de puissance du rotor : ($C_Q = P/\rho\pi R^2 V_e^3$)

C_{Zm} : coefficient de traction moyen du rotor : ($C_{Zm} = 6\, C_T/\sigma$)

D : diamètre du rotor ($D = 1.5$ m) ou de l'hélice ($D = 0.85$ m)

FM : Figure de mérite : ($FM = T^{3/2} / \Omega Q (2\pi\rho R^2)^{1/2}$)

K_1, K_2 : coefficients de translation des lignes tourbillonnaires marginales

n : fréquence de rotation des pales, t/s

$OXYZ$: système de coordonnées fixe défini sur la Figure 4

P : puissance du rotor ou de l'hélice, ($P = 2\pi nQ$), W

r : distance radiale comptée à partir de l'axe de rotation, m

R : rayon du rotor ou de l'hélice

T, Q : traction et couple du rotor ou de l'hélice, N et N.m

t : temps, s

U, V, W : composantes de la vitesse définies sur la Figure 4

V_∞, V_e : vitesse à l'infini et vitesse à l'extrémité des pales ($V_e = \Omega R$), m/s

Z_b, C_b : coefficients de traction et de puissance réduits du rotor, ($Z_b = 200 C_T/\sigma$; $C_b = 200\, C_Q/\sigma$)

α : basculement du rotor en vol d'avancement, deg.

α_o : pas général à $\xi = 0.7$ sur l'hélice, deg.

γ : paramètre de fonctionnement ($\gamma = V_\infty / nD$)

Γ : circulation sur la pale ou dans le sillage, m^2/s

ξ : rayon réduit ($\xi = r/R$)

λ , μ : paramètres d'avancement ; hélice ($\lambda = \gamma/\pi$) ; rotor ($\mu = V_\infty / V_e$)

θ_v : distribution du vrillage de pale, deg.

θ, $\theta_{.75}$: pas général du rotor à $\xi = 0.75$

ψ : azimut de la pale, deg.

ψ_b , ψ_s : périodicité azimutale, et azimut correspondant au sillage lointain, deg.

ν , ρ : viscosité cinématique et masse spécifique de l'air N/(m,s) et Kg/m^3

σ : solidité du rotor ($\sigma = bc/\pi R$)

τ, χ : coefficients de traction et de puissance de l'hélice ($\tau = T/\rho n^2 D^4$) ; ($\chi = P/\rho n^3 D^5$)

η : rendement de l'hélice : ($\eta = \gamma\tau/\chi$)

ω, Ω : vitesse angulaire : ($2\pi n$) , rad/s

ωt : phase, deg.

INDICES INFERIEURS

t, e : relatifs au tourbillon d'extrémité ou à l'extrémité de la pale

ni : relatif à la nappe interne

1. INTRODUCTION

L'élaboration de codes fiables, capables de prédire les performances des voilures tournantes en conditions de vol variées demeure actuellement un défi lancé aux aérodynamiciens.

Les méthodes de calcul couramment utilisées font appel au concept de lignes ou surfaces portantes et à des modèles de sillages plus ou moins évolués (éléments rectilignes ou courbes). Ils procèdent suivant une méthode itérative mettant en jeu l'influence réciproque du champ tourbillonnaire et des répartitions de charges sur le rotor. Ces codes incluent généralement la mise en équilibre du sillage dont la géométrie et l'intensité des tourbillons sont consistantes avec la charge des pales et le champ des vitesses induites. Les différentes itérations de la procédure prévoient donc une remodélisation de la géométrie du sillage jusqu'à ce que la convergence soit atteinte, dans le plus grand nombre de calculs proposés, sur le coefficient de traction, déterminé par avance, ou plus rarement sur une distribution de circulation prescrite par l'expérience.

Des exemples non exhaustifs de ces calculs, baptisés "SME" (sillage mis en équilibre) sont donnés dans les références (1) à (22). Ils concernent des rotors et des hélices en vol stationnaire et de translation (références (1) à (15)) et des rotors en vol d'avancement (références (16) à (22)). De plus, des revues de synthèse (références (20) et (22)) montrent clairement l'aide que peuvent apporter ces codes dans la détermination des comportements aérodynamiques détaillés des voilures tournantes opérant suivant différents types de vols.

Néanmoins, la littérature citée ci-dessus met en évidence certaines faiblesses des méthodes de calcul, notamment dans le cas du vol stationnaire pour des pales à vrillage non linéaire et/ou à extrémités évolutives. La mise en équilibre du sillage s'avérant plus sensible dans le cas du vol stationnaire que dans celui de translation, il s'agit donc, pour chaque type de vol étudié, d'identifier la technique "SME" adéquate. En outre, ces techniques impliquent des temps de calcul importants en l'absence de conditions initiales connues, comme c'est le cas pour des pales à vrillages non linéaire et à extrémités évolutives.

Les difficultés induites par les processus de convergence et les temps de calcul conduisent à mettre en équilibre la ligne tourbillonnaire d'extrémité seulement, alors que la nappe interne obéit à une loi prescrite par l'expérience (références (13)-(16)).

Enfin, de nombreux calculs basés sur la méthode "SME" nécessitent une variation de pas général en cours de procédure afin de pouvoir assurer la convergence sur le coefficient de traction prescrit, qui est une donnée d'entrée. La validation du code repose alors sur des comparaisons calcul-expérience limitées à des mesures locales de vitesses et de géométrie de sillage. Très peu de recherches ont porté sur un modèle plus complet dont la validation pourrait aussi être étendue à des comparaisons portant sur des quantités aérodynamiques globales (Figure de mérite par exemple).

La présente étude a eu pour but d'accroître considérablement nos données expérimentales afin d'améliorer, dans le sens décrit ci-dessus, les codes "SME" actuellement utilisés à l'IMFM, et de les valider dans une large gamme de paramètres.

Ainsi, dans le cas du vol stationnaire, un nouveau modèle basé sur une distribution de circulation de pale prescrite est proposé ; le coefficient de traction n'est plus une donnée d'entrée mais une valeur finale calculée, le calcul s'effectuant sans avoir recours à une variation du pas général.

Dans le cas de l'hélice en vol de translation, le modèle adopté propose la mise en équilibre de la ligne tourbillonnaire d'extrémité et de la nappe interne.

Dans ces deux cas envisagés, la modélisation du sillage lointain s'appuie sur les résultats expérimentaux, et les caractéristiques aérodynamiques globales et locales peuvent être prédites sur une large gamme de paramètres de fonctionnement.

Enfin, des confrontations entre l'expérience et un code de calcul de rotor en vol d'avancement (code METAR) sont présentées et permettent d'ores et déjà d'apprécier les portées de ce code.

2. MOYENS D'ESSAIS ET DE MESURE

Les expériences ont été conduites dans la soufflerie elliptique de l'IMFM à veine ouverte (3,3 x 2,2 m^2, l = 3 m ; $V_\infty \leq$ 50 m/s) sur des maquettes de rotors d'hélicoptère et d'hélices. Les photographies 1a), 1b) et 1c) montrent respectivement la maquette du rotor d'hélicoptère en vol stationnaire et en vol d'avancement (vue depuis l'aval) et la maquette d'hélice en vol de translation (vue depuis l'amont).

Le rotor a un moyeu articulé équipé de pales dont on peut faire varier le nombre et la forme géométrique. La géométrie des rotors et les conditions d'essais sont résumées sur la Figure 2a. La Figure 2b donne la géométrie des pales de l'hélice (NACA 64 A608, vrillage, épaisseur et corde). Les différents jeux de pales de rotor d'hélicoptère numérotés de 1 à 7 sont présentés sur la Figure 3.

Les moyens de mesure appropriés à la détermination de. écoulements instantanés autour des pales dans le proche et lointain sillage comprennent des fils chauds c ...isés, la vélocimétrie laser et des visualisations. Les efforts globaux (traction et couple) sont mesurés à l'aide de jauges de contrainte fixées sur le mât supportant les maquettes. Les détails techniques relatifs à ces moyens d'essais et de mesure peuvent être consultés dans les références (6), (12), (13), (23) et (24).

Le champ de vitesse 3-D est mesuré par deux techniques complémentaires : la sonde à fils chauds croisés qui est déplacée en aval du plan de rotation par un support motorisé (voir Figure 1c), et la vélocimétrie laser 2-D.

La Figure 4 représente le système de coordonnées fixe (OXYZ) utilisé pour les essais "hélice", dans lequel les composantes U, V, W du vecteur vitesse en un point M du sillage sont mesurées et représentées ensuite par une série de Fourier à l'ordre 10. L'enregistrement des vitesses aux fils chauds croisés est synchronisé sur la rotation des pales. Le vélocimètre laser (VL) opère en mode "rétrodiffusion", et possède une cellule de Bragg pour détecter le signe de la vitesse. L'enregistrement des informations délivrées par le compteur peut être effectué en modes "continu" ou "stroboscopé". Le vélocimètre est monté sur un chariot à 3 degrés de liberté (Figure 5). La position azimutale de la pale et deux composantes du vecteur vitesse sont simultanément stockées à l'aide de deux buffers (voir Fig.5). Les traitements statistiques et histogrammes sont ensuite assurés par un micro ordinateur.

Les trajectoires (r_t, Z_t, ψ_t) des tourbillons issus de l'extrémité des pales sont déterminées par deux techniques complémentaires : l'une basée sur des visualisations, l'autre sur une exploration au fil chaud; la première est utilisée très près du disque de rotation des pales, la seconde plus en aval. De plus, la technique au fil chaud donne la position de la limite du sillage lointain qui se caractérise par des instabilités. Ces techniques sont détaillées dans les références (6) et (23).

La mesure de la circulation à une section r de la pale peut être obtenue à partir de deux techniques suivant qu'il s'agit du vol stationnaire ou du vol d'avancement du rotor d'hélicoptère. Dans le cas où l'écoulement n'est pas axisymétrique (vol d'avancement) la méthode utilise (Fig. 6a) l'intégration du vecteur vitesse suivant le contour rectangulaire défini à une phase ψ constante. La circulation Γ est alors donnée par la formule :

$$\Gamma = \oint \vec{V} d\vec{\ell} = \sum_{i=1}^{18} Vi.\ d\ell i \qquad (1)$$

Vi est la vitesse aux points i du contour.

Si l'écoulement est axisymétrique (vol stationnaire), le contour choisi est encore rectangulaire comme le montre la Figure 6b mais s'étend de pale à pale. Dans ce cas il suffit de relever la variation de la vitesse avec l'azimut ψ (quand ce dernier varie entre 0 et $2\pi/b$) en deux points U et L situés au-dessus et au-dessous du disque de rotation. Il est alors aisé de montrer que la circulation peut s'écrire[12]

$$\Gamma = \oint \vec{V}\, \vec{d\ell} = \int_0^{2\pi/b} [\, V_U(\psi) + V_L(\psi)\,]\ r\, d\psi \qquad (2)$$

On voit ainsi que la première méthode (ψ = cte) nécessite de déplacer le volume de mesure suivant le contour déterminé et d'effectuer des mesures "stroboscopées" à la phase ψ à l'aide du V.L.. La seconde présente l'avantage de ne pas avoir à déplacer le volume de mesure et d'enregistrer les valeurs délivrées par le V.L. en mode continu.

Le grand nombre de points de mesures ainsi obtenu suivant le contour d'intégration améliore d'autant la précision de la mesure.

Les résultats obtenus sur les pales rectangulaires à vrillage linéaire (Fig. 3) ont permis de donner une formule de synthétisation valable pour le vol stationnaire sous forme de séries de Glauert :

$$\Gamma(\xi) = \sum_{i=1}^{10} \gamma_n \sin(n\,\phi(\xi)) \qquad (3)$$

où ϕ est relié au rayon réduit par l'expression

$$\phi(\xi) = \mathrm{Ar\,cos}\ [(2\,\xi - 1 - \xi_o) / (1 - \xi_o)]$$

où ξ_o est le rayon réduit du moyeu.

Les coefficients γ_n sont des polynômes du 3ème degré en θ et b :

$$\gamma_n = \gamma^1_n(b)\,\theta + \gamma^2_n(b)\,\theta^2 + \gamma^3_n(b)\,\theta^3 \quad \text{pour} \quad 1 \leqslant n \leqslant 10$$

$$\gamma^j_n(b) = \alpha^j_n\, b + \beta^j_n\, b^2 + \delta^j_n\, b^3 \quad \text{pour} \quad 1 \leqslant j \leqslant 3$$

Les valeurs numériques de ces coefficients sont données dans la référence (12).

A titre d'exemple la Figure 7 montre la concordance des points expérimentaux avec les lois synthétiques données par la formule 3. Le pas général est égal à 6° et le nombre de pales prend les valeurs 2, 3 et 4. On peut aussi constater que le niveau de la circulation croît et que le maximum se déplace vers l'extrémité lorsque le nombre de pales augmente.

3. CODES "ROTOR D'HELICOPTERE EN VOL STATIONNAIRE" (SMEROT)

Ces codes ont pour nom générique SMEROT (Sillage mis en équilibre de rotors). La description détaillée de ces codes figure dans les références (12) et (13). Nous en rappellerons ici les étapes principales.

La pale est modélisée par une ligne portante et le sillage est composé d'un nombre fini de filaments tournillonnaires lachés par les pales. Une partie de ceux-ci, localisés vers l'extrémité, s'enroulent rapidement pour former la ligne tourbillonnaire marginale dont l'intensité est forte, les autres filaments de moindre intensité, constituent la nappe interne.

On peut alors distinguer deux procédures suivant que le calcul est mené à C_T prescrit ou à Γ prescrit.

3.1. Code à C_T prescrit (SMEROT - C_T)

La Figure 8 donne l'organigramme d'un tel code. On constate que le C_T est une donnée d'entrée et que la géométrie initiale et les vitesses induites (pas 0) sont déduites des formules empiriques, données dans les références (1) et (2), dépendant de C_T , σ , et θ . De plus, le sillage lointain est représenté par un cylindre semi-infini ; le sillage est jugé lointain pour un tourbillon issu d'une pale après un temps de parcours de celui-ci qui correspond à une rotation $\psi_s = 5\pi/b$ de la pale (cette valeur a été obtenue expérimentalement au fil chaud).

Le sillage est ensuite mis en équilibre ; cette procédure intéresse seulement la ligne marginale d'extrémité, la nappe interne est prescrite par les formules empiriques des références (1) et (2). Trois boucles d'itération (voir Figure 8) sont répétées dans cette opération, jusqu'à ce que le vecteur vitesse calculé devienne tangent à la géométrie de la ligne marginale (pas 2) et jusqu'à ce que la convergence soit réalisée sur la distribution de circulation et sur le C_T (pas 3). La boucle d'itération du pas 1 requiert une variation $\Delta\theta$ du pas général. Le temps de calcul nécessité par ce code sur IBM3081 est de l'ordre de 3mn CPU.

Des comparaisons calcul-expérience ont été réalisées (références (6),(12), (13)) pour différentes configurations de rotor faisant varier le nombre de pales rectangulaires à vrillage linéaire ($2 \leqslant b \leqslant 4$) et le pas général ($4^0 \leqslant \theta \leqslant 12^0$).

Les Figures 9a et 9b montrent le résultat de ces comparaisons portant, à titre d'exemple, sur la distribution de circulation (Rotor No. 7, Fig. 3, $b = 5$, $\theta = 10^0$).

Sont aussi portés sur ces figures les résultats de calcul d'autres auteurs (réfs. (5), (11), (15) et (25)) qui attestent de la validité des codes utilisés en particulier sur la prédiction du maximum de circulation qui se produit à $\xi = 0.9$. Les calculs proposés dans les références (15) et (25) présentent une bonne concordance sur toute l'envergure de la pale. Le principal reproche qui peut être fait aux calculs à C_T constant ici présentés est la nécessité de "retoucher" le pas général en cours de calcul et de "dénaturer" en quelque sorte la géométrie d'origine du rotor que l'on s'est fixé en donnée d'entrée. Ainsi le calcul IMFM présenté sur la Figure 9a converge après une variation $\Delta\theta = 1^0$: toute comparaison avec les charges globales du rotor devient par suite sujette à caution comme commenté dans les références (11), (12) et (16).

3.2. Code à Γ prescrit (SMEROT - Γ)

La Figure 10 présente l'organigramme du code à Γ prescrit mis au point à l'IMFM, qui permet de s'affranchir de l'inconvénient dont il vient juste d'être question.

Les données d'entrée sont les mêmes, excepté le C_T qui devient une inconnue du calcul.

La distribution de la circulation le long de la pale est prescrite suivant la formule (3), et la géométrie initiale du sillage est identique à celle décrite dans le code de la Figure 8. La procédure générale du calcul est alors réduite à une seul boucle d'itération portant sur la mise en équilibre du sillage effectuée de la même façon que sur la Figure 8. Le pas général est maintenu constant, et après convergence, le C_T peut être calculé et comparé à l'expérience, ainsi que les valeurs locales du sillage (géométrie, vitesse).

A titre d'exemple, la Figure 11 présente une comparaison avec l'expérience, des calculs obtenus à partir des codes à C_T prescrit et Γ prescrit. Cette comparaison porte sur les coordonnées radiales et axiales(r_t, Z_t) des tourbillons lachés par l'extrémité des 4 pales du rotor 7 pour $\theta = 8^0$. Cette figure montre la supériorité du code à Γ prescrit sur celui à C_T prescrit qui nécessite une variation du pas général dans ce cas de $1{,}5^0$.

Concernant le champ des vitesses, la variation de la composante axiale W avec l'abscisse radiale a été calculée à cinq phases ψ de rotation de la pale, dans un plan aval $Z/R = 0.11$. Le rotor est quadripale et son pas général θ vaut 10^0. La Figure 12 présente le résultat des calculs issus des deux codes précédemment décrits et la comparaison aux expériences. Là aussi, les prédictions du code à Γ prescrit sont meilleures que celles à C_T prescrit, en particulier lorsque l'influence de tourbillons marginaux devient forte dans le plan de mesure (c'est-à-dire à $\psi = 0^0$ et $\psi = 81^0$). Est également représentée sur la figure, la valeur de W, donnée par la théorie classique de quantité de mouvement (ou théorie des anneaux) qui est indépendante de la phase. On notera la prédiction acceptable fournie par cette théorie simplifiée d'une mise en oeuvre rapide.

Enfin, la Figure 13 donne la comparaison essais-calcul (code Γ prescrit) réalisée sur la figure de mérite pour le rotor quadripale No. 7. La théorie des anneaux est également portée sur la courbe. L'accord entre les différentes quantités mises en jeu est acceptable jusqu'à des Zb de l'ordre de 20, valeur au-delà de laquelle des phénomènes de décrochage du rotor interviennent. Notons que la comparaison calcul-expérience sur la figure de mérite n'est pas réalisable avec le code à C_T prescrit.

En conclusion, les validations effectuées à partir de nombreuses expériences réalisées sur les rotors en vol stationnaire ont montré l'avantage de l'utilisation d'un code à Γ prescrit et, d'une façon plus générale, les bonnes prédictions obtenues par les codes "SMEROT" excepté les cas de tractions élevées et les pales à vrillage non linéaire et à extrémité évolutive.

Des progrès restent à accomplir notamment pour les rotors No. 3, 4, 5 de la Figure 3.

4. CODE "HELICE EN VOL DE TRANSLATION" (SMEHEL)

Ce code a pour nom générique SMEHEL (sillage mis en équilibre d'hélices). Les nombreuses expériences réalisées au fil chaud sur la caractérisation du sillage d'hélice (voir ref. 23) ont conduit à l'élaboration de formules de synthétisation de la contraction r_t et de la convection Z_t des tourbillons issus de l'extrémité des pales.

Pour $0.2 \leqslant \gamma \leqslant 1.0$ et $23^0 \leqslant \alpha_o \leqslant 32.5^0$ ces formules peuvent s'écrire :

$$r_t/R = A + (1 - A)\, e^{-\psi/B} \qquad \text{pour} \quad 0 \leqslant \psi \leqslant \psi_s \tag{4}$$

$$Z_t/R = K_1 \, (\psi/\psi_b) \qquad \text{pour} \quad 0 \leqslant \psi \leqslant \psi_b \tag{5}$$

$$Z_t/R = K_1 + K_2 \, (\psi/\psi_b - 1) \qquad \text{pour} \quad \psi_b \leqslant \psi \leqslant \psi_s \tag{6}$$

A et B dépendent de α_o et γ suivant les lois :

$$A(\alpha_o,\gamma) = P_A(\gamma) + \alpha_o Q_A(\gamma) \tag{7}$$

$$B(\alpha_o,\gamma) = P_B(\gamma) + \alpha_o Q_B(\gamma) \tag{8}$$

P_A, Q_A, P_B et Q_B sont des polynômes du 2e ordre en γ^2.

K_1 et K_2 sont des fonctions de λ/λ_T où λ_T est le paramètre d'avancement à la traction nulle. Les valeurs des coefficients ci-dessus sont données dans les références (13), (23).

La position azimutale du sillage lointain suit la loi :

$$(\psi_s - \psi_b) / (b\ \psi_b) = 1/4 \{ 8.5 - \alpha_o /10 - \gamma(2+\gamma) \} \tag{9}$$

Les différentes relations (4) à (9) font intervenir les paramètres α_o et γ, alors que les formules de synthétisation relatives au sillage du rotor en vol stationnaire dépendent de σ, θ et C_T (voir paragraphe 3).

Le code de calcul de l'hélice en translation dont les pales sont représentées par une ligne portante, fait intervenir une mise en équilibre complète du sillage, dans un système de référence attaché aux pales.

La pale et le sillage sont alors modélisés comme présenté sur la Figure 14. Np points de calcul sont répartis sur la pale et occupent le milieu de chaque lanière tourbillonnaire s'echappant dans le sillage dont le nombre $N_L = Np + 1$. Les points de calcul sont concentrés vers l'extrémité et le moyeu où les gradients de circulation sont plus forts.

La connaissance de la ligne marginale tourbillonnaire (r_t, Z_t) permet de représenter la nappe interne pour $i = 1, 2, \ldots N$ à partir des équations :

$$r^i_{ni}/R = \xi r_t(\psi) \qquad \text{pour} \quad 0 \leqslant \psi \leqslant \psi_s \tag{10}$$

$$Z^i_{ni}/R = H(r,0).\ \psi \qquad \text{pour} \quad 0 \leqslant \psi \leqslant \psi_b \tag{11}$$

$$Z^i_{ni}/R = H(r,0).\ \psi_b + H(r,\psi_b)(\psi - \psi_b) \qquad \text{pour} \quad \psi_b \leqslant \psi \leqslant \psi_s \tag{12}$$

où les pas $H(r,0)$ et $H(r,\psi_b)$ s'expriment en tout point comme des fonctions de U, V, W :

$$H(U,V,W,) = \pi/180.\ (V_\infty + W) / \{ \Omega + (U\cos\psi - V\sin\psi)/r \} \tag{13}$$

Le sillage lointain ($\psi > \psi_s$) est ensuite représenté conformément au schéma de la Figure 15

Des cylindres, de densité de circulation dΓ/dr constante, prennent le relais de chaque filament issu de la pale et mis en équilibre avec un rayon égal à celui du filament qu'ils prolongent.

La procédure de calcul de mise en équilibre[27] est alors effectuée comme le montre le diagramme de la Figure 16.

Les valeurs d'entrée permettent de calculer tout d'abord la ligne marginale et la position du sillage lointain à partir des équations (4) à (9).

Avant d'aborder le premier pas de calcul, la nappe interne correspondant à la ligne marginale de départ est calculée dans le pas 0 par les formules (10) à (13), en supposant que le pas de cette nappe est égal au paramètre d'avancement ($Z_{ni}/R = \lambda\psi\ (\pi/180)$). La mise en équilibre complète sur la ligne marginale et la nappe interne s'effectue ensuite suivant l'itération du pas 1. La convergence est supposée atteinte lorsque le champ des vitesses est tangent à la fois à la ligne marginale et aux lignes internes,

et que les valeurs z_{ni}^{n} et z_{ni}^{n-1} obtenues aux pas n-1 et n vérifient l'inéquation

$$\text{Max} \mid z_{ni}^{n} - z_{ni}^{n-1} \mid < \epsilon \text{ avec } \quad \epsilon = 10^{-4}$$

Les performances globales de l'hélice sont alors calculées (τ, χ, η) de même que les quantités locales telles que la distribution de circulation le long des pales ou le champ instantané des vitesses.

Le calcul, mené à pas général constant, requiert le même temps d'exécution que le rotor en vol stationnaire, soit environ 3 mn CPU sur IBM 3081.

La validation du code a porté d'une part sur les quantités globales, comme l'illustrent, à titre d'exemple, les Figures 17a, b, c qui montrent les comparaisons calcul-expériences réalisées sur les variations de la traction avec γ pour trois valeurs différentes du pas général. On notera l'excellent accord obtenu avec des écarts maximums de l'ordre de 7 % enregistrés à faible γ et fortes charges.

Il a, d'autre part, été possible de tester le calcul sur des grandeurs locales. La Figure 18 présente les variations de la vitesse radiale $Vr = (U^2+V^2)^{1/2}$ calculées et mesurées dans un plan situé à Z/R = 0.221. Ces vitesses sont tracées dans un repère en rotation avec les pales qui sont localisées à $\psi = 0°$, $90°$, $180°$, $270°$. La confrontation calcul-expérience est généralement bonne dans tout le champ. La position du tourbillon prédite par le calcul est bien recoupée par l'expérience bien que les vitesses dans la région du tourbillon lui-même montrent quelques différences ($\psi = 10°$). Les plus grands écarts se produisent dans la zone du moyeu où le calcul est à améliorer par une prise en compte de la géométrie réelle de cette partie du rotor.

5. CODE "ROTOR d'HELICOPTERE EN VOL D'AVANCEMENT" (METAR)

Ce code, mis au point à l'Aérospatiale (appelé METAR : Modèle d'Etude de l'Aérodynamique des Rotors), est décrit dans les références (28) et (29). Il est construit sur un modèle de ligne portante et sillage prescrit. Il n'est pas tenu compte de l'influence du sillage lointain, le sillage proche s'arrêtant après 3 rotations des pales.

Les différentes étapes du calcul sont reportées sur le diagramme de la Figure 19 . Après introduction des valeurs d'entrée (caractéristiques géométriques, caractéristiques aérodynamiques des profils, conditions de vol), le pas 0_a donne une estimation du C_T et des vitesses induites par la méthode de Meyer Drees en supposant que la circulation est constante le long de la pale et varie simultanément avec l'azimut. Le pas 0_b , à partir des résultats de 0_a , donne la géométrie du sillage et la trajectoire de la ligne tourbillonnaire d'extrémité suivant une forme simplifiée déduite des lois empiriques dans les références (17) et (18).

Les coefficients de la matrice d'influence peuvent ensuite être écrits.

La Figure 20 montre comment le disque rotor et le sillage ont été discrétisés. Le rotor est divisé en 10 cercles concentriques ($1 \leqslant j \leqslant 10$) et 24 azimuts ($0 \leqslant i \leqslant 24$) où i = 0 correspond à $\psi = 0$. Les points de calcul sur les pales sont notés : P_b (i,j) et ceux du sillage P_w (i,j,k) où k représente l'âge du tourbillon et varie depuis k = 0 (émission depuis la pale à $\psi = 0°$) jusqu'à k = 72 ($\psi = 3 \times 360° = 1080°$) par saut de 15°. A chaque saut, la vorticité correspondante est lachée dans le sillage et se conserve dans une maille élémentaire convectée. Il est ensuite tenu compte de l'influence de tous ces éléments tourbillonnaires sur les points de calcul du disque rotor.

Le pas suivant (1 sur la Figure 16) procède au travers d'une boucle itérative, au calcul de la distribution de circulation le long de la pale (1a) puis au calcul des vitesses induites (1b), enfin, au test de convergence sur le champ des vitesses. Après convergence du calcul, les valeurs de C_T , Γ et des vitesses induites sur la pale sont calculées.

La validation de ce code est actuellement en cours à l'IMFM où de nombreuses expériences sont entreprises sur un rotor maquette en vol d'avancement (rotor No. 7).

Les premières confrontations réalisées portent sur la variation du C_T en fonction du paramètre d'avancement μ . La Figure 21 fait état de divergences entre calcul et expérience d'autant plus fortes que μ est grand. Aux faibles valeurs de μ , par contre, le code semble mieux prédire les valeurs mesurées de C_T.

Dès à présent, il semble nécessaire, afin d'améliorer le code METAR, de prévoir une extension incluant la mise en équilibre du sillage comme cela a été réalisé pour les codes décrits dans les paragraphes 3 et 4.

6. CONCLUSIONS

Les caractéristiques aérodynamiques de rotors d'hélicoptères et d'hélices opérant en vol stationnaire ou de translation ont été étudiées à la fois à partir de codes numériques et d'expériences réalisées sur maquettes en soufflerie.

Pour chaque configuration de vol, l'effort a porté sur la validation et l'amélioration de codes de calcul utilisant des méthodes de mise en équilibre du sillage, la validation et l'amélioration étant elles-mêmes basées sur les résultats expérimentaux portant à la fois sur les quantités aérodynamiques globales et locales. Les conclusions suivantes ont ainsi pu être tirées :

1. Pour les rotors d'hélicoptères au point fixe, l'amélioration des codes "SME" est obtenue par l'utilisation d'une méthode à Γ prescrit. L'avantage sur le code plus classique à C_T prescrit réside en particulier sur le maintien, au cours de la procédure, d'un pas général θ constant, et sur la réduction du calcul à une seule boucle d'itération. Il est de plus possible de prédire les charges aérodynamiques

pour une géométrie de rotor donnée. Enfin, les comparaisons calcul-expériences effectuées sur les valeurs locales telles que le champ des vitesses ou la géométrie du sillage montrent que le code à Γ prescrit conduit à de meilleures prédictions. Il serait toutefois souhaitable de pouvoir étendre cette méthode aux rotors à vrillage non linéaire et fortement chargés, et d'envisager de l'appliquer aux cas des rotors *en vol de translation*.

2. La mise en équilibre complète de la ligne marginale et de la nappe interne a été utilisée dans le cas d'hélices *en vol de translation*, avec prise en compte du sillage lointain à l'aide de cylindres à densité de circulation constante. Le code mis au point, qui tient compte de la position du sillage lointain à l'aide d'une formule empirique, prédit correctement à la fois les efforts globaux subis par les pales et les valeurs locales telles que le champ de vitesses. Il a été aussi possible de calculer un modèle de géométrie de sillage réaliste qui peut être d'une aide déterminante dans la résolution des problèmes d'intéraction entre le sillage de l'hélice et le fuselage par exemple.

Toutefois, une amélioration de l'écoulement dans le voisinage du pied de pale peut également être attendue par la prise en compte de la géométrie du moyeu.

3. Dans le cas du rotor d'hélicoptère en vol d'avancement, le code METAR, basé sur un sillage prescrit, semble donner des prédictions moins acceptables lorsque la paramètre d'avancement croît. Une amélioration peut être apportée par l'introduction de la mise en équilibre du sillage et par l'extension des comparaisons calcul-expériences, en particulier celles portant sur la distribution de circulation le long des pales et les champs de vitesse du sillage. C'est le programme de recherche que s'est fixé l'IMFM dans le futur proche.

Remerciements : La présente recherche a été en partie supportée par la "Direction des Recherches Etudes et Techniques" sous le contrat No. 85/115.

Références :

(1) LANDGREBE, A.J., "The wake geometry of a hovering helicopter rotor and its influence on rotor performance", Journal of American Helicopter Society, Vol. 17, No. 4, October 1972, pp.3-15.

(2) KOCUREK, J.D. and TANGLER, J.L., "A prescribed wake lifting surface hover performance analysis", Journal of American Helicopter Society, Vol. 22, No. 11, January 1977, pp. 24-35.

(3) SULLIVAN, J.P., "The effect of blade sweep on propeller performance", A.I.A.A. Paper No.77-716, A.I.A.A. 10th Fluid and Plasma Dynamics Conference, Albuquerque, June 1977.

(4) SCHMA, J.M. and CLARK, D.R., "A lifting surface method for hover/climb airloads", Proceedings of the 35th Annual American Helicopter Society Forum, Washington, May 1979.

(5) TUNG, C., "Rotorcraft Wakes", Communication at the French/US MOU on Helicopter Rotors, Moffett Field, May 1987.

(6) MARESCA, C., NSI MBA, M. and FAVIER, D., "Prédiction et vérification expérimentale du champ des vitesses d'un rotor en vol stationnaire", AGARD-FDP on Aerodynamics Loads on Rotorcraft, CP-334, Paper No. 7, May 1982.

(7) MILLER, R.H., "Rotor hovering performance using the method of fast free wake analysis", Journal of Aircraft, Vol. 20, No. 3, March 1983, pp.257-261.

(8) MORINO, L., KAPRIELIAN, Z. and SIPCIC, S.R., "Free wake analysis of helicopter rotors", Proceedings of 9th European Rotorcraft Forum, Paper No. 2, Stresa, September 1983.

(9) BLISS, D.B. and QUACKENBUSH, T.R., "A new approach to the free wake problem for hovering rotor", Proceedings of 10th European Rotorcraft, Paper No. 14, The Hague, August 1984.

(10) BLISS, D.B., TESKE, M.E. and QUACKENBUSH, T.R., "Free wake calculations using curved vortex elements", Proceedings of 1st International conference on Rotorcraft Basic Research, Research Triangle Park, February 1985.

(11) GRABER, A., and ROSEN, A., "A parametric investigation of a free wake analysis of hovering rotors", Proceedings of 12th European Rotorcraft Forum, Paper n° 22, Garmish-Partenkirchen, September 1986.

(12) MARESCA, C., FAVIER, D. and NSI MBA, M., "A prescribed radial circulation distribution of a hovering rotor blade", Proceedings of 12th European Rotorcraft Forum, Paper No. 23, Garmish-Partenkirchen, September 1986.

(13) FAVIER, D., NSI MBA, M., BARBI, C. and MARESCA, C., "A free wake analysis for hovering rotors and advancing propellers", Proceedings of 11th European Rotorcraft Forum, Paper No. 21, London, September 1985 ; see also, Vertica, Vol. 11, No. 3, March 1987, pp. 493-511.

(14)CHEN, C.S., VELKOFF, H.R. and TUNG, C., "Free-wake analysis of a rotor in hover", A.I.A.A. Paper 87-1245, A.I.A.A. 19th Fluid and Plasma Dynamics Conference, Honolulu, June 1987.

(15)STEINHOFF, J. and RAMACHANDRAN, K., "A vortex embedding method for free wake analysis of helicopter rotor blades in hover", Proceedings of 13th European Rotorcraft Forum, Paper No. 11, Arles, September 1987.

(16)RAND, O. and ROSEN, A., "An unsteady prescribed wake model for a helicopter rotor in forward flight", Journal of American Helicopter Society, Vol.30, No. 4, October 1985, pp.11-21.

(17)EGOLF, T.A. and LANDGREBE, A.J., "Helicopter rotor wake geometry and its influence in forward flight. Volume I - Generalized wake geometry and wake effects on rotor airloads and performance", NASA CR 3726, June 1983.

(18)EGOLF, T.A. and LANDGREBE, A.J., "Helicopter rotor wake geometry and its influence in forward flight. Volume II - Wake geometry charts", NASA CR 3727, June 1983.

(19)ELLIOTT, J.W., ALTHOFF, S.L., SELLERS, W.L. and NICHOLS, C.E., "Inflow velocity measurements made on a helicopter rotor using a two-component laser velocimeter", A.I.A.A. Paper 87-132, A.I.A.A. 19th Fluid and Plasma Dynamics Conference, Honolulu, June 1987.

(20)MARTIN, R.M., ELLIOTT, J.W. and HOAD, D.R., "Experimental and analytical predictions of rotor blade vortex interaction", Journal of the American Helicopter Society, Vol. 31, No.4, October 1986, pp. 13-20.

(21)JOHNSON, W., "Recent developments in rotary wing aerodynamic theory", A.I.A.A. Journal, Vol. 24, No. 8, August 1986, pp. 1219-1244.

(22)LANDGREBE, A.J., "Overview of helicopter wake and airloads technology", Proceedings of 12th European Rotorcraft Forum, Paper No. 18, Garmish-Partenkirchen, September 1986.

(23)FAVIER, D. and MARESCA, C., "Etude du sillage 3D d'une hélice aérienne quadripale", AGARD-FDP on Aerodynamics and Acoustics of Propellers, CP-366, Paper No. 15, October 1984.

(24)NSI MBA, M., MEYLAN, C., MARESCA C.and FAVIER, D., "Radial distribution circulation of a rotor in hover measured by laser velocimeter", Proceedings of the 10th European Rotorcraft Forum, Paper No. 12, The Hague, August 1984.

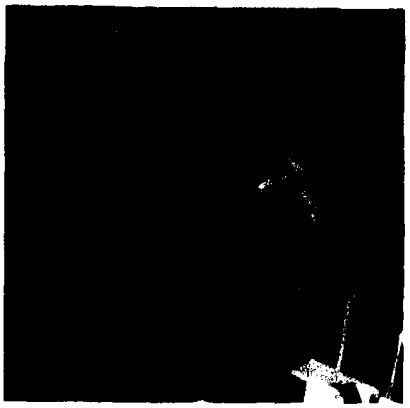
(25)MULLER, R.H.G., "The influence of winglets on rotor aerodynamics", Proceedings of 12th European Rotorcraft Forum, Paper No. 34, Garmish-Partenkirchen, September 1986.

(26)REDDY, K.R. and GILBERT, N.E., "Comparison with flight data of hover performance using various rotor wake models", Proceedings of 13th European Rotorcraft Forum, Paper No. 12, Arles, September 1987.

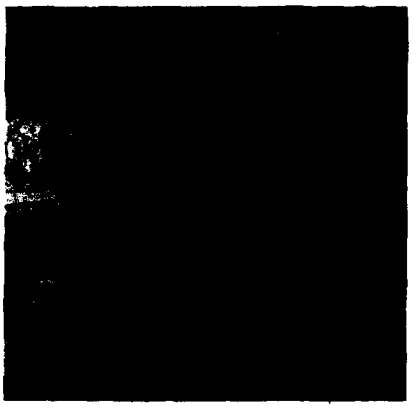
(27)ETTAOUIL, A., "Etude numérique du champ aérodynamique d'une hélice aérienne isolée ou en interaction avec une voilure. Validation par comparaison avec l'expérience", Thesis of Doctorat, I.M.F.M. Université d'Aix-Marseille II, Septémber 1987.

(28)LAMBERT, C., "Modélisation d'un sillage type Egolf et Langrebe en vol d'avancement", Aérospatiale Report, H/BE 1986-10, October 1986.

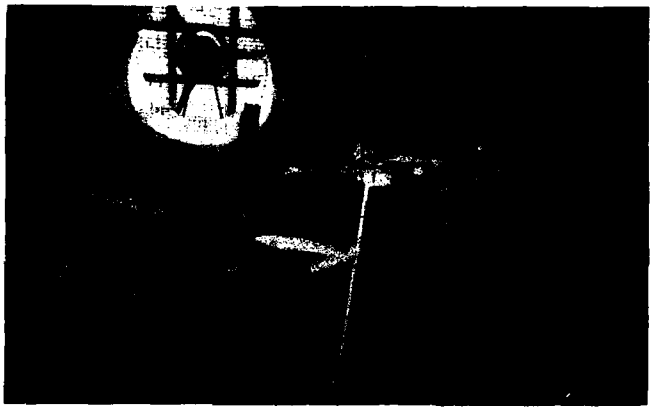
(29)TOULMAY, F., "Modèle d'étude de l'aérodynamique rotor (METAR). Formulation et application au rotor SA 349-pales G.V.", Aérospatiale Report H/BE/R.37176, 1986.



a)



b)



c)

Fig. 1 : Maquettes de rotor d'hélicoptère et d'hélice montées en soufflerie.
a) Vol stationnaire ; b) Vol d'avancement ; c) Vol de translation

a)

Modèles / Conditions	ROTOR		HELICE
	Stationnaire / Avancement		Translation
Diamètre D	1.50 m		0.85 m
Moyeu ξ_0	0.22		0.176
Fréquence de rotation	143 t/s	120-180 t/s	140-280 t/s
Vitesse extrémité de pale	107 m/s	100-190 m/s	60-120 m/s
Conicité a_0	2.5°	variable	0°
Nombre de pales b	2-6	2	4
Profil de pales	OA 209 - BV 23010		NACA 64 A 408
Corde de pales c	0.05		voir Fig. 2b
Vrillage de pales θ_t	Linéaires et non linéaires		voir Fig.2b (NL)

b)

ξ	0.176	0.300	0.400	0.500	0.600	0.700	0.800	0.900	1.000
t/c	0.187	0.091	0.085	0.082	0.080	0.073	0.052	0.051	0.051
c/R	0.205	0.292	0.280	0.242	0.203	0.174	0.155	0.143	0.134
θ_t (°)	28.3	20.8	25.1	9.66	4.53	0.00	-4.5	-8.3	-11.5

Fig. 2 : Caractéristiques géométriques et conditions d'essais des rotors et hélices.

DEFINITION DES ROTORS

Numéro du rotor	Vrillage	Forme en plan	Profil
1	-8°		BV 23010
2	-14°		BV 23010
3	-8,3° non linéaire		OA 209
4	-8,3°	d=60°	OA 209
5	-8,3°		OA 209
6	-8,3°	0,95R R	OA 209
7	-8,3°		OA 209

a=0,15c
b=0,25c
d=0,60c

Fig. 3 : Définitions géométriques des rotors d'hélicoptères (vol stationnaire).

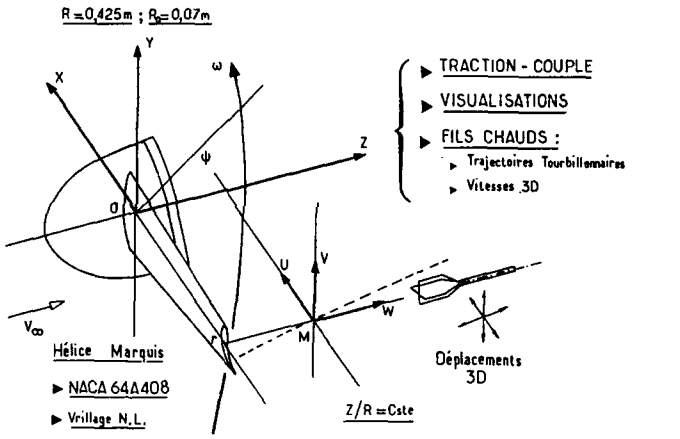


Fig. 4 : Système de référence et composantes du vecteur vitesse. Essais sur l'hélice "Marquis".

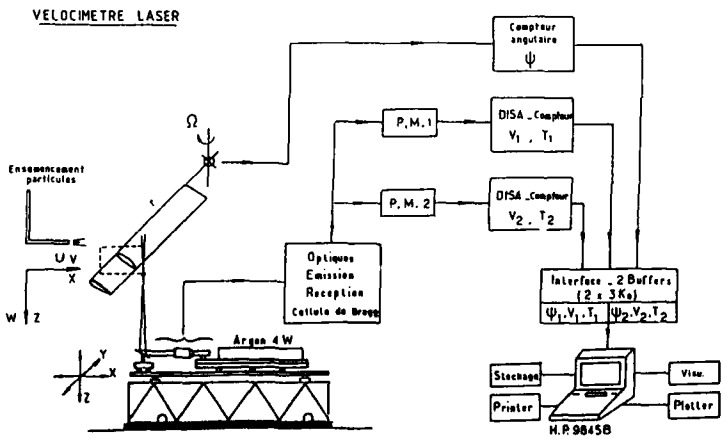
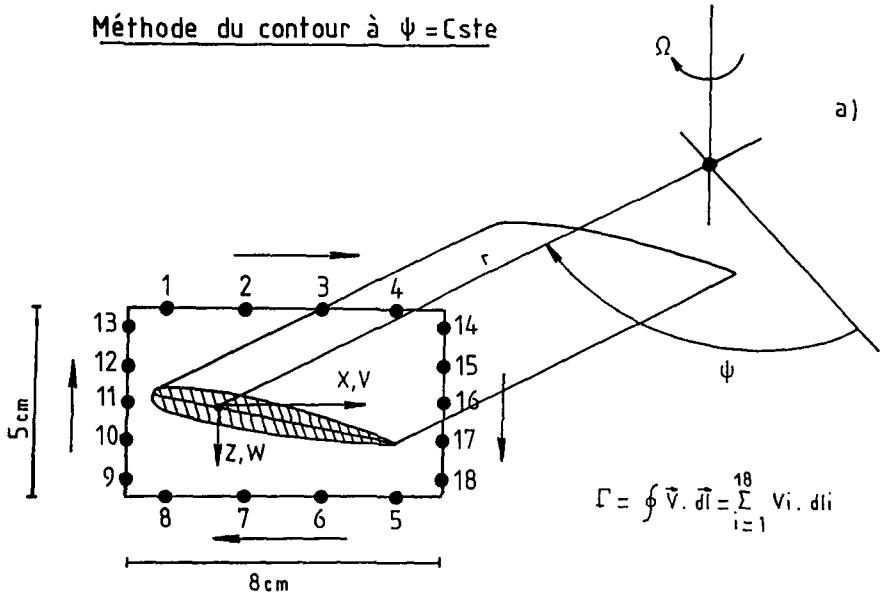


Fig. 5 : Organigramme de la vélocimétrie laser.

VOL QUELCONQUE

Méthode du contour à ψ = Cste



$$\Gamma = \oint \vec{V} \cdot d\vec{l} = \sum_{i=1}^{18} Vi \cdot dli$$

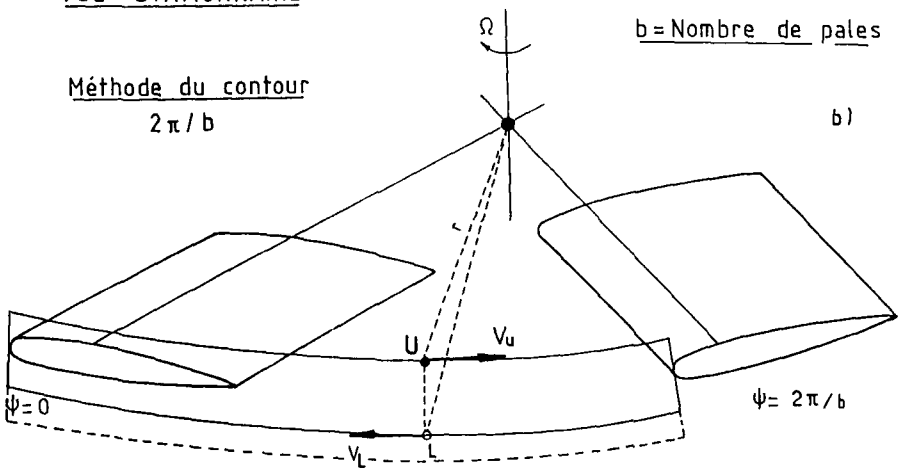
a) Vol quelconque

VOL STATIONNAIRE

b = Nombre de pales

Méthode du contour

$2\pi / b$



$$\Gamma = \oint \vec{V} \cdot d\vec{l} = \int_{0}^{2\pi/b} [V_u(\psi) + V_L(\psi)]\, r\, d\psi + 0$$

b) Vol stationnaire

Fig. 6 : Principe de la mesure de la circulation.

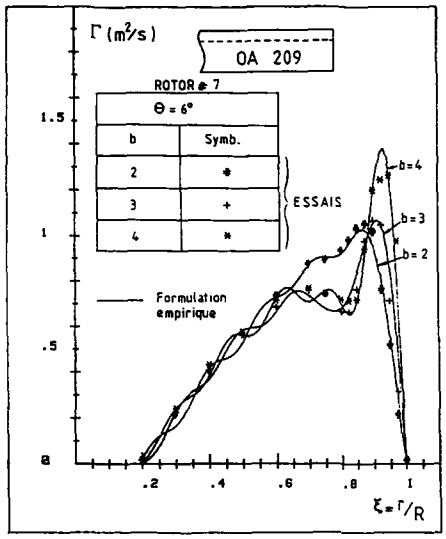


Fig. 7 : Représentation de la distribution de circulation en vol stationnaire par une formulation empirique.

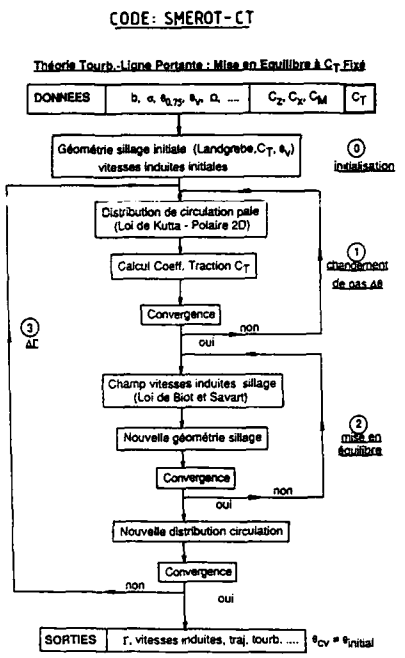


Fig. 8 : Diagramme du modèle SMEROT-CT.

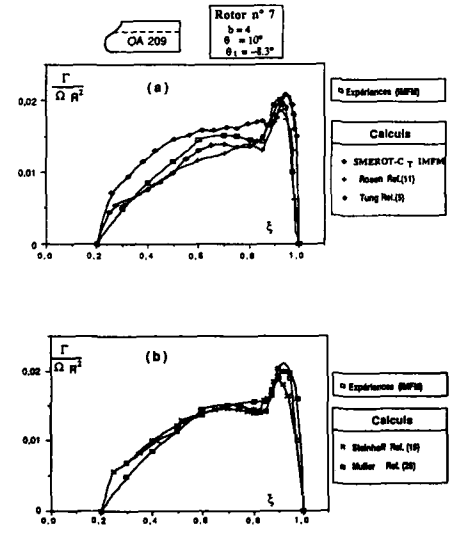


Fig. 9 : Comparaison calculs/expériences sur la répartition de la circulation le long des pales en vol stationnaire.

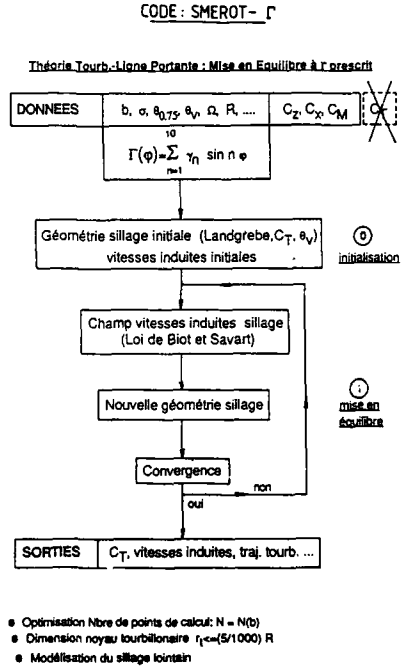


Fig.10 : Diagramme du modèle SMEROT-Γ.

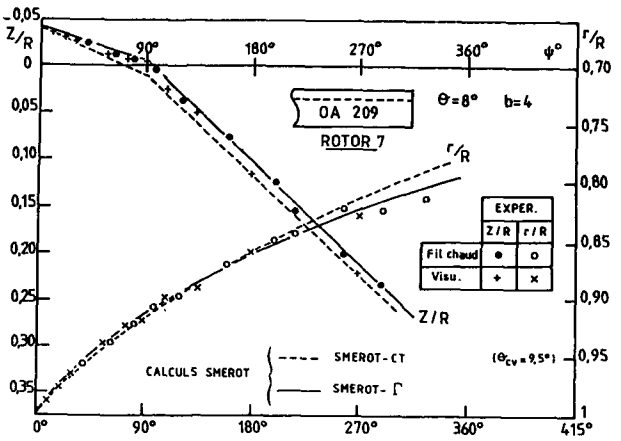


Fig.11 : Comparaison calculs/expériences sur les trajectoires tourbillonnaires d'extrémité.

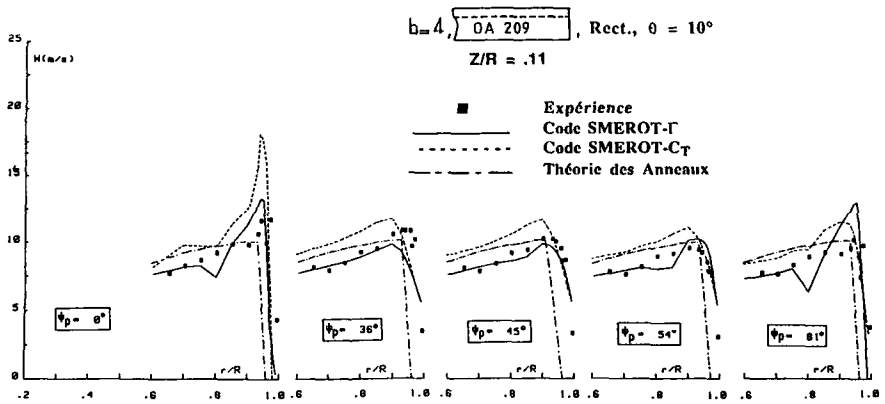


Fig.12 : Comparaison calculs/expériences sur le champ des vitesses en vol stationnaire.

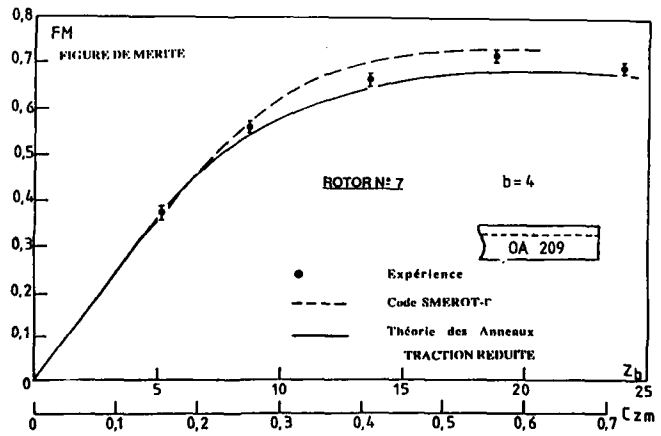


Fig.13 : Comparaison calculs/expériences sur la figure de mérite en vol stationnaire.

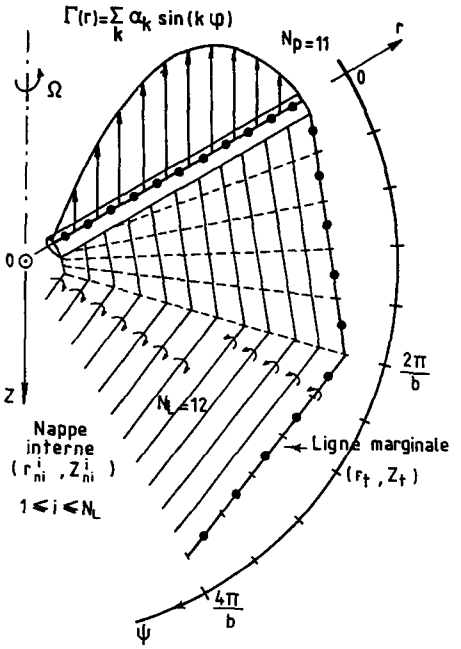


Fig.14 : Représentation de la pale et du sillage de l'hélice en vol de translation.

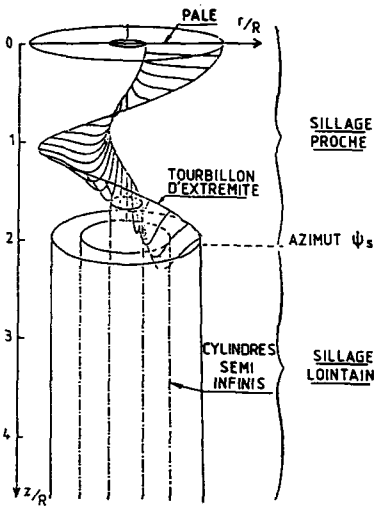


Fig.15 : Représentation du sillage proche et lointain de l'hélice en vol de translation.

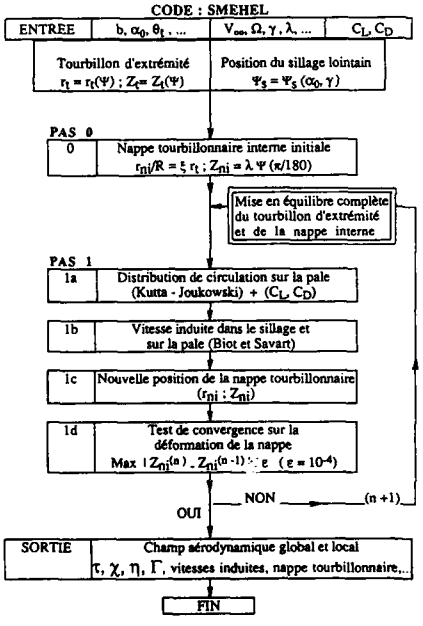


Fig.16 : Organigramme du code SMEHEL.

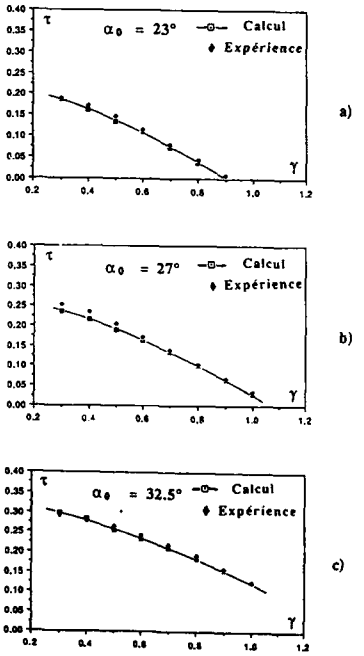


Fig.17 : Comparaison calcul/expériences sur le coefficient de traction en vol de translation.

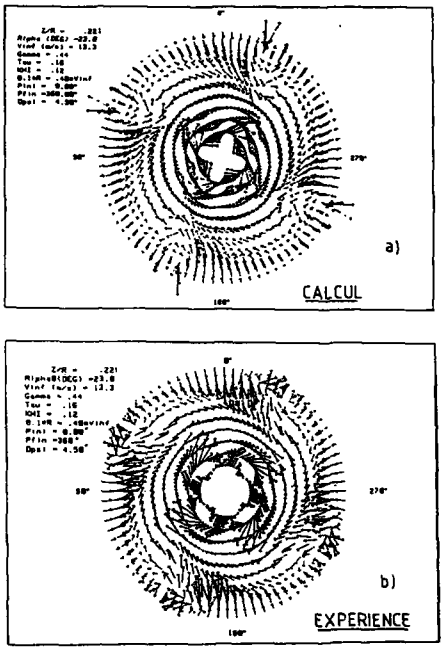


Fig.18 : Comparaison calcul/expériences sur le champ radial des vitesses en vol de translation.

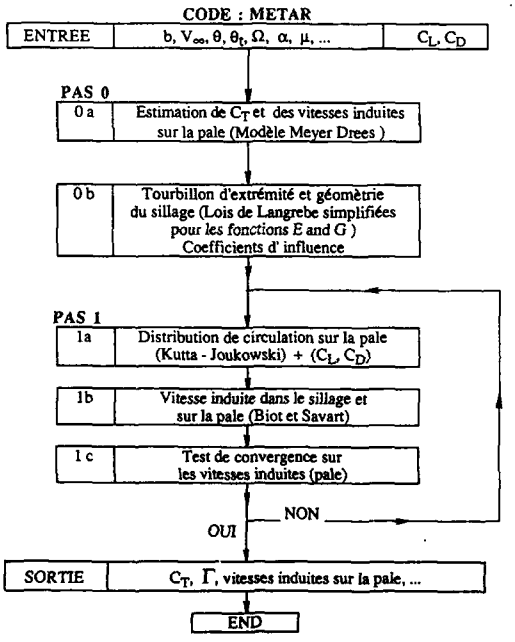


Fig.19 : Organigramme du code METAR en vol d'avancement.

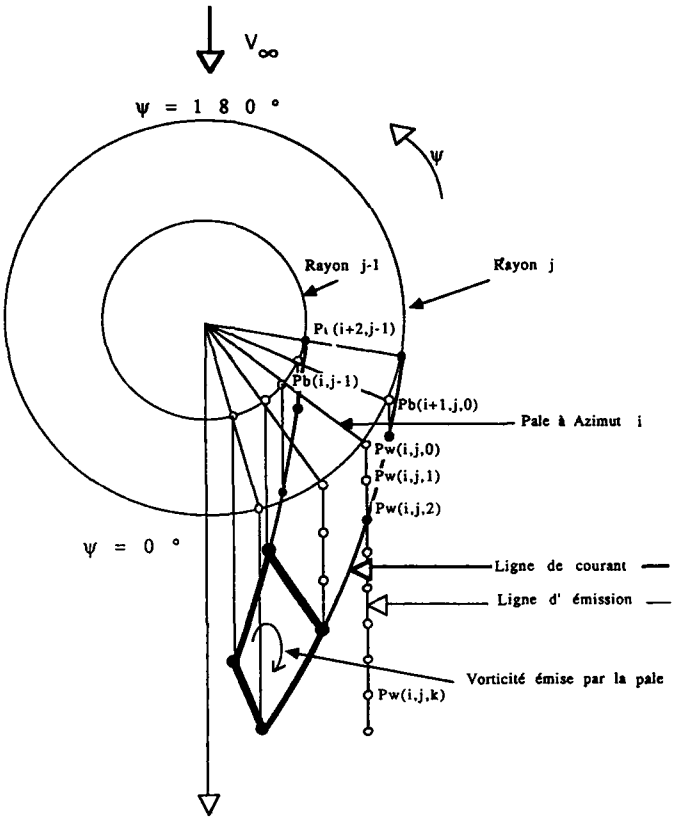


Fig.20 : Représentation des points de calcul sur les pales et dans le sillage en vol d'avancement.

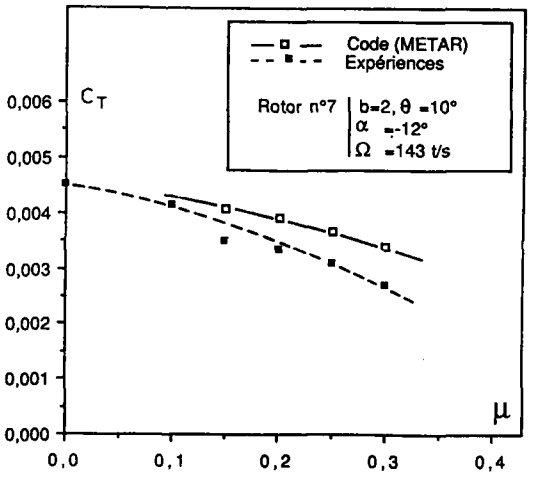


Fig.21 : Comparaison calcul/expériences sur le coefficient de traction en vol d'avancement.

VALIDATION OF A 3D EULER/NAVIER-STOKES FINITE VOLUME SOLVER FOR A RADIAL COMPRESSOR

by

Lars-Erik Eriksson
Division of Hydro- & Gas Dynamics
NTH - The Norwegian Institute of Technology
N-7034 Trondheim, Norway

and

Jan Tore Billdal
Division of Fluid Dynamics, SINTEF
The Foundation for Scientific and Industrial Research
at the Norwegian Institute of Technology
N-7034 Trondheim, Norway

SUMMARY

The application of a time-marching Euler/Navier-Stokes solution procedure to 3D compressible turbomachinery flow is described. The method is based on the cell-centered finite-volume technique and explicit Runge-Kutta time-stepping. A centered and compact difference scheme is used to obtain the velocity and temperature gradients needed in the viscous flux terms and a standard algebraic turbulence model is included in the method. Computational results for the well known Eckardt impeller show that the viscous model comes significantly closer to the experimental data than the Euler model. The results of a thin-layer version of the viscous solver are in very close agreement with those of the full Navier-Stokes solver.

INTRODUCTION

Numerical procedures for the simulation of steady compressible flow, either external or internal, have developed rapidly during the last ten years. Of those methods which are based on the unsteady Euler equations or Navier-Stokes equations it could be argued that finite volume methods currently are the most popular. In the case of internal flows one of the earliest successful finite volume Euler solvers was developed by Denton[1]. For external flows the Runge-Kutta finite volume method by Jameson et al[2] is perhaps the best known Euler solver and variations of this original scheme have recently been applied to internal flows also[3]. The authors' own experiences with a Runge-Kutta finite volume Euler solver for computing fully three-dimensional transonic flow fields in radial compressors[4,5] have been very encouraging and clearly indicate the potential of this type of scheme. However, the results also indicate that for radial compressors it is important to include viscous effects, especially in the radial part of the flow channel, and this has motivated us to generalize our numerical solution procedure to the unsteady Navier-Stokes equations. Such extensions of this type of method have been reported recently[6,7,8] with promising results.

The purpose of this paper is to present a fully 3D time-marching Euler/Navier-Stokes solver for radial compressors and to present detailed comparisons between experimental and computational (both inviscid and viscous) results for a test case. The test case we have chosen is the well known Eckardt impeller[9]. In the following paragraphs we first briefly outline our numerical method, with special emphasis on the viscous flux terms and turbulence modelling, and then present the results in a form which facilitates comparisons with experimental data.

NUMERICAL METHOD

Our computation procedure[4,5,8] is based on the cell-centered finite volume method and a three-stage explicit time integration scheme, but differs from the original scheme by Jameson[2] in the construction of artificial damping terms and boundary conditions. In order to extend this method from the Euler equations to the Navies-Stokes equations we need the gradients of the velocity components u,v,w and temperature T. There are at least three different ways of accomplishing this, but here we choose to compute these gradients directly at the cell wall centers where they ar needed to evaluate the viscous flux terms. This is done by the chain rule and completely centered differences of x,y,z,u,v,w,T with respect to the computational coordinates ξ,η,ζ. A brief description of the method is presented below.

Full Navier-Stokes Equations

Applying the cell-centered finite volume discretization technique to the full Navier-Stokes equations on an arbitrary non-orthogonal structured grid we obtain the semi-discrete equation

$$\begin{aligned} VOL_{ijk}\frac{d}{dt}Q_{ijk} &+ F_{i+\frac{1}{2},j,k} - F_{i-\frac{1}{2},j,k} \\ &+ G_{i,j+\frac{1}{2},k} - G_{i,j-\frac{1}{2},k} \\ &+ H_{i,j,k+\frac{1}{2}} - H_{i,j,k-\frac{1}{2}} = VOL_{ijk}\,R_{ijk} \end{aligned} \qquad (1)$$

where

VOL_{ijk} = volume of grid cell ijk

Q_{ijk} = $[\rho, \rho\bar{v}, \rho(e+\frac{1}{2}v^2)]$ at center of cell ijk

$F_{i+\frac{1}{2},j,k}$ = integrated flux of mass, momentum, energy through cell wall between cells ijk and i+1,j,k

G,H = corresponding fluxes in j and k directions

R_{ijk} = lower order terms, at center of cell ijk

The fluxes in the three coordinate directions are computed in the following manner: The inviscid (Euler) part is computed in the standard manner, i.e. by using averages of cell-centered values as approximations of wall-centered values. The viscous part is calculated by first approximating the gradients of u,v,w,T at wall centers and then using these values directly in evaluating the diffusive fluxes. However, for the standard definition of the viscous stress terms, ie.

$$\bar{\bar{\tau}} = \mu\,(\,\nabla\bar{v} + \tilde{v}\nabla\,) - \frac{2}{3}\mu\,(\nabla\cdot\bar{v})\,\bar{\bar{I}} \qquad (2)$$

it is possible to combine these two steps and thereby obtain a simple expression for the integrated flux. For example, the integrated flux of momentum due to viscosity between grid cells ijk and i+1,j,k can be approximated by

$$\begin{aligned} \bar{\bar{\tau}}_{i+\frac{1}{2},j,k}\cdot\overline{\overline{SI}}_{i+\frac{1}{2},j,k} \cong \mu_{i+\frac{1}{2},j,k}\,VOL^{-1}_{i+\frac{1}{2},j,k}\,\Big[\,&(\overline{\overline{SI}}\cdot\overline{\overline{SI}})\,\frac{\partial\bar{v}}{\partial i} + (\overline{\overline{SI}}\cdot\overline{\overline{SJ}})\,\frac{\partial\bar{v}}{\partial j} \\ &+ (\overline{\overline{SI}}\cdot\overline{\overline{SK}})\frac{\partial\bar{v}}{\partial k} + (SI\cdot\frac{\partial\bar{v}}{\partial i})\overline{\overline{SI}} + (\overline{\overline{SI}}\cdot\frac{\partial\bar{v}}{\partial j})\overline{\overline{SJ}} + (\overline{\overline{SI}}\cdot\frac{\partial\bar{v}}{\partial k})\overline{\overline{SK}} \\ &- \frac{2}{3}(\,\overline{\overline{SI}}\cdot\frac{\partial\bar{v}}{\partial i} + \overline{\overline{SJ}}\cdot\frac{\partial\bar{v}}{\partial j} + \overline{\overline{SK}}\cdot\frac{\partial\bar{v}}{\partial k})\overline{\overline{SI}}\,\Big]_{i+\frac{1}{2},j,k} \end{aligned} \qquad (3)$$

where all terms inside the large bracket are evaluated at i+½,j,k. The metric term $\overline{\overline{SI}}(i+\frac{1}{2},j,k)$ is here the standard normal surface area vector ($\bar{n}S$) for the cell wall between grid cells ijk and i+1,j,k and is therefore easily obtained. However, the corresponding normal surface area vector in the j direction, $\overline{\overline{SJ}}$, is in the standard implementation only defined for integer i,k values and fractional j values and we are thus forced to construct $\overline{\overline{SJ}}(i+\frac{1}{2},j,k)$ in a nonstandard manner. Here we choose to approximate it by averaging the four nearest available vectors, i.e.

$$\overline{\overline{SJ}}_{i+\frac{1}{2},j,k} \cong \frac{1}{4}\,(\overline{\overline{SJ}}_{i,j-\frac{1}{2},k} + \overline{\overline{SJ}}_{i,j+\frac{1}{2},k} + \overline{\overline{SJ}}_{i+1,j-\frac{1}{2},k} + \overline{\overline{SJ}}_{i+1,j+\frac{1}{2},k}) \qquad (4)$$

For the same reason we approximate $\overline{\overline{SK}}(i+\frac{1}{2},j,k)$ by

$$\overline{\overline{SK}}_{i+\frac{1}{2},j,k} \cong \frac{1}{4}\,(\overline{\overline{SK}}_{i,j,k-\frac{1}{2}} + \overline{\overline{SK}}_{i,j,k+\frac{1}{2}} + \overline{\overline{SK}}_{i+1,j,k-\frac{1}{2}} + \overline{\overline{SK}}_{i+1,j,k+\frac{1}{2}}) \qquad (5)$$

The remaining metric term VOL^{-1} is finally approximated by

$$VOL^{-1}_{i+\frac{1}{2},j,k} \cong \frac{1}{2}\left(VOL^{-1}_{i,j,k} + VOL^{-1}_{i+1,j,k} \right) \tag{6}$$

The derivatives of the velocity vector $\bar{v} = (u,v,w)$ with respect to the three coordinate directions i,j,k are approximated by

$$\left(\frac{\partial \bar{v}}{\partial i}\right)_{i+\frac{1}{2},j,k} \cong \bar{v}_{i+1,j,k} - \bar{v}_{i,j,k}$$

$$\left(\frac{\partial \bar{v}}{\partial j}\right)_{i+\frac{1}{2},j,k} \cong \frac{1}{4}\left(\bar{v}_{i,j+1,k} + \bar{v}_{i+1,j+1,k} - \bar{v}_{i,j-1,k} - \bar{v}_{i+1,j-1,k} \right) \tag{7}$$

$$\left(\frac{\partial \bar{v}}{\partial k}\right)_{i+\frac{1}{2},j,k} \cong \frac{1}{4}\left(\bar{v}_{i,j,k+1} + \bar{v}_{i+1,j,k+1} - \bar{v}_{i,j,k-1} - \bar{v}_{i+1,j,k-1} \right)$$

Finally, the viscosity μ is obtained by

$$\mu_{i+\frac{1}{2},j,k} \cong \frac{1}{2}\left(\mu_{i,j,k} + \mu_{i+1,j,k} \right) \tag{8}$$

which means that μ need only be defined and stored at cell centers. Equations (3)-(8) constitute a formula by which the viscous momentum flux across a constant-i cell wall can be approximated in terms of the standard metric quantities $\bar{SI}$,$\bar{SJ}$,$\bar{SK}$,VOL used in the inviscid case. Analoguous formulas can be written for the corresponding fluxes in the j and k directions and the energy fluxes due to viscosity and heat conduction can also be approximated in this manner.

Since the approximations discussed above for the viscous terms are completely centered and also as compact as possible they are consistent with the second order accuracy obtained for the inviscid terms. A practical demonstration of the accuracy of the overall scheme is presented in Fig 1, where a 2D laminar viscous solution for a NACA 0012 airfoil at M_∞=0.85, α=0, Re=500 (test case A5 of ref 10) is shown for both a coarse 65x33 and a fine 129x65 grid. The fact that both grids give virtually identical results serves to verify the scheme and to indicate its inherent accuracy.

Thin Layer Approximation

In the case of high Reynolds number flow with thin (usually turbulent) boundary layers, it is natural to use a computational grid which reflects the fact that gradient normal to the walls are much larger than streamwise gradients. This leads to grid cells of very high aspect ratio in the boundary layer regions, a feature which can be used to minimize the computational work involved. In the case of a radial compressor, assuming a standard H-type grid with i=streamwise direction, j=blade-to-blade direction and k=hub-to-shroud direction, it is clear that gradients in the j and k directions will be much larger than those in the i direction in the wall regions. This fact leads to a considerable simplification of the viscous flux terms. First of all, the viscous fluxes in the i direction can be neglected. Next, all terms in the j and k fluxes involving i-derivatives can be ignored. Finally, if the corner regions are ignored, all k-derivatives in the j fluxes and all j-derivatives in the k fluxes can be discarded. This gives us the remaining thin layer[11] terms

$$\bar{\tau}_{i+\frac{1}{2},j,k} \cdot \bar{SI}_{i+\frac{1}{2},j,k} \cong 0 \tag{9}$$

$$\bar{\tau}_{i,j+\frac{1}{2},k} \cdot \bar{SJ}_{i,j+\frac{1}{2},k} \cong \mu_{i,j+\frac{1}{2},k} VOL^{-1}_{i,j+\frac{1}{2},k} \left[(\bar{SJ}\cdot\bar{SJ})\frac{\partial \bar{v}}{\partial j} + \frac{1}{3}(\bar{SJ}\cdot\frac{\partial \bar{v}}{\partial j})\bar{SJ} \right]_{i,j+\frac{1}{2},k}$$

$$\bar{\tau}_{i,j,k+\frac{1}{2}} \cdot \bar{SK}_{i,j,k+\frac{1}{2}} \cong \mu_{i,j,k+\frac{1}{2}} VOL^{-1}_{i,j,k+\frac{1}{2}} \left[(\bar{SK}\cdot\bar{SK})\frac{\partial \bar{v}}{\partial k} + \frac{1}{3}(\bar{SK}\cdot\frac{\partial \bar{v}}{\partial k})\bar{SK} \right]_{i,j,k+\frac{1}{2}}$$

which are much simpler than the corresponding complete terms and which do not add much computational work to that needed for the inviscid flux terms.

Turbulence Model

The turbulence model used in this work is the algebraic Baldwin-Lomax model[11]. Although the validity of this model can be questioned for the type of flows computed here, it was chosen as a base line model because of its simplicity. A brief outline of its implementation for turbomachinery flow is given below.

In the case of turbomachinery flow, assuming a standard H-type grid with i=streamwise direction, j=blade-to-blade direction, k=hub-to-shroud direction, we have three different regions to consider: 1) the region upstream of the blades, 2) the region between the blades, and 3) the region downstream of the blades. In the first region we only have the hub and shroud walls to deal with, i.e. k=1 and k=kmax, since we impose periodic conditions at j=1 and j=jmax. The implementation of the turbulence model is thus straightforward in this region. In the second region the situation is more complex since we now have four solid walls (j=1,j=jmax,k=1,k=kmax) to deal with. Here we solve the problem by applying the turbulence model only in four specified nonoverlapping wall regions and then extending the definition of μ_T to the remaining areas (corners and central region) by transfinite interpolation. Finally, in the third region we have the same situation as in the first region except for the wake from the blade trailing edge. Since our grid is not adapted to the wake position we here choose to ignore the effect of wake turbulence and thus treat the third region in the same manner as the first one. This simplification can be justified if we are mainly interested in the flow in the first and second regions.

Additional Features

Just as in the inviscid case we use the concept of local time step scaling in order to accelerate the convergence to steady state. In the estimation of the local spectral radius of the semi-discrete scheme (1) the effect of the viscous terms has been included so that the method works equally well regardless of whether it is the inviscid or the viscous terms which dictate the maximum time step.

The boundary conditions used for the viscous solution procedure are identical to those used for the Euler solver except for the solid wall conditions, where the no-slip condition is imposed and either a temperature or a wall heat flux is specified. For the Eckardt impeller case the zero wall heat flux condition was used since no wall temperature data was given.

Computer Implementation

The four main computer codes involved in this work, a grid generation code, an Euler code, a full Navier-Stokes code and a thin layer N-S code, have been vectorized for and run on a well known vector processor (Cray XMP). Except for the grid code, which is based on transfinite interpolation and therefore consumes negligible amounts of CPU time, the codes have all been structured so as to take maximum advantage of the vectorization effect. Typical speeds for the various codes are as follows: Euler and thin layer N-S codes ~ $20 \cdot 10^{-6}$ sec/grid point/time step, full N-S code ~ $50 \cdot 10^{-6}$ sec/grid point/time step. The performance of the full N-S code can probably be improved by 10-15% by minor changes.

For the viscous computations a previously obtained inviscid solution was used as initial solution. Since the inviscid and viscous flow codes were run on different grids an interpolation code was used to transfer the inviscid solution from the "inviscid" grid to the "viscous" grid. A considerable amount of CPU time was saved through this procedure.

Typically grid sizes and numbers of time steps for the Eckardt impeller are as follows: Inviscid solution - 1000 steps on a 61 x 17 x 17 grid. Viscous solution - 2000 steps on a 61 x 30 x 30 grid, starting from the interpolated inviscid solution. The solutions were considered to be stationary when the mass flow at several stations distributed between inflow and outflow varied less than 1%.

RESULTS

Description of the test case

Dr. D. Eckardt performed between 1970 and 1977 at DFVLR, Cologne, a detailed investigation of the flow within several high-speed centrifugal impellers. Using an advanced laser velocimeter he measured the absolute velocity pattern, the flow angle distribution and turbulence intensity. The first results from his work were published in the middle of the seventies[9], and were then the first data giving an overall picture of the flow within a centrifugal compressor impeller running under realistic conditions. Therefore, Eckardt's measurements have been used by several scientists as a test case for checking and calibrating theoretical/numerical methods.

The impeller we consider here is a radial discharge type with 20 blades. Fig 2 shows the main dimensions in a meridional plane along with the locations of the five cross-flow planes where the measurements were done. A detailed description of the impeller geometry can be found in[12]. The calculations presented here are for the optimum design point with a mass flow rate of 5.31 kg/s and rotational speed of 14000 rpm. At this condition the impeller tip speed is 293.2 m/s and the static pressure rise over the impeller is about 1.5:1.

Fig 3 shows contour plots of measured meridional velocity normalized with rotor tip speed. At planes I and II, i.e. the inducer, the flow exhibits a potential character with positive slope of velocity from pressure side to suction side and from hub to shroud. At plane III, which is located in the area where the flow shifts from axial to radial, the start of a wake can be seen in the shroud/suction corner. This wake develops rapidly downstream and at planes IV and V a pronounced jet/wake is observed. At outlet it occupies a quarter of the flow area. The jet/wake pattern in the radial part of the impeller is caused by viscous effects. The influence of Coriolis forces on the suction side boundary layer combined with a deceleration along the shroud surface, implies that the flow separates in the shroud/suction corner. Due to the appearance of a secondary flow, low-energy fluid from the boundary layers are fed into the wake. An increase in the intensity of secondary flow downstream of plane II indicates that this wake grows rapidly.

Inviscid calculation

Fig. 4 shows a 3D view of the inviscid H-grid. The flow filed is discretized by 17 equally spaced streamwise surfaces, 17 equally spaced bladewise surfaces and 61 spanwise surfaces (leading and trailing edges of the blade corresponding to respectively spanwise surfaces 15 and 52).

Experience with the Euler code has shown that the use of measured values of static pressure tends to produce a solution with higher mass flow than measured. Hence, to get the correct mass flow in the impeller we specified an exit static pressure 0.1 bar higher than measured by Eckardt. Fig 5 shows velocity vectors at suction surface, midpitch and pressure surface. Fig 6 shows contours of meridional velocity in the five cross flow planes corresponding to Eckardt's planes I-V, while Fig 7 shows the secondary flow in the same planes. A comparison of the plots of isolines shows that the agreement between measurements and calculation is good in the inducer and up to plane III, due to the potential character of the flow. Downstream of plane III, our inviscid calculation cannot simulate the jet/wake pattern of the flow. Looking at the secondary flow we can see the two passage vortices, starting in plane II and continuously increasing in intensity up to rotor exit. At plane V the two vortices have merged together. Due to the secondary flow in the channel there is a deviation between the relative flow and the blade, Fig 8. At hub and midchannel the flow has a pronounced component towards the pressure side of the blade, while at shroud it is directed towards the suction side of the blade. At exit this effect is usually called the slip effect of centrifugal impeller.

Thin-layer Navier-Stokes calculation

The grid size is in this case 61*30*30. This code gives almost the correct mass flow in the impeller (within 1.7%) with the use of the same exit static pressure as measured by Eckardt. Fig 9 shows velocity vectors in five meridional planes between suction- and pressure side of the blades. Fig 10 shows contours of meridional velocity in the five cross-flow planes corresponding to Eckardt's measurements planes I-V, while Fig 11 shows the secondary flow in the same planes. A comparison of the isolines shows the first evidence of three-dimensional boundary layer accumulation already at plane II. The wake grows rapidly from this point and causes a significant blockage in the flow. The extent of this wake is too large when compared with measurements, but the overall wake development seems to be realistic. Comparing the plots of secondary velocity with the same plots for the inviscid case, we see that the structure of the flow is the same in both cases for all the five cross-flow planes, but especially in the radial part of the impeller there are some deviations due to the extra vorticity created in the viscous case. Fig 12 shows the velocity vectors in five streamwise surfaces between hub and shroud. This flow is closely related to the secondary flow in the channel.

Full Navier-Stokes calculation

We have here used the same grid as for the thin-layer Navier-Stokes calculation. Fig 13 shows contours of meridional velocity in the five cross-flow planes. When compared with the solution from the thin layer Navier-Stokes calculation, Fig 10, only very small deviations can be seen.

The calculated static pressure distribution (p/p_{inlet}) on the shroud wall for both the inviscid and viscous case is compared with Eckardt's instantaneous shroud static pressure measurements, Fig 14. The long lightly-loaded inducer is clearly seen, as well as the rise in pressure to a static pressure ratio of approximately 1.5 at the impeller exit and the subsequent rise in the vaneless diffuser. It is evident that the viscous solution is significantly closer to the experimental data than the inviscid solution especially in the outlet region.

CONCLUSIONS

The results presented above indicate that an inviscid (Euler) flow model can predict the compressible flow in a radial compressor with reasonable accuracy from the inlet to

the transition area between the axial and radial part of the channel. Downstream of this area it is clear that the viscous effects are significant and cannot be ignored. The corresponding results of the viscous flow model are unquestionably closer to reality in this region, even though the predicted start and subsequent development of the shroud/suction side wake is not quite right. There are several possible explanations for this overpredicted wake, but the most likely one is perhaps the primitive turbulence model used. Since the algebraic turbulence model used gives very little turbulent mixing outside the wall regions, it is possible that the wake growth rate in the calculation is too high once most of the wake is outside the wall region. However, there is also the possibility that a blade-fixed shroud (calculations) may give a different wake development than a non-rotating shroud with tip leakage (experiments). This effect has not yet been investigated with the present method.

As mentioned in the previous section the obtained viscous flow solution comes fairly close to the measured mass flow-pressure ratio combination (1.7% error in mass flow for the correct pressure ratio), in contrast to the Euler solution where the pressure ratio had to be significantly increased (~0.1 bar) to obtain the same mass flow. This fact indicates that the viscous solution procedure gives more or less the right amount of entropy production, i.e. the turbulence model works quite well in a global sense.

The comparison between the thin-layer version and the full version of the Navier-Stokes solver shows that the thin-layer approximation is valid for this type of flow. This means that not only can all streamwise viscous fluxes and all crosswise viscous fluxes involving streamwise gradients be ignored, but also the cross-derivative terms of the crosswise viscous fluxes. As mentioned previously this simplifies the viscous flow code substantially and makes it practically as fast as the Euler code on the same grid.

The results obtained here demonstrate beyond any doubt that explicit time-stepping schemes are of practical use for both inviscid and viscous flows. The use of local time step scaling and interpolation procedures to transfer solutions from one grid to another are possibly the key factors here. Since the grid used for viscous flow simulation is like an Euler grid in the interior of the channel and like a Navier-Stokes grid in the wall region, it is likely that the use of local time step scaling increases the speed of transient waves along the center region of the channel and thereby accelerates the overall convergence. Furthermore, by using an inviscid solution as initial solution for the viscous flow solver it is clear that the transient waves involved will be much smaller and the number of time steps needed for the convergence criteria to be satisfied will be correspondingly smaller.

Acknowledgement

The authors would like to thank Prof. H. Nørstrud at the Division of Hydro- & Gas Dynamics, NTH, for initiating this work, for providing us with the necessary computer resources and for valuable technical discussions. We would also like to thank Dr. Ing. Stud. Erland Ørbekk for much valuable help with computer graphics.

REFERENCES

1. Denton, J.D., "A Time Marching Method for Two- and Three-dimensional Blade-to-Blade Flow", Aeronautical Research Council R&M 3775, 1975.

2. Jameson, A., Schmidt, W. and Turkel, E., "Numerical Solutions of the Euler Equations by Finite Volume Methods Using Runge-Kutta Time-Stepping Schemes", AIAA Paper 81-1259, June 1981.

3. Subramanian, S.V. and Bozzola, R., "Application of Runge-Kutta Time Marching Scheme for Computation of Transonic Flows in Turbomachines", AAIA Paper 85-1332, July 1985.

4. Eriksson, L.E., "Simulation of Transonic Flow in Radial Compressors", Computer Methods in Applied Mechanics and Engineering 64, 1987, pp. 95-111.

5. Billdal, J.T. and Wilson, A., "Radial Compressor Design Using a Euler Solver", Presented at NATO/AGARD Symposium: Technology for Advanced Aero Engine Components, Paris, May 4-8, 1987.

6. Haase, W., Wagner, B. and Jameson, A., "Development of a Navier-Stokes Method Based on a Finite-Volume Technique for the Unsteady Euler Equations", Proc. 5th GAMM Conf. on Num. Meth. in Fluid Mech., eds. M. Pandolfi & R. Piva, Notes on Num. Fluid Mech., Vol. 7, Vieweg, Braunschweig , 1984, pp. 99-107.

7. Muller, B. and Rizzi, A., "Runge-Kutta Finite-Volume Simulation of Laminar Transonic Flow over a NACA 0012 Airfoil Using the Navier-Stokes Equations", FFA TN 1986-60, Stockholm, 1986.

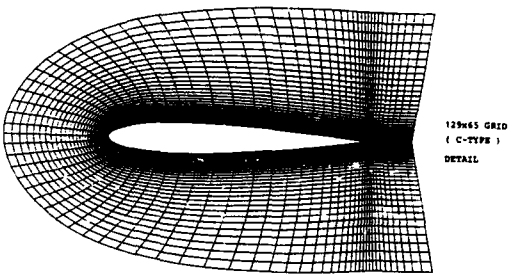
8. Eriksson, L.E., "A Finite Volume Solution Technique for the Navier-Stokes Equations Governing Viscous Compressible Flow", HOG Report No. 8, Trondheim, 1987.

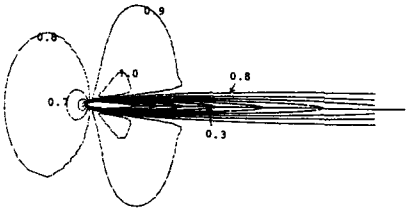
9. Eckhardt, D., "Detailed Flow Investigations Within a High-Speed Centrifugal Compressor Impeller", Journal of Fluids Engineering, Trans. ASME, Series I, Vol. 98, pp. 390-402, 1976.

10. Bristeaux, M.O. and Periaux, J., "Problem (A): External 2D Flow Around a NACA 0012 Airfoil", Proc. of GAMM Workshop on Numerical Simulation of Compressible Navier-Stokes Flows, Nice, Dec. 4-6, 1985, to be published by Vieweg, Braunschweig, 1986.

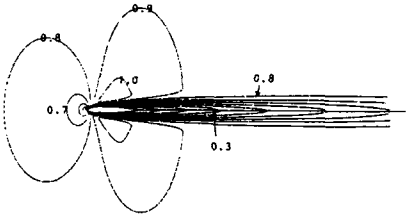
11. Baldwin, B.S. and Lomax, H., "Thin Layer Approximation and Algebraic Model for Separated Turbulent Flows", AIAA 16th Aerospace Sciences Meeting, Huntsville, Alabama, Jan. 16-18, 1978.

12. Schuster, P. and Schmidt-Eisenlohr, U., "Flow Field Analysis of Radial and Backswept Centrifugal Compressor Impellers. Part 2: Comparison of Potential Flow Calculations and Measurements", ASME Publication of Performance Prediction of Centrifugal Pumps and Compressors, pp. 87-95, March 1980.





VISCOUS SOLUTION ON 65x33 C-TYPE GRID AROUND
NACA 0012 AIRFOIL, M_∞=0.85, α=0°, Re=500.
MACH CONTOURS, ΔM=0.1



VISCOUS SOLUTION ON 129x65 C-TYPE GRID AROUND
NACA 0012 AIRFOIL, M_∞=0.85, α=0°, Re=500.
MACH CONTOURS, ΔM=0.1

Fig.1 2D laminar viscous flow with present method.
NACA 0012 airfoil, M_∞=0.85, α=0 , R_e=500.

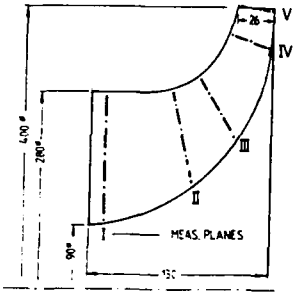


Fig. 2 Meridional cross-section of the DFVLR rotor, dimensions in mm. I-V, measurement planes in the impeller.

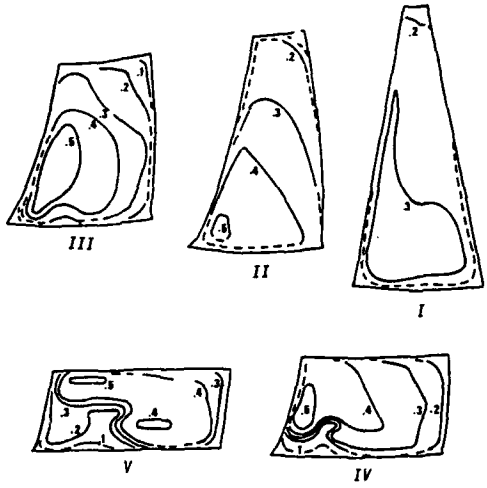


Fig.3 Eckardt's measured countours of meridional velocity normalized with tip speed at the five measurement planes I-V in the impeller.

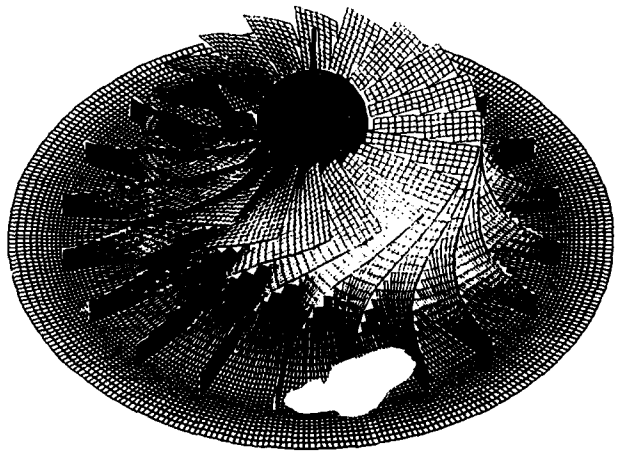


FIG.4 3-D PERSPECTIVE VIEW OF THE INVISCID GRID (61X17X17)

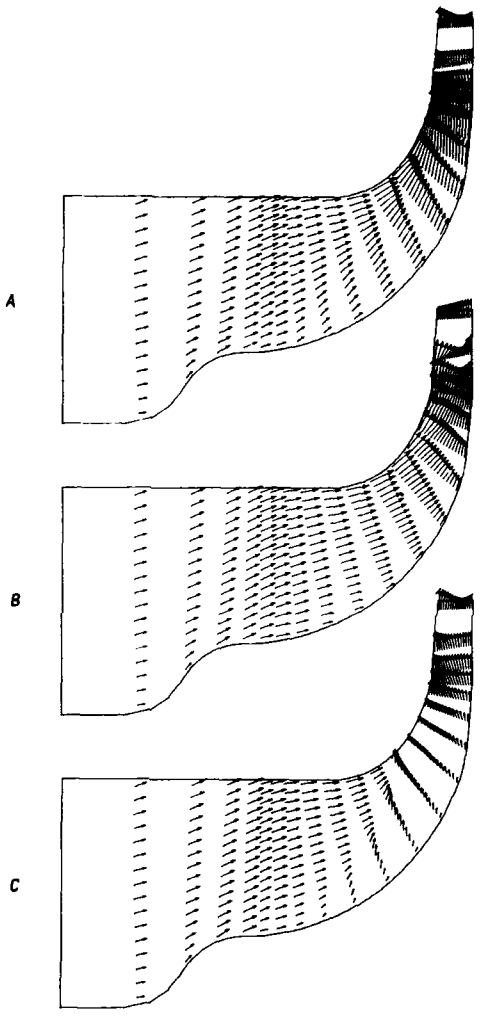


FIG.5 INVISCID CALCULATION : VELOCITY VECTORS AT
A)SUCTION SIDE B)MID PITCH C)PRESSURE SIDE

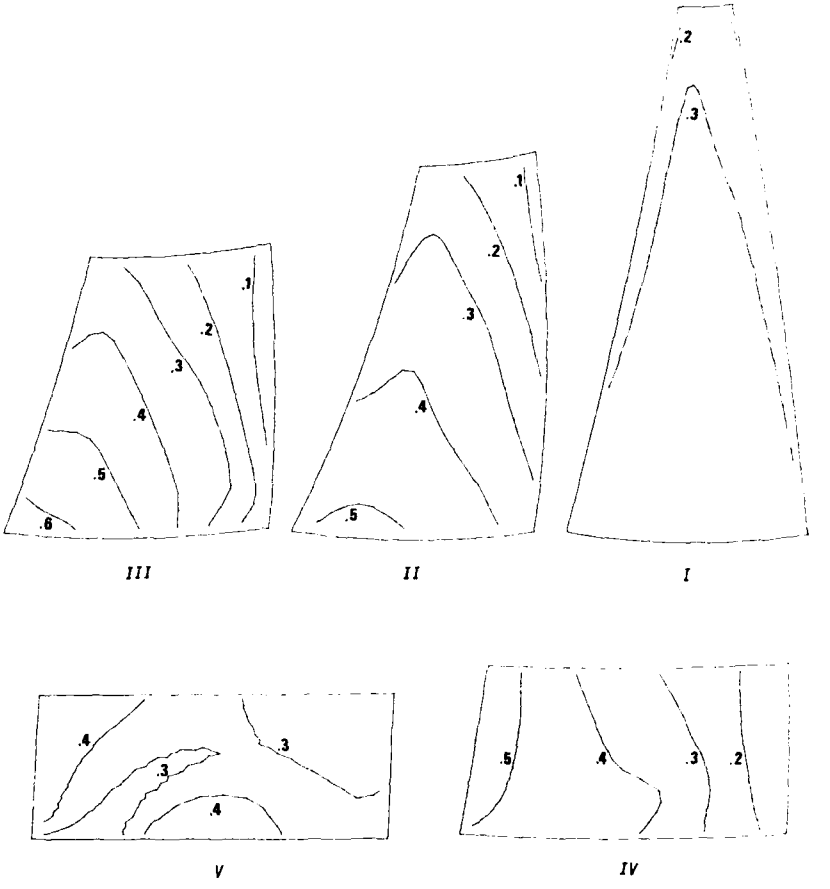


FIG.6 INVISCID CALCULATION : CONTOURS OF MERIDIONAL VELOCITY AT THE FIVE MEASUREMENT PLANES I-V IN THE IMPELLER

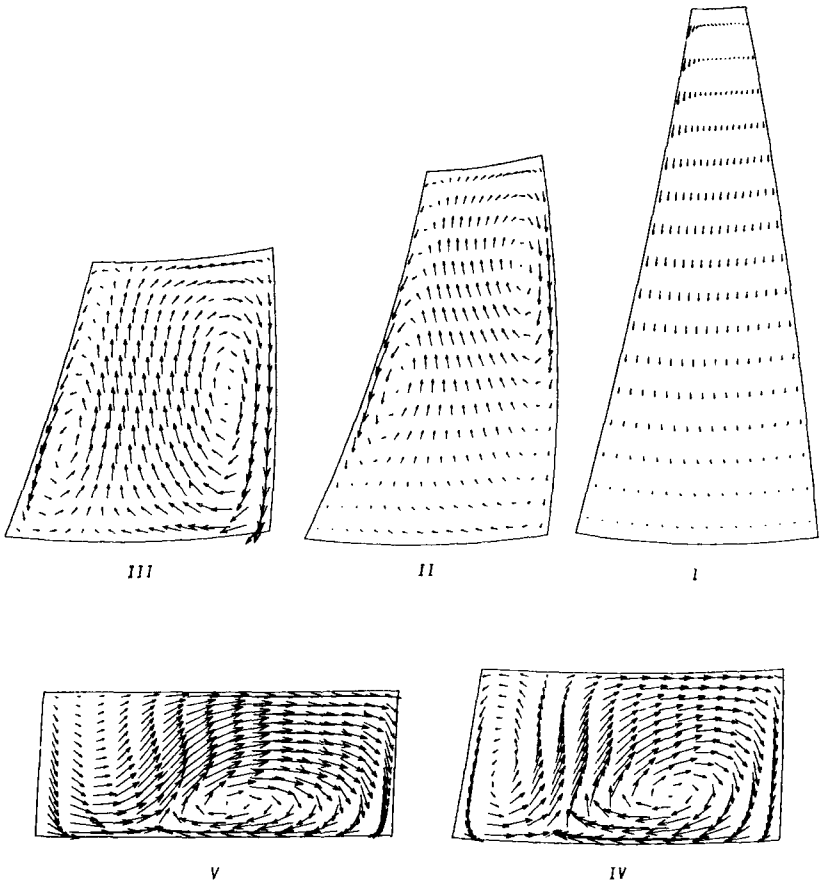


FIG.7 INVISCID CALCULATION : SECONDARY VELOCITY VECTORS AT THE FIVE MEASUREMENT PLANES I-V IN THE IMPELLER

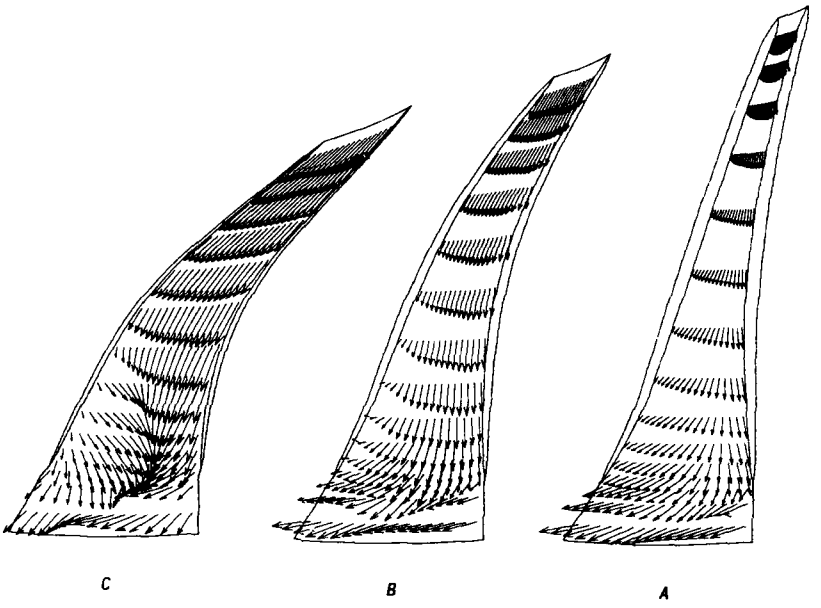


FIG.8 INVISCID CALCULATION : VELOCITY VECTORS AT
A)NEAR HUB B)MID-CHANNEL C)NEAR SHROUD

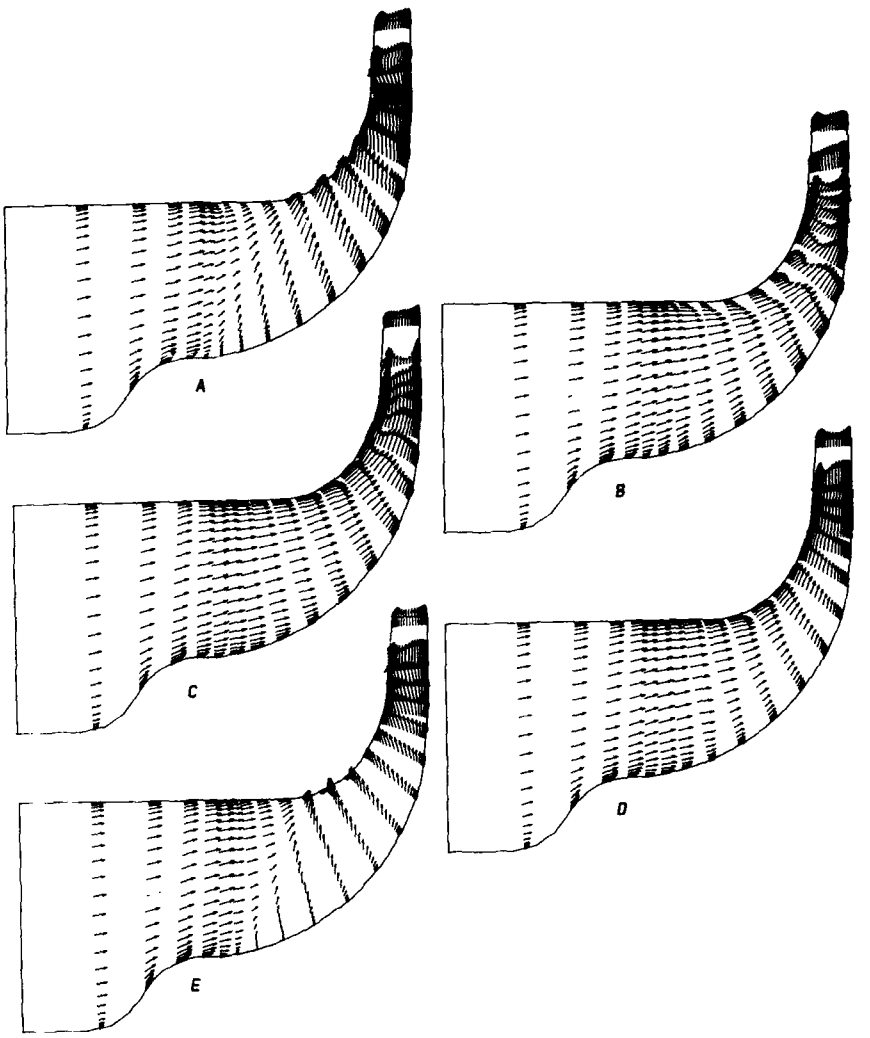


FIG.9 THIN LAYER CALCULATION : VELOCITY VECTORS AT
A)1.1% FROM SUCTION SIDE B)14.1% FROM SUCTION SIDE
C)MID PITCH D)14.1% FROM PRESSURE SIDE
E)1.1% FROM PRESSURE SIDE

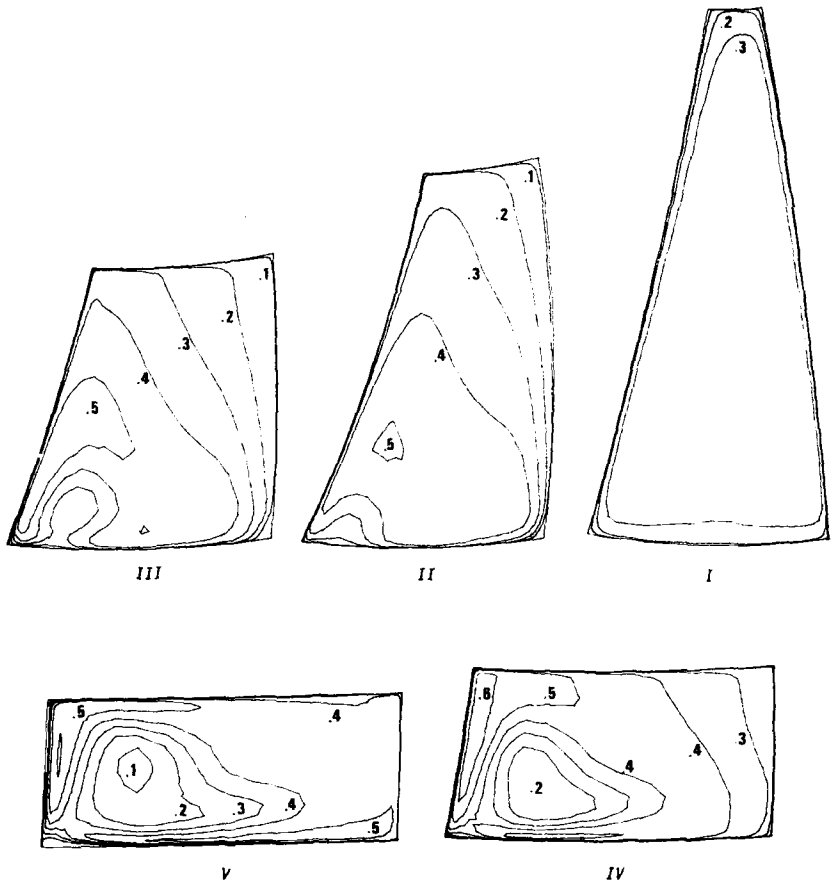


FIG. 10 THIN LAYER CALCULATION : CONTOURS OF MERIDIONAL VELOCITY AT THE FIVE MEASUREMENT PLANES I-V IN THE IMPELLER

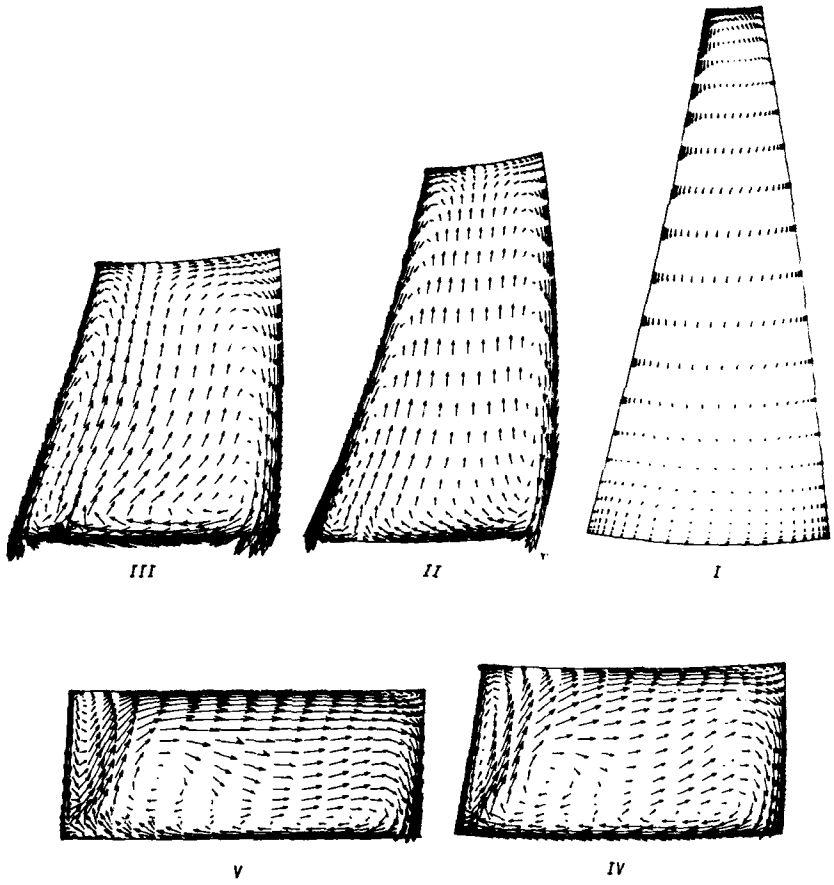


FIG.11 THIN LAYER CALCULATION : SECONDARY VELOCITY VECTORS AT THE FIVE MEASUREMENT PLANES I-V IN THE IMPELLER

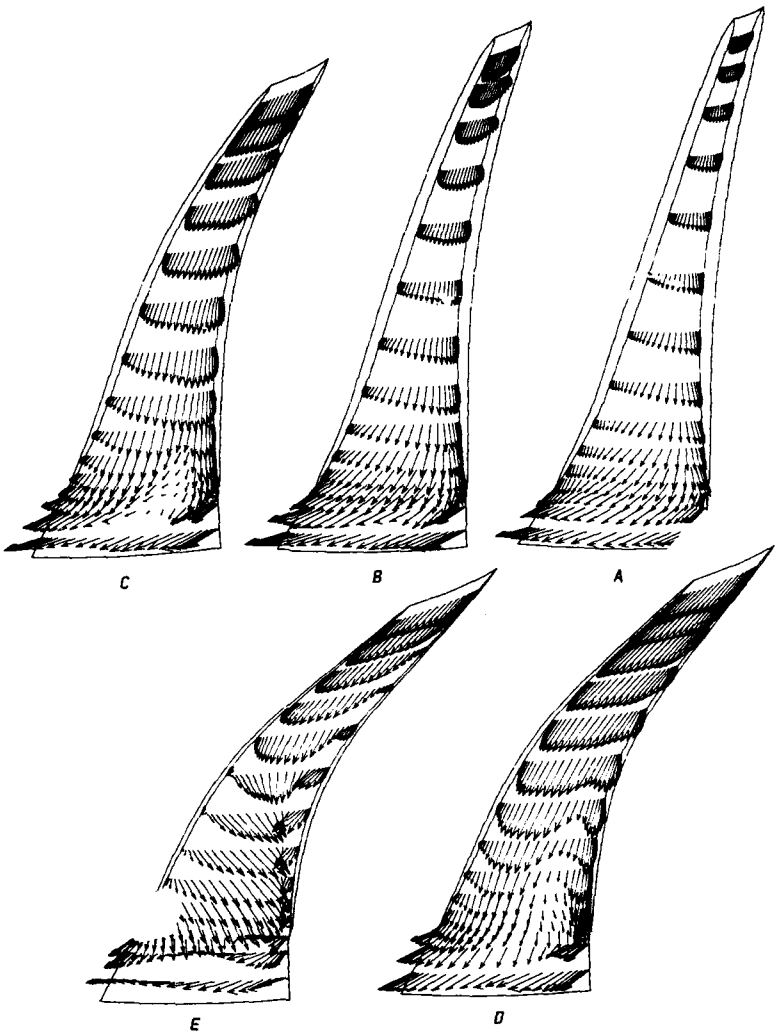


FIG. 12 THIN LAYER CALCULATION : VELOCITY VECTORS AT
A) 1.1% FROM HUB SURFACE B) 14.1% FROM HUB SURFACE
C) MID CHANNEL D) 14.1% FROM SHROUD SURFACE
E) 1.1% FROM SHROUD SURFACE

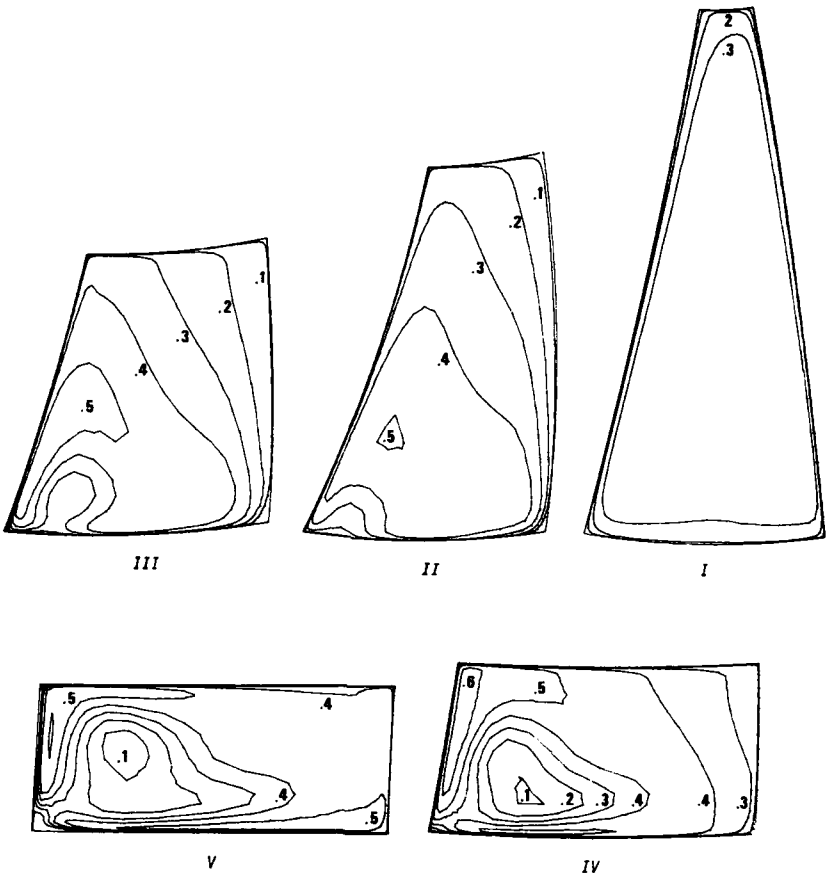


FIG. 13 FULL N-S CALCULATION : CONTOURS OF MERIDIONAL VELOCITY AT THE FIVE MEASUREMENT PLANES I-V IN THE IMPELLER

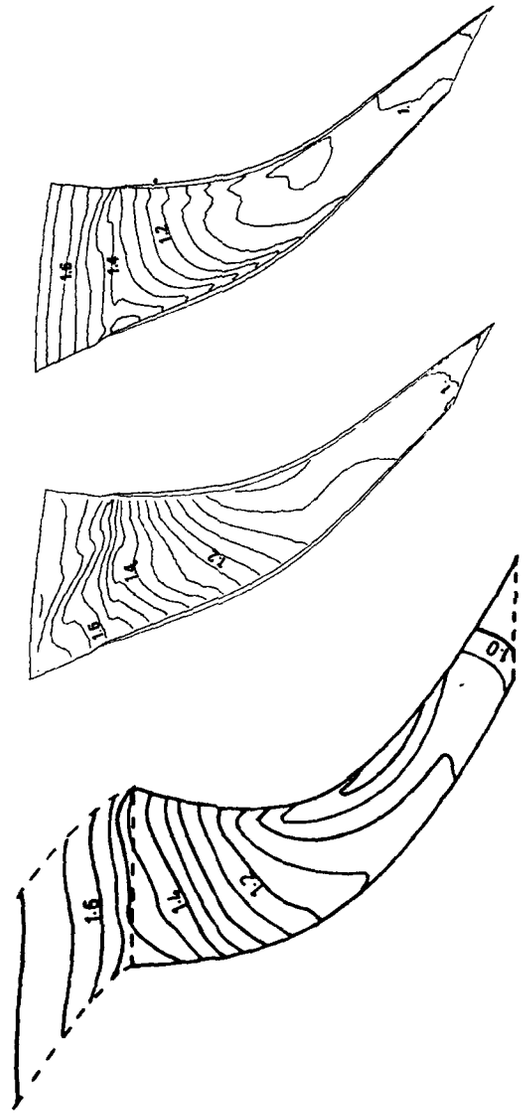


FIG. 14 CONTOURS OF STATIC PRESSURE RATIO ON THE SHROUD SURFACE
A)ECKARDT'S MEASUREMENTS B)INVISCID CALCULATION
C)VISCOUS CALCULATION

Computation of Transonic 3D Cascade Flow and Comparison with Experiments

H.-W. Happel / B. Stubert

MTU Motoren- und Turbinen-Union München GmbH
Dachauer Straße 665, 8000 Munich 50, FRG

SUMMARY

The inviscid turbomachinery flow within a single stator or rotor blade row is computed by a time-marching 3D Euler code. With respect to rotor blades, the conservation laws are formulated in a rotating frame. The numerical scheme is explicit and first order accurate in time and space. Explicit numerical viscosity terms are added to the Euler equations to achieve a stable solution process. In order to save computer time, local time stepping and a grid refining procedure are used in the calculations. The computational efficiency of the code is demonstrated for realistic blade geometries. The comparison with measurements proves the code to be a useful tool for calculating the 3D flow through turbomachinery cascades.

NOMENCLATURE

$\vec{C}$	correction vector
$\vec{e}$	unit vector
e_{rot}	total internal energy with respect to the rotating frame
$\vec{F}$	flux vector
$\vec{H}$	source vector
n	number of time steps
N	number of time steps for one period
p	static pressure
r	radial coordinate
$\vec{S}$	surface vector
t	time
$\vec{U}$	state vector
w	velocity
z	axial coordinate
α	smoothing coefficient
β	flow angle
γ	ratio of specific heats
ε	slope angle of stream surface
ξ,η	curvilinear coordinates
φ	tangential coordinate
ω	angular velocity

Subscripts

a,b,c,d	cell vertex indices
i,j,k	grid point indices in tangential, axial, and radial direction
r	in radial direction
z	in axial direction
l,m	summation indices
φ	in tangential direction
0	updating time level

Superscripts

n	time level index
$\overline{(\,)}$	averaged value
$\vec{(\,)}$	vector
$\tilde{(\,)}$	volume averaged value

INTRODUCTION

The tendency to reduce the number of stages in turbomachinery components results in an increase in stage loading which leads to transonic flow within the blade rows. As the unsteady Euler equations are hyperbolic for subsonic as well as for supersonic Mach numbers, time-marching Euler codes are widely used for the prediction and analysis of transonic flow. The fast development of computer hardware in the last years now allows the industrial use of 3D Euler calculations in turbomachinery with an acceptable accuracy. That means it is possible to discretize the equations with a sufficiently fine grid.

In industrial turbomachinery design the flow is still treated as a steady-state problem today. Therefore, the unsteady Euler equations are used to start from an initial guess to a steady-state solution for a single blade row. In order to design a multistage turbomachine a so-called quasi-3D procedure is used. The fully 3D unsteady turbomachinery flow is approximated by calculating several 2D solutions along hub-to-tip surfaces (S2) as well as blade-to-blade surfaces (S1) and iterating between the two kinds of 2D solutions [2]. In practice it is normally satisfactory to perform only one hub-to-tip solution along a mean S2 stream surface and several blade-to-blade solutions along axisymmetric S1 stream surfaces.

The optimized quasi-3D solution can be refined by 3D Euler computation within discrete blade rows. Therefore, the computational grid has to be extended about one axial chord length upstream and downstream of the cascade in order to assume uniform boundary conditions in circumferential direction. Although the direct influence of the adjacent cascades is lost, the 3D calculation of a single blade geometry is of interest to study lean and bow effects of the blade stagging, for example, or to estimate the choking limit of the cascade.

GOVERNING EQUATIONS

The unsteady 3D Euler equations written in the well known vector notation

$$\int_V \frac{\partial \vec{U}}{\partial t}\, dV = -\int_O \left[\vec{F}_r\, dO_r + \vec{F}_\varphi\, dO_\varphi + \vec{F}_z\, dO_z \right] + \int_V \vec{H}\, dV \qquad (1)$$

$$\vec{U} := \begin{pmatrix} \varrho \\ \varrho w_{rc} \\ \varrho r(w_\varphi + \omega r) \\ \varrho w_z \\ \varrho e_{rot} \end{pmatrix}$$

$$\vec{F}_r := \begin{pmatrix} \varrho w_r \\ (\varrho w_r^2 + p)\cos\Delta\varphi - \varrho w_\varphi w_r \sin\Delta\varphi \\ \varrho r(w_\varphi + \omega r)\, w_r \\ \varrho w_z w_r \\ (\varrho e_{rot} + p)\, w_r \end{pmatrix} \qquad \vec{F}_\varphi := \begin{pmatrix} \varrho w_\varphi \\ \varrho w_r w_\varphi \cos\Delta\varphi - (\varrho w_\varphi^2 + p)\sin\Delta\varphi \\ \varrho r(w_\varphi + \omega r)\, w_\varphi + p \cdot r \\ \varrho w_z w_\varphi \\ (\varrho e_{rot} + p)\, w_\varphi \end{pmatrix}$$

$$\vec{F}_z := \begin{pmatrix} \varrho w_z \\ \varrho(w_r \cos\Delta\varphi - w_\varphi \sin\Delta\varphi)\, w_z \\ \varrho r(w_\varphi + \omega r)\, w_z \\ \varrho w_z^2 + p) \\ (\varrho e_{rot} + p)\, w_z \end{pmatrix} \qquad \vec{H} := \begin{pmatrix} 0 \\ \omega\varrho\left[(2w_\varphi + \omega r)\cos\Delta\varphi + 2w_r \sin\Delta\varphi\right] \\ 0 \\ 0 \\ 0 \end{pmatrix}$$

are solved in integral form.

The total internal energy e_{rot}

$$e_{rot} := \frac{\gamma}{\gamma - 1}\frac{p}{\varrho} + \frac{1}{2}\left(w_r^2 + w_\varphi^2 + w_z^2 - (\omega r)^2\right) \tag{2}$$

is specified for a rotating frame with uniform angular velocity ω. Equation (2), being valid for a calorically perfect gas (γ = const.), gives the closure relation for the static pressure p in the flux terms.

For flow calculations in turbomachinery it is obvious to use cylindrical coordinates. The transformation of the conservation laws into a cylindrical coordinate system, however, produces additional source terms in the momentum equations in radial and circumferential direction. These are caused by a tangential variation of the unit vectors $\vec{e}_r$ and $\vec{e}_\varphi$. To avoid those additional terms two modifications are introduced. Firstly, the radial momentum equation is replaced by a cartesian formulation relative to a fixed radial direction for all grid points. Secondly, the momentum equation in circumferential direction is replaced by the moment of momentum equation in axial direction. Because of this formulation, source terms only originate from the centrifugal and Coriolis forces in the radial momentum equation in a rotating frame.

FINITE VOLUME DISCRETIZATION

The discretization of the physical domain depends on the actual blade geometry. Generally the computational domain is limited by the blade surface, the periodic boundaries, and the inlet and outlet planes, Fig. 1. To obtain a uniform grid around the blade two types of grid generation are available for this Euler code. An H-grid for compressor cascades and relatively thin turbine blades and a C-grid for blunt turbine profiles. Both grid types have regions where the cells are highly distorted, the H-grid near the leading and trailing edge and the C-grid in the region around the trailing edge. On the other hand a C-grid allows grid points to be distributed at the pressure and suction sides independently of each other.

The conservation laws are applied to overlapping control volumes. These are composed of eight basic volumes taking the common nodal point close to the centre of the control volume as reference point.

For calculating the basic volumes, the hexahedra are composed of five tetrahedra, [3]. The volume of one tetrahedron is determined by

$$V_{T_{abcd}} = \frac{1}{6}\begin{vmatrix} r_a & (r\varphi)_a & z_a & 1 \\ r_b & (r\varphi)_b & z_b & 1 \\ r_c & (r\varphi)_c & z_c & 1 \\ r_d & (r\varphi)_d & z_d & 1 \end{vmatrix} \tag{3}$$

where the subscripts (a b c d) refer to the four vertices of the tetrahedron, Fig. 2. Then the basic volume is given by

$$V = V_{T_{1452}} + V_{T_{4857}} + V_{T_{5276}} + V_{T_{4723}} + V_{T_{5247}} \tag{4}$$

The convection term in equation (1) is approximated by

$$\int\left(\vec{F}_r\, dS_r + \vec{F}_\varphi\, dS + \vec{F}_z\, dS_z\right) \approx \bar{\vec{F}}_r \iint r\, d\varphi dz + \bar{\vec{F}}_\varphi \iint dr dz + \bar{\vec{F}}_z \iint r\, dr d\varphi\,. \tag{5}$$

The surface integrals are determined by a numerical mapping (Fig. 3)

$$S_r = \int_0^1\int_0^1 r(\xi,\eta)\frac{\partial(\varphi,z)}{\partial(\xi,\eta)}\, d\xi d\eta \qquad S_\varphi = \int_0^1\int_0^1 \frac{\partial(r,z)}{\partial(\xi,\eta)}\, d\xi d\eta \qquad S_z = \int_0^1\int_0^1 r(\xi,\eta)\frac{\partial(r,\varphi)}{\partial(\xi,\eta)}\, d\xi d\eta \tag{6}$$

to a unit square using bilinear shape functions for the radius

$$r(\xi,\eta) = r_a(1-\xi)(1-\eta) + r_b\xi(1-\eta) + r_c\xi\eta + r_d(1-\xi)\eta \tag{7}$$

and for the circumferential and axial coordinates, respectively. The fluxes F_r, F_φ and F_z are averaged by

$$\vec{F} = \frac{1}{4}(\vec{F}_a + \vec{F}_b + \vec{F}_c + \vec{F}_d). \tag{8}$$

BOUNDARY CONDITIONS

For subsonic axial velocities the theory of characteristics provides four boundary conditions in the inlet and only one in the exit plane.

In the inlet plane the radial distributions of

- the relative stagnation temperature,
- the relative stagnation pressure,
- the relative flow angle β_z = arc ctg (w_φ/w_z) (for subsonic inflow), and
- the slope of the axisymmetric blade-to-blade stream surfaces ξ = arc tg (w_r/w_z)

are imposed assuming uniform values in circumferential direction. If the relative inflow Mach number is supersonic (but w_z is subsonic) the radial distribution of the circumferential component w_φ of the relative velocity is held constant instead of the relative flow angle β_z. Then the unique incidence condition being a function of back pressure is automatically satisfied as a part of the solution.

In the exit plane the static pressure is prescribed only at midspan position, because the corresponding radial distribution is a result of the Euler solution. In order to obtain a uniform static pressure distribution in circumferential direction, the radial equilibrium is fulfilled after each time step using volume-averaged values

$$\left(\overline{\frac{\partial p}{\partial r}}\right) = -\frac{1}{V}\left[\int_S \rho w_r \vec{w}\, d\vec{S} - \int_V \rho \frac{(w_\varphi + \omega r)^2}{r}\, dV\right] \tag{9}$$

of the static pressure gradient in radial direction. The integration of the right hand side of equation (9) is performed over all basic elements at constant radius in pitchwise direction.

As a 3D flow problem is determined at any point in space by a total of five state variables, the axial momentum equation is additionally used in the inlet plane, and all conservation laws with the exception of the energy equation are discretized in the exit plane.

The periodic boundaries (upstream and downstream of the blade row) are treated in the same way as interior nodal points, combining information from the left and right boundary to construct a regular control volume, Fig. 1.

Along the solid walls no mass and energy flux cross the surface because the normal component of the velocity is zero everywhere. The transport of momentum and moment of momentum only consists of the pressure forces perpendicular to the surface. The conservation principles are applied to half or quarter elements and the transient changes are attached to the nodal point of reference lying on the solid walls.

NUMERICAL SCHEME

In order to obtain a stable explicit time-marching algorithm of the discretized Euler equations numerical viscosity must be introduced. The resulting numerical error in the Euler solution can be reduced by the so-called damping surface technique [4]. The characteristic property of this method is the periodic addition of viscous terms during the whole calculation. Numerical viscosity is introduced by the volume-averaged state vector at time level n and is reduced by the lagging correction vector at time level n_o.

Defining a volume-averaged state vector of the control volume $V_{i,j,k}$

$$\vec{\tilde{U}}_{i,j,k} := \frac{1}{\Delta V_{i,j,k}} \sum_{l=1}^{8} \left(\int \vec{U}\, dV\right)_l \tag{10}$$

with the approximation

$$\int \vec{U}\, dV = \frac{V}{8} \sum_{l=1}^{8} \vec{U}_l \tag{11}$$

of the volume integrals of the eight surrounding basic volumes V and using a lagging correction vector

$$\vec{C}_{i,j,k}^{\,n_o} := (1 - \alpha) \left[\vec{U}_{i,j,k}^{\,n_o} - \vec{\tilde{U}}_{i,j,k}^{\,n_o} \right] \tag{12}$$

the unsteady 3D Euler equations are discretized as

$$\vec{U}_{i,j,k}^{\,n+1} = \vec{\tilde{U}}_{i,j,k}^{\,n} + \vec{C}_{i,j,k}^{\,n_o} - \frac{\Delta t}{\Delta V_{i,j,k}} \left[\int_S (\vec{F}_r dS_r + \vec{F}_\varphi dS_\varphi + \vec{F}_z dS_z)^n - \int_V \vec{H}\, dV \right] \tag{13}$$

for the nodal point of reference (i,j,k) close to the centre of the control volume. The transport terms are positive for fluxes leaving the control surface.

During the period of N time steps n_o is constant. At the time level $n = n_o + N$ the correction vector is updated by $n_o = n$ and therefore the discretization becomes an Euler-Lax combination

$$\begin{aligned} \vec{U}_{i,j,k}^{\,n+1} = \vec{\tilde{U}}_{i,j,k}^{\,n} &+ (1 - \alpha) \left[\vec{U}_{i,j,k}^{\,n} - \vec{\tilde{U}}_{i,j,k}^{\,n} \right] \\ &- \frac{\Delta t}{\Delta V_{i,j,k}} \left[\int_S (\vec{F}_r dS_r + \vec{F}_\varphi dS_\varphi + \vec{F}_z dS_z)^n - \int_V \vec{H}\, dV \right] \end{aligned} \tag{14}$$

for the first step of the new period. When the steady-state solution is reached the value of the added viscosity terms decreases. The smoothness of the Euler solution can be adjusted by the smoothing coefficient α, which should be in the range between one and three per cent. The number of N should be chosen as small as possible to increase the convergence rate of the calculation. Although a one-dimensional von Neumann stability analysis yields N equal the number of grid points in flow direction, for many calculations N equal 10 to 15 per cent of the number of grid points in axial direction provide sufficient stability.

The explicit numerical viscosity as well as the boundary discretization using half and quarter elements along the solid surfaces cause first order accuracy in space, while the scheme is also first order accurate in time. For steady-state solutions the latter aspect is less important.

ACCELERATION OF CONVERGENCE

As explicit time-marching procedures are time-consuming with respect to the Courant-Friedrichs-Lewy condition, the convergence is accelerated using local time stepping, because only the steady-state solution is required. This is very useful in connection with grid spacing, in order to achieve a Courant number close to unity everywhere. Furthermore, a two or three level grid-refining procedure reduces computer time.

COMPUTATIONAL RESULTS

The application of the code is demonstrated for two cases of transonic turbomachinery flow. The first calculation deals with a turbine stator and the second one with a compressor rotor. With respect to the thick leading edge the turbine stator is discretized with a C-grid. A meridional view of the periodic boundary and a blade-to-blade section of the C-grid is sketched in Fig. 4a. The surface pressure distributions of the hub, mid and tip section are in quite good agreement with the measured data, Fig. 5. In all sections the flow is strongly accelerated up to a shock on the suction side near the trailing edge. According to the pressure distributions Mach number contours of the three sections are also plotted in Fig. 5.

A further calculation was made for the transonic flow within the first rotor of a low pressure compressor. The calculation of a single compressor rotor without the following stator can require a modification of the compressor duct to avoid annulus blockage. In Fig. 4b the discretization of the compressor rotor using an H-grid is sketched in the meridional (dashed line for the original annulus) and a blade-to-blade section. A purpose of this calculation is to determine the choking flow rate within the rotor, which is identified by a closed sonic line from the suction to the pressure side in the hub section.

Unfortunately, measurements of pressure or velocity distributions along the blade surface are not yet available. The comparison is only possible with the measured choking flow rate through the whole compressor stage. As the mass flow through a given 3D geometry is determined by the back pressure, in the first calculation the "measured" choking flow rate is verified by variation of the static pressure at midspan position in the exit plane. The calculated isomach contours on the left hand side of Fig. 6 and Fig. 7 indicate no choking condition in the hub region. Therefore, in a further calculation the back pressure is decreased in order to reach the "computed" choking flow rate, which is about three per cent higher than the measured one. This result seems to be realistic based on an inviscid calculation. The corresponding isomach contours are plotted on the right hand side of Fig. 6 and Fig. 7. The closed sonic line between suction and pressure side in the hub section (see Fig. 7, r-h side) is characteristic for the "computed" choking flow rate.

CONCLUSIONS

The time-marching 3D Euler code is a good tool for reviewing the fully 3D aerodynamic properties of isolated stator or rotor blades after a quasi-3D turbomachinery design. Furthermore, the 3D influence of differently staggered blades can be studied.

ACKNOWLEDGEMENTS

The reported work was performed at MTU Motoren- und Turbinen-Union München GmbH and was supported within research programmes of the German Bundesministerium für Forschung und Technologie and Bundesministerium der Verteidigung (Ministry of Research and Development and Ministry of Defence). The permission to publish the results is gratefully acknowledged.

REFERENCES

[1] DENTON, J.D.: "An improved time-marching method for turbomachinery flow calculation", ASME paper 82-GT-239 (1982)

[2] WU, C. H.: "A general theory of three-dimensional flow in subsonic and supersonic turbomachines of axial-, radial- and mixed-flow types", NACA TN 2604 (1952)

[3] RIZZI, A., ERIKSSON, L.-E.: "Computation of flow around wings based on the Euler equations, J. Fluid Mech., Vol. 148, pp. 45-71 (1984)

[4] COUSTON, M., McDONALD, P. W., SMOLDEREN, J. J.: "The damping surface technique for time dependent solutions to fluid dynamic problems", VKI TN 109 (1975)

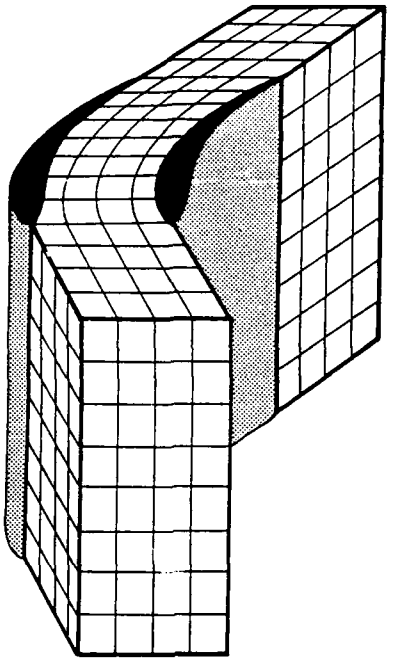


FIG. 1: DISCRETIZED PHYSICAL DOMAIN

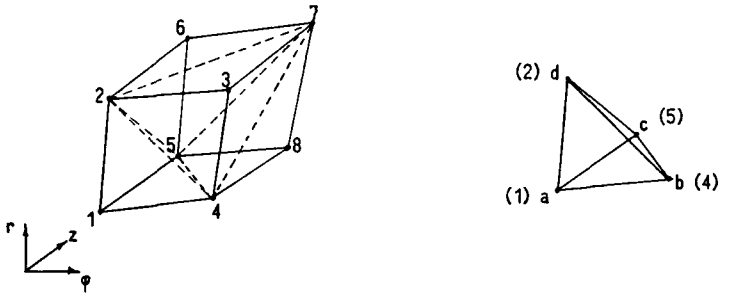


FIG. 2: BASIC VOLUME COMPOSED OF 5 TETRAHEDRA

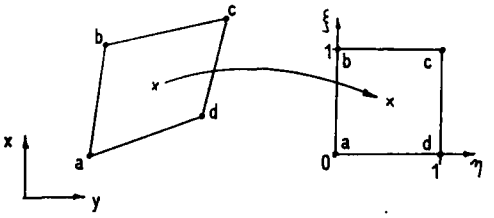
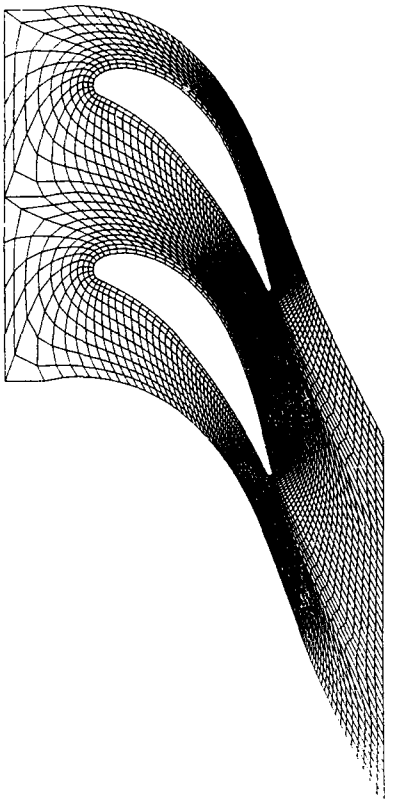
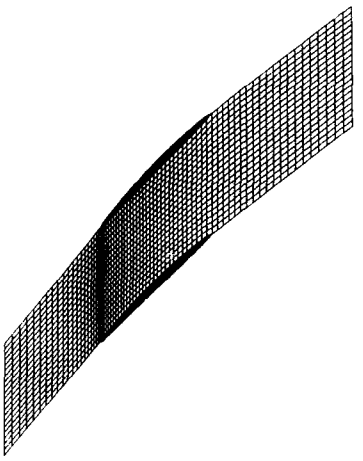


FIG. 3: MAPPING OF A SURFACE INTEGRAL



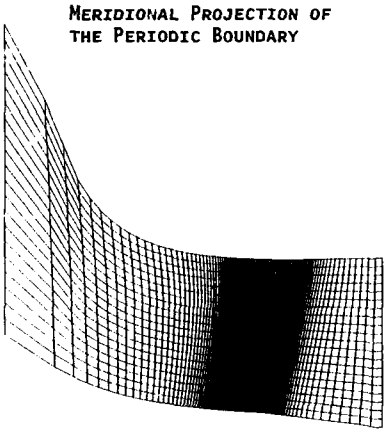
BLADE-TO-BLADE

SECTIONS



MERIDIONAL PROJECTION OF THE PERIODIC BOUNDARY

MERIDIONAL PROJECTION OF THE PERIODIC BOUNDARY AND BLADE SURFACE



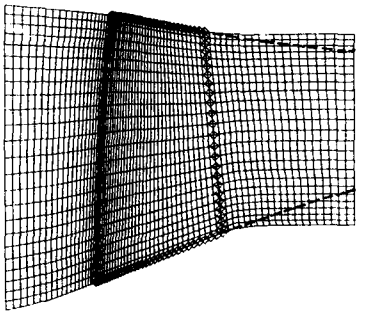


FIG. 4 A: C-GRID OF THE TURBINE STATOR

FIG. 4 B: H-GRID OF THE LOW PRESSURE COMPRESSOR ROTOR

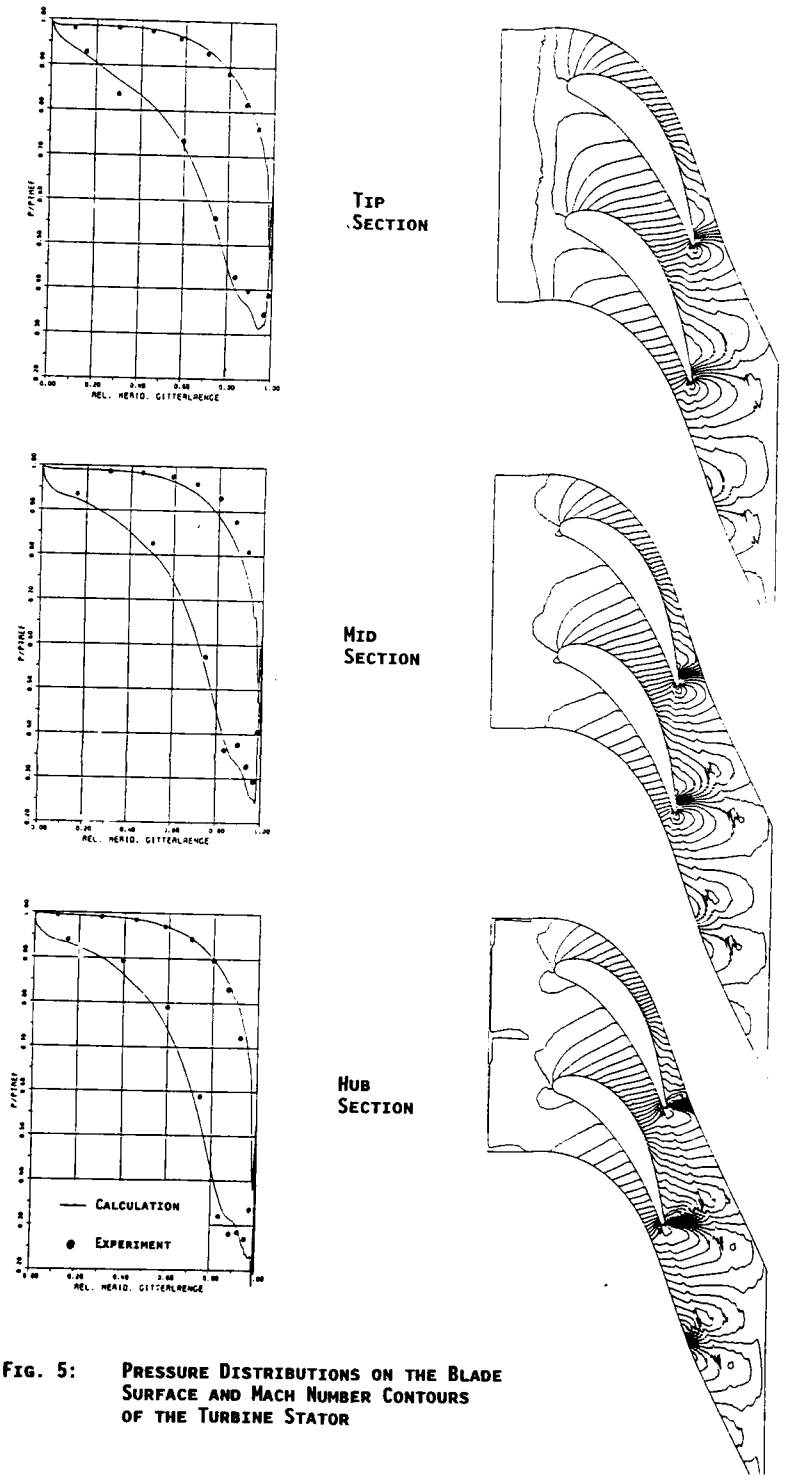


FIG. 5: PRESSURE DISTRIBUTIONS ON THE BLADE SURFACE AND MACH NUMBER CONTOURS OF THE TURBINE STATOR

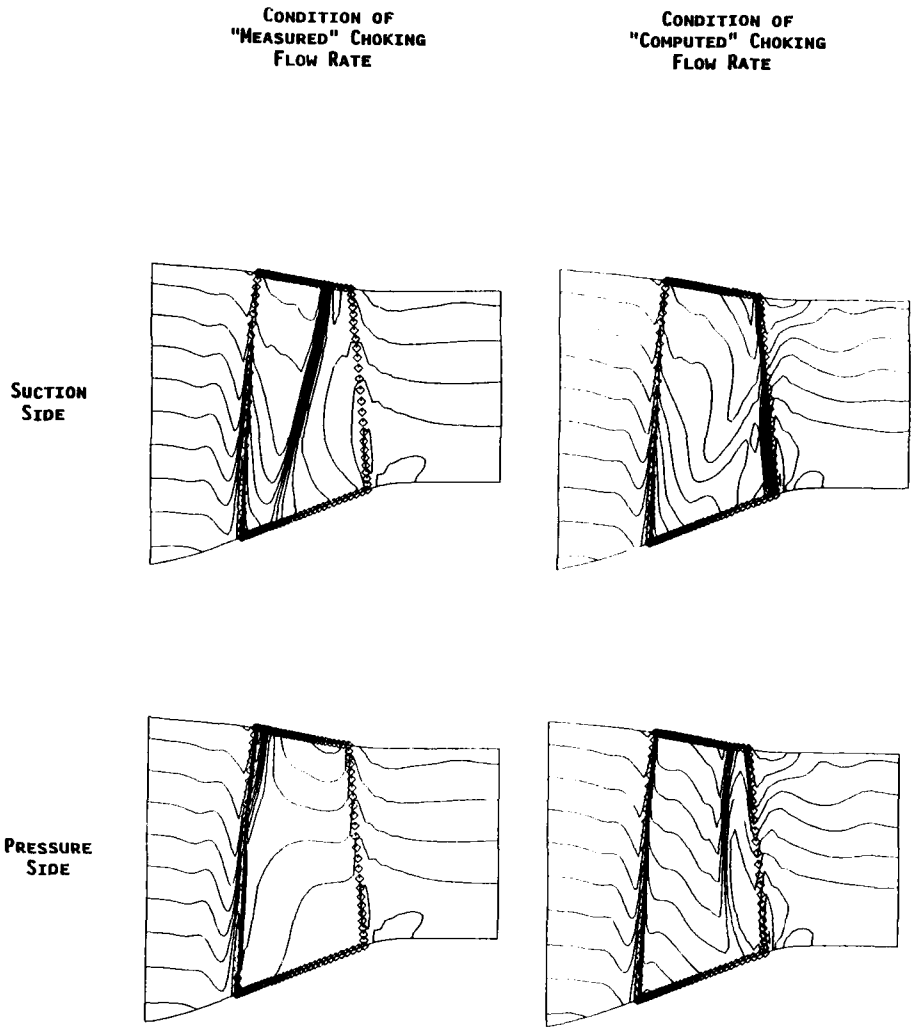


Fig. 6: Mach Number Contours on the Rotor Blade Surface for "Measured" and "Computed" Choking Flow Rate

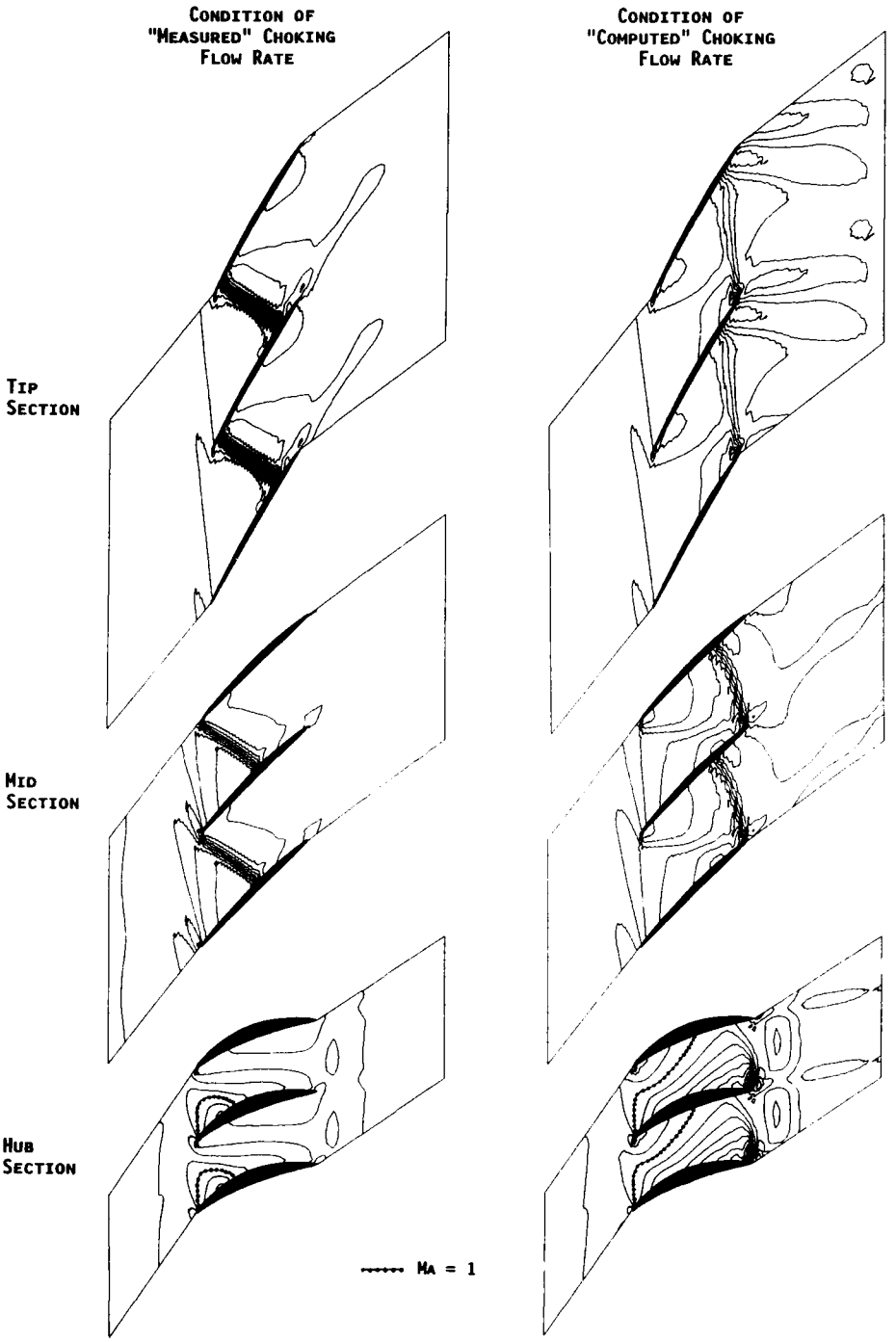


Fig. 7: Mach Number Contours in Blade-to-Blade Sections of the Low Pressure Compressor Rotor.

NUMERICAL AND EXPERIMENTAL INVESTIGATION OF ENGINE INLET FLOW WITH THE DORNIER EM2 SUPERSONIC INLET MODEL*

by

H.Buers and S.Leicher
Dornier GmbH – BF 10
Postfach 1420
D-7990 Friedrichshafen 1
Federal Republic of Germany

and

P.A.Mackrodt
DFVLR
Göttingen
Federal Republic of Germany

ABSTRACT

Numerical and experimental investigations have been conducted with the Dornier EM2 supersonic, fixed geometry, side mounted inlet to improve the performance in the supersonic flight regime. A ramp bleed system was installed to stabilize the inlet flow. The design procedure for the bleedsystem is described and some representative results from windtunnel tests are presented to confirm the procedure. The theoretical investigations were executed with a block structured Euler program, which allowed a more accurate modelling of the realistic aircraft geometry. To simulate boundary layer effects at the ramp of the inlet an outflow velocity perpendicular to the ramp was introduced. The calculated and the experimental data were in good agreement.

1. INTRODUCTION

For many years Dornier has been envolved in the design and development of supersonic inlets for future fighter aircrafts. These investigations, sponsored by the German Ministry of Defense, resulted in improved theoretical design tools and their validation by sub- and supersonic tests on windtunnel models.

The Dornier inlet design procedure is based on the principal to look for a simple, weight and money saving solution. The EM2 supersonic inlet, discussed in this presentation, is a side mounted, D-shaped inlet of fixed geometry (Fig. 1-1). The splitter plate has been designed as an eight degree ramp for flow precompression.

The EM2 model was tested at the DFVLR Göttingen in the supersonic flight regime and in the low speed regime at the DFVLR facilities at Braunschweig. The test results for MA > 1.6 showed a remarkable reduction in the permissible operating range of the engine. The buzz limit, which occurs for the throttled down engine, was shifted to higher mass flow ratios (Fig. 1-2). Since at these Machnumbers the buzz limit depends on the flow situation at the ramp ahead of the inlet tube, which is evident from the Schlieren-pictures in Fig. 1-2, a ramp bleed system was designed in order to reduce the shock induced separation. Thus it was expected to extend the operating range of the engine by shifting the buzz limit to smaller mass flow ratios. Furthermore it was expected, that the flow at the engine face place (EFP) would get less flow distortion and achieve higher pressure recovery.

* This study was sponsored by the German Ministry of Defense, RÜFo IV

2. EM2 RAMP BLEED SYSTEM

2.1 Design Procedure

Based on the idea to build a simple, low cost system the design of the bleed system had to meet the conditions:

- suction is to be accomplished by a porous wall section at the ramp ahead of the lip section;
- suction is to be initiated by a natural pressure drop between the suction area at the ramp and the bleed exit.

The design and test procedure was given by the following steps [20]:

- numerical investigations of the flow field for the fuselage/inlet configuration with a 3D-Euler code;
- boundary layer calculations for the ramp flow, based on the Euler calculations;
- evaluation of former windtunnel tests with the EM2 inlet model;
- definition of the bleed region at the ramp;
- calculation of the required bleed flow;
- design of the bleed components for the model installation;
- extension of theoretical design tools for calculation of bleed effects;
- windtunnel tests;
- comparison of tested and calculated data.

2.2 Numerical Investigations

The accuracy and reliability of numerical results much depends on the accurate representation of the geometry in the calculations, especially if small local effects are considered.

2.2.1 Grid Generation

The grid has been developed completely interactive and menue driven, by the combination of existing CAD-software together with application-oriented programs including the capabilities of a grid generator developed at Dornier /1/. The method allows the construction of blocked and/or unblocked contour conformal grids, which are needed for the later application of the finite volume flow solver. The grid around the EM2 forebody with a side-mounted inlet consists of four block groups in i-direction comprising 18 blocks and about 237.000 grid points. It can be looked at as a grid of the HO-type; H-type in the flow direction and O-type in circumferential direction. The first two circumferential block- rings consist of three blocks while the later two comprise five. The grid is generated by adapting the block arrangement as good as possible to the configuration while keeping the number of blocks as small as possible. Figure 2-1 shows the surface grid, the grid of the symmetry and the downstream farfield plane. The thicker lines indicate block interfaces. Also faded in is the internal grid of the inlet channel. In the third block- ring a new block was inserted just before the inlet, causing two additional blocks in the circumferential direction. The upstream faces of these three blocks degenerate into a single li[illegible] This clearly can be seen in Fig. 2-1, where the block

boundaries at the farfield are plotted. Some details of the grid are shown in the next two figures. The grid of a horizontal plane located at the middle of the inlet shows one special feature of the grid. The block directly in front of the inlet entrance plane has twice as much lines in i-direction as the neighbouring one (Fig. 2-2) in order to get a good resolution of the shocks expected to show up here for supersonic freestream conditions. Figure 2-3 shows two vertical grid planes, the first one is situated near the lip of the inlet while the second one is the engine face plane. The form of the cross section of the inlet channel varies from an almost half circle to a nearly real circle, while the grid is inside of H-type.

2.2.2 Euler Calculations

In order to reduce the numerical and financial expenses, the flow boundary conditions at the engine face station were taken from the previous windtunnel tests without any adjustment.

Flow Solver

The Euler equations are solved basically by the numerical scheme developed by Jameson, Schmidt and Turkel /2/. This is a central difference finite volume method combined with a blended second and fourth order dissipation. The steady state is reached by applying a Runge Kutta type time stepping scheme with an arbitrary number of stages. In order to accelerate local time stepping, enthalpy damping and implicit residual averaging is used. By using a sequence of mesh refinements (multi level grid technique) and applying a multigrid method /3/ at each of these levels acceptable good convergence rates for 3-D cases have been achieved. In order to be able to treat blocked grids a Multi Block Version (MBV) of the method has been developed /4, 5, 6, 7/, which is optimized with regard to computing time as well as to the amount of I/O, which has to be performed. It allows in and out of core computations depending upon the number of grid points and the amount of main storage being available. The method has been applied to external and internal flow problems with and without viscous effects.

Results

First results of the EM2 forebody inlet configuration have already been shown in /4/. Some are comparisons between experimental and theoretical cp-distribution along the fuselage side wall and in two cross sections at the bleed design Machnumber M = 1.63, shown in Fig. 2-4 and 2-5.

Of further interest were the behaviour of the shock system for different compressor entrance pressures at the design point and the influence of viscous effects for the design of a boundary layer suction system at the ramp in order to spread the possible operating range of the engine.

In Fig. 2-6 the pressure and Machnumber distributions near thu ramp are plotted for the three different engine face plane pressures. the ratio between EFP pressure p_E and the pressure at infinity p_∞ varies from 3.4 over 3.55 to 3.77. As expected the normal shock moves upstream with increasing throttling. Fig. 2-7 shows the behaviour of the total pressure along the fuselage and demonstrates quite good an agreement with theory for a pre-shock Machnumber of 1.4 (theory: loss in total pressure of about 5.8 %). The figures 2-8 and 2-9 inform about the invluence of the high and the low EFP-pressure ratios (Fig. 2-6) on the Machnumber distribution in the inlet midplane.

2.2.3 Ramp Boundary Layer Calculations

Based on the Euler results the boundary layer of the ramp was investigated by an inverse method /18/. The calculated displacement thickness was used to determine the bleed mass flow and the distribution of the boundary layer shape factor $H_{1,2}$ was used to look for the required extension of the suction area.

2.3 Bleed Installation at the EM2 Model

2.3.1 Location of the Suction Area

As mentioned above the design of the ramp bleed system is based on former high speed tests [19] with the EM2 inlet model and calculations of the flow at the ramp. Fig. 2-10 informs about the criteria, which determined the suction area. The bleed starts at the point, where the boundary layer calculations indicated the growth of the parameter $H_{1,2}$ for the throttled engine. The suction region is terminated immediately ahead of the lip-section and is divided into three segments (see Fig. 2-11) to avoid recirculation, which could be initiated by the high static pressure rise in front of the inlet lip.

2.3.2 Required Bleed Flow

The required bleed mass flow was calculated in such a way, that the suction removes boundary layer material in the order of the displacement thickness; that is for one segment (throttled engine):

$$\dot{m}_{bl} = \rho_r v_r b_s \delta^x$$

with:

ρ_r, v_r: local density and velocity, calculated from former windtunnel tests,
δ^x : displacement thickness from boundary layer calculations, and
b_s : extension of the suction area across the flow (see Fig. 2-11).

The total bleed flow at the design condition was in the order of 3 % of the mass flow through the engine face plane.

2.3.3 Porosity of the Suction Area

For the design of the wall-porosity of the suction region the bleed mass flow was corrected for roughness effects and for the efficiency fo the bleedholes according to the data of /8, 9, 10/.

For the EM2 1:7 model the porosity was achieved by perpendicular holes of 0.5 mm diameter (order of displacement thickness) spaced 1 mm apart. The hole arrangement of the three segments resulted in 18 % porosity for the first two cells and 24 % for the third one. (The windtunnel tests also covered the investigation of different porosity arrangements with variation in hole number and hole diameter.)

2.3.4 Bleed Exits

The bleed flow from the ramp was channeled separately for each cell via pipes to the lower side of the fuselage (see Fig. 2-12). The bleed flow could be throttled by electrically driven flaps at the tube exits.

2.3.5 Test Set of the Model

Static pressure tubes were installed at the fuselage side wall and the ramp in a horizontal line according to the ramp center line. Additional orifices were situated at the bottom of each suction cell for plenum pressure survey, and further probes were placed in the bleed tubes to calculate the bleed mass flow.

Since the main purpose was to check the flow quality at the engine face plane, most of the test instrumentation was installed at that station, which is part of the DFVLR test modul, described in para. 3.1.2.

3. BLEED TESTS WITH THE EM2 INLET MODEL

3.1 Experimental Setup

3.1.1 Windtunnel

The Transonic Wind Tunnel of the DFVLR-AVA Göttingen (TWG) is a continuous blowing (Göttingen-type) tunnel with a cross sectional area, A, of 1 m x 1 m (Fig. 3-1). The horizontal walls of the transonic test section (d in Fig. 3-1) are slotted to keep wall interferences small, whereas the vertical walls are solid. In the subsonic range ($0.5 < Ma_\infty \leq 0.9$) the Mach numbers are controlled by an adjustable second throat diffuser (e). To achieve transonic velocities ($0.9 \leq Ma_\infty \leq 1.2$) and for boundary layer suction an auxiliary compressor is provided. For measurements at supersonic speeds ($1.3 \leq Ma_\infty \leq 2.0$) the model is mounted in the supersonic test section (c) and the Mach-numbers are controlled by an adjustable Laval nozzle (b). By variation of the stagnation pressure, p_0, between 0.3 and 1.6 bar the Reynolds number (Re) ranges depicted in Fig. 3-2 are covered.

More detailed descriptions of the tunnel are given by Ludwieg et al. /11/, Hottner & Lorenz-Meyer /12/, and Lorenz-Meyer /13/.

3.1.2 Test Equipment

The described measurements should determine the distributions of total and static pressure in the EFP from which the pressure recovery, η, and the static distortions (e.g. DC60) should be calculated. For this purpose a pneumatically driven, rotatable pitot rake was provided (Fig. 3-3) which was equiped with twelve arms spaced by 30°, each of which carries 5 pitot probes at five radii (Fig. 3-4). By rotation of the rake by 15° it was possible to get the pitot pressure at 120 positions in the EFP. To measure the static pressure, eight orifices are located each at cowl and hub of the test modul (Fig.

3-4). All pressure measurements were done with the aid of electronic multiport sensors (PSI-system, see /14/ which make possible, to scan more than 200 pressure orifices in about 20 seconds.

The engine mass flow rate was adjusted with the aid of an electrically driven choking cone (Fig. 3-5) with a cone angle of 64°.

3.1.3 Test Procedure

The measurements were performed at the three Mach numbers Ma_∞ = 1.63, 1.79, and 2.00 with two angles of attack, α = 0° and 5°, and also of yaw, β = 0° and 3°. The Reynolds number, Re_∞, was kept at values between 0.6 and 0.7 x 10^7 m^{-1} by varying the stagnation pressure, p_0.

To ensure the effectivity of the boundary layer bleed system and - simultaneously - to keep the bleed mass flow as low as possible (to avoid losses in inlet performance) it was necessary to find out the optimum bleed flow rate. For this purpose at first with fully closed bleed chokes the buzz onset of the inlet was determined by gradually closing the main choking cone. As a reliable criterion for buzz onset - used in many tests before /15, 16, 17/ - the dynamic behaviour of the static pressure on the wall of the inlet duct, 50 mm upstream of the CFP, was observed. The output of a dynamic pressure transducer (Kulite) mounted in that position shows a sudden rise from the constant value at normal operating conditions (Fig. 3.6) to large amplitudes when buzz occurs (Fig. 3-7). In the next step the bleed exits were fully opened and by further throttling of the engine mass flow the buzz onset - now occuring at significantly lower mass flow rates than without bleed - was determined again. In the last step each of the three bleed exits was separately closed as far as it was possible without affecting the buzz onset. With these optimum choke settings, starting from the buzz onset, the inlet mass flow rate was gradually increased until the main choking cone was fully open and at four to six different mass flow rates between these positions the distribution of total pressure and the static pressures at hub and cowl were taken.

From the distributions of pitot and static pressure measured not only the pressure recovery, η, and the static distortion parameters (e.g. DC60) were calculated, but also the mass flow rate was determined. To get the mass flow rate correctly, the influence of the boundary layer at the cowl must be considered (the boundary layer at the hub is assumed to be very thin and therefore neglected). To this end the radial distribution of the pitot pressure is approximated by a third order spline function which uses the static pressure at the respective position at the cowl as an additional point of support. This method has led to very good results at all DFVLR inlet measurements so far /15, 16, 17/.

3.2 Test Results

3.2.1 Effect of Bleed on Engine Entrance Flow

The efficiency of the ramp bleed system has been demonstrated by its influence on the flow quality at the engine face station. Some characteristic values concerning the flow quality are the total pressure recovery factor η and the flow distortion factor DC60. The value η gives the ratio between total pressure at engine face and free stream, whereas DC60 indicates the local fluctuation in total pressure for a 60 degree segment of the engine face plane.

Fig. 3-8 demonstrates, that with ramp bleed for all engine operating conditions the total pressure recovery is improved by 1 to 2 percent, combined with a remarkable shift of the buzz limit to smaller engine mass flow ratios. With ramp bleed the distortion level is reduced by about 25 % in nearly the total engine operating range, as given in Fig. 3-9.

3.2.2 Effect of Bleed on the Boundary Layer

An additional impression of the effectivity of the boundary layer bleed at the inlet ramp is given by a comparison of the distributions of total pressure inside the boundary layer with and without bleed. A small pitot rake with seven probes situated at distances from the wall between 1.5 mm and 12.5 mm was arranged immediately downstream of the inlet ramp. The total pressure distributions measured are plotted in Fig. 3-10 for Ma_∞ = 1.63 at two mass flow rates. At the higher mass flow rate (≙ 75 %) without bleed the boundary layer is relatively thick (at Ma_∞ = 1.63 more than 6.5 mm) and becomes considerably thinner (< 1.5 mm) when ramp bleed is applied. At lower mass flow rates (near the buzz onset) the boundary layer thickness seems to stay unchanged by bleed, but the loss in total pressure decreases. The fact is that without bleed the boundary layer separates downstream of the normal shock at the ramp; application of bleed prevents separation and hence the loss in total pressure. More distant from the wall (h ≥ 6.5 mm) with bleed applied, the total pressure decreases a little bit, which is the result of an alternation in shock configuration caused by the application of the ramp. With boundary layer suction the total pressure level at the rake station nearly gives the value for isentropic compression (Fig. 3-10).

4. COMPARISON OF CALCULATED AND MEASURED RESULTS OF THE FLOW

The Euler calculations show, especially for the larger scale of Fig. 2-6, that the inviscid results indicate some discrepancies to the test results, regarding the shock position. The experimental data from the previous wind tunnel tests /19/ show the pressure rise more upstream due to viscosity.

Within the scope of this inlet study the theoretical design tools should be improved to achieve better agreement with test results. The Dornier Euler Program was modified to treat boundary layer effects at the ramp. Based on the calculated displacement thickness (see para. 2.2.3) blowing velocities were introduced for the inlet flow calculations.

4.1 Boundary Layer from Test and Euler Pressure Distribution

Fig. 4-1 shows a comparison between the displacement thickness growth referring to the experimental (without suction) and the theoretical pressure distribution (with blowing). The premature transition in the experiment probably results from roughness effects and/or windtunnel turbulences. The calculated suction velocities from the measured bleed flow of the three cells are compared with blowing velocities of the theoretical investigations in Fig. 4-2. As demonstrated, the magnitude as well as the distribution between experimental suction and theoretical blowing is quite similar.

4.2 Euler Calculations with Simulated Boundary Layer

To account for viscous effects at the inlet ramp the well known equivalent source concept was used for the calculations of the inlet flow. The influence of the blowing can be seen in the Fig. 4-3. The normal shock moves quite a bit upstream. Figure 4-4 compares the viscous and inviscid cp-distribution along the fuselage side wall with the experiment. Simulating the viscous effects improves the result substantially. The remaining differences may be caused by the grid, being still to coarse, by to much artificial dissipation in the theory and by the differing massflux ratios of the Euler calculations and the measurement.

5. CONCLUSION

A theoretical and experimental investigation of the ramp bleed system for a supersonic engine inlet has been conducted. The demonstrated way to achieve sufficiently good agreement between theory and experiment by local grid refinement and local treatment of viscous flow effects gives the possibility to use more complex calculation methods with agreeable amount of computing time.

The windtunnel tests proved the efficiency of the simple ramp bleed system for the improvement of the engine entrance flow quality. Better pressure recovery, lower buzz limits and less distortion were achieved.

/1/ W. Seibert

An Aproach to the Interactive Generation of Blockstructured Volume Grids Using Computer Graphics Devices
First International Conference on Numerical Grid Generation in Computational Fluid Dynamics, Landshut, West Germany, 14th - 17th July, 1986

/2/ A. Jameson, W. Schmidt, E. Turkel

Numerical Solutions for the Euler Equations by Finite Volume Methods Using Runge Kutta Time Stepping Schemes
AIAA Paper 81-1259, 2981

/3/ A. Jameson, T.J. Baker

Multigrid Solution of the Euler Equations for Aircraft Configurations
AIAA Paper 84-0093, Jan. 1984

/4/ S. Leicher

Numerical Solution of Internal and External Inviscid and Viscous 3D Flow Fields
AGARD, 58th Meeting on Applications of Computational Fluid Dynamics in Aeronautics, 7th - 10th April 1986, AIX-en provence, France

/5/ S. Leicher

Analysis of Transonic and Supersonic Flows around Wing-Body-Combinations
ICAS 84-1.2.2, 1984

/6/ S. Leicher

Numerical Solution of 3D Invisdic Flow Fields around Complete Aircraft Configurations
ICAS 86-1.3.2, 1986

/7/ A. Jameson, S. Leicher, J. Dawson

Remarks on the Development of a Multiblock Three-Dimensional Euler Code for out of Core and Multiprocessor Calculations
Progress in Scientific Computing, Vol. 6, Birkhaeuser, Boston. 1984

/8/ J. Syberg, J.L. Koncsek

Bleed System Design Technology for Supersonic Inlets
Journal of Aircraft, Vol. 10, No. 7, July 1973

/9/ W.F. Wong

The Application of Boundary Layer Section to Suppress Strong Shock-Induced Separation in Supersonic Inlets
IAA Paper 74-1063

/10/ L.G. Hunter, J.A. Cawthon

Improved Supersonic Performance for the F16 Inlet Modified for the J 79 Engine
AIAA Paper 84-1272

/11/ Ludwieg, H.; Lorenz-Meyer, W.; Schneider, W.

Der Transonische Windkanal der Aerodynamischen Versuchsanstalt Göttingen
Jahrbuch 1966 der WGLR, S. 145-155

/12/ Hottner, T.; Lorenz-Meyer, W.

Der Transonische Windkanal der Aerodynamischen Versuchsanstalt Göttingen (zweite Ausbaustufe)
Jahrbuch 1968 der DGLR, S. 235-244

/13/ Lorenz-Meyer, W.

Der Transonische Windkanal 1 m x 1 m der DFVLR-AVA Nr. 4 in 'Beiträge zur experimentellen Strömungsmechanik'
Festschrift z. 65. Geburtstag von H. Ludwieg, DFVLR-AVA IB 251-77 A 37 (1977)

/14/ Juanarena, D.B.

A Multiport Sensor and Measurement System for Aerospace Pressure Measurements
25th Annual ISA Aerospace Symposium, May 1979

/15/ Schneider, W.; Mackrodt, P.-A.

Leistungsmessungen an einem Modell mit Rumpfseiteneinlauf (EM2)
DFVLR-AVA IB 222-84 C 01 (1984)

/16/ Mackrodt, P.-A.

Leistungsmessungen am Modell EM2 mit Rumpfseiteneinlauf in transonischer Anströmung
DFVLR-AVA IB 222-85 C 09 (1985)

/17/ Mackrodt, P.-A.; Schmitz, D.

Experimentelle Untersuchungen an einem Unterrumpf-Rampeneinlauf bei Überschallanströmung
Jahrbuch der DGLR 1986 I, Bonn 1986, 86-142, Seiten 303-311

/18/ H.W. Stock

Inverse Verfahren zur Berechnung der turbulenten Grenzschicht und Kopplung mit Eulerverfahren
Dornier-Bericht Nr. 19/85 B, 1985

/19/ H. Buers

RÜFo Überschalleinläufe
Pitot-Seiteneinlauf-Modell EM2
Experimenteller Teil, Abschlußbericht
Dornier-Bericht Nr. 31/85 B

/20/ H. Buers

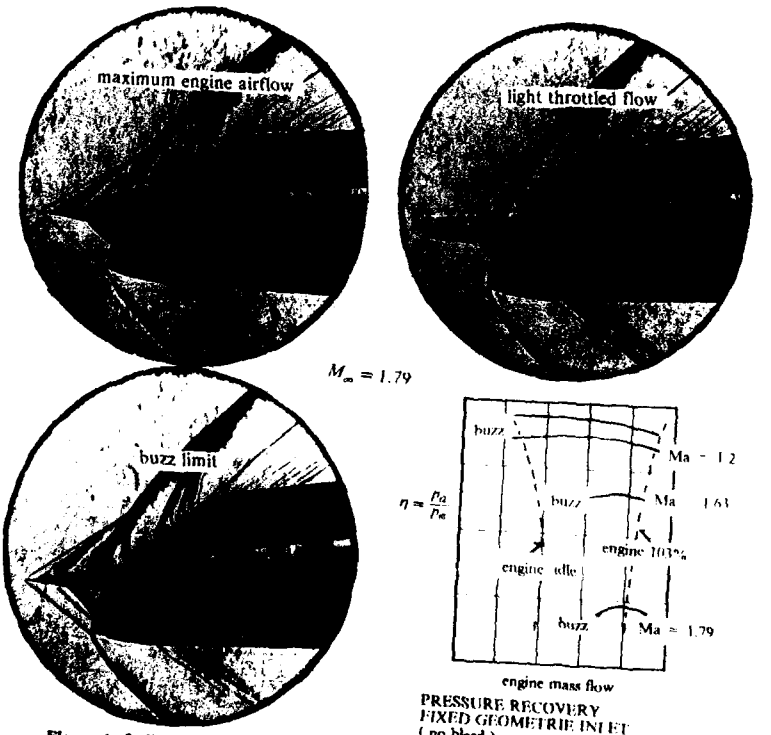
Pitot-Seiteneinlauf-Modell EM2 mit Grenzschichtabsaugung auf der Rampe
Abschlußbericht
Dornier-Bericht Nr. 29/87 B

Nomenclature

A	area
b_s	extention of suction area across flow direction
$\dot{m}$	engine mass flow
$\dot{m}_{ref}$	maximum engine air flow (choked throat)
U_∞	free stream velocity
V_r	local velocity at the ramp
V_W	blowing velocity at the ramp (theory)
V_W	suction velocity at the ramp (experiment)
p_∞	static pressure freestream
p_E	static pressure at engine face plane
p_{to}	total pressure freestream
$\bar{p}_{t2}$	total pressure at engine face plane (mean value)
p_r	localtotal pressure at the ramp
α	angle of attack
β	angle of sideslip
δ^*	displacement thickness
ρ_r	local density at the ramp
η	pressure recovery $\bar{p}_{t2}/p_{t0}$
Ma, M	Machnumber
Re	Reynoldsnumber
$H_{1,2}$	boundary layer shape factor
EFP	engine face plane



Figure 1- 1: DORNIER EM2
SUPERSONIC INLETMODEL



PRESSURE RECOVERY
FIXED GEOMETRIE INLET
(no bleed)

Figure 1- 2: SCHLIERENFOTO
SHOCK DEVELOPMENT AHEAD OF THE INLET

DORNIER

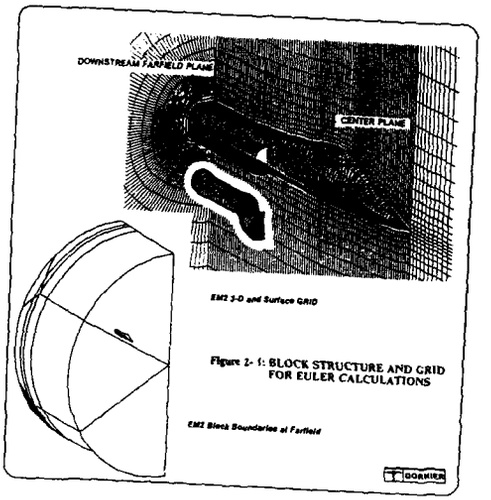


Figure 2- 1: BLOCK STRUCTURE AND GRID FOR EULER CALCULATIONS

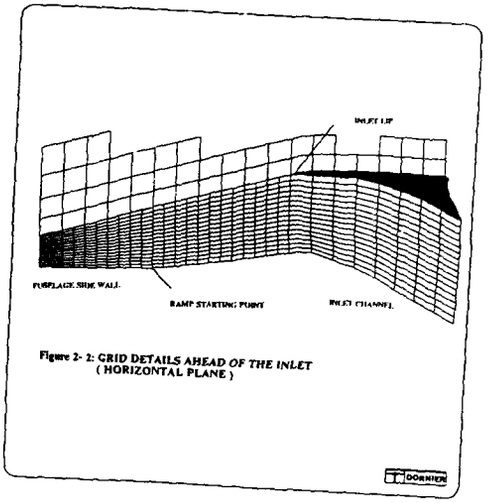


Figure 2- 2: GRID DETAILS AHEAD OF THE INLET (HORIZONTAL PLANE)

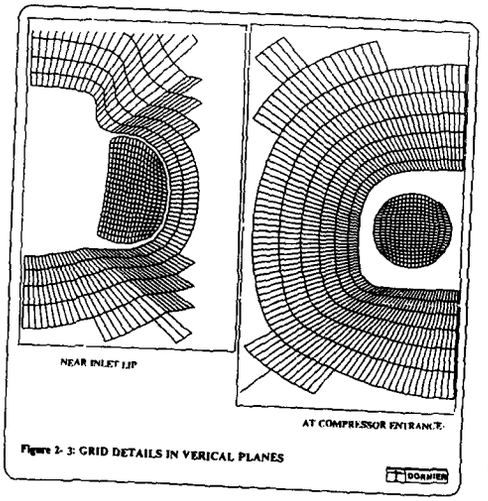


Figure 2- 3: GRID DETAILS IN VERICAL PLANES

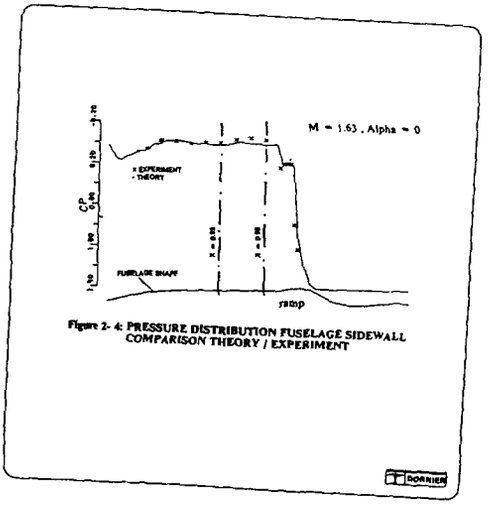


Figure 2- 4: PRESSURE DISTRIBUTION FUSELAGE SIDEWALL COMPARISON THEORY / EXPERIMENT

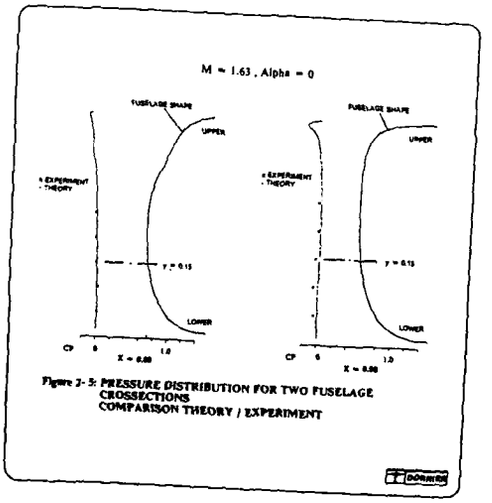


Figure 2- 5: PRESSURE DISTRIBUTION FOR TWO FUSELAGE CROSSECTIONS COMPARISON THEORY / EXPERIMENT

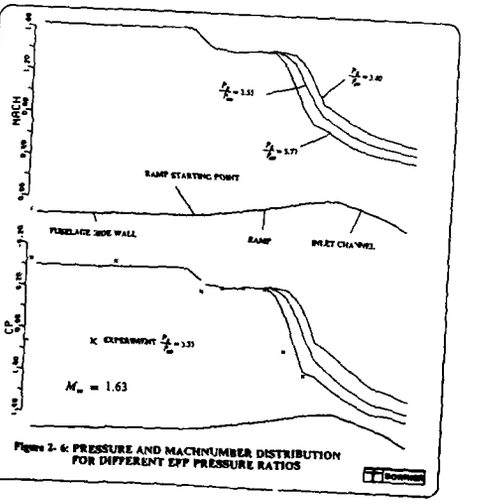


Figure 2- 6: PRESSURE AND MACHNUMBER DISTRIBUTION FOR DIFFERENT EFF PRESSURE RATIOS

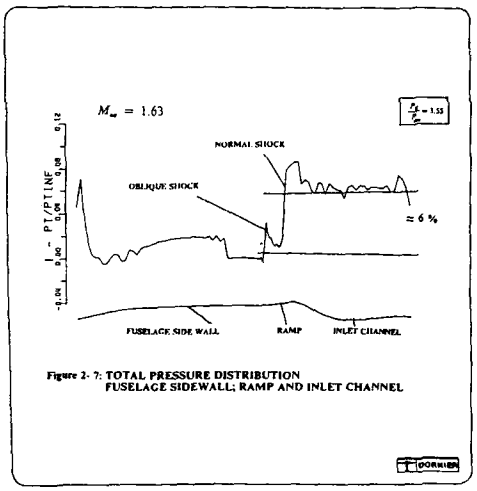


Figure 2- 7: TOTAL PRESSURE DISTRIBUTION
FUSELAGE SIDEWALL; RAMP AND INLET CHANNEL

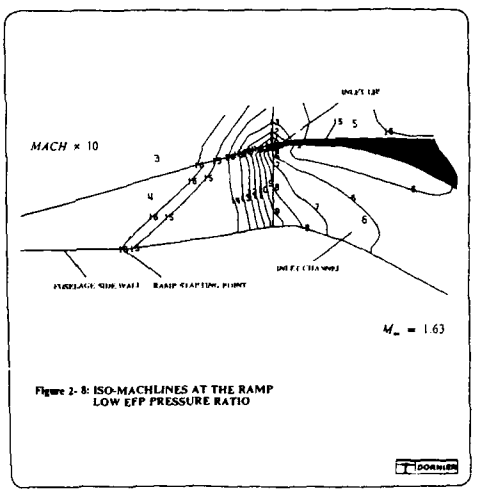


Figure 2- 8: ISO-MACHLINES AT THE RAMP
LOW EFP PRESSURE RATIO

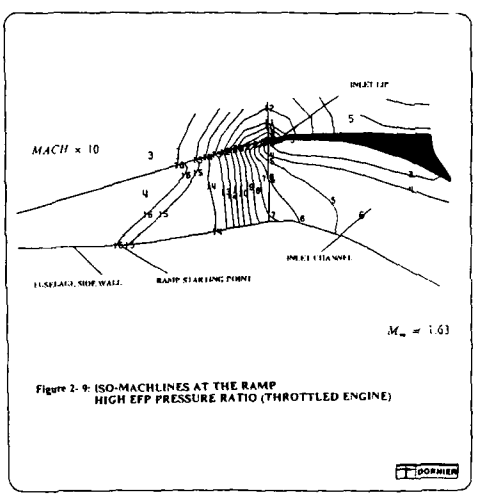


Figure 2- 9: ISO-MACHLINES AT THE RAMP
HIGH EFP PRESSURE RATIO (THROTTLED ENGINE)

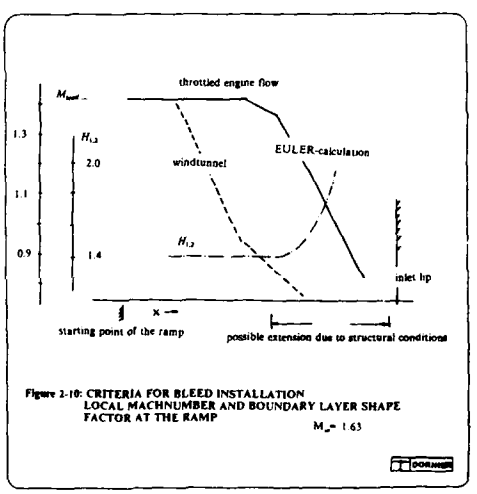
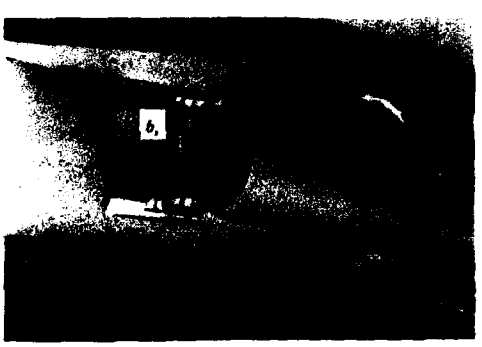
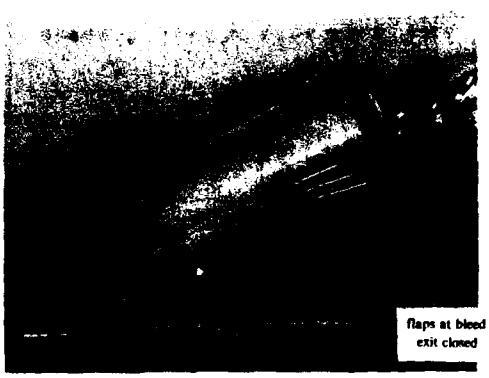


Figure 2-10: CRITERIA FOR BLEED INSTALLATION
LOCAL MACHNUMBER AND BOUNDARY LAYER SHAPE
FACTOR AT THE RAMP
M_∞ = 1.63



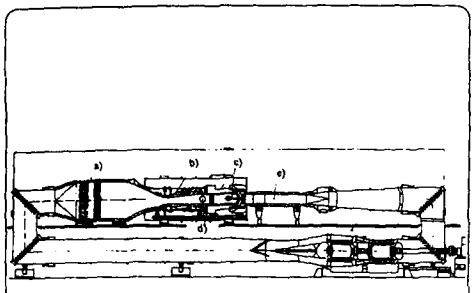
front bleed cell rear bleed cell

Figure 2-11: SUCTION REGION AT THE RAMP
(CELLS WITHOUT POROUS COVER PLATE)



pressure probes for flow calculation

Figure 2-12: BLEED EXITS AT THE LOWER
SIDE OF THE FUSELAGE



a) screens and honeycombs

b) adjustable Laval nozzle

c) supersonic test section

Figure 3- 1: TRANSONIC WINDTUNNEL OF THE DVFLR GÖTTINGEN

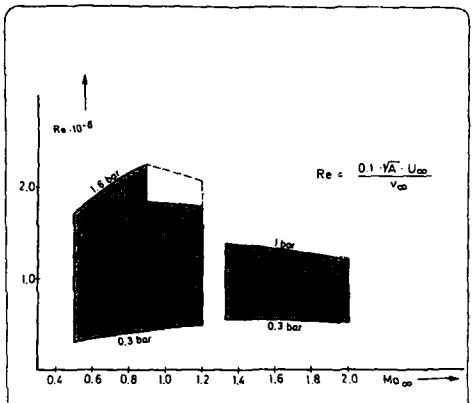


Figure 3- 2: REYNOLDSNUMBER RANGE OF THE TWG

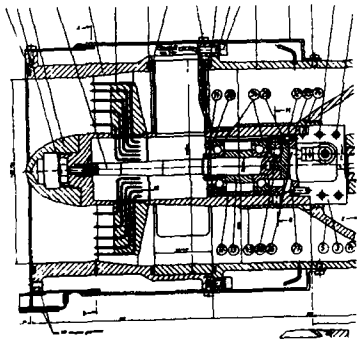


Figure 3- 3: CUTAWAY DRAWING OF THE PITOT RAKE

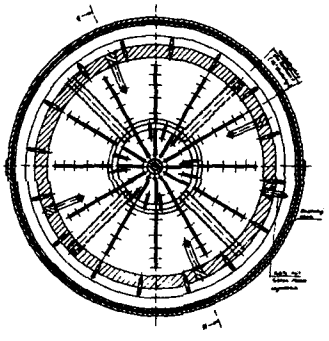


Figure 3- 4: FRONTAL VIEW OF THE PITOT RAKE

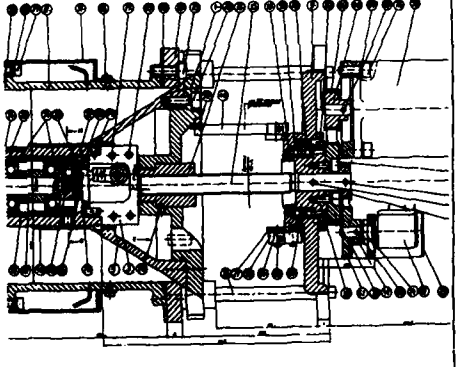


Figure 3- 5: CUTAWAY DRAWING OF THE MAIN CHOKING CONE



Figure 3- 6: KULITE SIGNAL FOR BUZZ INDICATION (NO BUZZ)

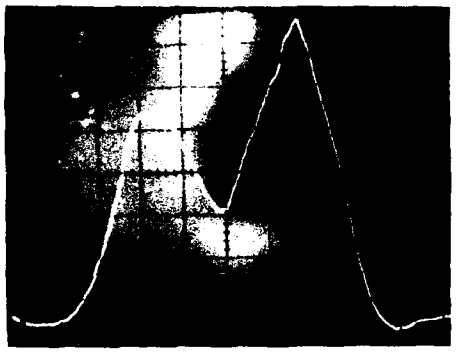


Figure 3- 7: KULITE SIGNAL FOR BUZZ INDICATION
SIGNAL LEVEL AT BUZZ

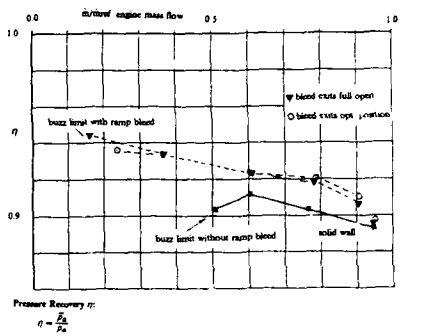


Figure 3- 8: TOTAL PRESSURE RECOVERY
WITH AND WITHOUT RAMP BLEED

DORNIER

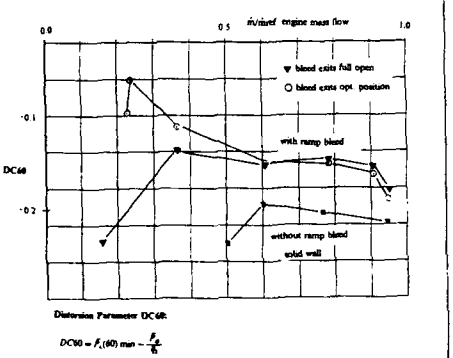


Figure 3- 9: FLOW DISTORSIONS PARAMETER DC60
WITH AND WITHOUT RAMP BLEED

DORNIER

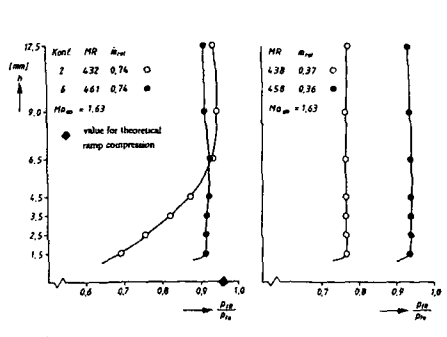


Figure 3-10: TOTAL PRESSURE RECOVERY OF THE
BOUNDARY LAYER AT INLET LIP

DORNIER

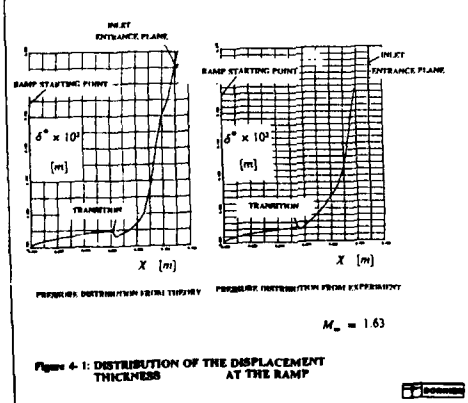


Figure 4- 1: DISTRIBUTION OF THE DISPLACEMENT
THICKNESS AT THE RAMP

DORNIER

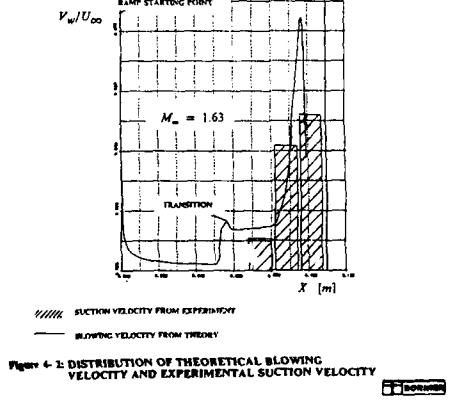


Figure 4- 2: DISTRIBUTION OF THEORETICAL BLOWING
VELOCITY AND EXPERIMENTAL SUCTION VELOCITY

DORNIER

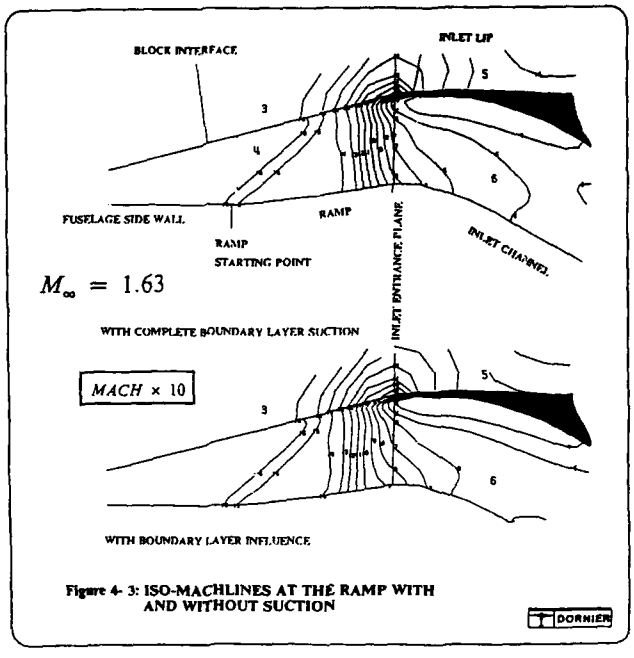


Figure 4- 3: ISO-MACHLINES AT THE RAMP WITH AND WITHOUT SUCTION

DORNIER

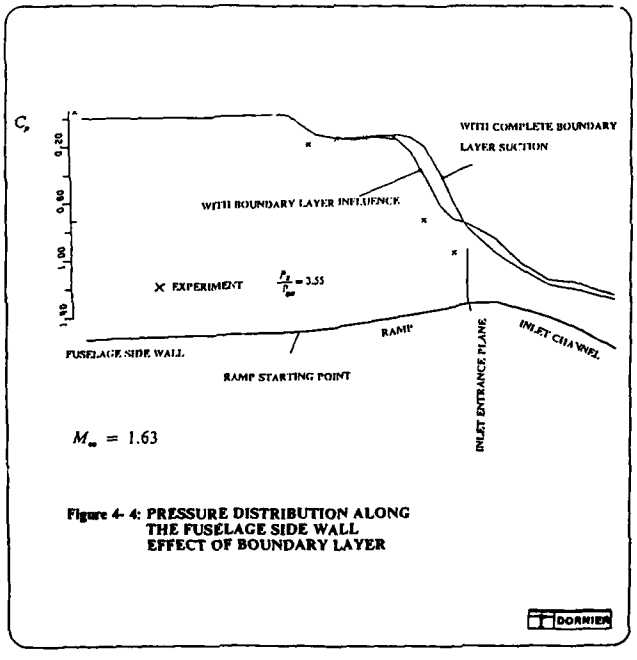


Figure 4- 4: PRESSURE DISTRIBUTION ALONG THE FUSELAGE SIDE WALL EFFECT OF BOUNDARY LAYER

DORNIER

EFFORTS TOWARD THE VALIDATION OF A COMPUTATIONAL FLUID DYNAMICS CODE FOR ANALYSIS OF INTERNAL AERODYNAMICS

by

R.G.Semmes, D.G.Arbiter and R.D.Dyer
Deputy for Engineering
Aeronautical Systems Division
Air Force Systems Command
United States Air Force
Wright-Patterson AFB, Ohio 45433
USA

SUMMARY

A two dimensional/axisymmetric, Reynolds averaged Navier-Stokes code (PARC2D) was selected to aid Aeronautical Systems Division engineers in the analysis of internal aerodynamics problems. Before implementing the code in actual systems application, the code's results were compared with experimental data to determine the extent of its usefulness. The configurations chosen for code validation were (1) a two-dimensional hypersonic inlet, (2) an axisymmetric convergent-divergent nozzle, and (3) an axisymmetric subsonic diffuser.

The paper discusses the ability of the method to readily perform engineering predictions on internal aerodynamics problems. Sample grids for each configuration as well as comparisons of computational and experimental results will be presented.

The PARC2D code was able to predict the hypersonic inlet flowfield trends and shock structure but had difficulty adequately predicting forebody losses. PARC2D provided good agreement with experimental data for both the convergent-divergent nozzle as well as the subsonic diffuser.

LIST OF SYMBOLS

A_e	nozzle exit area, cm^2
A_t	nozzle throat area, 45.60 cm^2
d_e	nozzle exit diameter, cm
d_m	nozzle maximum diameter, 15.24 cm
d_t	nozzle throat diameter, cm
j	grid coordinate - streamwise direction
k	grid coordinate - normal to stream
l_c	axial length of nozzle *convergent* section, cm
l_d	*axial* length of nozzle divergent section, cm
N-S	Navier-Stokes
P_p	pitot pressure, Pa
P	static pressure, Pa
P_t	total pressure, Pa
P_{to}	stagnation pressure, Pa
$P_{t\infty}$	freestream total pressure, Pa
P_∞	freestream static pressure, Pa
$(P_t/P_\infty)_{des}$	design nozzle pressure ratio
Station, STA	axial location, cm
U	axial velocity, cm/s
U_e	axial velocity at boundary layer edge, cm/s
X, X Station	axial location, cm
1	cowl leading edge shock
2	shock reflected off centerbody
3	shock reflected off cowl
δ	boundary layer height, cm

INTRODUCTION

The Aeronautical Systems Division (ASD), Deputy for Engineering, has a need to analyze complex configurations of developmental and operational systems. Engineers do not always have the benefit of experimental diagnostic testing to resolve the aerodynamic impacts of proposed configuration designs or modifications. The need exists, therefore, to acquire the ability to efficiently and accurately analyze a wide range of aerodynamic problems. In the field of internal aerodynamics, computational fluid dynamics codes exist which could possibly fulfill this need.

Because viscous effects are significant in the analysis of internal flowfields, a full Navier-Stokes (N-S) model was identified to perform our analysis of duct flow problems. ASD is a systems development organization, therefore, the resources did not exist to devote to code development, so the N-S code acquired for system application had to be existent, supporting documentation available, and hopefully already being applied to internal aerodynamic problems.

The N-S code selected (ref 1) was the two-dimensional(2-D)/axisymmetric, Reynolds averaged Navier-Stokes code PARC2D. The 2-D/axisymmetric version was initially selected for a starting point to determine the codes idiosyncrasies and capabilities prior to working with the three-dimensional version. The PARC2D code makes use of the conservative form of the Navier-Stokes equations. An implicit central-differencing algorithm is used. Artificial viscosity is used for solution stability. Variable time steps are used, both temporal and spatial, to improve the efficiency of the code. The turbulence model is a Baldwin-Lomax style algebraic model. Numerous options are available within the code including: axisymmetric and 2-D equations, inviscid, thin shear layer or fully viscous solutions, and a choice of a laminar or turbulent boundary layer. Boundary conditions can be set anywhere in the flowfield. The inputs include: the grid, thermodynamic properties at the boundaries, flowfield type, artificial viscosity parameters, iteration controls, and output requirements.

Having selected the PARC2D code, a variety of candidate problems typical of future application was selected to validate the code for our application. The configurations chosen for code validation were selected based on adequate configuration definition, surface and off-body flowfield data availability, and the validity of a 2-D or axisymmetric assumption. Based on these requirements, the configurations chosen for code validation were (1) a two-dimensional hypersonic inlet, (2) an axisymmetric convergent-divergent nozzle, and (3) an axisymmetric subsonic diffuser. Surface pressure data, flowfield pressures and velocities, and boundary layer characteristics were used as the basis for comparison.

RESULTS

HYPERSONIC INLET:

The first case chosen for evaluation was a two dimensional inlet designed to operate at a freestream Mach number of 7.4. Geometric definition and experimental results were taken from a study conducted at NASA-Ames Research Center described in reference 2. The inlet geometry is shown in Figure 1. The grid developed for this case, shown in Figure 2 is an "H" type grid designed to minimize the number of points outside the region of interest. Three hundred grid points were applied in the streamwise direction (J direction) with one hundred ten points used perpendicular to the flow (K direction). In boundary layer regions the grid was packed using the following rule: approximately 20 points in the boundary layer, with the first two points off the wall located so that the velocity at the second point is subsonic and less than 10 percent of the velocity at the edge of the boundary layer. The leading edges of physical surfaces were also packed to provide proper flow resolution in these regions of large pressure gradients. The case was run using the fully viscous option. Boundary layer transition from laminar to turbulent was set based on the experimental onset of transition.

Comparison of the computational and experimental flowfield shock structures provides insight into the quality of the prediction. Figure 3 compares the computed shock locations with the experimental results measured using pitot pressure probes. From this comparison several important differences can be seen. The PARC2D code predicts a cowl shock (labelled "1" in Figure 3) impinging on the centerbody upstream of the experimental reflection location. The difference may be due to a larger predicted stand off distance of the cowl leading edge shock. The result of the early centerbody impingement of shock "1" is that the reflected shock, labelled "2" in Figure 3, is stronger than the experimental one and strikes the cowl early. The increased strength of shock "2" is caused by a greater slope of the centerbody surface at the computational reflection location in comparison to the slope of the centerbody at the experimental reflection location. Similarly, the third shock, labelled "3", appears stronger and reflects from a location upstream of the experimental location.

After comparing the general flowfield, the capability of PARC2D to predict static pressure was examined. Figure 4 shows the comparison of the surface static pressure ratios (P/P_{∞}) along the centerbody, and as expected from the discussion of the analytical shock locations, the predicted static pressure rise due to the cowl shock impingement on this surface is early and the value of the total shock induced compression is higher. A small expansion region near STA 120 is not predicted by PARC2D. The drop in predicted static pressure ratio at the end of the inlet is a result of the imposed boundary condition and could be remedied with input refinements.

Static pressures on the cowl surface were also examined (see Figure 5) and the numerical results show good correlation in the compression region prior to Station 115.0. Downstream of this location, the code overpredicts the compression due to the cowl surface curvature. At Station 122.0 an expansion prior to the reflected shock impinging on the cowl surface is not predicted by PARC2D. This expansion is the result of the cowl shock curving towards the centerbody as it enters the boundary layer. The experiment expansion wave parallels the reflected shock wave as they approach the cowl where as the computed expansion wave intersects the reflected shock wave and is dissipated. An overprediction of the compression downstream of this expansion occurs because of the stronger shocks discussed earlier. As seen in the centerbody results the static pressure is forced to the boundary condition value at the downstream end of the flowfield and can be solved with proper boundary conditions.

Data are presented in Figure 6 comparing values of predicted Mach number and pitot pressure ratio to experimental results at the entrance to the inlet, STA 81.28. PARC2D results match the experimental data quite well except in the boundary layer. For both the Mach number and pitot pressure plots in the near wall region (Figures 6a and 6b), a deviation from the expected profiles can be seen. It is speculated that a dominance of artificial viscosity in the region of large gradients near the wall causes an underprediction of the flowfield's kinetic terms. Relaxation of the artificial viscosity parameter will be attempted for future efforts. Figure 7 shows the comparison of prediction with experiment at STA 104.14. The losses shown by experiment, between the inlet entrance and this station, below the cowl shock are not predicted by PARC2D. The pitot pressure profile is also overpredicted outside the boundary layer and although the levels are not consistent, the variation of pitot pressure correlates well with experiment. As indicated by the pitot pressure and Mach number profiles, the cowl shock is predicted to be closer to the centerbody than the experimental shock. At the inlet throat, Station 125.7, the predicted Mach number (Figure 8a) agrees with the experimental results. The same boundary layer discrepancies seen in the upstream stations are again evident at this location. Agreement with experimental pitot pressures, however, (Figure 8b) has deteriorated considerably from station 104.14. Given that Mach number is in agreement with experiment, the initial conclusion is that a total pressure loss in the duct was missed by the PARC2D prediction.

Further examination of total pressures showed a discrepancy between experiment and PARC2D throughout the duct. The experimental data indicated approximately a 25% loss in total pressure from the forebody to the inlet entrance whereas the PARC2D solution and isentropic relationships result in only a 15% loss. Through the duct, however, both experiment and PARC2D show the same variation in total pressure indicating that the difference in solutions occurs between the forebody leading edge and the inlet entrance. This discrepancy is masked at the upstream stations due mainly to the nature of pitot pressures.

A comparison of predicted and experimentally derived boundary layer heights were examined next to determine the code's performance in this area (Figures 9 and 10). The experimental values were obtained using total temperature as an indication of boundary layer height. It was difficult to determine the top of the predicted boundary layer because after the first cowl shock reached the centerbody, the values of total temperature, total pressure, and velocities were continuously varying. The predicted boundary layer heights were obtained by examining all three parameters. The two parameters yielding the closest results were averaged to give a computational height; usually velocity and total pressure.

Figure 9 shows the boundary layer growth on the centerbody. The thicker boundary layer around Stations 100.0 and 105.0 is probably due the computational switch from laminar to turbulent flow. This switch was set to begin a turbulent calculation where experiment showed the onset of transition, not the onset of turbulent flow. This early implementation of a turbulent calculation leads to a thicker boundary layer downstream. The thicker boundary layer coupled with an early shock impingement is evidenced by the early boundary layer compression predicted by the code. The computed shock boundary layer interaction length and boundary layer compression level, however, agrees well with experiment. The cowl boundary layer height (Figure 10) indicates the same trends as the centerbody. The boundary layer is initally thicker, the compression begins earlier, and the compression level and shock boundary layer interaction length are in agreement with experiment.

CONVERGENT-DIVERGENT NOZZLE:

To examine the code's usefulness in the transonic and low supersonic Mach number regime, case 2, an axisymmetric convergent-divergent nozzle (ref 3) was chosen. The nozzle has a design nozzle pressure ratio of 4.25. The convergent section contracts at a 42.35 degree angle over a centerline length of 4.36 cm. The divergence angle is 2.12 degrees and acts over a centerline length of 12.19 cm (Figure 11). One hundred and thirty grid points were applied in the streamwise direction with dense packing in the convergent section and through the throat while maintaining orthogonality to the nozzle wall (Figure 12). Sixty grid points were used radially with dense enough packing to meet the boundary layer packing requirements outlined in the previous case. Two cases were run; one at the design pressure ratio and one above design at a nozzle pressure ration of 7.03.

At the two nozzle pressure ratios the code shows good overall agreement with the experimental surface static pressure distribution (see Figure 13). The predicted expansion, however, begins further upstream than indicated experimentally. Regridding and refinement of physical coordinates was unsuccessful in correcting this discrepancy. No further experimental data is available to analyze the cause of this difference, but its significance on the complete solution is small. The code accurately predicted the pressure variation through the throat and downstream into the divergent section. Due to the large convergence angle, the flow overexpands at the throat creating a shock which transverses the nozzle and impinges on the nozzle wall in the divergent section at $x/d_m=0.75$. The corresponding static pressure rise on the nozzle wall is predicted by the code but it occurs slightly upstream from the experimental location. Again this difference is small and the overall PARC2D solution is considered acceptable for the available experimental data.

SUBSONIC DIFFUSER:

Case 3 is a subsonic diffuser (ref 4) with a total diffusion angle of 12 degrees acting over a centerline length of 107.5 cm. A constant area, 21.6 cm long, boundary layer build-up section upstream of the diffuser section was included in the model to analyze the effects of boundary layer thickness. One hundred and forty grid points were used in the streamwise direction with eighty used in the radial direction (Figure 14). In the streamwise direction, the grid was more closely packed where the duct transitions from the constant area section to the diffuser section. Radially, the grid was packed tightly towards the duct wall for boundary layer analysis. An inlet pressure ratio (P / P_{to}) of 0.80 was selected for comparison of PARC2D results with the experimental surface pressure distribution and boundary layer profiles. At this pressure ratio, both a thin shear layer analysis and a fully viscous solution were calculated.

For the thin shear layer approximation, the code accurately predicted the surface static pressure distribution (Figure 15). The largest deviation from experimental results being approximately 3% at the diffuser exit. This 3% discrepancy may be due to the assumption of a flow-through condition at the exit plane. The boundary layer profiles, however, do not agree with experimental data and in general show unrealistic trends (Figure 16). The profile shapes of the PARC2D solution predict a much thinner boundary layer with the height at the exit being only 25% of the experimental boundary layer height.

The failure of the thin shear layer approximation to accurately predict boundary layer profiles could result from a combination of the pressure ratio chosen for analysis and the grid spacing used to model the flow. At an inlet pressure ratio of 0.80 and a diffusion angle of 12 degrees, the flow is near separation which could preclude a thin shear layer approximation. During initial runs of this case when a laminar solution was sought, separation in the diffusion section was predicted by the code indicating flowfield conditions at or near separation and the need to run a full Navier-Stokes solution. In addition, a thin shear layer should be modeled so that in the boundary layer, the distance between k equals constant lines does not vary in the streamwise direction. Failure to model the diffuser accordingly introduced the need for a streamwise variation in viscosity which is not computed for a thin shear layer case.

When the fully viscous solution was examined, both the surface static pressures and the boundary layer profiles showed good correlation with measured values (Figures 15 and 17). As seen in Figure 13, the thin shear layer approximation and fully viscous solution have essentially the same surface static pressure distribution but the boundary layer prediction of the fully viscous case (Figure 17) improves vastly over the thin shear layer assumption. The boundary layer height of the fully viscous case has thickened to agree with experimental data and the boundary layer profiles have assumed expected shapes. The edge velocities are generally 99.9% of the core flow velocity whereas in the thin shear layer case, edge velocities of 102% of the core flow were found to exist. The fully viscous boundary layer profiles are still slightly flat but agree with experimental results closely enough for satisfactory definition of diffuser performance.

CONCLUSIONS AND RECOMMENDATIONS

CONCLUSIONS

HYPERSONIC:

1. The code accurately predicted Mach number profiles throughout the inlet.
2. The shock boundary layer interaction predictions were acceptable. The overall boundary layer height, however, was overpredicted and may be resolved in part by an appropriate choice of transition location.
3. The code overpredicted the overall compression through the inlet.
4. The code accurately predicted the total pressure variation from the entrance to the throat of the inlet.
5. The code did not correlate with experiment as to the total pressure loss from the forebody leading edge to the inlet entrance.
6. The code was unable to predict the near wall boundary layer profiles.

SUBSONIC:

1. The code accurately predicted surface static pressure distributions.
2. The fully viscous case accurately predicted boundary layer profiles.
3. The thin shear layer was unable to produce acceptable boundary layer profiles in regions near separation.

SUPERSONIC:

The code accurately predicted surface static pressure distributions.

RECOMMENDATIONS

1. The PARC2D code may be applied without further refinement to the analysis of appropriate subsonic and supersonic internal flows.
2. The code may be applied to flows in the hypersonic regime for general flowfield analysis.
3. With the following modifications, the code may be applied to the hypersonic regime for complete flowfield definition:
    a. Modification of the artificial viscosity term.
    b. Further validation of the code for forebody flowfield prediction.
4. The authors recommend the code be further validated in the hypersonic regime with another experimental case.

REFERENCES

1. Phares, W. J.; et al: Application of Computational Fluid Dynamics to Test Facility and Experiment Design, AIAA 86-1733, 1986.

2. Gnos, A. Vernon; et al: Investigation of Flowfields Within Large Scale Hypersonic Inlet Models, NASA TN D-7150, 1973.

3. Carson, George T. Jr.,; Lee, Edwin E. Jr.: Experimental and Analytical Investigation of Axisymmetric Supersonic Cruise Nozzle Geometry at Mach Numbers from 0.60 to 1.30, NASA TP 1953, 1981.

4. Copp, Martin R.; and Klevalt, Paul L.: Investigation of High-Subsonic Performance Characteristics of a 12 Degree 21-Inch Conical Diffuser, Including the Effects of Change in Inlet-Boundary-Layer Thickness, NACA RML9H10, March 1950.

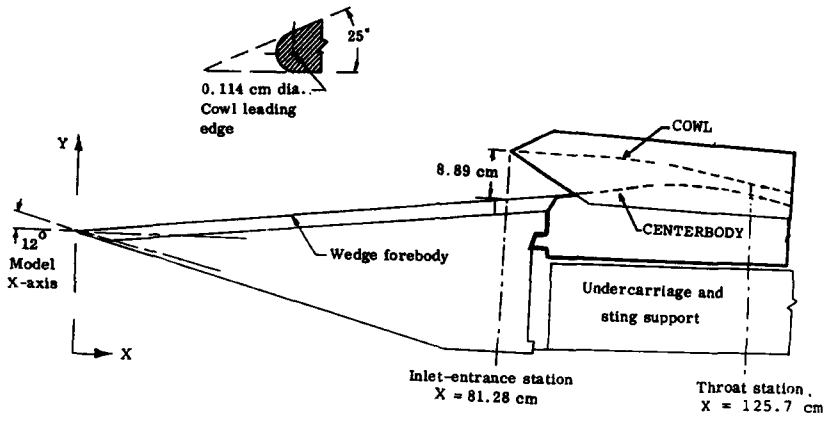


FIGURE 1. - GEOMETRIC DESCRIPTION OF HYPERSONIC INLET.

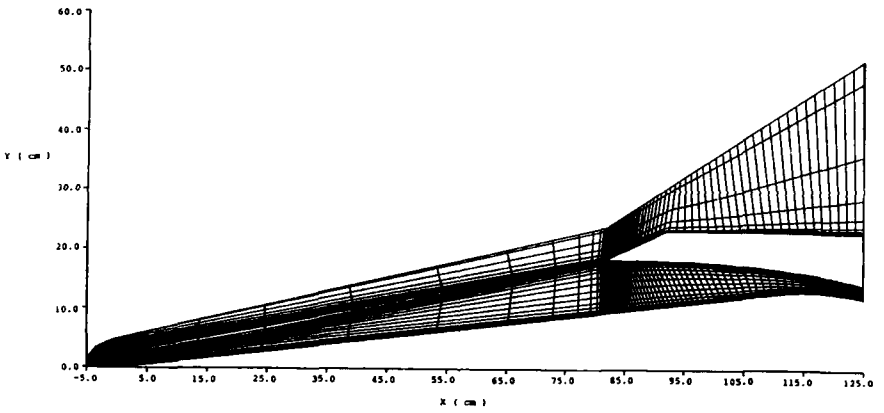


FIGURE 2. - HYPERSONIC INLET GRID, EVERY FIFTH GRID POINT.

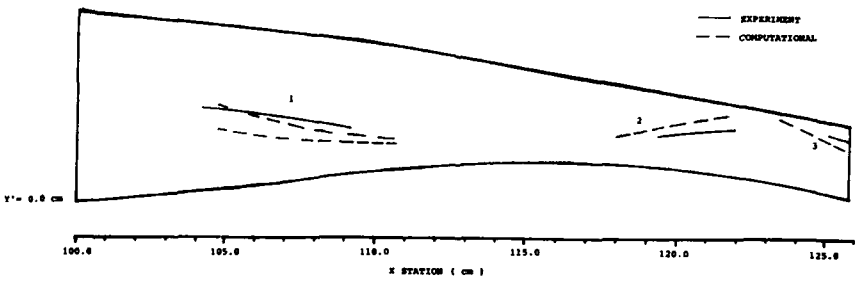


FIGURE 3. - COMPARISON OF EXPERIMENTAL AND PREDICTED INTERNAL SHOCK LOCATIONS FOR THE HYPERSONIC INLET.

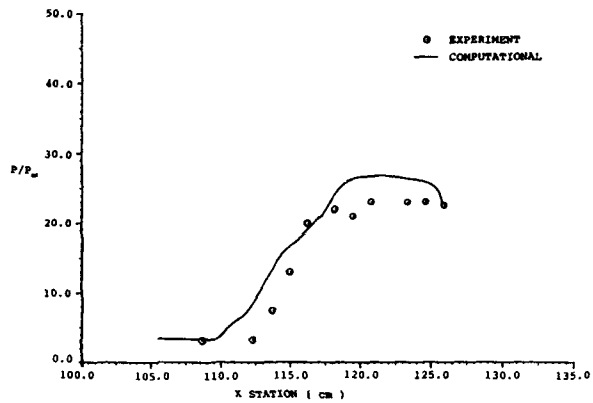


FIGURE 4. - CENTERBODY SURFACE STATIC PRESSURE DISTRIBUTION FOR THE HYPERSONIC INLET.

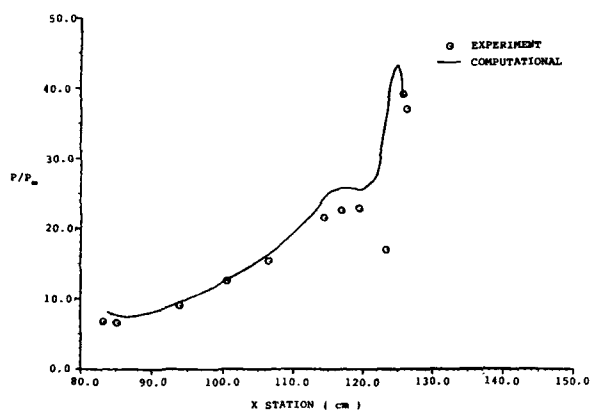
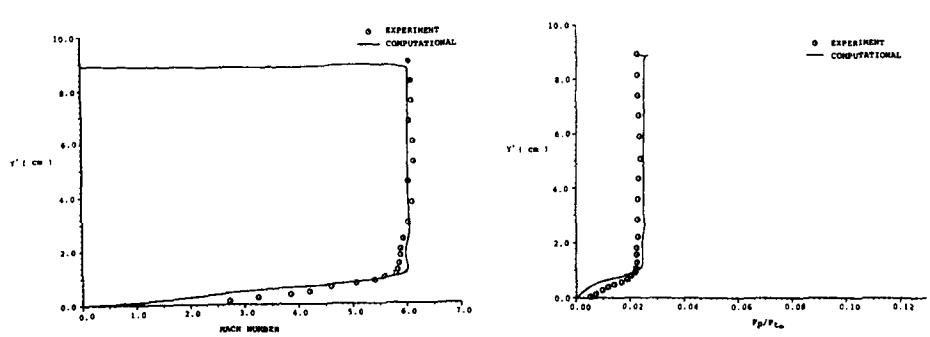


FIGURE 5. - COWL SURFACE STATIC PRESSURE DISTRIBUTION FOR THE HYPERSONIC INLET.



A B

FIGURE 6. - FLOWFIELD COMPARISON AT X STATION 81.28 FOR THE HYPERSONIC INLET.

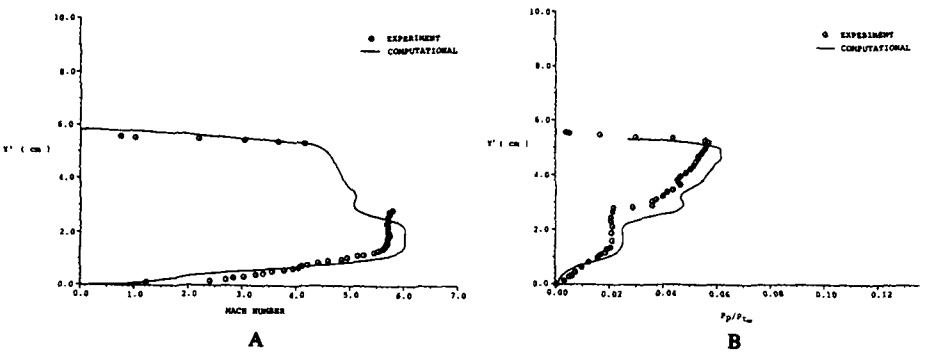


FIGURE 7. - FLOWFIELD COMPARISON AT X STATION 104.14 FOR THE HYPERSONIC INLET.

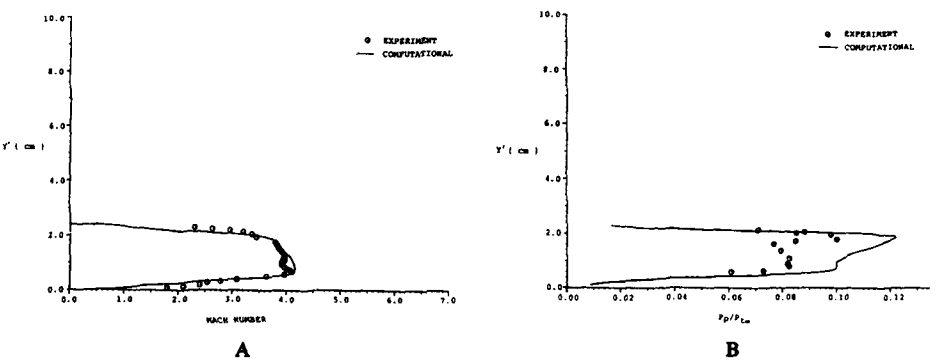


FIGURE 8. - FLOWFIELD COMPARISON AT X STATION 125.7 FOR THE HYPERSONIC INLET.

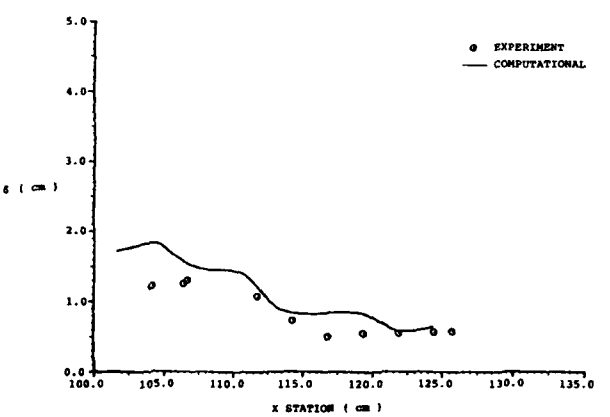


FIGURE 9. - CENTERBODY BOUNDARY LAYER THICKNESS FOR THE HYPERSONIC INLET.

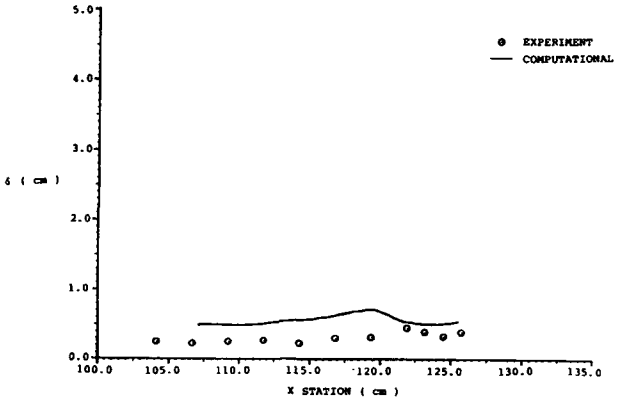
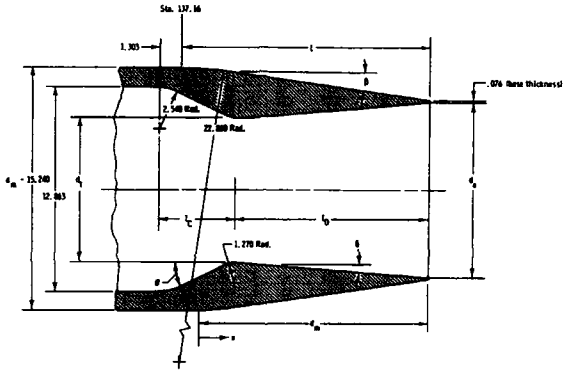


FIGURE 10. - COWL BOUNDARY LAYER THICKNESS FOR THE HYPERSONIC INLET.



$(P_t/P_\infty)_{des}$	A_e/A_t	d_t/d_m	l_c/d_m	l_D/d_m	θ,deg	δ,deg	l/d_m	d_e/d_m
4.25	1.25	0.5	0.286	0.8	42.35	2.12	1.0	0.559

FIGURE 11. - GEOMETRIC DESCRIPTION OF THE CONVERGENT-DIVERGENT NOZZLE.

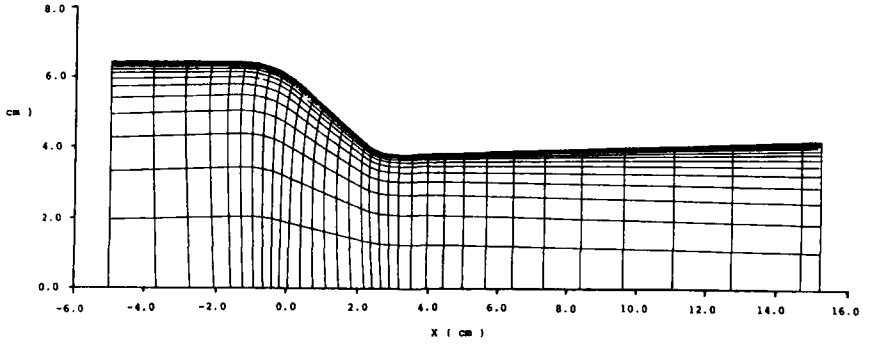


FIGURE 12. - CONVERGENT-DIVERGENT NOZZLE GRID, EVERY FIFTH GRID POINT.

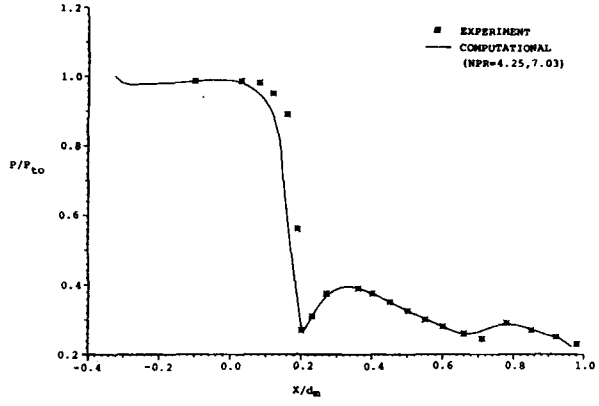


FIGURE 13. - SURFACE STATIC PRESSURE DISTRIBUTION FOR THE CONVERGENT-DIVERGENT NOZZLE.

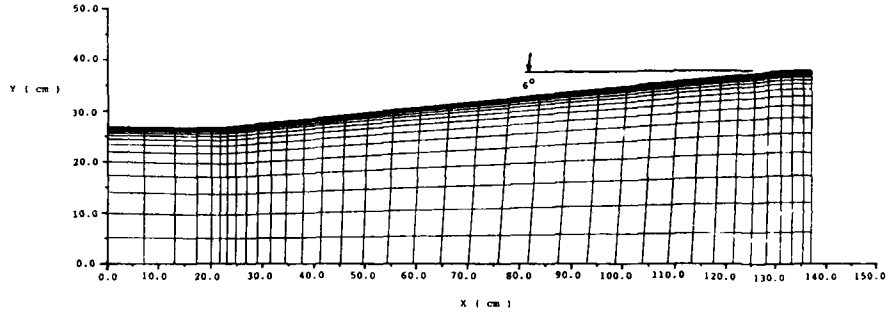


FIGURE 14. - SUBSONIC DIFFUSER GRID, EVERY FIFTH GRID POINT.

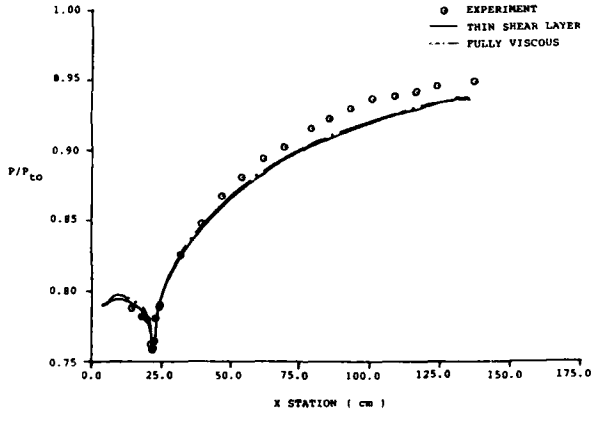


FIGURE 15. - SURFACE STATIC PRESSURE DISTRIBUTION FOR THE SUBSONIC DIFFUSER.

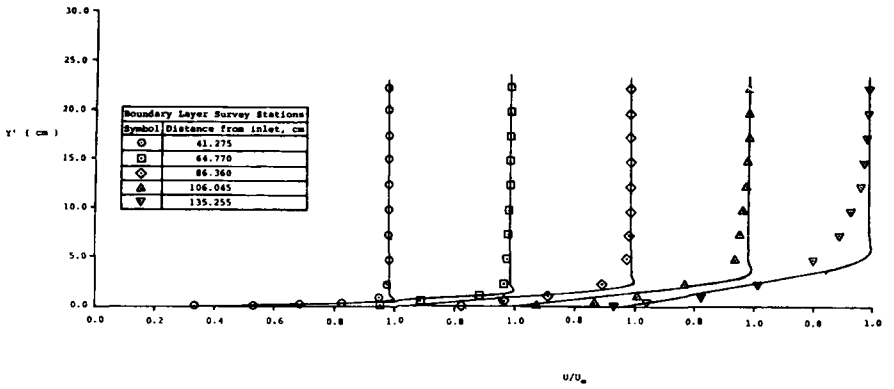


FIGURE 16. - BOUNDARY LAYER PROFILES FOR THE THIN SHEAR LAYER SUBSONIC DIFFUSER CASE.

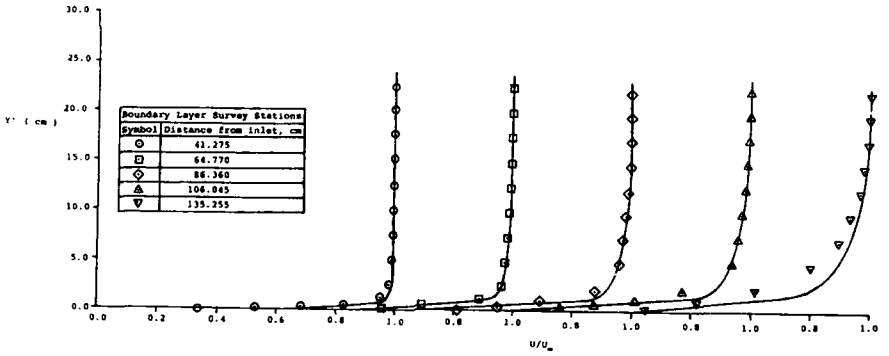


FIGURE 17. - BOUNDARY LAYER PROFILES FOR THE FULLY VISCOUS SUBSONIC DIFFUSER CASE.

Measurements and Computations of Swirling Flow in a Cylindrical Annulus

R.J. Kind, Professor
F.M. Yowakim, Graduate Student
P.M. Reddy, Graduate Student

Department of Mechanical and Aeronautical Engineering
Carleton University, Ottawa, Canada K1S 5B6

SUMMARY

Comprehensive measurements have been completed for four swirling flows in a cylindrical annulus. Nominal swirl angles were 0, 15, 30 and 45 degrees. The data include static and total pressure distributions, axial and tangential wall shear stress components, and profiles of the mean velocity components and of the Reynolds shear and normal stresses. The work was intended to provide data for validation of computational methods. Consistency checks indicate that the data are of high quality and suitable for this purpose. Space limitations only permit presentation of some of the data in this paper.

The paper also outlines a computational method which was used with simple mixing-length turbulence models to compute development of the measured flows. The computations have demonstrated that a simple mixing length model gives excellent predictions of the swirling flow near the annulus walls.

1. Introduction

Wall-bounded swirling flows occur in turbomachinery, cyclone separators, electrical machinery and other equipment. Despite their practical importance, the opportunities to validate computational fluid dynamics codes for such flows are limited by the scarcity of suitable experimental data. Swirling flows involve strongly curved streamlines; current computational methods have difficulty in accurately predicting even simpler two-dimensional curved flows [1] and their ability to predict swirling flows cannot, therefore, be taken for granted. This paper presents experimental data for several swirling flows in an annular duct having constant inner and outer radii, r_i and r_o respectively. The data are considered to be of high quality and suitable for validation purposes. Also presented are the results of computations using a finite-difference method with simple mixing-length turbulence models.

Previous experimental work includes that of Yeh [2], Scott and Rask [3] and Scott and Bartelt [4]; these authors have published mean flow data for swirling flow in annuli. The present experiments are the first to include comprehensive measurements of Reynolds stresses in such flows. Four flows, having nominal swirl angles of 0, 15, 30 and 45 degrees, were measured. The annulus radii r_i and r_o had values of 0.127 and 0.203m, respectively. The Reynolds number based on mean axial velocity, $\bar{U}$, and hydraulic diameter, $D_h = 2(r_o - r_i)$, was 3.1×10^5. $\bar{U}$ was about 32 m/s.

Recent theoretical work on swirling flows has concentrated on numerical methods, rather than analytical or integral methods. Numerical methods for solving the Navier-Stokes equations for duct flows are well developed, for example Gosman et al. [5], Patankar and Spalding [6] and Briley [7]. If there is no reverse flow or re-circulation, the equations can be parabolized by neglecting the streamwise diffusion terms; a marching solution is then possible. The difficulty lies in finding suitable turbulence models to represent the Reynolds stresses. Data which include Reynolds stresses are thus particularly useful.

Yamamoto and Millar [8] found that computations using a two-equation ($K - \varepsilon$) turbulence model did not give good predictions of Scott and Rask's [3] results. Koosinlin and Lockwood [9] used both an algebraic Reynolds stress model and a mixing length formulation based on the more complex model for prediction of swirling boundary layers on spinning discs and cylinders. Predictions of the two models were found to be about equal in quality. Koosinlin et al. [10] obtained good predicitons of swirling boundary layers on spinning cones, discs and cylinders using a mixing length model in which the mixing length was made a function of local swirling flow Richardson number as proposed by Bradshaw [11]. Lilley and Chigier [12] and Lilley [13] have suggested that non-isotropic turbulence models are necessary for good prediction of flows with strong swirl. The present computations made use of mixing-length models based on suggestions of Lilley and Chigier [12] and Galbraith et al. [14]. As will be seen, these appear to be capable of giving good predictions for at least the near-wall regions of the flows.

2. Description of Experiments

2.1 Apparatus

Figure 1 shows a schematic of the swirl tunnel used to produce the measured flows. Air from a 2-stage axial blower passed through a honeycomb into a settling chamber. The settling chamber was fitted with three screens, the first one graded, to produce uniform stagnation pressure in the flow entering the contraction leading into the annular working section.

A row of inlet guide vanes (IGV's) at the start of the working section was used to impart swirl to the flow. The vane angle was adjustable to give the desired swirl angle; the vanes were removed to obtain the non-swirling flow. The wakes of the IGV's decayed quite rapidly with downstream distance.

The working section ended with a row of straightening vanes so that the flow was discharged with negligible swirl. This avoided mismatch of radial pressure gradient at the annulus exit. The straightening vanes were 1.8m downstream of the IGV's, giving a test section length of 12.3 hydraulic diameters. Values of radii and Reynolds number are stated in the Introduction. The test section was made of mild steel; working surfaces were machined to a smooth finish and segments were accurately aligned so that inner and outer annulus walls were concentric and there were no significant discontinuities at joints. There were no struts or other obstructions between the IGV's and straightening vanes. The test section was fitted with static pressure taps in the outer and inner walls and five ports at which instrumentation could be traversed radially across the flow. Only one port was used at any given time, other ports being smoothly sealed.

Instrumentation consisted of a 3-hole cobra probe, a single channel of constant-temperature hot-wire anemometry (TSI-1053A), single-sensor hot-wire probes and Rosemount Model 831A pressure transducers. The transducer sensitivity was about 0.12mm of water per mV of output voltage. The cobra probe used tubes of 0.44mm ID, 0.73mm OD, the side tubes being chamfered at 60°. The mouth of the central tube was located on the axis of the 3.2mm diameter probe stem so that the probe could be rotated about this axis without changing the location of the mouth. DISA single-sensor normal (90°) and slant (45°) hot-wire probes, models 55P11 and 55P12 respectively, were used. Sensors were tungsten wires, 5µm diameter and 1.25mm long. Support prongs and probe holders were straight.

The cobra and hot-wire probes were traversed radially at each of the five instrumentation ports using a manual traversing gear. Probe stems or holders were radial with respect to the annular duct and the traverse gear allowed rotation about this radial axis. Radial position, absolute angular orientation and changes in angular orientation (yaw) of the probes could be determined within $\pm$0.03mm, $\pm$1 deg. and $\pm$0.1 deg., respectively.

A Hewlett-Packard 3054A data acquisition and control system was used to acquire and process the pressure and hot-wire anemometer data. The system comprised a HP-85A computer, a 3497A acquisition/control unit and a 3456A digital voltmeter. The latter had a nominal sensitivity of 1µV. RMS voltages were measured using a true RMS voltmeter set at a 3 sec. integration time constant.

2.2 Experimental Methods

The cobra probe was used only to measure the radial distribution of total pressure and as a Preston tube at the inner wall of the annular duct. At each measurement point the probe was nulled by yawing it until both side tubes gave the same pressure reading. Calibration showed that the central tube gave the correct total pressure when aligned within 5° of the resultant velocity direction in uniform flow. No displacement corrections were applied; available corrections were not expected to be valid because the mouth of this particular probe was very close to the stem (within 3mm).

When resting against the inner wall, the centre of the cobra probe's mouth was 0.37mm above the wall, corresponding to $y^{+} = 70$. Previous work by Rajaratnam and Muralidhar [15] and Prahlad [16] indicates that under such conditions a nulled yaw probe can be used to determine the resultant wall shear stress and its direction. The Preston-tube calibration of Head and Vasanta Ram [17] was used.

At each measurement point in the flow, six separate readings of mean and RMS anemometer output voltage were taken, three with the normal wire probe and three with the slant wire probe. The probes were rotated about their stems to a different azimuth angle, Ψ, for each of the three readings. Mean velocity and Reynolds stress components were deduced from these data as outlined below. Azimuth angles were selected as in Table 1 to minimize wake interference effects from the sensor-support prongs.

For the hot-wire probes, the instantaneous effective cooling velocity was assumed to follow the relationship suggested by Jorgensen [18]:

$$U_{eff}^2 = U_n^2 + k^2 U_t^2 + h^2 U_b^2 \qquad (1)$$

U_n, U_t and U_b are, respectively, the velocity components normal to the sensor in the plane of the prongs, tangential to the sensor and normal to the sensor and the prongs. The relationship between anemometer bridge output voltage and U_{eff} was found by calibrating the probes in the potential core of a free jet, with the probes oriented such that $U_t = U_b = 0$. This relationship is highly non-linear and it was fitted with a fourth-order polynomial. This polynomial relationship was used to calculate a linearized output voltage for any given bridge DC output. Multiplication of bridge RMS outputs by the local slope of the polynomial relation gave corresponding 'linearized' RMS voltages. This procedure is equivalent to that implemented in hardware form by the TSI Model 1052 linearizer [19] but with the availability of a computer data acquisition system the present method was judged to be more accurate and reliable. Checks showed that it gave the same results as when the hardware linearizer was used. The yaw and pitch sensitivity factors, k and h, were determined by separate calibration steps, using a

Table 1

Azimuth Angles for Slant and Normal Hot Wire Probes With Different Swirl Angles

Nominal Swirl (degrees)	Slant Probes Angle (degrees)	Normal Probes (degrees)
45	0, 45, 90	-45, 0, 90
30	0, 45, 90	-45, 0, 90
15	0, 45, 90	-45, 45, 90
0	0, 45, 90	-45, 45, 90

procedure similar to that suggested by Bruun and Tropea [20]. For k, two separate probe orientations in the calibration flow were used such that $U_b = 0$ and $U_t \neq 0$. Given eqn. (1) and the other calibration data, k can then be calculated. h was found similarly, using two orientations for which $U_t = 0$, $U_b \neq 0$. Orientations representative of those prevailing during the flow measurements were used for determining k and h.

The velocity components of eqn. (1) can be re-expressed in terms of the instantaneous axial, radial and tangential velocity components, (U + u), (V + v) and (W + w) in the annulus. Together with the calibration information, this yields a relationship between instantaneous anemometer output voltage and velocity components. Assuming low turbulence intensity (maximum of 14 percent in the present flows), this relationship can be expanded and split into two equations, one between linearized DC anemometer voltage and the mean velocity components, U, V and W and the other between linearized RMS voltage and the turbulence parameters $\overline{u^2}$, $\overline{v^2}$, $\overline{w^2}$, $\overline{uv}$, $\overline{uw}$ and $\overline{vw}$. Of course these equations also contain the sensor orientation angles α and ψ. α was 0 and 45 degrees for the normal and slant-wire probes respectively (these values were checked and found accurate within 0.2 degrees for all probes). As mentioned, a variety of values was used for azimuth angle ψ (see Table 1). These equations can be written for each of the six DC and RMS readings made at each measurement point and solved simultaneously for the flow parameters. The system would be over-defined for the mean velocity components and the mean equations were only written and solved for the three readings made with the slant wire probes. The slant wire probes were judged to have the best sensitivity for this purpose.

The above method of measuring mean flow and turbulence parameters is similar to the rotating probe method used by other investigators, for example Bissonette and Mellor [21] and So and Mellor [22]. Bruun [23] suggested that all six readings at each point could be taken with the same slant wire probes. Acrivlellis [24], as modified by Bartenwerfer [25], suggested a maximum of five measurements with a slant probe and the sixth with a normal probe. In the present work, attempts to take five readings with a single probe were unsuccessful; the resulting equations lacked linear independence. The procedure of three readings with each probe worked best. It should also be noted that Comte-Bellot *et al.* [26] found that orienting hot wire probes normal to the flow was not significantly inferior to aligning them with the stream direction.

Hot wire probes were re-calibrated about every three hours.

3. Computational Method and Turbulence Models

As will be seen later, the present experimental results showed that the behaviour of the Reynolds shear stresses near the annulus walls was consistent with relatively simple mixing-length models. It therefore appeared to be appropriate to assess the suitability of such models for computation of swirling flows in annuli. For this purpose a numerical method was formulated and implemented as a computer program.

The governing equations were expressed in terms of primitive variables. Incompressible axisymmetric steady flow was assumed. All lengths, velocities, pressure and kinematic viscosity (molecular and turbulent) were non-dimensionalized by (r_o-r_i), $\overline{U}$, $\overline{U}^2$ and $\overline{U}(r_o-r_i)$ respectively. $\overline{U}$ is the mean axial velocity in the annulus. In non-dimensional terms the continuity and momentum equations then become:

$$\frac{\partial U}{\partial x} + \frac{V}{r} + \frac{\partial V}{\partial r} = 0 \tag{2}$$

$$U\frac{\partial U}{\partial x} + V\frac{\partial U}{\partial r} = \frac{-\partial P}{\partial x} + \frac{\partial U}{\partial r}\left(\frac{(\nu + \nu_{rz})}{r} + \frac{\partial \nu_{rz}}{\partial r}\right) + (\nu + \nu_{rz})\frac{\partial^2 U}{\partial r^2} \tag{3}$$

$$\frac{W^2}{r} = \frac{\partial P}{\partial r} \tag{4}$$

$$U\frac{\partial W}{\partial x} + V\frac{\partial W}{\partial r} + \frac{VW}{r} = \left(\frac{\partial W}{\partial r} - \frac{W}{r}\right)\left(\frac{(\nu + \nu_{r\theta})}{r} + \frac{\partial \nu_{r\theta}}{\partial r}\right) + (\nu + \nu_{r\theta})\frac{\partial^2 W}{\partial r^2} \tag{5}$$

These equations are for a cylindrical coordinate system (x, r, θ) with mean velocity components U, V, W and turbulent fluctuation velocities u, v, w. The axial viscous and turbulent diffusion terms were assumed negligible so that the equations are parabolic and the non-dimensional radial velocity terms have been neglected in the radial momentum eq. (4). ν is the non-dimensional kinematic molecular viscosity. The axial and tangential kinematic eddy viscosity components are defined in the usual way:

$$\nu_{rx} = -\overline{uv}/(\frac{\delta U}{\delta r}) \tag{6}$$

$$\nu_{r\theta} = -\overline{vw}/(r\frac{\delta}{\delta r}(\frac{W}{r})) \tag{7}$$

The mixing lengths, ℓ_{rx} and $\ell_{r\theta}$, were assumed to be related to the eddy viscosity components as suggested by Lilley and Chigier [12]; that is

$$\ell_{rx}^2 = \nu_{rx}/[(\frac{\delta U}{\delta r})^2 + (r\frac{\delta}{\delta r}(\frac{W}{r}))^2]^{1/2} \tag{8}$$

$$\ell_{r\theta}^2 = \nu_{r\theta}/[(\frac{\delta U}{\delta r})^2 + (r\frac{\delta}{\delta r}(\frac{W}{r}))^2]^{1/2} \tag{9}$$

The symbols in eqns. (6) to (9) can be interpreted either as the non-dimensional or as the corresponding dimensional parameters. A number of models were tried for the mixing lengths, ℓ_{rx} and $\ell_{r\theta}$. Predictions obtained with three of these models are compared with the experimental data in this paper.

Equations (2) to (5) were solved using a fully-implicit finite-difference marching scheme taken largely from Hornbeck [27]. Central- and forward- difference expressions were used for the radial and axial derivatives, respectively. Variable grid spacing was used in the radial direction, with successive radial intervals in the ratio 1.15 for most calculations. The spacing was increased from the inner wall until about the mean radius and then decreased towards the outer wall of the annulus.

The no-slip boundary condition is applied at the inner and outer walls. Radial distributions of U, V, W and $\partial P/\partial x$ must be available at the initial station in order to start the computation. About four grid points were typically within the laminar sublayer at each streamwise step. The product of the molecular viscosity and the appropriate velocity gradient at the wall therefore gave the wall shear stress components.

The axial momentum eq. (3) is solved first. The radial velocities are then obtained by integration of the continuity eq. (2). The tangential momentum eq. (5) can then be solved. The radial momentum eq. (4) can then be integrated to obtain the radial pressure distribution. Since the axial pressure gradient is required to solve eq. (3), an iterative procedure is required. The axial pressure gradients of the previous step are used as initial values and all four equations are solved. If the resulting mean axial velocity differs from $\overline{U}$, the pressure on the outer wall is adjusted while $\delta P/\delta r$ is left unchanged. This gives new estimates for $\delta P/\delta x$ and the calculations are repeated until converged. The calculation thus predicts the pressure variation along the annulus walls. Difficulties were sometimes experienced in starting the calculations when no good estimates of the axial pressure gradients at the first station were available. With perseverance, estimates which led to convergence would eventually be found. It was found helpful to set the radial velocity to zero for the first few steps.

The computer program was verified by computation of various laminar flows for which exact solutions are available. Overall conservation of axial and angular momentum was checked and found to be closely satisfied for all computations. Most of the computations used 101 radial grid points and a non-dimensional axial step length of 0.13. Convergence was checked by increasing the number of radial grid points and decreasing the step length; computed results were virtually unchanged. Numerical errors are believed to be negligible.

The three mixing length models reported on in this paper are summarized in Table 2. All three models make use of Van Driest damping [28] near the walls; A^+ was assigned the usual value of 26 and y^+ was based on the resultant wall shear stress. Model B uses an extended form of the Galbraith et al. [14] modified mixing length near the annulus walls. Galbraith et al. showed that incorporation of the ratio of local to wall shear stress in the mixing length formula gives better consistency with the observed persistence of the logarithmic law-of-the-wall even when rather strong adverse pressure gradients are present. Their work was for two-dimensional plane boundary layer flows. Analysis of the present experimental data indicated that the same idea, as expressed in model B of Table 2, also gives improved correlation with the near-wall behaviour of swirling flows in annuli. Model C of Table 2 is the only one which incorporates curvature correction terms. Away from the walls, the mixing length models are particularly simple. The work of Moore [29, 30] indicates that such models can be adequate even in very complex flows. δ is taken as the distance from the wall to the axial-velocity maximum; since this is not generally at the mean radius, δ has different values for the inner and outer portions of the annular flows and the mixing length is discontinuous at the axial-velocity maximum.

Table 2 - Mixing Length/Eddy Viscosity Models

Model	Main Source	Axial Mixing Length Distribution		Tangential Mixing Length Distribution	
		Near-wall region $\ell_o = Ky(1-e^{-y+/A+})$	Away from the wall	Near-wall region $\ell_o = Ky(1-e^{-y+/A+})$	Away from the wall
A	Patankar and Spalding	$\ell_{rx} = \ell_o$	$\ell_{rx} = 0.08\delta$	$\ell_{r\theta} = \ell_{rx}$	$\ell_{r\theta} = \ell_{rx}$
B	Galbraith Sjolander and Head	$\ell_{rx} = \ell_o\sqrt{\frac{\tau_{rx}}{\tau_{x,w}}}$	$\ell_{rx} = 0.08\delta$	$\ell_{r\theta} = \ell_o\sqrt{\frac{\tau_{r\theta}}{\tau_{\theta,w}}}$	$\ell_{r\theta} = 0.08\delta$
C	Bradshaw	$\ell_{rx} = \ell_o(1- Ri)$ (concave wall) $\ell_{rx} = \ell_o/(1+ Ri)$ (convex wall)	$\ell_{rx} = 0.08\delta\,(1- \beta Ri)$ or $\ell_{rx} = 0.08\delta/(1+\beta Ri)$	$\ell_{r\theta} = \ell_{rx}$	$\ell_{r\theta} = \ell_{rx}$
eddy viscosity all models		$\nu_{rx} = \ell_{rx}^2\left\{\left[\frac{\delta U}{\delta r}\right]^2 + \left[r\frac{\delta(W/r)}{\delta r}\right]^2\right\}^{1/2}$		$\nu_{r\theta} = \ell_{r\theta}^2\left\{\left[\frac{\delta U}{\delta r}\right]^2 + \left[r\frac{\delta(W/r)}{\delta r}\right]^2\right\}^{1/2}$	

$$Ri = 2W\frac{\delta(rW)}{\delta r}\Big/r^2\left\{\left[\frac{\delta U}{\delta r}\right]^2 + \left[r\frac{\delta(W/r)}{\delta r}\right]^2\right\}$$

β = 1.5 for inner wall $K = 0.4$

β = 2.5 for outer wall

4. Results and Discussions

4.1 Consistency Checks on the Experimental Data

A number of checks for axisymmetry and consistency were applied to the data. Such checks included: (a) mean axial velocity, $\overline{U}$, constant within $\pm$0.7 percent; (b) outer wall static pressure near start of annulus circumferentially uniform within $\pm$1.5 percent of $0.5\rho\overline{U}^2$; (c) dynamic pressure at mid-radius circumferentially uniform within $\pm$3 percent at all stations; (d) axial and angular momentum between stations 1 and 5 conserved within $\pm$20 percent of the force or torque due to skin friction stresses on the annulus walls; this is equivalent to $\pm$1.7 percent or better of the initial momentum or angular momentum; (e) comparison of static pressures measured by inner-wall taps with those determined by integration of the radial momentum equation from the outer wall; (f) comparison of total pressures measured with the 3-hole probe with those computed from the static pressures and the mean velocity and normal Reynolds stress data; (g) comparisons of wall shear stresses measured by Preston tube with those determined from Clauser plots and by extrapolation of the Reynolds shear stresses measured within the flow. The comparisons of (e), (f) and (g) were always very satisfactory; examples can be seen in the figures which present the experimental results.

4.2 Error Estimates for Experimental Data

Errors can arise from effects of velocity gradients over the slant wire probes, neglect of higher order turbulence terms in the data reduction equations, imperfect calibration and linearization, position and orientation errors, and sensitivity and repeatability limitations. A detailed error analysis is given by Yowakim [31]. The maximum error on the mean velocity components U and W is estimated at 4 percent and is mainly due to neglect of turbulence terms, calibration errors and repeatability limitations. The radial velocity V is very small and estimated errors on it were over 100 percent; consequently no data for V are presented and it was set to zero in the data reduction calculations. The maximum error is estimated at 15% on the Reynolds stresses $\overline{uv}$, $\overline{vw}$, $\overline{u^2}$ and $\overline{w^2}$ and at 20% on $\overline{uw}$ and $\overline{v^2}$. As outlined, the Reynolds stresses are obtained by simultaneous solution of six equations representing six separate readings; the errors arise mainly from sensitivity and repeatability limitations. Wall shear stresses are estimated to be accurate within $\pm 0.0003(0.5\rho\overline{U}^2)$.

The quality of the data is perhaps best indicated by the small scatter seen in the figures and by the very good agreement between results obtained by different techniques.

4.3 Experimental Results

Complete data for all four flows are presented by Yowakim [31]. Only selected data are presented in this paper with the emphasis on the 30 degree swirl flow. More data on the 45 degree swirl flow are presented in another paper [32].

Figure 2 shows the distributions of wall static pressure along the inner and outer walls of the annulus for all four flows. The values measured on the inner wall are seen to agree closely with those calculated by integration of the radial momentum eqn. (4) from the outer wall.

The axial and tangential components of wall shear stress were determined independently of one another by a Clauser-plotting technique based on an extended form of the law of the wall [31, 33]. Figure 3 shows examples of the Clauser plots. Wall shear stresses determined in this way are presented in Fig. 4; the values measured by the Preston-tube technique are also shown and agreement is seen to be good. The shear stresses on the outer wall are seen to be generally higher than those on the inner wall. This reflects the unstable and stable gradients of angular momentum near the outer and inner walls, respectively.

Figure 5 shows radial distributions of the mean axial and tangential velocity components at the first and last measurement stations of the annular duct. The distributions can be integrated to obtain the swirl number, that is the ratio of tangential to axial momentum fluxes divided by the radius of the outer wall. At station 1 the swirl number has values of 0.23, 0.47 and 0.87 for the flows with nominal swirl angles of 15, 30 and 45 degrees, respectively. The swirl number decreases gradually along the annulus due to the retarding torque exerted by the tangential component of the wall shear stress.

Radial distribution of the axial and tangential Reynolds shear stresses, $\rho\overline{uv}$ and $\rho\overline{uw}$, are shown in Fig. 6 for the 30 degree swirl flow. Note that the Reynolds stress data are entirely consistent with the wall shear stress values determined by the Clauser plotting and Preston tube techniques.

The normal Reynolds stresses, $\rho\overline{u^2}$, $\rho\overline{v^2}$ and $\rho\overline{w^2}$ in the 30 degree swirl flow are presented in Fig. 7. The turbulence is seen to be an-isotropic; as might be expected, the radial fluctuation intensity, $\overline{v^2}$, is distinctly less than the other two intensities, especially in the vicinity of the annulus walls.

Mixing lengths and eddy viscosities have been determined from the data. Figure 8 presents some results for the two components of mixing length.

4.4 Computational Results

Computations for all four measured flows were carried out using the turbulence models of Table 2 and others. Some computed results for the 30 degree swirl flow are compared with the experimental data in this paper. These comparisons are quite typical of the results in general. Comparisons between computed and measured results for the 45 degree swirl flow are available in [34].

Computed wall shear stresses are compared with the experimental data in Fig. 9. Agreement with experiment is fairly good and there are no major differences between the three turbulence models. Model B is a little more successful in predicting the difference between shear stress values on the inner and outer walls but is less successful in stabilizing at the correct values near the start of the calculations. Neither of these are, however, general trends. All three of these turbulence models are very similar near the walls and the differences in predicted wall shear stresses are mainly the result of differences in predicted velocity distributions in the core region of the annulus, that is away from the walls.

Computed and experimental mean velocity profiles are compared in Fig. 10. All three turbulence models give fairly good predictions of the axial velocity profiles. Predictions of the tangential velocity profile are not quite as good, especially for turbulence model C. It should be noted that it is easier to obtain good predictions of the axial velocity profiles because continuity requires that the mean axial velocity, $\overline{U}$, have the same value for all profiles.

Even though the present simple turbulence models produce only fair predictions of tangential velocity profiles, Reddy et al [34] have shown that these predictions are much better than those obtained by Yamamoto and Millar [8] using a more complex two-equation ($k-\varepsilon$) turbulence model.

The main success of the present simple mixing-length turbulence models is in predicting the near-wall region of the measured swirling flows. This success is illustrated in Fig. 11 where predicted and measured velocity distributions are plotted in law-of-the-wall coordinates. The agreement is seen to be good. The good agreement in the near-wall region is not surprising in view of the fact that the near-wall mixing length models, particularly that of model B, Table 2, agree well with the experimental data, as seen in Fig. 8. The agreement in Fig. 11 would be even better if better

turbulence models for the core region of the flow were available, since wall shear stress predictions would then be more accurate than those of Fig. 9. The predicted wall shear stresses of Fig. 9 were used to non-dimensionalize the computed velocity components for plotting in Fig. 11.

4.5 Remarks

Experimental evidence for a wide variety of wall-bounded flows indicates that the law-of-the-wall is very persistent [14, 1] and fails only in relatively extreme cases, such as in very severe pressure gradients. As discussed elsewhere [33], the present experiments show that the law-of-the-wall also applies at the convex and concave walls of an annular duct with swirling flow. Accurate prediction of the near-wall region of wall-bounded flows is of crucial importance because of its dominant influence on wall shear stress. Computational methods must therefore place great emphasis on correct performance near walls.

The near-wall model B of Table 2 is considered to be very satisfactory. It has been shown to produce excellent predictions of swirling flow near both the inner and the outer walls of an annular duct. Moreover it is very simple and easy to incorporate in computational methods. The correct law-of-the-wall behaviour is automatically obtained when it is used so that there is no need to incorporate special wall functions as is frequently done. Chen and Patel [35] have recently shown that even the best available wall functions lack the flexibility inherent in the other approach, that is the use of a turbulence model that is valid right to the wall.

Simple mixing length and eddy viscosity models are purported to lack universality and to be somewhat arbitrary. They do however lead to recovery of the law-of-the-wall and, as mentioned above, the law-of-the-wall is in reality quite persistent. Moreover, recent investigations into coherent structures in wall-bounded turbulent flows suggest that simple turbulence models may have a sounder physical basis than previously supposed. For example the observations of Head and Bandyopadhyay [36] indicate that the outer part of turbulent boundary layers is composed largely of vortex loops inclined at a characteristic angle to the wall. These loops appear to originate close to the wall and would be expected to play an important role in momentum transfer across the shear layer. In view of both this and the practical success of the simple turbulence models, it seems inappropriate to dismiss them at this time.

The work on swirling flows in ducts is continuing, with the emphasis on developing improved turbulence models for the core region of the flow.

5. Conclusions

Mean flow and turbulence parameters have been measured in four swirling flows in an annular duct. The data are comprehensive and of high quality and are suitable for validation of computational fluid dynamics codes.

The data show that a simple mixing-length turbulence model is valid near the annulus walls.

Computations have demonstrated that use of a simple mixing length model results in very good predictions of flow behaviour in the crucial near-wall regions of the swirling annular flows.

6. Acknowledgements

The experimental work was initiated by D.A.J. Millar who was responsible for development of the annular swirl tunnel facility. The financial support of the Natural Sciences and Engineering Research Council, under its Operating Grants program, is also gratefully acknowledged.

7. References

1. Kline, S.J., Cantwell, B.J., Lilley, G.M. (eds.) proc. 1980-81 AFOSR-HTTM-Stanford Conference on Complex Turbulent Flows; Comparison of Computation and Experiment, Stanford University, Stanford, CA, Vol. II, 1981.

2. Yeh, H., "Boundary Layer Along Annular Walls in a Swirling Flow", Trans. ASME, J. Basic Eng., Vol. 80, pp. 767-776, 1958.

3. Scott, C.J. and Rask, D.R., "Turbulent Viscosities for Swirling Flow in a Stationary Annulus", Trans. ASME, J. Fluids Eng., Vol. 95, pp. 557-566, 1973.

4. Scott, C.J. and Bartelt, K.W., "Decaying Annular Swirl Flow With Inlet Solid Body Rotation", Trans. ASME, J. Fluids Eng., Vol. 98, pp. 33-40, 1976.

5. Gosman, A.D., Pun, W.M., Runchal, A.K., Spalding, D.B. and Wolfstein, M., "Heat and Mass Transfer in Recirculating Flows, Academic Press, London, 1969.

6. Patankar, S.V. and Spalding, D.B., "A Calculation Procedure for Heat, Mass and Momentum Transfer in Three-Dimensional Parabolic Flows", Int. J. Heat Mass Transfer, Vol. 15, pp. 1787-1806, 1972.

7. Briley, W.R., "Numerical Method for Predicting Three-Dimensional Steady Viscous Flow in Ducts, J. Comp. Phys., Vol. 14, pp. 8-19, 1974.

8. Yamomoto, A. and Millar, D.A.J., "A Calculation of Laminar and Turbulent Swirling Flows in Cylindrical Annuli", in: Flow in Primary, Non-Rotating Passages in Turbomachines, ed. Herring, H.J., Soler, A. and Steltz, W.G., ASME, N.Y., pp. 89-98, 1979.

9. Koosinlin, M.L. and Lockwood, F.C., "The Prediction of Axisymmetric Turbulent Swirling Boundary Layers", AIAA Journal, Vol. 12, pp. 547-554, 1974.

10. Koosinlin, M.L., Launder, B.E. and Sharma, B.I. - "Prediction of Momentum, Heat and Mass Transfer in Swirling Turbulent Boundary Layers", Trans. ASME, J.Heat Transfer, Vol. 96. pp. 204-209, 1974.

11. Bradshaw, P., "Effect of Streamline Curvature on Turbulent Flow", AGARD-ograph 169, 1973.

12. Lilley, D.G. and Chigier, N.A., "Nonisotropic Turbulent Stress Distribution in Swirling Flows from Mean Value Distributions, Int.J. Heat Mass Transfer, Vol. 14, pp. 573-585, 1971.

13. Lilley, D.G., "Nonisotropic Turbulence in Swirling Flows, Acta Astronautica, Vol. 3, pp. 919-933, 1976.

14. Galbraith, R.A. McD., Sjolander, S. and Head, M.R., "Mixing Length in the Wall Region of Turbulent Boundary Layers, Aero. Quart., Vol. XXVII, pp. 97-110, 1977.

15. Rajaratnam, N. and Muralidhar, D., "Yaw Probe Used as Preston Tube", The Aeronautical Journal, Vol. 72, pp. 1059-1060, 1968.

16. Prahlad, T.S., "Yaw Characteristics of Presston Tubes", AIAA J., Vol. 10, No. 3, pp. 357-359, 1979.

17. Head, M.R. and Vasanta Ram, M.R., "Simplified Presentation of Preston Tube Calibration", Aero Quarterly, Vol. XXII, pp. 295-300, 1971.

18. Jorgensen, F.E., "Directional Sensitivity of Wire and Fiber-film Probes", DISA Information, No. 11, 1971.

19. TSI Inc., "TSI Instruction Manual for Model 1052 Linerizer", Thermo-Systems Inc., St. Paul, Minnesota, 1975.

20. Bruun, H.H. and Tropea, C., "Calibration of Normal, Inclined and X-Array Hot Wire Probes", University of Karlsruhe SFB 80/M/170, 1980.

21. Bissonnette, L.R. and Mellor, G.L., "Experiments on the Behaviour of an Axisymmetric Turbulent Boundary Layer With a Sudden Circumferential Strain", J. Fluid Mech., Vol. 63, pp. 369-413, 1974.

22. So, R.M.C. and Mellor, G.L., "Experiment on Convex Curvature Effects in Turbulent Boundary Layers", J.Fluid Mech., Vol. 60, pp. 43-62, 1973.

23. Bruun, H.H., "A Review of Conventional and Some Advanced Hot-wire Measurements and Their Physical Interpretation", von Karman Inst. for Fluid Dynamics, Lecture Series 96, 1977.

24. Acrivlellis, M., "An Improved Method for Determining the Flow Field of Multidimensional Flows of Any Turbulence Intensity", DISA Information, No. 23, 1978.

25. Bartenwerfer, M., "Letters to the Editors - Comments on: The Method for Analyzing Hot-wire Signals", DISA Information, No. 24, 1979.

26. Comte-Bellot, G., Strohl, A. and Alcaraz, E., "On Aerodynamic Disturbances Caused by Single Hot-Wire Probes", Trans ASME, J. of Applied Mechanics, Vol. 38. pp. 767-774, 1971.

27. Hornbeck, R.W., "Numerical Marching Techniques for Fluid Flows with Heat Transfer, NASA SP-297, 1973.

28. van Driest, E.R., "On Turbulent Flow Near a Wall, J.Aero.Sci., Vol. 23, pp. 1007-1011, 1956.

29. Moore, J. and Moore, J.G., "A Calculation Procedure for Three-Dimensional, Viscous, Compressible Duct Flow. Part II-Stagnation Pressure Losses in a Rectangular Elbow", Trans. ASME, J.Fluids Eng., Vol. 101, pp. 423-428, 1979.

30. Moore, J. and Moore, J.G., "Performance Evaluation of Linear Turbine Cascades Using Three-Dimensional Viscous Flow Calculations", Trans. ASME, J. Eng. Gas Turbines and Power, Vol. 107, pp. 969-975, 1985.

31. Yowakim, F.M., "Experimental Investigation of Turbulent Swirling Flow in an Annulus", Ph.D. thesis, Carleton University, Ottawa, Ontario, Canada, 1985.

32. Yowakim, F.M. and Kind, R.J., "Mean Flow and Turbulence Measurements of Annular Swirling Flows", submitted to ASME J. Fluids Eng., 1987.

33. Kind, R.J., Yowakim, F.M. and Sjolander, S.A., "The Law of the Wall for Swirling Flow in Annular Ducts", submitted to ASME J.Fluids Eng., 1988.

34. Reddy, P.M., Kind, R.J. and Sjolander, S.A., "Computation of Turbulent Swirling Flow in an Annular Duct", proc. Fifth Int. Conf. on Numerical Methods in Laminar and Turbulent Flow, Montreal, Vol. 5, Part 1, pp. 470-481, 1987.

35. Chen, H.C. and Patel, V.C., "Practical Near-Wall Turbulence Models for Complex Flows Including Separation", AIAA Paper No. 87-1300, June 1987.

36. Head, M.R. and Bandyopadhyay, P., "New Aspects of Turbulent Boundary-Layer Structure, J. Fluid Mech., Vol. 107, pp. 297-338, 1981.

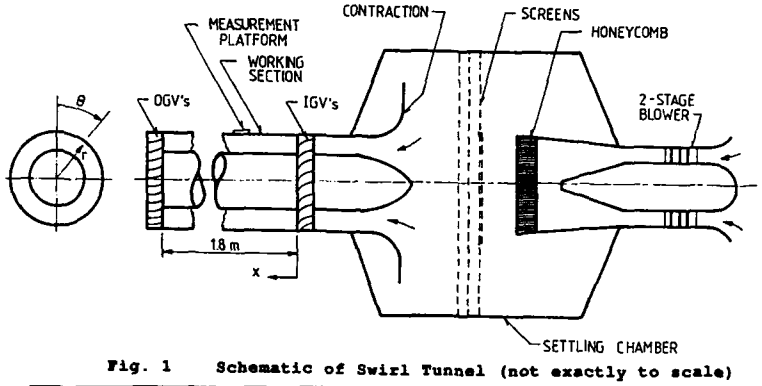


Fig. 1 Schematic of Swirl Tunnel (not exactly to scale)

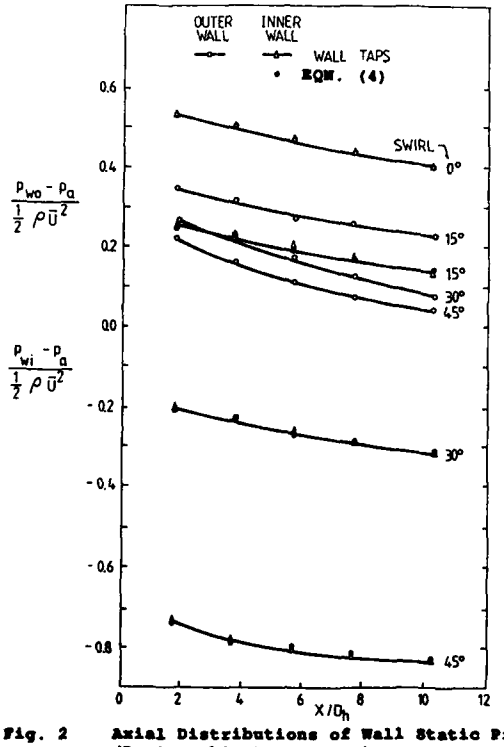


Fig. 2 Axial Distributions of Wall Static Pressures (P_a is ambient pressure)

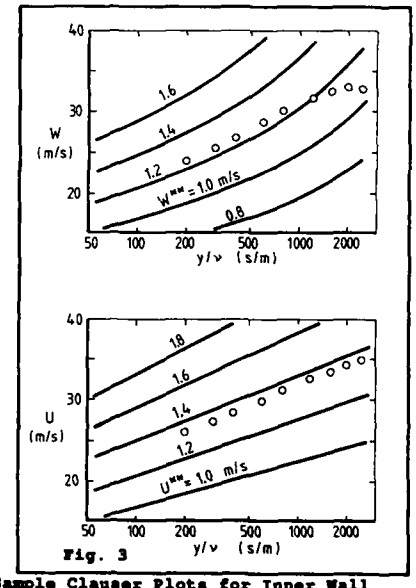


Fig. 3 Sample Clauser Plots for Inner Wall
o = data, 45° swirl flow, x/D_h = 10.3
——— = law of wall relations [33]

$U^{**} = \tau_{x,w}/\sqrt{\rho\tau_w}$; $W^{**} = \tau_{\theta w}/\sqrt{\rho\tau_w}$;

τ_w = resultant shear stress.

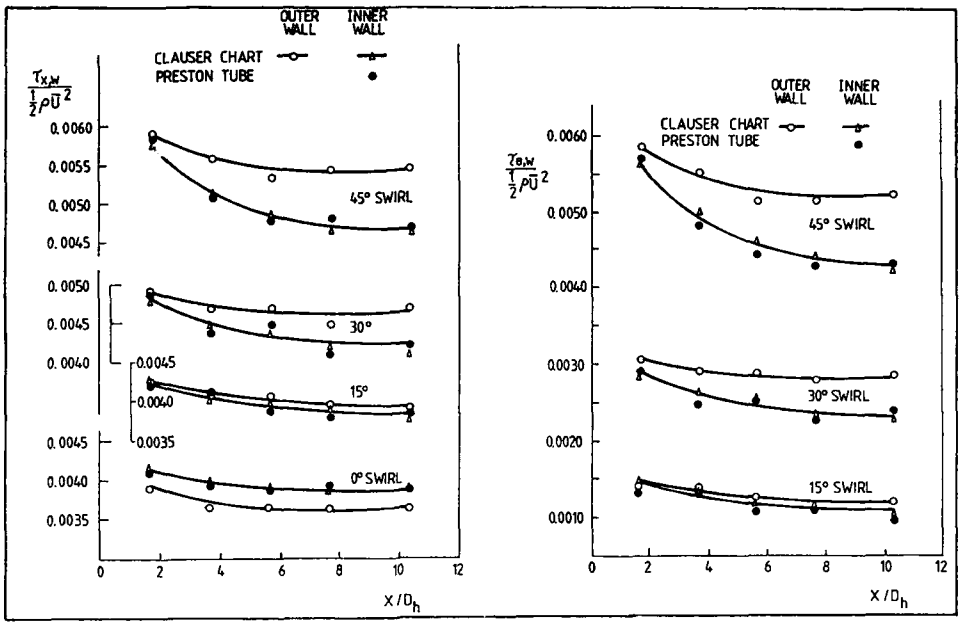


Fig. 4 Axial Distributions of Axial and Tangential Components of Wall Shear Stress

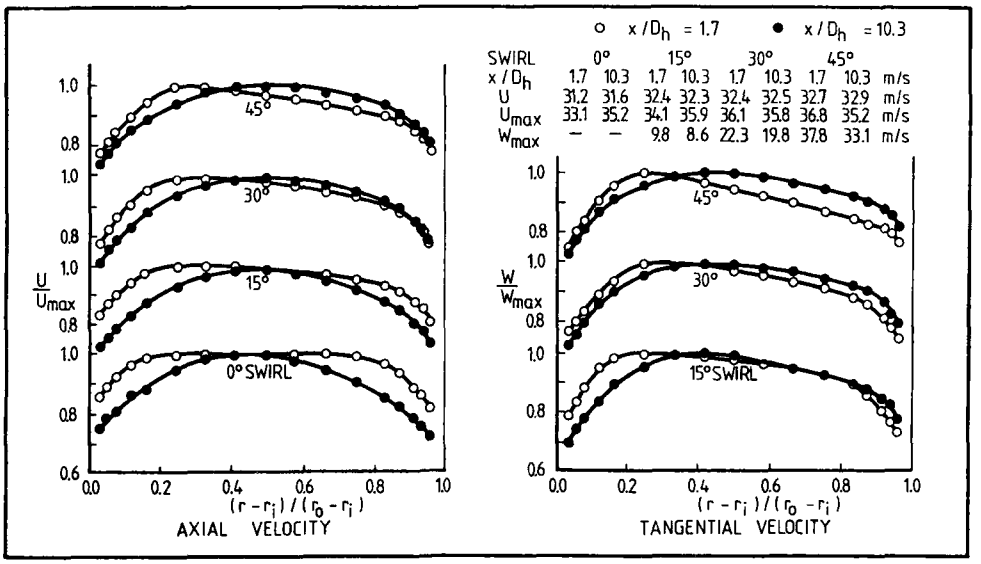


Fig. 5 Radial Distributions of Axial and Tangential Mean Velocity at First and Last Measurement Stations

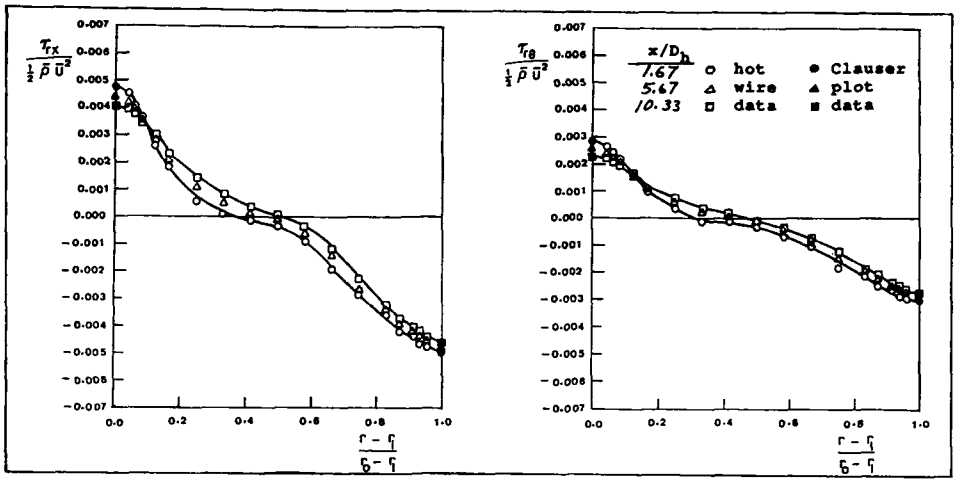


Fig. 6 Radial Distributions of Axial and Tangential Reynolds Stresses in 30° Swirl Flow

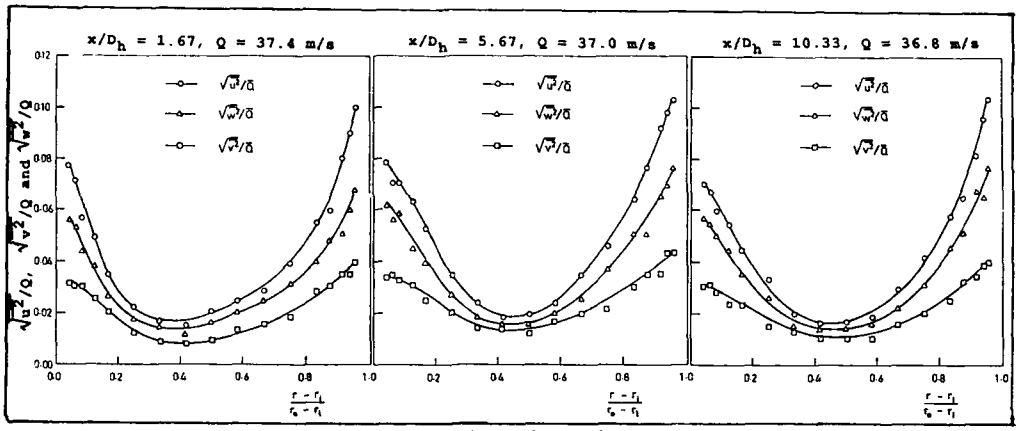


Fig. 7 Radial Distributions of Normal Reynolds Stresses
(Q = radially averaged resultant mean velocity)

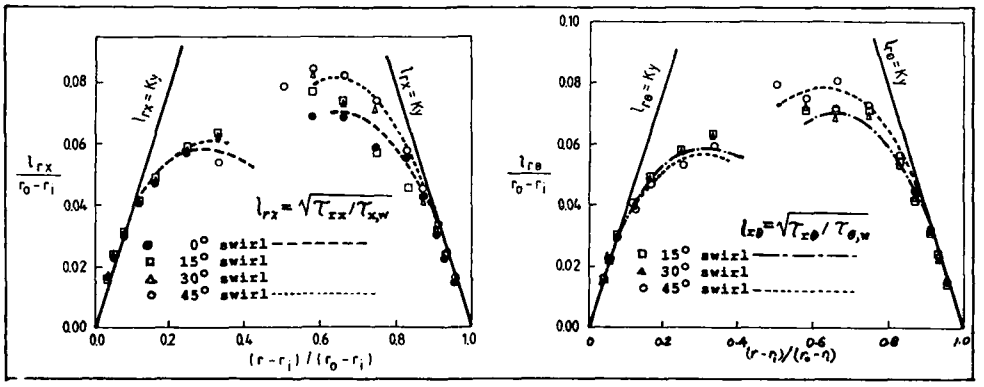


Fig. 8 Radial Distributions of Axial and Tangential Mixing Lengths at x/D_h = 10.3

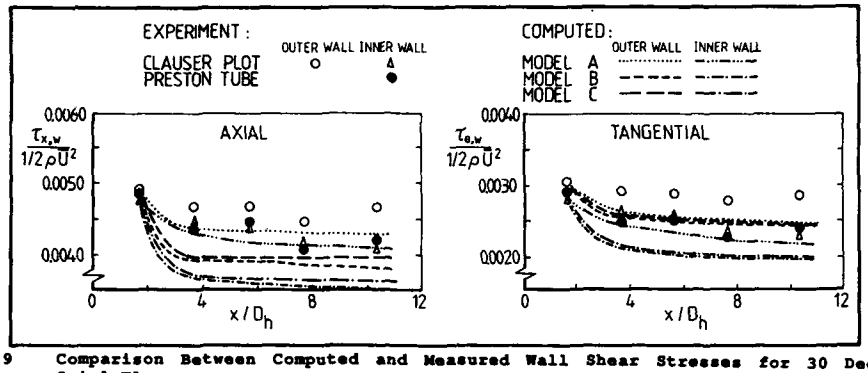


Fig. 9 Comparison Between Computed and Measured Wall Shear Stresses for 30 Degree Swirl Flow

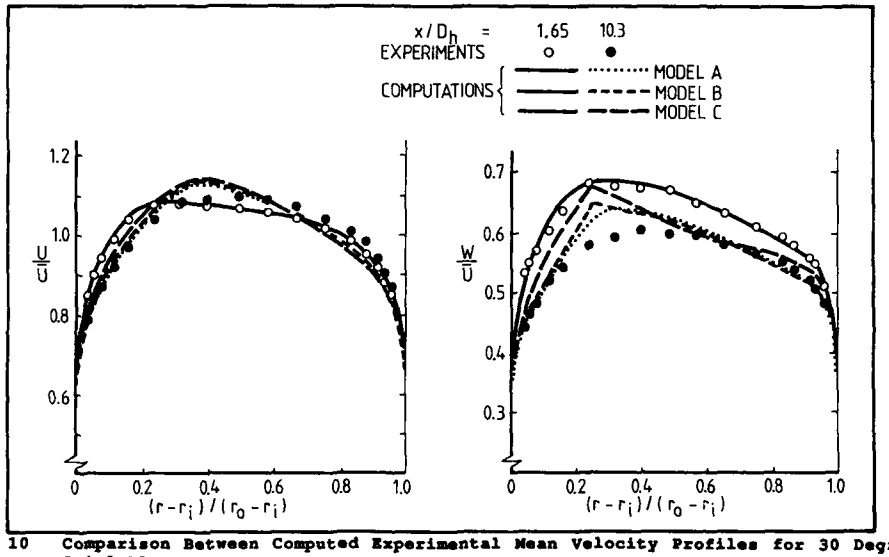


Fig. 10 Comparison Between Computed Experimental Mean Velocity Profiles for 30 Degree Swirl Flow

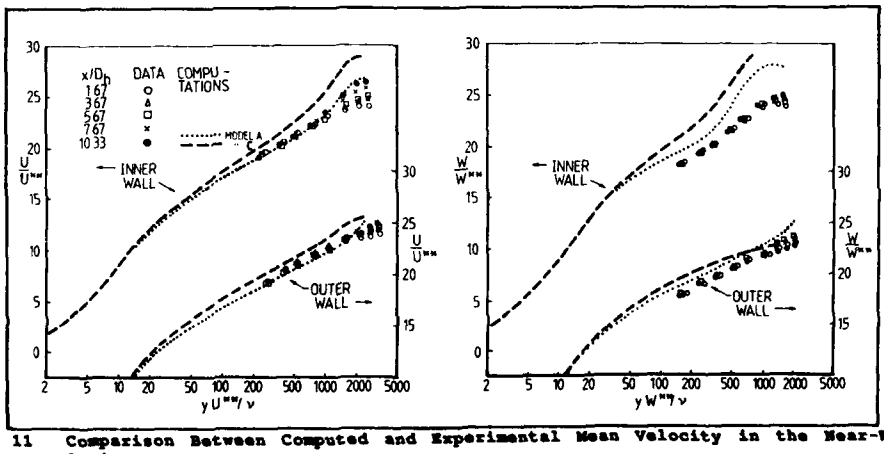


Fig. 11 Comparison Between Computed and Experimental Mean Velocity in the Near-Wall Region

ON THE VALIDATION OF 3-D NUMERICAL SIMULATIONS OF TURBULENT IMPINGING JETS THROUGH A CROSSFLOW

J.M.M. Barata*, D.F.G. Durão*, M.V. Heitor* and J.J. McGuirk**

*Instituto Superior Técnico
Mechanical Engineering Department
Av. Rovisco Pais
1096 Lisboa Codex
PORTUGAL

**Imperial College of Science and Technology
Mechanical Engineering Department
London SW7 2BX
ENGLAND

ABSTRACT

Laser-Doppler measurements of the flow field resulting from the impingement of a single axisymmetric jet against a wall after penetrating a confined cross flowing stream are presented and used to validate numerical predictions of the flow. The experiments have been carried out for a Reynolds number (based on jet exit conditions) of 60000, corresponding to a jet to crossflow velocity ratio of 30 and for a jet exit 5 jet diameters above the opposing wall. This study provides a basis for better understanding of several related but more complex practical flow fields. The data is particularly suitable for the evaluation of the accuracy of the turbulence model used in several numerical methods currently under development for the prediction of this type of flow. As an example of this latter use, calculations are presented of the three-dimensional flow characterised by the measurements. A standard "k-ε" turbulence model is used in these calculations. The difficulty of assessing turbulence model performance in these complex flows due to the intrusion of numerical diffusion errors is demonstrated by comparing calculations on both coarse and fine meshes and by improving the accuracy of the discretisation of the convection terms using the high order QUICK method. The ability of the model calculations to simulate both the mean and the turbulence fields is examined, particularly in the imediate vicinity of the stagnation point.

NOMENCLATURE

D - diameter of the jet
H - height of the crossflow channel
k - turbulence kinetic energy
Re - Reynolds number
U - horizontal velocity, $U = \overline{U} + u'$
V - vertical velocity, $V = \overline{V} + v'$
X - horizontal coordinate (positive in direction of crossflow)
Y - vertical coordinate (positive in direction of jet flow)
Z - transverse coordinate (positive on right side of cross-flow duct looking upstream)

subscripts

j - jet-exit value
o - crossflow value

1. INTRODUCTION

Single or multiple jets issuing into a crossflow are typical of many engineering problems, such as the discharge of exhaust gases from a chimney into the atmosphere or of waste liquids into water, film cooling of turbine blades, dilution jets in gas-turbine combustors and thrust vector control of rocket trajectories. If the crossflow is also confined, as in the present case, further complexity may be introduced by jet impingement; here the most important practical relevance is to the flow field beneath a short take-off/vertical landing, STOVL, aircraft close to the ground. In this apllication the lift jets interact strongly with the ground plane resulting in lift losses, in enhanced entrainment close to the ground (suckdown), in engine thrust losses following re-ingestion of the exhaust gases and in possible aerodynamic instabilities caused by fountain impingement on the aircraft underside.

The study of a single jet in crossflow which subsequently undergoes impingement on a ground plane provides a basis for understanding the essential dynamics of these more complex practical flowfields. The provision of detailed flow field measurements will also allow the validation of numerical solutions of the governing equations of motion and the associated turbulence models. The present paper provides laser-Doppler measurements of the velocity characteristics of the flow produced by a single round jet discharged through the upper wall of a rectangular water channel of large cross section (.50 x .10 m) at right angles to the channel flow. The work follows that of (1) and is particularly devoted to the experimental validation of computational codes.

Some qualitative information relevant to the flow beneath STOVL aircraft in ground vicinity has been provided recently by the flow visualisation studies of (2) for H/D < 4 without a crossflow. Much of the measurements reported so far have concentrated on the unconfined problem or on relatively large impingement heights (typically H/D > 10) and low jet-to-crossflow velocity ratio (predominantly V_j/U_∞<20). References (3) to (5) provide measurements of jet trajectories and mean velocity and temperature profiles for values of V_j/U_∞<10. The data of (6) and (7) provide more detailed measurements, but for H/D of 24 and for velocity ratios of 2 and 16. References (8) and (9) present results for more relevant impingement heights (8 and 3 respectively), but again the velocity ratio range falls short of the interesting region (i.e. less than 8). Turbulence measurements in impinging jet flows are even more rare: (10) reports LDV measurements (including those of shear stress) but for unconfined flow and for a velocity ratio of 2.3; (11) have used hot-wire techniques in jets in crossflow, but for extremely low velocity ratios (0.5-2) and, therefore, of little value in the present context. This gap in available data was first addressed by reference (1), who reports LDV measurements of impinging jets in crossflow for a velocity ratio between the jet and the crossflow of 30 and for the jet exit 5 jet-diameters above the ground plate. The results are extended in the present work to the validation of first-and second-order numerical schemes.

Numerical calculations of impinging jets through a crossflow for high velocity ratios and small impingement heights have also been attempted by (1) based on a first-order scheme. Reference (13) did report some preliminary calculations of impinging jets in crossflow, but little attention was given to the strongly impinging case due to the lack of experimental data. Although a two equation "k-ε" model was employed in these calculations, the use of first order upwind differencing and very coarse meshes made any statements on turbulence model accuracy impossible due to the intrusion of numerical diffusion. The "k-ε" model of turbulence was also used by (14) to predict flow situations relevant to the STOVL problem but, again, the results remain to be evaluated against experimental data. Reference (15) has also addressed the question of false diffusion in 3D jets-in-crossflow calculations and found necessary to adopt the higher order QUICK discretisation for the convective terms in order to obtain numerically accurate solutions. The calculations presented in this paper were obtained with a highly modified version of the code used by (13) and follow those reported by (1) with the "k-ε" turbulence model and the hybrid numerical scheme. The present results are new, in that they provide examination of a two-equation model performance in this type of flow based on detailed measurements.

The following section describes the experimental method, gives details of the flow configuration, of the laser Doppler velocimeter and of the errors incurred in the measurements. Section 3 presents and discusses the results and section 4 summarizes the main findings and conclusions of this work.

2. FLOW CONFIGURATION, EXPERIMENTAL TECHNIQUE AND MEASUREMENT PROCEDURE

The experiments were carried out in a horizontal water channel, 1.50m long and 0.5 m wide, made of perspex, as shown schematically in figure 1. The apparatus was built to allow multi-jet impingement experiments with variable blockage ratio, H/D, but in the present study a single jet of 20 mm exit diameter has been used at a fixed impingement height of 5 jet diameters. The crossflow duct extends 20D upstream and 55D downstream of the jet entry which is symmetrically located at 12.5D from each side wall. The jet unit comprises a nozzle with an area contraction ratio of 16 and a settling chamber 0.56m long, which begins with a 7° flow distributor followed by flow straighteners. The facility has a recirculating system whereby both jet and crossflow water is drawn from a discharge tank and pumped to a constant-head tank or supplied to the jet unit via control valves. The uniformity of the crossflow was ensured by straighteners and screens.

The origin of the horizontal, X, and vertical, Y, coordinates is taken at the centre of the jet exit in the upper wall of the tunnel: X is positive in the crossflow direction and Y is positive vertically downwards.

The present results were obtained for a jet exit mean velocity of 3 m/s, giving rise to a Reynolds number based on the jet exit conditions of 60000. The nozzle exit turbulence intensity was measured to be approximately 2%. The crossflow mean velocity used was 0.1, corresponding to a velocity ratio between the jet and the crossflow of 30. Measurements obtained in the crossflow without the jet have shown that the local turbulence intensity of the crossflow was 18% and that the wall boundary layer in the jet impingement region had an uniform thickness around 10 mm.

The experimental equipment and measurement procedure used in this study have been explained in detail by (1) and only a brief description will be given here. The velocity field was measured by a dual-beam, forward-scatter laser velocimeter, which comprised an argon-ion laser operated at a wavelength of 514.5 nm and a nominal power of around 1 W, sensitivity to the flow direction provided by light-frequency shifting from acousto-optic modulation (double Bragg cells), a 310 mm focal length transmission lens and forward-scattered light collected by a 150 mm focal length lens at a magnification of 0.76. The half-angle between the beams was 3.48° (4.64° in air) and the calculated dimensions of the measuring volume at the e^{-2} intensity locations were 2.225 and 0.135 mm. The horizontal, U, and vertical, V, mean and turbulent velocity components were determined by a purpose-built frequency counter interfaced with a microprocessor, as described by (16). The fluctuating velocity components were also used, together with those at 45°, to compute the local shear stress distribution, $\overline{u'v'}$. Measurements were obtained up to 2mm from the ground plate with the transmitting optics inclined half-angle of beam intersection and with the scattered light collected off-axis. Results obtained 20 mm above the ground plate with both the on-axis and the off-axis arrangements have shown a close agreement, within the precision of the equipment.

Errors incurred in the measurement of velocity by displacement and distortion of the measuring volume due to refraction on the duct walls and the change in refractive index were found to be negligibly small and within the accuracy of the measuring equipment. No corrections were made for sampling bias, and the systematic errors that could have arisen were minimized by using high data rates in relation to the fundamental velocity fluctuation rate, as suggested for example by (17) and (18). Non-turbulent Doppler broadening (systematic) errors due to gradients of mean velocity across the measuring volume, e.g. (19), may affect essentially the variance of the velocity fluctuations, but for the present experimental conditions are sufficiently small for their effect to be neglected: the maximum error is of the order of $10^{-4}\ V_j^2$, and occurs at the edge of the jet. Transit broadening has been shown by (20) to be the principal source of error

in laser velocimetry: for the present optical configuration the related signal-to-noise ratio is about 69 and the maximum error in the variance of the velocity fluctuations is of the order of $2 \times 10^{-3} V_j^2$.

The number of individual velocity values used in the experiments to form the averages was always above 10 000. As a result, the largest statistical (random) errors were 1.5% and 3%, respectively for the mean and variance values, according to the analysis referred by (21) for a 95% confidence interval.

3. RESULTS AND DISCUSSION

The results are presented and discussed under two headings: the first considers contours of mean and turbulent velocities, and the second compares experimental results with predictions obtained with the "k- " model of turbulence together with two numerical schemes. The contours have been drawn using a bi-cubic interpolation between measurements obtained along 11 (eleven) vertical profiles and 14 (fourteen) horizontal profiles in the region $-10<X/D<7$ and $0.75<Y/D<4.9$.

Prior to the present detailed measurements the visualization studies of (1), also obtained for Re_j=60000 and V_j/U_o=30, have identified an initial potential-core jet region and an impingement region characterized by considerable deflection of the jet. This becomes almost parallel to the ground plate and originates a recirculating flow region far upstream of the impinging jet. A second recirculation zone was detected on the wake of the impinging jet due to deflection of the crossflow. The following paragraphs examine this qualitative description of the flow and extend the analysis of the results of (1) to the validation of numerical schemes.

3.1 Mean and turbulent velocity characteristics

Figure 2 shows contours of the mean velocity components $\overline{U}$ and $\overline{V}$ for H/D=5 and V_j/U_o=30 and quantify the mean flow characteristics of the impinging jet and of the radial wall-jets for these conditions. The deflection of the impinging jet by the crossflow is noticed by the location of the impingement point at about X/D=0.2. This deflection of the impinging jet is observed in (1) through peaks in the horizontal profiles of the horizontal velocity component on the downstream edge of the jet and is associated with the flow asymmetry indicated by the contours of the mean vertical velocity, $\overline{V}$, figure 2(b). It is expected that this asymmetry varies with the velocity ratio V_j/U_o, but the results suggest that for a wide range of conditions, the flow in the vicinity of the jet is largely controlled by complex inviscid dynamics, so that the influence of turbulence on the flow development may be weak and limited to the far flow-field, as also discussed by (11).

Figure 2(a) identifies the upstream recirculating flow region noted before, due to the interaction of the crossflow with the upstream wall jet. It consists in a scarf vortex wrapped around the jet with its size and strength expected to increase with the velocity ratio V_j/U_o. The second recirculating flow region formed in the wake of the impinging jet, away of the ground plate, due to deflection of the crossflow is identified by the contour of zero axial velocity and it is expected to be not significantly affected by the velocity ratio V_j/U_o.

Figure 3 shows contours of measured turbulent characteristics for V_j/U_o=30 and indicates two regions of intense velocity fluctuations, i.e. the shear layer surrounding the impinging jet and the impingement zone itself. Both are located in the zones where the highest mean velocity gradients occur and are associated with near-Gaussian velocity probability distributions suggesting the absence of discrete frequency oscillations. Along the impinging jet, the asymmetry of the distributions of the normal stresses is associated with the comparatively large mean velocity gradient that occurs along the downstream edge of the jet. The influence of the velocity ratio V_j/U_o upon the shape of the contours of the figure 3 is expected to be small, although the maxima of the stresses may increase as V_j/U_o increases. The results also show that the flow is anisotropic. Along the impinging jet, with the exception of the initial potential core, $\overline{v'^2}$ is the largest stress with $\sqrt{\overline{u'^2}}/\sqrt{\overline{v'^2}} \geq 0.7$. On the other hand, along the wall jets the peak values of $\overline{u'^2}$ are the largest with $\sqrt{\overline{u'^2}}/\sqrt{\overline{v'^2}} \leq 2.3$.

The contours of the shear stress $\overline{u'v'}$, figure 3(c), quantify the turbulent diffusion along the impinging and wall jets. The sign of the shear stress is consistent with the direction of the mean flow, with near zero values at the centre of the impinging jet. The shear stress is positive along the downstream edge of the impinging jet and shows that faster moving elements of jet fluid (i.e., v'>0) tend to move outwards into the wake of the jet (u'>0). Similarly, the shear stress is negative along the upstream edge of the jet because there the faster moving elements of jet fluid are associated with negative horizontal velocity fluctuations. Along the wall jets a similar analysis holds and the shear stress is positive upstream of the jet exit and negative otherwise. For example, the results show that in the downstream wall-jet the faster elements of jet fluid (u'>0) tend to move away from the wall (v'<0) giving sise to negative values of Reynolds shear stress. The present results also show that away from the impinging zone the sign of the shear stress u'v' is related with the sign of the shear strain in accordance with a turbulent viscosity hypothesis, i.e. $\overline{u'v'}=-\nu_T (\partial\overline{U}/\partial Y+\partial\overline{V}/\partial X)$, where ν_T is a turbulent viscosity. Along the impinging jet the shear strain $\partial\overline{V}/\partial X$ dominates and $\overline{u'v'}=-\nu_T \partial\overline{V}/\partial X$, while along the wall jets $\partial\overline{U}/\partial Y>|\partial\overline{V}/\partial X|$ and the shear stress changes its sign and may be represented by $\overline{u'v'}=-\nu_T \partial\overline{U}/\partial Y$. Around the impinging point the values of $\partial\overline{U}/\partial Y$ and $\partial\overline{V}/\partial X$ have the same order of magnitude and the "thin shear layer approximation", e.g. (22) and (23), is no more valid. The gradient diffusion approximation does not represent the flow because it is subject to strongly stabilizing curvature and the turbulent structure of this zone is probably influenced by extra rates of strain, e.g. (24). It is noted that in agreement with this analysis the correlation coefficient of shear stress in the impingement region is smaller than 0.2 while its maximum value along the impinging and wall jets is about 0.55 and, therefore, close to the values found in undisturbed shear layers, e.g. (22).

3.2 The numerical simulation of the flow field

The detailed nature of the mean and fluctuating velocity measurements present in the previous section make the data eminently suitable to validate numerical calculations of the flow. Numerical predictions are presented using the "k-ε" model of turbulence together with the first order hybrid numerical scheme

implemented in 3-D meshs of 30x17x17 and 60x34x34 nodes to quantify the magnitude of numerical errors. In addition, calculations are also presented here improving the accuracy of the discretization of the convection terms of the transport equations through the use of the high order QUICK (quadratic upstream weighted) method.

Figure 4 shows typical measured and calculated vertical profiles of the mean velocity components $\overline{U}$ and $\overline{V}$ and quantifies the similarity of the profiles. The figure shows clearly the formation of both upstream and downstream wall jets after jet impingement. The presence of the scarf vortex far upstream of the jet exit is noted in the profile at X/D=-4 by the relatively large positive values of $\overline{V}$ (i.e., downwards) away of the ground plane compared with those values measured close to the wall. An important feature of the flow also shown in figure 4 is that the upstream wall-jet follows the ground plate until separation occurs, while the downstream wall-jet is associated with negative (i.e. upward) mean vertical velocities and, therefore, is slightly directed away from the ground plate with a maximum inclination of 3.8^{o} at X/D=2.5 for V_j/U_o=30.

Figure 5 extends the previous figure and shows typical measured and calculated profiles of turbulent quantities. The results confirm the previous analysis in that regions of intense velocity fluctuations occur along the zone characterized by the highest mean velocity gradients.

Figure 4 and 5 quantify the effect of refining the mesh on the accuracy of the calculation method based on the hybrid scheme. They compare measured vertical profiles of mean and turbulent velocity characteristics with predicted values using a coarse mesh of 30x17x17 nodes and a fine mesh of 60x34x34 nodes (X, Y, Z respectively). This is the finest mesh that can be used with the computer storage available and gives results that may be considered as grid independent. The grid spacing was non-uniform with grid lines particularly clustered in the vicinity of the shear layers and impinging zone. The results show that although the mean axial velocity profile is well predicted with the two meshes, the predicted mean vertical velocity and turbulent levels are considerably improved by grid refinement. The analysis is extended in figure 6 by the comparison between measured and predicted horizontal profiles of mean and turbulent quantities close to the ground plate, at Y/D=4.7. The results suggest that, even with fine meshes, there are regions of the flow where the turbulent viscosity assumption is innaplicable. Beyond the fact that the shear stress is considerably overpredicted along a large region of the flow, the sign of the calculated values near the impinging zone is wrong because, as noted before, the gradient hypothesis does not represent the flow in this region. In spite of the failure of the turbulence model to predict the structure of the impinging zone, it should be pointed out that the corresponding effect on the simulation of the mean flow is not significant, as shown in figure 4, because the flow is dominated by large pressure gradients (similar observations are however not valid if the wall heat transfer is to be calculated).

The ability of the "k-ε" model to simulate the mean flow was further analysed by increasing the order of the discretization of the convection terms in the transport equations using the QUICK method together with the coarse mesh of 30x17x17 nodes. Figure 7 compares measured particle tracks (or streaklines) over 0.2 seconds on the vertical plane of symmetry with predicted velocity fields using the hybrid and QUICK methods. The figure allows a clear visualization of the impinging jet and of the upstream scarf vortex and shows that the two numerical schemes may predict the gross features of the flow, although the QUICK method requires coarser meshes. Predictions obtained with the QUICK method implemented in a mesh of 30x17x17 are similar to those with the hybrid method with a fine mesh of 60x34x34. Both methods allows a good agreement with the measurements but still overpredict the length of the scarf vortex by about 2D. Both the QUICK and the hybrid scheme do not simulate the upward tilting of the downstream jet, at least at the extent observed in the measurements.

4. CONCLUSIONS

Laser-Doppler measurements have provided information of the mean and turbulent velocity characteristics of the flow created by a single round jet impinging on a ground plate through a confined crossflow for H/D=5 and V_j/U_o=30. The experimental results have allowed to validate numerical calculations of the flow based on the solution of the finite difference form of the fully tridimensional Navier-Stokes equations, incorporating the turbulence viscosity concept. The following is a summary of the more important findings and conclusions of this work.

o The impinging jet penetrates strongly through the crossflow, although is slightly bent with the stagnation point at x/D=0.2. The deflected jet becomes almost parallel to the ground plate and the upstream wall-jet terminates in a scarf-vortex. The downstream wall-jet lifts from the ground plate.

o The shear layer surrounding the impinging jet and the impingement zone are characterized by intense velocity fluctuations with maximum values coincident with the highest mean velocity gradients. The distribution of shear stress is consistent with that of shear strain in the sense of a gradient diffusion hypothesis with exception of the impingement zone, which is dominated by strong stabilizing curvature effects.

o Grid independent numerical calculations of the flow are presented with the hybrid scheme implemented in a mesh of 60x34x34 nodes and quantify the importance of grid refinement to reduce numerical errors. Similar predictions were obtained with the high order QUICK method implemented in a coarse mesh of 30x17x17, representing the gross features of the mean flow. In the impingement zone, however, the shear stress, $\overline{u'v'}$, is not predicted correctly and this is independent of numerical influences and confirms that this zone is not represented by a turbulent viscosity hypothesis.

ACKNOWLEDGEMENTS

The present work was partially supported by the U.K. Ministry of Defense (RAE, Farnborough) and has been performed in collaboration between the "Centro de Termodinamica Aplicada e Mecanica dos Fluidos da Universidade Técnica de Lisboa", C.T.A.M.F.U.T.L, and the Fluids Section of the Imperial College of Science and Technology.

The assistance of Mrs Margarida Cristóvão in typing this paper is gratefully acknowledged.

REFERENCES

1. Barata, J.M.M., Durão, D.F.G., Heitor, M.V. and McGuirk, J.J. (1987). Experimental and Numerical Study on the Aerodynamics of Jets in Ground Effect. To appear in Exp. in fluids. Also, Tenth Symposium on Turbulence, University of Rolla-Missouri, Missouri, 22-24 Sept. 1986.

2. Saripalli, K.R. (1983). Visualisation Studies of Jet Impingement Flows at McDonnell Douglas Research Laboratories. Flow Visualisation III, Univ. Michigan, Sept. 6-9.

3. Keffer, J.F. and Baines, W.D. (1963). The Round turbulent jet in a Cross-wind. J. Fluid Mech., Vol. 15, pp. 481-496.

4. Ramsey, J.W. and Goldstein, R.J. (1972). Interaction of a Heated jet with a Deflecting Stream. NASA CR 72613.

5. Kamotani, Y. and Greber, I. (1972). Experiments on a Turbulent Jet in a Cross Flow. AIAA Journal, Vol. 10, pp. 1425-1429.

6. Sugiyama, Y. and Usami, Y. (1979). Experiments on the Flow in and around Jets directed normal to a Crossflow. Bulletin JSME, Vol. 22, pp. 1736-1745.

7. Shayesteh, M.V., Shabaka, I.M.N.A. and Bradshaw, P. (1985). Turbulent Structure of a Three-dimensional Impinging Jet in a Crossflow. AIAA 23rd Aerospace Sciences Meeting, Reno-Nevada, 14-17, Jan. 1985.

8. Kamotani, Y. and Greber, I. (1974). Experiments on Confined Turbulent Jets in a Cross-flow. NASA CR-2392.

9. Stoy, R.L. and Ben-Haim, Y. (1973). Turbulent jets in a confined cross-flow. J. Fluids Engng., Vol. 95, pp. 551-556.

10. Crabb, D., Durão, D.F.G. and Whitelaw, J.H. (1981). A round jet normal to a crossflow. J. Fluids Engng., Vol. 103, pp. 142-153.

11. Andreopoulos, J. (1985). On the structure of jets in a crossflow. J. Fluid Mech., Vol. 157, pp. 163-197.

12. Andreopoulos, J. and Rodi, W. (1984). Experimental investigation of jets in a crossflow. J. Fluid Mech., Vol. 138, pp. 93-127.

13. Jones, W.P. and McGuirk, J.J. (1980). Computation of a round turbulent jet discharging into a confined cross-flow. Turbulent Shear Flows 2, pp. 233-245.

14. Childs, R.E. and Nixon, D. (1985). Simulation of impinging turbulent jets. AIAA 23 rd Aerospace Sciences Meeting, Reno-Nevada, 14-17 Jan. 1985.

15. Demuren, A.O. (1983). Numerical calculations of steady three-dimensional turbulent jets in a cross flow. Comput. Meth. Appl. Mech. and Engrg., Vol. 37, pp. 309-328.

16. Heitor, M.V., Laker, J.R., Taylor, A.M.K.P. and Vafidis C. (1984). Introduction Manual for the FS model 2 Doppler-Frequency counter. Imperial College, Mech. Engng. Dept. Report FS/84/10.

17. Dimotakis, F. (1978). Single scattering particle laser-Doppler measurements of turbulence. AGARD CP 13, paper 10.7

18. Erdmann, J.C. and Tropea, C.D. (1981). Turbulence-induced statistical bias in laser anemometry. Proc. 7th Biennal Symp. on Turbulence. Rolla-Missouri.

19. Durst, F., Melling, A. and Whitelaw, J.H. (1981). Principles and practice of laser-Doppler anemometry. 2nd. ed., Academic Press, New York.

20. Zhang, Z. and Wen, J. (1987). On principal noise of the laser Doppler velocimeter. Exp. in Fluids, Vol. 5, pp. 193-196.

21. Yanta, W.J. and Smith, R.A. (1978). Measurements of turbulent-transport properties with a laser-Doppler velocimeter. AIAA paper 73-169, 11th Aerospace Science Meeting, Washington.

22. Castro, I.P. and Bradshaw, P. (1976). The turbulence structure of a highly curved mixing layer. J. Fluid Mech., Vol. 73 (2), pp. 265-304.

23. Cebeci, T. and Bradshaw, P. (1977). Momentum transfer in boundary layers. Hemisphere Publ. Corp. Washington.

24. Bradshaw, P. (1973). AGARD ograph 169.

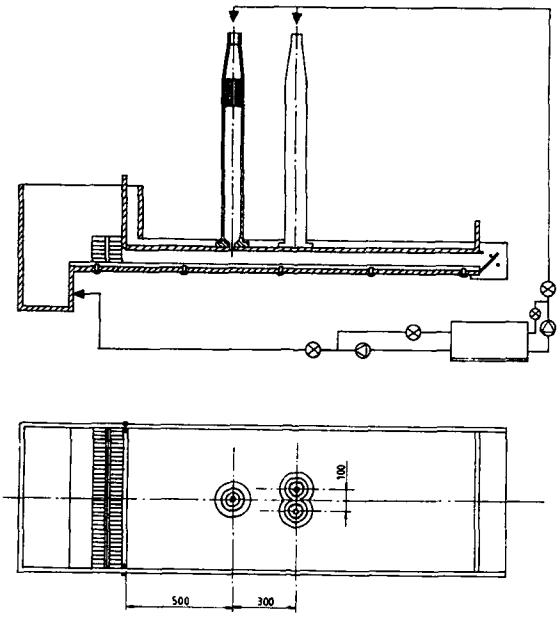
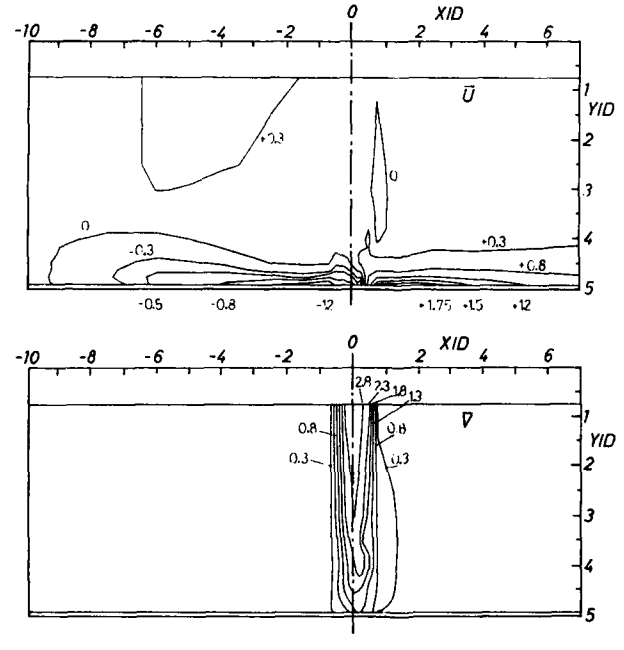


Fig. 1 - Diagram of flow configuration



(a)

(b)

Fig. 2 - Contours of measured mean velocity characteristics for V_j/U_o=30 and H/D=5

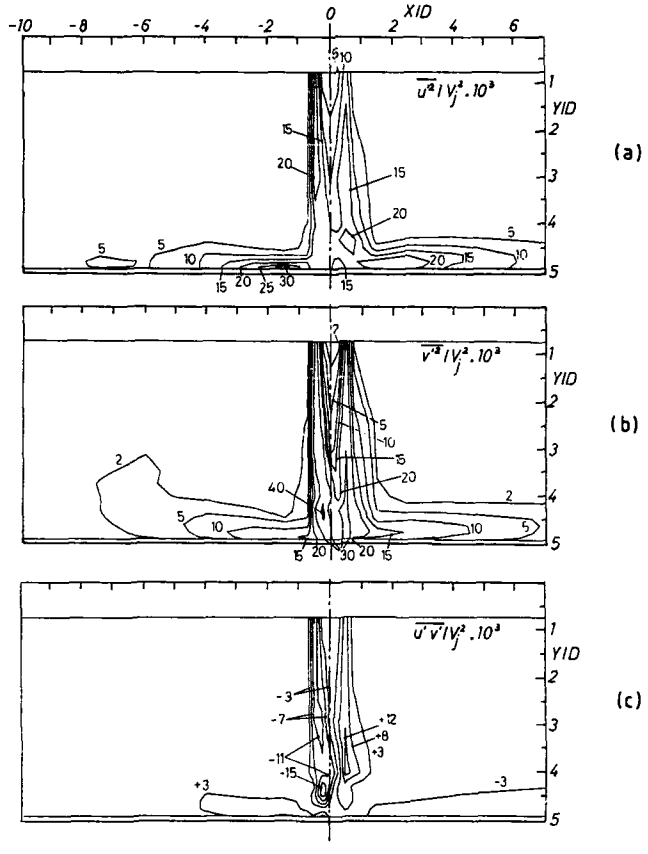


Fig. 3 - Contours of measured fluctuating velocity characteristics for V_j/U_o=30 and H/D=5

a) $\overline{u'^2}/V_j^2$; b) $\overline{v'^2}/V_j^2$ c) $\frac{\overline{u'v'}}{V_j^2} \times 10^3$

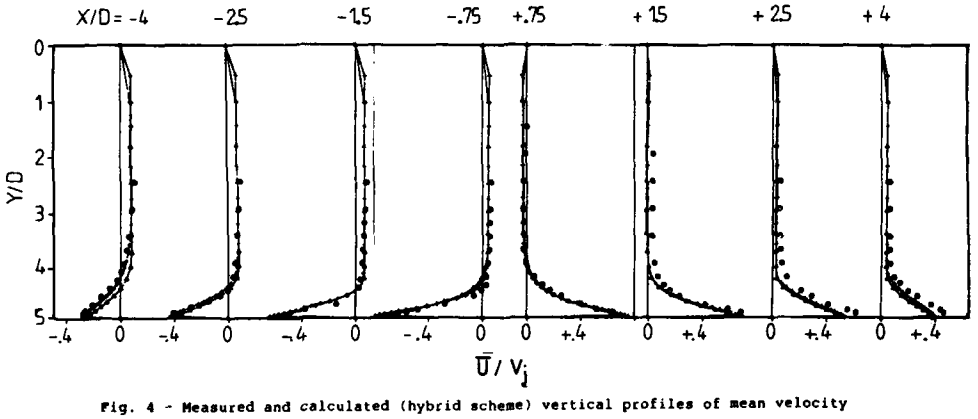
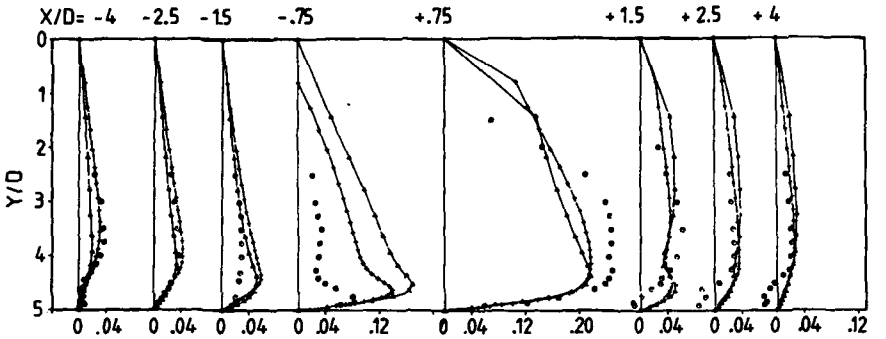


Fig. 4 - Measured and calculated (hybrid scheme) vertical profiles of mean velocity characteristics for V_j/U_o=30 and H/D=5

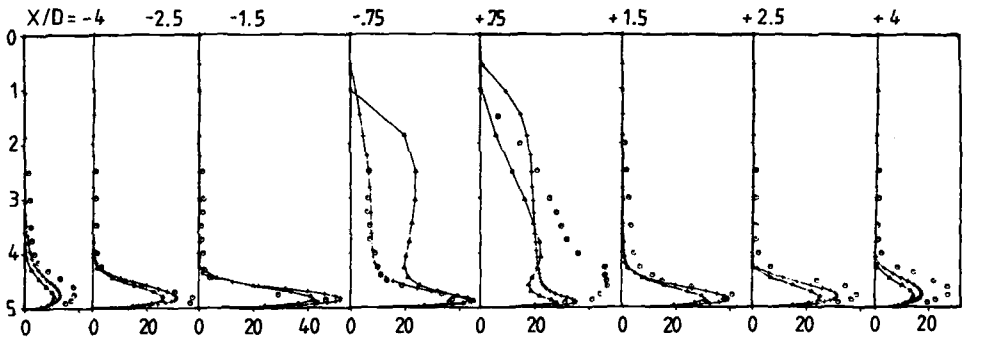
Ⓜ measured; ++ calculated (60 x 34 x 34); Δ—Δ calculated (30 x 17 x 17)

a) $\overline{U}/V_j$; b) $\overline{V}/V_j$

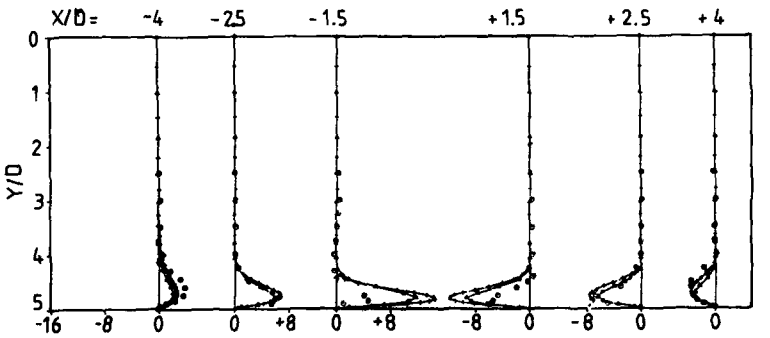


b) $\bar{v}/v_j$

Fig. 4 (cont.) ⓘ measured; ++ calculated (60 x 34 x 34); △—△ calculated (30 x 17 x 17)



a) $(\overline{u'^2} + \overline{v'^2})/V_j^2 \times 10^3$



b) $\overline{u'v'}/V_j^2 \times 10^3$

Fig. 5 - Measured and calculated (hybrid scheme) vertical profiles of turbulent velocity characteristics for V_j/U_o=30 and H/D=5
ⓘ measured; ++ calculated (60 x 34 x 34); calculated (30 x 17 x 17) △—△

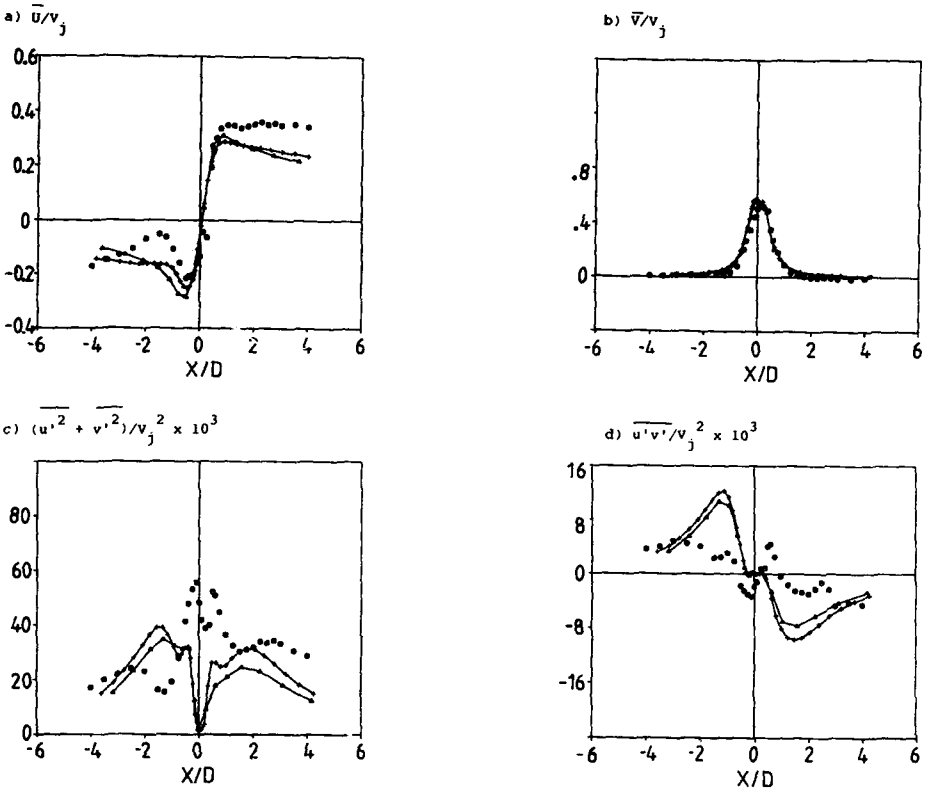
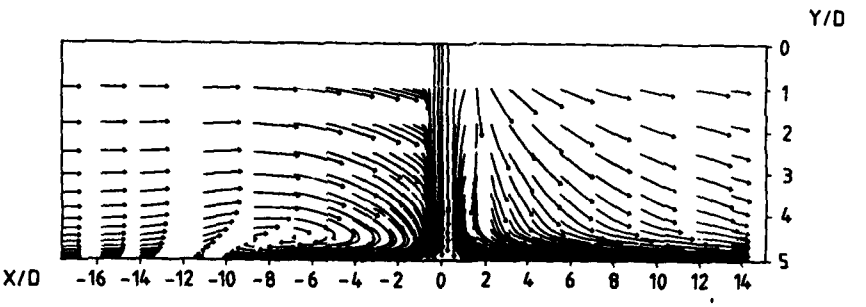


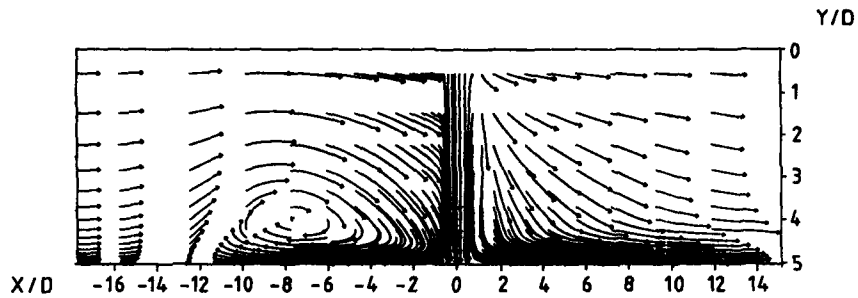
Fig. 6 - Horizontal profiles of mean and turbulent velocity characteristics for V_j/U_o=30 and H/D=5 at Y/D=4.7

measured; ++ calculated (60 x 34 x 34); △—△ calculated (30 x 17 x 17)

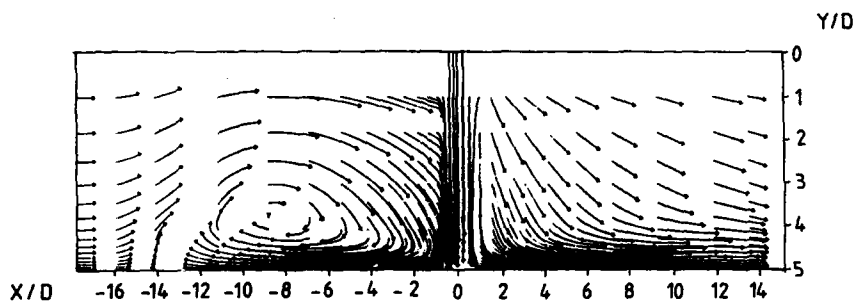


a) Calculations with hybrid scheme (30 x 17 x 17)

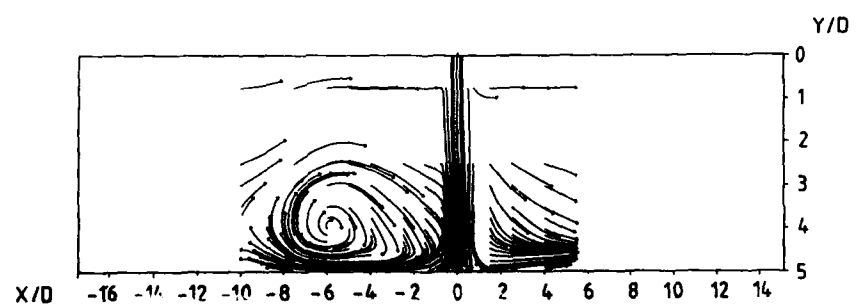
Fig. 7 - Streaklines over 0.2 s for V_j/U_o=30 and H/D=5



b) Calculations with hybrid scheme (60 x 34 x 34)



c) Calculations with QUICK scheme (30 x 17 x 17)



d) Measurements

Fig. 7 (cont.)

Time-dependent numerical simulation of the starting flow of an incompressible fluid past a downstream-facing step.

M. Ciofalo
Dipartimento di Ingegneria Nucleare, Universitá di Palermo, Viale delle Scienze, 90128 Palermo, Italy.

M.W. Collins
Thermo-Fluids Engineering Research Centre, The City University, Northampton Square, London, EC1V 0HB, U.K.

SUMMARY

An impulsively-generated transient flow of an incompressible fluid past a complex-shaped body is investigated numerically using the two-dimensional Navier-Stokes equations. The geometry is a flat plate with a backward-facing step and a blunt trailing edge. Reynolds numbers, based on free-stream velocity and step height, range from 50 to 500. Results are compared with flow visualization data in water. The influence of boundary and initial conditions, differencing scheme, time stepping, pressure-velocity coupling algorithm and other computational parameters is discussed. A literature review is included of experimental and predictive studies on laminar and transitional flow past backsteps.

NOMENCLATURE

H	Step height
L_1	Length of plate upstream of the step
L_2	Length of the splitter plate downstream of the step
L_3	Length of the region downstream of the plate included in the computational domain
M	Total mass flow rate
N	Number of outer (pressure-velocity coupling) iterations
p	Pressure
RF	Residual reduction factor (ratio of final/initial residual) for stopping the linear equation iterative solvers
S	Strouhal number for vortex shedding = $H/(\Delta t u_o)$
t	Time
u_o	Reference velocity (= velocity of motion of the plate)
u,v	Velocities in the streamwise and cross-stream directions
x,y	Coordinates in the streamwise and cross-stream directions
z	Coordinate in the spanwise direction

Greek symbols

δ	99% boundary layer thickness
δ^*	boundary layer displacement thickness
Δt	Time step
$\Delta\tau$	Non-dimensional time step
$\delta\tau$	Non-dimensional interval between consecutive vortex pairs
ϵ_M	Mass source residual (sum of the absolute values of nett mass fluxes in-out of the control volumes) required to stop the outer iterations.
ν	Kinematic viscosity
τ	Non-dimensional time = tu_o/H
ψ	Stream function

Subscripts

c	Centre of smoke filament
e	Rear end of smoke filament
H	Step height
M	Mass
R	Reattachment
w	Wake
o	Reference

1. INTRODUCTION AND LITERATURE SURVEY

1.1. Laminar and transitional flows past backward-facing 90° steps have been investigated both experimentally and numerically for their relevance to the mechanics of flow separation, reattachment, and transition. Some of the most important experimental works on this subject are summarized in Table 1; reference is made to the geometry and nomenclature shown in Figure 1.

Table 1. Summary of experimental works on laminar and transitional backstep flow

Authors	Ref.	Fluid	R	e.r.	a.r.	d.r.	Exp. technique
Moore (60)	1	Air	1000-5000	<1.1	~1	~47	Pitot, visual.
Goldstein et al (70)	2	Air	100-500	<1.1	~0.6	~50	Hot-wire, visual.
Denham & Patrick (74)	3	Water	50-250	1.5	6.6	13.3	LDA, visual.
Honji (75)*	4	Water	50-500	<1.1	Undef.	42	Visualization
Sinha et al.(81)	5	Air	150-1000	<1.1	~1.3	34-140	Hot-wire, visual.
Armaly et al.(83)	6	Air	100-8000	3	12	20	LDA
Aung (83)**	7	Air	85-850	<1.1	~0.7	36-71	Hot-wire.

* Starting (transient) flow ** Also heat transfer measurements

With the single exception of the paper by Honji[4], therefore, all these investigations regard steady-state conditions. The two issues most frequently addressed, and relevant to the present study, are the behaviour of the reattachment length and the conditions for transition to turbulence of the separated shear layer.

a) Reattachment length

The reattachment length x_R, once non-dimensionalised with respect to the step height H, is primarily a function of the Reynolds number.

As can be seen particularly well from the results of Armaly et al.[6], which cover the whole range of R from laminar to fully turbulent, x_R/H increases up to a Reynolds number of about 10^3, then decreases and attains an almost constant value in fully turbulent flow. The maximum of x_R is associated with transition to turbulence. The mechanisms involved are discussed well by Aung[7]. Maxima of x_R/H are variously reported between 12 and 28 (while fully-turbulent values are more closely clustered in the range 5-7).

The main results from Refs.1-7 are summarised in Figure 2. The Reynolds number R is based on maximum inlet velocity and on step height. Only some of the many experimental points have been reported from the work by Goldstein et al.[2], and only Laser-Doppler data from that by Denham and Patrick[3]. The wide scatter of data can partly be explained by the influence of secondary factors affecting the reattachment length, and varying widely from one set of experiments to another (see Table 1). These factors are discussed below.

I. Thickness δ of the boundary layer at separation.

The ratio δ/H should have a direct influence on x_R/H. For generic separation bubbles an early paper by Cramer[8] proposed the following correlation, based on rather over-simplifying assumptions:

$$x_R/\delta^* = (R_{\delta^*}/3)\ ((H/\delta^* + 1)^2 - 1) \qquad (1)$$

in which δ^* is the displacement thickness of the boundary layer at separation. Assuming $\delta^* = 0.29\delta$ for a laminar boundary layer, equation (1) may be re-written as:

$$x_R/H = 0.084\ (\delta/H)^2 R\ ((\frac{3.45}{\delta/H} + 1)^2 - 1) \qquad (2)$$

which predicts an increasing x_R/H for increasing δ/H. However, Goldstein et al.[2], who used two different development lengths L_d (Figure 1), and hence two different values of δ/H for each R, observed no significant variation in x_R/H though L_d/H changed from 6 to 50. Moreover, they found that equation (1) correlated their data only if the factor $^1/_3$ was reduced about 25 times!

On the other hand results by Aung[7], who used two different values of H, indicated a decrease in x_R/H with increasing δ/H (see Figure 2), i.e. a trend opposite to Cramer's correlation (1). The expansion ratio was very low (<1.1) for both values of H, so that no effect of this parameter could be made responsible for the variation in x_R/H.

Hence, experimental findings are ambiguous on this point. It may be added that a predictive study by Aung, Baron and Tsou[9] indicates that, when R is fixed, x_R/H increases with increasing δ/H if R is larger than about 100, while otherwise decreases.

II. Adverse pressure gradients

Another parameter possibly affecting the reattachment length is the adverse pressure gradient, obviously related to the expansion ratio e.r. = L/2 for a parallel-walled channel (Figure 1). Goldstein et al.[2] found that x_R did not vary appreciably when the test-section wall opposite to the step was modified so that the duct had an expansion ratio slightly less than 1. However, to the authors' knowledge, no systematic study on this parameter has been conducted for laminar flow, so one has to resort to uncertain comparisons between separate sets of data by different experimenters (see Table 1 and Figure 2). Such a comparison seems to indicate that x_R/H decreases with increasing e.r., at least for large e.r. (compare results by Armaly et al., obtained with the highest e.r.= 3, with the others). However, it should be observed that systematic studies on the effect of the adverse pressure gradient on x_R do exist for turbulent flow, and they show an opposite trend, i.e. an increase in x_R for increasing e.r. or adverse p gradient (see Narayanan et al.[10], Kuehn[11], Mori et al.[12]). No satisfactory explanation of this apparent discrepancy will be attempted here.

III. Channel aspect ratio.

A last factor possibly affecting x_R - and more generally, the overall flow behaviour - is the channel aspect ratio $\Delta z/L$ (Figure 1), or the step aspect ratio $\Delta z/H$. Once more, unfortunately, a lack of systematic investigation on this parameter for laminar flows should be noted. Comparison between different sets of experiments sheds scarce light on the subject. It is generally accepted, however, that side-wall effects and secondary spanwise flows become negligible if $\Delta z/H$ is larger than ~10.

b) Transition of the separated shear layer

The same factors influencing the reattachment length are likely to affect the transition to turbulence of the shear layer separating from the step corner. However, besides the obvious influence of the Reynolds number R, only the effect of the ratio δ/H (or equivalent parameters) has been satisfactorily investigated.

As was already pointed out in an early paper by Owen and Klanfer[13], transition to turbulence is associated with a decrease in the length of the separation bubble. In the curves of Figure 2, onset of transition can be identified with the departure from a linearly increasing trend, which occurs between R = 500 and 1000. These values are consistent with the early criterion proposed by Tani and Sato[14] for roughness elements:

$$R\ \delta_t/\delta > 840 \qquad (3)$$

in which H is the roughness height, δ_t is the thickness of the boundary layer at the transition point, and δ is the thickness of the boundary layer at the roughness element. Transition is here implied to occur after reattachment.

Similarly, Cramer[8], for a wide class of separating flows, proposed the simple transition criterion:

$$R_{\delta^*} > 500 \qquad (4)$$

in which R_{δ^*} is the Reynolds number based on the boundary layer displacement thickness δ^*.

On the other hand, with specific reference to backsteps, Roshko and Lau[15] proposed a criterion based on the ratio δ/H:

$$\delta/H < 1 \qquad (5)$$

The two approaches are synthetized in a more comprehensive criterion proposed by Goldstein et al.[2]; they conclude that the shear layer remains laminar only if both:

$$\delta^*/H > 0.4 \qquad (6')$$

and

$$R < 520 \qquad (6'')$$

are satisfied, and undergoes transition otherwise.

No systematic study on the effect of secondary factors on transition exists, so that no definite conclusion can be drawn. Comparing in Figure 2 the results by Sinha et al.[5] (obtained with e.r. < 1.1 and a.r. = 1.3 and showing a maximum of x_R at R = 820) with those by Armaly et al.[6], (obtained with e.r. = 3 and a.r. = 12 and showing an x_R still increasing at R = 1700) one may infer that small values of either the expansion ratio or the aspect ratio (or both) facilitate transition.

1.2. Several predictive studies on laminar flow past backsteps have been published. However, they have been generally used more as validation tests for numerical methods than as a means of investigating the physical aspects of the flow. Some papers are mainly concerned with heat transfer predictions and only marginally with the flow field. Most relate to steady-state conditions, and two-dimensional flows. One of the most interesting recurrent issues is the dependence of the results on the assumed inlet conditions. Atkins et al.[16] using finite differences, and Thomas et al.[17] using finite elements, solved the Navier-Stokes equations in the two-dimensional stream function-vorticity form, and simulated the experiments by Denham and Patrick[3]. Both found good agreement in the reattachment length (in the range R = 25 to 250) if the experimental velocity profiles were used at inlet, while x_R was overpredicted using a fully-developed (parabolic) profile.

This is consistent with the observation made by Aung et al.[9] that - at least in computations - x_R/H increases with δ/H for a given R.

The same trend was found by Chiu and Pletcher[18] who solved the Partially Parabolized Navier-Stokes equations (PPNS), and by Hackman et al.[19], who included comparisons between cartesian and curvilinear grids and alternative differencing schemes.

Hall and Pletcher[20] used a rather complex viscous-inviscid interaction procedure. In the viscous region, they solved the boundary layer equations (in stream function - u velocity formulation) with the so-called FLARE approximation, which neglects streamwise convection in the recirculation bubble. Good agreement was achieved for R = 100 with data by Armaly et al.[21], but the reattachment length was overpredicted for the data by Aung[22]. The paper by Hall and Pletcher also includes heat transfer predictions.

A similar technique was used by Kwon and Pletcher[23,24] who simulated experiments by Eriksen[25] at R = 100 to 500. Their paper also includes turbulent flow predictions.

To the authors' knowledge, no predictive study of transient laminar flow has been presented so far for backward-facing steps. Vortex shedding was predicted by Celenligil and Mellor[26] in turbulent flow using a Reynolds stress transport closure model. Vortices were shed cyclically at R = 50,000 with a period $\Delta\tau$ ($=\Delta t\ u_0/H$) of about 10. Time-averaged fluid dynamic quantities were in good agreement with experimental results obtained by Kim et al.[27].

2. REFERENCE EXPERIMENT AND COMPUTATIONAL MODEL

2.1. The experimental results used as reference data for the simulations described below are probably the only ones available in literature on the starting and developing flow past a backward-facing step. They were obtained at the University of Mancheater by Honji[4]. He used a flat plate with a backward-facing step of height 1.85 cm, immersed in a large water tank and attached to a motor-driven carriage that could be started impulsively at a constant speed between 0.1 and 10 cm/s.

The experimental set-up and the relevant dimensions are shown in Figure 3.

The flow was visualized by the aluminium-dust method, showing instantaneous streamlines, and by electrochemically produced smoke, emitted by a brass strip attached to the surface of the plate, showing streaklines.

Results are reported in Ref.4 for Reynolds numbers R from 95 to 475. They include the movement of the reattachment point and of smoke filaments with time, and various photographic records of streamlines and streaklines. All results refer to the midplane of the plate.

Such flow observations allowed the author to draw the following qualitative picture of the flow behaviour.

For all values of R, the initial flow field (immediately after the onset of motion) is a potential flow. Then, a laminar boundary layer starts growing on the plate upstream of the step, and a recirculation bubble downstream of it.

The further evolution of the recirculation bubble depends critically on the Reynolds number. For R < 120, it remains single and grows gradually with time towards a steady configuration. For 120 < R < 140, a secondary counter-rotating vortex appears at the lower corner. For R > 140 also a third eddy, co-rotating with the main recirculation bubble, appears immediately downstream of the upper (separation) step corner.

If R < 200, the secondary vortices die away with time, and a steady recirculation bubble is established, while for R > 200 the primary vortex is pushed downstream and shed before a steady bubble can be established.

Unfortunately, most observations do not include the region downstream of the splitter plate. However, some tests were conducted with the plate removed, so that a blunt rearward-facing edge of thickness 2 H was obtained. Wake oscillation and vortex shedding were observed for R > 200, with no evidence for secondary vortices like those developed behind the step.

Most observations were carried out up to a non-dimensional time $\tau = t\ u_0/H$ of only 30. As the length of the upstream plate is about 40 H, for $\tau = 40$ the perturbation created by the leading edge of the plate (though carefully rounded) would reach the step and possibly affect the flow field near it.

For the experimental conditions, the transition criterion expressed by equation (6) predicts laminar reattachment even at R = 500, if the steady-state boundary layer thickness is used. However, it should be observed that during the early stages of the transient the separating boundary layer is thin, so that transition to turbulence would occur at all R if criterion (6) were valid for starting flows.

2.2. The experiments described above were simulated by solving the time-dependent two-dimensional Navier-Stokes equations using the primitive variables (u, v, p) and a pressure-velocity coupling approach. The computer code employed was FLOW3D Release 2, recently developed at the Harwell Laboratories. Its main features and options are summarized in Table II. The code's architecture and general characteristics are described by Burns et al.[28]. Details of the computational treatment of the equations, with emphasis on non-orthogonal grids, are given by Burns and Wilkes[29].

The code is highly vectorized for use on parallel computers. All the simulations described here were run on the Harwell CRAY-2. Auxiliary routines were added to generate streaklines (simulating smoke filaments) and to visualize them, with a view to creating animations[30].

Table II. Main characteristics of FLOW3D Release 2

A. CAPABILITIES	
Type of Flow	Laminar/Turbulent (k-ε model) Steady/Transient 2D / 3D Incompressible/Compressible Non-Buoyant/Buoyant (Boussinesq approximation) Isothermal/Non-isothermal
Grid	Cartesian/Body fitted (Rhie & Chow[31] approach)
Co-ordinates in physical space	Cartesian/Cylindrical
Further options	Transport of additional scalars Heat conduction in solid regions Solids or thin surfaces in the flow Porous regions Periodicity or symmetry in any direction
B. NUMERICAL METHODS	
Pressure/velocity coupling algorithms	SIMPLE, SIMPLEC, PISO, PISOC
Space-differencing schemes	Central (CD), upwind (UW), hybrid upwind (HU), 2nd order upwind (HUW), 3rd order upwind (QUICK)
Linearized equation solvers	Line relaxation (LRLX), preconditioned conjugate gradients (ICCG), Stone's Strongly Implicit Method (SIP) etc.
C. FORESEEN EXTENSIONS	
Large eddy simulation, two-phase flows, free-surface flows, adaptive grids, alternative turbulence models (Reynolds stress transport).	

3. COMPARISON AND EVALUATION OF NUMERICAL METHODS.

3.1. The main objectives of the simulations described here were:
- to test the capability of the code and its basic algorithms to reproduce (both qualitatively and quantitatively) the transient flow behaviour.
- to compare and evaluate alternative numerical options and algorithms.

To this purpose, preliminary simulations were run varying the following parameters:
- Computational grid (extent of the computational domain, number and distribution of the grid points).
- Boundary and initial conditions.
- Spatial differencing scheme (with emphasis on the effect of upwind).
- Pressure/velocity coupling algorithm.

Also, in addition to transient simulations, steady-state computations were performed.

The main results of this preliminary study are summarized below. Final simulations are presented and compared with experimental data in Section 4.

3.2. Computational grid and boundary conditions

The computational grid which was adopted is shown in Figure 4(a). A detail of the step region is shown in Figure 4(b). It is a cartesian grid with 187 control volumes in the flow in the streamwise direction (x) and 90 cross-stream (y). As FLOW3D treats a two-dimensional problem as a three-dimensional one with two planes of symmetry, the actual size of the grid is about 52,000 control volumes. All quantities (u, v and p) are defined at the centres of the control volumes, and the Rhie and Chow algorithm[31] is used to express convective fluxes through the boundaries of each volume, avoiding recourse to a staggered-grid formulation, while at the same time preventing chequerboard oscillations.

The grid is selectively refined near walls and other regions where strong spatial variations of flow quantities are expected.

The use of a cartesian grid simplifies the numerics, allowing a saving of 20% - 30% in memory and computing time. No comparison was performed with a body-fitted grid, however for a backstep geometry Hackman et al.[19] found that numerical differencing errors were smaller for a cartesian grid than for a body-fitted one.

The whole length of the plate upstream of the step is included in the computational domain (Figure 1). This allows "natural" boundary conditions (plug u-velocity profile) to be imposed at the inlet and the development of the boundary layer on the plate to be computed as a part of the solution. The assumption of a uniform (plug) inlet profile for u is reasonably accurate as the leading edge of the plate was carefully smoothed in Honji's experiments to prevent flow separation (Figure 3).

The outlet boundary conditions are equivalent to:

$$\partial v/\partial x|_{out} = \partial p/\partial x|_{out} = 0 \qquad (7')$$

$$\partial u/\partial x|_{out} = \text{constant} \qquad (7'')$$

where the constant is determined by imposing global continuity.

As these conditions express a fully developed flow at outlet, they would be completely inadequate if the computational domain were truncated before or close to the trailing edge of the plate, where reverse flow and unsteadiness are present. Preliminary simulations with such a "short" grid, limited to the region above the plate, confirmed this, yielding non-converging or unphysical results. Hence a region of length L_3 = 56 cm (twice the length of the splitter plate) was included downstream of the trailing edge. This also allowed the wake's behaviour to be simulated and visualized. Of course, it was necessary to include in the computational domain a region below the plate (the plane in which the plate lies is not a plane of symmetry).

Free stream conditions (symmetry with respect to y) were imposed at a distance 5 H from each side of the plate:

$$\partial\phi/\partial y|_{y=\pm 6H} = 0 \qquad (8)$$

In the water tank used in the experiments of Ref.4, the walls were at a distance of about 19 H from both sides of the plate. As we are using a reference frame moving with the plate, rigorous boundary conditions should be imposed as moving wall conditions:

$$u = u_0, \qquad v = \partial p/\partial y = 0 \qquad (8')$$

for $y = \pm 20$ H.

However, this would be computationally challenging, requiring either an excessive number of grid points, or too coarse a grid, or else a steep variation of the y-spacing between consecutive meshes (with the related so-called "l½-order" errors). Conditions (8) were proved to be adequate, in the sense that displacing the y-boundaries from ±6 H to ±8 H was found to alter insignificantly the flow field in the region $-2 H < y < 2 H$.

Relative grid independence was demonstrated in that a variation in the mesh stretching (ratio of minimum to maximum grid spacing) in both the x- and y-direction from about 0.1 to 0.5 modified computed results by less than a few percent.

With the 187 x 90 grid of Figure 4, the maximum value of Δx is close to H. Hence the maximum cell Peclet number $u\,\Delta x/\nu$ is close to the Reynolds number R, based on the step height (up to ~500). Such high values were feared to compromise the stability of the computational algorithms, as it is well known that for $u\,\Delta x/\nu > 2$ the matrices of the linearized flow equations lose diagonal dominance and may become difficult to handle for the respective solvers, unless upwind differencing is used. However, as discussed below, problems with central differencing were encountered only for steady-state computations at R > 125, while in the time dependent simulations stability problems did not arise even using central differencing up to R = 500.

3.3. Steady-state computations

Stationary solutions were sought for R = 50 to 500, using the SIMPLEC pressure-velocity coupling algorithm with a tight convergence criterion. For $R \lesssim 125$, stable fully-converged solutions were obtained using both central (CD) and hybrid upwind (HU) differencing. At R > 125 CD-based computations became unstable. Though stability might probably have been improved using small under-relaxation parameters, this was not attempted and only HU results were considered. Up to R = 125 results from CD and HU were barely distinguishable. At R > 200, convergence became difficult even with HU, suggesting that no steady solution existed, the asymptotic flow being oscillatory. For instance, Figure 5(a) shows the computed streamline pattern for R = 500. The figure clearly suggests that wake oscillation and vortex shedding would characterize the time-dependent flow behaviour under these conditions, as was confirmed by transient simulations (Section 4). Correspondingly, poor convergence was attained by the steady-state computation (the mass residual was oscillating around 5 x 10^{-2} M after some hundreds iterations of SIMPLEC).

For comparison purposes, the computed steady state lengths of the primary recirculation bubble downstream of the step (x_R) and of the wake reverse-flow region behind the splitter plate (x_w) are reported, expressed in step heights, in Figure 5(b) as functions of R. For R > 200 the recirculation bubble reaches the end of the splitter plate and merges with the wake, so that its length ceases to be defined. Values of x_R may be compared with experimental results collected in Figure 2. Present predictions lie above all experimental data. However, as will be discussed in Section 4, corresponding transient predictions agree with experimental results for this geometry.

3.4. Transient simulations: influence of initial conditions

To start the transient flow simulations, three alternative initial conditions were tested:

(A)	$u = 0$	everywhere	(9)
(B)	$u = u_0$	everywhere	(9')
(C)	$u = 0$ $u = u_0$	for $\lvert y\rvert < H$ elsewhere	(9'')

In all cases, v and p were assumed to be 0 everywhere, and a plug u-velocity profile was assumed at the inlet.

Conditions (C) are based on assuming that the fluid behind the plate is entrained by its impulsively-started motion. They satisfy continuity, while conditions (A) and (B) do not.

The predicted reattachment length is shown in Figure 6 for R = 125 and initial conditions (A), (B) and (C), in the interval τ = 0 - 20. Experimental results[4] for R = 126 are included for comparison. No significant difference is found between conditions (A) and (B). Using condition (C) the reattachment length is overpredicted, especially for small values of τ. The difference between the curves becomes smaller for increasing τ. Clearly, the simpler conditions (A) or (B) seem more appropriate. Among them, condition (B) allowed a significant reduction in computation time with respect to (A), clearly because it approximates better the (potential) flow that is established for very short values of τ, and was chosen for all the subsequent simulations.

3.5. Time stepping

Final simulations were run using a time step $\Delta t = 0.2\ H/u_o$ (i.e. $\Delta\tau = 0.2$). The corresponding Courant number $u_o\ \Delta t/\Delta x$, based on nominal velocity, was about 1.5 for the smallest meshes (near the step corner). Stability problems did not arise as fully implicit backward-differencing in time was used. An alternative stable time-differencing algorithm (Crank-Nicholson), available among the code's options, was not fully explored. However, preliminary tests did not show any significant change in the results, while the computation time was slightly longer.

When central-differencing was used for the spatial derivatives, time-step independency was demonstrated for $\Delta t = 0.2\ H/u_o$, in the sense that further reduction of Δt did not change appreciably the results. This was not the case when hybrid-upwind was used; the issue is addressed in the following section.

3.6. Spatial differencing schemes

Transient simulations were run using both central differencing (CD) and hybrid-upwind differencing (HU). At all Reynolds numbers, use of HU reduced significantly the computation time (40% for R = 200), accelerating convergence at each time step. However, the numerical viscosity thus introduced resulted in a significant reduction of the predicted reattachment length and in a disappearance of several fine flow structures resolved by using CD. The effect, as expected, was larger at large Reynolds numbers.

Use of HU resulted also in a strong sensitivity to both the value of the time step and the convergence criterion These effects are illustrated in Figure 7. Figure 7(a) compares the values of x_R/H predicted with CD and HU for $\Delta\tau$ = 0.2, 0.1, and 0.05 at R = 200. The convergence criterion was $\epsilon_M = 5.10^{-4}$ in all cases. Experimental data are also reported.

Using CD no sensitivity is found. Using HU, x_R decreases significantly with decreasing $\Delta\tau$.

Figure 7(b) compares results obtained using CD and HU for $\epsilon_M = 5.10^{-4}$ and 1.10^{-4}. The time step was $\Delta\tau = 0.2$ in all cases. Again CD results are insensitive to ϵ_M, while HU results increase with decreasing ϵ_M.

These results amply justify the preference for central differencing though a price must be paid in computing time.

As an alternative to CD and HU, the third-order accurate QUICK scheme[32] was tested. Results were disappointing, as it yielded poor convergence leading to long computing times and/or instability.

3.7. Pressure-velocity coupling algorithm

Four alternative algorithms for pressure-velocity coupling are available in FLOW3D [29] as shown in Table II.

SIMPLE is the prototype of them all. It was first introduced by Patankar and Spalding[33] for parabolic flows and then extended to elliptic flow situations[34]. Essentially, it is based on a two-step iterative cycle, in which a guessed pressure field is introduced in the momentum equations to evaluate velocities, and then a pressure-correction equation, derived by enforcing continuity under certain simplications, is solved to obtain an improved guess. A convenient convergence parameter, expressing the amount by which the continuity equation is <u>not</u> satisfied, is the mass-source residual, ϵ_M, i.e. the sum of the absolute values of all nett mass fluxes into or out of every control volume in the computational domain. ϵ_M can be made non-dimensional by dividing it by total flow rate $\dot{M}$.

SIMPLEC was proposed by Van Doormal and Raithby[35] as an improvement to SIMPLE. It is based on a more consistent expression for the coefficients of the discretized pressure-correction equation, and has been shown to allow faster convergence for problems dominated by pressure gradients and drag forces. For a number of model problems, SIMPLEC has proved less sensitive than SIMPLE to selection of under-relaxation factors[28].

In the PISO algorithm, an additional pressure-correction step is performed at each iteration to improve the solution of the momentum equations while maintaining continuity. For transient problems, it may be used as a non-iterative algorithm and as such it was introduced by Issa[36]. In fact it allows a satisfactory solution to be reached in a few, or even in a single, iteration. This requires, however, that at each cycle the set of linearized flow equations is solved with high accuracy, so that the advantage of reducing the number of outer iterations may be overcome by the increase in the number of inner iterations of the linear equation solvers.

Finally, the same modifications for SIMPLEC may be equally applied to PISO, yielding the PISOC algorithm.

All four methods described were tested in transient flow for some Reynolds numbers. With the iterative algorithms, (SIMPLE or SIMPLEC), results were found to be barely sensitive to the convergence criterion ϵ_M, provided $\epsilon_M/\dot{M} < 10^{-3}$ when central differencing was used. A slightly lower stopping value ($\epsilon_M/\dot{M} = 5.10^{-4}$) was selected for all the final simulations.

A comparison of the performances of the four algorithms is summarized in Table III. It refers to R = 125 and to a simulation from τ = 0 to 10 with $\Delta\tau$ = 0.1 (100 steps). In all cases, an under-relaxation factor of 0.7 was used for u and v. A factor of 0.5 was also applied to p when SIMPLE was used. In Table III the stopping criterion for the solution of the linearized momentum equations is indicated. It expresses the residual reduction factor RF = ratio of final to initial residual required to stop the inner iterations. A value two times smaller was used in all cases for the pressure-correction equation.

As expected, convergence was slower for the first few time steps, in which the flow develops from the initial conditions ($u = u_o$ everywhere), and then was rapidly accelerating. This was clearly shown when using SIMPLE or SIMPLEC by a rapid decrease in the number of iterations required per each time step. When using PISO or PISOC as non-iterative algorithms, the solution was significantly different from the corresponding fully-converged SIMPLE/SIMPLEC solution, showing that - particularly during

the first stages of the transient - accuracy was not preserved. After 30 - 40 steps, a single iteration was sufficient also to SIMPLE or SIMPLEC to achieve the required convergence, so that the extra computational effort implied by PISO and PISOC was not paid back. PISO and PISOC were also tested with a larger maximum allowed number of iterations (10); the SIMPLE/SIMPLEC solution was recovered at all time steps, but the computation time increased significantly (to 853 s and 800 s respectively).

Table III. Comparison of Pressure-velocity coupling algorithms

Algorithm	SIMPLE	SIMPLEC	PISO	PISOC
Stopping criterion ϵ_M/M	10^{-3}	10^{-3}	-	-
Maximum number of iterations	100	100	1	1
RF (momentum equations)	0.1	0.1	0.01	0.01
CPU time (s)	758	424	670	620

An obvious conclusion is that PISO (PISOC) should not be used when the flow is varying smoothly and a moderate degree of convergence is required, as in such cases even SIMPLE (SIMPLEC) are likely to require a single iteration per time step. Moreover using PISO (PISOC) with a single iteration per step is "dangerous" in that poor accuracy may be achieved in those time steps during which the flow is varying sharply.

It should be mentioned that accuracy problems (phase errors) with PISO and PISOC have been reported in FLOW3D studies on the stability of plane Poiseuille flow to two-dimensional disturbances (George test) and related problems[37].

Comparing SIMPLE with SIMPLEC, and PISO with PISOC, it is also apparent that a consistent, if moderate, advantage is offered by the modification of Van Doormal and Raithby[35].

On the basis of the results described above, SIMPLEC was chosen for the final simulations.

3.8. Linear equation solvers

In most simulations, the linearized momentum and pressure-correlation equations were solved using Stone's Strongly Implicit Procedure (SIP) for the former and a pre-conditioned conjugate gradient method (ICCG) for the latter. Using a line relaxation method (LRLX) instead of SIP did not alter the computational effort or the results significantly. Instability arose when SIP was replaced by either a sweeping version of SIP or a pre-conditioned CG-squared method (CGSQ). However, no systematic study on the performances of these solvers was conducted. More details on the subject are given by Kightley and Jones[38].

3.9. Summary of Computational Options

The modelling and numerical options selected as optimal (or at least reliable) after the parametric study discussed above, and adopted for the final transient flow simulations, are summarized in Table IV.

Table IV Summary of Computational Options

Reynolds number range	50 - 500
Pressure velocity coupling	SIMPLEC
Stopping criterion for outer iterations	$\epsilon_M/M = 5 \times 10^{-4}$
Under-relaxation factor (u,v)	0.7
Under-relaxation factor (p)	1.0
Linear equation solver (u,v)	SIP
Linear equation solver (p)	ICCG
Reduction factor (u,v)	0.1
Reduction factor (p)	0.05
Spatial differencing scheme	Central differencing
Time differencing scheme	Fully implicit backward
Time step	$\Delta t = 0.2\ H/u_o$
Number of time steps	1000
Grid	Cartesian selectively refined
Number of nodes	187 x 90 (x3)
Maximum cell Peclet number	~R
Maximum cell Courant number	~1.5
Storage requirement	3.6 Mwds
CPU time	2 - 4 s/time step

4. TRANSIENT FLOW PREDICTIONS AND COMPARISON WITH EXPERIMENTAL DATA

4.1. Boundary Layer Development

Immediately after the onset of motion, a potential flow develops around the plate. The corresponding streamlines are shown for R = 200 and τ = 0.1 in Figure 8. The stream function is normalised so that it ranges from -1 to 1 between the lower and upper free stream boundaries. This initial flow field is practically independent of the Reynolds number.

Successively, a boundary layer grows on the plate upstream of the step (and on the lower face of the plate), while a recirculation region starts to develop downstream of the step, and a second one in the wake of the splitter plate. The thickness of the boundary layer at separation, as observed in Section 1, has been shown to affect numerical predictions of reattachment length, so that its accurate prediction is an important issue. For the present case, Honji[4] reports an initial growth of the boundary layer uniform along the plate and following approximately the law:

$$\delta = 3.66\ (\nu t)^{1/2} \qquad (10)$$

δ being the 99% boundary-layer thickness.

On the other hand, once steady-state conditions are attained δ must vary along x as:

$$\delta_{ss} \approx 5(\nu x/u_o)^{1/2} \qquad (10")$$

The computed values of δ at R = 200 are reported as functions of time, and compared with equations (10') and (10") in Figure 9(a) for the two points A and B in Figure 8. They are at distances 37 cm and 74 cm respectively from the leading edge of the plate.

It can be seen that (10') is followed closely up to $\tau \approx 20$ for both points A and B. For larger values of τ, the asymptotic (steady state) values predicted by (10") are approached first at point A and then at B.

The evolution of the profiles of u(y) with time is reported in Figure 9(b).

4.2. Reattachment length and related quantities

The increase of the predicted reattachment length with time is shown in Figure 10 and compared with available experimental data. The general agreement is good. However, experimental data suggest that the slope of the x_R versus τ curves increases with R, while the predictive results exhibit a (very slight) opposite trend. It should be observed that, as at high Reynolds numbers the reattaching shear layer spreads, flow visualization may have over-estimated the reattachment length.

The overall trend of the computed reattachment length in the range τ = 0 to 200, and R = 50 to 500, is shown in Figure 11(a). Several additional remarks can be made.

First, asymptotic conditions are reached for values of τ increasing with the Reynolds number. Second, for R > 200 the recirculation length overtakes the length L_2 of the splitter plate, so that the separation bubble merges with the wake downstream of the splitter plate. For R < 200 all curves exhibit an overshoot beyond the asymptotic mean value, followed by oscillations around it if R > 50. The amplitude of the oscillations increases slowly with R, being about $\pm H/2$ for R = 150, and their frequency increases too. As discussed in Section 4.4., this frequency is the same as for vortex shedding downstream of the splitter plate, hence oscillations of the recirculation region down the step are clearly induced by the periodic detachment of vortices from farther downstream.

It should be recalled that steady-state computations showed convergence problems increasing with the Reynolds number. As anticipated in Section 3.3., this is clearly related to the fact that no true steady solution exists for R > 50. However, it is noteworthy that the values of x_R predicted (for R < 200) by steady-state simulations, even with imperfect convergence, coincide within 1 or 2% with the mean asymptotic values computed in transient mode.

The way in which the predicted values of x_R vary with τ and R is more clearly shown in Figure 11(b), which reports x_R/H versus R at different τ's. Curves τ = const. are enveloped on the left by a solid line corresponding to the maximum (overshoot) values. The broken line represents the asymptotic mean values around which x_R oscillates. All curves τ = const. exhibit a maximum around R = 100.

A quantity related to the reattachment length is the distance x_e by which the rear end of the smoke filament, emitted from the upstream plate in the experiments (Figure 12), travels with time. Values of x_e versus τ are reported in Ref.4 for several values of R. Smoke filaments follow flow streaklines and were simulated by computing the instantaneous positions of particles emitted at each time step from assigned starting points and travelling with the flow. Simple linear interpolation and backward differencing in time was used. Printer plots of such simulated filaments are shown as examples in Figure 12 for R = 100 (a) and 200 (b) at τ = 20.

Curves of x_e versus τ for the simulated filament starting from the step corner are reported in Figure 13, and compared with experimental results for various Reynolds numbers. Agreement is good, and the trend of the data (slope increasing with R) is correctly predicted.

The time evolution of quantities x_c and y_c, indicated in Figure 12, is also reported in Ref.4 for R = 142. Experimental data are compared in Figure 14 with predictions at the close Reynolds number of 150.

4.3. Qualitative flow behaviour as a function of the Reynolds number

In Section 2, the main qualitative conclusions drawn by Honji from his observations were summarized. The predicted flow behaviour is shown in Figure 15(a - f). Streamline plots in the near-step region are reported for R = 50, 100, 150, 200, 300 and 500 at τ = 10, 20, 40, 60, 100.

For R < 100, Figure 15(a,b), a single recirculation bubble develops gradually. For R = 150, Figure 15(c), a secondary counter-rotating eddy is formed near the lower corner at low τ, and then dies away. The incipient appearance of a third eddy near the upper corner is also visible for low values of τ. For R = 200, Figure 15(d), this third eddy (rotating as the main one) is clearly visible for τ = 20 and 40. It eventually merges with the main bubble (τ = 60). For R = 300, Figure 15(e), the third eddy does not merge with the first, but pushes it downstream and takes its place. Also the lower corner eddy is seen to be shed downstream. Finally, at R = 500 Figure 15(f), three co-rotating eddies are clearly visible at low τ; they push one another downstream until a final (almost steady) configuration with a single recirculation bubble is reached.

This predicted behaviour is in good agreement with the visualization results of Honji. The appearance of the third eddy close to the upper step corner was indicated in them not only by the aluminium dust-visualized streamline pattern, but also by the appearance of a kink in the smoke filament separating from the step corner. A similar kink is clearly visible in the corresponding simulated filament for R > 150, while it does not exist at lower R (Figure 12).

The time instant for the first appearance of the kink decreases with increasing R, again in good agreement with the experimental results. It should be mentioned that, when the hybrid-upwind differencing scheme was used, many flow structures visible in Figure 15 were smoothed away and disappeared. In particular, a clear upper corner eddy was predicted only for R > 300, and the three-eddy pattern visible in Figure 15(f) for R = 500 was replaced by a two-eddy pattern.

4.4. Wake Oscillation and Vortex Shedding

At all Reynolds numbers investigated except the lowest (R = 50), wake oscillation and vortex shedding was predicted downstream of the splitter plate's blunt trailing edge. Examples are shown in Figure 16, which refers to R = 300 and τ = 70, 75, 80. Three consecutive shade-plots of the stream function (b), and the corresponding simulated streaklines (a), are reported. Vortices are shed in couples with a non-dimensional period $\delta\tau_o \approx 12$, corresponding to a non-dimensional shedding frequency

(Strouhal number) $S = 1/\delta\tau_o \approx 0.08$. They detach alternately from the upper and lower corner of the splitter plate and are carried downstream with the mean flow. The "simulated filament" technique was found to be particularly effective to visualize the vortex pattern even with the poor resolution offered by printer plots as those in Figure 16. Essentially, the same technique - but with high resolution graphics - was used by Eaton[39] to study the detailed vortex shedding mechanisms behind a cylinder in crossflow.

The non-dimensional time interval $\delta\tau$ between consecutive vortex couples was predicted to increase with time for all values of R, until an asymptotic cyclic regime was reached with $\delta\tau = \delta\tau_o$. This is shown in Figure 17(a). The asymptotic period $\delta\tau_o$ decreased with R, i.e. the Strouhal number increased with R as shown in Figure 17(b).

The predicted S-versus-R dependence can be well described by:

$$S \approx 0.018\ R^{0.266} \qquad (11)$$

It should be observed, Figure 17(a), that even the merging of the recirculation bubble downstream of the step with the wake region, which takes place about $\tau \approx 70$ for $R \geq 200$, does not modify the vortex shedding period. The fact that vortex shedding is predicted even for low Reynolds numbers (100) is not surprising. In fact, it is induced in the mixing zone by the strong asymmetry of the two shear layers separating from the lower and upper sides of the plate. The former is an ordinary and thick laminar boundary layer, while the latter is either the thin redeveloping boundary layer after reattachment ($R < 200$) or is no less than a recirculation region protruding from the splitter plate ($R \geq 200$).

When hybrid-upwind differencing was used, vortex shedding was predicted only for $R > 200$. For these conditions, however, the predicted Strouhal number was not much different from that predicted using central differencing. Changing the boundary conditions by moving the free-stream boundaries from $y = \pm 6H$ to $y = \pm 10\ H$ did not affect significantly the Strouhal number nor the amplitude of the wake oscillations.

More computational results for the test-cases discussed above can be found in Ref.40. A detailed analysis of the overall flow behaviour, with particular emphasis on vortex shedding and its relevance to thermal mixing problems, will be presented in Ref.41.

5. SUMMARY AND CONCLUSIONS

The overall behaviour of a complex, time-dependent, developing flow was predicted in the range R = 50 - 500. Agreement with available experimental results was good when central differencing was used, and the results were satisfactorily demonstrated to be independent of grid size, time stepping and convergence crtieria.

The increase of the reattachment length with time, the behaviour of streaklines, and the time-dependent structure of the recirculation bubble, were predicted with remarkable accuracy. Vortex shedding was predicted at Reynolds numbers ≥ 100. The Strouhal number increased as $R^{0.266}$.

Use of upwinding deleted fine flow structures or shifted the Reynolds number value for their appearance. Moreover, it introduced unacceptable sensitivity to the time step value and to the convergence criteria, and prevented vortex shedding for $R < 200$.

Among the various pressure-velocity coupling algorithms tested, SIMPLEC was estimated to be the best compromise between accuracy and computing time.

6. ACKNOWLEDGEMENTS

The work was carried out while one of the authors (M. Ciofalo) was spending a NATO fellowship at The City University, London (Industrial Research Training Award No.0769/86).

Computational facilities, including the use of FLOW3D, Release 2, and of the CRAY-2 computer, were provided by AERE Harwell. The authors are specially grateful to Dr.Ian Jones and Mrs. Suzanne Simcox for their help and advice.

REFERENCES

1. MOORE, T.W.F. "Some Experiments on the Reattachment of a Laminar Boundary Layer Separating from a Rearward-Facing Step on a Flat Plate Aerofoil". J. Roy. Aero. Soc., Vol.64, pp.668-672, November 1960.
2. GOLDSTEIN, R.J., ERIKSEN, V.L. OLSON, R.M. and ECKERT, E.R.G. "Laminar Separation, Reattachment, and Transition of the Flow over a Downstream Facing Step". Trans. ASME D, (J. Basic Eng.), Vol.92, pp.732-741, 1970.
3. DENHAM, M.K. and PATRICK, M.A. "Laminar Flow over a Downstream-Facing Step in a Two-Dimensional Flow Channel". Trans. Inst. Chem. Eng., Vol.52, pp.361-367, 1974.
4. HONJI, H. "The Starting Flow down a Step". J. Fluid Mech., Vol.69, pp.229-240, 1975.
5. SINHA, S.N., GUPTA, A.K. and OBERAI, M.M. "Laminar Separating Flow Over Backsteps and Cavities - Part I: Backsteps". AIAA Journal, Vol.19, pp.1527-1530, 1981.
6. ARMALY, B.F., DURST, F., PEREIRA, J.C. and SCHONUNG, B. "Experimental and Theoretical Investigation of a Backward-Facing Step Flow". J. Fluid Mech., Vol.127, pp.473-496, 1983.
7. AUNG, W. "An Experimental Study of Laminar Heat Transfer Downstream of Backsteps". Trans ASME C, (J. Heat Transfer), Vol.105, pp.823-830, 1983.
8. CRAMER, K.R. "On Laminar Separation Bubbles". J. Aero. Sci., Vol.25, pp.143-144, 1958.
9. AUNG, W, BARON, A, and TSOU, F.K. "Wall Independency and Effect of Initial Shear-Layer Thickness in Separated Flow and Heat Transfer" Int. J. Heat Mass Transfer, Vol.28, pp.1757-1771, 1985.
10. NARAYANAN, B., KHADGI, Y.N. and VISWANATH, P.R. "Similarities in Pressure Distribution in Separated Flow Behind Backward-Facing Steps". The Aero. Quarterly, Vol.25, pp.305-312, 1974.
11. KUEHN, D.M. "Effects of Adverse Pressure Gradient on the Incompressible Reattaching Flow Over a Rearward-Facing Step". AIAA Journal, Vol.18, pp.343-344, 1980.
12. MORI, Y., UCHIDA, Y. and SAKAI, K. "A Study of the Time and Spatial Structure of Heat Transfer Performances Near the Reattaching Point of Separated Flows". Procs. 8th Int. Heat Transfer Conf., San Francisco, 1986, pp.1083-1088.

13. OWEN, P.R. and KLANFER, L. "On the Laminar Boundary Layer Separation from the Leading Edge of a Thin Aerofoil" Royal Aircraft Establishment Report, No.Aero-2508, Oct.1953.
14. TANI, I. and SATO, H. "Boundary-Layer Transition by Roughness Element" J. Phys. Soc. Japan, Vol.11, pp.1284-1291, 1956.
15. ROSHKO, A. and LAU, J.C. "Some Observations on Transition and Reattachment of a Free Shear Layer in Incompressible Flow" Procs. Heat Transfer and Fluid Mech. Institute,(Ed. A.F. Charwat), Stanford Univ. Press, pp.157-167, 1965.
16. ATKINS, D.J., MASKELL, S.J. and PATRICK, M.A. "Numerical Predictions of Separated Flows". Int. J. Num. Meth. in Eng., Vol.15, pp.129-144, 1980.
17. THOMAS, C.E., MORGAN, K. and TAYLOR, C. "Finite Element Analysis of Flow over a Backward-Facing Step" Computers & Fluids, Vol.9, pp.265-278, 1981.
18. CHIU, I.T. and PLETCHER, R.H. "Prediction of Heat Transfer in Laminar Flow over a Rearward-Facing Step Using the Partially-Parabolized Navier-Stokes Equations". Procs. 8th Int. Heat Transfer Conf., San Francisco, 1986, pp.415-420.
19. HACKMAN, L.P., RAITHBY, G.D. and STRONG, A.B. "Numerical Predictions of Flow over Backward-Facing Steps". Int. J. Num. Meth. in Fluids, Vol.4, pp.711-724, 1984.
20. HALL, E.J. and PLETCHER, R.H. "Application of a Viscous-Inviscid Interaction Procedure to Predict Separated Flow with Heat Transfer". Trans. ASME C, (J. Heat Transfer), Vol.107, pp.537-563, 1985.
21. ARMALY, B.F., DURST, F. and KOTTKE, V. "Momentum Heat and Mass Transfer in Backward-Facing Step Flows" Procs. 3rd Symp. on Turbulent Shear Flows, Davis, USA, 1981 (Preprints).
22. AUNG, W. "Heat Transfer in the Separated Region Beyond a Rearward-Facing Step" Ph.D. Thesis, University of Minnesota, USA 1969.
23. KWON, O.K. and PLETCHER, R.H. "A Viscous-Inviscid Interaction Procedure - Part I: Method for Computing Two-Dimensional Incompressible Separated Channel Flows" Trans. ASME I, (J. Fluids Eng.), Vol.108, pp.64-70, 1986.
24. KWON, O.K. and PLETCHER, R.H. "A Viscous-Inviscid Interaction Procedure - Part II: Application to Turbulent Flow Over a Rearward-Facing Step". Trans. ASME I, (J. Fluids Eng.), Vol.108, pp.71-75, 1986.
25. ERIKSEN, V. "An Experimental Investigation of the Laminar Flow of Air over a Downstream Facing Step". M.S. Thesis, University of Minnesota, USA, 1968.
26. CELELIGIL, M.C. and MELLOR, G.L. "Numerical Solution of Two-Dimensional Turbulent Separated Flows Using a Reynolds Stress Closure Model". Trans. ASME I, (J. Fluid Eng.), Vol.107, pp.467-476, 1985.
27. KIM, J., KLINE, S.J. and JOHNSTON, J.P. "Investigation of Separation and Reattachment of a Turbulent Shear Layer Flow over a Backward-Facing Step". Report MD-37, Thermosci. Div., Dept. of Mech. Eng., Stanford University, USA, 1978.
28. BURNS, A.D., JONES, I.P., KIGHTLEY, J.R. and WILKES, N.S. "FLOW3D, Release 2: User Manual" UKAEA Report (Draft form) AERE Harwell, July 1987.
29. BURNS, A.D. and WILKES, N.S. "A Finite Difference Method for the Computation of Fluid Flows in Complex 3D Geometries". UKAEA Report, AERE-R-12342, Harwell, 1987.
30. CIOFALO, M. "Auxiliary Routines for FLOW3D, Release 2" Thermo-Fluids Eng. Res. Centre, The City University, London, 1988 (To be Issued).
31. RHIE, C.M. and CHOW, W.L. "A Numerical Study of the Turbulent Flow Past an Aerofoil with Trailing Edge Separation". AIAA Journal, Vol.21, pp.1525-1532, 1983.
32. LEONARD, B.P. "A Stable and Accurate Convective Modelling Procedure Based on Quadratic Upstream Interpolation". Comp. Meth. in Appl. Mech. and Eng., Vol.19, pp.59-98, 1979.
33. PATANKAR, S.V. and SPALDING, D.B. "A Calculation Procedure for Heat, Mass and Momentum Transfer in Three-Dimensional Parabolic Flows". Int. J. Heat Mass Transfer, Vol.15, pp.1787-1806, 1972.
34. PATANKAR, S.V. "A Calculation Procedure for Two-Dimensional Elliptic Situations". Num. Heat Transfer, Vol.4, pp.409-425, 1981.
35. VAN DOORMAL, J.P. and RAITHBY, G.D. "Enhancements of the SIMPLE Method for Predicting Incompressible Fluid Flows". Num. Heat Transfer, Vol.7, pp.147-163, 1984.
36. ISSA, R.I. "Solution of the Implicitly Discretized Fluid Flow Equations by Operator-Splitting". J. Comp. Phys., Vol.62, pp.40-65, 1986.
37. GAVRILAKIS, S. Personal Communication, 1988.
38. KIGHTLEY, J.R. and JONES, I.P. "A Comparison of Conjugate Gradient Preconditioning for Three-Dimensional Problems on a CRAY-1". Comp. Phys. Comm., Vol.37, pp.205-214, 1985.
39. EATON, B.E. "Analysis of Laminar Vortex Shedding behind a Circular Cylinder by Computer-Aided Flow Visualization". J. Fluid Mech., Vol.180, pp.117-145, 1987.
40. CIOFALO, M. "Computation of Turbulent Recirculating Flows with Heat Transfer Using FLOW3D - Progress Report - October-December 1988". Thermo-Fluids Eng. Res. Centre, The City University, London, 1988. (To be issued).
41. CIOFALO, M. and COLLINS, M.W. "Vortex Shedding and Thermal Mixing Past a Plate with a Backward-Facing Step in High Reynolds Number Laminar Flow". To be presented at 6th Int. UIT Conf. on Fluid Flow and Heat Transfer, Bari, Italy, June 9-10, 1988.

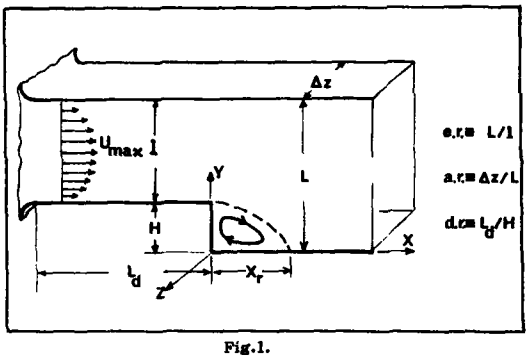


Fig.1.

Geometry and nomenclature for a backward-facing step.

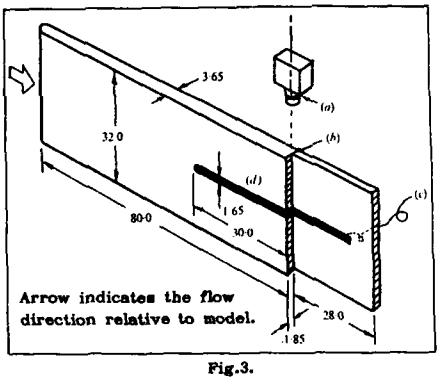


Fig.3.

Set-up for the experiments described in Ref.4. (a) Camera, (b) Step, (c) Power supply, (d) Brass strip. Dimensions in cm.

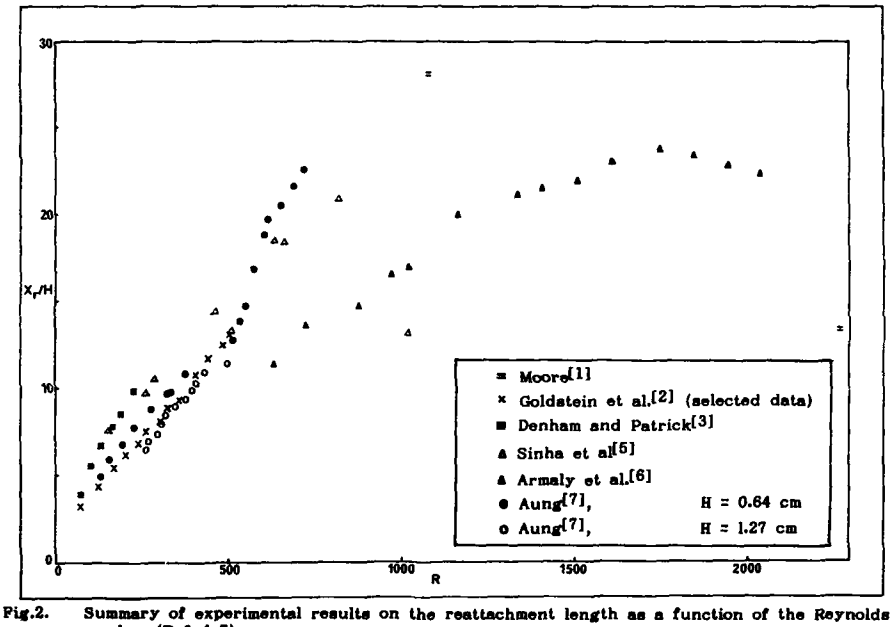
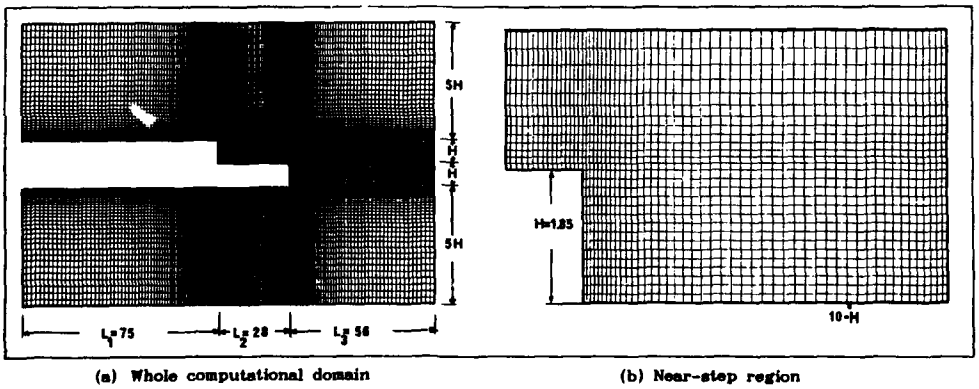
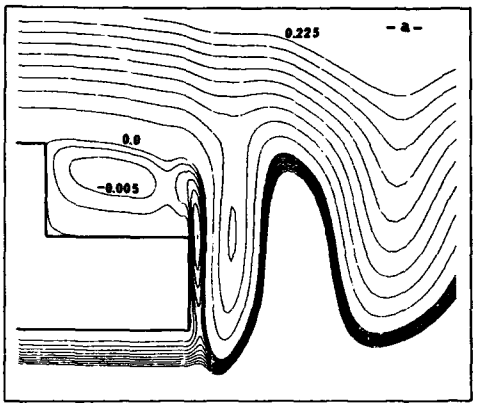


Fig.2. Summary of experimental results on the reattachment length as a function of the Reynolds number (Refs.1-7).

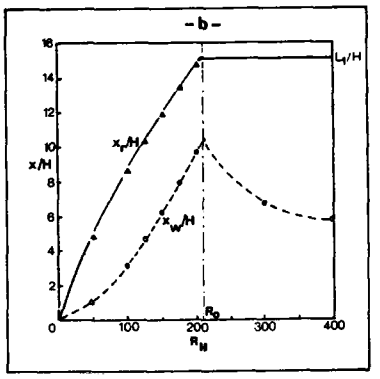


(a) Whole computational domain (b) Near-step region

Fig.4. Computational grid (dimensions in cm). The y-scale is 5 times the x-scale.



(a) Streamlines for R = 500



(b) Length of the two recirculation regions versus Reynolds number

Fig.5. Steady state results

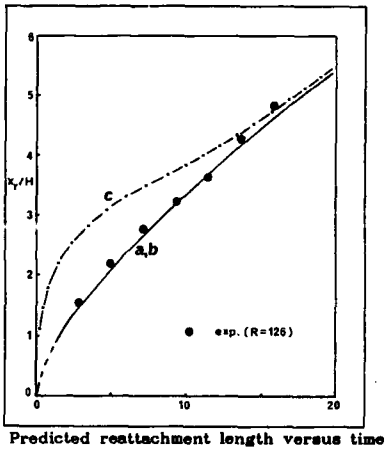


Fig.6. Predicted reattachment length versus time for different initial conditions (R = 125).
(a) u = 0 everywhere, (b) u = u_o everywhere
(c) u = u_o for $|y| < H$ and 0 elsewhere.

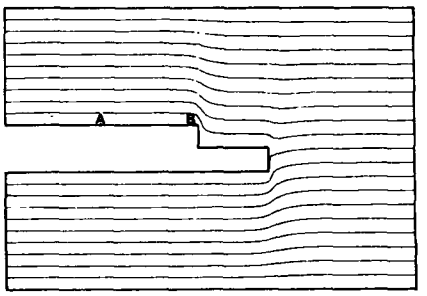


Fig.8. Instantaneous streamlines immediately after the onset of motion (R = 150, τ = 0.1)
Increment between curves is $\Delta\psi$ = 0.1

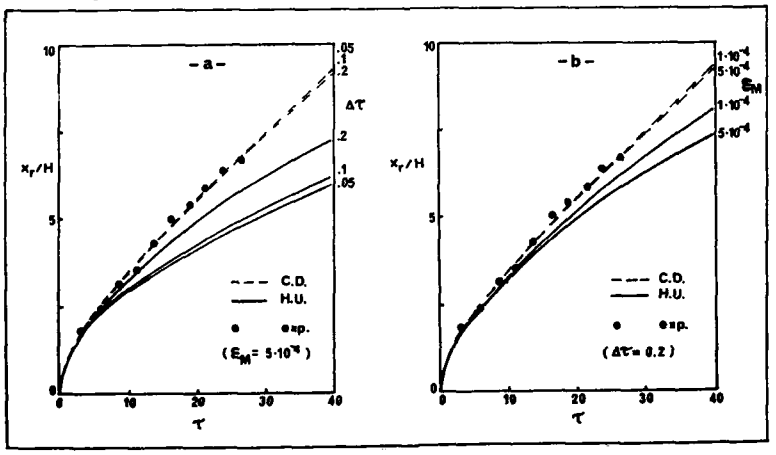
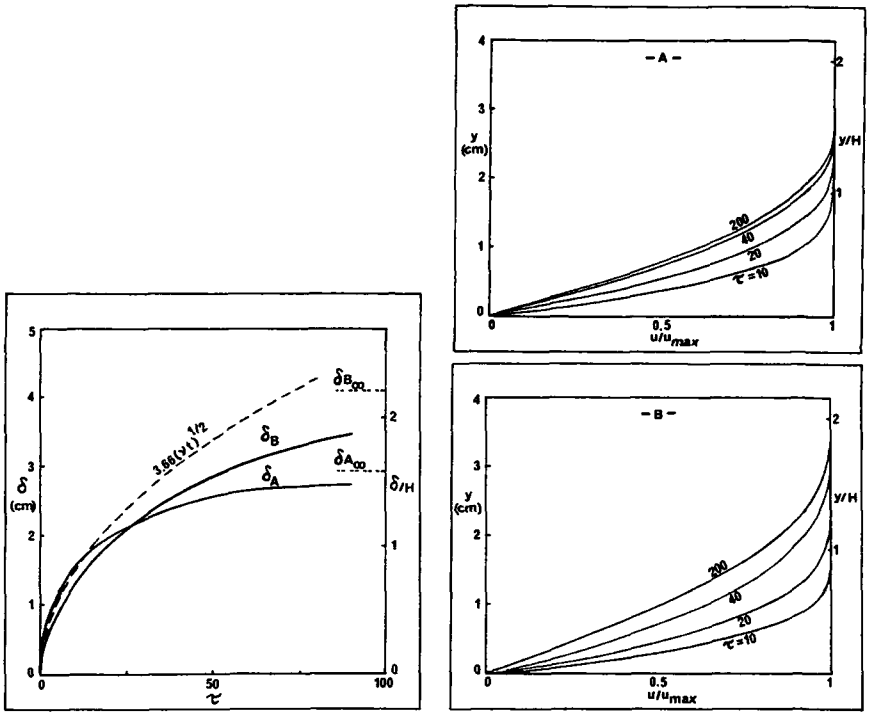


Fig.7. Influence of the spatial differencing scheme on the sensitivity to (a) time step and (b) convergence criterion (R = 200).



(a) Thickness of the boundary layer versus time (b) Evolution of the profiles of u(y).

Fig.9. Boundary layer evolution on the upstream plate at points A, B of Fig.8 (R = 200).

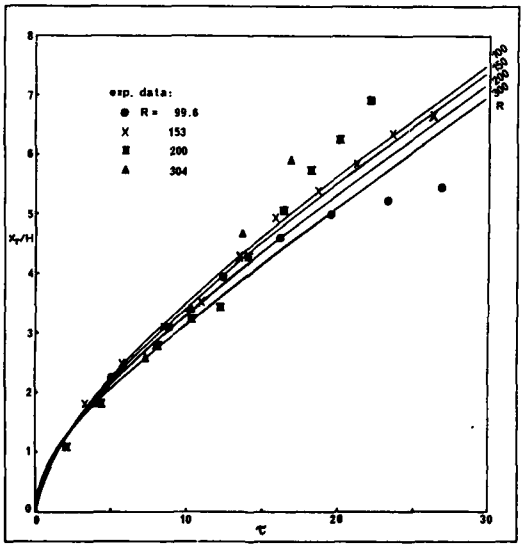
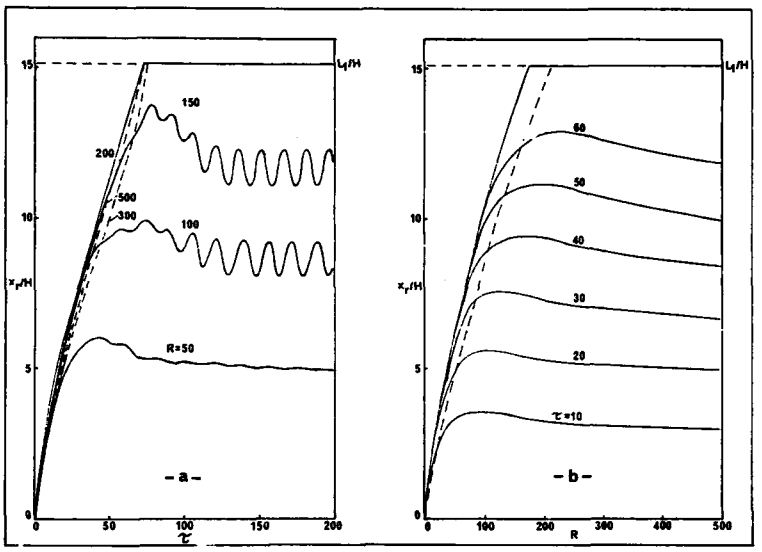


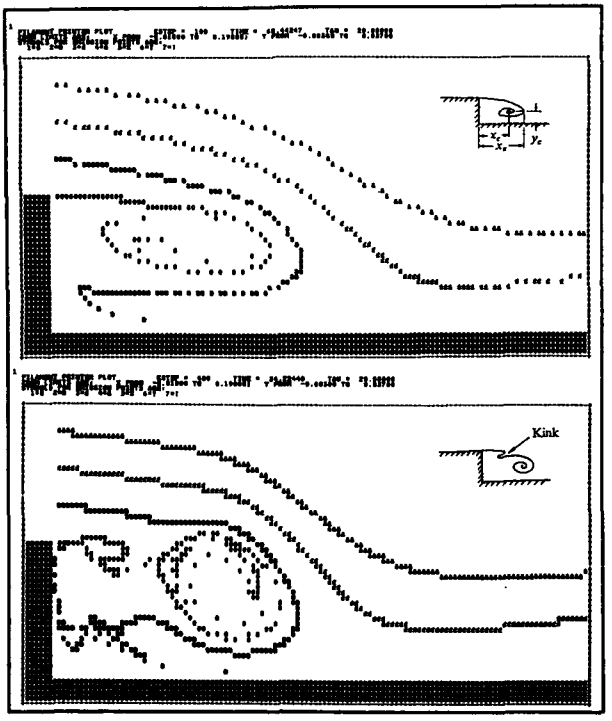
Fig.10. Computed versus experimental reattachment lengths.



(a) x_R versus time for different R

(b) x_R versus R for different times. The dashed curve represents the mean asymptotic reattachment length.

Fig.11. Summary of predicted reattachment length evolution.



(a) R = 100

(b) R = 200

Fig.12. Simulated smoke filaments: characteristic quantities and appearance of kink at high Reynolds numbers. τ = 20.

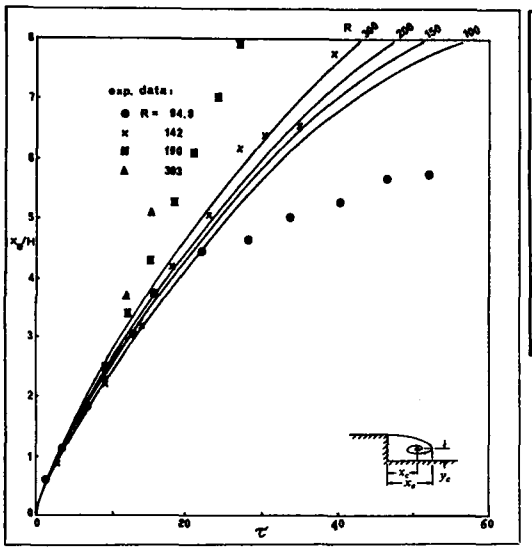


Fig.13. Predicted versus experimental evolution of x_e (distance travelled by the rear end of the filament) for various R.

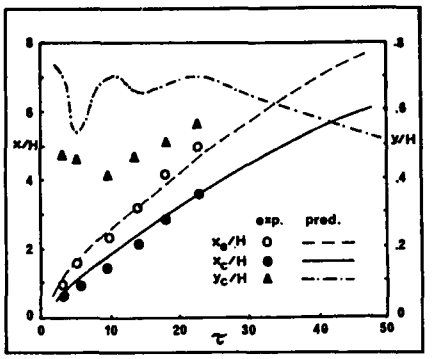


Fig.14. Predicted versus experimental evolution of characteristic quantities, x_e, x_c and y_c (Fig.12) for R = 150.

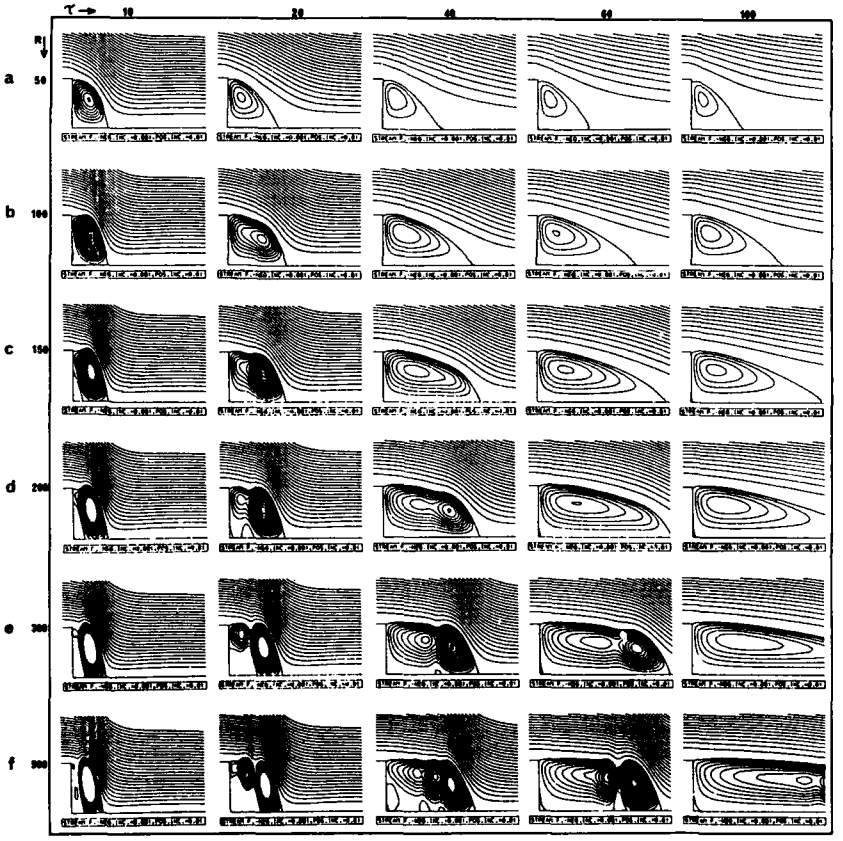
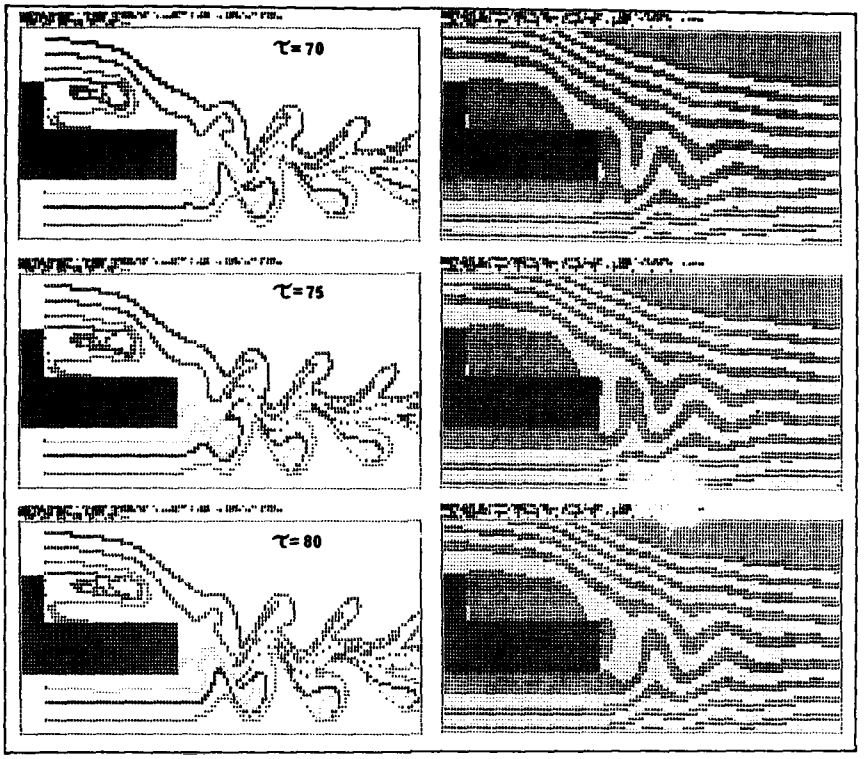
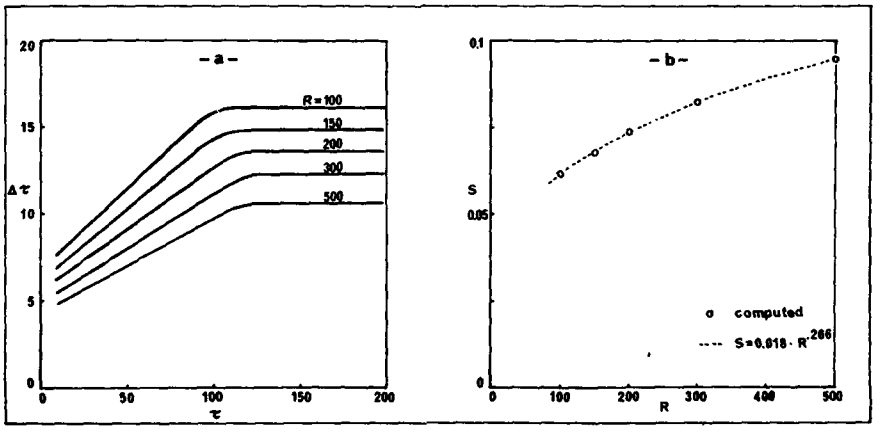


Fig.15. Predicted evolution of the streamline pattern for R = 50 to 500 and τ = 10 to 100.



(a) Filaments (streaklines) (b) Stream function

Fig.16. Shaded plots of the stream function and simulated smoke filaments showing periodic vortex shedding downstream of the splitter plate (R = 300).



(a) Non-dimensional interval $\Delta\tau$ between consecutive vortices versus time for different Reynolds numbers.

(b) Strouhal number versus Reynolds number after periodic shedding is attained.

Fig.17. Characteristic parameters of vortex shedding.

A COMPARATIVE STUDY AND VALIDATION OF UPWIND AND CENTRAL-DIFFERENCE NAVIER-STOKES CODES FOR HIGH-SPEED FLOWS

by
David H. Rudy, Ajay Kumar, James L. Thomas, Peter A. Gnoffo
NASA Langley Research Center
Hampton, Virgina, USA 23665-5225
and
Sukumar R. Chakravarthy
Rockwell International Science Center
Thousand Oaks, CA, USA 91360

SUMMARY

A comparative study has been made using four different computer codes for solving the compressible Navier-Stokes equations. Three different test problems were used, each of which has features typical of high-speed internal flow problems of practical importance in the design and analysis of propulsion systems for advanced hypersonic vehicles. These problems are the supersonic flow between two walls, one of which contains a ten-degree compression ramp, the flow through a hypersonic inlet, and the flow in a three-dimensional corner formed by the intersection of two symmetric wedges. Three of the computer codes use similar recently-developed implicit upwind-differencing technology, while the fourth uses a well-established explicit method. The computed results were compared with experimental data where available.

SYMBOLS

C_f	skin-friction coefficient
L	length of computational domain
M	Mach number
p	static pressure
p_p	pitot pressure
p_t	total pressure
T	static temperature
T_t	total temperature
x,y,z	spatial coordinates
ϵ	eigenvalue limiter
γ	ratio of specific heats

Subscripts:

w	wall
wedge	wedge surface
∞	free stream

INTRODUCTION

Before any computer code which numerically solves the Navier-Stokes equations can be used with confidence as an analysis or design tool, the range of the validity of the solution procedure and physical modeling must be known. The verification process requires three distinct types of testing: (1) internal consistency checks; (2) comparison with other codes; and (3) comparison with experimental data.

The first of these tests consists of checking the code for proper conservation of mass, momentum, and energy. The simplest such test would be verifying that the code can preserve free-stream flow. Other tests would include the computation of flows for which analytic solutions are available. In these cases, studies can be made on the effects of grid refinement and the effects of variations of numerical method parameters such as artificial viscosity controls.

The second level of testing is the comparison of computed results with those obtained using other similar but well-established codes that also solve the time-dependent Navier-Stokes equations. Comparisons could also be made with results from boundary-layer codes or space-marching parabolized Navier-Stokes codes.

The final verification test is the comparison of computed results with highly accurate benchmark experimental data sets. The basic quantities that need to be compared with the experiment include surface pressure, pressure profiles, shock shape, mass flux, surface heat transfer and skin friction, total-pressure recovery, and boundary-layer profiles. Typically, however, only a limited subset of these types of data is available for any particular experiment.

The present paper presents a comparison of results from four different computer codes for solving the compressible Navier-Stokes equations using three different flow problems. These test problems all have features typical of high-speed internal flow problems of practical importance in the design and analysis of propulsion systems for advanced hypersonic vehicles.

DESCRIPTION OF CODES

Three of the four computer codes use similar recently-developed upwind-difference technology and represent the current state-of-the-art in computational fluid dynamics. The first of these, CFL3D (Computational Fluids Lab 3-D code), was developed by Thomas for the thin-layer Navier-Stokes equations and is described in Ref. 1. This code uses a finite-volume method in which the convective and pressure terms are differenced with the upwind-biased flux-difference splitting technique of Roe. The resulting discretization is third-order accurate. The differencing for the diffusion terms representing shear stress and heat transfer effects corresponds to second-order-accurate central differencing. The time-differencing algorithm is a spatially-split approximate factorization method.

The second upwind code, USA-PG3 (Unified Solution Algorithm - Perfect Gas, 3-D), was developed by Chakravarthy.[2] The corresponding two-dimensional version is denoted USA-PG2. In these codes, the convection terms are modeled using a family of high-accuracy total-variation-diminishing (TVD) upwind-biased finite-volume schemes based on Roe's approximate Riemann solver. Second derivative viscous terms in the full Navier-Stokes equations, except cross-derivative terms, are modeled with conventional central-difference approximations. The cross-derivative terms are treated so that their discretization also contributes to the diagonal dominance of the implicit time discretization. For the present calculations, the implicit formulation was solved using approximate factorization methods.

The third upwind code, LAURA (Langley Aerothermodynamic Upwind Relaxation Algorithm), is a finite-volume, single-level storage implicit upwind-differencing algorithm developed by Gnoffo[3, 4] to solve both the Navier-Stokes and thin-layer Navier-Stokes equations with particular emphasis on external, reacting, hypersonic flows over blunt bodies with detached shocks. The perfect-gas version of the code is implemented for this study. An alternating-directional-sweep Gauss-Seidel substitution strategy is used to relax the governing equations. The method uses Roe's averaging procedure and a symmetric TVD scheme for flux definition. The scheme is second-order accurate except in the vicinity of flow structures (i.e., shocks) in which the gradient of Riemann-like variables across adjacent computational cell walls changes sign. At such points the scheme reduces to first-order accuracy. The present version of the code does not contain a turbulence model and, therefore, will be used only for the two laminar flows considered in the present study.

The fourth computer code was developed by Kumar[5, 6, 7] and uses the original unsplit explicit technique of MacCormack[8] to solve the full Navier-Stokes equations. The two-dimensional version of the code, denoted NASCRIN (Numerical Analysis of SCRamjet INlets), is described in Refs. 5 and 6, while the three-dimensional version, SCRAMIN (SCRAMjet INlets), is described in Ref. 7. The numerical technique is a two-step, predictor-corrector scheme which is second-order accurate in both space and time. These codes have been successfully used for a number of high-speed internal flow calculations such as the studies of scramjet inlet flow fields of Kumar.[5, 7]

RESULTS

The first test problem, shown in Fig. 1, is a two-dimensional case with laminar supersonic flow between two walls. The upper wall is kept parallel to the free stream, while at the lower wall, the flow undergoes a 10° compression at 2 cm. from the leading edge and then a 10° expansion at 4 cm. The total length of the flow domain is 10 cm. with an initial distance between the two walls of 2 cm. At the present time, no experimental data exist for this problem. However, this problem was chosen since it contains many of the features of a typical complex internal flow including the interaction of a shock wave and an expansion fan as well as the interaction of a boundary layer and a shock wave, the latter resulting in a separated flow region. The inflow Mach number was 5.0 and the Reynolds number based on the inflow conditions and the length of the flow domain was 1.14×10^7. An adiabatic-wall boundary condition was applied at each wall. Computations were made with all four codes on two grids. The first of these grids had 51 uniformly-spaced points in the streamwise direction and 51 points in the normal direction stretched to cluster points in the boundary layers along each wall. The second grid contained 101 points in each direction with the spacings between points equal to half of those in the 51 x 51 grid. A solution for a 201 x 201 grid was also obtained using only CFL3D.

The computed pressure and skin friction along the lower and upper walls are shown for all four codes in Figs. 2 and 3, respectively for both the 51 x 51 grid and the 101 x 101 grid. As shown, the wall pressures computed by all of the codes are in good agreement with noticeable differences in the separated-flow region at the base of the compression ramp and at the intersection of the ramp shock with the upper-wall flow. The peak pressure on the upper wall is approximately 5 for the coarser grid and approximately 5.8 for the finer grid and occurs further upstream as the grid is refined. Greater differences are seen in the skin-friction values, which were all computed using two-point one-sided differences for the derivative of the velocity. Along the upper wall, downstream of the leading edge and ahead of the separated-flow region, the grid refinement results in a convergence of skin friction which closely matches the values obtained from weak-interaction theory. In the separated regions, the levels are quite different for the four codes even on the 101-point grid, indicating further grid refinement is required. In general, the trend is an increase in the upstream extent of separation with increasing grid refinement. The NASCRIN

solution shows the least amount of separation and also shows oscillations in the computed skin friction near the separation and reattachment points. The largest negative values of skin friction occur near the impingement of the ramp shock. On the finer grid, all of the methods show a thin separation region upstream of this impingement. This overall trend is consistent with experimentally observed interactions of shock waves with laminar boundary layers. Downstream of the interaction, the values of skin friction all approach a common asymptotic value. In all of the calculations, the adiabatic-wall boundary condition was implemented by using zero gradients of pressure and total temperature at the wall instead of the more commonly used zero gradient of static temperature. In a related grid refinement study, for supersonic flow over a flat plate, use of the total temperature boundary condition tended to improve the prediction of the adiabatic wall temperature, especially on a coarse grid.

All of the LAURA results used a symmetric limiter introduced by Yee,[9] defined by Equation (4e) of Ref. 9. Of the three limiters suggested by Yee in that report, (Equations 4c-e), the third gave the highest pressure jump across the reflected shock in the ramp problem, consistent with the non-oscillatory results of the other two upwind methods. Both the ramp and the corner flow problems were found to be much less demanding than blunt body flows with regard to the required magnitude of the eigenvalue limiter, ϵ (Harten's entropy fix), used in the evaluation of the upwind dissipation within LAURA. The minimum value of ϵ as a fraction of the free-stream velocity magnitude was equal to 0.005 whereas the minimum value in blunt body flows is approximately 0.1. Smaller values resulted in non-converging solutions or physically incorrect solutions. Conversely, large values of ϵ (i.e., $\epsilon > .05$) caused losses in the adiabatic-wall temperature in the ramp problem. These losses are believed to be caused by a breakdown in the reflected cell boundary condition to approximate a zero energy flux across the cell wall in the presence of both a coarse grid (cell Reynolds number of order 100 based on sound speed and mesh height at the wall) and large ϵ.

Fig. 4 shows the effect of grid refinement on the pressure contours. All of these calculations were made with CFL3D. This figure indicates the increased resolution of the shock waves on the finest grid and, as evident from the movement of the separation shocks, the increased extent of the separated regions on the finer grids.

The second test problem, shown in Fig. 5, is the P8 inlet,[10] which represents inlet configurations typical of a hypersonic airbreathing vehicle. This 2-D inlet was designed to provide an internal compression ratio of 8. The forebody wedge is a 6.5-degree wedge intended to match a design Mach number of 6 at the inlet entrance under the test conditions of a free-stream Mach number of 7.4, allowing for boundary-layer displacement effects. The Reynolds numbers based on free-stream conditions is 8.86×10^6 per meter. The total pressure is 4.14×10^6 N/m^2, the total temperature is 811 degrees Kelvin, and the wall temperature is 303 degrees Kelvin. In the experiment, transition to turbulence occurred on both the centerbody and the cowl surfaces. Calculations incorporating a transition region were made with three of the codes, CFL3D, USA-PG2, and NASCRIN. Calculations assuming fully turbulent flow on both surfaces were also made with the two upwind codes, CFL3D and USA-PG2. In the experiment, the cowl lip was blunted with a diameter of 0.114 cm. However, for the computations, the upper and lower surfaces of the cowl were extended to form a sharp leading edge to simplify the construction of a grid. The grid that was used for the two implicit upwind codes contained 215 points in the streamwise direction which were clustered at the cowl leading edge. There were 101 points in the normal direction clustered at the upper and lower surfaces. A slightly less-refined grid was used for the NASCRIN calculation to allow a larger time step to be used with the explicit algorithm in that code. All of the calculations were made assuming equilibrium conditions at the tunnel test section corresponding to a ratio of specific heats, γ, of 1.4. Furthermore, all of the computations were made using the Baldwin-Lomax[11] turbulence model.

Mach number profiles are shown in Fig. 6 for both the transitional and fully-turbulent calculations in comparison with the experimental values at the cowl inlet station. Transition regions were specified to correspond approximately to the experimental values. The turbulent eddy viscosity was linearly increased from zero to the fully-turbulent value over the length of 5.9 in. (15 cm.) along the centerbody beginning at 10.8 in. (27.5 cm.) and over a length of 3.94 in. (10 cm.) along the cowl surface beginning at 41.3 in. (105 cm.). As shown, the transitional results agree best with the data. The transitional computations and the experiment both indicate a boundary-layer thickness of about 0.5 in., whereas the turbulent computations show a boundary-layer thickness slightly above 0.6 in.

Computed wall pressures are compared with experimental results in Figs. 7 and 8 for the transitional and turbulent calculations, respectively. Computed pressure contours using USA-PG2 for the region from 43.0 to 50.1 in. are shown in Fig. 9. For all of the calculations, the pressures are generally overpredicted from 46 to 48 in. on the centerbody and from 40 to 48 in. on the cowl. The pressure rise at 44 in. on the centerbody is due to the impingement of the cowl shock. The pressure rise at 49 in. on the cowl is associated with the impingement of the reflected shock onto the cowl (Fig. 9). The locations of both shocks are sensitive to the incoming boundary-layer thickness. The NASCRIN calculation shows better agreement with experimental data for the transitional calculation although the reflected shock impingement is still downstream of the experimental results. The disagreement of this calculation with the two upwind results can partly be attributed to the differences in the grids used. The fully-turbulent calculations shown in Fig. 8 agree well with each other and indicate the

closest agreement with the location of the impingement of the reflected shock in the experiment.

Predicted pitot-pressure and total-temperature profiles are compared in Figs. 10 and 11 with experimental data for two different locations in the inlet. In Fig. 10(a), all of the codes predict a pitot pressure of .025 above the boundary layer and below the cowl shock on the wedge centerbody. This value is higher than the experimental value of .021. Ng, Benson, and Kunik[12] demonstrated close agreement with the experimentally-measured level in that region using a γ of 1.38. Calculations made with CFL3D with a γ of 1.38 also indicate close agreement of pitot pressure with experimental data throughout the inviscid portion of the profile. However, this choice of γ cannot be justified based on the temperature present in the experiment. The value of γ in the reservoir is nominally 1.35. However, the free-stream value of temperature is no more than approximately 100 degrees Kelvin. Thus, the ratio of specific heats would be expected to be 1.4 in the inviscid portions of the flow. Real-gas effects may be important, however, in the flow field induced by the presence of the pitot probe since the temperature increases rapidly across the shock ahead of the tube to a value near that of reservoir conditions. Pitot-tube pressures were calculated with equilibrium real-gas relations, but only a slight effect was found, which could be compensated for by using an "effective" value of γ of 1.396 in the pitot-tube formula for perfect gases. The effect of the equilibrium real-gas assumption becomes more important at higher stagnation temperatures.

The Mach number at the cowl inlet station outside of the wedge shock determined from real-gas pitot formulas using the measured pitot pressure data is 7.6. This indicates a longitudinal variation in Mach number of approximately 0.01 per foot, which is in agreement with the wind-tunnel calibration measurements (Appendix A of Ref. 10). Agreement of the computed and experimental pitot pressures thus requires incorporation of the longitudinal Mach-number gradient into the calculations.

In all of the computations, the shock from the cowl lip is located above that measured experimentally at 40.9 in. (104 cm.). This may be a result of the wedge approximation to the cowl leading edge. The turbulent cowl computations produce a thicker boundary layer in the leading-edge region than in the transitional calculations in which the flow is laminar in that region. The effect of this thicker boundary layer is to increase the leading-edge interaction and lower the position of the observed cowl shock at x = 40.9 in. The local increase in pitot pressure near the cowl surface at x = 49.2 in. (125 cm.) shown in Fig. 10(b) is associated with the impingement of the reflected cowl shock onto the cowl surface. Those calculations which more closely predict the cowl shock location at x = 40.9 in., i.e., the NASCRIN transitional calculation and the two upwind turbulent calculations, Fig. 11(b), also more closely predict the overall flow-field interaction pattern downstream of this location. Considering the above-mentioned discrepancies, the boundary-layer thicknesses do appear to be well-predicted based on the pitot-pressure and total-temperature profiles, and all of the methods predict similar thicknesses.

The final test problem is the supersonic flow in a three-dimensional symmetric corner formed by the intersection of two wedges with equal wedge angles of 9.48 degrees as shown in Fig. 12(a). The flow in such a corner is representative of the flow inside a scramjet inlet. A sketch of the flow field is shown in Fig. 12(b). This complex flow field consists of an oblique corner shock wave joining the two wall shocks, embedded internal shocks which extend from the two shock intersection points toward the wedge surfaces, slip lines which converge toward the intersection of the wedges and which separate the flow crossing the corner shock from the flow crossing the two wall and internal shocks. Calculations were made for both laminar and turbulent supersonic flow and compared with the experimental data obtained by West and Korkegi.[13] In both cases, the Mach number was 3.0, the free-stream temperature was 105 degrees Kelvin, and the wall temperature was 294 degrees Kelvin. The grids used in both cases had 35 equally-spaced points in the streamwise direction and 61 points in both directions in each crossflow plane clustered at the wedge surfaces.

Computed results for the laminar flow case are shown in Fig. 13. The Reynolds number for this case was 3.07×10^6 per meter. The density contours for this case at a cross-plane near the downstream outflow boundary at X = .0724m computed using USA-PG3 are shown in Fig. 13(a). A comparison with the experimentally observed flow structure shows that the flow features are well-predicted. A comparison of the sidewall pressure distribution with experimental data is shown in Fig. 13(b). The pressure has been normalized using the experimental pressure value, P_{wedge}, on the wedge surface, which was 1.98 times the free-stream pressure. In general, the computed pressures for all of the codes follow the trends in the experimental data. The difference between the predicted locations of the internal shock obtained from the four codes as well as the overprediction of the pressure level outside of this shock by three of the codes may be due in part to the relative coarseness of the grid in these regions. In coarse-grid regions, the solutions obtained by each code are sensitive to the dissipation inherent in each numerical scheme. Therefore, grid refinement is required to resolve the differences between the codes.

Computed sidewall pressure values for the turbulent case are shown in Fig. 14. The Reynolds number chosen for this case was 8.66×10^6 per meter. Although the number of grid points remained the same, the grid was more highly stretched at the wall than in the laminar case. All of the codes again used the Baldwin-Lomax[11] turbulence model in these calculations. The experimental data shown are from the highest and lowest

Reynolds numbers for which experimental data are given in Ref. 13. Once the flow becomes turbulent, there is very little change in the sidewall-pressure distribution over the range of experimental Reynolds numbers. The computational Reynolds number was approximately a factor of three lower than the lower of the two experimental Reynolds numbers. As in the laminar case, the pressure levels follow the trends of the data although pressure levels are again overpredicted in the relatively coarse grid region. In addition to dissipation effects related to the coarseness of the grid, the differences between the solutions may also be due in part to differences in the determination of the length scales for the turbulent shear stresses in the Baldwin-Lomax turbulence model.

CONCLUSIONS

A comparative study has been made using four different computer codes for solving the compressible Navier-Stokes equations. Three different test problems were used, each of which has features typical of high-speed internal flow problems of practical importance in the design and analysis of propulsion systems for advanced hypersonic vehicles. Three of these codes use similar recent implicit upwind-differencing technology, while the fourth uses the explicit MacCormack method.

The flow between two walls, one of which contains a ten-degree compression ramp, contains the interaction of a laminar boundary layer and a shock wave at a relatively high Reynolds number, and details of the flow in the resulting separated flow upstream of the impinging shock were found to be sensitive to the resolution of the grid that was used. Agreement of the results from the four codes was found only in the region outside of the separated-flow region. For the P8 inlet, the overall flow structure and the boundary-layers of velocity and temperature were in general, well-predicted. Discrepancies between the computed and experimental levels of pitot pressure and total temperature outside the boundary layer were found. These discrepancies can be atttributed to a longitudinal gradient in free-stream Mach number which was not incorporated into the computations. For the three-dimensional flow in a corner formed by the intersection of two symmetric wedges, it was found that the complex flow structure was qualitatively predicted by all of the codes for both laminar and turbulent cases.

REFERENCES

1. Vatsa, V. N.; Thomas, J. L.; and Wedan, B. W.: Navier-Stokes Computations of Prolate Spheroids at Angle of Attack. AIAA Paper 87-2627-CP, 1987.

2. Chakravarthy, S. R.; Szema, K-Y.; Goldberg, U. C.; Gorski, J. J.; and Osher, S.: Application of a New Class of High Accuracy TVD Schemes to the Navier-Stokes Equations. AIAA Paper 85-0165, 1985.

3. Gnoffo, P. A.: Application of program LAURA to Three-Dimensional AOTV flow fields. AIAA Paper 86-0565, 1986.

4. Gnoffo, P. A.; McCandless, R. S.; and Yee, H. C.: Enhancements to Program LAURA for Computation of Three-Dimensional Hypersonic Flow. AIAA Paper 87-0280, 1987.

5. Kumar, A.: Numerical Analysis of the Scramjet-Inlet Flow Field by Using Two-Dimensional Navier-Stokes Equations. NASA TP-1940, 1981.

6. Kumar, A.: User's Guide for NASCRIN - A Vectorized Code for Calculating Two-Dimensional Supersonic Internal Flow Fields. NASA TM-85708, 1984.

7. Kumar, A.: Numerical Simulation of Scramjet Inlet Flow Fields. NASA TP-2517, May 1986.

8. MacCormack, R. W.: The Effect of Viscosity in Hypervelocity Impact Cratering. AIAA Paper 69-354, 1969.

9. Yee, H. C.: Numerical Experiments with a Symmetric High-Resolution Shock-Capturing Scheme. NASA TM-88325, 1986.

10. Gnos, A. V.; Watson, E. C.; Seebaugh, W. R.; Sanator, R. J.; and DeCarlo, J. P.: Investigation of Flow Fields Within Large-Scale Hypersonic Inlet Models. NASA TN D-7150, April 1973.

11. Baldwin, B.; and Lomax, H.: Thin-Layer Approximation and Algebraic Model for Separated Turbulent Flows. AIAA Paper 78-257, Jan. 1978.

12. Ng, W.-F.; Benson, T. J.; and Kunik, W. G.: Real Gas Effect on the Numerical Simulation of a Hypersonic Inlet. Journal of Propulsion and Power, Vol. 2, No. 4, July-August 1986, pp. 381-382.

13. West, J. E.; and Korkegi, R. H.: Supersonic Interaction in the Corner of Intersecting Wedges at High Reynolds Numbers. AIAA J., vol. 10, no. 5, May 1972, pp. 652-656.

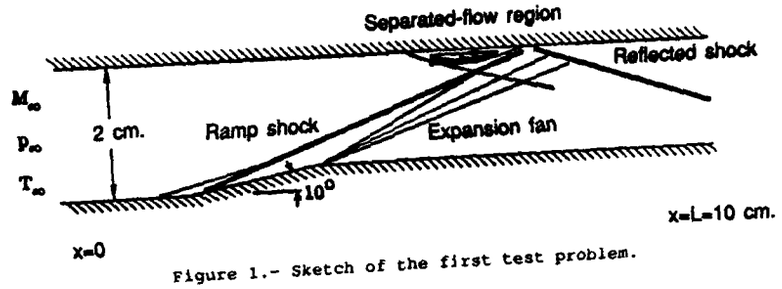
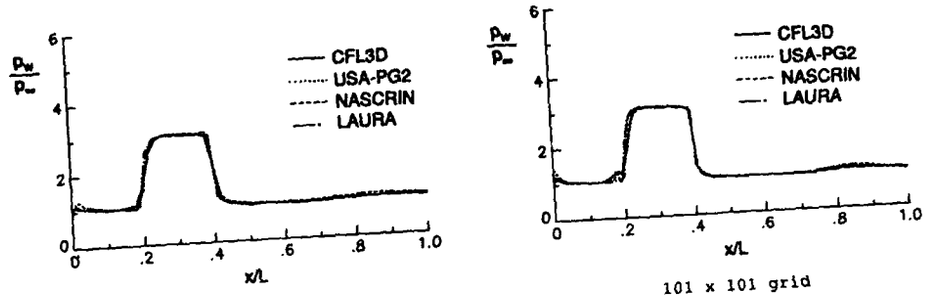
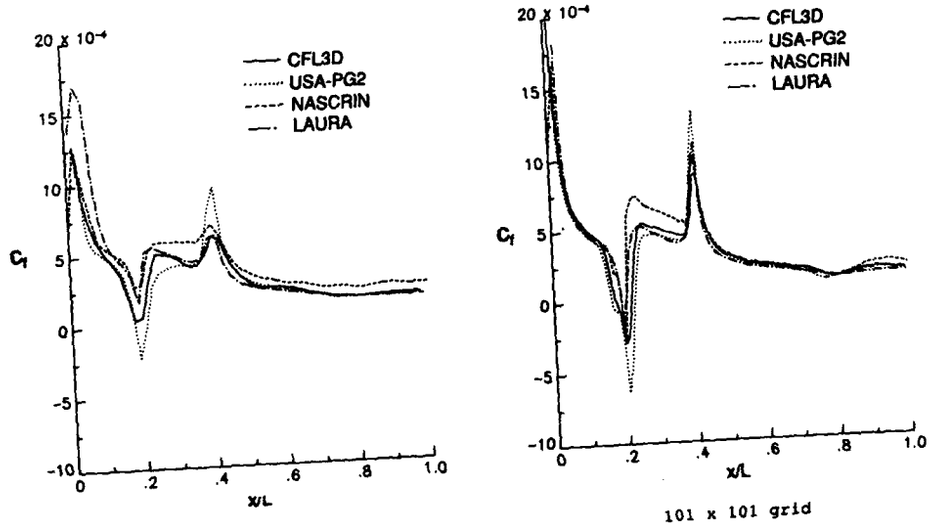


Figure 1.- Sketch of the first test problem.

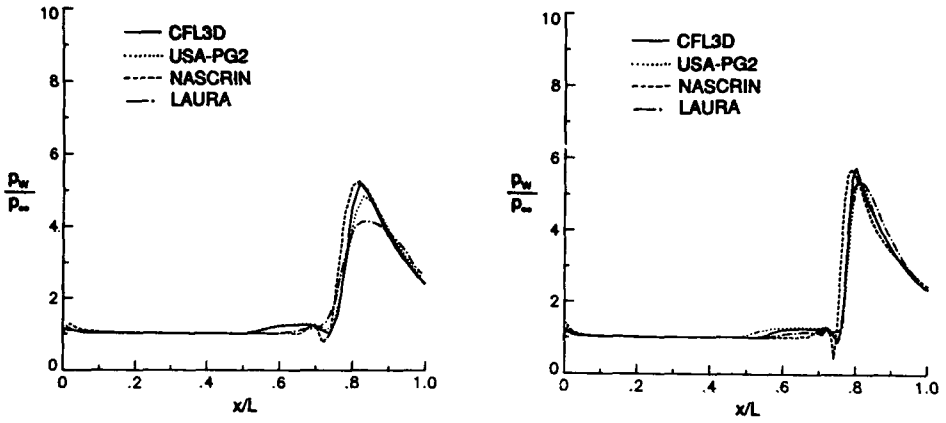


(a) pressure



(b) skin friction

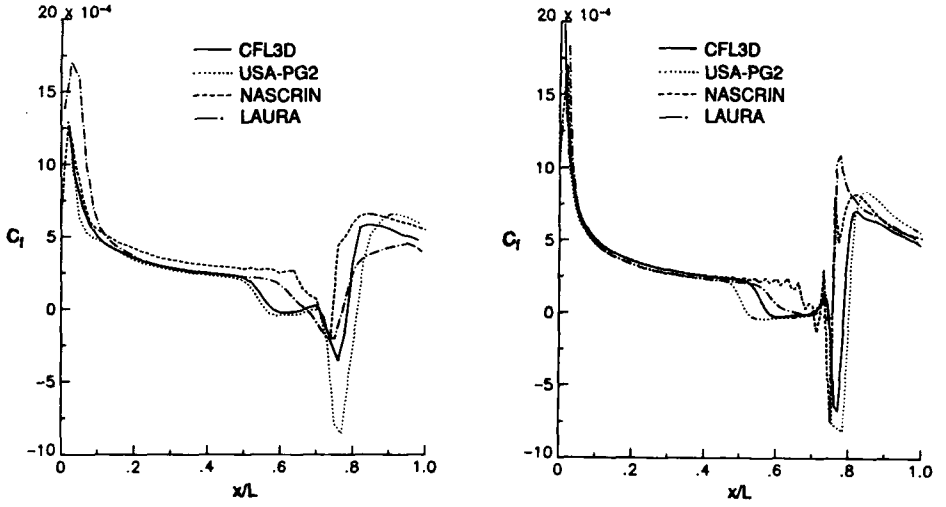
Figure 2.- Computed pressure and skin friction on lower wal..



51 x 51 grid

101 x 101 grid

(a) pressure



51 x 51 grid

101 x 101 grid

(b) skin friction

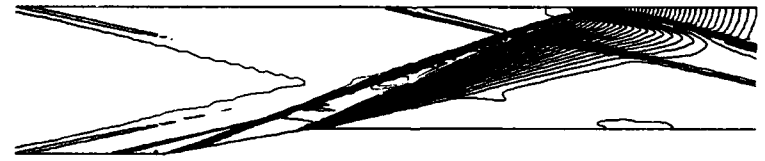
Figure 3.- Computed pressure and skin friction on upper wall.



(a) 51 x 51 grid



(b) 101 x 101 grid



(c) 201 x 201 grid

Figure 4.- Pressure contours computed with CFL3D.

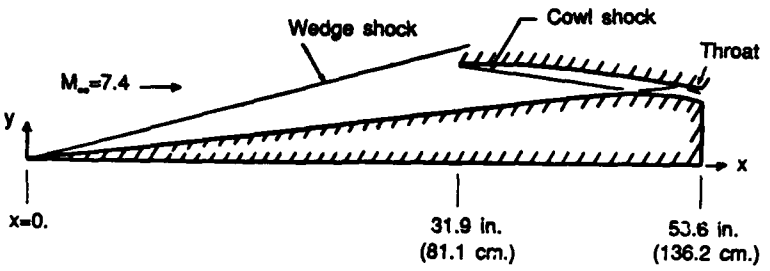
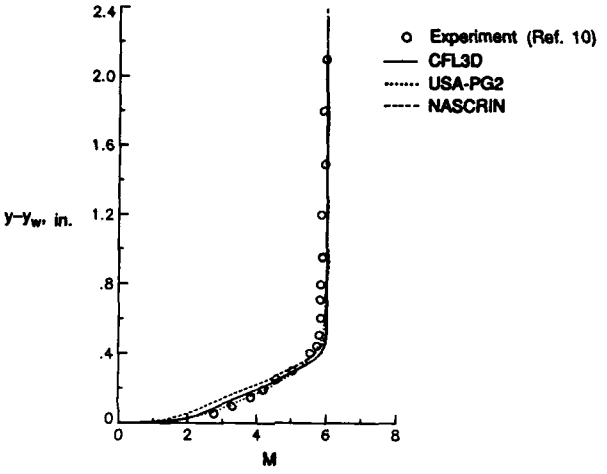
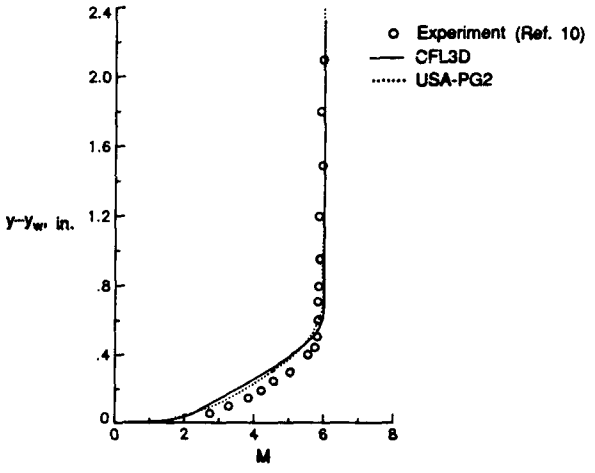


Figure 5.- P8 hypersonic inlet geometry.

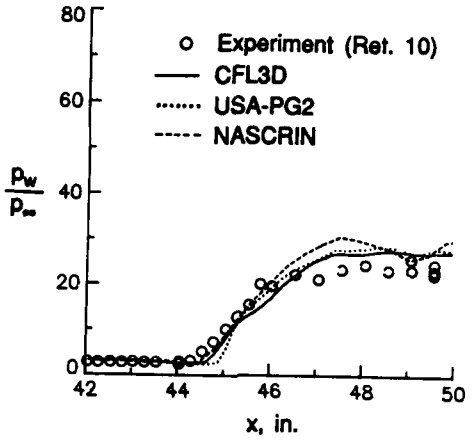


(a) transitional computation

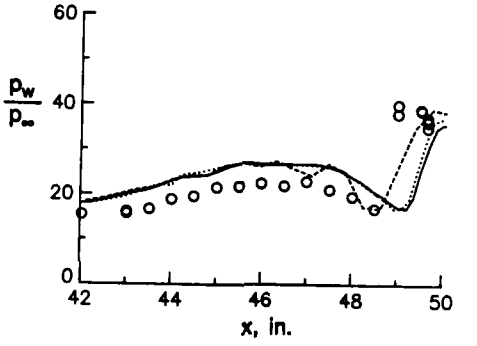


(b) fully turbulent computation

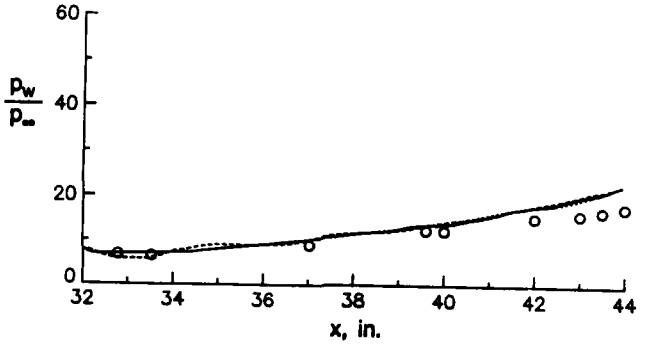
Figure 6.- Comparison of computed and experimental Mach number profiles at cowl inlet station. x = 31.9 in. (81.1 cm.).



(a) centerbody

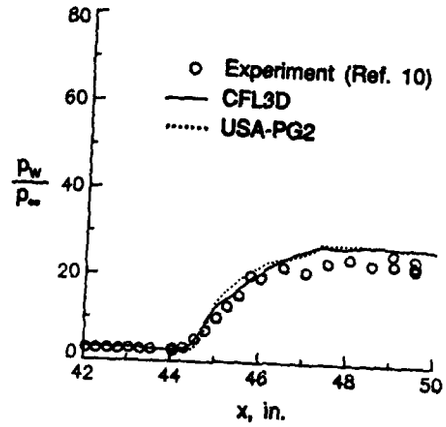


(b) cowl

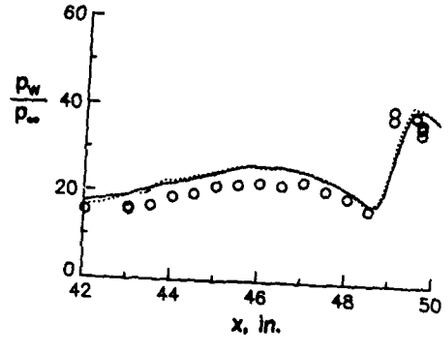


(c) cowl leading edge

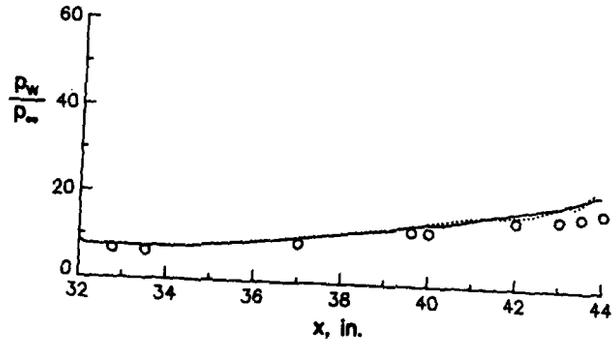
Figure 7.- Comparison of computed and experimental surface pressure. Transitional computation.



(a) centerbody

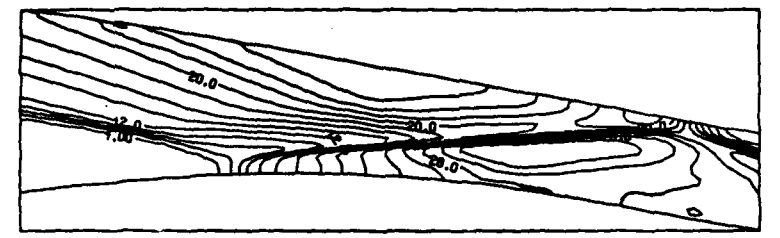


(b) cowl

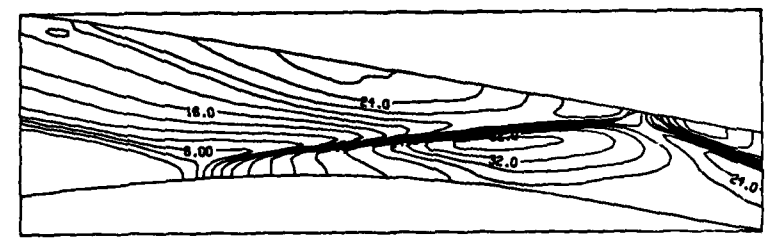


(c) cowl leading edge

Figure 8.- Comparison of computed and experimental surface pressure. Fully turbulent computation.



(a) transitional

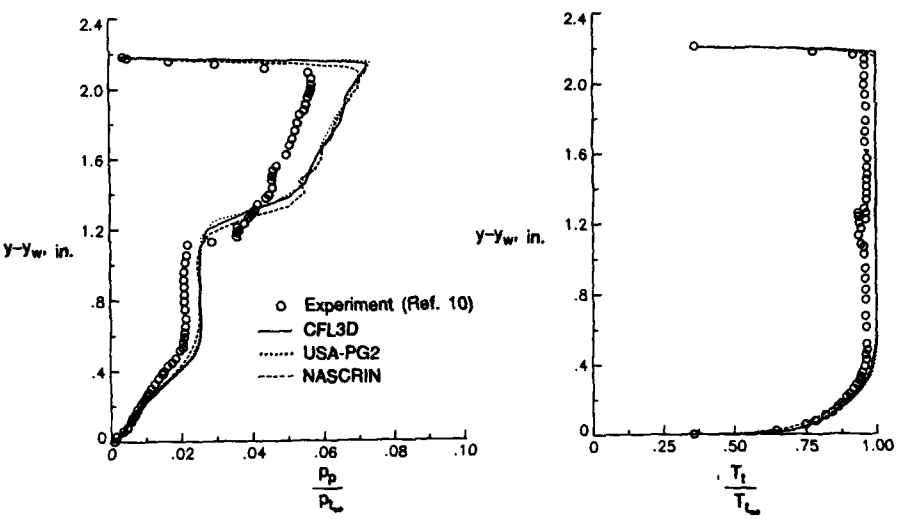


x=43.0 in.
(109.2 cm.)

50.1 in.
(127.3 cm.)

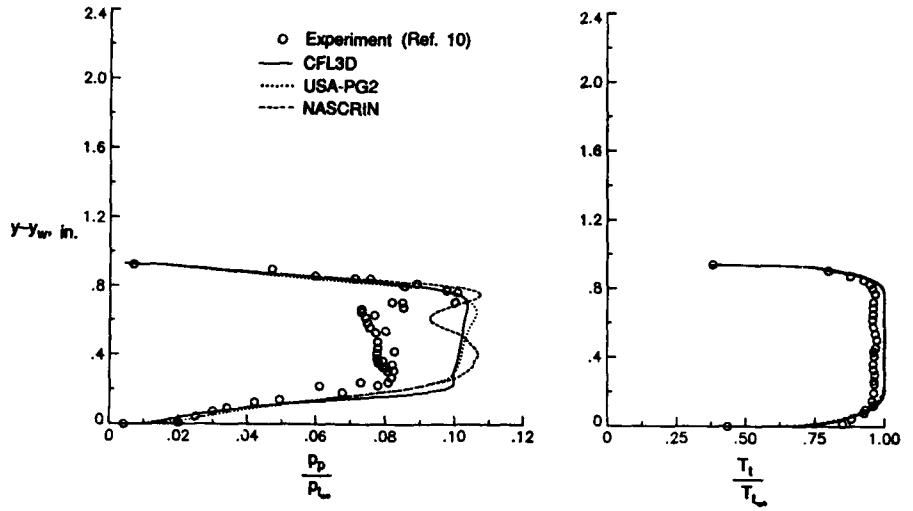
(b) fully turbulent

Figure 9.- Pressure contours computed using USA-PG2.



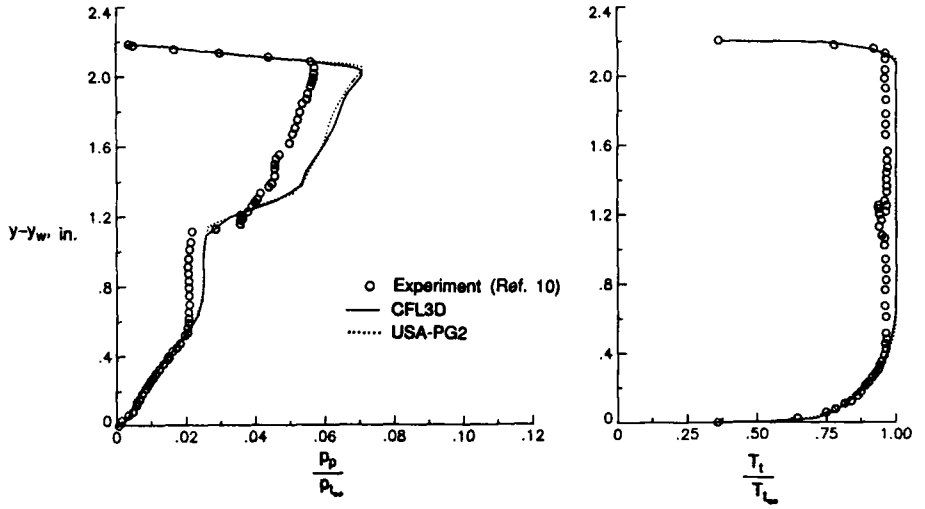
(a) x = 40.9 in. (104 cm.)

Figure 10.- Comparison of computed and experimental pitot-pressure and total-temperature profiles. Transitional computation.



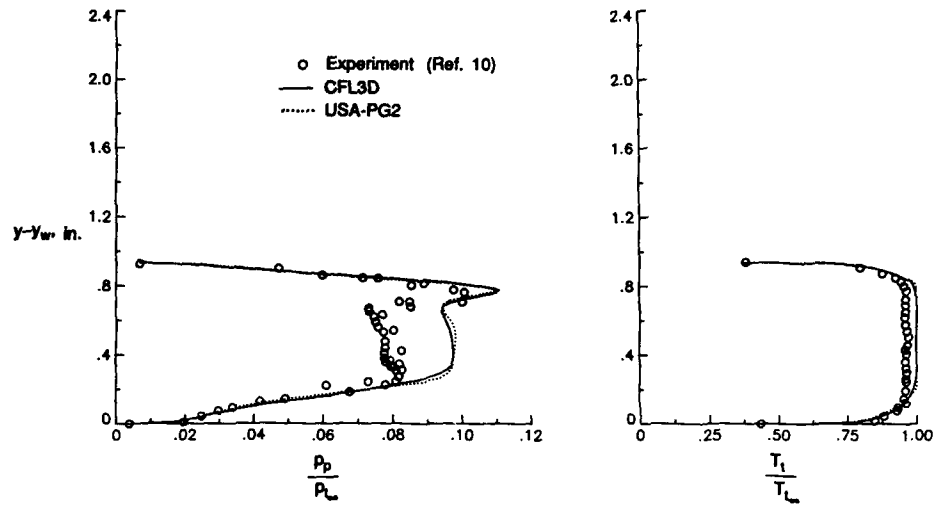
(b) x = 49.2 in. (125 cm.)

Figure 10.- Concluded.



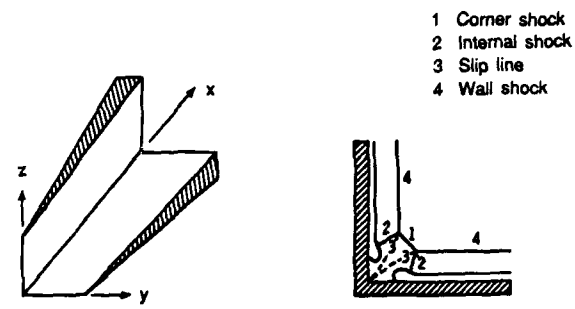
(a) x = 40.9 in. (104 cm.)

Figure 11.- Comparison of computed and experimental pitot-pressure and total-temperature profiles. Fully turbulent computation.



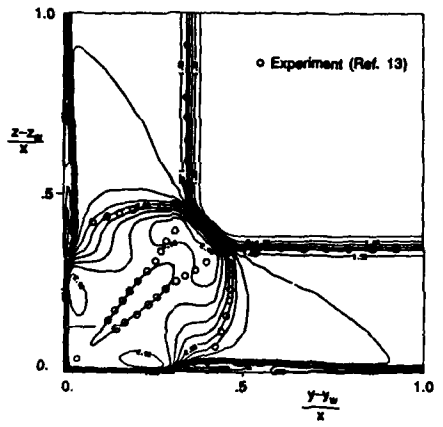
(b) x =49.2 in. (125 cm.)

Figure 11.- Concluded.

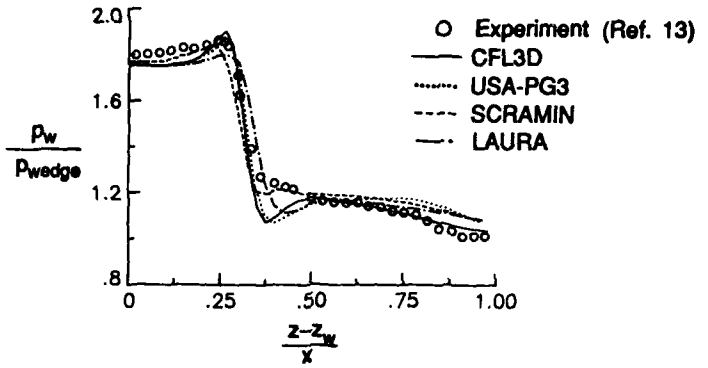


(a) corner geometry (b) flow structure in cross-flow plane

Figure 12. Corner flow problem.



(a) Computed density contours using USA-PG3. x = 0.0724 m.



(b) Comparison of computed and experimental surface pressure. x = 0.0724 m. for CFL3D and SCRAMIN and x = 0.0733 m.for USA-PG3 and LAURA.

Figure 13.- Computed results for laminar corner flow.

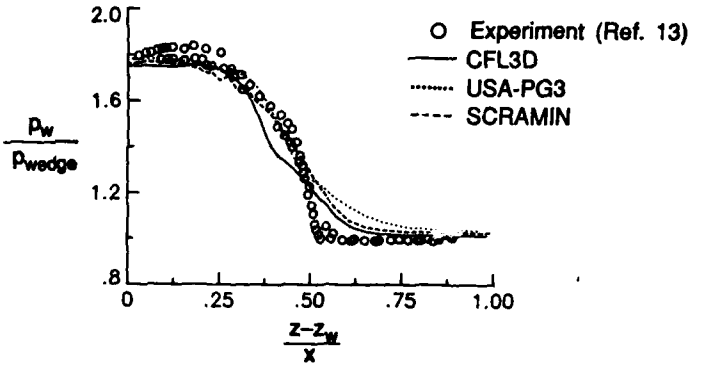


Figure 14.- Comparison of computed and experimental surface pressure for turbulent corner flow. x = 0.0724 m. for CFL3D and SCRAMIN and x = 0.0733 m. for USA-PG3.

VALIDATION OF COMPUTATIONAL FLUID DYNAMICS
2 - 5 MAY 1988
Lisbon, Portugal

ROUND TABLE DISCUSSION

Randy Graves, NASA

Dick Bradley opened the Symposium some three days ago, and unfortunately Dick had to return to the U.S. and could not be here for the closing session. I am Randy Graves, and I am standing in for Dick. I would like to say a couple things before we get started. First off, when we have the discussion session which will follow Peter Sacher's technical review, would you, if you have something to say, please identify yourself clearly as to your name and your affiliation, because everything will be recorded, and later transcribed for the record.

Well, we started off a little over three days ago with Dick's introduction where he gave some definitions of calibration and validation and we looked at four kinds of experiments. I think, looking back over the thirty some papers and also the approximately twenty papers in the poster session, I think we have seen, over this time period, a number of cases of validation, calibration, and a wide range of experiments. I think, looking at the poster session in particular, that there was a lot of good interaction, and I hope that when we get to the discussion period, it will raise some interesting discussions as well as questions. I think there are a lot of unanswered questions. A couple of them came up on the first day, which have been deferred to the discussion session.

So what I would like to do now is introduce Peter Sacher, who is our Technical Evaluator for the Symposium, and Peter will lead off with his review. That will be followed then by our discussion period, and I will return to the podium to moderate the discussion period.

Peter Sacher, MBB

Thank you, Randy. Let me just start these remarks with how much I appreciate the opportunity to act as an evaluator here for this meeting. It was not easy to follow all these presentations this week. We had a new record of papers: fifty-eight, including the poster session. So, if some of my remarks are possibly too provocative or too much criticism, forgive me. I may revise it in the written version. There is a background within AGARD on databases, and the experience we have had in comparison of experimental and computational results. This is nothing new, and this effort was going on at least for the last decade. (Fig. 1) We have a pretty good set of test cases for external and even for internal flows, and there have been a couple of working groups working on test cases just performing comparisons between CFD and experiments. Now, something has changed by the goal of this meeting, and I will try to follow the outline given by Bradley and Schmidt. The goal of this meeting was to address the design and analysis capabilities which have to be user-friendly, cost-effective, numerically accurate and fully verified by detailed experimental comparisons. That is directly taken out of the call for papers. (Fig. 2) So we have the objectives of the symposium to identify the level of agreement of physical models and numerical solution algorithms with experimental data, to identify regions of validity, identify flow regions where significant gaps exist, and to perform qualitative and quantitative error analyses.

Outlined a little bit more in detail was the goal by the criteria for validation given during the excellent presentation of Dick Bradley, also by Povinelli in the session later on. There are requirements that the numerical code must be able to accurately model the critical flow physics. (Fig. 3) Validation occurs when accuracy and limitations of both the experimental data and the code algorithm are known and understood. Now let us go through the symposium and my impression to try to identify where we have followed or met the requirements given by these definitions.

One remark on the status of CFD codes. It was not mentionned too much during this week, but everyone notices that we have research codes, pilot codes and production codes (see Fig. 4), and I think we were talking the whole week on research codes, and, well, sometimes on pilot codes in use at different companies producing a large amount of data which we have just compared with experiments, but not validated. We had a really good session number one. At least the aim of this meeting was very well defined and prescribed - a good start on Monday morning. The driving motivation for the code calibration comes from industry. That is a fact, and could clearly be seen in the first presentations. But first of all, before comparing and validating numerical results, the validation numerically had to be done. That means the proof of consistency, stability, convergence, uniqueness of the solutions, and I have an old view foil from Yoshihara, from Boeing Co. Fig. 5, who has identified classes of sources of errors in numerical methods. And, I think this was not mentionned too often during this meeting, some errors are inevitable. They are given by the choice of the equations. There are some classes of solutions where physical flow does not exist. We have the numerical algorithm and, combined with it, an error of discretization. And we have the solution of our system of equations which is of limited accuracy, and the convergence has to be proven. All this has to come first, and then, of course, the validation by experiment.

We have heard about four classes of experiments, experiments for the principal understanding of the physics of flow and, of course, to find out models for CFD codes. The third class was the calibration test, often used in project work in industry, and, last but not least, the aim of this symposium, the validation of CFD codes, needs a special kind of very carefully prescribed measurements. I was missing validation by flight tests. This is something which comes in addition to this procedure. Perhaps we often make validation for an unrealistic range of Reynolds numbers, and the limitation of this validation by tests was not always clearly defined and prescribed. We also need the definition of sensitivity, parameters of sensitivity, of the influence of a systematic variation of parameters which are, of course, dominating the flow.

After session one, which I assume to have been a good one, the next sessions follow the classes of geometries. We have to deal with 2-D airfoils, 3-D wings, wing-bodies, and then of course internal

flows. In session two for airfoils, we have well-defined experimental databases. The initial conditions and test boundary values are well prescribed and known. And we are able to take account of the effect of the wind tunnel representations in computational fluid dynamics. So validation and calibration were given for different classes of test cases, and classes of computer codes. I should say that boundary layer codes are still in use and valid instruments, valuable instruments during project work. Viscous inviscid interaction using small perturbation theory, full potential flow equations and Euler have been shown, and often in good agreement, at least in cases with weak shocks and non-separated flow. But there is a problem, even in 2-D, with transition. We will see later more with transition than with turbulence. And, of course, with 3-D separation, which is the special subject of Working Group number 10 in AGARD now. Concerning Navier-Stokes solutions, parametric studies on grid size, time steps, turbulence models often performed for steady and unsteady solutions, good agreement was shown, at least for some cases. But I would have preferred to see cases where differences or discrepancies exist. I have often seen, in practical work, and from the literature, that a special turbulence model validated for a certain class of airfoil fails completely if you change to another class of airfoil geometry. Surprising to me, at the end of this session, there is a great potential in adaptive grid embedding techniques. The flow grid overall density says nothing. The local density needed depends on sensitivity regions where shocks, curvature or other physical effects occur. That seems to be of great importance to save computer time.

Session three, vortex flow, there is a big controversy on the discussion of the validity or the approach to compare results from Euler calculations with experiments. I should say that we have in the case of simplest geometric shape, a fully developed 3-D flow, a rather complex flow field. And we have seen the international vortex flow experiment gives a good database, and, at least for this case, we cannot complain about too good agreement with experiments or even by comparisons of numerical data with each other. There is a large effort in Euler calculation. We must state that. But there is nearly no validation at all. But there is some tendency to validate at least the Euler codes by numerical checks. The validity of comparison with experiments is at least questionable. No Euler flow exists in real life, of course. Is the vortex flow really dominating for medium angle of attack, let us say ten degrees, or is the vortex viscous flow interaction dominating, is there shock viscous flow interaction, still not present in the Euler code? Well, you have seen Navier-Stokes solvers, surprisingly, do not improve the situation, at least for the vortex flow experiment.

Session four, wing bodies, we have seen a large database on large aspect ratio wings, and several attempts to use it for comparison with Navier-Stokes codes. One major problem is the treatment of the wind tunnel walls in CFD, we have seen only two contributions being able to take account for that. A big question was on 3-D transition. Should these experiments have been made with free or with fixed transition? I think we need both. And there is the big question of the laminar or turbulent boundary layer shock interaction. The conclusion at present is, even for attached flow, the Navier-Stokes results are not yet validated, at least following the outcome of this session. The reason may be, only a few, too few solutions are available, have been presented, perhaps mainly due to the extremely high cost of the calculations. There are some other remarks on the wing body session. There is some tendency in applying still potential flow codes. I have seen, for unsteady flow, remarkable extension of the small perturbation approximation, and this has been validated. There has been an introduction of exact relations for entropy, shock strength, and for vorticity in methods solving the potential flow equation. There is some kind, you can say, of correlation or empirically extending the region of validity. But these approaches are really promising. Some examples of very carefully performed experiments designed for code validation were shown in papers number 17 and 18. But also two contributions were purely reporting on the state of the art of CFD codes in project industry work.

The session on high speed flows was relatively short, only five contributions, but at least three of them were good examples for the subject of the meeting. They were describing experiments tailored and designed to certain limited problems like the separation on blunt body shapes. And, also in this session the development and modification of the computer code to take account of the physical effects was driven by industrial motivation, the force induced separation is a need to know in the missile work. A chance, let me say, has been missed by our U.S. people to use the opportunity to report on intensive work which has been done concerning the validation of hypersonic flow codes during the development of the shuttle orbiter. There was only one paper describing facilities and the existent codes.

Session six on turbo machinery, an excellent introduction to the internal flow problem, and again a good definition of what validation does mean, given by Povinelli in the paper number twenty-five. Then we had the paper on cascades and validation of Euler codes for internal flows, which are a little bit questionable to apply. The rest, unfortunately were not aligned to the subject of the meeting, again. They were just reporting on availability of a variety of CFD codes in industry.

The last session, intakes and ducts, where the internal flow is, of course, by no means simpler than the external flow. All complications due to viscosity, compressibility, vorticity and so on are still present, and perhaps more dominating than in external flow. But in some cases, boundary conditions are better defined, with one exception. There is an additional complexity, the initial condition, the inflow profile is generally not known, especially for aircraft intakes. And the use of inviscid Euler flow codes, is again questionable. But also here an excellent example for carefully performed code validation tests was given by the very last paper yesterday evening, by Kind, paper number thirty-four, and he has shown how to use boundary layer and shear stress measurements to look at the impact of different formulations of turbulence models in CFD codes.

So let me come to some concluding remarks. I have formulated eighteen statements, let me just go over quickly. Good news first. Some positive statements: (1) I got the impression that experimental and numerical working engineers are coming more and more together, and this meeting here is a good example for this interaction between those disciplines, which have been too long separated in the past. (2) The research institutes working more or less experimentally are running now their own CFD codes. (3) It is a good tendency that numerical and experimental flow simulation are more and more understood as complementary tools. Those approaches need each other. (4) Nobody talks anymore of replacement of wind tunnels by the computer. I am really happy to find that. (5) We have had very good experience in our poster session. This is also a positive remark. Some of the people displaying their paper inside told me

that they would have preferred to stay inside the poster session outside. It is easier to discuss with the people walking around than to stand up here before the audience. I think I would recommend that our panel at least should continue with poster sessions, perhaps with one modification. Why should we not leave the poster display from the beginning of the week till the end of the meeting, just having it for permanent discussion?

Now some criticism. (6) As I said before, the code validation process was often misunderstood as comparison of results. (7) Code validation by numerical verification, e.g., in terms of stability, convergence, uniqueness is often not shown in the papers. But I hope to find it in the written versions. (8) Comparison, in many cases, has been done with too complex configurations, geometries, or have been applied to too complex flows. (9) The dominating parameters and their sensitivity and their limitation have not been identified and separately investigated. The systematic parameter variation was not always transparent to me. (10) The driving motivation in many cases came from industry, which does not have time for systematic basic tests. (11) There are still databases needed for carefully selected prescribed flow problems, much more extensive than has been done within the vortex flow experiment, the DFVLR experiment, or for the three or four databases I have seen for internal flows. (12) The topic of cost, computer cost, was not addressed at all. (13) There is further need of improvment of models to represent transition, very important 3-D transition, three-dimensional separation, turbulence models, real gas effects, reacting gases. We have not seen too much in session five on high speed. And, of course, heat transfer, and so on. (14) No one was talking about the limits of applicability found by CFD or experiments. I miss a definition of the range, the individual range of the validation. (15) Some of these papers seem to me coming two years too late. They should have been submitted to the symposium in Aix, which was titled CFD Applications. (16) There is a need for validation of experiments too. In industry, we have an iron rule, an iron law: never try to use the same model in different wind tunnels. Repeating tests and establishing quality requirements is necessary, absolutly necessary, and we have to start with doing benchmark tests. (17) More emphasis should have been devoted on disagreement between computed and measured results Where the curves disagree is the interesting region, and should have been discussed much more why it occurs, than the agreement, which is sometimes harder to explain than the disagreement. (18) My final remark concerns the poor quality of some presented viewgraphs of some papers. I realize that the quality of the format has nothing to do with content or the value of the paper, of course. But it is a matter of politeness to the audience to present data in a proper format.

In summary, this symposium was certainly a step in the right direction, but perhaps not far enough.

Bradley started with the statement, "Nobody believes the result of a CFD calculation except the one who has generated it". I have some doubt that during this week too many have been converted to believers.

R. Graves

Peter, thank you very much. That was a very perceptive and somewhat provocative summary for the meeting. I think that with the 18 points that he just went over we have a good starting point for the open discussion. Just before we begin, I want to remind you again to please come forward and take the microphone, state your name clearly and your affiliation so that we can transcribe the discussion later.

With that I do not have to provide any lead-in for the discussion period, so we are now open for discussion.

K. Gersten, Bochum University

I was worrying about Dr. Bradley's paper on his philosophy. First of all I had difficulties with the semantics, the "code" obviously meant in his paper "prediction method". Prediction method, if I understood it correctly, usually has three parts in it. Simplifying Navier Stokes equation, I am talking about the Reynolds averaged Navier Stokes equations, for example, steadiness, inviscid, parabolizing or incompressibility or things like that. Second, turbulence modelling and third the numerical procedure. In my feeling always codes were referring to numerical procedures, but obviously the word code is used differently. There is no question about it that 1 and 2 were always existing before computers existed, so in principle, numerical procedure means CFD and I would like to make a provocative statement saying that validation of part 1 and 3 is unfair to do it with experiments. Turbulence modelling, of course, it is clear you have to compare it with experiments. I want to just explain why I think it is not acceptable to take a posteriori justifications by experiments for number 1 and 3. Number 1 was simplifying Navier Stokes equations and I should mention Van Dyck's book in which he distinguishes between rational and irrational approximations. I would think that if you have a rational approximation no a posteriori justification by experiment is necessary. One should avoid irrational approximations. A famous example was von Karman - Tsien formula or rule. That was irrational; you couldn't prove it systematically to higher accuracy and so it was just a rule and nothing else. If people start cancelling out terms in the Navier Stokes equations, that usually leads to an irrational approximation. If you avoid that, then justification comes from other sources, not from experiments. Steadiness for example, stability theory, inviscid code, has the justification from boundary layer theory. Parabolizing comes from a perturbation procedure with a certain slenderness parameter. Experiments to check numerical procedures, if I would ask my colleagues from applied mathematics to check their codes, their procedures, with experiments, they would think I am kidding. That was what I wanted to say, it may be provocative, but you want to have a lively discussion.

R. Graves

Do we have an answer to that?

L. Roberts, Stanford University

I have one or two remarks that follow very closely on the remark that Prof. Gersten just made. I should start out by saying that I am very impressed with the sheer volume of activity that is now taking place and has been generated over the last two or three years on this subject. I have a suggestion that relates

to the need for more care and discipline in formulating critical or definitive questions that need to be validated. I was very impressed with the formulation of the Garteur wing experiment that was in the poster session. It is clear that a great deal of thought has gone into the formulation of that experiment. We need more such thinking to address certain specific questions, not simply to make a comparison of CFD with experiment. For example, in very simple terms, if one were to try to determine whether the approximation of a flow being irrotational was adequate, then one ought to really just compare a potential calculation with an Euler calculation. That is all that is required to determine whether the approximation of irrotationality is a good one. You do not need experiments and the introduction of experiments into that comparison is simply additional information that is not needed and may be confusing. Similarly, if one is concerned whether the boundary layer approximation is a good one, one needs only to compare an Euler calculation plus a boundary layer calculation with a Navier Stokes calculation. That is the proper comparison to determine whether a boundary layer approximation is adequate. There is no point in introducing experiments into that comparison. It would be confusing to compare a potential code with a boundary layer calculation against a Navier Stokes equation, because there are two possible sources of error there. It isn't clear whether the error comes from the boundary layer approximation or comes from the fact that you have used a potential flow approximation instead of a full Euler code in that comparison. Those are the kind of comparisons that need to be made that do not need experiments. Similarly, I don't think that it is necessary to validate the physics of the Euler approximation, nor the physics of laminar flow. There is nothing in the physics that the Euler representation describes that is uncertain. There is nothing really in laminar flow that is uncertain, so there is no need to compare either of those with experiment. I think though that clearly the big chore in front of us is to validate the turbulent physics. There it is important that we do compare Navier Stokes calculation with experiment. Anything less than the Navier Stokes calculation on the CFD side introduces additional possible sources of approximation, sources of error, and it would be confusing to compare say an Euler code with experiment because the comparison is not valid. There are physical processes in the experiment that cannot possibly be captured by the Euler approximation and so I think that we need always to compare the Navier Stokes with the experiment. Perhaps we can avoid comparisons in which more than one possible source of error are made present. A comparison in which the numerics and the physical model assumptions and the measurements all introduce individual errors which cannot be distinguished in the comparative answer is not very useful thing to do.

W. Schmidt, Dornier

How do you know that Navier Stokes is good enough? But actually this is more or less the last part. I think what you do is you talk about real world and ideal world. Before World War I people built airplanes that flew very nicely without knowing Navier Stokes in detail. Now we have to build airplanes that are fairly advanced and we need lots of additional information that we have to get from tools that we can afford and we understand. This is forcing us to use to some extent inadequate methods. But we have to know to which extent inadequate methods would be good enough for certain jobs. This is also what has to be validated. It is very important to have both simpler methods and complex ones. The vehicle toolbox needs validation in order to know to which extent they can be used and where.

L. Roberts, Stanford University

I think that is part of the point that I was trying to make. In order to validate your approximation you need to isolate what that question is and answer that question and not necessarily compare with some other data which doesn't answer the original question. I am in agreement that we need approximate methods. I would like to be sure that people are asking the right questions to justify the approximation and not introducing extraneous information in the comparison.

S. Bogdonoff, Princeton University

I want to congratulate Mr. Sacher for a very interesting and very concise review of this meeting. As an experimentalist, I have the feeling that there aren't many of us in this group. I would like to make a couple of comments. First, several speakers have talked about Euler solutions. I would like to point out that the Euler equation doesn't have viscosity, but all numerical solutions do. There is a numerical "viscosity" that comes in to all of the Euler computations. This was pointed out to me, in some detail, by my computational friends. There is one place where I disagree with Len Roberts. I think that the most valuable thing that one can do in computation (outside of all of the things you have talked about, meshes, etc.), is to compare computational methods. I disagree with Len with regard to the fact that you should only compare experiment with Navier Stokes. I would suggest that you need Euler, PNS, any other approximation you can get, and Navier Stokes, to compare with the actual experiment. If you have the right experiment and the right computations, you learn a tremendous amount about the physics. I think that the major contribution which I have gotten from computation, and I have been fortunate to work with a couple of major computational programs, is that what I thought was important in the experiment was not the physics that turned out to be critical. For many of the things we are talking about, I don't believe that we know the physics in adequate detail. Sometimes a comparison of the computations and the experiment gives you some lead. I believe, for example, that most 3-d flows are inviscid-rotational flows, even though many people still think that they are viscous flows. There is a thin viscous layer, but it doesn't seem to be the primary driver. One last comment specifically with regards to the experiments. I am appalled at the use of experiments that were made over the past 40 years to do computational "validation". Those experiments were carried out to do specific things for many reasons, but they were surely not designed for computational validation. I know of very few experiments which were carried out 30 years ago or 20 years ago, or even 10 years ago that have the quality, the basic resolution, and the parameter variations that are required for computational validation. I would suggest that developing a code and then looking for some experiments to validate it is unreasonable. The experiments that you need to validate a code, I believe, have to be designed specifically for that task. You should have computations to tell you what kind of details you need from the experiment, what range of parameters, what kind of instrumentation you need to really test if the code is worth anything or not. I suggest that we have a sociological problem of people developing codes, other people doing experiments, and other people designing vehicles. I really don't believe that we are going to get very far, in the long run, in developing the potential that is clearly here in computation if we don't do those things together in a

much, much more detailed way than we have in the past. I think that this was an excellent meeting from my point of view. I won't disagree at all with Mr. Sacher's view that it really didn't do what the title said, but the idea that we are at least talking together about the problem is important. It is absolutely critical that, when you have such meetings, you make some effort to get many experimentalists, perhaps seated alternately with the computation experts, because I think that you have to be that close to do the job that is really required.

E. Reshotko, Case Western Reserve

This is a comment to both Professors Gersten and Roberts. We are not here to validate the physics, we are here to validate a computational tool that tries to represent the physics. Therefore, the emphasis has to be on the computational tool. It would be nice if we understood all the physics. We don't understand all the physics yet, particularly when it comes to turbulent flow. That presents a bit of an obstacle, but the basic validation here is the validation of the computational capability.

While I have the microphone I would like to make a few remarks about the topic of transition that appeared in Peter Sacher's summary. None of what I saw here today in any way computes transition. In order to compute transition from first principles one would have to start with a 3-dimensional, unsteady, time-accurate Navier Stokes code suitable for laminar flow. I did not see any such code tested at this meeting. I am not sure even if one was presented at this meeting capable of the range of parameters where transition could be captured. Therefore, it means that for most of the codes that were tested at this Conference, transition had to be imposed. Turbulent stresses had to be switched on at some arbitrary condition. Probably the time has come to consider the use of codes where transition can in fact be computed. This requires codes that have the necessary spatial resolution. I am acquainted with people who are using spectral finite element codes that do have the resolution necessary to compute transition. Perhaps such algorithms should be considered by more people in order to get the kind of detail needed to calculate through the transition process and into the initial portions of the turbulent flow. One final remark has to do with what constitutes a proper experiment. There is a belief that a solution of the time-accurate 3-dimensional Navier Stokes equations even in a limited domain with a limited physical objective constitutes an experiment that can be used for code validation. Certainly this is at the root of the work of the Center for Turbulence Research at NASA-Ames. One should perhaps pay more attention to the experiments that are being generated numerically as an aid to turbulence modelling.

D. Papailiou, Patras

I would like to make some comments on the particular subject of turbulence modelling. I think that we have to be very happy that we can recognize in this meeting that there is a trend during the last two or three years of trying to validate turbulence models as compared to the past when people were arbitrary about using all their work, not concerned about turbulence modelling at all. I want to make two comments. There is an arbitrary choice in the models that are used in the numerical schemes. There is no correlation between the physical aspects represented by a model and the particular problem that the numerical scheme is going to solve. As a result of that there is no apparent explanation of the discrepancies which are occurring in the results of these schemes. There is another point which I want to make. It is apparent to me that different parameters will show different sensitivity in different models. That means if you get a pressure distribution apparently you might not have any difference if you get a variety of models in your results. If you go to velocity distribution you might check some differences. If you go to turbulence characteristics like Reynolds stresses or intensities then you might find that different models might give you different results. We have to be very, very careful when we try to check and validate a turbulent model what parameters we choose in order to validate this. Now there is one more comment I want to make. There are a couple of experiments which show that the old mixing-length concept is still valid and gives in many cases very good results as compared to more sophisticated models. I would like to say that in my view there is not a unique model that will solve or can be used in all the problems that we have to solve. We have to very careful when we try to pick up a model for a particular problem. This has to be carefully selected.

T. Tjonneland, Boeing

It is interesting first of all to see the interest of academia in CFD. I want to make some comments from the industrial user viewpoint. You can tell Bradley that I am fully committed to using CFD. CFD will be used in the aerospace industry. However, we must have better tools to design airplanes with.

My comments will reflect the work that was done here this week, some lessons we have learned using CFD, and pick-up on Prof. Bogdonoff's comments made earlier in the week that our CFD tools are not well validated. We are using the available codes for design, but maybe we should use our Navier-Stokes codes to define the important aspects of the flow and the physics that we should be worrying about in a code. A good example for this approach is the F5 wing experiment. Various codes were used for modelling the lift and drag on that airfoil. No company would ever commit a design with that much variation in predicted lift to drag of an airfoil. That is a pitiful performance and we must go back and find out what is wrong here. Clearly, one of the key ingredients of that problem is our understanding of the flow. We couldn't even agree if the flow was laminar or transitional ahead of the shock on the wing, i.e. if it was a laminar shock boundary interaction or a turbulent interaction. We cannot hope to predict the lift and drag accurately without a better understanding of the flow that at this point can only come from a better experiment. I think that that is a lesson we have to learn and one CFD can contribute to. Don't solve the whole problem until you understand the dominant physical processes. Another thing I would like to comment on is the problem with the Euler codes. These are a dangerous weapon, because they do have some numerical viscous damping that can yield results that look like physical answers. So let's try not to use Euler codes where the real physics involve viscous interactions. Let us look at the work presented for an external compression inlet aperture region. That flow is dominated by shock wave boundary layer interactions and using Euler codes for that is inappropriate. Again let's understand the key physical aspects and use tools that are most applicable at least. We still have enough trouble doing it with the right tools. In that case, only a Reynold's-averaged Navier Stokes code can solve that problem.

Another troublesome point was in the last paper from Langley, an excellant paper, but again, it raises the problem that Bogdonoff pointed out to us earlier. We "almost" had the code validated but still the predicted total pressure did not agree very well with the experiment. The other flow properties seem to be well predicted, the static pressure is good, boundary layer profile is good, but total pressure is way off. If the total pressure is far off, maybe we shouldn't assume that the tunnel Mach number was wrong or that the total pressure in the tunnel was wrong. Total pressure is one of the toughest things to get right in a simulation. It is a derived quantity, so you can't compute it after the fact and say this is a take-what-you-get type of operation. If you want a validated code you should look for the most critical part of the flow and for the toughest variable to get right and look at that. You will find out the mesh requirement we generally use is just putting the mesh closely spaced next to the wall to pick up the boundary layer. If you want to predict total pressure through the stream and a shock going through it you had better have plenty of fine mesh there too. Don't stretch the mesh through the stream where you have total pressure variation. Use some kind of an error norm or something to find out where critical flow gradients that determine a parameter like total pressure occur, for example, and place the mesh so you can pick up those gradients, because like Bogdonoff says, if you don't have total pressure right, probably everything else is wrong, too. It just looks close to right. So I think that we have a ways to go, but CFD can certainly help us look at the critical aspects and select the best tool for that problem, not just try anything. I think that we are far enough along to be able to know the physics that are critical and the tools to use for that.

I will summarize my comments with this. AGARD has a very viable mission. We need better focus to even meet the objectives for this particular meeting. Let us keep trying to improve the focus and get CFD so it can predict lift and drag on airfoils, for example. At this time that goal seems remote, but in the meantime we have to continue to use CFD and to make it better and better. I think AGARD has a fantastic mission to carry on in this particular field.

W. Oberkampf, Sandia, USA

I would like to make two points, one of these is emphasizing a point that has been made by Professor Bogdonoff and some of the other speakers before; that is, using Euler solutions on separated flow problems, most notably at this Conference on delta wings. It seems to me that there is a serious question whether we should continue that procedure. As Professor Bogdonoff pointed out, there is artificial viscosity in these solutions. Authors that have cared to look at grid convergence on these problems have shown that they are not converging and it seems to me to raise the question whether we should continue with that procedure. The second point has to do with the Navier Stokes solutions, whether it is on delta wings or whether it is on cones for separated flows. I would like to recall about 20 years ago when finite difference solutions for boundary layer problems were very common. We had grids in the boundary layer that were on order of 50 to 100 points in the boundary layer. We had spatial steps in the parabolic solution of the boundary layer equations that were on the order of 1/10 of the boundary layer thickness. We had excellent solutions. The grids that I see, particularly in 3-dimensional solutions, seem to be very coarse. Suppose you talk about laminar flow, forget about turbulence modelling right now, it seems to me that we are a long way from the kinds of grid resolution that we need to solve 2-dimensional, and particularly 3-dimensional solutions. With the increase in computer power that is continuing we would improve these solutions a lot with finer grid resolution.

J. Slooff, NLR Amsterdam

My main observation during this meeting was very much in line with what Peter Sacher said and also with the remarks by Professor Roberts and Professor Gersten. I also tried to come up with a conclusion on that observation. If we, in a more limited sense, define as the objective of CFD code validation, to establish error norms both in the numerical and physical sense and sensitivity of those error norms to mesh topology and mesh density for various classes of configurations, and if we project that against what we have seen and heard this week, then there was a huge gap, as Peter Sacher already indicated, between what the general concensus is apparently on the definition of validation and what actually seems to be done. What seems to be missing is something like a generalized scenario of how you do that kind of thing. I almost hesitate to come up with a scenario because it seems so obvious in many cases how to do it. Yet, very few people over the past four days have really used some kind of scenario, and if they did, they didn't tell us about it. I'll show you what I think ought to be part of such a scenario. It is by no means intended to be complete, and I'm sure cannot be used in many circumstances and is therefore idealistic. Yet, I would like to make the point, because nobody seems to be doing it.

What we ought to do with any numerical method is first of all check for free stream consistency. I don't think everybody is really doing that. Then if we want to validate codes for incompressible irrotational flow (panel methods), I am thinking about 3-dimensional codes in particular, the next thing to do would be to simulate limiting 2-dimensional solutions obtained from, for instance, conformal mapping theory. We could transform those into infinite swept wing solutions and do the same thing. In that case we would have to use skewed meshes, instead of the straight meshes we would have in a real 2-d case, and we could find out something of the sensitivity of our solution to mesh skewness. Then I think almost everybody, including myself, probably has forgotten that there exist an isolated number of 3-dimensional exact analytical potential flow solutions, for instance for ellipsoidal bodies. I don't think that anybody is making use of those. Those are idealized cases. Finally, we should try to obtain error norms for recognized high-accuracy solutions for generic configurations representing the classes of configurations that we are interested in. That requires certain organized efforts because producing high-accurate solutions requires a lot of computing time. There have been some efforts going in Europe and in the U.S. to produce such high-accuracy solutions which can be used as a benchmark then for other codes. You will notice, that the fact that there are not many people interested in developing panel methods anymore has not prevented me from putting this up. The reason is that I think it equally applies to full potential flow methods. They should be capable of doing these incompressible cases just as well as incompressible methods. In addition to that, of course, we have the 2-D exact hodograph solutions which could also be transformed into exact infinite swept wing solutions. Euler codes should in principle be capable to do the same thing, and one should check that also. Here's where I disagree with Leonard Roberts who would rather do it the other way around. I would like to check first whether an Euler code can produce 2-D

irrotational flows solutions correctly, and what number of mesh points I will need to have an acceptable error. With boundary layer codes the situation is somewhat different. There we should check with existing exact solutions like Blasius and so forth and some recognized experimental test cases like from the Stanford Olympics, the Trondheim trials and other games that have been around us in the past 10 years or so. With the zonal methods, one has to do all the things that I have listed above, so that the more complex a method becomes, the more work has to be done in order to validate. The same goes for Reynolds averaged Navier Stokes equations. You may have noticed that I have not introduced any comparison with experiment until I have viscosity in some way in my model. I think that this is the way that we should operate.

M. Carr, ARA, UK

I endorse the comments of Professor Sloof regarding the philosophy of method validation; whether one can adhere to all the processes in practice is another matter. I wish to raise two specific items. First, the work of the GARTEUR Action Group which I presented at this meeting involved three-dimensional flow solvers. A major problem in the analysis arose from the fact that most flow solvers are based on specific grids. This can be a cause of discrepancies between methods thus making analysis difficult. There I encourage method developers to produce flow solver codes which are grid independent. It would then be possible to investigate the effect of different grids and indeed topologies on flow solvers as well as making the task of comparing different flow solvers easier.

My second point is that much of the discussion on code validation in this session pertains to an ideal world. Many method developers are employed to produce improved codes that will be used by other people in research and project studies. Thus one has to persuade potential users that using the codes is worthwhile, not because it solves the Navier-Stokes equations superbly, because none of them do, but that one has demonstrated the capability of the method and established confidence for the specific problems of interest. This includes demonstrating that if the code is being used in aerodynamic design, the results of the code will not be misleading. Thus although the method will not produce precisely the correct result it will point the designer in the right direction. Therefore, overall, there is an onus on CFD method developers to demonstrate confidence in the methods and impart that confidence to users, since ultimately the success of a CFD code is based on its effective use.

G. Lilley, Southampton University

It is very easy to agree with everything that has taken place in this discussion. I feel very privileged to be invited here as an observer, and I have learned along with others, a great deal about the state of the art in CFD in these classes of flows that are required by the aircraft industry. One can realize, as we have now seen after these few days of lectures, what the state of the art is. The major problem that we face today is that we are dealing with flows built up of a number of building blocks. The crucial issues that have come up and have been mentioned in this discussion are that we need one building block related to transition, another relating to turbulence modelling and a further building block relating to separation. That really brings me to the point which again was mentioned by others. We are trying to validate the codes with generally all these three major physical problems present, and the codes clearly are inadequate for dealing with any one of them. Therefore, to attempt a validation on these very complex flows involving in general a uniform flow, a viscous inviscid interaction, an interaction between a complicated wake or separated flow is really too difficult. Therefore, in spite of the work that has been done by all the various code generators and indeed the various solvers, it was really asking an impossible question, of having an exact validation of these codes with experimental data. I was very much involved as many of you know, in what was mentioned by one or two speakers, the Stanford Olympics. I like to think of the 1980/81 Stanford meeting as being an attempt to validate the various turbulent flow codes against well-conceived experiments and experiments which were independently evaluated and where the experiments were looked at very carefully for accuracy, and then to make the comparison with the best of the codes that were available. If any of you remember, and I am sure all of you in this audience do, the agreement in many cases between those codes available in 1981 and the experimental data wasn't very good. Although as the years have gone on, some of the discrepancies have been sorted out, mainly in relation to the numerics, it still remains an open question as to how good many of these turbulent flow models are on very much simpler complex, turbulent flows than those considered in this conference. My belief is, and I am still involved in trying to get the complex turbulent flows meeting together as an extension from the Stanford meeting, that until we really get to grips with zonal calculations on very much simpler turbulent flows in which there is transition, in which there is an attached 3-dimensional layer, interaction with corners, etc. and involving separation, I think that it is going to be very, very difficult to be able on the basis of the kind of comparisons that were made in this meeting to see where we have got to improve our turbulence flow modelling. An important new development is the work at Stanford and Ames, especially with the new Turbulence Center at Stanford, in which various numerical experiments involving direct and large eddy simulation and other methods are generating from the computer a large amount of information which is related to the physics of some of these perhaps simpler turbulent flows and seeing how that information either confirms or in fact modifies some of our basic turbulent flow models and the physics of the flow associated with them. It is quite clear from that work at Stanford at the present time that as flows become more and more complex, so the large scale turbulent flow will get more and more complicated. It is therefore not clear at this stage if the results of the work at Stanford will confirm under what conditions a simple turbulent flow model, such as one involving an eddy viscosity, can be used to predict complex turbulent flows to engineering accuracy. It is a very big and open question. I believe that the way ahead is to continue with research on flows much simpler than the ones that we were attempting to use at this conference in relation to the validation of CFD codes.

H. Hornung, California Institute of Technology

I like expensive wines very much and I used to be able to get hold of expensive wines very easily by betting my numerical colleagues that they couldn't do a computation of a certain simple flow in a certain time. This is getting more difficult and I think that it is a nice thing that it is getting more difficult. I think that as numerical fluid mechanics is getting more mature, people's claims of what they can do are diminishing. This is a very fortunate thing, because some years ago, they could just about do

everything, on paper anyway. So I have actually observed that in isolated cases numerical fluid mechanics has stood the extreme test of being able to discover new effects. That has happened in some very few isolated cases. I think that though the optimism of the CFD people is reducing as they get wiser, their capability is fortunately increasing tremendously. Some of that I have heard in this meeting, too, in particular, the reduction of the extreme claims is a very healthy sign.

W. Schmidt, Dornier

I would like to make a small comment on what you said. I think that you should be aware of the fact that there are many people in CFD that are very much concerned about their results and their details, possibly more than experimentalists. The forcing item in doing more detailed experiments is coming from the CFD side because they can see in thousands of points all flow details which you never saw in the experiment. I doubt if such details will be available in experimental data even during the next five years.

My actual comment is somewhat different. I got somewhat concerned in this discussion today that everybody is discussing flow modelling on the basis of the equation of the models. I never heard anybody discussing the modelling of boundary conditions. Everybody is discussing the highest possible modelling of turbulence, but nobody says what is the effect of the non-smooth, non-ideal surface on turbulence modelling or on transition. How much attention do we actually pay on the quality of our surface? Which experimentalist can tell me how smooth his surface really is?

S. Bodgonoff, Princeton

I want to end on a very positive note. Much of what I have heard the computational people talk about is much simpler perhaps than you have assumed. On the basis of rather limited experience we have found that 3-dimensional flows are infinitely easier to work on than 2-dimensional flows. I believe that the concentration on 2-dimensional flows is a real barrier to the advancement of CFD. I would like to point out that nothing in nature is 2-dimensional. Nowhere in a 3-dimensional flow will you ever get the gradients that you get in the 2-dimensional flow. If you look at the mathematics the singularities in two dimensions are much stronger than the singularities in three dimensions. I would also like to point out that there is the beginning of some information that indicates that the worry about turbulence may be much more critical in 2-d than in 3-d. Much of what our 3-dimensional work indicates that the main value of the Navier Stokes solutions has been to show that most of the flow is inviscid-rotational. This is not true in 2-d. I really believe that computation can do much more than most of you think that it can do. I sure hope that I am right.

R. Graves, NASA

Before I turn over the meeting to our Chairman for the closing remarks, I would just like to thank all of you for participating. In particular, I want to thank Peter Sacher again for his excellent overview of this meeting. Now I would like to turn over the meeting to Derek Peckham, Chairman of the FDP.

D. Peckham, Chairman FDP

It is time to bring this Symposium to a close and before we break for lunch and then return for the technical status review on drag prediction and analysis from CFD this afternoon, to which everybody is invited to attend, I would like to make a few closing remarks. I hope you have found the Symposium informative, stimulating and that you will return to your computer terminals with a clearer idea on what is required of code validation. On behalf of the Fluid Dynamics Panel I would like to thank all the speakers for their presentations, the audience for your active participation and also all the presenters at the poster session.

Also on your behalf I would like to thank the Program Committee for organizing this meeting, in particular, the Co-Chairmen of the Program Committee, Dick Bradley and Wolfgang Schmidt and the session chairmen for all their efforts. Also to Randy Graves for leading the final discussion period. Next I wish to thank General Borges for opening our Symposium on Monday, Dr. Bell for providing these excellent facilities for our meeting and also Professor Falcao, the Portugese Panel member for all his work in making the meeting arrangements so successful. Now the smooth running of the meeting depends very much on the efforts of our Panel Executive, Mike Fischer and his secretary Anne-Marie Rivault; I would like to thank them on your behalf. I would like to thank also Margarida Cristovao, Martha Pereira, Maria Ana De Carvalho Rosa and Gilberto Prado for their assistance. Also from the Abro agency who arranged our hotel accommodation and some of the trips for our ladies, Louisa Alfonso and Isabel Marcido. Also, upstairs we have the projectionists to thank. These meetings would not be possible without our interpretors who have worked so hard during this week. I would like to thank on your behalf Mrs. Celie, Mrs. de Susbielle and Mr. de Liffiac. I will conclude with some advertising for our future programs. In October in Cesme, Turkey we have a Symposium on Fluid Dynamics of Three-Dimensional Turbulent Shear Flows and Transition. Next year in the spring, 22 - 25 May, in Norway we have two specialist meetings; one on Computational Methods for Aerodynamic Design (Inverse) and Optimization and the second one on Applications of Mesh Generation to Complex 3-D Configurations. Next in the fall in October in Spain we have a Symposium on Aerodynamics of Combat Aircraft Controls and of Ground Effects. I hope that many of you will be able to attend some of these meetings. Finally, we have present at our meeting this week Dr. Marsters, Director of the National Aeronautical Establishment in Canada who is the AGARD National Delegate for Canada who would like to make a few comments to end our meeting.

Dr. Marsters, NAE Canada

Thank you very much Derek. I am very mindful of the fact that whatever I say is eating into your lunch hour, so I will try to be very brief. As a National Delegate it is a great pleasure to be able to be here and to participate in the meeting. I understand that it is not a very common event to have National Delegates attend meetings. It turns out that we National Delegates are a bit far from the mainstream. Some people even think that when one outlives one's usefulness as a researcher, one becomes elegible to become an AGARD National Delegate. Even as a manager of research these days, however, I find that the

continuity or the conservation laws that you use in your daily work are useful to me as well. Continuity in the form of resources to be able to see the research go forward. We have to maintain the existing momentum so that there is a conservation of momentum problem facing us, and we also have a conservation of energy for if continuity of resources holds, there is no new energy available to deal with the on-going research. There is also the task of the manager it turns out to deal with conversion of energy, where every once in a while it seems you must sit down with some of your favorite researchers, look them in the eye and assist them in converting their potential energy into some form of directed kinetic energy. There is even a more challenging task. That is to reduce randomness, to increase order and therefore, to violate the second law of thermodynamics. These are the trials that come to one after one has outlived ones usefulness as a researcher. This is the second panel meeting of AGARD that I have attended this week. The first two days I was at a Structures and Materials Panel Meeting and it is interesting to see the contrast in the way these things operate. I would like to congratulate the organizers, the Panel Chairmen and all the Panel members for the excellent meeting. I have enjoyed my observations and conversations here. The local Committee and the AGARD headquarters people have all done an excellent job. I would like to particularly comment on what I think was a highly successful poster session. I think that you found the key to making poster sessions truly useful. I think that key lies in the fact that people's attention was not diverted from the poster sessions by having simultaneous presentations in this meeting hall. It seems to me to be one of the best poster sessions that I have seen operate. I don't know whether you have really achieved the objectives as far as validation is concerned. I think that Mr. Sacher has already pointed this out in very clear terms so that we go away from here not sure that we have done much more validation than we had before the meeting. I am concerned also sometimes with the use of the term "prediction" for the methods that we use because in my dictionary prediction means foretelling those things which have not yet happened. Sometimes we still seem to have difficulty in confirming things that have already happened by using CFD. Despite the great strides that I see made in computational fluid dynamics I am not yet very worried about the near term closure of our wind tunnels at the National Aeronautical Establishment. I would like to compliment Mr. Sacher for his review of the meeting. It was very much to the point and was in some cases bluntly critical and probably justifiably so. I would like before I close to call your attention to the mission of AGARD which you will find on about the second page of your large thick bound volume. I would like you to reflect on this, reflect on the goals of the meeting as you finish up here and go back to your work. I would like you to bear these in mind. Many of you will be attending meetings again and the mission of AGARD includes the exchange of scientific and technical information. The last word, information, is particularly well chosen. In view of some of the remarks that have been made in the last few days I am glad that it is information and not fact. On behalf of AGARD, thank you for attending and participating in this Symposium.

DATA BASE FOR CODE VALIDATION

- 1979 AGARD-AR-138/FDP WG 04
  EXPERIMENTAL DATA BASE FOR COMPUTER PROGRAM ASSESSMENT
- 1981 GAMM WORKSHOP 2D TESTCASES
  FOR POTENTIAL/EULER FLOW CODES
- 1982 AGARD-AR-702 /(ADDENDUM NO. I 1984)
  COMPENDIUM OF UNSTEADY AERODYNAMIC MEASUREMENTS
- 1984 NASA NTF DELTA WING MODEL
  DATA BASE FOR THEORY DEVELOPMENT
  AIAA 84-2150
- 1985 AGARD-AR-211/FDP WG 07
  TESTCASES FOR INVISCID FLOW FIELD METHODS
- 1986 AGARD-RAR-226/FDP WG 08
  AERODYNAMICS OF AIRCRAFT AFTERBODY
- 1986 INTERNATIONAL VORTEX FLOW EXPERIMENT
  ON EULER CODE VALIDATION
  FFA STOCKHOLM (SEE PAPER NO. 10)

Fig. 1 AGARD Activities related to Data-Bases

CALL FOR PAPERS

(Bradley/Schmidt)

GOAL OF CFD

Design and analysis capability, user friendly, cost effective, numerical accurate and fully verified by detailed experimental comparisons.

OBJECTIVES OF THE SYMPOSIUM

- Identify the level of agreement of physical models and numerical solution algorithms with experimental data
- Identify regions of validity for given flow solvers
- Identify flow regimes where significant gaps exist and further work is warranted.
- Perform qualitative and quantitative error analysis and identify error bands for both the experimental data and CFD solutions.

Fig. 2 Objectives of the Symposium

CALL FOR PAPERS

(Bradley/Schmidt)

CODE VALIDATION

- Insure that the mathematical and numerical schemes employed in the code accurately model the critical physics of the flow field.

SOLUTION EVALUATION

- Demonstration of the effects of
  - geometric modeling
  - mesh resolutions
  - math. algorithms
  - turbulance models
  - reacting gas models
  - convergence criteria

  on the accuracy of numerical solutions representing various mathematical and physical models.

Fig. 3 Definition of "Code-Validation"

- RESEARCH CODES
  Test Results for Development and Validation
  (single-user-application)
- PILOT CODES
  Ready for Inhouse Use
  (multi-user-applications)
- PRODUCTION CODES
  Ready for Transfer to other places
  (multi-company-application)

Fig. 4 Status of CFD Codes

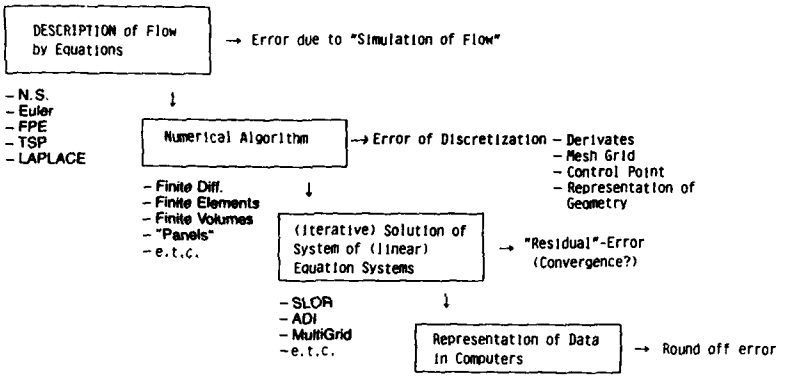


Fig. 5 Sources of Errors in numerical Flow Codes

REPORT DOCUMENTATION PAGE

1. Recipient's Reference	2. Originator's Reference	3. Further Reference	4. Security Classification of Document
	AGARD-CP-437 Volume 1	See Page ii	UNCLASSIFIED

5. Originator Advisory Group for Aerospace Research and Development
North Atlantic Treaty Organization
7 rue Ancelle, 92200 Neuilly sur Seine, France

6. Title VALIDATION OF COMPUTATIONAL FLUID DYNAMICS
Volume 1: SYMPOSIUM PAPERS AND ROUND TABLE DISCUSSION

7. Presented at the Symposium of the Fluid Dynamics Panel in Lisbon, Portugal, 2—5 May 1988.

8. Author(s)/Editor(s)	9. Date
Various	December 1988
10. Author's/Editor's Address	**11. Pages**
Various	604

12. Distribution Statement This document is distributed in accordance with AGARD policies and regulations, which are outlined on the Outside Back Covers of all AGARD publications.

13. Keywords/Descriptors

Fluid dynamics	Experimental data
Algorithms	Validity
Computation	Comparison

14. Abstract

AGARD's Fluid Dynamics Panel has sponsored a Symposium with the specific intent of examining activities, both computational and experimental, directed toward validating or calibrating CFD codes over a broad spectrum of fluid-dynamics study areas. The objectives of the Symposium were to identify the level of agreement of numerical solution algorithms and physical models with experimental and/or analytical data, to identify regions of validity for given flow solvers, and to identify flow regions where significant gaps exist and further work is waranted.

AGARD Conference Proceedings No.437 Volume 1 Advisory Group for Aerospace Research and Development, NATO VALIDATION OF COMPUTATIONAL FLUID DYNAMICS – Volume 1: SYMPOSIUM PAPERS AND ROUND TABLE DISCUSSION Published December 1988 604 pages AGARD's Fluid Dynamics Panel has sponsored a Symposium with the specific intent of examining activities, both computational and experimental, directed toward validating or calibrating CFD codes over a broad spectrum of fluid-dynamics study areas. The objectives of the Symposium were to identify the level of agreement of numerical solution algorithms and physical models with P.T.O.	AGARD-CP-437 Vol.1 Fluid dynamics Algorithms Computation Experimental data Validity Comparison	AGARD Conference Proceedings No.437 Volume 1 Advisory Group for Aerospace Research and Development, NATO VALIDATION OF COMPUTATIONAL FLUID DYNAMICS – Volume 1: SYMPOSIUM PAPERS AND ROUND TABLE DISCUSSION Published December 1988 604 pages AGARD's Fluid Dynamics Panel has sponsored a Symposium with the specific intent of examining activities, both computational and experimental, directed toward validating or calibrating CFD codes over a broad spectrum of fluid-dynamics study areas. The objectives of the Symposium were to identify the level of agreement of numerical solution algorithms and physical models with P.T.O.	AGARD-CP-437 Vol.1 Fluid dynamics Algorithms Computation Experimental data Validity Comparison
AGARD Conference Proceedings No.437 Volume 1 Advisory Group for Aerospace Research and Development, NATO VALIDATION OF COMPUTATIONAL FLUID DYNAMICS – Volume 1: SYMPOSIUM PAPERS AND ROUND TABLE DISCUSSION Published December 1988 604 pages AGARD's Fluid Dynamics Panel has sponsored a Symposium with the specific intent of examining activities, both computational and experimental, directed toward validating or calibrating CFD codes over a broad spectrum of fluid-dynamics study areas. The objectives of the Symposium were to identify the level of agreement of numerical solution algorithms and physical models with P.T.O.	AGARD-CP-437 Vol.1 Fluid dynamics Algorithms Computation Experimental data Validity Comparison	AGARD Conference Proceedings No.437 Volume 1 Advisory Group for Aerospace Research and Development, NATO VALIDATION OF COMPUTATIONAL FLUID DYNAMICS – Volume 1: SYMPOSIUM PAPERS AND ROUND TABLE DISCUSSION Published December 1988 604 pages AGARD's Fluid Dynamics Panel has sponsored a Symposium with the specific intent of examining activities, both computational and experimental, directed toward validating or calibrating CFD codes over a broad spectrum of fluid-dynamics study areas. The objectives of the Symposium were to identify the level of agreement of numerical solution algorithms and physical models with P.T.O.	AGARD-CP-437 Vol.1 Fluid dynamics Algorithms Computation Experimental data Validity Comparison

experimental and/or analytical data, to identify regions of validity for given flow solvers, and to identify flow regions where significant gaps exist and further work is warranted. Papers presented and discussions held at the Symposium of the Fluid Dynamics Panel in Lisbon, Portugal, 2—5 May 1988.	experimental and/or analytical data, to identify regions of validity for given flow solvers, and to identify flow regions where significant gaps exist and further work is warranted. Papers presented and discussions held at the Symposium of the Fluid Dynamics Panel in Lisbon, Portugal, 2—5 May 1988.
ISBN 92-835-0489-5 Vol.1 ISBN 92-835-0490-9 Vol.2 ISBN 92-835-0491-7 set of 2 vols.	ISBN 92-835-0489-5 Vol.1 ISBN 92-835-0490-9 Vol.2 ISBN 92-835-0491-7 set of 2 vols.
experimental and/or analytical data, to identify regions of validity for given flow solvers, and to identify flow regions where significant gaps exist and further work is warranted. Papers presented and discussions held at the Symposium of the Fluid Dynamics Panel in Lisbon, Portugal, 2—5 May 1988.	experimental and/or analytical data, to identify regions of validity for given flow solvers, and to identify flow regions where significant gaps exist and further work is warranted. Papers presented and discussions held at the Symposium of the Fluid Dynamics Panel in Lisbon, Portugal, 2—5 May 1988.
ISBN 92-835-0489-5 Vol.1 ISBN 92-835-0490-9 Vol.2 ISBN 92-835-0491-7 set of 2 vols.	ISBN 92-835-0489-5 Vol.1 ISBN 92-835-0490-9 Vol.2 ISBN 92-835-0491-7 set of 2 vols.